CRYOCOOLERS 13

Edited by
R. G. Ross, Jr.

a publication of the
International Cryocooler Conference

CRYOCOOLERS 13

A publication of the International Cryocooler Conference

CRYOCOOLERS 13

Edited by

Ronald G. Ross, Jr.
Jet Propulsion Laboratory
California Institute of Technology
Pasadena, California

Springer

Proceedings of the 13th International Cryocooler Conference,
held March 29–April 1, 2004 in New Orleans, Louisiana

ISSN: 1570-2235
ISBN: 0-387-23901-4

Printed on acid-free paper.

Printed in the United States of America.

9 8 7 6 5 4 3 2 1 SPIN 11335245

springeronline.com

Preface

The last two years have witnessed a continuation in the breakthrough shift toward pulse tube cryocoolers for long-life, high-reliability cryocooler applications. New this year are papers describing the development of very large pulse tube cryocoolers to provide up to 1500 watts of cooling for industrial applications such as cooling the superconducting magnets of Mag-lev trains, cooling superconducting cables for the power industry, and liquefying natural gas. Pulse tube coolers can be driven by several competing compressor technologies. One class of pulse tube coolers is referred to as "Stirling type" because they are based on the linear Oxford Stirling-cooler type compressor; these generally provide cooling in the 30 to 100 K temperature range and operate at frequencies from 30 to 60 Hz. A second type of pulse tube cooler is the so-called "Gifford-McMahon type." Pulse tube coolers of this type use a G-M type compressor and lower frequency operation (~1 Hz) to achieve temperatures in the 2 to 10 K temperature range. The third type of pulse tube cooler is driven by a thermoacoustic oscillator, a heat engine that functions well in remote environments where electricity is not readily available. All three types are described, and in total, nearly half of this proceedings covers new developments in the pulse tube arena.

Complementing the work on low-temperature pulse tube and Gifford-McMahon cryocoolers is substantial continued progress on rare earth regenerator materials. These technologies continue to make great progress in opening up the 2 - 10 K market. Also in the commercial sector, continued interest is being shown in the development of long-life, low-cost cryocoolers for the emerging high temperature superconductor electronics market, particularly the cellular telephone base-station market. At higher temperature levels, closed-cycle J-T or throttle-cycle refrigerators take advantage of mixed refrigerant gases to achieve low-cost cryocooler systems in the 65 to 80 K temperature range. Tactical Stirling cryocoolers, the mainstay of the defense industry, continue to find application in cost-constrained commercial applications and space missions; the significant development here is the cost-effective incorporation of Oxford-like flexure spring piston supports so as to achieve an extended-life, low-cost product.

The objective of *Cryocoolers 13* is to archive these latest developments and performance measurements by drawing upon the work of the leading international experts in the field of cryocoolers. In particular, this book is based on their contributions at the 13th International Cryocooler Conference that was held in New Orleans, Louisiana, on March 29 - April 1, 2004. The program of this conference consisted of 123 papers; of these, 88 are published here. Although this is the thirteenth meeting of the conference, which has met every two years since 1980, the authors' works have only been made available to the public in hardcover book form since 1994. This book is thus the sixth volume in this new series of hardcover texts on cryocoolers.

Because this book is designed to be an archival reference for users of cryocoolers as much as for developers of cryocoolers, extra effort has been made to provide a thorough Subject Index that covers the referenced cryocoolers by type and manufacturer's name, as well as by the scientific or engineering subject matter. Extensive referencing of test and measurement data, and application and integration experience, is included under specific index entries. Contributing organizations are also listed in the Subject Index to assist in finding the work of a known institution, laboratory, or manufacturer. To aide those attempting to locate a particular contributor's work, a separate Author Index is provided, listing all authors and coauthors.

Prior to 1994, proceedings of the International Cryocooler Conference were published as informal reports by the particular government organization sponsoring the conference — typically a different organization for each conference. A listing of previous conference proceedings is presented in the Proceedings Index, at the rear of this book. Most of the previous proceedings were printed in limited quantity and are out of print at this time.

The content of *Cryocoolers 13* is organized into 15 chapters, starting with papers describing the development of a new class of space cryocoolers to provide cooling in the 4-18 K temperature range. The next several chapters address cryocooler technologies organized by type of cooler, starting with regenerative coolers; these include Stirling cryocoolers, pulse tube cryocoolers, Gifford-McMahon cryocoolers, thermoacoustic refrigerators, and associated regenerator research.

Next, recuperative cryocoolers including Joule-Thomson, and sorption cryocoolers are covered. The technology-specific chapters end with a chapter on unique sub-Kelvin, magnetic, and optical refrigerators. The last three chapters of the book deal with cryocooler integration technologies and experience to date in a number of representative space and commercial applications. The articles in these last three chapters contain a wealth of information for the potential user of cryocoolers, as well as for the developer.

It is hoped that this book will serve as a valuable source of reference to all those faced with the challenges of taking advantage of the enabling physics of cryogenics temperatures. The expanding availability of low-cost, reliable cryocoolers is making major advances in a number of fields.

Ronald G. Ross, Jr.

Jet Propulsion Laboratory
California Institute of Technology

Acknowledgments

The International Cryocooler Conference Board wishes to express its deepest appreciation to the Conference Organizing Committee, whose members dedicated many hours to organizing and managing the conduct of the Conference, and wishes to express its appreciation to Lockheed Martin for its financial contribution. Members of the Organizing Committee of the 13th ICC included:

CONFERENCE CO-CHAIRS
John Hendricks, *ACE*
Louis Salerno, *NASA/ARC*

CONFERENCE ADMINISTRATOR
Devon Binder, *Centennial Conferences*

PUBLICATIONS
Ron Ross, *Jet Propulsion Laboratory*

TREASURER
Ray Radebaugh, *NIST*

PROGRAM CHAIRMAN
Eric Marquardt, *Ball Aerospace*

PROGRAM COMMITTEE
Stuart Banks, *NASA / GSFC*
Barrett Flake, *AFRL*
Robert Mohling, *Tech. Appl., Inc*
Rod Oonk, *Ball Aerospace*
John Pfotenhauer, *Univ. of Wisconsin*
Ken Price, *Raytheon*
Jeff Raab, *NGST*
Klaus Timmerhaus, *Univ. of Colorado*

In addition to the Committee and Board, key staff personnel made invaluable contributions to the preparations and conduct of the conference. Special recognition is due Laurie Huget, Executive Director of the Cryogenic Society of America, who managed the registration activities.

Contents

Space Pulse Tube Cryocooler Developments 85

Commercial and Industrial Pulse Tube Cryocoolers 133

Ball Aerospace 4-10 K Space Cryocoolers

D.S. Glaister[1], W. Gully[1], R.G. Ross, Jr[2], R. Stack[1], E. Marquardt[1]

[1]Ball Aerospace and Technologies Corporation
Boulder, CO 80306
[2]Jet Propulsion Laboratory
California Institute of Technology
Pasadena, CA 91109

ABSTRACT

This paper describes the design, development, testing and performance at Ball Aerospace of long life, 4-10 K temperature space cryocoolers. For temperatures down to 10 K, Ball has developed long life Stirling cycle cryocoolers. For temperatures to 4 K and below, Ball has developed a hybrid Stirling/J-T (Joule-Thomson) cooler. The hybrid cooler has been verified in test to 3.5 K on a Ball program and a 6 K Development Model is in development on the NASA/JPL ACTDP (Advanced Cryocooler Technology Development Program). The Ball ACTDP cooler Development Model will be tested in 2005. The ACTDP cooler provides simultaneous cooling at 6 K (typically, for either doped Si detectors or as a precooler for sub-Kelvin refrigerators) and 18 K (typically, for optics or shielding), with cooling stages also available at 40 and 180 K (typically, for thermal shields or other components). The ACTDP cooler is under development for the NASA James Webb Space Telescope (JWST), Terrestrial Planet Finder (TPF), and Constellation X-Ray (Con-X) missions. The 4-10 K coolers are highly leveraged off previous Ball space coolers including multiple life test and flight units.

INTRODUCTION

Ball Aerospace has specialized in space cryogenics, and specifically low temperature applications (<60 K) for over 40 years. This includes over 150 space flights of cryogenic hardware to date, 18 years of mechanical refrigerator or cryocooler development, and over 11 years of development of multistage Stirling coolers.

Consistent with the application trend to replace cryostat or dewar cooling systems with cryocoolers, Ball has concentrated their technology developments in the cryocooler area over the last decade. This has resulted in multiple cryocooler product lines. Each product is optimum for different application envelopes, and each is based on proven long-life designs. Our Stirling cryocoolers are very compact and power efficient. Our Joule-Thomson coolers have inherent load leveling capability and are optimum for providing stable temperatures over distributed cooling interfaces. Our hybrid cryocoolers combine the advantages of both Stirlings and J-Ts and are optimum for low temperature (<10 K) applications.

Cryocoolers 13, edited by R. G. Ross, Jr.
Springer Science+Business Media, Inc., New York, 2004

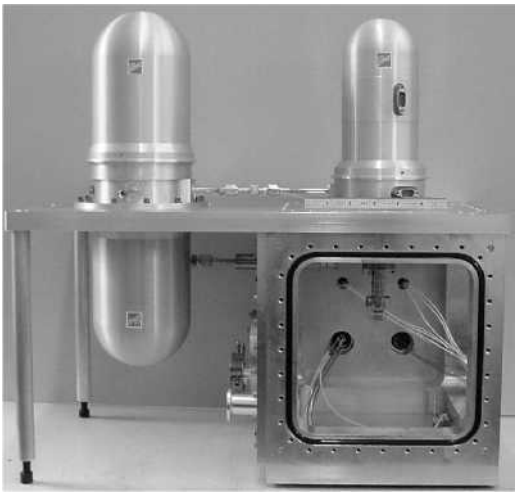

Figure 1. 2-Stage SB235 is designed for simultaneous cooling of detectors at 35 K and optics at 110 K

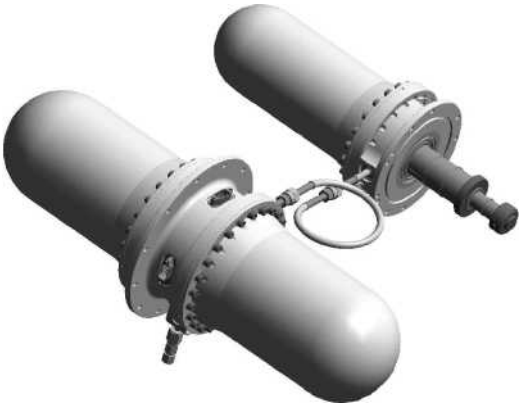

Figure 2. 2-Stage SB235E is a higher capacity model derivative of the SB235 and is designed for simultaneous cooling of detectors at 35 K and optics at 110 K.

STIRLING CRYOCOOLERS

Coolers for Moderate to Higher Cryogenic Temperatures

Ball Aerospace has been building long life, multi-stage Stirling coolers since 1989. These include flight qualified 1, 2, and 3-stage coolers.

At temperatures above about 60 K, our 1-stage SB160 cooler is preferred. Two SB160 units (flight and engineering model/flight spare) were delivered (in 1999 and 2000) for the HIRDLS (High Resolution Dynamic Limb Sounder) instrument on the NASA (National Aeronautics and Space Administration) Aura EOS (Earth Observation System) platform scheduled for launch in June 2004.[1] To date, several thousand hours have been accumulated on the HIRDLS engineering model and over 27,000 hours on the SA160 development unit predecessor.

Below 60 K and/or for simultaneous cooling of two different temperatures, our next generation 2-Stage coolers are more optimum and include the SB235 model and the SB235E derivative, shown in Figures 1 and 2, respectively. These are build-to-print, qualified coolers that

Figure 3. 3-Stage SB315 is a high capacity cooler optimized for cooling below 15 K.

are designed for simultaneous cooling of detectors at 35 K and optics at about 110 K and were the baseline for the TRW/Raytheon Space Based Infra-Red System–Low (SBIRS-low) Program Definition and Requirements Review (PDRR) program. The SB235 has a nominal performance of 1.0 W at 40 K and 2.0 W at 110 K for 85 W of motor power.[2] The SB235 has passed qualification level environmental test verification and is in life test at the Air Force Research Laboratory (AFRL) with about 2500 hours of accumulated run time. The SB235E has a nominal performance of 1.0 W at 41 K and 7.0 W at 110 K for 100 W of motor power. The SB235E is currently in assembly at Ball.

Our previous generation 2-stage cooler, the 30 K or SB230, was environmentally qualified and delivered to NASA GSFC (Goddard Space Flight Center) for life test.[3,4] It currently has accumulated over 20,000 hours with over 11,000 hours on the displacer after a design change.

Low Temperature Stirling Coolers

Ball's 3-stage Stirling coolers are optimum for cooling of multiple stages and/or below 30 K. For the Air Force Research Laboratory (AFRL), Ball developed a 3-stage cooler, the 35/60 K or SB335, which was highly leveraged off the GSFC SB230 design. This cooler has a nominal performance of 0.4 W at 35 K simultaneously with 0.6 W at 60 K for about 60 W of motor power. An SB335 unit completed environmental testing and is on life test at AFRL with close to 25,000 hours accumulated to date.[5]

A development unit of the SB335 was also employed on the Ball NASA 6 K Explorer Cooler program to develop technology advances for cooling to below 15 K. The 6 K Explorer Program demonstrated cooling with a relatively small cooler to temperatures below 12 K.[6] These enhancements were incorporated into the current SB315 or Advanced Cryocooler Technology Development Program (ACTDP) precooler shown in Figure 3. The SB315 combines the high capacity of our SB235 coolers with the 3-stage cold tip design from the SB335 to produce a high capacity <15 K low temperature cooler. A Development Model of the SB315 cooler is being built on NASA/JPL's ACTDP program.[7,8] On the ACTDP program, the SB315 will serve as a precooler for a Joule-Thomson (J-T) cooler that provides simultaneous cooling at 4-6 K and 18 K. The nominal performance of the ACTDP SB315 is 0.3 W at 15 K simultaneously with 1.0 W at 40 K and 2.0 W at 180 K for 180 W of motor power.

A Breadboard (BB) of the SB315 is also being built on an internal Ball program. This BB should verify the thermodynamic performance of the ACTDP precooler. In addition, the BB will be modified and tested for 10 K cooling. Predictions indicate that the SB315 should be capable

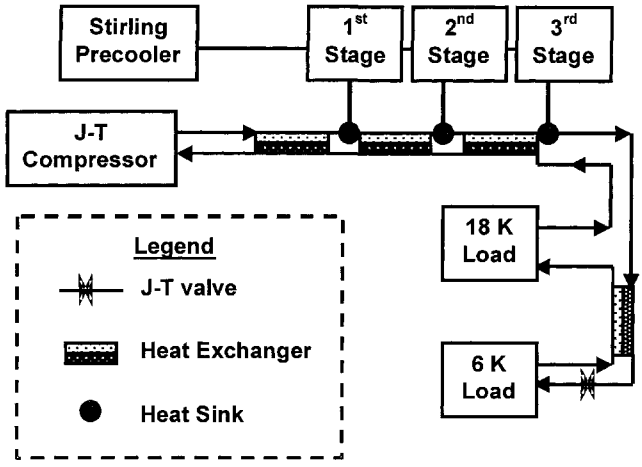

Figure 4. Ball hybrid cooler designs our Stirling and J-T cycles to produce very low temperature cooling.

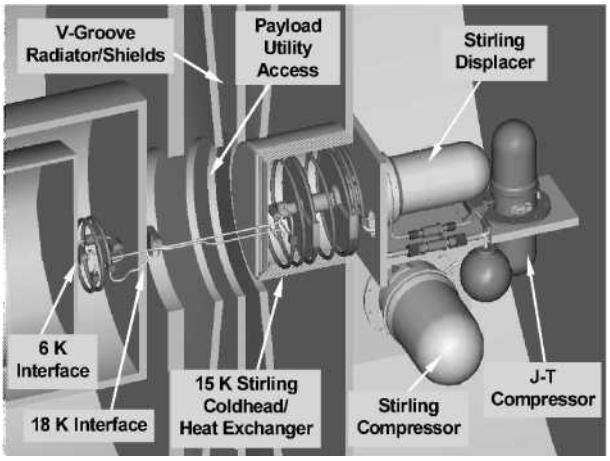

Figure 5. Ball 4-6 K Cooler integrated into TPF type application.

of 100 mW or more of cooling at 10 K. Initial verification with the BB of both the ACTDP precooler and 10 K performances should be completed by August 2004.

HYBRID CRYOCOOLERS

Introduction

For very low temperature (<10 K) cooling, Ball has combined our Stirling and J-T products to create a line of hybrid coolers.[9,10,11] As shown in Figs. 4 and 5, Ball's latest ACTDP hybrid is a cooling system that combines the best features of each thermodynamic cycle to produce low temperature cooling. The system uses the mass and power efficient Stirling as a precooler to perform the bulk of the cooling to temperatures around 15 K. Then, it uses the low temperature efficiency of the recuperative (vs. regenerative for the Stirling) J-T cooler to perform the last stages of cooling to 6 K and below. An additional benefit is the ability of the J-T to provide remote cooling (for both the 4-6 K and 18 K stages) through long, very thin, flexible lines. Thus,

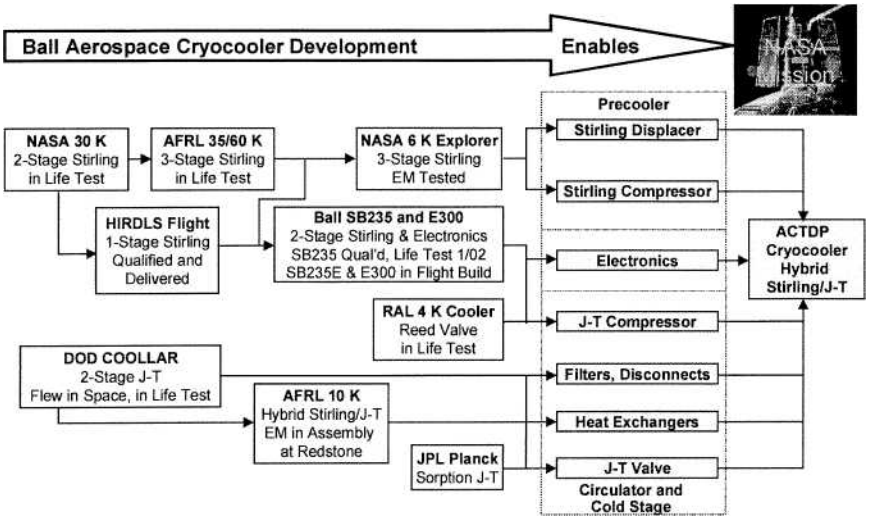

Figure 6. ACTDP 4-6 K Cooler is highly leveraged off previous developments.

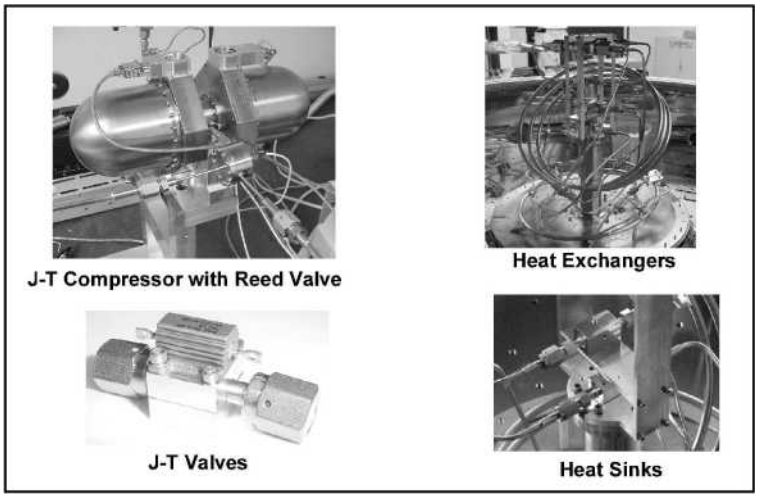

Figure 7. 4-6 K Breadboard Cooler hardware.

the J-T allows the cooling system to remotely locate the compressors over 20 meters from the cryogenic instrument.

4-6 K or ACTDP Cooler

The hybrid J-T/Stirling design is the baseline for the NASA/Ball ACTDP cooler. The nominal performance of the Ball ACTDP cooler is 30 mW at 6 K (or 20 mW at 4 K) simultaneously with 150 mW at 18 K for 125 W of motor power. Figure 5 shows a potential integration of the Ball ACTDP cooler into the NASA Terrestrial Planet Finder (TPF) mission. As shown in Figure 6, a key aspect of the ACTDP cooler is that it is highly leveraged off previous developments at Ball. In fact, every component in the system has been proven in test at some level. During the ACTDP Study Phase, this culminated in the successful integration and test of a breadboard cooling system (refer to Fig. 7 for hardware photos and Fig. 8 for test data plot). This breadboard has demonstrated cooling at 6 K (35 mW), 5 K (21 mW), and 4 K (12 mW).

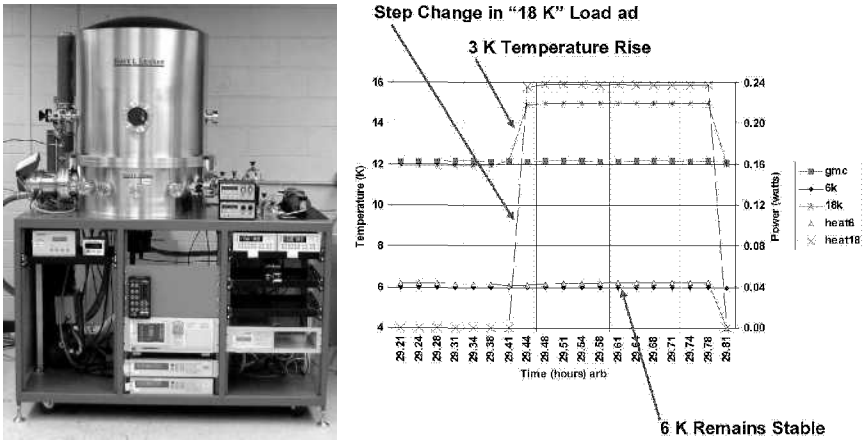

Figure 8. 6 K Breadboard Cooler testing showing simultaneous 6 and 18 K cooling with temperature stability even through a step change in the 18 K load.

Integration Features

Unique features in our hybrid coolers facilitate their mission integration. As previously mentioned, they have capabilities for very remote heat transport (and with no moving cold head parts). Our hybrids have also been designed to not require cryogenic radiator precooling assistance. This allows them to be equally applicable to Earth and non-Earth orbit missions and to minimize stray light and thermal back load on the cryogenic instruments. As a result of integration studies performed on the JWST[12], Constellation-X, and other systems, we have developed relatively mature thermal/mechanical integration designs, including structural supports and thermal insulation that have been accounted for in the thermodynamic performance. Understanding that the integration of a 4-6 K cooler will usually cross several system interfaces, we have built-in quick disconnects with proven heritage on our Cryogenic On-Orbit Long Life Active Refrigerator (COOLLAR)[13] and NICMOS flight programs. Our hybrid coolers use only a single phase, gaseous working fluid and have no zero-g concerns or 1-g testing limitations. We also have independent control of 6 and 18 K heat loads and the capability, in real-time on-orbit, to adjust to factor of two changes in the ratio of the 6 and 18K loads.

CONTROL ELECTRONICS

Ball understands that a cryocooler is the combination of a mechanical refrigerator system and the control electronics to drive it. We have paid special attention to the development of high reliability electronics for over a decade. This covers three generations of electronics. The E100 is in life test with the SB230 and SB335 coolers. The E200 (shown in Figure 9) was delivered with the SB160 on the HIRDLS program. The E300 is our electronics for SB235, SB315, and hybrid coolers. The E300 features include closed loop temperature and vibration control, high reliability (95% at 10 years), radiation tolerance to 100 krad and beyond, a comprehensive set of telemetry, an isolated power supply ground, and active current ripple suppression.

ACKNOWLEDGMENT

The authors would like to acknowledge the support of the various government agencies and personnel that have sponsored cooler technology developments at Ball through the years. This includes JPL, NASA GSFC, AF SMC SBIRS Low, and AFRL. We would also like to recognize the contributions of our teammates on the ACTDP: Redstone Engineering and CTS.

Figure 9. Ball E200 electronics delivered on the HIRDLS flight program.

REFERENCES

1. Kiehl, W.C., "HIRDLS Instrument Flight Cryocooler Subsystem Integration and Acceptance Testing," *Cryocoolers 11*, Kluwer Academic/Plenum Publishers, New York (2001), pp. 769-773.
2. Gully, W.J. et al., "Thermodynamic Performance of the Ball Aerospace Multistage Stirling Cycle Mechanical Cooler," *Cryocoolers 12*, Kluwer Academic/Plenum Publishers, New York (2003), pp. 45-50.
3. Berry, D. et al., "System Test Performance for the Ball Two-Stage Stirling-Cycle Cryocooler," *Cryocoolers 9*, Plenum Press, New York (1997), pp. 69-77.
4. Gully, W.J et al., Qualification Test Results for a Dual-Temperature Stirling Cryocooler," *Cryocoolers 10*, Plenum Publishing Corp., New York (1999), pp. 59-65.
5. Bruninghaus, C.H.Y., Tomlinson, B.J., and Abhyankar, N., "Performance Characterization of the Ball Aerospace 35/60K Protoflight Spacecraft Cryocooler," *Cryocoolers 12*, Kluwer Academic/Plenum Publishers, New York (2003), pp. 51-58.
6. Gully, W.J., "Development of a 12K Stirling Cycle Precooler for a 6K Hybrid Cooler System," *Cryocoolers 11*, Kluwer Academic/Plenum Publishers, New York (2001), pp. 63-68.
7. Ross, R.G., Jr., Boyle, R.F., Key, R.W. and Coulter, D.R., "NASA Advanced Cryocooler Technology Development Program," *Proceedings of the International Society of Optical Engineering (SPIE) Conference*, Waikoloa, Hawai, August 22-28, 2002.
8. Ross, R.G., Jr., Boyle, R.F., and. Kittel, P., "Overview of NASA SPACE Cryocooler Programs — A 2003 Summary," *Adv. in Cryogenic Engin.*, Vol 49B, Amer. Inst. of Physics, New York, 2004, pp. 1197-1204.
9. R. Levenduski, R., Gully, W. and J. Lester, J. "Hybrid 10 K Cryocooler for Space Applications," *Cryocoolers 10*, Plenum Publishing Corp., New York (1999), pp. 505-511.
10. Glaister, D.S. et al., "A 10 K Cryocooler for Space Applications," *Cryocoolers 11*, Kluwer Academic/ Plenum Publishers, New York (2001), pp. 577-586.
11. Oonk, R.L., "Low-Temperature, Low-Vibration Cryocooler for Next Generation Space Telescope Instruments," *Cryocoolers 11*, Kluwer Academic/Plenum Publishers, New York (2001), pp. 775-782.
12. Ross, R.G., Jr. "A Study of the Use of 6K ACTDP Cryocoolers for the MIRI Instrument on JWST," *Cryocoolers 13*, Kluwer Academic/Plenum Publishers, New York (2005), this proceedings.
13. R. Fernandez, R. and R. Levenduski, R., "Flight Demonstration of the Ball Joule-Thomson Cryocooler," *Cryocoolers 10*, Plenum Publishing Corp., New York (1999), pp. 449-456.

NGST Advanced Cryocooler Technology Development Program (ACTDP) Cooler System

J. Raab, R. Colbert, D. Harvey, M. Michaelian, T. Nguyen, M. Petach, R. Orsini, E. Tward, and M. Waterman

Northrop Grumman Space Technology (NGST)
Redondo Beach, CA 90278 USA

ABSTRACT

The NGST ACTDP cooler system features a three-stage integral pulse tube cooler coupled, as a precooler, to a 6 K Joule-Thomson (JT) cooler. The system is configured to provide remote cooling (12 m) at 18 and 6 K. The cooler is being developed under contract to the Jet Propulsion Laboratory with the objective of providing cooling for future NASA space observatory missions such as Terrestrial Planet Finder (TPF), Constellation X, and James Webb Space Telescope (JWST). The cooler development effort is to deliver an engineering model cooler with rack electronics that provide a flight-simulated interface.

This paper presents a cooler system overview and data collected during cooler development testing to date. Designed conservatively for a 10-year life, the hybrid cooler is required to provide 150 mW of cooling at 18 K together with 30 mW of cooling at 6 K while rejecting to 300 K and minimizing input power to the electronics. The total mass of the cooler and electronics system is less than 40 kg. The software driven control electronics provide the cooler control functions that are fully re-configurable and based on the NGST flight-qualified Advanced Cooler Electronics (ACE) with minor modification to measure and control temperatures in the 6 K range.

INTRODUCTION

The NASA Advanced Cryocooler Technology Development Program (ACTDP) objective is to develop active cooling systems for cooling remote sensors of space applications in the 5 to 10 K temperature range.[1] Additionally, the ability to provide a second cooling temperature in the 18 K range is required. The NGST ACTDP cooling system consists of a three-stage pulse tube precooler, a JT cooler, and control electronics—all based on flight heritage NGST hardware that has been adapted to the sub-10 K cooling requirements of the ACTDP program. The NGST effort is under contract with the Jet Propulsion Laboratory, with the current phase 9 months into a program scheduled for 31 months.

A schematic representation of the key components of the NGST ACTDP cooler system is shown in Figure 1. A valved compressor is used for the JT loop and incorporates the use of reed valves integrated with a flight qualified HEC (High Efficiency Cooler) compressor.[2] The pulse tube precooler also uses an existing HCC (High Capacity Cooler) compressor design[3] integrated with a three-stage pulse tube that provides gas precooling at 85, 35, and 17 K for the JT cooler. The JT

Cryocoolers 13, edited by R. G. Ross, Jr.
Springer Science+Business Media, Inc., New York, 2004

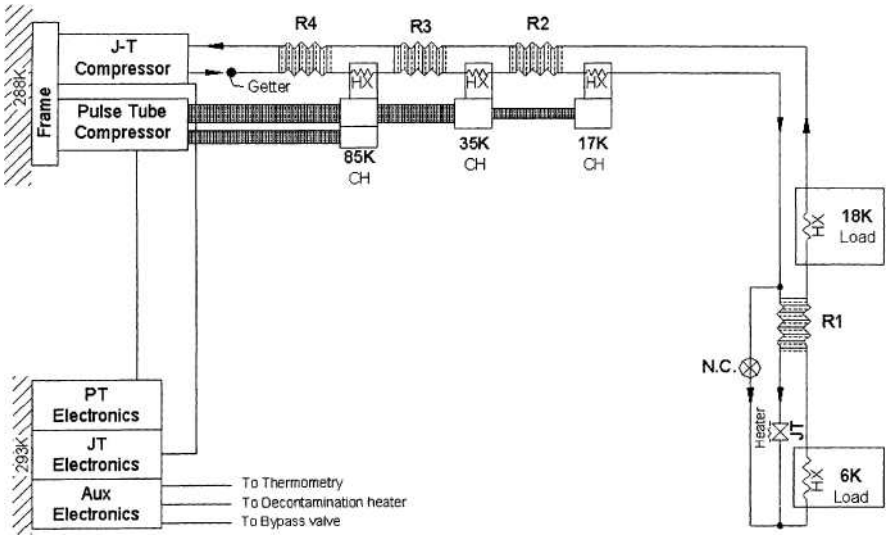

Figure 1. Schematic of NGST ACTDP cooling system.

precooling is achieved with the use of three recuperators operating from 300 K to 85 K (recuperator R4), 85 K to 35 K (recuperator R3), and 35 K to 17 K (recuperator R2). A 17 K to 18 K recirculating gas heat exchanger (HX) is used to provide cooling at 18 K with the exiting gas connected to an 18 K to 6 K recuperator (R1). The 6 K cooling for the sensor is provided by expansion through a JT valve. The 18 K cooling stage and JT valve are remotely located (12 to 20 m typically) from the pulse tube gas precooler. Also included in the JT cooler are room temperature getters, room temperature and cryo particulate filters, a JT decontamination heater, and a 100 K to 18 K bypass valve. The bypass valve is required to cool down potentially large (90 kg) thermal masses associated with the sensor. The JT cooler also has field joints that allow integration of the JT cooler coldhead into instrument systems independent of the JT compressor and pulse tube precooler. The JT cooler and pulse tube precooler are controlled with the Advance Cryocooler Electronics (ACE).[4] The ACE for the JT cooler and pulse tube precooler use an existing flight-qualified design with minor modification to replace the PRT thermometry with cernox thermometry and to interface with the auxiliary electronics. The auxiliary electronics is required to provide additional thermometry and heaters required for the cooling system.

COOLER SYSTEM

The three stage mechanical precooler (Figure 2) rejects heat at the centerplate of the compressor. Inside the compressor, flexure springs support the moving-coil linear motor that drives the pistons. The springs maintain alignment for the attached non-contacting pistons that oscillate and compress gas into the pulse tube cold heads. A small clearance between the cylinder and the piston seals the compression space. Two opposed compressor halves vibrationally balance the compressor. The compressor is operated at a frequency between 35 and 40 Hz.

The pulse tube cold heads are bolted to the compressor centerplate and are sealed with metal seals. The centerplate conducts heat to the radiator. The cold head components are arranged coaxially: mounting flange, regenerator, cold block, with the pulse tube, and warm-end heat exchanger body (or orifice) internal to the mounting flange and regenerator. The cold heads are surrounded by the JT cooler recuperators and the 35 K and 17 K cold head are enclosed in an 85 K radiation shield. A stainless steel orifice line connects the gas from the orifice to the reservoir tank that is either incorporated into the compressor end cap (85 K and 35 K stages) or mounted on the 85 K cold head (17 K stage).

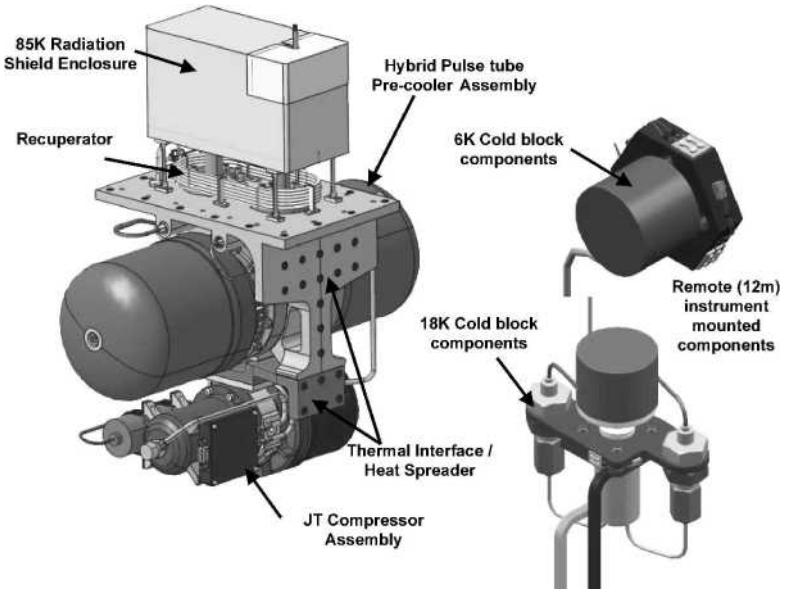

Figure 2. Integral vibrationally balanced pulse tube pre-cooler and JT compressor.

The internal wiring in the compressor is stranded PTFE (cross-linked Teflon) insulated wiring. All wiring exits the centerplate through ceramic-insulated pins in a D-shell feedthrough for the cooler drive power. A separate connector is used for redundant cernox thermometers on the 17 K cold block and a thermistor attached to the centerplate. An accelerometer is mounted on the compressor centerplate. Together with the signal conditioning electronics, the accelerometer provides a feedback signal to the vibration control algorithm in the ACE.

For the JT cooler (Figure 2) the compressor is as described previously for the precooler except it is the smaller HEC type. The compressor centerplate has been modified to incorporate reed valves to facilitate the DC flow required for JT operation. The JT cooler operates at 2X the precooler operating frequency. The JT gas flows through a zirconium room temperature getter, stainless steel tubing recuperators and transfer lines to the 18 K and 6 K cooling stages. The 18 K and 6 K cooling blocks are copper and have redundant thermometry and trim control heaters. Additionally the 6 K cold stage has the JT restriction for gas expansion and a decontamination heater.

An envelope for the bus-mounted cooler components, pulse tube precooler and JT compressor, is shown in Figure 3.

One of the two identical electronics boxes that are used to drive and control the precooler and JT cooler is shown in Figure 4. The electronics are a next generation of advanced cooler electronics based on our high-reliability flight designs currently on orbit and integrated on multiple instruments awaiting launch. The ACE represent a smaller, lighter weight, radiation hard (300 krad), and more reliable evolution of our previous cooler electronics. The functions of the electronics are to: (1) convert the 28 Vdc primary power to the secondary isolated power, (2) provide primary bus current ripple suppression, (3) drive the cooler, (4) provide communication with the host, and (5) control the cooler with a processor using software resident in EEPROM. The software performs the following functions:

- Transmits spacecraft command and cooler telemetry via the RS422 data bus,
- Collects cooler state of health data,
- Controls cold block temperature,
- Balances vibration force by controlling the waveform of the pistons,
- Provides safety protection to the cooler.

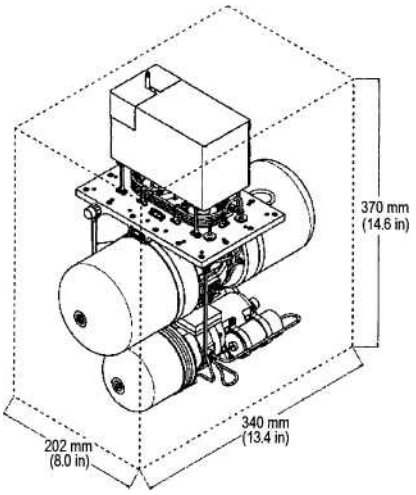

Figure 3. NGST ACTDP envelope for the mechanical cooler.

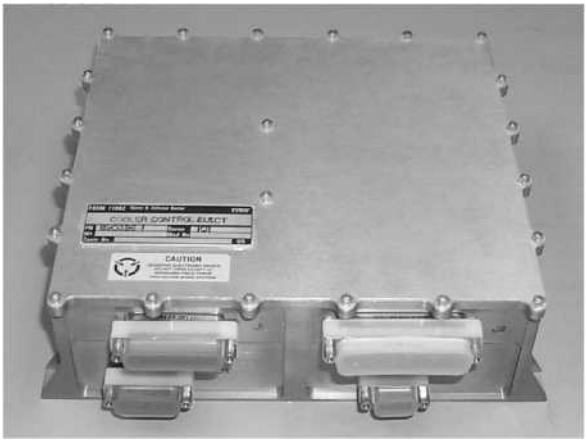

Figure 4. Advanced Cryocooler Electronics (9.20 in × 7.85 in × 2.91 in).

COOLER SYSTEM CAPABILITIES

Table 1 summarizes the cooler system weight and capabilities. Figure 5 shows the load line for the pulse tube precooler with data collected from 3rd stage unit testing. The requirement shown is a derived requirement that includes the required net cooling at the remote cold head as well as the required gas precooling for the JT cooler. Figure 6 shows a cool down curve based on analysis with the system performance model. The thermal mass used is 90 kg of aluminum. Because of the large thermal mass, a by-pass valve is incorporated into the design to allow JT helium flow to by-pass the JT restriction at temperatures greater than 18 K. Without the by-pass, the system would not cool down.

Figure 6 illustrates the system performance during cool down. Three key operating points on the cooling capacity specification define the system power. These points are steady state operation at 6 K and two pinch points during cool down at 18 K during the bypass mode and at 12 K during the JT orifice-controlled cool down.

Table 1. Cooler System Description.

Instrument	Capabilities
Mass	**(Kg)**
PT Pre-cooler	18.5
JT Cooler	7.1
Electronics (2 ACE and AUX)	7.8
Cables	3.3
Integrating Structure	0.7
Total	37.1
Nominal Operating Condition	
Cooling Load 18K	150mW
Cooling Load 6K	30mW
Heat Reject Temperature	300K
Bus Power steady state	228W
Peak cool down power	236W
Operating Temperature Range (TMU)*	-20 to 50°C
Non-operating Temperature Range (TMU)	-40 to 70°C
Operating Temperature Range (ACE)	-20 to 60°C
Non-operating Temperature Range (ACE)	-35 to 75°C
Launch Vibration (TMU)	14.2 Grms, 1 min
Launch Vibration (ACE)	14.2 Grms, 1 min
Launch Vibration JT cooler 18K and 6K comp.	25.8 Grms, 1 min
Bus Voltage Range	21V to 42V
Ripple Current	100 dB micro amps
Communication Protocol	RS422/1553B
Lifetime	10 years

*TMU = Thermal Mechanical Unit

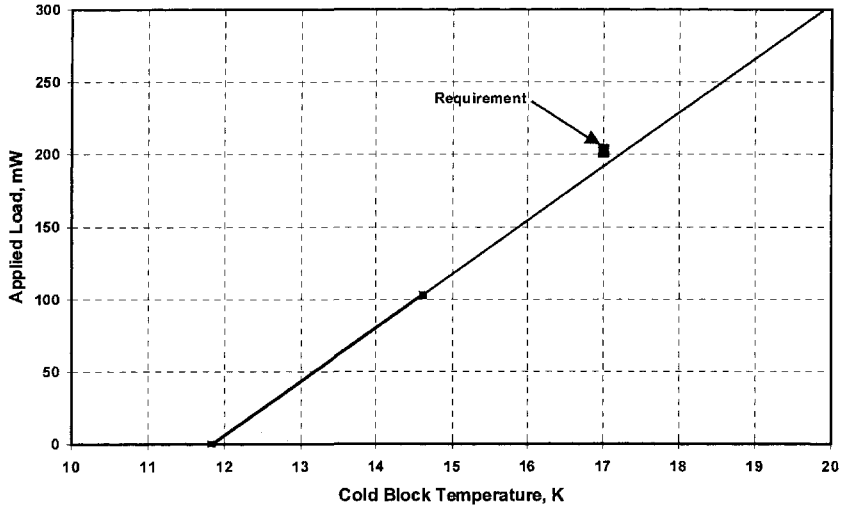

Figure 5. Pulse tube pre-cooler third stage performance with 35 K reject temperature.

CONCLUSIONS

Northrop Grumman Space Technology has demonstrated the feasibility of providing cooling for space scientific instruments at 6K. The system currently in development is an evolution of existing flight-proven designs and hardware. This approach minimizes the technical and schedule risks of developing new designs.

ACKNOWLEDGMENT

The work described in this paper was carried out by Northrop Grumman Space Technology and sponsored by the Jet Propulsion Laboratory ACTDP Project.

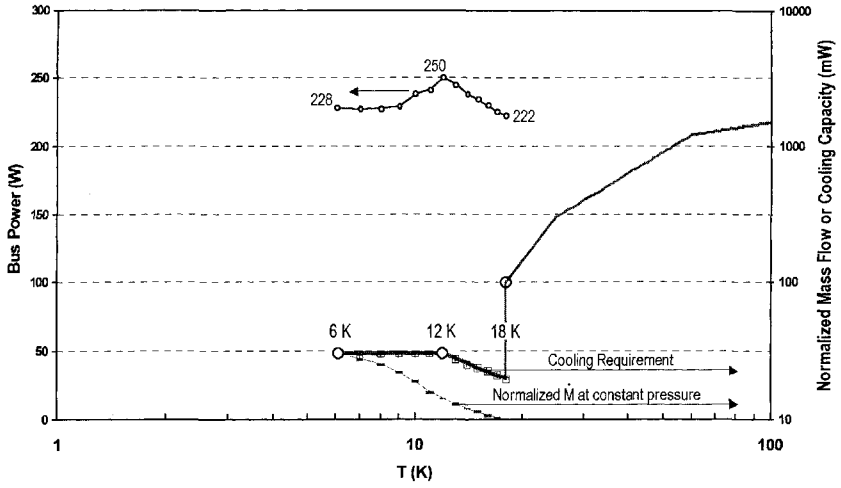

Figure 6. System performance during cooldown.

REFERENCES

1. Ross, R.G., Jr., Boyle, R.F., and. Kittel, P., "Overview of NASA SPACE Cryocooler Programs — A 2003 Summary," *Adv. in Cryogenic Engin.*, Vol 49B, Amer. Inst. of Physics, New York (2004), pp. 1197-1204.

2. Bailey, P.B., Dadd, M.W., Hill, N., Cheuk, C.F., Raab, J., Tward, E., "High Performance Flight Cryocooler Compressor," *Cryocoolers 11,* Kluwer Academic/Plenum Publishers, NY (2001), pp. 169-174.

3. Jaco, C., Nguyen, T. Harvey, D., Tward E., "High Capacity Staged Pulse Tube," *Cryocoolers 13,* Kluwer Academic/Plenum Publishers, NY (2004).

4. Danial, A., Davis, T, Godden, Harvey, D., J., M. Jackson, McCuskey, J., Valenzuela, P., "Advanced Cryocooler Electronics for Space," *Cryocoolers 13,* Kluwer Academic/Plenum Publishers, NY (2004).

A Study of the Use of 6K ACTDP Cryocoolers for the MIRI Instrument on JWST

R.G. Ross, Jr.

Jet Propulsion Laboratory
California Institute of Technology
Pasadena, CA 91109

ABSTRACT

The Mid Infrared Instrument (MIRI) of the James Webb Space Telescope (JWST) is a demanding application for the use of space cryocoolers. During calendar year 2003 an extensive study was carried out examining the application to this mission of hybrid 6K/18K J-T cryocoolers developed by NASA as part of their Advanced Cryocooler Technology Development Program (ACTDP). Among the most challenging requirements of the MIRI application were the requirements to cool down the ~90 kg 6 K cooling load in less than 30 days and to restrict the location of the compressors with their heat dissipation and vibration generation to a remote spacecraft position some 12 meters away from the cryogenic load. Because the hybrid 6K/18K J-T cryocoolers have unique load-carrying capability as a function of temperature, the cooldown requirement was the primary consideration in cooler sizing. This paper presents the lessons learned and performance achieved in the MIRI cryocooler application. In the final proposed configuration, all of the MIRI/JWST design considerations were successfully met. Although the cryocooler option was eventually deselected in favor of a solid-hydrogen stored cryogen system, the cryocooler study offered an important opportunity for understanding and refining the performance and integration capabilities of this important new class of low-temperature space cryocoolers.

INTRODUCTION

Chosen to replace the Hubble Space Telescope (HST), which was launched in 1990, the James Webb Space Telescope (JWST) is designed to examine the Universe in wavelengths between 0.6 and 28 microns during a mission lasting up to ten years. Unlike HST, which is in a Shuttle-accessible low-Earth orbit, JWST is designed to be located in deep space in an Earth-tracking L2 orbit. This location, a fixed 1.5 million km from Earth, will allow JWST's large ~6-meter telescope (illustrated in Fig. 1) to be passively cooled to ~35 K to enable unique new science.

The JWST instrument responsible for imaging the longest wavelengths is referred to as the Mid Infrared Instrument (MIRI). This instrument is being jointly developed by the European Space Agency (ESA) and NASA, with the Jet Propulsion Laboratory as manager. The MIRI instrument focal plane arrays require cooling to below 6.8 K, and its optics to below 15 K to suppress background noise levels to acceptable levels. Thus, unlike the other JWST instruments, MIRI requires supplemental active cooling to achieve temperatures on the order of 6 K.

Cryocoolers 13, edited by R. G. Ross, Jr.
Springer Science+Business Media, Inc., New York, 2004

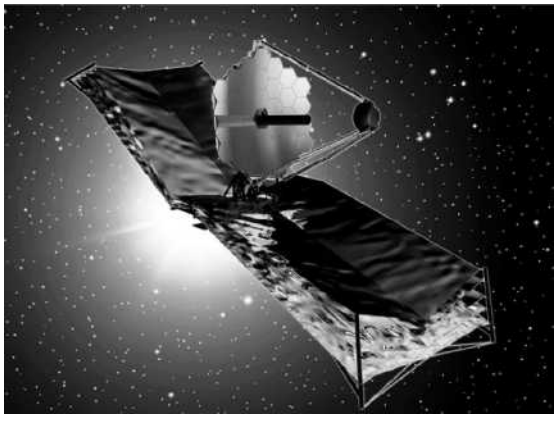

Figure 1. Overall James Webb Space Telescope configuration.

During the cryocooler/dewar trade study, two alternative approaches were examined by the MIRI team to provide the needed cooling: 1) a solid hydrogen cryostat, and 2) a 6 K/18 K mechanical cryocooler, the latter based on the cooler concepts being developed as part of NASA's Advanced Cryocooler Technology Development Program (ACTDP). Although the solid hydrogen stored cryogen system option was eventually selected in favor of a cryocooler, the cryocooler study offered an extremely valuable opportunity for understanding and refining the performance and integration capabilities of the ACTDP cryocooler concepts in an actual flight application.

THE MIRI CRYOCOOLER DESIGN CONCEPT

The cryocooler design concept for the MIRI application derives from three distinct areas: 1) the MIRI instrument itself, which represents the cooling load, 2) the overall JWST observatory, which provides most of the structural, thermal, electrical, and configurational interfaces, and 3) the ACTDP cryocoolers, which provide their own individual performance constraints. During the course of the cryocooler study the JWST observatory, and the MIRI instrument in particular, underwent modest configurational iterations typical of this stage in any project's development. Thus, the details presented here reflect the state of development in the spring of 2003, and are likely to be somewhat different from the design that exists at this time—a year later—or will exist in the future.

JWST Integration Concept

Figure 2 illustrates some of the configurational details of the JWST observatory at the time of this cooler integration study. In the JWST concept, the science instruments, including MIRI, are housed in the large ~35 K Integrated Science Instrument Module (ISIM) enclosure on the back of the ~35 K telescope. During launch, the telescope reflector is in a folded position with the telescope tower hard-mounted to the top of the spacecraft bus. After launch, the telescope reflector unfolds, and the entire tower and ISIM rise up approximately 1.5 m from the spacecraft bus to provide thermal and vibration isolation between the two. Thus, all cabling or plumbing connecting the ISIM instruments to the spacecraft must undergo this ~1.5 meter deployment, must be highly flexible, and must have minimal thermal conductance.

The overall JWST thermal compartmentalization places a constraint that any room-temperature cryocooler compressors be located in the spacecraft bus approximately 12 meters away from the cryogenic loads in the ISIM. Thus, the compressor-coldhead connection must also accommodate the 1.5 meter in-space deployment of the telescope away from the spacecraft following launch. One key advantage of this deployment is a much relaxed requirement on cryocooler-generated vibration compared with, for example, HST. For JWST, the cryocoolers are assumed to be vibration-isolated from the spacecraft structure using standard vibration isolation mounts with perhaps a 15 Hz mounting frequency.

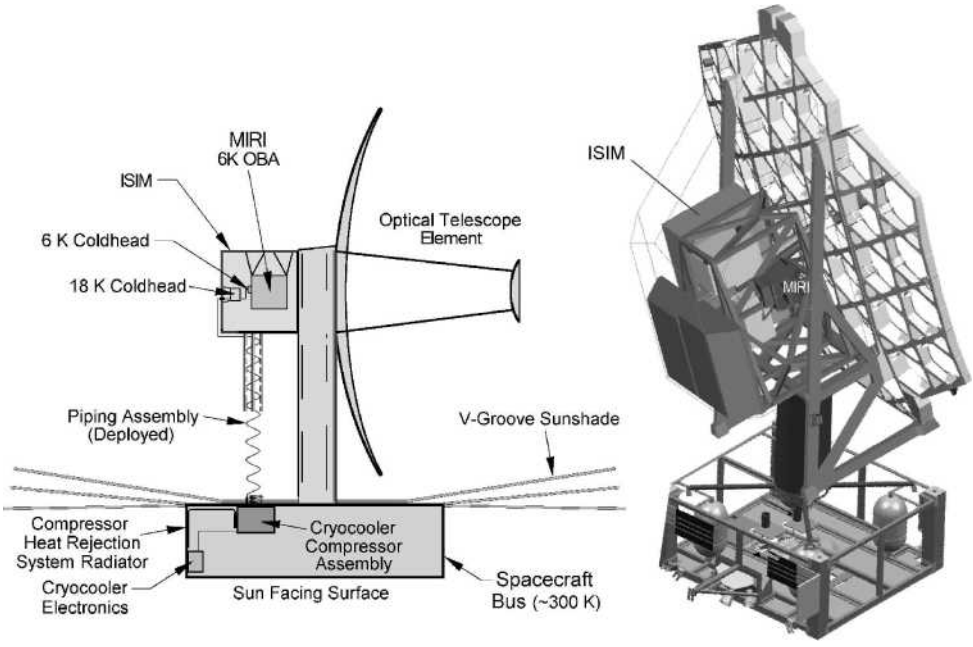

Figure 2. Overall James Webb Space Telescope configuration and cryocooler integration concept.

In terms of reliability and redundancy, an important implication of JWST's orbital location is that periodic repair and refurbishment, like was successfully used many times on HST, will not be possible with JWST. Thus, reliability and long life will be particularly important for this mission.

MIRI Instrument Concept

Figure 3 illustrates the generic concept of the MIRI instrument at the time of this cooler integration study. Structurally, the instrument is supported from the Integrated Science Instrument Module (ISIM) on the back of the JWST telescope via three pairs of low-conductivity struts. Strictly speaking, the instrument consists of three relatively low-power focal planes (~1 mW each) that require cooling to <6.8 K, plus a ~90 kg Optical Bench Assembly (OBA) that has to be cooled to below ~15 K. However, to avoid requiring two cooling temperatures, the instrument design in 2003 had the entire instrument integrated at roughly the same 6 K temperature.

In terms of refrigeration capacity, the primary cryogenic load presented to the cooler is approximately 10 mW, associated with conduction down the struts from the ~35 K ISIM structural interface, plus approximately 12 mW of radiation load to MIRI from the ~40 K ISIM enclosure, plus 5 mW (inc. margin) for the focal planes. The radiation loading assumes the presence of MLI blankets

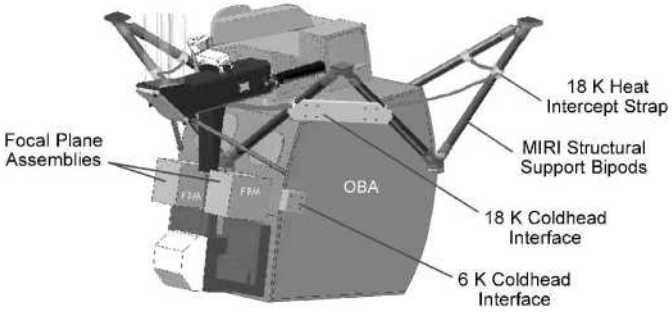

Figure 3. MIRI instrument conceptual design.

on most of the instrument's surfaces, but does not include the application of an external radiation shield, which was ruled out by the instrument provider because of integration difficulties.

A second key cryocooler capacity requirement was to cool the ~90 kg mass of the instrument from ~100 K to 6 K in less than 30 days in space, and quicker, if possible, during ground testing.

ACTDP Cryocooler Concept

In 2002, NASA initiated the Advanced Cryocooler Technology Development Program (ACTDP) as part of JPL's Terrestrial Planet Finder (TPF) project to develop the needed cryocooler technology for this class of space applications. The goal of the ACTDP activity is to build and test working models of up to three candidate cryocooler designs capable of providing 30 mW of cooling at 6 K together with 150 mW of cooling at 18 K.[1,2] Two of the ACTDP concepts, the Ball Aerospace and Northrop Grumman (formerly TRW) designs, are particularly well suited to the remote cooling requirements of the JWST application.[3,4] These two concepts, illustrated in Figs. 4 and 5, combine Stirling or pulse tube precoolers with a separate Joule-Thomson (J-T) stage that can provide simultaneous 6 K and 18 K cooling to a remote load many meters away from the compressor suite. For the MIRI application, as noted in Fig. 2, the compressor suite would be located in the JWST spacecraft bus, while the J-T coldhead would be mounted within the 35 K ISIM, adjacent to the MIRI instrument (see Figs. 2 and 4). This very clean mechanical interface allows the coolers and instrument to follow there own separate development and test paths and to be easily integrated together late in the ISIM integration and test phase.

Because the ACTDP cryocoolers have an ~18 K stage with greater than 150 mW of capacity as part of their design, this 18K stage was used to intercept heat flowing down the MIRI structural bipods and electrical cabling, thus lowering the 6 K cooling load by over 35%. These 18 K heat interceptors are schematically noted in Figs. 3 and 4.

In terms of cooling performance, the ACTDP hybrid coolers have a unique cooling trend versus temperature, quite different from pure regenerative coolers such as pulse tube and Stirling coolers. This is caused by the very different cooling behavior of the helium J-T system, which decreases

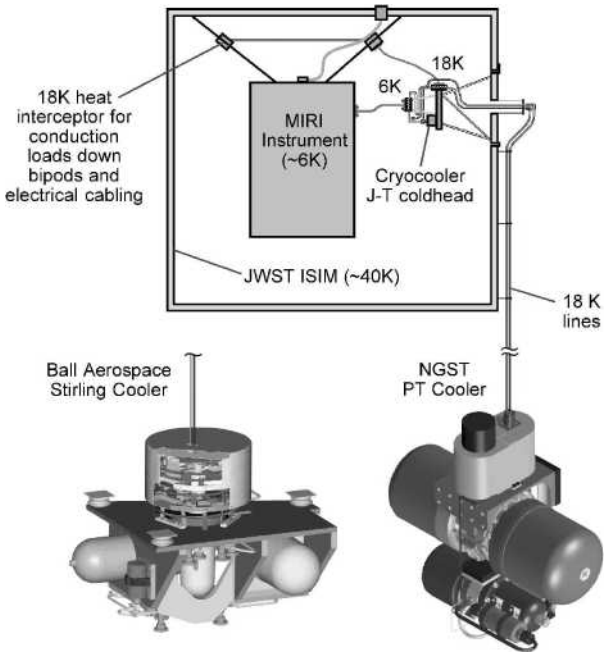

Figure 4. MIRI cryocooler conceptual design showing both Northrup Grumman (NGST) and Ball Aerospace ACTDP cryocooler compressor suite concepts.

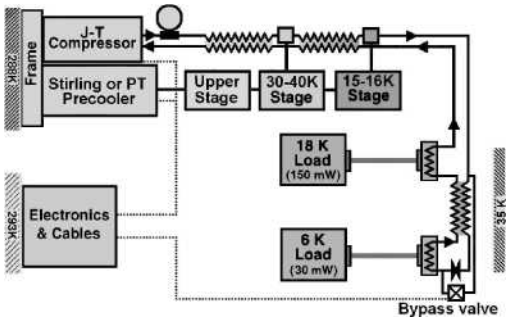

Figure 5. ACTDP hybrid J-T cryocooler flow diagram.

dramatically in cooling capacity with increasing precooling temperature as shown in Fig. 6. To provide augmented cooling capacity at elevated temperatures, the ACTDP coolers are fitted with valves that bypass the J-T working fluid around the J-T valve and the last recuperative heat-exchanger stage as shown in Fig. 5. Thus, at elevated temperatures, the J-T loop serves as a helium gas heat transfer loop to transfer the cooling capacity of the Stirling or pulse tube precooler directly to the 6 K and 18 K loads. This vastly increased cooling capacity above the bypass-valve closure temperatures is noted in Fig. 6. Also visible in Fig. 6 is the point of least cooling capacity, which occurs at temperatures just below the bypass valve closure temperature. This dip in cooling capacity below the bypass valve closure temperature presents an important pinch-point that must be carefully addressed to insure that the cryogenic load—here the MIRI instrument—can be cooled down to its final 6 K operating temperature.

MIRI CRYOCOOLER COOLING LOADS

Given the conceptual cooler configuration discussed above, Table 1 tabulates rough estimates of the expected cooling load contributions in the final 6 K equilibrium operating state of the MIRI instrument. It also includes a column of margined loads that include a 2x contingency factor to cover the uncertainties that exist in the load estimates this early in the design process. The largest loads on the 18 K stage are seen to be the heat interceptor loads from the MIRI graphite reinforced plastic (GRFP) struts, and the parasitic loads on the 18 K refrigerant lines, shown in Fig. 7, that run between the JWST spacecraft and the ISIM.

The far right column of Table 1 includes any end-of-life (EOL) load additions expected from load elements that can be expected to increase over the course of the JWST mission. These EOL

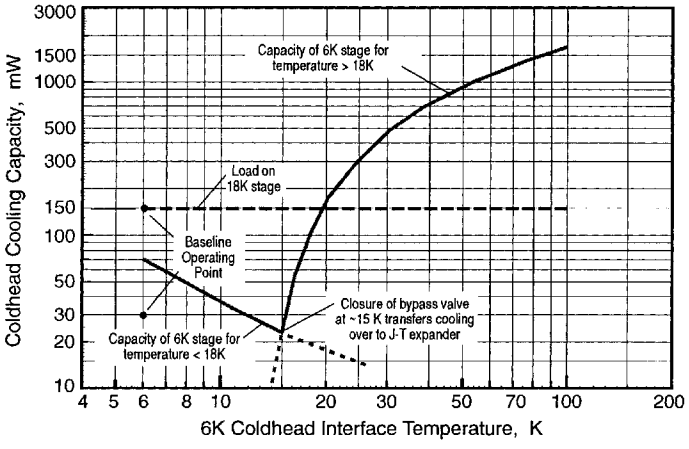

Figure 6. ACTDP cooling capacity versus temperature of the 6 K load.

Table 1. MIRI Cooler Baseline Loads with 18 K Heat Interceptor.

ITEM	Cryocooler Load (mW)		
6K Stage Loads	**BOL Best Estimate**	**BOL w/ Margin**	**EOL w/Margin**
MIRI radiation load from ISIM (40K)	7.2	11.8	12
MIRI Focal plane electrical dissipation	3.0	4.9	4.9
MIRI Electrical Harness conduction from 18 K intercept	* ~~8.3~~ 3.5	~~13.8~~ 5.8	5.8
MIRI Structural support conduction from 18K intercept	~~5.3~~ 2.0	~~11.5~~ 4.3	4.3
Radiation load on flexbraid connecting 6K stage to MIRI OBA	0.05	0.1	0.1
Radiation load on 6K stage from 18K stage (1500 cm^2)	0.1	0.2	0.2
Support conduction from 18 K stage to 6K stage (0.5 kg)	1.15	2.3	2.3
Redundant cooler J-T & bypass valve lines from 18 K stage (3)	0.1	0.2	0.2
Conduction from redundant cooler J-T heater and temp sensor leads	0.05	0.1	0.1
Total 6 K cryocooler load	17.15	29.7	~30.0
18K Stage Loads			
MIRI structural conduction Intercept Load	10.0	20.0	20.0
MIRI harness conduction Intercept Load	15.0	30.0	30.0
Radiation load on 18K flexbraid to MIRI structure intercept	0.05	0.1	0.1
18K coldstage support conduction from 35K ISIM	2.2	4.4	4.4
Redundant cooler J-T lines from 35 K ISIM (2 lines, each 50 cm)	0.1	0.2	0.2
Harness conduction for J-T heater and temp sensors	0.04	0.1	0.1
Quick-cooldown & defrost-mode bypass valve harness conduction	0.1	0.1	0.1
Radiation load on 18K stage from 40K ISIM (1200 cm^2)	1.0	2.0	2.0
18K line conduction from 35K ISIM feedthrough	1.0	2.0	2.0
Heat conducted down to 6K stage from 18K stage	-0.35	-0.7	-0.7
18K line support conduction external to ISIM (10 m)	10.0	20.0	20.0
Radiation load on 18K lines external to ISIM (10 m)	18.1	36.2	72.0
Total 18K cryocooler load	57.2	114.4	~150

*Crossed out numbers are original loads prior to inclusion of 18K heat interceptor

increases are dominated by increased radiation loading on the ~18 K refrigerant lines. Figure 7 describes the effective background radiation temperature seen by the refrigerant lines as a function of position up the JWST observatory tower. The resulting thermal radiation load is proportional to the fourth power of this background temperature and linearly proportional to the surface emittance of the lines and their external surface area. Also important is the conductance of the standoffs required to support the refrigerant lines from the tower structure. These and other conductance loads in Table 1 were estimated based on scaling previously proven cryogenic support designs.[5] Although the conductance is not subject to increase over time, the surface emittance of the lines can be expected to increase due to gettering of water vapor on the external surface of the 18 K lines over the course of the mission.[6]

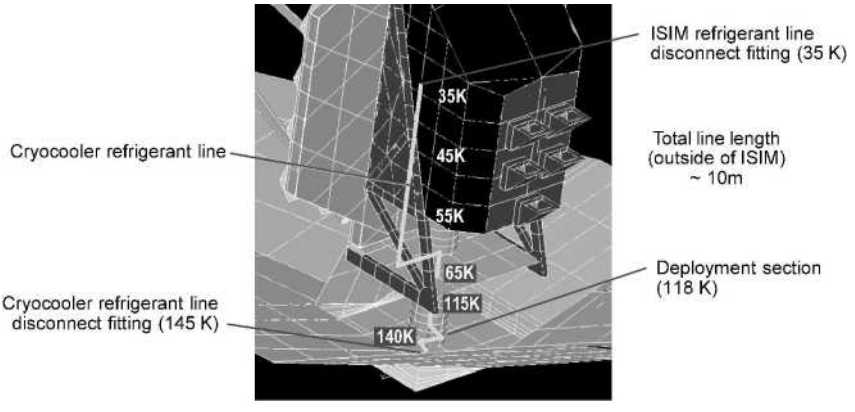

Figure 7. Radiation environment for the 18 K fluid lines that run between the spacecraft and the ISIM.

Two approaches to dealing with the radiation load increase have been considered: 1) wrapping the refrigerant lines with adequate multilayer insulation (MLI) to limit load growth over the JWST mission to the design level, or 2) incorporating a periodic defrost mode whereby warm, uncooled gas is passed through the lines to raise their temperature sufficiently (>160 K) to evaporate condensed moisture when the design load level is reached. The 72 mW line radiation load at EOL in Table 1 is felt to be an achievable goal for this EOL radiation design load for the refrigerant lines.

In reviewing the 6 K loads, it is seen that they are dominated nearly equally by the MIRI instrument radiation loads from the ~40 K ISIM, and by the MIRI conduction loads down the GFRP bipods from the 18 K heat-interceptor temperature. Because the 40 K ISIM will effectively getter all water vapor to negligible levels, increased surface emittance of the MIRI instrument should be very small. The only contribution would be from gases such as nitrogen and oxygen that are immobile at 6 K, but have vapor pressures above 10^{-4} torr at 35 K, and thus are not gettered by the ISIM surfaces.

CRYOCOOLER SIZING TO ASSURE THAT MIRI CAN BE COOLED DOWN

Because of the unique thermal performance of the hybrid ACTDP cryocoolers versus temperature, the cooldown performance of the overall MIRI cryogenic system must be carefully engineered. As shown in Fig. 5, the most critical temperature range for this type of cooler is between the bypass valve turnoff temperature and the ultimate 6 K load temperature. Figure 8 details the estimated MIRI loads and the ACTDP refrigerator performance over this temperature range. Also shown is a conceptual estimate of the input power required and how it might be throttled back as the final 6K operating point is achieved. Better power data must await breadboard testing of the ACTDP coolers.

In Fig. 8, the refrigerator is sized to provide approximately 50% more capacity than the sum of the total 6K loads in Table 1 in the critical 12 to 18 K temperature range. Note that when this is done, the refrigerator has substantial over capacity at 6K (>70 mW) compared to the 6K operational load of 30 mW. Thus, for this type of application, the 6 K operational load is not the sizing condition; the critical sizing condition is the ability to cool down from 18 K to 12 K.

Note also that the lack of an 18 K radiation shield around the MIRI instrument exacerbates the cooldown issue by allowing a near-constant radiation load to exist in this critical 18 to 12 K temperature range. In contrast, the presence of the 18 K heat interceptor on the support structure causes the structural conduction loads to be zero at 18 K, and to climb relatively linearly between 18 and 6 K. Thus, the radiation loads on the MIRI instrument dominate the sizing of the cryocooler's 6K stage.

This unique thermal behavior of the hybrid ACTDP-type cryocoolers requires that the thermal load be managed more thoughtfully than with a conventional regenerative cryocooler, where the sizing condition is invariably at just the lowest operating temperature.

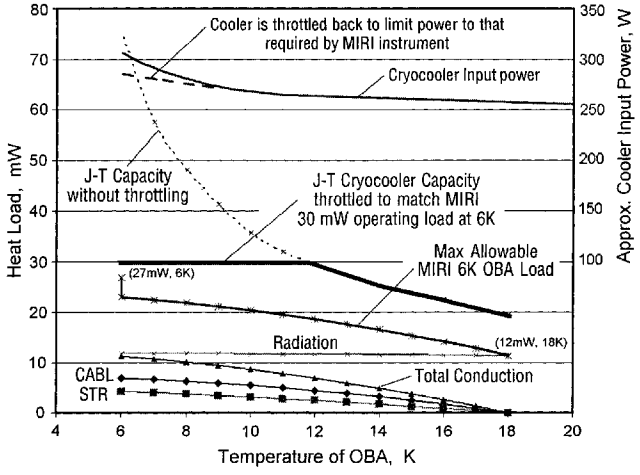

Figure 8. ACTDP cooling performance compared to the MIRI cooling loads.

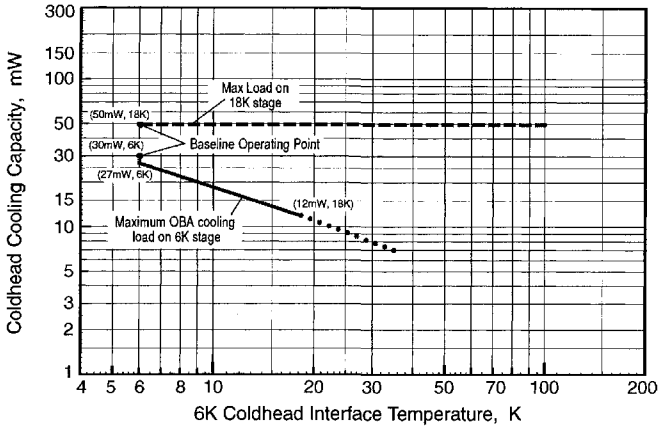

Figure 9. Example maximum allowable load requirement for ACTDP-type hybrid cryocooler.

Figure 9 displays an example design requirement for the maximum MIRI instrument load to be presented to the cryocooler. This plot presents the requirement as a 'not to be exceeded' load envelope as a function of temperature below 18 K, together with a simultaneous not-to-be-exceeded allocation for cooling from the cryocooler's 18 K stage. The numbers in this requirement are consistent with the margined MIRI loads presented in Table 1.

As a complement to the maximum-load requirement given in Fig. 9, the minimum allowable cryocooler performance must also be specified over the entire temperature range to insure that a positive margin exists between the cryogenic load and the cooler performance at all temperatures. An example of such a 'minimum allowable' cryocooler cooling performance for the MIRI application is shown in Fig. 10.

Predicting Instrument Cool-Down Time

Given the instrument's heat capacity, the instrument loads as detailed in Fig. 8, and the estimated cryocooler performance as shown in Fig. 6, one can estimate the predicted time for initial instrument cooldown. Figure 11 presents data on the specific heat of representative spacecraft materials as a function of temperature. For the 90-kg MIRI instrument the cooldown estimates can be based on the properties of aluminum, which is the dominant material in its design. Note that the specific heat of aluminum drops by a factor of 1000 between room temperature and 6 K.

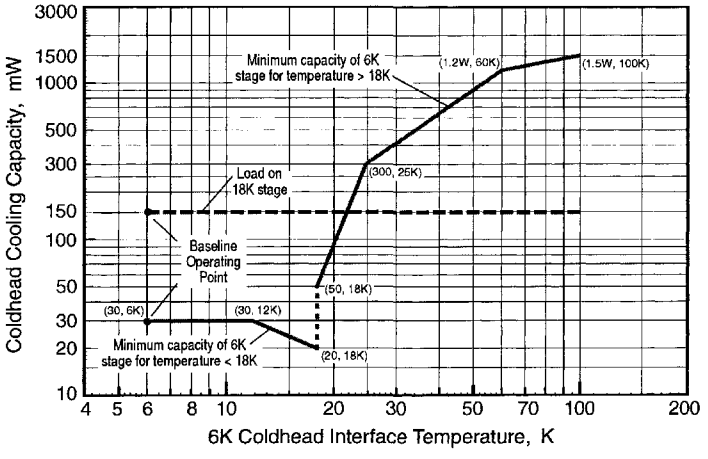

Figure 10. Example cooling performance requirement for ACTDP-type hybrid cryocooler.

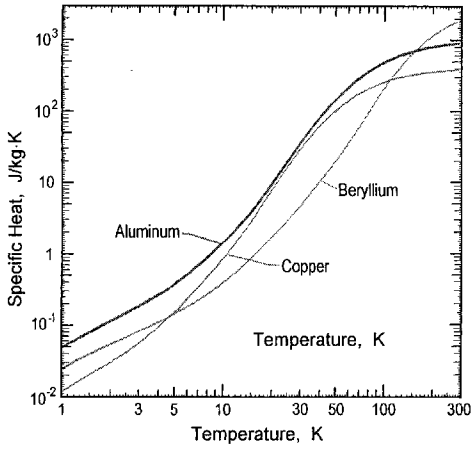

Figure 11. Specific heat versus temperature for representative spacecraft metals.

Figure 12 illustrates the predicted cooldown dynamics of the MIRI instrument from a starting temperature of 100 K. In flight, the MIRI instrument would be allowed to cool passively through radiation and conduction to the ISIM until the ISIM approaches its equilibrium temperature of around 40 K. At this point it is estimated that the MIRI instrument would have cooled to around 60 K. Thus, the predicted cooldown time after the cryocooler is energized would be approximately 7 days, with roughly equal time spent before and after the bypass valve is closed.

This calculation illustrates that, even with a very large (~90 kg) cold load, the cooldown time is quite acceptable with this type of cooler, largely because the specific heat of materials drops so precipitously at these low temperatures.

Predicting Instrument Warm-up and Re-cooldown Times

During the course of any space-science mission, there are events that may require power to the instruments to be turned off. These can be safety shutdowns or planned warm-ups for decontamination. With such an event, it is important that the instruments return to normal operation as soon as practical to maximize the science data collection. Figure 13 predicts the warm-up dynamics of the MIRI instrument in the event that the ACTDP cryocooler is turned off. Note that the low heat capacity of the instrument at 6 K results in a relatively rapid warm-up, with the instrument approaching the ISIM background temperature in a day or two after it is turned off. From Fig. 12, it can be seen that the cooler can return the instrument to operating temperature in about four days, which is felt to be quite reasonable.

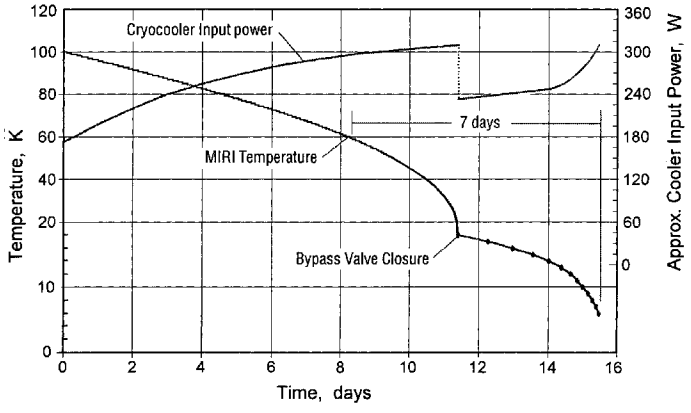

Figure 12. Predicted cooldown of the MIRI instrument versus time using an ACTDP cryocooler.

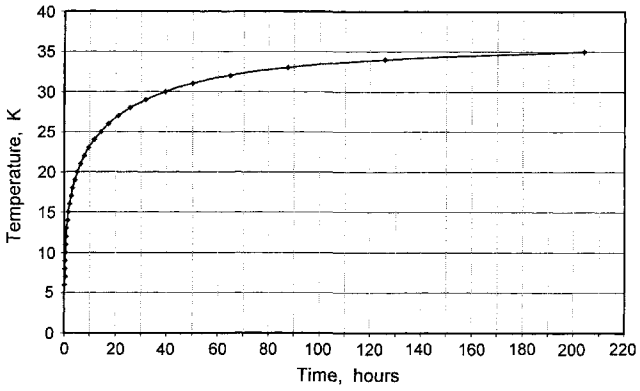

Figure 13. Predicted warm-up of the MIRI instrument versus time when the cryocooler is turned off.

SUMMARY

Because the MIRI Instrument on JWST is a demanding, yet representative application for the future use of space cryocoolers, it offered an important opportunity for understanding and refining the performance and integration capabilities of the hybrid J-T 6K/18K coolers being developed by NASA as part of their Advanced Cryocooler Technology Development Program (ACTDP). Among the most challenging requirements were the requirement to cool down the ~90 kg instrument in well less than 30 days and to restrict the location of the compressors to a remote spacecraft position some 12 meters from the cryogenic load. In the final analysis, the ACTDP cryocoolers successfully met all of the MIRI/JWST design considerations and were shown to provide an attractive option for meeting the cooling needs of future NASA missions.

ACKNOWLEDGMENT

The work described in this paper was carried out at the Jet Propulsion Laboratory, California Institute of Technology, and was sponsored by the NASA JWST MIRI project and the NASA TPF project through an agreement with the National Aeronautics and Space Administration. Special thanks are due Dean Johnson of JPL, Willy Gully and Dave Glaister of Ball Aerospace, and Manny Tward, Mike Petach, Debbie Fitzgerald, Bill Morelli, Allen Bronowicki, and John Pohner of Northrop Grumman Space Technologies for their technical support during the MIRI cryocooler accommodation study.

REFERENCES

1. Ross, R.G., Jr., Boyle, R.F., Key, R.W. and Coulter, D.R., "NASA Advanced Cryocooler Technology Development Program," *Proceedings of the International Society of Optical Engineering (SPIE) Conference*, Waikoloa, Hawaii, August 22-28, 2002.
2. Ross, R.G., Jr., Boyle, R.F., and Kittel, P., "Overview of NASA SPACE Cryocooler Programs — A 2003 Summary," *Adv. in Cryogenic Engin.*, Vol 49B, Amer. Inst. of Physics, New York (2004), pp. 1197-1204.
3. Glaister, D. et al., "Ball Aerospace 4-10 K Space Cryocooler," *Cryocoolers 13*, Kluwer Academic/ Plenum Publishers, New York (2005), this proceedings.
4. Raab, J. et al., "Advanced Cryocooler Technology Development Program (ACTDP) Cooler System," *Cryocoolers 13*, Kluwer Academic/Plenum Publishers, New York (2005), this proceedings.
5. Ross, R.G., Jr., "Estimation of Thermal Conduction Loads for Structural Supports of Cryogenic Spacecraft Assemblies," *Cryogenics*, Vol. 44, Issue: 6-8, June - August, 2004, pp. 421-424.
6. Ross, R.G., Jr., "Cryocooler Load Increase due to External Contamination of Low-ϵ Cryogenic Surfaces," *Cryocoolers 12*, Kluwer Academic/Plenum Publishers, New York (2003), pp. 727-736.

Lockheed Martin 6K /18K Cryocooler

J. Olson, P. Champagne, E. Roth, B. Evtimov, R. Clappier, T. Nast

Lockheed Martin Advanced Technology Center
Palo Alto, CA USA

T. Renna, B. Martin

Lockheed Martin Commercial Space Systems
Newtown, PA USA

ABSTRACT

Under contract with the Jet Propulsion Laboratory (Advanced Cryocooler Technology Development Program), Lockheed Martin's Advanced Technology Center (LM-ATC) is developing a four-stage pulse tube cryocooler and electronic controller to provide simultaneous cooling at 6 K and 18 K. LM-ATC successfully completed the design phase of the program, where a robust, simple pulse tube cryocooler system was designed to meet JPL's cryocooler needs. The simplicity of LM-ATC's approach, with a single compressor, coldhead and electronic controller, makes it very appealing for the large observatories (Constellation-X, Terrestrial Planet Finder, and the James Webb Space Telescope) that require high reliability.

The cryocooler is designed simultaneously to provide 20 mW of cooling at 6 K and 150 mW cooling at 18 K while conductively rejecting heat at 290K. The Lockheed Martin pulse tube is a simple four-stage coldhead with no moving parts, driven by a linear flexure-bearing compressor, powered by a high-efficiency electronic controller. The controller provides simultaneous temperature control at both 6 K and 18 K, vibration cancellation, and bus current ripple suppression.

This paper summarizes the characteristics of the system and the status of the program.

INTRODUCTION

In March 2002, LM-ATC and three other cryocooler teams began study contracts with the Jet Propulsion Laboratory (JPL) to examine the feasibility of building a long-life mechanical cryocooler capable of meeting the cryogenic needs of several large NASA programs. These needs include providing cooling simultaneously at both 6 K and 18 K, low mass, low power consumption, high reliability, fast cool-down time, and long separation between the cooler's moving parts and the cold parts of the spacecraft. Lockheed Martin chose a simple cryocooler design based on our recent success with low-temperature pulse tubes.[1]

Cryocoolers 13, edited by R. G. Ross, Jr.
Springer Science+Business Media, Inc., New York, 2004

Following successful completion of the study contract September 2002, LM-ATC was one of three teams selected to enter a risk reduction phase of the program, wherein prototype hardware is being built and tested.

STUDY PHASE

Requirements

The study phase began March 2002. The system requirements were defined by JPL, and are shown in Table 1. The requirements stem from a number of cryocooler features desired by the primary NASA customers, Constellation-X (Con-X), Terrestrial Planet Finder (TPF), and the James Webb Space Telescope[2] (JWST). These programs all had cooling needs at approximately the same temperatures, 6 K and 18 K. TPF and JWST had the need to deploy the cold section of the spacecraft, requiring a long separation between the cold parts and any heat- or vibration-generating component (namely, the compressor and electronics). It was initially thought that the observatories would require redundant cryocoolers in order to achieve sufficient reliability, so a specification was included to minimize the redundant cooler's off heatloads. There was an option during the study phase to include the use of a radiator at approximately 100K in order to increase the cooler's efficiency, but this option was dropped by LM-ATC because it added unnecessary complexity for only a modest improvement in efficiency.

Cryocooler System

The LM-ATC cryocooler design is very simple, and is shown in Figure 1. The system consists of 3 main components, the pulse tube coldhead, the compressor, and the electronic controller. A looped heat pipe is used to remove heat from the pulse tube coldhead.

The coldhead design is based heavily on previous cryocoolers developed by LM-ATC with IRAD funding.[1,3] The coldhead is a four-stage pulse tube with no moving parts and no tight tolerances. The coldhead is structurally robust and efficiently packaged. Such a coldhead is more complex than a single-stage pulse tube, but the complexity and reliability of pulse tube cryocoolers is determined primarily by the compressor and electronics, not by the relatively simple coldhead, so the additional complexity of four stages is of only minor importance. Furthermore, a four-stage pulse tube is simpler than proposed hybrid systems that mate a multiple-stage pulse tube or Stirling cooler to a Joule-Thomson cooler, because it does not use the more troublesome cryocooler components: the J-T expander and the moving displacer. Finally, systems that utilize a J-T expander to do the final stage of cooling require the the use of

Table 1. ACTDP requirements.

Requirement	Specification	LM-ATC Design
Cooling @ 6K / 18K	20 mW / 150 mW	20 mW / 150 mW
System Power	150 W	156 W
System Mass	40 kg	24.5 kg
Off Heat Load @ 6K	<1 mW	6 mW
Off Heat Load @ 18K	<25 mW	52 mW
Cooldown Time with 50g/250g Cu added mass at 6K/18K	50 hours (24 hours goal)	23 hours with 1000g Cu added mass at each stage
Transfer Line Length	1.5–5 m	1.5 m baseline

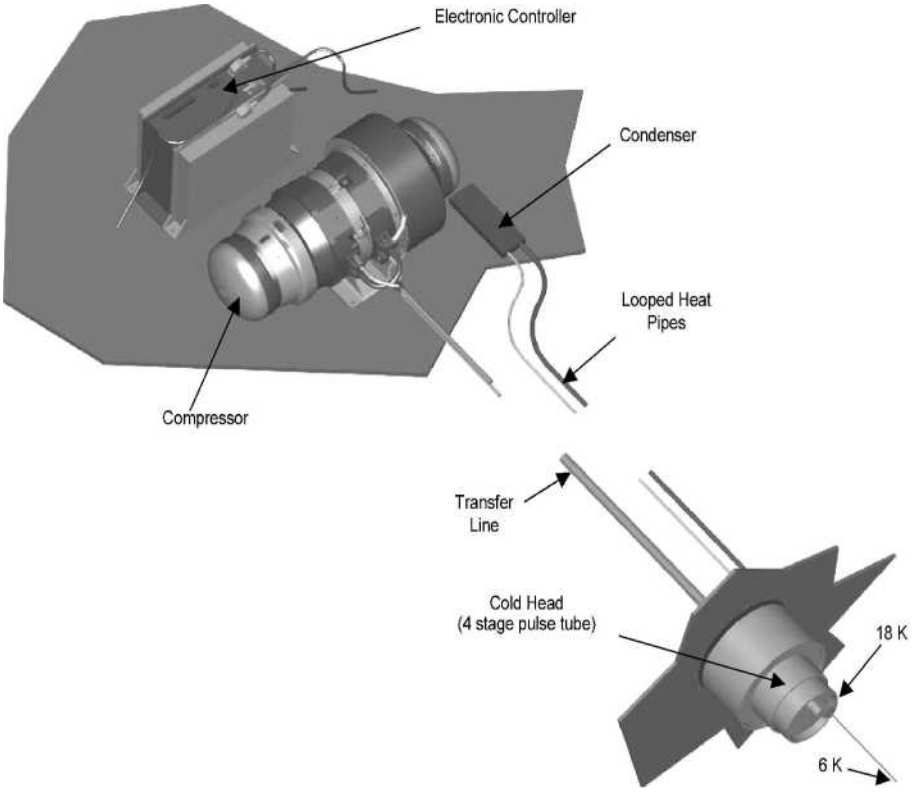

Figure 1. LM-ATC's chosen configuration for the ACTDP cryocooler system. A simple 4-stage pulse tube coldhead is driven by a standard flexure-bearing clearance-seal compressor, powered by an electronic controller. The split system design allows a separation of several meters between the compressor and coldhead.

a by-pass valve to avoid slow cool-down times when cooling a large thermal mass, whereas the 4-stage pulse tube has a large cooling capacity when the system is warm, allowing it to cool kilograms of material to 6 K in just a few days time.

The pulse tube coldhead is driven by a linear flexure-bearing clearance-seal compressor that is identical in complexity to compressors used on LM-ATC's single-stage and two-stage pulse tubes, and thus adds no additional complexity to the system. LM-ATC uses a moving magnet design that places the electrical coil outside the working gas space, eliminating the primary source of contamination from the working fluid. Furthermore, the moving magnet configuration eliminates flexing electrical leads, and eliminates all hermetic electrical feed-throughs into the pressure vessel. The ACTDP program uses our MEGA-series compressor, which has a swept volume in excess of 30 cm^3 and an operating frequency of approximately 30 Hz, and is similar to the compressor used for our high capacity two-stage pulse tube cooler.[4]

The compressor is powered by a simple high efficiency electronic controller. The electronic controller includes vibration control, a passive launch lock circuit that prevents the pistons from hitting the end stops while unpowered during launch, and current ripple suppression which limits ripple current to less than 1 amp peak to peak during nominal operation. In contrast to the hybrid systems, LM-ATC's system requires just a single controller, leading to reduced mass and increased reliability. Controller studies were funded as part of the study phase.

Results

LM-ATC successfully completed the study phase in September 2002. We designed a simple, efficient system with a robust coldhead, with high reliability even in a non-redundant configuration. The design results are shown in Table 1.

The predicted system power to deliver 20 mW at 6 K + 150 mW at 18 K is shown in Figure 2 as a function of transfer line length. Based on these results, we concluded that transfer line lengths in excess of 5 m require prohibitively large system power for the simple 4-stage pulse tube system, and so we selected a baseline length of 1.5 m.

RISK REDUCTION (PROTOTYPE HARDWARE) PHASE

Requirements

Following the completion of the study phase, and based on input from the three funding sources (Con-X, TPF, and JWST), the system requirements were refined by JPL, and design work began in earnest. The cooling load requirements were made firm at 20 mW at 6 K and 150 mW at 18 K (they were only guidelines during much of the study phase). A heat rejection temperature goal of 288 K was added in order to prevent condensation during laboratory testing, but otherwise the specifications remained unchanged.

The Con-X program found it desirable for the 1st stage to operate at 90 K, so we redesigned the coldhead to decrease the temperature of that stage. During the study phase, the design predicted a 1st stage temperature of 110 K, so only modest modification was required to decrease this to 90 K, and this modification only increased the predicted system power by 3 W.

At the time of the completion of the study phase, both the JWST and TPF programs had a need for a deployable coldhead, requiring approximately 20-meter separation between the compressor and coldhead. The biggest disadvantage of our simple pulse tube approach is that it does not allow a separation greater than a few meters without excessive power (see Figure 2) and

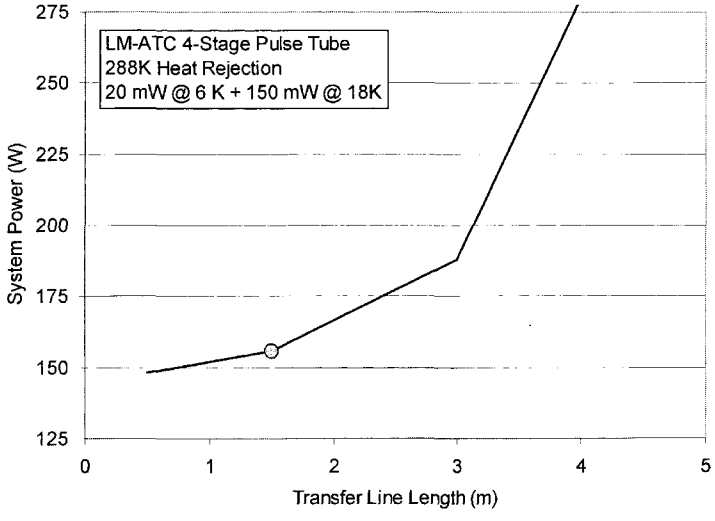

Figure 2. Predicted system power as a function of the separation between the compressor and coldhead. The 4-stage pulse tube is an efficient system for the ACTDP requirements. The cooling powers and heat rejection temperature are constant. Transfer line lengths in excess of 3 m require a prohibitively high system power. Our baseline design point is shown as a gray circle.

so we were instructed by JPL to focus instead on the Con-X configuration, where the separation is likely to be less than one meter. The cooler being built for the risk mitigation phase has a 1.5m long transfer line between the coldhead and compressor. In the time since completion of the study phase, JWST has officially baselined a solid cryogen cooler, and TPF has changed their configuration to allow for much shorter separation distances, so the decision to focus on the shorter transfer line seems in hindsight a very prudent one.

Cryocooler System

No major conceptual changes were necessary during the risk reduction phase. We matured the coldhead design using technology used on our GIFTS[5] and RAMOS[6] cryocoolers, so that the coldhead is an all-welded design that is readily flight qualifiable for future program needs.

One major benefit of the 4-stage pulse tube system is fast cooldown time. Unlike a J-T cooler, the cooling power is very large at higher temperatures. For example, with the entire cold-head at 100 K, the 4th stage has 500 mW of cooling power at nominal system power. For this reason, the cryocooler can cool large thermal masses in a relatively short time. The requirement is to cool 50 g of Cu to 6 K and 250 g of Cu to 18K in less than 50 hours; the predicted time to cool 1000 g of Cu at each stage is 23 hours, limited in part by the heat capacity of the regenerator matrices, which is comparable to or greater than the heat capacity of that mass of copper. With 10 kg of Cu on the 6 K stage, the predicted cooldown time is 7 days, as shown in Fig. 3.

Program Status

At this time we are building a prototype cold head and an engineering model compressor.

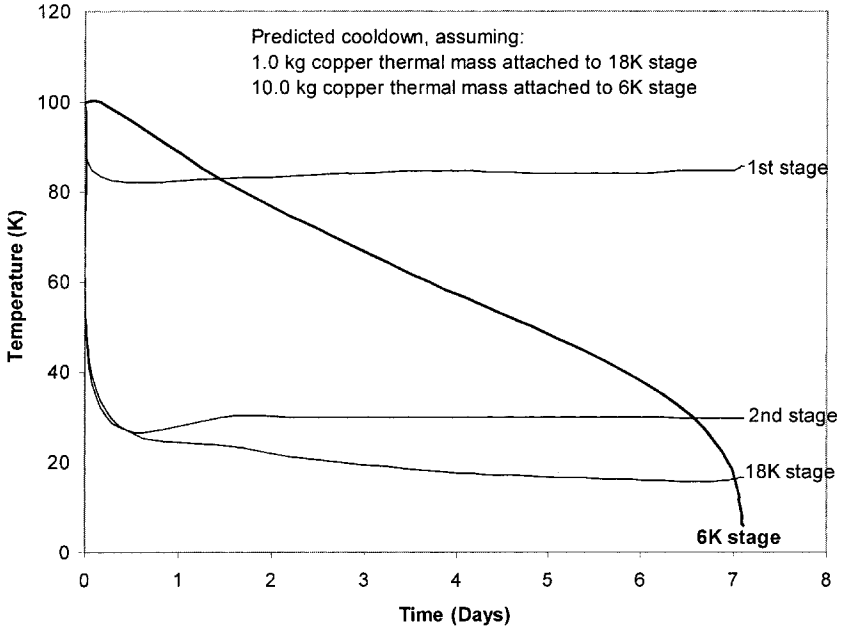

Figure 3. Cooldown curve for the LM-ATC 4-stage pulse tube cooler, assuming a 100K temperature when the cooler is turned on. The coldhead reaches its operating temperature in 7 days, despite cooling 10.0 kg of copper to 6 K and 1.0 kg of copper to 18K.

The development of the electronics has been deferred until later in the program at JPL's request. We have received nearly all of the parts for the coldhead and compressor, and assembly of these elements has been initiated.

CONCLUSION

Lockheed Martin's Advanced Technology Center has designed a robust, simple, high-efficiency 4-stage pulse tube cryocooler to meet the needs of NASA's powerful observatories. The cooler is designed to provide 20 mW of cooling at 6K simultaneously with 150 mW of cooling at 18K. The predicted system power is 156W, with a 288 K heat rejection temperature and a 1.5 m separation between the compressor and coldhead. We anticipate testing the prototype hardware in April of 2004.

ACKNOWLEDGMENT

We wish to acknowledge the support and sponsorship of this project by the Jet Propulsion Laboratory California Institute of Technology.

REFERENCES

1. Olson, J., Nast, T.C., Evtimov, B., Roth, E, "Development of a 10K Pulse Tube Cryocooler for Space Applications," *Cryocoolers 12,* Kluwer Academic/Plenum Publishers, New York (2002), pp. 241-246.
2. Ross, R.G., "A Study of the Use of 6K ACTDP Cryocoolers for the MIRI Instrument on JWST," *Cryocoolers 13,* Kluwer Academic/Plenum Publishers, New York (2005).
3. Nast, T.C., Olson, J., Evtimov, B., Kotsubo, V., "Development of a Two-Stage Pulse Tube Cryocooler for 35 K Cooling," *Cryocoolers 12,* Kluwer Academic/Plenum Publishers, New York (2002), pp. 213-218.
4. Foster, W.G. et al., "Development of a High Capacity Two-Stage Pulse Tube Cryocooler," *Cryocoolers 12,* Kluwer Academic/Plenum Publishers, New York (2002), pp. 225-232.
5. Nast, T.C. et al., "Lockheed Martin Two Stage Pulse Tube Cryocooler for GIFTS," *Cryocoolers 13,* Kluwer Academic/Plenum Publishers, New York (2005).
6. Frank, D. et al., "Lockheed Martin RAMOS Engineering Model Cryocooler," *Cryocoolers 13,* Kluwer Academic/Plenum Publishers, New York (2005).

Status of Pulse Tube Cryocooler Development at Sunpower

K. B. Wilson
Sunpower, Inc.
Athens, OH 45701

D. R. Gedeon
Gedeon Associates
Athens, OH 45701

ABSTRACT

Sunpower, Inc. and Gedeon Associates continue to develop linear-compressor driven pulse tube cryocooler technology under SBIR funding from NASA Goddard Space Flight Center. The first Phase II development effort between November 1999 and November 2001 established that a single-stage pulse tube driven by Sunpower's manufactured linear compressor technology achieves efficient performance and promises to reach mass production costs similar to Sunpower's commercial Stirling cryocoolers. In addition, efficient cooling with a two-stage cold head was demonstrated at 30K. Sunpower and Gedeon Associates recently completed another SBIR program from NASA Goddard Space Flight Center to develop a three-stage, high frequency, linear-compressor driven pulse tube cryocooler for cooling below 10 K.

This paper reviews the development history of pulse tube technology at Sunpower Inc., updates the status of the single-stage pulse tube cryocooler, and presents the results of the three-stage pulse tube cryocooler development program.

INTRODUCTION

Sunpower, Inc. has been developing Stirling cycle cryocoolers for nearly fifteen years and currently manufactures the CryoTelTM commercial line of low-cost, high-efficiency Stirling cryocoolers. The Stirling cryocoolers make use of a linear compressor, which is well suited for driving a pulse tube cryocooler. Sunpower's linear compressor technology can also be found in domestic household refrigerators and cryosurgical devices.

Gedeon Associates has developed modeling and optimization software for twenty years, and introduced the commercial "Sage" software ten years ago. The Sage graphical interface allows the user to assemble a single or multistage pulse tube cryocooler model from interconnected component pieces, then to optimize that model interactively.

Combining the relative experience in linear compressors and pulse tube modeling and design, Sunpower and Gedeon Associates have worked together for over four years developing high-efficiency, linear-compressor-driven pulse tube cryocoolers (PTC's). To date, NASA Goddard Space Flight Center in Greenbelt, MD has funded two collaborative Sunpower/Gedeon SBIR Phase II programs.

Cryocoolers 13, edited by R. G. Ross, Jr.
Springer Science+Business Media, Inc., New York, 2004

The goal of the first research effort was to demonstrate high efficiency in a single-stage PTC driven by Sunpower's linear compressor technology, which at that time was being manufactured for Sunpower's model M87 Stirling cryocooler.[1] The single-stage approach was to build a u-tube configuration after gaining experience with an in-line configuration. As a secondary goal, a second-stage u-tube cold head was to be constructed as an add-on to the single-stage u-tube configuration for a two-stage PTC. Each build incorporated inertance-tubes functioning as acoustic tuning devices between the pulse tube and reservoir volume. Performance for each configuration (in-line, u-tube and two-stage) was demonstrated at 100W electrical input power. The ultimate objectives were to establish the commercial potential of linear-compressor driven PTC's and whether they could be cost-competitive with the Sunpower M87 Stirling cryocooler.

The recently-completed SBIR Phase II program focused on the development of a high-frequency, linear-compressor driven three-stage PTC for cooling below 10K. Building on the multi-stage construction experience gained in the previous program, a new cryocooler was designed, fabricated and tested. Testing of particulate regenerators was conducted on an oscillating-flow regenerator test rig located at Sunpower on loan from NASA Glenn Research Center. Empirical data from this testing was used in the design and optimization of the second and third-stage cold heads which employed particulate regenerators. A 30 Hz, 300 We dual-opposed linear compressor was fabricated early in the program while the regenerator testing was underway. The cold head was built and tested sequentially: the first-stage cold head was tested as a stand alone single-stage PTC, then the second-stage cold head was added for a two-stage cryocooler. Finally the third-stage cold head was fabricated and tested to conclude the program.

SINGLE AND TWO-STAGE PULSE TUBE DEVELOPMENT REVIEW/UPDATE

Figures 1 through 3 show the pulse tube configurations that were constructed and tested. Detailed results from this effort were presented previously[1] and Table 1 summarizes the findings of the single and two-stage pulse tube development program.

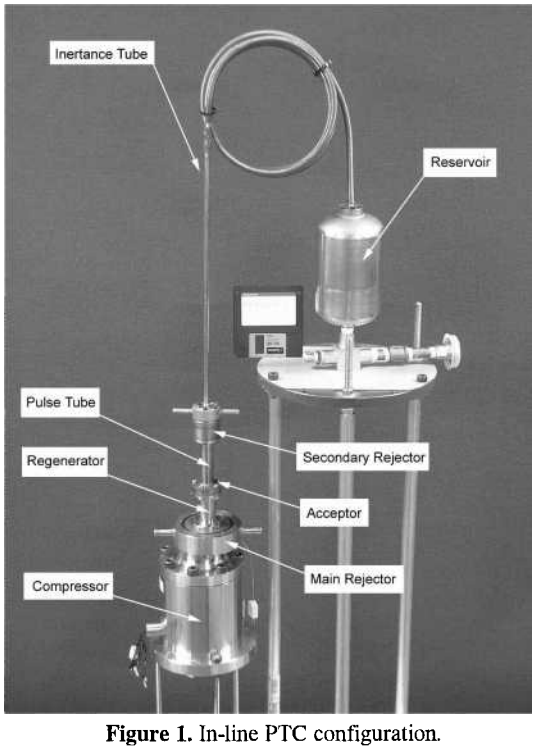

Figure 1. In-line PTC configuration.

Table 1. Summary of single and two-stage PTC development program (100 We input for all tests).

	In-line Configuration	U-Tube Configuration	2-Stage Configuration
1st Stage Lift	5.2 W @ 77K	4.8 W @ 77K	No-load @ ~80K
2nd Stage Lift			260 mW @ 30K

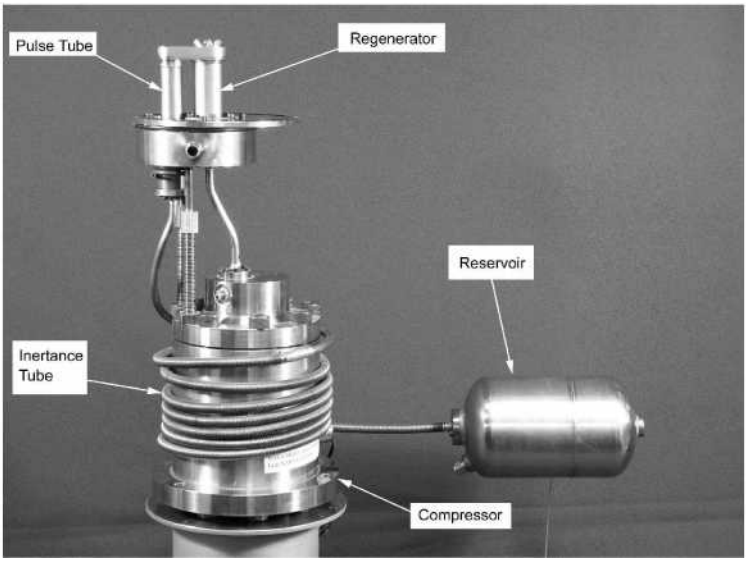

Figure 2. U-tube configuration.

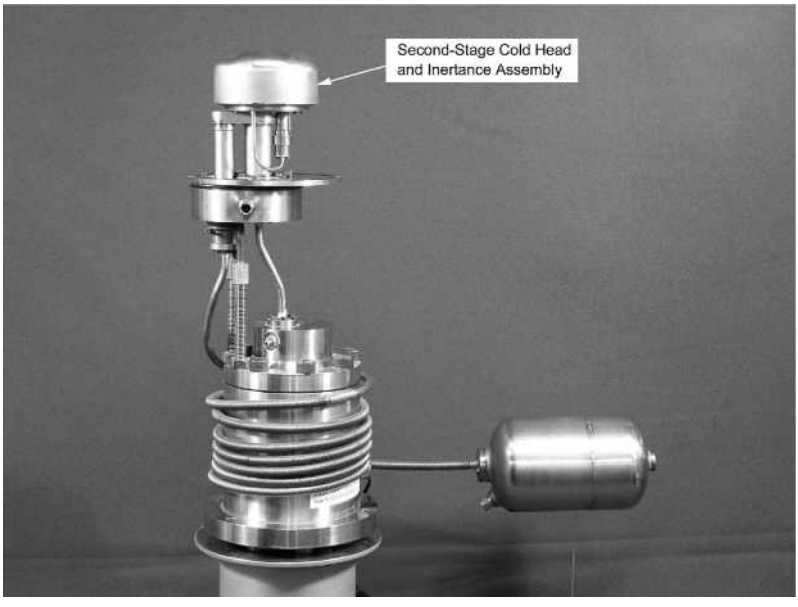

Figure 3. Two-stage PTC configuration.

At the beginning of the three-stage PTC development program, the hardware from the single and two-stage PTC program was used as a test bed for design improvements. One such design improvement increased the performance of the single-stage hardware. The original design of the heat exchangers used woven copper screens soldered to a copper housing. Dr. Ray Radebaugh at

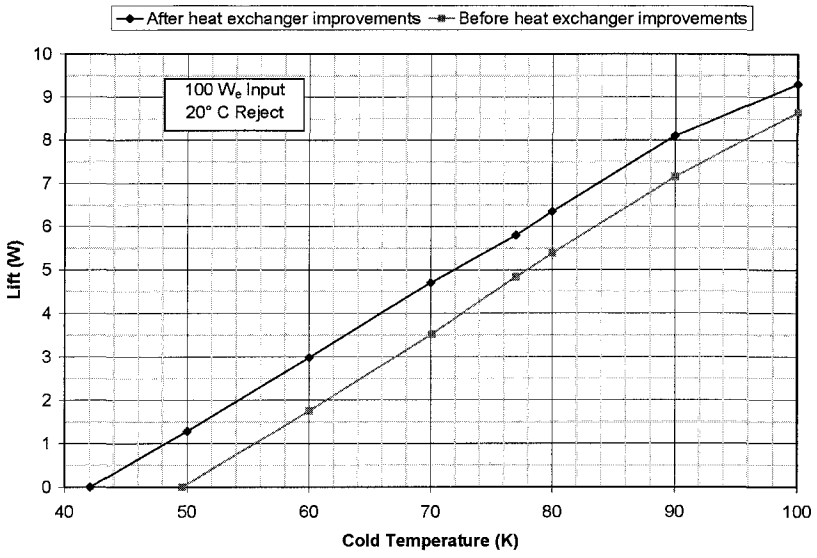

Figure 4. Performance of in-line PTC, before and after heat exchanger improvements.

NIST suggested that we try diffusion bonding to join the screens and their housing. We wanted to try the new bonding process simply to allow greater flexibility in the assembly technique of the three-stage cold head. However, we found that this new bonding procedure also increased the performance of the in-line PTC as shown in Figure 4. The in-line configuration now lifts 5.8 W at 77 K with 100 We input. Diffusion-bonded heat exchangers were never implemented into the u-tube and two-stage configurations from the original SBIR program.

Since the ultimate objective of the program was to establish the commercial potential of the single-stage u-tube PTC versus the production M87 Stirling cryocooler, we performed a preliminary cost study on a production design of the u-tube prototype. The component cost of the single-stage PTC was very similar (within a few percent) to that of the M87 Stirling cryocooler. Assembly costs should be similar to, if not lower than, those of the M87. So the preliminary analysis suggested that a single-stage u-tube PTC should be cost competitive with the Sunpower Stirling cryocooler.

THREE-STAGE PULSE TUBE DEVELOPMENT

As a result of the success of the first SBIR program, NASA Goddard Space Flight Center awarded a second SBIR Phase II contract to develop a three-stage PTC for cooling below 10K. The two-year contract, beginning in January 2002, involved the design, fabrication and testing of a three-stage cold head driven by a high-frequency, dual-opposed linear compressor. We employed the multi-staging u-tube design and construction techniques derived in the first SBIR program, with improvements in the bonding of heat exchangers as discussed earlier. Additionally, there were new challenges in the design and fabrication of low-temperature particulate regenerators. The cryocooler was constructed sequentially, allowing us to test the first stage as a stand-alone single-stage cryocooler to compare to the simulated results. Then we added the second-stage cold head and tested a two-stage PTC, followed by the three-stage PTC.

Linear Compressor (Pressure Wave Generator)

After evaluating design trades between performance of the cold head and compressor requirements relating to its size and mass, we decided on a 200 We, 30 Hz, dual-opposed-piston linear compressor. Actually, the linear motors are 150 We per side, 300 We total for the dual-opposed unit but the design point was targeted at 200 We. The 200 We level was more acceptable for the

Table 2. Features of the dual-opposed linear compressor.

Mass	11 kg
Physical Envelope	141ϕ mm x 335 mm OAL
Frequency	30 Hz
Electrical Power	300 W (150 W per side)
Total Swept Volume	100.8 cc
Charge Pressure	25 Bar

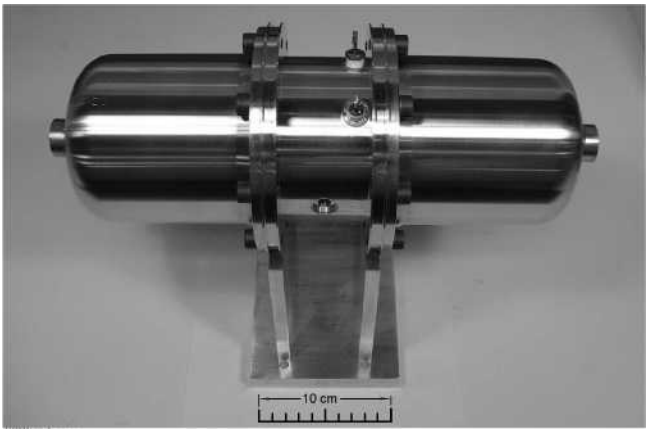

Figure 5. Dual-opposed linear compressor for three-stage PTC.

normal operating point of a spaceflight cryocooler and also allowed for some reserve power during cooldown. The prototype linear compressor is shown in Figure 5, with its features listed in Table 2.

Low Temperature Regenerators

Sunpower had no prior experience with packed-particle regenerator matrices that would be needed for the second and third stages of the cryocooler, so the program began by recommissioning an existing oscillating-flow test rig for use in characterizing regenerator flow resistance and heat transfer. Oscillating-flow testing gave us a way to directly compare the pressure-drop and heat-transfer correlations used in the Sage simulation with experiments. The test rig was originally developed by Sunpower and Gedeon Associates under NASA funding. It was designed to measure thermal energy flow down a regenerator sample subject to oscillating helium flow, similar to that which occurs in actual cryocooler operation. Data reduction software takes the results from a large number of data points at varying frequency, pressure, flow amplitude, and other data points, and derives general-purpose correlations for friction factor and Nusselt number using parameter estimation techniques. The hardware and data-reduction software are documented in a NASA contractor report.[2] The rig was last operated in 1993 and it was necessary to spend some time bringing the various pieces up to date and learning how to use them again. Once the hardware and software were functional, a few shakedown pressure-drop tests were run to verify that the rig was operational.

After studying construction designs for particulate regenerators, we established an epoxy-bonding technique similar to the process described by E. Luo, et al.[3] Initial testing of regenerator samples in the oscillating flow test rig required us to modify our overall regenerator design and bonding technique until we arrived at a robust design that could withstand substantial pressure amplitudes across the structure. To optimize the epoxy technique and address the effects of epoxy bonding on gas flow we first ran some nitrogen steady-flow pressure-drop tests on a number of matrices. Steady-flow tests are much simpler to conduct than an oscillating-flow test and quickly allowed us to evaluate the quality of a particular process. After several design and test iterations we had a satisfactory design and construction technique for the epoxy-bonded particulate regenerator matrix. The oscillating-flow testing was completed and the results were used for correlation of the Sage model-

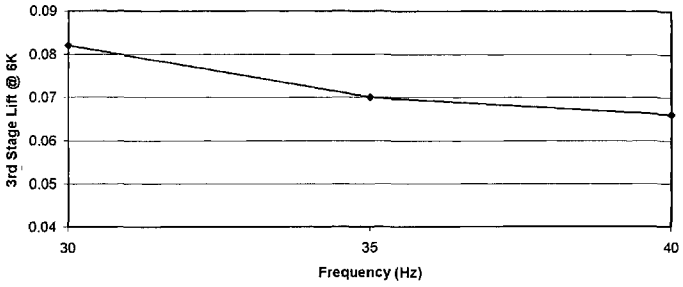

Figure 6. Simulated third-stage heat lift as a function of frequency.

ing software. Once this was done we were able to model and optimize the second and third stages of the cryocooler.

Spherical lead particles were used in the second stage regenerator and Er_3Ni rare-earth particles were used for the third-stage regenerator. Due to the expense of the Er_3Ni, no oscillating-flow testing was conducted with this material, only with the lead material.

Cold Head Modeling and Design

Initial studies of the effect of operating frequency suggested that lower frequencies would yield better results. For example, Figure 6 shows simulated third-stage cooling power as a function of frequency. Each data point represents a completely optimized machine. At 6 K, cooling power goes up from about 66 mW to 82 mW as frequency goes from 40 Hz down to 30 Hz. Below 30 Hz the size and mass of the compressor start to become issues, so we chose 30 Hz as our design-point frequency. These optimizations took place before we had oscillating flow characteristics for particulate regenerators, so only general trends were valid, not absolute cooling powers. For subsequent optimizations we lowered third-stage temperature down to 4.5 K and found that there was an even larger dependence on frequency as the low temperature decreased. These preliminary cold-head optimizations also highlighted the need for better understanding of packed-particle regenerators.

Our approach was to optimize the three-stage cold head for some design point and then investigate the performance at selected off-design conditions. We felt that the most important design condition was with the pulse tube orientation other than in the favorable cold-end-down position. Sage has the capability to simulate pulse tube orientation by way of a gravitational-stabilization factor included in the calculation of the manifold-induced pulse tube convection loss. Without the gravitational-stabilization factor the manifold convection loss corresponds to weightless operation. It also roughly corresponds to terrestrial horizontal orientation, except for an unknown amount of free-convection with the gravitational field acting perpendicular to the axis of the pulse tube. Originally we optimized the cold head for coldend down performance, then checked the performance in a weightless environment. We found the off-design performance was drastically less than the optimized performance. So the gravitational-stabilization factor was turned off during cold head optimization, making the design point a weightless environment. The hope was that a cold head designed for weightless operation would not perform too much worse than one optimized for cold-end-down orientation. This did indeed turn out to be the case. The main difference between the two optimizations was that the pulse tubes are somewhat thinner in the weightless optimization and the turning-manifold flow areas somewhat larger.

The second-stage regenerator was designed as an entirely lead matrix. In the third-stage regenerator we considered two options: 1) a layered structure of lead and Er3Ni, with lead for the first 30% of volume then Er3Ni for the remaining 70%, and 2) a monolithic packing of only Er3Ni. Due to the expense of the Er3Ni we decided on the layered regenerator. Table 3 shows the final simulated results of the performance of the optimized three stage cold head as well as the simulated design of stand-alone two and single-stage cold heads, all with 200 W PV power.

Table 3. Final predicted performance results of Sage simulation (200 W PV power).

	3 Stage Cold Head	2 Stage Cold Head	1 Stage Cold Head
1st Stage Lift	4.8 W @ 80K	4.9 W @ 80K	15.8 W @ 80K
2nd Stage Lift	270 mW @ 27K	600 mW @ 20K	
3rd Stage Lift	10 mW @ 5.5K		

Figure 7. Assembled three-stage cold head without inertance assemblies.

Fabrication

The machining of the manifold components of each stage were outsourced to a precision CNC machine shop specializing in the use of CAD/CAM technology. Other than those components, all parts were machined at Sunpower, Inc. Most joining processes, such as the diffusion bonding of the heat exchangers, brazing and welding were also outsourced. However, some specialized joining techniques of the inertance assemblies were developed in-house.

Figure 7 shows the assembled three-stage cold head without the inertance assemblies. Figure 8 shows the entire pulse tube cryocooler test setup. The first-stage inertance tube is wrapped around the first-stage reservoir mounted perpendicular to the linear compressor.

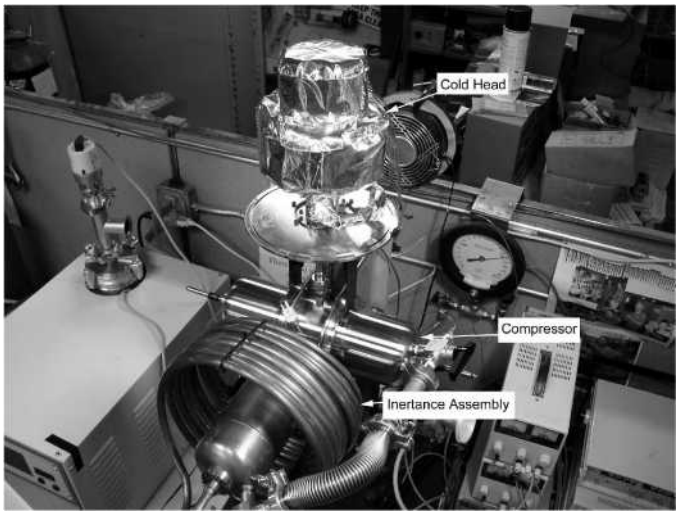

Figure 8. Experimental setup of three-stage PTC.

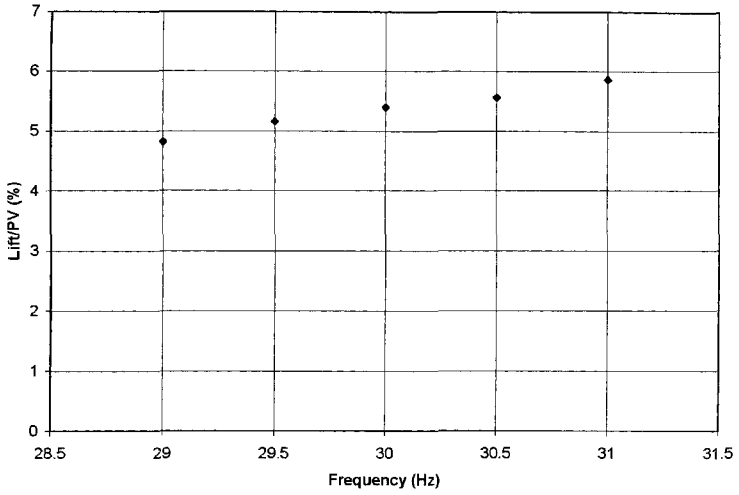

Figure 9. Frequency-dependent performance of single-stage cold head.

First-Stage Testing

The first stage consistently achieved about 9.2 W of lift at 80 K with 200 We input power. Compressor PV power was also measured and the compressor was found to be operating very efficiently, typically from 87% to 90%. With equivalent piston amplitude between Sage and experiment, Sage predicted compressor PV power quite closely, but predicted a higher cooling power.

Testing suggested that efficiency would increase by running at a higher operating frequency. Figure 9 shows the single-stage experimental performance for fixed piston amplitude versus varying operating frequency. Later testing of the first-stage inertance assembly revealed some insight into the performance by showing that the inertance assembly was optimally tuned around 35 Hz. This means that for a given piston amplitude, the largest amount of PV power produced was at 35 Hz. Of course the inertance assembly is only one piece of the system, so as the frequency increases to gain performance in the inertance assembly, other factors can change such as the mechanical tuning of the linear compressor.

Second Stage Testing

Figure 10 shows the experimental measurements and Sage predictions for second-stage cooling power as a function of temperature. During the testing the first-stage temperature remained close to 85 K, the compressor piston amplitude was about 11.3 mm (corresponding to about 160 W PV power input) and the first-stage cooling power ranged from about 0.5 W down to 0.1 W. The plot shows that Sage and experiment are similar.

Part of the discrepancy is due to Sage over-predicting the pressure amplitude in the compression space. When the pressure amplitude in Sage is decreased, simply by decreasing the piston amplitude, the agreement to the experimental load curve is much better. Conversely, increasing the experimental compressor pressure amplitude should bring the experimental cooling power close to the Sage prediction.

Third-Stage Testing

Unfortunately by the time we had the three-stage PTC assembled and ready to test, our funding for the program was virtually depleted. Therefore we were only able to run one three-stage PTC performance test and the performance was less than the target performance for the cryocooler. Our most plausible explanation of what happened is that we had underestimated the load imposed on the second stage by the presence of the third stage. As a result the second stage stalled at a temperature higher than 27 K as designed. This left the third-stage inertance assembly out of tune with the

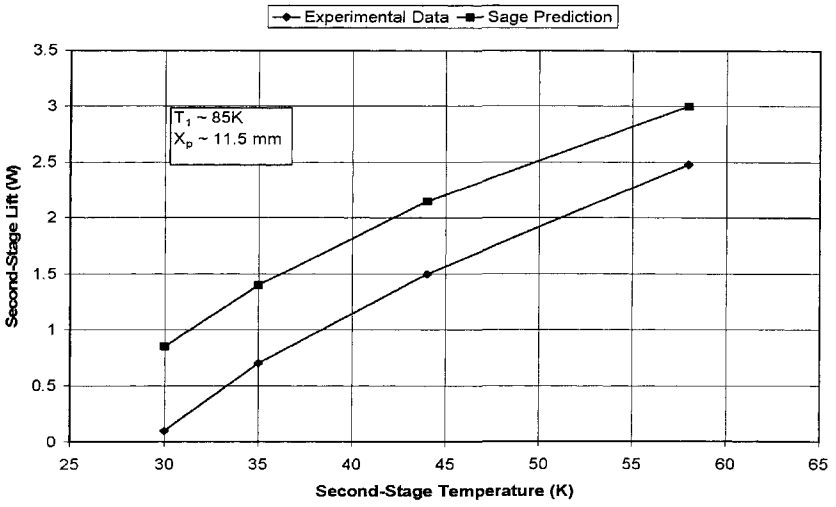

Figure 10. Comparison of experimental data and Sage-predicted performance on second-stage cooling power.

result that the third stage also stopped cooling at a temperature higher than anticipated. We feel the resolution to the problem is simply a matter of diverting less PV power from the second stage by suitable modification to the third stage regenerator, possibly something as simple as increasing its flow resistance. The result of that should be to allow the second stage to continue cooling to its intended operating temperature, at which time the third stage should also begin to perform as intended.

CONCLUSIONS

Sunpower, Inc. and Gedeon Associates have completed two SBIR Phase II development programs under funding from NASA Goddard Space Flight Center. The first SBIR program demonstrated that single and two-stage pulse tube cryocoolers driven by the same commercial linear compressor technology used in Sunpower's Stirling cryocoolers have high efficiency and are commercially viable. In the second SBIR program a three stage pulse tube cryocooler driven by a dual-opposed linear compressor was constructed and tested. There were many benefits to this development program including the modeling and fabrication of low-temperature regenerators and the design and construction techniques for multistage cold heads. Performance of the two-stage cold head was verified to be in close agreement with simulation. Available program resources were exhausted prior to completion of the technical goals. The next steps in the troubleshooting of the three-stage PTC have been identified and further funding is being pursued.

ACKNOWLEDGMENTS

We would like to thank NASA Goddard Space Flight Center for their continual support in the development of pulse tube technology at Sunpower, Inc.

REFERENCES

1. K.B. Wilson and D.R. Gedeon, "Development of Single and Two-Stage Pulse Tube Cryocoolers with Commercial Linear Compressor," *Cryocoolers 12*, Kluwer Academic/Plenum Publishers, New York (2003), pp. 139-147.
2. D. Gedeon and J.G. Wood, "Oscillating Flow Regenerator Test Rig: Hardware and Theory with Derived Correlations for Screens and Felts," NASA CR 198442, Feb. 1996.

3. E. Luo et al., "Fabrication and testing on monolithic single bin bed by low temperature epoxy bonding," *Adv. in Cryogenic Engineering*, Vol. 47B, Amer. Institute of Physics, Melville, NY (2002), pp. 1011-1018..

Development of a Small-Scale Collins-Type 10 K Cryocooler for Space Applications

C.L. Hannon[1], B.J. Krass[1], J. Gerstmann[1], G. Chaudhry[2], J.G. Brisson[2] and J.L. Smith Jr.[2]

[1]Advanced Mechanical Technology, Inc.
Watertown, MA, USA 02472

[2]Cryogenic Engineering Laboratory
Massachusetts Institute of Technology
Cambridge, MA, USA 02139

ABSTRACT

Future spacecraft cooling and sensing systems will require advanced multi-stage cryocoolers capable of providing continuous cooling at multiple temperature levels ranging from 10K to 95K. A multi-stage 10K cryocooler is under development that applies microelectronic sophistication to achieve high efficiency in a reliable, compact design. The cryocooler is based upon a novel modification of the Collins cycle, a cycle commonly used in many high-efficiency terrestrial cryogenic machines. Innovations of the design include *floating piston expanders* and electromagnetic *smart valves*, which eliminate the need for mechanical linkages and thereby reduce the input power, size, and weight of the cryocooler in an affordable modular design. The *floating piston expander* and *smart valves* have been successfully developed in room temperature experiments using a series of proof-of-concept component prototypes. These experiments enabled the development of a sophisticated LabView based control algorithm. In parallel to this effort, a manufacturing method was developed to enable production of very long continuous lengths of small bore finned tubing. This tubing is used in the highly effective recuperative heat exchanger associated with each stage of the cryocooler. A three stage engineering prototype has been designed that integrates the *floating piston expander* and recuperative heat exchanger as a functional cryocooler. The engineering prototype has been assembled and is currently undergoing development testing. This paper will present the results of the room temperature component development testing, the design of the engineering prototype, the results of initial engineering prototype development testing, and the direction of future development.

INTRODUCTION

Many current cryocoolers, most notably Stirling and pulse-tube types, have achieved compactness and reliability by adopting mechanically simple cold head configurations at the expense of thermodynamic efficiency. Large multi-stage terrestrial cryogenic refrigerators are able to achieve higher thermodynamic efficiencies, but do so by employing mechanically complex designs that are not feasible at a small scale. The ideal 10 K spacecraft cryocooler would have an efficiency com-

Cryocoolers 13, edited by R. G. Ross, Jr.
Springer Science+Business Media, Inc., New York, 2004

parable to that of large terrestrial machines, i.e., a power requirement less than 1 kW per watt of cooling at 10 K, with the compactness and reliability of a pulse-tube or Stirling cryocooler. An efficient multi-stage 10 K cryocooler with many of the above attributes is currently under development by AMTI in collaboration with the Cryogenic Engineering Laboratory at MIT. This design achieves compactness and reliability by using modern microelectronics to enable complex valve timing in a mechanically simple yet efficient cold head design. The cryocooler is based upon a novel modification of the Collins cycle that is used in many high-efficiency terrestrial cryogenic machines. The technology concepts enabling this innovative design were presented previously[1]. A system schematic is illustrated in Fig. 1.

A comparison of the thermodynamic performance of refrigeration at 4 K clearly shows the potential for successful cryocooler design using the new paradigm. The large-scale, high-efficiency machines based on the conventional Brayton and Collins cycles routinely operate with input powers of about 740 W per Watt of refrigeration, which is only 10 times the ideal Carnot power at 4 K. Small commercial sub-10 K Gifford-McMahon and pulse tube cryocoolers capable of about 1W of cooling at 4 K have been available for several years (Daikin, Aisin Seiki, Cryomech, Sumitomo, Leybold). These devices typically require about 5 kW - 8 kW per Watt of cooling at 4 K[2], which is about 70 to 100 times the Carnot requirement. The modified Collins cycle under development is particularly well suited for cryocoolers operating from 4 K up to about 30 K, above which temperature the thermodynamic losses of the mechanically simpler cryocoolers become less dominant.

FLOATING PISTON EXPANDER

The *floating piston expander* (FPE), first studied by Jones[3] and further developed by Smith[4], is a key element in the cryocooler concept. By employing a floating piston, the expander provides a highly effective expansion at a high-pressure ratio without the size, weight, and geometric constraints of a mechanical crosshead to stroke the piston and operate the cold valves via pull rods. The expander consists of a piston (or displacer) that floats with the gas in a closed cylinder. At the cold-end of the cylinder, high-pressure gas is admitted through a smart electromagnetic inlet valve, and low-pressure gas exits through a smart electromagnetic exhaust

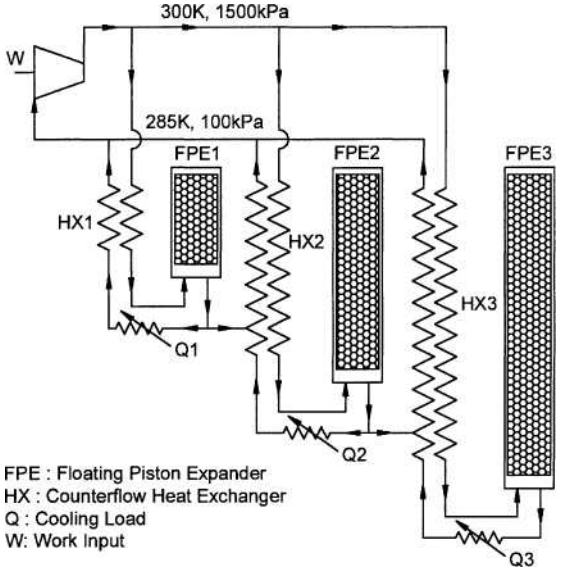

Figure 1. Modified Collins Cycle

valve. A microprocessor controls the opening and closing of the valves to achieve efficient expansion of the gas, and to minimize losses in the valves. The piston floating in the cylinder moves to keep the pressure in the warm-end displacement volume nearly the same as the pressure in the cold-end volume. The warm end has multiple electronic solenoid valves that connect to reference-pressure reservoirs. The warm end valves are flow-control throttling valves that control the velocity of the floating piston by controlling the rate of gas flow into and out of the warm cylinder volume. With this configuration, the helium pressure on the warm end of the piston is always essentially the same as the pressure on the cold end. The piston floats quasi-statically on the gas in the cylinder with low velocities set by the throttling of the gas in and out of the warm cylinder volume. The cold valves always open when there is essentially no pressure difference across the valve. This reduces the actuating force required of the cold valve actuators.

Figure 2 illustrates the general configuration of the first prototype FPE built for this project. Four valves at the warm-end control gas flow in and out of the warm-end volume. The high pressure gas source acted as the highest reference-pressure reservoir, and the atmosphere acted as the lowest reference-pressure reservoir. A single intermediate-pressure reservoir was provided that was connected to the warm-end volume by two valves. (For clarity in Figure 2, only one valve is shown connecting to the reservoir.) With warm-end connections to the high-pressure source and to atmosphere, a significant amount of high pressure gas bypassed the cold-end expansion volume. This configuration had been chosen so that at the start of both the intake and exhaust events, the pressure difference across the piston would be nearly zero. This would prevent rapid and uncontrollable piston acceleration.

Experience with the first FPE configuration demonstrated that piston dynamics were controllable even with small pressure differences across the piston. An alternative warm-end configuration was built that eliminated the connections to the high-pressure source and to atmosphere. It is clear that the Figure 2 configuration can be approximated in a closed warm-end configuration if a large number of reservoirs are connected to the warm-end volume with pressure levels cascading down from just less than system high pressure to just greater than system low pressure. With a large enough number of warm-end pressure levels the differential pressure across the piston at the start of the intake and exhaust events can be minimized. With four warm-end valves available, four reservoirs were installed so that the warm-end was closed. This configuration is illustrated in Figure 3. Pressure in each of the four reservoirs was pre-set, with the highest pressure reservoir set to slightly less than the system high pressure level and the

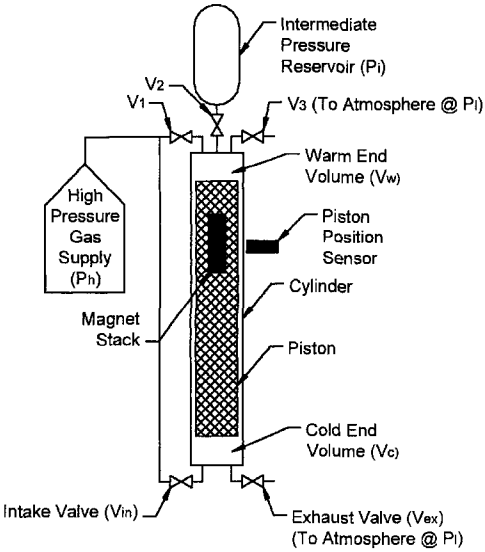

Figure 2. Single Reservoir FPE

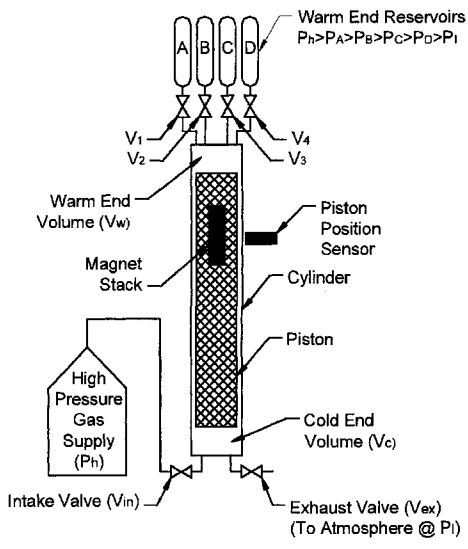

Figure 3. Four Reservoir FPE

lowest pressure reservoir set to slightly higher than the system low pressure level. The other two reservoirs were set to a high-intermediate pressure and low-intermediate pressure, respectively. In operation, the four reservoir pressures self-adjusted to steady state levels based on the valve timing criteria.

The ideal steady-state expansion cycle is shown as a PV diagram in Figure 4. The cycle starts with the piston in a position where the cold volume is a minimum and the pressure in the warm volume is equal to the pressure in reservoir A (state 1 on the diagram). At this point, all valves are closed. The cycle proceeds as follows:

- **Process 1-1a (Blow-in)** The inlet valve is opened. Helium at high pressure (P_h) enters the cold volume. The pressure in the cold end is driven up to P_h. The piston moves up, compressing the gas in the warm volume.
- **Process 1a-2 (Intake)** The inlet valve is kept open and the warm end valve V_1 (leading to reservoir A) is opened. Helium flows from the warm volume into reservoir A. High pressure helium continues to flow into the cold volume, maintaining the pressure inside the cylinder at P_h. When the cold volume has reached a cut-off volume V_{co}, the inlet valve is closed.
- **Process 2-3 (First expansion)** Warm valve V_1 is kept open. Helium from the warm volume flows into reservoir A. The pressure in the cylinder decreases. The helium in the cold volume expands so that the pressure in the cold end matches the pressure in the warm end. When the pressure in the cylinder falls to P_A, valve V_1 is closed.
- **Process 3-4 (Second expansion)** Warm valve V_2 is opened. Helium now flows from the warm volume into reservoir B. The helium in the cold volume expands further. This process continues until the pressure in the cylinder reaches P_B, at which point valve V_2 is closed.
- **Process 4-5 (Third expansion)** Warm valve V_3 is opened. Helium flows from the warm volume into reservoir C, while the helium in the cold volume expands. V_3 is closed when the pressure in the cylinder equals P_C.
- **Pressure 5-6 (Fourth expansion)** Warm valve V_4 is opened. Helium flows from the warm

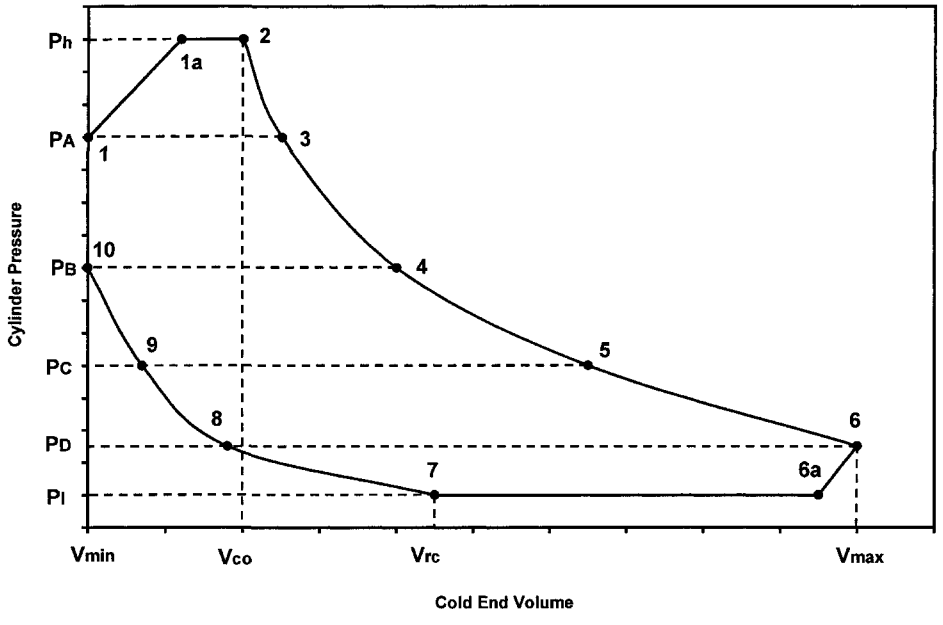

Figure 4. Four Reservoir Ideal P-V Diagram

volume into reservoir D. The helium in the cold volume continues to expand. V_4 is closed when the cylinder pressure equals PD.

- **Process 6-6a (Blow-down)** The exhaust valve is opened. Because the pressure in the cylinder (P_D) is greater than the outlet pressure (P_I), helium from the cold volume flows through the exhaust valve. The pressure in the cylinder falls, and the helium in the warm volume begins to expand. This process continues until the pressure in the cylinder equals P_I.
- **Process 6a-7 (Exhaust)** The exhaust valve is kept open, and the warm valve V_4 is opened. Helium from reservoir D (at a pressure P_D) flows into the warm volume. The piston moves downwards forcing the helium in the cold volume out through the exhaust valve. Through this process, the pressure in the cylinder stays at P_I. This process continues till the cold volume has reached the recompression volume V_{rc}, at which point the exhaust valve is closed.
- **Process 7-8 (First recompression)** Valve V_4 is kept open. Helium from reservoir D continues to flow inside the warm volume. The piston moves down, compressing the helium in the cold volume. The process continues until the pressure in the cylinder equals P_D. At this point, V_4 is closed.
- **Process 8-9 (Second recompression)** Warm valve V_3 is opened and helium from reservoir C enters the warm volume. The piston moves down and the pressure in the cylinder rises to P_C, at which point V_3 is closed.
- **Process 9-10 (Third recompression)** Warm valve V_2 is opened and helium from reservoir B enters the warm volume until the cylinder pressure reaches P_B. V_2 is closed at the end of the process.
- **Process 10-1 (Fourth recompression)** Valve V_1 is opened and helium from reservoir A enters the warm volume. The pressure inside the cylinder rises to P_A, at which point the valve is closed and the cycle is repeated.

It is possible that the piston will reach bottom dead center at some point during one of the four recompression processes. If this happens, the pressure in the cold volume will not change until Process 1-1a begins. The pressure in the warm volume will continue to increase as described above. Thus there will be a pressure differential across the piston until the cycle reaches state 1.

The original prototype was modified to connect each of the four warm-end valves to individual reservoirs. The initial charge in each reservoir was supplied by gas from a common high pressure manifold. Fill and purge valves allowed pressure levels to be pre-set in each reservoir. In practice it was important to carefully set the pressure levels in reservoirs A and D since these determine the duration of the blow-in and blow-out steps. The pressure for reservoirs B and C only needed to be preset to reasonable intermediate pressures. In operation, the pressure levels in reservoirs B and C settled to "natural" steady state levels based on overall cycle timing. Some adjustment of the pressures in reservoirs A and D was required in operation to maintain the desired differentials to system high and low pressure. Eventually the control system will be developed to self-monitor and adjust those pressures using slight variations in valve timing.

The performance of the four reservoir prototype is shown in Figure 5. Several cycles are plotted on a P-V diagram. All have the same characteristic shape and closely match the ideal P-V diagram shown in Figure 4. Piston acceleration and velocities during the blow-in and blow-down steps proved to be very reasonable and controllable. As with the earlier single reservoir prototype, the four reservoir prototype was operated as an open system where expanded gas was vented to the atmosphere. As expected, the overall rate of gas consumption was significantly diminished. Based on the success of this prototype, all further expander development will be based on this configuration.

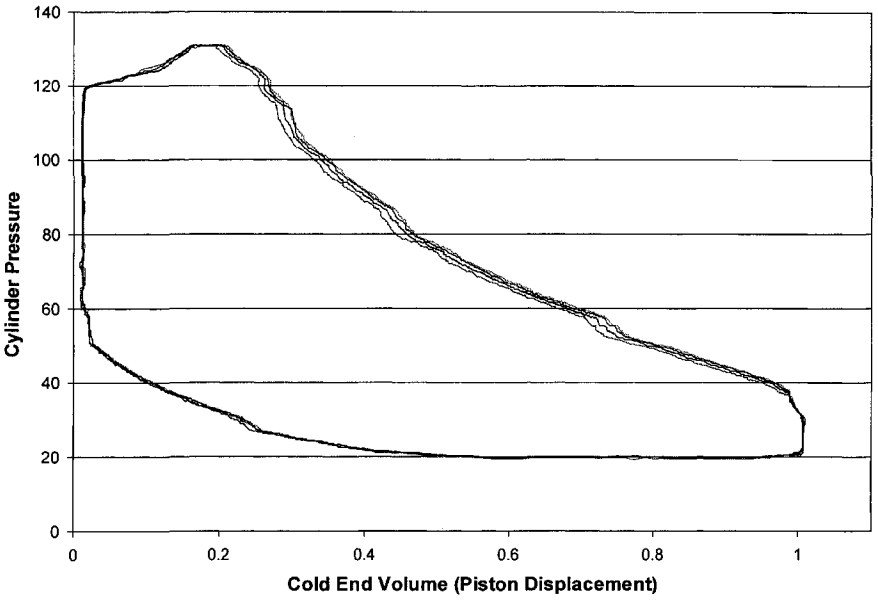

Figure 5. Four Reservoir Prototype PV Diagram

ELECTRO-MAGNETIC SMART VALVES

The FPE prototypes were supplied with prototype electro-magnetic *smart valves* at the cold end. As shown in Figure 6, the valve arrangement is a concentric design, with the exhaust valve located concentricly outside of the inlet valve. For both the inlet and exhaust valves, action is by the motion of a valve disk relative to a valve plate, which is also the cylinder head of the expander. When against the plate, the valve disk is held against the valve seats by the gas pressure difference across the valve ports and by permanent magnets acting as a valve spring. The valve is opened by a magnetic field that pulls the valve disk away from the plate. The valve port area of each valve consists of three small-diameter holes through the plate equally spaced on a circle. As in compressor valves, multiple ports with small dimensions result in a small valve lift for the required flow area. The small lift allows an optimum magnetic design for a quick opening and closing valve with minimum impact stress.

A toroidal yoke of ferromagnetic stainless steel surrounds a ring coil of copper wire. The valve disk of ferromagnetic stainless steel is separated from the flat face of the yoke by a small air gap that decreases as the valve disk moves to open the valve. When current flows in the coil, magnetic field flows through the yoke, across the air gap, through the valve disk and back to the yoke creating closed flux lines around the coil. The magnetic field crossing the air gap causes an attractive force between the valve yoke and the valve disk that is sufficient to lift the valve disk off of the non-magnetic cylinder head against the gas pressure difference across the valve. When the current is turned off the attractive force between the yoke and the disk is near zero (there is some residual magnetic flux in the yoke). The disk is pulled back to the cylinder head plate by permanent magnets mounted in the plate and by the pressure difference generated as the gas flow is interrupted.

The circuits that supply current to the valve actuator coils are designed to minimize the resistive (I^2R) heating in the cold valve coils. A high current pulse is supplied for a few milliseconds to crack the valve open. As the valve opens, the pressure differential across the valve decreases rapidly as does the force from the permanent magnets. This allows a much lower current level to complete the valve opening and hold the valve open for the 70-100

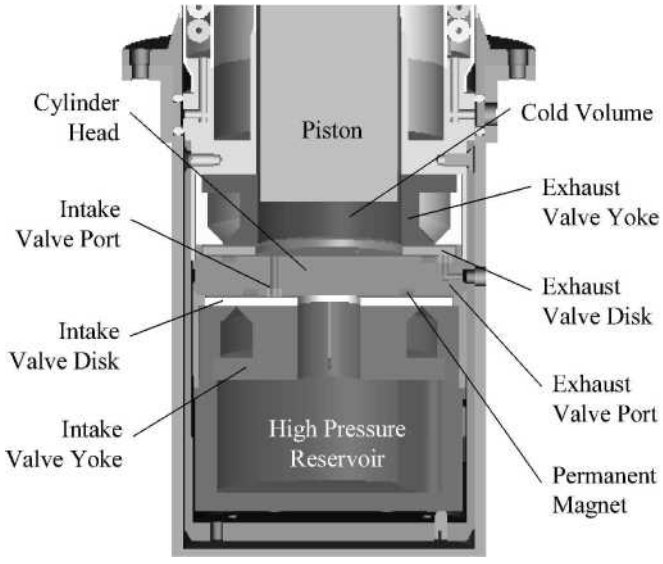

Figure 6. Electromagnetic *Smart Valve*

milliseconds required to complete an intake or exhaust event. (The small air gap in the magnetic flux path when the valve is open requires only a low current level to produce a sufficiently high magnetic force between the valve disk and the yoke so that the valve is held open.) Since resistive heating in the coil is proportional to the square of the current level, this approach reduces the resistive heating load integrated over a complete intake or exhaust event to less than 1 mW.

A typical current-voltage response is shown in Figure 7. To initiate actuation of the intake valve, the voltage is driven to its extreme negative potential which results in a rapid current rise to about 140 mAmps which was the pre-set peak current pulse level. After about 6 msec, the

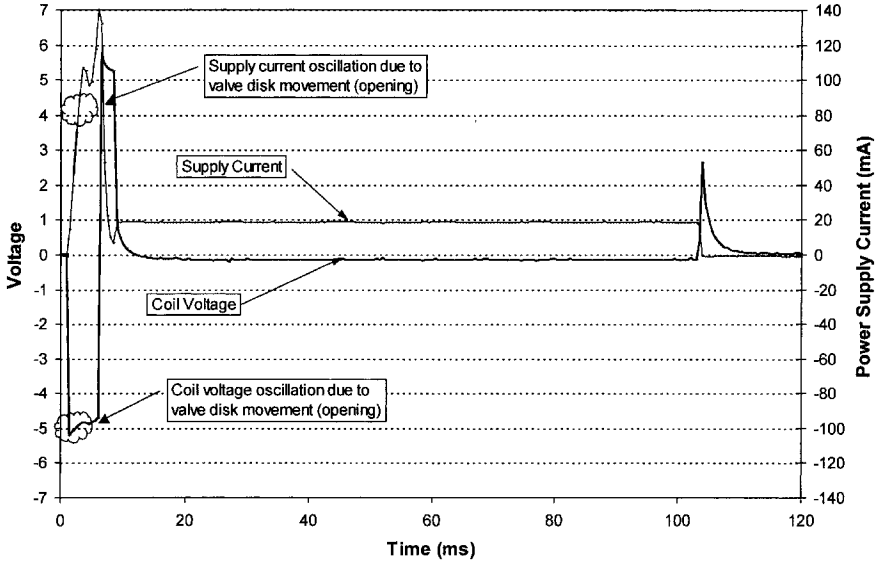

Figure 7. *Smart Valve* Shaped Voltage-Current Pulse

voltage is driven to its positive extreme to rapidly reduce the current from the peak level to its pre-set holding level of 20 mAmps. Only a nominal voltage is required to supply the holding current. To close the valve, the voltage is again driven positive to pull the current down to zero, at which point the voltage rapidly decays to zero. Transients can be seen in the voltage trace at the valve opening that are related to the dynamics of the valve disk and its effect on the magnetic field and coil inductance.

SINGLE CRYOCOOLER STAGE PROTOTYPE TESTING

Over the course of this project four distinct prototype expanders were assembled for room temperature testing. These early prototypes enabled the development of LabView based software to control the expansion cycle, the development of lightweight pistons and a piston position sensor, demonstration of the smart electromagnetic valves and the high-speed switching current supply for the smart valves. During testing of these prototypes a significant cooling effect could be sensed by touching the cold end of the expander, and on humid days there was an obvious build up of condensation and even frost. However, since the tests were conducted in the open, it was not possible to measure thermodynamic performance because heat transfer to the ambient environment was an overwhelming loss mechanism.

A new prototype has been fabricated and assembled which will be the first prototype cryocooler. This prototype is designed to be the lowest temperature stage of a three-stage cryocooler arranged as illustrated in Figure 1, and will be used to measure the thermodynamic performance potential of the cycle. The warm and cold end configurations are identical to that of the most recent room temperature prototype, but this prototype will include an integral heat exchanger and the entire apparatus will be installed in a an evacuated cryostat. The pre-cooling stream from the second stage will be simulated by helium gas supplied from a dewar. Where the previous prototypes had all operated as open systems in which expanded low pressure gas was exhausted to the atmosphere, a packaged two-stage compressor is used to supply up to 15 bar helium to the prototype cryocooler.

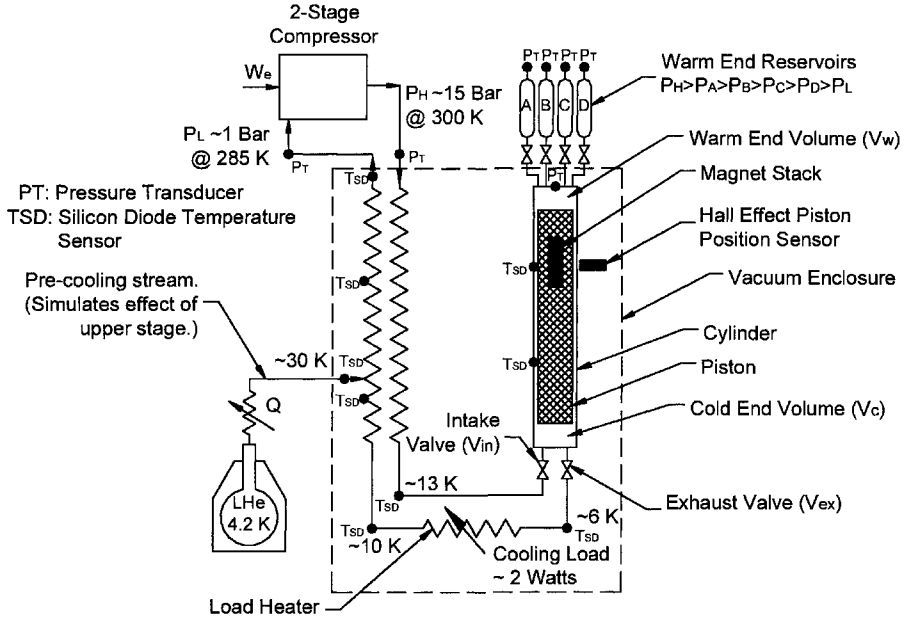

Figure 8. Schematic of Prototype Third Cryocooler Stage

The prototype single-stage cryocooler is illustrated schematically in Figure 8. Pressure transducers are provided to measure cylinder pressure, the reservoir pressures and the compressor suction and discharge pressures. A total of 10 silicon diode temperature sensors are also provided. Only cylinder pressure, the reservoir pressures and piston position are required for cycle-to-cycle control of the expansion cycle. The remaining pressure transducers and the temperature sensors are provided to measure thermodynamic performance and to characterize cryocooler performance. The heat exchanger for this prototype was designed in such a way that the expander can initially be assembled without the heat exchanger to enable measurement of the expander efficiency. Copper tubes connect the warm-end connections to and from the compressor to the cold-end intake and exhaust valves. After the expander efficiency data has been collected, the FPE assembly can be removed from the stage enclosure and the heat exchanger can be added to assembly.

As of the writing of this paper, the expander, less its heat exchanger, has been assembled and instrumented. Shakedown testing of the test apparatus has been completed such that repeatable cyclic operation of the expander has been achieved. A P-V diagram (Figure 9) has been obtained and the performance of this expander is observed to be very similar to that of the previous prototype, and to more closely match the characteristic shape of the ideal P-V diagram illustrated in Figure 7. During this preliminary testing a minimum cold-end temperature of about 245 K was measured with a pressure ratio of about 9:1 and a high pressure warm-end temperature of 300 K. The cold-end temperature was measured by a temperature sensor intended to measure the temperature of the high-pressure gas at the discharge of the heat exchanger. In the configuration used for shakedown testing it was the best positioned sensor to assess the cold-end temperature. The actual minimum temperature is assumed to have been lower. The configuration used to measure expander efficiency will provide for a direct measurement of the expanded low-pressure gas.

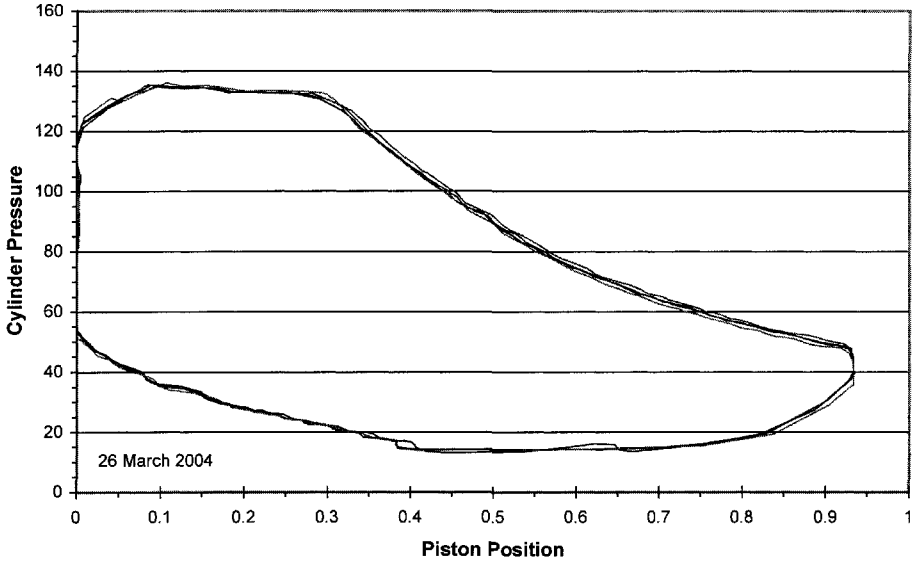

Figure 9. P-V Diagram for Single Cryocooler Stage Prototype

FUTURE WORK

Expander efficiency will be measured shortly and operation as a single-stage cryocooler should begin by mid-to-late Spring 2004. Data from the single-stage prototype will guide the design of a complete 3-stage cryocooler prototype. The current control system will be developed to enable dedicated microprocessor control of cycle-to-cycle operation with supervisory control by a higher level algorithm. It is expected that the 3-stage prototype will be assembled and under test by the Summer of 2005.

ACKNOWLEDGEMENTS

This work was supported by a series of SBIR Grants from the Missile Defense Agency. Previously Contract No. DASG60-01-C-0051 administered by the U.S. Army Space and Missile Defense Agency, and currently Contract No. F29601-02-C-0155 administered by the U.S. Air Force Research Laboratory.

REFERENCES

1. Hannon, C.L., Gerstmann, J., Traum, M., Brisson, J.G., Smith Jr, J.L., "Development of a Medium-Scale Collins-Type 10 K Cryocooler," *Cryocoolers 12*, Kluwer Academic/Plenum Publishers, New York (2003), pp. 587-594.
2. CILTEC Cryocooler Database, available on the Internet from the Center for Interfacing Low-Temperature Electronics and Coolers, www.ciltec.org.
3. Jones, R.E. and Smith Jr., J.L., "Design and Testing of Experimental Free-Piston Cryogenic Expander," *Advances in Cryogenic Engineering,* **45B,** Kluwer Academic/Plenum Publishers, New York (2000), pp. 1485-1491.
4. Smith Jr., J.L., Brisson, J.G., Traum, M.J., Hannon, C.L., and Gerstmann, J., "Description of a High-Efficiency Floating Piston Expander for a Miniature Cryocooler," *Proceedings of IMECE2002*, Vol. 3, Paper Number IMECE2002-33402, American Society of Mechanical Engineers, New York (2002).

STI's Solution for High Quantity Production of Stirling Coolers

Amr O'Baid, Andreas Fiedler, Abhijit Karandikar

Superconductor Technologies Incorporated
Santa Barbara, CA 93111

ABSTRACT

The mission of Superconductor Technologies Inc. (STI) is improving the quality of wireless. Through the use of its patented High Temperature Superconductor (HTS) technology, STI has created a cryogenic receiver front-end (CRFE) used by major wireless operators to enhance their network performance. The "Sapphire" cryocooler is a key component in the STI SuperLink product family. Since 1999, more than 4,000 Sapphire cryocoolers have been deployed with over 44 million hours of accumulated run time. The current generation of cryocooler has an efficiency of 16.7 W/W and a 6 W lift at 77 K with 100 W input power and 35°C heat rejection temperature.

STI's Sapphire cryocooler is not only suitable for wireless industry products, but for other applications where low cost, high efficiency, and field-proven reliability are decisive components for enabling product commercialization. The wireless communication industry demands products that are cost effective and extremely reliable, typically with MTBF requirements in the hundreds of thousands of hours. Field data confirms that the Sapphire cryocooler has met and even exceeded these requirements.

Performance data are presented along with reliability data from the field and in-house testing. Various methods of thermal management of the cryocooler in systems are also discussed.

INTRODUCTION

For seven years, STI has been producing Stirling cycle cryocoolers as part of their CRFE products for the wireless communication industry. The free piston, gas-bearing cryocooler is a critical component that contributes to the overall receiver system's lifetime and reliability. Cryocooler reliability data, therefore, is continuously tracked and updated. To date, the product has demonstrated an MTBF of greater than 500,000 hours based on reliability data from the field and in-house lifetest results. This has far surpassed STI's original goal of 50,000 hours. The extraordinary MTBF of > 500,000 hours has remained consistent over the last two years even with an increased number of deployed systems. The "Invisible Cooler," which is small, lightweight, and highly reliable has become a reality. STI's unique cryocooler design has a new name: "Sapphire."

Figure 1 shows STI's flagship product, the SuperLink Rx 850, one of over 4,000 maintenance-free SuperFilter and SuperLink Rx units deployed worldwide. In this figure, the Sapphire cryocooler is surrounded with a shroud to optimize forced-convection cooling of the unit using a fan.

Cryocoolers 13, edited by R. G. Ross, Jr.
Springer Science+Business Media, Inc., New York, 2004

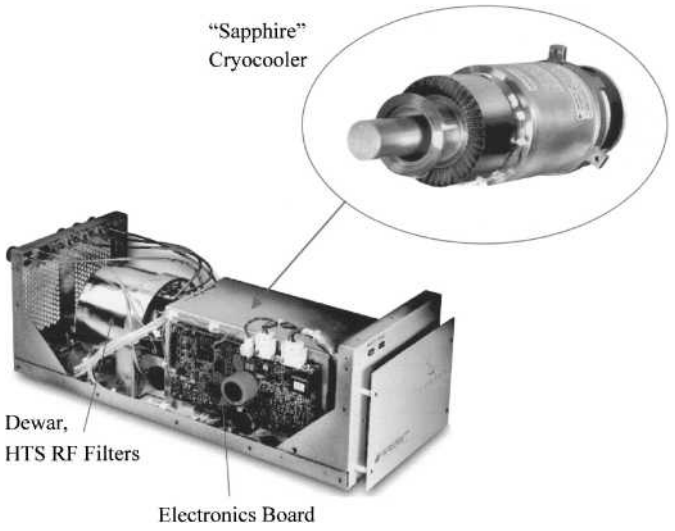

Figure 1. STI's flagship product, SuperLink Rx 850.

Cryocooler Performance

The Sapphire cryocooler is used in conjunction with a dewar and HTS RF filters based on "thin-film" technology that operates at a temperature of 77 K. The cooler has a heat load of 3.5 W from the dewar and is designed to operate over the complete ambient temperature range of -40°C to +60°C. The coldfinger temperature is regulated with the electronics board shown in Fig. 1.

STI's cryocooler has more than sufficient heat lift even under the worst-case conditions. The performance and physical characteristics of the Sapphire cryocooler are listed in Table 1. Figure 2 shows the heat lift of the Sapphire cryocooler as a function of input power for three different heat rejection temperatures.

RELIABILITY DATA FROM THE FIELD

STI has more than 4,000 units operating in the field. The combined run time is over 44 million hours. Of these units, 460 coolers have each > 26,280 accumulated hours (three years). Table 2 shows summary statistics for the STI units in the field. Figure 3 shows the accumulated run time and the number of coolers in the field as a function of time.

As part of STI's rigorous reliability and continuous improvement program, a thorough Pareto analysis is conducted on a regular basis to identify potential cryocooler design and reliability improvements. This resulted in cryocooler design changes in Q1 2002. Since that time over 2,600 coolers have been built, accumulating over 15 million hours in the field. Only three of these units have failed, and these failures were not wear-related.

Table 1. Performance and physical characteristics of the Sapphire cryocooler.

Heat lift	6 W of lift at 77K and 35°C heat reject temperature
Nominal input power	100 W input power at 6 W, 77 K and 35°C
Maximum input power	140 W, 60 Hz
Weight	7.5 lbs.
Dimensions	3.5 inches OD x 11.5 inches length
Operating orientation	Any
Ambient temperature	-40°C to +60°C
Vibration output	2.2 N with passive balancer

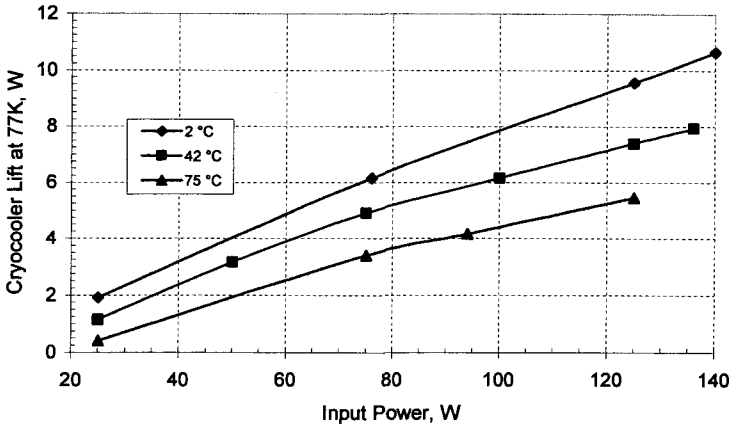

Figure 2. Cryocooler lift at 77 K vs. input power for various heat reject temperatures.

There are various ways to determine MTBF, such as Wiebull, exponential distribution, and lognormal. The method chosen depends on the nature of the product, and the types of failures that result. As part of the qualification of the cooler, tests were conducted to determine the Hazard Rate or Instantaneous Failure Rate (IFR) as a function of time. Commonly known as the "bathtub curve," the results clearly show no infant mortality in Fig. 4. In addition, the IFR does not change over time so there is no indication of wear out. By inspecting the units returned from the field as well as from ongoing reliability testing at STI (see next section), this has been validated.

Table 2. Statistics for STI coolers in the field as of March 2004.

Infant mortality	No
Wear out seen to date	No
Total number of coolers	> 4,000
Average hours per cooler	18,000
Cryocoolers with > 1 year run time	>1,600
Cryocoolers with > 3 years run time	460
Cumulative hours	> 44 million hours
MTBF	> 500,000 hours
Results of Continuous Improvement/Refinement: After Q1 2002	
Number of coolers	> 2,600
Cumulative hours	15 million hours
MTBF	Unknown (only 3 units failed)

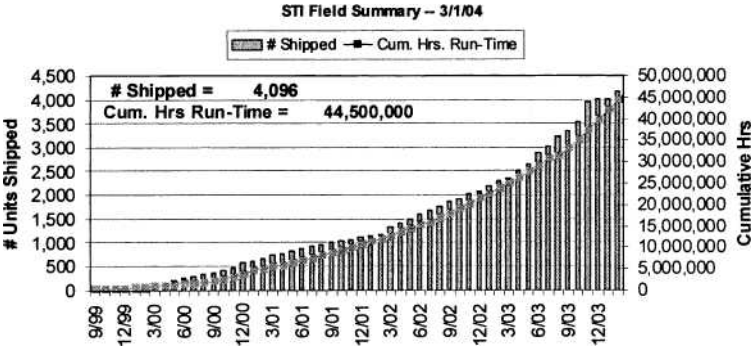

Figure 3. Field summary: number of units shipped vs. time.

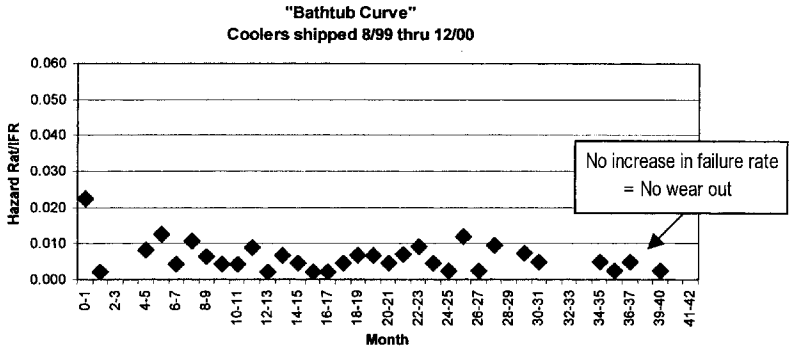

Figure 4. "Bathtub Curve" - Hazard rate or Instantaneous Failure Rate (IFR) vs. time; hazard rate or Instantaneous Failure Rate (IFR) equals the number failing in the next time period, having survived up to that time period.

Typical MTBF calculations are done using the exponential distribution. This methodology only applies if the product shows no infant mortality and a constant failure rate (no wear out). Since the Sapphire cryocooler at this point has met these two main criteria, this methodology is applicable. The equation for calculating MTBF using the exponential distribution methodology becomes simply: MTBF (hours) = Total accumulated run time (hours)/number of failures.

For units produced since Q1 2002, the MTBF is nearly 5 million hours. While this clearly demonstrates a highly reliable unit, ironically, not enough failures of this configuration have occurred to determine a statistically significant MTBF. However, the 500,000-hour MTBF number for the entire population of coolers in the field is statistically significant.

IN-HOUSE LIFE TEST

A few years ago, STI began additional in-house lifetime tests in order to determine the run time until wear out, thereby evaluating the latest design improvements. Ten optimized design coolers, introduced in Q2 2002, are currently operating at or close to worst-case conditions, defined as elevated cryocooler heat rejection temperature (between 35°C and 60°C) and maximum heat load or input power. Five of the ten lifetest coolers are operating with a regulated coldfinger temperature of 77 K. The remaining coolers are tested with the maximum possible input power achievable by the limitations of the electronics board. Figures 5 and 6 show measurement results and the test setup for the five temperature-regulated cryocoolers.

The heat reject temperature, input power, heat load, and cold-end temperature data for these lifetime coolers is recorded every 10 minutes on a continuous basis. This allows any variation in

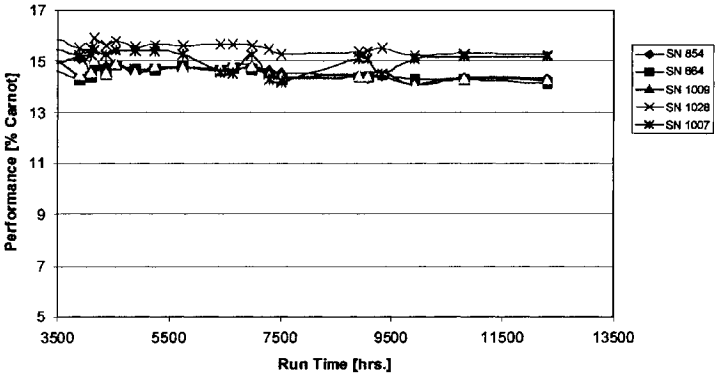

Figure 5. Performance results of temperature regulated lifetime coolers.

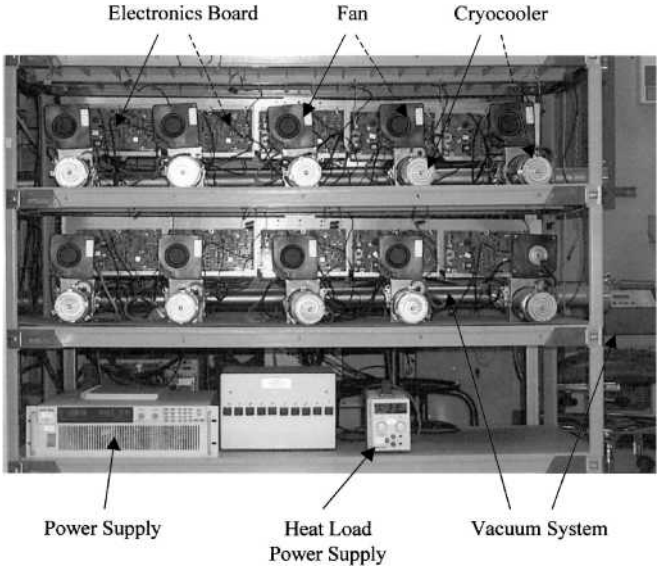

Figure 6. One of STI's in-house lifetime test stations.

cryocooler performance to become immediately apparent. Figure 5 shows the stable performance of all coolers within a range of 14% to 16 % of Carnot. All units with a current run time of more than 12,000 hours have shown nearly no performance variations during the last 2,000 hours, and therefore result in no wear out.

OUTDOOR CRFE SYSTEM - SUPERLINK RX 1900

SuperLink Rx 1900 is STI's newest product, an integrated duplexed CRFE for outdoor applications. The fully weatherized unit includes a SuperLink receiver and up to six dual duplexers.

The key requirement for SuperLink Rx 1900 (see Fig. 7) is that it operate outdoors without a fan for thermal management. This resulted in developing a Sapphire cryocooler with a modified heat rejecter and heat pipes as shown in Fig. 8 and described in the next section.

Passive thermal management design of SuperLink Rx 1900

The indoor units (e.g. SuperLink Rx 850) operate in semi-protected, air-conditioned environments in cellular service-provider shelters. This conditioned air safely circulates through the unit and the fins on the cryocooler heat rejecter. The use of forced convection greatly simplifies the thermal management while minimizing the system weight.

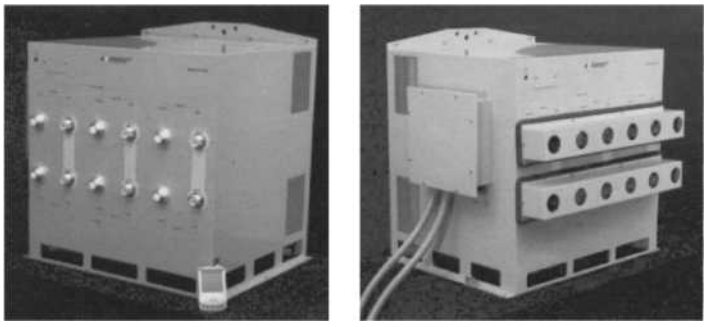

Figure 7. STI's SuperLink Rx 1900 for outdoor applications.

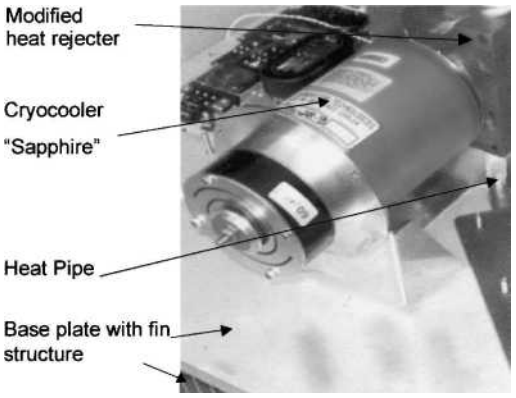

Figure 8. Heat pipe version of the cryocooler."Sapphire."

In contrast, the outdoor units (e.g. SuperLink Rx 1900) are exposed to a variety of ambient environmental conditions, including temperature extremes such as rain, snow, high humidity, and windblown dust. The requirement to operate reliably for a long period of time under these conditions eliminates the possibility of circulating air through the unit enclosure, pushing the design toward a sealed, insulated thermal heat management concept.

Most of the heat generated by the system (65%) comes from the Stirling cryocooler. The remainder is generated from other unit components such as the second stage amplifiers, PCB, AC/DC power converter, and the amplifier power supply. All of these components are designed to mount directly on the flat surface of the heat sink to expedite heat removal. Some of the system components are shown in Fig. 8.

To reject heat from the Stirling cryocooler to the outside environment, a temperature delta of no more than 20°C must be maintained between the cryocooler heat rejecter zone and the ambient air. To accomplish this requirement without circulating ambient air through the enclosure, a heat pipe/heat sink combination is used to remove the heat passively through conduction and free convection. A heat sink with fins is used to transfer heat to the ambient air. To replace the finned heat rejecters with an efficient heat pipe interface (< 1°C temperature delta), a variation of the Sapphire cryocooler was designed. A heat pipe structure thermally connects the cryocooler heat rejecter zone to the finned heat sink, which transfers heat to the ambient air. The use of a heat pipe/heat sink combination in place of relatively lower reliability fans results in a product with long life and high reliability.

STI shipped over 50 SuperLink Rx 1900 systems last year, incorporating into its products the use of highly reliable passive cooling to serve the outdoor needs of the cellular industry.

"NEMA" Standard

The outdoor enclosure unit, including a thermal management system, is designed to meet the National Electrical Manufacturers Association (NEMA) 4X standard. NEMA 4X enclosures are constructed for either indoor or outdoor use to provide a degree of protection to personnel against incidental contact with the enclosed equipment. In addition, the NEMA 4X enclosures provide a degree of protection against falling dirt, rain, sleet, snow, windblown dust, splashing water, hose-directed water, corrosion, and external formation of ice.

ALTERNATIVE CRYOCOOLER APPLICATIONS

The Sapphire cryocooler can be used for a variety of applications where low cost, high reliability, high performance, and long life are important or critical. Some examples include, but are not limited to the following:

- Medical devices
- Cold electronics: microprocessors, infrared detectors for focal plane arrays, and gamma-ray detectors
- Freezers for biomedical specimens
- Micro liquid Oxygen and liquid Nitrogen generators

SUMMARY

STI's Sapphire cryocooler has demonstrated field-proven reliability of greater than 500,000 hours MTBF, combined with high efficiency, high power density, and cost effective manufacturability. These critically important achievements are necessary to ensure STI's success in the wireless communication industry. To date, STI has delivered more than 4,000 cryo-cooled receiver units, accumulating over 44 million hours of run time. A total of 460 coolers have been operating for more than three years. The latest generation, of which over 2,600 units have shipped since Q2 2002, has demonstrated even higher MTBF. This conclusion is also based on field test results as well as in-house tests at STI. The SuperLink Rx 1900 is equipped with a modified version of the Sapphire cryocooler where heat removal is managed by using heat pipes and convection cooling to serve the outdoor needs of the cellular industry. Sapphire can be used for a variety of applications where low cost, high reliability, high performance, and long life are important or critical.

REFERENCES

1. Hanes, M. and O'baid, A., "Performance and Reliability Data for Production Free Piston Stirling Cryocooler," *Cryocoolers 12*, Kluwer Academic/Plenum Publishers, New York (2003), pp. 75-78.
2. www.suptech.com

Raytheon RS1 Cryocooler Performance

M.C. Barr, K.D. Price, G.R. Pruitt

Raytheon Space & Airborne Systems
El Segundo, CA, USA 90245

ABSTRACT

Over the past fifteen years Raytheon has developed a line of high reliability, long life, high efficiency flight qualified Stirling cryocoolers. Raytheon is currently manufacturing a low rate production lot of single-stage Stirling (RS1) cryocoolers to support its internal laboratory needs. The cryocooler features an Oxford-class design and is required to provide 3.3 W heat lift at 58K with an operational life in excess of 8 years. Initial testing indicates that this cryocooler has a measured heat lift capability in excess of 4 W at 58K. This paper will discuss performance trades on engineering units currently in test providing insight to effects of screen packing densities, transfer line configuration and operational charge pressure. Good correlation of performance with the analytical model is demonstrated with some path for improvement identified. Life test update of legacy RS1 cryocooler designs is also provided.

DESIGN OVERVIEW

The RS1 Cryocooler, as reported at SCW 2003[1], is the latest in a family of single-stage, split-Stirling cryocoolers. The design of the Raytheon RS1 Cryocooler (Figure 1) was described in detail at SCW 2003 convened in Girdwood, AK in September 2003. Since the last report on performance a number of engineering trade studies have been performed to establish sensitivity

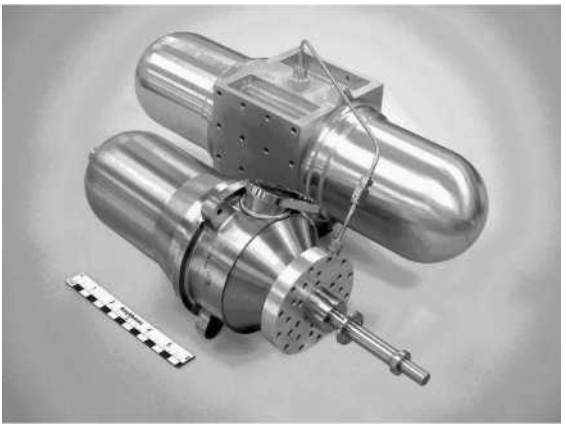

Figure 1. Raytheon RS1 cryocooler.

Cryocoolers 13, edited by R. G. Ross, Jr.
Springer Science+Business Media, Inc., New York, 2004

to design and operational parameters and to further validate the accuracy of the analytical model used to predict performance. Results of this testing are reviewed and discussed in the following section.

RS1 PERFORMANCE OVERVIEW

Performance mapping of the RS1 was reported at SCW 2003.[1] Since this last report tests have been conducted to assess sensitivity to design features (regenerator screen packing density, and transfer line configuration) and a key operational variable (charge pressure).

Performance vs. Screen Pack

The initial assessment considered was the sensitivity of performance to screen pack. For this evaluation performance was predicted for screen counts of 1016 (36% fill factor) and 920 (33% fill factor). Figures 2 and 3 illustrate the effect of screen pack on RS1 performance. Figure 2 depicts heat lift performance; Figure 3, specific power performance.

Figure 2 shows measured vs. predicted performance at 40 atm charge pressure operation. Both performance curves demonstrate compliance with the RS1 heat lift requirement of 3.3 W at 58K. There is excellent correlation between test data and predicted results from the thermodynamic math model. Correlation of predicted performance matches the lower fill factor performance within 5% over the data range reported. The analytical model also predicted the improved performance trend associated with the lower packing density that was demonstrated in the data, though the extent of the improvement was somewhat under predicted.

Figure 3 compares operational efficiency of the two screen packs considered. Specific power for the lower packing density (920 screens) configuration demonstrates a small improvement in efficiency compared with the higher packing density (1016 screens) configuration.

Performance vs. Charge Pressure

The next study conducted was to assess performance vs. charge pressure. For this study the RS1 cryocooler was assessed at two charge conditions: 40 atm and 36 atm. Results are provided in Figures 4 and 5. Figure 4 depicts heat lift vs. predicted results for the two charge conditions, and Figure 5 depicts specific power for the two conditions.

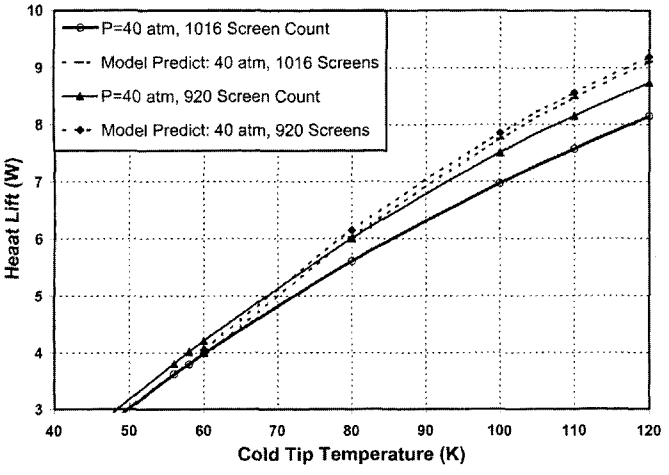

Figure 2. Performance vs. screen count. Results are compared for screen packs of 1016 count and 920 count; charge pressure is held constant at 40 atm. Results show improved performance levels are obtained with the lower packing density. Both configurations meet RS1 performance requirement of 3.3 W at 58K.

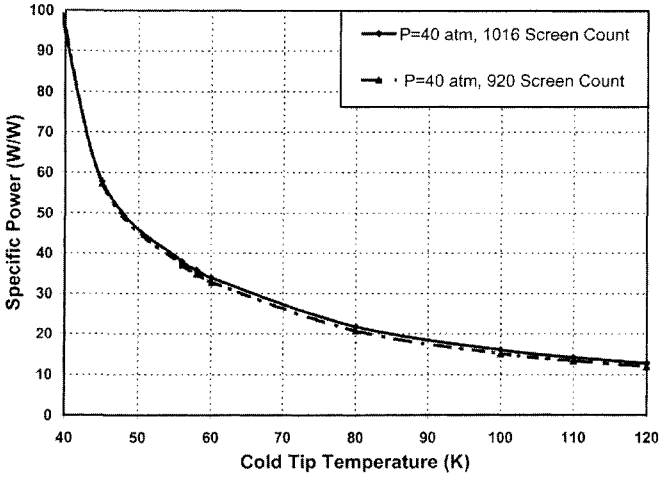

Figure 3. Comparison of operational efficiency vs. regenerator screen pack. Specific power of 920 screen count and 1016 screen count regenerator configurations are compared. Both configurations meet the RS1 requirement of 38 W/W at 58K. A slight improvement associated with the lower packing density is observed.

As expected, increasing the charge pressure increases capacity. The maximum capacity at 58 K for 36 atm is 3.8 W, compared to 4.1 W for 40 atm. Figure 4 again reinforces the ability of the analytical model to predict performance; results are within 2% of measured at 60K and within 6% of measured at 120K. The performance curves demonstrate compliance with RS1 requirements for both charge pressures.

Figure 5 depicts operational efficiency vs. charge pressure. A key observation is the gain in operational efficiency associated with the lower charge pressure. Whereas specific power for the 40 atm condition is measured at 34.5 W/W, the corresponding specific power for the 36 atm condition is measured at 32.5 W/W, a 6% improvement. Thus a trade off between efficiency and capacity has been characterized in the charge pressure setting. For the stated requirement of 3.3 W at 58K, the lower charge pressure is thus the better selection given that it meets the capacity requirement with substantial margin while achieving the better operational efficiency.

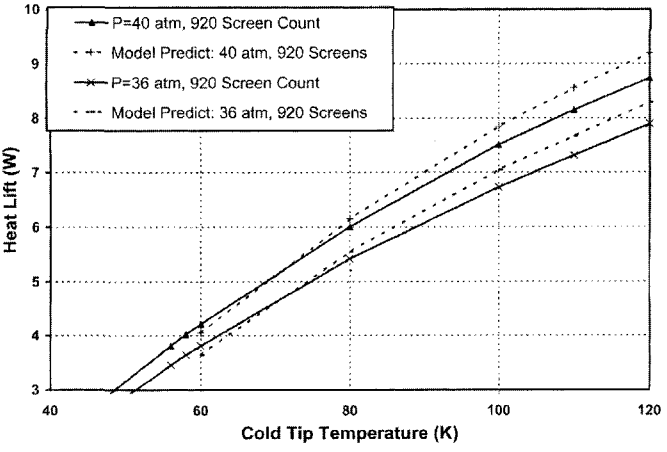

Figure 4. Performance vs. charge pressure. Results are compared at 40 atm and 36 atm for a regenerator pack of 920 screens. Results show excellent correlation with predicted values up to 120K. Both configurations meet RS1 performance requirement of 3.3 W at 58K.

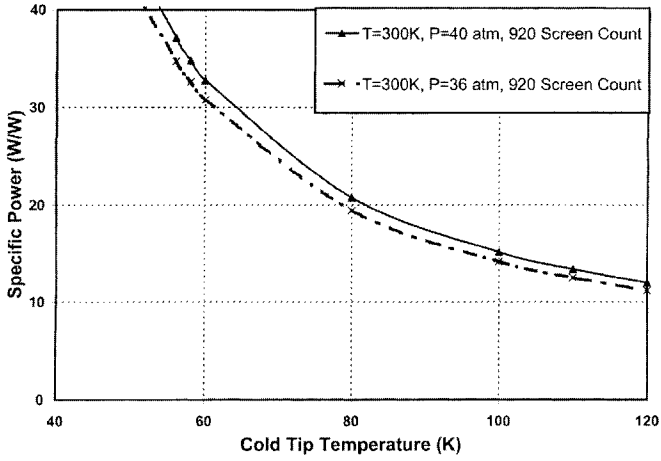

Figure 5. Comparison of operational efficiency vs. charge pressure. Specific power at 40 atm charge and 36 atm charge are compared for a regenerator pack of 920 screens. Both configurations meet the RS1 requirement of 38 W/W at 58K with substantial margin. The lower charge condition results in an efficiency gain of ~ 6% at 58K.

Performance vs. Transfer Line Configuration

The final trade considered was the impact of transfer line configuration on overall performance. Two conditions were assessed – an "S" configuration transfer line approximately 10" long with 4 bend radii of ~ 1" each and a bench test line configuration (T508) approximately 10" long with 2 bend radii of ~ ½" each. A comparison of test results with the analytical predictions is shown in Fig. 6.

These results show a small impact on performance at 58K (~ 2%) and a larger impact at higher operational temperatures (~ 4% variation between line configurations at 120K).

Overall these performance evaluations provide further validation of the analytical model to predict cryocooler performance. Results, in general are within a few per cent over the operational range of interest. The testing performed has highlighted a path to improved performance of the

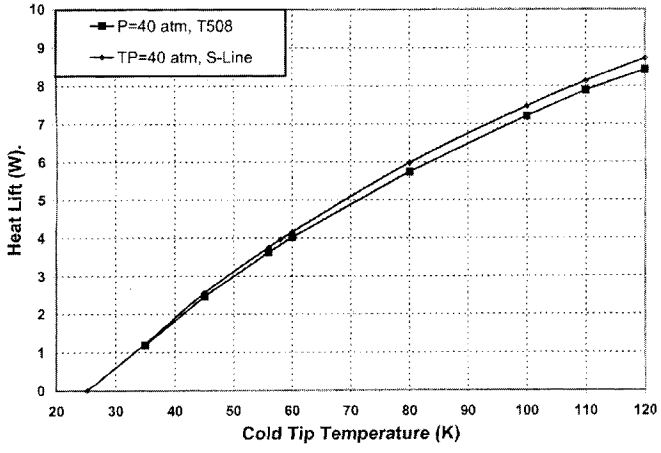

Figure 6. Comparison of performance vs. transfer line configuration. Heat lift comparison of S-configuration vs T-508 configuration transfer lines. The observed impact at 58K is less than 2% from predicted results.

Table 1. Summary of Hughes/Raytheon Stirling Cryocooler Programs.

Program	Year	Units	Performance*	Mass	Life Testing
SSC	90 – 94	2	2W @65K for 55 W in	18.5 kg	24,000+ hrs
ISSC	93 – 97	4	2.1W @60K for 80 W in	18.5 kg	23,500 hrs x 2
PSC	94 – 97	1	3.1W @60K for 90 W in	12.6 kg	30,000+ hrs
SBIRS Low	95 – 99	5	3.1W @60K for 90 W in	17.2 kg	38,000+ hrs
RS1	00 – 03	2 (+15)	3.3W @58K for 108 W in	14 kg	-

* with heat reject at 293K

RS1 through tailoring of the regenerator packing density and operational charge pressure to achieve higher operating efficiency.

RS1 Life Test Update

Life test summary of RS1 legacy cryocoolers is included as Table 1. Two cryocoolers are currently in test, the PSC cryocooler in test at AFRL and the SBIRS Low cryocooler in test at Raytheon. Over 115,000 hours of life testing have been accumulated to date on all coolers listed with no observed failures.

SUMMARY

In summary, several engineering trade studies were conducted to assess potential performance gains versus configuration. Good correlation was established with the analytical model, both in absolute accuracy and in predicting subtle trends. This illustrated the model's utility for exploring parametric changes to improve overall performance margin. Analytical results, supported by measured data, identified improvements in operational efficiency that were realized through tailoring of regenerator screen pack density and operational charge pressure. Life testing of the RS1 legacy design cryocoolers continues without any observed life test failures.

REFERENCES

1. Barr, M.C., Price, K.D., and Pruitt, G.R., "Long-Life Cryocooler Performance and Production," *Cryogenics*, Vol. 44, Issue: 6-8, June - August, 2004, pp. 409-412.

Ball Aerospace Next Generation 2-Stage 35 K SB235 Coolers

E.D. Marquardt, W.J. Gully, D.S. Glaister, R. Stack
Ball Aerospace and Technologies Corporation
Boulder, CO 80306

N. Abhyankar, E. Oliver
Air Force Research Laboratory
Kirtland AFB, NM 87117

ABSTRACT

This paper describes the design, development, testing, and performance of the Ball Aerospace SB235 and SB235E long life, 2-stage space cryocoolers optimized for dual temperature simultaneous cooling at 35 K and above. The SB235 and its model derivative SB235E are 2-stage coolers designed to provide simultaneous cooling at 35 K (typically, for HgCdTe detectors) and 100 K (typically, for the optics) and were baselined for the Raytheon SBIRS Low Track Sensor. A qualification unit SB235 was developed and has accumulated 2500 hours in a life test at the Air Force Research Laboratory (AFRL). The SB235 and its higher capacity derivative SB235E were designed for high cooling capacity, power and mass efficiency, and producibility for multiple unit build applications.

INTRODUCTION

Ball Aerospace has specialized in multi-stage low-temperature coolers from the beginning of our cryocooler program. We believe that the Stirling is the cryocooler of choice for high-efficiency low-temperature cooling because of its unmatched low-temperature performance. Ball developed a series of multistage coolers on the NASA 30 K MLVC program and its Flight program derivatives. Building on that experience we have made a next generation 2-Stage cooler with twice the cooling capacity in the same size package in a highly-producible design.[1,2] This cooler, the SB235, has undergone flight qualification vibration testing and is currently under life test at AFRL.

The SB235 cooler was initially designed to match the cryogenic requirements of the SBIRS-Low program, which were nominally 0.8 W at 35 K and 2.5 W at 115 K. Because these loads have tended to grow over time, we are now working on a higher heat lift version, the SB235E cooler, that we expect will carry 1 W at 41 K and 7 W at 110 K.

Cryocoolers 13, edited by R. G. Ross, Jr.
Springer Science+Business Media, Inc., New York, 2004

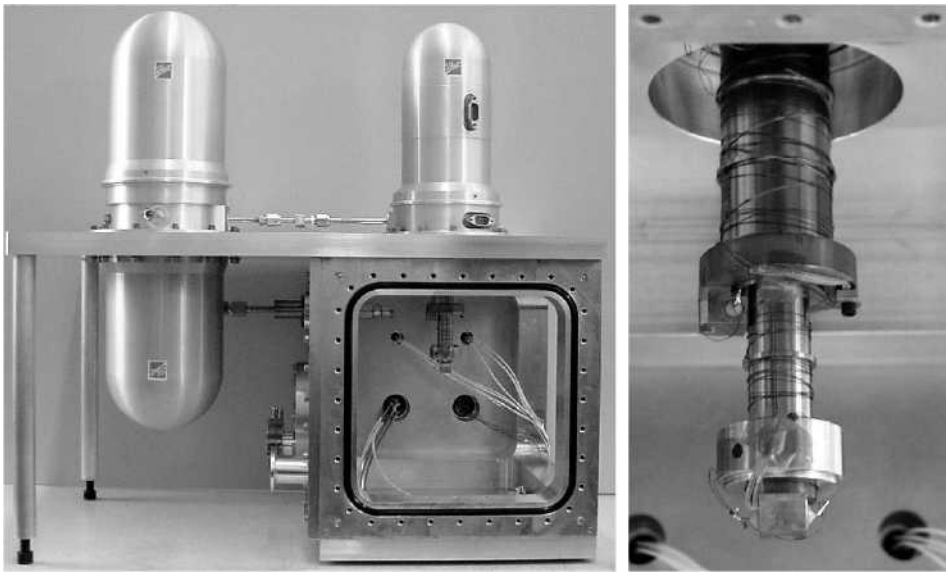

Figure 1. SB235 Qualification unit with close-up of the cold head.

SB235 MODEL CRYOCOOLER DESCRIPTION

The SB235 is a 2-stage Stirling cooler with a split design separating the compressor and cold head, shown in Figure 1. Dual opposed pistons are used in the compressor with a flexure bearing supported clearance seal. The expander is also flexure supported, and has a two-stage piston to generate cooling at 35 K and 115 K. It employs a counterbalance for active vibration control.

The cooler incorporates many features from our previous coolers. It includes a fixed regenerator that allows high side loads and protects the displacer clearance seal. Advanced EMI reduction techniques are used to achieve very low EMI emission levels for a system using a Pulse Width Modulated (PWM) power supply. Also, it employs the technology we have developed to insure non-contacting. On the 30 K program, where our research coolers were equipped with internal sensors that monitored the clearance gaps[3], we learned that low-frequency stiction tests were not sufficient to prove that a cooler was non-contacting during full power operation. We developed a scheme, which includes mechanical design, methods of part fabrication, and a sensitive electronic alignment, that results in full non-contacting operation. We include the sensors in the cooler during its initial alignment, but eliminate them once proper performance has been ascertained.

We show our simple two-stage cold interface in Figure 1 (right photo). Unlike a pulse tube, the Stirling requires only a single small diameter penetration in any radiation shield, and all warm end parts are removed from the cryogenic zone. The detailed design of the fixed regenerator displacer provides excellent thermal contact between the working fluid in the cooler and the external interface.

The performance requirements for the cooler are shown in Table 1. The cooler meets these requirements in the area of thermal performance and vibration, but without our final version of the electronics we have not tested radiation hardness or completed the full set of EMI tests.

Table 1. SB235 2-stage cooler design performance requirements.

Specification	SB235
Cooling Capacity	0.8 W @ 35 K 2.5 W @ 115 K
Reliability	99.5% cooler at 5 yrs
Mass	10.5 kg
Cooler Volume	14 cm x 28 cm x 40 cm
Vibration	< 0.1 N
Operating Temperature Range	-40 to 55 °C
Survival Temperature Range	-60 to 80 °C
Temperature Control Stability	0.01 K with varying heat rejection temperature
Radiation Tolerance	>100 krad
Launch Loads	15 g peak sine vibration 13 grms random vib
Electronics Interface	RS-422
EMI/EMC	Mil-Std 461E

PERFORMANCE CHARACTERIZATION

Performance Mapping

Ball delivered the SB235 cooler to the Air Force Research Laboratory at Kirtland Air Force Base for extensive characterization. They are characterizing the SB235 by mapping the cooler performance at 12 different cold-stage and mid-stage temperature combinations under a variety of parameters including stroke, frequency, phase angle, and heat rejection temperature. This

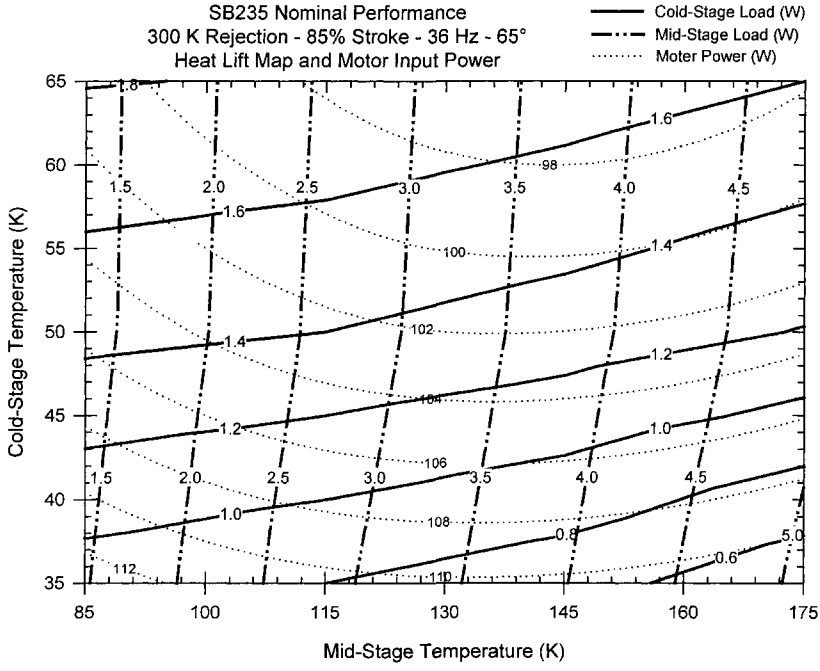

Figure 2. Nominal SB235 performance map. Contour plot shows available heat lift for both the cold-stage (solid lines) and the mid-stage (dot-dot-dash lines). Also included is the motor input power (dotted).

provides a large database of experimental data to allow cooler performance predictions for a wide variety of applications over a large temperature range. Testing is performed by setting the heat rejection temperature and controlling the heat loads on both cold-stages to maintain fixed temperatures. Next the phase angle, stroke, and frequency are varied in 75 different combinations. Performing this over 3 different cold-stage temperatures, 35 K, 50 K, and 65 K, and 4 mid-stage temperatures, 85 K, 115 K, 145 K, 175 K, results in 900 data points for each heat rejection temperature.

Figures 2 and 3 are a sample of the 75 graphs that could be plotted. Figure 2 represents nominal operation, while Figure 3 represents the dramatic increase in cooling that can be obtained by commanding the cooler to run at higher stroke and operating frequency. In both cases they demonstrate how the mid-stage heat lift is almost unaffected by the cold-stage temperature, although the cold-stage heat lift is somewhat affected by the mid-stage temperature. If they were totally independent, the heat lift lines would form a rectangular grid.

In a different type of experiment, we showed how the cooler could provide different amounts of heat lift at two fixed stages. We fixed the cold-stage and mid-stage temperatures at 35 K and 115 K respectively and varied stroke and phase angle at fixed frequency. The results shown in Figure 4 demonstrate how the Stirling cooler can be adjusted to match a wide range of required loads at both stages. With a 0.5 W load at 35 K and by adjusting the stroke and phase angle, the heat lift at 115 K will be between 1 W and 3.5 W. This can be accomplished on orbit to adjust for the real conditions in space. This is a unique ability of the Stirling cooler. Changing the frequency is the only way a pulse tube can shift the heat lift ratio but the frequency will have a much smaller effect. Changing the frequency of the SB235 will also shift the curves shown in Fig. 4 to provide an even larger range of the heat lift ratio.

In a final experiment we demonstrate how the heat rejection temperature affects the heat lift at the two stages. As shown in Fig. 5 the ambient temperature primarily affects the mid-stage, which makes sense since the regenerator loss term is proportional to the temperature gradient.

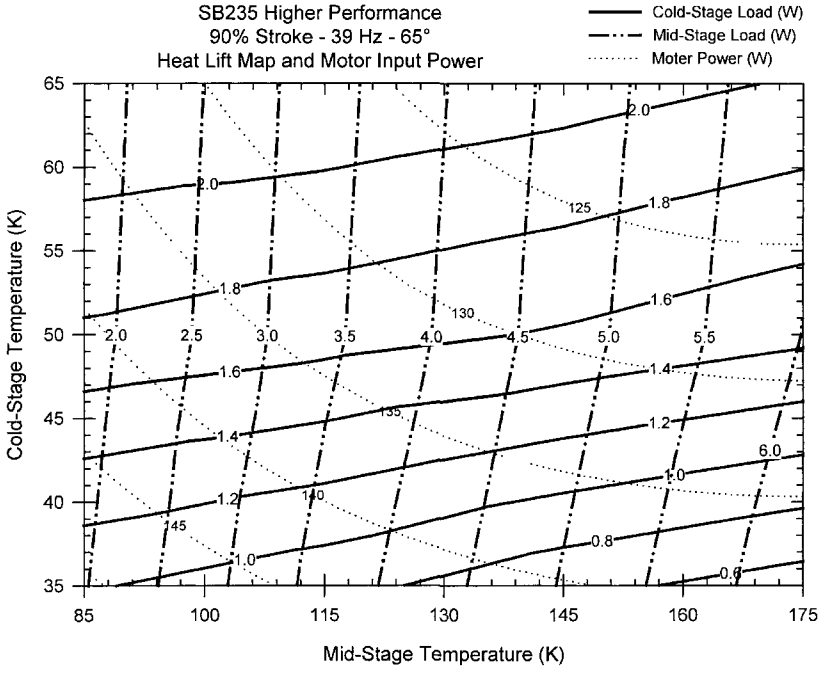

Figure 3. Higher heat lift performance map. Contour plot shows available heat lift for both the cold-stage (solid lines) and the mid-stage (dot-dot-dash lines). Also included is the motor input power (dotted).

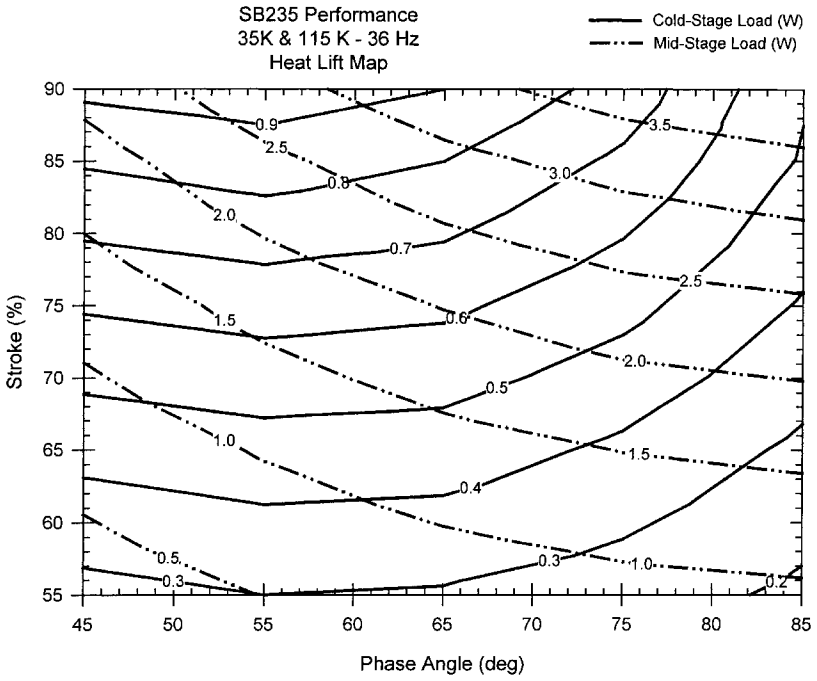

Figure 4. Constant temperature contour plot shows available heat lift for both the cold-stage (solid lines) and the mid-stage (dot-dot-dash lines).

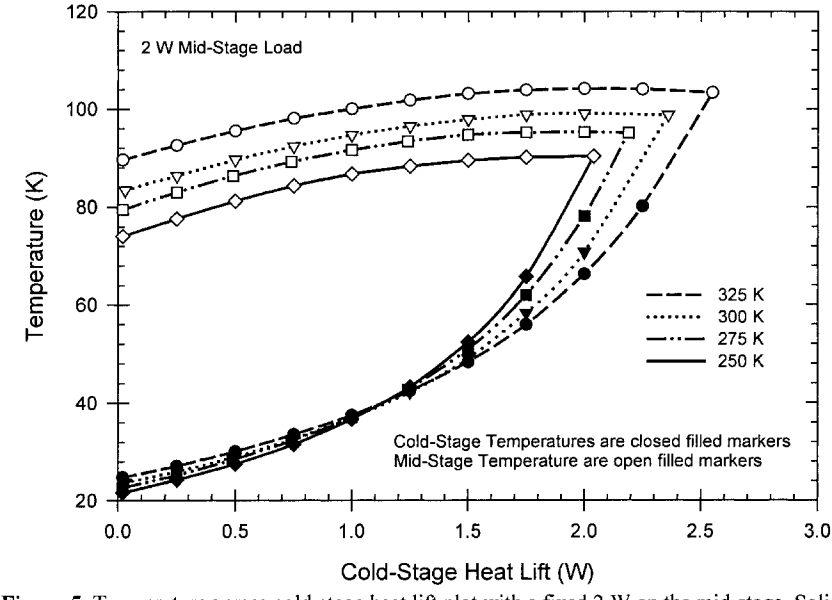

Figure 5. Temperature verses cold-stage heat lift plot with a fixed 2 W on the mid-stage. Solid filled markers are the cold-stage temperature; open markers are the mid-stage temperature.

Figure 6. SB235 under life test at AFRL.

Life Test

The SB235 qualification unit is currently under performance characterization and life test at AFRL, shown in Fig. 6. All the data shown in the earlier figures was taken at AFRL. The unit currently has over 2500 hours of life testing and testing will continue for the foreseeable future.

SB235E MODEL CRYOCOOLER

As mentioned, we are currently working on an 'enhanced' model designed for larger cooling loads. It is only slightly larger in size and mass while providing about twice the cooling power of the SB235; 3.2 W at 56 K and 14.6 W at 120 K. A thermal breadboard is currently under construction for performance testing in the fall of 2004.

REFERENCES

1. E.D. Marquardt, W.J. Gully, D.S. Glaister, and G.P. Wright, "The Next Generation Ball 35 K Cryocooler," in *Advances in Cryogenic Engineering: Proceedings of the Cryogenic Engineering Conference*, Vol. 47, edited by Susan Breon et al., American Institute of Physics (2002), pp. 1117-1122.
2. W.J. Gully, D.S. Glaister, E.D. Marquardt, R. Stack, and G.P. Wright, "Thermodynamic Performance of the Ball Aerospace Multistage Stirling Cycle Mechanical Cooler," in *Cryocoolers 12*, edited by R.G. Ross, Jr., Kluwer Academic/Plenum Publishers, New York (2003), pp. 45-50.
3. W.J. Gully, H. Carrington, W. Kiehl, T. Davis, and B.J. Tomlinson, "Qualification Test Results for a Dual-Temperature Stirling Cryocooler," in *Cryocoolers 10*, edited by R.G. Ross, Jr., Kluwer Academic/Plenum Publishers, New York (1999), pp. 59-66.

Development of the LSF95xx 2nd Generation Flexure Bearing Coolers

J.C. Mullié, P.C. Bruins, T. Benschop, M. Meijers

THALES Cryogenics B.V.
Eindhoven, The Netherlands

ABSTRACT

Thales Cryogenics has been working on high reliability cryocoolers since 1997. During this period two cooler series have been developed, the LSF91xx series for cooling powers up to 3 W at 80 K and the LSF93xx series for cooling powers up to 8 W at 80 K. As a result of several design improvements, it was possible to decrease the length and mass of our flexure-bearing coolers. These improvements have been applied in the new LSF95xx series. With the length and mass reduction, the LSF95xx complies with the SADA II specification with respect to envelope and mass. Based on this, being the first manufacturer offering a full flexure-bearing supported cooler that fits within the SADA II envelope, Thales Cryogenics has been selected in several new (military) programs with their LSF coolers.

By using a moving magnet configuration in all our flexure-bearing coolers, the risk with respect to contamination problems due to outgassing has been diminished because the coils are not part of the helium circuit. Furthermore, all connections in the LSF95xx are laser-welded, which means that there is no additional locking required inside the cooler. By using a different magnet design, no magnet segments have to be glued together, which decreases the risk of out gassing and increases the robustness even more.

This paper describes the trade-offs that have been considered in the design phase, and gives a detailed overview of the test results, the status of the qualification program, and the resulting specification of the LSF95xx cooler series.

INTRODUCTION

The first generation of Thales' LSF91xx flexure bearing compressors was introduced in 1999. The flexure-supported moving magnet concept is generally recognized as the most robust and reliable implementation of a Stirling compressor. By making this concept available in volume production, Thales set a first and important step to introduce Stirling and Stirling-type pulse tube cryocoolers into civil and industrial markets. Further, interest was raised in the space community, as the design and fabrication methods turned out to be suitable for making space-worthy coolers for a fraction of the cost generally associated with space cryogenics.

From the world of military infrared systems, it was soon recognized that the significant increase in MTTF (as compared to conventional cryocoolers) gives a large potential in reducing cost-of-use and increasing maintenance intervals. Space constraints, as well as standards such as the SADA envelope, limited the applicability of the LSF91xx series cryocoolers in military applications.

Cryocoolers 13, edited by R. G. Ross, Jr.
Springer Science+Business Media, Inc., New York, 2004

In four years of production of the LSF91xx, and in the design of compressors for a number of space programs, Thales has obtained extensive experience in building and designing flexure compressors. It was therefore decided to design a moving magnet flexure cooler using the cold finger of an existing Thales contact-seal SADA II cooler, but fitting into the SADA envelope.

The compressor design is now used as the basis of the LSF95xx series of cryocoolers. The series contains the LSF9599, with a 1/2" SADA compatible cold finger, and the LSF9597, with a 1/4" IDCA cold finger; the cold finger interfaces with the same dewar as Thales' rotary monobloc coolers. Furthermore, a number of slip-on coolers such as the LSF9580, LSF9587, LSF9588 and LSF9589 are available.

DESIGN

Magnetic Circuit Design

A mass reduction study was conducted on the LSF93xx compressor in order to use it in the LSF9330 for the Cryosystem space application. In this study, it was found that it is advantageous to replace the 16 magnet segments used in the motor by a single magnetized ring. For the mass and size reduction of the LSF95xx, it was decided to use the same approach. The magnetized ring is more robust than separate magnet segments, thus making the design even more suitable for applications where the cooler is subjected to severe shock and vibration. Furthermore, the segmented design may have trapped gas volumes in the gaps between the segments, thus requiring great care in cleaning and drying of the compressor in production. The magnetized ring is a single piece, thus the design further reduces potential outgassing into the helium space. The biggest advantage, however, is the fact that the design enables a reduction in moving mass for the same magnetic flux in the motor.

Flexure Support Design

In the first generation LSF91xx coolers, the pistons are supported at both ends by flexure packs. This gives the axial and radial stiffness required to support the piston even under high transverse loads. Each flexure pack consists of two flexures (thus eight flexures per compressor). Using a combination of FEM calculations and extensive fatigue tests,[1] Thales has continued to refine their Algor®-based FEM flexure optimization tool. A new spring steel material is found that has a 10% higher fatigue threshold than the old spring steel. Combined with the lower moving mass, this material made it possible to design flexures that can support the loads in a single-flexure arrangement, as shown in Fig. 1. Thus, in the LSF95xx, each piston is supported by one flexure at each end. Consequently, the compressor contains only four flexures, and the length has been reduced from 165 mm to 122 mm.

Compressor Housing Design

Having gained experience from the severe safety constraints in civil and space applications, the housing of the compressor is optimized to reduce stresses in the housing material. For general applications, the optimized housing is made of AISI 304L (yield strength = 170 N/mm²) and laser

Figure 1. Single flexure arrangement (1 flexure per piston side) and LSF95xx compressor.

welded. This provides a robust housing with a burst pressure well above the required two times the maximum design pressure. For applications requiring compliance with MIL-STD-1522, the housing can be made of AISI 321 (yield strength = 205 N/mm^2) and electron-beam welded.

Modularity

Parallel to the approach chosen for the LSF91xx series, the compressor was designed as much as possible in a modular concept. Adaptation to the various Thales' cold fingers is possible with the exchange of a minimum number of parts. This makes it possible to build even small series of coolers for economically acceptable costs.

SPECIFICATION AND PERFORMANCE

In the design of the LSF95xx, special care was taken to make sure that the weight and size reduction did not impact compressor efficiency. Therefore, the performance specifications of the LSF95xx series were made identical to those of the LSF91xx series. A summary of the performance of the LSF95xx compressor with existing Thales cold fingers is given in Table 1. As many heatsink designs clamp around the center part of the compressor, the fact that the LSF95xx has the same diameter as the LSF91xx means that the two designs are to a large extend interchangeable.

Dynamic Impedance

For integration of a cooler in a system, the dynamic impedance $Z=U^2/P$ of the cooler often is important. For a cooler drive electronics that provides a fixed voltage, a too high dynamic impedance would imply that there is not enough power going into the cooler. With a too low dynamic impedance, the high power drawn by the cooler may cause problems in the system power supply or in the thermal budgets. For interchangeability, the dynamic impedance of the LSF95xx was designed to be equal to that of the LSF91xx. As the dynamic impedance is influenced by many variables—such as system damping, piston resonance conditions, friction, piston stroke and coil impedance—this proved to be an important constraint in the design process.

QUALIFICATION

As the cold fingers and the performance of the LSF95xx series are identical to the LSF91xx series, it was not necessary to re-qualify the coolers for their performance in combination with the various dewars and applications of our customers. Since the magnet circuit, moving mass, piston mounting and flexure material have changed, a delta-qualification was performed on radiated magnetic field, induced vibration and acoustic noise, shock and vibration, and flexure fatigue / lifetime. The results of this qualification program are described in the next paragraphs.

Table 1. LSF95xx performance summary.

COOLER TYPE	UNIT	LSF9580	LSF9597	LSF9588	LSF9589	LSF9599
coldfinger/ approx dewar bore	mm	5	1/4"	10	13	1/2" SADA
Dimensions compressor (diam x L)	mm	60x122	60x122	60x122	60x122	60x122
Cooling power @ 80 K, 23C	mW	600	650	1600	2800	1500
Input power	W	40	40	160	100	60
Typical cooldown time to 80 K	min	9' @850J	8'@850J	7' @850J	5'@850J	13'@1440J
IDCA or slip on		Slip on	IDCA*	Slip on	Slip on	IDCA*
MTTF	hour	>20,000	>20,000	>20,000	>20,000	>20,000
Mass	< kg	1.7	1.7	1.8	1.9	1.8

Electromagnetic Interference

Electromagnetic interference is measured according to MIL-STD-461D, as specified. The results are given in Fig. 2.

Induced Vibration

Induced vibration is measured on two prototype compressors driving 1/4" IDCA cold fingers. Axial forces are below 1.7 N_{rms}, and radial forces are below 0.35 N_{rms}. A typical vibration spectrum for the compressor is depicted in Fig. 3 for operation near full stroke.

Acoustic Noise

Sound power measurements, as shown in Table 2, are performed in a reverberant room. From the sound power measurements, the resulting sound pressure at 5 meters distance is extrapolated assuming that at this distance, the cooler may be modelled as a monopole (point) source. It is found that at 5 m distance, in most frequency bands, the sound pressure is below the threshold of human hearing of 20 μPa.

Shock and Vibration

In order to verify the robustness of the new flexure design, a shock and vibration test program was performed. A number of coolers were successfully tested in Thales' Environmental Test Lab

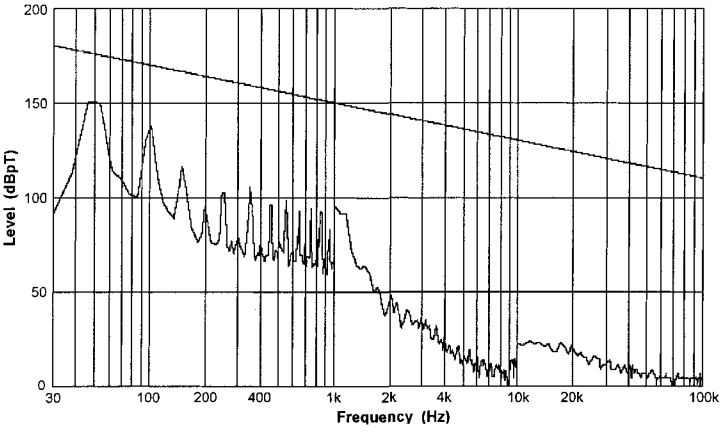

Figure 2. Magnetic interference of LSF95xx.

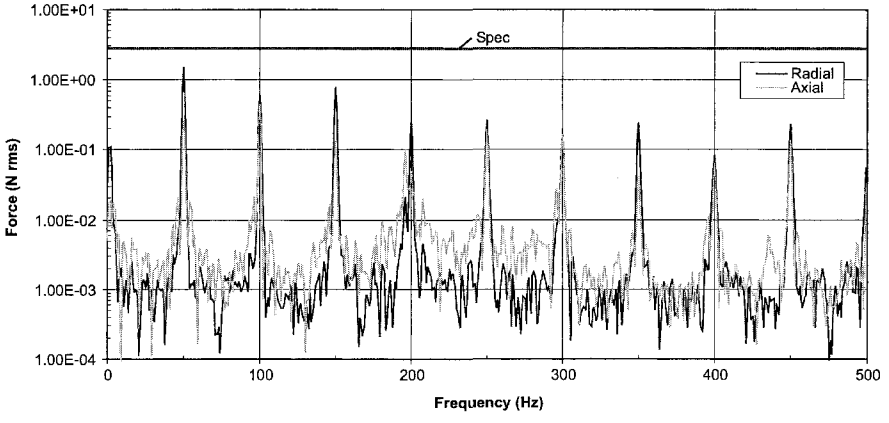

Figure 3. Typical vibration spectrum of an LSF9597.

Table 2. Sound power (0 dB =1´10^{-12} W) and sound pressure (0 dB =2´10^{-5} Pa) measurements.

f (Hz)	Sound power (dB)		Sound pressure @5m (dB)	
	LSF9588	LSF9597	LSF9588	LSF9597
63	x	x	x	x
125	10.0	3.9	-15.2	-21.1
250	12.5	12.2	-12.3	-12.9
500	21.1	21.5	-4.4	-3.5
1000	15.0	15.1	-10.1	-10.1
2000	19.5	13.5	-5.6	-11.5
4000	22.0	13.3	-3.1	-11.7
8000	25.2	34.0	-0.2	8.9
Overall (dB (A))	**34.5**	**34.8**	**9.5**	**9.8**

(ETL). For repetitive shock testing, the coolers are subjected to 2000 shocks of 20 g, 6 ms, in each direction, thus a total of 6000 shocks with the cooler non-operating. The resistance to shocks while operating is tested by subjecting the cooler to three shocks of 100 g, 11 ms, in each axis.

Random vibration testing consists of a 12.2 g_{rms} random pattern in the frequency range of 20-2000 Hz. This test is performed in two directions, for 3 hours in each direction. Finally, each qualification cooler is subjected to a sinusoidal vibration test where the frequency range of 5-2000 Hz is swept through 10 times at 1 octave per minute, in two directions. The level ramps up to 1 g peak from 14-23 Hz, and then ramps up further to 5 g peak from 52-2000 Hz.

Flexure Fatigue and Lifetime Testing

In the design phase of the flexures, FEM calculations and fatigue tests were performed in parallel. A large number of flexures, mounted exactly as they are in the compressor, are tested for more than 10^7 cycles (Wöhler fatigue curve) to support the FEM fatigue calculations. In the compressor design, the actual stroke of the pistons is limited so that the flexures stay 35% below their fatigue limit.

Apart from the mounting method of the flexures, the flexure material and the design of the magnet circuit, the LSF95xx is conceptually identical to the LSF9lxx. The reliability of the flexure mounting is proven in the fatigue tests, as well as in the shock and vibration tests. The magnetic circuit of the LSF95xx is even less susceptible to outgassing than the moving magnet design used in the LSF91xx. Thus, the lifetime results of the LSF91xx can be extrapolated to the LSF95xx. An overview of on-going lifetime tests is given in Table 3. A number of LSF95xx coolers will be added to the lifetime test setup in the coming period.

MTTF Calculation (Based on LSF91xx)

The calculation procedure as described below is used to determine MTTF figures of long lifetime cryocoolers. First, a FMECA (Failure Mode Effects Criticality Analysis) analysis was performed based on the available experience in cryogenic coolers. The output of the FMECA is a list of identified critical parts or functions in the cooler from the MTTF point of view.

For the parts subject to wear, we assume that the failure rate is constant (random failure). The tests results of lifetime tests already performed on similar parts are then considered. From these results, we determine the MTTF of the part or function with MTTF=$\sum$(running hours)/(number of failures). When no failures are observed, we take MTTF=$\sum$(running hours).

For the calculation of the MTTF of the complete cooler, we again assume that the failure rate is constant (random failure). This simplification can be justified by the considerations that all the different components inside the cooler follow different distributions. As a consequence, the system behaves in a unpredictable way (random failure) with a constant failure rate. This is supported by experience figures. Therefore, we calculate the MTTF of the cooler as MTTF = $1/\lambda$ with λ being the summation of the failure rate of each component over the number of components in the cooler for which a λ_i is defined. Using the list of failure mechanisms as reported by Ross[2] and filling it with

Table 3. Overview of lifetime tests on LSF91xx coolers.

Cooler type	# operating hours	remarks
LSF9188	32799	
LSF9188	32602	Of which 400 hours in centrifuge (up to 10 g)
LSF9180	28229	
LSF9180	16273	Stopped for destructive analysis
LSF9110	21446	Pulse tube cold finger
LSF9320	13234	
LSF9320	20142	
LSF9188	18371	
LSF9188	18391	
LSF9320	12427	
LSF9320	12667	
total	226581	

Table 4. Thales 9199 reliability and MTTF calculation.

FAILURE MECHANISM	conventional coolers[1]	Thales LSF 9199		
	Stirling + balancer w/ back to back compressor	LSF 9199 stirling	*MTTF*	= 1/MTTF
Excessive Internal Cooler Contamination	3	1	226581	4.41E-06
Hermetic Seal or Feedthrough Leak	2.5	0.5	226581	4.41E-06
Comp. Flexure Breakage (fatigue)	0.1	0.1	226581	4.41E-06
Comp. Motor Wiring Isolation Breakdown	1	0.2	226581	4.41E-06
Comp. Piston Alignment Failure	0.2	0.2	226581	4.41E-06
Comp. Piston Blowby due to Seal Wear	1	1	226581	4.41E-06
Comp. Piston Position Sensor Failure	1	0		
Expander Structural Failure (launch)	0.2	0.2		
Expander Blowby (wear)	3	3	205135	4.87E-06
Expander Motor Wiring Isolation Breakdown	0.5	0		
Expander Spindle Alignment Failure	0.2	0.2	205135	4.87E-06
Expander / Balancer Position Sensor Failure	1	0		
total failure probability (%)	**13.7**	**6.4**	***total MTTF***	**27601.23**

figures from Thales experience, Table 4 gives the resulting figures for the reliability and MTTF. Note that the resulting MTTF of 27,601 hours is changing every day, as the lifetest coolers that are reported in Table 3 are all still operating.

CONCLUSIONS AND FUTURE WORK

The development of the LSF 95xx second-generation flexure bearing compressors has led to a 35% reduction in mass and a 33% reduction in compressor volume. All other cooler performance characteristics have either improved or stayed the same. The shorter compressor design has slightly less margin with respect to hitting of the end stops. This implies that under axial acceleration, the input power to the cooler during cooldown may have to be limited. A test campaign will be started soon to establish the allowable values.

REFERENCES

1. Benschop, A.A.J., Mullié, J., Meijers, M., "High Reliability Coolers at Thales Cryogenics," *Proceedings of SPIE* (2000), pp. 385-393.

2. R.G. Ross, Jr., "Cryocooler Reliability and Redundancy Considerations for Long-Life Space Missions," *Cryocoolers 11*, Kluwer Academic/Plenum Publishers, New York (2001), pp. 637-648.

CMC One-Watt Linear Cooler Performance Map at Higher Input Power

D. T. Kuo and M. Schmitt

CMC Electronics Cincinnati
Pasadena, CA 91107

ABSTRACT

The performance characteristics of CMC's One-Watt Linear Cooler (Model B1000) are presented here for ranges of parameter values beyond the envelope defined by its commercial specification. CMC evaluated the B1000 cooler for a new airborne platform with a challenging cooldown requirement. This paper illustrates the mapping of a cryocooler performance envelope to determine the optimal operating point for this application. A key component of this performance map is CMC's Linear Drive Cooler Electronics (LCDE). The versatility of the LCDE is demonstrated over the range of these tests.

INTRODUCTION

CMC Stirling-cycle cryocoolers are well suited for applications requiring high thermodynamic efficiency and from lightweight consideration. More specifically, CMC's B1000 Cooler is further differentiated by its robust design margin to allow its operating range to be extended to meet fast cooldown requirement. This paper shows the process that CMC engineers followed to establish the operating envelope of the B1000 Cooler. The presentation of the performance envelope is preceded by a brief introduction of the hardware.

The cooler components, identified in Figure 1, consist of a dual-opposed-pistons linear compressor that generates an AC pressure waveform to drive a displacer within the dewar. The compressed helium refrigerant is cooled along the length of the moving regenerator and expanded in the volume formed by the tip of the regenerator and the dewar wall. The cold expanded gas absorbs heat from the load and returns to pre-cool the regenerator for the next cycle. Coupling of the regenerator and pistons is achieved through a gas transfer tube. The Stirling-cycle is used to analyze its thermodynamic performance. Within the compressor, voice-coil linear actuator provides the force to compress the refrigerant. Alternating current flowing in the coil acts in concert with the magnetic flux within the airgap of the field assembly, to convert electrical to mechanical energy. The coils are driven at resonance to maximize efficiency. A hockey-puck electronics module is shown mated to one end of the cylindrical compressor. There are two main functions performed by the linear cooler drive electronics (LCDE): 1) DC to AC power converter and 2) temperature controller. CMC's LCDE features a programmable digital processor to allow greater flexibility in its operation. More details of its capabilities are described in a following section. Figure 2 shows the next level of integrated dewar cooler assembly (IDCA).

Cryocoolers 13, edited by R. G. Ross, Jr.
Springer Science+Business Media, Inc., New York, 2004

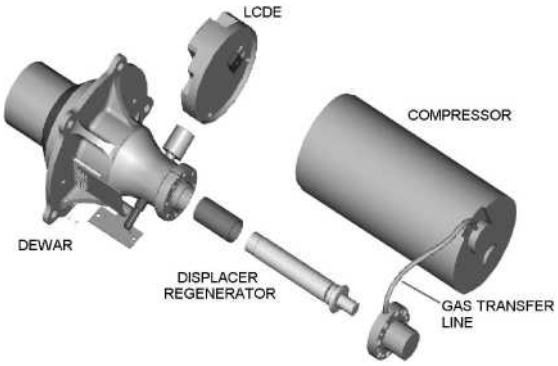

Figure 1. Exploded view of the integrated dewar cooler assembly (IDCA).

GENERAL CHARACTERISTICS

Cryogenic temperature operation is only possible with good thermal isolation of the refrigeration source from the hot environment. Thermal isolation is accomplished with a supporting structure that has low heat conduction and high vacuum to eliminate convection. Radiation heat transfer is minimized with the use of highly reflective coatings. All these features are embodied within the dewar shown above in Fig. 1. There's also the need for effective heat rejection to produce good thermodynamic performance. The sources of heat include cooler electronics, losses in the motor, and the heat of compression. Primary surfaces for heat rejection are: the compressor outside diameter, gas transfer tube, and expander endcap. The best efficiency is achieved by maintaining these surfaces at, or as close as possible to, the system heat sink temperature. These guidelines were applied in the design of the IDCA (Fig. 2) and in the performance map under a new set of operating conditions specified by the program. CMC set out to define the limits for its B1000 Cooler by optimizing parameters including operating frequency, gas pressure, and piston stroke limits as a function of heat sink temperature. The results of these optimization efforts are described in subsequent sections.

COOLDOWN CHARACTERISTICS

Factors affecting cooldown time include the thermal mass of the regenerator, the supporting structure within the dewar, and the refrigerated components, such as focal plane array (FPA), coldshield, and filter. Typical cooldown characteristic of the IDCA at 23 C ambient temperature is

Figure 2. Integrated Dewar Cooler Assembly (IDCA).

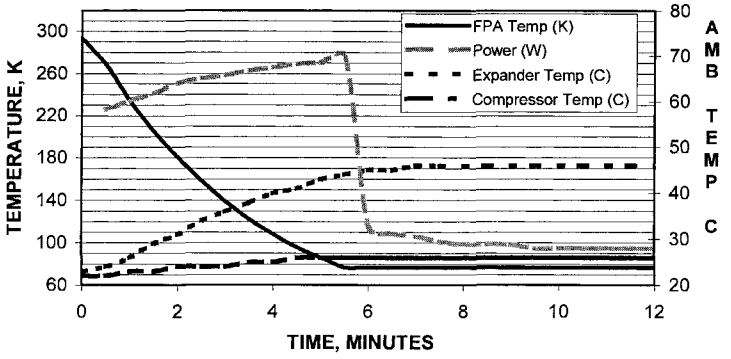

Figure 3. IDCA cooldown characteristics at 23C ambient temperature.

shown in Fig. 3. After a step increase in drive voltage after turn-on, the power consumption rises gradually until the operating set point is reached; at set point, the LCDE throttles the power back to a lower level required to maintain set point temperature. Other parameters plotted in the graph include the compressor and expander case temperatures. It is customary to design heat sinks to limit the temperature rise to less than 15 C above ambient temperature. Figure 3 shows that the expander was not adequately heat sunk with greater than 20 C rise. Figure 4 shows a longer cooldown from elevated temperature. Longer cooldown from elevated temperatures are due to the greater amount of thermal energy that has to be pumped. Figures 3 and 4 represent the performance baseline of the B1000 cooler before the re-optimization for a new requirement.

OPTIMIZATION APPROACH

The characteristics of the cooler can be modeled with the classical equation of motion for a damped spring-mass system driven by a forcing function. A number of hypotheses and constraints for the optimization includes:

1) Cooling efficiency is highest at the resonant frequency.
2) Cooldown time is best at maximum piston stroke and resonance.
3) Resonance frequency changes with ambient temperature.
4) Resonant frequency is a function of operating pressure.

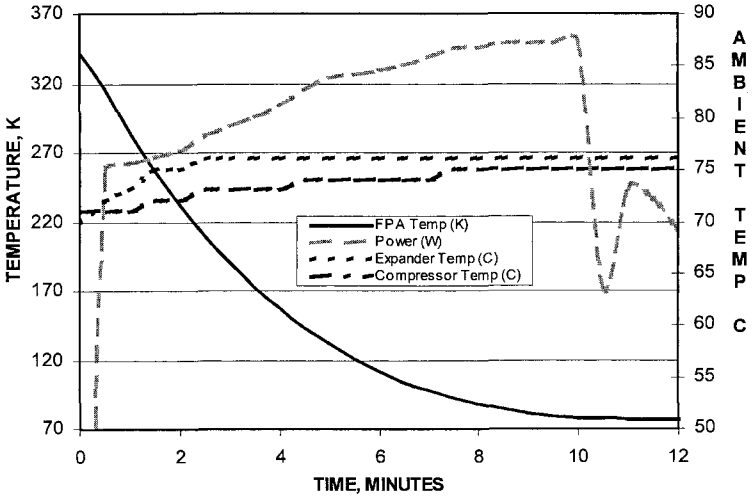

Figure 4. IDCA cooldown characteristics at 71C ambient temperature.

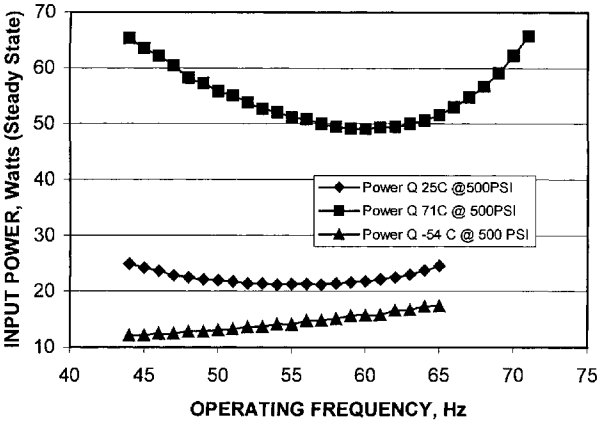

Figure 5. Steady-state input power at various ambient temperatures and frequency.

5) Optimization for faster cooldown is at the expense of higher steady state power and reliability.
6) Compressor size and weight should not exceed standard cooler envelope, and is to be reduced if possible.

The point of interest for this paper is to determine if faster cooldown time requirement can be achieved without violating size and weight constraints. A second point of interest is to determine the best balance between optimizing the parameters for fast cooldown while minimizing the adverse effect of higher steady-state power. Higher steady-state power reduces the life of the cooler.

Figure 5 shows that the dependency of the cooler efficiency (steady-state input power) on drive frequency. The best range to operate the B1000 cooler is between 55-65 Hz. This frequency range applies to the entire ambient temperature range for this product. For this test, the refrigeration temperature was maintained at 77 K while the input power was measured at successively higher frequencies beginning around 45 Hz. This frequency sweep was performed for the cooler at three ambient temperature conditions of −54C, 25C and 71C. Also note that the cooler charge pressure is 500 psig for these tests. The next variable to be examined is the effect of charge pressure on input power.

Figure 6 shows the best steady state performance for a range of charge pressures. For this cooler configuration, the lowest steady-state input power is attained with a 575 psig operating pressure. The input power is higher for pressures above and below this level. Again, the refrigeration tem-

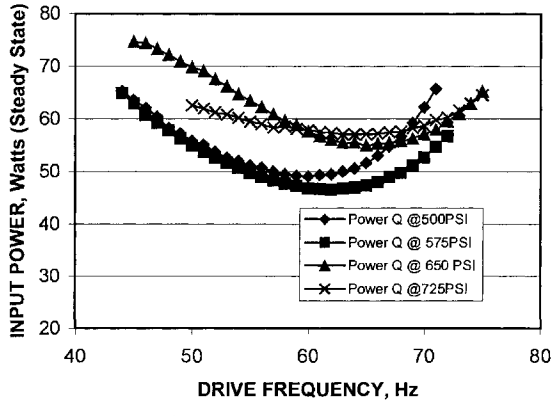

Figure 6. Steady-state input power at various charge pressures and frequencies; ambient temperature at 62C.

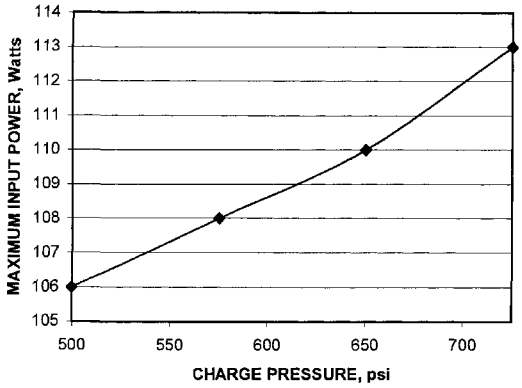

Figure 7. Input power at various charge pressures operating at 71°C ambient temperature.

perature was kept at a constant of 77K throughout these tests. The cooler was charged to each pressure level and evaluated for input power for frequency range between 45-75 Hz. Charge pressure started from the standard 500 psig and increased to 575, 650 and 725 psig, respectively. The conclusion from Figures 5 and 6 is that the optimum operating point for the CMC B1000 cooler is at the drive frequency of 62 Hz and a charge pressure of 575 psig at the ambient temperature of 62 C.

Figure 7 shows the maximum not-to-exceed power, approximately 108 Watts, for the operating points of 62 Hz and 575 psig. The maximum power is at the point in which the compressor pistons reaches full stroke and is touching the mechanical end stops. This physical limit can be altered only if the length of the compressor is increased. The LCDE is then programmed not to exceed this upper drive voltage (power) limit.

Finally, after identifying the best drive frequency, operating pressure and maximum input power, we can now determine if the cooldown time specification can be met. Figure 8 confirms that the system specification for cooldown time can be met with the previously chosen parameters. In summary, the optimized operating point for CMC's B1000 cooler satisfies the new program specification for cooldown time and with sufficient end-of-life margin. Life test data, presented in References 1 and 2, is the subject of future update. An update set of B1000 performance curves is provided in Figs. 9, 10 and 11.

LCDE FEATURES

CMC's LCDE is a microprocessor based controller and driver for all of CMC's cryocoolers. Some of the key features are as follows:

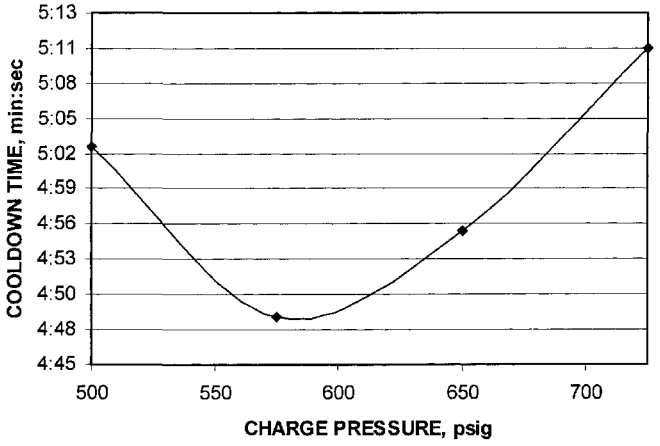

Figure 8. Optimized cooldown performance at 62 C ambient temperature

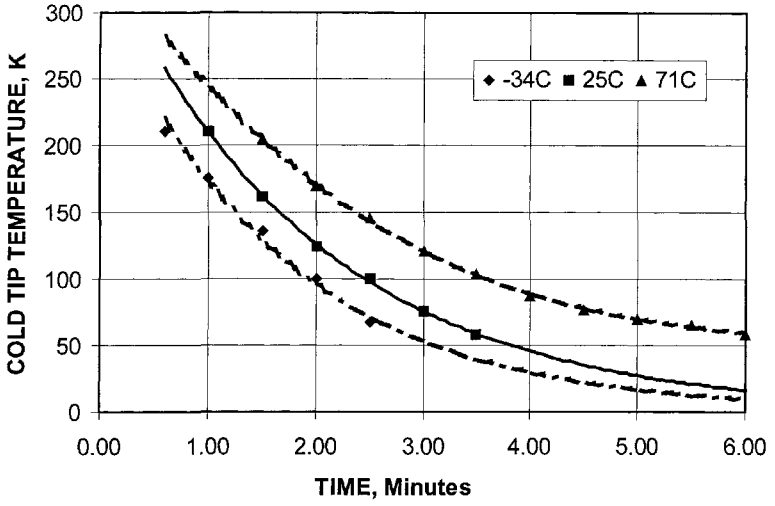

Figure 9. CMC B1000 cooldown performance with optimized parameters.

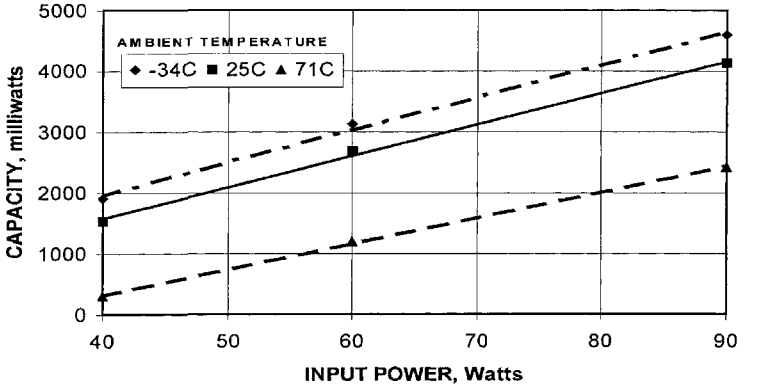

Figure 10. CMC B1000 refrigeration capacity at 77 K with optimized parameters.

1) Sinusoidal or (waveshaped) drive signals.
2) Two (2) temperature set-points (Primary and Standby).
3) Thermal shutdown.
4) Adjustable drive frequency: 20-76 Hz.
5) Dual frequency drive.
6) Scalable steady-state drive frequency as a function of ambient temperature.
7) Rate Power Output: 110 Watts.
8) Power efficiency: > 85% at all power levels.
9) Warranty timer. This unit has a built in digital hour meter.
10) RS-422 serial interface.
11) History data of temperature profile.
12) Works with 17-32 VDC power input. This controller provides over-voltage and under-voltage and reverse voltage protection.
13) Output current sense circuit protection.
14) One milliamp current source and a 1 to 1 buffered temp diode output.
15) Temperature ready indication.

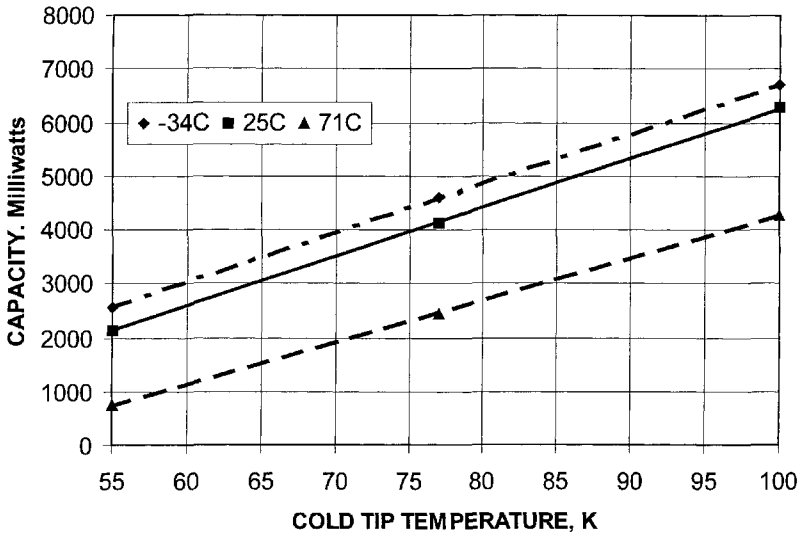

Figure 11. CMC B1000 cooler input power with optimized parameters at various ambient temperatures.

Our linear coolers run most efficiently when driven with a sine-wave. The controller is programmed for a standard sine-wave output and can be tailored for specialized waveform, if necessary. Two temperature set-points allows the IDCA to run in a standby mode, usually at a higher refrigeration temperature than primary mode. The advantages of a two-mode operation are power management, and faster cooldown to ready mode. The LCDE has an internal sensor that will shutdown if it gets too hot. The default temperature is 95 C. An LCDE feature that stands out is its flexibility with drive frequency. The drive frequency is set through software; additionally, a dual drive-frequency mode and a frequency versus ambient temperature mode can squeeze more efficiency out of the cooler. One drive frequency can be dedicated for faster cooldown and a second drive frequency can be used for steady-state operation throughout the ambient temperature range. The LCDE is rated for up to 110 Watts and delivers this power at better than 85% efficiency. A warranty timer can be accessed through a RS-422 serial interface as well as many preventive-maintenance-health (PMH) features such as: number of cooldown cycles completed, accumulated run time, accumulated watt-hour consumed. Protection circuitry includes over-voltage and under-voltage from 17-32 Vdc power input, and output current sense for catastrophic failure protection. The controller provides a one-milliamp constant current source for diode temperature sensor excitation; a one-to-one buffered output signal is available for temperature monitoring. Last but not least, an opto-coupled temperature ready signal is available for system management.

REFERENCES

1. Yuan, S.W., "CMCEC Life Test Results and Related Issues," *Cryocoolers 12*, Kluwer Academic/Plenum Publishers, New York (2002), pp. 79-85.

2. Kuo, D.T., "BAE's Life Test Results on Various Linear Coolers and Their Correlation with a First Order Life Estimation Method," *Cryocoolers 11*, Kluwer Academic/Plenum Publishers, New York (2000), pp. 665-671.

Characterization of the NGST 150 K Mini Pulse Tube Cryocooler

N. S. Abhyankar[1], T. M. Davis[2], D. G. T. Curran[3]

[1] Dynacs Military and Defense, Inc
Albuquerque, NM, USA

[2] Space Vehicles Directorate
Air Force Research Laboratory
Albuquerque, NM, USA

[3] The Aerospace Corporation
El Segundo, CA, USA

ABSTRACT

The Air Force Research Laboratory (AFRL) Cryogenic Technology Research Facility (CTRF) is characterizing the performance of the Northrop Grumman Space Technology (NGST), previously TRW, 150 K mini pulse tube (MPT) cryocooler. This cooler was developed under the AFRL 150 K Protoflight Spacecraft Cryocooler (PSC) Program supported by the Missile Defense Agency (MDA), then Ballistic Missile Defense Organization, (BMDO). Although this cooler has a smaller heat load capacity than other long-life space cryogenic coolers, it has been successfully used in a variety of scientific and military space applications providing cooling of focal planes, optics, and sensors for instruments such as SABER, CX, Hyperion, and the projected STSS Flight Demonstration System (FDS).

This paper presents the results of characterization of one of the NGST 150 K MPT cryocoolers performed at AFRL Cryogenic laboratory. The thermodynamic performance of the cryocooler is described in terms of the performance envelope over a range of rejection temperatures and operating parameters to provide system designers and mission evaluators with specific knowledge on the capability of this cooler. Analytical relations among variables such as input power, heat load, cold end temperature and rejection temperature are examined.

INTRODUCTION

The Air Force Research Laboratory managed and MDA sponsored 150 K MPT PSC cooler is one of the successful cryocooler development programs for space applications initiated in the early nineties. This cooler was built by NGST with a first engineering model[1] delivered in 1993. Since then eleven units plus spares have been built by NGST, six were launched and four are operational in space. Coolers were built for the following payloads:

Cryocoolers 13, edited by R. G. Ross, Jr.
Springer Science+Business Media, Inc., New York, 2004

- HSI (Hyper Spectral Imager) and LEISA (Linear Etalon Imaging Spectral Array) (The Lewis satellite which included experiments with cryocoolers was de-orbited shortly after the launch),
- SABER (Sounding of the Atmosphere using Broadband Emission Radiometry) for Utah State University's Space Dynamics Laboratory (SDL) and NASA Langley Research Center. (SABER is one of four instruments on NASA's TIMED, Thermosphere-Ionosphere-Mesosphere-Energetics and Dynamics, satellite which is still active in space. It is capable of obtaining a set of global measurements of temperature, pressure, winds, chemical composition, and energy inputs and outputs.),
- CX sensors on US military satellites,
- Hyperion (NMP EO1 New Millennium Program Earth Observing-1), and the
- Track sensor on STSS FDS (Space Tracking and Surveillance System's Flight Demonstration System) mission that is not launched yet.

The MPT coolers on SABER, CX, and Hyperion have been in continuous operation since launch. The cooler was originally designed for focal plane cooling at 73K prior to its application at 150K. Although initial AFRL design requirements called for efficient operation at the 150 K, 1 W load, the specifications were tailored to meet each mission's needs (e.g. Hyperion 0.84 W to 1.2 W maximum at 110K)

It is to be noted that the "miniature" aspect of the cryocooler is no longer valid due to technological improvements over the decade in compressors and regenerator materials, and better understanding of the pulse tube and ancillary mechanisms. Recently, NGST developed a "miniature" pulse tube cryocooler[2] for a design point of 1.5 W at 65 K that is smaller than the mini unit reported here. Lockheed Martin Advanced Technology Center in Palo Alto has developed a single stage NASA "mini" pulse tube cooler[3] with design points of 0.3 W at 65 K (15 W input power) and 3 W at 80 K (76 W input power). A two-stage miniature pulse tube flight cryocooler (MPTFC) developed jointly by the National Institute of Standards and Technology (NIST) and Lockheed Martin Astronautics Operations in Denver was flown twice in 1998 and 2001 on NASA space shuttle payloads.[4] European consortiums under the European Space Agency have also developed two miniature coolers, one[5] for 0.8 W at 80 K and another[6] for 1.2 W at 80 K.

The Air Force Laboratory's interest in characterization of the older generation 150 K MPT cooler lies in its application for the STSS FDS to be launched in 2007. In addition, there is interest in identifying potential failure modes (or anomalous behavior) with the cooler since different versions of the cooler have shown unexpected behavior during acceptance and on-orbit testing. Anomalies have included minor performance changes, both improvement and reduction, and failure of a component in the electronics involving the position control sensor (Hyperion). The performance changes were tracked to residual particulate (Stop-off) remaining from a brazing process that affected the cold head tuning. The component failure on the Hyperion cryocooler[7] electronics was quickly corrected with a software on-orbit patch installation. As a result of this patch the cooler continued to operate with nominal performance and the payload was able to provide five to six images per day.

The unit under characterization here was designated by NGST as number 2 among the series of MPT coolers that have been produced. Earlier, the Air Force laboratory had received unit number 6 based on the contractual agreement for the 150 K program, whereas number 2 was delivered to SDL for its preparation to be launched on SABER. Number 6 had been loaned to the FDS program for 10,000 hours of life testing at Raytheon facilities. The coolers are operated from stand-alone flight electronics custom made for individual coolers or rack electronics for ground use. During the acceptance testing of unit number 2 at SDL, it was found that the cooler data points were not repeatable for the same environment and control conditions due to the previously described residual particulate. The non-repeatable nature of this particular unit required it to be replaced by another cooler for the mission. The Air Force unit number 6 that had completed testing at Raytheon was sent to SDL. It was subsequently further characterized and flown on the SABER mission

presently in operation. The exchanged unit number 2 was returned to AFRL from SDL for characterization in the 24-inch vacuum chamber and is the subject of this paper.

Hardware Description

The cryocooler is an integral type orifice pulse tube cooler with an in-line single compressor and balancer capable of minimizing vibration induced by the compressor piston. The piston is supported by flexure springs maintaining alignment and providing non-contacting piston motion. An accelerometer with external signal conditioner and amplifier is placed on the support plate of the cooler to monitor induced vibration during the normal operation. In the laboratory, the cooler is driven with manual drive electronics having separate control knobs for controlling magnitude and offset of the compressor piston. For normal ground-support and on-orbit operations, the cooler is equipped with drive electronics having both temperature and vibration control. More details on the 150 K MPT have been published previously.[1,8,9]

In Figure 1, the MPT cooler is shown in the integrated configuration in the CTRF 24-inch vacuum chamber. The cold end is shown pointing upward in the "0" degree orientation. It is instrumented with a temperature-measuring diode and a heater. A set of thermocouples is placed at various locations to monitor rejection temperature on the support plate and temperature distribution elsewhere on the unit. The central support plate also provides the thermal interface for the chiller fluid that maintains the rejection temperature. The support stand is specially designed to allow change in orientation of the cooler from the vertical-up position (0 degrees) to the downward position (180 degrees) in selected intervals.

The temperatures, input power to the compressors, compressor and balancer strokes, and applied heat load to the cold end are monitored with the help of instruments through the General Purpose Interface Bus (GPIB) interface communication. A LabVIEW based data acquisition and monitoring software is developed with provision for round-the-clock operation.

A typical characterization schedule consists of evaluating the cooler for different operational scenarios. Among them, the common ones are cool down, design point verification, load lines,

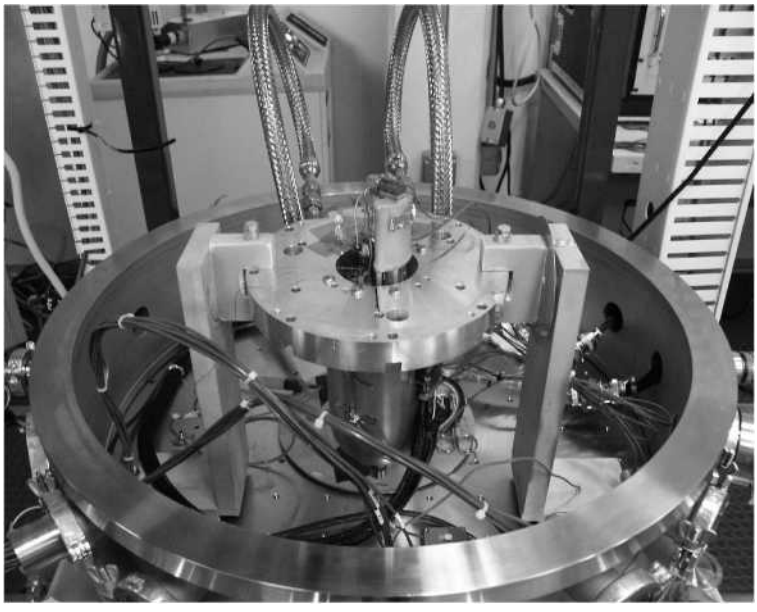

Figure 1. NGST MPT integrated in a 24" vacuum chamber with a rejection interface plate.

performance envelopes, optimum-search for operational frequency and offset, transient response during orbital variation, and thermal cycle and thermal vacuum tests. A baseline parameter set is repeated between major tests to track any performance change.

PERFORMANCE ENVELOPE

A performance map (also known as Ross plot) is shown in Figure 2 for 300 K rejection temperature to depict in-depth information about performance of the cooler. The carpet plot or performance map is generated by interwoven lines of constant temperature and input power to help mission planners estimate input power for expected equivalent load on the cold end at a temperature suitable to meet the sensor requirement. The data points required to generate such a map consist of load variation for fixed input power. They can also be obtained from constant stroke settings if it is more easily controllable than the input power. For the MPT, without the control electronics, constant power data points were obtained for cold end temperature below the desired 170 K limit for STSS application. Linearity or a close second order variation of cold end temperature versus heat load for constant power value is used to calculate constant temperature lines. The lines are drawn for a full range of coldhead temperature of 80 to 170 K at a rejection temperature of 300 K shown in Figure 2. The dotted lines indicate constant specific power in watts per watt. The circular dots are the measured data points for 150 K used to confirm the constant temperature calculation procedure. The lines are extrapolated moderately to indicate the trends in the behavior above 25 Watts although care must be taken since this does not mean that cooler settings will allow tests at those power values.

In Figures 3-5, maps are presented for rejection temperatures of 320, 270, and 245 K to cover the operational range in orbit as specified for the thermal cycle and thermal vacuum tests. Due to stroke and offset limitations, the high power points at low temperatures of 270 K and 245 K were not attainable and hence the performance map is restricted in this region and should not be used for permissible cooler operation. The constant temperature data points at 150 K again verify the procedural accuracy of the performance map. The performance improvement at lower rejection temperatures is evident by the shift in constant temperature lines towards lower specific power.

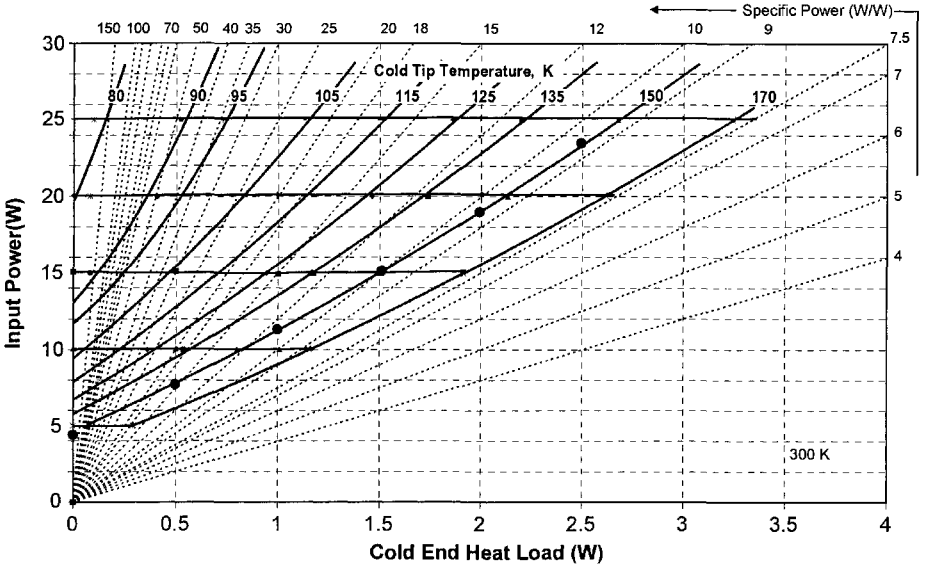

Figure 2. Performance map at a rejection temperature of 300 K.

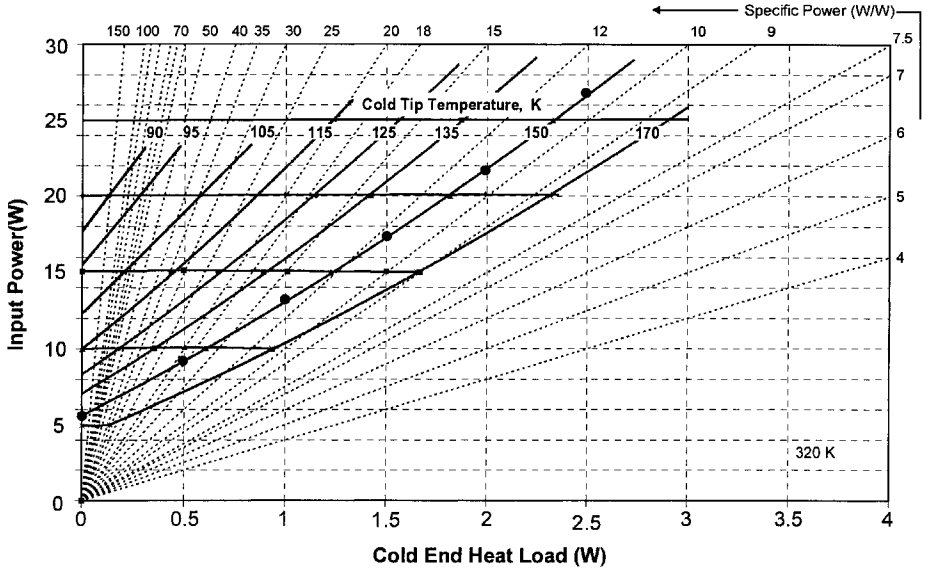

Figure 3. Performance map at a rejection temperature of 320 K.

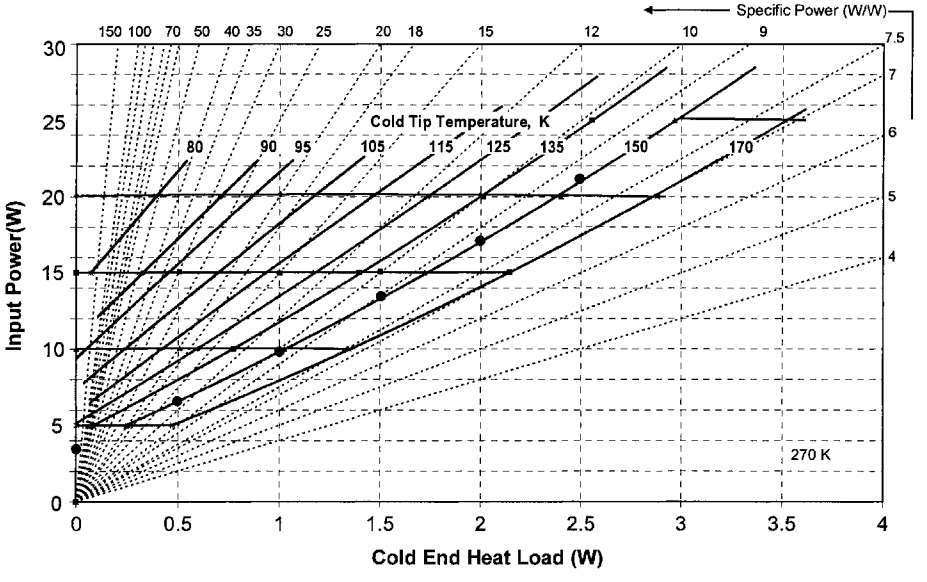

Figure 4. Performance map at a rejection temperature of 270 K.

PERFORMANCE MODELING

The pictorial display of performance data at different rejection temperatures provides a quick-look representation for cooler comparison and selection; however, it poses mathematical difficulty in building a cooler data model. The available measured data with variation of independent variables as heat load (Q_L), cold end temperature (T_c), input power (P_i), and rejection temperature (T_r) is sufficient for a multivariable model development. The difficulty lies in the selection of type of fit, powers, and combination of the variables when one variable is represented in terms of others. Due to complexity in thermodynamic modeling of any cooler, their representation in non-dimensional

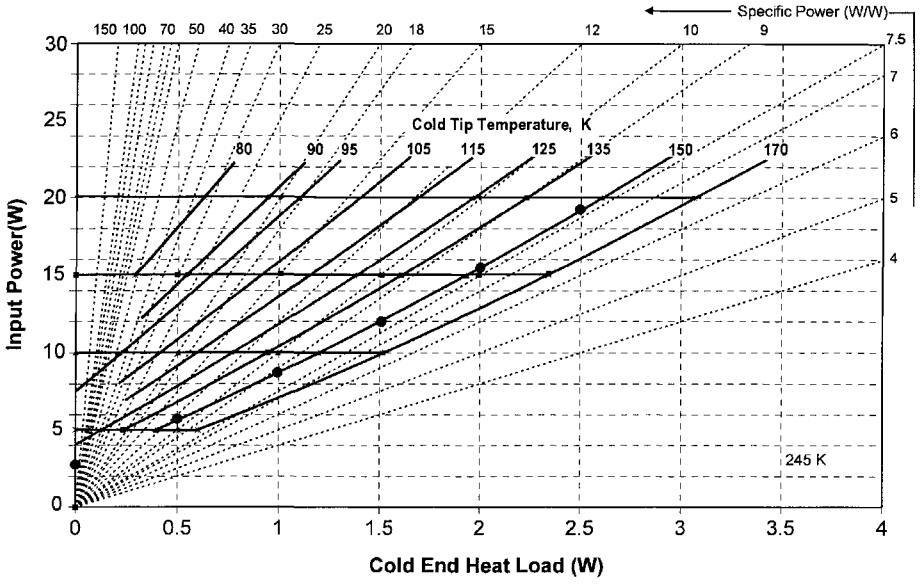

Figure 5. Performance map at a rejection temperature of 245 K.

form does not lead to elegant relations. The coefficient of performance (Q_L/P_i) as an inverse of specific power and its ratio with Carnot efficiency $T_c/(T_r-T_c)$ as percent (%) Carnot efficiency are considered to be guiding terms for the model development. The % Carnot efficiency as a function of cold end temperature is highly nonlinear for the range of load capacity and rejection temperature. Assumptions have to be made for practical considerations and display. For example, the performance maps presented above assume that the constant power line between T_c and Q_L, based on the visual inspection, can be represented in a quadratic relation. This allows a quantitative understanding of the cooler's behavior for particular cases as shown in Figures 2-5.

Based on the available data, an attempt was made to represent input power in terms of T_c, T_r, and Q_L. The variables and their coefficients for two possible sets or fits are given in Table 1.

The two sets of terms chosen for the curve-fit are explained as follows. The first set is based on the rationale that the input power is zero when the cooler is not running and when $T_c=T_r$ with load $Q_L=0$. The constant term is kept for adjusting off nominal values and the effect of parasitic losses while a minimum number of terms are provided to represent non-linearity. The second set of terms are selected based on another fit applied to limited data only for the 150 K constant temperature load lines at all four rejection temperatures (its coefficients are not suitable for extending to the

Table 1. Input power curve-fit data variables and coefficients for mini-PT model representation.

Set 1 Terms	Set 1 Coefficients	Set 2 Terms	Set 2 Coefficients
1	2.9500	1	26.353
Q_L	0.4533	Q_L	0.8477
Q_L^2	0.6076	Q_L^2	0.6129
$Q_L*(T_r/T_c-1)$	7.0764	T_c	-0.2009
$(Q_L*(T_r/T_c-1))^2$	-0.4601	T_r	0.0903
(T_r/T_c-1)	-1.3610	$Q_L*(T_r/T_c-1)$	6.4509
$(T_r/T_c-1)^2$	2.6746	$(Q_L*(T_r/T_c-1))^2$	-0.3622
		(T_r/T_c-1)	-31.695
		$(T_r/T_c-1)^2$	15.473
		$(T_r/T_c-1)^3$	-3.2443
		$(T_r/T_c-1)^4$	0.34942

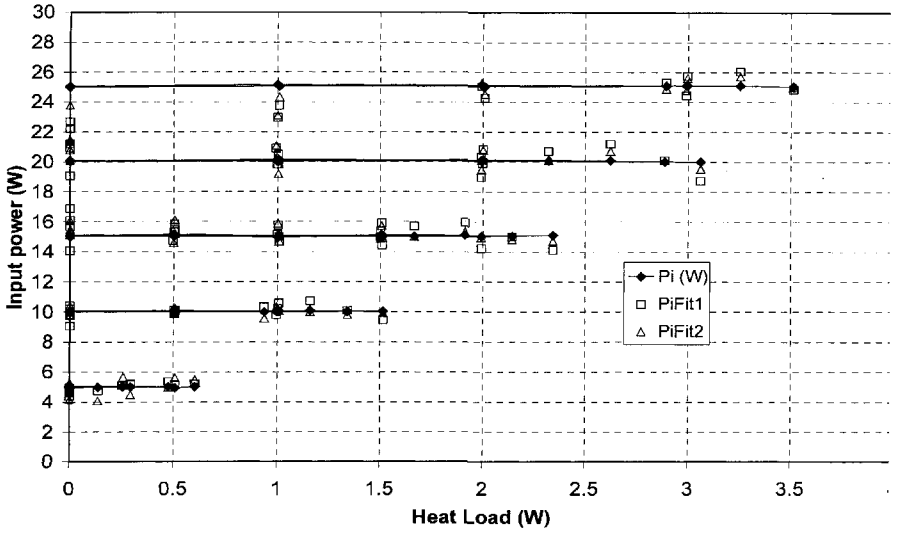

Figure 6. Curve-fit for entire data with set 1 and set 2 terms.

entire data and thus only the form is tried as a second set.) The calculated values from set 1 and 2 terms in Table 1 along with the measured input power are shown in Figures 6 and 7. It appears that set1 parameters (Rsquared correlation fit value ~ 0.979 for set1 as against 0.988 for set2) are sufficient for most of the cases except in the low load and power ranges for all rejection temperatures. Considering the range of parametric values and their spread, the curve fit with set 1 terms is reasonable for general estimation of input power. Similar representation can be studied for estimating load Q_L as a function of (T_c, P_i, T_r) and T_c as a function of (Q_L, P_i, T_r) if desirable. Inverting one relation to another may not be feasible due to the involved nonlinearities.

Parasitic self load was calculated based on a series of no load and loaded warm-up data from the lowest temperature at 300 K rejection temperature. The load value varied with the cold end

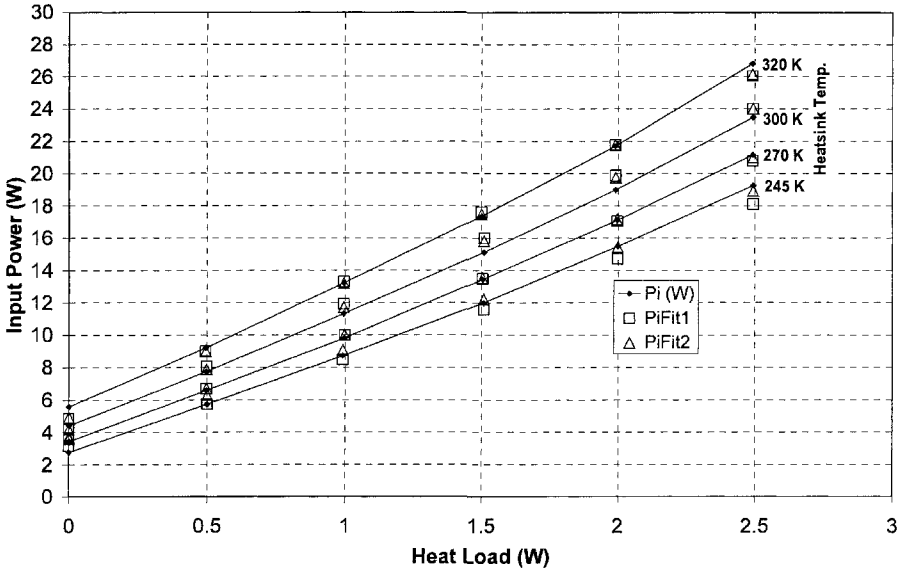

Figure 7. 150 K constant temperature load lines with close curve fit.

temperature, about 1 W at 95 K and 0.6 W at 150 K. The value obtained is high considering the cooler nominal operation condition to be 150 K at 1 W. Upon inspection, it was discovered that the heater lead wire used was of 26 gage instead of the twisted phosphorous-bronze pairs rated for cryogenic temperature. As a result, for given temperature and given input load, the required power is expected to be higher in the above discussion. The performance data presented above should then be viewed with this understanding. Further testing will be performed with lower gauge lead wires and the instrumentation heat leak will be reevaluated for its effect on the performance measurements.

The angle orientation study on the MPT has not shown as dramatic an effect as was seen in previous tests on the High Efficiency Cooler[10], due to lower MPT input power requirement (at high end ~ 25 W for mini-pulse tube as against ~150 W for HEC.) For the MPT there was no preferentially high power at 135 degrees from vertical. The vertical-up position (0 degree) appeared to be a stable configuration with repeatable data. However at the horizontal position, 90 degrees, the load line appeared to follow two curves, indicating unstable performance. As indicated in the introduction section, this anomaly was assumed to be due to debris in the bypass line. Future evaluation of the cooler will include thermal cycle and thermal vacuum tests to be followed by long term endurance evaluation to identify any other anomalies and failure mechanisms.

The 150 K mini-pulse tube development program has already paved a way for a series of advanced pulse tube cryocoolers for space implementation. With the success, NGST has developed high efficiency[11] and high capacity[12] coolers with single or multistage applications.

REFERENCES

1. Chan, C.K., Jaco, C., Raab J., Tward, E., Waterman M., "Miniature Pulse Tube Cooler," Proceedings of the Seventh International Cryocooler Conference, vol. 7 (1992), pp. 50-56.
2. Tward, E., Nguyen, T., Godden, J., Toma, G., "Miniature Pulse Tube Cooler," *Adv. in Cryogenic Engineering*, Vol. 49B, Amer. Institute of Physics, Melville, NY (2004), pp. 1326-1329.
3. Nast, T.C., Champagne, P.J., Kotsubo, V., Olson, J., Collaco, A., Evtimov, B., Renna, T., Clappier, R., "Miniature Pulse Tube Cryocooler for Space Applications," *Cryocoolers 11*, ed. R. G. Ross, Jr., Kluwer Academic/Plenum Publishers, (2001), pp. 145-154.
4. Ladner, D.R., Radebaugh, R., Bradley P.E., Lewis, M., Kittel, P., Xiao, J.H., "On-Orbit Cooling Performance of a Miniature Pulse Tube Flight Cryocooler," *Cryocoolers 12*, ed. R.G. Ross, Jr., Kluwer Academic/Plenum Publishers, (2003), pp. 777-787.
5. Trollier, T., Ravex, A., Charles, I., Duband, L., Mullie, J., Bruins, P., Benschop, T., Linder, M., "Miniature 50 to 80 K Pulse Tube Cooler for Space Applications," *Cryocoolers 12*, ed. R. G. Ross, Jr., Kluwer Academic/Plenum Publishers, (2003), pp. 165-171.
6. Gibson, A. S., Hunt, R., Charles, I., Duband, L., Crook, M., Orlowska, A.H., Bradshaw, T.W., Linder, M., "Design and Characterization of a Miniature Pulse Tube Cooler," *Cryocoolers 12*, ed. R. G. Ross, Jr., Kluwer Academic/Plenum Publishers, (2003), pp. 173-182.
7. "Pre-Launch, Launch and Early Orbit Operations," Earth Observing-1, EO-1 Launch Page, http://eo1.gsfc.nasa.gov/miscPages/launch.html.
8. Tward, E., Chan, C.K., Jaco, C., Godden, J., Chapsky, J., Clancy, P., "Miniature Space Pulse Tube Cryocoolers," *Cryogenics*, vol. 39, no. 8 (1999), pp. 717-720.
9. Chan, C.K., Clancy, P., Godden, J., "Pulse Tube Cooler for Flight Hyperspectral Imaging," *Cryogenics*, vol. 39, no. 12 (1999), pp. 1007-1014.
10. Yarbrough, S. A., Abhyankar, N., Tomlinson, B. J., and Davis, T. M., "Performance Characterization of the TRW 95 K High Efficiency Cryocooler," *Adv. in Cryogenic Engineering*, Vol. 49B, Amer. Institute of Physics, Melville, NY (2004), pp. 1277-1284.
11. Tward, E., Chan, C.K., Raab, J., Nguyen, T., "High Efficiency Pulse Tube Cooler," *Cryocoolers 11*, ed. R. G. Ross, Jr., Kluwer Academic/Plenum Publishers, (2001), pp. 163-167.
12. Chan, C.K., Nguyen, T, Jaco, C., "High Capacity Two-Stage Pulse Tube Cooler," *Cryocoolers 12*, ed. R.G. Ross, Jr., Kluwer Academic/Plenum Publishers, (2003), pp. 219-224.

Performance Test Results of a Miniature 50 to 80 K Pulse Tube Cooler

T. Trollier and A. Ravex (1)
I. Charles and L. Duband (2)
J. Mullié, P. Bruins and T. Benschop (3)
M. Linder (4)

(1) Air Liquide Advanced Technology Division, AL/DTA
Sassenage, France
(2) CEA/DSM/DRFMC/Service des Basses Températures
Grenoble, France
(3) THALES Cryogenics B.V.
Eindhoven, The Netherlands
(4) European Space Agency, ESA/ESTEC
Noordwijk, The Netherlands

ABSTRACT

An Engineering Model (EM) of a Miniature Pulse Tube Cooler (MPTC) has been designed, manufactured and tested in partnership between AL/DTA, CEA/SBT and THALES Cryogenics. Prior to the EM manufacturing, a development phase was performed with an in-line architecture for the cold finger and using an existing flexure bearing compressor from THALES Cryogenics.[1] The optimized development model pulse tube cooler demonstrated a cooling capacity of 1 W at 82 K with 25 watts PV work and 288 K heat rejection temperature. Based on this experience, the EM cooler reported on here has been designed and manufactured with a U-shaped architecture to provide a more compact cooler for improved integration. In this paper, thermal and mechanical test results for the new EM cooler are presented and analyzed for various heat sinking temperatures, input powers, and orientations.

INTRODUCTION

The objective of the work was to optimize, design, and manufacture, at pre-qualification level, a 50-80 K Engineering Model (EM) Miniature Pulse Tube Cooler (MPTC) which is commercially competitive in both performance and cost within the future space cryocooler market. It should offer significant advantages over the presently available technology and should require no, or only minor, delta qualification for direct use in future spacecraft applications. The overall performance specification was to demonstrate a cooling capacity of 1 W at 80 K with 32 W maximum electrical input power and with a heat sinking temperature of 288 K. The mass budget was limited to 3 kg, and the design should survive standard launch loads.

Cryocoolers 13, edited by R. G. Ross, Jr.
Springer Science+Business Media, Inc., New York, 2004

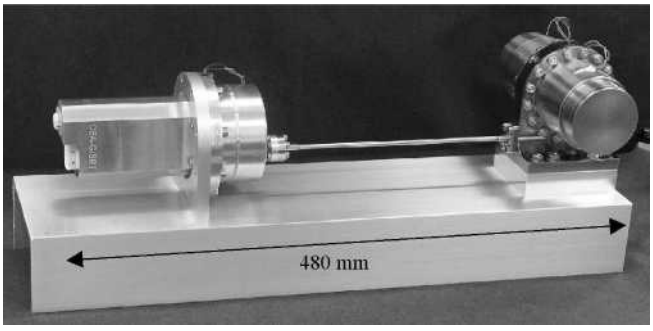

Figure 1. Final assembly of the MPTC Engineering Model.

MPTC DESIGN

The final Engineering Model design is shown in Fig. 1. The total length of the MPTC is 480 mm, including 200 mm for the interconnecting pipe. The overall mass of the EM is 2.8 kg.

In the design of the cold finger, the regenerator and the pulse tube are mounted parallel to one another onto a flange in a U-shaped configuration. This configuration was selected for the EM to provide good cryogenic performance in a compact, robust, and simple design that enhances integration compared to the in-line configuration. The flange is made of aluminium for high thermal heat transfer and mechanical stiffness. The hot flange is designed such that it integrates the buffer volume and the warm-end heat exchangers. The inertance tube is wound inside the buffer volume. Both the tube of the regenerator and the pulsation tube are made of thin-walled titanium alloy Ti-6Al-4V in order to reduce the parasitic heat leaks. The pulse tube EM incorporates a snubber that is used as a launch bumper to prevent any excessive lateral motion of both tubes and to significantly reduce the mechanical stress on the tubes at the flange location. This snubber is also made of aluminum. A low conductivity fiberglass part is placed between the cold block and the snubber cylinder to ensure low parasitic heat losses in case of contact during operation. In normal conditions, there is no contact between the snubber and the cold block of the pulse tube.

The compressor design is built around a moving-magnet linear motor that drives the pistons in a dual opposed configuration into a common compression chamber. The moving magnet linear motor offers significant advantages over the conventional moving-coil design. This innovative concept allows the coils, which are the main source of gas contamination, to be placed outside the working gas. Additional advantages are the absence of flying leads and glass feedthroughs to supply current to the coils. Flexure-bearings are used in order to have a radial clearance between the piston and the cylinder. These flexure-bearings are round discs made of spring steel with 3 arms. With this kind of flexure bearings, a very high radial stiffness can be achieved. The coil holders are made of titanium alloy in order to reduce eddy current losses and to combine high mechanical stiffness and low density. The two compressor halves are mounted on a dedicated nickel plated aluminium alloy "center plate" that contains all the mechanical, thermal and electrical interfaces of the compressor and the two cylinders. Bolted flanges are directly machined into the titanium alloy block of the coil holder. Gas containment is achieved by means of metallic seals.

MPTC THERMAL VACUUM PERFORMANCE TESTS

A dedicated thermal test bench has been built. The MPTC cold finger and compressor are mechanically and thermally anchored to separate cold plates in which ethylene glycol flows to allow for testing with various heatsink temperatures. The platform is attached to a flange that closes the vessel in order to perform the tests under high vacuum.

For the test results described below, the connecting pipe is 200 mm long and the compressor drive frequency is 50 Hz. Also, the referenced heatsink temperature is defined as the set-point

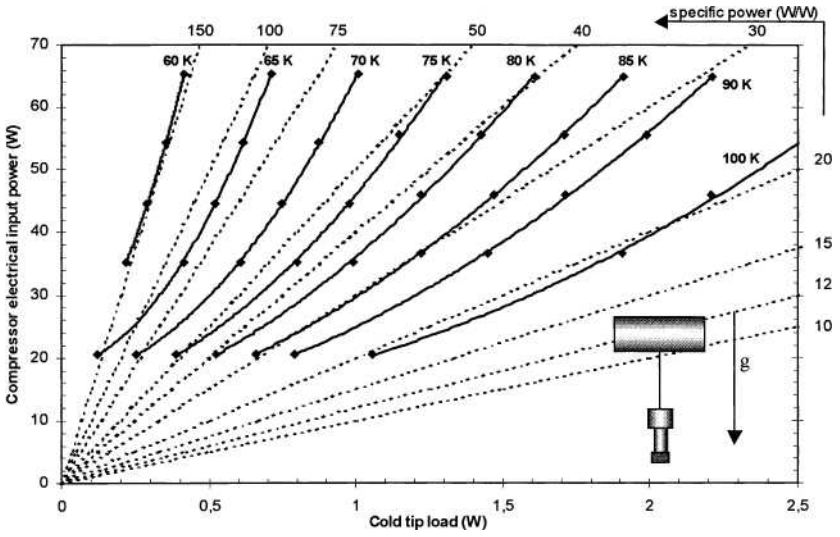

Figure 2. Performance map of the MPTC (288 K heatsink temperature and 0° tilt angle).

temperature of the coolant at the inlet of the cold-finger and compressor cold plates. The thermal vacuum test campaign consisted of tests over the following ranges of parameters:

- Input power ranging from 35 to 65 watts
- Cooling capacity from 0 to 2 watts
- Heatsink temperature from 237 K to 310 K
- Mounting orientation with respect to gravity vector: 0° tilt angle (cold finger vertical with cold tip down), 90° tilt angle (cold finger horizontal) and 180° tilt angle (cold finger vertical with cold tip up)

Figure 2 presents the performance map for the MPTC plotted for various input powers and applied heat loads for a 288 K heatsink temperature (coolant inlet temperature) and for 0° tilt angle (cold finger vertical with cold tip down). For 80 K, the design point is 1 W cooling capacity with 35 W electrical input power to the compressor (35 W/W specific power). As shown in the figure, the performance decreases for high input powers (50 to 65 W) due to a decrease of the compressor efficiency and warm-up of the compressor and cold-finger flanges. The performance decreases also for low applied heat loads due to the predominance of parasitic heat losses. An optimum is found in the 30 to 40 W electrical input power region (design point).

Taking the above performance of 1 W at 80 K for 35 W electrical input power for 288 K heat sinking and 0° tilt angle as the reference performance, various mounting orientations had the following impacts (see Fig. 3):

- An increase of 6.3 K with 180° tilt angle (cold finger vertical with cold tip up). The performance reduced to 1 W at 86.3 K / 35 W input which corresponds to 240 mW lost in cooling capacity (i.e. 24 %). That means also that the input power must be increased to 43.4 W to recover the 1 W cooling capacity at 80 K.
- An increase of 2.7 K with 90° tilt angle (cold finger horizontal). The performance is then reduced to 1 W at 82.7 K / 35 W input power. This corresponds to about 105 mW lost in cooling capacity (i.e. 10%).

As shown in Fig. 4, the impact of the orientation on performance losses is reduced for higher input powers and higher cooling capacities. For 65 W input power and 2 W applied heat load, the cold tip temperature is not affected anymore between 0° and 90° tilt angles for 288 K reference heat sinking conditions. The parasitic convective effect is obviously a function of the temperature gradient between the warm end and the cold tip temperatures. Larger input powers lead to larger gas displacements in the pulsation tube, which reduce the convection as well.

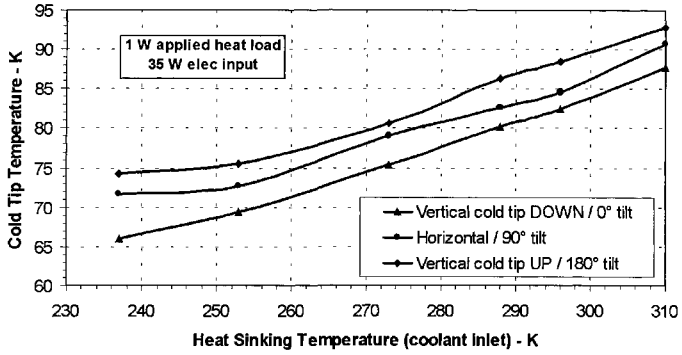

Figure 3. MPTC performance for various heat sinking temperatures and gravity orientations.

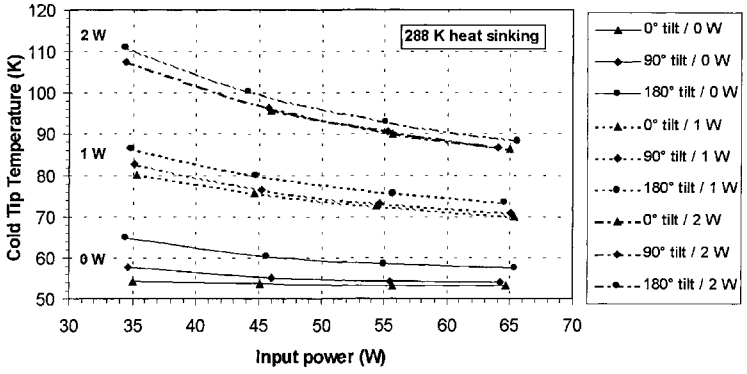

Figure 4. MPTC performance for various orientations, cooling powers, and input powers.

The natural convection heat transfer inside the pulsation tube while the cooler is not operating (OFF mode) has been studied. The pulsation tube is filled with 40 bars of helium and the tube wall is considered as adiabatic. The cold tip temperature is set at 80 K, while the hot end is set at 298 K. Using the simulation results to which we add the measured conduction and radiation contribution (determined to be 465 mW), we have plotted in Fig. 5 the predicted parasitic heat loss as a function of gravity orientation and compared it with the experimental results. The modelling of the natural

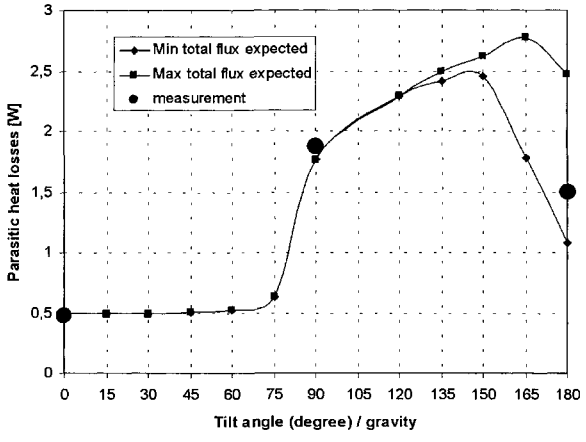

Figure 5. Parasitic heat loss measurements compared with predictions (80 K / 300 K).

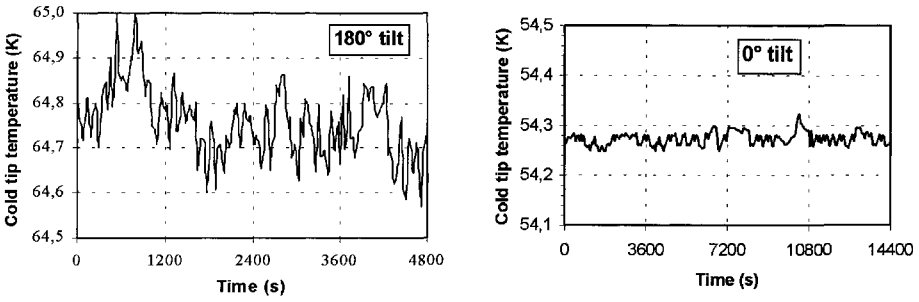

Figure 6. Cold tip temperature stability for 180° and 0° tilt angle (35 W and 288 K heat sinking).

convection allows for very good prediction of the MPTC parasitic heat losses in the horizontal orientation (less than 8% error). It indicates, also, that the parasitic heat losses for a non-operating cooler on the ground would be maximal for a tilt angle between 150° and 165° (about 2.5 W).

As shown, for tilt angles above 120°, there is no stationary solution. For 180°, the heat flux varies between 1 W and 2.5 W (including 465 mW of conduction and radiation losses). During the experimentation (operating mode), we noticed temperature instabilities of 0.5 K with the 180° tilt orientation, while the temperature stability for 0° tilt was better than 0.1 K (see Fig. 6).

MPTC MECHANICAL PERFORMANCE TESTS

Induced vibrations

The interface reaction forces produced by the MPTC have been measured directly with force transducers at the test article mounting interface against a seismic foundation (blocked force approach). Induced vibrations are directly measured with the quadratic summation of the forces in each of the 3 axes. The environmental vibration level of the bench is controlled in order to obtain a convenient signal/noise ratio. Figure 7 shows the induced vibration in the three axes with 36 W input power delivered by the CDE (the cooler was not heat sunk during the tests). For the fundamental driving frequency of 50 Hz, the levels are below 0.1 N in the cold finger axis (X), below 0.8 N in the compressor axis (Y), and below 0.1 N in the radial axis (Z). However, the harmonics show higher levels and particularly in the 300-500 Hz region where the levels reach 1.5 N, 4 N and 2.4 N, respectively, in the X, Y and Z axes. This evolution can be attributed to some coupling modes with the test fixture in the 500 Hz region, and to the excitation of some resonance frequencies of the cooler (the first resonance frequency of the compressor being calculated at 431 Hz).

Modal Analysis

The MPTC was equipped with six accelerometers and placed on a shaker. Sine surveys were performed with 0.5 g input before and after each high-loading test depicted herein in order to get the resonance frequencies of the MPTC cold finger. As shown in the Fig. 8, the resonant frequency in the Y-axis was found to be 151 Hz, which is in very good agreement with the predicted mode (respectively 153 Hz). For the Z axis, not shown, the measurement was 285 Hz (versus 283 Hz predicted). In the Y axis, the 0.5 g sine survey spectra indicates that contact is occurring between the cold tip and the snubber. An acceleration of 29 g for 150 Hz corresponds to a 0.31 mm displacement, which is the gap set between the cold tip and the snubber (0.3 mm).

Sine Vibration

Sine vibration tests were performed successfully in each of the three mutual axes with the following parameters: frequency bandwidth 5-100 Hz, amplitude +/- 12 mm from 5 to 20.5 Hz, 20 g peak from 20.5 Hz to 60 Hz, 8 g peak from 60 to 100 Hz. During the test the MPTC was not operating and the drive coils were short-circuited.

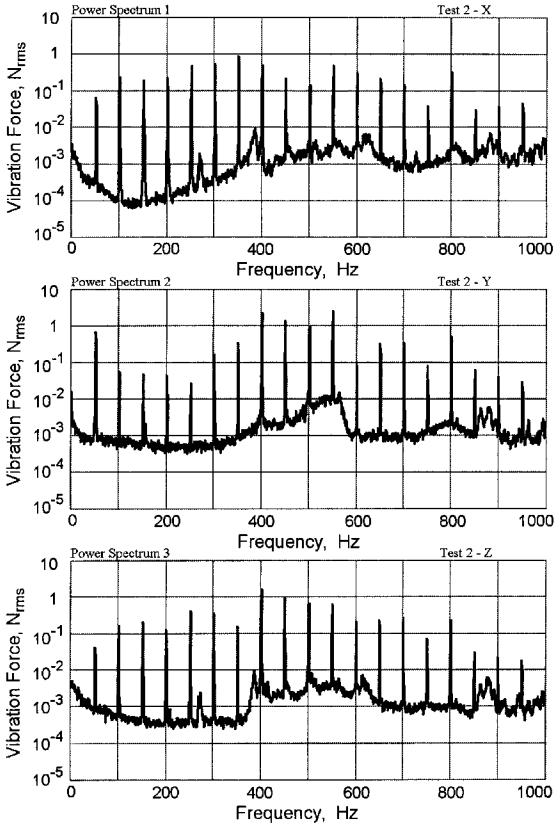

Figure 7. MPTC induced vibration for 36 W input at 50 Hz.

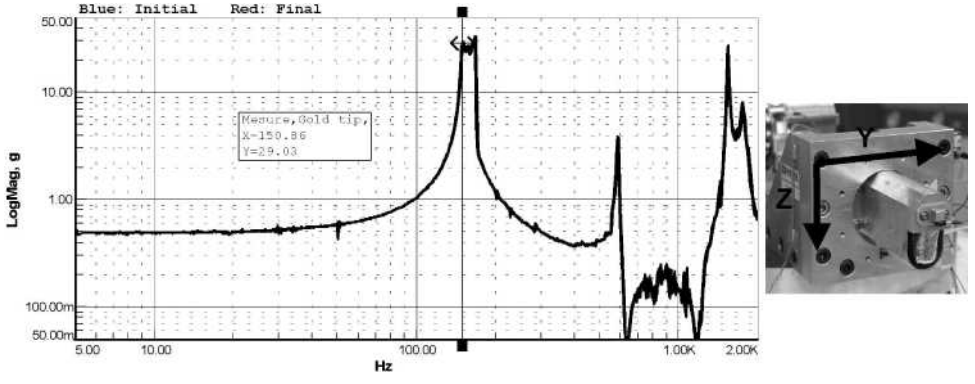

Figure 8. 0.5 g sine survey before and after high level sine vibration test: cold tip - Y axis

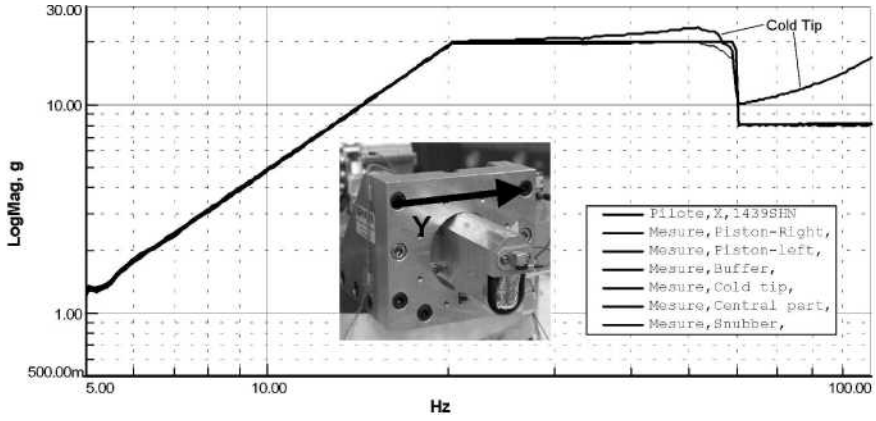

Figure 9. High level sine sweep test response: all points - Y axis

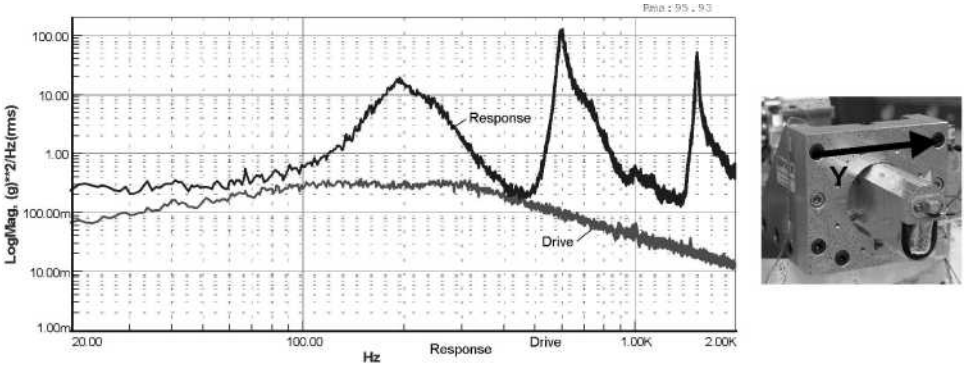

Figure 10. High level random vibration response: cold tip - Y axis

Six accelerometers were placed on the cold tip, the snubber, the buffer (mechanical anchorage of the cold finger), the center plate (mechanical anchorage of the compressor), and at each extremity of the coil holders (piston left and right). The platform was piloted and controlled with two separated accelerometers. Figure 9 presents the results for the high level sine test performed in the Y axis.

Random Vibration

After performance of the high level sine vibration tests in all three axes and the thermal vacuum verification tests, the MPTC was shaken with the following random vibration parameters in each axis:

- Frequency bandwidth: 20-2000 Hz
- Drive coil condition: shorted
- Power spectral density: +3 dB/Oct from 20 to 100 Hz
  0.3 g^2/Hz from 100 Hz to 300 Hz
  -5 dB/Oct up to 2000 Hz
- Overall level: 13.1 g_{rms}
- Duration: 150 sec/axis

Figure 10 presents the PSD vibration levels measured at the cold tip during loading in the Y axis. The flat aspect of the cold tip PSD output around 150 Hz indicates that it is contacting at its 150-Hz first-mode resonance frequency. Although this cold tip response corresponds to a high level of acceleration (95.9 grms), the MPTC successfully passed the random load in this axis.

CONCLUSIONS

The MPTC EM demonstrates very good cryogenic performance of 1 W at 80.2 K with 35.3 W electrical input power at 50 Hz corresponding to 26.2 W PV work (considered as the measured input power minus the measured Joule losses). The cold finger warm end temperature was 301.6 K and the compressor flange temperature was 298.2 K. Parasitic heat losses of 465 mW have been measured between 80 K and 300 K. The impact of heatsink temperature, gravity orientation, input power, and heat load have been measured and analyzed over a wide range. The MPTC has been characterized to have less than 0.1 N of induced vibration in the cold finger axis and 1 N in the compressor axis at the 50-Hz drive frequency. Finally, the MPTC has been submitted to high level sine and random vibration profiles.

This extensive test campaign provides very good knowledge of both the operational and OFF performance of the MPTC for consideration in future projects.

ACKNOWLEDGMENT

This work was performed in the framework of a Technological Research Program funded by the European Space Agency. We acknowledge the financial and technical support of the European Space Research and Technology Centre (ESA/ESTEC, Contract N°14896/00/NL/PA).

REFERENCES

1. T. Trollier, A. Ravex, L. Duband, I. Charles, T. Benschop, J. Mullié, P. Bruins and M. Linder, "Miniature 50 to 80 K Pulse Tube Cooler for Space Applications," *Cryocoolers 12*, Kluwer Academic Publisher/ Plenum Publishers, New York (2003), pp. 165-171.

Performance of Japanese Pulse Tube Coolers for Space Applications

A. Kushino, H. Sugita and Y. Matsubara

Institute of Space Technology and Aeronautics
Japan Aerospace Exploration Agency
Tsukuba, Ibaraki 305-8505, Japan

ABSTRACT

We report results from an experimental evaluation of Japanese Stirling-type pulse tube coolers operating at 60–80 K, with potential application to future satellite applications. Three commercial samples were driven under vacuum conditions of below ~10^{-2} Pa. The cooling capacities, cooldown times, and the vibration generated by the cold heads and compressors were measured systematically. With room-temperature heat-sink conditions, the cooling capacities at 77K ranged from 2 W to 3.4 W among the three coolers when driven with an effective input power of 100 W. The measured coolers were estimated to be similar to those of US flight coolers used in a previous infrared mission, and the results strongly suggest that Japanese coolers are worth being developed for space use; though, the present input power of 100 W is somewhat large. Displacements of the cold heads during operation depended on the cooler mounting to the base plate and were measured to be ~3 to 13 μm_{pp}—a value considerably larger than the displacement levels of US flight pulse tube coolers. The vibration of the cold head could be suppressed, even in the present integral-type configuration, if the cold head is placed at the node of vibrations.

INTRODUCTION

Mechanical cryocoolers are used to cool low temperature sensors aboard satellites. In particular, conventional Stirling coolers have been used in several Earth observing missions. Examples are Terra/ASTER[1], Terra/MOPITT[2] and ADEOS-II/GLI.[3] The advantages of such mechanical cryocoolers when compared to cryogens are small volume, light weight, and reliability. Since the 1990s, NASA has launched pulse tube coolers in orbit.[4] They work without any moving mechanics at their cold heads.

In NASDA, ISAS and following JAXA, which started at 1st of October 2003, several satellite missions have been proposed for the near future. Many of them include cryogenic sensors as listed in Table 1. Although there are several kinds of commercial pulse tube coolers[5,6] in Japan, mainly developed for high-Tc superconducting filters for cellular phone systems on the ground, Japanese pulse tube coolers have not yet been used in space. Conversion of commercial coolers designed for ground applications to space use could lead to lowered costs compared to directly developing flight models.

We have investigated the performance of Japanese commercial pulse tube coolers as candidates for conversion to Japanese flight coolers in the future. In particular, cooler induced vibration

Cryocoolers 13, edited by R. G. Ross, Jr.
Springer Science+Business Media, Inc., New York, 2004

Table 1. Japanese satellite missions already adopted or being proposed with cryogenic sensors.

	Expected launch	Cryogenic sensor	Cooler (Temperature)
MTSAT-1R/JAMI[7]	Nov. 2004	IR detector	Pulse tube (60K)
Astro-EII[8]	Feb. 2005	X-ray spectrometer	Stirling (20K)+ADR (60mK)
Astro-F[9]	2005	IR detector	Stirling (20K)
SELENE[10]	2006	γ -ray spectrometer	Stirling (80K)
GOSAT[11]	2007	IR spectrometer	Pulse tube (60K)
JEM/SMILES[12]	2008	SIS mixer	Stirling (20K)+JT(4.5K)
VSOP-2[13]	>2010	Radio receiver	TBD
SPICA[14]	>2010	IR spectrometer	TBD
NeXT[15]	>2010	X-ray spectrometer	TBD

is one of the most important properties to be investigated for sensitive sensors, and should be suppressed to as low as possible. In the next section, three pulse tube coolers used in this evaluation are described. This is followed by a description of the experimental setup and the measurement results. Discussion and conclusions are presented at the end.

PULSE TUBE COOLERS

In 2002, we surveyed Japanese commercial pulse tube coolers that had a cooling capacity of about 1W at liquid nitrogen temperatures for an electrical input power of 100 W. Such cooling capacity can match the cooling needs of infrared spectrometers with HgCdTe detectors, which are often used on board Earth observing satellites. The weight was desired to be less than about 10 kg, and a high-frequency 'Stirling-type' drive configuration was required.

The selected coolers are shown in Fig 1. All three coolers control phase between the He gas pressure and its displacement using an inertance tube with buffer tank. The He gas is charged to 2.5~3 MPa. The linear compressors have moving-coil driven twin opposing pistons to cancel vibration. One sample, SP2000, has a U-shaped pulse tube configuration, where the regenerator and pulse tube are aligned in parallel; the other two have in-line pulse tube configurations. To drive them in vacuum, metal blocks were attached to the compressors to transfer heat from their hot heat exchangers to a base plate. The basic specifications are listed in Table 2. The power factors η (the ratio between the effective and the apparent power) were separately measured. They were: 0.85 (SPR-02A), 0.92 (SP2000), and 0.99 (CZX1A0Z1) at the lowest temperatures, respectively.

EXPERIMENTAL APPARATUS

The following measurements of the cooling characteristics were performed at JAXA Tsukuba Center. Each cooler was entirely enclosed in a vacuum chamber, where a vacuum level of $\sim 10^{-2}$ Pa was maintained to simulate space operation.

Figure 1. Three pulse tube coolers on base plates in the vacuum chamber.

Table 2. Basic specification of the three coolers. The weight includes that of the metal blocks to reject heat, which are shown in Fig. 1.

Supplier	AISIN Seiki	Daikin Industries	Fuji Electric
Model	SPR-02A	SP2000	CZX1A0Z1
Weight (kg)	8.7	16	10.2
Height (mm)	300	250	340
Width (mm)	250	300	190
Compressor diameter (mm)	90	110	90
Configuration	Inline	U-shaped	Inline

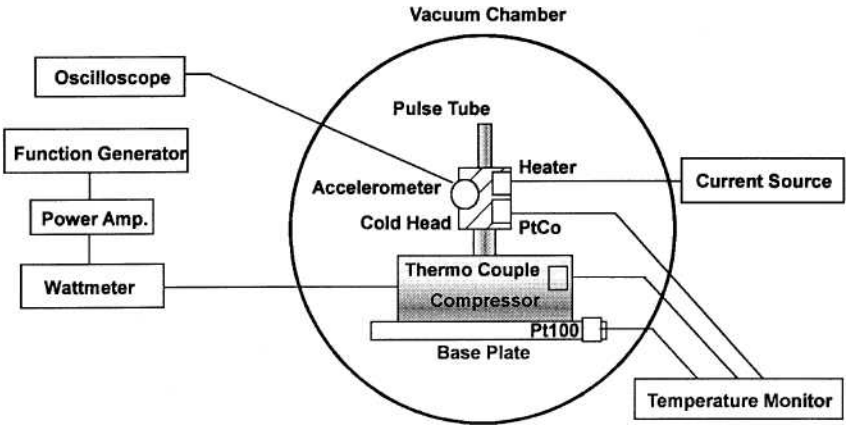

Figure 2. Systematic drawing of the cooler drive and measurement system.

The electrical input power to drive the compressor pistons was a sinusoidal wave supplied by a function generator and a power amplifier. The voltage, current and resultant effective power were monitored by a wattmeter placed between the compressor and the amplifier. Temperatures at the cold heads, copper base plates, and compressors were measured using PtCo, Pt100 resistive thermometers and T-type thermocouples, respectively. A load resistance of about 50 Ω was also attached to the cold head to evaluate the cooling capacity. Heat from the hot heat exchanger was rejected to the base plate under the compressor, which was kept at a fixed temperature between about 272 and 313 K by circulating a mixture of water and ethanol. Vibration generated by the coolers during operation was measured using a 3-axis accelerometer, which also enabled measuring the displacements. Except during vibration measurement, the cold head was wrapped with multilayer insulation (MLI) to suppress parasitic radiation loads from the 300 K chamber. The experimental setup is shown schematically in Fig. 2. The driving frequency was selected to be 50 Hz, which is the frequency commonly used for grid-based electrical appliances in Japan.

COOLDOWN TIMES

Figure 3 shows cooldown plots from a starting temperature of 273 K for various base plate temperatures. The coolers were driven with a fixed effective power of 100 W, which is the rated value of the three coolers. Times to 77 K differed by about 1000 sec, even for a single cooler, due to the wide range in base plate temperatures (~40 K). When the base plate temperature was 300 K, times ranged from 2000–2500 sec among the three coolers, and this was about 1.5 times longer than for the Japanese Stirling cooler flown on board the EOS-Terra satellite.[1] This is because the movement of He gas in the pulse tube cooler becomes worse at low temperature.[16] However, this slower cooldown time won't matter very much for the long—order of a year—observations in orbit.

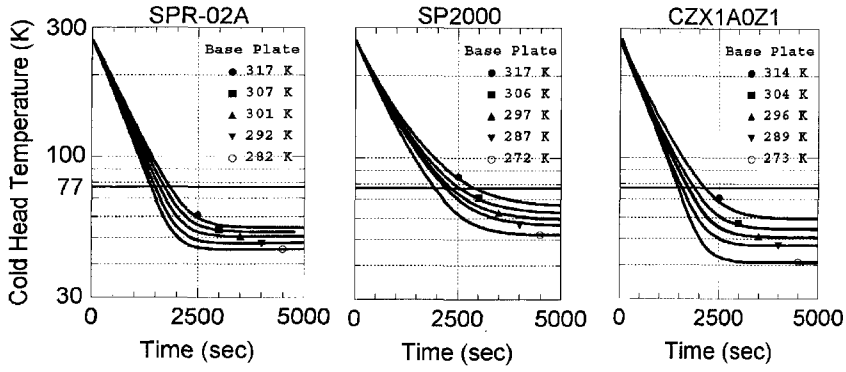

Figure 3. Cold head temperatures as functions of time from 273K. Base plate temperatures are shown by the symbols. Coolers are driven by 50Hz/100W.

COOLING CAPACITIES

The cooling capacity of each cooler was measured by measuring the power applied to a resistive heater attached to each cold head. The results are shown in Fig. 4. The cooling capacity is seen to increase almost linearly with cold head temperature in the measured temperature range between 40 K and 80 K. The best cooling capacity at 77 K, with the base plate kept at room temperature, was 3.4 W. The flight pulse tube cooler for the EOS-Aqua/AIRS experiment is estimated to have a cooling capacity of 3.3 W at 77 K with a baseplate temperature of 297 K and with an input power of 100 W.[17] This suggests that the Japanese commercial pulse tube coolers have enough capacity to be used at least for a similar application, i.e., infrared HgCdTe detectors for Earth observation.

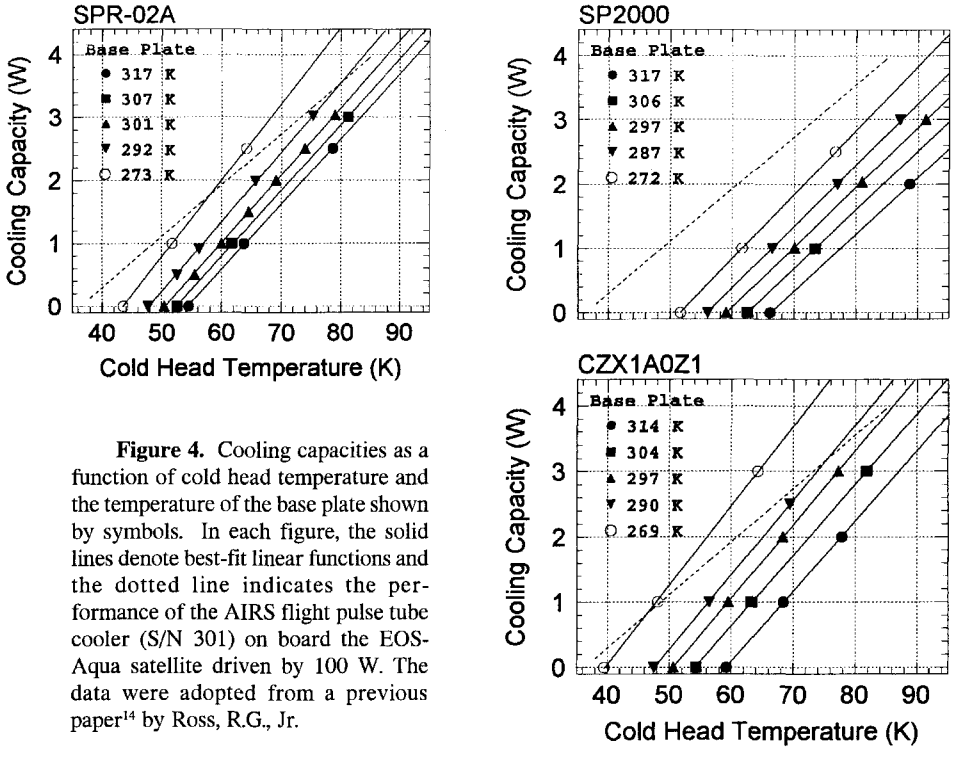

Figure 4. Cooling capacities as a function of cold head temperature and the temperature of the base plate shown by symbols. In each figure, the solid lines denote best-fit linear functions and the dotted line indicates the performance of the AIRS flight pulse tube cooler (S/N 301) on board the EOS-Aqua satellite driven by 100 W. The data were adopted from a previous paper[14] by Ross, R.G., Jr.

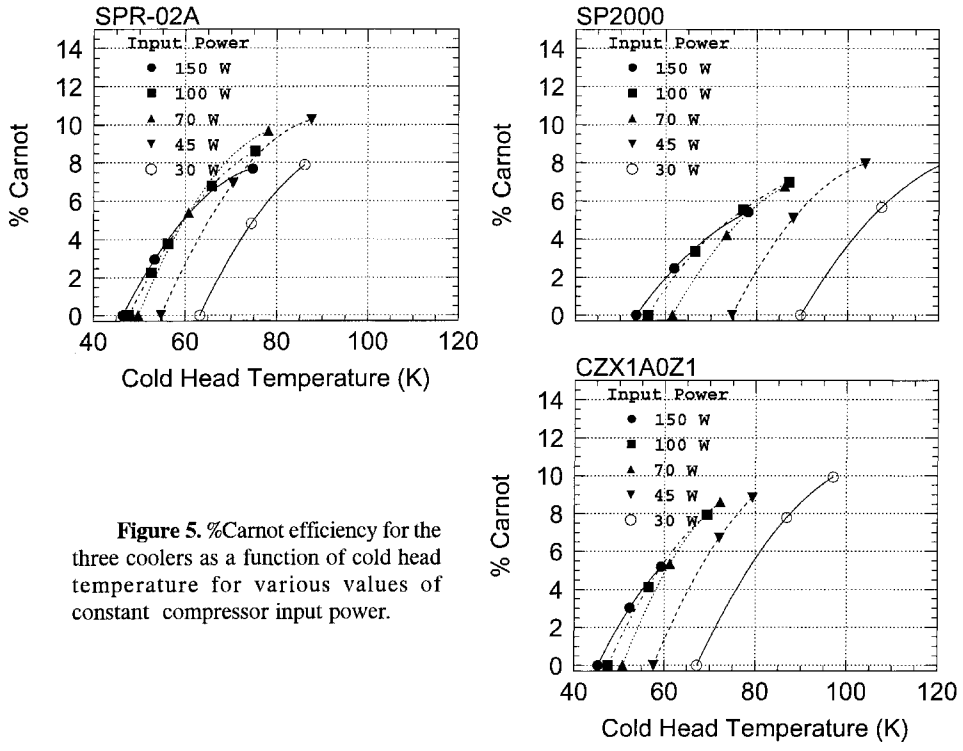

Figure 5. %Carnot efficiency for the three coolers as a function of cold head temperature for various values of constant compressor input power.

Moreover, if we can obtain a lower heat rejection temperature for the pulse tube coolers, the cooling capacity will be significantly increased as shown in Fig. 4.

In real missions, the available electrical input power to the compressors ranges from 45 W[1] to several hundreds of watts.[18] We also measured the cooling capacities when the coolers were driven by effective powers from 30 W to 150 W. Figure 5 shows the %Carnot efficiency as a function of cold head temperature and effective input power. For each cooler, the larger the input power is, the better the %Carnot efficiency is. Below about 77 K, good performance was not obtained when the cooler was driven with an input power less than ~70 W.

VIBRATION

Each cooler was mounted to the copper base plate using metal blocks that were tailored for each cooler. Then, the generated vibration at the beginning of cooldown from room temperature was measured using accelerometers located on both the cold head and on the compressors. The three axes were defined as shown in Fig. 6, i.e., X is the direction of movement of compressor pistons, and Z is normal to the base plate.

Results of displacements are shown in Table 3. The compressor of SPR-02A had very low vibration compared to that at its cold head; this behavior was not observed with the other two coolers. This is because the compressor of SPR-02A was directly fixed to the base plate through its bottom side, and the other two were fixed at rather high positions near the cold heads. However, the present μm order displacements were about 10 times larger than those achieved on the flight pulse tube cooler of EOS-Aqua/AIRS (0.2μm).[19] Such high levels may cause degradation of the spectrographic performance of the sensors. Thus, to achieve an order of magnitude smaller vibration level, the cold head should be placed at the node of vibration. It is not necessary to split the cold head from the compressor using a long capillary tube that will deteriorate the cooling capacity. Indeed, the flight pulse tube coolers of AIRS are integral-types.

Table 3. Displacement at the cold head and compressors. The units are μm_{pp}.

Cooler	SPR-02A		SP2000		CZX1A0Z1	
Accelerometer at	cold head	compressor	cold head	compressor	cold head	compressor
x -displacement	3.4	2.8	8.3	6.4	4.5	2.9
y -displacement	5.6	3.2	12.7	6.4	2.7	10.3
z –displacement	3.8	2.8	3.7	5.9	4.2	9.2

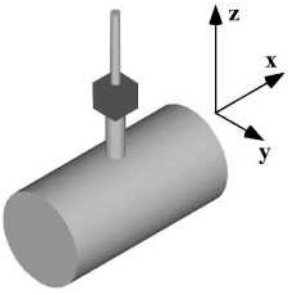

Figure 6. Definition of the 3-axes in the vibration measurement.

CONCLUSION

We successfully drove three kinds of Japanese commercial pulse tube coolers operating at 60–80 K under vacuum conditions. Cooling capacities, when driven with 100 W, were similar to those of previous flight coolers. We observed that vibration depends on cooler mounting to the base plate. An evaluation summary is presented in Table 4. We conclude that Japanese pulse tube coolers are worth being developed for future space use.

ACKNOWLEDGMENT

The authors deeply thank the suppliers of the pulse tube coolers, who kindly allowed us to evaluate good Japanese samples. We appreciate all the members in the thermal engineering group at JAXA, especially Dr. S.Toyama and Mr. T. Kobayashi with their helpful advice and technical support through the experiments. A.K. was a research fellow at JAXA and financially supported.

REFERENCES

1. Kawada, M. et al., "Performance Characteristics of the ASTER Cryocooler in Orbit," *Cryocoolers 12*, Kluwer Academic/Plenum Publishers, New York (2003), pp. 737-746.
2. Hackett, J. P., et al., "Layout and packaging of the MOPITT instrument," *Proc. of SPIE*, vol. 4486, (2002), pp. 122-130.

Table 4. Summary of the present evaluation.

Pulse tube cooler	**SPR-02A**	**SP2000**	**CZX1A0Z1**
Lowest temperature (K)	48	56	48
Power factor	0.85	0.92	0.99
Time to 77K (min)	25	37	26
Cooling capacity at 77K (W)	3.2	2.0	3.4
Cooling capacity per weight (W/kg)	0.37	0.13	0.33
%Carnot at 77K in 100W input	8.9	5.6	9.4

3. Kurihara, S., et al., "Calibration and instrument status of ADEOS-II Global Imager," *Proc. of SPIE*, vol. 5234 (2004), pp. 11-19.

4. See the URL at "http://www.astronautix.com/craft/lewis.htm"

5. Yasukawa, Y., et al., "Design and Test of a 70 K Pulse Tube Cryocooler," *Cryocoolers 12*, Kluwer Academic/Plenum Publishers, New York (2003), pp. 157-164.

6. Hiratsuka, Y., et al., "Development of a Lightweight Pulse-Tube Cryocooler," *Adv. in Cryogenic Engineering*, Vol. 49B, Amer. Institute of Physics, Melville, NY (2004), pp. 1360-1367.

7. Raab, J., et al., "JAMI Flight Pulse Tube Cooler System," *Cryocoolers 12,* Kluwer Academic/Plenum Publishers, New York (2003), pp. 191-197.

8. Inoue, H., "The Astro-E mission," *Advances in Space Research*, vol. 32 (2003), pp. 2089-2090.

9. Shibai, F., et al., "ASTRO-F mission," *Proc. of SPIE*, vol. 4850 (2003), pp. 162-169.

10. Kobayashi, N., et al., "SELENE Gamma Ray Spectrometer Using Ge Detector Cooled By Stirling Cryocooler," *Proc. of the 35th Lunar and Planetary Science Conference*, March 15-19, 2004, League City, Texas, in press.

11. See the URL at "http://www.jaxa.jp/missions/projects/sat/eos/gosat/index_e.html"

12. Seta, M., et al., "Submillimeter-Wave SIS Receiver System for JEM/SMILES," *Advances in Space Research*, vol. 26, Issue 6 (2000), pp. 1021-1024.

13. Murata, Y., et al., "The Next Space VLBI Mission following VSOP," *Proceedings of the IAU 8th Asian-Pacific Regional Meeting*, vol. 2 (2002), pp. 21-22.

14. Nakagawa,T., "SPICA: a new space telescope for mid- and far-infrared astronomy," *Advances in Space Research*, vol. 30, Issue 9 (2002), pp. 2129-2134.

15. Kunieda, H.,et al., "New X-ray Telescope Mission (NeXT)," *Proceedings of the New Century of X-ray Astronomy*, vol. 251 (2001), p. 220.

16. Hiratsuka,Y., private communication.

17. Ross, R.G., Jr., "AIRS Pulse Tube Cooler System-Level and In-Space Performance Comparison," *Cryocoolers 12,* Kluwer Academic/Plenum Publishers, New York (2003), pp. 747-754.

18. Shirey, K.A., et al., "Space Flight Qualification Program for the AMS-02 Commercial Cryocoolers," *Cryocoolers 12,* Kluwer Academic/Plenum Publishers, New York (2003), pp. 37-44.

19. Ross, R.G., Jr., "AIRS Cryocooler System Design and Development," *Cryocoolers 9,* Kluwer Academic/Plenum Publishers, New York (1997), pp. 885-894.

High Capacity Staged Pulse Tube

C. Jaco, T. Nguyen, D. Harvey, and E. Tward

Northrop Grumman Space Technology
Redondo Beach, CA, USA

ABSTRACT

The High Capacity Cryocooler (HCC) is being designed to provide large capacity cooling at 35 K and 85 K for space applications in which both cold focal planes and optics require cooling. The compressor is scaled from the High Efficiency Cryocooler compressor and is capable of using input powers up to 700 W. The two linear pulse tube cold heads are integrated with the compressor into an integral cryocooler. Provision is made to provide a thermal strap between the cold heads in order to improve efficiency. The cooler is undergoing acceptance testing that includes thermal performance mapping over a range of reject temperatures and power levels, launch vibration testing and self induced vibration testing.

INTRODUCTION

The High Capacity Cryocooler (HCC) as shown in Figure 1 is a two-stage pulse tube cooler developed to provide a long life, low mass, higher efficiency space cryocooler on missions such as the Space Tracking and Surveillance System (STSS). The cooler has an objective to extend the performance of proven, high efficiency, lightweight pulse tube cooler technology to larger capacity, lower temperature and staged operation.

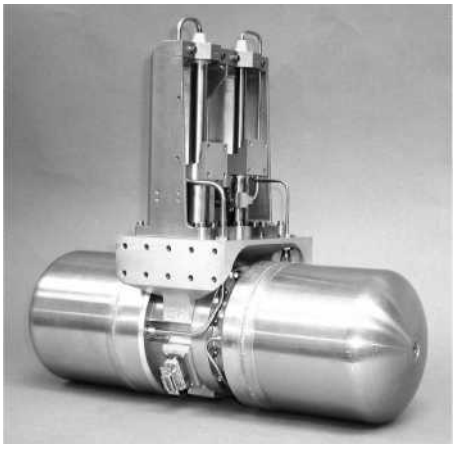

Figure 1. Two-stage high capacity cryocooler.

Cryocoolers 13, edited by R. G. Ross, Jr.
Springer Science+Business Media, Inc., New York, 2004

Table 1. Typical cooler characteristics.

Cooling load at 85 K	19.11 W
Cooling load at 35 K	1.9 W
Input power	500 W
Reject temperature	300 K
Maximum input power capability	700 W
Cooler mass	14.3 kg

Because of its high efficiency and very low mass/unit capacity, the HCC can be applied to simultaneously cool long wave infrared (LWIR) focal planes (as low as 30 K) and optics (60 K to 150 K). The HCC performance is not restricted to the design point of 2 W at 35 K and 16.5 W at 85 K and has a wide spectrum of cooling temperatures and cooling loads for various input power and heat reject temperatures. The HCC achieves low input power and large cooling load because of the efficiency of its pulse tube cold heads and its efficient compressor. The low mass results from the use of the second-generation flexure compressor technology developed with Oxford University and productionized for Northrop Grumman by Hymatic Engineering.[1]

CRYOCOOLER

The cooler characteristics are summarized in Table 1. The HCC two-stage cold heads are designed in an integral parallel configuration. In this design, the 1st and 2nd stage cold heads are mounted directly on the compressor center plate. The oscillating flow from the compressor is split into the two cold heads in proportion to their required thermal design performance. The parallel two-stage cold head configuration has many advantages. First, there is minimal interference in the thermal performance of the two stages, i.e., changes in cooling at one stage has a small effect on the other stage. Second, the regenerators are maintained at reasonable sizes even at the HCC high cooling requirements. This minimizes the performance issues associated with very large regenerator sizes. Third, the heat strap between the cold heads is a very effective tool to control the load balancing between the two stages. Fourth, the heat leak to the lower temperature stage is trapped by the upper temperature stage in both a single cooler and in a standby redundant configuration resulting in improved efficiency.

The two-stage cold head is mounted onto a back-to-back compressor designed to achieve both long lifetime and vibration balance. The flexure springs are very stiff in the direction perpendicular to the driven motion (much stiffer than gas or magnetic bearings) so that close tolerance gas gap seals can be maintained and wearing seals can be eliminated. The flexures themselves are designed for maximum stress levels well below the material endurance limits. Their reliability is validated in the compressor since over 10^7 cycles are accumulated in 4 to 5 days with these compressors. The working fluid is dry helium with no lubricants. The drive is a direct voice coil motor similar to a loudspeaker drive, thereby eliminating linkages.

The cooler components are shown in Figure 2. The linear cold heads are attached to the centerplate and hermetically sealed with a metal C-ring. The cold heads containing the regenerators, cold blocks, pulse tubes and orifice blocks are mechanically supported against launch loads by a support structure. The two 6.45 cm^2 cold block interfaces are gold plated and located near the midpoint of the cold heads. The 35 K cold head is provided with redundant calibrated platinum resistance thermometers used for temperature control. The thermal strap between the 85 K cold block and the 35 K regenerator provide overall system power reduction. Also located on the centerplate is an accelerometer that is used to sense cooler self-induced vibration. The accelerometer preamplifier, which is mounted on the centerplate, amplifies the accelerometer signal for transmission to the control electronics. Here it is used as an error signal in a feedback loop to reduce the vibration to very low levels. The compressor end caps, which also enclose the reservoir, are hermetically sealed by metal C-rings. The centerplate incorporates simple and effective mechanical and thermal interfaces to payloads. The primary mechanical mounting interfaces of the compressor

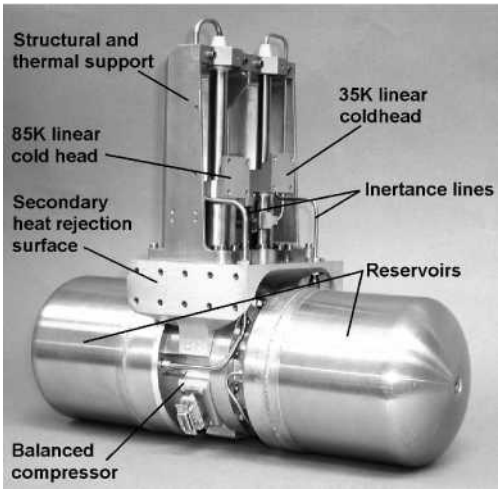

Figure 2. HCC cooler components.

can adequately remove up to 400 W of heat by direct conductive heat transfer to the mount surface. For greater input powers, a secondary thermal interface is provided for extra heat removal capability.

After assembly, the bake out process performed on the cooler reduces volatile condensables and water in the machine to negligible levels. All Northrop Grumman coolers are hermetically metal sealed to have effective zero detectable leakage rates of helium fluid. The processes have been verified by life tests of similar pulse tube coolers and in flight history of the seven other Northrop Grumman pulse tube units that are currently in orbit.

COOLER PERFORMANCE

Figure 3 shows a typical performance map of the two-stage cooler at fixed stroke and reject temperature. Note that at fixed upper temperature load as the applied load on the lower temperature stage is reduced from the maximum value shown of 2.25 W to 0 W, the temperature of the upper

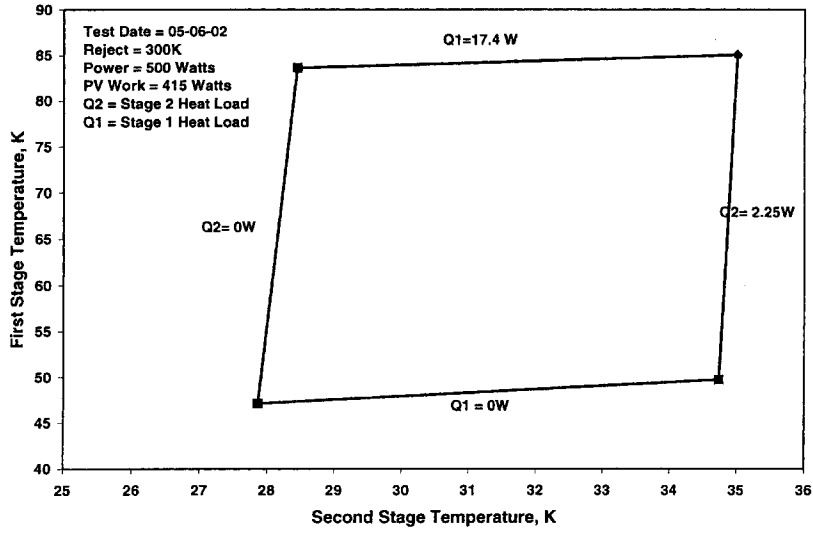

Figure 3. Two stage cold head performance map.

Table 2. HCC performance at different temperatures of first stage.

Stage 1 Temperature	Stage 1 Load	Stage 2 Temperature	Stage 2 Load	Input Power
85 K	16.8 W	35 K	2 W	501 W
111 K	12.55 W	35 K	0.7 W	209 W

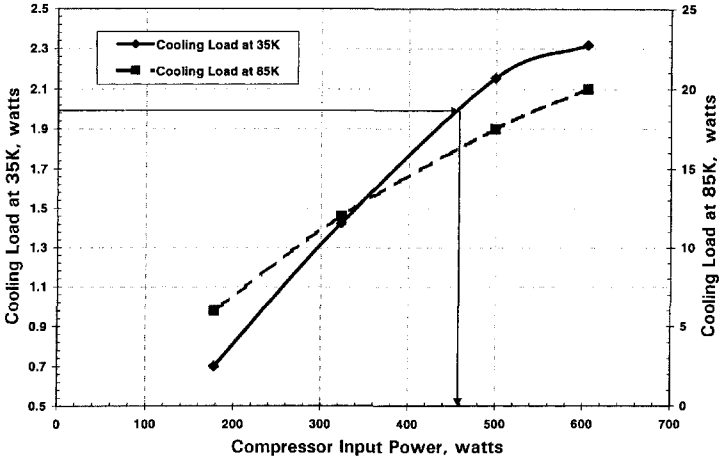

Figure 4. Two stage cold head performance as function of input power.

stage is affected only by a few degrees. Similarly, when the load on the lower temperature stage is held fixed and the load on the upper temperature stage is varied from 17.4 W to 0 W, the lower temperature stage temperature varies by less than 1 K. This implies that the thermal performance of each cold head is independent of the other.

In a parallel multistage configuration, there is little interference between the stages. This is very important in reducing risk for an immature payload design. Figure 4 shows the performance of the HCC cooler as a function of the input power. As the input power is reduced, the cooling loads are reduced while maintaining the efficiency of the system. In these measurements the HCC cooler maintains its efficiency as the input power is reduced from 500 W to 178 W. The HCC cooler can be optimized at different first stage cooling temperatures. Table 2 summarizes the performance at two cooling loads at 35 K and different temperatures of the first stage.

The High Capacity Cryocooler is undergoing acceptance testing prior to its delivery to the Air Force. The complete suite of acceptance tests includes thermal performance mapping over a wide range of reject temperatures and power levels, launch vibration testing, and thermal vacuum tests. The engineering model cooler was tested under the random launch vibration shown in Figure 5,

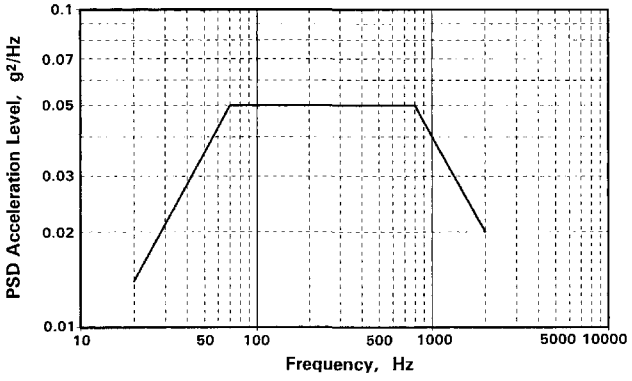

Figure 5. Random vibration profile.

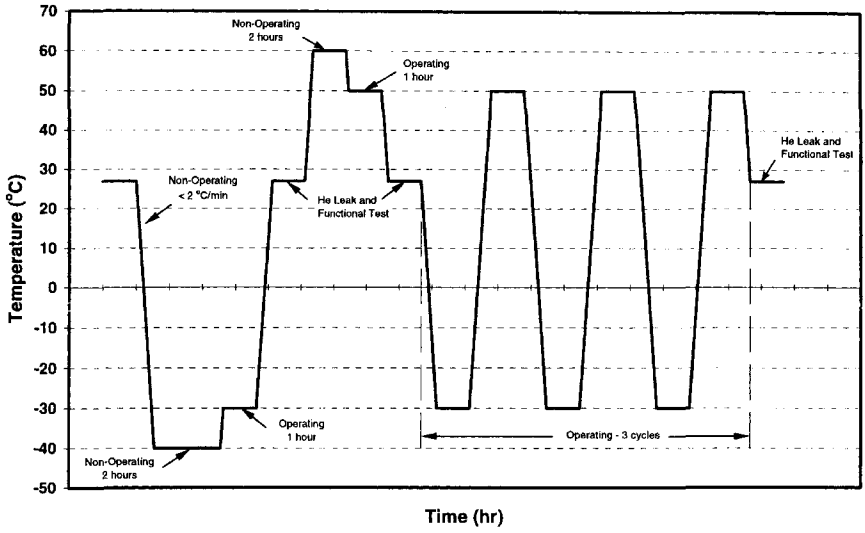

Figure 6. Thermal cycle test.

Table 3. Thermal, stress and dynamic margin for qualification levels.

Components		Requirement	Capabilities
Center Plate	Temperature Rise @ 400W	≤ 20 K	16.7 K
	Interface Heat Flux @ 400W	≤ 25 W/in^2	17.6 W/in^2
85 K Cold Head	Safety Factor (Yield)	≥1.5	4.4
	Safety Factor (Ultimate)	≥2.5	5.9
	Margin of Safety (Q=90)	≥0	1.55
	1st Mode	≥250 Hz	770 Hz
35 K Cold Head	Safety Factor (Yield)	≥1.5	2.8
	Safety Factor (Ultimate)	≥2.5	3.2
	Margin of Safety (Q=90)	≥0	0.27
	1st Mode	≥250 Hz	511 Hz
H-Bar	1st Mode	≥250 Hz	594 Hz

which are acceptance levels. The overall random vibration level is 8.65 Grms. The cooler was also acceptance tested under different thermal conditions.

The thermal cycle profile is shown in Figure 6. Extensive thermal and dynamic analyses were conducted on the HCC. The results of the analyses are summarized in Table 3.

ACKNOWLEDGMENT

This work was sponsored by the MDA and was performed for the Air Force Research Laboratory (AFRL), Kirtland AFB, NM, under contract number F29601-01-C-0226. The support of Thom Davis and Adam Smith of AFRL is gratefully acknowledged.

REFERENCES

1. Tward, E., et al., "High Efficiency Cryocooler," *Adv. in Cryogenic Engineering*, Vol. 47B, Amer. Institute of Physics, Melville, NY (2002), pp. 1077-1084.
2. Chan, C.K, Nguyen, T., and Jaco, C., "Two-Stage Pulse Tube Cooler," *Crycoolers 12,* Kluwer Academic/Plenum Publishers, New York (2003), pp. 219-224.

Lockheed Martin RAMOS Engineering Model Cryocooler

D. Frank, E. Roth, P. Champagne, J. Olson, B. Evtimov, R. Clappier, T. Nast

Lockheed Martin Advanced Technology Center
Palo Alto, CA 94304 USA

T. Renna and B. Martin

Lockheed Martin Commercial Space Systems
Newtown, PA 18940 USA

ABSTRACT

Lockheed Martin's Advanced Technology Center (LM-ATC) is developing the cryocooler system for the United States infrared instrument on the Russian-American Observational Satellites (RAMOS) under contract to the Space Dynamics Laboratory. The project is presently fabricating the engineering model, which consists of the cryocooler and electronic controller.

LM-ATC's cryocooler is robust and simple, consisting of a two-stage coldhead with no moving parts, driven by a linear flexure-bearing compressor and powered by a high-efficiency electronic controller that includes ripple suppression and vibration cancellation. A distance of up to one meter separates the coldhead and compressor.

The controller provides temperature control at 75K. The cryocooler is designed simultaneously to provide 0.75 W of cooling at 75K and 6 W cooling at 130K while rejecting heat at 313K. Total system power is 117 W and the exported vibration is less then 0.2N. This paper presents the status of the engineering model and overall system characteristics.

INTRODUCTION

The RAMOS instrument requires system cooling at two different temperatures. The program selected LM-ATC's two-stage pulse tube based on its maturity and simplicity. The cryocooler consists of a compressor driving a two-stage pulse tube coldhead, powered by cryocooler control electronics (CCE).

The RAMOS instrument consists of two cryocooler systems (Figure 1). One cryocooler is utilized as a redundant system and is not operating under normal condition. The cryocooler is a split system with the coldhead mounted on the instrument vacuum shell and the compressor on a spacecraft panel. This leads to a system with a long transfer lines between the coldhead and compressor. The primary cryocooler has the shorter line. Each cryocooler has a dedicated CCE.

The coldhead is a simple two-stage pulse tube based on LM-ATC's cryocooler that was developed under Independent Research and Development (IRAD) funding in 1998-1999[1]. The coldhead

Cryocoolers 13, edited by R. G. Ross, Jr.
Springer Science+Business Media, Inc., New York, 2004

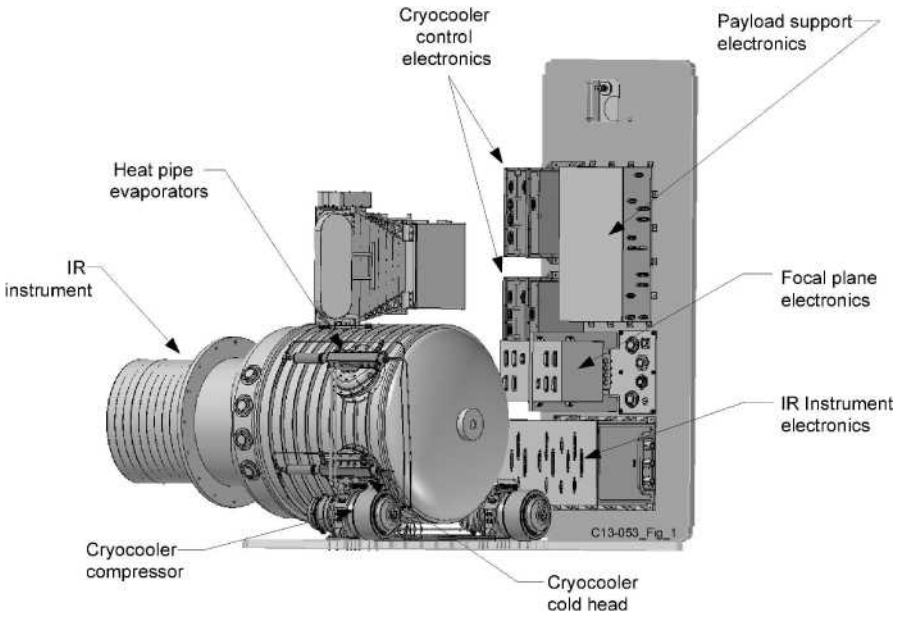

Figure 1. RAMOS United States Subsystem. The subsystem instrument contains two cryocoolers with one acting as a redundant system.

was redesigned to provide high efficiency thermodynamic performance at the RAMOS heat loads and operating conditions, and to allow flight-like featured such as weldability to be included in the design.

The compressor is our MIDI size, an intermediate size from our series of LM-ATC developed linear flexure-bearing clearance seal compressors. The MIDI compressor provides a range of swept volumes of 6-10 cm^3. This compressor, which is also used on the GIFTS program[2], uses the moving magnet design favored by LM-ATC because it places the motor coil outside the working gas space, eliminating the coil epoxy (the primary source of contamination) from the gas space, eliminating electrical feed-throughs into the gas space, and eliminating flexing electrical leads.

The CCE is a high efficiency controller based on a design developed under IRAD at Lockheed Martin. It provides control for the compressor and contains innovative concepts for ripple suppression and vibration cancellation from a feedback loop to an accelerometer. The CCE also includes the launch lock feature to prevent the pistons from striking the end stops during launch and a stroke limitation during operation. The CCE is designed to operate over an input voltage range of 20 – 40 Vdc and suppress the conducted ripple current to less than 1.0 amp peak-to-peak at maximum cooling. The spacecraft interface for command and telemetry is RS-422.

TWO-STAGE PULSE TUBE CRYOCOOLER

The cryocooler heat map is shown schematically in Figure 2. The compressor operates near resonance and is driven by the CCE. The compressor is attached to the pulse tube coldhead with a transfer line between 0.6m and 1m in length. The heat rejection of the CCE and compressor is performed at the mounting interface. Heat from the cold head is rejected by means of a heat pipe evaporator attached to its warm flange.

TWO-STAGE PERFORMANCE PREDICTION

The following predicted performance characteristics of the system were presented at the critical design review during the development phase of the program in 2003. The predicted perfor-

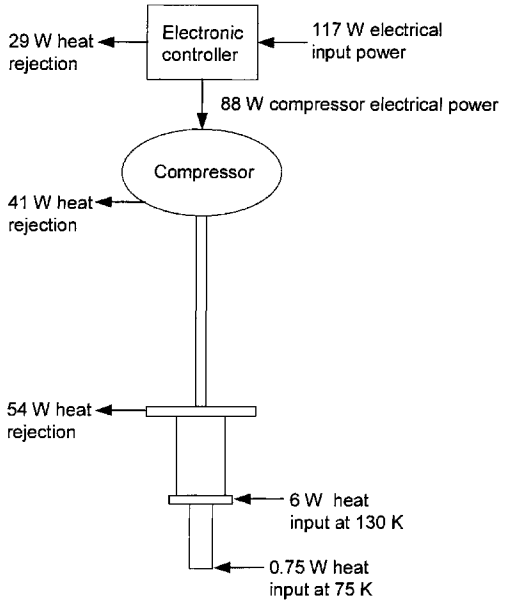

Figure 2. Heat map of cryocooler system. The cryocooler system provides 0.75W cooling at 75K and 6W cooling at 130K with only 117 W system electrical power. This heat map is for the system with a 1 m transfer line.

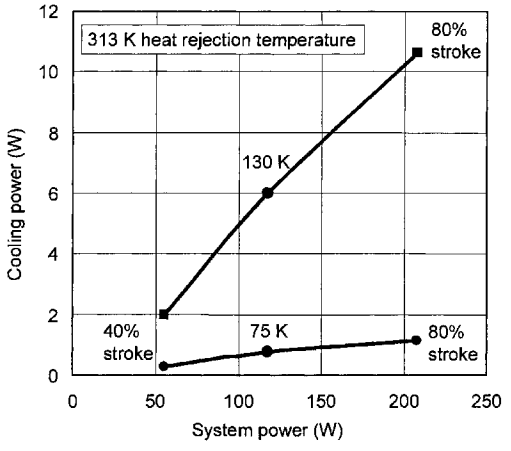

Figure 3. Cooling power versus system power at 75K and 130K and a 1 m transfer line.

mance of the cryocooler is shown in Figure 3, which shows the cooling power at the two stages as a function of system electrical power.

Figure 4 shows the sensitivity of cooling power with cold tip temperatures. The input power and compressor drive frequency were fixed at the nominal condition.

As previously stated, the RAMOS system has a redundant cryocooler. The redundant cryocooler is nominally not operating and therefore the parasitic heat load must be removed from the operating unit. It is important that the parasitic heat load be minimized such to maximize the instrument cooling by the primary operating unit. Figure 5 shows the predicted parasitic of a non-operating RAMOS coldhead that is thermally grounded to the instrument while the primary cooler is operating.

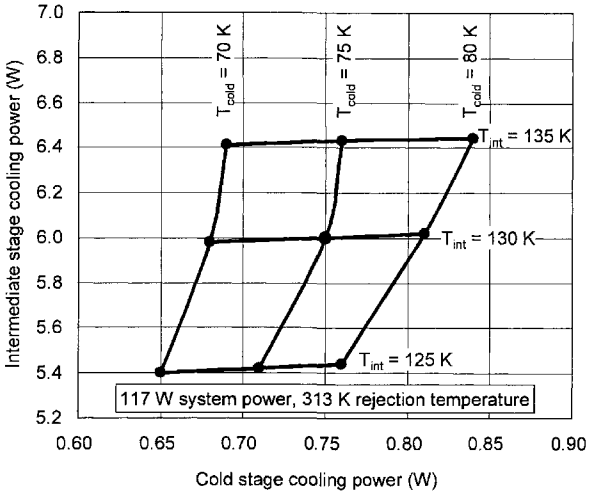

Figure 4. Sensitivity of cooling power with cold tip temperatures. This sensitivity is the performance at the nominal operating frequency, system power and heat rejection temperature with a 1 m transfer line

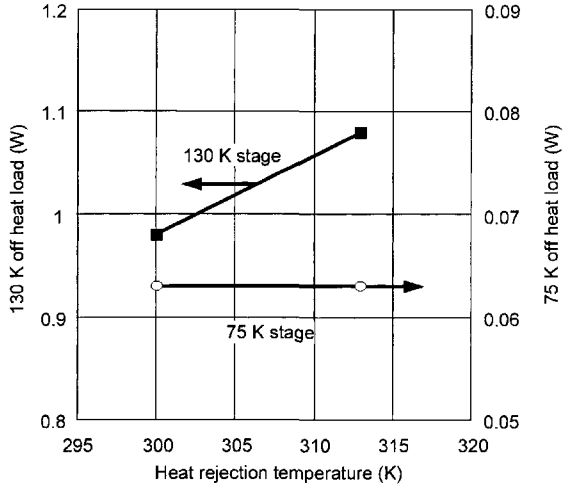

Figure 5. Parasitic heat load of the redundant non-operating coldhead while thermally grounded to the cooled instrument.

PROGRAM STATUS

At this time, the assembly of the EM cryocooler is near completion. The compressor has been fully assembled and is under test. The coldhead is being assembled for integration with the compressor. The CCE brassboard has been assembled and tested and is presently being used to test the special test equipment that will be used to test and qualify the flight units.

The EM compressor is shown in Figure 6 during induced vibration testing on a spring stand without a coldhead. This stand-alone compressor test showed promising results that the cryocooler being operated with vibration cancellation of the CCE would meet the 0.2 N requirement. In addition the compressor has been successfully tested for a number of performance characteristics such as miscellaneous losses, characteristics of the flexure-bearing system, and operation and survival at the required temperature extremes. The measured weight of the compressor is 4.1 kg.

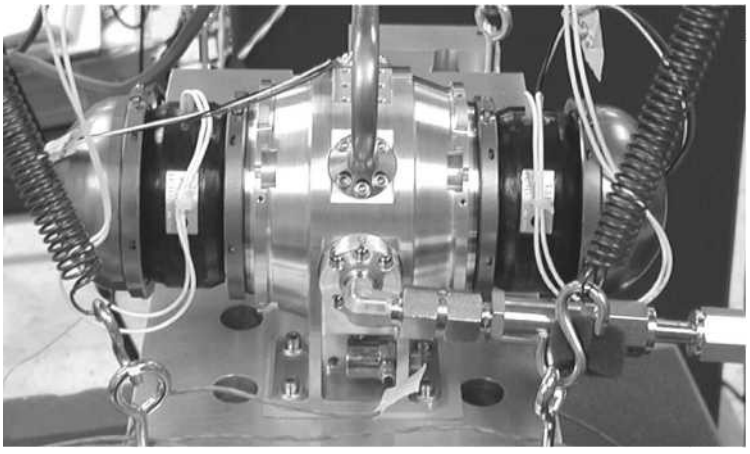

Figure 6. Engineering Model on spring stand facility testing for induced vibration.

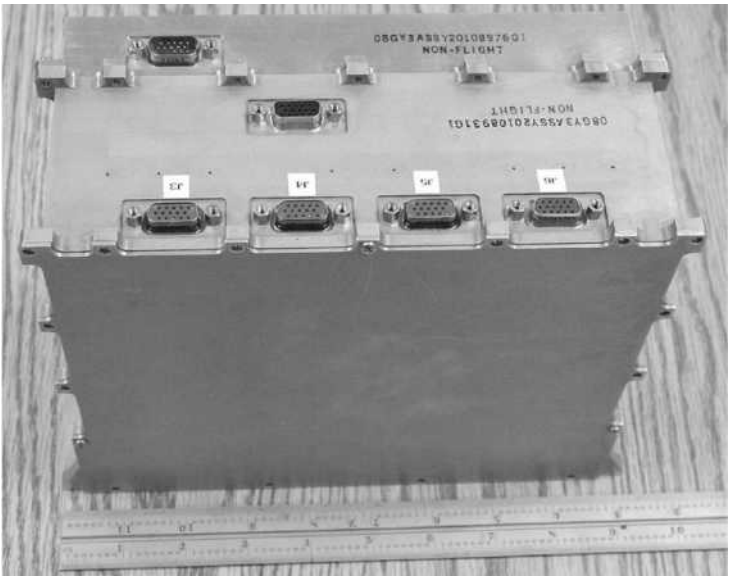

Figure 7. Lockheed Martin cryocooler control electronics brassboard

As previously stated, the CCE brassboard has been completed and tested and is shown in Figure 7. It consists of three circuit boards: the power supply board, the control board, and the ripple suppression board. The CCE also contain a passive launch lock circuit to protect the compressor during unpowered launch conditions.

The testing of the CCE brassboard has been completed. The results of these tests show an efficiency of 80% over the range of input voltages while providing the required compressor power. Testing demonstrates the tare power consumption is below 5W. Thermal tests were performed over a range of −55 to 75 °C. Based on the brassboard, which physically duplicates the flight configuration, the weight of the flight CCE is 3.4 kg.

The coldhead is in its assembly phase with all parts fabricated. The warm flange, which interfaces with the heat pipe evaporator and vacuum shell of the instrument, is shown in Figure 8. The coldhead is an all welded and brazed system. The interfaces with the instrument consist of shrink fits with the female sides of the interface on the coldhead stages. The weight of the Coldhead is estimated at 1.8 kg including the longest transfer line.

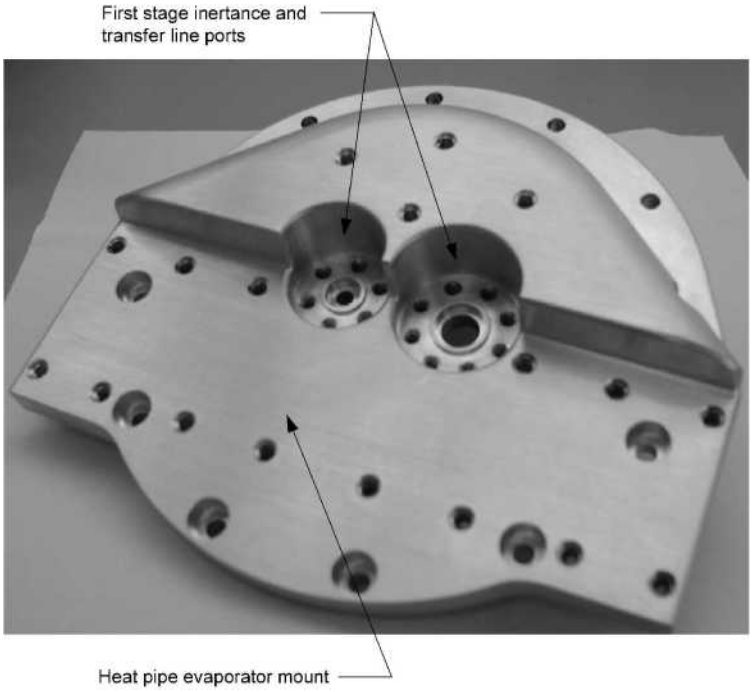

Figure 8. Coldhead warm flange. This flange interfaces with the heat pipe evaporator and the instrument vacuum shell

ACKNOWLEDGMENT

This work was supported under contract to the Space Dynamics Laboratory, North Logan, UT 84341 USA.

REFERENCES

1. T. Nast et al., "Development of a two-Stage Pulse Tube Cryocooler for 35K Cooling," *Cryocoolers 12*, Kluwer Academic/Plenum Publishers, New York (2003), pp. 213-218.
2. T. Nast et al., "Cryocooler Development for the Geosynchronous Imaging Fourier Transform Spectrometer (GIFTS) Instrument," *Cryocoolers 13*, Kluwer Academic/Plenum Publishers, New York (2005).

Lockheed Martin Two-Stage Pulse Tube Cryocooler for GIFTS

T. Nast, D. Frank, E. Roth, P. Champagne, J. Olson, B. Evtimov, R. Clappier

Lockheed Martin Advanced Technology Center
Palo Alto, CA 94304 USA

T. Renna and B. Martin

Lockheed Martin Commercial Space Systems
Newtown, PA 18940 USA

ABSTRACT

Lockheed Martin's Advanced Technology Center (LM-ATC) is developing the cryocooler system for the Geosynchronous Imaging Fourier Transform Spectrometer (GIFTS). This is a NASA New Millennium Program (NMP) Earth Observing-3 mission to demonstrate revolutionary science enabling technologies. One of the new technologies for future generation remote sensors is the two-stage pulse tube cryocooler.

Lockheed Martin is presently fabricating two cryocooler flight models, which includes the cryocooler and electronic controller.

LM-ATC's cryocooler approach employs a unique staging arrangement, which results in high power efficiency, compact, efficient packaging and interfacing and excellent reliability. It is robust and simple, consisting of a two-stage coldhead with no moving parts, driven by a linear flexure-bearing compressor and powered by a high-efficiency electronic controller that includes ripple suppression and vibration cancellation. The design is a "split" system in which the compressor and cold head are separated by a transfer line.

The approach allows on orbit adjustment of the relative cooling loads and temperatures of the two stages.

The controller provides precise temperature control at 55K. The cryocooler is designed to simultaneously provide cooling of 1.5 W at 55 K and 8 W at 140 K while rejecting heat at 300 K. Total system power is projected to be 150 W, and the exported vibration is expected to be less than 0.2 N. This paper presents the status of the flight model and overall system characteristics.

INTRODUCTION

The GIFTS instrument requires system cooling at two different temperatures, one for the focal plane and one for the optics. The GIFTS program selected LM-ATC's two-stage pulse tube based on its maturity and advanced technology. The cryocooler consists of a moving magnet compressor driving a two-stage pulse tube coldhead, powered by cryocooler control electronics (CCE).

Cryocoolers 13, edited by R. G. Ross, Jr.
Springer Science+Business Media, Inc., New York, 2004

Table 1. GIFTS cryocooler system design point.

Cooling load at 55 K	1.5 W
Cooling loads at 140 K	8.0 W
Input Power	155 W
Reject Temperature	300 K
Maximum Input Power Capability	180 W
System Weight	9.1 kg

Although the program's initial formulation base-lined a redundant system employing two cryocoolers, one operating and one standby, the high reliability figures for the cryocooler system allowed the use of a single cryocooler without backup.

A summary of the cooler system's design-point characteristics is given in Table 1.

The coldhead is a two-stage pulse tube based on LM-ATC's cryocooler that was developed under Independent Research and Development (IRAD) funding in 1998-1999.[1] The coldhead was optimized to provide high efficiency thermodynamic performance at the GIFTS heat loads and operating conditions, and to provide flight design features including all welded or metal seals.

The compressor is an intermediate size (MIDI) from our series of LM-ATC developed linear flexure-bearing clearance seal compressors. The MIDI compressor provides a range of swept volumes of 6-10 cm^3. This compressor, which is also used on the RAMOS program[2], uses the moving magnet design favored by LM-ATC because it places the motor coil outside the working gas space, eliminating the coil epoxy (the primary source of contamination) from the gas space, eliminating electrical feed-throughs into the gas space, and eliminating flexing electrical leads.

The CCE is a high efficiency second-generation controller based on a design developed under IRAD at Lockheed Martin. It provides control for the compressor and contains innovative concepts for ripple suppression and vibration cancellation from a feedback loop from an accelerometer. The CCE also includes the launch lock feature to prevent the pistons from striking the end stops during launch and a stroke limitation during operation. The CCE is designed to operate over an input voltage range of 20 – 40 Vdc and suppress the conducted ripple current to less than 1.0 amp peak-to-peak at maximum cooling. The spacecraft interface for command and telemetry is RS-422.

TWO-STAGE PULSE TUBE CRYOCOOLER PERFORMANCE

The cryocooler heat map is shown schematically in Figure 1. The compressor operates near resonance and is driven by the CCE. The compressor is attached to the pulse tube coldhead with a short transfer line. The heat rejection of the CCE and compressor is performed at the mounting interface. Heat from the cold head is rejected by means of a heat pipe evaporator attached to its warm flange.

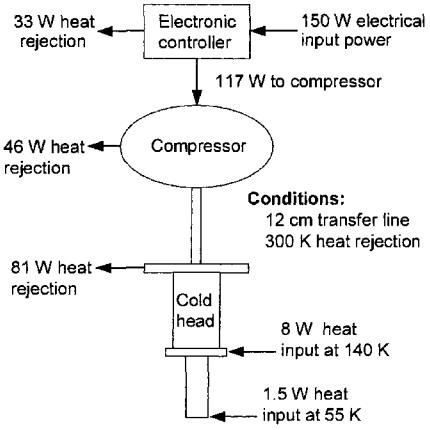

Figure 1. Heat map of cryocooler system. The cryocooler system provides 1.5 W cooling at 55 K and 8 W cooling at 140 K with only 150 W system electrical power.

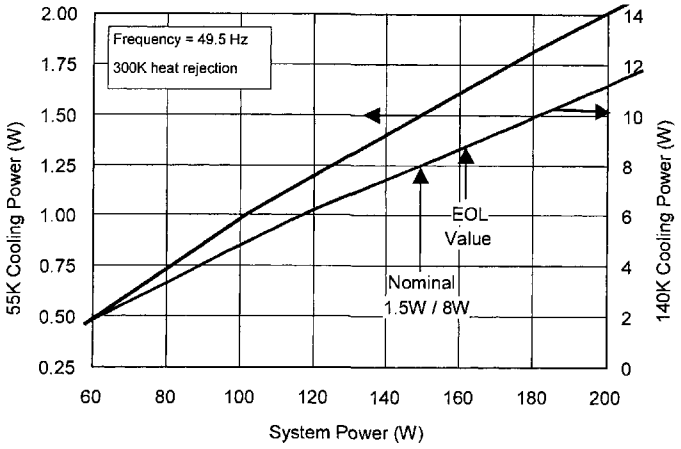

Figure 2. Cooling power versus system power at 55 K and 140 K.

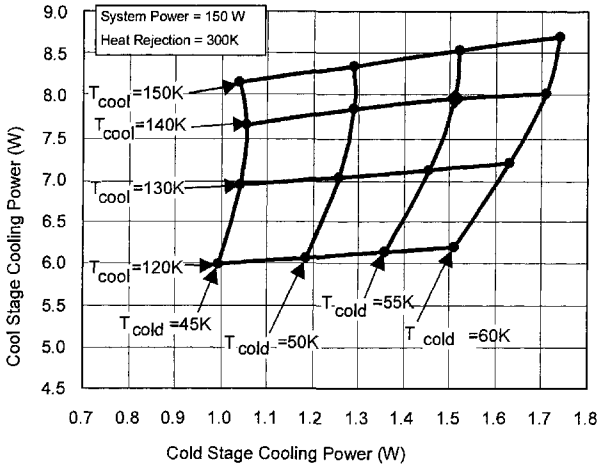

Figure 3. Sensitivity of cooling power with cold tip temperatures. This sensitivity is the performance at the nominal operating frequency, system power and heat rejection temperature with a 1 m transfer line.

Two-stage Performance Prediction

The following predicted performance characteristics of the system were presented at the critical design review in 2003. The predicted performance of the cryocooler is shown in Figure 2, which shows the cooling power at the two stages as a function of system electrical power. The nominal cooling conditions are satisfied with a stroke of 75 % of the maximum operating stroke, providing a large margin for increased cooling.

Figure 3 shows the sensitivity of cooling power with cold tip temperatures. The input power was fixed at the nominal condition. The data shows the two stages are only weakly coupled; a change in temperature or cooling load on one has a relatively small affect on the other.

Capability to Change Relative Cooling Loads at the Two Stages

Generally, advocates of the Stirling-cycle cryocoolers cite one of the advantages of Stirling coolers is the ability to change the relative cooling loads at the two stages by changing the phase lag between compressor and displacer by commands to the electronics. A properly designed pulse tube system also has this capability, and one example is shown in Figure 4. In many programs the relative cooling at the two stages of a cryocooler are not precisely known until the sensor development is

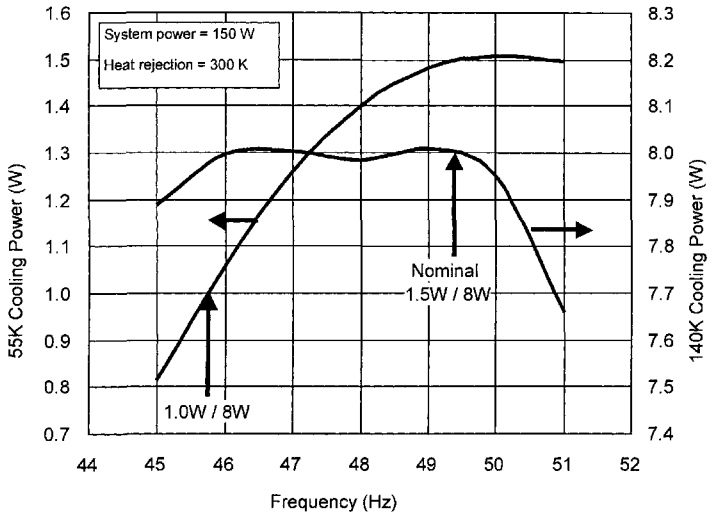

Figure 4. On orbit controllability of heat loads at the two stages.

well along, in many cases after the cryocooler design and operating parameters are well established. In this case, the optics heat load is fairly well known, but there is some uncertainty in the focal plane load. The effect of changing the operating frequency and the stroke on the cooling levels at the two stages is shown in Figure 4. The power input for this case is held constant, and the effect of frequency change is shown. The figure shows that the optics load at 140 K can be held essentially constant at 8 W, while the focal plane load varies from 1 W to 1.5 W. This is one scenario of variation in loads; many other cases can be satisfied by variations in the stroke and frequency and power input. These changes can all be made by commands to the electronics while on orbit.

PROGRAM STATUS

At this time (April 2004), the assembly of the FM cryocooler is near completion. The compressor has been assembled and tested. The assembly of the two flight model cold heads are near completion. The CCE brassboard has been assembled and tested and is presently being used to test the special test equipment that will be used to test and qualify the flight units.

The FM compressor is shown in Figure 5 during induced vibration testing on a spring stand without a coldhead. This stand-alone compressor test showed promising results that the cryocooler

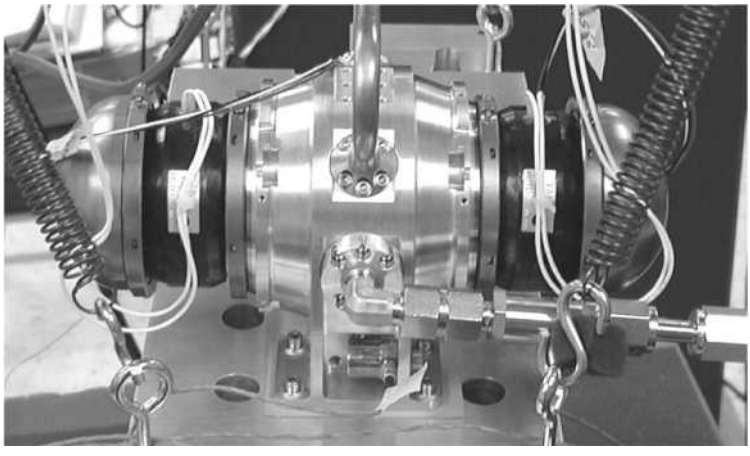

Figure 5. Engineering Model on spring stand facility testing for induced vibration.

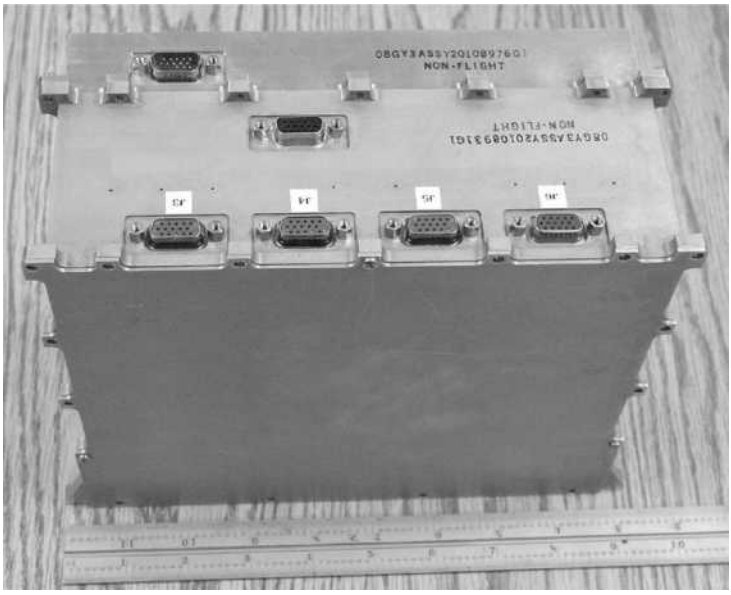

Figure 6. Lockheed Martin cryocooler control electronics brassboard.

being operated with vibration cancellation of the CCE would meet the 0.2 N requirements. In addition, the compressor has been successfully tested for a number of performance characteristics such as miscellaneous losses, characteristics of the flexure-bearing system, and operation and survival at the required temperature extremes. The measured weight of the compressor is 4.1 kg.

As previously stated, the CCE brassboard has been completed and tested and is shown in Figure 6. It consists of three circuit boards: the power supply board, the control board, and the ripple suppression board. The CCE also contain a passive launch lock circuit to protect the compressor during unpowered launch conditions.

The testing of the CCE brassboard has been completed. The results of these tests show an efficiency of 80% over the range of input voltages while providing the required compressor power. Testing demonstrates the tare power consumption is below 5 W. Thermal tests were performed over a range of –55 to 75 °C. Based on the brassboard, which physically duplicates the flight configuration, the weight of the flight CCE is 3.4 kg.

The coldhead is in its final assembly phase with all parts fabricated. The warm flange, which interfaces with the heat pipe evaporator and vacuum shell of the instrument, is shown in Figure 7.

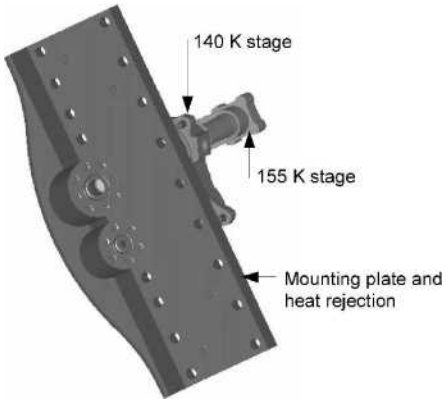

Figure 7. Cold head assembly.

The coldhead is an all welded and brazed system. The interfaces with the instrument consist of a bolted connection. The weight of the Coldhead is at 1.4 kg.

ACKNOWLEDGMENT

This work was supported under contract to the Space Dynamics Laboratory, North Logan, UT 84341 USA. The funding was provided by NASA/Langley

REFERENCES

1. T. Nast et al., "Development of a two-Stage Pulse Tube Cryocooler for 35K Cooling," *Cryocoolers 12*, Kluwer Academic/Plenum Publishers, New York (2003), pp. 213-218.
2. T. Nast et al., "Lockheed Martin RAMOS Engineering Model Cryocooler," *Cryocoolers 13*, Kluwer Academic/Plenum Publishers, New York (2005), this proceedings.

Second Generation Raytheon Stirling/Pulse Tube Hybrid Cold Head Design and Performance

C.S. Kirkconnell, K.D. Price, K.J. Ciccarelli, and J.P. Harvey

Raytheon Company
El Segundo, CA, USA 90245

ABSTRACT

Raytheon is in initial test of a second generation two-stage Stirling/pulse tube hybrid cold head for use in long life space cryocoolers. The Stirling/pulse tube configuration provides excellent thermodynamic performance by optimally combining the strengths of both technologies. The cold head is designed for optimal performance at a second stage temperature of 40 K and a first stage temperature of 110 K with nominal capacity of 1 W at the lower stage and simultaneous 7 W at the upper stage. The inherent load shifting capability of this configuration permits efficient operation of the cooler over a wide range of temperatures and heat loads. Load shifting is accomplished through varying the phase angle of the Stirling displacer piston relative to the pressure wave. Load shift data on the new cold head is provided. Lessons learned from the testing of the initial brassboard regarding component sizing have been incorporated into this second generation design. The quantitative improvement provided by those design changes is presented. The second generation cold head design is currently being incorporated into a flight design warm-end expander motor assembly with Oxford-class flexure and clearance technology typical of Raytheon flight-qualified production cryocoolers for space. The expander is driven by an Oxford-class compressor of similar design legacy to other Raytheon designs.

INTRODUCTION

The testing and modeling efforts described herein represent the continuation of a roughly four-year development effort to design a new type of space cryocooler, namely a Stirling/pulse tube hybrid. The initial concept and perceived advantages of the Stirling first stage/pulse tube second stage were first discussed at the 11th International Cryocooler Conference in 2000.[1,2] Brassboard test results were presented two years later at the 12th International Cryocooler Conference, in which measured capacity data from 35 K to 112 K (second stage temperature) was presented.[3] As discussed in a recently presented and soon to be published paper from the 2003 Cryogenic Engineering Conference, the brassboard effort was followed by extensive model correlation efforts which have led to an improved cold head design.[4] The present effort documents the completion of the build of the improved expander, updates the previously published performance predictions with the as-built predictions, accounting for actual heat exchanger and regenerator porosities, final void volume measurements, etc., and provides some results from the very first stages of the testing, which commenced in March 2004.

Cryocoolers 13, edited by R. G. Ross, Jr.
Springer Science+Business Media, Inc., New York, 2004

TEST CONFIGURATION

The second generation Raytheon Stirling/Pulse Tube Two-Stage (RSP2) expander is shown in Fig. 1. As described in a previous paper, the primary differences between the expander shown and the initial brassboard unit are in the component sizing of the second stage components and the improvement of gas porting and heat rejection at the transfer line port.[4] The displacer motor assembly and end cap were reused from the original brassboard unit. The spiral flexures used in the expander have direct legacy to the Raytheon production line of single-stage Stirling cryocoolers and have been shown to be long-life, reliable, and consistent with the design goal of minimum vibration output in three axes. The expander is shown mounted to a tooling ring that mates with a vacuum dewar can to permit bench top testing, which is an improvement over the original unit with respect to testability.

The original unit featured the surge volume as an integral part of the first stage manifold. The new expander permits operation with two different phase shift configurations. The first configuration to be tested, which is the configuration that corresponds to the data provided in the subsequent section, has the surge tank bolted and thermally sunk to the first stage manifold. The inertance tube is thus isothermal (nominally, neglecting friction heating) at the first stage temperature. Thermodynamically, this is the same as the original brassboard unit. The second phase shift configuration features the surge volume outside the vacuum dewar, at ambient temperature. Thus the inertance tube connects the warm end of the pulse tube at the first stage temperature to ambient. Modeling results indicate that properly optimized inertance tubes will yield roughly equivalent cryocooler performance using either configuration. Cryocooler integration is typically eased by locating mass and volume away from the cryogenic zone, so the latter configuration is probably the most generally desirable, should the modeling predictions be validated by test. Photographs of the inertance tube and surge volume being used to test the "all cryogenic" configuration are provided in Fig. 2.

The compressor, which is shown together with the expander in the test fixture in Fig. 3, is being reused from the initial testing. The RSP2 compressor can be configured for either 6.0 cc or 7.5 cc peak-to-peak swept volume, the adjustment being made by switching to a piston-cylinder set of different piston diameter. Based upon the modeling optimization and the resulting desire to match the expander and compressor resonant speeds at about 50 Hz, the compressor has been configured in the small bore, 6.0 cc, configuration. The compressor design is discussed more extensively elsewhere.[1-3]

Figure 1. Second generation RSP2 expander with tooling ring for vacuum dewar integration. Inertance tube and surge volume, which may be either cryogenic or ambient, not shown.

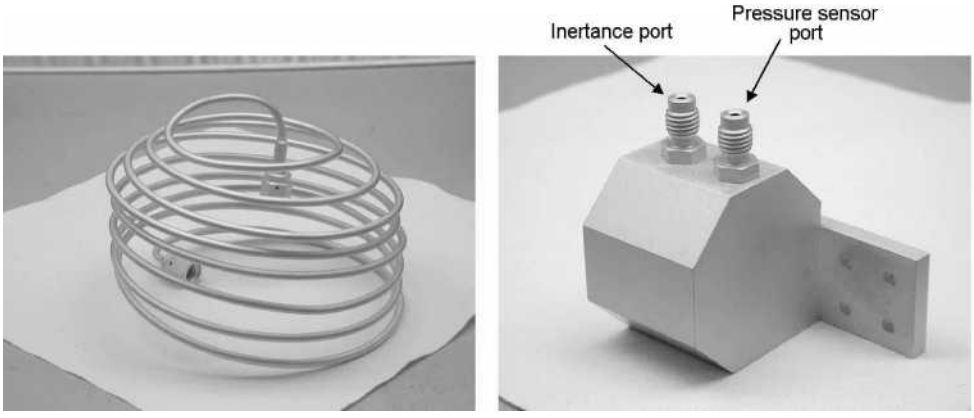

Figure 2. Cryogenic phase shift hardware. Inertance tube (left) and surge tank (right) for RSP2 expander shown. Inertance tube constructed from standard tubing and gold plated to reduce parasitic loading due to radiation. Surge volume bolts to first stage manifold through four through holes clearly seen in the photo.

PERFORMANCE PREDICTIONS

The brassboard test data was used to develop and correlate a thermodynamic simulation model that provides simultaneous solution of the mass, momentum, and energy equations throughout the cryocooler. The model has been correlated using a fixed orifice phase shifter with cryogenic (first stage temperature) surge volume, a cryogenic surge volume and inertance tube, and an ambient surge volume with an inertance tube. Performance predictions based upon the nominal drawing dimensions were provided previously.[4] Now that the cryocooler build has been completed, the model has been updated to account for the as-built dimensions. This type of

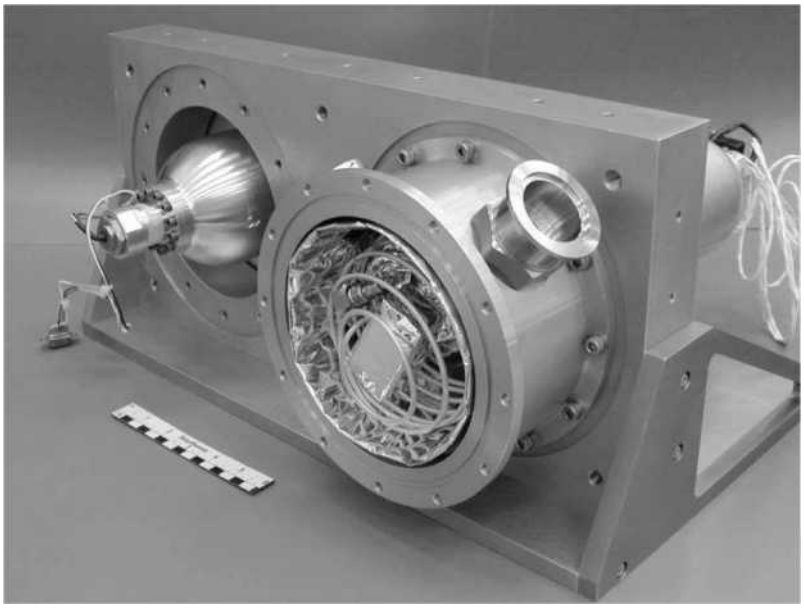

Figure 3. Complete RSP2 test configuration with compressor and expander mounted in test fixture.

correction has the potential for significant impact primarily with respect to the regenerator mesh, given the nominally +/- 10% manufacturimg and lot variation possible in wire diameter. This affects void volume, heat exchanger effectiveness, and pressure drop. The first test configuration utilizes the cryogenic surge volume and inertance tube, so the first model updates, and the only ones available as of this writing, are for that configuration.

The updated performance predictions indicate that the material and manufacturing deviations from nominal should have a fairly benign impact on the cryocooler performance. The updated prediction is 1.1 W at 40 K, 6.6 W at 110 K, for 124 W pressure-volume (PV) power. The cold head performance is essentially the same, though it has been determined that the optimum inertance tube is roughly 50 cm longer than the one built. A 10% efficiency improvement is expected when that correction is implemented. A PV power instead of motor power prediction is reported because of a programmatic decision to reuse the less efficient compressor motors from the brassboard unit instead of upgrading to the new design. The new motors are in final assembly as of this writing. The decision to reuse the existing motors was made so that the only fundamental differences between this test configuration and the previous one are limited to the expander, recalling that the intent of the test is to characterize and measure the cold head improvements. The projected efficiency of the compressor with the new motors is 75%, which projects to a motor power of 183 W for the design point.

Figures 4 and 5 show the projected performance of the new RSP2 cryocooler over a wide range of second stage temperatures for two selected first stage temperatures. These temperature regimes largely envelope the thermal control requirements of long wave infrared (LWIR) sensor systems, where the second stage cools the focal plane and the first stage cools the optics. The only parameters permitted to vary between these plots are those that are easily controlled in test, namely, operating frequency, strokes, and phase angle, i.e., Figures 4 and 5 depict operation of the same cooler. This is illustrative of the wide operational range over which this cooler functions efficiently.

Initial testing has commenced as of this writing. A preliminary, low power steady operating point of 4.3 W at 150 K + 1.1 W at 60 K for 72 W input PV power has been achieved. This agrees well with the corresponding model prediction for this operating condition (4.1 W at 150 K + 1.3 W at 60 K for 67 W input power, as shown in Fig. 5), particularly at this very early stage of the testing prior to any model correlation or cryocooler optimization. This agreement bodes well for the near term realization of the performance described in Figs. 4 and 5.

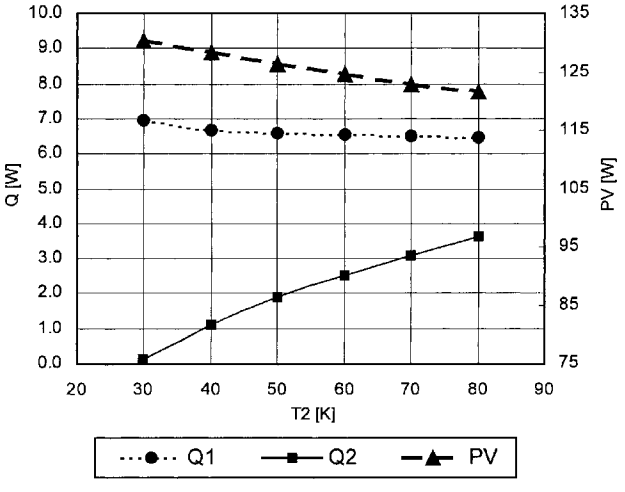

Figure 4. Second stage load and power curves with T1 (first stage temperature) held constant at 110 K. Q1 = first stage heat lift, Q2 = second stage heat lift, PV = compressor input pressure-volume (thermodynamic) power.

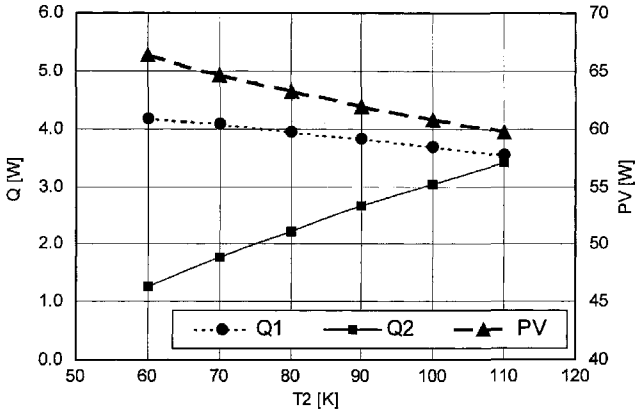

Figure 5. Second stage load and power curves with T1 (first stage temperature) held constant at 150K. Legend same as Figure 4. Note that this is a significantly lower power case than Figure 4, with the compressor running at about 50% stroke.

SUMMARY

The fabrication and final assembly of a second generation RSP2 expander has been completed and has entered initial testing. Test plans call for characterization of the cryocooler over a wide range of frequencies, charge pressures, phase angles, stroke amplitudes, and operating temperatures (first stage, second stage, and rejection temperature). Following the initial test phase with the cryogenic surge volume, the ambient surge volume configuration will be implemented and the characterization tests repeated.

In parallel with these tests, efforts have commenced on the fabrication of a flight-qualified version of the RSP2. The compressor design is essentially the same as the one presently in test with the primary exceptions being the incorporation of piston position sensors housed within the pressure volume, the use of hermetic feedthroughs, and the incorporation of an improved motor electromagnetic design that fits within the same envelope as the present motor. Thus the piston-cylinder, flexure assembly, internal mounting features, and basic housing designs are left unchanged.

The flight version of the expander incorporates a new motor assembly design that permits greater flexibility in the sizing of the displacer piston diameter. This will permit the use of essentially the same expander warm end design for cryocoolers ranging from the size discussed herein up to substantially higher capacity.

ACKNOWLEDGEMENTS

The authors would like to acknowledge the support of Thom Davis and the Air Force Research Lab at Kirtland AFB, who have permitted use of the compressor in support of these test activities.

REFERENCES

1. Kirkconnell, C. S., Price, K. D., Barr, M. C., and Russo, J. T, "A Novel Multi-Stage Expander Concept," *Cryocoolers 11*, Kluwer Academic/Plenum Publishers, New York (2001), pp. 259-263.
2. Price, K. D. and Urbancek, V., "95 K High Efficiency Cryocooler Program," *Cryocoolers 11*, Kluwer Academic/Plenum Publishers, New York (2001), pp. 183-188.
3. Price, K. D. and Kirkconnell, C. S., "Two Stage Hybrid Cryocooler Development," *Cryocoolers 12*, Kluwer Academic/Plenum Publishers, New York (2003), pp. 233-239.
4. Finch, A.T., Price, K.D., and Kirkconnell, C.S., "Raytheon Stirling/Pulse Tube Two-Stage (RSP2) Cryocooler Advancements," *Adv. in Cryogenic Engineering*, Vol. 49B, Amer. Institute of Physics, Melville, NY (2004), pp. 1285-1292.

Efficient 10 K Pulse Tube Cryocoolers

C. Wang
Cryomech, Inc.
Syracuse, New York, USA

ABSTRACT

Two 10 K pulse tube cryocoolers, Models PT805 and PT810, have been developed and commercialized at Cryomech to provide cooling from 8 K to 20 K. The PT805 provides 3.5 W at 10 K and 48 W at 80 K, simultaneously, for 4.6 kW power input. The PT810 provides 10 W at 10 K and 40 W at 49 K, simultaneously, for 7.6 kW power input. These pulse tube cryocoolers have almost the same efficiency, cooling capacity, and cooling speed as that of 10 K Gifford-McMahon (GM) cryocoolers. A test demonstrated that the two-stage pulse tube cryocooler is less sensitive to the air contamination than 10 K GM cryocooler. The pulse tube refrigerators developed at Cryomech are expected to have mean time between maintenance (MTBM) > 5 years. The PT810s have been used for cryopumps and demonstrate their advanced features in the field.

INTRODUCTION

Cryomech, Inc. has developed a series of 4 K pulse tube cryocoolers, Models PT403, PT405, PT407 and PT410 to provide 0.3 W to 1.0 W at 4.2 K.[1,2] These 4 K pulse tube cryocoolers have opened many challenging applications in cooling Nuclear Magnetic Resonance (NMR) and and Magnetic Resonance Imaging (MRI) magnets, precooling dilution refrigerators, Adiabatic Demagnetization Refrigerators (ADR) and sorption coolers, cooling sensitive devices like Superconducting Quantum Interference Device (SQUID) magnetometers, etc. These applications demonstrate the great advantages of pulse tube cryocoolers over GM cryocoolers with respect to vibration, temperature stability, reliability, and lifetime.

Cryopumps have been the largest commercial application of cryocoolers in the past ten years. Because of their clean pumping, high vacuum (~10^{-8} torr), and high pumping speed, cryopumps have been adopted widely by the semiconductor industry. The cryopump requires a ~80 K cooling station to condense water and hydrocarbon vapors and a ~15 K cooling station to condense and trap air gases. Nearly all cryopumps use a two-stage Gifford-McMahon (GM) cryocooler as the cooling source. However, the vibration caused by the moving displacer in the GM cryocooler has become a problem in the last few years as the circuit line widths in semiconductor fabrication have become more and more narrow. In some applications, a complicated vibration eliminator has to be used for the cryopumps to reduce the vibration transferred to the fabrication equipment.

10 K cryocoolers are still being used for cooling the radiation shield of superconducting magnets, laboratory cryostats, etc. Without rare earth materials in the 2nd stage regenerator, 10 K pulse tube cryocoolers will be lower in manufacturing cost and will provide less magnetic distortion of sensitive measurements. A few groups[3,4] are working on 10 K two-stage pulse tube cryocoolers.

Cryocoolers 13, edited by R. G. Ross, Jr.
Springer Science+Business Media, Inc., New York, 2004

In order to meet the cooling requirements from 8 K to 20 K, we have developed and commercialized two pulse tube cryocoolers, Models PT805 and PT810. The features and performance of these models are introduced in this paper.

PULSE TUBE COLD HEAD

The two-stage pulse tube cryocooler includes a pulse tube cold head and a helium compressor package. The PT805 uses a CP950 compressor with a nominal input power of 4.6 kW. The PT810 uses a CP980 compressor with a nominal input power of 7.8 kW.

Figures 1 and 2 show photos of the PT805 and PT810 pulse tube cold heads. The PT805 and PT810 are very similar to the PT405 and PT410 4K pulse tube cryocoolers.[2] Their schematics are given in Reference 2. The regenerator efficiency at the temperature above 8 K is much higher than at the temperature of 4 K. The 10 K pulse tube cryocoolers have shorter 2nd stage regenerators than that of 4 K versions. Only lead spheres are filled in the 2nd stage regenerator of the PT805 and PT810. The first stage regenerators are packed with phosphor bronze screens. Both the PT805 and PT810 use a double-inlet configuration.

It has been confirmed that the vibrations in the PTR cold heads mainly come from the stretching of the tubes generated by gas compression and expansion. The rotary valves of the PT805 and PT810 have been integrated in the warm end of the cold head. A special version with a remote rotary valve is also available at Cryomech for all two-stage pulse tube cryocoolers. In this version, the rotary valve and motor is separated from the pulse tube expander by three feet.

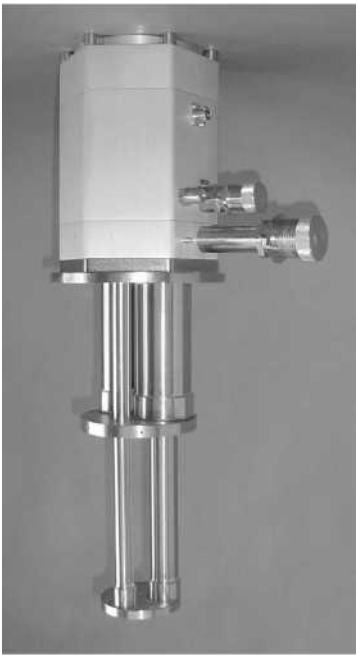

Figure 1. Photograph of the PT805 cold head

Figure 2. Photograph of the PT810 cold head

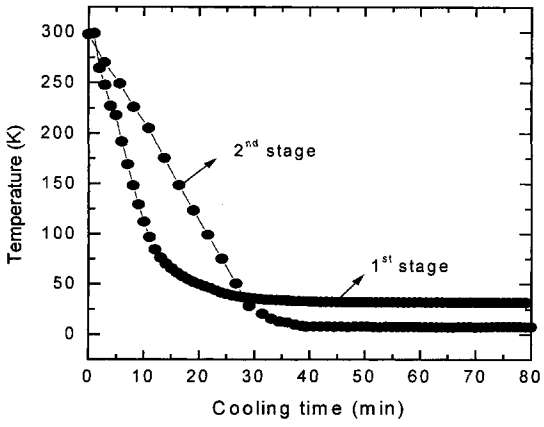

Figure 3. Cool-down characteristics of PT805

PERFORMANCE

1. Performance of PT805

Figure 3 shows the cool down curves of the PT805. It takes 40 minutes for the 2nd stage to reach the bottom temperature of 7.6 K. The 1st stage reaches the bottom temperature of 31.8 K in ~40 minutes. Figure 4 gives the cooling load map of the PT805. It can achieve 3.5 W at 10 K on the 2nd stage and 32 W at 65 K on the 1st stage simultaneously, or achieve 10 W at 20 K and 48 W at 78 K, simultaneously. The input power of it is 4.3 kW at the temperatures of 7.6 K and 31.8 K on both stages and 4.8 kW for the temperatures of 20 K and 78 K.

The PT805 was tilted to test orientation effects with and without heat loads on both stages. The results are given in Figs. 5(a) and 5(b). After tilting the cold head over 30 degree, the performance of the PT805 on both stages dropped significantly.

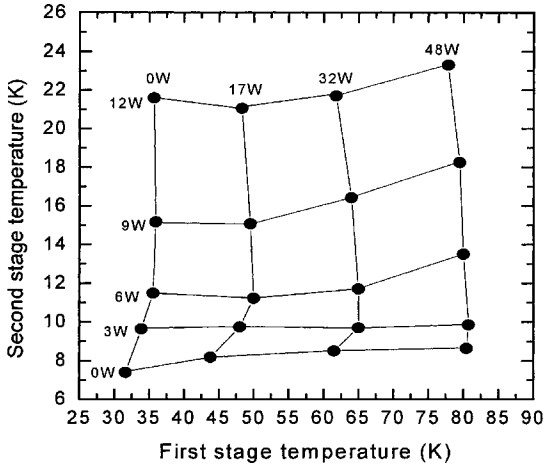

Figure 4. Cooling load map of the PT805

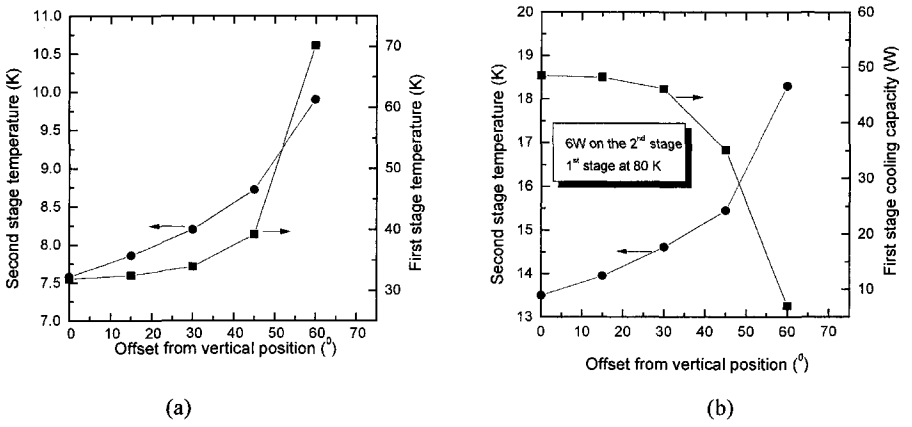

Figure 5. Orientation effects on the performances of PT805: (a) without heat loads on both stages; (b) with heat loads on both stages

2. Performance of PT810

Figure 6 shows the cool-down characteristics of the PT810. The 2nd stage reaches a bottom temperature of 6.4 K in 35 minutes, and the 1st stage reaches a temperature of 31.4 K in 55 minutes. Comparing the cooling speed of the PT805 and PT810 to that of the 4 K pulse tube cryocoolers, Models PT405 and PT4101,2, the PT805 and PT810 have a faster cooling speed.

A cooling load map of the PT810 cooler is given in Fig. 7. This cooler can provide 10 W at 10 K on the 2nd stage and 40 W at 49 K on the 1st stage, for which it consumes 7.6 kW of input power. It also provides 15 W at 16.2 K and 80 W at 72 K, simultaneously, for 7.8 kW input.

The orientation effects on the performance of the PT810 are shown in Figs. 8(a) and 8(b). The PT810 appears to be a little less sensitive than the PT805. This might be due to the higher pressure differences in the PT810. Tilting the cold head greater than 40 degrees will cause significant degradation of the performances. For all of our two-stage pulse tube cryocoolers, we recommend that the tilted angle should be less than 30 degrees without significantly losing the performances.

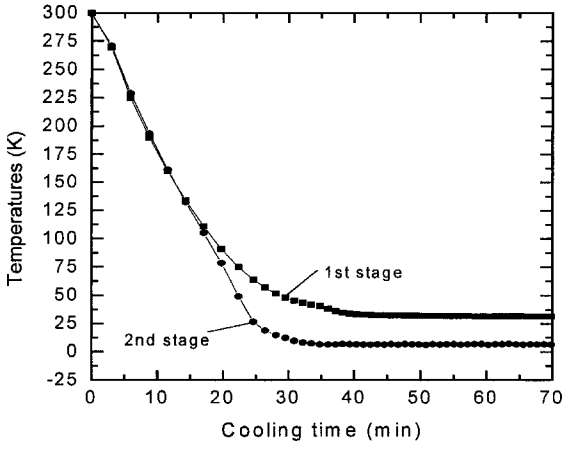

Figure 6. Cool-down characteristics of the PT810

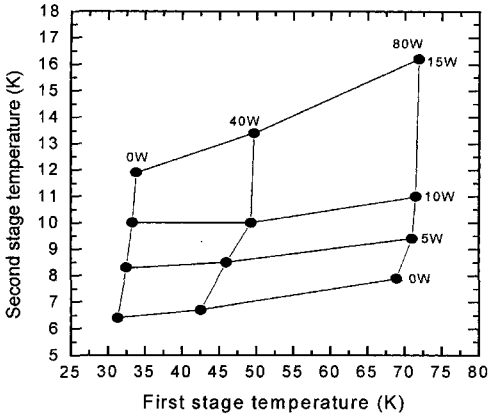

Figure 7. Cooling load map of the PT810

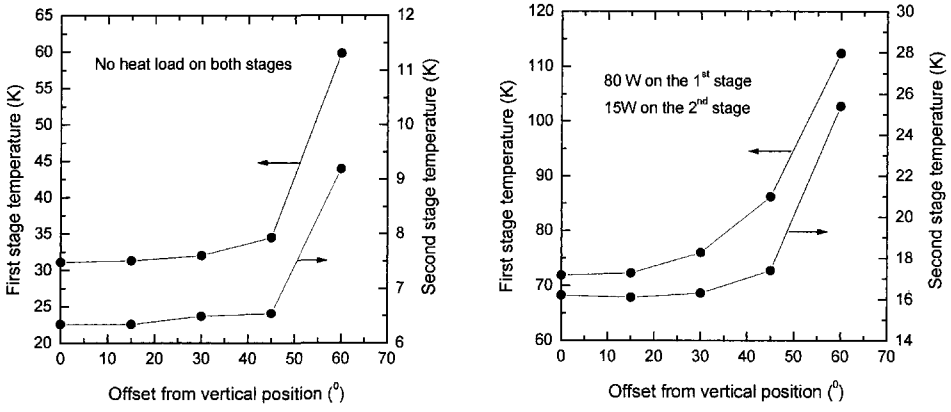

(a) (b)

Figure 8. Orientation effects on the performances of the PT810 (a)without heat loads on both stages; (b)with heat loads on both stages.

Table 1. Performance comparisons of pulse tube cryocoolers with GM cryocoolers (60Hz power operation)

Company & Cryocooler Model	Type	Compressor model & input power	1st & 2nd stage cooling capacity	Cooling speed
Cryomech PT805	2-stage PT *	CP950 4.7 kW	48W @ 80K with 10W @ 20K	32min From 300K to20K
CTI 1020	2-stage GM*	9600 5.0 kW	35W @ 77K with 12W @ 20K	Not available
APD M208S	2-stage GM	HC8 4.5 kW	35W @ 77K with 10W @ 20K	40 min From 300K to 20K
Cryomech PT810	2-stage PT	CP980 7.6 kW	40W @ 49K with 10W @ 10 K	31 min From 300K to 10K
SHI SRDK-408S	2-stage GM	CSW-71 7.5 kW	35W @ 45K with 6.3W @ 10 K	<60min From 300K to 10K

* PT-Pulse tube cryocooler; GM-GM cryocooler

Figure 9. The world's first cryopumps using pulse tube cryocoolers, courtesy of XL Technology Systems, Inc.

The performances, input powers and cooling speeds of the PT805 and PT810 are compared with the similar models of commercial GM cryocoolers in Table 1. The PT805 and PT810 have almost the same cooling capacities, efficiencies and cooling speeds as the GM cryocoolers. The performances of the GM cryocoolers of CTI, APD and Sumitomo Heavy Industry are obtained from their product catalogs. All the performances are given at the operations of 60 Hz power input.

CRYOPUMP WITH THE PT810 PULSE TUBE CRYOCOOLER

The world's first cryopumps with the PT810 pulse tube cryocooler have been successfully manufactured by XL Technology Systems, Inc. Their photograph is given in Fig. 9. Two arrays in the cryopump are cooled down to proximately 77 K and 15 K, and pump all gases to the vacuum of $<10^{-8}$ Torr. These cryopumps have been used in thermal vacuum test facilities for space simulation as well as vacuum coating system and vacuum process system. They demonstrated their advanced features of extra low vibration and long MTBM over the traditional cryopump with GM cryocoolers in the field. These cryopumps from XL Technology System, Inc. are in patent pending.

MAINTENANCE INTERVAL OF 10 K PULSE TUBES

Currently, the maintenance interval of the 10 K GM cryocooler is ~10,000 hours[5]. Cryomech's goal is to provide the 10 K pulse tube cryocooler with MTBM > 5 years (43,800 hours). Three possible service requirements for the Pulse Tubes in five years are: 1. adsorber in the compressor package; 2. rotary valve and valve plate in the cold head; 3. contamination in the cold head. These three service requirements were investigated and given below.

1. Lifetime of the Adsorber

The lifetime of the adsorber was mainly determined by the oil carryover which passes through the oil separator and reaches the adsorber. We have redesigned the oil separator and the adsorber to improve their efficiencies for the pulse tube cryocoolers. A quality control process has been developed to monitor the oil carryover rate before the adsorber. This measurement is taken during the operation of the complete cryocooler, throughout several cool downs. Each system is monitored for nearly a week. Figure 10 shows measured oil carryover rates in some of

the CP900 series compressors from our production line. The CP900s are controlled to have oil carryover of less than 80 mg/day (29 g/year). In a test of an in-house pulse tube over a few months, a total of 250 g oil was allowed to pass through the oil separator and into the adsorber. We found there is no oil passing through the adsorber and no contamination in the cold head. The measurement of the maximum oil adsorption of adsorber is still undergoing. The statistic measurements of the oil carryover and the adsorber performance give us confidence that we will be able to recommend 5 years MTBM for the compressor.

2. Lifetime of the Rotary Valve

The rotary valve includes valve and valve plate. Without the moving displacers, the pulse tube cryocooler does not generate wear particles from the moving of the displacer seals in the GM cryocoolers. This results in less wear on the valve and valve plate.

Also, the pulse tube is working at a lower speed of 1.4 Hz instead of 2 (50 Hz power) or 2.4 Hz (60 Hz power) for the GM cryocoolers. This is a benefit to the lifetime of the rotary valve. Different valve and valve plate materials have also been studied at Cryomech to provide less wear and longer operation time.

After 12,000 hours running, we checked one rotary valve of our two-stage pulse tube cryocooler. It was found that the valve wore only 0.03 mm and there was no significant wear on the valve plate. The valve is designed to have normal function with the wear < 1 mm. We predict that the valve and valve plate will last more than five years.

3. Contamination Sensitivity of the Pulse Tube Cryocooler

We have set up a procedure and process for the purification of the helium gas in the whole system. This process was verified to efficiently decrease the gas contamination to a very low level, which ensures the long term running of the pulse tube cryocoolers.

A two-stage 4 K pulse tube cryocooler has been tested for contamination sensitivity. The impact of air contamination was studied and is shown in Fig. 11. The pulse tube cryocooler has less sensitivity than two-stage GM cryocoolers to air (78% N_2, 20% O_2) contamination. After adding 600 torr·liter of air in the system, the first lost 2 W at the temperature of 65 K and the 2nd stage temperature increased by 0.1 K. This feature enables the two-stage pulse tube cryocooler to operate for a long time without performing cold head service.

Since the first PT405 pulse tube cryocooler was delivered to a user in July 1999, a few hundred pulse tube cryocoolers are working in the field. So far, we have not had any requirements of routing services for replacing the adsorber and the rotary valve. There has been no report on the performance degradation of our pulse tube cryocooler. All of this information supports us toward the goal of providing the Pulse Tubes with five years MTBM.

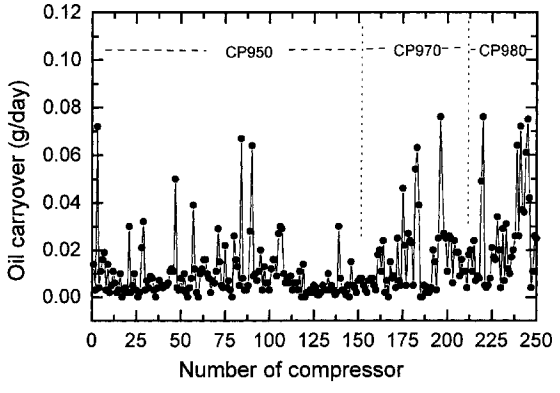

Figure 10. Oil carryover of CP900 series compressor package

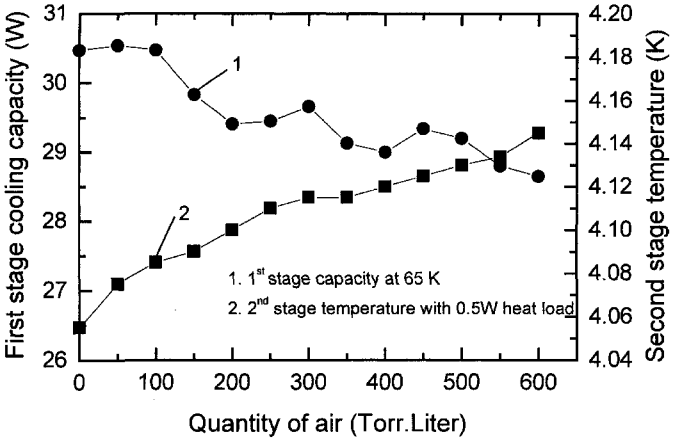

Figure 11. Impact of air contamination in the PT405.

CONCLUSION

Efficient two-stage pulse tube cryocoolers, Models PT805 and PT810, have been developed and commercialized at Cryomech for cooling from 8 K to 20 K. The PT805 and PT810 provide almost the same cooling capacity, efficiency and cooling speed as the commercial GM cryocoolers. The 10 K two-stage pulse tube cryocoolers are expected to have MTBM greater than five years and open the applications for cryopump industry etc.

ACKNOWLEDGMENT

The author would like to thank XL Technology Systems, Inc. who provided the photograph and applications of the cryopump with a pulse tube cryocooler.

REFERENCES

1. Wang, C. and Gifford, P.E., "0.5W Class Two-Stage 4 K Pulse Tube Cryorefrigerator," *Advances in Cryogenic Engineering*, Vol. 45A, Kluwer Academic/Plenum Publishers, New York (2000), pp.1-8.

2. Wang, C. and Gifford, P.E., "Development of 4 K Pulse Tube Cryocoolers at Cryomech," *Advances in Cryogenic Engineering*, Vol. 47B, AIP, Melville, New York (2002), pp. 641-648.

3. Siegel, A. and Haefner, H.U., "Investigation to the Long-Term Operation Behavior of GM-Pulse Tube Cryocoolers," *Advances in Cryogenic Engineering*, Vol. 47B, AIP, Melville, New York (2002), pp. 903-910.

4. Gao, J., "IGC-APD Advanced Two-Stage Pulse Tube Cryocoolers," *Advances in Cryogenic Engineering*, Vol. 47B, AIP, Melville, New York (2002), pp. 683-690.

5. Catalog of GM cryocoolers from Sumitomo Heavy Industry.

Development of Stirling-Type Coaxial Pulse Tube Cryocoolers

L.W. Yang and G. Thummes

University of Giessen and TransMIT-Center of Adaptive Cryotechnology and Sensors
D-35392 Giessen, Germany

ABSTRACT

We report on recent progress in the development of two versions of coaxial Stirling type pulse tube cold fingers that were designed for operation on commercial linear Stirling compressors with nominal input power of 200 W (Leybold Polar SC7) and of 100 W (AIM SL400), respectively. The coaxial cold finger driven by the AIM SL400 compressor at 100 W input power reaches a no-load temperature below 40 K and provides a cooling power of 3.6 W at 80 K. Between 50 W and 120 W input power, the COP (cooling power/input power) at 80 K is larger than 3%. The other coaxial cold finger driven by the Leybold POLAR SC7 compressor achieves a COP of 3.3-3.7% at 100-250 W input power. For comparison, the performance data of the U-type and inline versions of the above pulse tube cold fingers are also presented in this paper. The cooling performance of the different pulse tube cold fingers is compared by means of the coefficient of performance based on the motor power of the linear compressors.

INTRODUCTION

In the past five years, we have been developing Stirling-type pulse tube cryocoolers (PTCs) for the potential replacement of commercial Stirling cold fingers.[1-4] The PTC cold fingers were designed for operation with commercial linear compressors, i.e. the compressor of the SL200 or SL400 Split-Stirling cooler of AEG Infrared Modules (AIM) and that of the Polar SC7 Split-Stirling cooler of Leybold Vacuum. This development was part of the joint project "High temperature superconductors and novel ceramics for future communication technology" that was supported by the German Government (BMBF).

For practical reasons, at the early stages of the development we have chosen a U-shaped configuration of pulse tube and regenerator.[1] Later on, for the purpose of comparison also inline versions of the PTC cold fingers have been built and tested.[2-4] For many applications a coaxial geometry of the PTC cold head is desirable, because this most resembles the compact shape of a Stirling cold finger. Here we report on the development and test of two coaxial PTC cold fingers for operation with the above-mentioned compressors. The cooling performance is compared to that of the corresponding of U-shaped and inline versions of the cold fingers.

Cryocoolers 13, edited by R. G. Ross, Jr.
Springer Science+Business Media, Inc., New York, 2004

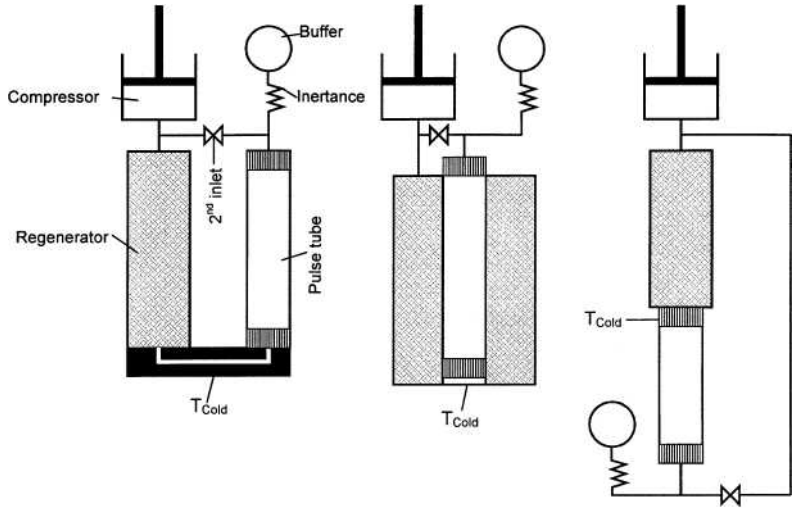

Figure 1. Three typical configurations of pulse tube coolers; (a) U-shaped, (b) coaxial, (c) inline; T_{Cold} indicates the position of the cold tip.

COOLER DESCRIPTION

Fig. 1 illustrates the three typical geometrical arrangements of pulse tube and regenerator in a pulse tube cooler. In inline configuration, there are no losses from curved gas flow at the cold tip. Therefore high performance pulse tube coolers[5, 6] usually employ an inline configuration. However, in an inline PTC the cold tip is located in the middle of the cold finger, which makes thermal interfacing rather delicate. In contrast, the U-shaped and coaxial geometry allows easy access to the cold tip. For many applications, the coaxial arrangement, as shown in Fig. 1 b), is to be preferred, because this most resembles the compact shape of a Stirling cold finger.

During the course of the project, we have realized all of the three PTC configurations in Fig. 1. Each PTC cold finger was built in a smaller and a larger version either designed for operation on the AIM SL200/SL400 or the Leybold Polar compressor, respectively.

A more detailed description of the cooler design and test setup has been given previously.[1,3] The inertance line[7, 8] between the warm end of pulse tube and the buffer volume (Fig. 1) consists of a series network of capillaries with different diameters and lengths. In addition, the smaller PTC cold fingers with SL400 compressor are operated with second inlet flow resistance to gain optimum performance.[1-4] The larger versions with Polar compressor operate efficiently without second inlet.[3, 4]

For all of the results presented below, the length of the transfer line that connects compressor and cold finger was 20 cm for the PTCs with SL400 compressor and 8 cm for the PTCs with Polar compressor. The warm end of the PTC cold fingers was cooled by water. The coolers were operated at a frequency of 40 Hz, which was found to be close to the optimum frequency. The helium charging pressure was 30 bar.

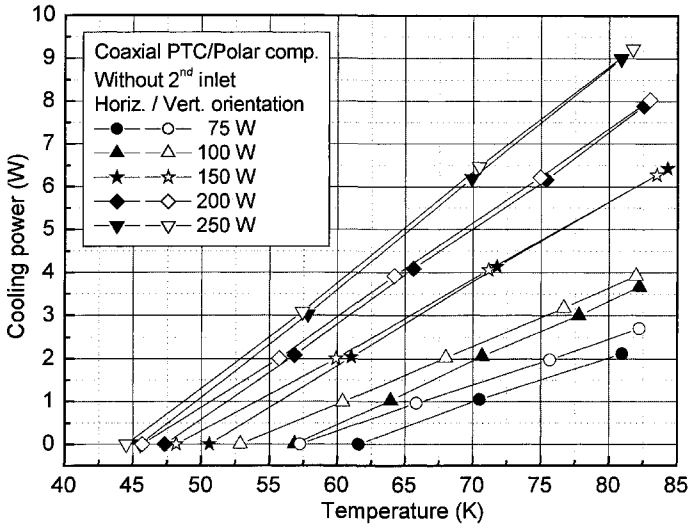

Figure 2. Cooling power versus temperature for the coaxial PTC with Polar compressor at different input power from 75 – 250 W; operation without second inlet; full symbols: horizontal cold finger, open symbols: vertical cold finger with cold end facing downwards.

PERFORMANCE OF PULSE TUBE COOLERS WITH POLAR COMPRESSOR

Coaxial PTC

The coaxial PTC cold finger for operation with the Polar compressor was designed and fabricated following previous experience[3, 4] gained with the corresponding U-shaped and inline PTC versions.

Fig. 2 displays the cooling power as function of temperature at different input power for vertical (with cold tip facing downwards) and horizontal orientation of the cold finger. In vertical orientation, upon increasing the input power from 75 W to 250 W, the minimum no-load temperature drops from 57.3 K down to 44.5 K and the available cooling power at 80 K increases from 2.45 W to 8.8 W.

As seen from Fig. 2, in horizontal orientation of the cold finger the cooling performance is slightly degraded. Fig. 3 shows the increase in cold tip temperature, $T_{horizontal}$-$T_{vertical}$, upon changing the orientation of the cold finger from vertical to horizontal position either without applied heat load or at a fixed load of 3 W. It follows from Fig. 3 that the temperature rise is much more pronounced without heat load and at lower compressor input power. At input powers of 150 W and higher the orientation effect on cooling power is rather small. For example, at 100 W input power the cooling power at 80 K is 3.34 W in horizontal orientation compared to 3.63 W in the vertical case, which corresponds to a reduction of cooling power by 8 %.

The degradation in cooling performance in horizontal orientation can be related to an enhanced heat transfer from gravity-induced natural convection of helium gas in the pulse tube, which is superimposed on the oscillatory gas displacement.[3] Streaming from natural convection in the pulse tube is dampened when the driving force for the oscillatory gas movement in the pulse is larger than the buoyant force from the density gradient in the gas column. This qualitatively

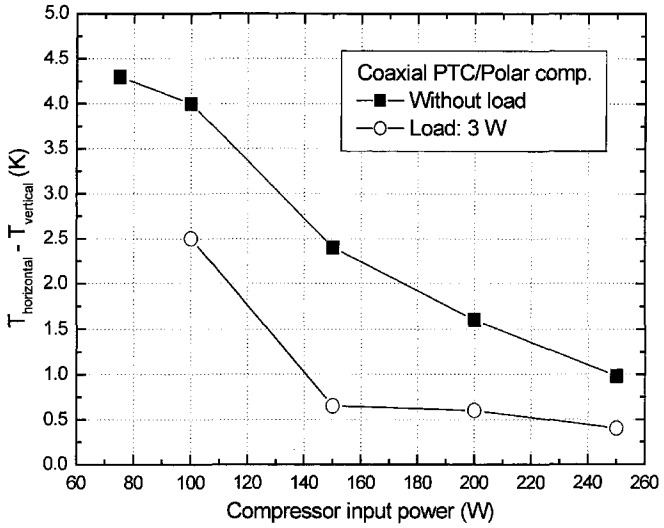

Figure 3. Difference of horizontal and vertical cold tip temperature as function of compressor input power at an applied heat load of 3 W and without load; coaxial PTC with Polar compressor.

explains the reduction of the orientation effect with increasing load or increasing input power in Fig. 3.

Performance Comparison of the Three PTC Configurations with Polar Compressor

Fig.4 compares the cooling power of the coaxial PTC with that of the inline[4] and U-shaped[3,4] versions at an input power of 100 W and 200 W to the Polar compressor. All data in Fig. 4 were obtained with the cold finger oriented horizontally and at a filling pressure of 30 bar.

As seen from Fig. 4, the cooling performance of the U-shaped and the coaxial cold finger are quite similar. With both cold fingers, the same cooling capacities of 3.35 W and 7.4 W at 80 K are available at input powers of 100 W and 200 W, respectively. The inline PTC provides even higher cooling capacities of 4.0 W and 8.7 W at 80 K with 100 W and 200 W, respectively.

These results suggest that the inline configuration is the optimum geometry of the pulse tube cold finger. However, as shown below, the performance data of the other set of PTC cold fingers driven by the SL400 compressor do not confirm such a conclusion.

PERFORMANCE OF PULSE TUBE COOLERS WITH SL400 COMPRESSOR

The previously fabricated and tested U-shaped[3,4] and inline PTC cold fingers that were designed for operation with the AIM SL200 compressor achieved cooling powers of 2.9 W and 3.1 W at 80 K, respectively, at a compressor input power of 100 W. Recently an advanced version of the SL200, the SL400 linear compressor, has become available that promises a higher cooler efficiency.

One essential improvement of the SL400 is the increased efficiency of the linear motors. The motor power of the compressor can be defined as electrical input power minus the ohmic losses of the linear drive coils. The compressor motor efficiency is then given by the motor power divided by the electrical input power. From experiments, we obtained a motor efficiency of about 80% for the SL400 and about 72% for the SL200 compressor.

In the following, we present the cooling performance of the new coaxial PTC and of the previous U-shaped and inline PTC versions driven by the new SL400 compressor.

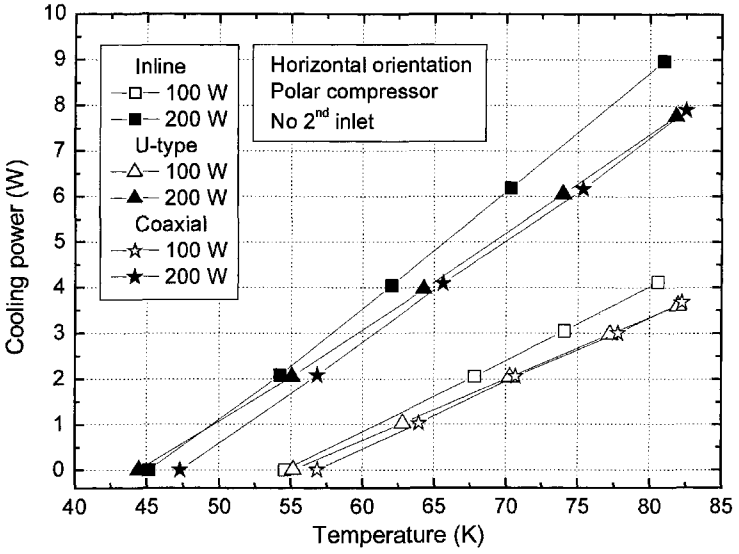

Figure. 4. Comparison of the cooling performance of three PTCs with different geometrical arrangement; cold finger versions with Polar compressor at 100 W and 200 W input power.

Coaxial PTC

Figure 5 shows cooling power versus temperature for the coaxial PTC with SL400 compressor at different compressor input power ranging from 30 W to 120 W. The data were obtained with the cold finger in horizontal position, and the second inlet was opened, except for one load line at 100 W input. With the second inlet opened, upon increasing the input power from 30 W to 120 W the minimum no-load temperature decreases from 63.3 K to 33.2 K and the cooling power at 80 K increases from 0.6 W to 4.3 W.

This coaxial PTC achieves an appreciable cooling power at 80 K also without second inlet, as seen from the two load lines in Fig. 5 at 100 W input power. At 100 W input, the cooler provides 3.3 W of cooling power at 80 K without second inlet compared to 3.6 W with the second inlet opened. However, without second inlet the no-load temperature is higher by about 12 K, so that the two load lines diverge at temperatures below 80 K.

Figure 6 displays the coefficient of performance (COP = cooling power/compressor input power) at 80 K as function of compressor input power for operation with and without second inlet. For input powers ranging from 50 W to 120 W the COP at 80 K is larger than 3% for both modes of operation. In Fig. 6, the COP without second inlet is about 9% lower than with second inlet. An exception occurs at the lowest input power of 30 W where the second inlet becomes ineffective.

Performance Comparison of the Three PTC Configurations with SL400 Compressor

Figure 7 shows a comparison of the cooling power of the three PTC configurations as function of temperature at an input power of 100 W. All data in Fig. 7 were obtained with the cold fingers in horizontal position and with the second inlet opened. Unlike the case in Fig. 4, for this set of PTC cold fingers the coaxial version attains the highest cooling power of 3.6 W at 80 K followed by the inline PTC with 3.53 W and the U-shaped PTC with 3.3 W at 80 K. This shows that a properly designed coaxial PTC can achieve similar or even better cooling performance than the corresponding inline PTC version.corresponding inline PTC version.

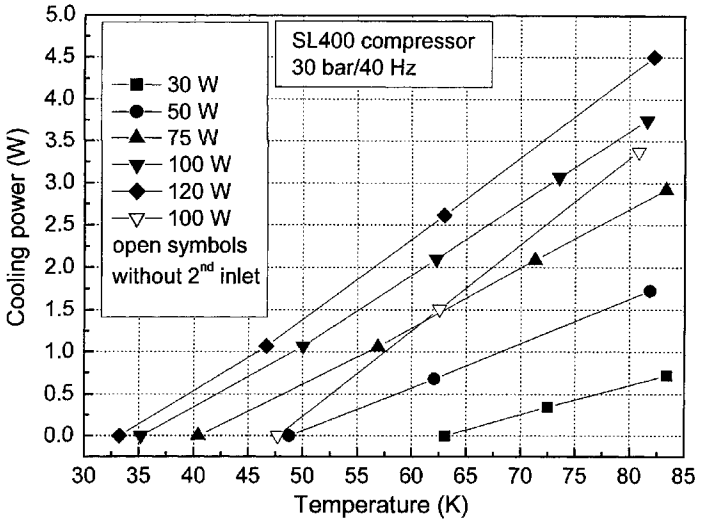

Figure 5. Cooling power versus temperature for the coaxial PTC with SL400 compressor at different input power from 30 – 120 W; full symbols: operation with second inlet, open symbols: without second inlet; horizontal cold finger.

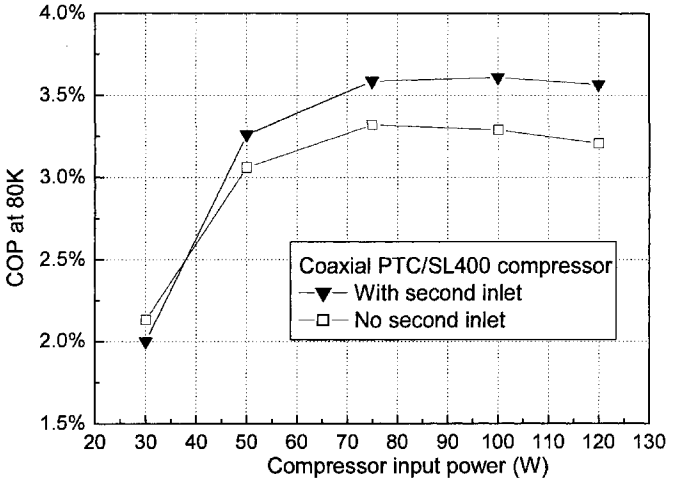

Figure 6. COP at 80 K as function of input power for the coaxial PTC driven by the SL400 compressor; operation with and without second inlet.

In comparison with the earlier performance data[3, 4] of the U-shaped and inline PTC driven by the SL200 compressor, the cooling power of the same cold fingers driven by the SL400 compressor is increased by about 14% at 80 K, which indicates the higher efficiency of the SL400 compressor.

COOLER EFFICIENCIES BASED ON MOTOR POWER

For the PTCs with Polar compressor at nominal input power of 200 W, the COP based on input power ranges from 3.7% to 4.4% at 80 K (Fig. 4). The corresponding COP for the coolers with SL400 compressor is 3.3% to 3.6% at nominal input power of 100 W (Fig. 7). The two new coaxial PTCs attain a highest COP of 3.6% to 3.7% at 80 K and nominal input power (Fig. 6).

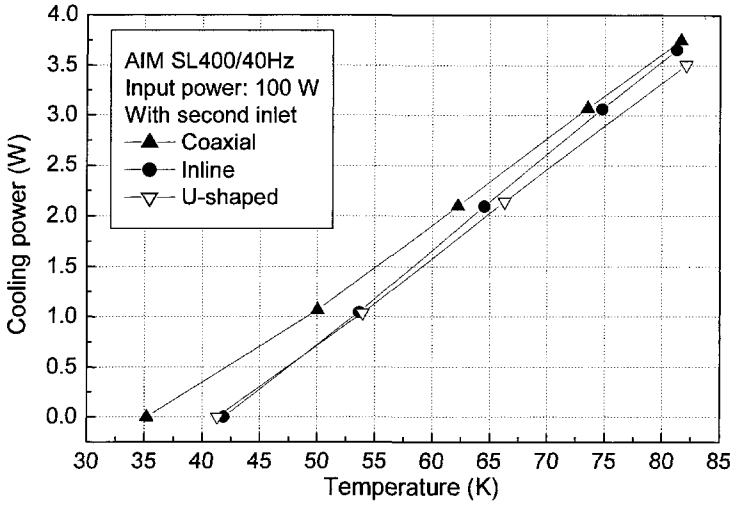

Figure 7. Cooling performance of the three configurations of PTCs driven by the SL400 compressor.

Since the two different compressors have different efficiencies, a more meaningful comparison of the performance of the two sets of PTC cold fingers would be based on the p-V-power of the compressors. Unfortunately, in our test setup the p-V-power of the two commercial compressors cannot be measured.

Therefore, for the purpose of comparison we have chosen the compressor motor power as reference, which is quite close to the p-V-power. From measuring the input power and the ohmic loss in the drive coils we deduced a motor efficiency of $\eta_{Motor} = 70\%$ for the Polar compressor, and, as already mentioned above, a motor efficiency of 80% for the SL400 compressor. The coefficient of performance based on motor power is given by $COP_{Motor\ power} = COP/\eta_{Motor}$.

Fig. 8 shows $COP_{Motor\ power}$ at 80 K as function of motor power for the two coaxial cold fingers and for the larger inline cold finger with Polar compressor. $COP_{Motor\ power}$ attains highest values of 6.3% and 5.4% for the inline and coaxial PTC with Polar compressor, respectively. The smaller coaxial PTC with SL400 compressor reaches a highest $COP_{Motor\ power}$ of 4.5%. This shows that the cold fingers with larger volume of pulse tube and regenerator can reach a higher efficiency than the smaller versions.

CONCLUSIONS

Our two newly developed coaxial PTC cold fingers, i.e. one larger version for operation with the Leybold Polar compressor and one smaller version for operation with the AIM SL400 compressor, achieve maximum coefficients of performance based on compressor input power of 3.7% and 3.6% at 80 K, respectively. Compared to the corresponding inline and U-shaped PTCs with SL400 compressor the coaxial cold finger exhibits the highest cooling performance. Moreover, the coaxial cold finger can operate without second inlet with only a slightly reduced cooling power of 3.3 W at 80 K and 100 W input as compared to 3.6 W in second-inlet mode.

All of the larger cold fingers with Polar compressor operate efficiently without second inlet, which makes the coolers mechanically simpler and more reliable. As opposed to the versions with SL400, from the PTCs with Polar compressor the inline cold finger reaches the highest cooling power of 8.7 W at 80 K and 200 W input, corresponding to a COP of 4.4% or $COP_{Motor\ power} = 6.3\ \%$.

Therefore, for our PTC cold fingers the optimum geometrical configuration with respect to high cooling performance is not so evident. In this context, it should be noted that a preliminary test of the larger coaxial cold finger with a modified flow distributor at the input to the regenerator indicates an increased cooling power of 8.0 W at 80 K and 200 W input. The corresponding COP of 4.0% already comes close to that of the inline version with Polar compressor.

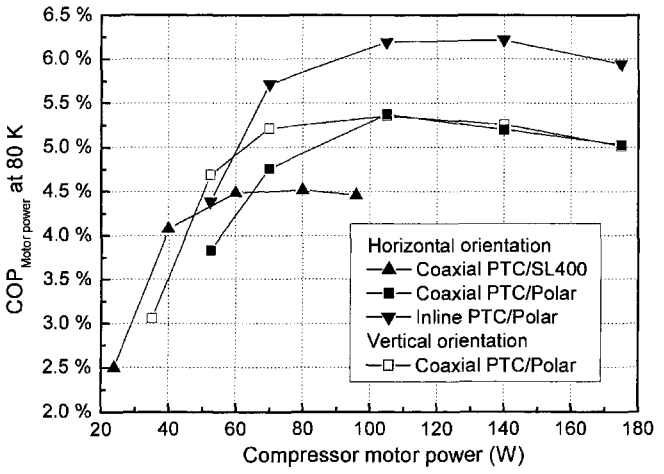

Figure 8. $COP_{Motor\ power}$ at 80 K as function of compressor motor power for three different PTCs.

For all cold fingers, there is a certain input power range approximately between half and full nominal input where the coefficient of performance varies only slightly (Fig. 7 and 8). This makes the coolers useful for applications with different cooling requirements.

The presently most efficient PTCs[5,6] that were designed for space applications reach a highest COP of about 6% based on compressor input power. For our PTCs, the existing transfer line between compressor and cold finger and heat conduction along the stainless steel tubes of regenerator and pulse tube may degrade the final performance.

ACKNOWLEDGMENTS

This work is supported by AEG Infrarot-Module GmbH (Heilbronn) and Leybold Vakuum GmbH (Cologne) under contracts to the German Ministry of Education and Research (BMBF).

REFERENCES

1. Yang, L.W. and Thummes, G., "Medium-size pulse tube coolers with linear compressor", *Adv. Cryog. Eng.*, vol. 47 A (2002), pp. 745-752.
2. Yang, L.W., Rolff, N., Thummes, G., and Häfner, H.-U., "Development of a 5 W @ 80 K Stirling-type pulse tube cryocooler", *Cryocoolers 12*, Kluwer Academic/Plenum Publishers, New York (2003), pp. 149-155.
3. Thummes, G. and Yang, L.W., "Development of Stirling-type pulse tube coolers driven by commercial linear compressors", *Proceedings of SPIE - Infrared Technology and Applications XXVIII*, vol. 4820, SPIE, Bellingham (2003), pp.1-14.
4. Yang, L.W. and Thummes, G., "High-Frequency Pulse Tube Coolers for HTS Applications", *Cryogenics and Refrigeration - Proceedings of ICCR'2003*, International Academic Publishers/World Publishing Corp., Beijing (2003), pp. 69-72.
5. Kotsubo, V., et al., "Development of pulse tube cryocoolers for HTS satellite communications", *Cryocoolers 10*, Kluwer Academic/Plenum Publishers, New York (1999), pp.171-179.
6. Tward, E., et al., "High efficiency pulse tube cooler", *Cryocoolers 11*, Kluwer Academic/Plenum Publishers, New York (2001), pp.163-167.
7. Gardner, D.L. and Swift, G.W., "Use of inertance in orifice pulse tube refrigerators", *Cryogenics*, vol. 37 (1997), pp. 117-121.
8. Radebaugh, R., "Development of the pulse tube refrigerator as an efficient and reliable cryocooler", *Proceedings of the Institute of Refrigeration*, vol. 96, IIR, London (1999-00), pp. 11-31.

Low Temperature High Frequency Pulse Tube Cooler Using Precooling

J.M. Poncet, I. Charles, A. Gauthier, T.Trollier*

CEA-Grenoble / Service des Basses Températures
Grenoble, Isère, France
* Air Liquide Advanced Technology Division, AL / DTA
Sassenage, Isère, France

ABSTRACT

A low-temperature stage pulse tube cooler is under development at CEA-SBT in partnership with Air Liquide (AL/DTA). This stage is designed to operate from an 80 K heat sink and to provide cooling power at 30 K. In a first phase, an experimental setup featuring a Gifford McMahon (GM) cooler as the precooling stage has been manufactured. The regenerator of the pulse tube stage includes a heat exchanger thermally coupled to the GM cold tip. The design is such that the temperature of this heat sink can be varied over a wide range of temperatures. A preliminary tuning of this experimental setup has been done. In this case, stainless steel meshes have been used even in the low-temperature area. The first results are encouraging, as a temperature lower than 30 K has already been achieved. Sensitivity to various parameters such as inertance, frequency, filling pressure and heat intercept temperature has been tested. The heat extracted at the intermediate heat exchanger has been measured using a shunt-type technique and is compatible with the use of our large-heat-lift pulse tube for precooling. For space applications, the precooling could be provided by a passive radiator. In order to increase the performance, we have examined the use of a regenerator material with better specific heat capacity in the cold area. Lead plated meshes have been manufactured and initial experimental results are presented. This cooler will provide inputs for the design of an integrated two-stage pulse tube cooler in the future.

INTRODUCTION

CEA / SBT has considerable experience with the development of both high- and low-frequency pulse tube coolers based on single-stage expanders, and with two-stage expanders at low frequency. In the framework of a European project aimed at the development of an HTS Analog to Digital Converter (Super ADC), 80 K and 30 K cold stages are required for the amplifiers and the ADC, respectively. The development of a 30 K pulse tube has been engaged in partnership with Air Liquide / DTA. The cooling needs at 30 K are predicted to be 300 mW. In order to combine this need with the dissipation at 80 K (few watts), it was decided to design a 30 K stage with the 80 K precooling provided by a large-heat-lift pulse tube cooler already developed at CEA / SBT. For simplification reasons, a single-stage pulse tube with an intermediate heat exchanger in the regenerator cooled by a Gifford McMahon cooler has been designed. In a second step, we will develop the two-stage machine. These points are discussed.

Cryocoolers 13, edited by R. G. Ross, Jr.
Springer Science+Business Media, Inc., New York, 2004

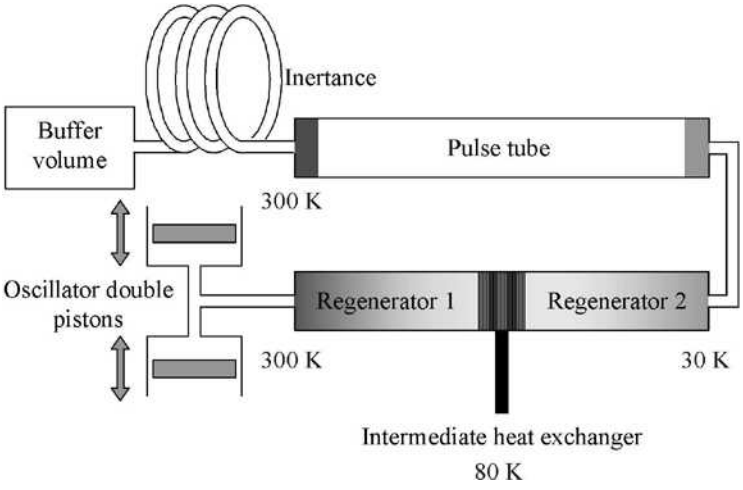

Figure 1. Schematic of the overall cryocooler configuration.

ARCHITECTURE CHOICE

Background on high frequency pulse tube coolers suggests that it will be difficult to achieve significant cooling power at 30 K with a single stage. To decrease the operating temperature, a two-stage pulse tube configuration can be used. This configuration is commonly used in low-frequency pulse tubes to achieve 4 K temperatures[1] and some high-frequency coolers have been reported.[2] It is also possible to use a single stage pulse tube with intermediate precooling. The low temperature pulse tube cold finger is similar to a single-stage pulse tube, but an intermediate heat exchanger is mounted into the regenerator (see Figure 1). This heat exchanger allows reducing the thermal losses of the regenerator and limits the parasitic losses on the cold tip. This architecture is simpler than a two-stage pulse tube and is well adapted for development purposes. It allows focussing on the second regenerator and pulse tube characteristics. In our case, a large heat lift is needed in the 80 K range. The load at 80 K (the one necessary for the application and the one necessary for the 30 K pulse tube) is compatible with a large-heat-lift pulse tube developed by SBT that is able to provide more than 5.5 W at 80 K.[3,6] A solution for the final application will be to use two pulse tubes as described and to develop a two-stage machine in a future step.

DESCRIPTION OF THE COOLER

A photograph of the cold finger is shown in the Figure 2. Thin stainless steel tubes are used for the regenerator and pulsation tube walls. The heat exchangers are made of cooper and are fabricated using Electro Discharged Machining (EDM). The pulsation tube hot-end heat exchanger is located in the vacuum vessel and is cooled by a water cooling circuit, as is the main heat exchanger. This cold finger is connected with a 300 mm transfer line to a conventional moving-coil linear compressor manufactured by Thales Cryogenics BV (UP 8220 type). This compressor is designed for about 200 W maximum electrical input power, and it is also water cooled. The regenerators were first filled with stainless steel meshes. Optimization of the phase shift is performed by an inertance tube located outside of the vacuum vessel.

EXPERIMENTAL BENCH

The cold finger is mounted into a vacuum vessel. The precooling of the intermediate heat exchanger is ensured by the use of a Ricor / Edwards 6-30 two stage GM cooler (see Fig. 3). The heat exchanger of the pulse tube is connected via a copper strap to the first stage of the GM cooler.

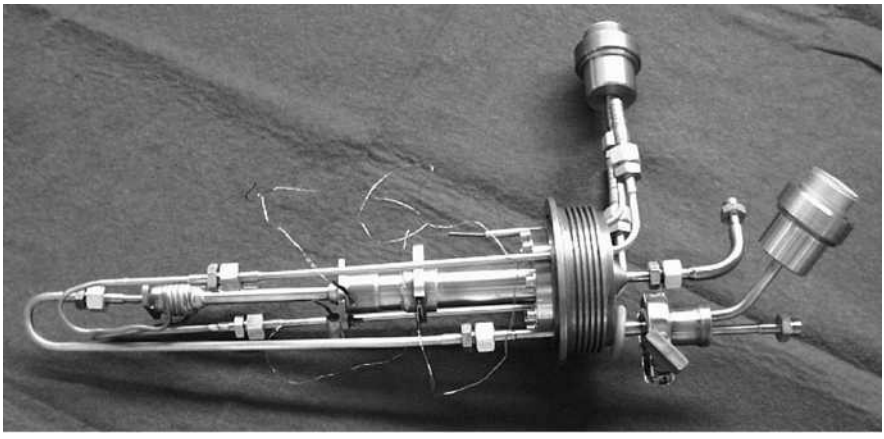

Figure 2. A view of the pulse tube.

Figure 3. 3D view of pulse tube with the Gifford McMahon machine.

The first stage GM is equipped with a heater in order to be able to control the temperature of this stage and consequently the temperature of the intermediate heat exchanger. A regulation loop has been used in order to operate at a given temperature of the pulse tube intermediate heat exchanger. The temperature of the intercept can be easily controlled over a large temperature range. A limitation occurs for temperatures lower than 50 K due to the lack of cooling capacity in the GM cooler. The Edwards GM 6-30 cooling capacity is the reason for its utilization rather than our large-heat-lift cooler, as it is able to reach a larger range of temperatures on the first stage. The second stage of the GM cooler is not used in our application.

The thermal copper strap has been calibrated prior to test with the pulse tube cooler through the use of a heater and two thermal sensors (see Fig. 4). For various temperatures of the GM first stage, the thermal gradient has been measured for a given applied thermal load at the strap extremity. Thus, by measurement of the gradient in the strap, it is possible to estimate the heat that is being extracted from the intermediate stage.

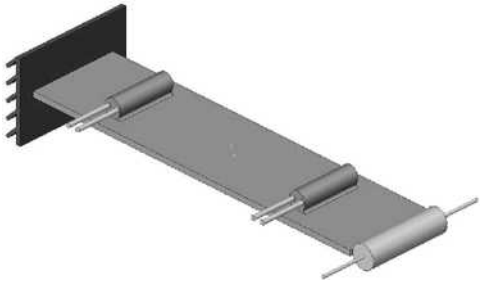

Figure 4. Calibration of the thermal copper strap.

A thermal shield has been manufactured with copper foil to protect the cold tip of the pulse tube from thermal radiation. This shielding is mechanically and thermally linked with the intermediate heat exchanger. The efficiency of this shielding is increased by the use of multilayer insulation (MLI). Some MLI has been installed directly on the tubes below the shielding and above this device.

The cold tip is equipped with a heater and a thermal sensor (Cernox) in order to be able to characterize the cooler (ultimate temperature and cooling curve). The intermediate heat exchanger is also equipped with a thermal sensor that is used for the thermal regulation loop.

REGENERATOR

To start the development, standard stainless meshes were used in both parts of the regenerator. Due to its specific capacity (see Figure 5), it is evident that stainless steel is not a good candidate for a second-stage regenerator that must work at temperatures down to 30 K. Lead balls, which exhibit a larger specific heat than stainless steel, is commonly used in two-stage GM and low-frequency pulse tubes. For high-frequency pulse tubes, where pressure drop into the regenerator is more critical, the ball shape is not well adapted due to the larger ratio of pressure drop to heat exchange (NPH/NTU).[4] As lead meshes are not commercially available, some commercial stainless steel meshes have been coated with lead (10 and 5 microns). This technique has been proposed and developed in 1986 by Cosier et al.[5] This allows a large increase in the specific heat while keeping

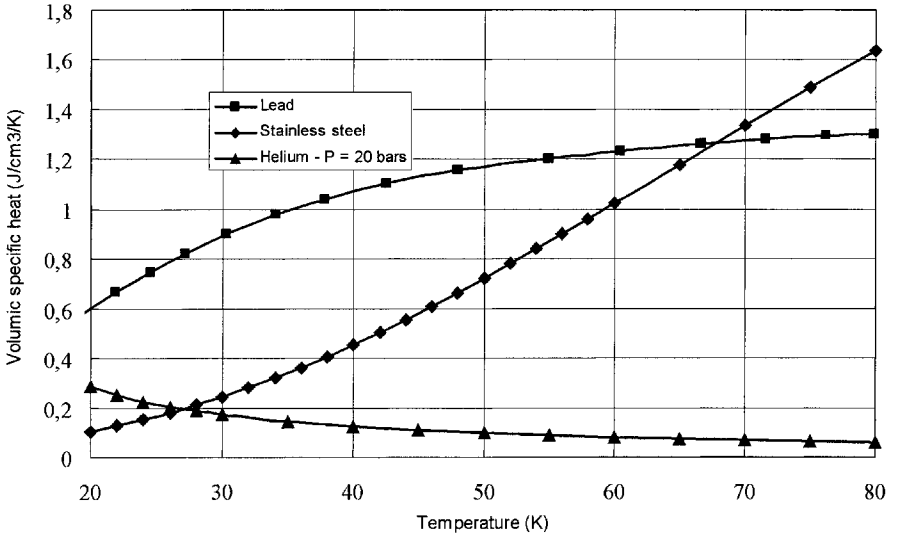

Figure 5. Comparison of specific heat.

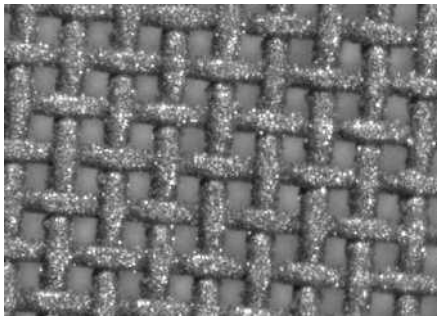

Figure 6. Stainless steel coated with lead.

a good shape for pressure drop and heat exchange aspects. Figure 6 shows such a mesh. Lead-coated meshes have been procured from JENA University with a deposit coating approximately 10 μm thick on the stainless steel meshes.

RESULTS AND ANALYSIS

As has been mentioned, first tests were conducted using stainless steel meshes. This is not the best material, but the interest was to verify other parameters like volume, aspect ratios, resonant frequency, filling pressure, etc during the procurement of the lead-coated meshes. To achieve a good global efficiency, it is necessary to design a pulse tube cold finger that works at the compressor's resonant frequency. Several configurations have been tested; for the first one, the global volume of the cold finger was too small, so it was not adapted to the oscillator. The maximum electrical power of our oscillator is about 200 W, and its resonance frequency is roughly 50 Hz. With the first PT version, the maximal PV work that could be supplied to the gas was low (100 W), and it was decided to change the volume of the cold finger in order to increase the PV work maximal value. By increasing the volume of the pulse tube, its optimum frequency was reduced, and the oscillator is better adapted, thus allowing greater PV work to be achieved.

In the framework of this development, it was decided to focus on the cold finger, and so the results are presented as a function of the mechanical power given to the gas (PV work). Figure 7

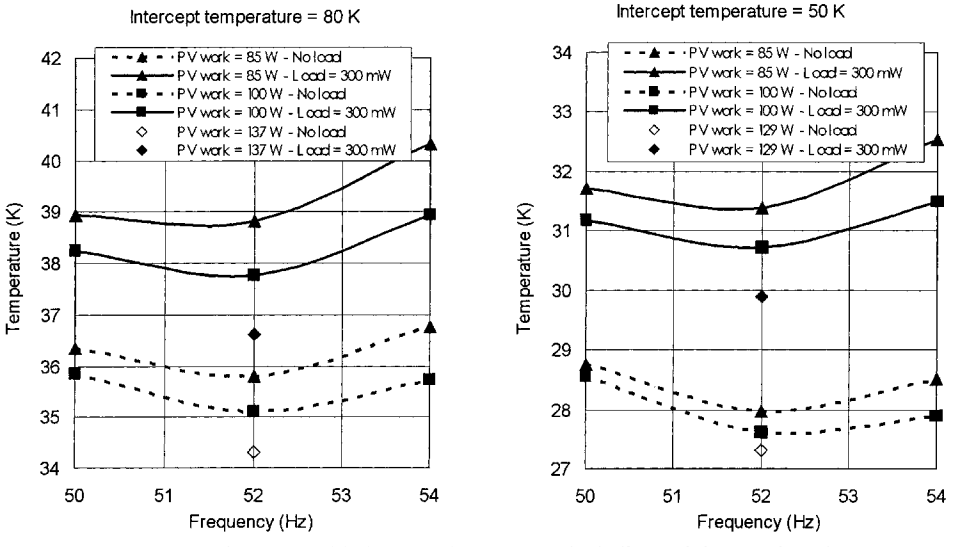

Figure 7. Performance with the second regenerator including stainless steel meshes.

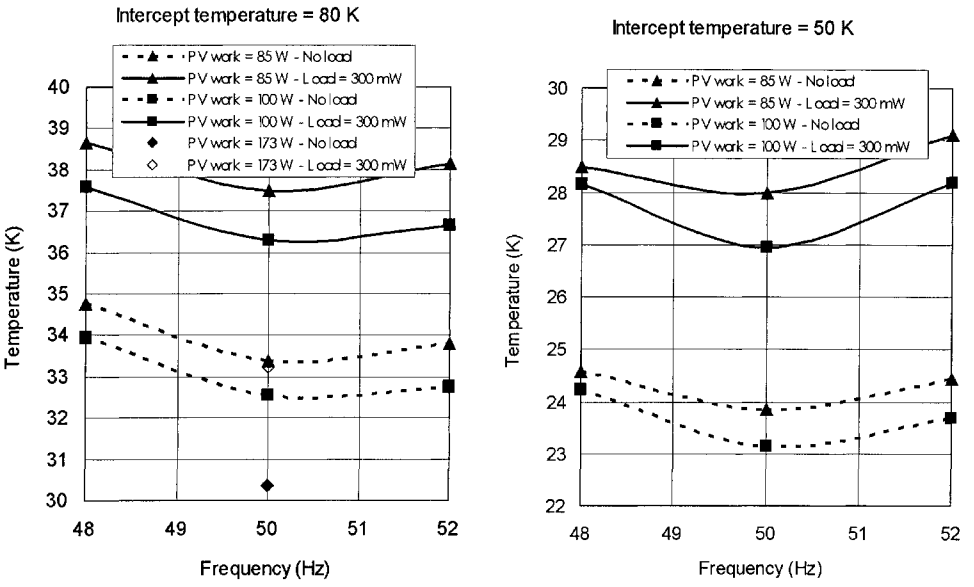

Figure 8. Performance with the second regenerator including lead-coated meshes.

presents our best results with stainless steel meshes. The optimum frequency of the pulse tube is 52 Hz, which is not yet the resonant frequency of the oscillator. However, optimization of the pulse tube was stopped, because, with lead coated meshes, a lower temperature is expected, so the apparent volume of the cooler will increase. Under these conditions, the optimum frequency of the tube will decrease. With the intercept at 50 K, a limit (no-load) temperature of 27.3 K was obtained with a PV work of 129 W. With 300 mW applied heat load, a temperature of 29.9 K was reached with the same PV work. With the intercept at 80 K, the limit temperature was a little above 34 K, and with 300 mW applied, the temperature obtained was 36.6 K. Of course, the load on the intercept heat exchanger increases when its temperature decreases. At 80 K, a typical value of the load that needed to be removed is 2 W, which is compatible with the large-heat-lift pulse tube already developed at CEA / SBT.

Lead plated meshes were next manufactured and are currently under test. In parallel, the regenerator of the second stage was slightly increased. The first results are presented in the Figure 8. With the heat intercept at 50 K, in comparison with the regenerator with stainless steel meshes, all the temperatures decreased by approximately 4 K. The no-load temperature obtained with a PV work of 100 W was about 23 K, and, with 300 mW applied the corresponding temperature, was 27 K. With the intercept at 80 K, the performance improvement was less. This can be explained by increased pressure drop in the regenerator. The thickness of lead deposit was a little higher than the specification, so the ratio between the pressure drop, the heat transfer coefficient, and the heat capacity of this device was not optimum. By increasing the intercept temperature, the loss due to the pressure drop was less balanced by the gain due to increased heat capacity. In the future, this point will be solved by using a lower lead thickness.

With the modification of the regenerator, we continued to increase the volume of the cold finger. That allowed further reductions in the optimum frequency of the cooler. The oscillator is close to its resonant frequency, and it is now possible to inject more PV work into the pulse tube. The highest value injected was 173 W under these conditions. With the intercept at 80 K, an ultimate temperature of 30.3 K was obtained. With 300 mW applied, the temperature reached was 33.2 K. For this test, the inertance tube was not yet optimized, and further improvements are foreseen and will be presented later.

CONCLUSION

A 30 K stage high-frequency pulse tube has been developed at CEA / SBT in collaboration with Air Liquide / DTA. The regenerator is divided into two parts separated by a heat intercept heat exchanger cooled down by another cooler (single stage pulse tube or other). This solution simplifies greatly the study of the second stage. Two types of low temperature regenerators have been tested (stainless steel meshes and stainless steel meshes coated with lead). A no-load temperature below 30 K has been reached with the first type of meshes and with the intercept at 50 K. With the second type of meshes and the same 50 K heat intercept temperature, all temperatures decreased by approximately 4 K. Currently, the ultimate temperature obtained is 23 K. With the heat intercept at 80 K, a ultimate temperature of 30 K has been reached, and 33 K has been reached with 300 mW applied on the cold tip. Further improvements are foreseen in the near future.

ACKNOWLEDGMENT

This work, performed in collaboration with Air Liquide DTA, was supported by the European Community (Super ADC program). We thank them for their support of our developments.

REFERENCES

1. J.M. Poncet, A. Ravex and I. Charles, "Developments on Single and Double Stage GM Type Pulse Tube Cryorefrigerators," *Cryocoolers 11*, Kluwer Academic/Plenum Publishers, New York (2001), pp. 229-233.
2. Wilson, K.B, Gedeon, D.R., "Development of Single and Two-stage Pulse Tube Cryocoolers with Commercial Linear Compressors," *Cryocoolers 12,* Kluwer Academic/Plenum Publishers, New York (2003), pp. 139-147.
3. Charles, L. Duband, J-Y. Martin, J.C. Mullié and P.C. Bruins, "Experimental Characterization of a Pulse Tube Cryocooler for Ground Applications," *Adv. in Cryogenic Engineering*, Vol. 49B, Amer. Institute of Physics, Melville, NY (2004), pp. 1373-1379.
4. Rühlich and H. Quack, "Investigations on Regenerative Heat Exchangers," *Cryocoolers 10*, Kluwer Academic/Plenum Publishers, New York (1999), pp. 265-274.
5. J. Cosier and R.M. Silvester, "Rigid leaded regenerator matrix for small closed-cycle refrigerators," *Cryogenics,* vol. 27 (1987), pp. 88-89.
6. I. Charles, J.M. Duval, L. Duband, T. Trollier, A. Ravex, J.Y. Martin, "High frequency large cooling power pulse tube," *Proceeding of the ICEC19* (2002), pp. 395-398.

Development of a Single Stage Pulse Tube Refrigerator with Linear Compressor

J. Yuan and J. Maguire

American Superconductor Co.
Westborough, MA 01581 USA

ABSTRACT

High frequency Stirling type pulse tube cryocoolers offer significant advantages in efficiency, size and reliability, over conventional Stirling coolers or low frequency GM type pulse tube refrigerators. This kind of cooler has potential application for HTS motors and generators. A baseline single stage Stirling type pulse tube cooler has been designed and constructed based on a thermodynamic model. An oil-free, linear motor driven compressor is used. The cooler has been tested for its cooldown and cooling capacity, with heat rejected by chilled water at 290 K. Initial testing indicates that the cooler can reach the best no load temperature of 37 K within 30 minutes and has a cooling capacity of about 50 W at 55 K and 140 watts at 80 K with an input power of 3.4 kW. 11% Carnot efficiency has been reached at 80 K. The dependency of cooler performance on pulse tube orientation and input power has been investigated. In addition, matching issues between cooler and compressor, and flow distribution issues within the pulse tube and regenerator, are discussed in the paper.

INTRODUCTION

High reliability, high efficiency, low cost cryocoolers are needed to cool commercial high temperature superconductor (HTS) devices. While practical Gifford-McMahon coolers are available today for most of these applications, Stirling-type pulse tubes offer an opportunity for a significant further improvement in reliability, efficiency and cost. As the cost of the HTS wire continues to drop, the performance continues to increase[1], and HTS systems are starting to be commercialized, the need for a better cryocooler continues to grow.

The present paper describes design, construction and test results of a high power single stage Stirling type pulse tube cooler developed at American Superconductor for HTS motor and generator applications. The cooler was driven by an oil free, clearance seal linear compressor or pressure wave generator. The cooler has been tested for its cooldown and cooling capacity with heat rejected by chilled water at 290 K. Initial test indicates that the cooler can reach a best no load temperature of 37 K within 30 minutes and has a cooling capacity of 50 W at 55K and 140 watts at 80 K with an input power of 3.4 kW. This results in 11% Carnot efficiency at 80 K. The dependence of cooler performance on the pulse tube orientation and input power is addressed. The matching issues between cooler and compressor are discussed.

Cryocoolers 13, edited by R. G. Ross, Jr.
Springer Science+Business Media, Inc., New York, 2004

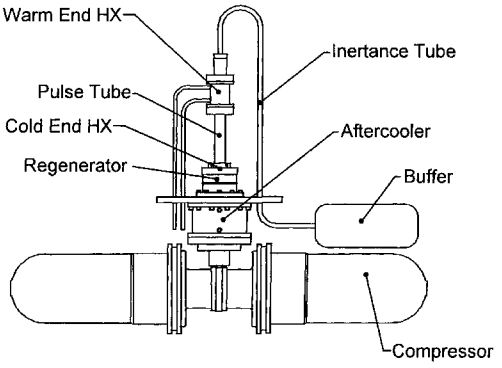

Figure 1. Cooler configuration.

COOLER DESIGN AND CONSTRUCTION

A schematic of the cooler with the pressure wave generator is represented in Fig. 1. As illustrated, the cooler utilizes an inline configuration with an inertance tube to provide a phase shift at the warm end of the pulse tube. To simplify the manufacturing process and minimize potential leaks, a unique aftercooler was designed and fabricated which can dissipate more than 4 kW heat. In this particular design, an aluminum core having a crossing pattern of holes for gas and coolant, respectively, has been brazed with an aluminum cage. The design allows us to scale up the aftercooler for a larger compressor without any difficulty. During the design process, special attention has been paid to the cold end heat exchanger to assure a smooth gas transition from the regenerator into the pulse tube and vice versa. A small water-cooled heat exchanger is placed at the warm end of the pulse tube. The warm-end heat exchanger contains a cavity through which cooling water circulates.

The baseline single stage Stirling-type pulse tube cooler has been designed and built based on the following design specifications:

- Mean Pressure 2.5 MPa
- Pressure Ratio 1.3 (inside pulse tube)
- Frequency 60 Hz
- Sink Temperature 290 K
- Cooling Capacity 100 Watts @ 55 K
- Compressor Input 3.2 kW

The design goal was to obtain 100W at 55 K with an input power of 3.2 kW. The essential design parameter pressure ratio was used as a starting point. The cooler geometry, including the size of pulse tube and regenerator was optimized at 55 K. A rather large phase angle between the mass flow rate at the entrance of the inertance tube and the pressure wave was selected to reach this optimized design. Since a gas piston is utilized to separate the cold and hot gas within the pulse tube, careful control of the gas columns within the pulse tube is a key to a successful pulse tube refrigerator. Figure 2 illustrates the gas P-V diagram within the pulse tube of the current design. In this particular design, the cold gas column is about 30% of the pulse tube volume.

Like the design of the other cryocoolers, the design of the pulse tube cooler required several iterations. During this process, particular efforts have been made on issues associated with a large scale Stirling type pulse tube cooler, such as flow distribution within the pulse tube and regenerator, and impedance matching between the pressure wave generator and the cooler.[2] To address the flow mal-distribution problem, a commercial CFD code has been employed. The study indicated that flow mal-distribution within the pulse tube and regenerator could be caused by a changing flow direction as in the case of a poorly designed U-shape configuration or by a changing flow area. This non-uniform flow could produce huge losses, which result in poor pulse

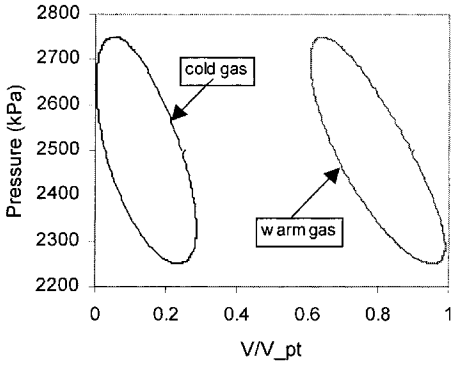

Figure 2. P-V diagram of cold and warm gas within pulse tube

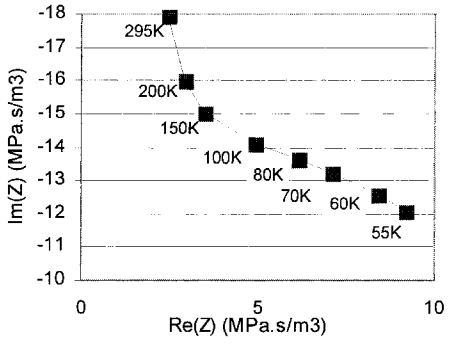

Figure 3. Cooler impedance as function of cold end temperature

tube performance. This issue becomes even more vital in a large scale, high frequency pulse tube due to its high volume flow rate and its tendency to have mal-distributed flow within the large cross sectional area of the regenerator and pulse tube.

Another key issue in designing a high frequency Stirling type pulse tube is the impedance matching issue between the compressor and the cooler. Theoretical investigation indicates that cooler input impedance is a function of cold-end temperature and compressor output impedance is coupled with cooler input impedance, especially when the compressor system stiffness is dominated by the gas spring. This makes the design of a cooler to operate over a wide range of temperature difficult, since in theory only one temperature can be perfectly matched with the compressor. As an example, our baseline cooler impedance as a function of cold-end temperature is illustrated in Fig.3. The plot suggests that a well-matched cooler system at operating temperature is not matched during the cool-down process.

COOLER TEST AND DISCUSSION

Cooling Capacity

The cooler has been tested for its cooldown and cooling capacity with heat rejected by chilled circulating water at 290 K. Initial test indicated that the cooler can reach the best no load

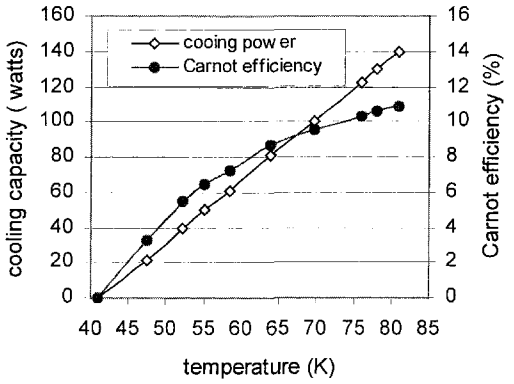

Figure 4. Cooling capacity and Carnot efficiency as a function of temperature

temperature of 37 K within 30 minutes. The optimized cooling capacity of the cooler as a function of temperature with a compressor input power of 3.4 kW is displayed in Fig. 4. The system has been designed to have a maximum cooling power at 55 K. As seen, the cooler produced 50 watts at 55 K and 140 watts at 80 K. Although, the cooler was designed with an operating frequency of 60 Hz, the overall system resonant frequency, when combined with compressor, was only 57 Hz. At this operating point, the PV power from compressor was about 2.4 kW, which resulted in a compressor efficiency of about 70%. This suggests that additional fine tuning of the entire system is needed to reach a higher system efficiency.

Orientation Dependence

The performance of a pulse tube refrigerator depending on the orientation is a well known problem[3]. The best performance is obtained when the pulse tube cold end is at the downward position, which we refer to as 0 degree in Fig.1. Tests have been carried out to investigate this effect on a lager-scale pulse tube to determine the severity of the problem. A series of tests have been performed by varying input power, orientation angle, and heat load on the cold head. Figure 5 illustrates the percentage of cooling power at different inclination angles relative to the vertical nominal position as shown in Fig.1. In general, pulse tube performance drops when the pulse tube is inclined. This effect, as observed in Fig. 5, is a strong function of operating temperature. The lower the operating temperature, the stronger this effect. For the case of input power of 3 kW, at 80 K the total cooling capacity drop is less than 5%, while at 50 K it drops more than 30% when pulse tube is in a horizontal position. However, one should notice that compared with a GM-type pulse tube (valved, low frequency), the orientation problem here is much less prominent. In particular, at 80 K the performance degradation of larger scale pulse tubes is almost negligible when the inclination angle is up to 90 degree. This is very encouraging for some HTS applications where the cooler is required to operate in an inclined position.

An additional point to be noted is that the input power plays an important role in the performance degradation when the pulse tube is inclined. Comparing Fig. 5 (a) and (b), one can observe that for the given pulse tube, the effect of inclined angle on the system performance is much stronger when the input power is high and operating temperature is low. At 50 K, the cooling power remains 40% with an input power of 3.6 kW, while the cooling power remains 65% with an input power of 3.0 kW when the inclination angle is 90 degrees.

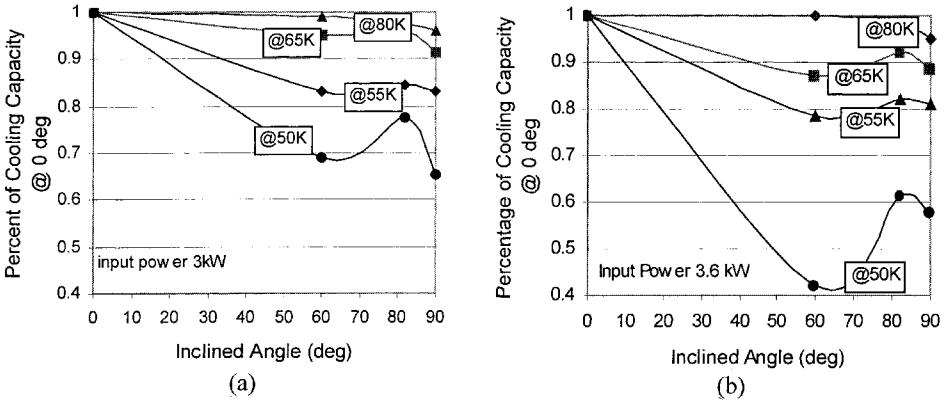

Figure 5. Dependency of cooling capacity on inclination angle

Parasitic Losses

As part of our efforts to identify the loss terms associated with the baseline pulse tube, investigations have been conducted into parasitic losses. Parasitic losses of the cooler have been measured based on cooler warm-up rate at 55 K with different heat loads. Figure 6 illustrates test data and projected parasitic losses at 55 K. A loss of 20 watts has been measured, which is in very good agreement with our prediction.

Effect of Inertance Tube

Experiments have been performed by adjusting the phase shift network at the warm end of the pulse tube. This adjustment directly affects the compressor performance, such as the resonant frequency, stroke and output PV power. Figure 7 shows cooler cooling capacity at 77 K and 55 K as a function of inertance tube length for constant inertance tube diameter and input power. The results indicate that there is an optimized inertance tube length for a given diameter. One should notice that the initial design point is not far away from the final optimized point, which lends credibility to our ability to predict the system parameters.

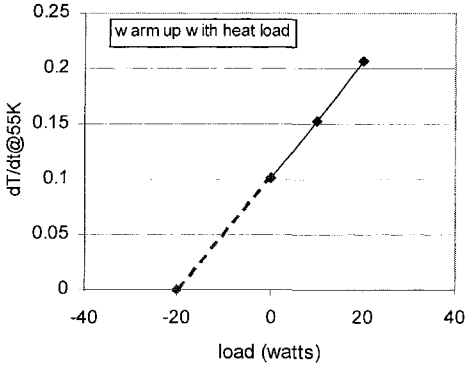

Figure 6. Parasitic losses at 55 K

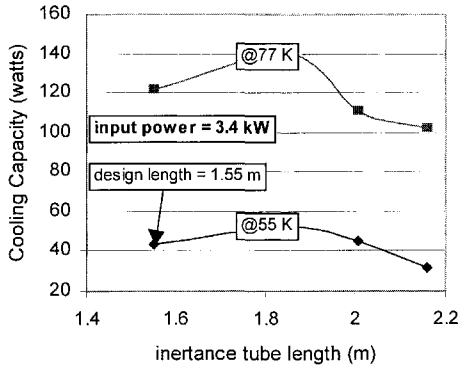

Figure 7. Cooler cooling capacity as a function of inertance tube length

Temperature Profile

Two temperature profiles were measured during the experiments. The first one was the axial temperature profile along the regenerator and pulse tube wall, while the second one was the circumferential temperature profiles of the pulse tube and regenerator at different planes. These temperature profiles provided information that can be used to diagnose problems inside the regenerator and pulse tube, such as non-uniform flow and poor packing of the regenerator. Figures 8 and 9 illustrate those two temperature profiles of our two different regenerator and cold end heat exchanger designs, referred as Design I and Design II. In those particular tests, a set of thermocouples was uniformly distributed on the middle plane of the regenerator and along the regenerator and the pulse tube wall. The temperature was measured when the cold end reached its ultimate temperature.

The temperature profiles of Fig. 8 demonstrated that the regenerator and pulse tube operation are perfectly normal. However, the circumferential temperature profiles of Fig. 9 indicate that Design I has a serious mass streaming issue within the regenerator. This result suggests that the circumferential temperature profiles are more critical in a large-scale Stirling type pulse tube cooler.

As expected, the ultimate temperature of Design II was 39 K while the ultimate temperature of Design I was only 62 K.

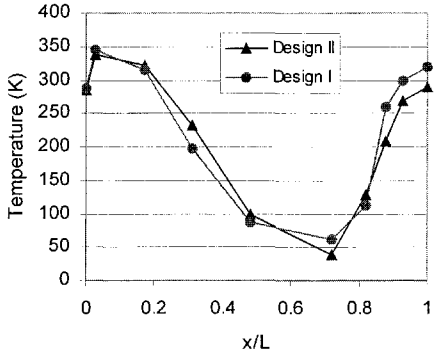

Figure 8. Temperature profile along regenerator and pulse tube

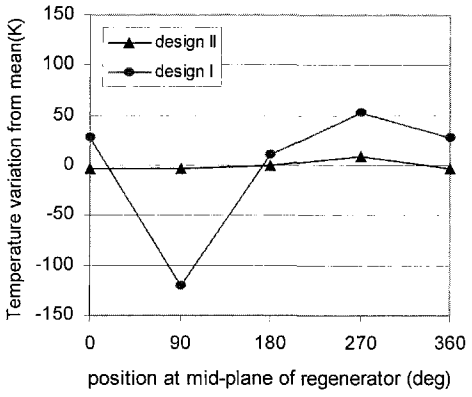

Figure 9. Temperature distribution around middle plane of two different regenerator design.

CONCLUSION

A single stage Stirling type pulse tube has been designed and constructed. It has been found that the single stage Stirling type pulse tube has the potential to produce a relatively high cooling capacity at 55 K. Theoretical and experimental studies indicate that a well-matched cooler system at operating temperature is not matched during the cool-down process. Tests have also shown that a mal-distribution problem in a large-scale pulse tube cooler could be avoided by carefully designing the regenerator and cold-end heat exchanger. At 80 K, the performance degradation of the large-scale pulse tube is almost negligible when the inclination angle is up to 90 degrees. Furthermore, the parametric study has shown that there is an optimized phase shift network. Further work is needed to improve our baseline pulse tube cooler utilizing the data obtained from our current tests.

ACKNOWLEDGMENT

The work described here was supported financially by American Superconductor Corp. The authors would like to thank the management and our coworkers at American Superconductor for their assistance and support, and Dr. Ray Radebaugh at NIST for his helpful discussions.

REFERENCES

1. Verebelyi, D.T., Schoop, U. et al., "Uniform Performance of Continuously Processed MOD-YBCO-coated Conductor Using a Textured Ni-W Substrate," *Superconductivity Science & Technology*, vol. 16 (2003), pp. L19-L22.
2. Martin, J.L. "Pulse Tube Cryocoolers for Industrial Applications," *Advances in Cryogenic Engineering*, 47A, American Institute of Physics, Melville, NY (2002), pp. 662-669.
3. Thummes, G., Schreiber, M., Landgraf, R. and Heiden, C., "Convective Heat Losses in Pulse Tube Coolers: Effect of Pulse Tube Inclination," *Cryocoolers 9,* Kluwer Academic/Plenum Publishers, New York (1997), pp. 393-402.

A Commercial Pulse Tube Cryocooler with 200 W Refrigeration at 80 K

J.H. Zia

Praxair Inc.
Tonawanda, NY 14150, USA

ABSTRACT

An electrically driven pulse tube cryocooler that produces 200 W of refrigeration at 80 K is now available from Praxair Inc. The unit can be used to provide refrigeration by de-superheating, liquefying and/or subcooling a stream of nitrogen. The electroacoustic transducer used in the cryocooler is a dual opposed piston, moving magnet design from CFIC Inc. The pistons maintain a clearance seal and thus no lubricants are needed. The electrical power consumed by the driver at full refrigeration load is 4.3 kW giving an overall efficiency of 13% of Carnot. The cryocooler as a whole is designed for high reliability and no routine maintenance.

The paper will describe the rapid evolution of the cryocooler from a laboratory-based prototype to a commercial offering. Experimental results from refrigeration performance tests and load curves will be described. A brief overview of continuing efforts to improve performance, efficiency and envelope size will also be provided.

INTRODUCTION

Large orifice pulse tube cryocoolers (OPTR's) offer the promise of the reliability and capacity required for operation of the new wave of high temperature superconducting (HTS) devices to be commercialized in the near future. These HTS devices include transformers, fault current limiters, motors, generators and cables. Truly commercial cryocoolers that satisfy the stringent availability and reliability criteria of electrical power HTS devices are rare.

The pulse tube technology group at Praxair Inc. is actively involved in developing commercial OPTR offerings for the electrical power HTS industry. Such cryocoolers can also be conveniently integrated into other applications. A commercial OPTR that produces 200 watts of refrigeration at 80 K, and consumes a nominal 4 kW of electrical power is now available. The unit is vertically oriented with the cold end of the thermal buffer tube lower than the warm end. Acoustic power is provided by a dual opposed piston pressure wave generator (PWG) from CFIC that produces acoustic power from 4200 Watts of electrical input power. The pistons use a clearance gap from the matching cylinder, hence there is no lubricant. The PWG is equipped with an internal water-cooling loop to remove heat generated by electrical losses in the coils and by viscous losses in the seal gap. Regenerator phasing is controlled by a dual valve inertance network. The 'cold-head' is insulated by an optional vacuum jacket. The cryocooler is mounted on a skid and an optional enclosure that includes connections for the cryogen, utilities and electrical power. An optional electrical controls

Cryocoolers 13, edited by R. G. Ross, Jr.
Springer Science+Business Media, Inc., New York, 2004

panel can be integrated into the enclosure: this provides voltage and frequency modulation capabilities. The electrical panel also houses safety shutdowns for electrical, vibration and over-temperature protection. A variable frequency drive inside the electrical panel provides the ability to control the cryocooler using customer process variables.

A laboratory precursor to this commercial cryocooler was successfully built and tested in 2003.[1] Major challenges addressed in the precursor were scaleup, management and amelioration of pulse tube streaming and optimization of refrigeration efficiency. These are typical of the issues encountered in laboratory scale OPTR's and quite different from the issues of developing a commercial cryocooler from a laboratory based unit. Reliability, continuous availability, ease of operation and integration were overarching requirements in the transition to the commercial unit.

PRODUCT TRANSITION ISSUES

Mechanical Design and Construction

The working gas in the OPTR is helium at a mean pressure of 2.5 MPa. Gas leakage and seal integrity are perennial problems with laboratory based OPTR's that are often constructed by bolting together flanged segments. Consequently, in the commercial product all individual segments were welded together to form a leak free envelope. The wall thickness of the envelope and welding procedures took into account the stress exerted by high-pressure helium inside the OPTR.

Three shell and tube heat exchangers were used in the OPTR. Since the tubes and shell were much smaller than traditionally encountered in the heat exchanger industry, a specialized fixture and brazing procedure was developed to join the tubes into the tube-sheets and subsequently, to join the tube bundle to the inside walls of the envelope. All brazing operations were performed per ASME specifications. Each heat exchanger was tested for leaks up to a pressure of 3.5 MPa and structural integrity (burst pressure) up to 4.3 MPa prior to brazing into the OPTR.

The regenerator consisted of layers of stainless steel wire mesh. The assembly of the regenerator into the envelope was complicated by the delicate nature of the mesh. There were concerns about undesirable oxidation/melting of the mesh due to heating of the envelope caused by welding. Therefore, specialized welding techniques were developed to overcome this problem.

The phase shift across the regenerator was controlled by a dual valve inertance network and compliance tank as described by Swift et al.[2] This allows freedom to access a range of complex impedances within the first and fourth quadrants. ASME code was also followed in fabrication of the inertance network and compliance tank. Once assembled (see Fig. 1), the entire helium envelope of the OPTR was burst tested to a pressure of 3.8 MPa and leak tested with helium to a pressure of 3.5 MPa. A second inertance network was later developed using only a single valve and a much smaller compliance tank. This had the advantage of providing the same phase shift (with reduced flexibility) with a much smaller profile, thus reducing the footprint and height of the cryocooler.

Safety

An insulating vacuum jacket was welded to the cold head. Cryogen inlet and outlet arms extended out from the jacket providing an insulated passage into and out of the cold head. To address the possibility of accidental pressurization of the vacuum jacket by cryogen leakage or rupture of the helium envelope, a bursting disc was placed at the inlet arm of the vacuum jacket.

The electrical controls panel also has monitoring equipment for temperatures of the process gas inlet and outlet, temperatures inside the PWG (for over-temperature protection in case of a cooling water failure) and vibration of the PWG. The dual opposed piston design of the PWG ensures complete cancellation of vibration, however in the unlikely case of a failure of a single piston, the resulting vibrations may cause damage to the cryocooler. The vibration monitor therefore provides a shutdown at a high vibration set-point to protect the cryocooler. Electrical overcurrent protectors were used for the PWG in compliance with NEMA electrical safety codes. Each

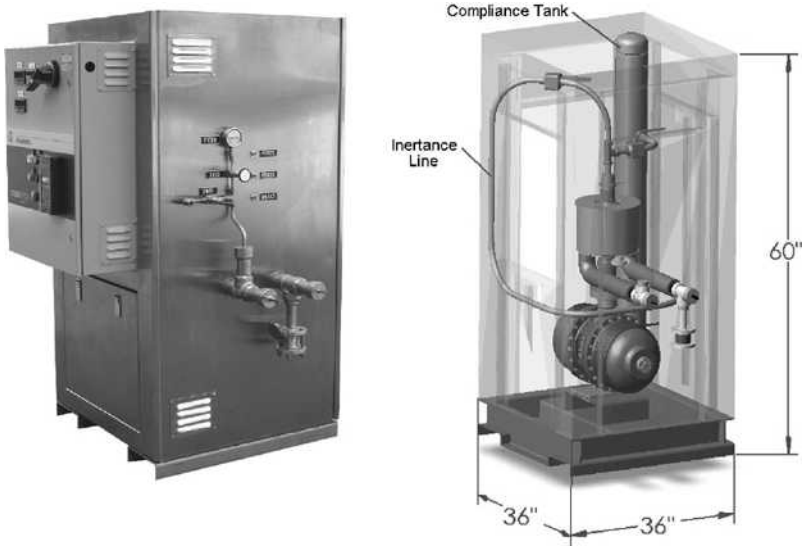

Figure 1. Left: the cryocooler in a stainless steel enclosure. Inlet and outlet lines for the cryogen can be seen. Right: a 3-D representation of the cryocooler inside the enclosure. The pressure wave generator sits at the base of the cryocooler, mounted on a skid.

device inside the electrical panel was UL certified (Underwriters Laboratories Inc.). The aim is to obtain UL certification for the electrical panel and eventually for the entire cryocooler.

PERFORMANCE

Refrigeration performance tests were carried out using nitrogen as the cryogenic fluid. In general, the frequency of the pressure waves produced by the PWG was maintained at 60 Hz, although the capability to vary this frequency was present. The refrigeration, Q_c, was measured as the cooling power delivered to a stream of nitrogen flowing through the cold heat exchanger. This was a true measure of the actual *useful* refrigeration to an HTS device or process that uses a liquid cryogen. Since on many occasions the outlet nitrogen stream was at least partially liquefied, an in-line electric heater was employed to re-vaporize the nitrogen and bring it back up to the inlet temperature. The lines and the heater were well insulated. Figure 2 is a simplified schematic of the setup described above.

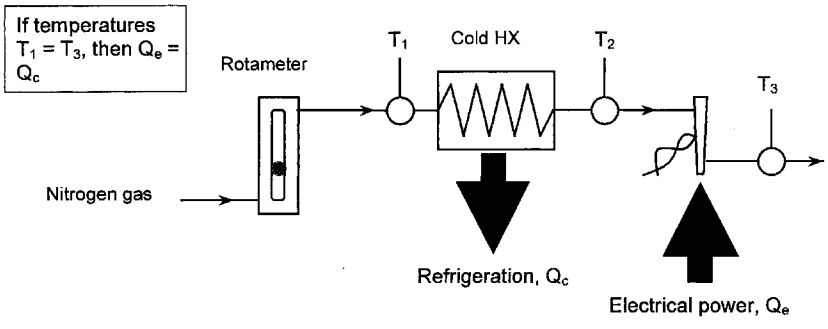

Figure 2. Schematic of the experimental setup for measuring the refrigeration power of the cryocooler. This setup was used when the nitrogen at the cold heat exchanger (HX) outlet was either gas or at least partially liquefied. For subcooled nitrogen, the downstream heater was replaced by an insulated dewar mounted on a scale.

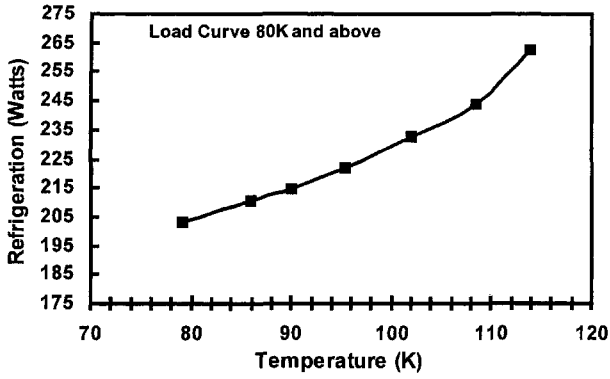

Figure 3(a). Load curve for cooling a gaseous nitrogen stream from ambient temperature.

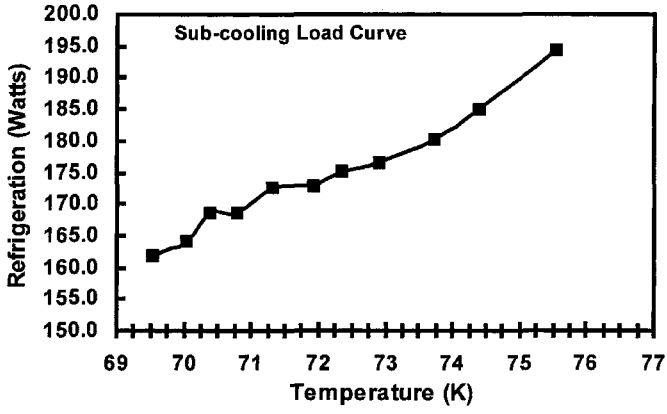

Figure 3(b). Load curve for sub-cooling a nitrogen stream.

A slightly different setup was used when the nitrogen was subcooled at the cryocooler exit. In this case, the heater was removed and the subcooled fluid allowed to flow into an insulated dewar. The rate of change of mass of the dewar was used to calculate the flow rate of the subcooled nitrogen.

When the temperature of the stream exiting the heater equals the temperature of the gas going into the cold heat exchanger, using a heat balance, the electrical power consumed in the heater is equal to the refrigeration delivered to the nitrogen stream. Since the experimental setup involved manipulating the electrical power into the heater until the temperature, T_3 was equal to T_1, a reasonable time was allowed in each run to reach thermal equilibrium (30-45 minutes). At a fixed cryocooler operating condition, the refrigeration temperature, T_2, could be varied by altering the nitrogen flow rate at the rotameter. The resulting load-curves are shown in Figs. 3a and 3b.

Optimization of Performance

Maximizing performance in this particular cryocooler involves two different optimizations that are linked to each other by the cold heat exchanger. The first consideration is the thermoacoustic performance of the cryocooler. Secondary, but just as important is the heat transfer performance of the cold heat exchanger.

Obtaining optimum thermoacoustic performance involves a delicate balance between optimum regenerator phasing and reducing pulse tube streaming. It is often the case that optimum regenerator phasing results in adverse phasing conditions in the pulse tube and the resultant streaming losses decimate the refrigeration. Following the work of Swift & Gardner[2], a pulse tube cryo-

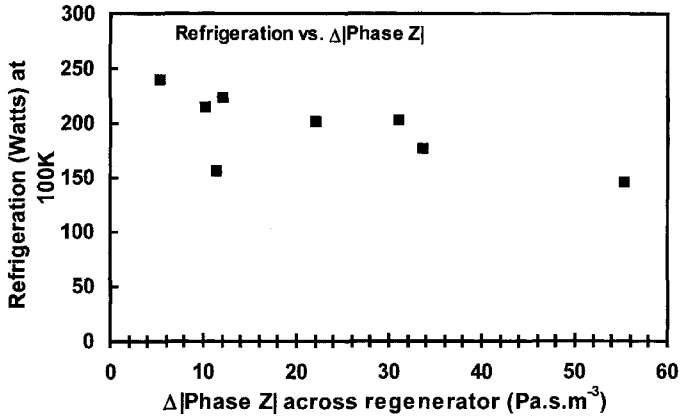

Figure 4. Variation in the regenerator heat pumping as a function of the phase angle, Phase(P-U) = Phase Z, across it.

cooler can mimic an efficient Stirling cryocooler when the oscillating velocity phase leads the oscillating pressure phase at the warm end of the regenerator and lags behind it at the cold end. It has been further established through experimental experience that maximum regenerator performance is obtained when the phase ($P_1 - U_1$) is equal in magnitude, but opposite in sign across the two ends of the regenerator. This observation is also noted in the work of Swift et al.[3] Provided sufficient phase flexibility in the inertance network (using a dual valve inertance) the phasing across the regenerator can be adjusted very close to the optimum. The existence of this optimum can be experimentally investigated by placing dynamic pressure transducers on both sides of the regenerator. Knowing the dimensions and operating conditions of the cryocooler (frequency, mean pressure, etc.) the phase (P_1-U_1), or Phase Z, where Z is the impedance, on both sides of the regenerator can be calculated. Additionally, a careful energy balance will yield the net heat pumping by the regenerator after accounting for streaming and conduction losses in the pulse tube. Figure 4 shows the results of such an experimental investigation. When the Phase Z is equal in magnitude but opposite in sign across the end of the regenerator, Δ|PhaseZ| across the regenerator will be zero. In this case the heat pumping by the regenerator will be maximized.

Work done on acoustic streaming in the pulse tube by Olson and Swift[4] suggests a similar phase optimum in the pulse tube. Indeed, merely optimizing the regenerator does not necessarily lead to maximum performance in the cryocooler. This is often due to adverse phasing conditions in the pulse tube that drive a second order flow from the cold end to the warm end (or vice versa). In general, one can employ a suitably tapered pulse tube to reduce streaming losses, however in this case commercial cost considerations favored a uniform diameter pulse tube. Careful sizing of the void volumes in the hardware and sufficient flexibility in the impedance of the inertance network during the hardware design process allowed a low cost, non-tapered pulse tube with a minimal streaming loss.

Stall Temperature

In order to carry out the stall/no-load temperature test a small silicon diode temperature sensor was placed inside the cold heat exchanger. The inlet and outlet arms were capped so that there was no cryogen flow. The cryogen side of the cold heat exchanger was filled with helium. Running the cryocooler in this manner quickly led to a steady state temperature of 62 K, as shown in Fig. 5.

Cold Heat Exchanger

The 'delivery of refrigeration' to the cryogen occurs as it flows through the cold heat exchanger. The original design of this heat exchanger was carried out using the work of Seume &

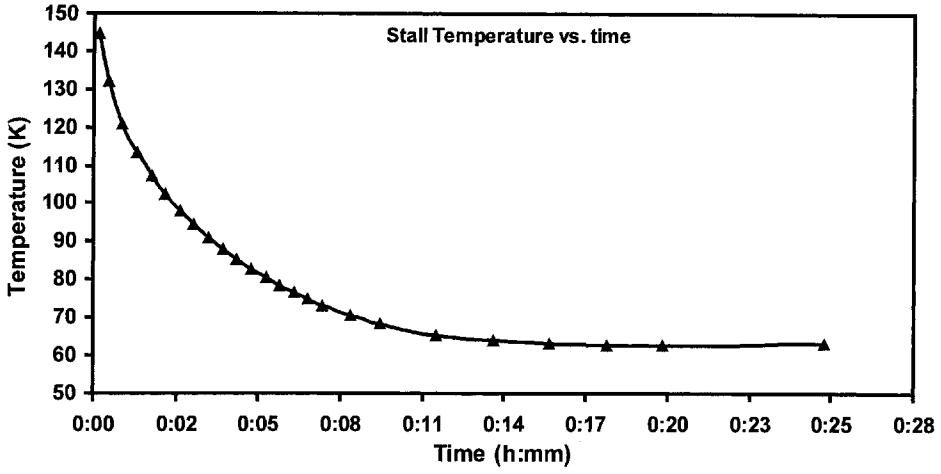

Figure 5. Temporal variation of temperature in the cold heat exchanger when there is no cryogen flow. The final steady state temperature of 62 K is the stall temperature.

Simon as a guide.[5,6] The resultant shell and tube heat exchanger had sufficient area for de-superheating a cryogen such as nitrogen down to its saturation temperature. However, for liquefaction and subcooling of the cryogen from ambient temperature, heat transfer limitations were seen. Therefore, the internal geometry of the heat exchanger was reconfigured to enhance the heat transfer on the shell side. Subsequent experiments suggested sufficient enhancement in the shell side heat transfer to produce subcooling in the cryogen (Fig. 3b).

PACKAGING

The cryocooler was packaged in a stainless steel 'all inclusive' cabinet with connections for cooling water, electric supply and cryogen flow. For better integration into a customer site, the cryocooler is also available as a bare, skidded unit without a vacuum jacket. Incremental, standard add-ons to the bare unit are the vacuum jacket, electrical controls panel, protective cabinet or enclosure, pressure and temperature monitoring instrumentation—including shutdowns for vibration and over-temperature protection.

With the benefit of the new, smaller inertance network, the standard package dimensions can be reduced significantly to an envelope volume of 20 x 30 x 60 inches. Additionally, for operation in countries with 60 Hz electrical supply, a variable frequency drive is not necessary and can be replaced with a suitably sized SCR (Silicon Controlled Rectifier) that is much smaller and lower cost.

CONCLUSION

Product engineering work on an electrically driven pulse tube cryocooler that produces over 200 W of refrigeration at 80 K has led to a commercial cryocooler product from Praxair Inc. The unit delivers refrigeration by de-superheating, liquefying and/or subcooling a cryogen such as nitrogen. Experimental tests using nitrogen as a cryogen have proven the refrigeration capability of the device. The electrical power consumed by the driver at full refrigeration load is 4.2 kW giving an overall efficiency of >13% of Carnot.

The unit has been engineered for long-term reliability and availability with a zero-maintenance philosophy. Considerable effort has gone into making the unit controllable, safe and durable for long term continuous or intermittent operation. The PWG used in the cryocooler is a dual opposed piston, moving magnet design from CFIC Inc. The pistons maintain a clearance seal and thus no lubricants are needed. There are, of course, no other moving or wearing parts.

The cryocooler can be configured with various standard options depending on customer requirements. The revised footprint of the unit allows it to fit through standard door frames. Additionally, a total weight of 300 lb allows the unit to be conveniently mounted at the 'point of use' of the refrigeration.

ACKNOWLEDGMENT

The author would like to thank Nancy Lynch (Praxair) and John Corey (CFIC) for collecting valuable parts of the experimental data. Product engineering work from Thurman Gordon and Robert Wingels (both Praxair) is gratefully acknowledged. Advice and guidance from Greg Swift (LANL) was invaluable in getting our laboratory precursor up and running.

NOMENCLATURE

P_1, first order pressure amplitude (Pa)
U_1, first order volumetric velocity amplitude (m^3/s)
Z, complex impedance ($Pa \cdot s \cdot m^{-3}$)

REFERENCES

1. Zia, J.H., "Design and Operation of a 4 kW Linear Motor Driven Pulse Tube Cryocooler," *CEC-ICMC 2003 Transactions*, in print (2004).
2. Swift, G.W., Gardner, D.L., "Use of Inertance in Orifice Pulse Tube Refrigerators," *Cryogenics*, vol. 37, (1997), pp. 117-121.
3. Swift, G.W., Gardner, D.L., Backhaus, S., "Acoustic Recovery of Lost Power in Pulse Tube Refrigerators," *J. Acoust. Soc. Am.*, vol. 105, (1999), pp. 711-724.
4. Olson, J.R., Swift, G.W., "Acoustic Streaming in Pulse Tube Refrigerators: Tapered Pulse Tubes," *Cryogenics*, vol. 37, (1997), pp. 769-776.
5. Seume, J.R, and Simon, T.W., "Oscillating flow in Stirling Engine Heat Exchangers," *21st Intersociety Energy Conversion Engineering Conference*, (1986), pp. 533-538.
6. Seume, J.R, and Simon, T.W., "A Survey of Oscillating flow in Stirling Engine Heat Exchangers," (1988) *NASA Contractor Report 182108*.

Large Scale Cryocooler Development for Superconducting Electric Power Applications (HTS-4)

N. Lynch

Praxair, Inc.
Tonawanda, NY 14150

ABSTRACT

The Department of Energy is sponsoring work at Praxair for HTS-4 to develop cryocooler hardware for high temperature superconducting electric power applications. The HTS-4 program goals specify an oil-free cryocooler capable of producing 1500 W at 72.5 K and 1050 W at 65 K, with a targeted 30% Carnot efficiency (minimum 25%). This highly reliable system's availability should be 99.9% (99.8% minimum) with a mean time to repair of 4 hours and a Mean Time Between Failures (MTBF) of 17,520 hours. The target system cost is $40 /watt of cooling at 65 K ($42K), and the maximum allowable cost is $60 /watt ($63K).

This paper discusses the technical approach to these ambitious goals. The design will be based on the successful 200 W pulse tube cryocooler built and demonstrated by our group. Program development areas include pressure wave generator improvements to increase efficiency and decrease weight and cost, as well as cold head development to increase efficiency and capacity.

INTRODUCTION

The Department of Energy (DOE) has selected Praxair, Inc. to develop advanced cryogenic refrigeration systems for High Temperature Superconducting power applications. Table 1 lists the goal and worst-case allowable values of key parameters as stated by the DOE for their cryocooler development program HTS-4 to support BSCCO or YBCO cable applications. The availability requirements noted in the table translate into a desired downtime of less than 9 hours per operating year, with a maximum down time of 17.5 hours per year. The MTBF requirements translates to a minimum of 2 years operation.

TARGET DEFINITION

The required Carnot efficiencies and refrigeration capacities of Table 1 translate into the electrical and acoustic power inputs summarized in Table 2. The rejection temperature, T_{hot}, was assumed to be 300 K. The numbers presented in Table 2 are extremely aggressive targets, as the Carnot efficiencies are much higher than those achieved in pulse tube cryocoolers to date. Our largest pulse tube cryocooler[1] produced 200 W refrigeration with 4200 W electrical input, corre-

Cryocoolers 13, edited by R. G. Ross, Jr.
Springer Science+Business Media, Inc., New York, 2004

Table 1. Target system parameters for HTS-4 cryocooler development program.

Range of Operation, K	65 – 80
Capacity at 72.5 K (Mid-point temperature), W	1500
Capacity at 65 K (Low end of temperature range), W	1050
Efficiency, % Carnot	
Goal	30
Min	25
Cryogenic System Availability	
Goal	99.9
Min	99.8
Mean Time to Repair, hours	4
Mean Time between Failures hours	17,520
Cost per cooling Watt at 65 K	
Goal	< $40
Max	$60
Cost	
Goal (< $40 / W at 65K)	$42 K
Max ($60 / W at 65K)	$63 K
Compressor / drive unit	Oil free
System Mass, kg	
Goal (< 0.5 kg / W at 65K)	525
Max (0.75 kg / W at 72.5K)	788

Table 2. Thermodynamic efficiency/power parameters for HTS-4 cryocooler.

Parameter	Goal Value		Worst-Case Allow.	
Refrigeration temperature, K	72.5	65	72.5	65
Capacity, W	1500	1050	1500	1050
% Carnot, electrical basis	30	30	25	25
(W electrical input) / (W refrigeration)	10.5	12.1	12.6	14.5
Electrical Input, kW	15.7	12.7	18.8	15.2
Acoustic power, kW (80% PWG efficiency)	12.6	10.1	15.1	12.1
% Carnot, acoustic basis	37.5	37.5	31.3	31.3

sponding to a Carnot efficiency of slightly more than 13%. These requirements are near those demonstrated by kinematic Stirling cryocoolers.

TECHNICAL APPROACH

The development will build upon the successful development of a 200 W cryocooler, and will include team members from Qdrive (CFIC) and Los Alamos National Laboratory (LANL). The driver will be a Qdrive's zero-oil resonant Pressure Wave Generator (PWG). The PWG is driven by dual-opposed, STAR™ linear motors mounted nose to nose in a common vessel at mean pressure. Both motors use clearance seal pistons on Qdrive's patented thin-flexure suspension.

To achieve HTS-4 performance, a three-phase project is proposed. It includes both cold head and PWG improvements to increase capacity and efficiency.

Phase 1 includes both coldhead development and PWG improvements. Coldhead development will focus on scaleup challenges as well as efficiency improvements. Design starting points include the 200 W cryocooler, as well as an existing, large-scale cold head developed by LANL for refrigeration at 130 K.[2,3] These two cold heads represent the largest pulse tube cryocoolers developed and built to date. The target refrigeration capacity for Phase 1 will be 1000 W, a five-fold scaleup of the current technology.

Figure 1. The 2x2 kW PWG before (left) and after (right) redesign to reduce size, weight and cost.

The new coldhead will be modular, allowing individual components to be easily changed. This will be crucial in extending beyond existing technology to increase capacity, and in particular, efficiency. The vacuum jacket housing will be constructed to accommodate components of varying diameters and lengths, enabling a large range of conditions and components to be tested. The coldhead will be fully instrumented, including dynamic pressure sensors and external thermocouples along the length and circumference of the pulse tube and regenerator to monitor any streaming processes. An inertance line with a bypass valve and line will be used to easily modify the phasing and the inertance network impedance. Primary issues in Phase I will be those associated with scaleup, in particular, streaming. Axial and circumferential temperature measurements will monitor streaming. Potential remedies include the tapered pulse tube, impedance network optimization, as well as basic design considerations to reduce the driving force for streaming cells to form.

The coldhead will be mounted on an existing, 2x10 kW Qdrive PWG. This PWG, one of the very first large PWGs developed by Qdrive, has demonstrated an electrical-to-acoustic conversion efficiency of ~ 72%.

In parallel with cold head development, Qdrive will develop an improved, second-generation large PWG. One development goal is to increase the PWG electrical-to-acoustic conversion efficiency from ~ 72% to 80% or higher. This will be accomplished with further refinements to the clearance seal and suspension systems. Additionally, improved drift control technology[4] will be extended to this larger range. Also, the entire PWG will be designed to reduce weight and manufacturing cost. This builds upon a redesign of the 2x2 kW PWGs, shown before and after in Figure 1, which significantly reduced the PWGs weight and cost.

The PWG Phase 1 development work will culminate in production and testing of a prototype PWG. This PWG will be the platform for Phase 2 development. Phase 1 work also includes programs targeted at other specific cryocooler components, including heat exchangers and PWG reliability.

Phase 2 will build upon the PWG and coldhead work in Phase 1 to further increase capacity and efficiency. The target capacity in this phase is a 1500 W cryocooler with a Carnot efficiency of 25% or greater. It will incorporate the improved PWG developed in Phase 1, and continue building upon the coldhead improvements demonstrated in Phase 1.

Phase 3 development will focus on meeting the cost, reliability and weight targets to complete the development of a fully commercial unit suitable for production and industrial use rather than a laboratory environment.

CONCLUSIONS

The DOE is sponsoring a cryocooler development program for High Temperature Superconductivity applications with aggressive cost and efficiency targets. Praxair, Inc. has been selected to lead a team, including Qdrive (CFIC) and Los Alamos National Laboratory to develop large, 1500 W at 72.5 K cryocoolers for use in superconducting cable applications. The program will be carried

out in three phases and include coldhead and pressure wave generator work. The design will be based on the successful 200 W pulse tube cryocooler built and demonstrated by our group. Program development areas include pressure wave generator improvements to increase efficiency and decrease weight and cost, as well as cold head development to increase efficiency and capacity.

REFERENCES

1. Zia, J. "A Commercial Pulse Tube Cryocooler with 200 W Refrigeration at 80 K," *Cryocoolers 13*, Kluwer Academic/Plenum Publishers, New York (2005).
2. Swift, G., *A Unifying Perspective for Some Engines and Refrigerators*, Acoustical Society of America (2002), p. 16-20.
3. Swift, G.W., Allen, M.S., Wollan, J.J., "Performance of a Tapered Pulse Tube," *Cryocoolers 10*, (1999), pp. 315-320.
4. Spoor, P., "Clearance-seal mass flux and equilibrium position shifts in solid and hollow free pistons," *Cryocoolers 13*, Kluwer Academic/Plenum Publishers, New York (2005).

The Effect of Mean Pressure on Large Pulse Tube Cryocoolers

Nancy Lynch

Praxair, Inc.
Tonawanda, NY 14150

ABSTRACT

We have been developing large scale, Stirling-type pulse tube cryocoolers. These cryocoolers are operated at or near 60 Hz and are directly powered by a dual-opposed linear motor pressure wave generator (PWG). The PWG is non-lubricated, requiring no oil removal from the helium working fluid. The PWG drives the unit directly, with no need for a rotating valve. The power input to the PWG and cryocooler can be scaled according to the refrigeration need, as opposed traditional refrigeration where capacity control is achieved by on-off operation.

These cryocoolers are hermetically sealed. As ambient conditions change, or cooling water temperature varies, the mean pressure in the cryocooler can vary over time. If the power input to the cryocooler changes, this will change the amount of heat produced by the motor and the motor temperature, which will also change the mean pressure.

Seemingly small changes in the mean pressure can affect cryocooler efficiency, capacity, and overall performance.

This paper presents simulation results showing how variation in the mean pressure impacts large cryocooler performance, in particular, the amount of refrigeration produced by the cryocooler. The paper also discusses various strategies for compensating for performance losses caused by mean pressure fluctuations.

INTRODUCTION

The mean pressure plays an important role in cryocooler design and optimization. Initially the designer must select the optimum cryocooler temperature while optimizing numerous other variables. While operating, the cryocooler may experience mean pressure fluctuations as a result of ambient temperature fluctuations or cryocooler input power level.

This paper addresses how to compensate for mean pressure changes that may occur during operation. We begin with a fixed geometry and design conditions and explore the effect of pressure on performance and identify what parameters can influence cryocooler performance when it is forced to operate away from its design pressure. All work presented here is based upon simulations done in SAGE. The cryocooler is based upon a nominal 60 Hz, oil free Pressure Wave Generator of the type provided by CFIC. The cryocooler is a single stage unit employing a stainless steel mesh regenerator and shell and tube heat exchangers. The impedance network employs a single inertance line of fixed length with an orifice to provide resistance.

Cryocoolers 13, edited by R. G. Ross, Jr.
Springer Science+Business Media, Inc., New York, 2004

Table 1. The impact of ambient temperature on mean operating pressure.

Condition	Temperature, F (C)	Mean Pressure, MPa
Cold Ambient Conditions	30 F (-1C)	2.4 MPa
Design Conditions	70 F (21C)	2.6 MPa
Hot Ambient Conditions	110 F (43C)	2.8 MPa

THE EFFECT OF MEAN PRESSURE ON CRYOCOOLER PERFORMANCE.

For a cryocooler design optimized for operation at 2.6 MPa and 60 Hz with a 70°F ambient temperature, Table 1 illustrates the mean pressure variations to be expected if the cryocooler is exposed to outdoor ambient temperatures from 30°F to 110°F. There may be other factors which might cause the operating pressure to deviate from the design pressure, such a slow loss of helium over time due to a small leak, or errors in pressurizing the cryocooler prior to operation.

Simulations were generated to determine the effect of mean pressure variation on cryocooler performance. Since changing the temperature at which heat is rejected will also impact cryocooler performance, the heat rejection temperature was not varied so that the impact of mean pressure could be studied directly. Further, the pressure wave generator was assumed to be operating at full capacity at the design point, meaning that it was simultaneously maintained at full stroke and current limitations. If the cryocooler were not operating at full capacity, it may be possible to simply increase power to the cryocooler to restore refrigeration capacity, admittedly at a lower efficiency. It was further assumed in this work that the vessel's maximum allowable working pressure was not exceeded as the mean pressure increased.

Figure 1 illustrates the effect of mean pressure variations on cryocooler performance under these conditions if no corrective action is taken. We see that the pressure fluctuation caused by ambient temperature variations are enough to cause a sizable performance degradation, up to 20% over the pressure range that may be experienced due to ambient variations, as measured by the predicted refrigeration capacity. In this plot, the cryocooler is assumed to be operating at full capacity, with both the current supplied to the PWG and stroke at their full allowed values. The effects of mean pressure changes impact the acoustic work delivered by the PWG to the cold head. If pressure is decreased at these conditions, the PWG will experience stroke limitations and the input power must be reduced to prevent the pistons from hitting each other or the back housing of the PWG. If the mean pressure increases, the stroke will decrease and work input fall, but the current cannot be further increased to restore full power to the cryocooler.

In an operating cryocooler, only a few parameters, namely the orifice diameter (provided a valve rather than a true orifice is employed) and frequency, can be easily manipulated. This cryocooler was assumed to have a single inertance line with no bypass line. Thus, additional simulations were generated that allowed either the orifice diameter or frequency to be adjusted for optimal performance.

Figure 2 compares the uncompensated cryocooler performance to that obtained by adjusting only the orifice diameter. We can see that there is only little to no improvement in cryocooler performance at off-design mean pressures.

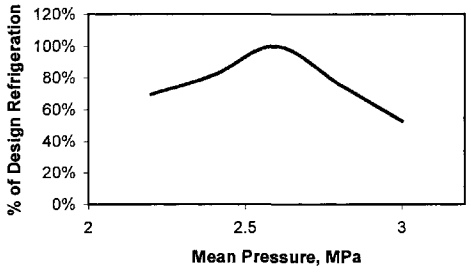

Figure 1. The impact of mean pressure fluctuation on cryocooler performance.

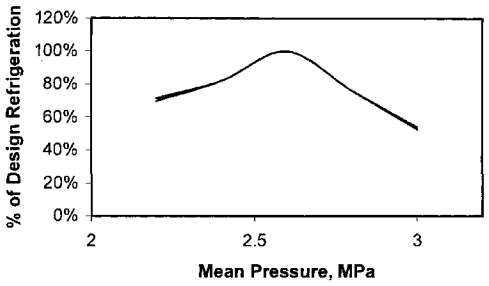

Figure 2. Use of the inertance valve to improve cryocooler performance when mean pressure fluctuations are present. The two lines are virtually indistinguishable, there is little improvement from orifice diameter optimization.

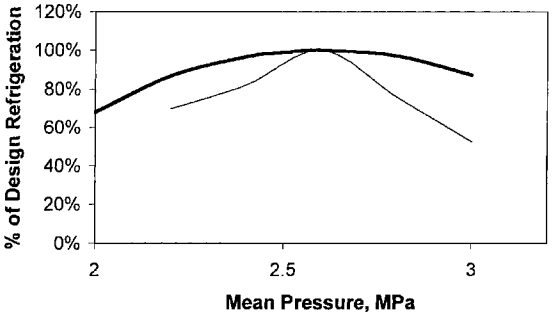

Figure 3. Effect of adjusting the drive frequency to improve cryocooler performance (maximize refrigeration) when mean pressure fluctuations are present. The thin curve is the original unoptimized performance, and the heavy curve is the performance with the drive frequency optimized for each pressure condition. There is significant improvement from frequency optimization.

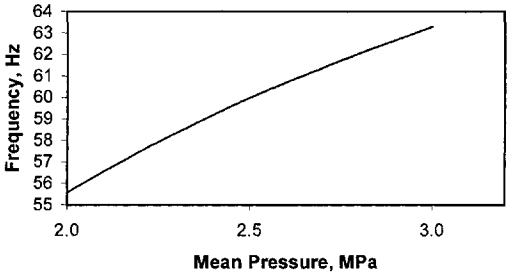

Figure 4. The optimum frequency as a function of mean pressure required to maximize cryocooler refrigeration when mean pressure fluctuations are present.

Figure 3 illustrates the cryocooler performance obtained by adjusting the frequency. We see that a significant improvement in predicted refrigeration can be obtained by optimizing the frequency to compensate for mean pressure fluctuations. By adjusting the frequency, the PWG can again operate closer to the full stroke and current limitations, increasing the work input to the cryocooler.

Figure 4 shows a plot of the optimized frequency versus the mean pressure with a fixed orifice diameter. At these points, the cryocooler is operating at or very near both full stroke and input current conditions. The area to the left and above of the line is an area where stroke limitations are encountered. In the area below and to the right of the line, current limitations are encountered. This line can be considered a "ridgeline" because both cryocooler input power and refrigeration capacity

fall as one moves away from this optimum line. Adjusting the frequency then, is a simple means of compensating for mean pressure fluctuations while the cryocooler is operating.

CONCLUSIONS

- Mean pressure fluctuations caused by ambient temperature variation can significantly impact the amount of refrigeration produced by a cryocooler operating at full capacity.
- Adjusting mean frequency is an effective way to counter the effects of mean pressure fluctuations.
- Adjusting the orifice diameter is not an effective way to counter the effects of mean pressure fluctuations.

Operation of Thermoacoustic Stirling Heat Engine Driven Large Multiple Pulse Tube Refrigerators

Bayram Arman, John Wollan, and Vince Kotsubo

Praxair, Inc.
Tonawanda, NY 14150

Scott Backhaus and Greg Swift

Los Alamos National Laboratory
Los Alamos, NM 87545

ABSTRACT

With support from Los Alamos National Laboratory, Praxair has been developing thermoacoustic Stirling heat engines and refrigerators for liquefaction of natural gas. The combination of thermoacoustic engines with pulse tube refrigerators is the only technology capable of producing significant cryogenic refrigeration with no moving parts. A prototype, powered by a natural-gas burner and with a projected natural-gas-liquefaction capacity of 500 gal/day, has been built and tested. The unit has liquefied 350 gal/day, with a projected production efficiency of 70% liquefaction and 30% combustion of an incoming gas stream. A larger system, intended to have a liquefaction capacity of 20,000 gal/day and an efficiency of 80 to 85% liquefaction, has undergone preliminary design.

In the 500 gal/day system, the combustion-powered thermoacoustic Stirling heat engine drives three pulse tube refrigerators to generate refrigeration at methane liquefaction temperatures. Each refrigerator was designed to produce over 2 kW of refrigeration. The orifice valves of the three refrigerators were adjusted to eliminate Rayleigh streaming in the pulse tubes. This paper describes the hardware, operating experience, and some recent test results.

INTRODUCTION

Praxair has been developing thermoacoustic liquefiers and refrigerators for liquefaction of natural gas and for other cryogenic applications. The liquefier development program is divided into two components: 1) pulse tube refrigerators driven by combustion-powered thermoacoustic Stirling heat engines (TASHEs), and 2) pulse tube refrigerators driven by linear motors. For the foreseeable future, the linear-motor-driven technology will be limited to low-power refrigeration and liquefaction applications.

Praxair's efforts to develop practical high-power combustion-driven thermoacoustic natural-gas liquefaction to eliminate the need for significant electric power in multi-kW cryogenic refrig-

Cryocoolers 13, edited by R. G. Ross, Jr.
Springer Science+Business Media, Inc., New York, 2004

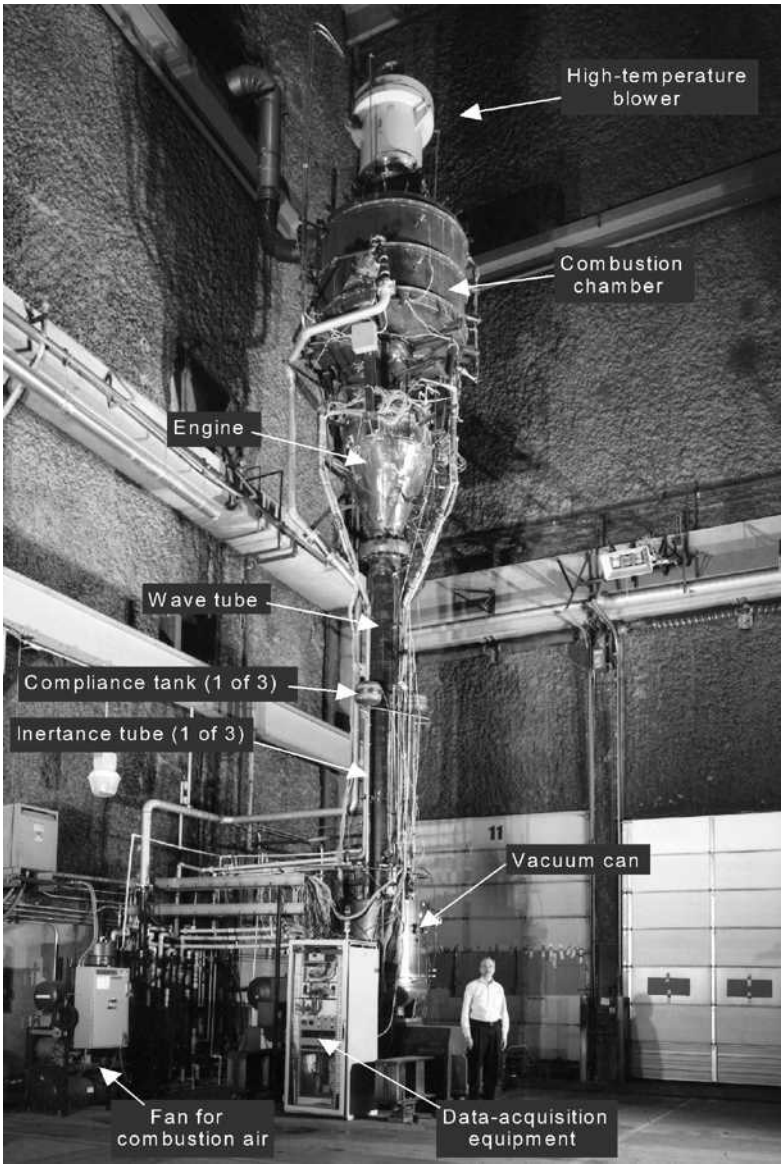

Figure 1. Photograph of 500-gal/day system in Denver, with project leader John Wollan.

eration began with its 2001 acquisition of the project from Chart, Inc. Chart's development effort was summarized by Wollan et al.[1] and Swift and Wollan.[2] After Praxair's acquisition of the project, extensive modifications were made to the acquired hardware: The refrigerators were kept intact, but the engine and burner were completely rebuilt, and a more sophisticated system for control and data acquisition was created.

The resulting system is shown in Figure 1, and a simple block diagram is shown in Figure 2. Heat from a high-temperature heat source (combustion of natural gas) provides useful energy to the system, heat is removed from a load (methane, experiencing cooling and liquefaction) at cryogenic temperatures, and waste heat is rejected to ambient temperature. Thermoacoustic processes in 30-bar helium gas accomplish the energy conversions and transport.

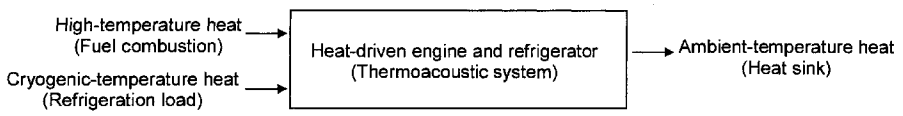

Figure 2. Simplest block diagram of the engine-driven refrigerator system. Heat is pumped from cryogenic temperature, high-temperature heat is consumed, and waste heat is rejected to ambient temperature, without any moving parts.

The major thermoacoustic subsystems are: (1) an engine to generate high-intensity acoustic power from high-temperature heat; (2) a wave tube (a nearly half-wavelength resonator) to transport the acoustic power from the engine to the refrigerators and to determine the 40-Hz operating frequency; and (3) refrigerators to generate useful cryogenic refrigeration while consuming the acoustic power. The engine is a thermoacoustic–Stirling hybrid heat engine.[3] The engine subsystem includes additional components to generate heat and transport it to the hot heat exchanger of the engine: a combustion chamber and a high-pressure, high-temperature, blower-driven[4] circulating-helium heat-transfer loop. The refrigerators are three inertance-enhanced orifice pulse tube refrigerators. A methane circulation loop provides the refrigeration load for the refrigerators. A cooling-water loop provides the ambient-temperature sink for the engine and the refrigerators.

This paper focuses on the pulse tube refrigerators and their performance. As shown schematically in Figure 3, the three refrigerators are driven in parallel by the acoustic power delivered by the wave tube. They are linked in series by the methane circulation loop, so that the first refrigerator precools the incoming methane to about 180 K, the second refrigerator cools the methane to liquefaction temperature and partially liquefies it, and the third refrigerator further liquefies the methane.

For thermal isolation, the three refrigerators are wrapped in a few cm of fine fiber insulation and enclosed in a single vacuum jacket pumped to about 10 microns. The three refrigerators are mounted on an annular 180° turning duct at the bottom of the wave tube. The refrigerators have similarities to the one that was used in the Cryenco-Los Alamos TADOPTR project,[5] with stainless-steel screen regenerators and tube-in-shell heat exchangers. A valve in series with each refrigerator's inertance enables phase adjustments. Initially, the inertance tubes were not water

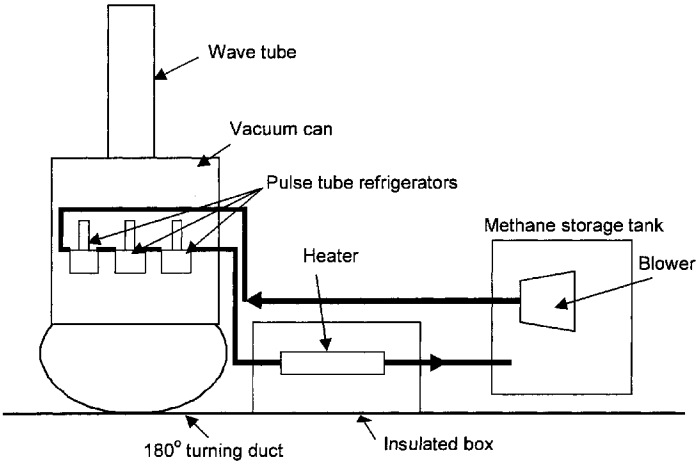

Figure 3. Pulse tube refrigerators and methane circulation loop.

cooled and they ran so hot that the reduced gas density in them provided insufficient inertance for efficient refrigerator operation. For the measurements reported here, the tubes were water-jacketed.

These three pulse tube refrigerators were designed to produce a total of 7 kW of refrigeration at methane liquefaction temperatures, so they are large, with regenerators of 20 cm diameter and pulse tubes of 10 cm diameter. All components are in line in each refrigerator, in the following sequence starting from the bottom: aftercooler, regenerator, cold heat exchanger, pulse tube, secondary ambient heat exchanger, orifice valve, inertance tube, compliance tank.

The third refrigerator is 3.4 cm lower than the second, to allow flow of condensed liquid methane from the second refrigerator's cold heat exchanger into the third refrigerator's cold heat exchanger via gravity without deep accumulation of liquid in the second refrigerator. The third refrigerator's cold heat exchanger has a liquid-level sensor.

The instrumentation on the refrigerators was kept to a minimum. Three pressure transducers[6] are located near the pressure node at the middle of the wave tube for measuring acoustic power[7] delivered to the lower half of the wave tube and the refrigerators. A fourth pressure transducer is mounted in the 180° turning duct, the common space at the entrance to the three refrigerator aftercoolers. Each refrigerator also has a pressure transducer in its compliance tank and at the top of its pulse tube, between the secondary ambient heat exchanger and the orifice valve.

Each pulse tube has three equally spaced thermocouples along its wall to indicate[8,9] pulse-tube streaming, which is discussed below. Several more thermocouples are mounted on the axial midpoints of the regenerators, on the inertance of the third refrigerator, and throughout the methane circulation loop.

Three separate cooling water streams are provided for the aftercoolers, the secondary ambient heat exchangers, and the water jackets around the inertance tubes. Flow meters are located in each of these three streams, to measure the total flow to the three aftercoolers, the three ambient heat exchangers, and the three water jackets, but the individual water flow rates are not measured.

A pressure-regulated, closed-loop methane circulating system provides the load on the refrigerators. This methane system, shown schematically in Figure 3, consists of a large storage tank, a circulating blower, a heater enclosed in an insulated box, and the associated drive and control electronics. The heater consists of three electric-resistance cartridges enclosed in tubes carrying the methane. The cooling power of the refrigerators is determined by measuring the electrical power required by this heater to vaporize the liquefied methane and reheat it back to the initial inlet-methane temperature. (The cooling power does not uniquely determine the liquefaction rate unless there is 100% liquefaction.) The methane pressure sets the cold-end temperature of the third refrigerator whenever there is a liquid-vapor interface in its cold heat exchanger.

EXPERIMENTS AND OVERALL PERFORMANCE

In a typical run, the burner is ignited to heat the hot heat exchanger of the engine to start the acoustic oscillations. During the engine startup, the refrigerator orifice valves are closed so there is negligible refrigeration, and the acoustic power produced by the engine is dissipated mostly in wave-tube losses. Once the desired acoustic amplitude is reached, the refrigerators' orifice valves are gradually opened to start refrigeration. Opening the orifice valves also increases the load on the engine, which causes a rise in the hot temperature of the engine and demands an increased fuel flow rate to the combustion system to maintain the desired acoustic amplitude. The engine operation is very stable and controllable. It typically takes two hours to go from one operating point to another and settle down to a sufficiently time-independent state that "steady-state" data can be acquired.

During attempts to reach performance goals, the highest system cooling power to date was 3800 W at 150 K, the temperature being determined by the methane pressure of 150 psia. This cooling power corresponds to 350 gal/day of liquefaction (though in fact the methane flow rate was greater than this, so the methane stream leaving the third refrigerator was less than 100%

liquid). Greater liquefaction rates and cooling powers have been prevented by a power handicap in the thermoacoustic engine, due to unforeseen inertance associated with end effects at some locations in the engine. These inertial effects can be avoided, or taken into account, in future hardware designs.

The power shortfall does not seriously affect the thermoacoustic efficiency. At the 350-gal/day operating point, a direct comparison of the refrigeration power to the rate at which fuel was fed to the burner yields an overall system efficiency of 45% liquefied, 55% burned. In other words, 45% of a pure methane stream arriving at the system would have been delivered as liquefied product, and 55% would have been burned, if pure methane instead of natural gas had been used as fuel for the burner. However, most of the combustion heat was lost up the flue and to heat leak from the combustion chamber, because no effort was made to minimize such losses in this hardware. A standard flue-gas recuperator and better combustion-chamber insulation, both needed for a commercially interesting system, would enable the delivery of 85% of the heat of combustion to the thermoacoustic engine. In this reasonably plausible imaginary situation, the efficiency at the 350 gal/day operating point would have been 70% liquefied, 30% burned.

SOME DETAILED PULSE TUBE REFRIGERATOR RESULTS

Experiments measuring the refrigeration power spanned many combinations of refrigerator orifice-valve openings, acoustic pressure amplitudes, and methane pressures. Although DeltaE[10] was used to design these refrigerators, the Sage program[11] was used to analyze and interpret the test results. (Whenever we have compared the results of these two codes, they have been similar.) Measured pressure amplitudes and phases, including the pressure differences across the regenerators, agreed reasonably well with the Sage models. Measured cooling powers were significantly below the Sage predictions.

In this paper, we present some details regarding streaming in the third refrigerator's pulse tube, while the orifice valves of the other two refrigerators were closed. A Sage inertance-network model was used to infer the volume flow rates from the measured pressures. In the Sage model, the oscillating mass flow at the entrance to the network and the valve opening were adjusted until the calculated pressure amplitudes matched the measured values in the compliance tank and at the top of the pulse tube. To establish confidence in this model, Figure 4 displays the good agreement between the measured and calculated differences between the pressure phases in the compliance tank and at the top of the pulse tube, as a function of the orifice-valve setting, for three different acoustic pressure amplitudes. In our notation, p_m is the mean pressure and $|p_1|$ is the amplitude of the fundamental component of the oscillating pressure.

With confidence established in the Sage model, it can be used to predict the phase difference between the pressure p_1 and volume flow rate U_1, which is a key parameter in the analysis of heat transport via Rayleigh streaming in pulse tubes by Olson and Swift.[12] According to their analysis, the streaming flow is minimized if the U_1–p_1 phase difference somewhere near the middle of the pulse tube is –50°, which corresponds in these refrigerators to a phase difference at the ambient end of the pulse tube ranging from –55° to –60°.

One obvious indication of minimum streaming is a linear pulse-tube temperature profile.[8,9] Using the three equally spaced thermocouples on the side of the pulse tube, a linear profile occurs when the normalized temperature, $1 - 2T_{mid}/T_{average}$, equals zero. In Figure 5, the normalized temperature is plotted versus the U_1–p_1 phase difference at the ambient end of the pulse tube. The temperature profiles become linear within about 10° of the expected phase difference, confirming that Olson and Swift's analysis is at least approximately applicable to these refrigerators.

Further confirmation of streaming suppression can be seen in the coefficient of performance (COP). The COP is the ratio of measured cooling power to modeled aftercooler input acoustic power, with the latter confirmed by measurements of the acoustic power[7] at the middle of the wave tube. The COP should be a maximum when streaming is minimized. Figure 6 displays the COP versus the U_1–p_1 phase difference, showing the maximum COP occurring at about the same phase difference as that yielding a linear pulse-tube temperature profile in Figure 5.

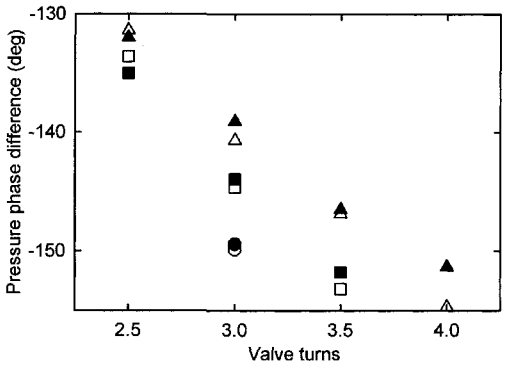

Figure 4. Compliance pressure phase minus pulse-tube pressure phase in the third refrigerator. Circles, $|p_1|/p_m$ = 3%, squares 5%, triangles 7%. Filled symbols represent experimental data, and open symbols represent Sage calculations.

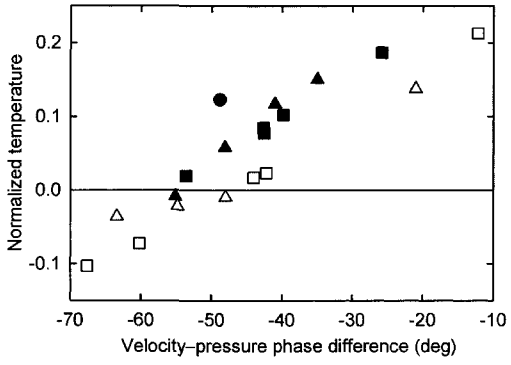

Figure 5. Normalized temperature vs. U_1–p_1 phase difference in the third refrigerator. Circle, $|p_1|/p_m$ = 3%, squares, $|p_1|/p_m$ = 5%, triangles 7%. The filled and open symbols represent data taken in different months. Filled symbols correspond to those of Figure 4.

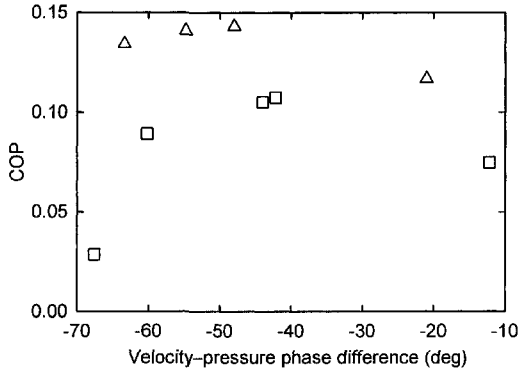

Figure 6. Coefficient of performance vs. U_1–p_1 phase difference for the data represented by open symbols in Figure 5.

CONCLUSIONS AND RECOMMENDATIONS

The multiple Stirling heat engine-driven pulse tube refrigerators run well and stably. Pressure amplitudes and phases, and regenerator pressure drops, agree reasonably well with computer models. A more extensive and comprehensive experimental study is needed for further improvement in the agreement between the predictions and experiments.

The inertance networks behave as expected. Water-cooling the inertance tube and orifice valve in pulse tube refrigerators of this size is essential to keep the gas density high enough to provide the expected inertance. Orifice valve adjustment easily allows minimization of pulse-tube streaming, as demonstrated by linear pulse-tube temperature profiles and maximization of the COP, at operating points close to those expected.

These analyses indicate that inertance models in programs like Sage[11] and DeltaE[10] are adequate for the turbulent flows in the inertances of large pulse tube refrigerators.

As with all large pulse tube refrigerators that have been manufactured and tested by our team, these three refrigerators do not perform as well as expected. At $|p_1|/p_m = 7\%$, the COPs are 30% below Sage's predictions.

Future experiments towards understanding regenerator internal streaming and other complex behavior are needed to improve understanding of such large pulse tube refrigerators. A vibration-balanced pair of CFIC's Q-Drive pressure wave generators[13] would be suitable for driving one of these three refrigerators.

The Los Alamos–Praxair team has made steady improvements in the thermoacoustic natural gas liquefaction system's efficiency:

- Coolahoop (NIST–Los Alamos)[14]
  10% liquefy, 90% burn (predicted from measured electrical heats)
- 140-gal/day TADOPTR (Los Alamos–Cryenco)[5]
  40% liquefy, 60% burn
- 500-gal/day TASHE-OPTR (the hardware described in this paper)
  70% liquefy, 30% burn (assuming a flue recuperator is used)
- 20,000-gal/day Cascade-OPTR[15] (current Los Alamos–Praxair preliminary design)
  80–85% liquefy, 15–20% burn

The planned 20,000 gal/day thermoacoustic liquefier technology should be able to compete with existing natural-gas liquefiers of comparable capacity, in terms of both efficiency and cost.

REFERENCES

1. Wollan, J.J., Swift, G.W., Backhaus, S.N., and Gardner, D.L., "Development of a Thermoacoustic Natural Gas Liquefier," *Proceedings of AIChE Meeting*, New Orleans LA, March 11-14 (2002). Also available at www.lanl.gov/thermoacoustics/Pubs/Wollan.pdf
2. Swift, G.W., and Wollan, J.J. "Thermoacoustics for liquefaction of natural gas," *GasTIPS*, vol. 8(4), (Fall 2002), pp. 21-26. Also available at www.lanl.gov/thermoacoustics/Pubs/GasTIPS.pdf
3. Backhaus, S.N., and Swift, G.W., "A Thermoacoustic-Stirling Heat Engine." *Nature*, vol. 399, (1999), pp. 335-338; "A thermoacoustic-Stirling heat engine: Detailed study," *Journal of the Acoustical Society of America*, vol. 107 (2000), pp. 3148-3166.
4. Piller Industrieventilatoren GmbH, Moringen, Germany, www.piller.de
5. Swift, G.W., Allen, M.S., and Wollan, J.J., "Performance of a tapered pulse tube," *Cryocoolers 10*, Kluwer Academic/Plenum Publishers, New York (1999), pp. 315-320.
6. Endevco, Inc., San Juan Capistrano CA, model 8510B-500.
7. Fusco, A.M., Ward, W.C., and Swift, G.W., "Two-sensor power measurements in lossy ducts," *Journal of the Acoustical Society of America,* vol. 91 (1992), pp. 2229-2235.

8. Duband, L., Charles, I., Ravex, A., Miquet, L., and Jewell, C., "Experimental results on inertance and permanent flow in pulse tube coolers," *Cryocoolers 10*, Kluwer Academic/Plenum Publishers, New York (1999), pp. 281-290.

9. Kotsubo, V., Huang, P., and Nast, T.C., "Observation of DC flows in a double inlet pulse tube," *Cryocoolers 10*, Kluwer Academic/Plenum Publishers, New York (1999), pp. 299-305.

10. Ward, W.C., and Swift, G.W., "Design Environment for Low Amplitude Thermoacoustic Engines (DeltaE)," *Journal of the Acoustical Society of America,* vol. 95 (1994), pp. 3671-3672. Software and user's guide available either from the Los Alamos thermoacoustics web site www.lanl.gov/thermoacoustics/ or from the Energy Science and Technology Software Center, US Department of Energy, Oak Ridge, Tennessee.

11. Gedeon, D., "A globally implicit Stirling cycle simulation," *Proceedings of the 21st Intersociety Energy Conversion Engineering Conference,* American Chemical Society (1986), pp. 550-554. Sage Version 3.0 software and user's guide available from Gedeon Associates, Athens, Ohio.

12. Olson, J.R., and Swift, G.W., "Acoustic streaming in pulse tube refrigerators: Tapered pulse tubes," *Cryogenics*, vol. 37, (1997), pp. 769–776; "Suppression of acoustic streaming in tapered pulse tubes," *Cryocoolers 10*, Kluwer Academic/Plenum Publishers, New York (1999), pp. 307-313.

13. CFIC, Inc., 302 Tenth St., Troy NY 12180, www.qdrive.com.

14. Radebaugh, R., McDermott, K.M., Swift, G.W., and Martin, R.A., "Development of a thermoacoustically driven orifice pulse tube refrigerator," *Proceedings of the Interagency Meeting on Cryocoolers*, October 24, 1990, Plymouth, Massachusetts, David Taylor Research Center publication 91/003, Bethesda MD 20084-5000, pp. 205-220.

15. Gardner, D.L., and Swift, G.W., "A cascade thermoacoustic engine," *Journal of the Acoustical Society of America,* vol. 114 (2003), pp. 1905-1919.

A Traveling Wave Thermoacoustic Refrigerator within Room Temperature Range

Yun Huang, Ercang Luo, Wei Dai, Zhanghua Wu

Technical Institute of Physics and Chemistry, CAS
Beijing, 100080, China

ABSTRACT

Thermoacoustic refrigerators use sound waves to generate cooling. Furthermore, they use inert gases that are friendly to the environment. Their unique working mechanism and promising future have attracted many researchers. This article focuses on the design of a traveling wave thermoacoustic refrigerator that works in the civil refrigeration range, since traveling wave refrigerators have higher efficiencies than standing wave refrigerators. According to linear thermoacoustic theory, two analytical methods, the lumped-element network and transfer matrixes, are discussed for analysis of the thermoacoustic systems. Several possible modes for achieving efficient thermoacoustic refrigeration are analyzed with the simplified lumped-element network method. Then, a feasible thermoacoustic refrigeration mode is chosen and optimized with the transfer matrix method. The goal is to achieve a relatively high cooling capacity at a temperature of 250 K. The calculation results show that, with helium, the refrigerator can have a cooling power of 80 W and achieve a COP of 2.86; this corresponds to a relative Carnot efficiency of 57%. According to this, we have constructed a refrigerator. It has achieved a no-load cooling temperature of 263 K when driven by a mechanical compressor with helium, and achieved a cooling power of 80 W at 274 K when driven by a standing wave thermoacoustic engine with nitrogen at the pressure ratio of 1.09.

INTRODUCTION

Thermoacoustic refrigerators have few moving parts, and they use inert gases that are friendly to the environment. Their unique working mechanism and promising future have attracted many researchers. Studies of thermoacoustic refrigerators have prospered in recent years. Most of them are concerned with pulse tube refrigerators driven by thermoacoustic engines, and standing-wave thermoacoustic refrigerators driven by thermoacoustic engines or loud-speakers.[1-4] Relatively less research has addressed traveling-wave thermoacoustic refrigerators.

This article focuses on the design of a traveling wave thermoacoustic refrigerator that works in the civil refrigeration range. In the first section, two analytical methods used in the design are introduced. In the second part, several possible modes are analyzed to find an efficient one with the lumped-element network method. In the third part, a traveling wave thermoacoustic refrigerator is designed using the transfer matrix method. Then, preliminary experiments with the refrigerator driven by both mechanical compressor and thermoacoustic engine are introduced.

Cryocoolers 13, edited by R. G. Ross, Jr.
Springer Science+Business Media, Inc., New York, 2004

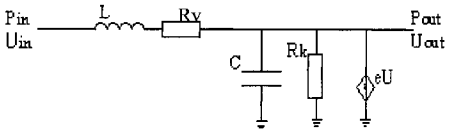

Figure 1. Lumped-element network.

ANALYTICAL METHODS

A traveling-wave thermoacoustic system is usually made up of a regenerator, compliance, inertance tube, thermal buffer tube (TBT), and heat exchangers. To have an efficient refrigerator, we need to understand the work mechanism of each part and assemble them together appropriately.

The wave equations and the energy-temperature equation are often coupled together to solve a problem. In our project, the temperature gradient in the system is small. So, without much error, the temperature distribution in the regenerator and in the thermal buffer tube can be assumed to be linear. Thus, only the wave equations are needed, and the lumped parameter network, or transmission matrix, of each component can be easily obtained.

Two simplified methods based on linear thermoacoustics: lumped element network [5] and transfer matrix,[6,7] are chosen for the design of the refrigerator.

Lumped Element Network

Acoustic systems are analogous to electrical circuits because of the similarities between the control equations for oscillating flow and those for electric circuits. This gives rise to lumped-element network theory. According to this theory, a channel, whose length is much smaller than the wave length, has the impedance features shown in Fig. 1.[5] In Fig. 1, the symbol L denotes the inertance of the gas in the channel, R_v viscous resistance, C the compliance of the gas in the channel, and R_k the thermal-relaxation resistance. The term eU represents a source or sink of volume flow, which arises only when the temperature gradient along the channel is nonzero. Different components have quite different properties in the thermoacoustic system, and they can be simplified according to the working circumstances. The regenerator, due to its geometrical characteristics and working conditions, is usually represented as a combination of a viscous resistance, a compliance, and a source of volume flow. Similarly, the compliance and inertance of the TBT, the compliance of the reservoir, and the inertance of the feed back tube are considered. In this way the thermoacoustic system can be expressed as a network.

Transfer Matrix

The transfer matrix method focuses on the input and output properties of the components. Given the input and transfer matrix, the output can be easily obtained. In some cases it is mathematically easier than the network method. The transfer matrix comes from the analytical solution of the system's control equations.

The following are transfer matrixes of the components based on linear thermoacoustic theory. Since the wave equations for the regenerator are very complex, we just quote the results achieved with the distributed lumped-element method by Swift.[8] For isothermal tubes, the transfer matrixes come from the analytical solution of the wave equations.

$$\textit{Regenerator}: \quad \begin{bmatrix} \tilde{p}_{out} \\ \tilde{u}_{out} \end{bmatrix} = \begin{bmatrix} 1+\dfrac{i\omega C_0 R_0}{2} g(\tau,b) & -\dfrac{\tau+1}{2} R_0 f(\tau,b) \\ -\dfrac{\tau \ln \tau}{\tau-1} i\omega C_0 & \tau \end{bmatrix} \begin{bmatrix} \tilde{p}_{in} \\ \tilde{u}_{in} \end{bmatrix} \tag{1}$$

$$\textit{Isothermal tubes}: \quad \begin{bmatrix} \tilde{p}_{out} \\ \tilde{u}_{out} \end{bmatrix} = \begin{bmatrix} \cos kx & \dfrac{-j\omega\rho_0}{A(1-f_\mu)} \dfrac{\sin kx}{k} \\ -\dfrac{A(1-f_\mu)}{j\omega\rho_0} k \sin kx & \cos kx \end{bmatrix} \begin{bmatrix} \tilde{p}_{in} \\ \tilde{u}_{in} \end{bmatrix} \tag{2}$$

Here k is the wave number, ρ the density, ω the angular frequency of the system, and τ the ratio of the refrigeration temperature and the room temperature. The terms f_k and f_μ are intrinsic functions of the sound wave channels.

The thermal buffer tube is located between the cold heat exchanger and the ambient heat exchanger. The TBT does have a temperature gradient, but its diameter is much larger than the thermal penetration depth, so f_{WT} (defined by the following non-dimensional complex factor in the continuity equation):

$$\frac{d\tilde{u}}{dx} = -\frac{1}{Z_C}\tilde{p} + f_{WT}\beta_0 \frac{dT_0}{dx}\tilde{u}$$

can be neglected. The compliance ($Z_C = \rho C_P / T_0\beta$) is the main embodiment of the temperature's effect on the gas. For an ideal gas, $T_0\beta$ is a constant. To simplify, the thermal buffer tube is distributed; this permits the transmission matrix for an isothermal duct to be used.

ANALYSIS OF POSSIBLE REFRIGERATION MODES

To obtain an efficient system, we have tried several types of modes. This section will give some analysis on three modes using the lumped-element network method. In a preliminary analysis of the system, the lumped element network has the advantage of simplicity and intuitiveness, though it is not an exact solution to the control equations.

Type One is shown in Fig. 2. Given the working conditions and the geometry of the components, we can generate the expressions for the volume flow rate in each component of the circuit. So we can have the expressions of the cooling power (Qc), the consumed energy (W), and the coefficient of performance (COP). The cooling power is assumed to be roughly equal to the acoustic work flowing out of the regenerator, and the consumed energy is the total energy supplied to the system. The expressions for these parameters are as follows:

$$Qc = 0.5\mathrm{Re}\left[P_R U_R^*\right] = \frac{1}{2}\frac{P^2\omega^2 LC}{R}\frac{1-\omega^2 LC}{\left(1-\omega^2 LC\right)^2 + \left(\omega L/\tau R\right)^2} \tag{3}$$

$$W = 0.5\mathrm{Re}\left[P(U_L - U_R)^*\right] = \frac{1}{2}\frac{P^2\omega^2 LC}{R}\frac{\left(1/\tau - 1 + \omega^2 LC\right)}{\left(1-\omega^2 LC\right)^2 + \left(\omega L/\tau R\right)^2} \tag{4}$$

$$COP = \frac{Qc}{W} = \frac{1-\omega^2 LC}{1/\tau - 1 + \omega^2 LC} = \frac{1-\omega^2 LC}{(T_0 - T_C)/T_C + \omega^2 LC} \tag{5}$$

To have cooling power means $Qc > 0$. So it is necessary to have $1 > \omega^2 LC > 0$. In addition, Eq. (3) and Eq. (5) show that the more $\omega^2 LC$ approaches zero, the more COP approaches the Carnot COP, but at the same time the more Qc approaches zero.

Type Two is shown in Fig. 3. The difference between Type One and Type Two lies in the location of the regenerator and the thermal buffer. The cooling power can be expressed as Eq. 6. The right side of Eq. 6 is obviously < 0, because the empty duct has positive inertance or compliance. That means it is impossible for the system to function as a refrigerator.

$$Qc = 0.5\mathrm{Re}\left[P_R U_c^*\right] = \frac{1}{2}\frac{(-\tau)P^2\omega^2 LC}{R\left[\left(1-\omega^2 LC\right)^2 + \left(\omega L/\tau R\right)^2\right]} \tag{6}$$

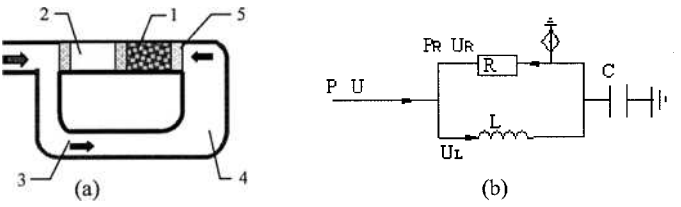

Figure 2. (a) Scale drawing of Type One; (b) Crude impedance diagram for Type One.
(1 regenerator, 2 thermal buffer, 3 inertance duct, 4 reservoir, 5 heat-exchanger, 6 mass (piston), 7 springs)

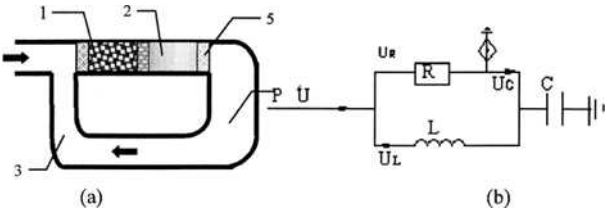

Figure 3. (a) Scale drawing of Type Two; (b) Crude impedance diagram for Type Two.

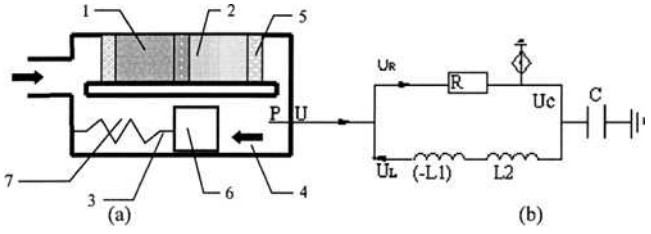

Figure 4. (a) Scale drawing of Type Three; (b) Crude impedance diagram for Type Three.
(1 regenerator, 2 thermal buffer, 3 inertance duct, 4 reservoir, 5 heat-exchanger, 6 mass (piston), 7 springs)

Type Three is shown in Fig. 4. Type Two has an empty inertance duct, while in Type Three there are a spring and piston in it. The spring functions like a negative inertance, which can be expressed as $-L_1 = -k/A^2\omega^2$, where k is the spring constant, and A is the cross sectional area of the piston or duct. The piston functions like a positive inertance $L_2 = M/A$, where M is the mass of the piston. So, the total inertance of the system is $L = (-L_1) + L_2$. According to Eq. (7), when the total inertance is negative, the cooling power is positive, so the system can work as a refrigerator. Similarly when $\omega^2 LC$ approaches zero, the COP approaches the Carnot COP, but the Qc approaches zero also. This system is, in essence, a free-piston Stirling refrigerator.

$$Qc = 0.5\mathrm{Re}\left[P_k U_c^*\right] = \frac{1}{2}\frac{(-\tau)P^2\omega^2(-L_1+L_2)C)}{R\left[\left(1-\omega^2 LC\right)^2 + \left(\omega L/\tau R\right)^2\right]} \tag{7}$$

$$W = 0.5\mathrm{Re}\left[P(U_R - U_L)^*\right] = \frac{1}{2}\frac{P^2\omega^2(L_2-L_1)C}{R}\frac{\left[\tau - 1 + \omega^2(L_2-L_1)C\right]}{\left[1-\omega^2(L_2-L_1)C\right]^2 + \left(\omega(L_2-L_1)/\tau R\right)^2} \tag{8}$$

$$COP = \frac{Qc}{W} = \frac{1}{1/\tau - 1 - \omega^2 LC/\tau} = \frac{1}{(T_0 - T_C)/T_C - \omega^2 LC/\tau} \tag{9}$$

DESIGN AND PRELIMINARY TESTS OF THE REFRIGERATOR

The goal of the study was to design a traveling-wave thermoacoustic refrigerator whose cooling power is about 100 W at 250 K. Since the Type One system maintains the advantage of no moving parts, it was chosen. Mainly, the transfer matrix method was used in the design. In the approximate analysis above, no loss except the loss caused by the flow resistance of the regenerator is considered. However, here, the loss caused by the dynamic heat conduction is also considered. The cooling power is the difference between the total power of the inlet and the outlet of the cold heat exchanger. The time averaged total power of one cross section is expressed as: [6]

$$E_x = W_x + Q_x = \frac{1}{2}\mathrm{Re}\left[\tilde{U}\tilde{P}^*\left(1 - T_0\beta_0 f_{qx}\right)\right] - AK_0\frac{dT_0}{dx} \tag{10}$$

In the design, the average pressure, the amplitude of the pressure oscillation, the oscillation frequency, and the working gas are supposed to be known. The geometry of the components is

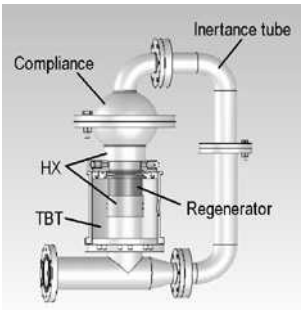

Figure 5. An assembly sketch of the refrigerator.

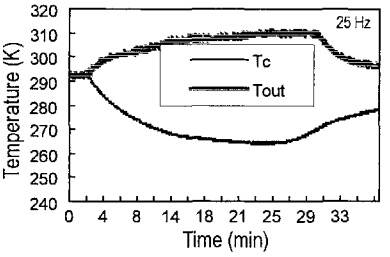

Figure 6. Tc is the cold end temperature and Tout is the temperature of the outlet of the compressor.

optimized to get enough cooling power with a relatively high COP. Calculations yielded a geometry that could achieve a cooling power of 80 W at 250 K, with a COP of 2.86, a Carnot efficiency of 0.57, and with helium at 2.0 MPa. To verify the design, the author also compared the results with the 'Thermoacoustic Simulator' in our Lab.[9] The difference is no more than 20%. Finally, the geometry of the refrigerator was fixed as shown in Fig. 5. The diameter of the inertance tube is 32 mm, and the diameter of the regenerator and TBT is 50 mm. The regenerator is made up of stainless screens. The cold and warm heat exchangers were cut using Electrical Discharge Machining (EDM). The warm heat exchanger is removable, while the cold heat exchanger is welded to the thermal buffer tube and the housing of the regenerator. The total height and width of the refrigerator are about 360 mm and 250 mm, respectively.

When the refrigerator was finished, the thermoacoustic engine was still under construction, so we reformed a conventional crankshaft compressor to supply the needed pressure waves. The reconstruction mainly consisted of three tasks: the removal of the valves, the alteration of the gas flow ways, and the separation of the lubricant oil. The swept volume of the mechanical compressor is about 80 cc, and the pressure oscillation is about 3.8% of the average pressure. The compressor can work at different frequencies with a frequency modulator. With this driver, the refrigerator achieved the lowest unloaded cooling temperature of 264 K with 2.0 MPa Helium. The pressure ratio was 1.08. Figure 6 shows the temperatures of the cold end and at the outlet of the compressor. The temperature at the outlet of the compressor reached 312 K because there is only an electric fan to cool it. After several experiments, the cold end could no longer cooled down. We supposed that some lubricant oil had entered the refrigerator, and disassembly showed oil had indeed accumulated in the regenerator. It greatly deteriorated the performance of the refrigerator. By now we have found a method to separate the oil completely. Further experiments will be done soon.

After the standing-wave thermoacoustic engine was finished, we coupled the refrigerator and the engine together. Details of the engine can be found in another paper.[10] Due to some abnormal phenomena with helium as the working gas, we initially used nitrogen. A cooling power of 80 W was achieved at 274 K when the average pressure was 3.1 MPa, and the amplitude was 1.39 bar. The frequency of the system was about 34 Hz despite of the varied pressures. Figure 7 shows the relationship between cooling temperature and cooling power. Figure 8 shows that when the cooling power changed, the amplitude of the pressure wave changed. During the experiments we found that Gendon streaming had a great impact on the refrigerator, and that suppression of the streaming can greatly improve the performance of the refrigerator. In the experiments we also found the inlet of the refrigerator and the connection of the TBT and inertance tube can be as cool as the cold end heat-exchanger. This may be caused by axial heat transfer, turbulence in the TBT, or something unknown. We will discuss this in detail in a future paper.

CONCLUSIONS

Two analytical methods in thermoacoustics have been used in the design. The lumped-element network is intuitive, but not accurate. In this article, it is used for preliminary analysis to select an

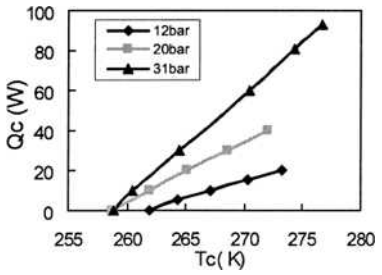

Figure 7. Measured thermal load versus temperature at the cold end under different average pressures.

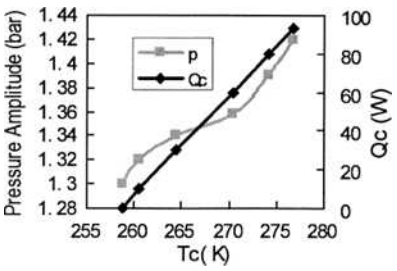

Figure 8. Measured thermal load at the cold end and the pressure amplitude at the inlet of the refrigerator at an average pressure of 31 bar.

initial configuration. The transfer matrix method is equivalent to solution of the control equations, and it was used for the design and optimization of the traveling-wave thermoacoustic refrigerator. Calculations show that, with helium, the refrigerator can achieve a cooling power of 80 W at 250 K with a COP of 2.86, which corresponds to 57% of Carnot efficiency.

Preliminary tests have been completed on the refrigerator. It achieved a cooling temperature of 263 K when driven by a mechanical compressor with helium at a pressure ratio of 1.08, and a cooling power of 80 W at 274 K when driven by a standing wave thermoacoustic engine with nitrogen at a pressure ratio of 1.09.

Up to now, the refrigerator works rather far from the design point due to limitations on the compressor side. If these limitations are eliminated, we believe that the system could perform much better. Besides, experiments will also be conducted to identify and suppress the various loss mechanisms to improve the performance further.

ACKNOWLEDGMENTS

This work is supported by the Chinese Academy of Sciences with project number: KJCX2-SW-W08.

REFERENCES

1. T.Jin, G.B. Chen et al, "A thermoacoustically driven pulse tube refrigerator capable of working below 120 K," *Cryogenics*, 41 (2001), 595-601
2. M.E.H. Tijani, et al., "Design of thermoacoustic refrigerators," *Cryogenics*, 42 (2002), pp. 49-57.
3. G. Swift, J. Wollan, "Thermoacoustics for Liquefaction of Natural Gas," *Gas TIPS*, Fall (2002), pp. 21-26.
4. S. Garrett, *Cool sounds–Environmentally friendly acoustic refrigerator for ice cream cabinets*, http://www.light-science.com/cosound.html
5. Greg Swift, *Thermoacoustics: A unifying perspective for some engines and refrigerators*, Acoustical Society of America (2002).
6. Xiao J. H, *Thermoacoustic effects and thermoacoustic theory for regenerative cryocoolers (heat engines)*, PhD Dissertation, Institute of Physics, CAS (1990).
7. E.C. Luo, "A simplified linearized thermoacoustic theory for Regenerative Cryocoolers," *Adv. in Cryogenic Engineering*, Vol. 45A, Kluwer Academic/Plenum Publishers, New York (2000), pp. 419-426.
8. S. Backhaus, G.W. Swift, "A thermoacoustic Stirling heat engine—Detailed study," *J. Acoust. Soc. Am*, 107, 6 (2000), pp. 3148-3166.
9. E. Luo, J. Wu and J. Yang, et al., "Thermoacoustic simulation for regenerative machines," *Adv. in Cryogenic Engineering*, Vol. 47A, Amer. Institute of Physics, Melville, NY (2002), pp. 828-83.
10. W. Dai, E.C. Luo et al., "Building a High-efficiency and Compact-sized Thermoacoustically-driven Pulse Tube Cooler," *Cryocoolers 13*, Kluwer Academic/Plenum Publishers, New York (2005).

Building a High-Efficiency and Compact-Sized Thermoacoustically-Driven Pulse Tube Cooler

W.Dai, E.C.Luo, Y.Zhou, J.F.Wu, W.X.Zhu

Technical Institute of Physics and Chemistry
Chinese Academy of Sciences
Beijing, China 100080

ABSTRACT

Thermoacoustic systems have attracted lots of attention in recent years due to their structural simplicity, high reliability, and potential for very high efficiency. There has been extensive research on standing wave and traveling wave systems, including both compressors and refrigerators. This article introduces our efforts towards building a high-efficiency and compact-sized thermoacoustically driven pulse tube cooler for temperatures below 80 K. Firstly, we have improved the heat exchangers in the thermoacoustic systems. By using Electrical Discharge Machining (EDM) cut heat exchangers, pressure ratios of 1.15/Helium and 1.22/Nitrogen have been obtained on a 1/4 wavelength standing wave system. Coupling the thermoacoustic compressor with a miniature pulse tube cooler has led to a lowest no-load temperature of 105.4 K. To reduce the size of the systems, we plan to use spring-mass resonators. The design and manufacture of two types of spring-mass resonators has just been completed, and tests will be done soon.

INTRODUCTION

Self-oscillating thermoacoustic compressor technology uses heat to generate pressure oscillations without any moving parts; this has attracted lots of research attention in recent years. The invention of traveling-wave type[1] and cascade type[2] systems has further boosted the passion for this kind of engine.

Besides the proper acoustic field design, heat exchangers are a particularly important part of thermoacoustic systems. Lowering the heat transfer temperature difference will effectively reduce the generation of irreversible entropy, thus improving the general efficiency. So, the first part of this article introduces our heat exchanger design and related experiments carried out on an ordinary standing wave thermoacoustic compressor outfitted with these new heat exchangers.

Combining the thermoacoustic compressor with a pulse tube cooler can lead to a cooler with no moving parts at all. So, the second part of the article introduces some experimental results obtained by coupling a miniature pulse tube cooler with our thermoacoustic compressor. The size incompatibility of the above combination presents a problem that limits this application of thermoacoustic compressors. Using a spring-mass resonator could lead to a smaller system size with suitable operating frequency for small-scale applications such as cryocoolers.[3] At this time, we have

Cryocoolers 13, edited by R. G. Ross, Jr.
Springer Science+Business Media, Inc., New York, 2004

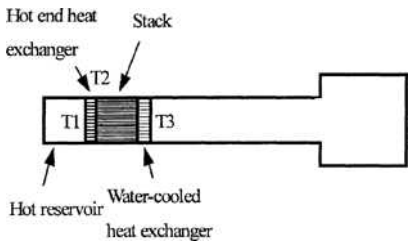

Figure 1. Illustration of standing-wave thermoacoustic compressor.

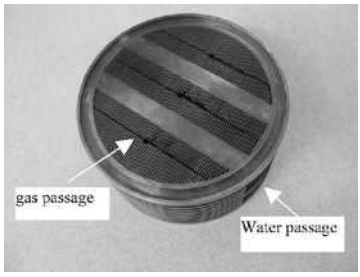

Figure 2. Photo of EDM-cut water-cooled heat exchanger.

just finished designing and manufacturing two different types of resonators; these are introduced in the last part of the article. Finally, conclusions are drawn with some discussion.

EXPERIMENT DETAILS

Standing Wave Thermoacoustic Compressor with New Heat Exchangers

As a first step toward achieving our target, a standing wave thermoacoustic compressor was built. The basic structure is shown as in Fig. 1. Most of the parts have an inner diameter of around 80 mm, while the resonance tube has an inner diameter of 50 mm. The stack is made from stainless steel mesh. Specifically, EDM technology was used in manufacturing the heat exchangers for both the hot-end heat exchanger and the water-cooled heat exchanger. Figure 2 shows a photo of a representative water-cooled heat exchanger. The side grooves and holes are for water to flow through. The gas passage consists of many narrow channels surrounded by copper fins formed by the EDM process. This design ensures heat exchanger integrity without any soldering work. The hot-end heat exchanger uses a similar design. To monitor the performance of this design, three sheathed K-type thermocouples have been placed at the hot-end heat exchanger exit, inside the hot-end heat exchanger block, and in the water-cooled heat exchanger exit. The experiments show that these heat exchangers perform quite well as seen in Fig. 3. Generally, when using helium as the working gas, the temperature difference between the gas and the copper block could be kept around 10 K, even with a heating power of 1.8 kW. Meanwhile, the gas temperature at the exit of the water-cooled heat exchanger could be kept around 15°C above the water temperature.

Table 1 gives some experimental results for our thermoacoustic system. During the experiments, frequency-jump behavior sometimes occurred. Table 2 gives a record of this behavior, which is primarily influenced by the hot reservoir volume, the resonance tube length, and the average pressure. All of these may be generalized as two important factors: relative position of the stack

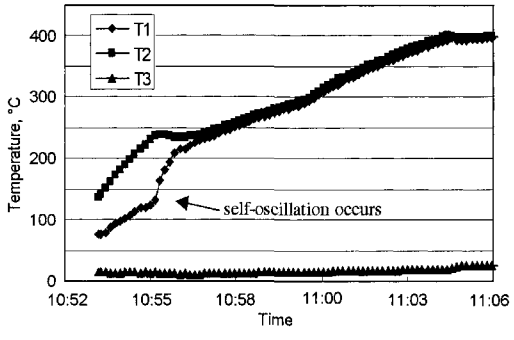

Figure 3. Temperature history of the three thermocouples shown in Fig 1.

Table 1. Typical experimental data on standing wave thermoacoustic compressor.

Gas Kind	Average Pressure	Resonator Tube	MeshNo.	Heater Power	Hot Temp	Frequency	Pressure Ratio
N_2	10bar	1.9m	20#	1.65kW	588℃	45.8Hz	1.22
He	35bar	3.5m	15#	2kW	553℃	82.7Hz	1.15
CO_2	10bar	2.1m	20#	2kW	506℃	30Hz	1.22

Table 2. Frequency jump behavior with 20# mesh.

Hot Reservoir Volume(cc)	Resonance Tube length(m)	Working Gas	Average Pressure(bar)	Jump behavior record
754	4	Helium	25.0	Start at fundamental frequency mode (≈ 72Hz), jump to ≈ 168Hz at 420℃
1274	4	Helium	25.0	Start at fundamental frequency mode (72.8Hz), no frequency jump happens
754	5	Helium	19.8	Start directly at high frequency mode (144Hz)
1274	5	Helium	25.5	Start at fundamental frequency mode (62Hz), jump to 135Hz at 400℃
1274	5	Helium	31.7	Start at fundamental frequency mode (64Hz), no frequency jump happens

and the ratio between the thermal penetration depth and the hydraulic diameter of the stack. However, more careful and systematic study is needed to uncover the quantitative rules that determine this bifurcation behavior.

Coupling Miniature Pulse Tube Cooler with the Thermoacoustic Compressor

For some preliminary tests, a coaxial double-inlet pulse tube cooler was coupled with the thermoacoustic compressor. The cooler was provided by the PTR group in our institute. The regenerator has an outside diameter of 10 mm and a length of about 50 mm. It should be mentioned here that the cooler was originally designed for a frequency around 50 Hz and a pressure ratio over 1.2. Figure 4 shows a photo of the main parts of the experimental setup. Figure 5 gives the cool-down curve of the pulse tube cold end when driven by the thermoacoustic compressor with a pressure ratio of 1.15 and a frequency of 82.7 Hz. The lowest no-load temperature is 105.4 K.

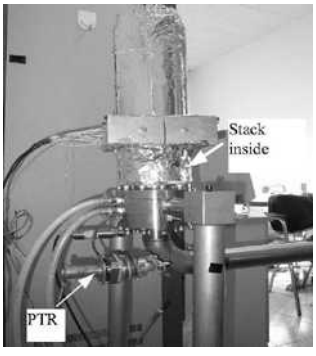

Figure 4. Photo of pulse tube cooler coupled with the thermoacoustic compressor.

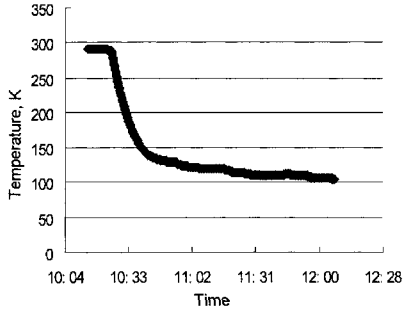

Figure 5. Cool-down curve of pulse tube cold end with charge pressure 32.6 bar, frequency 82.7 Hz.

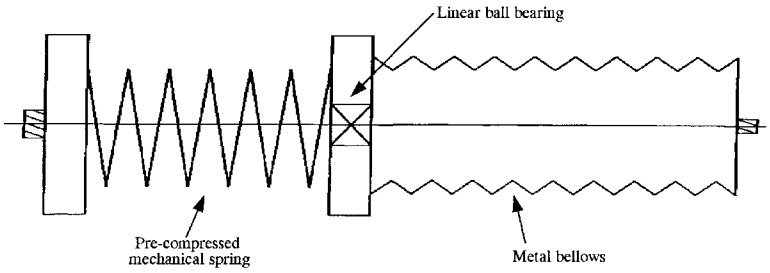

Figure 6. Basic structure of metal-bellows resonator.

We believe that when properly designed for working with thermoacoustic compressors, the pulse tube cooler should reach liquid nitrogen temperatures near 80 K.

Flexure Bearing Supported Piston and Bellows Subsystem

There is a size incompatibility in the above combination of pulse tube cooler with thermoacoustic compressor due to the requirement for a long resonance tube to control the oscillating frequency (see Fig. 4); this can present an obstacle to applying thermoacoustic compressors to small-scale cryocoolers. To remove this long resonance tube, spring-mass resonators can be used to control the resonant frequency by adjusting the mass or spring constant.

One way to realize this type of resonator is to use a flexure-bearing supported piston with clearance seal, which has been confirmed in Ref. 3. Another way, proposed in Ref. 4, is by using a metal bellows. The technology used in the first idea directly comes from the linear compressor structure. For this reason, it will not be addressed in detail. Our present focus is on using a metal bellows to realize the resonator structure, as this has the advantage of allowing a larger swept length.

Figure 6 illustrates the basic structure of the design. The bellows itself serves as both a spring and separator of the gas on the two sides. The bellows right surface is screw-fixed and sealed, while the other end is confined by a mechanical spring and supported by linear ball bearings that provide a low friction factor. Due to the space-separation nature of the metal bellows, the ball bearing can even be oil-lubricated. The mechanical spring on the left side is pre-compressed to make sure that the metal bellows remains in a compressed state, as the bellows can only endure an oscillating compression force with long lifetime. Additional mass can be screw-fixed on the axis to adjust the resonant frequency as required. Initial tests of this spring-mass subsystem show rather good resonating behavior. The next step will be to substitute the spring-mass resonator for the resonance tube generally used in thermoacoustic compressors.

CONCLUSIONS

We have built a 1/4-wavelength standing wave thermoacoustic compressor. It has performed quite well, which validates the heat exchanger design using EDM technology. At this time, the maximum pressure ratio we have obtained with helium is 1.15. Coupling it with a miniature pulse tube cooler has led to a lowest no-load temperature of 105.4 K. Future work will be done to integrate the spring-mass type resonator into the thermoacoustic compressor to reduce the system size. To obtain temperatures below 80 K, we are also designing a miniature pulse tube cooler working with a small pressure amplitude (<1.2) and relatively high frequency (70-80 Hz). We hope to finally realize a high-efficiency compact-sized thermoacoustically driven pulse tube cooler within this year.

ACKNOWLEDGMENT

This work is supported by Chinese Academy of Sciences with project number: KJCX2-SW-W08.

REFERENCES

1. Backhaus S. and Swift G.W., "A Thermoacoustic-Stirling Heat Engine," *Nature*, 399 (1999), pp. 335-338.
2. Gardner D.L. and Swift G.W., "A Cascade Thermoacoustic Engine," *J. Acoust. Soc. Am.*, 114 (4) (2003), pp. 1905-1919.
3. Matsubara Y., Dai W., Onishi T., Kushino A. and Sugita H., "Thermally actuated pressure wave generators for pulse tube cooler," *Proc.of ICCR 2003*, p.57.
4. Luo E., Liu H. and Wu J., "A new thermoacoustic engine with its resonant frequency freely controlled by metallic-bellow unit," *Adv. in Cryogenic Engineering*, Vol. 47A, Amer. Institute of Physics, Melville, NY (2002), p. 822.

Development of a Linear Compressor for Use in G-M Cryocoolers

John A. Corey, Erick L. James
CFIC-Qdrive, Troy, NY 12180

Ali Kashani, Ben Helvensteijn
Atlas Scientific, San Jose, CA 95120

Gregory L. Rhoads
Air Force Research Lab/PRPG, Wright-Patterson AFB OH 45433

ABSTRACT

A new compressor for Gifford-McMahon (G-M) cryocooler service has been designed and built using twin Clever Fellows Innovation Consortium (CFIC) STAR linear motors and special friction-free reed valves compatible with oil-free service. This fully-balanced arrangement eliminates all oil and other condensibles in the helium, as well as providing attitude independence and in-use mobility prohibited by conventional G-M compressors. Secondary oil management components and their failure modes are also eliminated. The design operating point matches pressures and flow for a Sumitomo 408 coldhead. Standard Qdrive 5 kW motors are used, giving significant capacity margin over the baseline compressor's 6 kW rating. Test results to date have demonstrated design-point flow and pressures, with significantly lower input power than the baseline compressor. The design is reviewed and test results are presented in this paper.

INTRODUCTION

The growing use of mid-size cryocoolers outside the laboratory environment has introduced some new and more stringent demands on their operation. The workhorse product, a Gifford-McMahon device that uses converted refrigeration compressors with oil-filled mechanisms, typically requires stationary, level placement during operation to avoid oil carryover into the cold regions where it congeals and impairs operation. Even in rated conditions, such coolers typically require regular service. Recently, large-scale acoustic Stirling coolers (sometimes misnamed 'pulse tube coolers') have been developed, with capacities of hundreds of watts, from oil-free linear-motor sources of many kilowatts. These are comparatively insensitive to orientation or even external vibration and shock loads during operation, but are not able to deliver cooling at temperatures below about 50K. The U.S. Air Force requires a mobile cryocooler, with cooling at temperatures from 4 to 20K, and asked if the current kilowatt-class linear motor drives might be adapted to an attitude-independent compressor for mobile G-M cryocooling. This paper reports on the results of that effort and the resulting prototype development of oil-free multi-kilowatt G-M compressors using CFIC STAR linear motors for standard G-M coldheads. In addition to the Air Force's needs, we expect these new compressors to find applications in many places where current devices impose higher costs through their reliability, service, and operational limits.

Cryocoolers 13, edited by R. G. Ross, Jr.
Springer Science+Business Media, Inc., New York, 2004

DESCRIPTION OF THE NEW COMPRESSOR

As in CFIC's acoustic Stirlings, the core of the new compressors is a pair of inline STAR motors, moving in balanced opposition. Indeed, the compressor design flows directly from past practice for pressure wave generators (PWGs), Figure 1. Where PWGs have facing pistons in a common space with a power delivery port, the compressor caps that central cavity, to act as a gas spring, and adds two outward-facing pistons in cylinders with inlet and outlet check valves.

Such compressors are not directly suited to use in ordinary gas compression, but must serve in closed-cycle, pre-charged systems like Gifford-McMahon cryocoolers (G-Ms). The mean pressure is a key design variable in these machines, because the gas spring and thereby the resonant frequency depends on it. A machine beginning from a low initial pressure would require a lower initial drive frequency, but in a G-M the charge pressure provides a near-constant mean level that keeps system resonance at a near-constant frequency. Two notable features are the friction-free, self-energizing reed valves, which operate successfully in a totally dry environment. The other is the need to provide water cooling to both heads and the motors of this system.

Dynamics and Control of Motion and Gas

Conventional reciprocating compressors also have valved chambers addressed by pistons, but the motions of those pistons are controlled by rigid linkages. Control is typically just switching on or off that prescribed motion, to deliver gas against a discharge head. In a resonant dynamic device, the reciprocating motion of the pistons is determined solely by the sum of the forces acting on it, not fixed quantities and strongly dependent on the motions they determine!

High-efficiency reciprocating power transfer requires near-resonant conditions to provide low-loss motion. In resonance, the stored energy of the moving element (instant sum of kinetic and potential energies) is constant in the absence of load, just as in steady rotation. Real power is delivered through the moving element by phase separation between its velocity and force oscillations. The frequency of motion is determined by the ratio of stiffness forces to inertial forces, to the 1/2 power, so a high stiffness and low moving mass are beneficial for compact devices operating at higher frequencies. STAR motors have lightweight plungers and derive significant axial stiffness from their intrinsic magnetic forces. 241-class motors (2 kW at 60 Hz) have open air natural frequencies of about 32 Hz. 297-class motors (5 kw at 60 Hz) have open-air natural frequencies of about 24 Hz. Still, these need considerable additional stiffness to operate efficiently at 50 or 60 Hz for compatibility with common power sources. For motors at this multi-kilowatt scale, with strokes of several centimeters, stress is too high for long-life mechanical springs, and additional magnetic springs add mass as much as stiffness. Only gas springs are practical, but fortunately they are already present in the central piston chambers of PWGs. Gas forces there are augmented by gas forces in the outboard compression chambers, but those are largely defined by the required flow and pressures. The central spring can be tuned, by choice of piston area and basic volume.

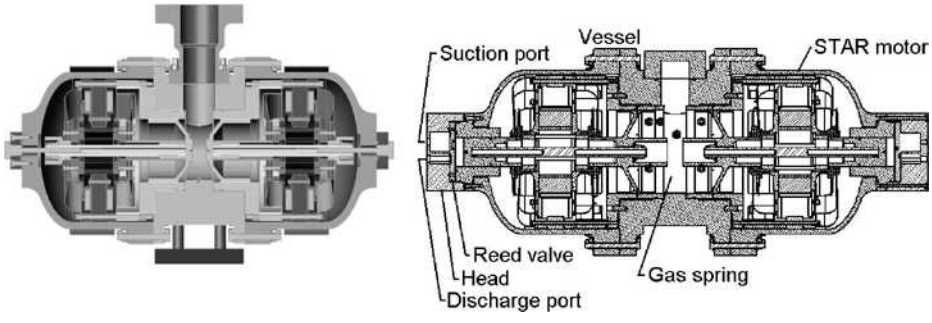

Figure 1. Baseline PWG and compressor sections.

To design such a machine requires advance knowledge of at least the inlet and discharge pressures, required flow rate, gas properties (inlet density, specific heats ratio, inlet temperature), intended frequency, the moving mass and intrinsic stiffness of the reciprocator, and the stroke amplitude and force available from the motor. These are respectively, Pin, Pdis, vdot, rho, Cp/Cv, Tin, f, m, k, X(t) and f(t). Variables to be determined include spring piston area, spring volume, compression piston area, and reciprocating mass (respectively, Ap, Vs, Ac, and m). Note that mass is both an input and result of this analysis, reflecting its iterative role as piston areas in particular change. Complete design further requires detailed understanding of valve dynamics, clearances, and secondary volumes and non-linear effects, but these are beyond the scope of this paper. A linearized and adiabatic model is described here.

Using an adiabatic compressor model and the target pressures and gas properties, a time history of pressure in the compression space can be derived. Analysis of this periodic function will provide a fundamental sinusoid and some higher harmonic functions. We consider only the fundamental and divide it into components in phase and in quadrature with the piston motion to extract the stiffness contribution to the resonant movement. That stiffness is combined with the motor's intrinsic stiffness and the calculated stiffness from the gas spring (which can be presumed adiabatic for this level of analysis). Total stiffness, combined with known masses (e.g., motor core) are combined with parametric structural models of the pistons to estimate total moving mass as a function of piston diameters. These two equations (the stiffness relation and mass relation) can be solved together to define the spring piston diameter. The desired flow rate, with the frequency and allowable stroke of the motor sets the compression piston diameter. A power and force check can be done, using the resultant stiffness and mass in an integrated dynamic model, to verify total system resonance at the desired frequency, stroke, power, and flow at target pressures.

Further analysis and control is required to address the stability of the mean piston position. There is no linkage constraining the piston motion to remain centered evenly about its rest position. That is, free-pistons (and these are nearly free in their allowed range of motion) can drift even while reciprocating. This drift is usually occasioned by the uneven flow of gas across imperfect seals, which can build pressure to one side and push the piston along. In this machine, the gas spring swept volume is a significant fraction of the mean volume, for compactness, so the non-linear effects of high pressure (relative to mean pressure) exacerbate the drifting tendency by further unbalancing the natural flow around the clearance seals. On the other hand, the spring chambers are very nearly adiabatic, so the pressure and motion are essentially in phase. To counter drift, these compressors use centerports that connect the front and rear gas volumes (relative to each piston) momentarily, as the piston passes its rest position. If there is no drift, then the pressures ahead and behind the piston will be equal at that moment. If there has been some net flow, then a pressure difference will exist as the piston passes its rest position, and a small corrective flow will arise in response. During piston excursions far from its rest position, the tiny port pairs in the piston and cylinder wall are not aligned, so flow is effectively stopped, preserving the main piston seal.

Fabrication

The new compressor uses two standard 5 kilowatt STAR motors, with maximum strokes of 26 mm. These motors use moving rare-earth magnets, multi-pole construction, and true-radial, torsionally-stiff flexure suspension. All have been proven in acoustic Stirling service, but an all-new, all-aluminum containment vessel was designed for this weight-sensitive application. It consists of a center body with cylinders for the central gas spring, plus two end vessels that enclose the motors and support the outboard compression cylinders and valve heads. Both spring and compression piston are combined with the moving magnets in a single, rigid plunger assembly, finish turned as a unit in each motor assembly to establish the several microns of running clearance that each uses as a wear-free working seal (refer to Fig. 1).

The demonstration system includes the basic compressor, power controls with safeties, and a closed-loop water cooling system for both the compressor motors and the compressed gas. All components and the system are solid-modeled to ensure packaging (Fig. 2). These auxiliaries have not been subjected to rigorous weight or size reduction efforts in this demonstration phase, but are co-mounted, separately-boxed on a common skid with the basic compressor. The power conditioning components are particularly specialized for this application, which must run from a variable-voltage DC battery electrical bus on a military vehicle. To achieve the alternating current required for the STAR motors, a synthetic, tunable-frequency sine wave is generated and used as the reference for twin switching-type servo amplifiers that independently drive each STAR motor from the common signal and the DC input. 200 volt, 50 Hz output power is synthesized in the power conditioning cabinet by a secondary inverter, to provide drive power for the fan, water pump, and cold-head motor (Sumitomo 408K).

Sensor-based safeties are provided for temperature of the motors, cooling water, amplifiers, and the compressed gas, maximum pressure of the gas, flow of water, piston overstroke, over-current, and electrical isolation. The coldhead connections and the combined helium-water fan-coil unit are common to the benchmark compressor, having been sourced from a donor machine (Sumitomo CSA-71).

The weight of this assembly is not optimized. A skid-mount approach was adopted to include the compressor, cooling and controls on a common base, but without a package integration activity, there is considerable redundant structure and mass. Total prototype mass is 265 kg, which does not yet compare favorably with the commercial baseline unit at 140 kg, despite its added burden of oil filters, separators, etc. Partly this is intrinsic in the larger pressurized volume (and vessel) of the linear machine, but is dominated by the base frame, with separate controls and cooling cabinets. The compressor itself, without these, is 146 kg. A comparison of overall dimensions reveals the impact of the prototype skid package, too. Compare the dimensions in Fig. 2 to 550W x 550L x 885H (mm).

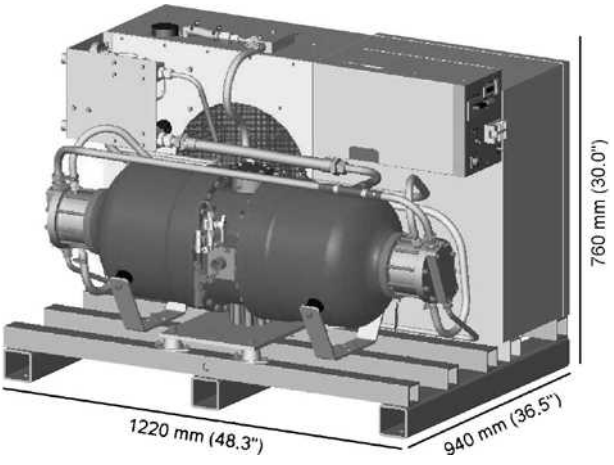

Figure 2. Solid model of prototype 8 kW oil-free liner compressor assembly.

Figure 3. Completed compressor assembly.

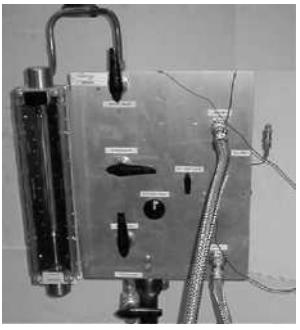

Figure 4. Load-flow board for mapping.

Test Procedure and Results

Once constructed, the compressor was subjected to approximately 100 hours of run-in and mapping testing during which time the optimum frequency and charge pressure were defined. The schedule did not provide for a mechanical iteration (modification to moving mass or gas spring volume) to adjust dynamics for a particular frequency, but the variable-frequency power electronics made it unnecessary to exactly match a line of 50 or 60 Hz. Rather, we scanned the range of operating conditions to identify and characterize the operating characteristics of this prototype compressor. This testing was done against a calibrated load orifice with flow meter and pressure sensors on either side, as shown in Fig. 4.

The resulting map of delivered flow as functions of charge pressure and pressure ratio for operation at 56 Hz is given in Fig. 5. The design charge level of 185 psig (12.8 MPa) is flanked by traces at 1 Bar more and less charge pressure. A much higher charge case (242 psig, 16.7 MPa) is included to show the stability and range of the machine, though the limits to capacity and pressure ratio are also evident for such an off-design condition.

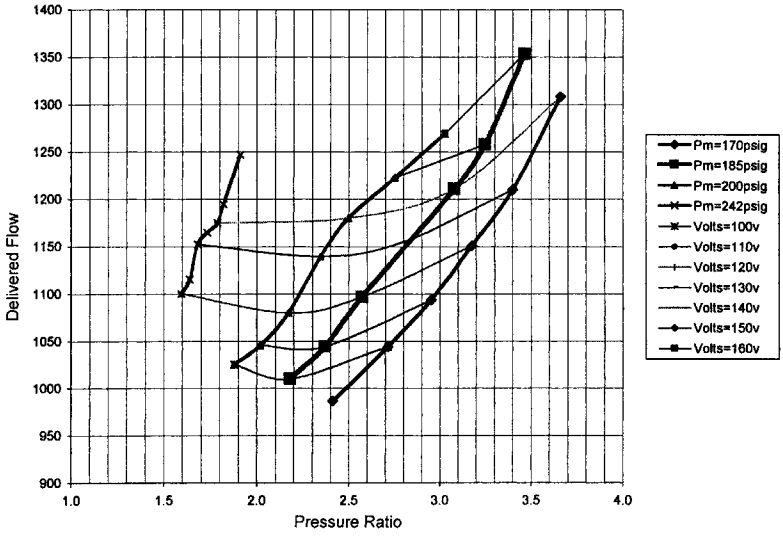

Figure 5. Dependence of 8 kW compressor flow on voltage for various charge pressures.

The optimal nature of 56 Hz at the target conditions is also shown by a frequency sweep curve (Fig. 6) at fixed charge pressure (178 psig/12.3 MPa). Here the actual design point is demonstrated (1340 litre/minute at a pressure ratio of 3.75). Actual pressures are slightly higher than the standard for the baseline compressor (0.66 to 2.5 MPa vs 0.54 to 2.3 MPa). Power consumption noted for the compressor was measured independently of the fan, pump, coldhead, and power conditioning equipment. Test capacity of the prototype is compared to the ratings of the production baseline unit in Table 1, below.

Baseline compressor capacity as quoted by the manufacturer is 1050-1200 litre per minute at 50 Hz and 1300 to 1400 at 60 Hz, which interpolates to 1260-1320 litre per minute at 56 Hz (where the prototype makes 1340). Rated power draw of the baseline unit is 7.5 kW at 60 Hz, where delivered flow is most comparable to this test. Corrected for pump and fan at 90 and 190 watts respectively, the tested oil-free compressor draws about 7.5 kW total, matching the efficiency of the baseline. Notably, the baseline unit draws up to 8.3 kW peak, where the modulation of the prototype linear compressor keeps peak draw no higher than rated power. Further improvements to manifolding and ducting, not within the scope of this project, can be expected to raise the linear unit's efficiency above the well-developed baseline performance.

After mapping against the test load, the design point was repeated with the actual coldhead attached. No vacuum enclosure or coldhead insulation was available, so this test confirmed only that the start-up and shutdown sequences were operational and that the compressor could manage those transients; in addition, the successful powering of the coldhead with auxiliary inverter power, and steady-state cooling (accumulation of air-source ice) was demonstrated. Future testing with the coldhead in a vacuum chamber is planned after delivery of the compressor to Atlas Scientific.

Table 1. Rated performance comparison of prototype and baseline compressors.

	Baseline	Prototype	(Units)
Frequency	60	56	Hz
Flow	1300-1400	1340	Std Litre/min
P-inlet	0.54	0.66	MPa
P-outlet	2.3	2.5	MPa
Power In (System)	7.5	7.5	kW

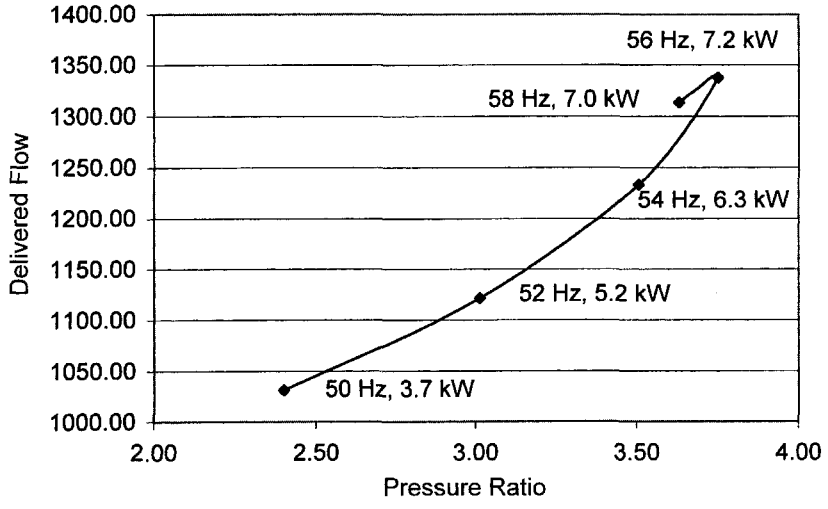

Figure 6. Dependence of 8 kW compressor flow on pressure ratio for various drive frequencies at full load current (178 psig charge, 70 amps).

Challenges

This project, although successful in meeting its performance goals, has not been without challenges. Indeed, these challenges have, so far, prevented final qualification and shipping of the first unit. The issues that arose, adding time to the development, include additional lightweight development to reduce compressor mass and conversion from AC to variable DC power. The development issues include: thermal management, adhesive performance at elevated temperatures, and stroke sensor performance at elevated temperatures. In addition, inlet noise, and start-up sensitivities are areas needing further development. Overall package dimensions and weight were given only modest attention in this effort and need attention in a next-generation system.

Of these, the most critical are those related to thermal management. Cooling is more critical in dry machines than in those with some oil present. In this machine, the presence of close clearance seals on large diameters makes proper thermal management even more important. In the design phase, we were careful to match thermal expansions and to use transient distortion control techniques adapted from our PWG practices in acoustic coolers. However, the absence of an adjacent heat exchanger (aftercooler) as in that experience base, combined with additional heat loads from the compression pistons, drove motor cavity temperatures significantly higher than typical in PWG duty, from about 50°C to about 70°C. The matching work was still functional, but we found two dependent problems. First, the LED and phototransistor of the optical stroke limit sensor lost sensitivity and became a source of random false shut-offs. This was addressed by improving the optical port reflectance and replacing the solid-state components with equivalents rated for service to 80°C.

More serious was the discovery, on disassembly for replacement of the sensor parts, that the primary adhesive that attaches the moving magnets to the plunger suffered cracking. Review of the specifications for the subject adhesive (DP-460 from 3M, commonly used for bonding magnets in motors) showed its glass transition to occur at 65-75°C, a range we had achieved. Adhesive strength drops significantly above this temperature.

Accordingly, we have entered into a recertification process with alternate adhesives to qualify one for this higher temperature service. We currently are testing joints with 100°C capacity and expect to rebuild the prototype compressor this month. In the meantime, we have improved the cooling at the heads and vessel on both this compressor and a similar one at the 4 kW size, in construction in parallel under the same sponsorship. That unit (Fig. 7) incorporates the lessons learned on the 8 kW unit and has begun testing, with delivered capacity of 850-900 litres per minute against similar pressures.

Figure 7. 4kW prototype compressor.

CONCLUSIONS

A new helium compressor for closed-circuit G-M cryocoolers (in two multi-kilowatt sizes) has been designed, built, and tested successfully. It is completely oil-free and delivers high-pressure flows comparable to the best of well-developed conventional compressors. It is based on well-proven drivers (pressure wave generators) for acoustic Stirling coolers, by addition of secondary pistons in chambers with friction-free reed valves. Demonstrated capacity of 1350 standard litres per minute from 0.6 to 2.5 MPa matches the requirements for a Sumitomo 408K coldhead, from 7.2 kilowatts of compressor input power. To date, approximately 100 hours of compressor load testing have been completed. Developmental issues met and overcome included sensor and adhesive limits in higher-temperature duty. At this writing, the initial prototypes (8 kw described in detail here, and a 4 kW second unit) are in preparation for delivery to the Air Force, and a first commercial trial unit, now under construction, has been sold.

The future for this new class of compressors is in applications where zero contamination, high reliability, motion/attitude insensitivity, and minimal maintenance are prized. Military field-deployment of superconductors, medical imaging, and mobile and remote cryostorage systems are example applications. Together with their acoustic Stirling cousins, these novel cryocompressors bring on-site cryogenics toward appliance-like practicality.

ACKNOWLEDGMENTS

This work has been supported by the US Air Force Research Laboratory (AFRL) through subcontracts with Atlas Scientific and Cryomagnetics, Inc. The authors wish to thank these sponsors and especially Chuck Oberly of AFRL and Ali Kashani and Mike Coffey, principals of our prime contractor-customers.

Compression Losses in Cryocoolers

J.S. Reed, G. Davey, M.W. Dadd and P.B. Bailey

Department of Engineering Science
Oxford University
Oxford, UK

ABSTRACT

Most of the loss mechanisms in Stirling and Pulse Tube cryocoolers are well documented and are relatively easy to analyze and estimate. One of these losses is related to the irreversible compression of gas in the cylinder, and the magnitude of this loss is such that it has a very significant impact on the overall system efficiency. Simple tests on a cryocooler give an estimate on the size of this loss, though the results of these tests include elements of other, known losses, such as clearance seal and pressure drop losses. The parametric variation of this 'lumped' loss suggests that it is not primarily due to these, or other known losses. Over a wide range of machines and conditions this 'lumped' loss varies with operating frequency, swept volume and pressure swing, suggesting that it is some kind of thermodynamic effect related to the area of the 'P-V' loop in the compression space.

This loss appears to be quite independent of the refrigeration cycle, and takes place in the ambient temperature part of the system as a result of cyclic pressure changes in a typical Stirling cycle geometry. The loss does depend on geometry, and is typically higher on a 'split' Stirling cycle machine than on a more compact 'integral' one.

This paper looks at the experimental data that is the basis of this loss, and compares these data with other studies carried out on compression losses in Stirling Cycle and other reciprocating machines.

INTRODUCTION

A typical Stirling cycle or Pulse Tube cryocooler consists of a compressor containing a reciprocating piston and a cold-head containing a regenerator. By supplying electrical power to the motor the piston performs work on the gas in the compression space and the cold head uses this work to transport heat from the cold end to the compression end. In the ideal case, the ratio of the heat lifted at the cold end to the work done on the gas at the warm end would be equal to that of a Carnot cycle operating between the same temperatures. In practice, however, this process is subject to a number of loss mechanisms that either reduce the effective amount of work input into the cycle or place additional heat loads on the cold-end. Understanding and reducing these loss mechanisms is the key to producing an efficient cryocooler.

Many of the loss processes present in a working cryocooler have been fairly well characterized by measurements and analyses. The data have shown, however, that these do not appear sufficient to account for the amount of power lost in working machines. Indeed the discrepancy is so large it seems to be the largest loss process for machines made in Oxford and has a profound impact on the

Cryocoolers 13, edited by R. G. Ross, Jr.
Springer Science+Business Media, Inc., New York, 2004

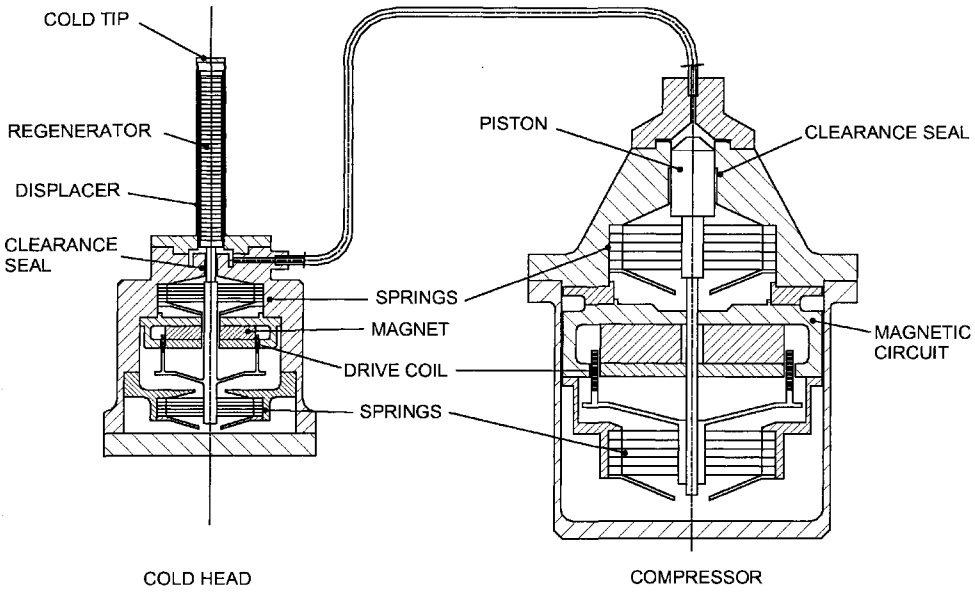

Figure 1. Schematic of original Oxford 'split'cryocooler

efficiency and design of these machines. It would therefore be highly desirable to develop an understanding of the physical mechanisms behind these so called 'compression losses' and hopefully reduce them in future devices.

For convenience, this paper relates to the classic 'Oxford' type of machine, with a moving coil linear motor and clearance seal suspension system; Figure 1 shows a typical machine. Compression losses are not unique to this particular 'split' configuration and are also present in 'integral' machines with the compressor and cold head close-coupled.

EXPERIMENTAL EVIDENCE

Although compression losses are observed in both types of machine, one advantage of a Stirling cycle over a pulse tube is the possibility of independently controlling the displacer and the compressor piston. One possible test is to drive the compressor while holding the displacer stationary. Under these circumstances there is no change in volume at the cold end of the machine, the cold end gas can do no work and hence there is no gross refrigeration. Ideally the gas should behave as a spring and no power should be absorbed. The fact that there is a significant power loss is indicative of loss processes that are not dependent on the refrigeration cycle. We will refer to this measurement of 'gas spring loss' as a 'compression loss' test.

Orlowska[1] carried out a thorough analysis of the losses in an early 'Oxford' Stirling Cryocooler, which was a machine of 3.15 cm^3 swept volume designed to give 1 watt of refrigeration at 80 K. She carried out compression loss tests on a complete cryocooler over a range of frequency and strokes. The shaft work (taken as $W_e - i^2R$) was measured and found to be very linear with frequency (Fig. 2).

Similar results have been obtained from every other machine built and tested at Oxford. For example, further evidence was obtained from the 'Ambient' cooler[2]; a machine of 4.3 cm^3 swept volume designed for a domestic freezer and giving 60 watts of refrigeration at 253 K. The results of these compression loss tests give a power input for each stroke that was approximately linear with frequency over the measured range (Fig. 2).

Both of these sets of results are for tests carried out on complete cryocoolers, but similar results are obtained when a compressor is attached to a dummy volume. In all cases the result of the compression loss test closely obeys:

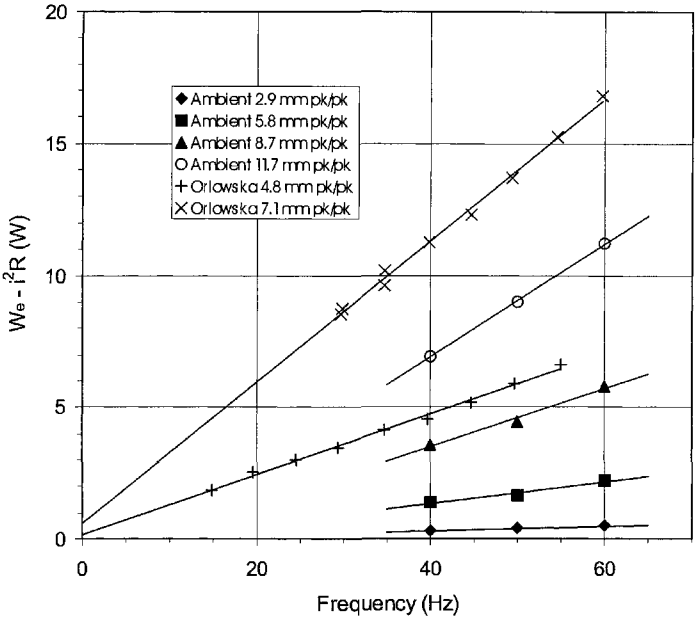

Figure 2. Compression loss data for two Stirling coolers.

$$W_e - i^2R = k\, f\, \Delta p\, \Delta V \tag{1}$$

where f is the frequency, Δp is the pressure swing (peak-to-peak), ΔV is the swept volume and k is a constant for a particular machine. The value of k was found to be between 0.1 and 0.2, tending to higher values for the traditional 'split' Stirling cooler, and lower values for an 'integral' machine. When compressors have been tested into a 'dummy volume', the values have been lower still.

The behavior of machines during this test is so consistent that it has been used as an accurate diagnostic tool. If, for example, the value of k increases at higher frequencies, there is invariably a pressure drop problem, and if it increases at low frequencies, then there is excessive seal leakage.

Inclusion of the 'compression loss' term is part of the cryocooler design process used at Oxford. Stirling cycle machines designed in this way have a measured performance very close to that predicted by the design model, and this has been found to be true over a wide range of sizes and temperatures.

STIRLING CYCLE LOSS MODEL

There are many ways of modeling Stirling cycle machines given in the literature, mostly based on the classic Schmidt analysis. A simplified version of the model used at Oxford is given in Fig. 3; only the major loss mechanisms are shown.

The diagram shows 'compression loss' as a separate term from the clearance seal and pressure drop losses. Experimentally, the 'Compression Loss' test gives a lumped value for many of the high temperature losses, including windage, pressure drop, heat transfer and clearance seal losses. To separate out these losses, it is useful to look at the parametric dependency of each one.

Seal Loss

Caused by leakage through the clearance seal, the loss is conventionally given by an analytical solution for laminar flow through an idealized seal as:

$$W_{seal} = \frac{\pi D t^3 (\Delta p)^2}{96 \mu L_{seal}} \tag{2}$$

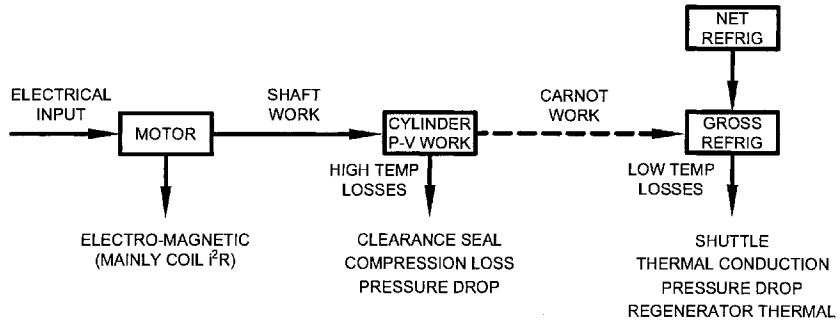

Figure 3. Schematic of Stirling cycle losses (simplified).

Thus, for a given machine, the seal loss is a function only of the pressure swing, and is independent of frequency. Figure 4 compares the measured compression loss of the ambient cooler at 11.7 mm stroke with the theoretical (and ideal) seal leakage loss. It should be noted that imperfections in the piston, cylinder and alignment can increase the magnitude of this loss, but there is no evidence that such imperfections will change its functional dependence.

Pressure Drop Losses

The power lost is proportional either to velocity squared (for laminar flow) or to velocity cubed (turbulent flow). In a complicated geometry, the total loss will be the sum of individual pressure drop terms; laminar flow will only be present in elements such as long pipes and heat exchangers. In practice the flow entry and exit terms (essentially turbulent) often dominate. The $\frac{1}{2}\rho v^2$ terms are further complicated by the variation of density through a cycle, but with a low volumetric compression ratio, the density change is much less than the velocity change. The theoretical pressure drop term for the ambient cooler is plotted on Fig. 4. The calculated values plotted here are for the machine operating as a cryocooler with the displacer moving. In a 'compression loss' test the

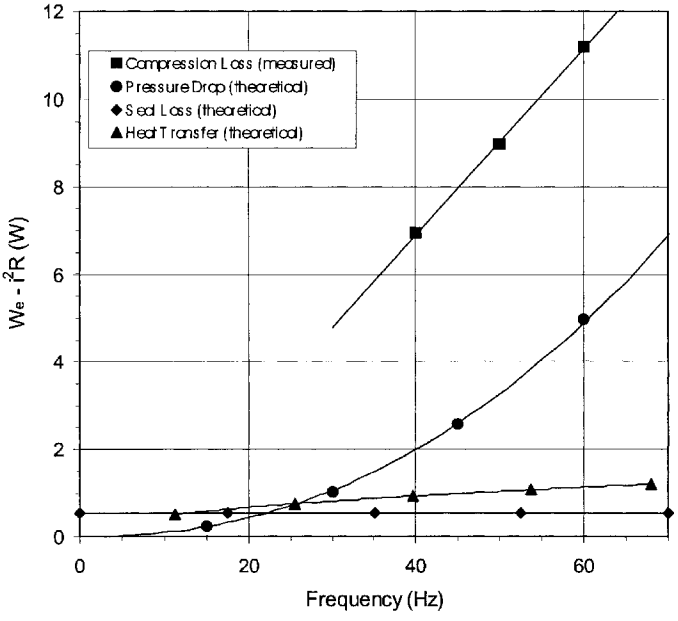

Figure 4. Measured compression loss for the Ambient cooler at 11.7 mm p-p stroke, compared with theoretical values for the expected loss mechanisms.

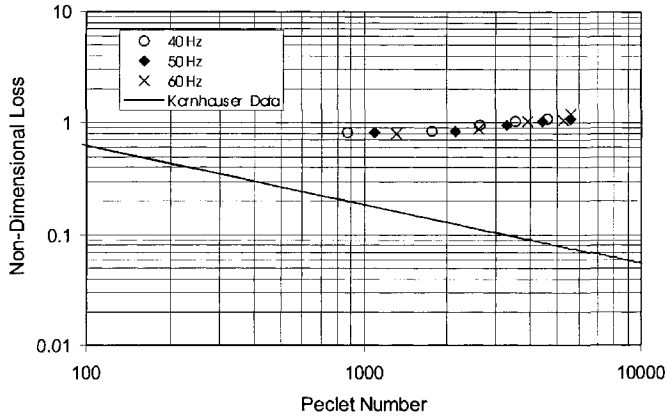

Figure 5. Compression Losses for the Ambient Cooler plotted non-dimensionally as a function of Peclet number. This is compared with an approximation to data from Kornhauser and Smith (Ref 3, Fig. 1) for the loss in a gas spring. The Peclet number is based on mean piston velocity, and the non-dimensional loss is based on the work of adiabatic compression.

displacer is stationary, and so the mass flow through the regenerator and heat exchangers will be significantly less, hence the curve as plotted can be regarded as an upper bound for the pressure drop loss for these tests.

Heat Transfer Losses.

In machines of the size and operating frequency considered here, there is insufficient heat transfer to keep the compression and expansion processes in the compressor cylinder isothermal. Instead, a more general polytropic process must be assumed, and significant temperature swings are probable.

Various authors have produced correlations for the losses expected in the geometry of a simple cylindrical gas spring. Kornhauser & Smith[3] described experiments with a closed, conventionally sealed piston, suggesting that the losses are small and the processes are nearly adiabatic. More recently this work has been extended to include gas inflows into the cylinder[4], and concludes that there are increased losses compared to the closed geometry. In addition to flows to and from the cylinder, there is the possibility of effects due to flow through the clearance seal. Hence the equivalent losses in a complete Stirling cooler are difficult to predict and there is little scope for determining such values other than by measurement. The authors are aware of others attempting to model these losses using computer based numerical methods, but without conclusive results.

Figure 5 shows data derived from Kornhauser & Smith[3], plotted non-dimensionally, together with equivalent values taken from the ambient cooler results; the Kornhauser & Smith data are also plotted in Fig. 4.

Other Loss Mechanisms.

There are several other active loss mechanisms that should be taken into account: electromagnetic losses (eddy current, magnetic hysteresis), mechanical friction, windage, thermal loss due to flow mixing, heat transfer loss 'behind the piston', etc. In various machines these losses have been measured and usually found to be small.

COMPRESSION LOSS MECHANISM

The major loss mechanisms identified for these machines have well known parametric dependencies. The results of 'compression loss' tests are inconsistent with any of these, and there are three possible explanations for this.

Firstly, it is possible that two of the mechanisms combine characteristics to give the observed behavior, which is a loss per cycle proportional to the compressor 'P-V' area. For instance, the heat transfer loss (which decreases with increasing frequency) could combine with the pressure drop loss (increasing with frequency) to give a loss per cycle. There are two arguments against this. The expected theoretical magnitudes of these individual losses are much smaller than the observed compression loss. In addition, it seems extremely unlikely that, given the wide range of machines which exhibit this phenomenon, the two losses always *exactly* sum to give a fixed 'loss per cycle.'

The second explanation is that it is possible that one of the other known loss mechanisms which we have judged to be insignificant is in fact much larger than we think. However, none of them appear to have the correct parametric dependency, and experimentation has so far indicated that they are small in magnitude.

The third reason, and in our view the most likely, is that there are one or more loss mechanisms active that are not properly understood or accounted for. The functional dependence gives the appearance of a thermodynamic phenomenon, with a magnitude proportional to the area of the compressor 'P-V' loop, and proportional to frequency.

CONCLUSION

A 'compression loss' is always observed in 'Oxford' type Stirling and pulse tube cryocoolers, and this is significantly higher than that predicted by existing loss mechanisms. It is postulated that this is either due to existing models of loss mechanisms being incorrect, or due to one or more unknown losses occurring in these machines. In either case data indicates behavior similar to a thermodynamic cycle, with the loss proportional to the work done on the gas in the compression space.

Work is currently under way at Oxford to try to determine the nature of these losses, in the hope that a fuller understanding of them may lead to an increase in cryocooler efficiency.

ACKNOWLEDGMENTS

We acknowledge the strong support of Thom Davis of AFRL who are funding the current program of work. We would like to thank Anna Orlowska for permission to use her data.

NOMENCLATURE

D	=	Piston diameter	W_e	=	Work in (electrical)
f	=	Frequency	W_{seal}	=	Work lost in the clearance seal
i	=	Current (rms)	Δp	=	Pressure swing (peak-to-peak)
k	=	Numeric constant	ΔV	=	Swept volume
L_{seal}	=	Length of clearance seal	μ	=	Gas viscosity
R	=	Coil resistance	ρ	=	Gas density
t	=	Seal radial clearance			

REFERENCES

1. Orlowska, A.H., "An Investigation of some Heat Transfer and Gas Flow Problems Relevant to Miniature Refrigerators," *DPhil Thesis*, University of Oxford, UK (1985), figure 5.6, page 5-21.

2. Green, R.H., Bailey, P.B., Roberts, L., Davey, G., "The Design and Testing of a Stirling Cycle Domestic Freezer," *Applications for Natural Refrigerants,* International Institute of Refrigeration, Aarhus, Denmark (1996), pp. 2.11–2.15.

3. Kornhauser, A.A., Smith, J.L., "The Effects of Heat Transfer on Gas Spring Performance," *Proc. 26th Intersociety Energy Conversion Engineering Conference,* American Nuclear Society, La Grange Park, Ill., USA, Vol 5 (1991), pp 180-185.

4. Catelmi, F.J., Gedeon, D., Kornhauser, A.A., "An Analytical Model for Turbulent Compression-Driven Heat Transfer," *ASME Journal of Heat Transfer,* Vol. 120 (1998), pp 617-623.

A Novel Method for Controlling Piston Drift in Devices with Clearance Seals

P. S. Spoor and J. A. Corey

Clever Fellows Innovation Consortium
Troy, NY 12180

ABSTRACT

The time-averaged mass flux through a free-piston clearance seal can cause shifts in the equilibrium piston position, which will reach an ultimate value for a given set of operating conditions if the piston is restrained by a mechanical or magnetic stiffness. The mass flux and resulting piston offsets can be particularly significant in systems where the reactive component of dynamic pressure on the pistons is large (e.g. where gas-spring stiffness is important). Here we derive simple expressions for the time-averaged mass flux through a clearance seal, assuming that the piston is acting against enclosed volumes on either side (i.e., is a double gas-spring) and predict the resulting piston offset. We consider the case of solid pistons, which have a clearance gap that is constant in time, and the case of hollow pistons, which can flex in response to the pressure waves and therefore have a time-varying clearance. We compare these predicted offsets to data on several pressure-wave generators, taken with the compression volumes capped (so that they resemble double-gas springs). Agreement with theory is excellent for most cases of interest. These results suggest that a properly designed piston can harness the pressure-induced flexing effect to reduce or eliminate piston drift. Such an "anti-drift" piston is built and tested, with promising results.

INTRODUCTION

The advent of high-power, efficient linear motors has enabled the development of resonant acoustic power conversion technology for turning electricity into sound power, or turning sound power into electricity, at the level of tens of kilowatts. Among the leading applications are acoustic cryocoolers, which are comprised of high-power resonant acoustic power sources, or pressure-wave generators (PWGs) driving high-frequency acoustic Stirling (e.g. "pulse-tube") refrigerators. These cryocoolers have no cold moving parts and no lubricants, and have no required maintenance and no intrinsic failure modes. Figure 1 shows a typical PWG configuration, showing twin-opposed linear motors compressing a common volume between them, and acoustic work flowing up through a delivery port. The reciprocating motion of these motors is ensured by the use of a suspension with relatively low axial stiffness, but high stiffness against rotation or rocking motion. Thus, the piston's pure axial motion is guaranteed by the suspension only, and the piston need never contact the bearing. The acoustic isolation of the front and back volumes is maintained by a tight, but unlubricated, clearance seal.

Cryocoolers 13, edited by R. G. Ross, Jr.
Springer Science+Business Media, Inc., New York, 2004

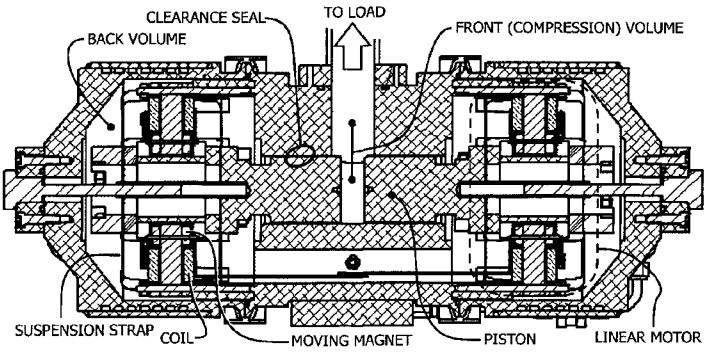

Figure 1. A pressure-wave generator showing twin opposed linear motors with clearance-seal pistons.

It is well known that free-piston devices of this sort are susceptible to shift of the equilibrium piston position off-center, due to nonzero time-averaged mass flux through the seal and the resulting unbalanced mean pressure difference that develops across the pistons. At the same time, considerations such as cost and power density are tending to drive PWG designs in directions that increase this susceptibility. The highest power machines have a large moving-magnet mass, which is most effectively balanced by using the reactive component of the acoustic pressure acting on the piston faces as the restoring force (rather than mechanical springs). This tends to move the design toward pistons with large frontal area, but hollow insides to keep them relatively lightweight. The larger piston diameter indicates a looser tolerance on the clearance gap. All these factors increase the time-averaged mass flux through a piston seal and the resulting piston offset. This offset compromises the machines by reducing their useful stroke.

The following is a guide to estimating piston offset and corrective flow necessary to combat piston offset, in a typical pressure-wave-generator (PWG). To simplify the analysis, we will make a number of assumptions that are valid in the limit of small oscillations, albeit not strictly true at the amplitudes these machines are intended to operate. We assume:

1. Adiabatic volumes on either side of each piston.
2. Oscillating pressure in phase with oscillating motion (gas-spring phasing).
3. Clearance gap much smaller than the thermal penetration depth of the working fluid.
4. Piston and cylinder at a uniform temperature T_0.
5. Acoustic displacement within the clearance seal much smaller than the seal length.
6. Drift velocity of mass flux much slower than the first-order acoustic velocity.

The above assumptions are valid for a typical system with a nominal clearance gap of 25 microns, a seal length of 50 to 100 mm, frequency 60 Hz, working fluid helium, and acoustic amplitude of less than 5%. Actual PWGs are often intended to run at acoustic amplitudes closer to 15 to 20%, so assumption #5 is certainly violated under nominal operating conditions.

The gas outside the seal is essentially adiabatic, whereas in the seal it is essentially isothermal, with zero axial thermal gradient. The pistons and cylinders are typically made of thick-walled aluminum, so an assumption of zero axial thermal gradient in the solid seems reasonable. For small amplitudes, the gas in the seal spends several cycles in intimate thermal contact with this solid, so it seems reasonable to suppose that the gas is essentially at uniform temperature within the seal. There is acoustic dissipation within the seal, of course, but it is nearly uniform along the length of the seal and of relatively low power density with respect to the available solid surface area. Then the density of the gas within the seal is

$$\rho(x) = \rho_0 \frac{P(x)}{P_0}, \tag{1}$$

where ρ_0 and P_0 are the ambient density and ambient pressure, respectively, x is the axial coordinate along the seal, and $P(x)$ is the total pressure as a function of position at any instant of time along the seal. There must be mathematical discontinuities in temperature and volume flow at the ends of the seal, according to this assumption, but we will ignore these for now.

Let

P_0 = mean or charge pressure,

p = acoustic ("excess") pressure, and

$P = P_0 + p$ = total pressure.

If the PWG is more or less like a gas spring, the pressure wave in front of the pistons is in almost perfect antiphase with the pressure in back (this is a good approximation for the biggest PWGs even when driving a load, and valid for our piston-drift tests, which are done with the PWGs capped). Then the total pressure on either side of the seal, as a function of time, is approximately

$$P_C(t) \cong P_0 + p_C \sin(\omega t)$$
$$P_B(t) \cong P_0 - p_B \sin(\omega t);$$

where p_C and p_B are the peak acoustic (oscillating) pressure amplitudes on the compression (front) and bounce (back) sides of the piston, respectively. Figure 2 shows the total pressures labeled on either side of a piston seal, and defines the compression-space side of the seal as x=L, and the back side as x=0, where L is the length of the seal. The piston is shown fully forward, so that at this instant in time, $P_C = P_0 + p_C$ and $P_B = P_0 - p_B$.

The mass flux through the seal as a function of x, assuming pure Poiseulle flow, is given by

$$\dot{m}(x) = \frac{\rho_0}{P_0} \frac{\Pi \delta^3}{12\mu} P(x) \cdot \frac{dP(x)}{dx}, \tag{2}$$

where ρ_0 is the ambient density, Π is the seal perimeter, δ is the clearance seal gap, and μ is the working fluid viscosity. Again, $P(x)$ is really $P(x,t)$, but we are considering the system at one instant in time, when the piston is fully forward (at the 'top of the stroke'). If we assume that mass flux through the seal is conserved (as opposed to volume flux), and we assume that the seal gap is constant, then $P(x) \cdot P'(x)$ is constant, and the pressure as a function of x in the seal is given by

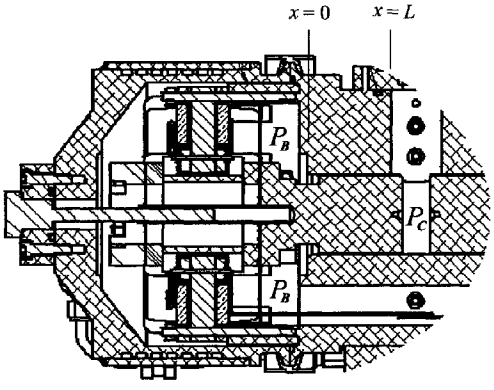

Figure 2. A closeup of one piston in the pressure-wave generator shown in Figure 1, with labels corresponding to variables referred to in the text.

$$P(x) = P_C\sqrt{1-(L-x)/x_0}\,, \quad P_C > P_B$$
$$P(x) = P_C\sqrt{(L-x)/x_0 - 1}\,, \quad P_C < P_B \tag{3}$$
$$P(x) = \text{constant}\,, \quad P_C = P_B$$

where

$$x_0 = \frac{(P_C/P_B)^2}{(P_C/P_B)^2 - 1}\cdot L\,.$$

Using this form for $P(x)$, the mass flux is found to be

$$\dot{m}(t) = -\frac{\rho_0}{P_0}\frac{\Pi\delta^3}{12\mu}\frac{\left(P_C^2(t) - P_B^2(t)\right)}{2L}\,. \tag{4}$$

If we assume a double gas spring with an oscillating volume $V_1\sin(\omega t)$, due to the piston oscillating against two possibly unequal volumes V_C and V_B, the time-averaged mass flux becomes, to second order in V_1/V:

$$\overline{\dot{m}(t)} \cong -\frac{\rho_0}{P_0}\frac{\Pi\delta^3}{12\mu L}\frac{P_0^2}{2}\gamma(2\gamma+1)\left[\left(\frac{V_1}{V_C}\right)^2 - \left(\frac{V_1}{V_B}\right)^2\right]. \tag{5}$$

If we have sensors in these volumes reading first-harmonic pressures $p_C\sin(\omega t)$ and $p_B\sin(\omega t)$, then this expression becomes

$$\dot{m}_{2,2} \cong -\frac{\rho_0}{P_0}\frac{\Pi\delta^3}{12\mu L}\frac{(2\gamma+1)}{4\gamma}\left(p_C^2 - p_B^2\right). \tag{6}$$

Obviously this is strictly true only for the case of a double gas spring. The factor containing γ would be different if, for instance, the front volume consisted only of a clearance volume between a piston and an isothermal heat exchanger.

Equation (6) gives the time-averaged oscillating mass flux through the seal, at least in the limiting case where there is no opposing mean-pressure gradient. In a closed system, the time-averaged flow of mass to one side of the seal means that an opposing DC pressure will build, opposing the time-averaged oscillating flow and causing a DC return flow. Eventually, the system will reach steady state, where the steady return flow caused by $\Delta P_{2,0}$ is equal to the time-averaged oscillating mass flux through the seal, i.e.

$$\dot{m}_{2,0} = -\dot{m}_{2,2}\,. \tag{7}$$

Approximating with $\dot{m}_{2,0} = \rho_0 U_{2,0}$, where $U_{2,0}$ is the DC return volume flow, we can write

$$\dot{m}_{2,0} = \rho_0\frac{\Pi\delta^3}{12\mu L}\Delta P_{2,0}\,. \tag{8}$$

We can combine (6), (7), and (8) to obtain

$$\Delta P_{2,0} = \frac{(2\gamma+1)}{4\gamma P_0}\left(p_C^2 - p_B^2\right). \tag{9}$$

If the piston has area A_P and is attached to a mechanical spring of stiffness K_M, then this second-order pressure difference will result in a constant offset x_0 given by

$$x_0 = \frac{(2\gamma+1)}{4\gamma P_0}\left(p_C^2 - p_B^2\right)\frac{A_P}{K_M}\,. \tag{10}$$

Since the time-averaged oscillating flow and the opposing DC return flow have to go through the same seal, the seal characteristics drop out of the final result for $\Delta P_{2,0}$. Also note that if the gas-spring system were perfectly symmetric, with equal volumes on either side of the piston, there should be no reason for mass to flow preferentially to one side or the other.

Flexing pistons

If the pistons are solid, and are perfectly centered in perfectly straight cylinders, and run perfectly parallel to the cylinder walls, then Eq. (12) may be a good approximation of actual piston behavior. [There is another, minor effect which we did not consider in the previous derivation, which is the offset resulting from the time-averaged pressure on either side of the piston. Because gas springs are nonlinear, with a stiffening nonlinearity which increases with the fractional volume change, the pistons are pushed *backward* slightly if the front volume is smaller than the back volume. The effect is small compared to the offset caused by the second-order mass-flux through the seal.] In large systems where gas-springing is important to the overall dynamics, pistons are large in diameter, making it difficult to perfectly center them in the bore and make them run perfectly true, and the pistons are often hollow to make them lighter. Since the flow through the seal is proportional to the seal gap cubed, even minor changes in the seal gap can have significant consequences on the flow. We will consider one such example: the flexing of hollow pistons due to the pressure difference across the piston wall, and the resulting time-and-pressure-amplitude-dependent seal gap that results.

Figure 3 shows a cutaway view of a piston from a 10 kW pressure-wave generator, which uses two opposing 5 kW linear motors with 7.25-inch diameter pistons. The pistons are aluminum, with a radial shell thickness of 0.25 inch, to keep them light. Figure 4(a) shows the same piston, with a finite-element model showing in exaggerated fashion how it might deflect with a 4.5 bar overpressure "external" (to the right) and an 0.8 bar underpressure "internal". This analysis assumes a linear pressure gradient in the seal, which is not quite right, but we will return to that issue in a moment. [The cylinder wall is not shown in this figure, but would run parallel to the text, at the top of the figure]. This is typical of what the piston might experience at the top of its stroke, when the pressure in the compression space is maximum and that in the back space is minimum. Figure 4(b) shows the piston at the bottom of its stroke, when the pressure difference is maximum in the other direction: high inside the piston, low outside.

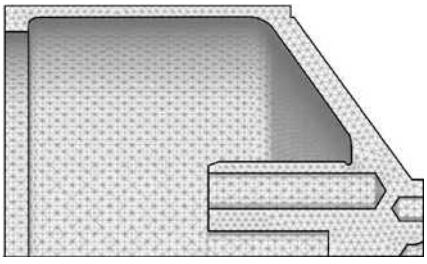

Figure 3. Cutaway view of a hollow piston from a 10 kW pressure-wave generator.

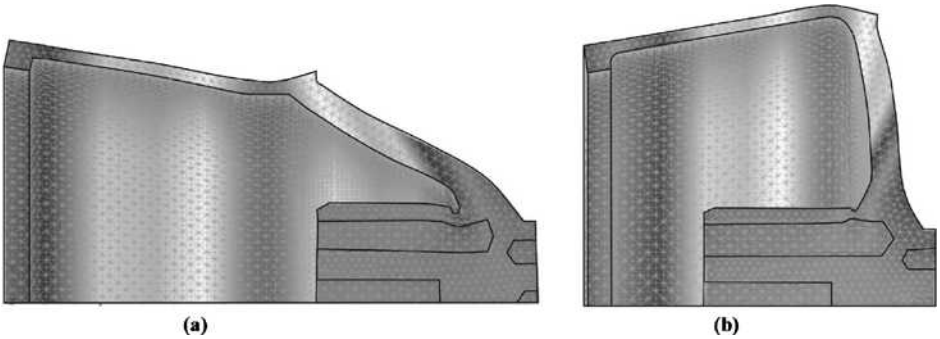

Figure 4. The piston of Fig. 3, with FEA analysis showing exaggerated strains when (a) the pressure is high in front and (b) when pressure is high in back.

In each case, the back end of the piston hardly deflects at all, since the inner and outer diameters of the piston shell experience the same pressure at that end. The front edge of the piston, however, deflects a full 0.0004 inch or 0.4 mil inward radially at the top of the cycle, and 0.34 mil outward at the bottom of the cycle. The nominal seal gap for these pistons is 1 to 2 mil, so this flexing makes the flow resistance of the seal substantially different depending on the direction of the pressure gradient. It will favor mass flux to the back side of the piston, since the seal is more open when the pressure is high on the front side, thus increasing the tendency of the piston to drift forward.

To predict the effect on the time-averaged mass flux and piston offset, we begin as before, by considering the pressure gradient through the seal. This is more of a challenge than the case of a constant seal gap, for as we see from Figs. 3 and 4, the seal gap may not have a simple analytic shape. Furthermore, the pressure gradient depends on the seal gap, which in turn is dependent on the pressure gradient. To simplify, we will *assume* a linearly varying seal gap, and ask what pressure gradient is necessary to preserve constant mass flux through the seal. Let the gap on the x=L side be $\delta_+ = \delta_0 + \Delta\delta$, where $\Delta\delta$ is the increase in the gap due to a radial pressure difference Δp across the piston if the compression space pressure is high. Then the gap as a function of x is $\delta(x) = \delta_0 + \frac{\Delta\delta}{L}x$. If mass flux is independent of x, $P(x)\cdot P'(x)\cdot\delta^3(x) = \text{constant}$. To obtain the time averaged mass flux, it is necessary to include the time-varying nature of the gap as well as the pressure. Since the gap is varying with the pressure across the piston, the seal gap is approximately $\delta(x,t) = \delta_0 + (\Delta\delta/L)\cdot x\cdot(P_C - P_B)\sin(\omega t)$. The math gets more complicated because $\Delta\delta/\delta_0$ is not small. However, if the mass flux is expanded to include terms up to $(\Delta\delta/\delta_0)^4$, it turns out that if the fractional pressure amplitude is not too large, the only significant terms that survive are first order in $\Delta\delta/\delta_0$. The second order mass flux becomes

$$\dot{m}_{2,2} \cong -\rho_0 \frac{\Pi\delta^3}{12\mu L}\left[\frac{(2\gamma+1)}{4\gamma P_0}\left(p_C^2 - p_B^2\right) + \frac{3}{2\delta_0}\frac{\Delta\delta}{\Delta p}\left(p_C + p_B\right)^2\right], \tag{11}$$

and

$$x_0 \cong \left[\frac{(2\gamma+1)}{4\gamma P_0}\left(p_C^2 - p_B^2\right) + \frac{3}{2\delta_0}\frac{\Delta\delta}{\Delta p}\left(p_C + p_B\right)^2\right]\frac{A_P}{K_M}. \tag{12}$$

Here $\Delta\delta/\Delta p$ is the rate of radial deflection with respect to radial pressure difference across the piston shell, obtained from FEA or hoop stress or some other source. This approximation assumes the maximum outward deflection equals the maximum inward deflection, and assumes that the seal gap is linear in x, neither of which is strictly true (as one can see from Fig. 4). The first term in Eq. (12) is the original second-order mass-flux term, and the second term is due to the flexing piston. Since the flow through the flexing piston seal is asymmetric, the piston offset does not disappear if the acoustic pressure amplitudes on both sides of the piston are equal. Also note that the first term, independent of the seal properties, is inversely proportional to the mean pressure. The second term, arising from the time-varying seal gap, is independent of the mean pressure. This gives a convenient way to distinguish effects due to variable seal gap in actual data, by varying the mean pressure.

Note also that the sign of $\Delta\delta/\Delta p$ can be made positive or negative depending on how the piston is shaped or oriented. If the piston were turned around so that the hollow "cup" were facing the compression space side, then the leading edge of the piston would experience no deflection, and the back end would deflect radially outward when p_C is high and inward when p_C is low. This would cause the two terms in (12) to have opposite signs, which suggests that if the amplitude of $\Delta\delta/\Delta p$ can be controlled by proper piston design, the piston flexing can be used to reduce or eliminate drift.

EXPERIMENT

Very simple experiments can be used to check the veracity of Eqs. (10) and (12). A pressure-wave generator such as the one shown in Fig. 1 is driven with the delivery port capped, pressure sensors in the front and back spaces, and displacement sensors on each motor. The piston offset is recorded as a function of dynamic pressure amplitude and can be compared directly to the predictions of (10) and (12).

We first consider a small PWG with solid pistons, similar to the one shown in Fig. 1. Flexing-piston effects should be absent, so Eq. (10) should apply. Figure 4 shows the results, for two different but nominally equivalent PWGs rated at 600 W pV output, with 2-inch diameter solid pistons. The piston drift in both PWGs appears to be well approximated by Eq. (10), especially at low amplitude. For PWG #2, we see that the piston offset is indeed doubled if the mean pressure is halved, as predicted by (10).

In the next experiment, we measure piston offsets and dynamic pressures for two nominally equivalent 10 kW PWGs, with pistons like those shown in Figs 3 and 4. Here, we expect flexing piston effects to dominate. Figure 6 shows the results. Indeed, Eq. (10), which does not include piston flexing, is a poor fit, while Eq. (12) is a surprisingly good approximation. We say 'surprisingly' because flexing piston results are sensitive to details of seal geometry such as nominal seal gap, piston bore taper, and so on, which may not be the same from unit to unit. One thing that may help keep variation between PWGs down is that the piston offset is the result of a second-order pressure difference arising from the total unbalanced mass flux through both pistons, so the effects of anomalies in any one piston are reduced by averaging over 2.

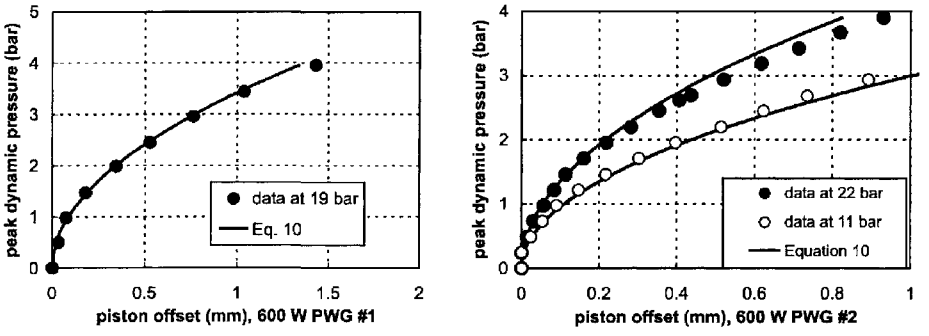

Figure 5. Piston offset data on two small (600 watt) PWGs with 2-inch diameter solid pistons.

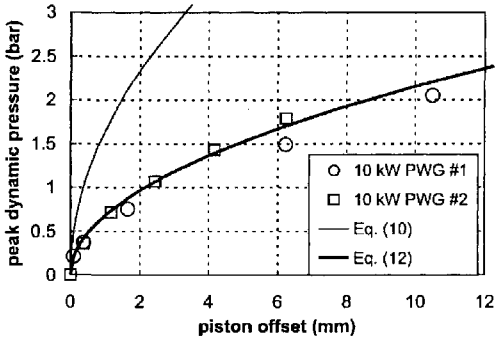

Figure 6. Piston-offset data for two large (10 kW) PWGs, with 7.25-inch diameter, hollow pistons.

Anti-Drift Pistons

The 10 kW data also underscores how serious the piston drift problem is in the larger PWGs. The pistons have a steady-state offset of over 10 mm at a peak dynamic pressure in the front space of 2.0 bar (with the wave in the back space at about 0.25 bar), and the maximum stroke amplitude for these motors is 15 mm. For the 20 kW PWGs, the drift is even stronger. Since it seems that the piston offset can be accurately predicted as a function of operating conditions and piston/seal geometry, it ought to be possible (as mentioned previously) to design a piston that has just enough of the right piston-flexing so that the net unbalanced flux through the seal is zero, without any appreciable second order static pressure difference.

We decided to test this idea on a 4 kW PWG, because calculation and measurements show that for this size, the two terms in Eq. (12) are approximately the same magnitude. For a standard piston design, this means that the pistons drift twice as much as they would if the pistons were solid. But it also means that if the pistons were turned around so the "cupped" side faced the front space, hence with the radial pressure difference across the piston shell reversed, there should be no net drift. The first term in Eq. (12) remains the same, but the second term changes sign.

Actually turning the pistons around backward is a difficult modification to a PWG, but it is possible to reverse the pressure gradient on the piston shell by adding a piece to the existing piston. In the standard piston design of this (now outdated) model, the piston is held onto a piston stem by eight machine screws. If four are used instead, the other four holes can be used as passageways to an inner annulus formed by a second piece that inserts inside the original piston, as shown in Fig. 7(a). The white arrow in Fig. 7(a) shows how fluid can enter the inner annulus through one of the unoccupied screw holes. The inner annulus is sealed in the back by an O-ring. Fig. 7(a) is an approximation to one possible practical embodiment of an antidrift piston, shown in Fig. 7(b), where an annular channel is milled out of the front side of the piston, leaving an outer shell with a free edge on the front side, but only adding a little extra "dead volume."

A 4 kW PWG was tested with standard pistons in place, then reassembled with "anti-drift" pistons of the type shown in Fig. 7(a), and tested again. The resulting piston offset data is shown in Figure 8. Indeed, the piston offset is dramatically reduced with the antidrift pistons. However, the resulting offset is not quadratic in wave pressure, but has some reversals of direction not predicted

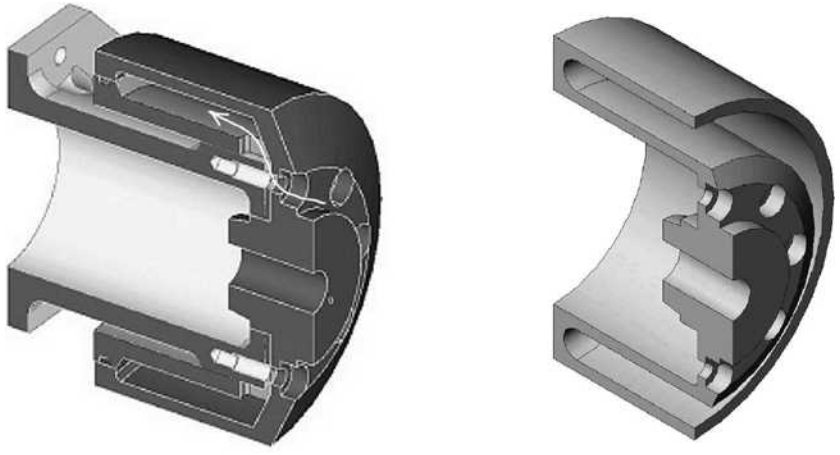

Figure 7. "Anti-drift" pistons, designed to have zero unbalanced mass flux through the clearance seal. In (a), a "standard" piston has been modified by means of an insert so that the inner diameter of the piston's outer shell now feels the pressure wave in the front space. In (b), a practical one-piece embodiment is shown.

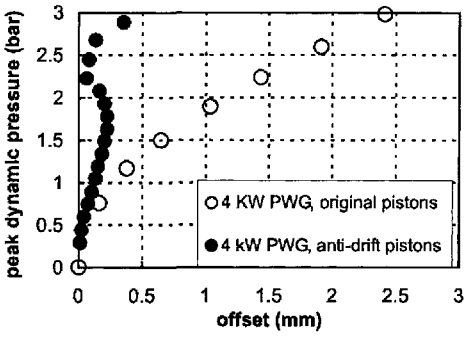

Figure 8. Piston-offset data for a 4 kW PWG with first normal and then "anti-drift" pistons.

by the theory. We tentatively attribute these to the sensitivity of the residual drift on details such as the relatively high flow resistance of the screw holes and imperfect sealing between the two parts of this composite piston. Pistons of the type shown in Figure 7(b) have been fabricated and installed in the same 4 kW PWG and await testing, but data was not available in time for this publication.

CONCLUSIONS

The dominant mechanisms that cause free pistons to drift axially from their nominal center positions are explained and quantified. The equations describing piston drift are verified with experiments on several different sized pressure-wave generators, which use free pistons activated by linear motors to provide acoustic power for acoustic-Stirling cryocoolers and other thermo-acoustic devices. The dominant mechanism for piston drift in large PWGs is found to be the flexing of hollow pistons in response to oscillating pressure differences across them. This phenomenon is shown to be useful for eliminating piston drift if the piston is properly designed.

ACKNOWLEDGMENT

This work was supported by Praxair, Inc.

Verification of Long Life Operation through Real Time Dynamic Alignment Tracking

W. J. Gully, E.D. Marquardt, and D. S. Glaister
Ball Aerospace and Technologies Corp.
Boulder, CO 80306

N. Abhyankar
Dynacs Engineering Co.
Albuquerque, NM 87106

T. Davis
Cryogenic Cooling Technology, Space Vehicles Directorate
Air Force Research Laboratory
Kirtland AFB, NM 87117

ABSTRACT

Oxford style mechanical cryocoolers rely on clearance seals to prevent wear between the pistons and cylinders. The support structure that maintains this clearance has to handle the large pneumatic forces that occur during operation in addition to the armature's weight. It is therefore more difficult to develop clearance seals that remain non-contacting during full power operation than when at rest.

A standard stiction ("static friction") test only confirms that a seal does not drag in quasi-static operation. To measure the clearance during operation requires a precise measurement of the piston location at high speeds. During the early development of long life space cryocoolers, Ball developed a unique system using proximity sensors that allowed for the measurement of the clearance gaps in real time under dynamic conditions. This system was critical to the development and verification of long life design features in Ball's space cryocooler product line.

This paper briefly describes that system and discusses measurements from the AFRL/Ball 35/60 K Stirling cycle mechanical cooler that has been in life test at the Air Force Research Lab (AFRL) Cryogenic Technological Laboratory. The data indicate that the cooler's clearance seals and alignment have remained essentially unchanged during more than 22,000 hours of continuous operation.

INTRODUCTION

During the development of mechanical cryocoolers in the mid 1990's, Ball developed an electronic means of indicating the alignment of the pistons within the cylinders. Although initially envisioned as an assembly tool, they were so useful that we integrated them into the cooler so we could monitor piston clearance during full power operation. The results obtained enabled us to determine the factors required for the cooler to be non-contacting under load. The process working

Cryocoolers 13, edited by R. G. Ross, Jr.
Springer Science+Business Media, Inc., New York, 2004

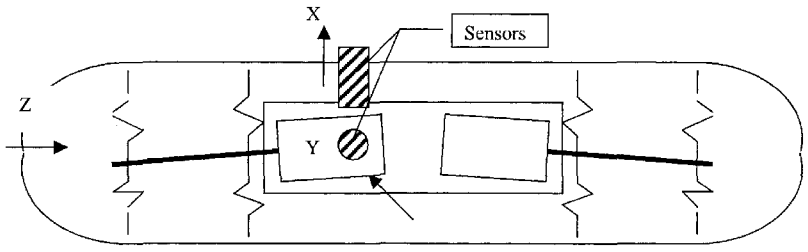

Figure 1. Unless nearly perfectly aligned, a piston will twist off axis and into the cylinder wall as it approaches top dead center because of pneumatic forces. We added sets of internal sensors to monitor these lateral deflections.

Figure 2. The three stage, Stirling cycle "35/60 K" cryocooler equipped with hermetic internal proximity sensors for monitoring the internal clearance gaps during the life test.

against alignment is depicted in the cartoon in Figure 1 of an opposed pair of compressors in a common housing. The figure shows how a spring-supported armature compressing gas in a central cylinder is deflected as the pistons approach top dead center. If not perfectly aligned, the piston tends to tip when faced with the high pressure. As it tips, high pressure spills down one side and low pressure spills up the other resulting in a substantial pressure difference across the piston. The pressure difference results in a substantial desabilizing force on the armature and the support system must be strong enough to react this force and keep the piston from touching the wall.

After our characterization tests[1,2] were over, we decided to leave the sensors in when we sealed the unit to see if there were any unexpected changes during subsequent tests. The sealed unit equipped with sensors is shown in Figure 2. Unfortunately, after the unit was characterized we discovered a problem and had to rebuild a portion of our displacer, which meant that we lost our data baseline. But a full set of data exists for our compressor, and we will discuss it in the remainder of the paper.

LIFE TEST AT AFRL

The cooler was delivered to the Cryogenic Technological Laboratory at Kirtland Air Force Base, NM in 2000, and entered an extended duration life test early in 2001. The cooler and its control electronics are shown together in an AFRL thermal test chamber in Figure 3. The cooler has logged more than 22,000 hours of operation in the ensuing three years. Performance data has been presented by AFRL in other presentations.[3] The life test has been suspended at intervals to allow for characterization tests, including these recent stiction and proximity sensor measurements.

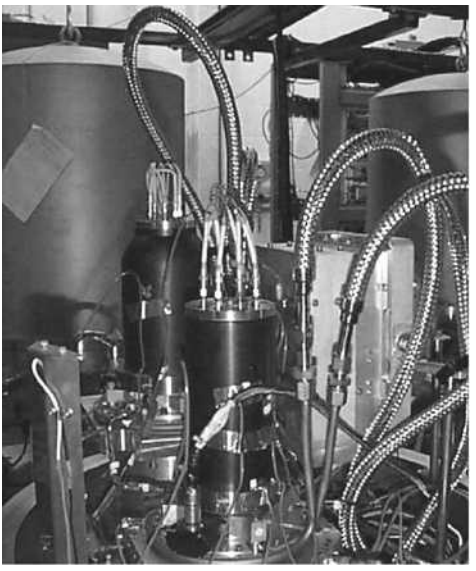

Figure 3. The cryocooler (foreground) and its control electronics (rear, right) installed in an environmental chamber at the Air Force Research Laboratory.[3]

Proximity Sensor Measurements

The sensors can be used in a variety of ways. The simplest measurement is to look at the gravitational sag of a static (non-operating) cooler. Next, we show the sensor output during a "quasi-static" stiction test. Finally, we present dynamic data from an operating cooler.

Static Fall

The simplest possible measurement is to note the location of the piston when we lay the cooler on its side. Obviously, it falls "down" in the direction that happens to be below the centerline. If we rotate the cooler about its long axis to change the downward direction, a plot of the X and Y deflections results in a circle, as shown in Figure 4. Because we were free to push the piston to the wall when it was in assembly, we know that the magnitude of the fall is about 40% of the clearance gap. The circle provides direct evidence of a substantial region of clearance around the compressor's neutral axis. Ideally, the cooler would operate around this neutral axis when operating vertically in 1-G or in 0-G.

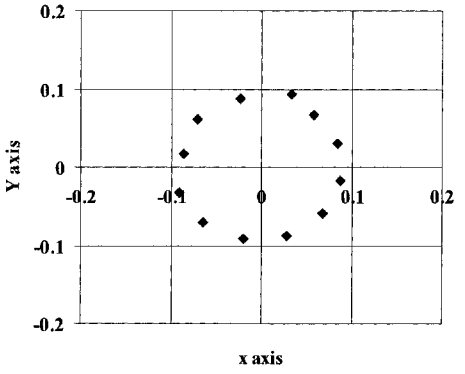

Figure 4. C1's piston gravitational sag as monitored by a pair of orthogonal sensors as a horizontal cooler is rotated around its long axis. From data taken at AFRL, September 1998.

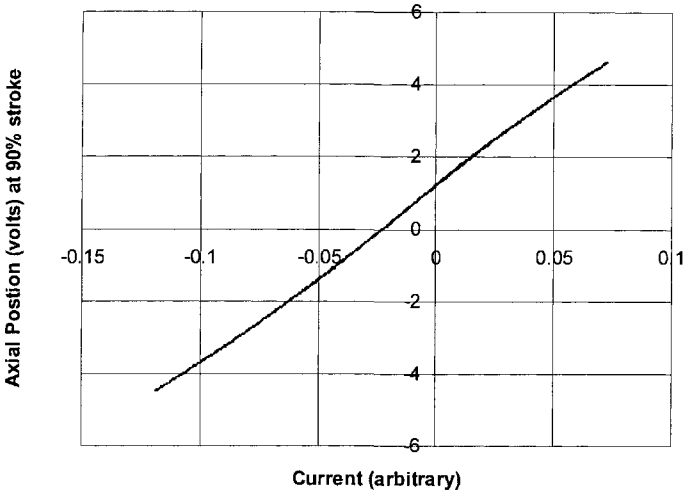

Figure 5. A stiction plot for the 2nd Ball compressor armature, January 2004.

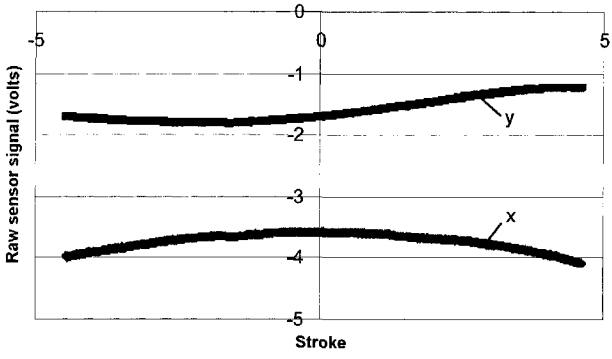

Figure 6. An example of the apparent but spurious radial motion in x and y directions during a stiction test that is actually a result of imperfections in the sensor target.

Stiction

The next interesting measurement is to monitor the apparent radial location of the piston as it moves axially during a stiction test. Ideally, we should see nothing as the piston travels straight down the cylinder. But actually, the proximity sensors show false signals because their targets are shifting along underneath and they end up looking at different regions of the target. These false signals are really imperfections in target form and alignment, and we record them during the stiction test.

Stiction tests are a good way to detect if the alignment has completely failed and the piston is actually rubbing along the cylinder. In the test the compressor is driven axially over its stroke very slowly to avoid pressure hysteresis. Then, a plot of *axial* position against current opens into a hysteresis loop. The loop opens because friction always opposes the motor force, so the force at any point will depend upon whether the piston is moving to the left or to the right. A recent stiction plot for compressor 2 is shown in Figure 5. The spurious x and y radial displacements taken from the proximity sensors during the test are shown in Figure 6.

The apparent radial motion of C2's piston during the stiction test is shown in Figure 6. We know from tests during its assembly that the apparent motion in Figure 6 is spurious and that the

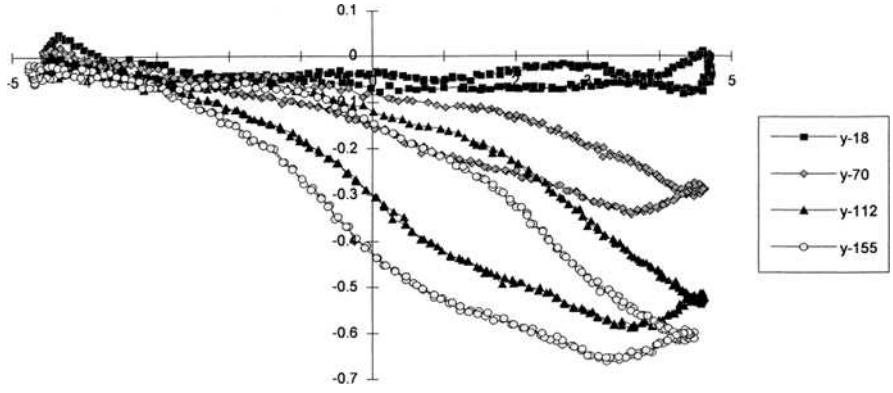

Figure 7. A plot of radial motion in the Y direction when the cooler is operating normally, as a function of charge pressure. We were able to manipulate the pressure before it was sealed.

piston actually travels in a straight line. The shifts in Figure 6 are due to imperfections in the target. We re-measured these patterns recently and found that they were, as expected, the same as when the cooler was built. This is essentially a background that has to be subtracted from the signal recorded for an operating cooler.

Dynamic Operation

The next step is to observe a cryocooler operating at power. A good example of what can be seen is shown in Figure 7 and discussed further in Reference 1. For reference, the available clearance (vertical axis) in this and subsequent figures is just short of ± 1 unit, and full stroke corresponds to ± 5 units on the horizontal axis.

The four traces illustrate three characteristic of the changes in the piston's radial motion as a function of charge pressure, as the compressor operates at full stroke at 36 Hz. First, the sideways deflection at top dead center (to the right in Figure 7) only occurs when there is a substantial pressure in the cooler, validating the model discussed in conjunction with Figure 1. Second, the curves often have other oscillations on them reflecting various damped armature modes. Finally, they are extended. We know that if a piston touches the wall its pattern shrinks significantly.

Recent Dynamic Measurements

We can no longer manipulate the cooler's pressure because it is sealed. But we can measure the dynamic excursions at comparable strokes and compare them with similar measurements made when the cooler was first built. We present our results in pairs, Figures 8 and 9 for compressor 1, and Figures 10 and 11 for Compressor 2. The first member of the pair was recorded in 1998, and the

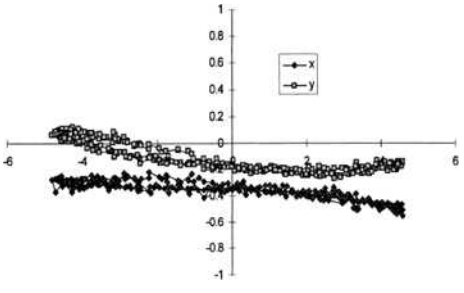

Figure 8. The x and y lateral motion in compressor C1 as a function of stroke when it was built, 1998.

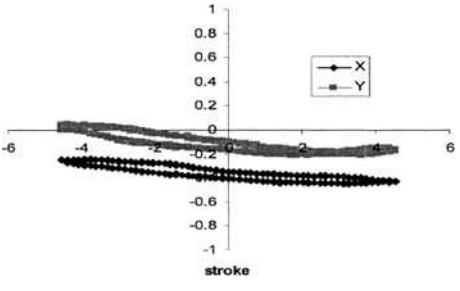

Figure 9. The x and y motion measured in 2004, is similar both in magnitude and in general form.

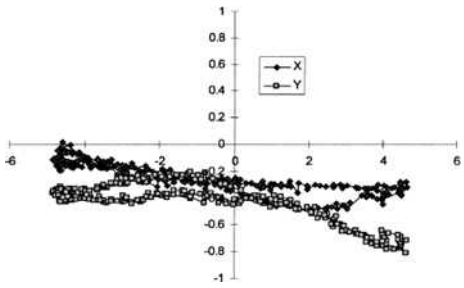

Figure 10. The x and y lateral motion of compressor C2 as a function of stroke when it was built in 1998.

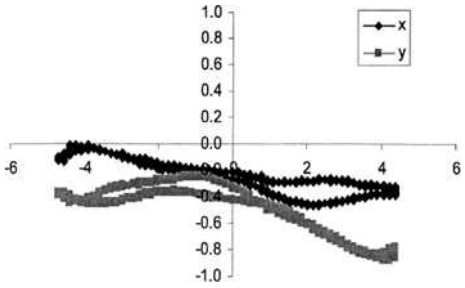

Figure 11. The x and y lateral motion of C2 as it appears today (2004) is again similar in magnitude and in general appearance.

second member was recorded in February, 2004. Both coolers are running at 90% stroke, at 36 Hz, at similar pressures, and in a vertical orientation. We see that the signals are similar in magnitude and appearance. As far as we can tell, there has been no substantial change in operation over the intervening years.

SUMMARY

Ball Aerospace equipped its engineering model 35/60 K Stirling cryocooler with internal proximity sensors. They were initially developed for aligning the cooler and for understanding the pneumatic forces that tend to push the pistons off center. But we left them in when we welded the cooler, something we don't ordinarily advocate, so we could monitor the cooler during its life test. In a flight cooler the information gained would not be worth the added risk and complexity of adding the sensors.

AFRL is conducting an extended duration life test of the Ball 35/60K multistage Stirling cycle mechanical cooler. At present, the cooler has logged more than 23,000 hours of operation. As part of this life test we are watching the proximity sensors for changes over time. It is comforting that recent measurements are similar to those taken when the cooler was first built. Although we should not be surprised, it is still amazing that a mechanism that has flexed nearly 3000 million times repeats its trajectory to within a fraction of a thousandth of an inch.

REFERENCES

1. Gully, W.J., *et.al*, in "Qualification Test Results for a Dual Temperature Stirling Cryocooler," *Cryocoolers 10*, Ross, R.G. Jr., ed., Kluwer Academic/Plenum Publishers, 1999, pp. 59-65.
2. Berry, D., *et.al*, "Two-Stage Cryogenic Refrigerator for High Reliability Applications," *Advances in Cryogenic Engineering*, Vol. 41, Kittel, P., ed., Plenum Press, NY, 1996.
3. Bruninghaus, C.H.Y., Tomlinson, B.J., and Abhyankar, N., "Performance Characterization of the Ball Aerospace 35/60K Protoflight Spacecraft Cryocooler," *Cryocoolers 12*, Kluwer Academic/Plenum Publishers, New York (2003), pp. 51-58.

Sensorless Balancing of a Dual-Piston Linear Compressor of a Stirling Cryogenic Cooler

V. Doubrovsky

Wolfson School of Mechanical and Manufacturing Engineering, Loughborough University, Loughborough, Leicestershire, LE11 3TU, UK

A. Veprik, N. Pundak

Ricor Ltd, Cryogenic and Vacuum Systems, En Harod Ihud, 18960, Israel

ABSTRACT

Long-life, highly reliable and low-cost miniature Stirling cryogenic coolers are the core components in a wide variety of cryogenically cooled electro-optic, high temperature super-conductive and vacuum applications. The linear compressors of such coolers are known to be the major source of harmful vibration disturbances affecting the operation of these inherently vibration sensitive systems.

The dual-piston approach to the design of the linear compressor yields intrinsically low vibration export and, therefore, is widely accepted across the industry. However, the residual vibration export originated from unavoidable technological tolerances, natural wear and contamination cannot be completely eliminated.

The ultra-low vibration export from a dual-piston compressor may be attained using active balancing. A dedicated digital controller normally relies on internal sensors (e.g. LVDT) for direct measuring of the pistons' motion or an external sensor (e.g. accelerometer or load cell) for measuring the residual vibration export. This eventually complicates the entire design and makes the cooler more expensive and less reliable.

The authors disclose the recent efforts made by Ricor towards the development, implementation and testing of a sensorless adaptive feed-forward controller for the balancing of dual-piston compressors. In this novel approach, the detection and synchronization of the pistons' velocities relies solely on the real-time data acquisition (motors' voltages and currents) and the general model of the linear "moving coil" or "moving magnet" motor.

The attainable performance of the controller was evaluated through the full-scale testing performed on the Ricor model K535 linear dual-piston Stirling cryogenic cooler.

INTRODUCTION

Linear Stirling coolers normally comprise a linear compressor providing for the pressure pulses and the reciprocal volumetric change of the working agent (typically Helium) in the expansion space of the cold finger.

Cryocoolers 13, edited by R. G. Ross, Jr.
Springer Science+Business Media, Inc., New York, 2004

The above linear compressors are typically driven by the linear "moving coil" or "moving magnet" motors. In the "moving coil" linear actuator an alternating current is passed through a coil attached to a piston assembly and located between the poles of a stationary permanent magnet. In a "moving magnet" approach the coil is fixed and the permanent magnet is attached to the piston assembly.

Since such coolers are often used in cryogenically cooled and inherently vibration sensitive electro-optic, high-temperature superconductive and vacuum applications, the issue of exported vibration originated by the imbalanced motion of the compressor's internal components becomes a concern governing the entire design approach. Nowadays, the above vibration export is typically controlled using a dual-piston design featuring a pair of opposed compressors arranged back-to-back with their pistons driven by the common current and, therefore, reciprocating in an opposite mode. In such a design, because of the common current and shared compression space, some sort of self-synchronization takes place and the vibration is virtually eliminated due to quasi-synchronized counter-motion of the above pistons. This simplest approach became prevalent across the industry and is used by the vast majority of the cryocooler manufacturers, including AIM, Astrium, BEI, DRS, Hymatic, Leibold, Matra-Marconi, Raytheon, Ricor, and Thales.

This method, however, does not allow for receiving deep dynamic balancing due to the unavoidable asymmetry of the opposite compressors (dissimilar wear, friction factors, spring constants, clearance seals, force of permanent magnets, etc.).

Better performance might be attained by connecting the opposed compressors in parallel, with the possibility of accurate manual adjustment of the relative phase and amplitude of the driving voltages to the compressors in order to provide for a minimum dynamic force export. The performance of such a balancing, however, strongly depends on the ambient temperature, heat load and spatial orientation of the cooler. Since the motors' currents in such a design are independent, the compressor losses the above self-synchronization feature. Moreover, this approach is not viable for controlling the vibration export at higher-order harmonics.

Another, more expensive, yet much more efficient solution is based on instant monitoring followed by the active adjustment of the motion of the pistons, relying on the system of automatic control producing the separate voltages to drive each motor. In this approach, one of the two back-to-back compressors is designated to be a "*Master*" and other one to be a "*Slave*." The "*Master*" motor is driven by the sinusoidal signal, the magnitude of which is determined by the temperature controller with the purpose of automatically maintaining the desired temperature of the cold finger tip. The "*Slave*" motor is driven by a voltage composed with the purpose of canceling the overall vibration export. In other words, the "*Slave*" compressor may be thought of as an active balancer relatively to the "*Master.*"

Obviously, the proper operation of such an active controller should rely upon an appropriate "*Observer*" evaluating the mentioned vibration export. There are two known approaches to implementing the above "*Observer.*"

The first one relies on using the resultant vibration estimator, e.g. external load cell or accelerometer.[1-4] There are some disadvantages related to using such an approach. To start with, such sensors and dedicated signal conditioners are quite expensive and have to be of a high quality to ensure monitoring of relatively low levels of vibration with high signal-to-noise ratio (especially when approaching low vibration levels). Further, there exist particular transfer paths between the actual force export and measured vibration signal. In some instances, depending on the dynamic properties of such a path and, therefore, the transfer functions involved, the entire active control system appears to be too sensitive or even unstable. Adding the correction circuitry may be helpful, but requires the preliminary knowledge of the dynamic properties of the host structure and, quite often, the on-site adjustment involving finding optimal placement for the vibration sensor and tuning the active controller. A final, additional possible complication is related to the presence of the vibration export from the cooler's expander, which becomes the dominating source after the vibration export from the compressor is essentially cancelled. Since the motion of the expander is lagged by approximately 90 degrees relative to the piston's motion,

it becomes impossible to provide for appropriate compensation. This leads to confusion of the controller and extra instability in its operation.

The second method relies on using pairs of motion sensors, (e.g. LVDTs, capacitance sensors, accelerometers) performing direct monitoring of the piston's motion. This method potentially yields much more accurate and stable active vibration control which, in this instance, is inherently independent of the dynamics of the host structure and vibration produced by the other components of the cooler. The obvious disadvantage is the need for the extra expense of two additional sensors and dedicated signal conditioners, feedthroughs, modification of the existing coolers, etc.

In this paper, the authors disclose the recent efforts made by Ricor towards developing a so-called sensorless approach to the balancing of dual-piston compressors in which the detection and synchronization of the pistons' motion relies solely on the general model of the linear "moving coil" or "moving magnet" motor and real-time monitoring of the motors' voltages and currents. The entire approach is based upon the idea of using a linear motor as a velocity sensor, as, for example, is discussed in [5] in relation to the stroke control in a single-piston compressor.

EQUIVALENT ELECTRICAL CUIRCUIT OF THE LINEAR MOTOR VELOCITY EVALUATION

The equivalent electrical circuit of an ideal linear "moving coil" or "moving magnet" motor can be effectively thought of as a series connection of a voltage source, resistor, inductor and back-emf source [6-9], which is governed by the well-known equation:

$$L\frac{dI}{dt} + RI + \alpha\frac{dX}{dt} = U, \tag{1}$$

where L and R are the motor inductance and active resistance, U is the driving voltage applied across motor terminals, I is the current through the motor coil, α is the motor velocity/voltage or, alternatively, force/current constant and X is the piston displacement.

Using indices "*m*" and "*s*" for the "*Master*" and "*Slave*" opposed motors, equation (1) yields:

$$L_m\frac{dI_m}{dt} + R_m I_m + \alpha_m\frac{dX_m}{dt} = U_m; \qquad L_s\frac{dI_s}{dt} + R_s I_s + \alpha_s\frac{dX_s}{dt} = U_s, \tag{2}$$

from which follows the simple rule for evaluating the piston's velocities:

$$\frac{dX_m}{dt} = \frac{U_m - L_m\, dI_m/dt - R_m I_m}{\alpha_m}, \qquad \frac{dX_s}{dt} = \frac{U_s - L_s\, dI_s/dt - R_s I_s}{\alpha_s}. \tag{3}$$

This relies on the motor's currents, voltages and the major motor's parameters, such as inductance, resistance and motor volt/velocity or force/current constants [5]. It is obvious that the accuracy of the evaluation of the velocities and, therefore, balancing performance depends strongly upon the accuracy of the evaluation of the above constants.

IDENTIFICATION OF MOTOR CONSTANTS

The values of the inductance and resistance of the motor were experimentally defined, based on measuring the stalled motor impedance at different currents and axial positions.

From experiment undertaken with the linear motor of a Ricor K535 cryogenic cooler, the value of the coil active resistance conducted at an ambient temperature of 23°C was found to be 0.4 Ohm for either motor practically independent of the piston position. The active resistance of the motor coil follows the well-known rule $R = R_0(1 + \beta\Delta T)$, where R_0 is the coil resistance at reference temperature, $\beta = 0.0039$ deg^{-1} is the temperature coefficient of electrical resistance for the High Conductivity Copper and ΔT is the temperature difference with regards to the reference temperature.

From experiment, the value of the motor inductance varies slightly from 5.6 mH to 5.8 mH depending on the piston position. It is important to note that this value is practically independent of the coil temperature and current.

Static evaluation of the force/current constant yielded a= 8.8 N/A practically independent of the coil temperature and current.

The above experimentation has shown that the motor's parameters which are required for calculations per Equations (3) are practically independent of the magnet axial position, motor current and temperature[6], although not the coil resistance, which, however, may be easily compensated for.

EXPERIMENTATION ON ACCURACY OF INDIRECT VELOCITY EVALUATION

Experimentation on the accuracy of the indirect measurement of the piston velocity has been conducted at a nominal driving frequency of 50Hz.

Figure 1a shows the schematics of the experimental rig where the linear motor (1) of the Ricor K535 cryogenic cooler was mounted upon the fixture (2) attached to the Newport pneumatically vibration isolated table (3). For the reference, the velocity of the piston assembly was directly monitored using the Bruel & Kjær Type 4383 accelerometer (4) and Type 2635 Charge Amplifier (5) operating in the Integrator mode. The motor was driven by the sinusoidal signal produced by the digital controller (6) relying on the National Instruments 7030/6040 E-series RT MIO board (see http://ni.com) using one full-size PCI slot of the dedicated PC (7) and running under the National Instruments LabView software. The electrical signal produced by the above controller through the power amplifier (8), relying on two off-the-shelf Advanced Motion Control series 50A servo amplifiers Type 50A20 and FC10010 filters (see http://www.a-m-c.com), as shown in Figure 1b, was supplied to the motor, the voltage and current of which were sensed by the dual-channel multimeter (9), as shown in Figure 1c, supplying the appropriate voltages to the above controller for the indirect evaluation of the motor velocity using Equation (3). The reference signal produced by the accelerometer was supplied to the controller for comparison.

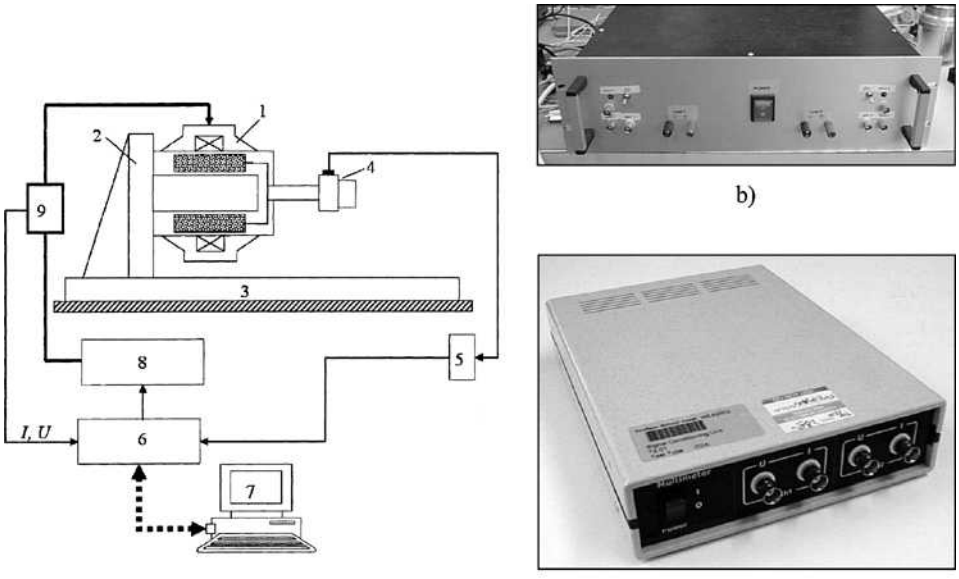

Figure 1. Experimentation on accuracy of indirect velocity evaluation.

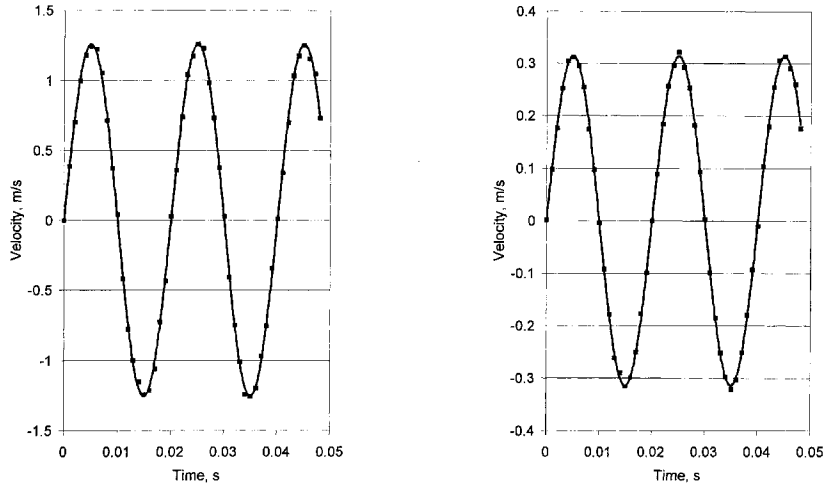

±4 mm stroke ±1 mm stroke

Figure 2. Accuracy of indirect motor velocity evaluation

In the course of experimentation, the motor parameters were treated as the tuning parameters and varied slightly around the values obtained from the above experimentation. As a result of this variation, the best fit was achieved at maximum stroke and then experiment was repeated at smaller strokes.

Figure 2 shows typical results of experimentation at ±4mm and ±1 mm strokes, respectively, where solid lines correspond to the velocity signal produced by the accelerometer and squares show that obtained using the calculation procedure per equation (3).

CONTROL ALGORITHM FOR ACTIVE BALANCING

Provided that the pistons have identical masses, the balancing would be accomplished if the above opposite pistons follow identical waveforms. This is typically achieved by matching the magnitudes and phases of the pistons' motions at the distinctive frequencies, namely, at the driving frequency and its higher harmonics.

This leads to a *narrowband frequency control* where the evaluation of the above harmonics may rely upon *heterodyne filtering* showing intrinsically exceptional performance in terms of being insensitive to the external disturbances such as shock, vibration and other disturbances containing frequencies equal to the driving frequency and its harmonics.

Since external temperatures and heat loading upon the cryogenic cooler vary slowly, the balancing controller may be relatively slow and, therefore, an adaptive feed-forward control with a *least mean square* (LMS) algorithm is quite suitable for our purposes. The basic theory behind the feedforward control using an LMS algorithm and its practical implementation can be found in references [9-13].

Figure 3 shows the schematics of such a controller, where ω is the angular driving frequency, the numerical value of which is supplied to Generator_1 producing two voltages, namely $\sin\omega t$ and $\cos\omega t$. One of these is used to drive the "*Master*" motor through the master power amplifier PA_m, the amplification factor of which is governed by the temperature PID controller comparing the current and the reference temperatures T and T_{ref}, respectively.

The voltage and current of the "*Master*" and "*Slave*" motors are then sensed using the appropriate multimeters and supplied to the Master and Slave Velocity Estimators calculating the velocities $\dot{X}_m$ and $\dot{X}_s$ using equations (3).

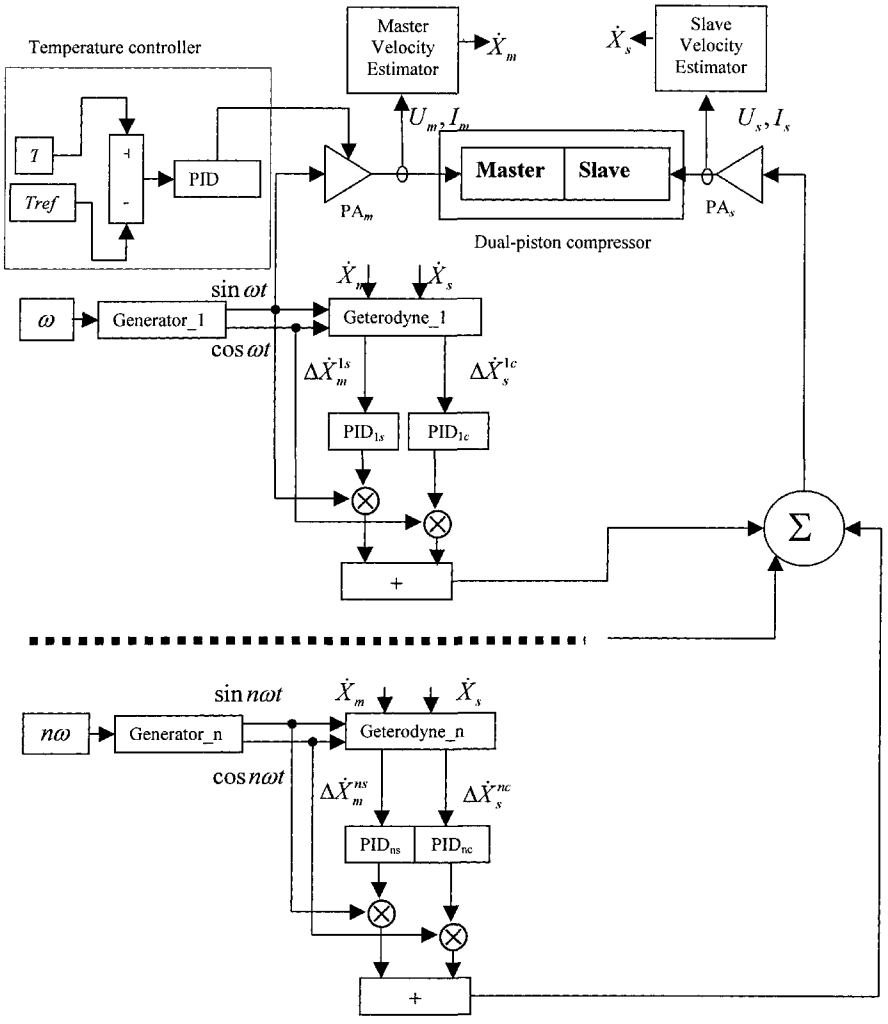

Figure 3. Adaptive feedforward control with heterodyne filtering

The two above voltages, $\sin\omega t$ and $\cos\omega t$, produced by Generator_1 are also supplied to Geterodyne_1 for the spectral analysis and evaluation of errors which are the actual differences between the *sine* and *cosine* components of the fundamental harmonics of the "*Master*" and "*Slave*" pistons velocities, namely: $\Delta\dot{X}_m^{1s}$ and $\Delta\dot{X}_m^{1c}$. These errors are then supplied to the inputs of the PID controllers PID_{1m} and PID_{1s}, the outputs of which, after summation, are supplied to the *"Slave"* power amplifier PA_s. The above controllers are tuned in such a manner as to eventually minimize the above errors, thus providing for a dynamic balancing of the fundamental component of the vibration export.

Similarly, the higher-order harmonic components may be eliminated. In Figure 4, the control is limited by n harmonics, as defined by the initial vibration export, application requirements and available computational resources.

PRACTICAL EVALUATION OF SENSORLESS BALANCING CONTROLLER AND EXPERIMENTATION ON ATTAINABLE PERFORMANCE

Figure 4 portrays the experimental rig (a) and its schematics (b). The Ricor K535 dual-piston linear Stirling cryocooler (1) was mounted upon the pneumatically vibration isolated Newport table (2) using the multi-component Kistler 9347B force link (3). Electrical output of the dynamometer through the Kistler charge amplifier Type 5010A (4) was passed to the Data Physics ACE Signal Analyzer (5) occupying the PCMCIA II slot of the dedicated notebook. This arrangement was calibrated and used for measuring the vibration export produced by the above cryocooler.

The two independent AC voltages were produced by the controller which was implemented as a National Instruments LabVIEW stand-alone application running on the above NI PCI 7030/6040 real-time board installed inside the dedicated PC (6). These voltages were then supplied to the above dual-channel power amplifier (7) through the connection box (8) and further used to drive the "*Master*" and "*Slave*" compressors, respectively.

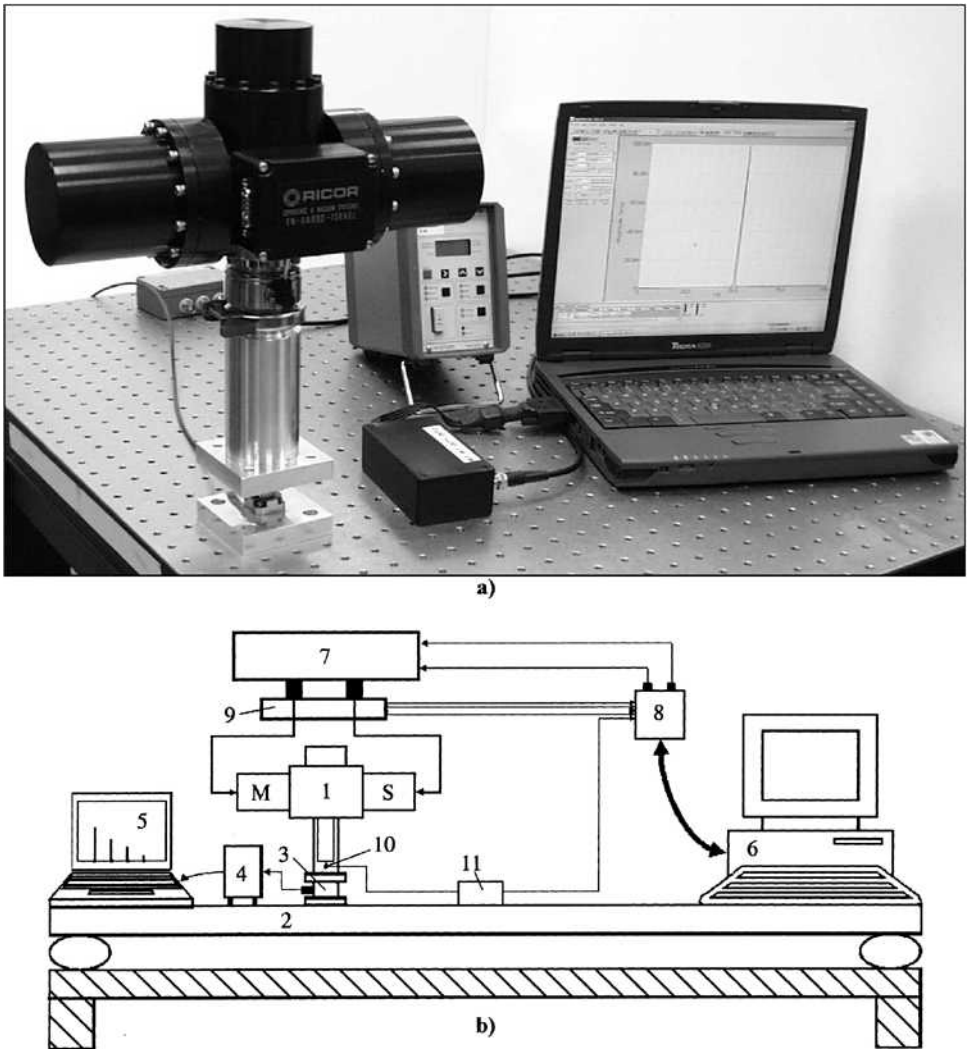

Figure 4. Experimental rig.

The multimeter (9) was used to monitor the motor's currents and voltages. The analogue outputs of the multimeter were then passed to the A/D inputs of the controller through the connection box. The electrical signal of the thermocouple (10), which was mounted upon the cold finger of a cryogenic cooler, through the conditioning amplifier (11), was supplied to the controller. This allows for the cooler operation in a closed loop mode.

Figure 5 shows the performance of the above controller maintaining the cold finger temperatures of 90 K and 60 K. Firstly, the cooler was driven using the above common current mode. Under these conditions the net power consumption was 30 W and 60 W, respectively. The vibration export produced in the above two cases is shown in Figure 5a,b. Then the cooler was driven using the above explained balancing controller suppressing the first two harmonics of the vibration export. Under these conditions the net power consumption remained 30 W and 60 W, respectively. The vibration export produced in this case by the balanced cooler is shown in Figure 5c,d. From Figure 5, the vibration export at the driving frequency was 23 and 27-fold reduced, and the vibration export at the first harmonic was 15 and 17-fold reduced.

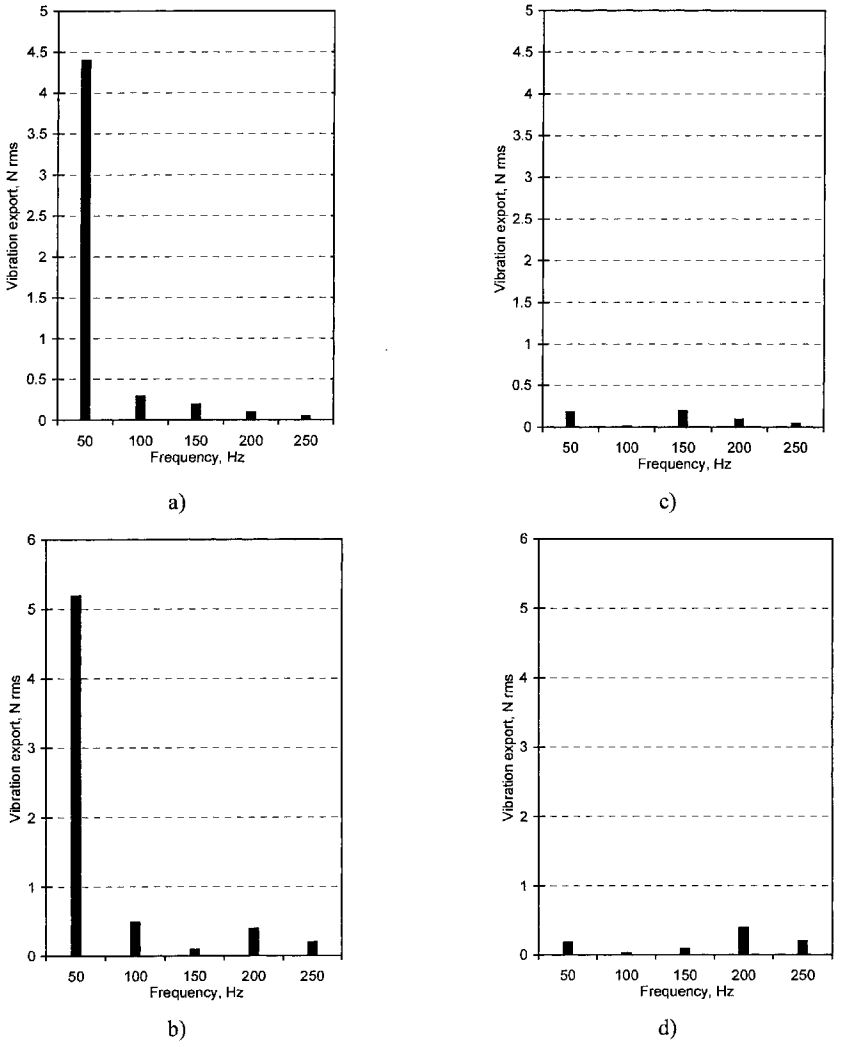

Figure 5. Performance of balancing controller at steady-state mode.

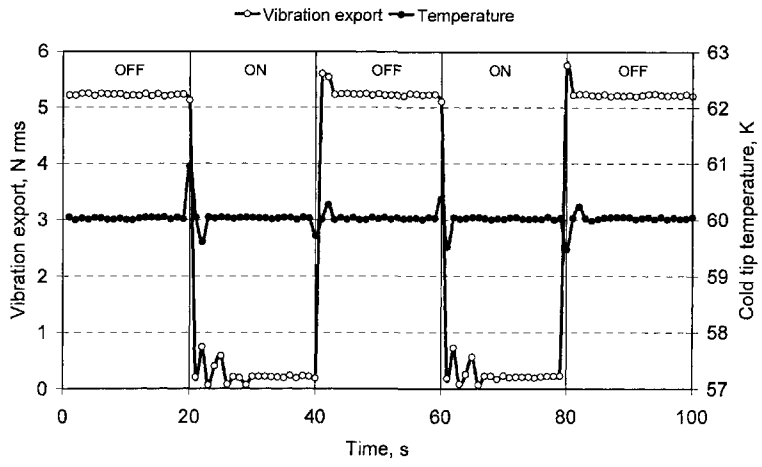

a)

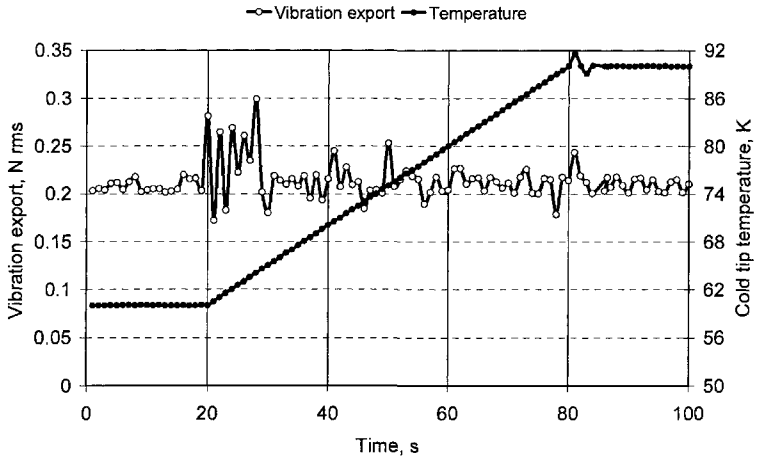

b)

Figure 6. Performance of balancing controller at transient processes.

Figure 6a shows the stability of the controller performance both in terms of vibration cancellation and cold finger temperature stabilization during transients produced by periodic switching from "Vibration controller ON" to "Vibration controller OFF" modes. Figure 6b shows the performance of the balancer controller during the transition from the cold finger temperature of 60K to 90K. From the above experimentation, the controller operation is quite stable and yields sufficient performance in terms of vibration and temperature control.

Also, it is shown that the temperature control, which is still the main feature of the controller, is not affected in any way by the balancer operation when in steady state. Weak deviations of the temperature from a required value were observed only during transition period.

CONCLUSIONS

The quasi-sensorless balancing method has proven to be feasible for active vibration control of the linear twin-piston compressor of the cryogenic cooler. Further efforts will be aimed at developing the temperature compensation and implementation of such an approach using a miniaturized industrial compact controller.

ACKNOWLEDGMENTS

We would like to show our appreciation to Israeli MOD and MOFAT under whose financial support the Project was undertaken. The authors are grateful to Mr. I. Zontag for his very helpful and enthusiastic support. Special thanks go to Mr. S. Riabzev and Mr. G. Vilenchik for the technical assistance during the experimentation stage of the Project.

BIBLIOGRAPHY

1. Flint E, Flannery P, Evert M and Anderson E, "Cryocooler disturbance reduction with single and multiple axis active/passive vibration control systems," published electronically at http://www.csaengineering.com/techpapers/techpapers.html, CSA Engineering, Inc.
2. Collins SA, Paduano JD, "Multi-axis vibration cancellation for Stirling cryocoolers," *Proceedings of the SPIE Cryogenic Optical Systems and Instruments Conference VI*, Orlando, FL, Vol. 2227 (1994), pp. 145-155.
3. Johnson DL, Collins SA, Ross RG, Jr., "EMI Performance of the AIRS Cooler and Electronics," *Cryocoolers 10*, Plenum Publishing Corp., New York (1999), pp. 771-780.
4. Yeoung-Wei A Wu, "Stirling-cycle cryogenic cooler using feed-forward vibration control," UK Patent 2279770 (1995).
5. Redlich, R, "Method and apparatus for measuring piston position in a free piston compressor," US Patent 5,342,176 (1994).
6. Redlich R, Unger R, Van der Walt, "Linear compressors: motor configuration, modulation and systems," *Proceedings of the International Compressor Engineering Conference*, Purdue University, West Lafayette, IN (1996).
7. Marquart E, Radebaugh, R, "Design Equations for linear compressor with flexure springs," *7th International Cryocooler Conference Proceedings*, Air Force Phillips Laboratory Report PL-CP—93-1001, Kirtland Air Force Base, NM, April 1993, pp. 783-804.
8. Narayankhedkar KG, Nagaraja N, Bapat SL and Patel LN, "Analysis of linear motor for electromagnetic driven cryocooler," *Proc. of International Conference on Cryogenics*, Macmillian India Ltd., New Delphi, India (1988), pp. 284-292.
9. Pollak E, Friedlaender FJ, Soedel W, Cohen, R. "Mathematical model of an electrodynamic oscillating refrigeration compressor," *Proc. of the Purdue Compressor Technology Conf.*, Purdue University, (1978), pp. 246-259.
10. Flint E, Anderson E, Flannery P, "Active/Passive Counter-Force Vibration Control and Isolation Systems," *Proceedings of the 2000 IEEE Aerospace Conference*, Big Sky MT (2000).
11. Anderson E, Evert M, Glease R, Goodding J, Pendelton S, Camp D, Fumo J, Jessen M, Cobb R, Erwin S, Jensen J, Satellite, "Ultraquiet Isolation Technology Experiment (SUITE): electromechanical Subsystems," *Proceeding of the 1999 SPIE Smart Structures and Materials Conference*, Volume 3674, (1999), pp 308-328.
12. Kou, S, Morgan, *Active Noise Control Systems*, John Wiley and Sons, New York (1996).
13. Widrow S, Morgan D, *Adaptive Signal Processing*, Prentice Hall Inc, Englewood Cliffs, NJ (1985).

Dynamically Counterbalanced Single-Piston Linear Compressor of a Cryogenic Cooler

A. Veprik, I. Nachman, N. Pundak

Ricor Ltd, Cryogenic and Vacuum Systems,
En Harod Ihud, 18960, Israel

ABSTRACT

Low vibration Stirling cryocoolers often rely on dual-piston linear compressors, the known disadvantages of which, as compared to their single-piston rivals, are: low reliability, increased power consumption, price, bulk, sensitivity to external vibration and g-forces. However, because of the inherently low level of vibration export, as required in numerous vibration sensitive electronic and electro-optic applications, the dual-piston approach has become prevalent in today's industrial practice.

The authors report on the novel patent pending approach to the passive control of a fundamental component of a vibration export from a single-piston compressor down to the levels typical for the actively controlled dual-piston rival. The technique relies on the principle of dynamic counterbalancing, where an auxiliary movable mass is, on the one hand, flexibly attached to a movable piston assembly and, on another hand, to the stationary compressor casing using auxiliary mechanical springs. The proper design of such a "spring-mass-spring" counterbalancer yields zero vibration export at minimum electrical power and current consumed by the motor.

Based on the theoretical analysis, the design of the single-piston compressor of 1 W at 77 K Ricor model K529N Stirling cryocooler was enhanced by adding such a counterbalancer. The obtained experimental results are in full agreement with the theoretical prediction. From experiment, the vibration export at driving frequency was reduced 57-fold at practically the same electrical current and power consumption as compared with the basic cooler.

INTRODUCTION

Linear Stirling coolers typically comprise a linear compressor providing for the required pressure pulses and the volumetric reciprocal change of a working agent (Helium, typically) in the expansion space of the cold finger.

The above linear compressors are typically driven by linear motors of the "moving coil" or "moving magnet" types. In the "moving coil" linear actuator an alternating current is passed through a coil attached to a piston assembly and located between the poles of a stationary permanent magnet. In a "moving magnet" linear actuator the coil is fixed and the permanent magnet is attached to the piston assembly.

The single-piston linear compressors are known to be major sources of harmful vibration export, which is produced by the cryogenic coolers. This is caused, primarily, due to an unbalanced motion of the moving piston assembly, where the resulting vibration export is, in essence, the force

Cryocoolers 13, edited by R. G. Ross, Jr.
Springer Science+Business Media, Inc., New York, 2004

of inertia developed by the moving parts with the magnitude being the product of the total moving mass, the magnitude of reciprocation and the driving frequency squared. The above imbalance leads to an essential vibration export comprising a well-pronounced fundamental frequency component, along with comparatively small higher-order harmonics. Since the prior-art designs do not allow for canceling such vibration at the source level, it is inevitably exported into the supporting structure to which the cooler is normally rigidly attached.

The simplest known approach to minimize this force relies on reducing the moving assembly mass, piston stroke and driving frequency. However, in so doing, the force export may be reduced to a particular limit only.

Another approach is based on using internal vibration isolation when the cylinder assembly is flexurally mounted inside the compressor casing and the gas transfer from the above movable cylinder assembly to the stationary casing relies on the flexible transfer line.[1] By choosing the natural frequency of such a vibration isolator to be well below the driving frequency, the vibration export may be essentially reduced. The drawback of such an approach is that under severe environmental conditions, such as shock, wideband random vibration, sine vibration with variable frequency and high g-forces, the above cylinder assembly is capable of developing excessive dynamic deflection damaging the internal transfer line along with the compressor interior. Tight tolerances, imposed on the free rattle space, call for the use of a stiff and heavily damped internal isolator, thus diminishing its performance. Additional drawback is that the lifetime of the internal flexible transfer line is limited.

A further approach is based on the principle of external vibration isolation when the entire compressor is supported from the enclosure of a cooled device using a compliant vibration-isolating and thermo-conductive interface. Examples of such an arrangement are disclosed, for instance, in US patents 5,129,232 and 5,864,273.[2,3] The known disadvantages of this approach are: complication of the mechanical design, increase in mass and bulk, sensitivity to external vibration, shock and g-forces, additional heat load on the cooler, complicated heat sinking and, therefore, degraded cooling performance.

In US patent 5,895,033[4] it is shown how a tuned dynamic absorber may be applied to the vibration protection of the sensitive equipment mounted in close proximity to the liner compressor. In this approach, the natural frequency of an auxiliary undamped spring-mass system, which is externally attached to the compressor housing, has to be precisely equal to the driving frequency. Since the compressor housing is normally attached rigidly to the system's enclosure, the known disadvantage of such an approach is that the relatively bulky dynamic absorber (20% of the entire system, typically) is required in order to achieve the desired vibration control. Further known disadvantages inherent to this approach are high sensitivity to even a small variation in the driving frequency and to environmental vibration and shock.

A combination of a stiff and heavily damped vibration isolation mounting and a tuned dynamic absorber is disclosed in[5] and US patent 4,860,543.[6] Using an optimally stiffened and damped vibration isolator allows the use of an essentially smaller dynamic absorber (20% of the compressor mass, typically). However, the above-mentioned sensitivity to the driving frequency, complication of mechanical design, heat sinking and degraded performance of such an arrangement, prevents this approach from being used in many practical applications.

Recent US patents disclose active vibration cancellation systems containing a vibration sensor, sophisticated digital controller and an actuator, as may be seen, for example, in US patents 5,582,013 and 6,169,404.[7,8] Such active systems yield very accurate suppression of vibration disturbance produced by the compressor. The disadvantages of this approach are, however, higher costs and bulk, lower reliability, additional power consumption in use and, consequently, additional heat emission.

The vibration export from the linear compressor may also be eradicated using a dual-piston design where the fine balancing of the fundamental and higher-order harmonics is usually attained by an active control system relying on appropriate sensors and a sophisticated digital controller, as disclosed, for example, in US patent 5,535,593.[9] This approach to vibration control in the linear compressors of Stirling cryogenic coolers has become prevalent in today's industrial practice. The

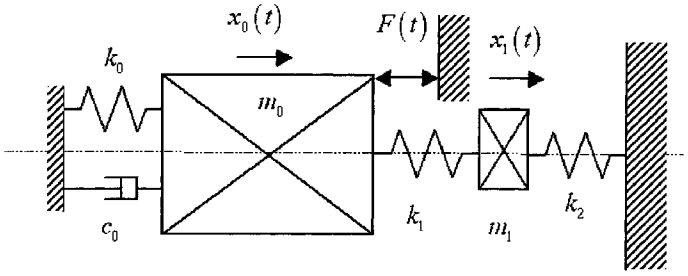

Figure 1. Dynamic model of a single-piston linear compressor with dynamic counterbalancer.

known disadvantages are, however: increase in price and bulk, decrease of reliability, cryocooler efficiency and excessive sensitivity to the g-forces.

It is, therefore, our primary objective to practically eliminate vibration export from the linear single-piston compressor of a Stirling cryogenic cooler without compromising the power consumed by the compressor motor while incurring minimally increased construction costs, allowing said cryogenic cooler to be sold at practically the same price as is prevalent today for prior-art coolers.

The above objective may be achieved by using a passive auxiliary "spring-mass-spring" counterbalancer, as detailed below.

DYNAMIC MODEL OF A SINGLE-PISTON LINEAR COMPRESSOR WITH DYNAMIC COUNTERBALANCER

In Figure 1, the piston assembly of total mass m0 is driven by the force $F(t) = a_i$, where a is the motor force/current constant and i is the motor current. It is important to note that the above driving force is applied to not only the piston assembly, but also to the compressor housing, as shown in Figure 1. The exact definition of gasodynamic forces produced by the piston motion is quite complex and determined by the entire cooler thermodynamics. A detailed knowledge of these forces, however, is not required for the purpose of the present study. In a simplistic approach[10], the entire gasodynamic interaction of the piston and the cylinder head may be thought of as a linear parallel spring-dashpot combination k_0 and c_0. The counterbalancer of total mass m_1 is driven by the piston through the first auxiliary spring having spring rate k_1 and flexibly attached to the stationary housing using the second auxiliary spring having spring rate k_2. The piston and counterbalancer motions are $x_0(t)$ and $x_1(t)$, respectively.

The equations of motion[11,12] take into account the interaction of mechanical and electrical subsystems; these are:

$$\left\{\begin{array}{l} m_0\dfrac{d^2x_0}{dt^2}+k_0x_0+c\dfrac{dx_0}{dt}+k_1\left(x_0-x_1\right)=\alpha i, \\ m_1\dfrac{d^2x_1}{dt^2}+k_1\left(x_1-x_0\right)+k_2x_1=0, \\ L\dfrac{di}{dt}+Ri+\alpha\dfrac{dx_0}{dt}=u. \end{array}\right\} \tag{1}$$

The vibration export may be easily calculated as a sum of all forces applied to the housing, that is:

$$Q(t)=-k_0x_0-c\frac{dx_0}{dt}+f(t)-k_2x_1=-k_0x_0-c\frac{dx_0}{dt}+\alpha i-k_2x_1\ . \tag{2}$$

From equations (1) and (2),

$$Q(t)=m_0\frac{d^2x_0}{dt^2}+m_1\frac{d^2x_1}{dt^2} \tag{3}$$

which is, in essence, the sum of the inertial forces developed by the moving masses.

From equation (3) it is seen that vibration export from such a compressor should be absent if the piston and counterbalancer reciprocate oppositely and the magnitudes of their reciprocation are related to the mass ratio, that is:

$$m_0 \frac{d^2 x_0}{dt^2} = -m_1 \frac{d^2 x_1}{dt^2}. \tag{4}$$

It is evident, that developing such a dynamic counterbalancing requires optimal tuning of its parameters, namely: the mass and rates of the two auxiliary springs. Now we turn our attention to finding such optimal parameters.

To start with, we make a transition into the frequency domain: $x_0(t) \Leftrightarrow X_0(j\omega), x_1(t) = X_1(j\omega); i(t) \Leftrightarrow I(j\omega)$ and $u(t) \Leftrightarrow U(j\omega)$, where $j = \sqrt{-1}$ and ω is the driving frequency. From equations (1), the appropriate complex spectra are:

$$\begin{aligned} X_0(i\omega) &= \frac{\alpha\left(-m_1\omega^2 + k_1 + k_2\right)}{D(j\omega)} U(i\omega), \\ X_1(i\omega) &= \frac{\alpha k_1}{D(j\omega)} U(i\omega), \\ I(i\omega) &= \frac{\left(-m_0\omega^2 + k_0 + k_1 + c_0 j\omega\right)\left(-m_1\omega^2 + k_1 + k_2\right) - k_1^2}{D(j\omega)} U(i\omega), \end{aligned} \tag{5}$$

where the complex determinant is

$$D(j\omega) = (Li\omega + R)\left[\left(-m_0\omega^2 + k_0 + k_1 + c_0 i\omega\right)\left(-m_1\omega^2 + k_1 + k_2\right) - k_1^2\right] + i\omega\alpha^2\left(-m_1\omega^2 + k_1 + k_2\right).$$

From equation (4), the vibration export is absent if

$$X_0(j\omega) m_0\omega^2 + X_1(j\omega) m_1\omega^2 = 0. \tag{6}$$

Using equations (5), from the condition of absence of vibration export (6) we find the simple condition of the compressor counterbalancing

$$m_0\left(-m_1\omega^2 + k_1 + k_2\right) + k_1 m_1 = 0$$

or

$$k_1 = m_0 \frac{m_1\omega^2 - k_2}{m_0 + m_1} \tag{7}$$

which is very important for the further analysis. This condition does not contain the parameters of the gasodynamic loading: gas spring rate k_0 and dashpot damping c_0. Such a compressor, therefore, will always be balanced independently of the ambient conditions and heat loading.

On the other hand, the above counterbalancer may be thought of as additional dynamic loading to the linear motor and, if improperly designed, may have a negative impact upon the motor current and power consumption. Now, therefore, we turn our attention to finding a spring rate k_2 so as to maximize the motor COP.

Without loss of generality, we consider further that the complex spectrum $U(j\omega)$ in equations (5) is purely real, that is $U(j\omega) = \mathbf{U}(\omega)$, where $\mathbf{U}(\omega)$ is the voltage magnitude.

From equations (5), the appropriate magnitudes are:

$$\begin{aligned} \mathbf{X}(\omega) &= \left|\frac{\alpha\left(-m_1\omega^2 + k_1 + k_2\right)}{D(j\omega)}\right| \mathbf{U}(\omega), \qquad \mathbf{X}_1(\omega) = \left|\frac{\alpha k_1}{D(j\omega)}\right| \mathbf{U}(\omega), \\ \mathbf{I}(\omega) &= \left|\frac{\left(-m_0\omega^2 + k_0 + k_1 + c_0 j\omega\right)\left(-m_1\omega^2 + k_1 + k_2\right) - k_1^2}{D(j\omega)}\right| \mathbf{U}(\omega). \end{aligned} \tag{8}$$

From equations (8), we find the magnitudes of the voltage $\mathbf{U}^*(\omega)$ and current $\mathbf{I}^*(\omega)$, which are required to support the desired magnitude of the piston motion Δ. These are:

$$\begin{aligned}\mathbf{U}^*(\omega) &= \Delta\left|\frac{D(j\omega)}{\alpha\left(-m_1\omega^2+k_1+k_2\right)}\right|,\\ \mathbf{I}^*(\omega) &= \Delta\left|\frac{\left(-m_0\omega^2+k_0+k_1+c_0j\omega\right)\left(-m_1\omega^2+k_1+k_2\right)-k_1^2}{\alpha\left(-m_1\omega^2+k_1+k_2\right)}\right|.\end{aligned} \tag{9}$$

Using equation (7), for the counterbalanced motor we find from equations (5) and (9)

$$I(i\omega) = \frac{k_0m_1-k_2m_0+c_0j\omega m_1}{\left(-k_2m_0R+k_0m_1R-c_0\omega^2m_1L\right)+j\omega\left(-k_2m_0L+k_0m_1L+\alpha^2m_1+c_0m_1R\right)}\mathbf{U}(\omega), \tag{10}$$

$$\mathbf{U}^*(\omega) = \Delta\left|\frac{\left(-k_2m_0R+k_0m_1R-c_0\omega^2m_1L\right)+j\omega\left(-k_2m_0L+k_0m_1L+\alpha^2m_1+c_0m_1R\right)}{\alpha m_1}\right|. \tag{11}$$

Further, the power consumed by the motor[13] is:

$$\mathbf{W} = \frac{1}{2}\mathrm{Re}\left[U(j\omega)I(j\omega)\right]. \tag{12}$$

Using equations (12), (10) and (11) we find:

$$\begin{aligned}\mathbf{W} &= \frac{\Delta^2}{2\alpha^2m_1^2}\times\\ &\times\left[\left(-k_2m_0R+k_0m_1R-c_0\omega^2m_1L\right)\left(k_0m_1-k_2m_0\right)+c_0m_1\omega^2\left(-k_2m_0L+k_0m_1L+\alpha^2m_1+c_0m_1R\right)\right]\end{aligned} \tag{13}$$

It is important to note that the magnitude of the current and the power consumed by the balanced motor simultaneously take minimum values

$$\mathbf{I}_0^{\min} = \frac{\Delta}{\alpha}\omega c_0, \quad \mathbf{W}^{\min} = \frac{\Delta^2\omega^2c_0}{2\alpha^2}\left(Rc_0+\alpha^2\right) \tag{14}$$

when

$$k_2 = k_0\frac{m_1}{m_0}. \tag{15}$$

From equations (9) and (15), the choice of the counterbalancer springs in the form

$$k_1 = \frac{m_0m_1}{m_0+m_1}\left(\omega^2-\frac{k_0}{m_0}\right), \quad k_2 = k_0\frac{m_1}{m_0} \tag{16}$$

yields not only zero vibration export, but also minimizes the net electrical power and current consumed by the motor.

It is important to note that absolutely the same values for current and power consumption may be obtained for the single-piston compressor with no counterbalancer attached and tuned to resonate when $k_0 = m_0\omega^2$.

From conditions (16) follows the frequency range where the above counterbalancer is viable

$$\omega > \sqrt{\frac{k_0}{m_0}}. \tag{17}$$

ESTIMATION OF DYNAMIC PROPERTIES OF THE LINEAR SINGLE-PISTON COMPRESSOR

The value of the equivalent gas spring rate k_0, which is required for the calculations of the counterbalancer springs, may be readily found using a curve-fitting procedure as applied to the experimentally obtained frequency response functions (FRF) of the single-piston compressor with

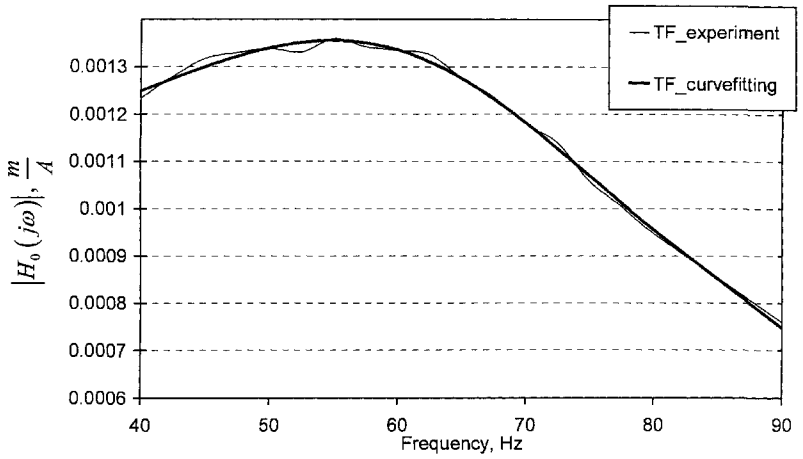

Figure 2. Frequency response function of the linear single-piston compressor.

no counterbalancer attached. It is further convenient to use a FRF relating the piston motion and the motor current.

From the well-known equation of motion of the single-mass linear motor:[11,12]

$$m_0 \frac{d^2 x_0}{dt^2} + k_0 x_0 + c \frac{dx_0}{dt} = \alpha i \tag{18}$$

follows the analytical form for the module of the above FRF:

$$|H_0(j\omega)| = \left| \frac{\mathbf{X}_0(j\omega)}{\mathbf{I}(j\omega)} \right| = \frac{\alpha}{\sqrt{\left(-m_0\omega^2 + k_0\right)^2 + \left(c_0\omega\right)^2}}. \tag{19}$$

Figure 2 shows typical (experimentally measured) dependence of the module of the above FRF on the driving frequency (thin line). During the experiment the Ricor model K529 cryogenic cooler was driven in a closed loop mode 77 K at 600 mW at normal ambient conditions and the driving frequency was slowly swept at the sweep rate 0.1Hz/s. Then the standard curve-fitting procedure, based on equation (19) with $m_0 = 0.053$ kg was applied. From the above procedure, the compressor parameters were estimated, these are:

$$k_0 = 8584 \frac{\mathrm{N}}{\mathrm{m}}, \; c_0 = 16.5 \frac{\mathrm{kg}}{\mathrm{s}}, \; \alpha = 8.6 \frac{\mathrm{N}}{\mathrm{A}}. \tag{20}$$

Superimposed in Figure 2 is also the analytical curve calculated using (19) with the above obtained values (thick line). The effective resonant frequency of the above compressor is 67 Hz.

DESIGN OF A DYNAMICALLY COUNTERBALANCED LINEAR SINGLE-PISTON COMPRESSOR

From the preliminary experimentation, the maximum heat lift produced by the Ricor cryo-cooler model K529N, operated at constant piston stroke over the range of the driving frequencies, takes place at 72 Hz. Since it is our intention to maximize the cooler's overall COP and since this frequency meets the condition (17), we, therefore, chose this frequency as a driving one. Further, from experiment, the maximal piston's stroke is $X_0 = 3.5$ mm. We further assume that the desired maximal counterbalancer stroke is $X_1 = 0.75$ mm. This imposes the stroke limit ± 4.25 mm for the first auxiliary spring, as required by the fatigue analysis.

After this assumption, from equation (6), the mass of the counterbalancer may be easily calculated as:

$$m_1 = \frac{\mathbf{X}_0}{\mathbf{X}_1} m_0 = 0.247 kg \tag{21}$$

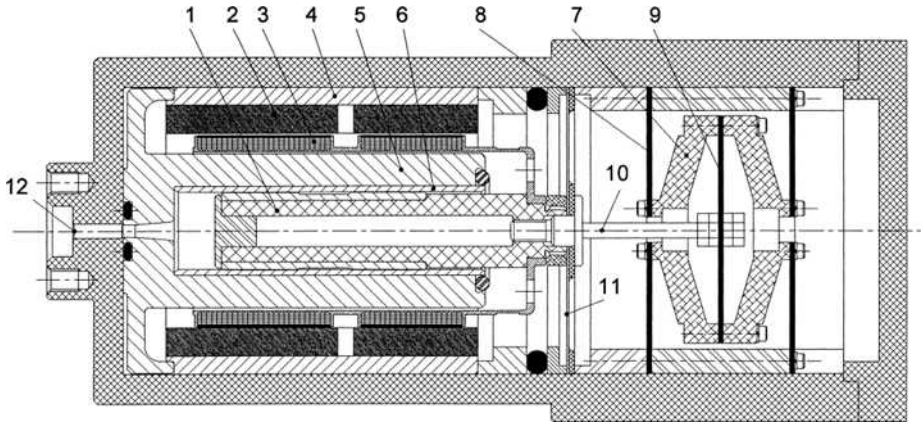

Figure 3. Linear single-piston compressor embodiment containing dynamic counterbalancer.

Then the ratios of the first and the secondary auxiliary springs were calculated per equations (16), these are:

$$k_1 = m_0 \frac{m_1\omega^2 - k_2}{m_0 + m_1} = \frac{m_0 m_1}{m_0 + m_1}\left(\omega^2 - \frac{k_0}{m_0}\right) = 1860\frac{\text{N}}{\text{m}}; \tag{22}$$

$$k_2 = k_0 \frac{m_1}{m_0} = 40240\frac{\text{N}}{\text{m}}. \tag{23}$$

The set of optimal values (16) includes the stiffness of the pneumatic spring which may vary with working conditions. This means that the compressor will not be always optimal in terms of power expenditure, yet it will always be balanced since condition (7) does not contain the gasodynamic spring and damper.

Based on the above analysis the linear compressor of the Ricor K529N 1 W cryogenic cooler was designed and manufactured.

Figure 3 shows the schematics of the above linear compressor with counterbalancer. The said compressor contains the piston assembly 1 which is driven by a "moving coil" linear actuator comprising radially magnetized magnet ring 2 and electrical coil 3. Outer and inner permandur yokes 4, 5 provide air gaps wherein the coil 3 reciprocates in a response to the AC current. The piston assembly 1 reciprocates inside the cylinder 6 with micrometer radial clearances, thus providing for the required dynamic seal. The said counterbalancer contains movable mass 7, which is located in the compressor rear space and is flexibly suspended from the compressor casing by a set of second auxiliary springs 8. The piston assembly is flexibly connected to the said counterbalancer using the first auxiliary spring 9 and connecting rod 10.

The electrical current is supplied to the moving coil from the stationary feedthrough (not shown) through the flexible PCB harness 11. The conduit 12 is used to transfer the gas oscillations to the cryocooler expander (not shown). The auxiliary springs were spiral shaped similar to the well-known Oxford springs[11] and optimized for spring rate, linearity and fatigue.

EXPERIMENTATION ON DYNAMICALLY COUNTERBALANCED LINEAR SINGLE-PISTON COMPRESSOR

In the experiment, the basic single-piston compressor of the K529N cryogenic cooler was compared with the enhanced counterbalanced model designed and manufactured as explained in the preceding section. Figure 4a shows the external layout of the above compressor with no rear cover and Figure 4b shows the principal components the counterbalancer: weights, springs and connecting rod.

Firstly, the above basic cryogenic cooler with unbalanced compressor was driven at 72 Hz in a closed loop mode under the specific heat loading. From experiment, the unbalanced compressor produces a dynamic force of 8.6 N rms at the driving frequency. Further, the same experimentation

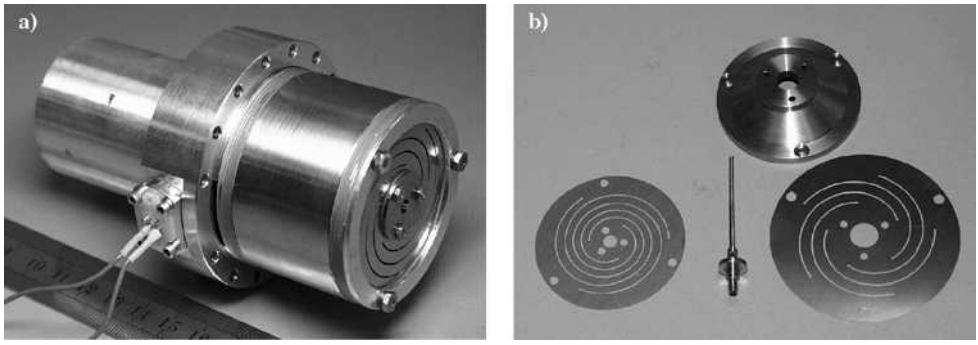

Figure 4. Layout of the counterbalanced linear compressor with no rear cover (a) and components of counterbalancer (b).

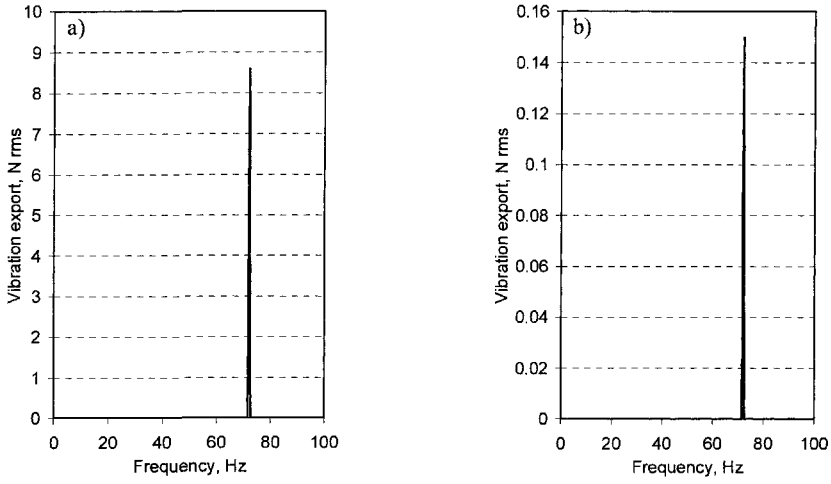

Figure 5. Vibration export from original (a) and counterbalanced (b) compressors.

was carried out with the cooler containing the counterbalanced compressor. By a fine tuning of the driving frequency, the vibration export was reduced 57-fold down to 0.15 N rms. It is important to note that in both cases the net current and power consumption remained practically the same. Figure 5 shows spectra of vibration export produced by the basic unbalanced (a) and counterbalanced (b) compressors.

Figure 6 shows, superimposed, the dependencies of the fundamental component of the above vibration export produced by the basic Ricor K529N (marked by ▪) and by the modified counterbalanced coolers (unmarked line) operating under similar working conditions in the range of the driving frequencies 70-75 Hz. From Figure 6, the level of vibration export of the modified counterbalanced compressor shows a deep and wide notch in the vicinity of the nominal driving frequency while reaching the previously mentioned lowest value of 0.15 N rms at 72 Hz. It is worth noting that over the entire frequency range considered, the vibration export from the modified counterbalanced compressor was significantly lower than that of the basic cooler.

COMMENTS ON DIFFERENCES BETWEEN TUNED DYNAMIC ABSORBER AND DYNAMIC COUNTERBALANCER

In spite of the visible similarity, the above dynamic counterbalancer differs greatly from the well-known tuned dynamic absorber. To start with, the tuned dynamic absorber is an auxiliary spring-mass system mounted upon the vibrating machine and tuned so as to have a natural frequency

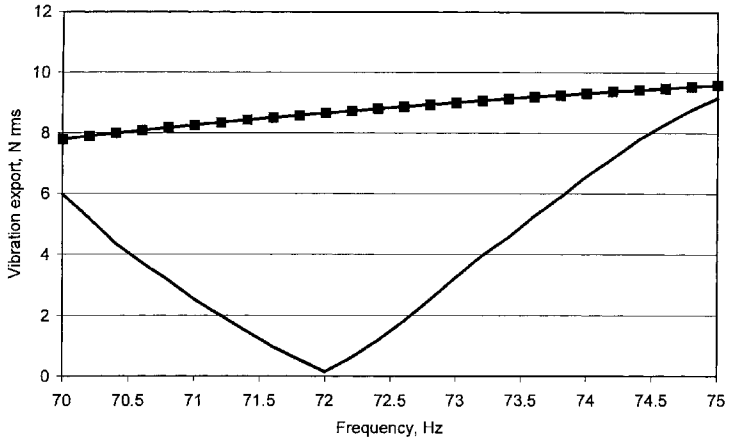

Figure 6. Vibration export from original and counterbalanced compressors at different driving frequencies.

precisely equal to the driving frequency. When properly tuned, the dynamic absorber through its motion develops a dynamic force, which counterbalances the excitation force and, therefore ultimately stabilizes the entire machine housing. Since such a dynamic absorber is driven through the machine housing vibration, its mass should be comparable to the entire machine mass. The typical mass ratio for dynamic absorber is 15-20%. A smaller mass ratio diminishes attainable performance, requires excessive deflection of the absorber mass and also makes the tuning procedure problematic since the useful antiresonant notch becomes too narrow.

In addition, the attainable performance of the tuned dynamic absorber strongly depends on the dynamic properties of the vibration isolated machine, namely additional damping and stiffness in the vibration isolator, which may be required for controlling the machine's rattle space and its mechanical stability. These diminish the suppression ratio at the driving frequency, as shown by Veprik et al.[5]

In contrast to the tuned dynamic absorber detailed above, the dynamic counterbalancer is an auxiliary spring-mass system attached flexibly upon the primary moving part and tuned so as, firstly, not to affect the magnitude and phase of the motion of the above moving part and, secondly, to develop the counterbalancing inertial force in such a manner as to cancel the overall force export.

Further, the required mass of the above counterbalancer should be comparable to the mass of the primary moving part but not to the mass of the machine as in the case of the tuned dynamic absorber; this yields enormous advantages in terms of bulk.

Further, due to the completely different operational principle, the design of the dynamic counterbalancer and its attainable performance do not depend at all upon the machine mass and method of its mounting: its operation will not be affected in any possible way even when the machine is rigidly mounted to even a very massive foundation.

CONCLUSIONS

The novel principle of dynamic counterbalancing of a single-piston linear compressor of a split Stirling cryogenic cooler is derived analytically. The simple analytical conditions yield an optimal design of the counterbalancer which is capable of practically eliminating the vibration export at the driving frequency at minimum power consumption. The results of analytical prediction are supported by full-scale experimentation in which the designed counterbalancer yielded 57-fold reduction of vibration export without practically affecting power and current consumption as compared with the basic cryocooler. Further attempts should be aimed at reshaping the above counterbalancer towards its miniaturization.

REFERENCES

1. Kawahara, et al. USA Patent 6,565,332 May 20, 2003.
2. Minas, et al, USA Patent 5,129,232, July 14, 1992.
3. Dean, et al, USA Patent 5,864,273, January 26, 1999.
4. Ross, et al, USA Patent 5,895,033. April 20, 1999.
5. Veprik A, Babitsky V, Pundak N, Riabzev S, "Passive vibration protection of linear split Stirling cryocooler for airborne infrared application," *Journal of Shock and Vibration*, vol. 7, no. 6 (2000), pp. 363-379.
6. Higham, et al, *Vibration isolation system for a linear reciprocating machine*, USA Patent 4,860,543, August 29, 1989.
7. Neufeld, *Electromechanical cryocooler*, USA Patent 5,582,013, December 10, 1996.
8. Eckels, *Vibration cancellation for C-shaped superconducting magnet*, USA Patent 6,169,404, January 2, 2001.
9. Wu, et al., USA Patent 5,535,593, July 16, 1996.
10. Dadd M, Davey G, Lion Stopatto P and Bailey P, "Vibration reduction in balanced linear compressors," *Proceedings of ICEC 17*, Bournemouth, UK, 14-17 July 1998, p.127-131.
11. Marquardt E, Radebaugh R and Kittel P, "Design equations and scaling laws for linear compressors with flexure springs," *7th International Cryocooler Conference Proceedings*, Air Force Phillips Laboratory Report PL-CP—93-1001, Kirtland Air Force Base, NM, April 1993, pp. 783-804.
12. Deuk-Yong Koh, Yong-Ju Hong, Seong-Je Park, Hyo-Bong Kim, Kwan-Soo Lee, "A study on the linear compressor characteristics of the Stirling cryocooler," *Cryogenics 42* (2002), pp. 427–432.
13. Kraus, J. and Fleisch, D., *Electromagnetics: with Applications*, McGraw-Hill Co. (1999).

Counterflow Pulse-tube Refrigerator

M.E. Will and A.T.A.M. de Waele

Department of Applied Physics, Eindhoven University of Technology
NL-5600 MB Eindhoven, The Netherlands

ABSTRACT

Regenerators in standard pulse-tube refrigerators are expensive, complicated, heavy, and contribute significantly to the losses in the cooler. In this research the regenerators are avoided by using two identical GM-type pulse-tube refrigerators operating in opposite phase. The two regenerators are replaced by one counterflow heat exchanger. This system is called Counterflow Pulse-Tube Refrigerator (CFPTR). A theoretical treatment is given for the optimization of pulse-tube refrigerators with heat exchangers and regenerators. For a single-stage system the heat exchanger performance will be compared with the regenerator performance based on irreversible entropy production.

A special feature of our system is that the position of the rotary valve and the heat exchanger can be interchanged, so the valve can work both at room temperature and at low temperature. A new design principle for the rotary valve has been used. It will be described and the performance will be discussed.

INTRODUCTION

Regenerators in pulse-tube refrigerators are large, heavy, expensive, and complicated. In addition they contribute significantly to the losses in the cooler. In this research the regenerators are avoided by using two identical pulse-tube refrigerators operating in opposite phase. The two regenerators are replaced by one Counterflow Heat Exchanger (CFHEx). The complete system is called Counterflow Pulse-Tube Refrigerator (CFPTR). Basically this concept was introduced for pulse-tube refrigerators by Matsubara[1] who proposed to replace the low-temperature regenerator by a heat exchanger. The system, discussed in this paper, has no regenerators at all. The experimental set-up will be discussed and some preliminary results are given.

A theoretical treatment is given to compare the fundamental difference between heat exchangers and regenerators. This comparison is based on entropy production due to four different processes. We discuss the preferred solution (optimized regenerator or optimized heat exchanger) in a temperature range of 40 to 200 K.

CONCEPT

The CFPTR consists of two identical subsystems, labeled one and two, working in opposite phase. Both subsystems consist of a pulse tube with a cold- and a hot-end heat exchanger, an orifice, and a buffer as usual. The heat, normally stored and released in the regenerator material, is now transported from one subsystem to the other in the heat exchanger.[2] Fig. 1 is a schematic

Cryocoolers 13, edited by R. G. Ross, Jr.
Springer Science+Business Media, Inc., New York, 2004

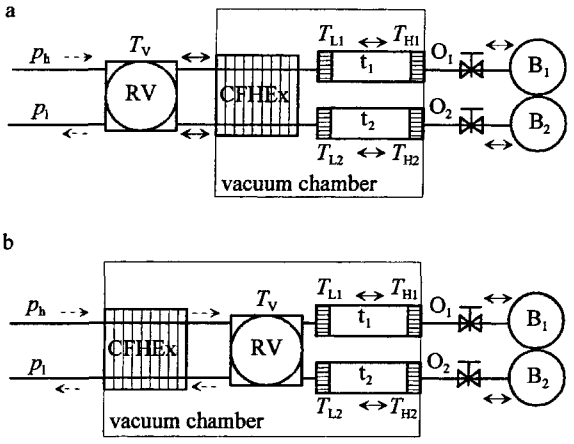

Figure 1. Schematic representation of the counterflow pulse-tube refrigerator. RV is the rotary valve. CFHEx is the counterflow heat exchanger. Subsystems one and two consist of a pulse tube (t) with a cold- and a hot-end heat exchanger, an orifice (O), and a buffer (B). The arrows give the possible gas flow directions (oscillating or steady). The temperatures at five different places in the system are also indicated. Fig. a has the rotary valve at room temperature. Fig. b has the rotary valve at low temperature.

representation of the system. A compressor generates a high pressure p_h and a low pressure p_l. The rotary valve connects subsystem one to p_h while p_l is connected to subsystem two. Half a period later it connects subsystem one to p_l and subsystem two to p_h etc. The flows in the two subsystems are opposite at all times. Due to the oscillating flow in the heat exchanger, there is also a regenerative effect in the heat exchanger. The performance of the heat exchanger is due to the sum of these two effects.

When the rotary valve is placed at low temperatures (Fig. 1b), the flows in the heat exchanger do not alternate (dashed arrows). In this case there is no regenerative effect in the heat exchanger and the performance of the heat exchanger is based on heat exchange only.

EXPERIMENTAL SET-UP

The rotary valve[3] that we use is schematically drawn in Fig. 2. The main parts are the rotor and the stator. The rotor and the stator make mechanical contact. In the rotor (Fig. 2b) four oval-shaped channels are made. This is done to have the same areas of the rotor at high and at low pressures during the cycle. In the stator (Fig. 2c) connections are made to the high- and the low-pressure sides of the compressor and to the two subsystems in a symmetric arrangement. In Fig. 2a one of the slots in the stator is connected to the high-pressure side. The other connections in the stator are made in a similar way, but the horizontal channels are positioned at other levels. The rotor has been made of rulon. The stator has been made of brass. The contact area of the stator has been smoothened and chromed. The major point of the valve is that the areas of the channels to p_l and p_h in the contact area are equal.

The pressure in the housing is p_{hs}. The force, pressing the rotor against the stator, is given by

$$F_t = \int (p_{hs} - p(\vec{r},t)) dA. \tag{1}$$

The pressure in the contact area between the rotor and the stator is $p(\vec{r},t)$. The ideal p_{hs} gives F_t=0 during the whole cycle, so there is no net force on the rotor. This ideal pressure is around the average of the high and the low pressures. However, in reality the pressure distribution $p(\vec{r},t)$ changes during the cycle because of slight differences in area at high and low pressures, contact area roughness, and pressure variations. If, at some time in the cycle the pressure distribution

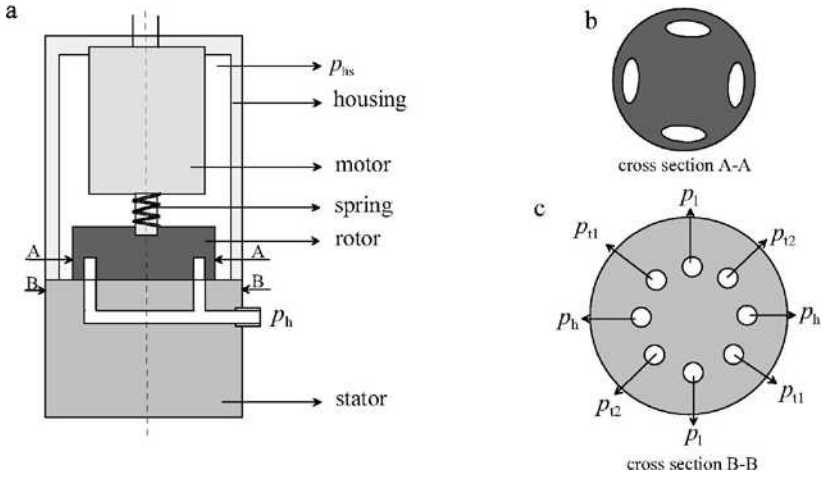

Figure 2. Schematic representation of the rotary valve. The rotor and the stator make mechanical contact. Four oval-shaped channels in the rotor (Fig. b) provide balanced forces on the rotor. In the stator (Fig. c) connections are made to the high- and the low-pressure sides of the compressor and to the two subsystems (t1 and t2). The pressure in the housing is p_{hs}.

results in a negative force, the rotor will be lifted a bit. Gas will flow from the high-pressure side of the compressor to the housing. The pressure in the housing will rise until it is high enough to result in a positive force on the rotor during the whole cycle.

The motor is driven by a constant voltage power supply (4.6 V). Due to the varying friction force the current through the motor will also vary. A typical time dependence of this current is given in Fig. 3. In this figure the high- and the low-pressure sides of the compressor, the pressures in the two tubes and in the housing are given as well. The dashed lines give the moments the valve starts to open (a), is completely open (b), starts to close (c), and is completely closed (d). The current is high when the valve is closed (between d and a). The specifications of the motor give a torque constant of 2.9 Nm/A. The maximum current is 0.1 A, so the maximum torque needed to rotate the rotor is 0.29 Nm. If we increase p_{hs}, the torque of the motor increases. The leak rate through the valve decreases with increasing p_{hs}. The typical leak rate for a torque of

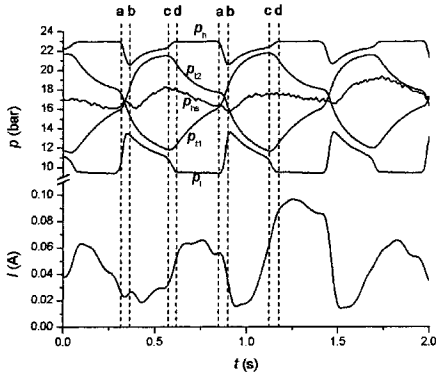

Figure 3. Pressures in the counterflow PTR. The pressures at the high- and the low-pressure sides of the compressor, in the two tubes, and in the housing are given. The amplitude of p_{hs} has been multiplied by a factor ten. At 'a' the valve starts to open, at 'b' the valve is completely open, at 'c' the valve starts to close, and at 'd' the valve is completely closed. The current of the motor is given in the lower plot.

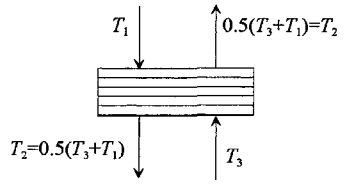

Figure 4: Schematic representation of a step heat exchanger.

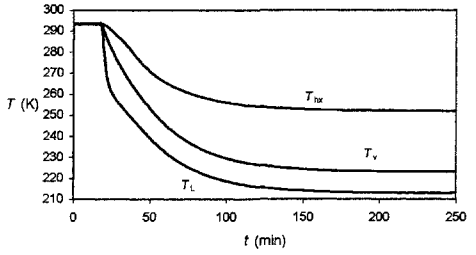

Figure 5. Cool-down curves for the coldest point, the valve and the middle of the heat exchanger.

0.29 Nm is 1% of the total flow. Increasing the pressure amplitude in the system increases the torque of the motor as well.

Preliminary set-up

In our preliminary set-up we use the rotary valve at low temperature (Fig. 1b), and a series of so called 'step heat exchangers' where the outgoing gas temperatures are the average of the two incoming gas temperatures (Fig. 4). The total efficiency is 0.76. The cool-down curves for the coldest point of the system (T_L), the valve (T_v) and halfway the heat exchanger (T_{hx}) are given in Fig. 5.

The rotary valve performs well at low temperature and at room temperature using a small motor to drive it. The lowest temperature reached so far is 213 K. According to calculations this system should reach a lowest temperature around 150 K. The difference is presently unknown. All system components will be improved to reach lower temperatures.

HEAT EXCHANGER VERSUS REGENERATOR: A FUNDAMENTAL COMPARISON

An optimized heat exchanger (good heat exchange, low flow resistance and simple construction) is of key importance for our investigations. The performances of heat exchangers and regenerators can be compared by calculating the entropy production rates by the four different irreversible processes: axial thermal conduction in the gas ($\dot{S}_{cg}$), axial thermal conduction in the material ($\dot{S}_{cm}$), heat exchange between the gas and the material ($\dot{S}_{hx}$), and flow resistance ($\dot{S}_f$).

The regenerator has an area of cross-section A_r, filling factor f, and is supposed to be filled with spherical particles with diameter d_h. The heat exchanger consists of N times two parallel tubes (one for the high- and one for the low-pressure side) each with flow cross-section $A_{hx}=0.25\pi d^2$. The area of the tube wall is A_{hw}. Fig. 6 shows a schematic cross-section of two tubes with the temperature profile. In the next sections the four different irreversible processes will be discussed. In order to avoid unnecessary complications we will treat the various contributions to lowest order in the temperature difference.

Conduction in the gas

For a regenerator the entropy production per unit length due to heat conduction in the axial direction in the gas can be written as[4]

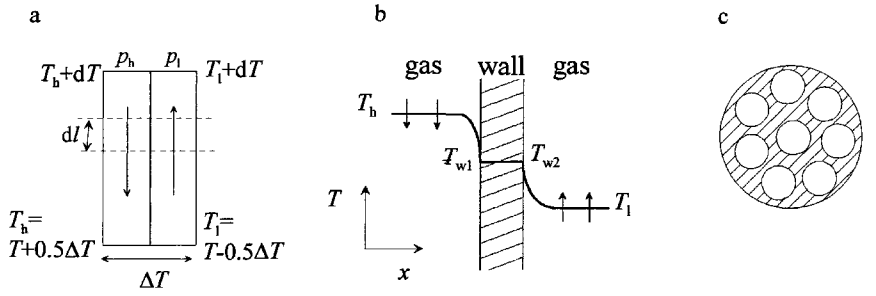

Figure 6. Schematic representation of a heat exchanger part. The arrows indicate the flow direction. Fig. a gives two tubes of the heat exchanger with the temperature profile. Fig. b gives the heat transfer through the wall of the tubes. The temperature distribution is given assuming constant temperature in the wall. Fig. c shows the way the tubes are assumed to be connected to each other. We assume that the tubes have contact to each other over the complete area and have an uniform temperature in the radial direction.

$$\frac{\mathrm{d}\dot{S}_{cg}}{\mathrm{d}l} = (1-f)A_r \frac{N_{ur}\kappa_{gr}}{T^2}\left(\frac{\mathrm{d}T}{\mathrm{d}l}\right)^2, \tag{2}$$

with κ_{gr} the effective coefficient of thermal conductivity of the gas, N_{ur} the Nusselt number for the regenerator, T the temperature, and l the length co-ordinate.

For the heat exchanger the entropy production can be derived from Eq. (2) with f=0. The entropy production can be written as

$$\frac{\mathrm{d}\dot{S}_{cg}}{\mathrm{d}l} = 2NA_{hx} \frac{N_{uh}\kappa_g}{T^2}\left(\frac{\mathrm{d}T}{\mathrm{d}l}\right)^2, \tag{3}$$

with N_{uh} the Nusselt number for the heat exchanger.

Conduction in the material

For the regenerator the entropy production due to axial heat conduction through the matrix material can be given as[4]

$$\frac{\mathrm{d}\dot{S}_{cm}}{\mathrm{d}l} = fA_r \frac{C_\kappa \kappa_w}{T^2}\left(\frac{\mathrm{d}T}{\mathrm{d}l}\right)^2, \tag{4}$$

with κ_w the thermal conductivity of the material. The effective coefficient of thermal conductivity of the matrix is smaller than the bulk coefficient of the matrix material due to the reduced contact surface of the different layers of matrix material. This is included in the coefficient C_κ.[5]

The entropy production for the heat exchanger can be obtained from Eq. (4) with f=1

$$\frac{\mathrm{d}\dot{S}_{cm}}{\mathrm{d}l} = 2NA_{hw} \frac{\kappa_w}{T^2}\left(\frac{\mathrm{d}T}{\mathrm{d}l}\right)^2. \tag{5}$$

Flow resistance

For the regenerator the entropy production due to flow resistance can be written as[4]

$$\frac{\mathrm{d}\dot{S}_f}{\mathrm{d}l} = \frac{C_z}{d_h^2}\frac{\eta \dot{n}^2}{A_r}\frac{V_m^2}{T}, \tag{6}$$

with C_z/d_h^2 the flow impedance factor, η the viscosity, V_m the molar volume, and $\dot{n}^2$ the mean square molar flow.

For the high-pressure side of the heat exchanger the formulae are

$$\frac{\mathrm{d}\dot{S}_{fh}}{\mathrm{d}l} = \dot{n}\frac{V_{mh}}{T_h}\frac{\mathrm{d}p_h}{\mathrm{d}l}, \tag{7}$$

with

$$\frac{\mathrm{d}p_\mathrm{h}}{\mathrm{d}l} = \frac{1}{2}\rho v^2 \frac{f_\mathrm{r}}{d_\mathrm{l}}, \tag{8}$$

with f_r the friction factor, ρ the density, p the pressure, and v the average velocity. Combining Eqs. (7) and (8) we get

$$\frac{\mathrm{d}\dot{S}_\mathrm{fh}}{\mathrm{d}l} = \frac{1}{2} f_\mathrm{r} M \frac{\dot{n}^3}{N^2 d_\mathrm{l} A_\mathrm{hx}^2} \frac{V_\mathrm{mh}^2}{T_\mathrm{h}}, \tag{9}$$

with M the molar mass of helium. When we sum the contributions of the high- and the low-pressure sides and assume $p_\mathrm{h} \approx p_\mathrm{l} = p$, we get

$$\frac{\mathrm{d}\dot{S}_\mathrm{f}}{\mathrm{d}l} = f_\mathrm{r} M \frac{\dot{n}^3}{d_\mathrm{l} N^2 A_\mathrm{hx}^2} \frac{V_\mathrm{m}^2}{T}. \tag{10}$$

Heat exchange between gas and material

For the regenerator this contribution to the entropy production can be written as[4]

$$\frac{\mathrm{d}\dot{S}_\mathrm{hx}}{\mathrm{d}l} = \beta A_\mathrm{r} \frac{\left(T_\mathrm{r} - T_\mathrm{g}\right)^2}{T_\mathrm{r} T_\mathrm{g}}, \tag{11}$$

with β the volumetric heat exchange parameter, which can be written as

$$\beta = \alpha_\mathrm{h} F = 12 f \frac{\kappa_\mathrm{gr} N_\mathrm{ur}}{d_\mathrm{h}^2}, \tag{12}$$

with α_h the heat exchange coefficient, and F the heat exchange surface area per unit volume. Under some general conditions the entropy production can be written as[5]

$$\frac{\mathrm{d}\dot{S}_\mathrm{hx}}{\mathrm{d}l} = \frac{1}{12 f} \frac{d_\mathrm{h}^2}{A_\mathrm{r}} \frac{C_\mathrm{p}^2 \dot{n}^2}{\kappa_\mathrm{gr} N_\mathrm{ur}} \frac{1}{T^2} \left(\frac{\mathrm{d}T}{\mathrm{d}l}\right)^2, \tag{13}$$

with C_p the molar heat capacity of the gas at constant pressure.

For the heat exchanger the assumption is made that the tubes make contact over the complete wall area. Using the heat transfer as given in Fig. 6b

$$\frac{\mathrm{d}\dot{S}_\mathrm{hx}}{\mathrm{d}l} \mathrm{d}l = \mathrm{d}\dot{Q} \left(\frac{1}{T_\mathrm{l}} - \frac{1}{T_\mathrm{h}}\right) = \mathrm{d}\dot{Q} \frac{\Delta T}{T_\mathrm{l} T_\mathrm{h}}, \tag{14}$$

with $\dot{Q}$ the heat flow

$$\mathrm{d}\dot{Q} = \frac{1}{2} \pi N \left(T_\mathrm{h} - T_\mathrm{l}\right) \kappa_\mathrm{g} N_\mathrm{uh} \mathrm{d}l, \tag{15}$$

so

$$\frac{\mathrm{d}\dot{S}_\mathrm{hx}}{\mathrm{d}l} = \frac{1}{2} \pi N \kappa_\mathrm{g} N_\mathrm{uh} \frac{\left(T_\mathrm{h} - T_\mathrm{l}\right)^2}{T_\mathrm{h} T_\mathrm{l}}. \tag{16}$$

When we have a steady state with small differences between the low- and high-pressure sides

$$\kappa_\mathrm{gl} N_\mathrm{ul} = \kappa_\mathrm{gh} N_\mathrm{uh} = \kappa_\mathrm{g} N_\mathrm{u}, \tag{17}$$

the energy balance gives

$$\dot{n} C_\mathrm{p} \mathrm{d}T = \frac{1}{2} N_\mathrm{u} \kappa_\mathrm{g} \frac{\pi d_\mathrm{l} \mathrm{d}l}{d_\mathrm{l}} \left(T_\mathrm{h} - T_\mathrm{l}\right), \tag{18}$$

so

Table 1. Entropy production rates due to various processes in the heat exchanger and the regenerator. In the last column the ratio is given.

	Heat exchanger	Regenerator	Ratio (hx/reg)
Axial conduction in the gas	$2NA_{hx}\frac{N_{uh}\kappa_g}{T^2}\left(\frac{dT}{dl}\right)^2$	$(1-f)A_r\frac{N_{ur}\kappa_{gr}}{T^2}\left(\frac{dT}{dl}\right)^2$	$\frac{2NA_{hx}N_{uh}}{(1-f)A_rN_{ur}}$
Axial conduction in the wall	$2NA_{hw}\frac{\kappa_w}{T^2}\left(\frac{dT}{dl}\right)^2$	$fA_r\frac{C_k\kappa_w}{T^2}\left(\frac{dT}{dl}\right)^2$	$\frac{2NA_{hw}}{fA_rC_k}$
Flow resistance	$f_rM\frac{\dot{n}^3}{N^2A_{hx}^2d_1}\frac{V_m^2}{T}$	$\frac{C_z}{d_h^2}\frac{\eta\dot{n}^2}{A_r}\frac{V_m^2}{T}$	$\frac{f_rM\dot{n}}{C_z\eta}\frac{d_h^2A_r}{N^2A_{hx}^2d_1}$
Heat exchange	$2\frac{C_p^2\dot{n}^2}{\pi\kappa_gN}\frac{1}{N_{uh}}\frac{1}{T^2}\left(\frac{dT}{dl}\right)^2$	$\frac{1}{12f}\frac{d_h^2}{A_r}\frac{C_p^2\dot{n}^2}{\kappa_{gr}N_{ur}}\frac{1}{T^2}\left(\frac{dT}{dl}\right)^2$	$\frac{24f}{\pi}\frac{A_r}{Nd_h^2}\frac{N_{ur}}{N_{uh}}$

$$T_h - T_l = 2\frac{C_p\dot{n}}{\pi\kappa_gN}\frac{1}{N_{uh}}\frac{dT}{dl}, \tag{19}$$

and

$$\frac{d\dot{S}_{hx}}{dl} = \frac{2C_p^2\dot{n}^2}{\pi\kappa_gN}\frac{1}{N_{uh}}\frac{1}{T^2}\left(\frac{dT}{dl}\right)^2. \tag{20}$$

Summary

We now collect the entropy production rates in the regenerator and in the heat exchanger (Table 1). We assume that the flow areas for the regenerator and the heat exchanger are equal

$$(1-f)A_r = 2NA_{hx} = A_t. \tag{21}$$

For the heat exchanger we use a minimum wall thickness δ_w needed to stand the pressure

$$\frac{\delta_w}{d_1} = \frac{p}{p_c}, \tag{22}$$

with p_c the breaking stress of the material. The total flow area of the channels of the heat exchanger can be given as

$$2NA_{hx} = A_t = \frac{1}{2}N\pi d_1^2, \tag{23}$$

and the total area of the walls

$$2NA_{hw} = 2N\pi d_1\delta_w = 4A_t\frac{\delta_w}{d_1} = 4A_t\frac{p_0}{p_c}. \tag{24}$$

The optimal regenerator and heat exchanger can be found by minimizing the entropy productions. This is dependent on the type of flow (laminar of turbulent) in the system.

Regenerator optimization

For the heat exchange we use a Nusselt number[5] N_{ur}=10. We assume that $\kappa_{gr}=\kappa_g$. The constant used for the conductivity of the matrix[5] is C_k=0.16. The constant for the flow impedance C_z has been obtained from measurements in our group and is equal to 1600.

If we are looking for the optimum grain size d_h we can write the total entropy production for the regenerator as

$$\frac{d\dot{S}_{tot}}{dl} = \frac{a_1}{d_h^2} + b_1d_h^2 + c_1, \tag{25}$$

with

$$a_1 = 1600\frac{1-f}{A_t}\eta\dot{n}^2\frac{V_m^2}{T}, \tag{26}$$

$$b_1 = \frac{1}{120}\frac{1-f}{f}\frac{1}{A_t}\dot{n}^2\frac{C_p^2}{\kappa_g}\frac{1}{T^2}\left(\frac{dT}{dl}\right)^2, \tag{27}$$

$$c_1 = \left(10(1-f)\kappa_g + 0.16\frac{f}{1-f}\kappa_w\right)\frac{A_t}{T^2}\left(\frac{dT}{dl}\right)^2. \tag{28}$$

The total entropy production is given in Fig. 7a as a function of d_h. It shows that there is a minimum entropy production for the optimum grain size diameter.

Heat exchanger optimization

Assuming laminar flow in the heat exchanger means for the friction factor[6] that

$$f_r = \frac{64}{R_e}, \tag{29}$$

with R_e the Reynolds number. Assuming fully developed laminar flow with uniform surface heat flux, the Nusselt number can be written as[6]

$$N_{uh} = \frac{hd_1}{\kappa} = 4.36. \tag{30}$$

Using stainless steel tubes the breaking stress is p_c=0.25×10^9 Pa.

If we are looking for the optimum number of tubes N, the total entropy production can be written as

$$\frac{d\dot{S}_{tot}}{dl} = a_2 N + \frac{b_2}{N} + c_2, \tag{31}$$

with

$$a_2 = 64\pi\eta\frac{\dot{n}^2}{A_t^2}\frac{V_m^2}{T}, \tag{32}$$

$$b_2 = \frac{0.46}{\pi}\dot{n}^2\frac{C_p^2}{\kappa_g}\frac{1}{T^2}\left(\frac{dT}{dl}\right)^2, \tag{33}$$

$$c_2 = \left(4.3\kappa_g + 0.028\kappa_w\right)\frac{A_t}{T^2}\left(\frac{dT}{dl}\right)^2. \tag{34}$$

The total entropy production as function of N shows a minimum as can be seen in Fig. 7b.

Typical entropy flows in the regenerator or heat exchanger are around 1 W/K. When we look at the total entropy production rates in Fig. 7 it can be seen that the curves are quite flat around the minimum. This means for the heat exchanger that a decrease of the number of tubes from 50.000 to 5.000 gives an increase of the entropy to 0.07 W/K for tubes of a length of 1 m, which is still acceptable. For three different temperatures the minimum entropy production and the optimized geometry have been calculated. The results are given in Table 2.

Assuming fully developed turbulent flow in the heat exchanger (R_e>>1000) means for the friction factor[6] and the Nusselt number[7]

$$f_r = \frac{0.33}{R_e^{1/4}}, \tag{35}$$

$$N_{uh} \approx 0.0343 R_e^{3/4}. \tag{36}$$

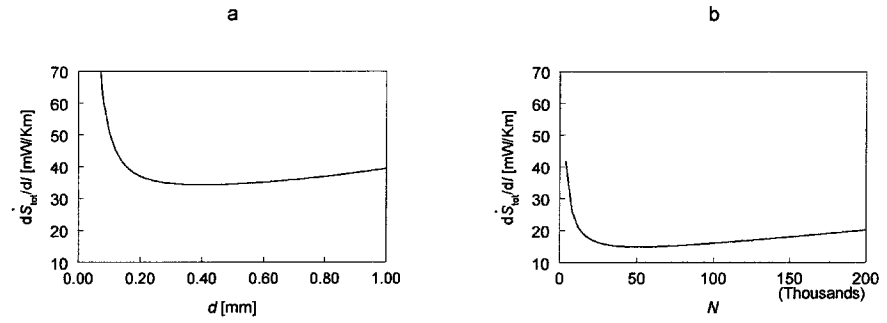

Figure 7. The total entropy production rate per unit length for laminar flow at 100 K. Fig. a: for the regenerator as function of the diameter of the spherical particles, Fig. b: for the heat exchanger as function of the number of tubes.

Table 2. Minimum entropy production rates at the optimum condition in the heat exchanger and the regenerator for different temperatures. The flow area in these calculations is A_t=10 cm^2.

	T [K]	200	100	40
Heat exchanger	N [10^3]	6.4	52	403
Heat exchanger	d_l [mm]	0.31	0.11	0.040
Heat exchanger	$d\dot{S}_{min}/dl$ [mW/Km]	2.7	15	66
Regenerator	d_h [mm] with f=0.5	1.1	0.4	0.14
Regenerator	$d\dot{S}_{min}/dl$ [mW/Km]	3.8	34	170

The total entropy production in the heat exchanger has the form

$$\frac{d\dot{S}_{tot}}{dl} = a_3 N^{5/8} + \frac{b_3}{N^{5/8}} + \frac{d_3}{N^{3/8}} + e_3. \tag{37}$$

with

$$a_3 = 0.72\pi^{5/8}\eta^{1/4}M^{3/4}\dot{n}^{11/4}\frac{V_m^2}{A_t^{19/8}T}, \tag{38}$$

$$b_3 = \frac{27}{\pi^{5/8}}\dot{n}^{5/4}\frac{C_p^2}{\kappa_g}\left(\frac{\eta}{M}\right)^{3/4}\frac{A_t^{3/8}}{T^2}\left(\frac{dT}{dl}\right)^2, \tag{39}$$

$$d_3 = \frac{0.075}{\pi^{3/8}}\left(\frac{\dot{n}M}{\eta}\right)^{3/4}A_t^{5/8}\frac{\kappa_g}{T^2}\left(\frac{dT}{dl}\right)^2, \tag{40}$$

$$e_3 = 0.028A_t\frac{\kappa_w}{T^2}\left(\frac{dT}{dl}\right)^2. \tag{41}$$

The total entropy production as function of N is given in Fig. 8. Looking at Fig. 8 we see that around 500.000 tubes are needed to reach the minimum entropy production rate. In a real set-up this will be very difficult.

If we calculate the Reynolds number of the gas flow at all possible N, we will see that already at small N the flow will become laminar instead of turbulent. This means that the optimum situation for the heat exchanger (lowest entropy production rate) is found for a situation with laminar flow.

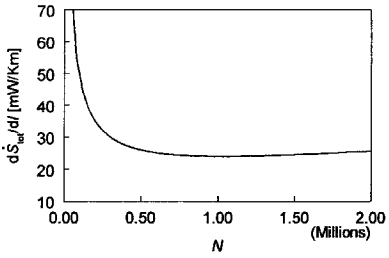

Figure 8. Total entropy production per unit length in the heat exchanger with turbulent flow as function of the number of tubes, at 100 K.

CONCLUSIONS

Theoretically a PTR working with an optimized heat exchanger should perform better than one with an optimized regenerator over the temperature range of 40 to 200 K. The optimized heat exchanger for 100 K will be built and placed in the set-up in the near future to verify the theory and improve the performance of the set-up. The rotary valve works very well at low temperatures.

ACKNOWLEDGMENT

This project is supported by the Dutch Technology Foundation (STW). The authors would like to thank L.M.W. Penders, L.C. van Hout, M.A.W. Bogers and H.H.J.M. van Helvoirt for their help in building the set-up.

REFERENCES

1. Gao, J.L., Matsubara, Y., "An Inter-Phasing Pulse-Tube Refrigerator for High Refrigeration Efficiency", *Proceedings of ICEC-16*, Elsevier, (1996), pp. 295-298.
2. Will, M.E., Zeegers, J.C.H., De Waele, A.T.A.M., "Counter-Flow Pulse-Tube Refrigerators", *Proceedings of ICEC-19*, Narosa Publishing House, New Delhi (2002), pp. 407-410.
3. Will, M.E., Tanaeva, I.A., Li, R., De Waele, A.T.A.M., "New Rotary Valves for Pulse-Tube Refrigerators", submitted to Cyogenics, (2004).
4. De Waele, A.T.A.M., Steijaert, P.P., Gijzen, J., "Thermodynamical Aspects of Pulse Tubes", *Cryogenics*, vol 37, no. 6 (1997), pp. 313-324.
5. Steijaert, P.P., *Thermodynamical Aspects of Pulse-Tube Refrigerators*, [PhD Thesis], Eindhoven University of Technology, (1999), pp.50,51, 100.
6. Incropera, F.P., De Witt, D.P., *Introduction to Heat Transfer*, John Wiley & Sons, New York (1985), pp. 338, 355.
7. Kakaç, S., Shah, R.K., Aung, W., *Handbook of Single-Phase Convective Heat Transfer*, John Wiley & Sons, New York (1987), pp. 4-32.

A Study of Performance Improvement of the Coaxial Inertance Tube Pulse Tube Cryocooler

Seong-Je Park, Yong-Ju Hong, Hyo-Bong Kim, and Yang-Hoon Kim*

Thermal and Fluid Systems Departments
Korea Institute of Machinery & Materials
Taejeon 305-600, Korea
*Department of Mechanical Engineering
Pusan National University
Pusan, 609-735, Korea

ABSTRACT

A pulse tube cryocooler (refrigerator) has no moving parts in its cold section, and, when driven by a linear compressor, has the potential of achieving higher reliability and lower vibration than other small refrigerators. The most compact and convenient pulse tube cryocooler for practical applications is the coaxial type. It can often replace Stirling cryocoolers without any change to the dewar or to the connection to the cooled device. The purpose of this study is to analyze the characteristics of a coaxial type inertance pulse tube refrigerator (IPTR), and to understand the principal factors governing its performance.

The key components of a coaxial-type IPTR include a linear compressor with two reciprocating pistons driven by linear motors, a regenerator, a pulse tube with its inertance tube, and a buffer (reservoir) volume. To ensure high performance of the coaxial-type IPTR, the design and operating parameters of the linear compressor and expander must be optimized.

Experimental results show that the operating frequency has a significant effect on a linear compressor's input power characteristics, and with a higher charge pressure of the working fluid, a higher pressure ratio can be achieved. To find optimal conditions of the coaxial type IPTR, the no-load temperature has been measured for various inertance tube volumes, operating frequencies, and charge pressures. In addition, cooldown and load characteristics have been determined.

INTRODUCTION

W.E. Gifford and R.C. Longsworth[1] first described the pulse tube cryocooler in 1964. This type of the pulse tube cryocooler is now called the basic pulse tube cryocooler. The performance of this type of pulse tube refrigerator has been greatly improved through the introduction of an orifice and buffer volume at the hot end of the pulse tube. R. Radebaugh et al. modified this type of the pulse tube refrigerator, which is called as the orifice pulse tube refrigerator, in 1986.[2,3]

Cryocoolers 13, edited by R. G. Ross, Jr.
Springer Science+Business Media, Inc., New York, 2004

In 1990, the double inlet pulse tube refrigerator, in which a bypass tube is connected between the pressure wave generator and the hot end of the pulse tube, was suggested by S. Zhu et al.[4] The refrigeration power per unit mass flow rate through the regenerator was greatly increased in the double inlet pulse tube refrigerator.

When driven at high frequency (30 to 60 Hz), a pulse tube refrigerator is referred to as a Stirling-type pulse tube, and the process of controlling the phase relationship between mass flow and pressure in the regenerator can become more difficult. A commonly used means of achieving optimal phasing in a Stirling-type pulse tube's expander is the inertance tube.[5] The inertance tube allows the phase shift to be tuned to make the pulse tube refrigerator operate as efficiently as a Stirling refrigerator.

More recently, de Boer[6] showed that the performance of the IPTR is superior to that of the OPTR over a limited range of frequencies, and the rate of refrigeration of the IPTR is governed by the dimensions of the inertance tube, the volume of the pulse tube, the conductance of the regenerator, the charge pressure, and the drive frequency.

Ravikumar et al.[7] showed that, as frequency increased, an "inertance tube" phase shifter enhanced the cooler performance in a region where an orifice or double-inlet deteriorated the performance. They also used a rotary valve along with a G-M compressor to experimentally investigate the dependency of performance on frequency of operation, inertance tube diameter, and length.

In this paper, we first discuss the cooling characteristics of the orifice type, the double inlet type, and the IPTR with a linear compressor. Then, the effects of the inertance tube volume, charge pressure, and operating frequency on the cooldown characteristics of the coaxial type IPTR are experimentally investigated.

EXPERIMENTAL DESCRIPTION

The structural shape of the coaxial type pulse tube refrigerator is shown in Fig. 1, and a schematic diagram of the experimental apparatus of the coaxial type IPTR is given in Fig. 2.

The coaxial type IPTR consists of two units: the compressor and the expander. The linear compressor, driven by linear motors, has two reciprocating pistons that generate the pressure wave that is transmitted to the expander. The expander, which generates the cooling, consists of a regen-

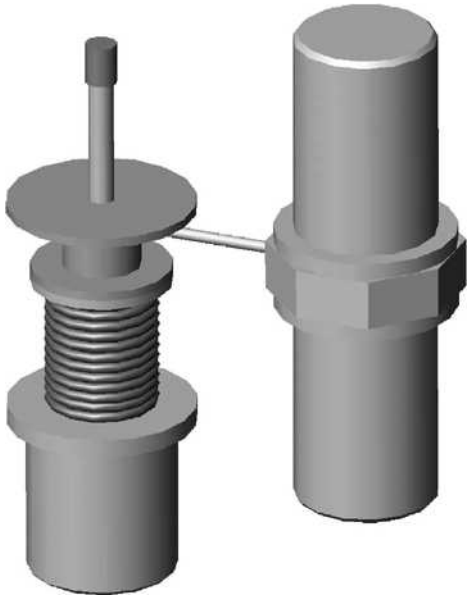

Figure 1. Structural shape of the coaxial type inertance pulse tube refrigerator

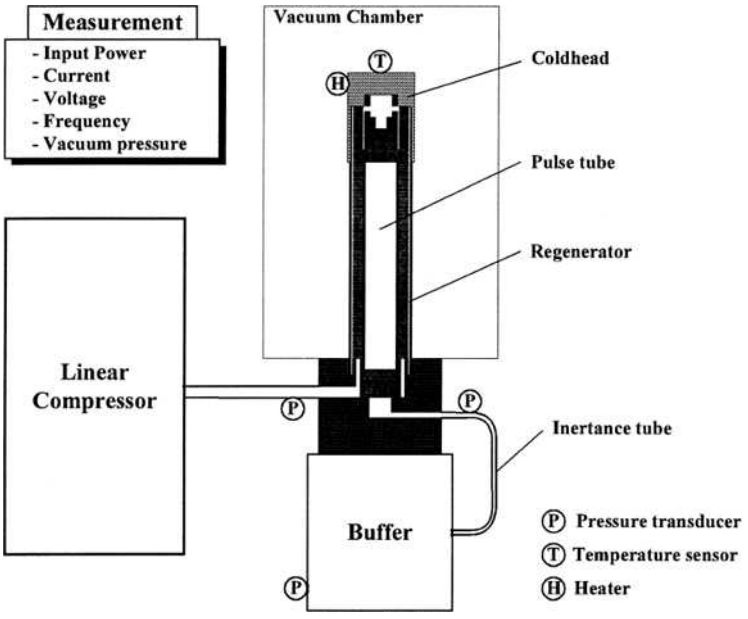

Figure 2. Experimental apparatus of the coaxial type inertance pulse tube refrigerator

erator, a pulse tube with its inertance tube phase shifter, and a buffer (reservoir) volume. In our system the linear compressor was a commercially-available unit (Leybold Polar SC-7 COM).

The coaxial type orifice pulse tube refrigerator and double inlet pulse tube refrigerator were constructed by exchanging the inertance tube for the orifice valve and inserting a double inlet valve between the exit of the compressor and the hot end of the pulse tube. The detailed specifications of the coaxial type IPTR are presented in Table 1.

An AC power supply was used to supply and control the operating frequency and the input voltage to the linear compressor. A silicon diode thermometer was attached to measure the temperature at the cold end, and a manganin resistance heater was provided at the cold end of the pulse tube to measure the cooling capacity. Piezoelectric pressure sensors were installed on the transfer line between the exit of the compressor and aftercooler and between the hot end of the pulse tube and reservoir to measure pressure oscillations.

The cold end was installed in a vacuum chamber, and the pressure of the vacuum chamber was maintained below 10^{-5} torr to reduce the thermal losses during measurements. After evacuating and purging with clean high-pressure helium gas to clean the regenerator of the pulse tube refrigerator,

Table 1. Specifications of coaxial type IPTR

Item		Coaxial type IPTR
Compressor		Polar SC-7
Charging pressure		20 ~ 30 bars (Helium)
Regenerator	Mesh	# 250
	Volume	10.1 cc
Pulse tube	Diameter	0.95 cm
	Volume	5.7 cc
Inertance tube	Diameter	1.3 / 1.9/ 2.7 / 3.0 mm
	Length	0.95 / 1.9 / 2.85 m
Buffer volume		1000 cc

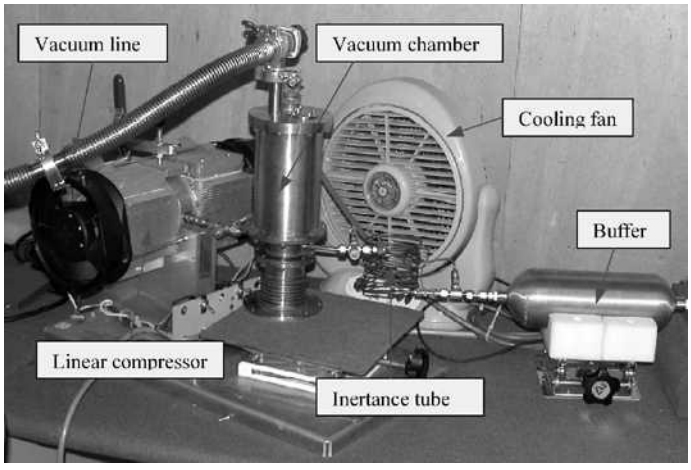

Figure 3. Coaxial type inertance tube pulse tube refrigerator

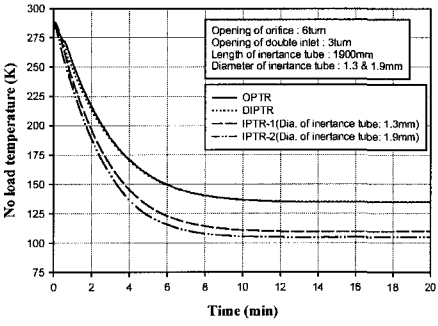

Figure 4. Cooldown characteristics of OPTR, DIPTR, IPTR-1, IPTR-2.

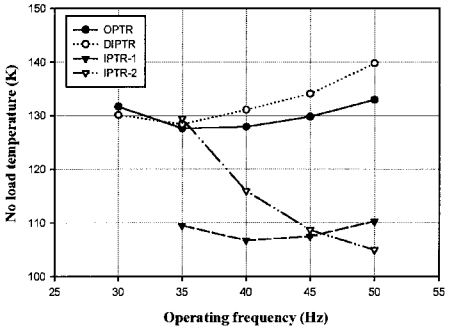

Figure 5. No load temperatures of the OPTR, DIPTR, IPTR-1, IPTR-2 with operating frequency.

the pulse tube refrigerator was connected to the linear compressor. Then, the system was charged up to about 20 to 30 bars. Figure 3 shows the test setup of the coaxial type IPTR.

EXPERIMENTAL RESULTS

As a preliminary investigation, the refrigeration performance of four types of pulse tube refrigerators was investigated: the orifice pulse tube (OPTR), the double inlet pulse tube (DIPTR), and two inertance-type pulse tubes (IPTR-1 and IPTR-2).

Figure 4 shows the cooldown characteristics of the orifice pulse tube, double inlet pulse tube and inertance type refrigerators at an operating frequency of 50 Hz. Charge pressure and input voltage were 25 kg_f/cm^2G and 30 V, respectively, and the maximum flow coefficient (C_v) for the orifice valve and double inlet valve was 0.03. Note that the cooldown rate of the inertance tube type pulse tube refrigerators was faster than that of the orifice and double inlet pulse tube refrigerators. The lowest no-load temperature of the OPTR, DIPTR, IPTR-1 and IPTR-2 were 134.8 K, 135.3 K, 110.2 K and 105.2 K, respectively.

Figures 5 and 6 show the dependence of cold head temperature and input power on the operating frequency for the orifice, double inlet, and inertance type pulse tube refrigerators. The resonant frequencies of the OPTR, DIPTR, IPTR-1 and IPTR-2 were about 35 to 40 Hz. The lowest temperature for the IPTR was lower than that for the OPTR and DIPTR. The lowest temperatures of the

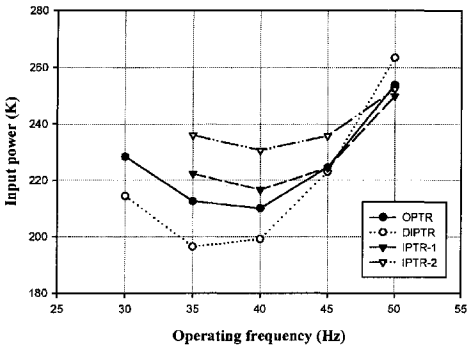

Figure 6. Input power of the OPTR, DIPTR, IPTR-1, IPTR-2 with operating frequency.

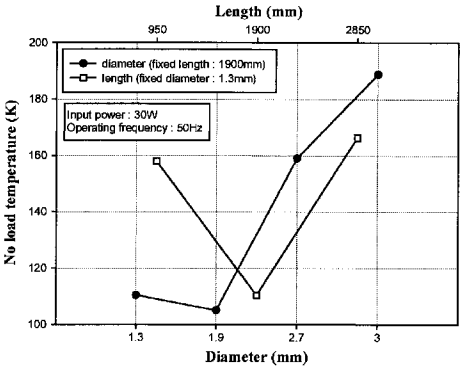

Figure 7. Dependence of no-load temperature on diameter and length of the inertance tube.

OPTR and DIPTR were measured at an operating frequency of 35 Hz, and the lowest temperatures of the IPTR-1 and IPTR-2 were measured at an operating frequency of 40 Hz and 50 Hz, respectively. The lowest input powers were measured approximately at an operating frequency of 40 Hz. In the case of the IPTR-2, the optimal operating frequency for lowest no-load temperature was 50 Hz, but the input current increased above the allowable current limit.

Figure 7 shows the variation of the cold head temperature with the diameter and length of the inertance tube for the coaxial IPTR. The optimal length of the inertance tube in the manufactured coaxial IPTR was 1900 mm, and the optimal diameter was in the range of 1.3 mm to 1.9 mm. In this experiment, operating pressure, charge pressure, and input voltage were 50 Hz, 25 kg_f/cm^2G and 30 V, respectively.

Figure 8 shows the dependence of cooldown characteristics on charge pressure for IPTR-1 at the operating frequency of 50 Hz and input voltage of 30 V. The length and diameter of the inertance tube were 1900 mm and 1.3 mm, respectively. With a charge pressure in the range of 22.5 kg_f/cm^2G to 30 kg_f/cm^2G, although the performance of the IPTR was almost constant, the best results for the cooldown time and the lowest temperature were achieved at a charge pressure of 25 kg_f/cm^2G.

Figures 9 and 10 show the variation of the cold head temperature and the input power with various charge pressures for the inertance tube type pulse tube refrigerator.

The lowest temperature and input power were obtained for a charge pressure of 25 kg_f/cm^2G and operating pressure of 40 Hz. As the charge pressure increased, the operating frequency for the minimum input power increased, tracking the increased resonance frequency. The lowest temperature was 107 K at a charge pressure of 25 kg_f/cm^2G and an operating pressure of 40 Hz.

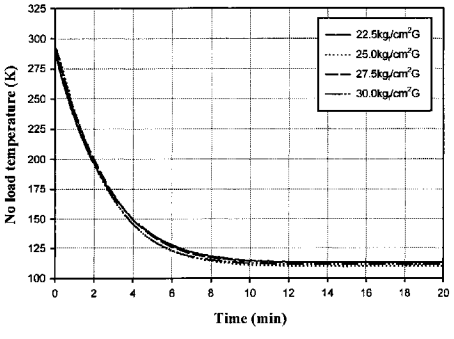

Figure 8. Cooldown characteristics with charging pressure of IPTR-1.

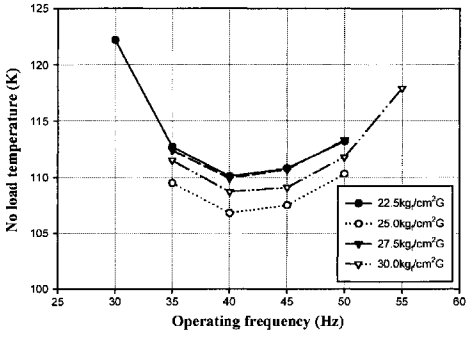

Figure 9. No load temperatures with charging pressure and operating frequency.

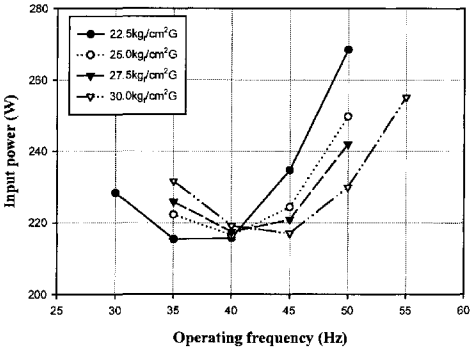

Figure 10. Input power with charging pressure and operating frequency.

For the coaxial type IPTR, which had the lower temperature and better performance, further studies of the regenerator, pulse tube, and structural design are needed.

CONCLUSIONS

To understand the parameters governing the performance of a pulse tube cryocooler we have investigated the cooling characteristics of the orifice type, the double inlet type, and the coaxial type IPTR with a linear compressor. We then measured the dependence of the performance of the coaxial type IPTR on inertance tube volume, charge pressure, and operating frequency. The following conclusions have been drawn from the experimental results.

(1) The cooldown rate of the inertance tube type pulse tube refrigerator was faster than that of the orifice and double inlet pulse tube refrigerators. The lowest no-load temperature of the OPTR, DIPTR, IPTR-1 and IPTR-2 was 134.8 K, 135.3 K, 110.2 K and 105.2 K, respectively.

(2) The optimal length of the inertance tube in the manufactured coaxial IPTR was 1900 mm, and the optimal diameter was in the range of 1.3 mm to 1.9 mm.

(3) The lowest temperature and input power were obtained at a charge pressure of 25 kg_f/cm^2G and an operating frequency of 40 Hz.

(4) As the charge pressure increased, the operating frequency for minimum input power increased because of the increase of the resonant frequency.

ACKNOWLEDGMENT

This work is supported by the "Dual use technology program."

REFERENCES

1. Gifford, W. E. and Longsworth, R. C., "Pulse Tube Refrigeration," *Trans. ASME J. of Eng. for Industry*, Paper No. 63-WA-210 (1964).
2. Mikulin, E. I., Tarasov, A. A. and Shkrebynock, M. P., "Low Temperature Pulse Tube Refrigeration," *Adv. in Cryogenic Engineering*, Vol. 29 (1984), pp. 629-637.
3. Radebaugh, R., Zimmerman, J., Smith, D.R., and Louie, B., "A comparison of three types of pulse tube refrigerators: new methods for reaching 60 K," *Adv. Cryogenic Engineering*, Vol. 31 (1986), p. 779.
4. Zhu, S. et al., "Double inlet Pulse Tube Refrigerators: An Important improvement," *Cryogenics*, 30 (1990), pp. 514-520.
5. Roach, P. R. and Kashani, A., "Pulse tube coolers with an inertance tube: theory, modeling and practice," *Adv. Cryogenic Engineering*, Vol. 43 (1998), p. 1895.
6. de Boer, P. C. T., "Performance of the inertance pulse tube," *Cryogenics*, Vol. 42 (2002), pp. 209-221.
7. Ravikumar, K. V. and Matsubara, Y., "Experimental results of pulse tube cooler with inertance tube as phase shifter," *Cryocoolers 10* (1999), pp. 291-298.

Measurements of Phase Shifts in an Inertance Tube

Michael A. Lewis, Peter E. Bradley, Ray Radebaugh, and Ercang Luo*

National Institute of Standards and Technology
Boulder, Colorado, USA

*Chinese Academy of Sciences
Technical Institute of Physics and Chemistry
Beijing China

ABSTRACT

Phase shifts and mass flows were measured at the inlet of an inertance tube, and the results are compared with transmission line models. The mass flow rates at the entrance to the inertance tube are obtained using a hot-wire anemometer. The hot wire was calibrated in oscillating flow conditions by mass flow rate comparisons at two other locations in the apparatus. Measurements were made and future work will attempt to show that by adjusting the diameters and lengths of the inertance tubes as well as the operating conditions, we will be able to independently identify the effects of resistive, inertance, and compliance components. We discuss the hot wire calibration procedure used to ensure self-consistency among the various transducers and system mass flowrate measurement calculations. The magnitude and phase of the inertance tube complex impedance are measured and discussed. The size of the inertance tube studied here was 1.5 mm diameter by 1.15 m long with frequencies between 30 and 70 Hz.

INTRODUCTION

The phase between flow and pressure in a pulse tube refrigerator has a large influence on losses in the regenerator. Inertance tubes shift this phase to more desirable values, but existing models for the phase shift need to be more experimentally verified. Measurements were made to calculate the mass flow rates and phase angle at the inlet of an inertance tube using hot wire anemometry. In order to make these measurements accurately, a systematic procedure had to be instituted to carefully measure mass flows and phase shift throughout the apparatus prior to the inertance tube installation. The experiments used a commercially available linear compressor with duel-opposed pistons of diameter 16.5 mm and a 10 mm peak-peak stroke. The maximum swept volume was 4.3 cm^3. At each end of the compressor there were LVDT rods threaded into the piston shaft that were contained in an o-ring sealed sensor housing. These piston position sensor devices provided a way of calibrating the piston position during operation and calculating a mass flow measurement at the piston face. This provides a mass flow measurement at one end of the system. At the other end of the system the mass flow at the reservoir volume inlet was measured using the pressure and temperature measurements along with the ideal gas law for the

Cryocoolers 13, edited by R. G. Ross, Jr.
Springer Science+Business Media, Inc., New York, 2004

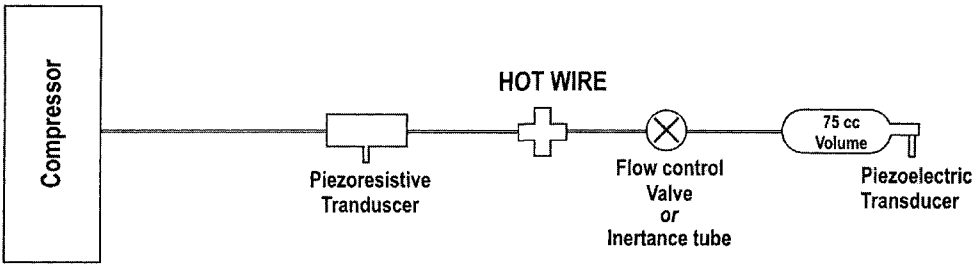

Figure 1. Experimental test schematic.

volume, assuming adiabatic behavior. The hot wire anemometer was originally calibrated using a mass flow meter reference standard at steady state flow conditions. This calibration equation needed to be corrected for the oscillating flow conditions under which the experiments were operated. Using the fundamental measurements at the reservoir volume and the calibrated piston displacement measurements we were able to recalibrate the hot wire anemometer under oscillating flow conditions and use the hot wire measurements for our inertance tube measurements.

MASS FLOW CALCULATIONS

The calibration test experiment consisted of the 4.3 cm^3 compressor, hot wire anemometers installed in stainless steel housing, flow control valve and reservoir volume. A schematic of the experiment can be seen in Figure 1. The flow control valve would later be replaced with the actual inertance tube to be tested. The associated volumes were 1.4 cm^3 from the compressor to the hot wire, 0.35 cm^3 from the hot wire to the flow valve, and 78 cm^3 within the reservoir volume to the flow valve. The diameter of the connecting tube was 2.56 mm. Temperature measurements were taken at the compressor, hot wire and reservoir volume. Pressure measurements were recorded at the compressor using a piezoresistive transducer and at the reservoir volume using a piezoelectric pressure transducer. The volume variation in the compressor was measured using a lock-in amplifier to read the output of the piston displacement sensor. Helium gas was used as the test fluid for all measurements. The mass flow measurement at the reservoir was calculated by

$$\left|\dot{m}\right|_r = \frac{2\pi f |P| V_{res}}{\gamma R T_{res}} \quad , \tag{1}$$

where f is the frequency, $|P|$ is the amplitude of the dynamic pressure, V_{res} is the volume of the reservoir, R is the gas constant per unit mass, and T_{res} is the temperature of the helium gas in the reservoir volume.

The mass flow measurement at the piston was calculated by

$$\left|\dot{m}\right|_p = 2\pi f |V| \rho \quad , \tag{2}$$

where $|V|$ is the magnitude of the volume variation of the piston and ρ is the average density.

The hot wire was originally calibrated using a commercially manufactured mass flowmeter over the expected operating range at steady state flow conditions. With the experimental operating condition being under oscillating flow conditions, comparisons with the mass flow rates measured at the compressor and the reservoir needed to be examined and corrections applied to account for this oscillating flow. The mass flowrates at the reservoir volume are calculated using fundamental measurements of pressure, temperature, known volumes, and gas constants. The mass flowrates measured at the compressor and at the hot wire were compared with the reservoir measurements for self-consistency.

CALIBRATION PROCEDURES FOR THE HOT WIRE

Experimental Conditions

The experimental conditions were average line pressures of 2.5 MPa, 2.0 Mpa, and 1.5 MPa with pressure ratios set at 1.1, 1.15, 1.2, 1.25 and 1.3. The operating frequencies were 70, 50 and 30 Hz. For the actual hot wire calibration in oscillating flow conditions the system was pressurized to the desired pressure and maintained during the experiment. The desired frequencies were set with a function generator. The pressure ratios were then set by adjusting the flow control valve, initially in the experiment, for the hot wire calibrations. Therefore, we would obtain data sets that had varying pressure ratios with constant line pressure, frequency, and electrical input power.

Compressor Mass Flow Corrections

The primary means of calibrating the hot wire anemometer for the oscillating flow is against the flow measured at the entrance of the reservoir. A secondary calibration source is the compressor, which is at the other end of the system. Measurements of the piston position give the mass flow at the piston face according to Eq. (2). When an oscillating pressure is present, the flow amplitude at any other location decreases for the increasing distance from the piston face, depending on the void volume between the piston and the location. With the valve closed, the flow is zero there, and the flow at the piston face is that required to produce a given pressure ratio in the void volume between the piston and the valve. The flow at the piston with the valve closed then becomes a correction term. When that term is subtracted from any measured piston flow with the valve open or with the valve replaced by an inertance tube, the result is the flow at the valve or the inertance tube entrance. The correction is actually a phasor that must be subtracted as a phasor from the flow measured with the same pressure ratio once the valve is opened. Figure 2 indicates this phasor subtraction to provide the corrected mass flow at the valve or inertance tube inlet when pressure oscillations exist. The pressure ratios are adjusted in these measurements by varying the compressor input power whenever the valve is open or interance tube is inserted.

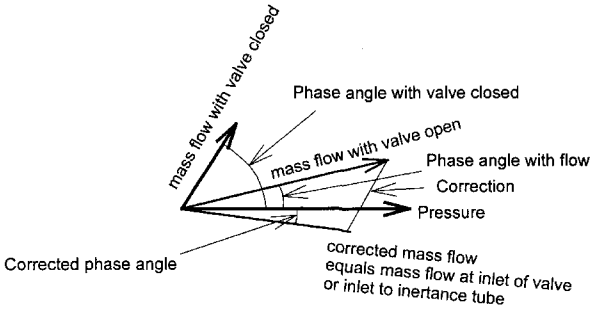

Figure 2. Phasor diagram with mass and phase correction technique.

Hot Wire Mass Flow Measurements and Phase Angle Calculations

The hot wire anemometer was made of 3.8 μm diameter tungsten wire and was originally calibrated in steady flow conditions with the procedure described by Rawlins.[1] A set of calibration coefficients was used in the data acquisition program to calculate a mass flow from the sensor output voltage. Using a Fourier series transformation of the signal, we were able to measure the phase angles of the hot wire with respect to the compressor. Tests were run under the experimental test program described earlier over all the pressure, frequency, and pressure ratios. During these experiments we were able to obtain mass flowrates at three locations in the system. These would be at the face of the piston, the hot wire using the original mass flow calibration, and at the reservoir volume. In principle, the reservoir mass flow determined from Eq. (1) and the compressor mass flow determined from Eq. (2), but corrected as shown in Fig. 2, should be the same whenever no inertance tube is present. Both results can then be used to calibrate the hot wire when no inertance tube is present. In practice, experimental uncertainties give rise to some differences between the two results. Because of the correction that must be applied to the compressor mass flow, we feel that this corrected value has about twice the uncertainty of the reservoir mass flow. Therefore, in using these two calibration values, we give twice the weight to the reservoir mass flow compared with the corrected compressor mass flow.

Calibration of the hot wire anemometer was performed with no inertance tube present, as indicated in Figure 1. Because the reservoir mass flow has the lowest uncertainty, that flow is used as the reference, and the other flows are expressed as a ratio to the reservoir mass flow, as shown in Figure 3 for an average pressure of 2.5 MPa and a frequency of 50 Hz. Other pressures and frequencies gave similar results. The upper curve shows the results from the hot wire based on the steady flow calibration. The curve below that is the corrected compressor mass flow, which is about 20% higher than the reservoir flow for low flows, but agrees well with the reservoir flow at higher flows. The reservoir mass flow could be represented by a horizontal line at 1.0. We note that the steady flow calibration of the hot wire agrees with the reservoir flow measurements in oscillating flow within the 5% experimental uncertainty for a high flow around 1.0 g/s. For lower flows, the steady flow calibration of the hot wire gives a flow about 40% higher than the reservoir flow. The steady flow calibration of the hot wire is then corrected for oscillating flow as shown by the lower curve in Figure 3. This new hot wire curve lies between the reservoir flow and the corrected compressor flow, but the reservoir flow is given the higher weight as discussed previously. We expect the new hot wire calibration curve has an uncertainty of about 10%. Figure 4 shows the measured phase angles of the flow at the three locations with respect to the compressor pressure versus the magnitude of the reservoir mass flow. Because the valve represents a purely resistive flow element, we would expect the flow to be in phase with the pressure.

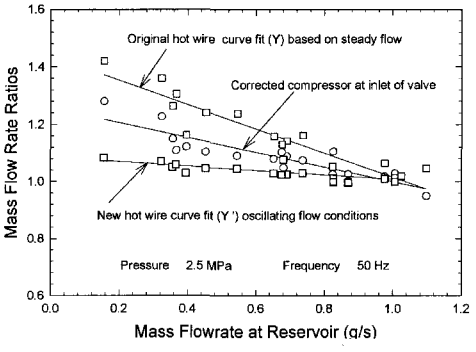

Figure 3. Hot wire curve fit using oscillating flow.

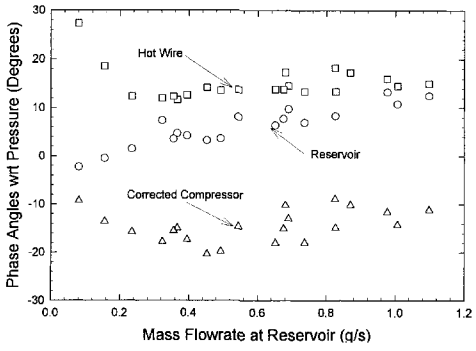

Figure 4. Phase shifts with respect to compressor pressure.

As can be seen in Figure 4. the corrected compressor values are lower than expected by about 15 degrees. The results for the reservoir phase are close to the expected 0 degrees for the lower flow rates, but then tend to drift up to about 10 degrees for the higher flow rates. The phase shifts from the hot wire are about 12 degrees higher than expected. No corrections were made to any of the phase data at this time, although a subtraction of 10 degrees from the hot wire may be warranted. These results indicate that the uncertainty associated with the phase measurements of the hot wire is about 10 degrees.

INERTANCE TUBE EXPERIMENTS

The inertance tube was installed exactly where the valve was located in the experiment with close attention to not changing any of the other volumes in the experiment. The stainless steel tube was 1.15 meters in length with an inside diameter of 1.57 mm. The hot wire correction for oscillation flow as discussed earlier was used to measure the mass flow at the inertance tube inlet.

The experimental test plan was completed on the inertance tube over the pressure, frequency and pressure ratio ranges as describe previously. Figure 5 shows the relative dynamic pressure amplitude at the inlet on the inertance tube for various average pressures over the mass flowrate range tested. The relative dynamic pressure ratio, P_1/P_0, is the ratio of the dynamic pressure amplitude to the average pressure.

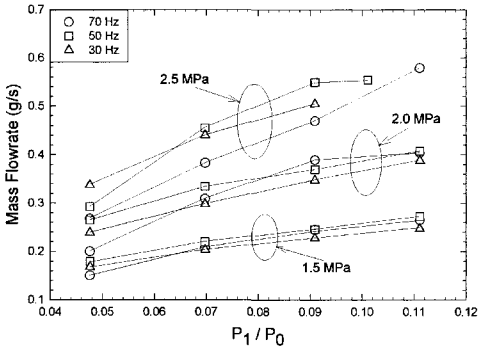

Figure 5. Dynamic pressure ratio at inlet of inertance tube.

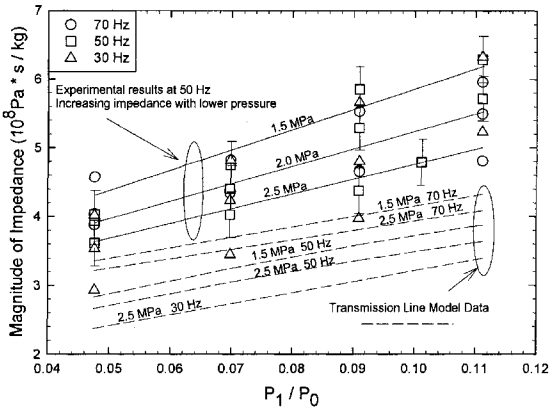

Figure 6. Magnitude of impedance at inertance tube.

We compared our measurements with those of a transmission line analysis modeling program developed at NIST. The magnitude of the impedance at the inlet of the inertance tube is shown in Figure 6. Data uncertainty bands of about $\pm$ 8% are indicated on the experimental results at 50 Hz and 2.5, 2.0 and 1.5 MPa. Solid lines are drawn within these uncertainty bands for these sets of data to indicate the approximate slope and the magnitude of the impedance. These experimental data results show agreement with the model in having a rising slope and increase of impedance with lower pressure. The uncertainty bands are located on these data points only for the purpose of clarity on the plot. All experimental data plotted have the same uncertainty value. The transmission line model data is shown using dashed lines. The results show that our measured magnitude of the impedance values are higher than those predicted by the model on the order of about 25 %.

The phase of the inertance tube impedance (pressure-flow) is shown in Figure 7. The results show that the measured phase angles are lower than those of the transmission line model. There is agreement with all three pressures tested for each of the frequencies. Error bars are shown for the 50 Hz data that indicate a $\pm$ 5 degree uncertainty. At 30 to 50 Hz it is lower by 8 to 10 degrees and at 70 Hz it is about 15-20 degrees. Although we made correction for the mass flows at the compressor, we did not correct for any phase-angle differences. From our data results it appears that a correction should have been made for the hot wire phase shifts of about 10-12 degrees, and this would have brought our measured values more in line with the transmission

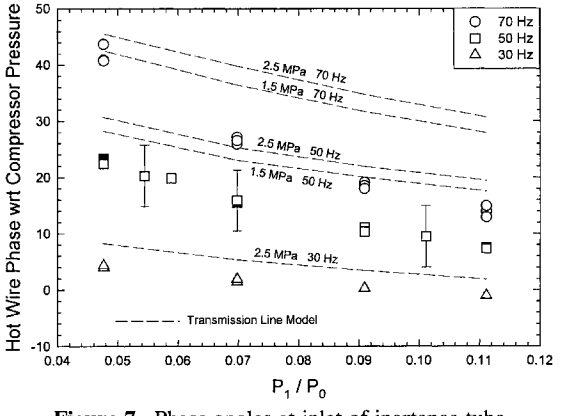

Figure 7. Phase angles at inlet of inertance tube.

line models for a given flow rate. However, as shown in Figure 6, the magnitude of the impedance from the model is about 25% lower than the measured value impedance. Therefore, for the same pressure ratio, the calculated flow is 25% higher than the measured values. For the same pressure ratio, the phase calculated from the model agrees with the measurement to within about 10 degrees.

In the entire set of model data shown, the conditions are assumed to be adiabatic and with a tubing surface roughness of one micron. If we assume isothermal behavior, the model predicts lower phase angles, with the largest change being at high pressure ratios and high frequencies. In our experiments, that would shift the 2.5 MPa and 70 Hz about 3 degrees lower toward the direction of the experimental data results. For all other cases, the calculated phase angle differences would be less than this 3-degree change. Similar effects of the impedance at isothermal conditions would predict an increase of impedance of 5 % at 2.5 MPa and 70 Hz, where again the maximum effect would be seen; this would shift the calculations toward the experimental results. At a surface roughness of 3 microns, the model calculates a decrease in phase shift by 2 degrees and an increase of impedance by 4 degrees. These effects are the same for all experimental test conditions.

CONCLUSIONS

We have developed a measurement technique using a hot wire anemometer to measure mass flows at the inlet of inertance tubes as well as phase shifts with respect to the compressor pressure. The hot wire calibration data were compared with mass flows at the compressor and reservoir locations in the experiments and a weighted curve fit to the data was calculated to obtain a reliable calibration for the hot wire in oscillating flow. The experimental results for the impedance of an inertance tube were compared with a transmission line model. The results showed that the transmission line model predicted impedance values about 25 % lower than the measured values. The model also predicted phase shifts that were higher than the measured values ranging from 8 degrees at the lower frequency range to 20 degrees at the higher frequency range. Corrections to the hot wire calibration from steady flow were made for the mass flow rate measurements in oscillating flow. However, no corrections were made for the phase angle measurements. With additional data analysis, it may be determined that a phase angle correction should also be applied that would give better agreement between the model and the measured data.

FUTURE RESEARCH

Additional experiments will involve longer length inertance tubes along with larger inside diameter tubing. We plan to extend the frequency range and increase the range of pressure ratios. With larger inside diameters we will need to utilize a larger compressor and increase the power flows.

REFERENCES

1. Rawlins, W.C., *The Measurement and Modeling of Regenerator Performance in an Orifice Pulse Tube Refrigerator*, Thesis to the Department of Chemical Engineering, University of Colorado, Boulder (1992), pp. 115-198.

Phase Shift and Compressible Fluid Dynamics in Inertance Tubes

Barrett Flake[1] and Arsalan Razani[2]

[1]Air Force Research Laboratory
Kirtland AFB, New Mexico, USA, 87117

[2]University of New Mexico
Albuquerque, New Mexico, USA, 87131

ABSTRACT

The phase shift between pressure and mass flow predicted by an analytic solution for incompressible oscillatory flow in an infinite tube is presented and compared with numerical solutions to the incompressible Navier-Stokes equations for an inertance tube computed by a commercial computational fluid dynamics (CFD) code. Compressible flow equations are also solved by the CFD program and the resulting phase shifts and temperature profiles are reported. A parametric study of the dependence of inertance tube phase shift upon diameter, frequency and length is presented. A turbulence model is included in some runs to evaluate the effect of turbulence on computed phase shift.

INTRODUCTION

Relatively long and small diameter "inertance tubes" have been used with pulse tube type cryocoolers to improve refrigeration performance. In a pulse tube cryocooler, a phase difference exists between pressure and mass flow and this difference depends upon operating parameters and location in the pulse tube.[1] Heat transfer performance at the cold and hot heat exchangers as well as the regenerator depends upon the phase difference between mass flow and pressure. However, phase shift can not be independently set at any given location in the pulse tube cryocooler. In orifice pulse tubes, the pressure and mass flow at the hot heat exchanger (right end of the tube) may be closely in phase. For a sufficiently large reservoir, when the pressure at the tube side of the orifice is at its maximum, the flow through the orifice is also at its maximum. For finite reservoirs, the mass flow will lead the pressure at the orifice. The mass flow leading angle increases with distance from the orifice down the pulse tube toward the cold end heat exchanger and increases more through the regenerator.

Altering the phase difference between mass flow and pressure at the hot end will cause a change in the phase difference at the cold end and in the regenerator. If the phase at the hot end is shifted such that the mass flow lags the pressure wave, the mass flow lead at the cold end and through the regenerator can be reduced resulting in improved pulse tube system performance. The advantage of altering the hot end phase shift is demonstrated in a "double inlet" pulse tube. In the double-inlet pulse tube, a small fraction of flow from the compressor is ducted through an

Cryocoolers 13, edited by R. G. Ross, Jr.
Springer Science+Business Media, Inc., New York, 2004

orifice to the hot end of the tube (bypassing the regenerator and pulse tube) such that the resulting total hot end mass flow lags the pressure. However, oscillating the fluid through the orifice and bypass requires some fraction of compressor work and the flow loop created between the compressor and hot end of the pulse tube can allow a net average or "DC" flow around the loop that tends to degrade to refrigeration performance.

An inertance tube offers the effect of mass flow lagging the pressure wave at the hot end of the pulse tube but without additional work from the compressor or creating the DC flow loop.[2] This work examines the dependence of the phase shift in an inertance tube upon tube geometry and operating parameters. The dependence is shown analytically for the case of a laminar, incompressible fluid in an infinitely long tube and is investigated numerically via a commercial CFD code (Fluent® [3]) for a compressible fluid (helium).

OSCILLATING INCOMPRESSIBLE FLOW INSIDE AN INFINITE TUBE - ANALYTIC SOLUTION

Analytic solutions for the time varying velocity distribution in the case of incompressible flow driven by a periodic pressure gradient in an infinite tube have been in the literature for some time.[4,5,6,7] Assuming negligible variations in the axial direction and only axial flow, a simplification of the Navier-Stokes equations yields

$$\frac{\partial u}{\partial t} = C\cos\omega t + \nu\left(\frac{\partial^2 u}{\partial r^2} + \frac{1}{r}\frac{\partial u}{\partial r}\right), \tag{1}$$

where u is the axial velocity, C is the amplitude of the pressure wave, ω is the frequency of oscillation, ν is the fluid kinematic viscosity and r is the radial direction in the tube. The periodic pressure gradient driving the flow is given by

$$\frac{dp}{dx} = -\rho C\cos\omega t\,, \tag{2}$$

where ρ is the fluid density.

As the objective in using an inertance tube is altering the phase shift between oscillating mass flow and pressure, it is instructive to consider the range of phase shift possible in this incompressible case. A negative pressure gradient drives flow in the positive x direction. The negative gradient corresponds to a positive gage pressure that is 180° out of phase with the oscillating pressure, $p(x,t)$ proportional to cos ωt. In a force balance, the pressure force is countered by the fluid inertia and viscous forces. For the case of an inviscid fluid ($\nu = 0$), the oscillating pressure would tend to accelerate the fluid during the positive half of the pressure cycle and decelerate the fluid in during the negative half. Therefor, peak positive velocity would occur at the end of the positive pressure half cycle (end of acceleration) and peak negative velocity would occur at the end of the negative half cycle as shown in the sinusoids of Fig. 1. Or, integrating Eq. (1) with $\nu = 0$ yields $u(t) = (C/\omega)$ sin ωt. This limiting case of an inviscid fluid corresponds to a mass flow that lags the pressure oscillations by 90°.

For the viscous case of a Newtonian fluid, Eq. (1) is solved assuming no slip at the wall (u = 0 at $r = a$, the tube wall radius,).

$$u(r,t) = -\frac{iC}{\omega}\left[1 - \frac{J_0\left(\sqrt{-i\lambda}\,\frac{r}{a}\right)}{J_0\left(\sqrt{-i\lambda}\right)}\right]e^{i\omega t} \tag{3}$$

where $\lambda = a^2\omega/\nu$ and J_0 is the zero order Bessel function. The velocity profile given by Eq. (3) demonstrates a phase difference between the fluid near the walls and the fluid in the core of the

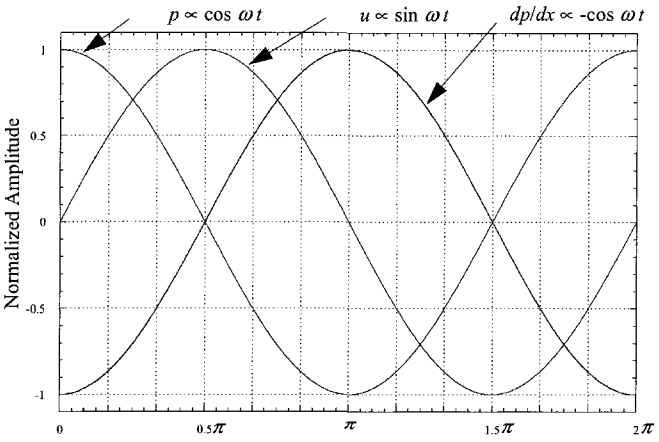

Figure 1. Normalized curves of pressure, pressure gradient and velocity for inviscid, incompressible oscillatory flow.

tube. This phase difference occurs as the pressure forces driving the flow are transmitted near instantaneously through the fluid, while the viscous stress at the wall takes some time to diffuse toward the core.[8] The magnitude of the phase difference depends upon the fluid properties, oscillating frequency and tube radius. As an example, Fig. 2 shows velocity profiles for a fluid having the density and viscosity of helium at 2 MPa and 300 K, oscillating at 50 Hz in a tube 2 mm in diameter. For this case the dimensionless frequency λ is 49.25 and the amplitude of the pressure gradient is 50 kPa/m. Note that when ωt is at $7\pi/8$, the core of the flow has a positive velocity while the flow near the wall is in the opposite direction. Just beyond $\omega t = 7\pi/8$, the negative mass flux near the wall equals the positive mass flux in the core resulting in a zero total mass flow rate which is out of phase with the core flow and the driving pressure oscillations. For this example case, when $\omega t \cong 0.93\pi$, the mean flow velocity is zero. Since the oscillating pressure passes through zero at $\omega t = \pi/2$, the pressure leads the mass flow by 77.2°.

To compare CFD prediction capability with the analytic velocity profile solution, an incompressible flow case was run for a 2 mm diameter tube 1 m long. The computational grid was 1000

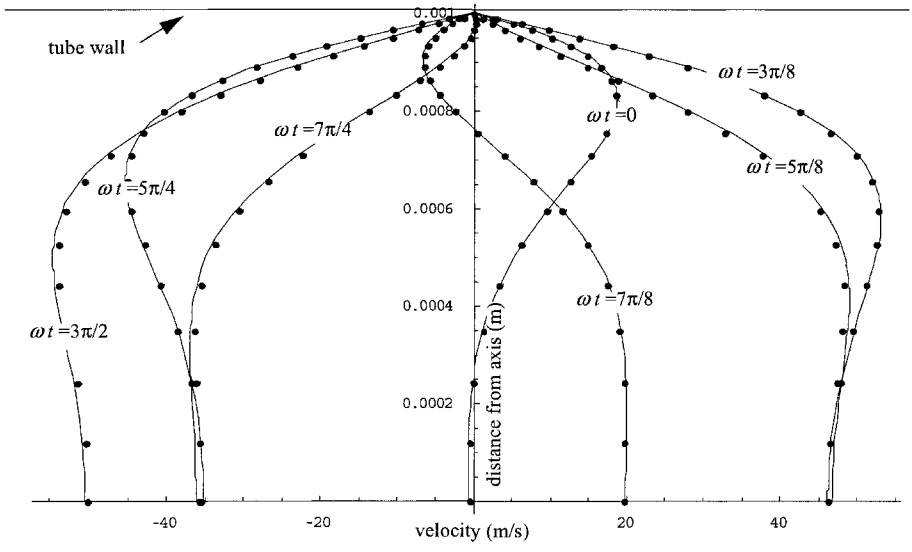

Figure 2. Velocity profiles from the analytic solution (Eq. (3)) and numerically calculated values (data points) for helium oscillating at 50 Hz in a 2 mm diameter tube.

cells along the length of the tube and 20 cells along the radius, with a more dense distribution near the tube wall. Constant fluid properties were set equivalent to those of helium at 2 MPa and 300 K ($\rho = 3.18$ kg/m^3 and viscosity, $\mu = 2.03$ kg/m-s). The boundary conditions included a sinusoidally oscillating pressure at the tube entrance with an amplitude of 50kPa while the tube outlet pressure was constant at 0 Pa (gage). Velocity data was recorded at the tube midpoint where the amplitude of the pressure gradient was approximately 50kPa/m. The computed data points are shown in Fig. 2 along with the analytic solution.

The velocity distribution of Eq. (3) can be integrated over the cross sectional flow area to give the mean cross sectional velocity $\bar{u}(t)$.

$$\bar{u}(t) = -\frac{iC}{\omega}\left[1 - \frac{2}{\sqrt{-i\lambda}}\frac{J_1\left(\sqrt{-i\lambda}\right)}{J_0\left(\sqrt{-i\lambda}\right)}\right]e^{i\omega t} \tag{4}$$

Evaluating the phase angle of this complex quantity yields the phase difference between mean velocity and pressure.

The phase shift between the pressure and the mean velocity given by Eq. (4) is plotted against the dimensionless frequency λ in Fig. 3. As λ tends toward zero (some combination of very low frequency, small tube diameter or very viscous fluid), the average velocity and pressure tend to be in phase. After the knee in the curve at around $\lambda = 20$, the phase difference asymptotically approaches 90°. For the example CFD case used to generate the points on Fig. 2, $\lambda = 49.3$ and corresponds to a phase difference of 77.2°.

A phase difference also exists between the average velocity and core velocity as illustrated by the velocity profiles in Fig. 2. The phase difference between average and core velocities has a maximum of 18.76° at $\lambda = 29.0$. The phase difference between the core velocity (Eq. (3) at $r = 0$) and the oscillating pressure is also plotted in Fig. 3. At $\lambda = 49.3$ (corresponding to the flow conditions of Fig. 2), the core velocity phase difference is 92.5°. Notice that in Fig. 2 at $\omega t = 0$, the core velocity is slightly negative, lagging the peak of the pressure oscillation by 2.5°. As the core velocity can be out of phase with the average velocity, care should be taken in experimental inertance tube measurements to distinguish whether core or average velocity is being measured.

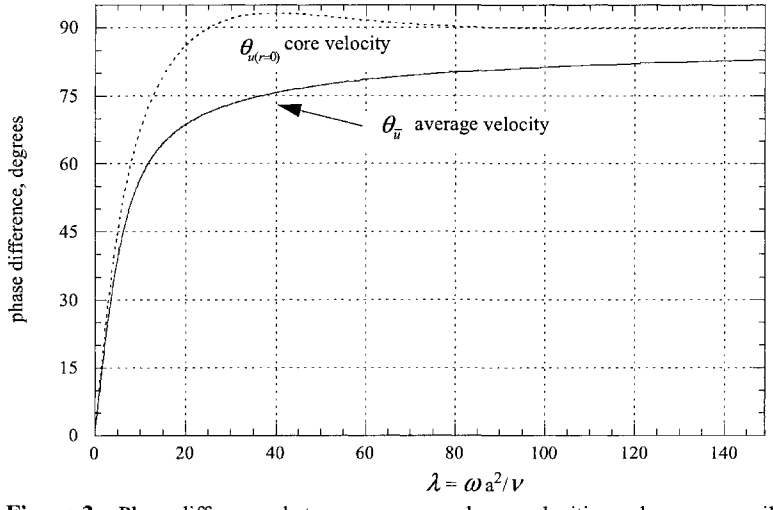

Figure 3. Phase differences between average and core velocities and pressure oscillations as a function of the dimensionless frequency, λ.

COMPRESSIBLE FLOW

For compressible flow, the force balance includes not only pressure, inertial and viscous terms, but also the reversible fluid compression and expansion associated with heating and cooling the fluid. The irreversible process of viscous dissipation is present in both compressible and incompressible flows, but is usually relatively small in low velocity flows and is not included in the calculations in this work.

In the incompressible case described above, the phase shift is independent of the pressure amplitude and, for an infinite tube, is not dependent upon length. Phase shift is dependent upon frequency, tube radius and fluid kinematic viscosity. For the compressible case, both pressure amplitude and tube length affect the phase difference at the inlet.

The commercial CFD code, Fluent®, numerically solves the time dependent mass, momentum and energy conservation equations and predicts flow field properties.[3] Fluent is used in this work to predict the inlet phase shift of inertance tubes for compressible fluids. The geometrical representation of the inertance tube assumed 2-D axisymmetric oscillating flow in a simple thin, long tube. A sinusoidally oscillating pressure of given amplitude and frequency was set at the tube inlet. The tube outlet was either fixed at zero gage pressure or the pressure was calculated to match that of a 1 liter fixed volume isothermal reservoir. Since energy conservation equations are solved in the compressible case, the tube side wall heat transfer must be specified. Two tube side wall thermal boundary conditions were evaluated, some cases had an isothermal boundary at 300 K while most cases had the boundary as adiabatic.

For all compressible flow cases, the inlet phase shift prediction was less than that given by the analytic solution for the incompressible flow case. In Fig. 4, inlet phase shift data points are plotted along with the analytic curve. The difference between the predicted compressible flow and analytic phase shift varied with tube diameter and length as well as driving pressure frequency and amplitude. The calculated phase shifts along with details for each case run is given in Table 1.

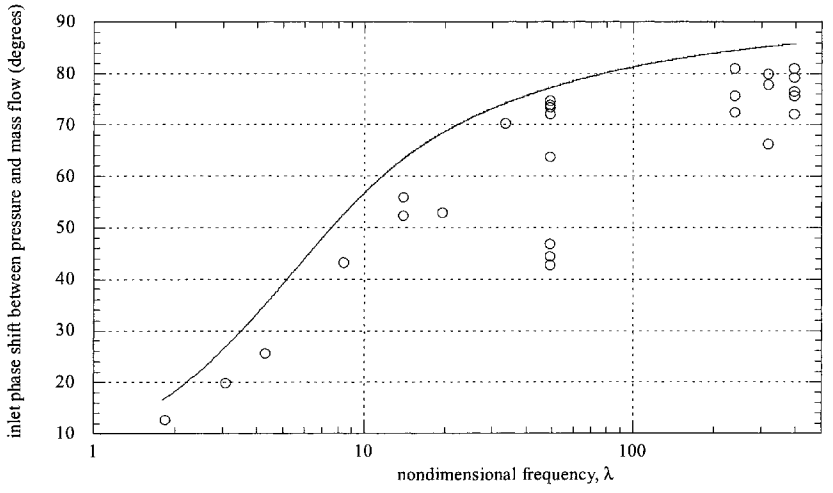

Figure 4. Computed phase difference between inlet mass flow and pressure for compressible flow cases (data points) and the analytic incompressible flow phase difference (curve of Eq. (4)) as a function of the dimensionless frequency, λ.

Case Studies

Several cases were run to compare predicted phase shift for compressible laminar flow in inertance tubes. The phase shift results are presented in Table 1. Based upon experimental reports on turbulence in oscillating flow (discussed below), most applications of inertance tubes on pulse tube cryocoolers will give rise to either partially or fully turbulent flow inside the inertance tube. However, the laminar cases are computationally quicker to solve and can demonstrate phase shift dependence upon pressure amplitude and tube length that may also be present in the turbulent cases. The general effect of turbulence is that of increased viscosity which corresponds to a decrease in dimensionless frequency, λ, and a decrease in the phase shift.

A substantial and historical body of research on turbulence in steady pipe flow exists where it is universally agreed that the transition from laminar to turbulent flow occurs for Reynolds numbers greater than 2100. The transition between laminar and fully turbulent flow in the oscillating case may be marked by turbulence that exists in only part of the period. For example, turbulent bursts may occur in the decelerating part of the period (flow under an adverse pressure gradient), then relaminarize during the accelerating portion. In a recent review of oscillating flow research [9], no existing uniform agreement on the transition from laminar to turbulent flow was found. Different flow parameters were used in characterizing the transition from laminar to turbulent oscillating tube flow. Some reports classified transition to turbulent flow by the Reynolds number, Re_δ, based upon the Stokes layer thickness, δ, and the amplitude of the center line velocity, U_0, and the non dimensional frequency λ used in Eq. (4) above.

$$Re_\delta = \frac{U_0 \delta}{\nu} \tag{5}$$

$$\delta = \sqrt{\frac{2\nu}{\omega}} \tag{6}$$

Various works cited in the review reported a transition to turbulence for a range of Re_δ between 110 and 1100.

The Reynolds number in terms of the amplitude of the oscillating mean flow velocity, $\bar{U}$ and tube diameter, D, was also used to categorize the conditions under which turbulent bursts first occur:

$$Re_{os} = \frac{\bar{U} D}{\nu} \tag{7}$$

The critical Reynolds number in this case is given as a function of a proportionality constant, K, and the square root of the dimensionless frequency, λ,

$$Re_{os,c} = K\sqrt{\lambda} \cdot \tag{8}$$

One report mentioned gave[10] the critical Reynolds number, $Re_{os,c} = 2450$ for $\sqrt{\lambda} < 1$ and $Re_{os,c} = 882\sqrt{\lambda}$ for $\sqrt{\lambda} > 7$, which agreed well with other reported experimental values. Considering the range of diameters, velocities and frequencies used in inertance tubes, almost all applications will include Re exceeding $Re_{os,c}$ with at least some part of the cycle will having turbulent flow.

A variety of turbulence models are available in the CFD code[3] and a k-ω turbulence model was used for the cases in this work. The standard k-ε turbulence model includes transport equations for the turbulent kinetic energy, k, and its rate of dissipation, ε. The k-ω model uses a specific dissipation rate, ω, which may be thought of as the ratio of ε to k. A recent report on using CDF to model pulsatile flow in stenotic vessels found that the k-ω model yielded better results

Table 1. CFD case summary of calculated inertance tube inlet mass vs. pressure phase difference along with specified boundary and flow conditions.

Case #	tube diameter (mm)	tube length (m)	frequency (Hz)	dimensionless frequency, λ	inlet phase shift (deg)	inlet pressure amplitude (kPa)	laminar or turbulent model	end pressure boundary P = 0 gage R = 1000 cc reservoir	tube side wall boundary A=adiabatic T=300K const
1	0.5	1.0	30	1.8	12.7	50	lam.	P	A
2	0.5	1.0	50	3.1	19.8	50	lam.	P	A
3	0.5	1.0	70	4.3	25.6	50	lam.	P	A
4	0.5	2.0	50	3.1	4.5	50	lam.	P	A
5	1.0	1.0	50	12.3	55.8	50	lam.	P	A
6	1.0	2.0	30	7.4	43.2	50	lam.	P	A
7	1.0	2.0	50	12.3	52.2	50	lam.	P	A
8	1.0	2.0	70	17.2	52.9	50	lam.	P	A
9	2.0	1.0	50	49.3	44.3	50	k-ε	P	A
10	2.0	1.0	50	49.3	72.0	50	lam.	P	A
11	2.0	1.0	50	49.3	63.7	150	lam.	P	A
12	2.0	2.0	30	29.6	70.2	25	lam.	P	A
13	2.0	2.0	50	49.3	74.7	25	lam.	P	A
14	2.0	2.0	50	49.3	73.3	50	lam.	P	A
15	2.0	4.0	50	49.3	46.8	50	lam.	P	A
16	5.33	3.84	30	238.4	81.0	40	lam.	R	T
17	5.33	3.84	40	317.9	80.0	40	lam.	R	T
18	5.33	3.84	50	397.4	75.6	40	lam.	R	T
19	5.33	3.84	50	397.4	81.0	40	lam.	R	A
20	5.33	3.84	50	397.4	79.2	140	lam.	R	A
21	5.33	3.84	30	238.4	75.6	30	k-ω	R	A
22	5.33	3.84	30	238.4	72.4	50	k-ω	R	A
23	5.33	3.84	40	317.9	77.8	40	k-ω	R	A
24	5.33	3.84	40	317.9	66.2	100	k-ω	R	A
25	5.33	6.0	40	317.9	35.1	100	k-ω	R	A
26	5.33	3.84	50	397.4	72.0	100	k-ε	R	A
27	5.33	3.84	50	397.4	76.5	100	k-ω	R	A
28	5.33	5.0	50	397.4	11.7	100	k-ω	R	A
29	5.33	6.0	50	397.4	-68.4	100	k-ω	R	A
30	5.33	8.0	50	397.4	-65.7	100	k-ω	R	A

than other available turbulence models[11]. However, without supporting experimental data, the numerical predictions in this work serve only to calculate a dependence of phase shift upon other flow parameters and to distinguish that phase shift in turbulent flow calculations is less than that in laminar flow.

Phase shift dependence upon tube geometry and flow conditions

All CFD computed phase shifts between inlet pressure and mass flow rate in the compressible flow cases were less than that predicted for the incompressible, infinite tube case (see Fig. 4). The difference generally increased with increases in frequency, inlet pressure amplitude and tube length. Fig. 5 includes three plots of phase shift versus tube length, frequency and inlet pressure amplitude.

The largest computed change was evident in a few cases with very long tube lengths. Phase shift for the 5.33 mm diameter tube at 50 Hz and 50 kPa pressure amplitude went from 76 ° to -66 ° as the tube length was increased from 3.8 to 8.0 meters. For the same tube operating at 40 Hz, the change from 3.8 to 8.0 m resulted in a less dramatic change (66 ° to 35 °). This change for mass flow lagging pressure to leading pressure for increased tube length was also predicted in earlier numerical work.[2] Other laminar flow cases generally demonstrated a reduction in phase shift with increased length.

The effect of increasing oscillating pressure frequency generally resulted in increased phase shift, just as in the incompressible flow case with increasing dimensionless frequency, λ. However, difference between the calculated phase shift of compressible flows and the analytic predictions for an incompressible fluid oscillating with the same frequency and tube diameter increased with increasing frequency.

Increasing the oscillating pressure amplitude increases the amplitude of the fluid velocity, uniformly resulting in a decrease in the phase shift.

Temperatures along the length of the tube.

For the adiabatic compressible flow cases, a temperature profile along the length of the tube was predicted. (Alternatively, a varying heat flux was predicted for the isothermal cases.) In the adiabatic cases, the cycle averaged fluid temperature near the middle of the length of the tube increased as the number of cycles increased. Comparing cases #18 (isothermal boundary) and #19 (adiabatic boundary), the adiabatic case with warmer tube walls results in a decrease in phase shift. For some given heat transfer relation (e.g. convective, conductive, radiative) between the outer tube and a heat source or sink, a quasi steady temperature profile could be determined. However, for the CFD runs in this report, only adiabatic and isothermal boundaries were set.

Fig. 6 shows a temperature profile averaged over one cycle along the inertance tube for case #8. The tube wall is adiabatic and this case has not reached a quasi-steady state (The cycle average temperature is still increasing with time). The profile was calculated after the simulation had run 60,000 time steps for at total of 148 cycles (2.1 s). The ends remain near the 300 K fixed inlet fluid boundaries, but the mid temperature has increased to 309.5 K.

SUMMARY

The phase difference between inlet mass flow and pressure in very long tubes was calculated from an analytic solution to an incompressible flow case and by use of a commercial CFD program for compressible flow. All CFD computed compressible flow cases demonstrated a decrease in the amount of phase shift by which mass flow leads pressure when compared with that predicted by the incompressible solution for equivalent diameter, frequency and viscosity. The general result of increased pressure amplitude and increased tube length was to decrease the phase difference.

The effect of changing the tube wall thermal boundary should be further investigated computationally and experimentally. For example, the influence of wrapping some portion of the

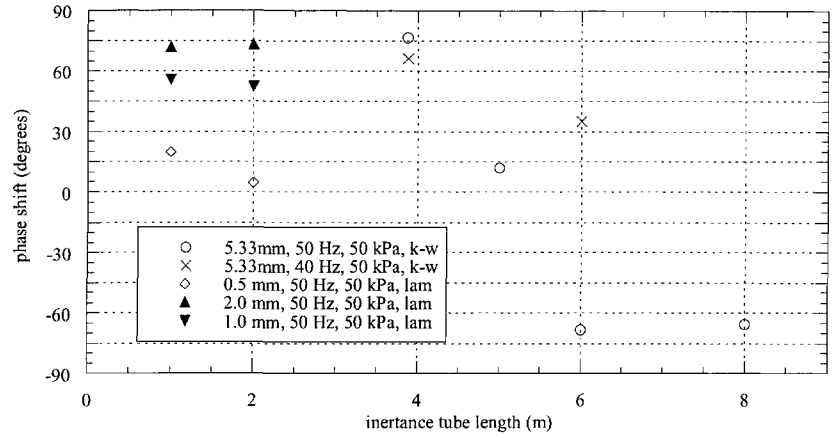

(a)

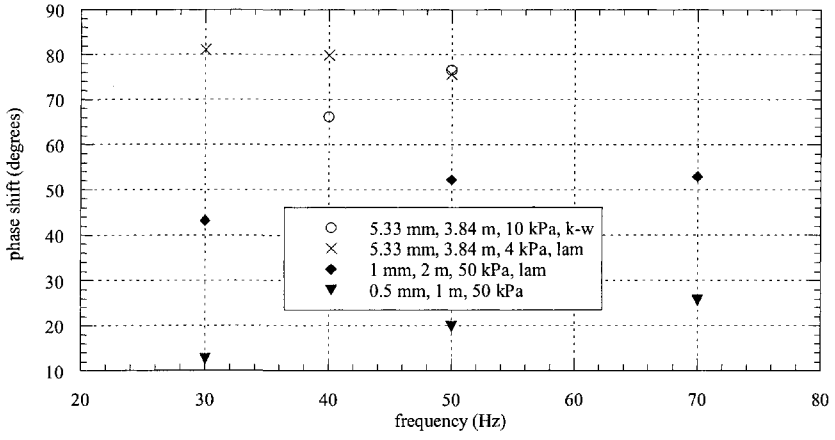

(b)

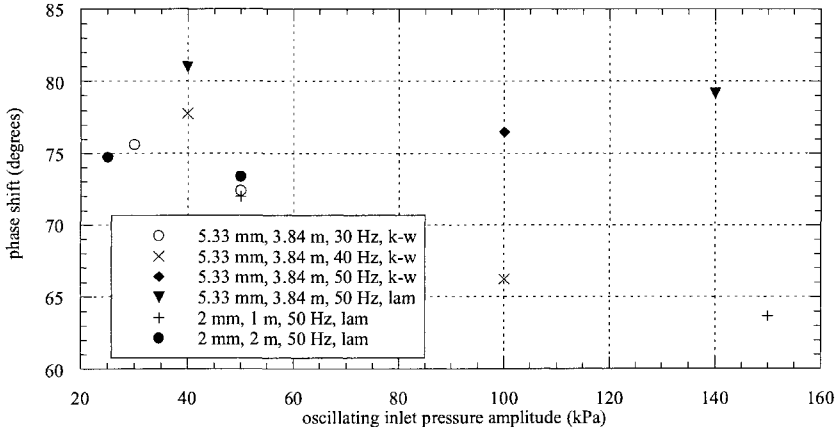

(c)

Figure 5. Inlet phase shift (mass lagging pressure) as functions of a) inertance tube length, b) frequency and c) inlet pressure amplitude.

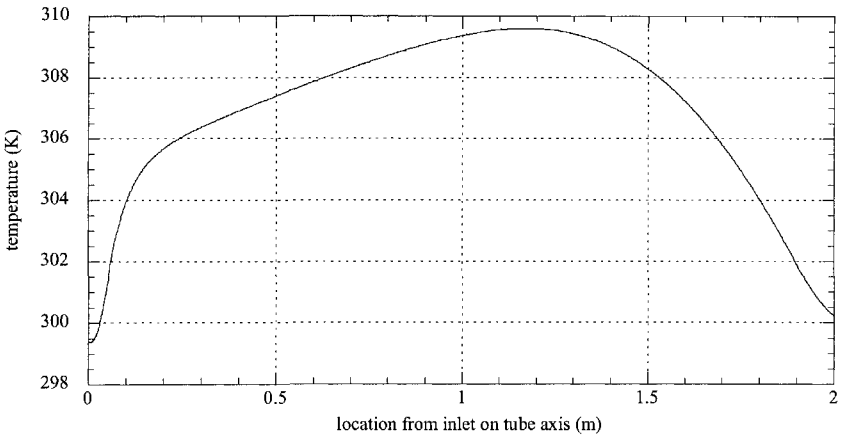

Figure 6. Axial fluid temperature averaged over one cycle. Data corresponds to case #8, after 148 cycles.

inertance tube around or near low temperature regions of the cryocooler upon inlet phase shift should be quantified by measurement and prediction.

This work has demonstrated a capability for CFD predictions of inertance tube performance. The CFD results match analytic prediction for the case of incompressible flow. The CFD calculations must be verified with experimental data to fully assess predictive capabilities. Further, these calculations are currently computationally expensive and are not suitable for the relatively quick predictions valuable to a cryocooler system designer. However, CFD inertance tube models, adequately validated with experimental data, can serve to fill in experimental data points over a wide range of operating conditions including, pressure frequency, amplitude, tube length, tube diameter, working fluid properties and tube thermal boundaries.

REFERENCES

1. Storch, P.J., Radebaugh, R. and Zimmerman, J.E., *Analytical Model for the Refrigeration Power of the Orifice Pulse Tube Refrigerator*, NIST 1342, Boulder, CO (1990).
2. Zhu, S.W., Zhou, S.L., Yoshimura, N. and Matusbara, Y., "Phase Shift Effect of the Long Neck Tube for the Pulse Tube Refrigerator," *Cryocoolers 9* (1997), pp. 269-278.
3. *Fluent 6.1 User's Guide*, Fluent, Inc., Lebanon, NH (2003).
4. Richardson, E.G. and Tyler, E., "The Transverse Velocity Gradients Near the Mouths of Pipes in Which an Alternating or Continuous Flow of Air is Established," *Proc. Phys. Soc. Lond.*, vol. 42 (1929), pp. 1-15.
5. Sexl, T., "Über die von E. G. Richardson entdeckten Annulareffeckt," *Z. Phys.*, vol. 61 (1930), pp 9-28.
6. Ito, H., "Theory of Laminar Flow Through a Pipe with Non-steady Pressure Gradients," *Rep. Inst. High-Speed Mech.*, Tohoku Univ., vol. 3, no. 30 (1953), pp. 163-180.
7. Rosenhead, L., *Laminar Boundary Layers,* Oxford University Press (1966), pp. 388-390.
8. Panton, R.L., *Incompressible Flow*, John Wiley & Sons, 1984, (1984), pp. 266-272.
9. Gündogdu, M.Y. and Carpinlioglu, M.O., "Present State of Art on Pulsatile Flow Theory," *JSME International Journal, Series B*, vol. 42, no. 3, (1999), pp. 384-397.
10. Ohmi, M., and Iguchi, M., "Critical Reynolds Number in an Oscillating Pipe Flow," *Bulletin of the JSME*, vol. 25, no. 200 (1982), p.165.
11. Varghese, S.S. and Frankel, S.H., "Numerical Modeling of Pulsatile Turbulent Flow in Stenotic Vessels," *J Biomech. Engrg.*, vol. 125, pp. 445-460.

CFD Simulation of Multi-Dimensional Effects in an Inertance Tube Pulse Tube Refrigerator

J.S. Cha[1], S.M. Ghiaasiaan[1], P.V. Desai[1], J.P. Harvey[2], and C.S. Kirkconnell[2]

[1]G.W. Woodruff School of Mechanical Engineering
Georgia Institute of Technology, Atlanta, GA 30332, U.S.A.

[2]Raytheon Space and Airborne Systems
El Segundo, CA 90245-0902, U.S.A.

ABSTRACT

Two entire Inertance Tube Pulse Tube Refrigerator (ITPTR) systems operating under a variety of thermal boundary conditions were modeled using a Computational Fluid Dynamics (CFD) code. Each simulated ITPTRs included a compressor, an after cooler, a regenerator, a pulse tube, cold and hot heat exchangers, an inertance tube, and a reservoir. The simulations represented fully coupled systems operating in steady-periodic mode. The objectives were to ascertain the suitability of CFD methods for ITPTRs and to examine the extent of multi-dimensional flow effects in various ITPTR components. The results confirmed that CFD simulations are capable of elucidating complex periodic processes in ITPTRs. The results also showed that a one-dimensional modeling is appropriate only when all the components in the system have large length-to-diameter (L/D) ratios. Significant multi-dimensional flow effects occur at the vicinity of component-to-component junctions, and secondary-flow recirculation patterns develop when one or more components have small L/D ratios.

INTRODUCTION

The design of Pulse Tube Refrigerator (PTR) systems has advanced incessantly since the invention of basic PTR[1], leading to improvements in their performance and lower achievable refrigeration temperatures. The major design variations introduced thus far include the Orifice Pulse Tube Refrigerator (OPTR)[2], double inlet OPTR[3], the modified OPTR[4], the multi-pass OPTR[5], and most recently the Inertance Tube Pulse Tube Refrigerator (ITPTR).[6] The exact nature of the physical phenomena underlying the operation of PTRs is not well-understood, however.[7,8] A fundamental difficulty in all PTRs is that their working fluid compression and expansion processes are not well-defined, and poorly-understood thermal relaxation and phase-lag phenomena dominate their operation. Crucial among these is the phase angle between pressure and mass flow. This phase angle is influenced by the wave resonance phenomena in BPTRs, and is adjusted by orifices and/or valves in various OPTR designs. In an ITPTR, the orifice valve of the simple OPTR is replaced by a long and slender (Inertance) tube that, with proper design, can cause an optimal phase lag between pressure and mass flow rate in the pulse tube.

Cryocoolers 13, edited by R. G. Ross, Jr.
Springer Science+Business Media, Inc., New York, 2004

Computational models have recently been developed for the simulation of the regenerator, or the entire PTR.[10-12] The Sage computer package [9] models an entire PTR assuming 1-D flow, and can optimize a system against a user-selected geometric parameter. The numerical model used by Ju et al.[10] is also 1-D and appears to simulate an entire PTR system. Simulation of a complete PTR system using CFD software packages has also been recently published.

Hozumi et al.[11] performed axi-symmetric and 3-D simulations of BPTRs and OPTRs, with an interest in the effects of gravity and orientation on system performance. Flake and Razani[12] conducted an axi-symmetric analysis of a BPTR and an OPTR, using the Fluent®[13] commercial CFD package, and indicated that the occurrence of recirculation patterns and streaming effects in the simulated pulse tube.

In this paper, we report on CFD simulations addressing the steady-periodic operation of two ITPTR systems. The objectives were to assess the feasibility of CFD simulation of ITPTRs, and to examine the extent and significance of multi-dimensional flow effects in these systems.

SIMULATED SYSTEMS

Two ITPTR systems referred to as MOD1 and MOD2 hereafter, were simulated, using the Fluent[13] code. A schematic of the ITPTR system is shown in Figure 1, and the geometric dimensions of all the components are listed in Table 1. The system designated as MOD1 is in fact identical to the experimental test apparatus of Kirkconnell et al.[14,15] and Harvey et al.[16], with the exception that MOD1 includes an inertance tube (IT) instead of an orifice. The MOD2 system is similar to MOD1, except that the regenerator, pulse tube, and inertance tube components of MOD2 have different geometric dimensions than MOD1.

Three different operational modes were simulated for MOD1 and MOD2 each, as summarized in Table 2. The three cases for each system address operation with an adiabatic cold end heat exchanger (CHX) (i.e., zero cooling load), a specified CHX cooling load, and a known CHX surface temperature. The boundary conditions depicted in Table 2 were the only parameters that were provided to the forthcoming CFD simulations. The entries that are shown in bold characters, furthermore, are calculated results from simulations. All other system boundaries were assumed to be adiabatic.

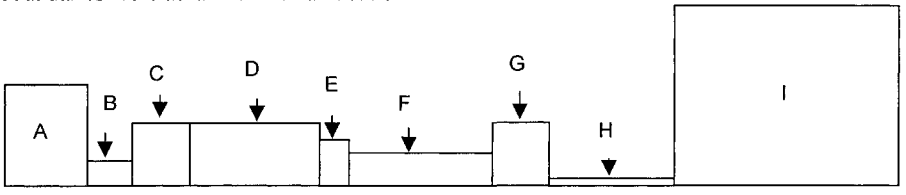

Figure 1. The Simulated ITPTR System.

Table 1. Dimensions of the Simulated Systems

	MOD1		MOD2	
Components	Radius (m)	Length (m)	Radius (m)	Length (m)
A (Compressor)	9.54E-03	7.50E-03	9.54E-03	7.50E-03
B (Transfer Line)	1.55E-03	1.01E-01	1.55E-03	1.01E-01
C (WHX1)	4.00E-03	2.00E-02	4.00E-03	2.00E-02
D (Regenerator)	4.00E-03	5.80E-02	1.00E-02	2.50E-02
E (CHX)	3.00E-03	5.70E-03	3.00E-03	5.70E-03
F (Pulse Tube)	2.50E-03	6.00E-02	7.50E-03	3.00E-02
G (WHX2)	4.00E-03	1.00E-02	4.00E-03	1.00E-02
H (Inert. Tube)	4.25E-04	6.84E-01	5.96E-04	1.07E+00
I (Surge Volume)	1.30E-02	1.30E-01	1.30E-02	1.30E-01

Table 2. Boundary Conditions for the Simulations

	MOD1			MOD2		
Components	Case 1	Case 2	Case 3	Case 4	Case 5	Case 6
WHX1 Wall Temperature (K)	293	293	293	293	293	293
CHX Wall Conditions	Adiabatic	1W load	150 K	Adiabatic	1 W load	282 K
WHX2 Wall Temperature (K)	293	293	293	293	293	293
CHX Load (W)	0	1	**6.39***	0	1	**2.57***
CHX Surface Temperature (K)	**87***	**100***	150	**278***	**280***	282

* These values were obtained from simulations.

CFD MODELS

The commercial CFD code Fluent®[13] was used. Given the assumed cylindrical and linear alignment of the simulated ITPTR systems, axi-symmetric, two-dimensional flow was assumed. Using a simple user defined function, the piston head motion was modeled as:

$$X = X_a * \sin(w*t) \tag{1}$$

where X_a= 4.511e-3 m, w = 213.62 r/s, and the time increment of 7.3529e-4 seconds were assumed.

Fluent is equipped with a dynamic meshing function that can create deformable mesh volumes. This function was utilized for modeling the compressor. Detailed nodalization of all components was performed, whereby regions deemed more sensitive, such as the vicinity of component-to-component junctions, were represented by finer mesh than others. The MOD1 and MOD2 systems were represented by a total of 4,325 and 4,366 nodes, respectively.

The mass, momentum and energy equations solved by Fluent for the forthcoming simulations are, respectively:

$$\frac{\partial \rho_f}{\partial t} + \frac{1}{r}\frac{\partial}{\partial r}(r \rho_f v_r) + \frac{\partial}{\partial x}(\rho_f v_x) = 0 \tag{2}$$

$$\frac{\partial}{\partial t}(\rho_f \vec{v}) + \nabla \cdot (\rho_f \vec{v}\vec{v}) = -\nabla p + \nabla \cdot (\tau) \tag{3}$$

$$\frac{\partial}{\partial t}(\rho_f E) + \nabla \cdot (\vec{v}(\rho_f E + p)) = \nabla \cdot \left(\hat{k} \nabla T + (\tau \cdot \vec{v})\right) \tag{4}$$

where

$$E = \hat{h} - \frac{p}{\rho} + \frac{v^2}{2} \tag{5}$$

and all properties represent the properties of the working fluid helium. The above equations apply to all components, except for CHX, WHX1, WHX2 and the regenerator. The latter 4 components are modeled as porous media, assuming that there is local thermodynamic equilibrium between the fluid and the solid structure in these components. The mass, momentum, and energy equations in the latter 4 components are:

$$\frac{\partial (\varepsilon \rho_f)}{\partial t} + \frac{1}{r}\frac{\partial}{\partial r}(\varepsilon r \rho_f v_r) + \frac{\partial}{\partial x}(\varepsilon \rho_f v_x) = 0 \tag{6}$$

$$\frac{\partial}{\partial t}(\varepsilon \rho_f \vec{v}) + \nabla \cdot (\varepsilon \rho_f \vec{v}\vec{v}) = -\varepsilon \nabla p + \nabla \cdot (\varepsilon \tau) - \left(\frac{\mu}{\beta}\vec{v} + \frac{1}{2}\hat{C}\rho_f |\vec{v}|\vec{v}\right) \tag{7}$$

$$\frac{\partial}{\partial t}\left(\varepsilon\rho_f E_f + (1-\varepsilon)\rho_s E_s\right) + \nabla\bullet\left(\vec{v}(\rho_f E_f + P)\right) = \nabla\bullet\left[\left(\varepsilon\hat{k}_f + (1-\varepsilon)\hat{k}_s\right)\nabla T + (\tau\bullet\vec{v})\right] \quad (8)$$

where $\varepsilon = 0.69$, $\beta = 1.06\times10^{-10}\,m^2$, and $\hat{C} = 7.609\times10^{4}\,m^{-1}$ were assumed. These parameters are based on the experiments of Harvey.[17]

For simplicity, all the simulations were done as transient processes, starting with an initial system temperature of 300 K for Cases 1-3, and 293 K for Cases 4-6. Simulations were continued until a steady-periodic state was obtained.

RESULTS AND DISCUSSION

General Observations

The variations of the cycle-average temperature of the CHX surface are depicted in Figure 2 for Cases 1, 2, 4 and 5, and show the development of steady-periodic states. For Cases 3 and 6, where a constant CHX surface temperature was imposed, steady periodic state can be easily recognized by plotting the temporal variation of the total rate of heat absorbed by the system through CHX (cooling load).

The axial distributions of cross-section and cycle-averaged temperature for Cases 1-3, under steady-periodic state, are displayed in Figure 3. Significant temperature gradients are predicted in the regenerator and the pulse tube. These profiles are evidently consistent with the known trends in data. The overall performances of the simulated systems are represented by the predicted entries in Table 2. Besides well-expected trends (e.g., higher cold tip temperatures with a cooling load of 1W, in comparison with cases with zero cooling load), an interesting observation is that simulation Cases 1-3 perform much better than Cases 4-6. The MOD1 system being made of models with large L/D, is evidently superior to the MOD2 system.

Multi-Dimensional Effects

Intuition suggests that multi-dimensional flow effects become more significant as a component's L/D ratio is reduced, and that the most significant multi-dimensional effects should occur at the vicinity of component-to-component junctions. Details of the simulation flow fields fully support these observations. Figures 4 and 5 depict the cycle-average temperature contours

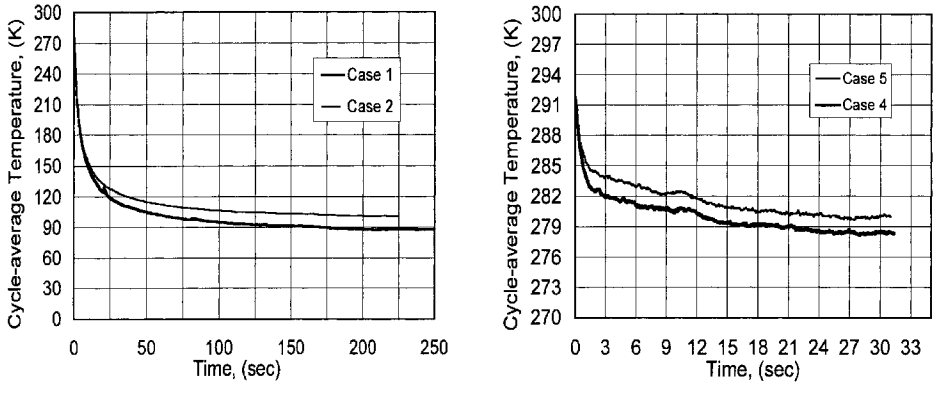

Figure 2. Temporal variations of cycle-average CHX surface temperature for simulation cases with a cooling load of 1W.

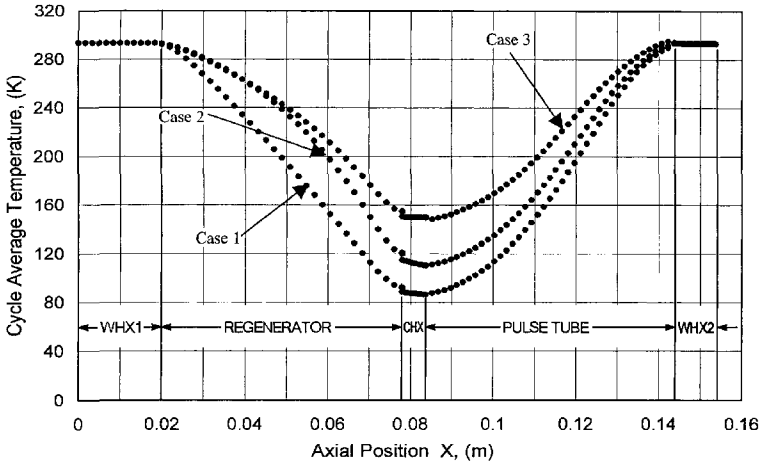

Figure 3. Axial distribution of cross-section and cycle-averaged temperature distributions under steady periodic for Cases 1-3 (MOD1 system).

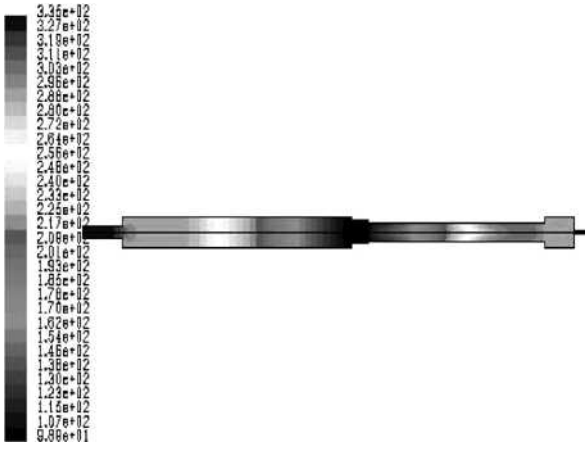

Figure 4. Steady-periodic cycle-average temperature contours for simulation Case 2.

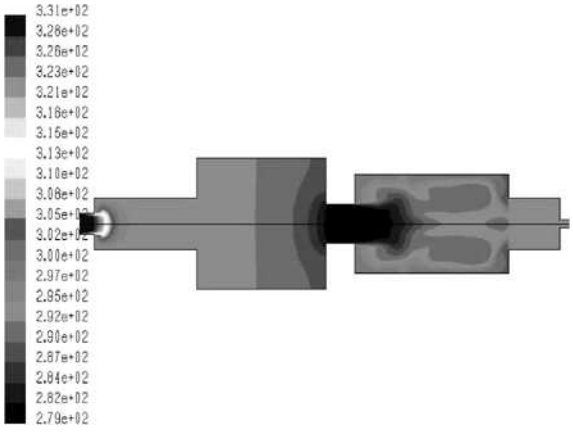

Figure 5. Steady-periodic cycle-average temperature contours for simulation Case 5.

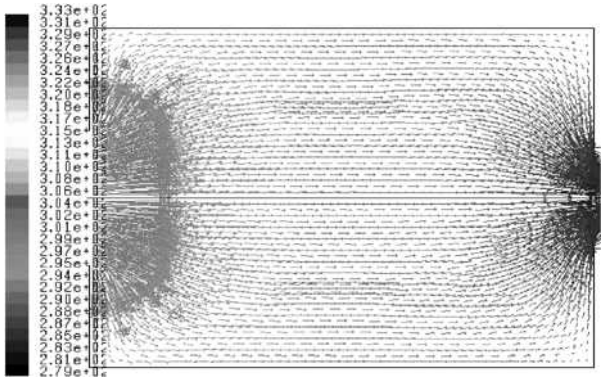

Figure 6. Snapshot of velocity vectors and temperatures [in K] in the regenerator of MOD2 system during the simulation Case 4.

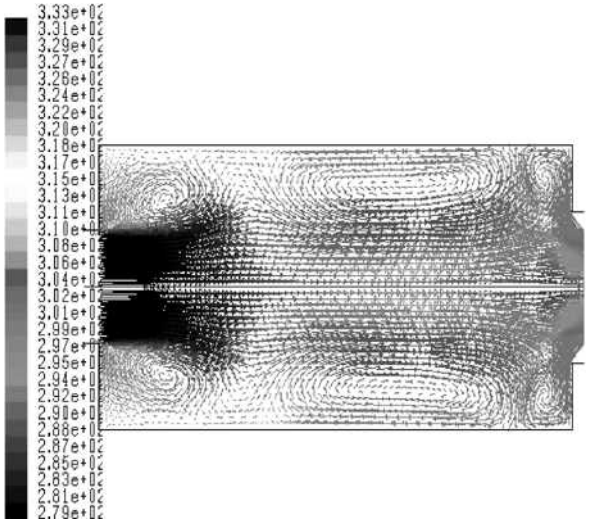

Figure 7. Snapshot of velocity vectors and temperatures [in K] in the pulse tube of MOD2 system during the simulation Case 4.

for Cases 2 and 5, respectively. The multi-dimensional effects in all simulations dealing with MOD1 system were relatively minor. Significant multi-dimensional effects occurred in MOD2 system, however. Typical snapshots of the fluid velocity and temperature distributions repre-senting the regenerator and the pulse tube of the MOD2 system are depicted in Figs. 6 and 7, respectively. The two figures are associated with Cases 4, under steady-periodic conditions. For both components, strong multi-dimensional effects occur near the two. The secondary flows, in the form of recirculation patterns are predicted for the pulse tube. The multi-dimensional flows undoubtedly impact pressure drop, dissipation and heat transfer processes, in particular in the regenerator. The multitude of recirculation pattern in the pulse tube cause undesirable mixing in the thermally stratified fluid, and is at least partially responsible for the poor overall performance of the MOD2 system.

CONCLUSION

Two entire ITPTR systems operating in steady periodic state under a variety of boundary conditions were numerically simulated using the CFD package Fluent. The objectives were to demonstrate the feasibility of CFD simulation of OPTRs, and to examine the multi-dimensional flow and

heat transfer effects. CFD simulations successfully predicted all the expected trends. They also showed that a 1-D analysis can be adequate only when all the components of the ITPTR have large length-to-diameter ratios. Significant multi-dimensional effects and working fluid recirculation occur when one or more components have relatively small L/D ratios. The recirculation patterns deteriorate the overall performance of the system.

ACKNOWLEDGEMENTS

The authors acknowledge gratefully the financial and technical support for this work by Raytheon Company.

NOTATION

$\hat{c}$ = Inertial Drag Coefficient
$\hat{h}$ = Enthalpy
$\hat{k}$ = Thermal Conductivity
P = Pressure
r = Radial coordinate
t = Time
T = Temperature
v = Velocity
w = Angular frequency (rad/s)
x = Axial coordinate
X = Piston displacement
X_a = Piston displacement amplitude

Greek letters

β = Permeability
ε = Porosity
μ = Absolute viscosity
ρ = Density
τ = Stress tensors

Subscripts

f = Fluid
s = Solid

REFERENCES

1. Gifford, W.E. and Longthworth, R.C., "Pulse-Tube Refrigeration," *Trans. ASME, J. Eng. Ind.* (series B), 86 (1964), pp. 264-268.
2. Mikulin, E.I., Tarasov, A.A., and Shrebyonock, M.P., "Low-temperature expansion pulse tubes," *Advances in Cryogenics Engineering*, vol 29, Plenum Publishing Corp., New York, pp. 629-637.
3. Zhu, S.W., Wu, P.Y., and Chen, Z.Q., " A single stage double inlet pulse tube refrigerator capable of reaching 42 K," ICEC 13 Proc. *Cryogenics*, 30 (1990), pp.256-261.
4. Wang, C., Wu, P., and Chen, Z., "Modified orifice pulse tube refrigerator without a reservoir," *Cryogenics*, 34 (1994), pp. 31-36.
5. Cai, J.H., Wang, J.J., Zhu, W.X. and Zhou, Y., "Experimental analysis of double-inlet principle in pulse tube refrigerator," *Cryogenics*, 33 (1993), pp. 522-525.
6. Zhu, S.W., Zhou, S.L., Yoshimura, N., and Matsubara, Y., "Phase shift effect of the long neck tube for the pulse tube refrigerator," *Cryocoolers 9*, Plenum Press, New York (1997), p. 269.
7. Ricardson, R.N. and Evans, B.E., "A review of pulse tube refrigeration," *Int. J. Refrigeration*, 20 (1997), pp. 367-373.
8. Popescu, G., Radcenco, V., Gargalian, E., and Bala, P.R., "A critical review of pulse tube cryogenerator research," *Int. J. Refrigeration*, 24 (2001), pp. 230-237.
9. Gedeon, D., *Pulse Tube Model-Class Reference Guide*, Gedeon Associates (1999).
10. Ju, Y.L., Wang, C. and Zhou, Y., "Numerical Simulation and Experimental Verification of the Oscillating Flow in Pulse Tube Refrigerator," *Cryogenics*, 38, pp. 160-176.
11. Hozumi, Y., Shiraishi, M., and Murakami, M., "Simulation of thermodynamics aspects about pulse tube refrigerator," *Adv. in Cryogenic Engineering*, Vol. 49B, Amer. Institute of Physics, Melville, NY (2004), pp. 1500-1507.
12. Flake, B. and Razani, A., "Modeling pulse tube cryocoolers with CFD," *Adv. in Cryogenic Engineering*, Vol. 49B, Amer. Institute of Physics, Melville, NY (2004), pp. 1493-1499.
13. Fluent Inc.,*Fluent 6 User Manual,* Fluent Inc (2003), p. 8-1.

14. Kirkconnell, C.S., *Numerical analysis of the mass flow and thermal behavior in high-frequency pulse tubes,* Ph.D. thesis, Georgia Institute of Technology, Atlanta (1995), GA.

15. Kirkconnell, C.S., Soloski, S.C., and Price, K.D., "Experiments on the Effects of Pulse Tube Geometry on PTR Performance," *Crycoolers 9*, Plenum Press, New York (1997), pp. 285.

16. Harvey, J.P., Kirkconnell, C.S., and Desai, P.V., "Comparison of Entropy Generation Rates in Various Stirling-Class Cryocooler Configurations," *Adv. in Cryogenic Engineering*, Vol. 49B, Amer. Institute of Physics, Melville, NY (2004), pp. 1519-1526.

17. Harvey, J.P., *Parametric study of cryocooler regenerator performance,* M.S. Thesis, Georgia Institute of Technology, Atlanta GA (1999).

Phase Angle Model for Pulse Tube with Secondary Orifice Using Lumped-Element Electrical Network Analysis

C. T. Nguyen, M. S. Haberbusch, A. J. Yeckley

Sierra Lobo, Inc.
Milan, Ohio, USA 44846

ABSTRACT

The pressure-flow phase angle is a key design parameter for optimizing pulse tube cryocooler performance. A high efficiency cryocooler requires an optimal phase angle that minimizes viscous dissipation losses in the regenerator and maximizes the acoustic power (PV) flow into the pulse tube. This will result in greater cooling capacity for a given amount of acoustic power delivered by the compressor. In a pulse tube cryocooler, the pressure-flow phase angle is driven by a combination of effects which include valve flow area, inertance tube size, and reservoir volume for a fixed working fluid flow rate. In this paper, the pressure-flow phase angle at the pulse tube is modeled using a simple lumped-element model RLC electrical network analysis. The RLC electrical network consists of a resistance component (R), an inertance component (L), and compliance component (C). The paper also addresses the effect of a secondary orifice (also referred to as a secondary valve) on the pressure-flow phase angle model. Phasor diagrams using vector representation are presented to visualize the direction and variation of the pressure-flow phase angle due to configuration changes in valves, inertance tubes, reservoir volumes, and working fluid flow rate. The model predictions will be compared to the established phase angle in-line theory method, as well as experimental results obtained with the Sierra Lobo pulse tube cryocooler developed under the NASA 2nd Generation Reusable Launch Vehicle Program.

INTRODUCTION

Much effort has been made to model the pressure-flow phase angle in the pulse tube cryocooler (Refs. 1, 2). An optimal phase angle results in a minimum flow rate and pressure drop through the regenerator. This results in higher pressure amplitude and larger cooling power for a given input PV power. In the pulse tube cryocooler, especially the smaller sizes, it is difficult to obtain an optimal large pressure-flow phase angle at the pulse tube due to the interdependence between volume flow rate, pressure amplitude, and pressure-flow phase angle. Meeting design specifications normally requires a tedious testing and tuning process to achieve the desired cryocooler performance parameters. In large pulse tube cryocoolers the flow rate into the reservoir is large, which may lead to a phase angle that is larger than the predicted optimum. In small pulse tube cryocoolers the working fluid flow rate is typically low.

Cryocoolers 13, edited by R. G. Ross, Jr.
Springer Science+Business Media, Inc., New York, 2004

Therefore, smaller than desired phase angles are seen in most practical small pulse tube cryocooler systems.

A secondary orifice is added to the system to provide additional pressure-flow phase angle shift. The presence of the secondary orifice also introduces the potential of DC flow which degrades system performance (Refs. 2, 3, and 4). The secondary orifice, typically a double-inlet valve, serves as a DC flow eliminator. Such an orifice adds the capability to create an equivalent pressure drop in the opposite direction to the DC flow pressure drop that is able to suppress the DC streaming. Due to the presence of the secondary orifice, the model for pressure-flow phase angle becomes more complicated. In this paper, the pressure-flow phase angle at the pulse tube of the cryocooler is modeled using the RLC electrical analog network. The pressure-flow phase angle is illustrated and presented using a phasor diagram with vector operations. Pressure-flow phase angle measurement methods are also presented.

PRESSURE-FLOW PHASE ANGLE MODELING IN THE ABSENCE OF A SECONDARY ORIFICE

Figure 1 shows the configuration of the reservoir, inertance tube, and the secondary orifice in the pulse tube cryocooler system. The continuity Equation of the working fluid entering the reservoir is:

$$\dot{m}_C = \frac{dM_C}{dt} \tag{1}$$

where $\dot{m}_c$ is mass flow rate of gas flowing into the reservoir, and M_c is the total mass of gas in the reservoir. Using the ideal gas equation, $\rho_m = {}^{P_m}\!/_{RT_c}$, and assuming a reversible and adiabatic reservoir, $dp_C = \gamma RT d\rho_C$, Equation 1 can be rewritten in terms of volume flow rate and pressure (Ref. 4):

$$u_C = \frac{V_r}{\gamma P_m}\frac{dp_C}{dt} \tag{2}$$

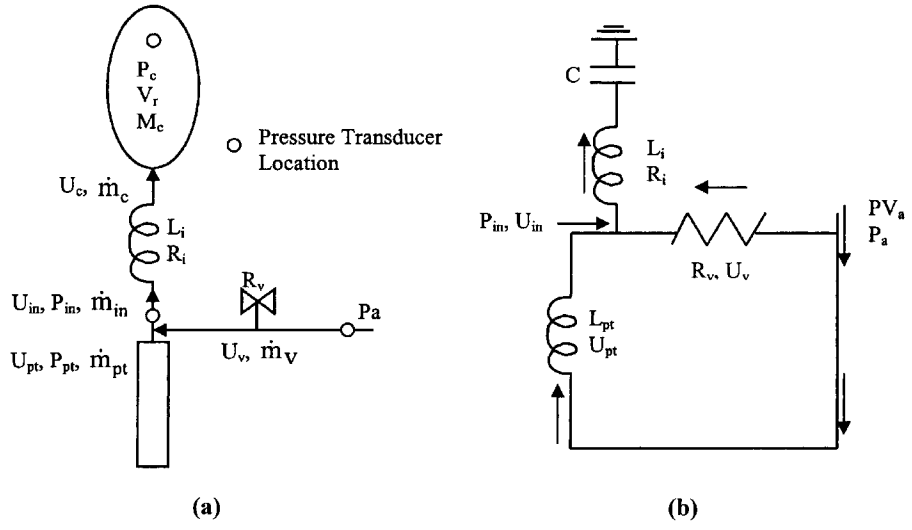

Figure 1. (a) Pressure-Flow Phase Angle Control System in the Pulse Tube Cryocooler; (b) Pressure-Flow Phase Angle Control System - Electrical Analog.

where γ is heat capacity ratio, T_c is gas temperature in the reservoir, V_r is reservoir volume, and R is the gas constant. Since pressure p_c and u_c are time-oscillatory complex quantities the pressure p_c in the reservoir and the volume flow rate into reservoir u_c can be written:

$$p_c = P_m + P_c e^{i\omega t} \tag{3}$$

$$u_c = U_c e^{i\omega t} \tag{4}$$

In Equations 3 and 4, P_m is the mean pressure and is a time-independent value; ω is the working fluid angular frequency. The mean volume flow rate is zero. The $P_c e^{i\omega t}$ and $U_c e^{i\omega t}$ terms are complex quantities, reflecting a time-varying phase-pressure angle and flow rate in oscillating flow. Here, P_c is the pressure amplitude in the reservoir, and U_c is the volume flow rate amplitude flowing into the reservoir. Substituting the value of p_c and u_c from Equation 3 and 4 into Equation 2, results in the following:

$$U_c = \frac{V_r}{\gamma P_m} i\omega P_c \tag{5}$$

The flow amplitude at the inertance tube inlet (U_{in}) leading the flow amplitude at the inertance tube outlet (U_c) is governed by the following equation:

$$U_c = P_{in} i\omega C_i + U_{in} \tag{6}$$

Where C_i is the compliance component of the inertance tube, and U_{in} is the flow rate amplitude into the inertance tube, the inertance tube is modeled as two components in the series: an inertance L_i and a viscous resistance R_i. The reservoir is modeled as a single compliance component C. Neglecting the inertance tube volume (C_i=0), the flow rate amplitude U_{in} is in phase with U_c, and they are the same amplitude, U_{in}=U_c. In the absence of the secondary orifice valve, U_{in} and U_{pt} are in phase and have the same magnitudes U_{in}=U_{pt}, and P_{in}=P_{pt}. The total acoustic impedance of the RLC series network using an electrical analogy (Figure 1b) in the absence of a secondary orifice is given by Equation 7:

$$Z = \frac{P_{in}}{U_c} = i\omega L_i + R_i + \frac{1}{i\omega C} \tag{7}$$

Where Z is total network acoustic impedance, P_{in} is inertance tube inlet pressure amplitude, L_i and R_i are inertance tube inertance and viscous resistance components, and C is reservoir capacitance. The total acoustic impedance in Equation 7, which represents the pressure-flow phase angle, consists of complex real and imaginary components that represent the phase angle between pressure and flow amplitudes in the oscillating flow. Equation 7 illustrates how the desired pressure-flow phase angle can be achieved by controlling the RLC components. The components in the RLC network such as inertance L, resistance R, and compliance C are defined using mechanical and acoustic terms (Ref. 2) and are given in Equations 8-10.

$$C = \frac{V_r}{\gamma P_m} \tag{8}$$

$$L_i = \frac{\rho_m l}{A} \tag{9}$$

$$R_v = \frac{4}{3\pi} \frac{K\rho_m}{A^2} U_{in} \tag{10}$$

$$R_i \cong \frac{\mu \Pi l}{A^2 \delta_v} \tag{11}$$

In Equations 8-11, V_r is the reservoir volume, r_m is the working fluid mean density, l is the length of the inertance tube, A is the cross sectional flow area, K is the head-loss coefficient for valves and fittings, μ is the viscosity, Π is the perimeter, δ_v is the viscous penetration depth, and U_{in} is the flow rate amplitude inlets of the inertance tube. Substituting Equation 8 into Equation 5 yields the following Equation:

$$U_c = i\omega C P_c \tag{12}$$

Equation 12 shows the flow into the reservoir leading the pressure in the reservoir by 90^0. Equation 12 is important since it provides the reference frame in the construction of the phase diagrams that represent modeling of the pressure-flow phase angles in the pulse tube cryocooler. Combining Equations 12 and 7 gives the pressure-flow phase angle equation at the pulse tube when the secondary orifice valve is closed:

$$P_{in} = P_c + R_i U_c + i\omega L_i U_c \tag{13}$$

Equation 13 consists of complex real and imaginary components that mathematically link the inlet to the inertance tube and the reservoir volume. The real component includes the reservoir pressure amplitude P_c and the inertance tube viscous resistance in phase with the reservoir volume flow rate amplitude (U_c). The imaginary component consists of the frequency, inertance, and reservoir volume flow rate. Equations 12 and 8 illustrate how the reservoir volume influences the flow amplitude, both of which contribute to the pressure-flow phase angle. It is desirable to size the pulse tube cryocooler reservoir large enough so as not to effectively change the amplitude of the volume flow rate.

PRESSURE-FLOW PHASE ANGLE MODELING IN THE PRESENCE OF SECONDARY ORIFICE

As the secondary orifice opens, mass flow rate into the reservoir $\dot{m}_{in}$ increases. The mass flow rate into the reservoir is governed by the following Equation:

$$\dot{m}_{in} = \dot{m}_{pt} + \dot{m}_v \tag{14}$$

Where $\dot{m}_{pt}$ and $\dot{m}_v$ are mass flow rates of working fluid at the pulse tube and secondary orifice. With the assumption that the working fluid at the secondary orifice is the same temperature at the warm end of the pulse tube and the pressure amplitude at the pulse tube is the same as the amplitude at the left side of the secondary orifice in Figure 1b, then the amplitude flow rate U_{in} can be written in terms of flow rate at the warm end of pulse tube (U_{pt}) and across the orifice (U_v):

$$U_{in} = U_c = U_v + U_{pt} \tag{15}$$

In pulse tube cryocoolers the regenerator component is typically designed using codes such as REGEN3.2, DeltaE, and SAGE. The regenerator component requires very careful design and review because once the system is integrated, it becomes an unchangeable component. Therefore, for much simpler analysis in this paper, the regenerator is removed from the acoustic and electrical analogs. Then, the relationship between the volume flow amplitudes in the pulse tube and the secondary orifice is shown with an electrical analog in Figure 1b (Refs. 1, 5):

$$R_v U_v = i\omega L_{pt} U_{pt} \tag{16}$$

In Equation 16, R_v and U_v are resistance and flow rate amplitude across the secondary orifice. L_{pt} is the inertance component of the pulse tube. Combining Equations 13, 15, and 16, the pressure-flow phase angle at the pulse tube in the presence of the secondary orifice is:

$$P_{pt} = P_c + (R_i - \frac{\omega^2 L_i L_{pt}}{R_v})U_{pt} + i(\omega L_i + \frac{\omega L_{pt} R_i}{R_v})U_{pt} \qquad (17)$$

Similar to Equation 13, Equation 17 consists of complex real and imaginary components. In the real component, besides P_c and R_i, the additional term $\omega^2 L_i L_{pt}/R_v$ with a negative sign indicates smaller flow resistance into the inertance tube. In the imaginary component, the additional term $\omega L_{pt} R_i/R_v$ with a positive sign is equivalent to the analog of having a longer inertance tube. The flow at the pulse tube (U_{pt}) lags the flow in the inertance tube (U_{in}). This will be demonstrated much more clearly in the next section where the phasor diagram is presented. All the above analysis provides the capability of using the secondary orifice to control the pressure-flow phase angle at the pulse tube to maximize the performance of the cryocooler.

Equation 17 reflects the effect of the secondary orifice in the control of the pressure-flow phase angle in the pulse tube cryocooler. As the secondary orifice valve opens, R_v becomes smaller; the flow into the inertance tube and reservoir has less resistance and accordingly there is an increase in the pressure-flow phase angle in the pulse tube. As the secondary orifice is closed, R_v becomes larger, and the flow into the inertance tube and reservoir becomes smaller; accordingly the pressure-flow phase angle in the pulse tube decreases. When the secondary orifice is completely closed, R_v goes to infinity, the magnitude of U_{pt} becomes U_c (since magnitude of $U_{in} = U_c$) and Equation 17 reduces to Equation 13.

PRESSURE-FLOW PHASOR DIAGRAM

Since pressure and flow are complex quantities in the oscillating flow of a pulse tube cryocooler, the real and imaginary components can be represented by vectors on a plane. These vectors have coordinates on two axes, real and imaginary. This allows for use of a visualization technique to observe the pressure-flow phase angle—the phasor diagram. The phasor diagram is constructed based on model equations that allow visualization of the change in pressure-flow phase angle quantitatively. Figure 2 shows the pressure-flow phase angle phasor diagram in the absence (a), and presence (b), of a secondary orifice valve. Figure 2a is constructed based on Equations 6 and 13, and Figure 2b is constructed based on Equation 17.

Figure 2 represents the pressure-flow phase angle in a typical pulse tube cryocooler. In Figures 2a and 2b, φ denotes the phase angle shift of the volume flow between the warm end of the pulse tube (U_{in}) and the inlet to the reservoir (U_c) due to the compliance component created by the small internal volume of the inertance tube. Figure 2a illustrates an important characteristic of the pressure-flow phase angle in pulse tube cryocoolers. In small cryocoolers, the flow rate amplitude into the reservoir U_c is so small that a long inertance tube is required to create a condition in which pressure leads flow rate. The long inertance tube creates a large pressure drop through the inertance tube, large flow phase angle shift, and small volume flow rate into the reservoir. Therefore, smaller pressure-flow phase angles are seen in most small pulse tube cryocoolers.

In large scale pulse tube cryocoolers, the volume flow rate amplitude increases while the pressure amplitude remains unchanged. Therefore to obtain smaller pressure-flow phase angles in large scale cryocoolers, the inertance tube needs to be shortened. Figure 2b shows the effect of the secondary orifice. The real component of Equation 17 is decreased due to the presence of the secondary orifice resistance and the imaginary component is increased. This results in a larger pressure-flow phase angle ($\varnothing_b > \varnothing_a$) in the pulse tube cryocooler. When the secondary orifice valve is opened, the imaginary component in the pressure-flow phase angle is large enough to maintain the same pressure amplitude in the pulse tube (P_{in}). If the secondary valve is closed, U_v vanishes, and Figure 2b simplifies to Figure 2a.

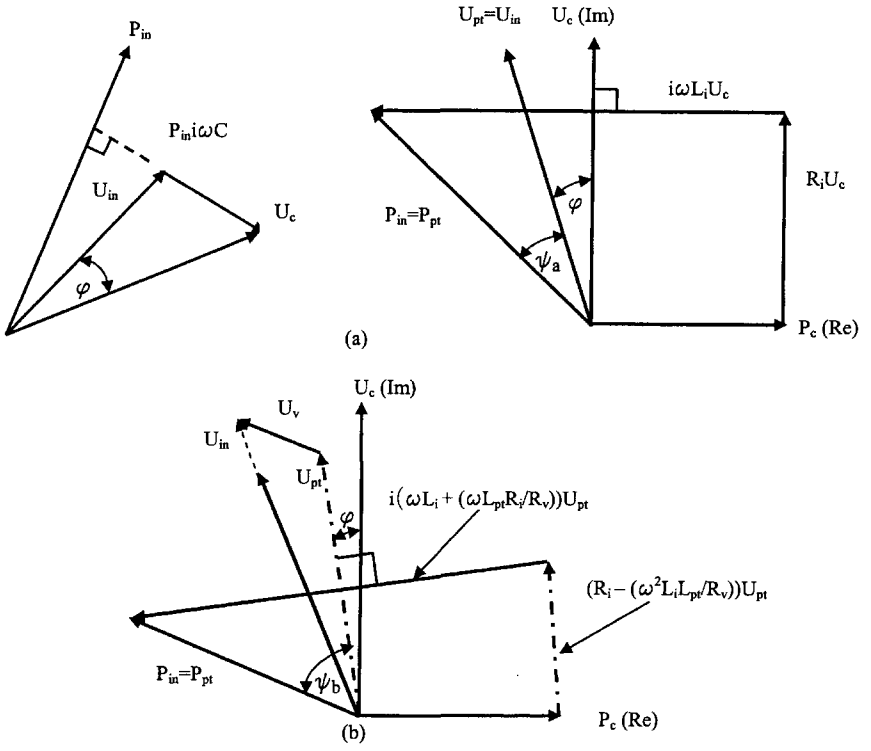

Figure 2. (a) Pressure-flow phase angle in the pulse tube when the secondary orifice valve is closed; (b) Pressure-flow phase angle in the pulse tube when the secondary orifice valve is opened.

MEASUREMENT METHODS

The actual pressure-flow phase angles for a real system can be determined from dynamic pressure measurements in the reservoir and the pulse tube. Figure 1 shows the locations of these pressure measurements in a pulse tube cryocooler. The optimal pressure-flow phase angle $\varnothing$ determines the maximum cooling capacity of the pulse tube cryocooler. In the absence of the secondary orifice the pressure-flow phase angle $\varnothing$ is simply the difference between the two pressure phase angles in the warm end of the pulse tube and inside the reservoir (as shown in Figure 1) minus 90°, minus the flow phase shift due to the compliance component of the inertance tube φ. Figure 3 illustrates the method used to determine the pressure-flow phase angle using dynamic pressure transducers.

When the secondary orifice is opened, the measurement becomes more complicated due to the additional load on the reservoir from the secondary valve. The acoustic impedance (Z_V) across an orifice consists of resistance component (R_V) in the electrical analog is:

$$Z_V = \frac{P_a - P_{pt}}{U_V} = R_V \tag{18}$$

Equation 18 shows that the flow (U_V) across the secondary valve is in phase with the pressure drop ($P_a - P_{in}$). Equation 15 shows that the magnitude of U_V is the difference between the volume flow rates U_{in}, when the secondary orifice is opened and closed. With pressure transducers located in the system as shown in Figure la, amplitudes as well as relative phase angles of P_a, P_{pt}, and P_c can be measured. In the phasor diagram, U_V is shown to be parallel to the ($P_a - P_{pt}$). This will make the flow-flow phase angle (φ) shift in the inertance tube smaller and the pressure-flow ($\varnothing$) phase angles in the pulse tube larger. If the secondary orifice opening is too large, the system perfor-

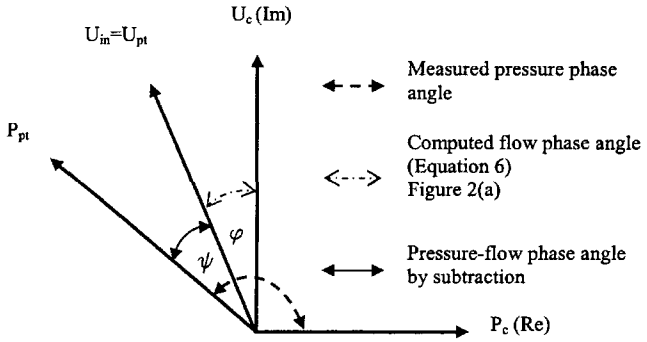

Figure 3. Method for determining pressure-flow phase angle using experimental dynamic pressure measurements (secondary orifice closed).

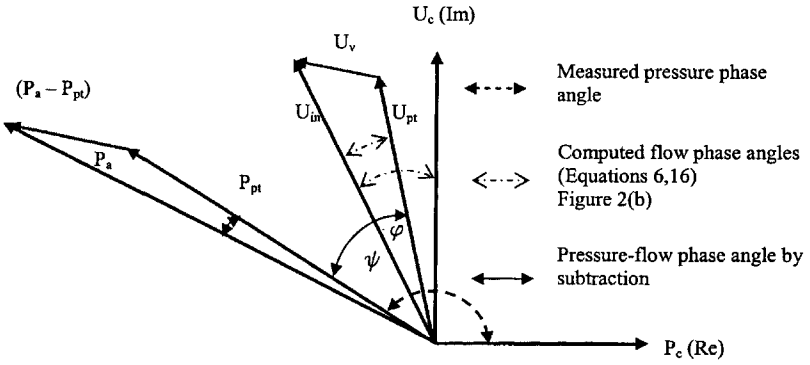

Figure 4. Method for determining pressure-flow phase angle using experimental dynamic pressure measurements (secondary orifice opened).

mance could see a negative effect due to DC flow, which is not discussed here. The optimal open area of the secondary orifice can be determined experimentally by monitoring the system performance. Steps to measure the pressure-flow phase angle in the pulse tube with a secondary orifice are shown in Figure 4.

SIERRA LOBO PULSE TUBE PRESSURE-FLOW PHASE MEASUREMENTS

Sierra Lobo has designed, fabricated and tested a two-stage pulse tube cryocooler under contract with Kennedy Space Center as part of the 2nd Generation Reusable Launch Vehicle program for oxygen and hydrogen propellant densification. This pulse tube cryocooler delivers 3.5 W at 60 K and 4 W at 20 K with 600 W of acoustic input power, and yields 11.2% Carnot efficiency (Ref. 6). The pulse tube was instrumented to monitor the phase angle in both the 1st and 2nd stage pulse tubes. Each pulse tube stage had a secondary orifice. Experimental test data were gathered on both stages with each secondary orifice closed and with each opened. Table 1 shows the lumped RLC network model prediction pressure-flow phase angle and the experimentally measured phase angles.

Table 1. Cryocooler Pressure-Flow Phase Angle Prediction & Measurements.

Pressure-Flow Phase at the Pulse Tube	Predicted	Experimental
1st Stage/Secondary Orifice Closed (degrees)	37	35
1st Stage/Secondary Orifice Closed (degrees)	21	18
2nd Stage/Secondary Orifice Opened (degrees)	37	38
2nd Stage/Secondary Orifice Opened (degrees)	21	26

Table 2(a). 1st Stage Pressure-Flow Phase Angle Model Comparisons.

Inertance Tube Length (m)	Lumped RLC Network Model	In-Line Theory
1	8	23.4
2	16	30.6
3	23	32.6
4	29	32.1
5	35	26.3
6	39	12.8
7	43	-4.3

Table 2(b). 2nd Stage Pressure-Flow Phase Angle Model Comparisons.

Inertance Tube Length (m)	Lumped RLC Network Model	In-Line Theory
1	9	15 4
2	17	17.3
3	24	15.1
4	30	8.4
5	34	-1.3
6	38	-12.7
7	41	-26.2

MODEL COMPARISONS

There are several theories used to model the pressure-flow phase angle in acoustic systems. A comparison between the lumped parameter model (RLC) and the distributed parameter in-line model (Ref. 7) is presented. Tables 2(a) and (b) show the model comparisons for different lengths of inertance tubes for both the first and second stages of a two stage pulse tube cryocooler.

The lumped RLC model shows reasonable agreement with the in-line model prediction for some inertance tube lengths. However, there are still substantial differences between the lumped RLC and in-line method model predictions. This is due to the negligible inertance tube compliance component and viscous dissipation through the inertance tube in the lumped RLC model. The accuracy of these models is yet to be determined over a broad range of operating conditions; therefore, all inertance tube modeling methods require improvement. Until an accurate model can be obtained, inertance tube experimental iterations will continue to be required during pulse tube testing to achieve the desire phase angle.

CONCLUSIONS

The pressure-flow phase angle modeling technique using the lumped model with RLC electrical network analogy has been shown to produce results that are in reasonable agreement with experimental data in some cases. More importantly, the phasor diagrams, developed using vector representation, provide a visualization tool for understanding the effects of various system components and their dimensions on the pressure-flow phase angle. A phasor diagram is introduced that illustrates the additional pressure-flow phase shift obtained by the use of a secondary orifice. This has been observed experimentally in the Sierra Lobo two-stage pulse tube cryocooler. A comparison of the lumped model theory with the in-line theory for calculating pressure-flow phase angles shows that there is much disagreement between the models. Additional test data is required with various ranges of inertance tube sizes and system operating conditions to further understand and improve pressure-flow phase angle design methods.

ACKNOWLEDGMENTS

The authors would like to acknowledge Sierra Lobo Corporate Officers: George Satornino, Dan Lowe, and Nabil Kattouah for their financial support of this work. The authors would also like to thank Dr. Ray Radebaugh of NIST for his technical review and assistance.

REFERENCES

1. Backhaus, S., Swift, G.W., "Thermoacoustic-Stirling Heat Engine: Detail Study," *Journal Acoustic Society America,* June, 2000.

2. Swift, G.W., *Thermoacoustics: A Unifying Perspective for some Engines and Refrigerators,* Condensed Matter and Thermal Physics Group, Los Alamos National Laboratory, 2000.

3. Radebaugh, R., *Foundations of Cryocoolers*, notes from the 12th International Cryocooler Conference short course, Cambridge MA, June 2002.

4. Hou, Y.K, et al., "The Role of the Orifice and the Secondary Bypass in a Miniature Pulse Tube Cryocooler," *Cryocoolers 12*, Kluwer Academic/Plenum Publishers, New York (2003), pp. 361-369.

5. Swift, G.W., "Thermoacoustic Engine," *Journal Acoustic Society America,* June, 1988.

6. Nguyen, C., Yeckley, A., Culler, A., Haberbusch, M., and Radabaugh, R., "Hydrogen/Oxygen Propellant Densifier Using a Two-Stage Pulse Tube Cryocooler," *Adv. in Cryogenic Engineering*, Vol. 49B, Amer. Institute of Physics, Melville, NY (2004), pp. 1703-1712.

7. Schunk, L., Pfotenhauer, J., Nellis, G., Radebaugh, R., and Luo, E., "Inertance Tube Optimization for KW-Class Pulse Tubes," *Adv. in Cryogenic Engineering*, Vol. 49B, Amer. Institute of Physics, Melville, NY (2004), pp. 1269-1276.

Numerical Simulations of Fluid Flow and Heat Transfer in Pulse Tubes

A.E. Schroth[1], M. Sahimi[1], and C.S. Kirkconnell[2]

[1]University of Southern California, Los Angeles, California, USA
[2]Raytheon, El Segundo, California, USA

ABSTRACT

Pulse tube refrigerators give rise to many loss mechanisms, particularly within the pulse tube component, which greatly affect their overall thermodynamic efficiency. These losses are not well understood, as a comprehensive model that can take into account the effect of such loss mechanisms does not currently exist. In addition, the difficulty of obtaining accurate experimental data has contributed to this lack of understanding. In this paper, a comprehensive model is developed which simulates the flow process and heat transfer within the pulse tube component of orifice pulse tube refrigerators. In the model, the fluid oscillations are simulated using two dynamic meshes that move periodically and have a specified phase difference. The model includes the pulse tube and cold and warm end heat exchangers at the end of the pulse tube. Simulation results for the dynamic evolution of the temperature and velocity profiles along the tube axis are presented for several case studies. The simulations indicate the formation of a wall jet near the tube wall, in agreement with experimental observations. They also confirm the existence of momentum streaming, as well as radial heat conduction losses to the pulse tube wall. The thermodynamic performance of the tube is also quantified and compared with the available experimental data.

INTRODUCTION

Cryogenic temperatures are required for cooling devices such as infrared detectors, focal plane arrays, superconductivity devices and other scientific devices for atmospheric monitoring and astronomy. Specially designed cryogenic refrigeration systems, such as cryocoolers, were designed to meet the demanding requirements for space flight and long term on-orbit operation. Cryocoolers provide the necessary refrigeration such that these devices may be maintained at cryogenic temperatures for stable and effective operation. The most common types of cryocoolers used today, according to Radebaugh [2000], are the Joule-Thomson (JT), Brayton, Stirling, Pulse Tube (PT) and Gifford-McMahon (GM). In particular, Pulse Tubes have recently achieved Carnot efficiencies as high as about 20% at 80 K and temperatures as low as 2 K has been achieved in pulse tube refrigerators. This has propelled pulse tubes from a laboratory curiosity to the point where it is now considered the standard for many space applications.

There are two theories that describe the refrigeration mechanism in the basic pulse tube refrigerator. In the surface heat pumping theory [Gifford and Longsworth, 1966], this phenomena was explained based on a thermodynamic analysis of transient heat transfer between

Cryocoolers 13, edited by R. G. Ross, Jr.
Springer Science+Business Media, Inc., New York, 2004

the fluid and its surrounding structure. At low frequency, surface heat pumping dominates, an effect that diminishes as the operating frequency increases. The pulse tube refrigeration mechanism was reanalyzed on the basis of enthalpy flow [Radebaugh, 2000] for an orifice pulse tube refrigerator and attributed to the cycle-averaged enthalpy flux in the pulse tube as a result of the phase shift effect between the mass flow rate and the pressure fluctuations. The theory behind PT refrigerators is very similar to that of the Stirling Refrigerators, except for the added benefit of having no moving parts in the cold end.

Pulse Tube Loss Mechanisms

The movement of the piston creates pressure oscillations throughout the PT refrigerator resulting in an oscillatory effect on the gas flow. The dynamic nature of this effect, in particular within the pulse tube component, and how this contributes to PT losses, is the focus of this research. The known secondary flows [Kirkconnell, 1995] that arise due to the interaction of the core and boundary layer flow necessitate a 2^{nd} order model. To date, numerical modelling of flows within the pulse tube component has been very limited and thus the loss mechanisms are not clearly understood, much less quantified. The losses occur when there are changes in enthalpy flow resulting in fluctuations in amplitude of the temperature oscillations. This is an irreversible process that generates entropy. Thus, this process is a loss mechanism [Lee et al., 1994]. In pulse tubes, these losses occur at the transition between heat exchangers (isothermal regions) and adiabatic regions.

The gross refrigeration power produced by a pulse tube cryocooler is further reduced by losses occurring in both the regenerator and in the pulse tube. Losses within the regenerator have been calculated accurately using various software packages, such as REGEN (developed at National Institute of Standards and Technology), DeltaE (Los Alamos National Laboratory), and ARCOPTR (Ames Research Center Orifice Pulse Tube Refrigerator). REGEN is a model for the regenerator only, incorporating the time-dependence of the oscillating parameters. It handles large amplitude oscillations as long as the ensuing pressure drops through the regenerator are small [Radebaugh et al., 1994]. ARCOPTR is based on one-dimensional thermodynamic equations for the regenerator and assumes all mass flows, pressure and temperature oscillations are small and sinusoidal. The results from ARCOPTR are the oscillating pressures, mass flows and enthalpy flows in each of the main components of the cooler [Roach and Kashani, 1996]. In comparison, DeltaE solves the one-dimensional wave equation based on the acoustic approximation (small amplitude). This software does not include any nonlinear effects resulting from high amplitudes. It is a linearized model that treats only the lowest order sinusoidal component of the oscillations. It can treat regenerators with large pressure drops and it used correlations for heat flow and friction that include non-linear effects that occur at high velocities [Swift and Ward, 1994].

The losses occurring within the pulse tube can also be calculated. However, the underlying cause of these losses is still not well understood and far from being quantified. The characterization of flows within pulse tubes cryocoolers has been a subject of both experimental and analytical interests in recent years. And though more efficient pulse tube configurations have been developed, the refrigeration losses in the pulse tube component have remained a significant percentage of the total available gross refrigeration capacity of these devices.

Some of these pulse tube refrigeration losses can be attributed to convective heat transfer within the pulse tube [Lee et al., 1994], which carries heat from the hot heat exchanger to the cold heat exchanger and thereby reduces the net cooling power. This convective driving occurs in the oscillatory boundary layer at the solid wall of the pulse tube. In the cyclic expansion and compression process, the gas elements close to the wall experience different viscous drag by the alternation of gas temperature and experience a net drift from the cold end to the hot end (called secondary mass flux). The Reynolds stresses in the viscous layer produce the forces that drive steady momentum streaming [Stuart, 1963]. The steady secondary mass flux is a quadratic quantity and thus nonvanishing when time-averaged over a cycle. According to [Lee et al., 1994], the steady mass flow is strongly dependent on the velocity amplitude, velocity gradient,

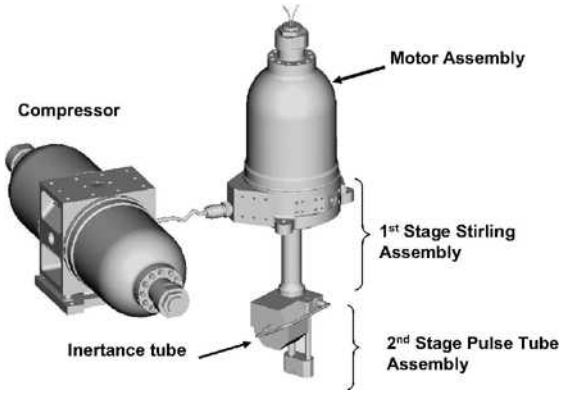

Figure 1. RSP2 Cryocooler cold head design

and on the velocity phase angle between the tube ends. Since the mass flux along the pulse tube must be zero, a flow streaming phenomena occurs in the center portion of the pulse tube, compensating for the secondary mass flux.

In orifice pulse tubes, an appropriate phase angle between velocity and pressure is required to produce favorable enthalpy flow. In a 2D linearized model developed by Lee et al. [1994], they concluded that the heat transfer between the gas and the tube wall produces enthalpy flow which is rejected to the tube wall and not to the hot heat exchanger. The necessity of a 2D model to understand and quantify these nonlinear effects was also demonstrated by Schroth et al. [2002]. Jeong [1996] investigated the same secondary flows in basic pulse tubes and confirmed the existence of large-scale streaming and the effects of axial temperature gradient. He showed analytically that the magnitude of the secondary flow increases as the axial temperature gradient (difference between the cold and hot heat exchangers of a pulse tube) increases. The entropy flow is negative at low temperatures (cryogenic), but positive at higher temperatures was reported by Radebaugh. [2003].

In the present study, a numerical model for simulating the detailed dynamic performance and characteristics of the oscillating flow in the pulse tube refrigerator is developed using FLUENT CFD software. The model simulates only the 2nd stage portion of the Raytheon Stirling/Pulse Tube Two Stage (RSP2) cryocooler [Finch et al., 2003] (see Figure 1). Numerical simulations are performed to study the various pulse tube loss mechanisms and their effect on overall performance and efficiency. Predictions made from the simulation are compared with the experimental data obtained from the RSP2 cryocooler in which good agreement was found for various operational configurations. Case studies are then developed in which investigations are made to determine how thermodynamic performance is affected by changes made to the properties of cold and warm heat exchangers. These changes include screen mesh size as well as overall heat exchanger lengths.

PHYSICAL AND SIMULATION MODEL

RSP2 Cryocooler

As previously mentioned, Raytheon is developing a two-stage Stirling/pulse tube cryocooler (RSP2) for long life space infrared (IR) sensor applications. This cryocooler, whose first stage utilizes a conventional Oxford-class Stirling expander, contains a second state pulse tube, in a U-turn configuration, whose expander is in intimate contact with the first stage cold end. This research contained in the paper focuses primarily on the simulation only the 2nd stage portion of the RSP2 cryocooler.

The Raytheon RSP2 cryocooler contains a unique feature in that it can vary refrigeration at two locations, having different operational temperatures, while still maintaining a relative

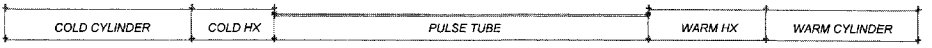

Figure 2. 2D Simulation Model (2nd Stage only, symmetric along bottom center-line)

constant efficiency. In other words, the refrigeration capacity, at each location, can be shifted, in real time, by adjusting the phase angle between the compressor and the expander piston, with minimal change in system efficiency. This unique advantage allows the cooler to perform over a wider range of load requirements compared to other approaches.

The RSP2 cryocooler was selected for simulation since a large performance database has been collected during its development and a correlated system level model has been developed. The experiment data contained within this database includes results obtained while varying the operating conditions and temperatures. This database forms the foundation of the model correlation efforts that will be conducted in this study. One of the key objectives of this research project is to perform numerical studies such that comparisons can be made between computational fluid dynamic (CFD) predictions to that of experimental data available from the RSP2 performance database.

Besides the regenerator, the 2nd stage portion of the RSP2 cryocooler consists of a cold and warm copper heat exchanger, and a pulse tube. The porosity of the heat exchangers is nominally from 0.60 to 0.75 depending on the size of the wire screen mesh. The operating wall temperatures of the cold and hot end heat exchangers, for the cases to be evaluated, varies from 45 K and 110 K. The operating mean pressure is nominally 3.0 MPa, with operational frequencies ranging from 34 Hz to 45 Hz.

Simulation Model

The RSP2 simulation model, shown in Figure 2, is representative of a Stirling/Pulse tube second stage assembly whose sizing is based upon test results from the RSP2 development program. The purpose of developing this model was to be able to predict the performance of the RSP2 Hybrid cryocooler based on the available experimental data. This would be a direct 2D simulation of the fluid flow and heat transfer occurring within the second stage portion of the cryocooler.

The key to this model was the development of a simulation approach that would produce the similar characteristic phase angle between the pressure and velocity waveforms, between the cold and warm sides of the pulse tube, as observed from the data collected from the RSP2 experimental database. These phase angles were produced by modeling a piston cylinder arrangement on both ends of the simulation model, whose piston surfaces form the outer edges of the grid network while still maintaining a closed system and conserving mass.

With the grid network meshed (i.e., cold and warm heat exchangers and pulse tube), the outer surfaces were position controlled, to following a period motion, varying the total volume within its network. Such movements would dynamically deform the internally meshed cells, removing and adding cell over its period. These surfaces followed a periodic motion, but with a controlled phase angle between their respective motion. The moving surfaces of the grid network, which deform the interior meshed cells, act as virtual *moving pistons*, oscillating the flow while maintaining conservation of mass. Extensive research was involved in the development of custom algorithms that automatically control the position of each moving surface, relative to each other. It was important that the simulation of the moving surfaces, for a closed system, would adequately conserve mass and energy. In many cases, it was found that the artificial movement of surfaces, if done improperly, could produce an oscillating change in total mass of the system, over a cycle, that could effect the overall system energy balance and produce instability in the numerical solution.

The simulation model consists of two pistons, cold and warm heat exchanger, and the pulse tube. The solver uses a finite volume approach to solve the governing equations describing the heat transfer and fluid flow in this system. Taking advantage of the symmetrical aspects of this

Table 1. Properties of copper wire screens

Mesh Size	Wire Diameter (mm)	Porosity	Mesh Distance (mm)	Hydraulic diameter (mm)
150	0.061	0.6993	0.140	0.1418
250	0.041	0.6582	0.120	0.0788
300	0.031	0.6938	0.100	0.0704
400	0.025	0.6677	0.083	0.0504

problem, only a 2D representation of the RSP2 Hybrid cryocooler was modeled. The symmetry axis (lying on the x-coordinate axis) runs down the centerline of the pulse tube. For 2D problems, the solver computes all integral quantities for an angle of 2π. Each area of interest was designated a separate face zone. A 2D regular, structured grid of mesh elements was then generated for each face zone using quadrilateral mesh elements. Use of the quadrilateral mesh element scheme is applicable primarily to faces that are bounded by four or more edges. As previously mentioned, the numerical model only simulates the 2nd stage portion of the RSP2 Hybrid cryocooler consisting of cold and warm heat exchangers, pulse tube, and pulse tube wall.

The pulse tube wall was modeled having material property of steel. The heat exchangers were modeled as homogeneous porous zones consisting of copper material, having a pore structure that exhibited a viscous and inertial resistance corresponding to that of mesh stacked copper interwoven meshed screens. Various sizes of mesh screens were evaluated as part of this study. Porosity values ranging from 0.60 of 0.75 were evaluated for each of the heat exchangers. The cold and warm pistons, piston cylinder walls, and heat exchangers were modeled as isothermal surfaces contributing to the overall heat transfer. The working fluid was modeled as ideal helium gas. Compressibility effects were assumed negligible based on the temperature range in which the available data was collected (45K to 120K).

Based on experimental mass flow rates, a laminar flow velocity formulation was selected for the solver. The predicted velocities were found to be well within the laminar flow range so the use of a turbulent model formulation was not required. The 2D axissymetric model assumes that no swirling flows within the 2nd stage portion of the cryocooler. There is no evidence from the experimental data that would suggest the existence of any significant amount of swirling flow.

Case Studies Definition

An area of interest regarding pulse tube cryocoolers is the effect of flow straightening caused by the cold and warm heat exchangers and its subsequent effect on thermodynamic performance. Flow straightening can occur by modifying the length of the heat exchanger as well as by changing the flow matrix properties (i.e., mesh size). The heat exchangers, in the RSP2 cryocooler consist of stacked copper meshed screens. The effect of changing the mesh size inside the heat exchanger should produce changes in pressure drop as well as the phase angle between the pressure and velocity wave. Variations in mesh size, regarding regenerators , has been reported by both Zhao et al. [1998] and Harvey [1999] in which similar conclusions have been drawn on the effect on pressure drop and resultant change in phase angle between the velocity and pressure wave.

Among many research groups, the design length of cold and warm heat exchangers, within pulse tube cryocoolers is not an exact science. There exist many rule-of-thumb standards for determining an adequate heat exchanger design length, but whose methods are rarely discussed, much less published. Often, the methods are regarded as proprietary information. In any event, the goal of this study is to shed some light on the effects on changes in heat exchanger lengths using predictions from the 2D simulation.

As mentioned earlier, changes in these flow characteristics are also dependent on the size of screen mesh used within the heat exchangers. The screen mesh sizes that will be evaluated, using the simulation model, includes 150, 250, 300, and 400 mesh screens made from interwoven copper strands. Since the simulation model is a 2D representation of the heat exchanger, the effective properties of the screen mesh (i.e., porosity, inertial and viscous

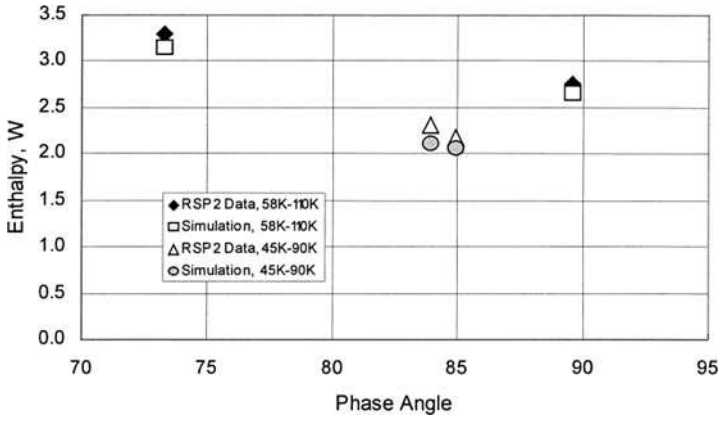

Figure 3. Comparison of enthalpy flow rates in pulse tube between experimental and predicted values for separate operational conditions.

resistances) are used in the formulation of the model. Table 1 describes the various screen mesh sizes evaluated and their properties.

SIMULATION RESULTS AND MODEL VALIDATION

Verification of the simulation model was first carried out by first establishing an internal energy balance and thus verifying the amount of work input into the system balanced by the total heat transfer occurring at the various surfaces. After which, predictions made from the model, was compared to the RSP2 cryocooler experimental data for various operating conditions.

Model Verification

In these simulations, the amount of PV compression and expansion power generated by the warm and cold pistons, respectively, was compared to the total surface heat flux, integrated over each of the isothermal surfaces. The PV power was calculated at each time step based on the product between the average absolute pressure and the rate of change in total volume. These values were then integrated over the cycle using Simpson's rule and divided by the characteristic time τ. The total heat transfer on the various surfaces were calculated using the same approach (i.e., cycle-averaged). Equation 1 shows the calculation used to determine the PV power:

$$PV\ \text{Power} = \frac{1}{\tau}\int_0^{\tau} p\frac{dV}{dt}d\tau, \tag{1}$$

where p is the absolute pressure, V is the volume, and τ is time. The rate of change of volume was based on the difference between the volume at the current times step and the previous time step divided by the time step size. The energy balance performed on each of the simulations indicated an error of less than 5% of the total energy of the system. In other words, the PV power compression plus the net heat transfer on the cold side balanced that with the PV power of expansion and net heat transfer on the warm side. Most of the error can be attributed to a poorly meshed grid near the isothermal surfaces. Future models will be performed using a higher grid mesh resolutions.

In comparing the results from the 2D simulation model to the RSP2 data, it was important to focus on the enthalpy flow in the pulse tube, since this represents the available gross refrigeration. Enthalpy flow in the pulse tube component was calculated using Equation 2 and

then cycled averaged. These predictions, for various flow configurations were compared to the actual enthalpy flow as demonstrated from the RSP2 development database.

$$h_{PT} = \rho U_{axial} c_P T, \quad (2)$$

The results are shown in Figure 3 in which the enthalpy in the pulse tube is calculated for a particular phase angle at two operation temperatures. These comparisons made in this figure were made at two separate operational temperatures settings and at various phase angles. The results show very good agreement the experiment data. Based on the preliminary results, the simulation appears to underestimate the enthalpy flow through the pulse tube in both cases that were examined. The total error between the actual and simulation was calculated to be less than 10% overall.

Figures displaying the pressure versus overall volumetric change of the working gas are shown in Figure 4. The PV diagram (bottom) shows the refrigeration performance of one example simulation model configuration.

Case Studies Predictions

Having completed the energy balance, the model was then exercised for a set of experimental conditions corresponding to the RSP2 cryocooler experimental data points. The results obtained show a definite trend in cryocooler performance as the entrance effects/mixing is reduced at the ends of the pulse tube. This coarseness of this current preliminary model prohibits the direct assessment of meaningful flow patterns. However, changes in heat exchanger pressure drop, as well as the changes in phase angle (between the pressure and velocity wave), is shown

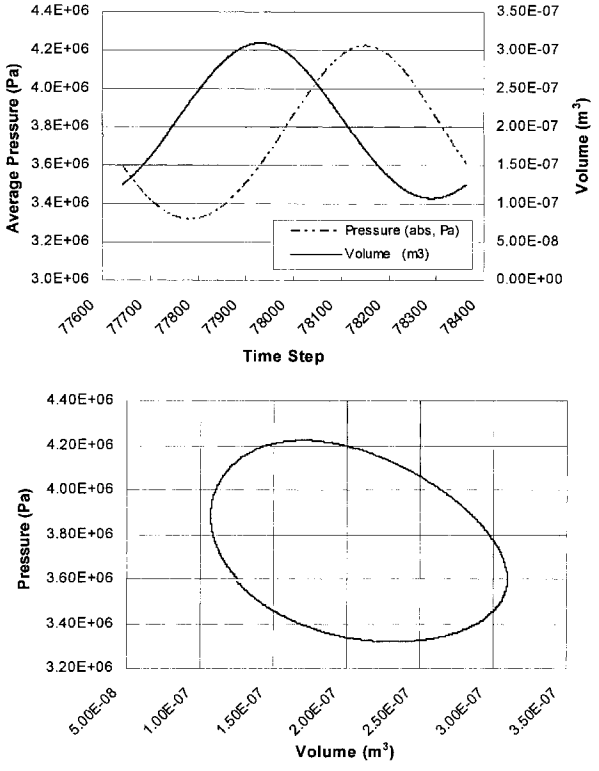

Figure 4. PV Diagrams resulting from the simulation model (cold side)

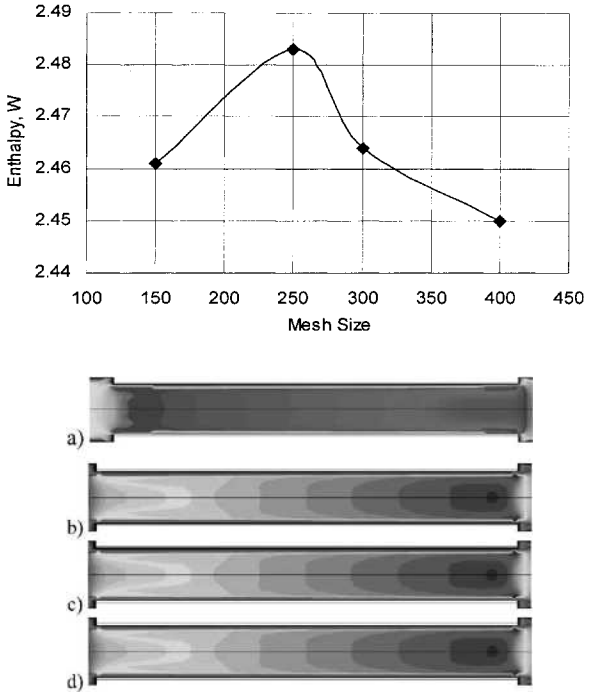

Figure 5. Variation in Enthalpy (gross cooling power) across the pulse tube as a function of mesh size. Below, velocity contours for the various mesh sizes (symmetry axis mirrored at center-line) 5a) 400, 5b) 300, 5c) 250, 5d) 150

to affect the overall gross cooling power flowing through the pulse tube (see Figure 5, top). The reduction in enthalpy flow, when the mesh screen sized is increased, was observed to be small but not negligible. Figure 5a-d illustrates the influence of the mesh size on flow straightening in regards to the velocity profiles. For each sub-figure shown, a contour plot of the velocity is shown, corresponding to the various sized screen mesh, at the exact same crank angle position. Notice the decrease amount of disturbance caused by the increased size of the mesh screen size. As the mesh size decreases, the effect on flow straighten becomes less and less effective as expected. The changes between the 150 and 250 wire mesh size are practically indistinguishable. For this preliminary model, the coarseness of the grid mesh applied to this simulation, does not allow for an immediate qualitative analysis of the resultant flow structure. However, immediate work is currently in progress to develop adequately refined meshes to ascertain these effects.

As the mesh size is increased from 150 through 400 mesh screens, it was observed that the pressure drop across the cold heat exchanger increased as expected, though very small. These resultant changes in the pressure drop was also accompanied by changes in phase angle between the pressure and velocity waves, which was also expected.

Figure 6 shows the effect of varying the length of the cold and warm heat exchanger lengths and its effect on the flows within the pulse tube. Based on this preliminary model, it appears that changes in overall heat exchanger length have a negligible effect on performance (i.e., enthalpy flow). It is apparent that the current model requires a much finer grid to resolve these effects. The flow fields, shown in Figure 6, show very little difference for each heat exchanger length.

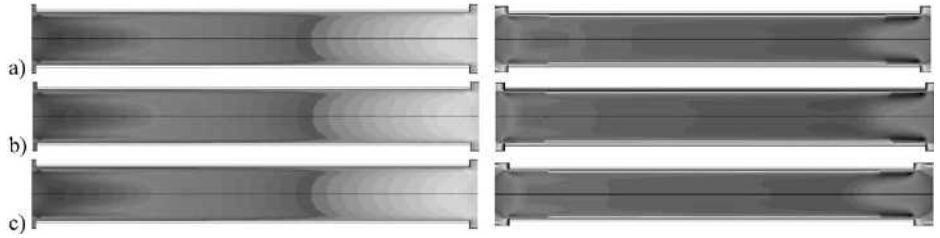

Figure 6. Velocity contours for various heat exchanger lengths corresponding to percentage increases from the reference size (symmetry axis mirrored at center-line) a) 0%, b) -10%, c) -20%

RESULTS AND CONCLUSIONS

A 2D model of the fluid flow and heat transfer, modeling the 2nd stage portion of a Stirling/Pulse Tube cryocooler was presented which was correlated to Raytheon's RSP2 cryocooler development work. Model validation efforts produced excellent agreement based on energy conservation and prediction of enthalpy flow across the 2nd stage pulse tube component.

A prediction on the effect of changes in wire mesh size was performed using the simulation model. The changes in mesh screen size, within the cold and warm heat exchanges, affected both the pressure drop and phase angle relationship of the oscillating flow. As the mesh size increased, both the pressure drop and phase angle increased. The current preliminary model could not resolve differences in thermodynamic performance when heat exchanger lengths were increased. Further action to increase model resolution is currently progress.

ACKNOWLEDGMENT

This work was supported by Raytheon Company under a grant given to the University of Southern California.

REFERENCES

1. Finch, A.T., Price, K.D., and Kirkconnell, C.S., "Raytheon Stirling/Pulse Tube Two-Stage (RSP2) Cryocooler Advancements," *Adv. in Cryogenic Engineering*, Vol. 49B, Amer. Institute of Physics, Melville, NY (2004), pp. 1285-1292.
2. Gifford, W.E. and Longsworth, R.C., "Surface Heat Pumping", *Advances in Cryogenic Engineering*, vol. 11 (1966), pp. 171-179.
3. Harvey, J.P., Master's Thesis, Georgia Institute of Technology (1999).
4. Jeong, E.S., "Secondary Flow in Basic Pulse Tube Refrigerators," *Cryogenics*, vol. 36 (1996), pp. 317-323.
5. Kirkconnell, C.S., *Numerical Analysis of the mass flow and thermal behavior in high frequency pulse tubes*, PhD Thesis, Georgia Institute of Technology (1995).
6. Lee, J.M., Kittel, P., Timmerhaus, K.D., and Radebaugh, R., "Steady secondary momentum and enthalpy streaming in the pulse tube refrigerator," *Cryocoolers 8*, Plenum Publishers, NY (1995), pp. 359-369.
7. Radebaugh, R., "A review of pulse tube refrigeration," *Adv. in Cryogenic Engineering*, vol. 35 (1990), pp. 1191-1206.
8. Radebaugh, R., "Development of the pulse tube refrigerator as an efficient and reliable cryocooler," *Proceedings of the Institute of Refrigeration of London (2000).*
9. Radebaugh, R., "Low Temperature and Cryogenic Refrigeration," *Series II: Mathematic, Physics and Chemistry*, vol. 99, Kluwer Academic Publishers, New York (2003), pp. 415-434.

10. Radebaugh, R., O'Gallagher, and A., Gary, J., *A numerical model for regenerator performance*, NIST (1994).

11. Roach, P.R., and Kashani, A., "A Simple modeling program for orifice pulse tube coolers," *Cryocoolers 9*, Plenum Press, NY (1997), pp. 327-334.

12. Schroth, A.E., Kirkconnell, C.S. Kirkconnell, Sahimi, M., "Numerical Model for Pulse Tube Using Method of Lines," *Cryocoolers 12*, KluwerAcademic/Plenum Publishers, New York (2002), pp. 379-387.

13. Stuart, J.T., *Laminar Boundary Layers*, Oxford University Press (1963), Chapter 7.

14. Swift, G.W., and Ward, W.C., "Design environment for low amplitude thermoacoustic engines," *Journal of the Acoustical Society of America*, vol. 95 (1994), p. 3671.

15. Zhou, Y., Ju, Y., and Jiang, Y., "Experimental Study of Oscillating flow characteristics for a regenerator in a pulse tube cryocooler," *Cryogenics*, vol. 38 (1998), pp. 649-656.

Visualization of Secondary Flow in Tapered Double-Inlet Pulse Tube Refrigerators

M. Shiraishi, M. Murakami* and A. Nakano

National Institute of Advanced Industrial Science and Technology (AIST)
Tsukuba, Ibaraki, 305-8564 Japan
*University of Tsukuba
Tsukuba, Ibaraki, 305-8573 Japan

ABSTRACT

Oscillating flow in a refrigerator with a tapered double-inlet pulse tube was studied using smoke-wire flow visualization. Two types of tapered pulse tubes (convergent and divergent) were studied and then compared with a cylindrical pulse tube (i.e., uniform cross section). Effects of a tapered tube on the suppression of secondary flow were investigated for improvement in cooling performance. Visualization showed that, if the strength of DC flow is adjusted to minimize convective secondary flow induced by acoustic streaming, DC flow has a stronger effect on secondary flow than does a tapered tube. The tapering of a tube was not an effective method to reduce the secondary flow in a double-inlet pulse tube. Cooling performance by the divergent tapered tube was slightly superior compared to that by the cylindrical tube, whereas that by the convergent tapered tube was significantly inferior.

INTRODUCTION

Use of a tapered tube at the pulse-tube section of a pulse tube refrigerator has been extensively studied for possible improvement in cooling performance (hereafter simply called "performance"). For clarity, here we define a tube that converges toward the hot end as a convergent tapered tube and a tube that diverges as a divergent tapered tube (see Fig. 1). For orifice pulse tube refrigerators, Olson and Swift[1] showed that the secondary flow could be suppressed by tapering the pulse tube and that the performance of convergent tapered tubes with an optimum taper angle was significantly superior than that of a cylindrical tube. Baek et al.[2,3] developed a two-dimensional model for pulse tubes valid for a wide range of taper angle, from divergent to convergent tapered tubes. Simulations using the model indicate that an increase in taper angle reduces the enthalpy flow loss associated with steady mass-streaming within the pulse tube. Previously, we observed secondary flow in orifice pulse tube refrigerators with tapered pulse tubes by using a smoke-wire flow visualization method.[4] We found that the performance of a convergent tapered pulse tube was slightly superior to that of a cylindrical tube, whereas the performance of a divergent tapered tube was inferior due to a strong secondary flow. Using numerical simulation of the mass flow in tapered pulse tubes and using corresponding experiments, Gao et al.[5] and Xu et al.[6] showed that the performance of convergent and divergent tapered tubes was superior to that of a cylindrical tube under

Cryocoolers 13, edited by R. G. Ross, Jr.
Springer Science+Business Media, Inc., New York, 2004

optimum conditions of frequency and taper angle.

For double-inlet pulse tube refrigerators, however, the performance of a divergent tapered tube was superior, based on experimental results of reference 6. However, in their experiments, the configuration of the tapered tube was a "two-step" pulse tube made of two nylon tubes with different respective internal diameters of 5 and 6 mm, and the refrigerator was a coaxial double-inlet refrigerator. These conditions differed from those of conventional pulse tube refrigerators, which have a rectilinear or a U-shaped configuration and tapered tubes with a constant taper angle. Due to these differences, the advantage of tapering a tube was not sufficiently confirmed by experiments for a double-inlet pulse tube refrigerator. Such confirmation requires direct observation of the flow phenomena. The effect of tapered tubes on flow behavior in double-inlet tapered pulse tubes, however, has not been studied in depth.

In this study, oscillating flow in double-inlet pulse tube refrigerators was observed by using a smoke-wire flow visualization method to clarify the effect of tapering a tube on the flow phenomena. The focus was on improvement in performance by reducing the convective secondary flow induced by acoustic streaming. First, the performance of refrigerators with a tapered pulse tube was evaluated by measuring the temperature difference between the hot and cold ends of the tube. Then, the convective secondary flow was investigated by smoke-wire flow visualization. Finally, based on these performance and visualization results, the effect of tapering a tube was determined.

EXPERIMENT

Two types of tapered tubes, convergent and divergent, were studied. The tapered tubes were made by cutting a transparent plastic tube (using a center lathe) and then polishing its inner surface. The cylindrical pulse tube was also made of transparent plastic. Figure 1 shows the configurations, nominal sizes, and taper angles of the tubes. The inside volume for each tube was determined by measuring the difference in weight before and after filling the tube with water; the volume of each

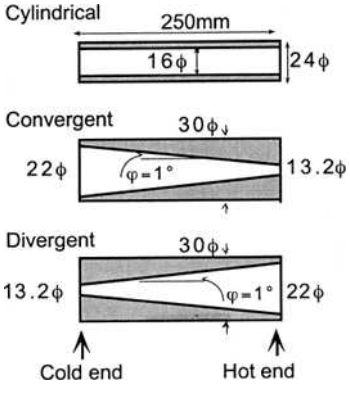

Figure 1. Configurations of pulse tube section. φ is a taper angle.

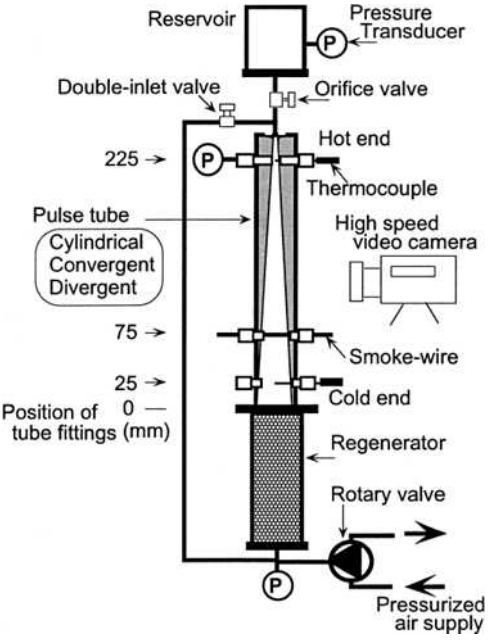

Figure 2. Experimental set-up of a tapered double-inlet pulse tube refrigerator used to visualize the flow in the pulse tube.

tapered tube was 60 cm^3 and that of the cylindrical tube was about 51 cm^3. Figure 2 shows a schematic of the experimental apparatus used to observe the flow. The pulse tube refrigerator was installed vertically, and the pulse tubes were joined with flanges to the regenerator to easily interchange the different pulse tubes. Each pulse tube had tube fittings at three positions; one fitting each for the smoke-wire, thermocouple, and pressure transducer. The regenerator was 35 mm in diameter, 160 mm long, and made of #100 stainless-steel screen with a wire diameter of 0.1 mm. The reservoir had a volume of roughly 7 times that of the cylindrical tube. The orifice and the double-inlet valves were needle valves. Each valve was fully open after 6 turns of the valve, and each turn was graduated into 25 divisions, thus totaling 150 "turn-divisions". The valve opening was expressed in these divisions as arbitrary units. Air was used as the working gas. The pressure oscillation was generated by introducing pressurized air of about 0.2 MPa into the rotary valve and then releasing it to the atmosphere. The smoke-wire was 0.1-mm-diameter tungsten wire. Both ends of the wire were soldered to copper supports acting as electrodes and as a fixing agent to keep the wire taut. The smoke-wire was tightened through the tube fittings at a position 75 mm from the end of the regenerator. Three pressure transducers (strain-gauge type) were respectively installed near the warm end of the regenerator, at the hot (at 225 mm from the end of the regenerator) end, and in the reservoir. Mineral-insulated thermocouples (CA) 0.15 mm in diameter were installed in the gas space and on the wall surface at the cold end (at 25 mm from the end of the regenerator) and the hot end (at 225 mm).

The performance of the pulse tube refrigerator was evaluated based on the temperature difference measured by the thermocouples on the wall surface. Due to the change in tube diameter, the radial temperature distribution in a tapered tube depends on the position in the pulse tube, thus making it somewhat difficult to directly compare the three types of pulse tubes. Therefore, we used the difference in wall temperature instead of gas temperature at the cold and hot ends. Thus a larger temperature difference corresponds to better performance. Secondary flow is enhanced under conditions of higher frequency and larger amplitude of pressure oscillation, causing an increase in velocity that makes observation of the flow difficult.[4] To visualize the induced secondary flow sufficiently, we therefore fixed the frequency at 6 Hz by considering the duration of emitted smoke-line at an adequate amplitude of pressure oscillation of about 1.2; amplitude is defined as the ratio between high and low pressures.

After the smoke-wire surface was coated with paraffin, the smoke-wire was installed in the tube and the lead wires were connected to a high-voltage pulse generator. The pulse tube was operated at a frequency of 6 Hz and an amplitude of pressure oscillation of about 1.2. After steady state was confirmed by monitoring the gas temperature, a smoke-line was emitted. The movement of the smoke-line was viewed and recorded using a high-speed video camera at a frame rate of 400 frames/s over five cycles of oscillation.

RESULTS AND DISCUSSION

Performance of the Pulse Tube Refrigerators

Prior to visualization, performance of each of the three different pulse tube refrigerators was investigated to determine the adequate conditions of the orifice and the double-inlet valves for observation under the prescribed conditions, namely, a frequency of 6 Hz and an amplitude of pressure oscillation of about 1.2. Performance was investigated as a function of the opening of the double-inlet valve (V_b) under a fixed opening of the orifice valve (V_o). Because preliminary visualization experiments showed that visualization was inadequate when $V_o > 30$ turn-divisions, performance of the double-inlet pulse tube refrigerator was determined by increasing V_o in intervals of 10 turn-divisions up to a maximum 30 turn-divisions. The reason that the visualization was inadequate when $V_o > 30$ turn-divisions was that the displacement of oscillating gas was then beyond the length of the pulse tube, and thus the smoke-line flowed out from the pulse tube section into the reservoir. Therefore, the movement of the smoke-line could not be recorded over a sufficient number of cycles of oscillation. Because at least five successive cycles of oscillation were required to successfully observe the secondary flow, opening of the orifice valve for visualization were chosen

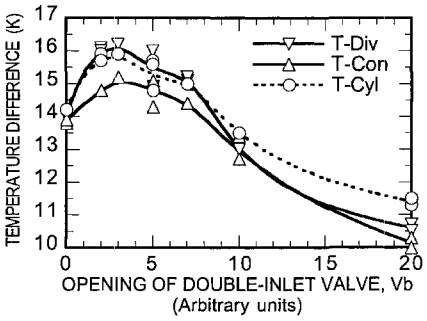

Figure 3. Performance of tapered and cylindrical pulse tubes at V_o = 20 turn-divisions. Performance was evaluated based on the difference in wall temperature between the hot and cold ends. T-Con represents convergent tapered tube, T-Div is divergent tapered tube, and T-Cyl is cylindrical tube.

as V_o = 10 and 20 turn-divisions. Figure 3 shows the measured performance (temperature difference) as a function of V_b at V_o = 20 turn-divisions. For all three pulse tubes, the performance increased with increasing V_b, peaking when V_b = 3 turn-divisions, and then decreased with increasing V_b when V_b > 3 turn-divisions. For all three pulse tubes, the optimum opening was V_b = 3 turn-divisions. The performance of the divergent tapered tube was superior to that of the other two tubes, although the difference in performance from that of the cylindrical tube was fairly small. These results differ from those previously reported[4] for orifice pulse tube refrigerators, where the convergent tapered tube showed the best performance.

Visualization of Secondary Flow

The conditions for visualization were determined based on the performance results shown in Fig. 3. As representative results for the effect of tapering a tube on the performance of double-inlet pulse tube refrigerators, we show here the visualization results for V_b = 0, 3, and 10 turn-divisions, V_o = 20 turn-divisions, 6 Hz, and an amplitude of pressure oscillation of about 1.2. Figures 4 and 5 show typical visualization results for the oscillation of the smoke-line during the first three cycles of oscillation in the convergent and divergent tapered pulse tubes, respectively. In both figures, (a), (b), and (c) correspond to the double-inlet pulse tube refrigerator when V_b = 0, 3 and 10 turn-divisions, respectively. For V_b = 0, the refrigerator was equivalent to an orifice pulse tube refrigerator. The smoke-line was emitted at the moment when the flow direction changed by a pressure variation from expansion to compression in a cycle. Frame 1 shows that the smoke-line just after being emitted from the smoke-wire, namely, the smoke-line was at almost the same position as the smoke-wire itself. Frames 3 and 5 show the smoke-line at the turning point where the smoke-line changed its direction of motion, namely, from toward the hot end to toward the cold end (Frame 3), called the hot-end turning point, and from toward the cold end to toward the hot end (Frame 5), called the cold-end turning point. Frames 2 and 4 show the smoke-line passing through the halfway point between the hot-end and cold-end turning points. The behavior evident in these five frames was the same as that in the next two cycles of oscillation.

Although details of smoke-line profiles depend on the configuration of the pulse tube, comparison between Figs. 4 and 5 reveals three major features in the smoke-line behavior common to all configurations when the double-inlet valve was opened. First, the displacement of oscillation decreased, as evidenced by the distance between the smoke-line at the hot-end and cold-end turning points (Frames 3 and 5, respectively). The displacement at V_b =3 turn-divisions decreased to about 20% of that at V_b = 0 turn-divisions (Fig. 4). This decrease in displacement was due to the effect of the double-inlet valve. Second, the smoke-line gradually shifted towards the hot end with time, as seen clearly from the change in smoke-line position between Frames 13 and 1 in Fig. 4(c). This shift in position of the smoke-line was due to DC flow that is inherently induced in double-inlet pulse tube refrigerators. Double-inlet pulse tube refrigerators have a closed-loop flow path in

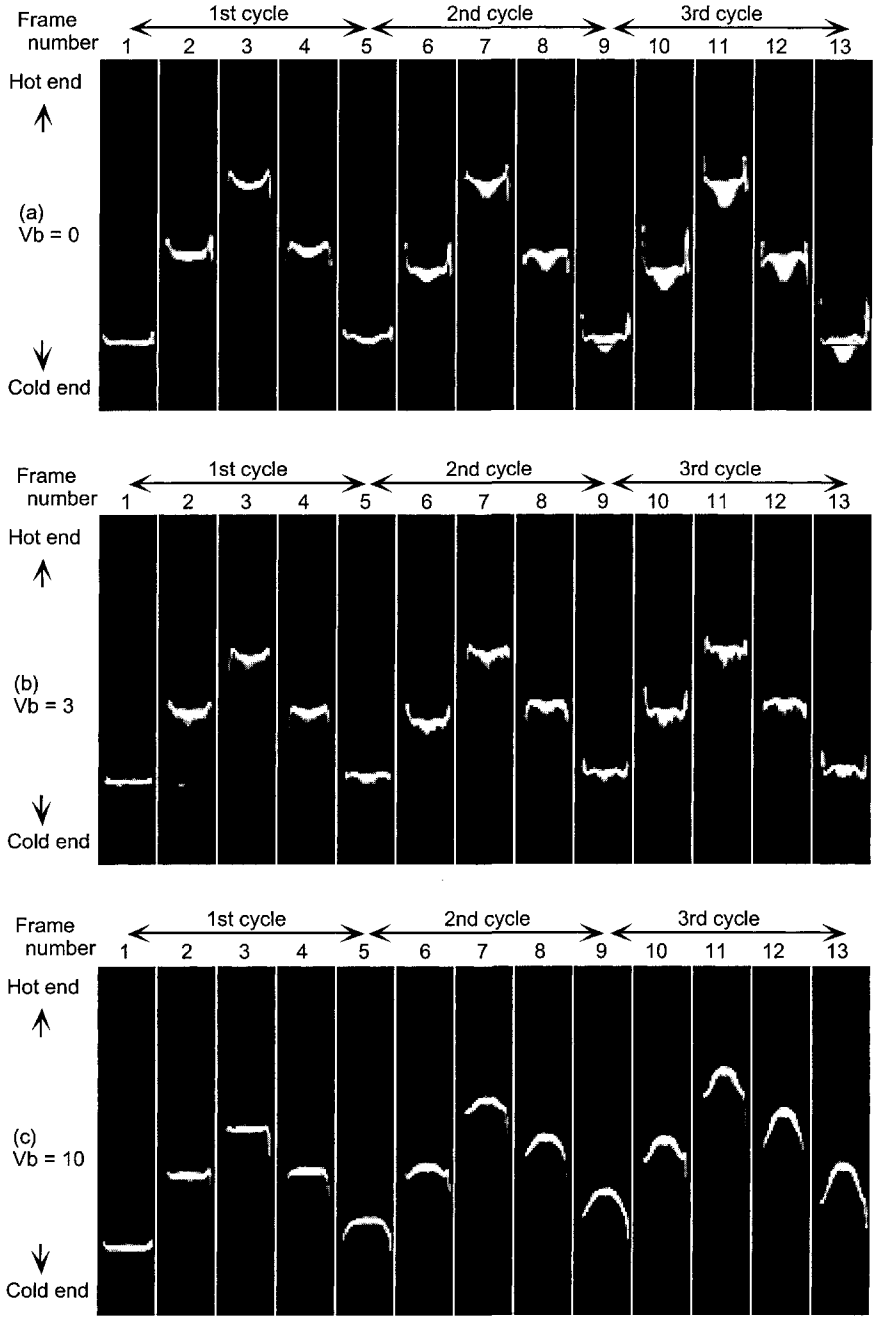

Figure 4. Typical visualization results for the convergent tapered tube during the first three cycles of oscillation at (a) $V_b = 0$; (b) $V_b = 3$; (c) $V_b = 10$. The smoke-line was emitted at the moment when the flow direction changed by a pressure variation from expansion to compression in a cycle; just after the smoke-line was emitted (Frame 1), at the turning point of the hot end where the smoke-line changed its direction of motion (Frames 3, 7, and 11), at the turning point of the cold end (Frames 5, 9, and 13), and halfway between these two turning points (Frames 2, 4, 6, 8, 10, and 12).

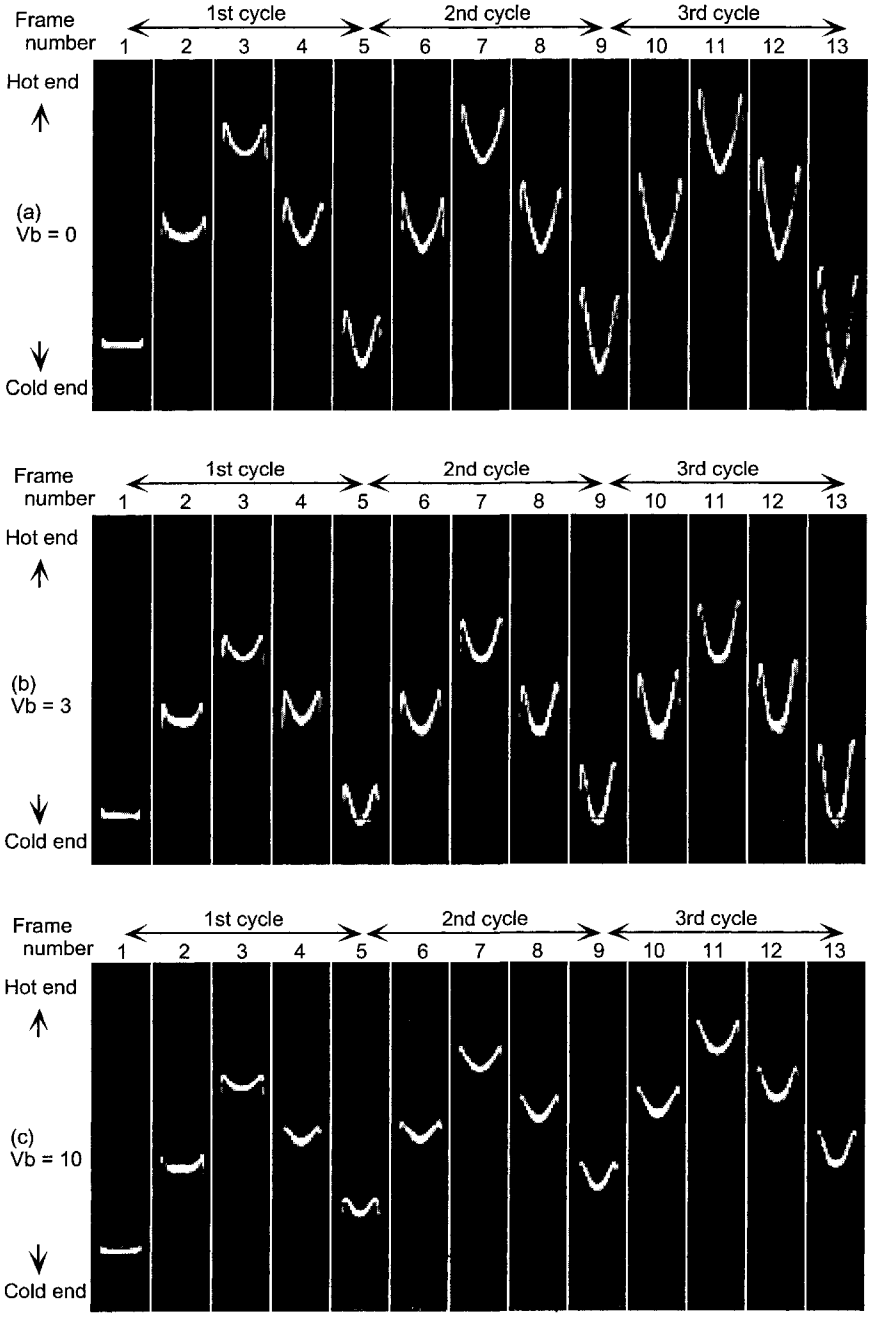

Figure 5. Typical visualization results for the divergent tapered tube during the first three cycles of oscillation at (a) $V_b = 0$; (b) $V_b = 3$; (c) $V_b = 10$. Conditions, parameters, and definitions are those defined for Fig. 4.

which the positive- and negative-direction flows due to pressure variation occur in each half cycle of oscillation. Mass flow of the positive-direction flow is not completely canceled by that of the negative-direction flow, and thus surplus mass flow during a cycle causes DC flow.[7] Third, the smoke-line was less elongated in the axial direction compared with the smoke-line when $V_b = 0$ turn-divisions, as evidenced by the distance between the leading edge of the smoke-line in the core region of pulse tube and that near the wall. This elongation of the smoke-line was again due to the DC flow.

To clarify the effect of a tapered tube on the secondary flow, we obtained the velocity profile of the secondary flow from these visualization results as follows. First, we digitized the smoke-lines at the hot-end turning point in the first five cycles of oscillation (such as Frames 3, 7, 11 in Figs. 4 and 5) by using an image-processing system. Then, we estimated the velocity profile of the secondary flow by using the change in the relative position of the smoke-line before and after a cycle, assuming that the change was due only to secondary flow. The obtained velocity profiles were thus an average profile for over a cycle. Figures 6, 7, and 8 show the obtained velocity profiles for various V_b in the convergent tapered tube, divergent tapered tube, and cylindrical tube, respectively. Here, negative and positive velocities in the figures correspond to flows going towards the cold end and hot end, respectively.

At $V_b = 0$, which corresponds to the configuration of an orifice pulse tube refrigerator, the velocity profiles for all three tubes indicate an axisymmetric convective secondary flow where gas in the core region goes toward the cold end while the associated return flow goes toward the hot end along the peripheral wall. This convective secondary flow, which is driven by an acoustic streaming[1] induced by the oscillating motion of the gas, is inherently induced in pulse tube refrigerators

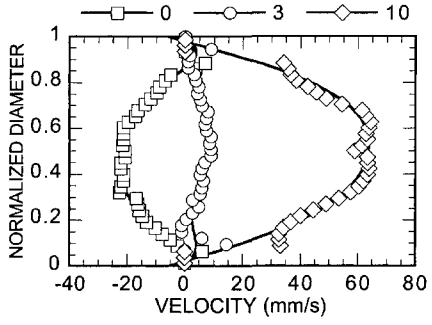

Figure 6. Velocity profiles of secondary flow in the convergent tapered tube for various V_b [turn-divisions]. Positive and negative values of velocity correspond to the flow going towards the hot and cold ends, respectively.

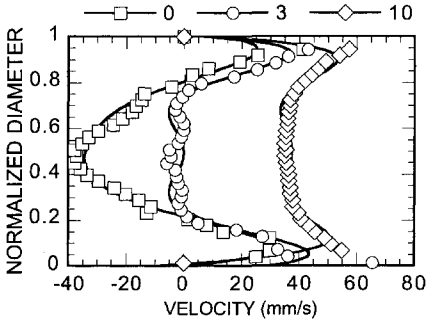

Figure 7. Velocity profiles of secondary flow in the divergent tapered tube for various V_b [turn-divisions]. Definitions are those defined for Fig.6.

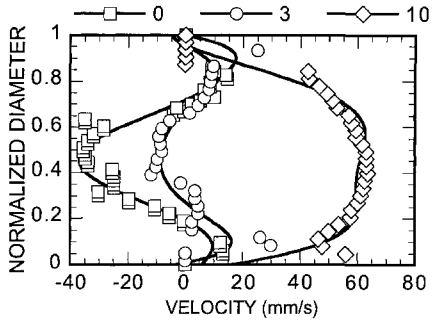

Figure 8. Velocity profiles of secondary flow in the cylindrical tube for various V_b [turn-divisions]. Definitions are those defined for Fig.6.

regardless of configurations and operating conditions. The velocity profile of the convergent tapered tube was much "flatter" (i.e. velocity of the leading edge in the core region was much slower) compared to that of either the divergent tapered tube or cylindrical tube. The shape of the velocity profile of the divergent tapered tube resembled that of the cylindrical tube, although the velocities of the leading edge in the core region and near the wall were faster than those for the cylindrical tube. These results agree well with those previously reported[4] for an orifice pulse tube refrigerator with a tapered tube.

At $V_b > 0$, which corresponds to the configuration of a double-inlet pulse tube refrigerator, DC flow is newly induced in the refrigerator. For example, Fig. 9 shows the representative velocity profile of DC flow derived from the velocity profiles of the convergent tapered tube in Fig. 6. The DC flow, which had a parabolic velocity profile, moved toward the hot end, and its strength increased with increasing V_b. In general, a secondary flow explicitly visualized by a smoke-line corresponds to an overall flow overlapped with several types of secondary flows. For the double-inlet pulse tube refrigerator installed vertically as shown in Fig. 2, the secondary flow at $V_b > 0$ formed as a superposition of the DC flow on the convective secondary flow at $V_b = 0$.[8] As a result of the superposition, the DC flow counterbalanced the convective secondary flow in the core region, causing a decrease in the velocity in the core region, while the DC flow superposed on the convective secondary flow near the wall, thus causing an increase in the velocity near the wall. At $V_b = 3$, the convective secondary flows in the core region were counterbalanced by the DC flow so that the velocities in the core region were significantly reduced. At $V_b = 10$, the DC flow increased and exceeded the convective secondary flow in the core region so that the entire flow (both in the core region and near the walls) moved toward the hot end.

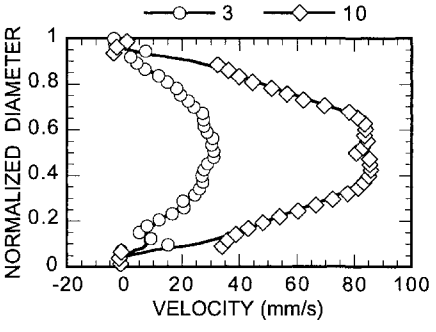

Figure 9. Typical velocity profiles of DC flow for various V_b [turn-divisions]. Profiles were derived from the velocity profiles of the convergent tapered tube in Fig. 6. Positive and negative values of velocity correspond to the flow going towards the hot and cold ends, respectively.

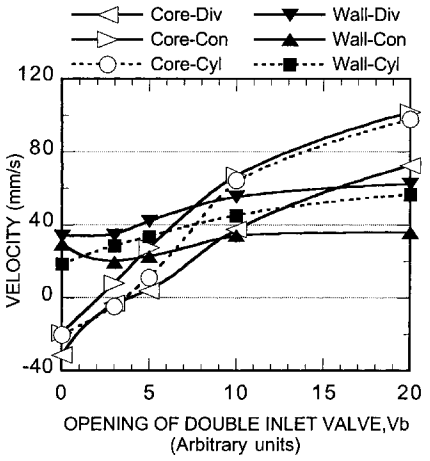

Figure 10. Representative velocities of secondary flow in the core region and near the wall of tapered and cylindrical tubes as a function of V_b[turn-divisions]. Positive and negative values of velocity correspond to the flow going towards the hot and cold ends, respectively.

To quantify the change in secondary flow in more detail, the velocities of three representative positions on the smoke-line were evaluated; the leading edges in the core region (V-core), near the right wall (V-right), and near the left wall (V-left). These positions were directly measured from observed smoke-lines at every turning point, and then the velocities were estimated from the change in those positions with time. Because the smoke-line dissipated into a broad line with time, the velocity profiles, especially near wall, were not clearly distinguishable due to elongation of the smoke-line parallel to the wall. Thus, determining the representative velocities with sufficient accuracy from the velocity profiles such as those in Figs. 6, 7 and 8 was somewhat difficult. Figure 10 shows the change in the velocities of the three positions with V_b. Here we present the V-left as the representative velocity of the leading edge near either wall because the difference between V-left and V-right was small due to roughly axisymmetric velocity profiles. For all three tubes, with increasing V_b, V-core monotonously changed from negative to positive velocity near $V_b = 3$ turn-divisions, and therefore the absolute values of V-core were a minimum near $V_b = 3$ turn-divisions. In contrast, for all three tubes, V-left had only positive values, indicating that the flow was only toward the hot end.

The results shown in Figs. 3 and 10 show that all pulse tubes of the configuration of a double-inlet pulse tube refrigerator effectively reduced the secondary flow in the core region, and thus improved the performance. Although the divergent tapered tube also improved the performance compared with that for the cylindrical tube, the improvement was relatively small. Moreover, performance and V-core for both the tapered and cylindrical tubes directly depended on the double-inlet valve. Comparison of performance improvement by the divergent tapered tube and that by adjusting V_b to the optimum opening indicates that, when the strength of DC flow is adjusted to minimize convective secondary flow, the DC flow is more effective at reducing the secondary flow in the core region. Therefore, for double-inlet pulse tube refrigerators, tapering of a tube is not an effective method to reduce heat loss caused by secondary flow. DC flow is inherently induced in double-inlet pulse tube refrigerators, and can therefore be used to reduce the secondary flow in the core region.

SUMMARY

Oscillating flow in tapered double-inlet pulse tube refrigerators was observed by using smoke-wire flow visualization. Effect of a tapered tube on the flow behavior of secondary flow was inves-

tigated by focusing on reducing the heat loss due to the secondary flow. Results showed that for a double-inlet pulse tube refrigerator, when the strength of the DC flow was adjusted to the optimum strength to minimize convective secondary flow in the core region, the DC flow more effectively reduced the secondary flow in the core region compared to the reduction by using a tapered tube. Moreover, performance of the divergent tapered tube was slightly superior compared to that of a cylindrical tube, whereas a convergent tapered tube was significantly inferior compared to that of either a divergent tapered tube or a cylindrical tube.

REFERENCES

1. Olson,J.R. and Swift,G.W., "Acoustic streaming in pulse tube refrigerators: tapered pulse tubes," *Cryogenics*, Vol. 37 (1997), pp. 769-776.
2. Baek,S.H., Jeong,E.S. and Jeong, S., "Two-dimensional model for tapered pulse tubes. Part 1: theoretical modeling and net enthalpy flow," *Cryogenics*, vol. 40 (2000), pp. 379-385.
3. Baek,S.H., Jeong,E.S. and Jeong, S., "Two-dimensional model for tapered pulse tubes. Part 2: mass streaming and streaming-driven enthalpy flow loss," *Cryogenics*, vol. 40 (2000), pp. 387-392.
4. Shiraishi,M., Ikeguchi,T., Murakami,M., Nakano,A. and Iida,T., "Visualization of oscillating flow phenomena in tapered pulse tube refrigerators," *Advances in Cryogenic Engineering*, vol. 47, American Institute of Physics, New York (2002), pp. 768-775.
5. Gao,C., He,Y. and Chen, Z., "Numerical simulation of convergent and divergent tapered pulse tube cryocoolers and experimental verification," *Proc. 6th Joint Sino-Japanese Seminar on Cryocooler and its Applications*, Lanzhou Institute of Physics, Lanzhou (2000), pp. 65-70.
6. Xu, M., He,Y., Gao,C., Chen, Z. and Li, J., "Experimental research of non-uniform cross-section pulse tube cryocooler (PTC)," *Proc. 6th Joint Sino-Japanese Seminar on Cryocooler and its Applications*, Lanzhou Institute of Physics, Lanzhou (2000), pp. 264-268.
7. Gedeon, D., "DC gas flows in Stirling and pulse tube cryocoolers," *Cryocoolers 9*, Plenum Press, New York (1997), pp. 385-392.
8. Shiraishi,M., Takamatsu,K., Murakami,M., Nakano,A., Iida,T. and Hozumi,Y., "Visualization of DC gas flows in a double-inlet pulse tube refrigerator with a second orifice valve," *Cryocoolers 11*, Kluwer Academic/Plenum Publishers, New York (2001), pp. 371-379.

Numeric Code for the Design of Pulse Tube Coolers

A. Hofmann

Thermo-Acoustic Consultant
D-76229 Karlsruhe, Germany*

ABSTRACT

The computer program FZKPTR is written for the design of two-stage 4K pulse tube coolers. However, it can be modified easily for describing manifold configurations of simpler systems such as low and high frequency (2 to 60 Hz) single-stage coolers. The program also provides basic routines for inertance tube phase shifters. The executable file will run with very fast response on any personal computer. User-defined operational parameters, geometries, and materials of the components are entered in a clearly structured matrix. The standard output is an array of data such as time-averaged temperature, amplitude and phase angle of pressure and volume flow as well as heat and work flow at any position of the system. Auxiliary quantities such as thermal and viscous penetration depth, swing of matrix temperature and many others can also be listed and plotted.

The code is based on the small amplitude thermoacoustic theory, but it is shown that reasonable results are also obtained for GM-type pulse tube coolers with rather high compression ratios. The input list has also provided empiric terms for adaptation of flow resistance and thermal conduction of any section. DC flows in both stages can be adjusted individually. Some examples for using the code will be given. The FZKPTR code will next become available to the public.

INTRODUCTION

Over the last decade pulse tube cooling has become one of the most important methods for small and medium scale cryogenic applications. Having no moving parts in the cold head, such kinds of coolers seem to be very simple devices. Their main function is based on the Stirling process, a gas cycle known for about 150 years. Many machines for transforming cyclic work flow of compressed gas into thermal energy and vice versa are being used in technology, and there is a broad basis on theoretical and experimental expertise in academic and industrial institutions. Surprisingly, not many of those data can be used directly for the design of pulse tube coolers. Partially this may be because of companies' privacy, and because pulse tube refrigerators were first developed by people in academic institutions who had not access to those design codes. On the other hand, aspects which were not relevant to conventional Stirling and Gifford-McMahon coolers had to be considered for pulse tube designs. A third aspect is that new cooler applications tend to very low refrigeration temperatures, to improved efficiency, and to more compact design. This has called

* Former address: Forschungszentrum Karlsruhe, Institute für Technische Physik
D-76021 Karlsruhe, Germany

Cryocoolers 13, edited by R. G. Ross, Jr.
Springer Science+Business Media, Inc., New York, 2004

for better methods of calculations for such systems. Numeric codes for such calculations have been developed by different groups, but some of such codes are on rudimentary levels so that they can be used only by the author. The code (REGEN3.1) developed at NIST[1,2,3] has been developed for regenerator design and does not comprise the complete cooler. The Los Alamos code DELTAE has been developed for the design of very general low-amplitude thermoacoustic engines. It is now commercially available.[4] However, we do not know whether it can be used for the design of multistage coolers with refrigeration temperatures in the 4 K range. The other commercial product SAGE[5] has resulted from a long period of development of conventional coolers, but it can also be applied to many different types of pulse tube coolers. All of these numeric codes will be very useful, they are very comprehensive, and, of course, each will certainly have specific advantages and disadvantages. Users interested in specific applications cannot avoid elaborate learning processes. Those codes were not available when we started our activities on pulse tube coolers, so we had to develop our own methods. This code FZKPTR[6] might be a valuable addition. It was developed for the design of two-stage pulse tube coolers with a 4 K refrigeration temperature. However, the model can also be applied to simpler single stage systems. Also, the inverse process as used for thermoacoustic drivers can be handled with the code. The physical basis (linear thermoacoustics) of our code, FZKPTR, is mainly the same as that of DELTAE developed at the Los Alamos National Lab. In contrast, our code includes real gas properties and temperature-dependent properties of a commercial solid material data base. Users should have respective licences.

THE CONCEPT OF THE PULSE TUBE REFRIGERATOR CODE FZKPT

The default version of our code is developed for describing a two-stage 4K pulse tube cooler as shown in Fig. 1. It may be used for the design of a cold head capable for lifting refrigeration powers $\dot{Q}_1$ and $\dot{Q}_2$ from temperatures T_1 and T_2, respectively. It yields the requirement of the compressor, namely the acoustic work flow (pV-power) resulting from pressure p, volume flow U, and phase angle φ at the outlet of the compressor. Furthermore, it yields the work flow to be extracted from both pulse tubes. The geometry and the intrinsic structure of all components may be modified so that the compressor power becomes as small as possible. This two-stage cold head is composed of up to 20 sections, and the internal structure of each section must be described by a number of parameters. Moreover, the code has to handle DC flows (small steady-state gas flow) to be individually adjusted in both pulse tubes, and it has to handle the ratio of gas flows, m_1/m_2, at the bifurcation of first and second stage. Altogether, there will be about 200 parameters to be modified for finding the best configuration. This is a rather difficult task. A computer code making all necessary iterations automatically would become very complicated. The better choice, we believe, is to modify the parameters manually and check the results for reasonableness. This procedure requires a fast response (within a few seconds) and a good overview on input and output data. Fast response means that restrictions in accuracy must be accepted.

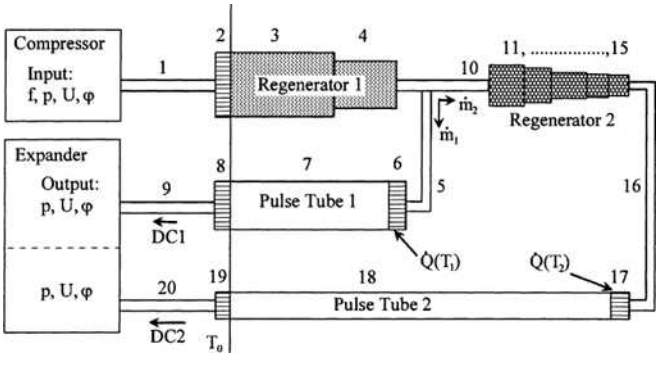

Figure 1. Schematic of the two-stage pulse tube cooler.

Table 1. List of typical input data of a two-stage 4K-PTR.

```
Example 1: 2-stage 4K-PTR
F      p0       p1/p0    SweptV   phi     TW      WREG1    WREG2       TOL
1.66   17.4E5   0.337    750e-6   45      300     0.001    0.001       1E-6

                    Length  TotalAr  b         bs       DeltaE    Jmat  MSTEP  FRF   CDF   A/I
'1_ Tube Compr_Reg1 ' 1.00   -1       5.00E-3   1.00E-3  0         3     1      1     1     'a'
'2_ Aftercooler     ' 0.020  26.4E-4  54.0E-6   8.40E-6  0         1     1      1     1     'a'
'3_ 1. REG. Part 1  ' 0.153  26.4E-4  39.0E-6   13.44E-6 19.9      3     10     1.0   0.1   'a'
'4_ 1. REG. Part2   ' 0.00   0        0         0        0        14     1      1.0   1     'a'
'5_ Tube REG1/PT1   ' 0.100  2.00E-3  1.00E-3   .0       25.0     1     1      1     1     'a'
'6_ Flow Conditioner' 0.015  15.2E-4  54.0E-6   8.4E-6   0        1     1      1.0   1     'i'
'7_ 1.PulseTube     ' 0.220  -1       22.0E-3   0.5E-3   0        3     10     1     1     'a'
'8_ WARMEND HX1     ' 0.020  15.2E-4  54.00E-6  8.4E-6   0        1     1      1.0   1     'a'
'9_ Tube PT1 to Exp.' 0.050  -1       2.0e-3    0.5e-3   0        3     1      1     1     'a'
'10_2. Reg, spacer 1' 0.001  4.52E-4  30.9E-6   11.7E-6  5.66     3     1      1.0   1     'a'
'11_2. Reg. Pb      ' 0.034  4.52e-4  23.40e-6  22.49e-6 0        14    10     1.0   0.32  a
'12_2. REG. spacer 2' 0.005  4.52E-4  0.5E-3    1.0e-3   0        3     1      1.0   1     'a'
'13_2. Reg. Er3Ni   ' 0.053  4.52e-4  23.40e-6  22.49e-6 0        62    100    1.0   2.0   'a'
'14_2. Reg. Spacer 3' 0.003  4.52e-4  1.0e-3    1.0e-3   0        3     1      1.0   1     'a'
'15_2. Reg. HoCu2   ' 0.039  4.52e-4  23.40E-6  22.49E-6 0        67    10     1.0   2.0   'a'
'16_Ltg.Reg.2 zu PT2' 0.080  -1       0.001     1.0e-3   0.       1     1      1.0   1     'a'
'17_Str.-Glaetter 2 ' 0.050  2.46e-4  0.45e-3   0.5e-3   0.671    1     1      1.0   1     'i'
'18_2. Pulsrohr, T1 ' 0.380  -1       9.5e-3    0.5e-3   0.       3     10     1     1     'a'
'19_Warmend HX2     ' 0.025  2.01E-4  54.0e-6   8.4e-6   0.0      1     1      1.0   1     'i'
'20_Ltg. PR2/Ventil ' 0.0001 -1       3.00e-3   1.0e-3   0        3     1      1     1     'a'
'Volumflow st1/st2  '    55          ! in percent (%)
'rel. dc-flow in PT1' 0.000
'rel. dc-flow in PT2' 0.00150
'Compressor:        '
'Swept volume, m^3  ' 43e-6          ! Volume of GM compressor capsule
'Frequency of grid  ' 50.0           ! in Hz
'He-Condensation    ' 0.00    1.0e5        ! Low rate in kg/s,  Pressure in Pa,
'Zyklus,j=1, n=0    ' 0
'List of suppl. var.' 0                    !yes=1, no=0
'Variable in Col.10 ' 19             !0 < integer < 23
'Variable in Col.11 ' 20             !0 < integer < 23
*******************************************************************************************
```

All input data are compiled in a list as shown in Table. 1. This list describes the real 2-stage 4K PTR operated in our laboratory. The compressor is described by the parameters of the upper block with the frequency F of the pulsating gas flow, the mean pressure p0, the ratio of pressure amplitude p1/p0, the swept volume of the compressor, and the phase angle between pressure and volume flow supplied by the compressor. The next lines describe the components 1 to 20 characterized by length, total cross sectional area, internal structure derived from hydraulic diameter and porosity, the change of enthalpy flow caused by intrinsic losses or by heat transfer, and the parameter JMat describing the material. MSTEP will control the listed output, and the last three columns are used for empirical corrections of terms that are not well known from literature, namely the friction loss (FRF) and the longitudinal thermal conductivity of the porous regenerator structures (CDF). The last column (A/I) provides the option for treating certain sections either as thermally insulated (adiabatic, a) or as isothermal (i). The next three lines are inputs for controlling the flow rated at the bifurcation of first and second stage and the DC flows in both pulse tubes. The last lines of the input list will be used for special studies that are beyond the scope of the present presentation. More details can be found in Ref. 6.

THE THEORETICAL BACKGROUND

The Basic Model

The calculations are based on the thermoacoustic theory[7,8,9,17] describing the conversion of mechanical and thermal energy of an oscillatory gas flow in ducts with solid walls. A very useful work on this problem has also been done by Xiao.[10] Our calculations are strongly based on that work, and we also use the same terminology.

The basic element is a circular channel with radius b and wall thickness b_s as shown in Fig. 2. The gas flow at the position x is described by the mean temperature T_0, the pressure

$$\tilde{p} = p_0 + \hat{p}e^{j\omega t} \tag{1}$$

and the volume flow

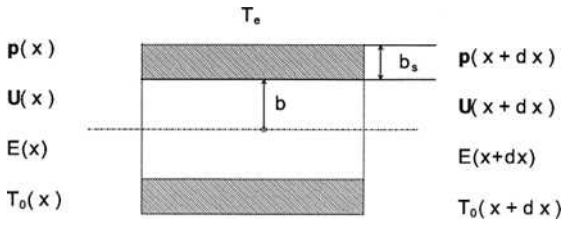

Figure 2. Geometry of the sound channel.

$$\tilde{U} = U_{DC} + \hat{U}e^{j(\omega t+\varphi)}, \qquad (U_{DC} << \hat{U}) \tag{2}$$

The fact that the volume flow U has no higher harmonics implies that the pressure amplitude must be small, namely POVERP<<1. This is taken into account when the following expressions are derived from Navier-Stokes equations. For laminar flow in circular channels, the shear force and the transversal heat flow can be described by analytic expressions. Hereby the two-dimensional problem is reduced to a linear one with

$$\frac{d\tilde{p}}{dx} = -Z_F\tilde{U} \quad , \qquad \frac{dT_0}{dx} = \frac{\frac{1}{2}\mathrm{Re}[\tilde{U}\tilde{p}^*(1-T_0\beta_0)f_{qx}]}{A_f K_e} \tag{3a,c}$$

$$\frac{d\tilde{U}}{dx} = -\frac{1}{Z_C}\tilde{p} + \beta_0\frac{dT_0}{dx}, \qquad \frac{dE_x}{dx} = -h_w U_w(T_0 - T_e) - \dot{m}_{DC}C_{p0}\frac{dT_0}{dx} \tag{3b,d}$$

So we have a system of 6 real type differential equations with the variables Re(p), Im(p), Re(U), Im(U), T_0, and the total axial energy flow E_x. The coupling coefficients Z_F, Z_C, f_{qx}, K_e are functions of channel geometries and of fluid and solid material properties. They are given by analytic expressions for simple geometries of the sound channels. We are using the terms as derived for circular channels[10]. Solving those equations yields all variables at any position of the system. And we also get the acoustic work and heat

$$W_x = \frac{1}{2}\mathrm{Re}[\tilde{U}\tilde{p}^*] \quad ^{\dagger} \tag{4}$$

and

$$Q_x = -\frac{1}{2}T_0\beta_0\, Re[\tilde{U}\tilde{p}^* f_{qx}] - A_f K_e\frac{dT_0}{dx} \tag{5}$$

respectively, and the longitudinal total energy (enthalpy) flow is $E_x = W_x + Q_x$. Equation (3d) describes the loss of total energy caused by heat transfer through the perimeter U_w and by a small DC flow, a term neglected in the basic thermoacoustic theory of Rott.

The basic assumptions of this model are:

1. The problem is two dimensional (constant cross sectional areas)
2. The sound field is at periodically working condition and the mean fluid velocity is zero
3. The acoustic amplitudes are low enough to avoid turbulence[17] so that:
   $Re_\omega = \rho_0 u\delta_\mu / \mu_0 << 500$
4. The displacement of gas particles is much smaller than the acoustic wave length:
   $(u/(2\pi a_0)<<1)$
5. The transverse heat flow from the solid wall to the environment is proportional to the temperature difference

---

† For harmonic functions of p and U=dV/dt, the following expressions are identical

$$W_x = f\oint pdV = f\int_0^{1/f}(p_0+\tilde{p})\tilde{U}dt = \frac{1}{2}\mathrm{Re}[\tilde{U}\tilde{p}^*] = \frac{1}{2}\hat{p}\hat{U}\cos(\varphi)$$

where the symbols 'tilde', 'hat' and 'asterisk' mark time dependent part, amplitude and conjugate of the variables, respectively

Many components of the PTR will be operated within an evacuated containment, thus there will be no overall transversal heat flow. This means that the coefficient of heat transfer, h_w, is zero at periphery with perimeter U_w. The other extreme for ideal heat transfer to the surrounding with temperature T_e. This means that $dT_0/dx=0$ in such components. Only these two extremes will be considered for the evaluation of cooler. The different section will be characterized by 'adiabatic' described by $(dE_x/dx)_1=0$ or by 'isotherm' described by $dT_0/dx=0$. The parameter 'A/I' in the input list is used to adjust any of the 20 sections either to 'a' (adiabatic) or to 'i' (isotherm).

ADAPTATION TO REAL REGENERATOR STRUCTURE

Intrinsic Structure. So far, the model is valid only for long circular ducts such as the pulse tubes and the connecting tubes. The model can also be applied to regenerators and heat exchangers consisting of bundles of circular channels. End effects are neglected, and it must be checked if the conditions for non-turbulent flow are fulfilled. But, most real regenerators are made from packages of wire mesh or microspheres. We describe such structures by equivalent packages of short circular channels which have such dimensions that a) the porosity, b) the wetted surface, and c) the flow resistance becomes the same for the real and the equivalent structures. Then we get the equivalent parameters

$$b = \frac{\varepsilon}{1-\varepsilon}\begin{cases} D_w/2 & \text{for mesh} \\ D_s/3 & \text{for spheres} \end{cases} \quad \text{and} \quad b_s = b\left(\frac{1}{\sqrt{\varepsilon}}-1\right) \tag{6}$$

where D_w and D_s are the diameters of wires and spheres, respectively. The channel diameter *2b* calculated in this manner is equal to the hydraulic diameter defined as four times the flow area divided by the wetted perimeter. It is in good agreement with data derived from other models.[11]

Pressure Drop and Heat Transfer. In the basic model, pressure drop and heat transfer from the fluid to the solid are calculated for laminar flow in very long ducts. Inlet and outlet effects are being neglected. Hence, pressure drop and heat transfer will be underestimated. To be more realistic, those channels have to be subdivided in many very short sections so that the end effects will dominate. Such configurations become similar to porous beds. Respective correlations for stacked mesh and for sphere-bed-matrices are given in literature.[12,13] The friction factor and the heat transfer coefficient (expressed by the Nusselt number) become power functions of the Reynolds number which proves to be in the range $30<Re<300$ for regenerators operated in the range $4\ K < T < 300\ K$. We have not succeeded to implement those correlations precisely into the theoretical model. But we believe that a reasonable correction is obtained by modifying the viscosity and the thermal conductivity of the fluid so that those terms yield the expected enhancement of pressure and heat transfer. Hence, we simply replace the viscosity η_0 by the apparent values

$$\eta_{apparent} = \eta_0(2.62 + 0.033\,Re)\cdot FRF \tag{7}$$

with

$$Re = \frac{\rho_0 \hat{U}\, 2b}{A_F \eta_0} \tag{8}$$

The pressure drop and heat transfer correlations given in Ref. 12 and 13 have been obtained for steady flow measurements, but recently it was shown[14] that the pressure drop does not change up to frequencies of 10 Hz. There is an enhancement at higher frequencies, but precise correlations are not known. We have therefore introduced an empirical factor 'FRF' (flow resistance factor), which will be read from the file of input data for each individual component. It is known that the heat transfer will be improved when the pressure drop increases. Assuming that the Prandtl number ($Pr = \eta c_p/k$) will not be changed, the apparent thermal conductivity becomes

$$k_{apparent} = \frac{\eta_{apparent} c_{p0}}{Pr_0} \tag{9}$$

In our code, those modified correlations are only applied to sections with small hydraulic diameters (2b < 0.5 mm). In other cases, the empiric correction term FRF may be used for taking account of other terms which may cause higher pressure drop than predicted by the laminar flow correlations. Reasonable values for the enhancement factor may be found in text books on fluid flow. In many cases, they will depend on the Reynolds number. For that purpose, we have implemented the option to list the Reynolds number at any position of the system together with the mentioned default variables. This option will be activated with the parameter 'List of suppl. var' given in the lowest lines of the input file. Up to 22 different variables can be selected to be printed in the output array.

Longitudinal Heat Conduction. In the basic model, the longitudinal heat flow is calculated as if the regenerator would be composed of a solid rod with the cross section as resulting from the total porosity and the total cross section. But, it is known that the effective thermal conductivity of stacked screens and of microsphere matrices is much smaller.[15] This conductivity degradation factor CDF is not well known in most cases. Taking this fact into account, the thermal conductivity of the solid material is decreased only in the expression where the term K_e describes the effective longitudinal conductivity

$$K_e = K_0 \frac{1}{\delta_K^2} \left| \frac{\tilde{U}}{A_f \omega} \right|^2 g_{qx} + K_0 + \frac{A_s}{A_f} K_{so} \cdot CDF \tag{10}$$

Here, the term K_{s0}, the thermal conductivity of the solid, has been replaced by $K_{s0} \times CDF$. However, in other equations describing the transversal heat flow, i.e. the thermal diffusion into the solid, which is characterized by the thermal penetration depth

$$\delta_s = \left(\frac{2K_{s0}}{\rho_{s0} C_{s0} \omega} \right)^{\frac{1}{2}} \tag{11}$$

the conductivity is not changed.

Materials. By default, the working gas is Helium with real gas properties derived from the HEPROP code. To the extent they are available, properties of solid materials are taken from CRYOPROP.[16] They are selected by the parameter JMat. Specific thermal data of other materials such as rare-earth compounds have been added. The thermal conductivity of those materials not known is set equal to that of stainless steel. This should be allowable for low frequency applications where the thermal diffusion depth δ_s is much greater than b_s, the thickness of the wall.

RUNNING THE CODE

The code is written in FORTRAN, but all calculations can be done with the executable file which runs on any PC. Thus, a compiler is not necessary. The code reads all data from the input file, and it calculates temperature, pressure, volume flow, phase angles, heat and work flow and many other parameters at any position of the system. Those data are written into ordered output lists which may be imported into graphic programs preferred by the user. Results are obtained within less than 3 seconds, and the output list can be checked just by a mouse click. Thus we get a very fast response and we can decide how the input must be modified for the next improvement. Making all iterations manually has the advantage that one will get a very good feeling for the processes going on in such coolers. Therefore in short time one can gain sufficient experience for modifying the input parameters in a reasonable way.

A user with no previous experience should begin with a less comprehensive system, such as one with a first-stage regenerator. All other components can be eliminated just by setting their length to zero. One should know that the irreversible losses of the regenerator increase with increasing temperature difference. When pressure, volume flow and temperature are given at the inlet of the regenerator, the parameter 'DeltaE', which is a measure of the regenerator loss, has to be

Table 2. Comparison of measurements and calculations done with PTR031120

Measurement							Calculation							
Q1	T1	Q2	T2	p	dm/dt	P_{el}	Q1	T1	Q2	T2	p	dm/dt	DC2	m_1/m_2
W	K	W	K	bar	g/s	kW	W	K	W	K	bar	g/s		
25	46.7	**0.51**	4.1	11.9...24.9	4.0	7	**25**	46.3	**0.67**	4.1	11.6...23.2	4.03	0.00150	0.55

modified so that the desired low end temperature is achieved. Then the first stage pulse tube and its 'DeltaE' are to be modified so that ambient temperature is achieved at its hot end. This 'DeltaE' is the effective refrigeration power of that stage.

RESULTS

4-K-PTR. The list of input data given by Table 1 describe a GM-type two stage pulse tube cooler as shown in Fig. 1. It has been operated in our laboratory. All parameters of size and materials have been transferred to the input list. The second stage regenerator is composed of Pb, Er_3Ni, and $HoCu_2$ (characterized by sections 12, 14, and 16). Among the many other parameters, we have measured temperatures and refrigeration powers at both stages, pressure at the hot end of the regenerator, and the mass flow (dm/dt) supplied by the compressor. The input parameters of the code, namely p0, p1/p0 (compression ratio),'swept volume' and the first stage refrigeration power have been modified for fitting those experimental data. Other parameters, such as the mass flow ratio at the bifurcation of stage 1 to stage 2 (m1/m2) and the DC flow—quantities which could not be measured—have been modified empirically to maximize the second stage refrigeration power.

The results are given in Table 2. For a 4.1 K second stage temperature, the model has predicted a refrigeration power of 0.67 W, whereas 0.51 W has been obtained in the experiment. This agreement is not bad. One should realize that the calculation shows that about 7.6 W of acoustic work flow (pV-power) is required at the cold end of the second stage pulse tube. Hence, the second stage losses are more than ten times the effective cooling power. A 10% error in the calculation of those losses would effect about 100% change of effective refrigeration. Moreover, the thermoacoustic model has been derived using a small-amplitude approximation and for a sinusoidal variation of pressure and flow rate. But here we have about 6 bar of pressure amplitude for 17.5 bar mean pressure, and the hot end gas flows are imposed by close/open valves. This will cause higher harmonics, which are not taken into account in the calculations.

The phase shifter has not been specified for this arrangement. The calculation only yields flow rate, pressure, and phase angle at the hot ends of the pulse tubes. Those data can be easily trans-

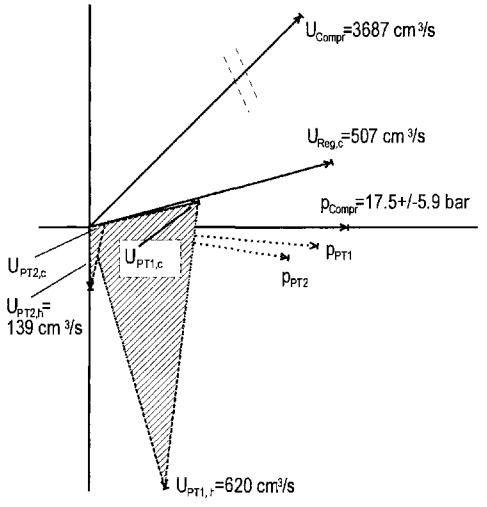

Figure 3. Pressure and volume flow phasors of the 4-K-PTR.

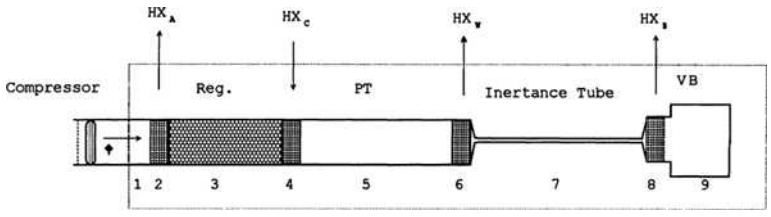

Figure 4. Scheme of a single stage pulse tube cooler with inertance tube phase shifter.

Table 3. Input file of a PTR with inertance tube phase shifter.

```
Example 2: Single stage 60Hz-PTR with parallel tube HX and innertance tube phase shifter
F       p0        p1/p0     SweptV    phi      TW       WREG1    WREG2        TOL
60     17.0E5     0.2       88e-6     45       300      0.001    0.001        1E-6

                        Length  TotalAr  b         bs       DeltaE    Jmat  MSTEP   FRF    CDF    A/I
'1_ Tube Compr_Reg1   ' 1.00    -1       5.00E-3    1.00E-3  0         3     1       1      1      'a'

                         Length  TotalAr  b         bs       DeltaE    JMat  MSTEP   FRF    CDF    A/I
'1_ Dead volume       '0.033    -1       29.0e-3    1.0e-3   0         3     1       1      1      'a'
'2_ Aftercooler       '0.050     6.28E-4  0.5e-3     0.5e-3   61.       1     1       5      1      'a'
'3_ 1. REG.           '0.065    26.4E-4  49.21E-6   11.83E-6 0         3     20      1      0.1    'a'
'4_                   '0        0         0         0        0         1     1       1      1      'a'
'5_ Branch st1/st2    '1e-6     -1        2e-3      0.5e-3   0         3     1       1      1      'a'
'6_                   '0        0         0         0        0         3     1       1      1      'a'
'7_                   '0        0         0         0        0         3     1       1      1      'a'
'8_                   '0        0         0         0        0         1     1       1      1      'a'
'9_                   '0        0         0         0        0         3     1       1      1      'a'
'10_                  '0        0         0         0        0         1     1       1      1      'a'
'11_                  '0        0         0         0        0         1     1       1      1      'a'
'12_                  '0        0         0         0        0         1     1       1      1      'a'
'13_                  '0        0         0         0        0         1     1       1      1      'a'
'14_                  '0        0         0         0        0         1     1       1      1      'a'
'15_Cold end HX       '0.05     6.28e-4  0.5e-3     0.5e-3   234       1     1       5      1      'a'
'16_Pulse tube        '0.120    -1       22.00e-3   0.5e-3   0         3     20      1      1      'a'
'17_WarmEnd HX        '0.05     6.28e-4  0.5e-3     0.5e-3   294       1     1       5      1      'a'
'18_Inertance Tube    '1.445    -1        3.5e-3    0.5e-3   0.0       3     20      10     1      'a'
'19_Buffer HX         '0        0         0         0        0         1     1       1      1      'a'
'20_Buffer volume     '0.1855   -1       30.00e-3   1.0e-3   0         3     20      1      1      'a'
'Volumflow PT1/Reg2 '   0              ! in percent (%)
'rel. dc-flow in PT1'0.00
'rel. dc-flow in PT2'0.000
'Compressor:        '
'Swept volume, m^3   '50.0e-6
'Frequency of grid   '50.0             ! in Hz
'He-Condensation     '0.00     1.0e5  ! Low rate in kg/s,  Pressure in Pa,
'Zyklus,j=1, n=0     '0
'List of suppl. var.'1                !yes=1, no=0
'Variable in Col.10 '21               !0 < integer < 23
'Variable in Col.11 '13               !0 < integer < 23
*****************************************************************************************************
```

ferred to piston type expanders. But they give also information for the design of other types of phase shifters and it also yields crude values for the timing of close/open valves. The phasor diagram for pressures and volume flows is shown in Fig. 3

Inertance Tube Phase Shifter. The basic equations (Eq. (3)) are the same for all components of the system. The only difference is given by the size, the intrinsic structure and the material. Hence the function of any of the 20 sections can be modified just with the parameters of the input list. Such an example is shown by Figure 4, a single stage cooler with inertance tube phase shifter. The respective input file is given in Table 3. This is a cooler operated with 60 Hz. It should be capable to lift about 200 W from 80 K. The calculation is done so that all work flow expanded from the pulse tube is dissipated in the inertance tube where adiabatic conditions have been assumed. The calculation will shows that the work flow is converted into heat flow, most flowing to the warm end heat exchanger HX_w. The size of the buffer volume will result from the fact that the flow rate must become zero at the closed end. The flow in the inertance tube will have high Reynolds numbers. Precise correlations for describing the respective pressure drop are not known. For more realistic calculations its value should be adjusted with the parameter FRF.

Other Configurations. Many other configurations can be handled by modification of the 20-section input list. Some more examples are given in Ref. 6. However, the source code can easily be modified if more components need to be considered. Also, properties of other materials can be implemented by adding arrays of specific heat and thermal conductivity data.

CONCLUSION

It has been shown that the present code can be used to study many different types of pulse tube coolers. All examples discussed here can be treated just by modification of a simple list of input data. No modification of the source code is required. However, one should always have in mind that the code is based on small-amplitude approximations. So, one should not expect too high an accuracy for the predictions. The code will be very valuable for getting a prototype design as a basis for further empirical improvements. It will also be very valuable to improve the understanding of the complicated thermal processes running in such systems.

The executable code of FZKPTR is now available to the public. Users interested in scientific or commercial use should contact the author (0721468784@t-online.de).

ACKNOWLEDGMENT

Most of this work was accomplished while I was a member of the FZK. The technical skill of Frank Gretschmann was indispensable for the experiments. I also thank Wolfgang Stautner from Oxford Magnet Technology for many critical comments on both experiments and calculations.

REFERENCES

1. P.J. Storch, R. Radebaugh, and J.E. Zimmermann, *Analytic Model for the Refrigeration Power of an Orifice Pulse Tube Refrigerator*, NIST Technical Note 1343 (1990).
2. Gary, J., Daney, D.E., and Radebaugh, R., "A Computational Model for a Regenerator," *Proc. Third Cryocooler Conference*, NIST Special Publication 689 (1985), p. 199.
3. Gary, J. and Radebaugh, R., "An improved numerical model for calculation of regenerator performance (REGEN3.1)," *Proc. Fourth Interagency Meeting on Cryocoolers*, David Taylor Research Center, Report DTRC-91/003 (1991), p. 165.
4. W.C. Ward and G.W. Swift, "Design Environment for Low-amplitude Thermoacoustic Engines," *J. Acoustic. Soc. Am.*, Vol 95 (1994), p. 3671. (http://www.lanl.gov/thermoacoustics/announce.html)
5. D. Gedeon, "Sage: Object-Oriented Software for Cryocooler Design," *Cryocoolers 8*, Ed. by R.G. Ross, Jr., Plenum Press, New York (1995), pp. 281-292.
6. A. Hofmann, "Instructions for Using the Numeric Code FZKPTR for the Design of Pulse Tube Coolers", *Wissenschaftliche Berichte des Forschungszentrum Karlsruhe*, FZKA 6929 (2003), ISSN 0947-8620.
7. Rott, N., *Thermally driven acoustic oscillations, Part III: Second order heat flux*, ZAMP 26 (1975), p. 43.
8. Rott, N. "Thermoacoustics," *Adv. Appl. Mech.* 20 (1980), p. 135.
9. G.W. Swift, "Thermoacoustics," *Encyclopedia of Applied Physics*, Vol. 21 (1997), pp. 245-264.
10. J.H. Xiao, "Thermoacoustic heat transportation and energy transformation. Part 1: Formulation of the problem," *Cryogenics* 35 (1995), p. 15.
11. E. Manegold, *Kapillarsysteme, Bd. 1*, Strassenbau, Chemie und Technik Verlags-GmbH, Heidelberg (1955), p. 422.
12. W.M. Kays and A.L. London, *Compact Heat Exchangers*, (Third Edition), McGraw-Hill Book Comp. NY (1984), ISBN 0.07-033418-8.
13. *VDI Wärmeatlas*, VDI-Verlag, Düsseldorf, 3. Auflage (1977).

14. K. Nam and S. Jeong, "Experimental study on regenerators under actual operating conditions,"*Adv. in Cryogenic Engineering*, Vol. 47B, Amer. Institute of Physics, Melville, NY (2002), p. 977.

15. M.A. Lewis, T. Kuriyama, F. Kuriyama, and R. Radebaugh, "Measurement of heat conduction through stacked screens," *Adv. in Cryogenic Engineering*, Vol. 43B, Plenum Publishing Corp., New York (1998), p. 1611.

16. Cryodata, Inc., http://www.cryodata.com/partners

17. Swift, G.W., *Thermoacoustics: A unifying perspective for some engines and refrigerators*, published by the Acoustical Society of America, ISBN 0-7354-0065-2 (2002).

Enthalpy, Entropy, and Exergy Flows in Ideal Pulse Tube Cryocoolers

P. Kittel

NASA Ames Research Center
Moffett Field, CA, USA, 94035-1000

ABSTRACT

Descriptions of how cryocoolers operate frequently take an energy-centric view. Such descriptions concentrate on the first law of thermodynamics, the conservation of energy. This approach can result in a complex description of the cooler in terms of energy and enthalpy flows.

An alternative is to take an entropy-centric approach. Closely related to this is the exergy-centric approach. These descriptions concentrate on the second law of thermodynamics, the generation of entropy or the destruction of exergy.

Both the energy-centric and exergy/entropy-centric approaches make use of the first two laws of thermodynamics and both approaches give equivalent descriptions of a cryocooler. However, the latter approach can be more useful as it can yield a simpler description, one that emphasis loss mechanisms.

This paper reviews the application of these approaches to pulse tube cryocoolers. For each component of ideal pulse tubes the effects of the component on the exergy, entropy, and enthalpy flows are found. The discussion concentrates on orifice type pulse tubes. While most of the discussion is applicable to cryocoolers driven by either Gifford-McMahon or linear compressors; the emphasis is on the latter.

INTRODUCTION

Enthalpy, entropy, and exergy analyses are useful tools for understanding thermodynamics of a system. In this paper, the thermodynamics of pulse tube coolers will be analyzed through the use of these quantities. Detailed thermodynamic models of pulse tube coolers have been presented by several previous authors using a variety of approaches.[1-5] The advantage of the exergy approach is that the fundamental thermodynamics of an ideal pulse tube and the principal loss mechanisms are simple to develop. The objective of this paper is to present the fundamental thermodynamics in a simple form. The basis of our approach is the thermodynamics of an open system. We will consider control volumes that include the working fluid only. Interactions with the regenerator, heat exchangers, and physical walls are limited to heat and work transfer.

We will follow the exergy approach of Bejan.[6] For an open system, the first law (energy conservation) is

$$\dot{E} = \sum_i \dot{Q}_i - \dot{W} + \sum_{in} \dot{m}h - \sum_{out} \dot{m}h \,, \qquad (1)$$

Cryocoolers 13, edited by R. G. Ross, Jr.
Springer Science+Business Media, Inc., New York, 2004

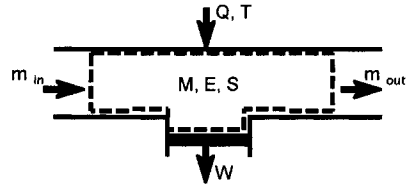

Figure 1. Schematic representation of a generalized control volume in an open system. The quantities M, E, and S can accumulate within the control volume. The nominal directions of the in- and outflows are shown. Note that heat flows are always associated with an external temperature.

where the inertance ($v^2/2$) and gravitational (gz) terms have been ignored. For many pulse tube applications these two terms are insignificant. If these terms are significant, such as the inertance term in an inertance tube; then they must be added to the enthalpy. The sign convention is chosen such that all heat flows, Q, into the system and all work done by the system are positive (see Fig. 1).

The second law (entropy conservation) is

$$\dot{S}_{gen} = \frac{d}{dt}S - \sum_i \frac{\dot{Q}_i}{T_i} + \sum_{out} \dot{m}s - \sum_{in} \dot{m}s \geq 0 \,. \tag{2}$$

Eqs. 1 and 2 can be combined and written in terms of exergy (rate of available work):

$$0 = -\frac{d}{dt}(E - T_o S) - \dot{W} + \sum_i \left(1 - \frac{T_o}{T_i}\right)\dot{Q}_i + \sum_{in} \dot{m}(h - T_o s) - \sum_{out} \dot{m}(h - T_o s) - T_o \dot{S}_{gen} \,, \tag{3}$$

where the terms represent the accumulation of non-flow exergy within the control volume; the transfer of exergy to the control volume by work, by heat transfer, and by mass flows in the inlet and outlet; and the final term is the exergy lost within the control volume. The reference temperature, T_o, is usually the environmental temperature, the external heat rejection temperature of the cooler. The internal exergy flow is $\dot{m}\xi$ where $\xi = h - T_o s$.

Eqs. 1-3 are true for all times. In the following discussion, we are only interested in steady state behavior integrated over a whole cycle. The following notation will be used to designate the cyclic integrals

for flows: $$X = \oint \dot{m}x = \oint \dot{m}\,dx = \oint \dot{m}\frac{dx}{dt}dt \tag{4}$$

and for accumulations: $$X = \oint \dot{X} = \oint \dot{X}\,dt \,. \tag{5}$$

In steady state operation, there can be no net accumulation. Thus, $X = 0$ for all accumulations. For time dependant variables the following notation will be used:

$$x = \langle x \rangle + \chi, \; \langle \chi \rangle = \oint \chi\,dt = 0, \text{ and } \chi \approx \chi_a \sin(\omega t + \phi_x) \,. \tag{6}$$

Eq. 1 can now be written as

$$E = 0 = \oint \dot{E} = Q - W + \oint_{in} \dot{m}h - \oint_{out} \dot{m}h \,, \tag{7}$$

where we have assumed that there are only single in- and outflows. For those pulse tubes with multiple inlets, the *in* and *out* integrals must be summed over all flows. Eqs. 2 and 3 become

$$S_{gen} = -\sum_i \oint \frac{\dot{Q}_i}{T_i} - \oint_{in} \dot{m}s + \oint_{out} \dot{m}s \geq 0 \,, \tag{8}$$

$$0 = -W + \sum_i \oint \left(1 - \frac{T_o}{T_i}\right)\dot{Q}_i + \oint_{in} \dot{m}(h - T_o s) - \oint_{out} \dot{m}(h - T_o s) - T_o S_{gen} \,, \tag{9}$$

and the exergy flow becomes $$\Xi = \oint \dot{m}\xi \tag{10}$$

If the working fluid is assumed to be an ideal gas, then

$$dh = c_P\,dT \tag{11}$$

and $$ds = c_P \frac{dT}{T} - R\frac{dP}{P} \,. \tag{12}$$

In adiabatic regions, $ds = 0$ and Eq. 12 becomes

$$c_P \frac{dT}{T} = R\frac{dP}{P} \,. \tag{13}$$

Integrating this yields

$$\frac{T}{\langle T \rangle} = \left(\frac{P}{\langle P \rangle} \right)^{\left(1 - \frac{1}{\gamma}\right)}, \tag{14}$$

where $\gamma = c_P/c_V$. Thus, in adiabatic sections the temperature and pressure oscillations are in phase.

We will also make the following assumptions. Pressure gradients that result from viscous flows are proportional to and in phase with the mass flow. Similarly, heat transfer is proportional to and in phase with temperature differences. All oscillating quantities are sinusoidal. These are the assumptions of small amplitudes and that the energy carried by higher harmonics is small compared to the total energy carried by the system.

IDEAL COMPONENTS

We will consider the components of an ideal pulse tube cooler (Fig. 2). These components are lossless except for those that require losses to function. In lossless components, $S_{gen} = 0$. Thus, the effects of viscous flow losses, secondary flows, and thermal conduction are ignored. As mentioned earlier, only steady state operation is considered. The reference temperature, T_o, is taken to be the ambient heat rejection temperature of the aftercooler. Fig. 2 also shows the heat and work flows into the control volume that includes the whole system. The system control volume is a closed system (no mass flows in or out). Thus the governing equations for the system, Eqs. 1-3 and 4-6, can be simplified by deleting the terms containing mass flow. The exergy only changes where there are work and flows across the system boundary or where entropy is generated.

Adiabatic Compressor

A schematic drawing of a compressor and its control volume are show in Fig. 3. The input work, $-W_{input}$, is provided by an external motor. Being adiabatic, $Q = 0$. There is only one mass flow, which we take as an outflow. Steady state operation requires $\langle \dot{m} \rangle = 0$. Eqs. 7-9 become

$$-W_{input} = \oint_{out} \dot{m}h = H_{out} = \Delta\Xi \text{ and } \oint_{out} \dot{m}s = 0 . \tag{15}$$

All of the work is converted to enthalpy flow out of the compressor. This is the only place in the system where work is done and since coolers are work absorbing, the exergy flow, $\Xi = -W_{input}$, is at its highest value here.

Adiabatic Transfer Line

If the transfer line (Fig. 4) connecting the compressor to the aftercooler is adiabatic, then $Q = 0$. Eqs. 7-9 become

$$H = \oint_{in} \dot{m}h = \oint_{out} \dot{m}h, \oint_{out} \dot{m}s = 0, \text{ and } \Delta\Xi = 0 . \tag{16}$$

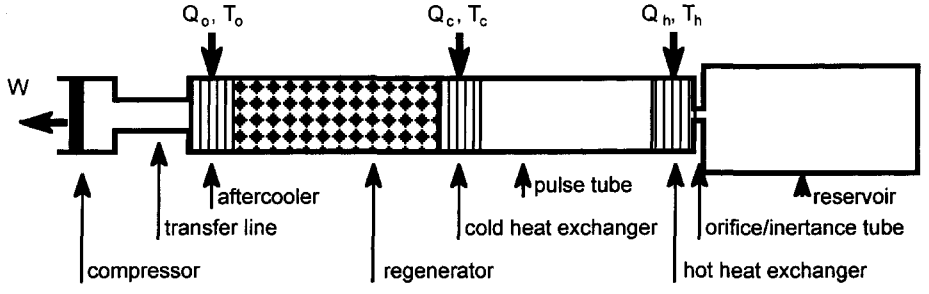

Figure 2. The principal components of an Orifice Pulse Tube Cooler showing the location and nominal direction of the heat and work flows for a control volume enclosing the entire cooler.

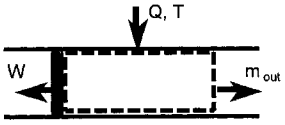

Figure 3. Control volume for the compressor. For an adiabatic compressor $Q = 0$.

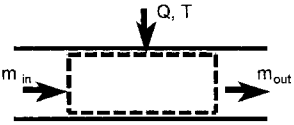

Figure 4. Control volume for the transfer line or pulse tube.

The enthalpy flowing in from the compressor equals the enthalpy flowing out to the aftercooler. In general, $\dot{m}_{in} \neq \dot{m}_{out}$. The mass flows are not equal because the compressibility of the gas results in the mass accumulated within the transfer line varying with the pressure.

Mass Accumulation

The rate of change of a mass of gas, M, in a fixed volume such as the transfer line, V, is given by mass conservation:

$$\frac{dM}{dt} = \dot{m}_{in} - \dot{m}_{out} = \dot{m} \,, \tag{17}$$

where $\dot{m}$ is the net mass flow into the control volume. For an ideal gas the equation of state is

$$M = \frac{PV}{RT} \,. \tag{18}$$

Differentiating this yields:

$$dM = M\left(\frac{dP}{P} - \frac{dT}{T}\right). \tag{19}$$

For an adiabatic volume, this can be simplified by using Eq. 13:

$$\frac{dM_s}{dt} = \dot{m}_s = \frac{M}{\gamma P}\frac{dP}{dt} \,. \tag{20}$$

This is the instantaneous mass accumulation due to an adiabatic pressure change (sometimes called the breathing mode). There are two notable observations about this equation. Firstly, $\dot{m}_s$ is independent of the temperature distribution in V. Secondly, for small amplitude pressure oscillations, $\dot{m}_s$ is in phase with dP/dt. Since dP/dt is out of phase with P and, by Eq. 14, out of phase with T, $\dot{m}_s$ and T are out of phase. Thus

$$\oint \dot{m}_s h = 0 \,. \tag{21}$$

The adiabatic accumulation of mass in steady state operation does not result in an enthalpy flow in adiabatic sections.

There is another source of mass accumulation, the accumulation due to the temperature difference between the inlet and outlet, $\dot{m}_T = \dot{m}_{in} - \dot{m}_{out}$. If the pressure is constant within the adiabatic control volume, then mass flow does not change the temperature or density of gas elements that remain within the control volume. This requires that the volume flows at the inlet and outlet be equal. Thus,

$$\dot{m}_{in} T_{in} = \dot{m}_{out} T_{out} \tag{22}$$

or

$$\frac{dM_T}{dt} = \dot{m}_T = \dot{m}_{out}\left(\frac{T_{out}}{T_{in}} - 1\right). \tag{23}$$

Here $\dot{m}_{in}$ and $\dot{m}_{out}$ are in phase and the accumulation results in no change in enthalpy flow.

We can now write a generalized mass flow equation that includes the two accumulation effects:

$$\dot{m}_{in} = \dot{m}_s + \dot{m}_T \,. \tag{24}$$

The terms on the right hand side are not, in general, in phase with each other. Thus, mass accumulation results in amplitude and phase gradients in the mass flowing through an adiabatic volume. If the enthalpy flow, H, in an adiabatic section is not zero, then the temperature must also have amplitude and/or phase gradients.

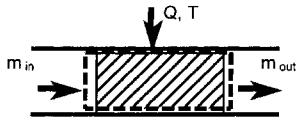

Figure 5. Control volume for a heat exchanger or regenerator. The hatched area represents the volume of the heat exchanger or regenerator. Only the working fluid is included in the control volume.

Aftercooler

Within the aftercooler (as in the following regenerator) (Fig. 5), there is perfect heat transfer between the gas and the heat exchanger. There is no temperature oscillation of the gas, $dT = 0$. Thus $dh = 0$ also. Eqs. 7-9 become

$$\oint_{in} \dot{m}h = H_{in} = -Q_o = -\oint_{out} \dot{m}T_o s = -T_o S_{out}, \text{ and } \Delta\Xi = 0 . \tag{25}$$

The heat rejected at the aftercooler is equal to the work done on the compressor, $W = Q_o$. Also, this heat is equal to $T_o S_{out}$, where S_{out} is the entropy flow in the regenerator. This entropy flows from the cold to the hot end of the regenerator. There is no change in the exergy flow because the exergy associated with Q_o is $(1 - T_o/T_o)\, Q_o = 0$.

Isothermal Compressor

In an isothermal compressor, there is no temperature oscillation and therefore no enthalpy flow. It is not reasonable to use an adiabatic transfer line with an isothermal compressor, as this defeats any advantage of isothermal compression by having the losses associated with two isothermal to adiabatic transitions (more about these losses in a later paper[7]). An isothermal transfer line is difficult to implement without significant viscous losses and will not be considered here. Thus, we will consider an integral isothermal compressor, which incorporates the aftercooler and hot end of the regenerator. Evaluating Eqs. 7-9 results in

$$W = Q_o = T_o S_{out} . \tag{26}$$

Eq. 26 is the same as a control volume containing an adiabatic compressor, and adiabatic transfer line, and an aftercooler. The difference between systems with an adiabatic compressor and an isothermal compressor is in the losses discussed in a later paper.[7]

Regenerator

The ideal regenerator (Fig. 5) has no void volume and no pressure drop. The first condition leads to $\dot{m}_{in} = \dot{m}_{out}$. In the regenerator as in the aftercooler and other heat exchangers, applying the condition $dT = 0$ to Eq. 12 results in

$$ds = -\frac{R}{P}\, dP . \tag{27}$$

In the absence of a pressure drop, dP/dz = 0, results in ds/dz = 0. i.e., there is constant entropy flow in a regenerator. This can be verified by applying Eqs. 7-9, which become

$$S_{in} = \oint_{in} \dot{m}s = \oint_{out} \dot{m}s = S_{out} \text{ and } \Delta\Xi = 0 . \tag{28}$$

It is interesting to note that these relations do not specify the temperature profile of the regenerator. Again, the exergy flow is constant because there are no losses or interaction outside of the system.

Cold Heat Exchanger

The cold heat exchanger is similar to the aftercooler (Fig. 5). The control volume has two mass flows. One flow, $\dot{m}_{out}$, is adiabatic, finite enthalpy flow but no entropy flow. The other flow, $\dot{m}_{in}$, has no temperature oscillations, finite entropy flow but no enthalpy flow. Applying Eqs. 7-9 yields

$$Q_c = \oint_{out} \dot{m}h = H_{out}, \; T_o S_{in} = \oint_{in} \dot{m}T_o s = -\frac{T_o}{T_c} Q_c \text{ and } \Delta\Xi = \left(1 - \frac{T_o}{T_c}\right) Q_c \tag{29}$$

The heat absorbed equals the enthalpy flow in the pulse tube; the corresponding entropy flows into the regenerator; and the corresponding exergy is added to the system. Combining Eq. 29 with Eqs. 25 and 28 yields

$$\frac{Q_o}{T_o} = -\frac{Q_c}{T_c}\,, \tag{30}$$

the familiar relation for an ideal Carnot cycle.

Pulse Tube - I

The ideal pulse tube is adiabatic (Fig. 4). It behaves like the adiabatic transfer line with $\dot{Q} = 0$, $\dot{m}_{in} \neq \dot{m}_{out}$. Evaluating Eqs. 7-9 yields

$$H = \oint_{in} \dot{m}h = \oint_{out} \dot{m}h\,,\ \oint_{out} \dot{m}s = 0\,,\ \text{and}\ \Delta\Xi = 0\,. \tag{31}$$

Neither of these equations specifies the temperature profile within the pulse tube. The enthalpy flow is constant and identical to the enthalpy flow out of the cold heat exchanger. However, since there is mass accumulation in the pulse tube, the mass flow decreases from the cold end to the hot end (see Eq. 22). To keep H constant, the temperature oscillation must vary along the length, increasing toward the hot heat exchanger. This is discussed in a later section.

Hot Heat Exchanger (Basic Pulse Tubes)

The hot heat exchanger is similar to the aftercooler with $\dot{m}_{out} = 0$ (Fig. 6). There is no temperature oscillation within the heat exchanger, thus there is no enthalpy flow inside it. Eq. 7 becomes

$$Q_h = -\oint_{in} \dot{m}h = -H_{in}\,. \tag{32}$$

Comparing to the relations (Eqs. 29 and 31) for the other components yields

$$Q_h = -Q_c\,. \tag{33}$$

As in the aftercooler, there is no exergy change associated with Q_h.

For a control volume surrounding the complete cooler, Eq. 7 becomes

$$W_{input} = Q_o + Q_c + Q_h \tag{34}$$

and the efficiency is

$$\eta = \frac{-Q_c}{W_{input}} = \frac{T_c}{T_o}\,. \tag{35}$$

This differs from the Carnot expression for an ideal cooler, $\eta = T_c(T_o - T_c)^{-1}$, because the work of expansion is not recovered.[8]

In the basic pulse tube the enthalpy flow in the pulse tube is dissipated in the hot heat exchanger. This is seen by applying Eq. 9

$$H_{in} = \oint_{in} \dot{m}h = T_o S_{gen}\,, \tag{36}$$

where S_{gen} is the entropy generated by the dissipation. This also causes a loss of exergy:

$$\Delta\Xi = -T_o S_{gen}\,. \tag{37}$$

In the hot heat exchanger of a basic pulse tube, the mass flow goes to zero, $\dot{m}_{out} = 0$. Thus, the only flow within the pulse tube is the accumulation flow. From the discussion on adiabatic flow, $\dot{m}$ is out of phase with P and T and $H_{in} = 0$. The ideal basic pulse tube produces no cooling. The cooling observed in real basic pulse tubes comes from non-ideal behavior. This is discussed in a later paper.[7]

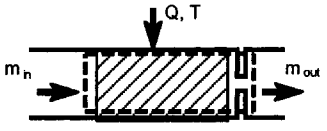

Figure 6. Control volume for the hot heat exchanger. The hatched area represents the volume of the heat exchanger. Only the working fluid is included in the control volume. For the basic pulse tube the orifice is closed and $\dot{m}_{out} = 0$.

Hot Heat Exchanger (Orifice Pulse Tubes)

In an ideal orifice pulse tube, the mass flow through the heat exchanger and orifice (Fig. 6) is constant and proportional to the pressure drop in the orifice. The outflow is into the reservoir, which is large enough to be isobaric and isothermal: $P_{out} = \langle P_{out} \rangle = \langle P_{in} \rangle$ and $T_{out} = \langle T_{out} \rangle = \langle T_{in} \rangle$. Thus,

$$\dot{m}_{in} = \dot{m}_{out} \propto (P_{in} - P_{out}) = \mathcal{P}_{in} . \tag{38}$$

The mass flow and pressure drop are in phase. Applying Eqs. 7-9 results in

$$Q_h = - \oint_{in} \dot{m} h = - H_{in} \tag{39}$$

and

$$H_{in} = \oint_{in} \dot{m} h = T_o S_{gen} . \tag{40}$$

where, by Eqs. 8 and 12

$$S_{gen} \approx \oint \dot{m} R \frac{\mathcal{P}}{\langle P \rangle} \tag{41}$$

is the entropy generated by the viscous pressure drop in the orifice.[6] There is a corresponding loss in exergy.

If the heat exchanger is treated as a separate control volume, then it is identical to the aftercooler,

$$\oint_{in} \dot{m} h = H_{in} = - Q_h = - \oint_{out} \dot{m} T_o s = - T_o S_{out} \text{ and } \Delta \Xi = 0 . \tag{42}$$

The orifice can also be treated as a separate control volume with

$$\oint_{in} \dot{m} T_o s = T_o S_{in} = - T_o S_{gen} \text{ and } \Delta \Xi = - T_o S_{gen} . \tag{43}$$

As with the basic pulse tube

$$Q_h = - Q_c = Q_o \frac{T_c}{T_o} = W_{input} \frac{T_c}{T_o} . \tag{44}$$

Pulse Tube - II

Entering the hot heat exchanger, the mass flow is in phase with the pressure (Eq. 38). Since the temperature oscillation is in phase with the pressure (Eq. 14), the enthalpy flow is at its most efficient here with mass flow and temperature in phase. This is not the case at the cold end of the pulse tube. There, the flow is increased and shifted in phase by the accumulation effects. The mass flows, Eq. 24, in the pulse can now be written as

$$\dot{m}_{in} = \dot{m}_s + \dot{m}_{out} \frac{T_{out}}{T_{in}} . \tag{45}$$

The $\dot{m}_a$ term does not contribute to the enthalpy flow. To maintain a constant enthalpy flow in the pulse tube the amplitude of the temperature oscillation, $\mathcal{T}$, must also vary:

$$\mathcal{T}_{in} T_{out} = T_{in} \mathcal{T}_{out} . \tag{46}$$

Inertance Tube

Replacing the orifice with an inertance allows more control over the phase shift between the mass flow and pressure in the pulse tube. However, for a control volume that encompasses all of the hot heat exchanger and inertance tube or orifice, the result of applying Eqs. 7-9 are the same:

$$Q_h = - \oint_{in} \dot{m} h = - H_{in} \tag{47}$$

and

$$H_{in} = \oint_{in} \dot{m} h = T_o S_{gen} . \tag{48}$$

These relations do not specify where within the control volume the entropy is generated and the heat is rejected. One might be tempted to assume that most of the entropy is generated and heat rejected in the hot heat exchanger. However, the author has observed significant heating along the inertance tube, indicating non-uniform entropy generation along the inertance tube.

Within the inertance tube, the inertia of the gas is significant. The energy, entropy, and exergy equations need to be changed to include the inertance of the gas. This is done by replacing $\dot{m}h$ with $\dot{m}(h + v^2/2)$ in Eqs. 1-3 and 7-9, where v is the gas velocity. The flow energy can transfer between enthalpy flow and kinetic energy flow without producing heat. This permits acoustic phenomena. The only constraint on enthalpy flow is that $H = 0$ at the reservoir. However, the radius of inertance tubes is often comparable to the thermal penetration depth. Thus, temperature oscillations and enthalpy flow are suppressed. However, there may be entropy flow, pressure, and kinetic energy gradients, which produce the heating:

$$\frac{dQ}{dz} = \oint \frac{d}{dz}\dot{m}(h + v^2/2) \tag{49}$$

and

$$\frac{dS_{gen}}{dz} = -\oint \frac{d}{dz}\frac{\dot{m}}{T}(h + v^2/2) + \oint \frac{d}{dz}\dot{m}s \,. \tag{50}$$

At the very least, there are viscous losses within the inertance tube, which generate entropy. The details of the workings of an inertance tube are beyond the scope of this paper.

SUMMARY

We have calculated the energy, entropy, and exergy flows for idealized pulse tubes. The results were derived from first principles based on fundamental thermodynamic relations for open systems. The results are summarized in Fig. 7 and in Table 1. These clearly show that the ideal pulse tube operates at constant enthalpy flow and that the ideal regenerator operates at constant entropy flow.

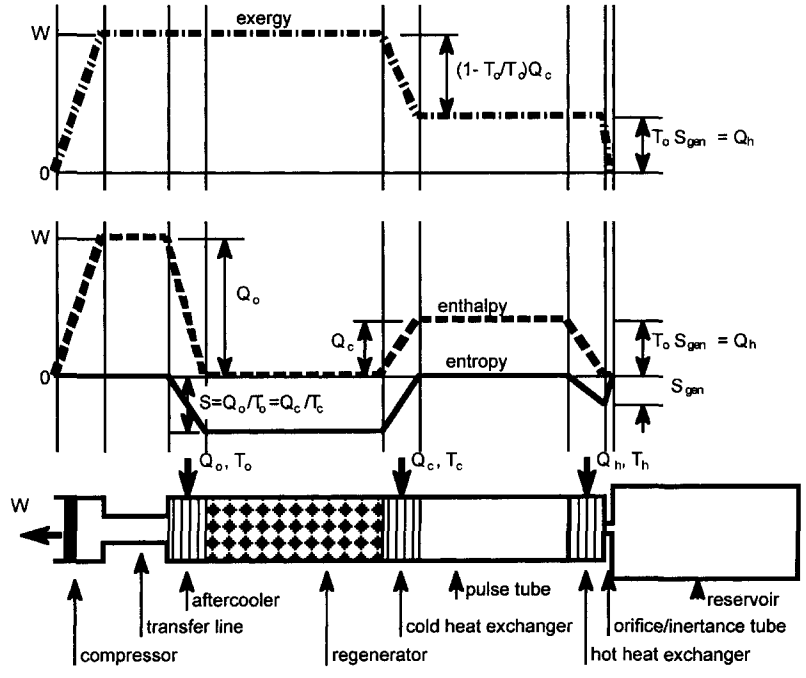

Figure 7. The exergy, enthalpy, and energy flows in the various components of a pulse tube.

Table 1. Summary of the enthalpy, entropy and exergy relationships.

Component	Characteristics		
Adiabatic compressor	$-W_{input} = H_{out}$,	$S = 0$,	$\Delta\Xi = -W_{input}$
Transfer line	H = constant,	$S = 0$,	$\Delta\Xi = 0$
Aftercooler	$Q_o = -H_{in} = T_o S_{out}$,		$\Delta\Xi = 0$
Regenerator	$H = 0$,	S = constant,	$\Delta\Xi = 0$
Cold heat exchanger	$Q_c = H_{out}$,	$S_{in} = -Q_c/T_c$,	$\Delta\Xi = (1 - T_o/T_c)\, Q_c$
Pulse tube	H = constant,	$S = 0$,	$\Delta\Xi = 0$
Hot heat exchanger/Orifice	$Q_h = -H_{in} = -T_o S_{gen} = \Delta\Xi$		
System	$W_{input} = Q_o = -Q_c\,(T_o/T_c)$, $Q_h = -Q_c$, $\eta = T_c/T_h$		

NOMENCLATURE

Roman

E	Energy
H	Enthalpy
M	Mass
P	Pressure = $\langle P \rangle + \mathcal{P}$
$\mathcal{P}$	Pressure, dynamic
Q	Heat
R	Gas constant (per kg)
S	Entropy
T	Temperature = $\langle T \rangle + \mathcal{T}$
$\mathcal{T}$	Temperature, dynamic
V	Volume
W	Work
X	General parameter
c	Specific heat
g	Gravitational acceleration
h	Specific enthalpy
m	Mass
s	Specific entropy
t	Time
x	General parameter
z	Height

Greek

Δ	Change (difference)
Ξ	Exergy
χ	General parameter
ϕ	Phase
γ	Specific heat ratio
η	Efficiency
ν	Velocity
ξ	Specific exergy

Other

$\langle\ \rangle$	Cyclic average
$\cdot$	Time derivative

Subscripts

a	Amplitude
c	Cold
gen	Generated
h	Hot
i	Index
in	Inflow
input	Input
min	Minimum
o	Reference
out	Outflow
P	Isobaric
s	Adiabatic
T	Isothermal
T	Temperature effect
V	Isochoric

REFERENCES

1. Storch, P.J., Radebaugh, R., and Zimmerman, J., *Analytical Model for Refrigeration Power of the Orifice Pulse Tube Refrigerator*, NIST Technical Note 1343 (1990).
2. Kittel, P., Kashani, A., Lee, J.M., and Roach, P.R. "General Pulse Tube Theory," *Cryogenics*, vol. 36, (1996), p. 849.
3. de Waele, A.T.A.M., Steijaert, P.P., and Gijzen, P., "Thermodynamic Aspects of Pulse Tubes," *Cryogenics*, vol. 37 (1997), p. 313.
4. de Boer, P.C.T., "Optimization of the Orifice Pulse Tube," *Cryogenics*, vol. 40 (2000), p. 701.
5. Razani, A., Flake, B., and Yarbrough, S., "Exergy Flow in Pulse Tube Refrigerators and Their Performance Evaluation Based on Exergy Analysis," *Adv. Cryo. Engin.*, vol. 49B, AIP Press, New York (2004), pp. 1508-1518.
6. Bejan, A., *Advanced Engineering Thermodynamics, 2ed Edition*, Wiley, New York (1997).
7. Kittel, P., "Enthalpy, Entropy, and Exergy Flow Losses in Pulse Tube Cryocoolers," *Cryocoolers 13*, Kluwer Academic/Plenum Publishers, New York (2005), this proceedings.
8. Kittel, P., "Ideal Orifice Pulse Tube Refrigerator Performance," *Cryogenics*, vol. 32 (1992) 843

Enthalpy, Entropy, and Exergy Flow Losses in Pulse Tube Cryocoolers

P. Kittel

NASA Ames Research Center
Moffett Field, CA, USA, 94035-1000

ABSTRACT

The enthalpy, entropy, and exergy flows in ideal pulse tube cryocoolers have been described previously. This paper will describe how these flows are affected by phenomena in non-ideal cryocoolers.

Frequently such descriptions take an energy-centric view. Such descriptions concentrate on the first law of thermodynamics, the conservation of energy. This approach can result in a complex description of the cooler in terms of energy and enthalpy flows.

An alternative is to take an entropy-centric approach. Closely related to this is the exergy-centric approach. These descriptions concentrate on the second law of thermodynamics, the generation of entropy or the destruction of exergy.

Both the energy-centric and exergy/entropy-centric approaches make use of both the laws of thermodynamics and both approaches give equivalent descriptions of a cryocooler. However, the latter approach can be more useful as it can yield a simpler description, one that emphasis loss mechanisms.

This paper applies the second law approach to pulse tube cryocoolers. The effects of a variety of loss mechanisms in the various components on the exergy, entropy, and enthalpy flows are discussed. The discussion applies to basic, orifice, and inertance type pulse tubes. Most of the discussion is applicable to cryocoolers driven by either Gifford-McMahon or linear compressors; the emphasis is on the latter.

INTRODUCTION

Enthalpy, entropy, and exergy analyses are useful tools for understanding thermodynamics of a system. In this paper, the thermodynamics of pulse tube coolers will be analyzed through the use of these quantities. Detailed thermodynamic models of pulse tube coolers have been presented by several previous authors using a variety of approaches.[1-5] This paper will use the approach we previously used for ideal pulse tubes.[6] The advantage of the exergy approach is that the fundamental thermodynamics of an ideal pulse tube and the principal loss mechanisms are simple to develop. The objective of this paper is to present the fundamental thermodynamics in a simple form. The basis of our approach is the thermodynamics of an open system. We will consider control volumes that include the working fluid only. Interactions with the regenerator, heat exchangers, and physical walls are limited to heat and work transfer.

Cryocoolers 13, edited by R. G. Ross, Jr.
Springer Science+Business Media, Inc., New York, 2004

We will follow the exergy approach of Bejan[7] and our earlier paper.[6] In the following discussion, we are only interested in steady state behavior integrated over a whole cycle. The following notation will be used to designate the cyclic integrals

for flows: $$X = \oint \dot{m}x = \oint \dot{m}\,dx = \oint \dot{m}\frac{dx}{dt}dt \tag{1}$$

and for accumulations: $$X = \oint \dot{X} = \oint \dot{X}\,dt\,. \tag{2}$$

In steady state operation, there can be no net accumulation. For time dependant variables the following notation will be used:

$$x = \langle x \rangle + \chi\,,\ \langle \chi \rangle = \oint \chi = 0\,,\ \chi \approx \chi_a \sin\left(\omega t + \phi_x\right)\,. \tag{3}$$

For a control volume (Fig. 1) in an open system, the first law (energy conservation) is

$$E = \oint \dot{E} = Q - W + \oint_{in} \dot{m}h - \oint_{out} \dot{m}h\,. \tag{4}$$

where the inertance ($\nu^2/2$) and gravitational (gz) contributions to the enthalpy have been ignored. We have assumed that there are only single in and out flows. The sign convention is chosen such that all heat flows, $\dot{Q}$, into the system and all work done by the system are positive.

The second law (entropy conservation) is

$$S_{gen} = -\sum_i \oint \frac{\dot{Q}_i}{T_i} - \oint_{in} \dot{m}s + \oint_{out} \dot{m}s \geq 0\,. \tag{5}$$

Eqs. 4 and 5 can be combined and written in terms of exergy (rate of available work):

$$0 = -W + \sum_i \oint \left(1 - \frac{T_o}{T_i}\right)\dot{Q}_i + \oint_{in} \dot{m}\left(h - T_o s\right) - \oint_{out} \dot{m}\left(h - T_o s\right) - T_o S_{gen}\,, \tag{6}$$

where the terms represent the transfer of exergy to the control volume by work, by heat transfer and by mass flows in the inlet and outlet, and the final term is the exergy lost within the control volume. The reference temperature, T_o, is usually the external heat rejection temperature of the cooler. The internal exergy flow is

$$\Xi = \oint \dot{m}\xi = \oint \dot{m}\left(h - T_o s\right)\,. \tag{7}$$

The set of governing equations, Eqs. 5-7, can be written in a terms of gradients. Since we are only considering a situation where work is done a one place, we will assume that there is no work done in a region of gradients. Consider a control volume of infinitesimal width, dz, where no work is done, then Eqs. 4-6 become

$$\frac{dE}{dz} = 0 = \frac{dQ}{dz} - \oint \frac{d}{dz}\dot{m}h\,, \tag{8}$$

$$\frac{dS_{gen}}{dz} = -\sum_i \oint \frac{d}{dz}\frac{\dot{Q}_i}{T_i} + \oint \frac{d}{dz}\dot{m}s\,, \tag{9}$$

and $$T_o\frac{dS_{gen}}{dz} = \sum_i \oint \frac{d}{dz}\left(1 - \frac{T_o}{T_i}\right)\dot{Q}_i - \oint \frac{d}{dz}\dot{m}\left(h - T_o s\right)\,. \tag{10}$$

Bejan[7] also gives convenient expressions for S_{gen} resulting from heat transfer across a temperature difference

$$\dot{S}_{gen} = \dot{Q}\frac{\left(T_h - T_c\right)}{T_c T_h} \approx \dot{Q}\frac{\Delta T}{T^2}\,, \tag{11}$$

where $T_h > T_c = T_h - \Delta T$ and $\Delta T << T_h$, and for S_{gen} due to pressure loss

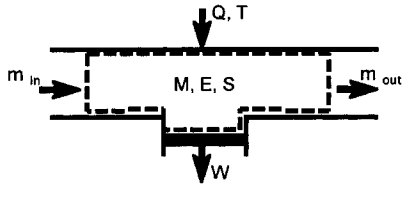

Figure 1. Schematic representation of a generalized control volume in an open system. The quantities M, E, and S can accumulate within the control volume. The nominal directions of the in- and outflows are shown. Note that heat flows are always associated with an external temperature.

$$\dot{S}_{gen} = \dot{m}R \ln\left(\frac{P_{in}}{P_{out}}\right) \approx \dot{m}R\frac{\Delta P}{P}, \tag{12}$$

where $P_{in} > P_{out} = P_{in} - \Delta P$ and $\Delta P << P_{in}$.

If the working fluid is assumed to be an ideal gas, then

$$dh = c_P\, dT \tag{13}$$

and

$$ds = c_P\frac{dT}{T} - R\frac{dP}{P}. \tag{14}$$

In adiabatic regions, $ds = 0$, thus Eq. 14 becomes

$$c_P\frac{dT}{T} = R\frac{dP}{P}. \tag{15}$$

Integrating this yields

$$T/\langle T\rangle = \left(P/\langle P\rangle\right)^{(1-1/\gamma)}, \tag{16}$$

where $\gamma = c_P/c_V$. Thus, in adiabatic sections the temperature and pressure oscillations are in phase.

We will also make the following assumptions. Pressure gradients that result from viscous flows are proportional to and in phase with the mass flow. Similarly, heat transfer is proportional to and in phase with temperature differences. All oscillating quantities are sinusoidal. These are the assumptions of small amplitudes and that the energy carried by higher harmonics is small compared to the total energy carried by the system.

NON-IDEAL COMPONENTS

Idealized (lossless) components were discussed in a previous paper[6] and will not be discussed in detail here. A variety of loss mechanisms will be discussed in this section. The same approach will be used, that of applying the exergy analysis as laid out by Bejan.[7] The approach assumes that the system (Fig. 2) is ideal except for the loss mechanism under consideration. Each loss mechanism is considered to be independent of other loss mechanisms. This approach assumes that interactions between loss mechanisms are higher order and can be ignored.

Compressor Losses

The analysis of the compressor must include the compressor losses. The compressor is no longer adiabatic and $Q \neq 0$. Now $Q_{loss} = W_{loss} = T_o S_{gen}$, where the losses are the sum of all the losses specific to the type and design of the compressor. These losses include seal leakage, viscous losses, heat transfer, rubbing friction, mechanical and magnetic hysteresis, joule heating, and eddy currents. Compressor losses will not be discussed here. Rather, this paper concentrates on the losses within the components of the cooler.

Pressure Loss in Regenerators and Heat Exchangers

Within the regenerators and heat exchangers, viscosity of the moving fluid results in a pressure gradient. In an ideal regenerator, $dh = 0$ and $dT = 0$. Thus the entropy and exergy equations, Eqs. 9 and 10, for a control volume of width dz become:

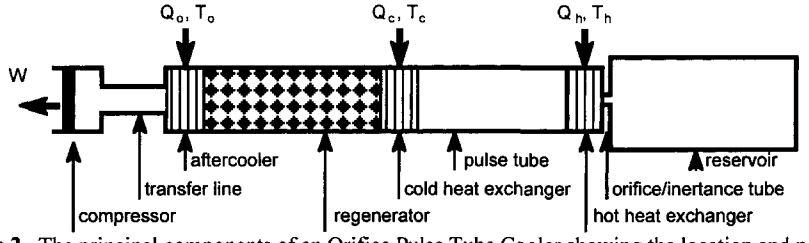

Figure 2. The principal components of an Orifice Pulse Tube Cooler showing the location and nominal direction of the heat and work flows for a control volume enclosing the entire cooler.

$$\frac{d\dot{S}_{gen}}{dz} = \dot{m}\frac{ds}{dz} = -\dot{m}R\frac{1}{P}\frac{dP}{dz} \text{ and } \frac{d\dot{\Xi}}{dz} = T_o\frac{d\dot{S}_{gen}}{dz}, \tag{17}$$

where Eq. 14 was used for ds. Note that a mass flow causes a decrease in the pressure, $\dot{m}\,dP/dz < 0$. If the pressure amplitude is small compared to the system's mean pressure, $\mathcal{P} \ll \langle P \rangle$, then Eq. 17 becomes:

$$\frac{d\dot{S}_{gen}}{dz} \approx -\frac{R}{\langle P \rangle}\dot{m}\frac{d\mathcal{P}}{dz}. \tag{18}$$

The entropy and exergy flows become:

$$\frac{dS}{dz} = \oint \frac{d}{dz}\dot{m}s = -\frac{R}{\langle P \rangle}\oint \dot{m}\frac{d\mathcal{P}}{dz} \text{ and } \frac{d\Xi}{dz} = T_o\frac{dS}{dz}. \tag{19}$$

Thus, S increases and Ξ decreases with decreasing pressure. (Recall that in ideal regenerators $S < 0$ and $\Xi > 0$.)

Integrating Eq. 19 over a cycle and along the length of the regenerator or heat exchanger yields the total entropy generated in the component over one cycle:

$$S_{gen} = \oint \int_0^l \dot{m}\frac{ds}{dz}dz \approx -\frac{R}{\langle P \rangle}\oint \int_0^l \dot{m}\frac{d\mathcal{P}}{dz}dz. \tag{20}$$

The latter expression can be evaluated by using the dP/dz versus $\dot{m}$ correlation that is appropriate for the flow conditions. For the regenerator, $T_o\,S_{gen}$ is the amount the exergy flow decreases from the hot end to the cold end. The entropy flow into the aftercooler is larger by $T_o\,S_{gen}$ than the entropy flow leaving the cold heat exchanger. These effects are shown in Fig. 3. At the aftercooler:

$$W_{in} = Q_o = T_o S_{out} = -T_o\left(S_{gen} + \frac{Q_c}{T_c}\right). \tag{21}$$

Pressure losses in other components also effects performance. The pressure loss in the aftercooler results in an additional S_{gen} that is added to Eq. 21. The pressure loss in the cold heat exchanger produces a heat load of $T_o\,S_{gen}$, reducing Q_c. These effects directly reduce the efficiency of the cooler. The pressure loss in the hot heat exchanger has no effect as it is just becomes part of the pressure loss that occurs at the orifice.

Heat Conduction in the Regenerator and Pulse Tube

Several of the components in a pulse tube cooler have temperature gradients. These include the pulse tube and the regenerator. In the ideal regenerator, $dh = 0$. Thus, the energy equation reduces to

$$\dot{Q}_{gas\,in} + \dot{Q}_{solid\,in} = -\left(\dot{Q}_{gas\,out} + \dot{Q}_{solid\,out}\right) = \dot{Q}_{regen}. \tag{22}$$

The heat conduction is constant along the length of an element. The balance of the heat conducted through the gas and the solid varies along the length in such a way as to keep the local temperature gradient, dT/dz, the same in the gas and in the solid. This is a complex situation.

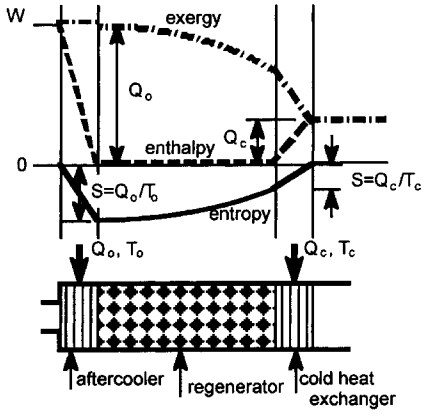

Figure 3. The exergy, enthalpy, and entropy flows as a result of the pressure drop losses discussed in the text. The effects are not shown to scale. Refer to the previous paper[6] for comparison to the ideal case.

We can ignore this complication by including the solid in the control volume. In the absence of significant temperature oscillations, Eq. 9 reduces to

$$\frac{dS_{gen}}{dz} = \frac{\dot{Q}}{T^2}\frac{dT}{dz} \tag{23}$$

and Eq. 10 become:

$$\oint \frac{d}{dz}\dot{m}\xi = 0 \,. \tag{24}$$

Thus, there is no effect on the entropy, enthalpy, or exergy flows in the components. The S_{gen} represents the increase in entropy that results from the flow of heat from the aftercooler to the cold heat exchanger. This reduces the heat rejected at the after cooler and increases the heat load on the cold heat exchanger.

Similarly, thermal conduction in the pulse tube reduces the heat being rejected at the hot heat exchanger by the heat flow in the pulse tube, Q_{pt}. This heat is an additional load on the cold heat exchanger.

The net effect of these heat flows is in reducing the heat absorbed by the cold heat exchanger to Q_c - Q_{regen} - Q_{pt} where Q_c is the cooling power for the ideal case.[6]

Adiabatic to Isothermal Transition Losses

There are three adiabatic to isothermal transitions in a pulse tube cooler. These occur at the transfer line to aftercooler transition, the cold heat exchanger to pulse tube transition, and the pulse tube to hot heat exchanger transition.

Two types of losses occur at these transitions. The first is the loss from converting from adiabatic to isothermal compression/expansion. Consider the difference between adiabatic and isothermal compressors. In adiabatic compression $PV^{\gamma} = const$ or

$$\left.\frac{\partial V}{\partial P}\right|_S = -\frac{V}{\gamma P} \,. \tag{25}$$

For isothermal compression: $PV = const$ or

$$\left.\frac{\partial V}{\partial P}\right|_T = -\frac{V}{P} \,. \tag{26}$$

Consider an element of gas in the transfer tube that is adiabatically compressed. When it reaches the aftercooler it is converted to the same state as an isothermally compressed element. This conversion occurs isobaricly.

For small amplitude compression of δP, a gas element would follow the paths shown in Fig. 4. The two paths start at the same (P, V, T) state. One element is compressed isothermally to state ($P+\delta P$, V-$V\delta P/P$, T). The other element is compressed adiabatically to state ($P+\delta P$, V-$V\delta P/\gamma P$, $T+\delta T$). In order to end at the same thermodynamic state, the second element would have to under go a second compression. The element cools and rejects heat during this isobaric and irreversible process. The irreversible heat is represented by the enclosed area in Fig. 4:

$$Q \approx -\left(\frac{\delta P}{P}\right)^2 \frac{RT}{2}\left(1 - \frac{1}{\gamma}\right) \,. \tag{27}$$

This is a second order effect and not important. It does represent some entropy generation, which reduces the entropy flow in the regenerator. Changing Eq. 27 from the simple cycle analyzed to the dynamic case in a pulse tube yields:

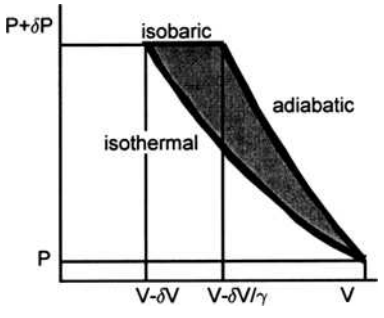

Figure 4. Comparison of a reversible isothermal compression vs. a reversible adiabatic compression followed by an irreversible isobaric compression. The difference is the shaded area, which represents the heat generated by the second route.

$$\dot{Q} \approx -\left(\frac{\mathcal{P}}{\langle P \rangle}\right)^2 \frac{R\langle T \rangle}{2}\left(1 - \frac{1}{\gamma}\right) \tag{28}$$

or

$$S_{gen} \approx \left(\frac{\mathcal{P}_a}{\langle P \rangle}\right)^2 \frac{R}{4}\left(1 - \frac{1}{\gamma}\right) . \tag{29}$$

The second loss comes from the total heat transfer in the aftercooler. All of the enthalpy flow in the transfer line is transformed into heat that is rejected. From Eq. 11 this is

$$S_{gen} \approx Q\langle \Delta T \rangle / \langle T \rangle^2 , \tag{30}$$

where ΔT is the temperature difference between the gas and the aftercooler. Eqs. 4-6 for the energy, entropy, and exergy balance in the aftercooler become

$$H_{in} = -Q_o = -\oint_{out} \dot{m} T_o s - T_o S_{gen} = -T_o\left(S_{out} + S_{gen}\right) . \tag{31}$$

Thus, this entropy generating terms reduces the entropy flow in the regenerator. This reduction affects the rest of the system, reducing the cooling available at the cold heat exchanger.

The same losses occur at both ends of the pulse tube where there are transitions from adiabatic flow to isothermal flow. At the cold heat exchanger, the entropy generation reduces the amount of cooling available for cooling at the cold heat exchanger. At the hot heat exchanger, this effect just becomes part of the entropy generated in the orifice.

Heat Transfer Losses in the Regenerator

In an ideal regenerator, there is sufficient heat transfer between the gas and the regenerator material to ensure that there is no temperature oscillation. In a real regenerator, there is small oscillating temperature difference, which drives the oscillating heat transfer. There is no net heat transfer:

$$Q = \oint \dot{Q} = 0 . \tag{32}$$

The oscillating temperature is

$$T_{g-w} = T_g - T_w , \tag{33}$$

where $T_{g-w} \ll T_o$. This temperature oscillation gives rise to an enthalpy flow:

$$H = \oint \dot{m}_{in} h = \oint \dot{m}_{out} h = \oint \dot{m} c_P T_{g-w} . \tag{35}$$

This enthalpy flow reduces the amount of heat rejected at the aftercooler by $\Delta Q = H$. The same amount of heat becomes a parasitic load on the cold heat exchanger. Thus, the net cooling ability is reduced by $\Delta Q = H$.

In addition to the creating enthalpy flow, the temperature oscillation also generates entropy. From Eq. 11 the entropy generated in a control volume infinitesimally thin is

$$\frac{d\dot{S}_{gen}}{dz} \approx \frac{T_{g-w}}{\langle T \rangle^2} \frac{d\dot{Q}}{dz} , \tag{36}$$

where $d\dot{Q}$ is the needed to bring an element of gas dz away to the local temperature:

$$\frac{d\dot{Q}}{dz} = -\dot{m} c_P \frac{d\langle T \rangle}{dz} . \tag{37}$$

Thus,

$$\frac{dS_{gen}}{dz} \approx -\oint \frac{T_{g-w}}{\langle T \rangle^2} \dot{m} c_P \frac{d\langle T \rangle}{dz} = H \frac{d}{dz} \frac{1}{\langle T \rangle} . \tag{38}$$

The entropy flow caused by the temperature oscillation can also be found from Eq. 9:

$$\frac{dS}{dz} = \oint \frac{d}{dz} \dot{m} s = \frac{dS_{gen}}{dz} . \tag{39}$$

Thus, there is an entropy flow gradient in the regenerator. The flow is from the cold heat exchanger toward the aftercooler and is greatest at the aftercooler. The affect of this gradient is to reduce the cooling available at the cold heat exchanger. Similarly, there is an exergy gradient:

$$\frac{d\Xi}{dz} = -T_o \frac{dS}{dz} . \tag{40}$$

Experience suggests that in regenerators operating at high temperatures $d\langle T \rangle / dz = -\alpha$ and T_{g-w} are nearly independent of position. Thus,

$$H \approx \text{constant}, \nabla S = \alpha H/T^2, \text{ and } \nabla \Xi = -\alpha H T_o/T^2. \quad (41)$$

These results are summarized in Fig. 5.

Combining the two effects and integrating the exergy loss over the length of the regenerator results in a reduction of cooling power by:

$$\Delta Q_c = -H\frac{T_o}{T_c}. \quad (42)$$

Heat Transfer Losses in Basic Pulse Tube

As was shown in the previous paper[6], the ideal basic pulse tube produced no cooling. This is a result of the mass flow being adiabatic and out of phase with the pressure and temperature oscillations. In practice, the basic pulse tube does produce a small amount of cooling, the result of heat transfer between the pulse tube wall and the gas. If we assume that this interaction results in small perturbations in h, s, T, and $\dot{m}$:

$$h = h_i + \eta, \; s = s_i + \sigma, \; T = T_i + \tau, \text{ and } \dot{m} = \dot{m}_i + \dot{\mu}, \quad (43)$$

where dh and ds are given by Eqs. 13 and 14 respectively and the perturbations are assumed to be small ($\eta \ll h_i$, $\tau \ll T_i$, and $\dot{\mu} \ll \dot{m}_i$) and out of phase with the ideal quantities:

$$\oint \dot{m}_i h_i = 0 \text{ and } \oint \dot{\mu}\eta = 0. \quad (44)$$

(Only the oscillating portions of h, s, T, and $\dot{m}$ contribute to the cyclic averages. So, only the oscillating terms need to be included in Eq. 43. Thus, $s_i = 0$.) The perturbations yield small enthalpy and entropy flows:

$$H = \oint \dot{m}h \approx \oint \dot{\mu}h_i + \oint \dot{m}_i\eta \text{ and } S = \oint \dot{m}s \approx \oint \dot{m}_i\sigma, \quad (45)$$

which result in cooling at the cold heat exchanger and dissipation at the hot heat exchanger.

One can estimate the size of the perturbations from a simple model of the basic pulse tube. Consider approximating the motion of an element of gas in the pulse tube as a four-step cycle. In this approximation of the ideal case, the element moves toward the hot heat exchanger as it is compressed adiabatically. The element pauses briefly at its maximum displacement without changing state. It then retraces its path expanding adiabatically. Finally it pauses at its initial starting point without changing state. In a real basic pulse tube, there is some heat transfer between the walls and our gas element. Assume this occurs only during the pauses and that the pauses are isobaric. Now, as heat is transferred, the gas cools and continues to move. Since the heat transfer only occurs for a short time, only the gas within the thermal penetration depth is cooled.

In analyzing this cycle we will assume small amplitude variations about mean values and that the wall temperature is steady and equal to the local mean gas temperature, $T_w(z) = \langle T_g(z) \rangle$. During the adiabatic legs, an element of gas is displaced a distance y_a (from Eq 25 with $\mathcal{V} = y_a A$):

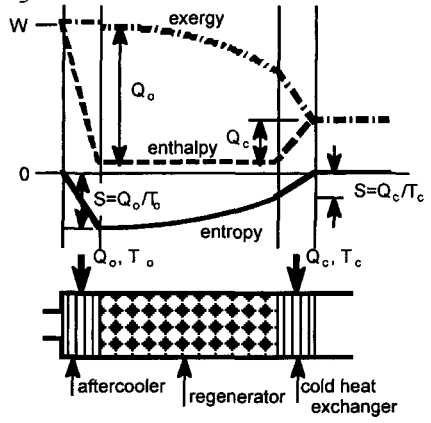

Figure 5. The exergy, enthalpy, and entropy flows as a result of the losses discussed in the text. The effects of regenerator ineffectiveness caused by imperfect heat transfer between the gas and the regenerator. The effects are not shown to scale. Refer to the previous paper[6] for comparison to the ideal case.

$$y_a = \frac{\mathcal{P}_a}{A}\frac{\langle \mathcal{V} \rangle}{\gamma \langle P \rangle} \tag{46}$$

where $\mathcal{V}$ is the volume between the gas element and the hot heat exchanger. After the compression, the heated and displaced gas element ends at a section of wall that is also hotter than the starting point. The temperature difference between the gas and the wall becomes:

$$\Delta T_{g\text{-}w} = \left.\frac{\partial T_g}{\partial P}\right|_S \mathcal{P}_a - \frac{\partial T_w}{\partial z} y_a \tag{47}$$

or

$$\Delta T_{g\text{-}w} \approx \frac{\mathcal{P}_a}{\langle P \rangle}\left[T_w\left(1 - \frac{1}{\gamma}\right) - \frac{\langle \mathcal{V} \rangle}{\gamma A}\frac{\partial T_w}{\partial z}\right]. \tag{48}$$

During the isobaric leg, the gas within the thermal penetration depth, λ, cools to the local T_w and the mean gas temperature changes by

$$\tau \approx \frac{2\lambda}{r}\Delta T_{g\text{-}w} \tag{49}$$

where $2\lambda/r$ is the ratio of the volume of the thermal penetration layer to the volume of the gas element. The enthalpy perturbation is $\eta = c_P \tau$. During the cooling, there is an additional displacement, δy, which can be found by $\delta V/\delta T|_P$ for an ideal gas:

$$\delta y_a = \frac{\langle V \rangle \tau}{A T_w} \tag{50}$$

The mass flows are proportional to the displacements. Thus,

$$\dot{\mu}_a = \frac{\delta y_a}{y_a}\dot{m}_a \tag{51}$$

One can now combine Eqs. 45-51 to calculate the mass flow and temperature perturbations and from those the enthalpy and entropy flows. Instead, we will find the phase shifts from these perturbations. The perturbations shift the phase of $\dot{m}$ and $\mathcal{T}$ by

$$\theta = \frac{\delta y_a}{y_a} \text{ and } \phi = \frac{\tau}{\mathcal{T}}. \tag{52}$$

These can be evaluated at the cold heat exchanger, yielding

$$\theta \approx (\gamma - 1)\phi \text{ and } \phi \approx \frac{2\lambda}{r}\left[1 - \frac{1}{\gamma - 1}\left(\frac{T_h - T_c}{T_c}\right)\right]. \tag{53}$$

where the temperature gradient was approximated by the mean temperature gradient.

The total phase shift is $\psi = \theta + \phi = \gamma\phi$ is small. The factor γ is the result of the assumed path of the secondary compression. We will generalize this to

$$\psi = \alpha\phi, \tag{54}$$

where α is a measure of how non-adiabatic the secondary compression is. Since, most of the gas is not in the boundary layer and therefore adiabatic, one might assume that the secondary compression is adiabatic. However, adiabatic flow does not result in an enthalpy flow.[6] Hence, $\theta = 0$ and $\alpha = 1$ for adiabatic flow. These phase shifts result in a small enthalpy flow:

$$H \approx \alpha \oint \dot{m}_i \eta = \alpha c_P \oint \dot{m}_i \tau \approx \frac{\alpha\phi}{2}\dot{m}_a c_P \mathcal{T}_a \approx \alpha\left(1 - \frac{1}{\gamma}\right)\frac{\phi}{2}\dot{m}_a c_P T_w \frac{\mathcal{P}_a}{\langle P \rangle}. \tag{55}$$

Since $\dot{m}_a T_w$ is constant along the pulse tube,[6] and $\Delta T_{g\text{-}w}$ is roughly constant,[1] ϕ and H are approximately constant. By Eq. 4, there is no net heat flow, $Q = 0$, between the gas and the wall.

When the term on the right hand side of Eq. 53 is 0, the phase shift and the enthalpy flow ≈ 0. This defines the minimum temperature a basic pulse tube can reach:

$$T_{c\min} \approx T_h/\gamma. \tag{56}$$

For T_h = 280 K, $T_{c\,min} \approx$ 168 K for helium and $T_{c\,min} \approx$ 200 K for air. A survey[8] of basic pulse tubes found that most had T_c above or near the minimum. The lowest temperature reached was 135 K in a large amplitude ($\mathcal{P}_a/\langle P \rangle = 0.56$) helium pulse tube.[9]

The heat transfer process described in this section applies to all pulse tubes. If the temperature gradient in the pulse tube is small ($T_c > T_{c\,min}$), then heat transfer to the wall increases the enthalpy flow. However, if the temperature gradient is large ($T_c < T_{c\,min}$), then the heat transfer reverses direction, decreasing the enthalpy flow.

The heat transfer induced phase shift results in an entropy flow, Eq. 45, where from Eq. 14 for the isobaric leg, $\sigma = c_P \tau / T_w = \eta / T_w$, and

$$\frac{dS}{dz} = \frac{1}{\alpha T_w} \frac{dH}{dz} . \tag{57}$$

Apply the assumption of constant phase angle to Eqs. 8-10 results in

$$H = \text{constant}, \; Q = 0, \; \frac{dS_{gen}}{dz} = \frac{dS}{dz} = 0 \text{ , and } \frac{d\Xi}{dz} = 0 . \tag{58}$$

These results are the same as in the ideal case[6] and are summarized in Fig. 6. Those gas elements that spend part of the cycle in one of the heat exchangers result in a net heat transfer from the cold heat exchanger to the hot heat exchanger, $H = Q_c = - Q_h$.

A more general solution allows $\nabla H \neq 0$. Again applying Eqs. 8-10 results in

$$\frac{dH}{dz} = \frac{dQ}{dz} = 0 \text{ , } \frac{dS_{gen}}{dz} = \frac{Q}{T_w^2} \frac{dT}{dz} - \left(1 - \frac{1}{\alpha T_w}\right) \frac{dH}{dz} \geq 0 \text{ , and } \frac{d\Xi}{dz} = \left(1 - \frac{T_o}{\alpha T_w}\right) \frac{dH}{dz} . \tag{59}$$

The condition that $\nabla \Xi \leq 0$ in the absence of work, leads to $T_w \geq \alpha T_o$ when $Q > 0$ (heat flowing from the wall to the gas). This is similar to Eq. 56.

Since the heat transfers occur across temperature differences of ΔT, there is entropy is generated. This effect was discussed earlier. Although, compared to the situation in the regenerator where all of the gas participated in the heat transfer, only the gas within the thermal boundary layer contributes in the pulse tube. Thus, reducing the size of the effect. The size of the boundary layer plays a critical role in the operation of the basic pulse tube. The discussion in this section leads to the conclusion that pulse tubes with a large fraction of the gas volume being within the boundary layer will be more efficient. I.e., basic pulse tubes will be more efficient if they are long, small diameter, and operate at low frequency. On the other hand, for orifice pulse tubes operating below $T_{c\,min}$, the opposite will be more efficient.

SUMMARY

The effect on entropy, enthalpy, and exergy flows of several loss mechanisms were analytically investigated. These included viscous pressure losses in heat exchangers and regenerators, losses due to heat conduction in regenerators, and losses due to heat transfer through out a cooler. The analyses showed that regenerator ineffectiveness, which results in internal gas temperature oscillations and an unwanted enthalpy flow, also results in an enhanced heat load on the cold heat exchanger. The enhanced load is $\Delta Q_c = - H \, T_o / T_c$. Heat transfer between the gas and the pulse tube wall is also responsible for the operation of the basic pulse tube. This phenomenon is a result of the adiabatic temperature change being larger than the temperature change of the wall with the associated displacement. This places a limit on the minimum temperature that a basic pulse tube can reach at $T_{c\,min} \approx T_h / \gamma$.

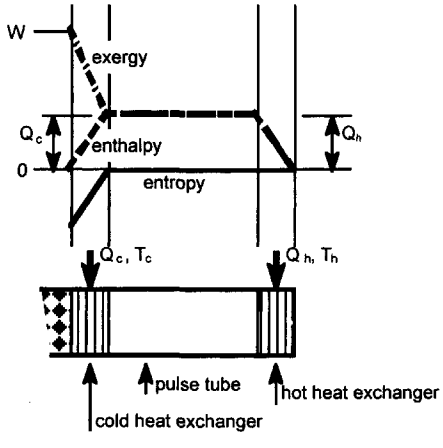

Figure 6. The exergy, enthalpy, and entropy flows as a result of the losses discussed in the text. The effects of heat transfer between the gas and the wall in the basic pulse tube. The effects are not shown to scale. Refer to the previous paper[6] for comparison to the ideal case.

NOMENCLATURE

Roman		Subscripts		Greek	
A	Cross sectional area	a	Amplitude	α	Non-adiabatic factor
E	Energy	c	Cold	Δ	Change (difference)
H	Enthalpy	g, gas	Gas phase	δ	Small change
P	Pressure = $\langle P \rangle + \mathcal{P}$	gen	Generated	Ξ	Exergy
$\mathcal{P}$	Pressure, dynamic	g-w	Gas to wall difference	χ	General parameter
Q	Heat	h	Hot	γ	Specific heat ratio
R	Gas constant (per kg)	i	Index	ϕ	Phase shift
S	Entropy	i	Ideal	η	Enthalpy perturbation
T	Temperature = $\langle T \rangle + \mathcal{T}$	in	Inflow	λ	Thermal penetration depth
$\mathcal{T}$	Temperature, dynamic	loss	Loss	μ	Mass flow perturbation
$V, \mathcal{V}$	Volume	min	Minimum	ν	Velocity
W	Work	o	Reference	θ	Phase shift
X	General parameter	out	Outflow	σ	Entropy perturbation
c	Specific heat	P	Isobaric	τ	Temperature perturbation
g	Gravitational acceleration	pt	Pulse tube	ψ	Total phase shift
h	Specific enthalpy	regen	Regenerator	ξ	Specific exergy
l	Regenerator length	s, S	Adiabatic		
m	Mass	solid	Solid part of heat exchanger or regenerator	Other	
r	Radius of pulse tube	T	Isothermal	$\langle\ \rangle$	Cyclic average
s	Specific entropy	t	Time	$\cdot$	Time derivative
t	Time	V	Isochoric		
x	General parameter	w	wall		
y	Displacement				
z	Distance				

REFERENCES

1. Storch, P.J., Radebaugh, R., and Zimmerman, J., *Analytical Model for Refrigeration Power of the Orifice Pulse Tube Refrigerator*, NIST Technical Note 1343 (1990).
2. Kittel, P., Kashani, A., Lee, J.M., and Roach, P.R. "General Pulse Tube Theory," *Cryogenics*, vol. 36, (1996), p. 849.
3. de Waele, A.T.A.M., Steijaert, P.P., and Gijzen, P., "Thermodynamic Aspects of Pulse Tubes," *Cryogenics*, vol. 37 (1997), p. 313.
4. de Boer, P.C.T., "Optimization of the Orifice Pulse Tube," *Cryogenics*, vol. 40 (2000), p. 701.
5. Razani, A., Flake, B., and Yarbrough, S., "Exergy Flow in Pulse Tube Refrigerators and Their Performance Evaluation Based on Exergy Analysis," *Adv. Cryo. Engin.*, vol. 49B, AIP Press, New York (2004), pp. 1508-1518.
6. Kittel, P., "Enthalpy, Entropy, and Exergy Flows in Ideal Pulse Tube Cryocoolers," *Cryocoolers 13*, Kluwer Academic/Plenum Publishers, New York (2005), this proceedings.
7. Bejan, A., *Advanced Engineering Thermodynamics, 2nd Edition*, Wiley, New York (1997).
8. Roach. P.R., private communication, also available at http://irtek.arc.nasa.gov/CryoGroup/PTDatabase/PTData-Basic.html
9. Lechner, R.A., and Ackerman, R.A., "Concentric Pulse Tube Analysis and Design," *Adv. Cryo. Engin.*, vol. 18, Plenum Press, New York (1973), p. 467.

A Model for Energy and Exergy Flow in an Orifice Pulse Tube Refrigerator

A. Razani[1,2], C. Dodson[2], N.S.Abhyankar[3], and B. Flake[1]

[1] Air Force Research Laboratory
Kirtland AFB, NM, USA 87117-5776
[2] University of New Mexico
Albuquerque, NM 87131
[3] Dynacs Engineering Co.
Albuquerque, NM 87106-4266

ABSTRACT

Rational bases for performance evaluation of cryocoolers are second law and exergy analyses. In this study, a model is proposed for the calculation of energy and exergy flow in an Orifice Pulse Tube Refrigerator (OPTR). Using a needle valve, it can be shown that the mass flow rate in the hot side of the OPTR, in general, can be written as a Fourier series expansion. Using the conservation of energy and the balance of exergy for the valve, a general formula for the timed-average irreversibility of the valve is obtained in which the usual, small amplitude approximation is removed. A numerical model is developed to investigate the effect of important system parameters on energy and exergy flow in the pulse tube components. Using the exergy balance on each component, the irreversibility of each component is determined. The goal of this study is to find the effect of important system parameters on the timed-average irreversibility of the distribution of components in the OPTR. It is shown that the regenerator contributes the most to the system irreversibility in a well-designed OPTR. Using the recent empirical relations for pressure drop and a simple model for thermal analysis in the regenerator, the exergy flow and irreversibility of different processes in the regenerator are determined.

INTRODUCTION

Orifice Pulse Tube Refrigerators (OPTRs) play an important role in satisfying the need for cryogenic cooling of space-based infrared detectors as well as electronics requiring coolers with high reliability, low vibration, and high efficiency. The thermodynamics of OPTRs have been under study by several investigators,[1-4] to just name a few. Exergy analysis is a powerful method for analysis and design of pulse tube refrigerators.[5,6] Exergy flow and analysis in the OPTRs for each component shows how the input exergy provided by the power input to the compressor is destroyed as the working fluid goes through its cyclic motion in the system. In this paper we concentrate on OPTRs because their basic components and relevant features conveniently show the application of the exergy method. In addition, a numerical model is developed to calculate the exergy flow in forward and backward directions as the working fluid goes through a cycle.

Exergy, like energy and entropy, is a property of the state of a system and measures the departure of the state from the system's state of the environment. For application to OPTRs, for

Cryocoolers 13, edited by R. G. Ross, Jr.
Springer Science+Business Media, Inc., New York, 2004

each component with one channel heat transfer with a thermal reservoir at the temperature T_R and one channel of inlet and exit mass transfer, the exergy balance can be written as[5]

$$< \dot{E}_D >=< \dot{m}e >_i - < \dot{m}e >_e - < \dot{W} > + < (1-\frac{T_o}{T_R})\dot{Q} > \quad (1)$$

Where e is the specific exergy carried with mass, and $\dot{E}_D$ is the rate of exergy destruction in the component. For a single-component working fluid, such as helium, in the absence of chemical, kinetic, or potential exergy, the specific exergy can simply be written as

$$e = h - h_o - T_o(s - s_o) \quad (2)$$

Where h is the specific enthalpy and s is the specific entropy and subscript "o" denotes the environment. Substituting Eq. (2) into Eq. (1) and using the vanishing average mass flow rate over a cycle yields

$$< \dot{E}_D >=< \dot{m}h >_i - < \dot{m}h >_e - T_o(< \dot{m}s >_i - < \dot{m}s >_e) - < \dot{W} > + < (1-\frac{T_o}{T_R})\dot{Q} > \quad (3)$$

Assuming the ideal gas law with constant thermophysical properties, the enthalpy and entropy in the above equation can be written, respectively as,

$$h = C_p(T - T_o), \quad (4)$$

$$s = C_p \ln(T/T_o) - R\ln(P/P_0). \quad (5)$$

OPTR MODEL

A model is developed to calculate the transient temperature, pressure, and mass transfer in a conventional OPTR for the purpose of evaluating the energy transfer, exergy transfer, and the irreversibility in each component of the pulse tube. The energy transfer in the pulse tube itself is based on the enthalpy flow model, assuming an ideal pulse tube[1]. Figure 1 shows an orifice pulse tube refrigerator with its basic components. Important equations are summarized below for different components.

A model for isothermal flow through a valve is used to calculate the mass flow rate m_o through the orifice[7].

$$\dot{m}_o = \pm k\sqrt{\left|P_o^2 - P_s^2\right|} \quad (6)$$

Where the proportionality constant, k, depends on the opening of the valve, and considered as an input in this model for parametric studies. P_o, and P_s are the pressures at the inlet and exit of the valve, respectively. The positive and negative signs in the above equation denote the forward and backward flow directions. Forward flow direction is defined from the compressor toward the valve (orifice). The general time dependent function P_o is an input in this model. Most calculations are reported for

$$P_o = p_a + p_o\cos(2\pi ft - \theta_o) \quad (7)$$

Where p_a is the average pressure in the system, p_o is the pressure amplitude, f is the frequency and θ_o is the phase angle. Assuming an ideal gas assumption for helium, the mass flow rate through the valve is related to the reservoir pressure by,

$$\dot{m}_o = \frac{V_s}{\gamma RT_o}\frac{dP_s}{dt} \quad (8)$$

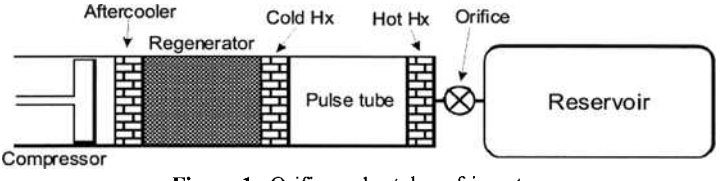

Figure 1. Orifice pulse tube refrigerator.

Where V_s is the reservoir volume, γ is the specific heat ratio, and T_o is the temperature of the environment. Solutions of Eqs. (6) to (8) show that the pressure in the reservoir is, in general, a periodic function with its average pressure $p_s \neq p_a$ and its amplitude and phase angle obtained from the solution of the equations[8].

The temperature and mass flow in the pulse tube is obtained using conservation of mass and energy, assuming an adiabatic pulse tube[7]. The temperature in the pulse tube is obtained from the solution of the following differential equation.

$$\frac{\partial T}{\partial t} = \frac{R}{C_p}\frac{T}{P}\frac{\partial P}{\partial t} - \frac{R}{A_t}\frac{T}{P}\frac{\partial T_a}{\partial x}\dot{m}_t \tag{9}$$

Where $\frac{\partial T_a}{\partial x}$ is the gradient of average temperature in the pulse tube, used as a parameter in this study, A_t is the pulse tube cross section, and $\dot{m}_t$ is the mass flow rate in the pulse tube. The mass flow rate at the hot side of the pulse tube is obtained from the following differential equation.

$$\dot{m}_{th} = \dot{m}_o + \frac{V_{HHX}}{RT_{HHX}}\frac{dP_{HHX}}{dt} \tag{10}$$

Where T_{HHX}, P_{HHX}, V_{HHX} are temperature, average pressure, and the void volume of HHX, respectively. The mass flow rate in the HHX is assumed to be proportional to the pressure drop in the HHX using a laminar flow model

$$\dot{m}_{HHX} = k_{HHX}(P_h - P_o) \tag{11}$$

Where the fluid conductance, k_{HHX}, for the HHX can be written in terms of the hydraulic diameter, flow area, length, and other flow parameters in the HHX using a laminar flow model. Solution of Eq. (9) for the hot side of pulse tube can be, in general, written as

$$T_h = T_{ih}\left(\frac{P_h}{P_{ih}}\right)^{R/Cp} e^{-\frac{R}{A_t}\frac{\partial T_a}{\partial x}\int_0^t \frac{\dot{m}_{th}}{P}dt} \tag{12}$$

Where the subscript i denotes the appropriate initial condition. The average of temperature at the hot side of T_{HHX} is related to heat transfer rate from the HHX and determines the temperature distribution at the hot side of the pulse tube using the energy balance for HHX. Eq. (12) clearly shows the effect of the gradient of the average temperature of the working fluid at the hot side of the pulse on the transient temperature distribution at the hot side. Mass flow rate at the cold side of the pulse tube is the solution to the following differential equation.

$$\dot{m}_{tc} = \frac{T_h}{T_c}\dot{m}_{th} + \left(\frac{V_t}{\gamma R T_c}\right)\frac{dP_t}{dt} \tag{13}$$

Where P_t is the pressure in the pulse tube with no pressure drop along the pulse tube and V_t is the volume of the pulse tube. An equation similar to Eq. (12) is used to calculate the temperature distribution at the cold side of the pulse tube. The temperature at the cold side of the regenerator is obtained from the energy balance in the CHX and regenerator. A simple thermal model is used to analyze the regenerator, considering regenerator inefficiency as a parameter. The mass flow rate and pressure drop in the regenerator is obtained using an experimentally-based correlation for the friction coefficient[9]. The differential pressure drop in the regenerator can be written as

$$dP = \frac{1}{2} f\rho u|u|\frac{dx}{D_{hr}} \tag{14}$$

Where f is the friction coefficient given by

$$f = \frac{C_1}{\mathrm{Re}} + C_2 = \frac{C_1\mu}{\rho u D_{hr}} + C_2 \tag{15}$$

Where C_1 and C_2 are the correlation coefficients for fluid friction and Re is the Reynold's number based on the hydraulic diameter D_{hr} in regenerator, μ is the viscosity and u is the

velocity of the working fluid. Assuming an ideal gas and writing the velocity in terms of mass flow rate, integration of Eqs. (14) and (15) gives the pressure at any point in the regenerator,

$$P(x,t) = \sqrt{P_{cr}^2 + 2\int_0^x [aT(x')\dot{m}_r(x',t) + bT(x')\dot{m}_r(x',t)|\dot{m}_r(x',t)|]dx'} \tag{16}$$

Where $a = C_1\mu R / 2A_r D_{hr}^2$, $b = C_2 R / 2A_r^2 D_{hr}$, P_{cr} is the pressure at the cold side of regenerator, and $T(x)$ is the spatial temperature distribution in the regenerator. The mass flow rate at any point in the regenerator, $\dot{m}_r$ is obtained from the following equation

$$\dot{m}_r(x,t) = \dot{m}_{cr}(t) + \int_0^x \frac{A_r}{RT(x')}\frac{dP_r}{dt}dx' \tag{17}$$

Where A_r is the flow area of the regenerator and viscosity is taken to be dependent on the temperature at any point in the regenerator. In this study, it is assumed that the temperature distribution in the regenerator is linear. Eqs. (16) and (17) are solved numerically to obtain the pressure and mass flow rate in the regenerator. Models similar to the Eqs. (10) and (11) are used to connect the cold side of pulse tube to the cold side of the regenerator.

$$\dot{m}_{rc} = \dot{m}_{tc} + \frac{V_{CHX}}{RT_{CHX}}\frac{dP_{CHX}}{dt} \tag{18}$$

$$\dot{m}_{CHX} = k_{CHX}(P_{cr} - P_c) \tag{19}$$

Where the subscript CHX refers to the cold heat exchanger. A simple model is used to calculate the thermal irreversibility in the regenerator and the cold and hot heat exchangers. The thermal analysis of the regenerator is based on the knowledge of the effectiveness of the regenerator ε as a parameter. The regenerator ineffectiveness λ is defined by

$$\lambda = 1 - \varepsilon = \frac{< \dot{m} h_{cr} >}{< \dot{m} h_{hr} >_{hot\ blow} - < \dot{m} h_{cr} >_{cold\ blow}} \tag{20}$$

Where subscripts *hr* and *cr* represent the hot and cold sides of regenerator, respectively. Assuming C_p is constant, the above equation can be written in terms of the temperatures of the hot and cold sides of regenerators. The temperature of the gas entering the regenerator at the hot side is taken to be the environmental temperature due to an assumption of a highly effective aftercooler. The temperature of the cold side of the regenerator is connected to the cold side of the pulse tube through the cold heat exchanger using a simple energy balance for CHX

$$\dot{Q}_{CHX} = (UA)_{CHX}(T_c - \bar{T}_{CHX}) \tag{21}$$

Where T_c is the temperature of the cold reservoir, $\bar{T}_{CHX}$ is the average temperature of the CHX and $(UA)_{CHX}$ is the thermal conductance of CHX. A similar equation is used for the hot heat exchanger by assuming that the exit temperature of the HHX is close to the environmental temperature.

$$\dot{Q}_{HHX} = (UA)_{HHX}(\bar{T}_{HHX} - T_o) \tag{22}$$

The model developed above can be used to capture the effect of important parameters on the energy and exergy flow in OPTRs.

RESULTS AND DISCUSSION

In order to calculate the energy and exergy flow in the OPTR, the transient pressure, mass flow rate, and temperature should be calculated in the pulse tube. The simple model developed in the previous section provides these quantities with a reasonable accuracy.

Irreversibility of an ideal OPTR

For an ideal OPTR, the only irreversibility occurs in the valve or orifice. Second law analysis of ideal OPTRs shows that the irreversibility of the valve is equal to the enthalpy flow in

the pulse tube[5]. The mass flow rate through the valve is given by Eq. (6) and, in general, can be expanded in a Fourier series[7]

$$m_o = \sum_{n=1}^{\infty} M_{on} \cos n(2\pi ft - \theta_o) \tag{23}$$

Since thermal exergy across the valve is assumed to be zero in ideal OPTRs, the exergy balance for the valve requires the destruction of all input exergy. Therefore, the irreversibility of the valve can be written as

$$< \dot{I} >_{valve} = RT_o \int \dot{m}_o \ln(\frac{P_o}{p_a}) dt \tag{24}$$

Using Eq. (7) and (20) and (21), the irreversibility of the valve can be written as

$$< \dot{I} >_{valve} = \frac{RT_o}{2} \sum_{m=1}^{\infty} \sum_{n=1}^{m} \frac{\dot{M}_{on}}{2^{m-1}} \frac{(-1)^{m-1}}{m} (\frac{p_o}{p_a})^m B[m,(m-n)/2] \tag{25}$$

Where B is the binomial function. For the ideal pulse tube, where the enthalpy flow and the irreversibility of the valve are equal, under the assumption of small amplitude approximation, Eq. (22) reduces to the familiar equation for enthalpy flow in an ideal pulse tube reported in literature

$$< \dot{I} >_{valve} = < \dot{m} h > = \frac{RT_o}{2} \dot{M}_{o1} \frac{p_o}{p_a} \tag{26}$$

This shows that the higher harmonics do not contribute to the enthalpy flow or irreversibility of the valve in ideal OPTRs. It should be pointed out that equation (22) represents an expression for the irreversibility of the valve removing the usual assumption of small amplitude approximation. Numerical calculations using Eq. (6), (7) and (24) as well as Eq. (25) show that the small amplitude approximation is very good in most cases.

To calculate the energy and exergy flows in OPTRs, the calculations are performed first for a thermally perfect OPTR. In this case, thermal irreversibility in the pulse tube, heat exchangers and the regenerator are absent. Table 1 shows the thermophysical properties and the nominal values for important parameters and the related equations used in calculations of energy and exergy flow in the OPTR. These values are used in the calculations unless the parameter is changed for parametric studies.

Figure 2 shows the results of calculations for mass flow rate for different locations at the inlet and exit of different components shown in Figure 1. The calculations are performed for a thermally perfect regenerator and the cold and hot heat exchangers. The calculations include the effect of pressure drop and void in the regenerator, CHX, and HHX. The calculations include the effect of pressure variation in the reservoir and the valve as modeled by Eqs. (6) and (8).

Table 1. Thermophysical properties and nominal values used in calculations.

Parameters, Equations	Nominal values (units)	Parameters, Equations	Nominal values (units)
p_a, Eq. (7)	1.5 (MPa)	k, Eq. (6)	$0.5*10^{-9}$ (Kg/s*Pa)
p_o, Eq. (7)	180 (kPa)	k_{HHX}, Eq. (11)	$2.76*10^{-7}$ (Kg/s*Pa)
V_s, Eq.(8)	0.001 m^3	k_{CHX}, Eq. (19)	$1.71*10^{-6}$ (Kg/s*Pa)
A_t, Eq. (9)	50.265 (mm^2)	V_{HHX}, Eq. (11)	1.0 (cm^3)
V_t, Eq. (13)	5.0265 (cm^3)	V_{CHX}, Eq. (19)	1.0 (cm^3)
L_r, Eq. (16)	7.5 (cm)	f, Eq. (7)	20 Hz
A_r, Eq. (16)	78.54 (mm^2)	λ, Eq. (20)	0.008
To, Eq. (5)	300 K	Porosity of regenerator	0.67
T_c, Eq. (13)	100 K	R, Eq. (9)	2076.9 (J/Kg*K)
$(UA)_{CHX}$	2 W/K	C_p	5192.6 (J/Kg*K)
$(UA)_{HHX}$	2 W/K	γ	1.667
C_1, Eq. (15)	33.6	D_{hr}, Eq. (16)	$3.33*10^{-5}$ (m)
C_2, Eq. (15)	0.337	η_{comp}	0.85

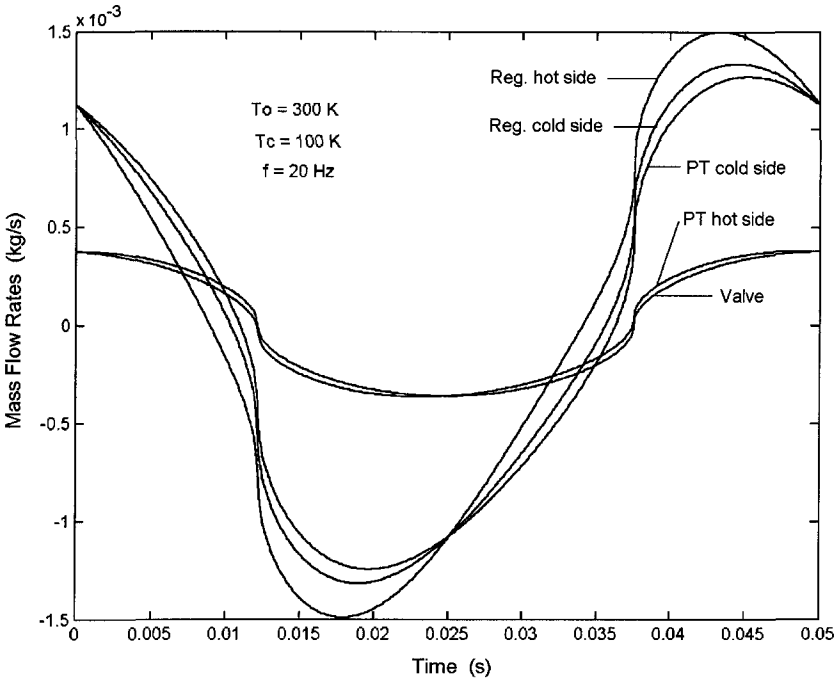

Figure 2. Mass flow rate for orifice pulse tube refrigerator for nominal values.

The effect of equation (6) for the valve on the mass flow rate through the system is clearly seen in the figure. This is mainly due to the fact that the mass flow rate depends on the derivative of pressure as indicated in Eqs. (10), (13) and (17). The phase difference between the mass flow rate at the hot side and the cold side of the pulse tube and mass flow rate at the valve are approximately, 10 and 33 degrees, respectively. Due to the relatively large volume of reservoir used in the calculations, the mass flow rate and pressure at the valve are almost in phase. Figure 2 also shows the effect of the void in the regenerator on the magnitude of the mass flow rate and corresponding phase shift. In addition, the results of calculations show a pressure drop and phase shift in pressure as modeled by Eqs. (14) to (17). It should be pointed out that the simple model used in these calculations captures important phenomena and sources of irreversibility due to friction and void in the system. Once the pressure, temperature, and mass flow rate at the inlet and exit of the components are determined, Eqs. (2) to (5) can be used to calculate the exergy flow into and out of the system components and exergy destruction (irreversibility) of the processes occurring within them. Separating the forward and backward exergy flow in the system facilitates the understanding of exergy flow in OPTRs and their thermodynamic analysis. The forward and backward exergy flow at any location is defined by,

$$\begin{aligned} <\dot{m}e>_{forward} &= <\dot{m}e>, \quad for \quad \dot{m} > 0 \\ <\dot{m}e>_{backward} &= <\dot{m}e>, \quad for \quad \dot{m} < 0 \end{aligned} \tag{27}$$

Figure 3 shows the pressure part, corresponding to the second term of Eq. (5) of the forward and backward exergy flow for a thermally perfect system. The nominal values are used in this calculation. The calculation includes the exergy destruction due to the pressure drop in the system. The magnitude of exergy flow is large because of large pressure in the system

compared to the environmental pressure of one atm. Numerical experimentation for a thermally perfect OPTR shows that the pressure and mass flow variations, especially in regenerator, which are mainly due to the fluid friction and void in the regenerator, have significant influence on the exergy flow in the system. Figure 4 shows the total exergy flow in the forward and backward directions, including the effect of regenerator inefficiency as defined in Eq. (20), effects of finite thermal conductance of the CHX and HHX, and conduction heat transfer in the regenerator. It should be pointed out that the magnitude of the exergy flow is given in Figures 3 and 4. Therefore, the difference of the magnitude of bar charts in the figures represents the exergy flow at any location over one cycle.

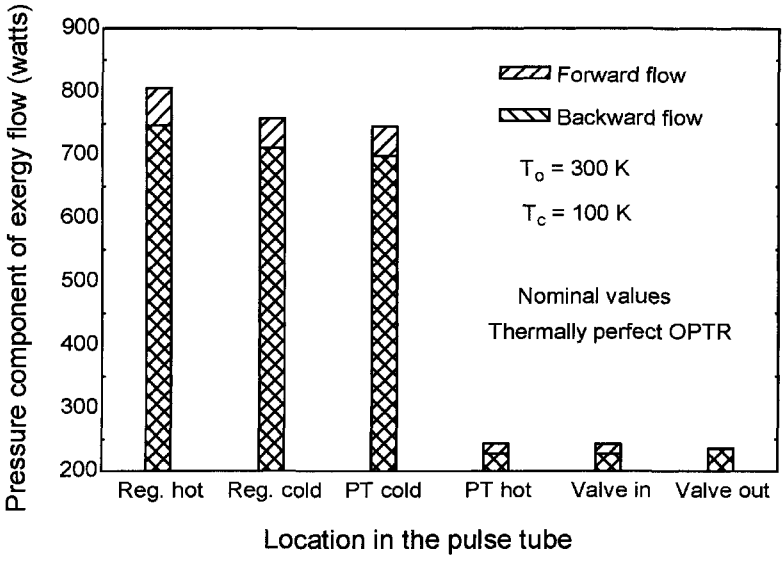

Figure 3. Pressure component of exergy flow in the forward and backward directions.

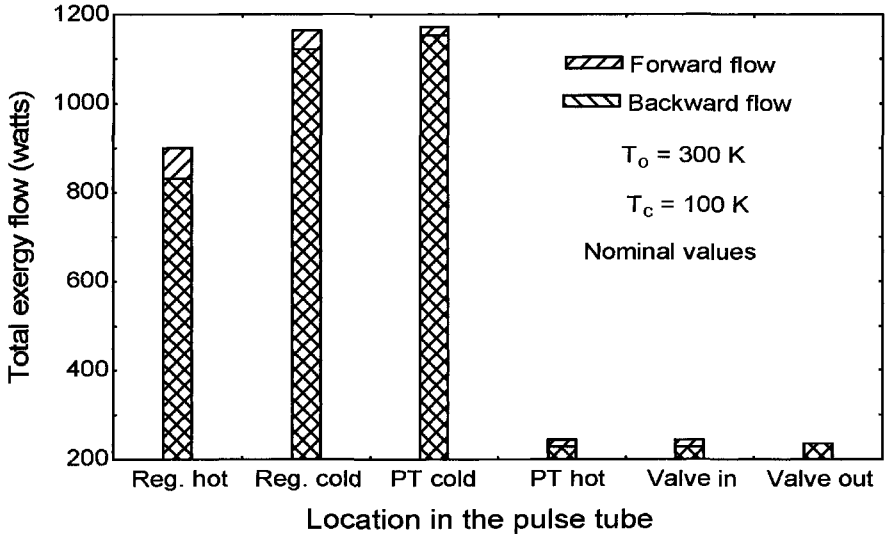

Figure 4. Total exergy flow in the forward and backward directions.

It is interesting to note that the working fluid acquires exergy from the matrix in the regenerator in the forward direction and returns it to the regenerator in the backward direction. Due to the thermal exergy destruction in the regenerator, there is a net loss in the process. In addition, there is thermal exergy destruction due to conduction heat transfer in the regenerator. Fluid friction in both forward and backward directions causes mechanical exergy destruction in both directions.

The exergy destruction for each component of OPTR is given in Figure 5. In this analysis the pulse tube itself is assumed to be ideal with no exergy destruction. In the model used in this study, the enthalpy flow in the pulse tube is assumed to be constant when the effect of conductance on the CHX and HHX is considered. The temperature variations at the hot and cold sides of the pulse tube due to finite thermal conductances in the CHX and HHX result in small exergy destruction in the pulse tube as shown in Figure 5. In actual OPTRs there are more complex phenomena occurring in the pulse tube itself resulting in additional exergy destructions due to heat transfer and fluid flow. Quantification of the pulse tube losses both theoretically and experimentally is under investigation in our laboratory. The COP (Coefficient of Performance) and Carnot COP for the refrigerator under thermally perfect and total conditions are also given in Figure 5 for comparison. In this analysis, the compressor is not modeled and it is assumed that its exergetic efficiency is 0.85. The irreversibility of the compressor given in Figure 5 is determined on this assumption.

Parametric studies show that the exergy destruction for each component changes as the parameters change and the optimization of the system must be based on minimum total exergy destruction for the entire system. Table 2 shows the effect of frequency and the valve parameter on exergy flow and destruction in the OPTR. The forward, backward and net exregy flow is reported in the table for three values of frequency and three values of valve parameter. The values of the parameters are chosen such that one occurs below and one higher than the nominal values for frequency of 20 Hz and the valve parameter of $k = 0.5*10^{-9}$ Kg/s*Pa. For all other parameters the nominal values are used as given in given in Table 1.

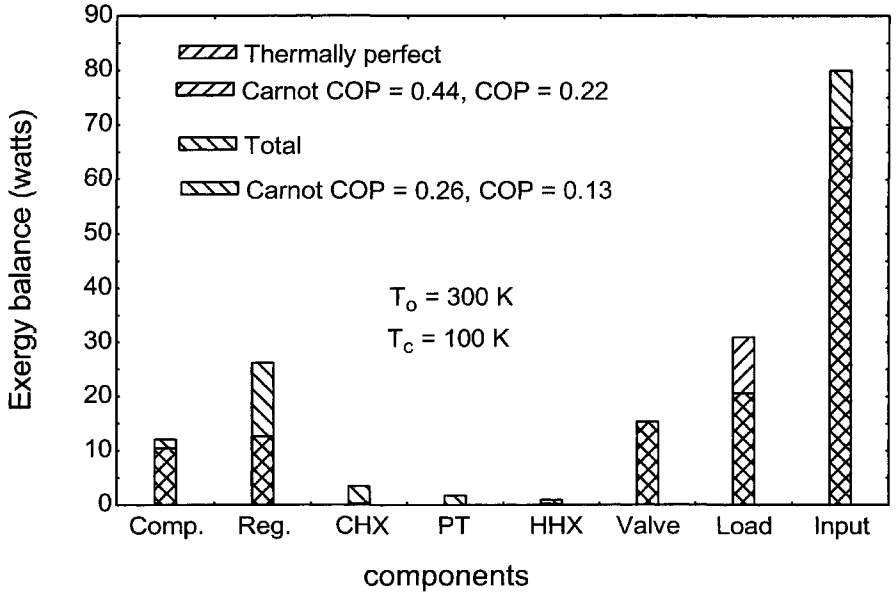

Figure 5. Exergy balance including the irreversibility of different components in the OPTR.

Table 2. Exergy flow at different locations in OPTR for three values of frequency and three values of valve parameter.

Location	Exergy flow (watts)	f=10 Hz k=0.5*10^{-9} (Kg/s*Pa)	f=20 Hz k=0.5*10^{-9} (Kg/s*Pa)	f=30 Hz k=0.5*10^{-9} (Kg/s*Pa)	f=20 Hz k=0.25*10^{-9} (Kg/s*Pa)	f=20 Hz k=0.75*10^{-9} (Kg/s*Pa)
Reg. hot Side	Forward	839.9	899.8	1023.1	563.3	1350.8
	Backward	776.1	831.7	947.6	533.6	1225.7
	Net	63.8	68.1	75.5	29.7	125.1
Reg. Cold Side	Forward	1137.0	1163.8	1230.8	641.5	1796.0
	Backward	1094.6	1121.6	1189.2	622.4	1728.7
	Net	42.4	42.2	41.6	19.1	67.3
PT Cold Side	Forward	1157.9	1170.9	1206.0	600.8	1846.2
	Backward	1139.9	1152.9	1188.0	592.5	1817.0
	Net	18.0	18.0	18.0	18.3	29.2
PT Hot Side	Forward	243.9	244.0	244.2	122.0	366.7
	Backward	227.7	227.8	227.9	114.1	341.8
	Net	16.2	16.2	16.3	7.9	24.9
Valve Inlet	Forward	242.7	242.7	242.8	121.4	364.1
	Backward	227.4	227.4	227.4	113.7	341.1
	Net	15.3	15.3	15.2	7.7	23
Valve exit	Forward	235.5	235.6	235.6	117.8	353.3
	Backward	235.5	235.6	235.6	117.8	353.3
	Net	0	0	0	0	0

CONCLUSIONS

A model, which captures the effect of important parameters on the energy and exergy flow in OPTRs, is developed. This model is used to calculate the exergy flows in the forward and backward directions at the inlet and the exit of each component of the pulse tube. The magnitudes of the forward and backward directions give insight into the losses occurring in each component. Through the exergy balance for each component, the exergy destruction is obtained for the components. In addition, the separation of mechanical and thermal exergy components gives insight into how the input exergy is transformed into product exergy at the load. It is shown that the pressure and mass flow variations significantly influence the exergy flow and consequently the exergy destruction in each component. The effect of the model for the valve used in this study influences the mass flow variation and the exergy flow as well. A general equation for the irreversibility of the valve based on a Fourier series expansion of the mass flow rate through the valve is obtained. Exergy analysis is a powerful method for thermodynamic understanding and quantification of losses in pulse tubes.

ACKNOWLEDGEMENT

One of the authors, C. Dodson, would like to thank the opportunity provided by the Space Scholars Program to participate and contribute to this investigation.

REFERENCES

1. Storch, P.J., Radebaugh, R., Zimmerman, J., Analytical model for refrigeration power of the orifice pulse tube refrigerator, NIST technical note 1343, (1990).

2. Kittle, P., Kashani, A. Lee, J.M., and Roach, P.R., "General pulse tube theory," *Cryogenics*, Vol. 34, no. 10 (1996), pp. 849-857.

3. de Boer, PCT, "Optimization of the orifice pulse tube," *Cryogenics*, Vol. 40, no. 11 (2000), pp. 701-711.

4. de Waele, ATAM, Steijaert, P.P., and Gijzen, J., "Thermodynamical aspects of pulse tubes," *Cryogenics*, Vol. 37, no. 6, (1997), pp. 313-324.

5. Razani, A., Flake, B., Yarbrough, S., "Exergy Flow in Pulse Tube Refrigerators and Their Performance Evaluation Based on Exergy Analysis," *Adv. in Cryogenic Engineering*, Vol. 49B, Amer. Institute of Physics, Melville, NY (2004), pp. 1508-1518.

6. Razani, A., Flake, B., Yarbrough, S., Abhyankar, N.S., "A Power-Efficiency Diagram for Performance Evaluation of Cryocoolers," *Adv. in Cryogenic Engineering*, Vol. 49B, Amer. Institute of Physics, Melville, NY (2004), pp. 1527-1535.

7. Kuriyama, F. and Radebaugh, R, "Analysis of mass and energy flow rate in an orifice pulse-tube refrigerator," *Cryogenics*, Vol. 39, no. 1 (1999), pp. 85-92.

8. Hou, Y.K., Ju, Y.L., Jing, W. and Liang, J.T., "The role of the orifice and the secondary bypass in a miniature pulse tube cryocooler," *Cryocoolers 12*, Kluwer Academic/Plenum Publishers, New York (2003), pp. 361-369.

9. Miyabe, H., Takahashi, S. and Hamaguchi, K., "An approach to the design of Stirling engine regenerator matrix using packs of wire gauzes," *Proceedings of 17th IECEC* (1982), pp. 1839-1844.

Development of New Cryocooler Regenerator Materials – Ductile Intermetallic Compounds

K.A. Gschneidner, Jr.[1,2], A.O. Pecharsky[1], and V.K. Pecharsky[1,2]

[1]Materials and Engineering Physics Program, Ames Laboratory
Iowa State University, Ames, Iowa 50011-3020

[2]Department of Materials Science and Engineering
Iowa State University, Ames, Iowa 50011-2300, USA

ABSTRACT

The volumetric heat capacities of a number of binary and ternary Er- and Tm-based intermetallic compounds, which exhibited substantial ductilities, were measured from ~3 to ~350 K. They have the RM stoichiometry (where R = Er or Tm, and M is a main group or transition metal) and crystallize in the CsCl-type structure. The heat capacities of the Tm-based compounds are in general larger than the corresponding Er-based materials. Many of them have heat capacities which are significantly larger than those of the low temperature (<15 K) prototype cryocooler regenerator materials $HoCu_2$, Er_3Ni and ErNi. Utilization of the new materials as regenerators in the various cryocoolers should improve the performance of these refrigeration units for cooling below 15 K.

INTRODUCTION

Lanthanide materials have been used as low temperature (<20 K) regenerators since 1990 because of their large magnetic entropies at their magnetic ordering temperatures[1]. This development allowed Toshiba scientists[2,3] to reduce the low temperature limit of a two stage Gifford-McMahon cryocooler from 10 to 4 K by replacing some of the Pb with Er_3Ni in the low temperature stage regenerator. Since then, Nd[4] and $HoCu_2$[5] have been used as replacements for Er_3Ni; and the $Er_{1-x}Pr_x$ alloys ($0 \le x \le 0.50$) as a substitute for Pb[6,7] for cooling down to between 60 and 10 K. $GdAlO_3$ ($T_C = 3.8$ K) has been employed to cool to 4 K when utilized in the coldest section of a compound regenerator[8]. Below we discuss our latest work on the development of regenerator materials – ductile intermetallic compounds which have high volumetric heat capacities in the vicinity of the magnetic ordering temperatures between 4 and 16 K.

EXPERIMENTAL DETAILS

The alloys were prepared by arc-melting stoichiometric amounts of the component materials on a water cooled copper hearth under an argon atmosphere. The alloys were generally turned over 6 times (except for ErIr which was turned over ~20 times) and remelted to ensure a homogeneous ingot. Weight losses after melting were negligible. The metals used in this study

Cryocoolers 13, edited by R. G. Ross, Jr.
Springer Science+Business Media, Inc., New York, 2004

were purchased from various commercial sources. The rare earth metals were 95 to 98 atomic percent pure with the major impurities being O, C and N, while the non-rare earth metals were 99.9+ atomic percent pure. The x-ray powder diffraction data were collected on an automated Scintag powder diffractometer using Cu K_α radiation to check on the phase purity and the crystallography of the samples. All of the samples were found to be single-phase materials within the limitations of the x-ray powder diffraction technique (typically 2 to 5 vol.% of an impurity phase). Most of the intermetallic compound samples were not heat treated because they were single phase alloys after arc-melting. ErRh and ErAu, however, were heat treated for 335 hours (2 weeks) at 900°C and rapidly quenched to room temperature to retain the B2 structure. The heat capacities at constant pressure were measured using an adiabatic heat-pulse-type calorimeter[9] from ~3.5 to ~350 K in zero magnetic field.

DUCTILE INTERMETALLIC COMPOUNDS

Magnetic lanthanide intermetallic compounds exhibit a wide range of magnetic ordering temperatures ranging from less than 1 K to nearly 1300 K. Of particular interest to the cryocooler industry are those compounds which order magnetically below 20 K[1]. Although many compounds have high heat capacities at the required temperature and thus would perform well as passive regenerator materials, their mechanical properties are far from ideal. In general, as most stoichiometric compounds, they are inherently brittle. Thus, they are nearly impossible to fabricate into sheets, jelly rolls, wires, and screens, which can be assembled into a regenerator which is more efficient than a packed bed of spheres. Furthermore, because of this brittleness the spheres can decrepitate and eventually leading to the failure of the regenerator and therefore the cryocooler. Thus, if one could make the brittle intermetallic compounds into ductile materials, or if one could find ductile intermetallic phases with suitable thermal properties, either development would be a major breakthrough in improving the efficiency of low temperature cryocoolers. Recently, we have discovered such a family of compounds which have unprecedented ductility (as high as 20%) and high fracture-toughness at room temperature[10]. This family of equiatomic compounds, RM, is made up of a rare earth (R) and a main group or transition metal (M) atoms, and has the B2, CsCl-type structure (see Fig. 1). There are over 120 known members in this family. Some of these binary RM phase have high heat capacities below 20 K [e.g. ErCu, $T_O \cong 8.5$ K and 13 K[11]; ErAg $T_O \cong 15.5$ K[12]; TmCu, $T_O \cong 6.5$ and 8 K[11,13]; and TmAg, $T_O \cong 7$ K[13] (the ordering temperatures listed here are those found in this study, which may differ slightly from earlier values reported in the literature)], and thus are of interest to the cryocooler community. Indeed, Biwa *et al.*[14] have proposed that ErAg be utilized as a

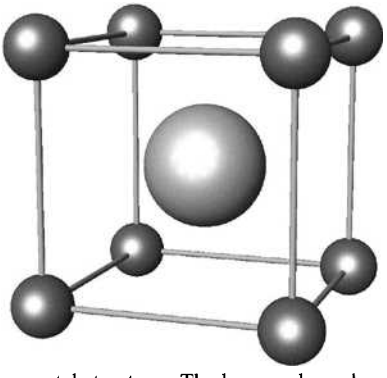

Figure 1. The B2 CsCl-type crystal structure. The larger sphere shown in the center of the unit cell represents the rare earth metal atom, while the smaller spheres on the corners represent the non-rare earth metal (a main group or a transition metal) atom.

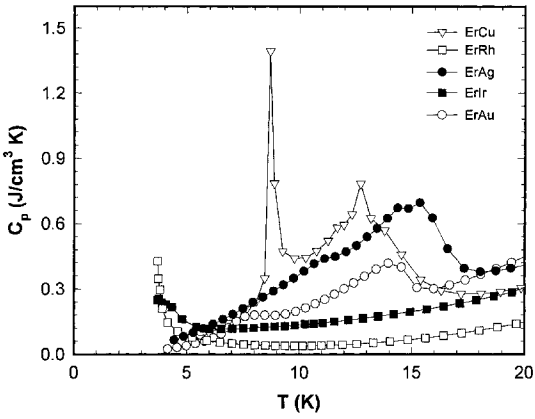

Figure 2. The volumetric heat capacities of ErCu, ErRh, ErAg, ErIr and ErAu from ~4 to 20 K.

regenerator material from 9 to 17 K, but they did not realize that this compound is a ductile intermetallic. In addition to their ductilities, these B2 compounds are stable in air and have good oxidation resistance at room temperature.

Alloying studies have been carried out on ErCu and TmCu to establish: (1) whether the two ordering peaks can be merged or shifted closer together to design an alloy which would have a larger heat capacity over a broader temperature range, and thus may increase the efficiency of the regenerator; and (2) how much the major heat capacity peak temperature (the lower ordering one) could be shifted upward or downward to give some flexibility in designing regenerators to fit a particular requirement.

RESULTS AND DISCUSSION

The pure B2 RM binary compounds studied include ErCu, ErRh, ErAg, ErIr, ErAu, TmCu and TmAg. In addition, many ternary R(M,M′) and (R,R′)M compounds were studied, especially the ErCu- and TmCu-base materials. The non-rare earth dopants include Al, Mn, Fe, Ni, Co, Zn, Ga, Ru and Ag, while the rare earth additives were Sc, Y, La, Ce, Pr, Nd, Gd, Tb, Dy, Ho, Er, Tm and Lu.

Binary B2 RM Compounds

The volumetric heat capacities of the binary ErM (where M = Cu, Rh, Ag, Ir, Au) B2, CsCl-type intermetallic compounds are shown in Fig. 2. Of these five compounds, only ErCu has two magnetic ordering temperatures (~8.5 and ~12.7 K), while the others probably have one magnetic transition: ErAg at about 16 K, ErAu at about 14 K, and ErRh and ErIr below 4 K. It is possible that ErAu may have a second magnetic transition at about 7.5 K but this needs to be verified by other physical property measurements such as the magnetic susceptibility or electrical resistivity. The upswing in the volumetric heat capacity below 5 K of ErRh and ErIr suggests that these two compounds might be good magnetic regenerator materials for cooling below 4 K, but lower temperature heat capacity measurements need to be made to verify the actual peak heat capacity values and their magnetic ordering temperatures. However, the high cost of Rh and Ir will prohibit their widespread use as regenerator materials, regardless of their ordering temperature and heat capacity peak value.

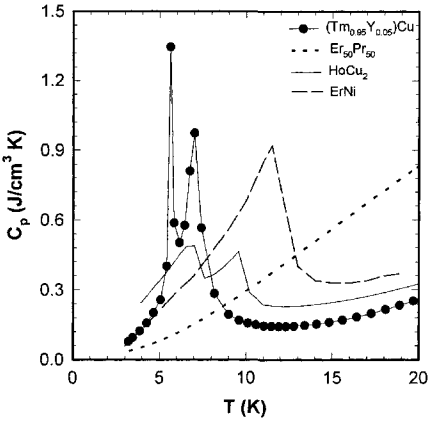

Figure 3. The volumetric heat capacity of $(Tm_{0.95}Y_{0.05})Cu$ from ~3 to 20 K. The corresponding volumetric heat capacities of the cryocooler prototype regenerator materials $Er_{50}Pr_{50}$, $HoCu_2$ and ErNi are also shown.

TmAg, which orders at 7.5 K, has a maximum heat capacity of 0.7 J/cm^{3}K, which is about 50% larger than the double peaks of $HoCu_2$, and would make an excellent replacement regenerator material for either $HoCu_2$ or Er_3Ni.

Rare Earth Additions

The substitutions of R = Sc, La, Ce, Pr and Nd for Er in $(Er_{0.9}R_{0.1})Cu$ have similar effects: the lower ordering temperature at ~8.5 K is wiped-out, the heat capacity at the upper peak (~12.7 K) is greatly reduced and shifted slightly to lower temperatures. The effect of Y is not nearly as drastic: both peaks are shifted to a lower temperature (8.5 to 7 K, and 12.7 to 12.2 K) and the magnitudes of the heat capacity peaks are greatly reduced, especially that of the 8.5 K peak. A similar behavior is observed for R substitution of Tm in TmCu, for R = La, Ce, Pr, and Nd. The substitution of Y for Tm in TmCu is, however, different from the $(Er_{1-x}Y_x)Cu$ alloys, where $0 \leq x \leq 0.15$. The temperatures and the peak volumetric heat capacity values of TmCu are lowered by Y doping. The upper peak temperature drops more rapidly than the lower one, so that they merge for $x = 0.15$. The volumetric heat capacity of $(Tm_{0.95}Y_{0.05})Cu$ is compared to those of the three low-temperature cryocooler prototype regenerator materials in Fig. 3. This alloy would be an excellent regenerator material for cooling down to 5 K.

The heavy lanthanides behave differently from the light lanthanides in that both peaks of pure ErCu still remain upon alloying. In the case of Gd and Tb dopants the peaks are shifted to a higher temperature and the volumetric heat capacities are considerably reduced. The substitution of Dy and Ho, in contrast to the other lanthanides, hardly has any affect on either the ordering temperature or the volumetric heat capacity, and Ho more so than Dy. For Dy, the temperature spread between the lower and upper ordering peaks is widened by about 2 K with low transition temperature shifted downward and the upper temperatures upward.

The substitution of Er for Tm (Tm-rich alloys) and Tm for Er (Er-rich alloys) on the volumetric heat capacity in the $(Tm_{1-x}Er_x)Cu$ pseudo binary system results in an increase of the upper heat capacity peak value of ErCu (1.4 J/cm^{3}K) to that of TmCu (2.8 J/cm^{3}K). The increase, however, is not linear, but has a sinusoid-like shape. The maximum value of the heat capacity for the lower magnetic ordering peak remains essentially constant (1.0 ± 0.3 J/cm^{3}K) as x varies from 0 to 1.0. In general, as x increases, the two ordering peaks shift slowly to higher temperatures.

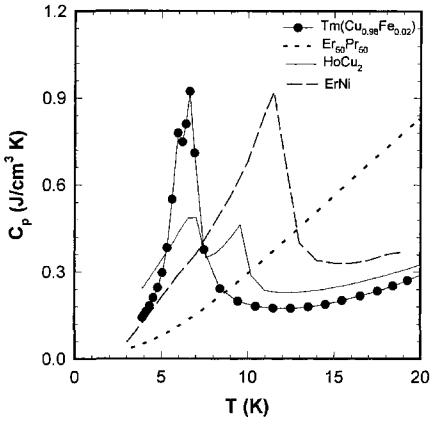

Figure 4. The volumetric heat capacity of $Tm(Cu_{0.98}Fe_{0.02})$ from ~4 to 20 K. The corresponding volumetric heat capacities of the cryocooler prototype regenerator materials $Er_{50}Pr_{50}$, $HoCu_2$ and ErNi are also shown.

Transition Metal Additions

The substitution of Mn, Fe, Co, Ni and Ru for Cu in $Er(Cu_{1-x}M_x)$ and $Tm(Cu_{1-x}M_x)$ have been studied. Nominally x was 0.05, but in some cases it was as large as 0.20 and as small as 0.02. In general, the two magnetic ordering peaks of the ErCu parent compound are shifted to lower temperatures, the upper one faster than the lower ordering peak, but only in the case of Ru additions did the two ordering temperatures merge. The volumetric heat capacities are significantly lowered, with Co additions having the largest effect followed by Ni, Fe and Mn in that order.

For TmCu, the transition metal substitutes caused the two magnetic ordering peaks to merge at $x \cong 0.05$. The heat capacity values at the ordering temperature are significantly reduced, again with Co having the greatest effect followed by Ni, Ru and Fe. The volumetric heat capacity of the $Tm(Cu_{0.98}Fe_{0.02})$ ductile intermetallic compound is shown in Fig. 4 along with the prototype regenerator materials $HoCu_2$, ErNi and $Er_{0.50}Pr_{0.50}$. It is seen that the Fe doped alloy has a much better volumetric heat capacity between 5 to 8 K than $HoCu_2$. But when compared to $(Tm_{0.95}Y_{0.05})Cu$ (Fig. 3) its heat capacity values are significantly smaller.

Main Group Metal Additions

The main group metals (M = Al, Zn and Ga), when substituted for Cu in the ErCu, behave significantly different from the previous alloying agents. The lower ordering peak is shifted to higher temperatures and tends to merge with the upper magnetic ordering peak, and the heat capacity maximum is increased over the undoped ErCu material. For the Al and Ga additions at $x = 0.05$, these compounds have large heat capacities between 12 and 17 K (for Al), and 12 and 18 K (for Ga). The volumetric heat capacity for $Er(Cu_{0.95}Ga_{0.05})$ along with the prototype materials is shown in Fig. 5. As far as we are aware this alloy has the highest heat capacity in 15 ± 3 K range of any known material.

The effect of Al and Ga substitutions for Cu in TmCu is different from that noted above for ErCu. In the Tm-based materials, the two ordering peaks merge between the two peaks of the TmCu compound, with a volumetric heat capacity value between those of the two peaks of TmCu. For the $Tm(Cu_{0.95}Al_{0.05})$ compound, the heat capacity is three times larger than that of $HoCu_2$.

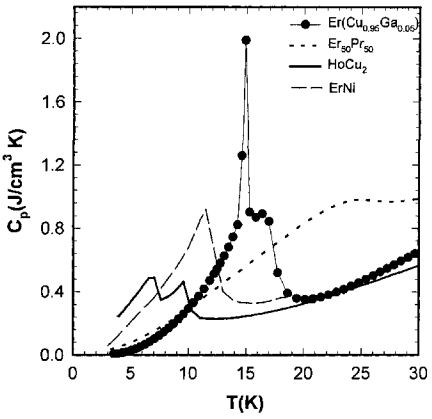

Figure 5. The volumetric heat capacity of $Er(Cu_{0.95}Ga_{0.05})$ from ~3 to 20 K. The corresponding volumetric heat capacities of the cryocooler prototype regenerator materials $Er_{50}Pr_{50}$, $HoCu_2$ and ErNi are also shown.

Recommended Regenerator Materials

Of the alloys studied, the best material for a regenerator which operates below 4 K is ErRh, followed closely by ErIr, see Fig. 2. But because of the cost of Rh and Ir, these two intermetallic compounds would see limited use.

There are eleven Er- and Tm-based B2 CsCl-type intermetallic compounds that could be used as a replacement for $HoCu_2$. The best is TmCu, which has a maximum heat capacity value more than six times larger than that of $HoCu_2$. However, when 5% Lu is substituted for Tm, i.e. $(Tm_{0.95}Lu_{0.05})Cu$ the peak maximum is lowered by about half of that of TmCu, but the breadth of the pair of peaks is wider and thus is more competitive with $HoCu_2$, see Fig. 6.

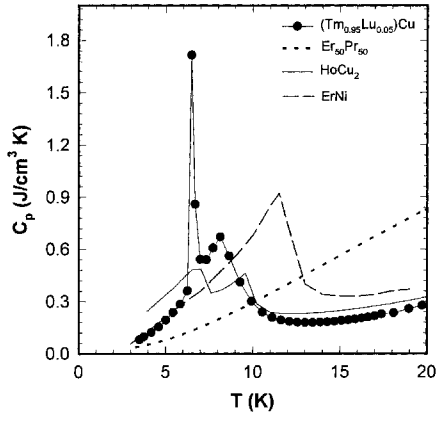

Figure 6. The volumetric heat capacity of $(Tm_{0.95}Lu_{0.05})Cu$ from ~3 to 20 K. The corresponding volumetric heat capacities of the cryocooler prototype regenerator materials $Er_{50}Pr_{50}$, $HoCu_2$ and ErNi are also shown.

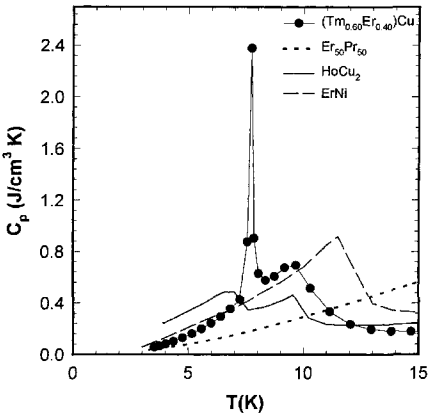

Figure 7. The volumetric heat capacity of $(Tm_{0.60}Er_{0.40})Cu$ from ~3 to 20 K. The corresponding volumetric heat capacities of the cryocooler prototype regenerator materials $Er_{50}Pr_{50}$, $HoCu_2$ and ErNi are also shown.

In the 6 to 9 K temperature range (i.e. between the $HoCu_2$ peaks and the ErNi peak) there are four ErCu-based materials and three $(Tm_{0.6}Er_{0.4})Cu$ compounds which have significant heat capacities and could be used as regenerator materials covering this region. The best of these is $(Tm_{0.6}Er_{0.4})Cu$, see Fig. 7.

There is one $(Tm_{1-x}Er_x)Cu$ alloy which would be competitive with ErNi prototype regenerator material, namely $(Tm_{0.2}Er_{0.8})Cu$, see Fig. 8. As a matter of fact the performance of the two materials as regenerators would be expected to be nearly the same if the two compounds were used as spheres. However, since $(Tm_{0.2}Er_{0.8})Cu$ is ductile, it can be fabricated into forms (parallel plates, monolithic perforated cylinders, etc.) which have much higher efficiencies than

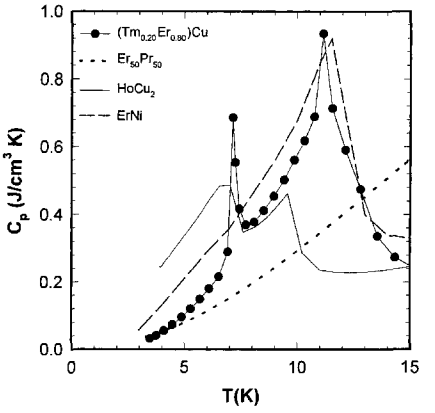

Figure 8. The volumetric heat capacity of $(Tm_{0.20}Er_{0.80})Cu$ from 3 to 20 K. The corresponding volumetric heat capacities of the cryocooler prototype regenerator materials $Er_{50}Pr_{50}$, $HoCu_2$ and ErNi are also shown.

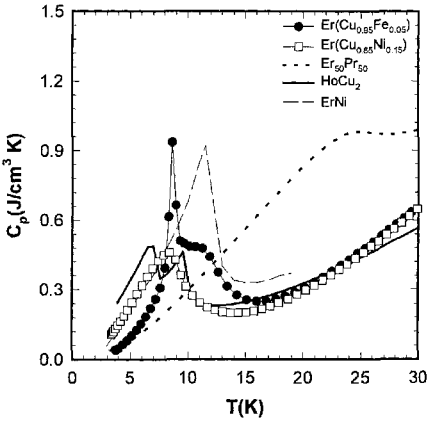

Figure 9. The volumetric heat capacities of $Er(Cu_{0.95}Fe_{0.05})$ and $Er(Cu_{0.85}Ni_{0.15})$ from ~3 to 30 K. The corresponding volumetric heat capacities of the cryocooler prototype regenerator materials $Er_{50}Pr_{50}$, $HoCu_2$ and ErNi are also shown.

packed particle beds.[15] But, since ErNi is a brittle intermetallic compound it is impossible, or nearly so, to fabricate into parallel plates, etc.

There is one major drawback to these Tm-based B2 intermetallic compounds, and that is the cost of Tm which can be 2 to 5 times more expensive than Er. There are, however, Er-based CsCl-type intermetallic compounds which are also better than the current prototypes, but they do not have nearly as large heat capacities as the Tm-based materials noted above. As a replacement for $HoCu_2$, the $Er(Cu_{0.85}Ni_{0.15})$ alloy is the best Er-based material, while for the 6 to 9 K temperature range $Er(Cu_{0.95}Fe_{0.05})$ would be the choice material, see Fig. 9.

For temperatures above 12 K there are three $Er(Cu_{0.95}M_{0.05})$ alloys, where M = Al, Zn and Ga, which would make excellent regenerator materials. The best being M = Ga, see Fig. 5.

SUMMARY

A large number of $(Er_{1-x}R_x)M$ and $(Tm_{1-x}R_x)M$ compounds have the B2 CsCl-type crystal structure and are also ductile. Several of them have heat capacities below 15 K, which are greater than those of the currently used prototype materials, such as $HoCu_2$, Er_3Ni and ErNi. In addition because the Er- and Tm-based intermetallics with the B2 structure are ductile, they can be easily fabricated into more efficient regenerator forms, while this is nearly impossible to do for the prototype compounds because they are brittle intermetallics. Furthermore, it has been shown that in general the Tm-based compounds are far better materials than Er-based compounds as regenerator materials because of their much higher volumetric heat capacities. When the ductile Er- and Tm-based B2 intermetallic compounds are utilized as regenerator materials for cooling below 15 K, the performances of cryocoolers will be improved, their efficiencies increased, and the no load temperatures will be lower as compared to the currently utilized regenerator materials ($HoCu_2$, Er_3Ni and ErNi).

ACKNOWLEDGEMENTS

Different aspects of this research were supported by Atlas Scientific, San Jose, California and by the Office of Basic Energy Sciences, Materials Sciences Division of the U.S. Department of Energy under Contract No. W-7405-ENG-82.

REFERENCES

1. Buschow, K.H.J., Olijhoek, J.F. and Miedema, A.R., "Extremely Large Heat Capacities Between 4 and 10 K," *Cryogenics*, vol. 15 (1975), pp. 261-264.
2. Sahashi, M., Tokai, Y., Kuriyama, T., Nakagome, H., Li, R., Ogawa, M. and Hashimoto, T., "New Magnetic Material R_3T System with Extremely Large Heat Capacities Used as Heat Regenerators," *Adv. in Cryogenic Engineering,* Vol. 35B, Plenum Publishing Corp., New York (1990), pp. 1175-1182.
3. Kuryama, T., Hakamada, R., Nakagome, H., Tokai, Y., Sahashi, M., and Li, R., Yoshida, O., Matsumoto, K. and Hashimoto, T., "High Efficient Two-State GM Refrigerator with Magnetic Materials in Liquid Helium Temperature Region," *Adv. in Cryogenic Engineering,* Vol. 35B, Plenum Publishing Corp., New York (1990), pp. 1261-1269.
4. Ackerman, R.A., *Cryogenic Regenerative Heat Exchangers*, Plenum Press, New York, 1997, p. 98.
5. Satoh, T., Onishi, A., Umehara, I., Adachi, Y., Sato, K. and Minehara, E.J., "A Gifford-McMahon Cycle Cryocooler Below 2 K," *Cryocoolers 11,* edited by R.G. Ross, Jr., Kluwer Academic/Plenum Publishers, New York, (2001) pp. 381-386.
6. Gschneidner, K.A., Jr., Pecharsky, A.O. and Pecharsky, V.K., "Ductile, High Heat Capacity, Magnetic Regenerator Alloys for the 10 to 80 K Temperature Range," *Cryocoolers 11,* edited by R.G. Ross, Jr., Kluwer Academic/Plenum Publishers, New York (2001), pp. 433-441.
7. Kashani, A., Helvensteijn, B.P.M., Maddocks, J.R., Kittel, P., Feller, J.R., Gschneidner, K.A., Jr., Pecharsky, V.K. and Pecharsky, A.O., "Performance of a New Regenerator Material in a Pulse Tube Cooler," *Adv. in Cryogenic Engineering*, Vol. 47A, Amer. Institute of Physics, Melville, NY (2002), pp. 985-991.
8. Tanaeva, I.A., Ikeda, H., van Bokhoven, L.J.A., Matsubara, Y., and de Waele, A.T.A., "Heat Capacities and Magnetic Moments of Potential Regenerator Materials at Low Temperatures," *Cryogenics* vol. 43 (2003), pp. 441-448.
9. Pecharsky, V.K., Moorman, J.O., and Gschneidner, K.A., Jr., "A 3–350 K Fast Automatic Small Sample Calorimeter," *Rev. Sci. Instrum.,* vol. 68 (1997), pp. 4196-4207.
10. Gschneidner, K. Jr., Russell, A., Pecharsky, A., Morris, J., Zhang, Z., Lograsso, T., Hsu, D., Lo, C.H.C., Ye, Y., Slager, A. and Kesse, D., "A Family of Ductile Intermetallic Compounds," *Nature Materials* vol. 2 (2003), pp. 587-590.
11. Morin, P., and Schmidt, D., "Competition Between Multi-q Antiferromagnetic Structures in Cubic Rare Earth-Copper Compounds," *J. Magn. Magn. Mater.,* vol. 21 (1980), pp. 243-256.
12. Hill, R.W., "The Specific Heats of ErAg and TbAg Between 0.5 and 21 K," *J. Phys. F: Met. Phys.* vol. 17 (1987), pp. 243-255.
13. Rawat, R. and Das, I, "The Similar Dependence of the Magnetocaloric Effect and Magneto-resistance in TmCu and TmAg Compounds and Its Implications," *J. Phys. Condens. Matter*, vol. 13 (2001), pp. L379-L387.
14. Biwa, T., Yagi, W. and Mizutani, U., "Evaluation of Low-temperature Specific Heats and Thermal Conductivities of Er-Ag Alloys as Regenerator Materials," *Jpn. J. Appl. Phys.,* vol. 35 (1996), pp. 2244-2248.
15. Barclay, J.A. and Sarangi, S., "Selection of Regenerator Geometry for Magnetic Refrigeration Applications," A.S.M.E. Annual Winter meeting, New Orleans (December 1984).

Status of the Development of Ceramic Regenerator Materials

T. Numazawa[1], K. Kamiya[1], T. Satoh[2], H. Nozawa[3] and T. Yanagitani[3]

[1]Tsukuba Magnet Laboratory, National Institute for Materials Science
Tsukuba 305-0003, Japan
[2]Cryogenics Department, Sumitomo Heavy Industries, Ltd.
Nishitokyo City, Tokyo 188-8585, Japan
[3]Ceramics Division, Konoshima Chemical Co. Ltd.
Kagawa 769-1103, Japan

ABSTRACT

This paper describes the status of recent developments of ceramic regenerator materials. First, improvement of the thermal and mechanical properties of Gd_2O_2S (GOS) regenerator material has been achieved. Since the heat capacity of GOS is very high (> 1 J/cm^3), with a λ type peak at 5.2 K, the thermal penetration depth is about 30% smaller than that of $HoCu_2$ below 6 K. Thus, a small particle size (less than 0.3 mm) with a high homogeneity is important for optimization of cooling efficiency. The recent introduction of Hot Isostatic Pressing (HIP) for fabricating GOS particles has been shown to be very effective in increasing the quality. Higher thermal conductivity and a withstanding pressure higher than 5 MPa have been achieved.

Secondly, new concept regenerators using a variety of ceramic materials have been considered. Multicomponent magnetic materials that consist of $(Gd_xTb_{1-x})_2O_2S$ have been fabricated for cooling temperatures above 6 K. Magnetic materials consisting of two magnetic elements show a broad heat capacity peak involving the combination of the two different heat capacity curves. By adjusting the heat-treatment conditions with catalyst materials there is a high potential for controlling the heat capacity curve using multicomponent magnetic materials.

In order to freeze the movement of the spherical magnetic materials in the regenerator, a 'solid' 4 K regenerator consisting of sintered GOS particles has been fabricated. Cooling-test results with the solid GOS regenerator show a certain level of decrease in the cooling capacity at 4.2 K. For a particle size of 0.4 mm in diameter, the cooling capacity at 4.2 K decreases by 20% compared with a regular regenerator with unsintered particles. However, this value is comparable to the cooling capacity achieved using only $HoCu_2$ for the lowest temperature portion of the 2nd regenerator.

INTRODUCTION

Ceramic magnetic regenerator materials (GAP = $GdAlO_3$ and GOS = Gd_2O_2S) have demonstrated improvement of the cooling performance of 4 K cryocoolers. For example, replacing $HoCu_2$ with GOS in a typical 4 K cryocoolers and be expected to increase the cooling capacity by 20% at 4.2 K.[1,2] A long-term operational test with GOS has been conducted successfully[3], and GOS is

Cryocoolers 13, edited by R. G. Ross, Jr.
Springer Science+Business Media, Inc., New York, 2004

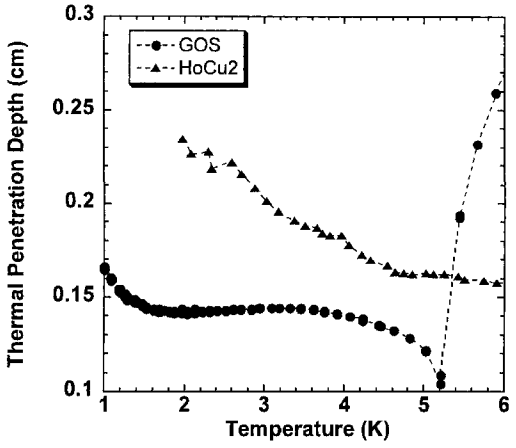

Figure 1. Thermal penetration depth of GOS and $HoCu_2$ at 1 Hz.

being used as a commercial regenerator material for 4 K cryocoolers. Efforts for improving the regenerator quality are continuing.

This paper first reports on recent improvements in the thermal and mechanical properties of GOS. Next, we show the status of the development of new-concept regenerators that make use of these ceramic magnetic materials as well as the fabrication flexibility offered by these materials compared with metallic compounds. Then, multicomponent magnetic materials for broadening the heat capacity curves and a 'solid' 4 K regenerator bases on sintered magnetic material are shown.

IMPROVEMENT OF QUALITY OF GOS REGENERATOR MATERIAL

Thermal conductivity is one of the important factors determining the thermal penetration depth of a regenerator material. Figure 1 shows the thermal penetration depth of GOS and $HoCu_2$. This value relates to the thermal conductivity and the heat capacity given in Fig. 2. Since the heat capacity of GOS becomes very high (> 1 J/cm^3) with a λ type peak at 5.2 K, the thermal penetration depth of GOS is roughly 30% smaller than that of $HoCu_2$ below 6 K. Thus, a smaller particle size (less than 0.3 mm in diameter), which is typical of that used in conventional regenerator materials, is required for the GOS regenerator material.

The spherical particles of GOS can be fabricated between 0.2 mm and 0.8 mm in diameter using a specially designed granulator with ultra-fine raw materials with a diameter of ~ 0.3 μm.[1] The

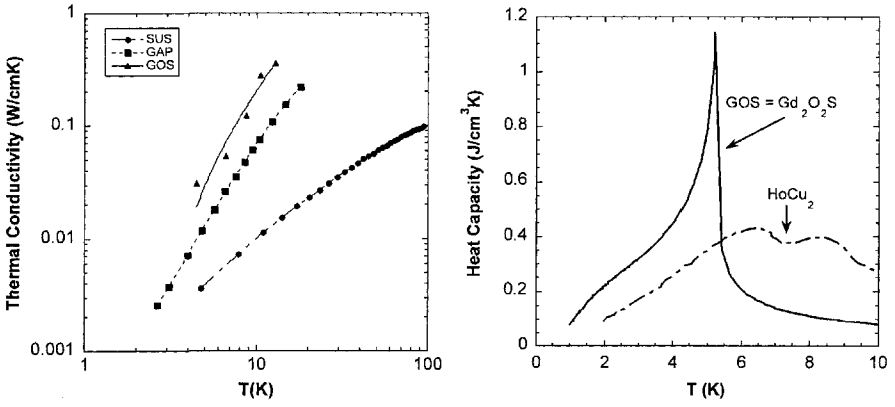

Figure 2. Conductivity of stainless steel, GOS and GAP, and volumetric heat capacity of GOS and $HoCu_2$.

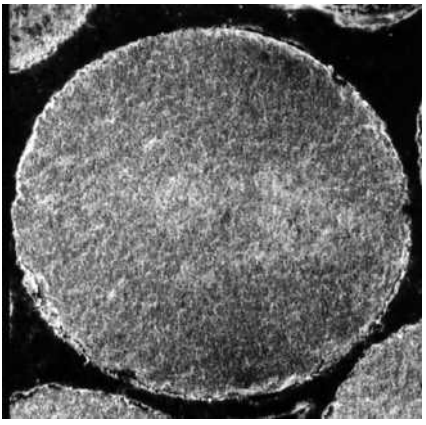

Figure 3. Cross sectional view of the GOS particle with diameter of 0.25 mm fabricated by HIP process.

thermal and mechanical properties of polycrystalline GOS show a high level of the quality as a regenerator material: thermal conductivity of 0.3 W/cm·K at 4 K and a Vickers hardness of 900. The relative density of the fabricated polycrystalline GOS is about 99 % compared to the theoretically predicted value. This indicates that void area still remains in the particles and that broken particles may be produced during long-term operation—although no broken powders have been observed. In addition, we found that the lower density also causes less thermal conductivity in the particles. Since our heat capacity measurement makes use of a heat relaxation method, the unsteady heat flow process in the sample can be observed directly through the temperature changes. The time dependent temperature curve normally shows a simple exponential shape, but if the sample has poor thermal properties, the curve becomes more complex including several different time constants. This is typically caused by poor uniformity of the density in the sample. Since it is difficult to measure the thermal conductivity of small particles with a diameter less than 1 mm, this experiment is useful to estimate the uniformity of regenerator particles.

We found evidence of such a density fluctuation in the GOS particles when the particle size became smaller than 0.3 mm. In order to increase the relative density of the GOS particles, we introduced Hot Isostatic Pressing (HIP) as a process at the final stage of the regenerator fabrication. By using HIP, the relative density of the GOS particles was increased up to 99.5%, and the uniformity of the density improved appreciably. Figure 3 shows a photograph of a cross section of a GOS particle of 0.25 mm diameter fabricated by the new HIP process. There is no observed void area, and consequently its time-dependent heat relaxation curve shows a typical simple exponential shape. The new fabrication process also increased the withstanding pressure of the particles. Since the regenerator materials are packed into a regenerator housing under high pressure, the regenerator materials must have enough strength to withstand the pressure. The fabricated GOS regenerator materials have achieved a withstanding pressure of > 5 MPa. These improved properties have contributed to achieving stable cooling capacity.

NEW REGENERATOR CONCEPTS BY THE CERAMIC MAGNETIC MATERIALS

It is difficult to cover a wide span of cooling temperatures with a single magnetic regenerator material, especially from 10 K to 4 K or lower temperatures. Thus, multilayer regenerators, which consist of several magnetic materials with different peak temperatures of the heat capacity, are useful to increase the performance of 4 K cryocoolers.[4] However, fabricating a multilayer regenerator is more complex, and therefore, may be less reliable and more expensive. We are seeking new, simpler methods for fabricating regenerators. In the present paper, two kinds of new approaches are described.

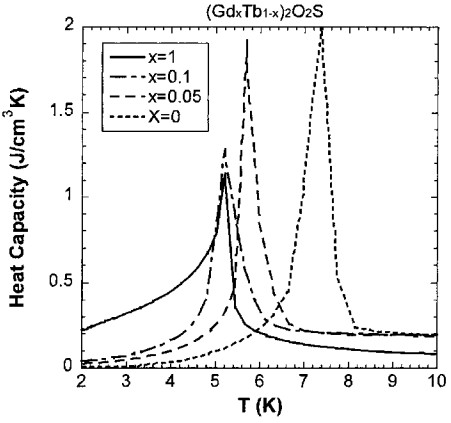

Figure 4. Volumetric heat capacity of $(Gd_xTb_{1-x})_2O_2S$ system.

Multicomponent Regenerator Materials

GOS shows a high volumetric heat capacity between 3 K and 5 K as shown in Fig. 2, but its heat capacity decreases significantly above the magnetic transition temperature of 5.2 K. Thus, other materials are needed to compensate for the lack of the heat capacity above 5.2 K. The material $(Gd_xTb_{1-x})_2O_2S$ has been proposed as a candidate for regenerator materials for temperatures between 6 K and 8 K.[5] Figure 4 shows heat capacity curves for fabricated bulk samples of $(Gd_xTb_{1-x})_2O_2S$. The heat capacity curves show a strong dependence on the composition x of Gd and Tb elements, and the range of $x < 0.1$ is found to provide a usefully high heat capacity for temperatures above 6 K.

When the heat treatment condition is optimized, the heat capacity data for newly fabricated $(Gd_{0.05}Tb_{0.95})_2O_2S$ shows a broad peak, as shown in Fig. 5. This suggests that the $(Gd_{0.05}Tb_{0.95})_2O_2S$ consists of several magnetic materials with slightly different transition temperatures; in other words, there remains several unreacted magnetic materials with different concentrations. However, if the heat treatment time is long enough, the material tends toward a single magnetic phase. This occurs much more clearly in small regenerator particles because of their small size. More thorough heat treatment like HIP is needed to improve the thermal and mechanical properties of the regenerator materials.

In order to satisfy these conflicting conditions between the reacting time and the heat treatment time, multicomponent magnetic materials have been considered. Figure 6 shows the heat capacity

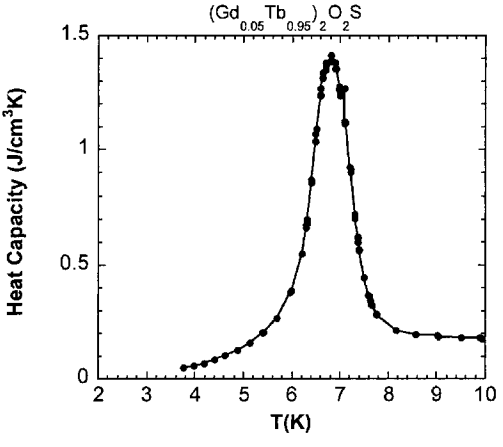

Figure 5. Volumetric heat capacity of $(Gd_{0.05}Tb_{0.95})_2O_2S$ with optimized heat treatment condition.

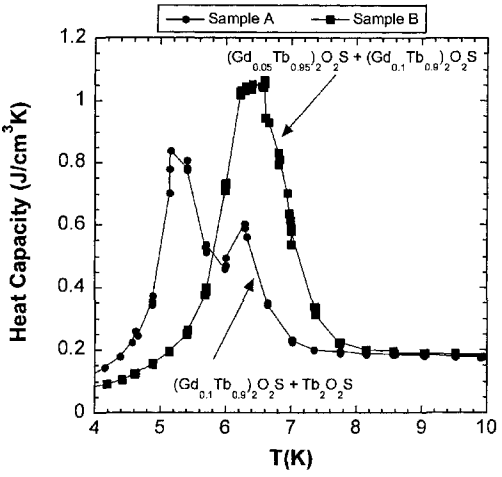

Figure 6. Volumetric heat capacity of multicomponent magnetic materials.
Sample A = $(Gd_{0.1}Tb_{0.9})_2O_2S + Tb_2O_2S$ and Sample B = $(Gd_{0.05}Tb_{0.95})_2O_2S + (Gd_{0.1}Tb_{0.9})_2O_2S$.

curves for fabricated multicomponent magnetic materials consisting of two magnetic elements. The sample A, $(Gd_{0.1}Tb_{0.9})_2O_2S + Tb_2O_2S$, shows two peaks in the heat capacity relating to two different curves. The sample B, $(Gd_{0.05}Tb_{0.95})_2O_2S + (Gd_{0.1}Tb_{0.9})_2O_2S$, shows a more integrated smooth curve without the two sharp peaks. The key parameters in the fabrication process are mainly heat treatment time, temperature, and catalyst material. The as-fabricated condition of sample B is much closer to that of a real regenerator particle. The disappearance of the sharp peaks with sample B suggests that the two magnetic phases are diffused uniformly in the sample, but both phases still hold their magnetic properties. This result shows that multicomponent magnetic materials have a high potential for allowing the heat capacity curve to be tailored for specific applications.

Solid Regenerator

Regenerator materials are exposed to the oscillating pressure changes brought about by the oscillatory helium gas flow in the regenerator. This causes collisions and friction between the regenerator particles, since the particles are slightly movable. Such motion of the particles occasionally results in damage to the regenerator material if the strength of the particles is not high enough. This is the main reason why 4 K regenerator materials must be fabricated into a spherical form with a high Vickers hardness and a smooth surface. A wire mesh regenerator is often used for the higher temperatures, and it is much easier to assemble into a regenerator. However, conventional 4 K regenerator materials are brittle, and consequently they are difficult to make into a wire form. If the regenerator particles are bonded firmly to each other, the motion of the particles can be frozen. This is the concept of a 'solid' type regenerator considered here.

Ceramic magnetic materials have a high potential for being made into solid regenerators using the sintering process. This is because the sintering temperature for ceramics is lower than their melting point, and therefore, this temperature margin makes it much easier to use a diffusion bonding method. Thus, we have applied this technique to the GOS regenerator particles. Figure 7 shows the fabrication process for achieving a solid, sintered GOS regenerator.

First, we prepared a cylindrical housing that was made of GOS with a wall thickness of 1 to 2 mm. Then we firmly pressed the GOS particles into the GOS housing with an amount of pressures similar to that used in packing a conventional regenerator. After the density of the regenerator reached a high enough value of ~ 4.2 g/cm³K, the GOS cylinder was heat-treated at a temperature of 1200 ~ 1500°C for several hours. Finally the GOS cylinder was machined to fit the 2nd regenerator of a cryocooler.

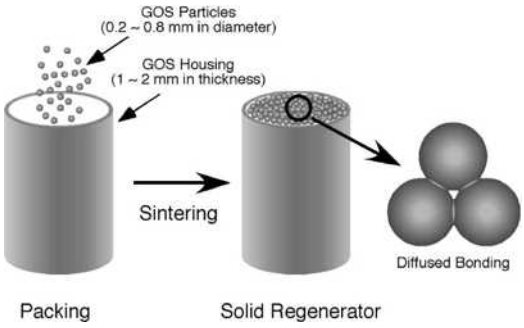

Figure 7. Fabrication process of 'solid' GOS regenerator.

Figure 8. Picture of the fabricated solid GOS regenerator.

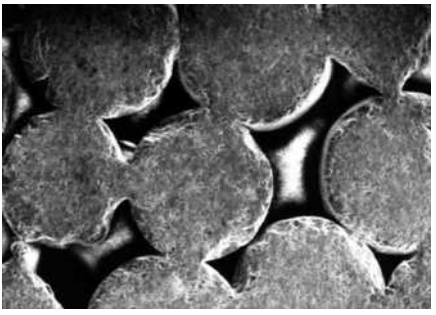

Figure 9. Cross sectional view of the solid GOS regenerator.

Figure 8 shows a picture of the fabricated solid GOS regenerator. The sintered GOS particles are tightly bonded with high homogeneity in the entire cylinder. Figure 9 shows a cross-sectional view of the solid GOS regenerator. The GOS particles are well bonded, and defects at the diffused bonding area are not found. Excessively long processing time during diffusion bonding results in distortion of the spherical particles and decreased void volume of the regenerator. Thus, the heat-treating time must be carefully controlled. In this experiment, the size of the sintered GOS regenerator is 29 mm in diameter and 30 mm in height. For this case, with GOS particles of 0.4 mm in diameter, the density of the sintered GOS particles without the GOS housing was ~ 4.7 g/cm^3, while that of the regularly packed GOS with 'free motion' was ~ 4.2 g/cm^3. Thus, the density increased by about 11 % by the sintering process, and this also decreased the void volume of the regenerator.

Thermal performance tests have been carried out with a Sumitomo SRDK-408D GM cryocooler with a cooling capacity of 1 watt at 4.2 K. The 2nd regenerator consisted of Pb, $HoCu_2$ and GOS, from the hot to the cold end. Three kinds of the sintered GOS regenerators with particle sizes of 0.25 mm, 0.4 mm, and 0.7 mm in diameter were prepared. Figure 10 shows the cooling capacity at 60 Hz operation as a function of 1st stage temperature and GOS particle size. As a reference, GOS particles of 0.4 mm in diameter without sintering were also tested. It is clear that the cooling capacity of the sintered GOS with 0.4 mm particle size is about 20% lower than that of the reference GOS without sintering. However, it is noticeable that the cooling capacity of the sintered GOS is comparable to that of the $HoCu_2$ regenerator material. This experimental condition has not been fully optimized for thermal efficiency. For example, the sintered GOS regenerator consists of both the sintered particles and the GOS housing, and the housing does not contribute effectively to the regenerator function, though the weight of the GOS housing occupies up to 10% of the total weight.

When the sintered particles size is changed from 0.7 mm and 0.25 mm, there is a strong correlation between the cooling capacity and the particle size. In particular, the 0.7 mm particle size

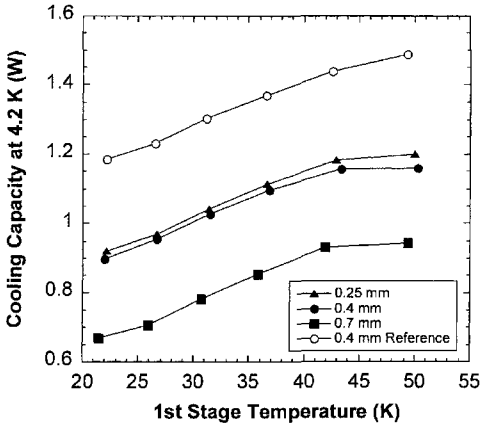

Figure 10. Cooling capacity at 4.2 K as functions of 1st stage temperature and the GOS particle size.

yields a decrease in cooling capacity by 20% compared to that with 0.4 mm-size particles. On the other hand, the 0.25 mm particles result in a slightly higher cooling capacity than with the 0.4 mm particles. This tendency is similar to that with the regular regenerator without sintering. Namely, decreased cooling capacity mainly comes from poor thermal diffusivity and smaller heat exchange area due to the larger size particles. For the smaller size particles, the pressure drop in the regenerator becomes larger because of the smaller volume of the cooling channels. However, the result for the 0.25 mm size particles suggests that the thermal diffusivity is still a dominant factor for the cooling capacity. Another factor in the thermal loss in the sintered regenerator is the thermal conduction loss caused by the better thermal links between the sintered particles. Also, there is some amount of additional axial heat conduction through the GOS housing wall and the small gap between the GOS housing and the regenerator housing. The conduction loss coming from the GOS housing can be reduced by using a thinner wall in future developments. However, the thermal loss from the bonded particles is essential to the method. Quantitative estimation of the thermal loss based on measuring the thermal conductivity of sintered particles is being investigated.

SUMMARY

The current development status of ceramic regenerator materials is summarized as:

1. Using the HIP fabrication process for generating GOS particles has achieved a relative density of 99.5% and a withstanding pressure of higher than 5 MPa.
2. The two-component material, $(Gd_{0.05}Tb_{0.95})_2O_2S$ + $(Gd_{0.1}Tb_{0.9})_2O_2S$ has shown that two magnetic phases can be diffused uniformly in a sample and retain their individual magnetic properties. Three or four components will be more effective in realizing a broader heat capacity curve.
3. A solid regenerator material achieved by sintering the GOS particles has been successfully fabricated, and the sintered material has been used in a real regenerator. The major thermal loss comes from thermal conduction through the bonded particles and the wall of the GOS housing.
4. Sintered regenerator magnetic materials provide for easier assembly and maintenance of the regenerator.

REFERENCES

1. Numazawa, T. et al., "A New Ceramic Magnetic Regenerator Material for 4 K Cryocoolers," *Cryocoolers 12*, Kluwer Academic/Plenum Publishers, New York (2003), p. 473.
2. Satoh, T. and Numazawa, T., "Cooling Performance of a 4 K GM Cryocooler with New Ceramic Magnetic Regenerator Materials", *Cryocoolers 12,* Kluwer Academic/Plenum Publishers, New York (2003), p. 397.

3. Ikeya, Y., Numazawa, T. and Li, R., "Improvement of 4 K GM Cooling Performance with a New Regenerator Material," *Cryocoolers 12,* Kluwer Academic/Plenum Publishers, New York (2003), p. 403.

4. Kuriyama, T., Takahashi, M., Nakagome, H., Hashimoto, T., Nitta, H. and Yabuki, M., "Development of 1 Watt Class 4 K GM Refrigerator with Magnetic Regenerator Materials," *Adv. in Cryogenic Engineering,* Vol. 39B, Plenum Publishing Corp., New York (1994), p. 1335.

5. Numazawa, T., Kamiya, K., Satoh, T., Nozawa, H. and Yanagitani, T., "Performance of Gd-Tb Oxysulfide Ceramic Regenerator Material for G-M Cryocoolers," *Adv. in Cryogenic Engineering*, Vol. 49B, Amer. Institute of Physics, Melville, NY (2004), pp.1598-1606.

Doped $AMnO_3$ Perovskites Suitable for Use in Magnetic Cooling Devices

A.S. Chernyshov[1], M.I. Ilyn[1], A.M. Tishin[1], O.Yu. Gorbenko[2], V.A. Amelichev[2], S.N. Mudretsova[2], A.F.Mairova[2] and Y.I. Spichkin[3]

[1]Physics Department of M.V. Lomonosov Moscow State University
Moscow, Russia, 119992
[2]Department of Chemistry of M.V. Lomonosov Moscow State University
Moscow, Russia, 119899
[3]Advanced Magnetic Technologies and Consulting, Ltd.
Moscow, Russia, 115114

ABSTRACT

The magnetocaloric properties of samples of $Sm_{0.55}Sr_{0.45}MnO_3$, $(Nd_{0.28}Eu_{0.72})_{0.55}Sr_{0.45}MnO_3$, and $(Nd_{0.46}Tb_{0.54})_{0.55}Sr_{0.45}MnO_3$ ceramics have been investigated in fields up to 1.4 T.

The adiabatic temperature change was measured by a direct method. It was established that the Curie temperature T_C and maximum specific adiabatic temperature change (per Tesla) near T_C in $Sm_{0.55}Sr_{0.45}MnO_3$, $(Nd_{0.28}Eu_{0.72})_{0.55}Sr_{0.45}MnO_3$, $(Nd_{0.46}Tb_{0.54})_{0.55}Sr_{0.45}MnO_3$ were 126, 112 and 76 K and 1.43, 1 and 1 K/T, respectively. The contributions to the magnetocaloric effect in $Sm_{0.55}Sr_{0.45}MnO_3$ were determined with the help of a thermodynamic model. It was shown that the main contribution at the magnetic phase transition is the contribution related with the exchange energy change.

INTRODUCTION

Doped $AMnO_3$ perovskites (manganites) displaying unusual physical properties (colossal magnetoresistivity and giant magnetostriction) also exhibit essential magnetic entropy change.[1-5] The latter circumstance, together with the ability to adjust magnetic ordering temperature by changing composition, makes them suitable for use in magnetic cryocoolers as effective materials for complex working bodies. However, the mechanisms of, and contributions to, the magnetocaloric effect (MCE) in these materials are not well understood. It should also be noted that the choice of the optimal dopant and the optimal doping level in the manganites is not well established in the literature. A number of recent papers have been concerned with the relationship between the tolerance factor t, cation size dispersion σ, and the structural, electrical, and magnetic properties of the perovskite-type manganites.[6-10] The tolerance factor t is defined as $t = (\langle r_A \rangle + r_O) / \sqrt{2}\,(r_{Mn} + r_O)$, where $\langle r_A \rangle$ is the mean radius of the A-site cations, r_{Mn} and r_O are the radii of the manganese and oxygen ions, respectively. It is known[11], that the value of $t = 1$ corresponds to the ideal cubic perovskite structure, and with a decrease of t the perovskite structure transforms to rhombohedral, and with further decrease of t, a perovskite becomes orthorhombic. Dispersion σ, defined as $\sigma^2 = \langle r_A^2 \rangle - \langle r_A \rangle^2$, describes a deviation of the

Cryocoolers 13, edited by R. G. Ross, Jr.
Springer Science+Business Media, Inc., New York, 2004

A-sites cations radii from the mean value. Analysis of literature data[12-15] points to the possible dependence of the magnetocaloric effect on both the tolerance factor of the perovskite structure t and on the dispersion σ. However, analysis of the data is complicated due to the fact that these parameters vary simultaneously.

In this work we directly measured the magnetocaloric effect of three ceramic compositions — $Sm_{0.55}Sr_{0.45}MnO_3$, $(Nd_{0.28}Eu_{0.72})_{0.55}Sr_{0.45}MnO_3$, $(Nd_{0.46}Tb_{0.54})_{0.55}Sr_{0.45}MnO_3$ — using the same value of the tolerance factor (t = 0.927) and the same strontium doping level (i.e. with the same Mn^{3+}/Mn^{4+} ratio) but different values of the σ (see Table 1). We also calculated the contributions to the MCE of $Sm_{0.55}Sr_{0.45}MnO_3$ on the basis of a thermodynamic model.

EXPERIMENTAL DETAILS AND THE MODEL

The ceramic samples were prepared by the folllowing procedure: ash-free paper filters were soaked with water solution of the metal nitrates with a total concentration of about 1 mol/l. Then the ash formed by burning of the dried filters was annealed at 700°C, the powder was pressed into pellets and sintered in air for 16 hours at 1200°C.

The phase purity and lattice parameters were controlled by X-ray diffraction, DSC (differential scanning calorimetry), SEM (scanning electron microscopy) and Raman spectrometry measurements. DCS was accomplished by a Netzsch STA-409 thermoanalyser with a sapphire single crystal as a reference material. Raman spectrometry measurements were performed with a triple monochromator system (Jobin-Yvon T64 000) in a subtractive arrangement and in a backscattering geometry of the incident laser light (514.5 nm line of an Ar^+-ion laser with power of up to 50 kW/cm^2). It was established, that all three samples were single phase with orthorohmbic perovskite structure. The position of the structure-sensitive $A_g(2)$ band in the Raman spectra is a highly sensitive indicator of the perovskite structural distortion.[16] We found the same position of the band for all three samples under study. The result corresponds to negligible variation of the tolerance factor or chemical stoichiometry in the series of the samples.

AC magnetic susceptibility was measured in the temperature range from 10 to 300 K using an APD cryogenic magnetometer (with magnetic field amplitude 10 Oe and frequency of 640 Hz). Direct measurements of the magnetocaloric effect have been carried out from 77 K to 300 K under quasi-adiabatic conditions. Magnetic fields up to 1.4 T were produced by an electromagnet (corrected for demagnetization factor); the typical time for establishing a specific known magnetic field was about 3 seconds. The cylindrical sample (4 mm diameter, 8 mm height, with the long axis along the magnetic field) was placed into an evacuated volume (vacuum about 10^{-3} torr) to reduce the heat exchange. The temperature was measured using a copper-constantan thermocouple.

The contributions to the magnetocaloric effect in $Sm_{0.55}Sr_{0.45}MnO_3$ were determined on the basis of the previously made magnetic and linear thermal expansion measurements.[17] For calculations, a thermodynamic model of the first order magnetic phase transition was used. The model considers a magnetic material in which one magnetic phase can be transformed to another by the field-induced first order magnetic phase transition occurring at a certain critical value of magnetic field. In this case the Gibbs energy in the corresponding magnetic state can be presented in general case as:[18,19]

$$G = G_{ex} + G_{me} + G_a - HI\,, \qquad (1)$$

where G_{ex} is the free energy of the exchange interaction, G_{me} is the energy of the magnetoelastic interaction, G_a is the anisotropy energy, and HI is the magnetic energy (I – magnetization, H – magnetic field). On the basis of Eq. (1) it is possible to calculate the magnetic entropy change ΔS_M and adiabatic temperature change ΔT related with the first order transition induced by the magnetic field. At the transition, the potentials of the magnetic phases should be equal, i.e. $G_1 = G_2$. From this condition it follows that at the transition:

$$\Delta G_{ex} + \Delta G_{me} + \Delta G_a = H_{cr}\Delta I\,, \qquad (2)$$

where the symbol Δ denotes the change of the corresponding parameter across the transition ($\Delta I = I_2 - I_1$) and H_{cr} is the critical magnetic field of the transition. The magnetic entropy change at

the transition can be calculated on the basis of eq. (2) and the magnetic Clausius - Clapeyron equation:

$$\frac{dH_{cr}}{dT} = -\frac{\Delta S_M}{\Delta I} \tag{3}$$

and has the form:

$$\Delta S_M^{tr} = -\left(\frac{\partial \Delta G_{ex}}{\partial T} + \frac{\partial \Delta G_{me}}{\partial T} + \frac{\partial \Delta G_a}{\partial T} - H_{cr} \frac{\partial \Delta I}{\partial T} \right), \tag{4}$$

where $\partial / \partial T$ denotes derivatives of the corresponding values on temperature. Then using equation:

$$\Delta T = -\frac{T}{C_{p,H}} \Delta S_M, \tag{5}$$

where $C_{p,H}$ is heat capacity and T – temperature, it is possible to determine the adiabatic temperature change at the transition:

$$\Delta T^{tr} = \frac{T}{C_{p,H}} \left(\frac{\partial \Delta G_{ex}}{\partial T} + \frac{\partial \Delta G_{me}}{\partial T} + \frac{\partial \Delta G_a}{\partial T} - H_{cr} \frac{\partial \Delta I}{\partial T} \right). \tag{6}$$

As one can see from Eqs. (4, 6), there are several contributions to the magnetocaloric effect at the first order transition (according to the sequence they appear in the parenthesis in Eqs. (4, 6)): the contribution from exchange, magnetoelastic, anisotropy, and magnetic energy changes. In order to calculate ΔS_M^{tr} and ΔT^{tr} temperature dependences one should know the temperature dependences of the values in Eqs. (4, 6).

H_{cr} and ΔI temperature dependences can be determined from experimental magnetization measurements. ΔG_a can be obtained from magnetic anisotropy constant data, but this contribution is usually small in comparison with others. The method of calculation of the magnetoelastic energy change is presented elsewhere.[20,21] ΔG_{me} can be calculated from data on the linear temperature expansion and the linear forced magnetostriction temperature dependency. ΔG_{ex} can be determined on the basis of $H_{cr}\Delta I$, ΔG_a and ΔG_{me} data and Eq. (2).

RESULTS AND DISCUSSION

Figure 1 shows the temperature dependency of the AC magnetic susceptibility of the investigated samples. There is a rapid rise in the susceptibility near the Curie temperature, which was determined to be 126, 112 and 76 K for $Sm_{0.55}Sr_{0.45}MnO_3$, $(Nd_{0.28}Eu_{0.72})_{0.55}Sr_{0.45}MnO_3$, $(Nd_{0.46}Tb_{0.54})_{0.55}Sr_{0.45}MnO_3$, respectively. As one can see from Fig. 1, the transition becomes broader and the maximum susceptibility decreases with increasing σ.

The temperature dependency of the adiabatic temperature change (ΔT) for $Sm_{0.55}Sr_{0.45}MnO_3$ is shown in Fig. 2. Measurements were performed with different magnetic field changes ΔH (up to 1.4 T) during heating and cooling of the sample. The MCE peaks were observed near the Curie temperature, and the maximum ΔT value was ~ 2 K at a temperature of 131 K and ΔH = 1.4 T, which corresponds to the specific adiabatic temperature change ($\Delta T/\Delta H$) of 1.43 K/T (for Gd $\Delta T/\Delta H$ = 2.9 K/T for ΔH = 2 T).[22] Although the MCE was field-reversible, the temperature hysteresis characteristic to the first order magnetic phase transitions was clearly observed. It should be also noted that the $\Delta T(T)$ peak in the compound was rather narrow—about 20 K (the second order MCE peaks are much broader: 60-80 K, and even more for Gd[16]). According to literature data[23,24], the heat capacity and the linear thermal expansion of $Sm_{0.55}Sr_{0.45}MnO_3$ also display a clear temperature hysteresis. Furthermore, linear thermal expansion is abruptly changed at the Curie temperature from the low-temperature (high magnetic moment) and low-volume to the high-temperature (low magnetic moment) and high-volume state, although usually

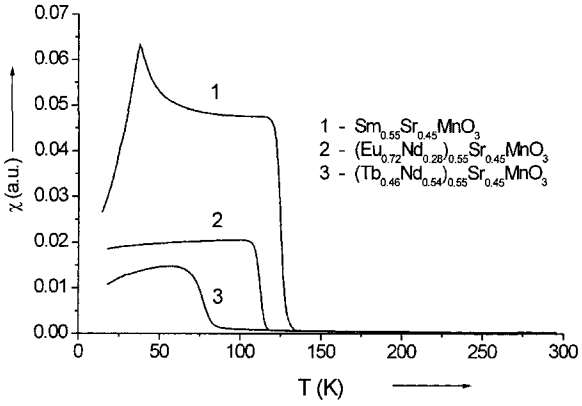

Figure 1. AC magnetic susceptibility temperature dependences: 1 - $Sm_{0.55}Sr_{0.45}MnO_3$, 2 - $Nd_{0.153}Eu_{0.397}Sr_{0.45}MnO_3$, 3 - $Nd_{0.299}Tb_{0.251}Sr_{0.45}MnO_3$.

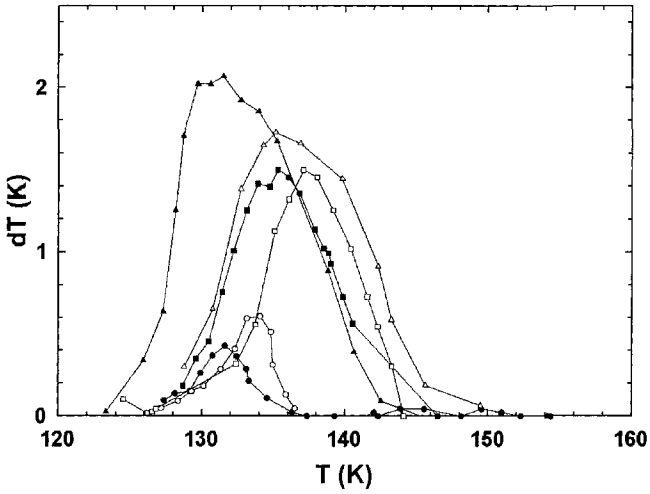

Figure 2. Magnetocaloric effect of $Sm_{0.55}Sr_{0.45}MnO_3$ as a function of temperature. ΔH = 0.5 T (circles), 1 T (squares) and 1.4 T (triangles). Data collected on the heating sample up (open symbols) and cooling it down (closed symbols).

The magnetovolume effect is a transition from a low-volume, low-moment to a high-volume, high-moment state.[25] So, it is possible to assume that the magnetic phase transition in $Sm_{0.55}Sr_{0.45}MnO_3$ is of the first order and possibly accompanied by a structural transition. DSC measurements revealed the latent heat of the transition of ~ 443 J/kg. It also should be noted that the magnetostriction behavior in $Sm_{0.55}Sr_{0.45}MnO_3$ (in particular, large negative volume magnetostriction (~ -4×10^{-4}) observed above the Curie temperature[24]) shows that above Curie temperature the material can be reverted into the low-temperature phase by the magnetic field.

In another two samples of ceramic perovskites — specifically $Nd_{0.299}Tb_{0.251}Sr_{0.45}MnO_3$ and $Nd_{0.153}Eu_{0.397}Sr_{0.45}MnO_3$ — one rare earth element (Sm) was replaced by a mixture of two differ-

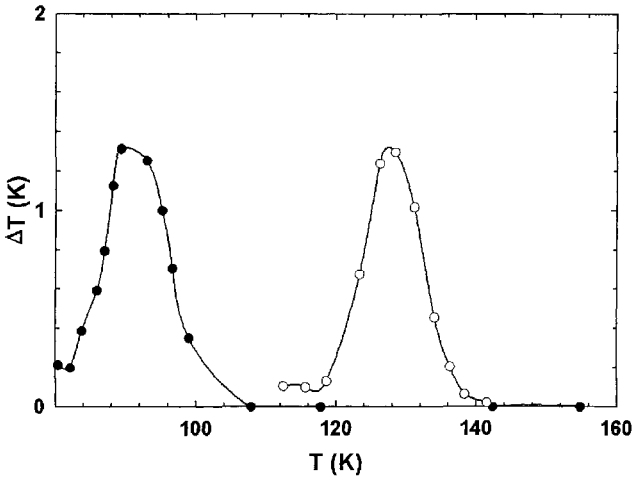

Figure 3. Magnetocaloric effect as a function of temperature for $Nd_{0.153}Eu_{0.397}Sr_{0.45}MnO_3$ (open symbols) and $Nd_{0.299}Tb_{0.251}Sr_{0.45}MnO_3$ (closed symbols).

ent rare earth elements (Nd+Tb and Nd+Eu, respectively). In both samples, the weighted average of the 3^+ rare earth ions radii was equal to that of the Sm^{3+} ion. Figure 3 shows the MCE temperature dependences measured in these samples for a magnetic field change ΔH = 1.4 T. The maximum specific adiabatic temperature changes for $(Nd_{0.28}Eu_{0.72})_{0.55}Sr_{0.45}MnO_3$ and $(Nd_{0.46}Tb_{0.54})_{0.55}Sr_{0.45}MnO_3$ were found to be ~ 1 K/T. The samples revealed the same MCE behavior as $Sm_{0.55}Sr_{0.45}MnO_3$. The maximums of MCE were observed at the lower temperatures and reached lower values than in $Sm_{0.55}Sr_{0.45}MnO_3$ without any monotonic dependence of the ΔT maximum value on the dispersion σ (see also Table 1). At the same time, one can see from Table 1 that under the constant values of the tolerance factor and the doping level the positions of MCE maximums and Curie temperature monotonically depend on the dispersion of the A-sites cations radii σ. This agrees well with the results relating the shift of Curie temperature with the variation of σ for the constant doping level.[10]

The results of calculations of contributions to the magnetic entropy change in $Sm_{0.55}Sr_{0.45}MnO_3$ on the basis of the thermodynamic model are presented in Fig. 4. As one can see, the main contribution comes from the change of the energy of the exchange interaction. This can be related with observed changes in the essential lattice parameter of this compound.[17,24] Earlier, we made analogous calculations for rare earth metals Tb, Dy, Er, and alloys $Tb_{0.5}Dy_{0.5}$, $Fe_{0.49}Rh_{0.51}$ and $Gd_5Si_{1.7}Ge_2$, where the first order magnetic first order transitions were observed.[26] It was found that the main contribution to the magnetocaloric effect in these materials also gave exchange energy change. The obtained results point to the possible driving force of the high magnetocaloric effect general for the first order magnetic phase transitions – modification of the exchange energy.

Using referenced data on the heat capacity[24], it is possible to calculate the adiabatic temperature change ΔT, which in general reproduces the $\Delta S_M(T)$ dependence. Its maximum value is ~1.5 K; this is the value related with the magnetic phase transition itself. Experimental value in $Sm_{0.55}Sr_{0.45}MnO_3$ for ΔH= 1.4 T is 2 K. The excess can be related with the paraprocess, which is especially large near a magnetic phase transition temperature.

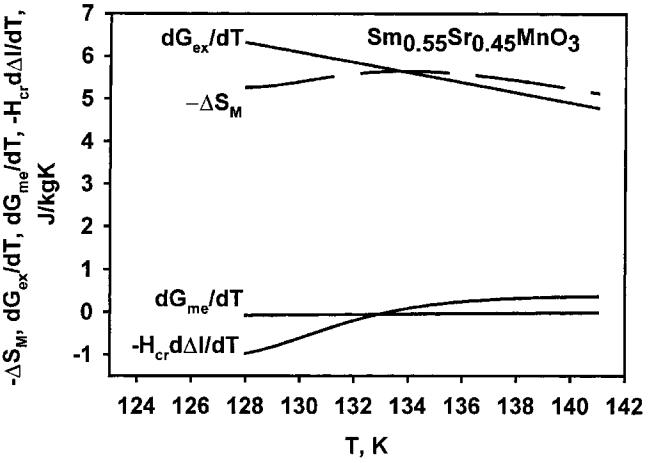

Figure 4. The temperature dependences of the magnetic entropy change ΔS_M under the transition and exchange $\frac{\partial \Delta G_{ex}}{\partial T}$, magnetoelastic $\frac{\partial \Delta G_{me}}{\partial T}$ and magnetic $-H_{cr}\frac{\partial \Delta I}{\partial T}$ contributions in it (see Eq. (4)) in $Sm_{0.55}Sr_{0.45}MnO_3$.

Table 1. Cation size dispersion σ^2, maximum MCE value ΔT_{max} and a temperature Θ, where the maximum value of the MCE occurs.

Sample	σ^2 (a.u.)^2	Θ(K)	ΔT_{max} (K)
$Nd_{0.299}Tb_{0.251}Sr_{0.45}MnO_3$	$8.5 * 10^{-3}$	90	1.4
$Nd_{0.153}Eu_{0.397}Sr_{0.45}MnO_3$	$8.0 * 10^{-3}$	127	1.4
$Sm_{0.55}Sr_{0.45}MnO_3$	$7.8 * 10^{-3}$	131	2.0

CONCLUSIONS

In this work the magnetocaloric effect of $Sm_{0.55}Sr_{0.45}MnO_3$, $(Nd_{0.28}Eu_{0.72})_{0.55}Sr_{0.45}MnO_3$, and $(Nd_{0.46}Tb_{0.54})_{0.55}Sr_{0.45}MnO_3$ ceramic manganites was investigated. It was shown that the character of the $\Delta T(T)$ dependences point to a first order transition at the Curie points in these materials. In the framework of a thermodynamic model of the first order magnetic phase transition, the main contribution to the MCE in $Sm_{0.55}Sr_{0.45}MnO_3$ was determined. It was shown that the model adequately describes the MCE in the vicinity of the magnetic phase transition. The main contribution to the MCE in $Sm_{0.55}Sr_{0.45}MnO_3$ comes from the exchange energy change under the transition. Together with our previous results on the contributions to the MCE at the first order magnetic phase transitions — in rare earth metals, and the alloys $Fe_{0.49}Rh_{0.51}$ and $Gd_5Si_{1.7}Ge_2$ — the obtained data highlight the very important role of this factor in forming of high MCE values at the first order phase transitions. It was also shown that under the constant values of the tolerance factor and the doping level, the positions of the MCE maximums and Curie temperature monotonically depend on the dispersion of the A-sites cations radii σ. However no monotonic dependence of the maximum adiabatic temperature change on the dispersion was found.

ACKNOWLEDGMENT

This work was supported by a grant from the Russian Fund of Basic Research.

REFERENCES

1. Guo, Z.B., Zhang, J.R., Huang, H., Ding, W.P., Du, Y.W., *Appl. Phys. Lett.*, vol. 70 (1997), p. 904.
2. Zhang, X.X., Tejada, J., Xin, Y., Sun, G.F., Wong, K.W., Bohigas, X., *Appl. Phys. Lett.*, vol. 69 (1996), p. 3596.
3. Szewczyk, A., Szymczak, H., Wisniewski, A., Piotrowski, K., Kartaszynski, R, Dabrowski B., Kolesnik, S., Bukowski, Z., *Appl. Phys. Lett.*, vol. 77 (2000), p. 1026.
4. Gschneidner, K.A., Jr., Pecharsky, V.K., *Annu. Rev. Mater. Sci.*, vol. 30 (2000), pp. 387-429.
5. Gschneidner, K.A., Jr., Pecharsky, V.K., *in: Intermetallic Compounds. Principles and Practice*, J.H. Westbrook and R.L. Fleischer, Eds., John Wiley and Sons, NY (2001), Vol. 3.
6. Ramirez, A.P., *J. Phys.: Condens. Matter*, vol. 9 (1997), p. 8171.
7. Rao, C.N.R., Arulraj, A., Cheetham, A.K., Raveau, B., *J. Phys.: Condens. Matter*, vol. 12 (2000), p. 83.
8. Raveau, B., Maignan, A., Martin, C., Hervieu, M., *Chem. Mat.*, vol. 10, (1998), p. 2641.
9. Woodward, P.M., Vogt, T., Cox, D.E., Arulraj, A., Rao, C.N.R., Karen, P., Cheetham, A.K., *Chem Mat.*, vol. 10, (1998), p. 3652.
10. Rodriguez, L.M., Attfield, J.P., *Phys. Rev. B*, vol. 58, (1998), pp. 2426.
11. Roth, R.S., Res, J., *Nat. Bur. Stand.*, vol. 58, (1957), p. 75.
12. Zhong, W., Chen, W., Ding, N., Zhang, A., Hu, *J. Magn. Magn. Mater.*, vol. 195 (1999), p. 112.
13. Guo, B., Du, Y.W., Zhu, J.S., Huang, H., Ding, W.P., Feng D., *Phys. Rev. Lett.*, vol. 78 (1997), p. 1142.
14. Bohigas X., Tejada, J., del Barco, E., Zhang, X.X., Sales M., *Appl. Phys. Lett.*, vol. 73 (1998), p. 390.
15. Guo, Z.B., Yang, W., Shen, Y.T., Du, Y.W., *Solid State Comm.*, vol. 105, (1998), p. 89.
16. Güttler, B., Skuja, L., Gorbenko, O.Yu., Kaul, A.R., Novozhilov, M.A., Babushkina, N.A., Belova, L.M., *in High density magnetic recording and integrated magneto-optics, MRS Proceedings*, vol. 517, (1998), p. 111.
17. Abramovich, A.I., Koroleva, L.I., Michurin, A.V., Gorbenko, O.Yu., Kaul, A.R., Mashaev, M.H., Shimchak, R., Kzhimanska, B., *Fiz. Tverd. Tela (Russia)*, vol. 44, no. 5 (2002), pp. 888 – 892.
18. Tishin, A.M., Spichkin, Y.I., *The Magnetocaloric Effect and Its Applications*, Institute of Physics Publishing, Bristol and Philadelphia (2003), p. 475.
19. Tishin, A.M., *Handbook of Magnetic Materials*, K.H.J. Buschow (Ed.) (1999), vol. 12, pp. 395 – 524.
20. Ewenson, W., Liu, S., *Phys. Rev.*, vol. 178 (1969), p. 783.
21. Cooper, B., Phys. *Rev. Lett.*, vol. 19 (1967), p. 900.
22. Dankov, S.Y., Tishin, A.M., Pecharsky, V.K., Gschneidner, K.A., Jr. Phys. Rev. B, vol. 57 (1998), p. 3478.
23. Aliev, A.M., Abdulvagidov, Sh. B., Batdalov, A.B., Kamilov, I.K., Gorbenko, O.Yu., Amelichev, V.A., *JETP Letters*, vol. 72, (2000), p. 464.
24. Abramovich, A.I., Koroleva, L.I., Michurin, A.V., Gorbenko, O.Yu., Kaul, A.R., *Physica B*, vol. 293, (2000), p. 38.
25. Morelon, L., Algarabel, P.A., Ibarra, M.R., Blasco, J., Garcia-Landa, B., Arnold, Z., Albertini, F., *Phys. Rev. B*, vol. 58, (1998), p. 14721.
26. Spichkin, Y.I., Tishin, A.M., *J. All. Comp.*, (2004), submitted for publication.

Improved Cooling Power by Means of a Regenerator Made from Lead Wire Mesh

A. Waldauf, T. Köttig, S. Moldenhauer, M. Thürk, and P. Seidel

Institut für Festkörperphysik, Friedrich-Schiller-Universität Jena
D-07743 Jena, Germany

ABSTRACT

The regenerator has had a significant influence on the development of refrigerators for cryogenic application. It is a key component in every cryocooler because it efficiently cools and heats up the gas as it flows between the compressor and the expansion space and vice versa. An essential parameter in the regenerator design is the heat capacity ratio.[1] In addition, the pressure drop across the regenerator must be minimized to achieve maximum p-V work in the expansion space.

This paper describes the design and the manufacturing process of a regenerator partially filled with lead screens in order to decrease the pressure drop compared to a regenerator filled with lead spheres. Furthermore they offer a high heat capacity ratio. Our four valve pulse tube refrigerator (FVPTR) was equipped with such a regenerator. The performance of this cooler is presented in this paper. This presentation includes experimental loss analysis as well.

At present the cooler provides a cooling power of 120 W at 74 K and 40 W at 34 K. The minimum no-load temperature achieved is 17 K.

INTRODUCTION

It is well known that lead is a common regenerator material for working temperatures between 20 and 50 K. Because of its low stability it is not possible to manufacture gauze discs from pure lead strands. Nowadays spheres with a typical diameter of approximately 200 μm are used. These spheres have two decisive disadvantages. Firstly it is very difficult to fix them at the right place in the regenerator, secondly they have a larger pressure loss than gauze discs.[2]

This work aimed at building a pulse tube cooler which has a high cooling performance in the entire temperature range between 20 and 80 K. To fulfill this approach we have designed a new regenerator with a lead wire mesh in order to decrease the pressure drop and to have a regenerator material with a high heat capacity at lower working temperatures. We chose a coaxial structure because this arrangement is the most compact and convenient one for current applications.[3] We have built the cooler in a four valve arrangement, which includes two additional valves at the hot end of the pulse tube to achieve the proper phase shift between pressure and volume flow.[4,5,6]

Cryocoolers 13, edited by R. G. Ross, Jr.
Springer Science+Business Media, Inc., New York, 2004

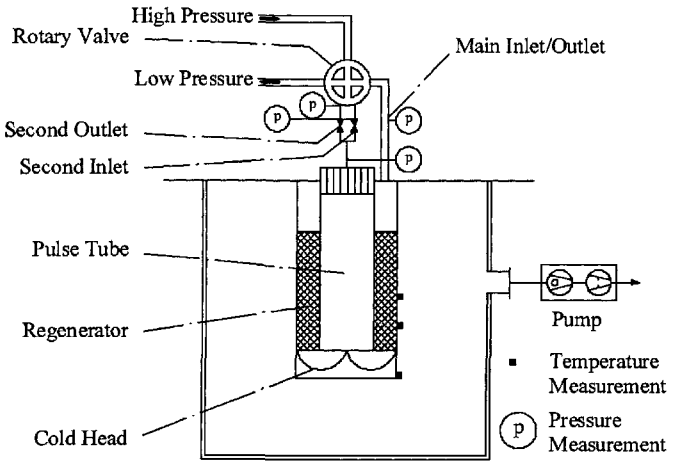

Figure 1. Schematic diagram of the FVPTR.

EXPERIMENTAL SET-UP

A schematic diagram of the refrigerator is shown in Fig. 1. The diagram also illustrates the location of the various sensors used to study the gas process during operation.[7] The pressure oscillation in the cold head is made by means of a rotary valve which is driven by a dc-motor. This valve connects the inlets and the outlets of the regenerator and of the pulse tube periodically to the high- or low-pressure side of a commercial helium-compressor (Leybold RW 6000, nominal input power 7 kW). A detailed cycle description is given elsewhere.[8]

The pulse tube has an inner diameter of 38 mm, a length of 317 mm and it is placed inside the annular screens in the regenerator. A specific material with a low thermal conductivity has been selected for the tube, which has a wall thickness of 1 mm. The regenerator tube has an inner diameter of 58 mm and a wall thickness of 0.75 mm. We chose the length as well as the arrangement of the regenerator in a way which minimises the heat exchange between pulse tube and regenerator. The total length of the regenerator is therefore 120 mm.

Description of the Manufacturing Process of the Regenerator

Primarily we used a stainless steel 200 mesh regenerator. In a further step we replaced the colder part of the regenerator (below 50 K) by lead screens. The section of the lead screens is about one third of the total length of the regenerator. It is essential to choose the right length in order to avoid an excessive pressure drop.

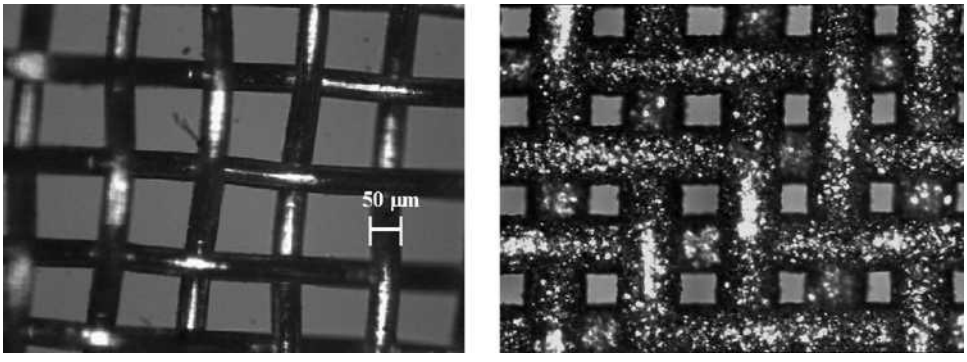

Figure 2. Screenview before and after electrostatic coating.

The lead screens were fabricated in the following way: At first we took bronze screens with 155 mesh and a wire diameter of 50 μm as a basic material in order to obtain mechanical stability. After a multi-staged cleaning and a chemical activation of the surfaces, which is an essential process in order to get a sufficient rugged lead coating, we deposited lead galvanically on the bronze mesh screens. The thickness of the lead was about 25 μm. A screenview before and after the deposition is shown in Fig. 2. It is important to obtain a rough lead surface in order to maximize the area of heat transfer. Therefore the composition of the electrolyte, the current density and the deposition time has to be optimised for a given screen geometry in oder to achieve optimal heat transfer and heat capacity ratio as well as convenient mechanical properties. The average porosity of the lead screens is 0.4 but it can be varied depending on the place in the regenerator. Still a further optimisation process is necessary to find out the best porosity distribution in the coldest part of the regenerator.

EXPERIMENTAL RESULTS AND DISCUSSION

Cooling Performance

At first we used a regenerator totally made of stainless steel. The FVPTR reached a minimum temperature of 32 K and a cooling power of 100 W at 75 K.

After we had replaced the cold end of the regenerator with lead spheres, the cooling power in the temperature region below 40 K was improved significantly. We reached a minimum temperature of about 23 K and a cooling power of 100 W at 72 K. The performance at higher cooling powers was better as well. This is due to improvements at the hot end of the pulse tube and to the decreased pressure drop of the lead screens in comparison to spheres. The cooling power of these two setups is shown in Fig. 3 (left).

After we slightly changed the arrangement of our thermal insulation, we even reached a minimum temperature of 17 K. The performance of the FVPTR for different filling pressures is shown in Fig. 3 (right). There p_M means the average pressure of the pulse tube at minimum temperature. The improvement of performance at increasing pressures can be seen.

We achieved a cooling power of 120 W at 74 K and 40 W at 34 K with an average pressure of 16.8 bar whereas in the lower temperature region the performance for different pressures was almost equal. It has to be mentioned that all these curves were measured without any readjustment of the cooler.

In two previous papers[8,9] we developed a model to represent P-V diagrams for a FVPTR, derived from measured pressure curves and the coefficient of discharge of the hot end inlet and outlet of the pulse tube.

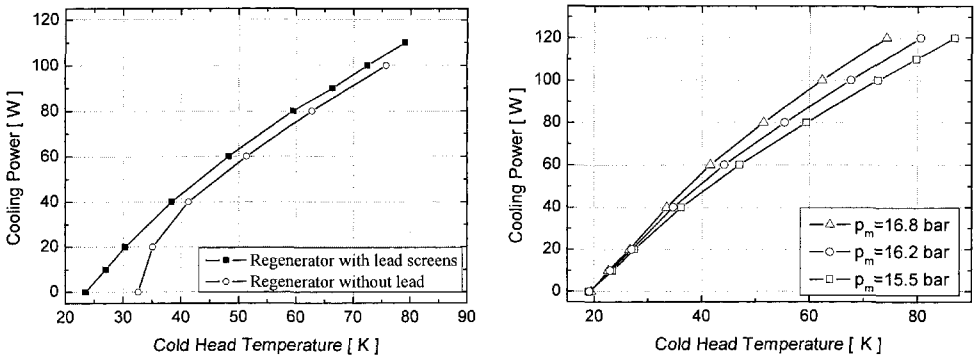

Figure 3. Cooling performance for different regenerators (left) and for different different filling pressures with the regenerator with lead screens (right)

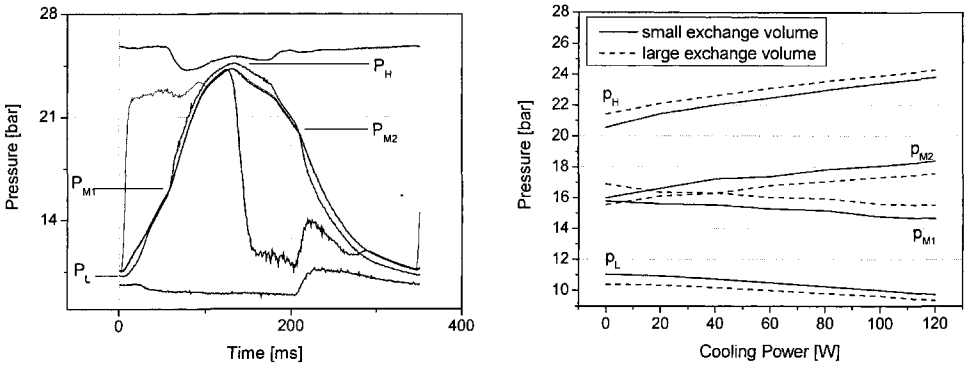

Figure 4. Typical pressure curves in a FVPTR (left) and characteristic of the two middle pressures and high and low pressure in dependence of the cooling power

This model has shown that the gross refrigeration power in a FVPTR strongly depends on the two intermediate pressures P_{M1} and P_{M2} (see Fig. 4 (left)). These two pressures were firstly introduced by Yuan et al. for a five valve pulse tube refrigerator.[10] They represent the pressure in the pulse tube after the gas has flown into and out of the reservoir or the pulse tube of a FVPTR, respectively. Fig. 4 (right) shows these two middle pressures as well as the high and low pressure in dependency on the cooling power. By means of this plot two typical features of a FVPTR can be seen.

Firstly the pressure difference between high and low pressure rises with increasing cooling power. This means that there is a higher gross refrigeration power for higher cooling power. Secondly the two middle pressures P_{M1} and P_{M2} split up for higher cooling power. Since $P_H - P_{M1}$ is the pressure difference for compression and $P_{M2} - P_L$ is the difference for expansion, larger pressure differences than in pulse tube coolers with passive phase shifters are available for refrigeration. In pulse tube coolers with passive phase shifters these two middle pressures coincide to one middle pressure.

Loss Analysis

Loss analysis is essential in the design and fabrication process of a pulse tube refrigerator. In this paper we report on the experimental analysis of the total static (e.g. conduction and radiation) and dynamic losses (e.g. regenerator and shuttle losses) of our FVPTR in coaxial design. Other references[11,12] describe a simple method to estimate the total static and dynamic losses and therefore the total losses at the cold head of the pulse tube cooler.

If the refrigerator is switched off at a certain temperature of the cold head, the total static losses are given by

$$\dot{Q}_{stat} = m \cdot c_p \cdot \Delta T \cdot \frac{1}{\Delta \tau} \tag{1}$$

where m is the mass, c_p the specific heat and ΔT the temperature distribution of the cold head. Since the determination of these values is not possible, a heat load P_{el} is supplied at the cold head

$$P_{el} + \dot{Q}_{stat} = m \cdot c_p \cdot \Delta T \cdot \frac{1}{\Delta \tau} . \tag{2}$$

For $1/\Delta\tau \rightarrow 0$ this equation results in

$$P_{el} = -\dot{Q}_{stat} . \tag{3}$$

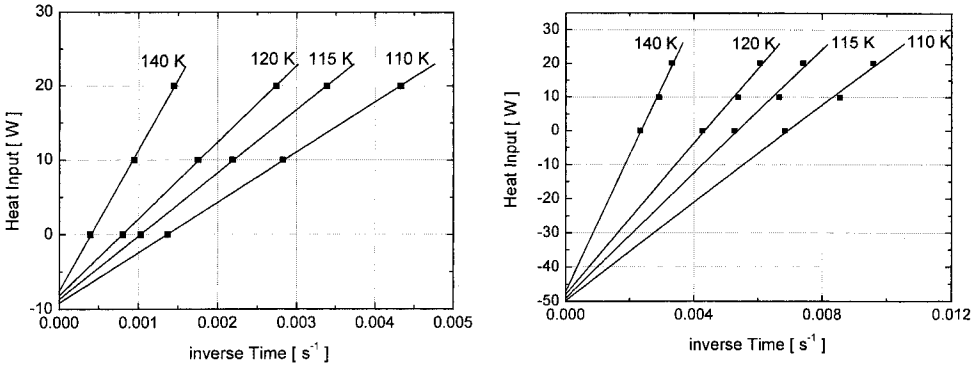

Figure 5. Total static (left) and total losses (right) of the FVPTR

To determine the static losses P_{el} is plotted against $1/\Delta\tau$ and $1/\Delta\tau$ is extrapolated to 0. Fig. 5 (left) shows such a measurement. In this way three different heat up curves for a heat load at the cold end of 0, 10, and 20 W are evaluated for temperatures above 90 K. We experimentally obtained a value of 8 W for the total static losses.

This method was also adapted to determine the dynamic losses of the refrigerator. In this case we have modified the cooler in such a way that during operation no p-V work is produced. This yields to the following equation for the cold head

$$P_{el} + \dot{Q}_{dyn} + \dot{Q}_{stat} = m \cdot c_p \cdot \Delta T \cdot \frac{1}{\Delta \tau} \tag{4}$$

and for $1/\Delta\tau \rightarrow 0$ this equation yields

$$\dot{Q}_{dyn} = - P_{el} - \dot{Q}_{stat} . \tag{5}$$

The experimental procedure was the following: Firstly the refrigerator was cooled down to 77 K by liquid nitrogen which flew into a vessel around the cold head. After the cold head had a temperature of 77 K and there was a linear temperature profile in the regenerator, the liquid nitrogen was blown out of the vessel and the cold head heated up. This procedure was done for different heat inputs at the cold head while the refrigerator was working and the dynamic losses are obtained in the same manner as the static losses. Fig. 5 (right) shows such a measurement. By means of this method we estimated the total dynamic losses to be 41 W at a frequency of 2.2 Hz.

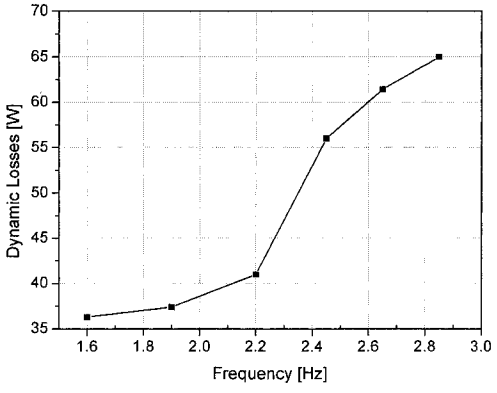

Figure 6. Frequency dependence of the dynamic losses

Fig. 6 depicts the frequency dependence of the total dynamic losses. A non-linear behaviour can be seen clearly. Furthermore, below the ideal working frequency of 1.9 Hz the dynamic losses are still decreasing. This frequency was found for no-load as well as load mode. This means that at lower frequencies the gross refrigeration power decreases faster than the dynamic losses. At higher frequencies the dynamic losses increase drastically because of the high regenerator losses.

CONCLUSION

This paper describes the manufacturing process of a regenerator partially made from lead wire mesh. A single stage FVPTR has been equipped with such a regenerator. The minimum no-load temperature achieved is 17 K. The cooling capacity is 120 W@74 K and 40 W@34 K. These values can be reached without any readjustment of the cooler.

In addition thermodynamic loss analysis has been done. We estimated the total static losses to be 8 W and the total dynamic losses to be 41 W at a working frequency of 2.2 Hz.

ACKNOWLEDGMENT

This work is partially supported by the German BMBF (No. 13 N 7395). We thank L. Föllmer and T. Hilprecht for technical assistance.

REFERENCES

1. Ackermann, R.A., *Cryogenic Regenerative Heat Exchangers*, Plenum Press, New York, 1997.
2. Kays, W.E., and London, A.L., *Compact Heat Exchangers*, McGraw-Hill, New York, 1964.
3. Köttig, T., Waldauf, A., Thürk, M., and Seidel, P., "Developments on GM-Type Pulse Tube Cryorefrigerators with Large Cooling Power," *Advances in Cryogenic Engineering*, Vol. 49B, Plenum Press, New York (2004), pp. 1445-1451.
4. Schmauder, T., Waldauf, A., Wagner, R., Thürk, M., and Seidel, P., "Investigation of a Single Stage Four-Valve Pulse Tube Refrigerator for High Cooling Power," *Cryocoolers* 11, edited by R.G. Ross, Plenum Press, New York (2001), pp. 327-336.
5. Waldauf, A., Thürk, M., Seidel, P., "Observation and control of temperature instabilities in a Four-Valve Pulse Tube Refrigerator," *Cryogenics*, vol. 44 (2004), pp. 75-79.
6. Blaurock, J., Hackenberger, R., Seidel, P., and Thürk, M., "Compact Four-Valve Pulse Tube Refrigerator in Coaxial Configuration," *Cryocoolers* 8, edited by R.G. Ross, Plenum Press, New York (1995), pp. 395-402.
7. Thürk, M., Brehm, H., Gerster, J., Kaiser, G., Wagner, R., and Seidel, P., "Intrinsic Behaviour of a Four Valve Pulse Tube Refrigerator," *Proc. of the 16th International Cryogenic Engineering Conference/ International Cryogenic Materials Conference* (1996), pp. 259-262.
8. Waldauf, A., Schmauder, T., Thürk, M., and Seidel, P., "Investigation of Energy Transport within a Pulse Tube," *Advances in Cryogenic Engineering*, Vol. 47A, edited by S. Breon et al., Plenum Press, New York (2002), pp. 753-759.
9. Waldauf, A., Schmauder, T., Thürk, M., and Seidel, P., "Affecting the Gross Cooling Power of a Pulse Tube Cryocooler with Mass Flow control," *Cryocoolers 12*, edited by R.G. Ross, Plenum Press, New York (2003), pp. 337-342.
10. Yuan, J., and Pfotenhauer, J., "A Single Stage Five Valve Pulse Tube Refrigerator Reaching 32 K," *Advances in Cryogenic Engineering*, 43, edited by P. Kittel, Plenum Press, New York (1998), pp. 1983-1989.
11. Yuanzhi, Z., and Fangzhong, G., "Measurement of losses in a miniature split stirling refrigerator," *Proc. of 4th Joint Sino-Japanese Seminar on cryocoolers and concerned topics (*1993), pp. 144-151.
12. Orlowska, A.H., Shuttle heat transfer, *Proc. of the ICEC 11* (1986), pp. 285-289.

A Low Porosity Regenerator Matrix for High Frequency Low Temperature Cryocoolers

D.R. Ladner, J.P. Martin, and P.S. Thompson

Equinox Interscience, Inc.
Wheatridge, CO 80403

ABSTRACT

A method has been devised to fabricate a uniform channel parallel plate heat exchanger suitable for high frequency low temperature regenerative cryocooler applications. The low porosity matrix design theoretically optimizes heat transfer and operating efficiency while minimizing losses, including thermodynamic losses in the matrix void volume, at higher operating frequencies than are currently achievable in regenerative cryocoolers designed for cooling below 15 K. Higher operating frequencies would enable efficient low mass valveless compressors to drive the coolers. To ensure that the thermal penetration depth is much larger than the matrix depth or inter-channel thickness at operating frequencies of about 30 Hz and at porosities as low as 10%, the channel small dimension must be less than about ~50 μm (0.002 inches) for typical matrix materials. For optimum heat exchanger effectiveness the deviation of the channel small dimension must be less than about 3 % from nominal to avoid significant flow maldistribution within the matrix gas volume. A simple and cost-effective fabrication method for reproducibly constructing such a matrix is discussed in terms of preliminary flow test results and predicted thermal performance as a function of matrix porosity. The method as currently implemented produces a continuum of high aspect ratio rectangular channels along a spiral length within a thin matrix disk component. The method also enables the design of a variable porosity matrix along the regenerator temperature gradient. Preliminary flow tests with disks having nominal 38 μm flow channels are consistent with the as-measured channel dimensions and matrix geometry.

INTRODUCTION

Rationale for Parallel Plate Matrix

Several attempts have been made by various researchers to produce a low porosity regenerator matrix having a parallel plate micro-channel flow geometry. Based on analytical and numerical modeling,[1,2] it is believed that a low porosity parallel plate matrix would optimize the heat transfer figure-of-merit while reducing the regenerator primary loss mechanism at temperatures below ~ 15 K, viz., compression losses in the matrix void volume.[3,4] However, the theoretically superior performance of a parallel plate matrix geometry,[5,6] compared to other geometries, such as collimated tubes,[7,8,9] packed spheres, or conventional screen matrix geometries, has not yet been

Cryocoolers 13, edited by R. G. Ross, Jr.
Springer Science+Business Media, Inc., New York, 2004

conclusively demonstrated. It has long been known that collimated flow channels should in principle provide superior heat exchange and lower pressure loss than flow channels which have the equivalent total flow area but involve more tortuous flow paths.[10,11,12] Figure 2 of Ref. 10 provides a comparison between the parallel plate, tube, and packed sphere geometries in terms of the nondimensional parameter $StPr^{2/3}/f$ plotted against the Reynolds number (N_R), where St is the Stanton number, Pr is the Prandtl number, and f is the Fanning friction factor. This parameter is a measure of the ratio of heat transfer to pressure loss that is useful in comparing different working fluids because it is independent of their thermophysical properties. It remains essentially constant over a large range of N_R for a given geometry. Figure 6-1 in Ref. 11 tabulates this parameter for laminar flow in several other cross-sectional geometries, including rectangular channels of different aspect ratios.

Equinox has developed regenerator design software that calculates regenerator matrix properties as a function of porosity n and channel geometry. The regenerator volume and aspect ratio, the required mass flow rate, and the matrix channel dimensions can be separately specified. Pressure drops, surface areas, matrix depth, thermal penetration depth, Reynolds number, and other parameters are computed and charted in an EXCEL® spreadsheet format. Fig. 1 below makes a geometrical comparison similar to Ref. 10 but plots $StPr^{2/3}/f$ against the matrix porosity. Although the results are nearly independent of channel size, porosity, and flow rate, the dimensions and flow rate used in Fig. 1 are stated for consistency with Figs. 2 to 4 below. The regenerator internal volume in this example is a 2 cm diameter x 4 cm long cylinder, and the laminar mass flow rate is 1 g/s. It is seen that the value of $StPr^{2/3}/f$ is ~0.39 for infinite parallel plates, ~0.36 for rectangular channels with an aspect ratio of 10:1, ~ 0.31 for tubes, and for equispaced spheres it varies weakly from ~0.04 at n = 0.30 to ~0.05 at n = 0.70 because the friction factor is a function of porosity. (Note that the minimum theoretical porosity for packed spheres is ~30%, although 38% is a typical practical limit.)

For a 4 K Gifford McMahon (G-M) cooler driven by a low frequency (~1 Hz) valve-type compressor, the regenerator matrix typically uses spheres of Pb, phosphor bronze, or rare earth compounds. The resultant 38% porosity is too large for efficient high frequency operation because of the compression losses in the matrix.[3] One approach to lower the porosity is to mix different size spheres, but this can result in a highly variable matrix geometry and unpredictable cold performance. In addition, care must be taken to prevent the tiny spheres from "leaking" into the flow system and causing damage to the coldhead components or the compressor. A "clean" quasi-parallel plate matrix with a high aspect ratio (a = w/d = width / height) therefore offers an attractive solution. If the rectangular channel height (small dimension d) is uniform, then the flow paths should provide evenly distributed heat exchange that involves the entire matrix mass.

A comparison of surface areas for the three finite channel geometries having the same characteristic dimensions as in Fig. 1 is shown in Fig. 2. Although the high aspect ratio rectangles provide a smaller matrix surface area for contact with the working fluid, the parameter $StPr^{2/3}/f$ is larger because of the lower ΔP. The surface area to ΔP ratio and the Nusselt number (Nu) to ΔP ratio are also larger for the rectangular geometry, so surface area alone is not sufficient to predict thermal performance. Because of the different channel geometries and channel distributions, the optimum "matrix depth," or inter-channel spacing, also varies with the porosity and geometry. Fig. 3 plots the matrix depth, i.e., the distance to the deepest part of the matrix material from the channel flow perimeter, as a function of the geometry and porosity. At a given operating frequency (30 Hz) and temperature (10 K), the ratio of the thermal penetration depth to the matrix depth should be large to enable optimum heat exchange between the working fluid (e.g., GHe) and the matrix bulk material. For porosities > 12 %, the matrix depth is smaller for the 10:1 rectangular channel geometry than for the tubes or spheres, and the thermal penetration depth to matrix depth ratio is therefore largest.

The most important figure-of-merit for regenerator performance is the NTU/ΔP ratio, which is maximized with the parallel plate or high aspect ratio rectangular flow geometries. This figure-of-merit is related to the parameter $StPr^{2/3}/f$ by

$$NTU/\Delta P = (StPr^{2/3}/f) \times 2\,\rho\,(A/\dot{m})^2/\,Pr^{2/3} \qquad (1)$$

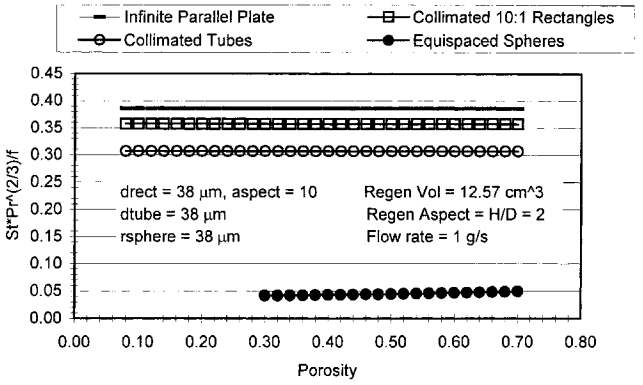

Figure 1. Plot of the ratio $StPr^{2/3}/f$ vs. porosity for three matrix geometries. Collimated 10:1 rectangular channels are in a "spiral-in-disk" configuration. Collimated tubes are in a triangular array. Spheres are equispaced.

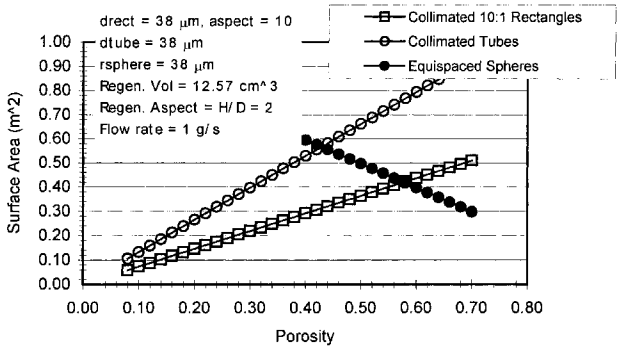

Figure 2. Plot of the surface area vs. porosity for three matrix geometries for the same characteristic dimension. Collimated 10:1 rectangular channels are in a "spiral-in-disk" configuration. Collimated tubes are in a triangular array. Spheres are equispaced.

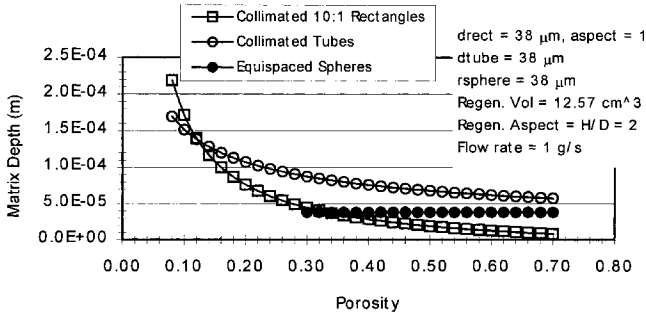

Figure 3. Plot of the matrix depth vs. porosity for three matrix geometries for the same characteristic dimension. Collimated 10:1 rectangular channels are in a "spiral-in-disk" configuration. Collimated tubes are in a triangular array. Spheres are equispaced.

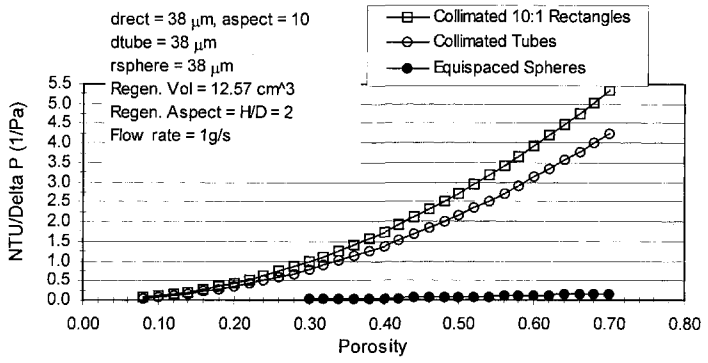

Figure 4. Plot of the ratio NTU / ΔP vs. porosity for three matrix geometries. Collimated 10:1 rectangular channels are in a "spiral-in-disk" configuration. Collimated tubes are in a triangular array. Spheres are equispaced. Values of NTU / ΔP are computed for GHe at 15 K.

where NTU is the number of transfer units,[13] ρ is the fluid density, A is the open (gas flow) area, and ṁ is the mass flow rate. Unlike the parameter $StPr^{2/3}/f$, the ratio NTU/ΔP, for a fixed regenerator sleeve cross-section and a fixed mass flow rate, is a function of the square of the matrix porosity, which varies as A. This parameter also varies with the working fluid properties and was computed here for GHe at 2.5 MPa at 15 K. It is seen in Fig. 4 that for a fixed flow rate the ratio of this figure-of-merit for any two geometries is identical to the corresponding ratio in Fig. 1. The ratio remains constant with decreasing porosity, while the figure-of-merit itself decreases. The parallel plate, or any rectangular channel with an aspect ratio > ~3:1, is superior to the other geometries at any porosity and at any channel dimension. Collimated tubes, e.g., formed as perforated disks, have figures-of-merit that are ~16 % lower than the 10:1 rectangular channels. The compression losses in the void volume nonetheless drive the matrix design toward the lowest porosities.[3,8] A better figure-of-merit would include the axial thermal conduction loss through the matrix. If the NTU/ΔP ratio is to be increased at a fixed porosity, then the regenerator sleeve area must scale up with the gas flow area. But the axial conduction will then also increase, so there is a practical limit at which axial conduction[14,15,16] becomes comparable to the compression loss. At a fixed porosity all collimated channel matrices will conduct heat equally in the axial direction, assuming equivalent matrix sections (e.g., disks), so the 10:1 rectangular channels would still provide the best overall figure-of-merit.

Previous Research

Two different approaches to construct a low porosity matrix have been reported by Chafe and Green.[6,7] In one case embossed Nd ribbon strips were wound in a spool to approximate the desired parallel plate geometry.[6] In a second case perforated Nd disks were stacked together to form a collimated capillary geometry.[7] Both approaches resulted in a modest reduction in operating temperature (4.5 K to 3.8 K) for a given input power and heat load (0.5 W). These tests were conducted with a modified G-M cooler whose low temperature packed sphere matrix was replaced by the Nd ribbon or disk components. Matrix porosities in the range of 13 to 20 % were achieved, with the best temperature reduction achieved with the lowest porosity. Given its much lower porosity, the measured flow impedance (pressure drop / mass flow rate) was also favorable compared to packed spheres, although our calculations show that it was still well above the theoretical value for that geometry. The experimental results nonetheless indicated modest

performance improvements over packed spheres. The researchers did not operate the G-M at a higher frequency nor attempt to modify a pulse tube or Stirling cooler regenerator.

M. Mitchell[17] has also fabricated and performed limited testing on an etched foil parallel plate regenerator matrix. The fabrication method requires a critically etched ribbon element to achieve both the flow channel and matrix spacing features along the entire regenerator length to ensure even flow distribution and to reduce axial conduction. It also involves critical splices in the foil to prevent bypass flow. However, this method has only been applied to stainless steel (not a suitable matrix material for < 15 K) and the theoretical matrix porosity is high, ~ 50 %.

Kelly et al.[9] have recently reported on the LIGA micro-machining process and its potential application to cryocooler regenerators. Their fabrication method employs a stack of 1 to 2 mm thick washers with collimated flow channels and porosities as low as 5 %. To achieve a uniform matrix depth over the matrix cross section, the symmetrically distributed channels would be identically round, hexagonal, or square (higher aspect ratios would be preferable). However, the authors indicate that there might be significant washer-to-washer porosity variation and that washer-to-washer channel alignment might be critical. Manufacturability of the LIGA matrix elements could be automated, but the washers would be expensive, because LIGA is a complicated multi-step process. It should also be noted that collimated tube matrix elements, which can achieve porosities comparable to our high aspect ratio rectangular channel matrix, have yet to be experimentally demonstrated because of the difficulty in fabricating micro-channels having the diameter uniformity required for uniform flow and heat exchange.

Marquardt and Radebaugh[5] have recently made measurements of the effectiveness of a 40 K miniature counterflow heat exchanger for Brayton cryocoolers. It is formed by diffusion bonding photo-etched components into an array of high aspect ratio rectangular channels. The authors note that flow maldistribution and channel deformation due to differential flow pressures are the primary design challenges. The measured effectiveness was 0.97, lower than the design value of 0.99, but better than similar comparably sized heat exchangers

The fabrication approaches used in the foregoing research efforts are complicated and expensive. The limited published performance data indicate that flow and heat transfer efficiency can deviate from theoretical predictions. The disagreement between the measured and theoretical values is probably attributable to a maldistribution of the flow. Low measured flow impedance, e.g., is caused either by peripheral bypass flow or internal flow through a significant fraction of larger-than-nominal passages, while high measured flow impedance is probably due to a failed or collapsed matrix design. Therefore, good agreement between experimental and theoretical flow impedance is a first criterion for validating a micro-channel matrix of known geometry.

EQUINOX RESEARCH

Matrix Description

For maximum efficiency at T < 15 K a regenerator matrix needs to have a low porosity *and* a matrix thickness that is much less than the thermal penetration depth at the operating frequency. These two constraints drive both the channel size and spacing. During our research we investigated several micro-machining methods (EDM, laser, molding by LIGA process, etc.) for fabricating matrix disks that would have a long uniform and continuous (as opposed to segmented) spiral flow channel to meet these constraints. The required flow channel dimension was d = 38 μm with a fixed separation between adjacent spiral turns to ensure low porosity and compatibility with the thermal penetration depth of the matrix material at ~30 Hz. The result was that none of these methods was acceptable either due to cost and / or reproducibility. We were led to find a simpler approach and therefore revisited the spiral geometry.[6] The simple approach taken here involves interleaved components and results in highly reproducible disks having a spiral array of 10:1 aspect ratio rectangular flow channels that closely approximate the parallel

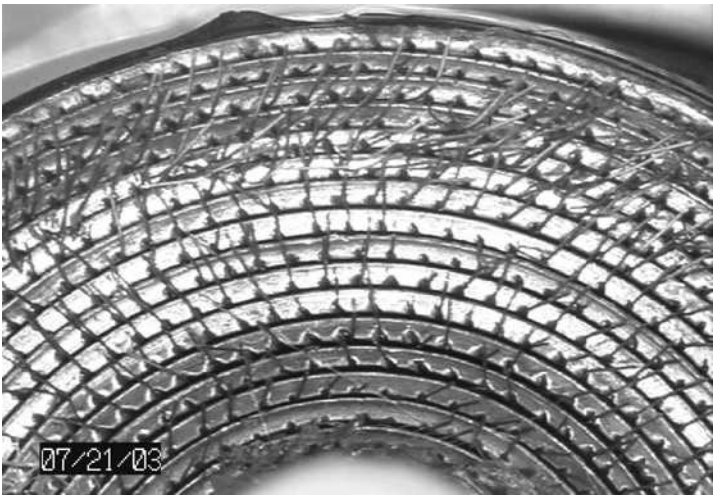

Figure 5. Photomicrograph of Pb alloy matrix disk #9 with 380 micron x 38 micron (10:1) rectangular flow channels and ~10% measured porosity.

plate attributes of a continuous spiral. The porosity and flow measurements presented below support this segmented "spiral-in-disk" design concept and the fabrication approach that we employed. Moreover, this inexpensive fabrication technique is workable for any flexible (preferably annealed) matrix material and can be automated with simple equipment. We successfully fabricated and flow tested several 6 mm and 4.7 mm thick disks of Pb alloy and Nd. A photomicrograph of a sample disk is shown before final processing in Fig. 5.

High Frequency Operation

The optimum regenerator matrix porosity is critically related to the magnitude of various frequency dependent and non-frequency dependent loss mechanisms.[3,4] Because the losses associated with axial heat conduction and working fluid heat transport become relatively less important at lower temperatures, the compression loss in the regenerator void volume can become dominant. These losses can be estimated, leading to optimized porosity and channel size (height d) gradients over the regenerator physical length and axial temperature range to optimize performance at a given operating frequency.

The segmented spiral channel in the Equinox regenerator disk provides the clean high aspect ratio (10:1) rectangular geometry needed to establish a hydraulic diameter ($D \sim 1.8d$) close to the infinite parallel plate value ($D = 2d$) to maximize the NTU/ΔP figure-of-merit at a given porosity and mass flow rate. To effect maximum heat exchange between the matrix material and the oscillating gas, the matrix depth, i.e., the half-separation between adjacent spiral channels (~ 9d/2 for a matrix porosity of 10%) must be small compared to the matrix material's thermal penetration depth, $d_\lambda = (\lambda/\pi cf)^{1/2}$, at the operating frequency f and the local matrix temperature. The volumetric heat capacity c and the thermal conductivity λ of the matrix typically increase with temperature. At f ~ 1 Hz and T = 15 K, d_λ ~ 2000 μm for many rare earth materials. Since d_λ varies as $1/f^{1/2}$, d_λ ~ 365 μm at f = 30 Hz. Thus the half-separation must be at least < 365 μm, and therefore d must be at least < 81 μm (~3.2 mils) for the desired 10% porosity matrix disk. A value of 170 μm for the half-separation would be much better, yielding d ~ 38 μm (~1.5 mil). By stacking several disks of thickness t and variable spiral channel dimension d, the porosity can be increased gradually toward the warm (~60 K) end to match the warm stage regenerator's fixed screen porosity of ~65%. The value of d_λ ~365 μm at f = 30 Hz and T = 15 K will decrease toward the 4 K end, leading to further reduction of channel

height d from 38 μm. However, the limit to that reduction is determined by the fabrication method; at this time the limit is ~ 20 μm without special processing. Non-uniformity of the disk channels would cause flow maldistribution through different areas of the disk. Since the mass flow varies as d^4 for a fixed aspect ratio, the mass flow rate variation in a given channel is four times larger than the channel variation. The flow would be disproportionately distributed in the widest channels, negating the heat exchange function of much of the matrix material. A goal of continuing research at Equinox is to experimentally determine the acceptable variation in d for the thousands of channels comprising the total flow cross section, i.e., the required channel distribution function. We estimate that a standard deviation of 1.25 μm for d = 38 μm would put 96% of the total flow within 15 % of the nominal value over 95 % of the matrix cross section.[18]

At this time the choice of matrix materials for fabricating these disks is more limited than for the packed sphere matrix. Although the highest volumetric heat capacities over the temperature range are desirable, achieving a uniform flow within the disk is also paramount. It is equally important to use well-characterized materials, since many rare earth compounds have high uncertainty in location of heat capacity peaks, i.e., paramagnetic transition temperatures. Fully annealed, both Nd and $Er_{0.5}Pr_{0.5}$ are pliable at room temperature and can be processed like lead alloy to achieve the uniform channels. Brittle disks would be susceptible to thermal and mechanical shock that could alter the flow channel uniformity, defeating the fundamental design. Nd and $Er_{0.5}Pr_{0.5}$ are also antiferromagnetic below their paramagnetic transitions, important for extending the matrix application to 4 K SQUID systems.

Data

Several Pb alloy and Nd matrix disks having measured porosities of ~11% were successfully fabricated at Equinox. The photomicrograph in Fig. 5 above shows a magnified portion of a disk cross section (Sample #9) during processing. Calibrated dimensional measurements across the disk diameter are in excellent agreement with the known matrix material dimensions and are consistent with the nominal channel height, d = 38 μm (1.5 mil). Fig. 6 plots the derived disk porosity for nine sample disks. Values were determined from measured component masses and the disk as-built dimensions. The disk-to-disk variation of ~5% is primarily due to the mass uncertainty. Equinox flow-tested the Pb alloy disks both individually and as a prototype regenerator stack at ambient temperature. Fig. 7 compares the measured flow impedance ($\Delta P/\dot{m}$) of each sample to the theoretical value for a disk having the nominal channel dimension d = 38 μm, the nominal 10:1 aspect ratio, the measured disk thickness (t = 6 mm), and the nominal total number of channels n = 1230. Neglecting the channel radius of curvature and

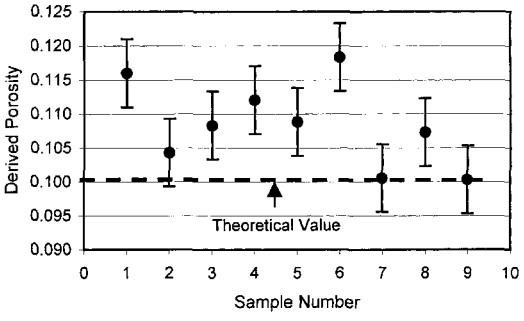

Figure 6. Plot of measured porosities of 9 disk samples. Dashed line is the ~10% theoretical value. The ordinate zero is suppressed. Error bars show the standard deviation.

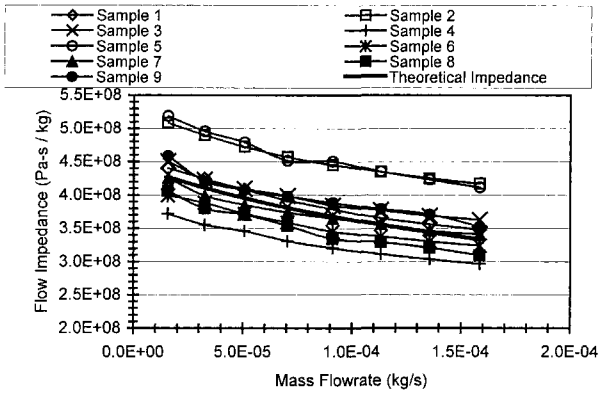

Figure 7. Measured GHe flow impedances vs. mass flow rate at 295 K and ~ 12 PSI ambient vent pressure for the individual disk samples. The solid line shows the theoretical disk impedance for the nominal 38 μm channels per Eqn. (2). The ordinate is suppressed.

end effects at the disk faces, the theoretical disk impedance is

$$Z_{th} = 12.37\eta t/na\rho d^4 \qquad (2)$$

where η and ρ are the viscosity and density of GHe at the ambient temperature and average pressure. The data curves are distributed fairly evenly about the theoretical impedance curve. From Eqn. (2) it was determined from the measured impedances that the *effective* channel height d for six of the nine samples was within ~3 % of the nominal value based on dimensional measurements of the matrix component materials. Fig. 8 plots these values; the standard deviation is 1.4 μm. We note that with increased fabrication experience, our final samples achieved increasingly better conformity to theoretical porosity and flow criteria. Fig. 9 shows the measured flow impedance for a stack of 3 disks (samples 7, 8, 9) assembled in a crude prototype regenerator configuration. The qualitative agreement is good, but the data lie slightly below the theoretical curve, possibly indicating weak bypass flow at the middle disk.

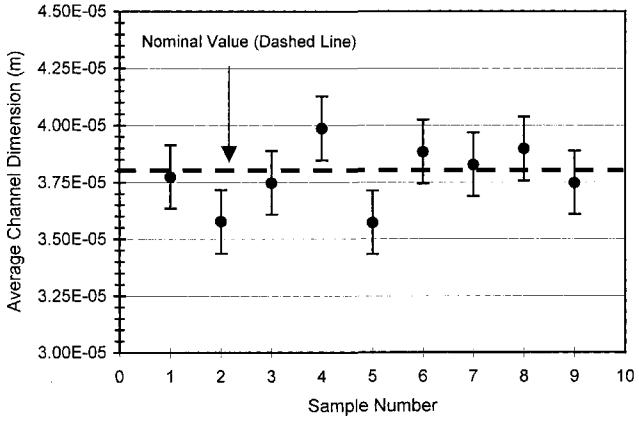

Figure 8. Plot of the derived rectangular channel height dimension d for 9 disk samples. Dashed line shows the nominal 38 μm value. The ordinate zero is suppressed. Error bars show the standard deviation.

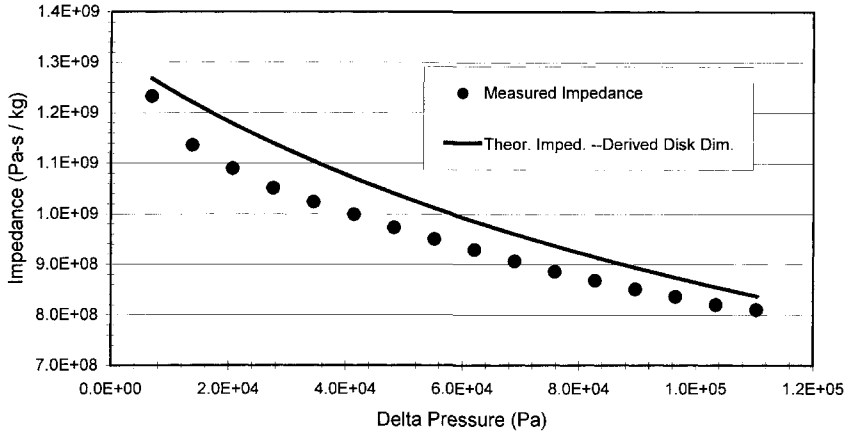

Figure 9. Measured GHe flow impedance at 295 K for a prototype matrix (3-disk stack). The solid line shows the theoretical impedance for the matrix using the "as measured" disk impedances from Fig. 7. The ordinate is suppressed.

Future Research

A primary research goal for matrix optimization using the segmented spiral-in-disk fabrication approach is to determine the optimum size and number of disks per unit length required to maximize the figure-of-merit and reduce axial heat conduction while also limiting any pressure losses associated with entrance/exit effects between disks. Current numerical models that assume a homogeneous regenerator matrix cannot do this. Thus, experimental optimization of the working length and aspect ratio of a prototype regenerator through in-situ cryogenic performance testing is fundamental to the matrix development. Such work is currently scheduled during 2004. The effect of graduated matrix porosity will also be investigated.

CONCLUSIONS

The theoretical regenerator matrix figure-of-merit, expressed as the NTU/ΔP ratio, is optimized with a parallel plate or high aspect ratio rectangular geometry. Prototype disks with porosities of ~11% for high frequency applications have been fabricated. A method for reproducibly achieving the matrix geometry with low porosity has been developed. Components with 10:1 rectangular flow channels have been produced in the form of a segmented spiral-in-disk channel. Preliminary ambient GHe flow tests in disks with nominal 38 μm flow channels indicate worst case effective dimensional uncertainties to be within ~1.4 μm of nominal, or ± 3.7 %. A prototype regenerator comprising a stack of these disks has a porosity of < 15 % and a flow impedance close to the theoretical value. Cryogenic performance testing is expected to confirm the Equinox fabrication approach and the application of this matrix for high frequency low temperature regenerators.

ACKNOWLEDGMENT

This research was supported by U. S. AFRL under SBIR Contract F29601-02-C-0157.

REFERENCES

1. Radebaugh, R., et al., "Modeling and Optimization of a High Frequency 10 K Pulse Tube Refrigerator," paper J2-1, *National Radio Science Meeting*, Univ. of Colo., Boulder, CO, Jan 2000.
2. Gary, J., and Radebaugh, R., "An Improved Numerical Model for Calculation of Regenerator Performance," *Proc. of the 4th Interagency Meeting on Cryocoolers*, David Taylor Research Center, 1990.
3. Radebaugh, R., et al., "Regenerator Development at 4 K: Effect of Volume and Porosity," *Adv. in Cryogenic Eng. 47A,* Amer. Institute of Physics, Melville, NY (2002), p. 961.
4. Pfotenhauer, J.M., et al., "Regenerator Loss Measurements at Low Temperatures and High Frequencies," *Cryocoolers 12*, Kluwer Academic/Plenum Publishers, New York (2003), p. 523.
5. Marquardt, E. and Radebaugh, R., "Compact High Effectiveness Parallel Plate Heat Exchangers," *Cryocoolers 12*, Kluwer Academic/Plenum Publishers, New York (2003), p. 507.
6. Chafe, J.N., Green, G.F., "Neodymium-Ribbon-Regenerator Cooling Performance in a Two-Stage Gifford-McMahon Refrigerator," *Adv. in Cryogenic Engineering*, Vol. 43, ed. by P. Kittel, Plenum Publishing Corp., New York (1998), p. 1589.
7. Chafe, J.N., Green, G.F., "Performance of Low-Temperature Gifford-McMahon Refrigerator Utilizing a Neodymium Disk Regenerator," *Adv. in Cryogenic Engineering*, Vol. 43, ed. by P. Kittel, Plenum Publishing Corp., New York (1998), p. 1783.
8. Hendricks, J., "Predicted Performance of a Low-Temperature Perforated Plate Regenerator," *Cryocoolers 12*, Kluwer Academic/Plenum Publishers, New York (2003), p. 483.
9. Kelly, K., et al. (2003), "LIGA-Fabricated High-Performance Micro-Channel Regenerators for Cryocoolers," Cryocoolers *12*, Kluwer Academic/Plenum Publishers, New York (2003), p. 489.
10. Radebaugh, R., and Louie, B., "A Simple First Step to the Optimization of Regenerator Geometry," *NBS Special publication 698*, 1995, p. 177.
11. Kays, W.M. and London, A.L., *Compact Heat Exchangers, 3rd Ed.*, McGraw Hill, New York, 1984, Fig. 6-1, p. 120.
12. Ackermann, R.A., *Cryogenic Regenerative Heat Exchangers*, Plenum Press, N.Y., 1997, p. 198.
13. Holman, H.P., *Heat Transfer, 4th Ed.*, McGraw-Hill Book Co., N.Y., 1976, pp. 403-415.
14. Lewis, M. and Radebaugh, R., "Measurement of Heat Conduction through Bonded Regenerator Matrix Materials," *Cryocoolers 12*, Kluwer Academic/Plenum Publishers, New York (2003), p. 517.
15. Ladner, D.R., "Measurement of Regenerator Thermal Conductivity Degradation Factors," Paper J2-3, *National Radio Science Meeting*, Univ. of Colo., Boulder, CO, Jan 2000.
16. Ladner, D.R., "Model for Two-Stage Pulse Tube Coldhead Parasitic Heat Load," *Advances in Cryogenic Engineering 47B*, American Inst. of Physics, Melville, NY (2002), p. 1149.
17. Mitchell, M.P., "Assembly Methods for Etched Foil Regenerators," *Adv. in Cryogenic Engineering*, Vol. 49, Amer. Institute of Physics, Melville, NY (2004), pp. 1592-1597.
18. Bevington, P.R., *Data Reduction and Error Analysis for the Physical Sciences*, McGraw-Hill Book Co., N.Y., 1969, Appendix C, pp. 307-309.

X-ray Lithography Fabricated Microchannel Regenerators for Cryocoolers

D.J. Guidry, J. T. Parker, A. B. McCandless, S. Motakef, and K. W. Kelly

International Mezzo Technologies, Inc.
Baton Rouge, LA, USA 70803

ABSTRACT

NASA, Air Force, Missile Defense Agency (MDA), and DoD repeatedly express the need for long-life, low maintenance space cryocoolers. Two types of cryocoolers that meet these requirements are the pulse tube and the Stirling coolers. One of the major factors limiting the efficiency of these coolers is the regenerator. Improving the regenerator performance would substantially increase the efficiency and thus reduce the power required to operate these coolers.

Recent advances in the field of microfabrication have resulted in the ability to create advanced geometries in lead and erbium alloys for use as regenerators in cryocoolers. The performance of cryocoolers, both in terms of power efficiency and the attainable cold end temperature, is strongly influenced by the geometry and cryogenic thermal properties of the regenerator material. These new fabrication techniques allow for the ability to reduce the pressure drop across the regenerator and improve the thermal capacity by optimizing the porosity, channel shape, channel size, and material of construction. Previous work indicates that the resulting regenerators support lower NPH/NTU values over current screens and powders used in cryocoolers.[1]

While these advanced geometries have already been formed in both lead and erbium, the technology can be expanded to include a wide variety of materials such as other rare-earth alloys, stainless steel, copper, and nickel alloys. A complete regenerator has been formed out of lead and is currently being evaluated. Improvements in the thermal performance of the regenerator will result in an overall improvement in regenerative cryocoolers, especially at the lower temperature ranges (<30K).

INTRODUCTION

Regenerative cryocoolers can be used to maintain the temperature of a device at cryogenic levels ranging from approximately 4 to 70 K. The performance of such cryocoolers, in terms of power efficiency and the attainable cold end temperature, is strongly influenced by the geometry and cryogenic thermal properties of the regenerator design and material. Depending upon the application, preferred regenerators typically have one or more of the following characteristics:

- High heat transfer area
- High wall-to-gas heat transfer
- Low axial conduction
- Low pressure drop loss
- High heat capacity
- Low dead (void) volume

Cryocoolers 13, edited by R. G. Ross, Jr.
Springer Science+Business Media, Inc., New York, 2004

Previously, wire meshes and packed beds of powders have been used as the thermally conductive components for regenerators in cryocoolers. For these systems, the pressure drop across the regenerators for a given unit of heat transfer is high (typically at or above about 6 NPH/NTU), resulting in low overall efficiency of the cryocooler.[1] This problem is particularly acute at low temperatures (below 30K) where manufacturing limitations have resulted in cryocoolers with regenerators consisting of packed beds of lead powders (for temperatures in the range of 10-30K) or magnetic intermetallic compound pellets (at temperatures below 10K). Packed powder beds have at least two disadvantages. First, they have very high pressure drops. Second, their porosity is fixed at approximately 38%, and cannot be reduced to more desirable values. Both factors are significant contributors to the low efficiency of cryocoolers employing packed powder beds.[2]

Regenerators made from stacked, porous plates through which fluid can flow have also been proposed for use in regenerators. Current plate designs suffer from losses of efficiency due to the difficulties in manufacturing thin plates with extreme precision to maximize the efficiency of heat transfer and fluid flow dynamics. Until now, available manufacturing methods (other than those for wire meshes and packed beds of spheres) used to fabricate the intricate geometries required in regenerators have been limited. Such options have included photoetching, excimer lasers, electron beam drilling, and conventional single electrode electro discharge machining (EDM). Each of these methods has major drawbacks that prevent it from being feasible for regenerator fabrication. Photoetching can only produce features that have aspect ratios less than two, resulting in plates that are less than 100 microns thick and have poor sidewall quality. Thousands of these plates have to be fabricated reliably for each regenerator formed. Excimer lasers have the ability to create the required geometry, but the process is extremely slow. Current lasers take about 10 seconds to drill a 50 micron hole in a 200 micron thick sheet of material. Using this process to create a complete regenerator in certain designs could take more than one month of processing time, which is not practical for production. Electron beam drilling is very fast and is capable of drilling hundreds of holes in a single second, but the smallest hole that can be drilled is 50 microns and the highest possible porosity is 8% due to a severe taper that develops during the process. Thus, electron beam drilling cannot be used to produce a thermodynamically optimal regenerator. In the case of conventional single electrode electro discharge machining (EDM), the process can create certain geometries, but is very slow and would be cost prohibitive for production. Thus, a need still exists for a way to fabricate regenerator plates that have characteristics that can improve the efficiency of the regenerators in which they are employed.

Mezzo has utilized two methods to fabricate disks for regenerators. The first method employs the LIGA process to directly mold lead disks. LIGA stands for X-ray LIthography, Electroforming (German: Galvanoformung), and molding (German: Abformung). As the name implies, this technology allows us to define high aspect ratio structures in a three-step microfabrication technique: x-ray lithography, followed by an electroforming step to produce a metallic molding die, which is then used to mold microcomponents. In the traditional LIGA process the mold is used to form polymer parts, but Mezzo has modified the process for the molding of lead. Mezzo utilizes the x-ray facility at the Center for Advanced Microstructures and Devices (CAMD) to perform its x-ray lithography. The LIGA process can produce structures as deep as 2000μm with lateral dimensions as small as a few microns. The sidewalls of these structures are extremely smooth with roughness measured in nanometers, and are essentially vertical with lateral dimensional variation/height on the order of 0.1μm/100μm. Due to low setup and production costs associated with the reproduction of microstructure via molding, LIGA promises to be a cost-effective mass production method, which can be used to produce highly accurate and complex microstructures for a wide variety of products.

Figure 1(a) is a series of molded lead plates that have been stacked to form a regenerator particularly suitable for a Stirling cycle cryocooler. Figure 1(b) is a micrograph of the molded lead sheet with an array of microchannels featuring an alignment aperture through which an alignment pin may extend, so that when stacked upon one another, each disk can be easily aligned with its adjacent counterparts. Each micro-channel is aligned with a corresponding micro-channel of an adjacent disk creating a continuous flow path through the stack.

The second regenerator manufacturing method developed at Mezzo begins with the formation of a molding die consisting of an array of microfeatures, typically microposts/microslots, which are

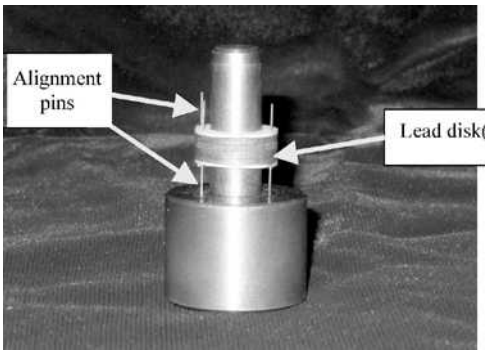

Figure 1(a): Stacked plate regenerator made from lead disks.

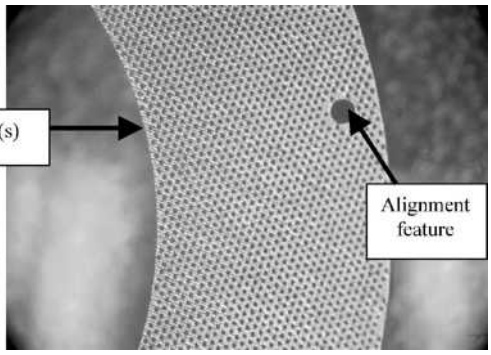

Figure 1(b): Micrograph of lead disk.

used to create through-channels, alignment features, and walls that form the perimeter of a single disk. In the case of molding lead, the LIGA tool is pressed into the lead using a combination of heat and pressure. In the second method, referred to as LIGA-EDM, the LIGA tool is used in conjunction with an EDM machine to form the disk for the regenerator. EDM technology began over fifty years ago and has been developed in recent years to allow for high precision and control over the process. EDM removes material using an electric spark and can be applied to any conductive material. In this technology, a high-frequency pulsed ac or dc current is applied through an electrode or wire to a material, which then melts and vaporizes the surface of the work piece. The electrode never comes into contact with the piece, but instead discharges its current through an insulating dielectric fluid across a very small spark gap.[3] This process has been combined with LIGA-fabricated electrodes in the past with success[4] and is applied towards fabricating regenerators in this work.

In order to fabricate a working regenerator using EDM, a LIGA tool consisting of an array of microposts or microslots, shown in Fig. 2, was fabricated. The LIGA tools act in a similar fashion as they do when they are used to mold materials. The LIGA tool is attached to the plunger (cutting) section of the EDM and is pushed into the material (Er) to be cut. As the micro posts are driven into the Er, material is removed to form the negative of the LIGA tool. The main advantage this method has over single electrode EDM methods is that hundreds of thousands of holes can be created in parallel, allowing for quick processing as shown in Fig. 3.

The LIGA-EDM manufacturing process allows for the production of custom engineered geometries of cryogenic materials, which when assembled into a working regenerator should result in highly efficient regenerators that would greatly improve the performance of cryocoolers. It also enables the fabrication of high-aspect ratio microchannel regenerator plates that are more precise

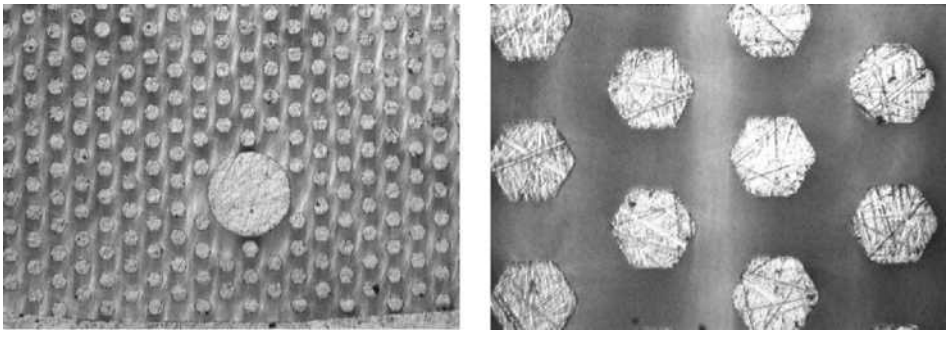

Figure 2. Close-up of completed nickel molding tool; the larger post in the figure on the left is the alignment post.

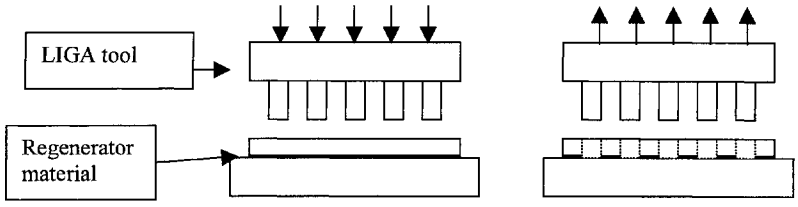

Figure 3. EDM process, figure on left is prior to EDM, figure on right is after EDM.

and economical than those produced by any other current method. The ability to design and engineer the shape and size of the regenerator provides the opportunity to both optimize the porosity of the regenerator and decrease the pressure drop across the length of the regenerator. The particular geometries of the microchannels in cross-section may vary substantially depending upon the desired porosity, other fluid dynamic considerations, and manufacturing practicalities. Thus, for example, the microchannels may have a smooth, unitary wall to form, in cross-section, a circular or elliptical shape, or the microchannels may have two or more walls which intersect at angles to form in cross-section a triangle, square, rectangle, hexagon, octagon, etc.

In certain regenerator designs, for example, each plate is a solid circular disk or a flat annular ring with:

- inner diameter preferably in the range of 0 to 6 centimeters
- outer diameter preferably in the range of 1 to 10 centimeters
- average thickness in the range of 100 to 500 microns
- hydraulic diameter in the range of 20 to 50 microns, and
- total height of the stack of plates preferably in the range of 1 to 20 cm.

The microchannels may be laid out in one of a variety of array formats. A preferred array format is one that is substantially uniform so that each microchannel is an equal distance away from each neighboring microchannel over the annular or circular disk. For low temperature applications (<20K), each plate preferably has a porosity in the range of 0.10 to 0.30. The sheet of thermally conductive material is typically metal or metal alloy with a thickness in the range of 100 to 500 microns. However, any material that is sufficiently thermally conductive and meets the physical and chemical requirements of the specific application may be used. In some applications, metals or metal alloys are particularly suitable and may be any conductive material in general (copper, stainless steel, Inconel, rare-earth alloys). However, due to their high heat capacity at cryogenic temperatures, Er-alloys and other intermetallic compositions such as HoSb, NdGe, PrGe, ErPr, Er_3Ni, or $Er_{0.5}Dy_{0.5}Ni_2$, are the preferred materials for cryocooler regenerators, particularly at temperatures below 15 K. Figure 4 shows micrographs of an erbium regenerator disk fabricated at Mezzo.

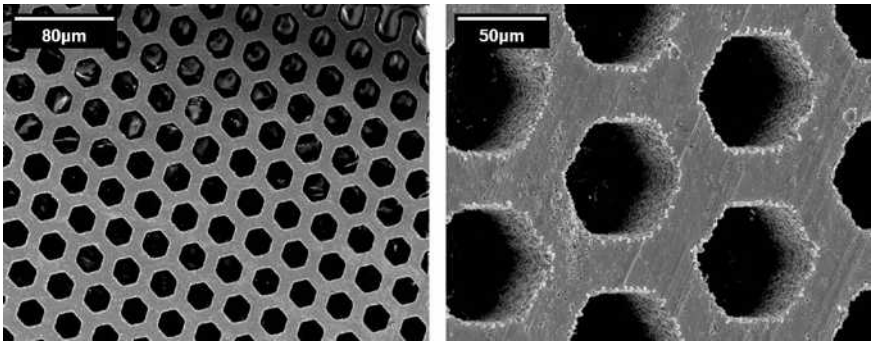

Figure 4. Erbium regenerator disk.

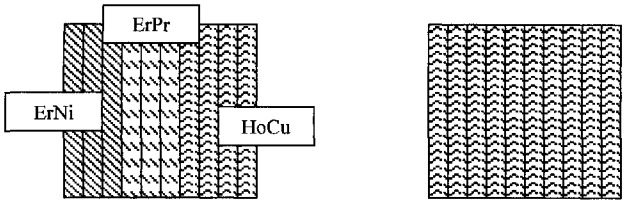

Figure 5. Multiple material regenerator (left); single material regenerator (right).

Materials at very low temperatures typically lose their specific heat (heat capacity), resulting in inefficiencies in the overall system. With the developed manufacturing method, multiple materials can be used in the cold region of a regenerator, allowing for high and uniform heat capacity throughout the regenerator. Figure 5 illustrates a regenerator formed using three different disk materials, as compared to a single material disk stack.

CONCLUSION

Previous work has highlighted the significant impact microchannel regenerators can have on cryocooler performance by both increasing the amount of heat stored and decreasing the pressure drop of the regenerator.[1] Models demonstrate the potential of microchannel regenerator plates to provide an optimal combination of channel geometry, porosity, and matrix material leading to substantial improvements over existing systems. In addition to performance factors, regenerators made with the described method also provide advantages in terms of ease of assembly and environmental safety, such as avoiding the hazards associated with the use of lead microspheres.

ACKNOWLEDGMENT

We would like to acknowledge the support of the Missile Defense Agency under contracts F29601-02-C-0279 and F29601-03-C-0023 administered by the Air Force Research Laboratory.

REFERENCES

1. Rühlich, I., Quack, H., "Investigations on Regenerative Heat Exchangers," *Cryocoolers 10*, Plenum Publishing Corp., New York (1999), pp. 265-274.
2. Ackerman, R., *Cryogenic Regenerative Heat Exchangers,* Plenum Press, New York (1997).
3. Guitrau, E.B., *The EDM Handbook*, Hanser Gardner Publications, Ohio (1997).
4. Takahata K., Gianchandani Y., "Batch Mode Micro-Electro-Discharge Machining", *Journal of MEMS,* vol. 11, no. 2 (2002), pp. 102-110.

Performance Investigation of Stirling-Type Nonmagnetic and Nonmetallic Pulse Tube Cryocoolers for High-Tc SQUID Operation

H. Z. Dang[1], Y. L. Ju[2], J. T. Liang[1], J. H. Cai[1], W. Dai[1] and Y. Zhou[1]

[1]Cryogenic Laboratory, Technical Institute of Physics and Chemistry
Chinese Academy of Sciences, Beijing 100080, China
[2]Nevis Laboratories, Department of Physics, Columbia University
Irvington, NY 10533, USA

ABSTRACT

Over 20 Stirling-type nonmagnetic and nonmetallic pulse tube cryocoolers (NNPTCs) intended to support the portable cryogen-free low-noise continuous operation of high-Tc SQUIDs have been constructed and tested at CL/TIPC/CAS. All cooler components in the vicinity of the SQUIDs' pickup loops are made of nonmagnetic and nonmetallic materials to eliminate cooler-generated interference and to realize direct coupling with the SQUIDs. The system designs are described, and the positive and negative effects of the use of nonmetallic materials on the cooler performance are analyzed. A set of experiments on 24 Stirling-type NNPTCs have been carried out to optimize the cooler geometry and working parameters, and to investigate the working principles of the coolers. Preliminary results are considered satisfactory, and the analysis and evaluation of the cooling performance and interference characteristics of this new-type pulse tube cooler are presented.

INTRODUCTION

Superconducting Quantum Interference Devices (SQUIDs) are the most sensitive magnetic flux-to-voltage sensors known so far. They have been utilized in a wide variety of applications such as biomagnetic research, geophysical surveys, nondestructive evaluation (NDE), and SQUID-based instrumentation for advanced scientific research.[1,2] For more than a decade since they appeared, liquid helium filled cryostats had been the only cooling option. In the 1970s, the concept of supplying a cryogen-free mechanical cooling system for low-Tc SQUIDs was proposed and reduced to practice soon afterwards.[3] However, progress was slow, and extensive applications were not realized. The advent of high-Tc SQUIDs in the late 1980s relaxed the cooling requirements and thus made the situation less severe. From then on, many attempts have been made to cool high-Tc SQUIDs with various types of cryocoolers.

Compared with cryogen-filled cryostats, the cryogen-free cryocoolers are mobile, user-friendly systems. They can realize turnkey operation, and there exists the possibility of operating the system in all orientations. Moreover, the flexible operating temperature may give potentially better SQUID performance (unlike the cryogens, whose operating temperatures are nearly fixed). Unfortunately,

Cryocoolers 13, edited by R. G. Ross, Jr.
Springer Science+Business Media, Inc., New York, 2004

cryocoolers introduce much more complicated interference than do cryogens. If no special measures are employed, the intensity of disturbances generated by commercially available cryocoolers are often hundreds of times the intrinsic noise level of the sensors; this can make the output of the SQUIDs meaningless. In fact, providing an appropriate low-noise mechanical refrigeration system for SQUIDs has been an enormous challenge since they appeared.

GM and Stirling cryocoolers have been the workhorses for cooling high Tc SQUIDs. But their moving displacers introduce distinct, sometimes severe, mechanical vibrations and electromagnetic interference (EMI) signals. These are often fatal for the SQUID operation and have required that the coolers be separated from the sensors in time or space. This has been named the *time-separation* or *space-separation* method, accordingly. In the *time-separation* concept[4], the cooler is turned off during the SQUIDs' operation, while a latent cold reservoir is used to keep the temperature stable; this results in non-continuous operation of the SQUIDs. Moreover, the frequent switching on and off aggravates the wear of the coolers. The *space-separation* method[5] is designed to substantially reduce the interference by increasing the distance between the cooler and the SQUIDs, thus supporting non-interrupted operation. However, it usually significantly adds to the size and complexity of the system, and requires more additional cooling power. These disadvantages associated with GM and Stirling coolers have greatly hindered their wider acceptance as a cooling system for high Tc SQUIDs.

Pulse tube cryocoolers (PTCs), on the other hand, are particularly attractive candidates for cooling high Tc SQUIDs because of the absence of moving parts at low temperatures. The feature has the potential for introducing much less vibration and EMI. For example, acceleration measurements[6] have shown that the vibration generated by PTCs is an order of magnitude less than that of GM and Stirling coolers. And, there exists the possibility of continuous operation of SQUID sensors when they are near or even attached directly to the coolers. Therefore, there has been a surge of interest in attempting to cool high Tc SQUIDs by PTCs since the mid 1990s; this is when mature PTC commercial products became available.[7]

STIRLING-TYPE NNPTCS

PTCs are divided into "Stirling-type" and "GM type" according to their drivers and operating frequencies. So far, nearly all PTCs developed for cooling high Tc SQUIDs have been of the GM type, whose structural features greatly constrain the potential applications of high Tc SQUIDs. For example, presently, the practical application of high Tc SQUIDs is heavily confined to biomagnetic measurements and diagnostics due to the clumsiness of the cooling system. Moreover, the mechanical vibration introduced by the rotary valve is still so severe that sometimes the *time-separation* or *space-separation* method has to be employed.[7,8,9] Stirling-type PTCs have many advantages over their GM type counterparts in terms of compactness, flexibility, and portability, due to their much smaller volume and much lighter weight (a reduction in volume or weight by a factor of 5 to 10). These merits greatly widen their potential application, especially in some special domains such as space and military, where SQUIDs are beginning to play an important role. Moreover, the vibration is damped further due to the absence of rotary valves, and this adds the possibility of coupling the SQUID sensors directly to the cold head. Therefore, we have attempted to develop a better cooling system based on Stirling type PTCs.

To realize the direct coupling of high Tc SQUIDs with the PTCs, another troublesome problem has to be solved in advance. Nowadays, nearly all components of the conventional PTCs are made of metallic materials or materials that exhibit marked remnant magnetization, such as OFHC copper cold heads, stainless steel tubes, stainless steel or copper regenerator matrix and flanges, etc. The magnetic components can also induce EMI because they generate Johnson noise, and then cause distortion of environmental fields. To solve the intractable problem in a simple and advisable way, we decided to fabricate all key components of the PTCs using nonmagnetic, nonmetallic, and electrically insulating materials. For short, we have named this pulse tube a NNPTC.[10]

The selection of materials for Stirling-type NNPTCs is important and arduous work. Based on a series of systematic experiments, we chose a special machinable ceramic for the cold heads and

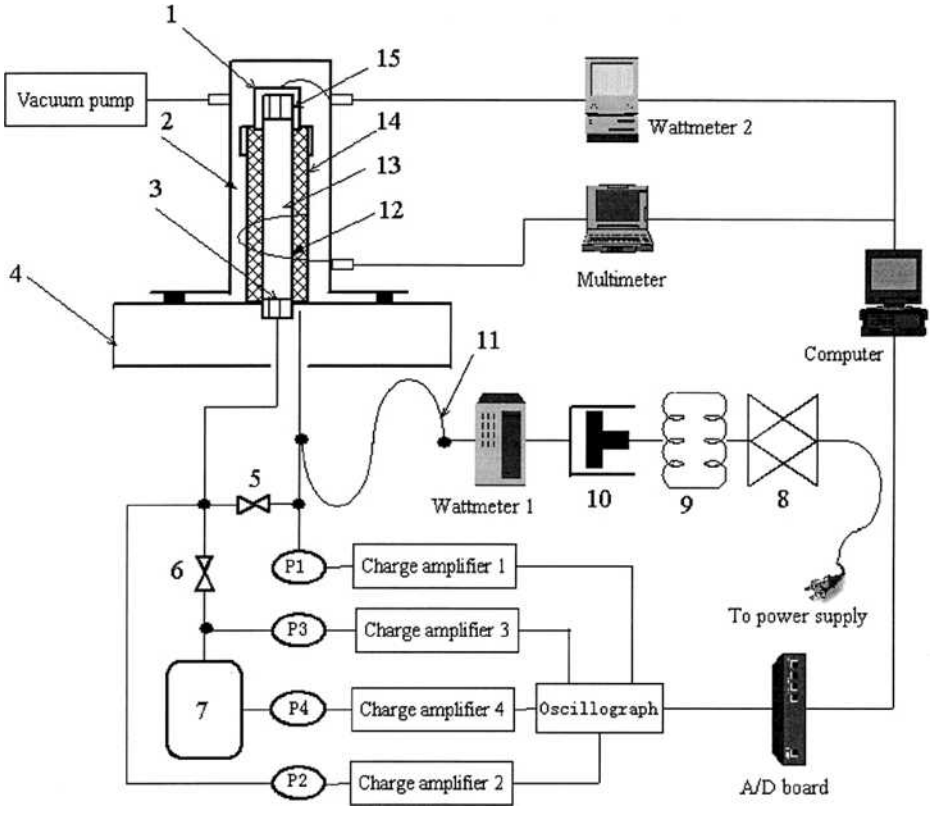

Figure 1. The schematic diagram of the system designed for high Tc SQUIDs. 1 - cold head; 2 - vacuum bonnet; 3 - flow straightener; 4 - hot end flange; 5 - double inlet; 6 - orifice valve; 7 - gas buffer; 8 - frequency converter; 9 - transformer; 10 - compressor; 11 - flexible tube; 12 - matrix; 13 - pulse tube; 14 - regenerator tube; 15 - flow straightener.

used stacked Nylon screens for the regenerator matrix. We fabricated the regenerator tubes using a special glass-filled epoxy resin and the pulse tubes with a kind of Nylon plastic. The vacuum bonnet and connecting flanges are made of acrylic glass, and all flow straighteners are of polytetrafluoroethylene plastic. All of the materials can be regarded as nonmagnetic, nonmetallic, and electrically insulating, and their mechanical, thermal, and cryogenic properties meet the corresponding requirements, respectively. More detail can be found elswhere.[10,11,12]

The characteristics of the Stirling-type NNPTCs are suitable for the construction of portable cryogen-free cooling systems with very low vibration. This includes the potential of supplying continuous low-noise cooling for high Tc SQUIDs, even when the sensors are attached directly to the cold head.

SYSTEM DESCRIPTION

A schematic diagram of the system specially designed for cooling high Tc SQUIDs is shown in Fig.1. The NNPTC is a single-stage coaxial type design. A special synthetic epoxy resin adhesive is used to make the connection between the tubes and the cold head and flanges; this makes the system more compact. The double-inlet configuration is adopted to get better performance, and the needed phase shift is achieved by adjusting the needle valves at the hot end of the pulse tube.

The compressor system consists of a frequency converter, a transformer, and a linear compressor. The transformer protects the compressor, and the frequency converter adjusts the operating

Table 1. The dimensional parameters of No.6 NNPTC.

Regenerator tube			Pulse tube			Regenerator matrix
Inner diameter	Wall thickness	Length	Inner diameter	Wall thickness	Length	Mesh
(mm)	(mm)	(mm)	(mm)	(mm)	(mm)	
11	1.25	60	5	0.75	74	400

frequency. To reduce the vibration generated by the compressor, it is connected to the NNPTC via a small-diameter flexible tube.

Four pressure transducers are used to measure the pressure drops through the orifice and double-inlet valves and the pressure variation in the gas buffer. A Pt-100 resistance thermometer is used to measure the cold-end temperature, and several other Pt-100 thermometers are placed along the external wall of the regenerator to monitor the temperature profile. A wattmeter is used to measure the input electrical power to the compressor, and another wattmeter is used to measure the cooling power of the cooler.

THE EFFECT ON PERFORMANCE OF USING NONMETALLIC MATERIALS

The Positive Effect

It is interesting that the use of nonmetallic materials for tubes and regenerator matrix results in a beneficial by-product, that is, the axial thermal conduction losses are reduced greatly due to the much lower thermal conductivities. For example, for a sample coaxial NNPTC, no.6, whose dimensional parameters are shown in Table 1, the sum of axial conductions loss through the tubes, stacked screens, and the working gas (helium) is only about 9.2% of that of a PTC with the same dimensions, but whose tubes and matrix are made of stainless steel.[12] It should be pointed out that the walls of the regenerator tubes in common metallic PTCs are seldom as thick as those of the nonmetallic tubes, so the actual decrease of the axial conduction loss would not be as great.

The Negative Effects of Use of the Selected Nonmetallic Matrix

For a given regenerator housing, there are two important factors that influence the performance of regenerators. They are the volumetric heat capacity of the matrix materials, c_m, and the thermal penetration depth in the solid matrix, λ_t. The volumetric heat capacity indicates how much heat per volume can be stored. We have computed the variation with temperature of the c_m for stainless steel and the three nonmetallic materials, Nylon, Kapton, and Teflon[11,12] and find that the c_m of Nylon is the highest of the three nonmetallic materials, but is only about 0.38–0.55 times that of stainless steel in the temperature range of 60–300 K; this indicates poorer regenerator performance compared with those with the metallic parts.

Based on thermoacoustics theory[13], the thermal penetration depth in the solid should not be smaller than the characteristic matrix dimension (which refers to the wire diameter of stacked screens) to avoid degrading the effective heat capacity. For high-frequency miniature PTCs working at liquid nitrogen temperatures and using 300–400 mesh stainless steel stacked screens, all of the wire will contribute toward the effective heat capacity, and we needn't consider the effect of the thermal penetration depth.[12,14] However, the situation is different for a Nylon matrix. The thermal penetration depth for Nylon is only 21.5–28.5% of that of stainless steel at the same frequency[12], and when the frequencies are between 30–80 Hz and the temperatures between 60–300 K, the thermal penetration depth for Nylon is of the same order of magnitude or smaller than the wire diameter of 400-mesh screens. Thus, we can not be sure that all of the wire will contribute toward the effective heat capacity. In order to reduce the negative effect, either a lower operating frequency or a larger mesh of screens would have to be adopted. It is difficult to produce the nonmetallic screens with too fine a mesh (we use 400-mesh Nylon screens in the experiments), so a lower operating frequency becomes inevitable.

According to calculations[12] for temperatures in the range between 60 and 300 K, to guarantee the same thermal penetration depth, the drive frequency of a NNPTC would have to be 0.045–0.090 times that of a PTC of the same dimensions with stainless steel screens. Because the optimum drive frequency for a conventional Stirling-type PTC is usually in the range of 35–65 Hz, the drive frequency of a NNPTC with Nylon matrix would need to be between 1.575 Hz and 5.85 Hz; this is impossible and meaningless for a Stirling-type PTC. So poorer performance of a NNPTC can be expected, and optimization of the cooler's construction becomes particularly important.

EXPERIMENTAL INVESTIGATION OF STIRLING-TYPE NNPTCS

During the last four years, 24 Stirling-type coaxial NNPTCs have been fabricated and tested systematically in the Cryogenic laboratory of the Technical Institute of Physics and Chemistry, Chinese Academy of Sciences (CL/TIPC/CAS). The experiments have focused on investigations of the effect of the cooler geometry and working parameters on cooling performance. The optimum parameters have been obtained, and the preliminary-target cooling capacities have been achieved.

Experimental Optimization of the Cooler Geometry

A theoretical model that includes the thermodynamic and the hydrodynamic behavior of gas parcels in an oscillating-flow regenerator was developed, and, based on the model, a preliminary set of optimum regenerator dimensions was obtained.[12] Then, a series of experiments was performed to address practical design issues and optimization of operational parameters.

To optimize the dimensions of the regenerator, two sets of experiments were carried out. For these, the same pulse tube was used, and the regenerator geometry was allowed to vary between test items in the same test set. For test set 1, the pulse tube measured 5 mm in inner diameter and 70 mm in length and had a wall thickness of 0.75 mm. The seven regenerators in the set all had the same volume, but had different aspect ratios (the ratio of the length to the inner diameter). The operating conditions were held constant at a mean pressure of 3.5 MPa and a frequency of 40 Hz. The input electric power was maintained at 72 W, and the swept volume of the specially-designed compressor was varied from 0 to 1.66 cm^3. Test set 2 had the same experimental parameters except that the pulse tube measured 5.5 mm in inner diameter and 76 mm in length. Figure 2 shows the variation in no-load temperature of the cold heads with the aspect ratio of the regenerators. The optimum aspect ratio of the regenerators is seen to be in the range of 5 to 6.

Next, another two sets of experiments (set 3 and 4) were conducted for pulse tube optimization. For set 3, the regenerator measured 11 mm in inner diameter and 57 mm in length, with a wall

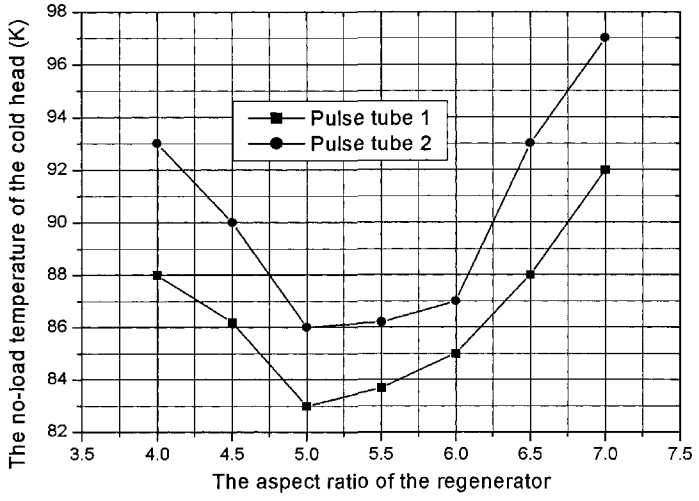

Figure 2. Variations of the no-load temperatures with the aspect ratio of the regenerators.

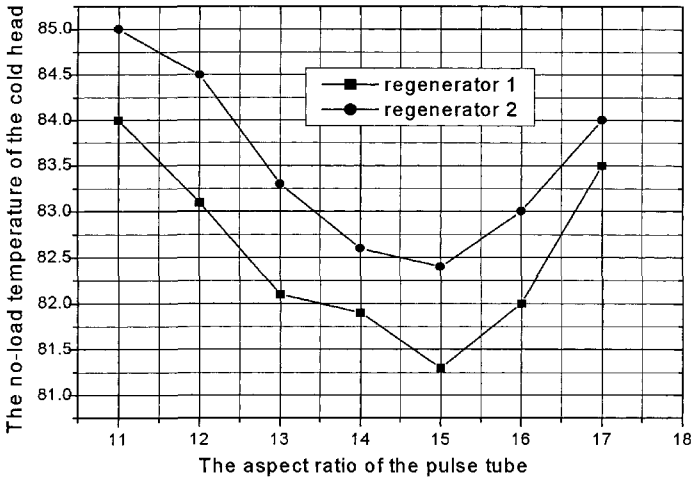

Figure 3. Variations of the no-load temperatures with the aspect ratio of the pulse tubes.

thickness of 1.25 mm. The seven pulse tubes defined a set of constant volume and variable aspect ratio. The charge pressure, operating frequency and the compressor were the same as was used in set 1 and set 2, but the input electric power was maintained at 70 W. Set 4 used another regenerator, which measured 11 mm in inner diameter and 60 mm in length. Figure 3 shows the variation in the no-load temperature of the cold heads with the aspect ratio of the pulse tubes. The optimum aspect ratio of the pulse tube is seen to be in the range of 13 to 16. It should be noted that temperature fluctuations were not as severe as those in the earlier regenerator-optimization experiments.

Finally, additional experiments were performed with the optimization variable being the ratio of the volume of the pulse tube to the void volume of the regenerator. The optimum ratio was found to be in the range of 0.5 to 0.6.[12]

Experimental Optimization of the Working Parameters

Based on the above optimizations of the pulse tube and regenerator geometry, several NNPTCs were fabricated and tested systematically to optimize the working parameters. These included operating frequency, charge pressure, input power, temperature of the hot end, opening of the valves, direction of the asymmetric double-inlet valve, orientation of the cold head, etc. In the following paragraphs we have chosen some representative experimental test data for presentation.

Figure 4 shows the frequency dependence of the no-load temperature of the cold head for the coolers. The optimum operating frequency is seen to be between 36 and 40 Hz. With the same geometry and working parameters, the optimum frequency for the conventional metallic PTCs developed in the same laboratory is usually around 50 Hz. The lower optimum operating frequency is attributed to the smaller thermal penetration depth, as discussed previously.[12]

Figure 5 shows the variation in the no-load temperature of the cold head with the temperature of the hot end for two coolers. The no-load temperature rises sharply with an increase of the temperature of the hot end. Cooling of the hot end is important to the optimization of the NNPTCs because of the lower thermal conductivities of the materials.

DC flow occurring around the loop formed by the regenerator, pulse tube, and the double-inlet is a well-known problem, and asymmetric resistance components are usually employed to reduce or cancel it. In the experiments, asymmetric double-inlet valves were used, and they are defined as in the positive direction when the needle points toward the warm end of the pulse tube; the opposite orientation is defined as in the negative direction. Figure 6 shows the cool-down curves for the no.5 cooler for the two directions. When in the positive direction, the no-load temperature is 10.6 K lower than that in the negative direction. We conclude that the direction of the intrinsic DC flow in the no.5 cooler is from the inlet of the regenerator to the hot end of the pulse tube via the double-

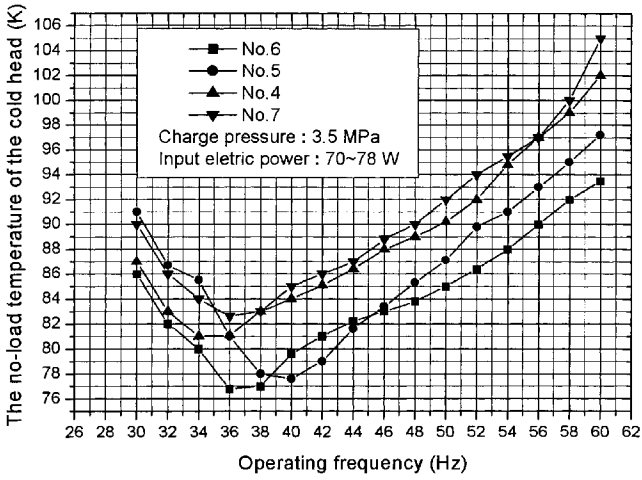

Figure 4. Frequency dependence of the no-load temperature.

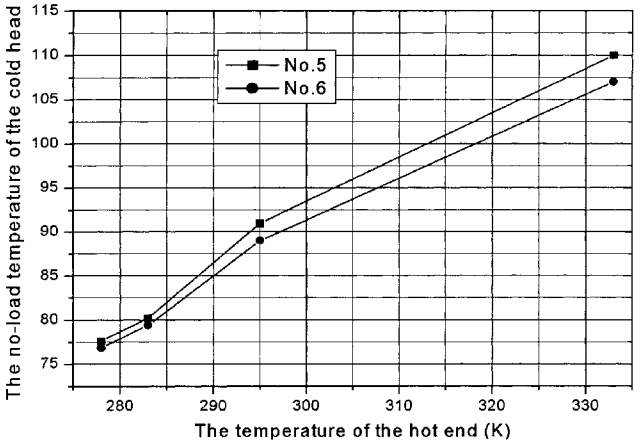

Figure 5. Variation of the no-load temperature with the temperature of the hot end.

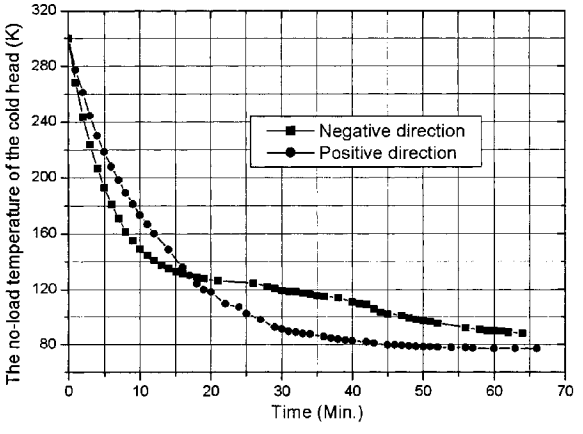

Figure 6. Cool-down curves for different directions of the double-inlet valves.

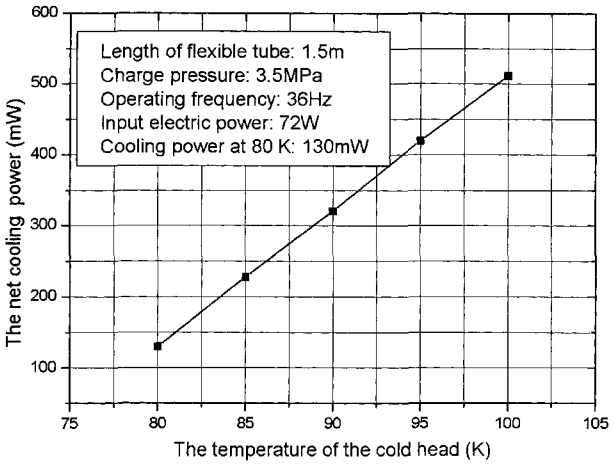

Figure 7. Temperature dependence of the net cooling power of the NNPTC.

inlet valve. We also observe that the cool-down curve when the double-inlet valve is in the negative direction is not as smooth as that in the positive direction, which can be attributed to the impact of a larger DC flow.

Typical Performance of the Stirling-type NNPTCs

At present, a cooling power of over 100 mW at 80 K with 70 W input electrical power has been achieved for the 24 Stirling-type coaxial NNPTCs.[11,12] As an example, we herein present the experimental parameters and results for the no. 6 cooler. Its dimensional parameters were shown earlier in Table 1. The operating frequency changes between 30 and 100 Hz, and the charge pressure varies from 2.0 to 3.6 MPa. Under the optimum working parameters, the no-load temperature reached 76.8 K after 80 minutes, and a cooling power of 130 mW at 80 K was achieved with 72 W of input electric power. The cooling capacity meets the basic cooling requirements of most high Tc SQUIDs, which require a cooling power from about 100 mW to a few hundreds watts. Figure 7 shows the temperature dependence of the cooling power of the no.6 cooler between 80 and 100 K.

The efficiency of the no.6 NNPTC at 80 K is about 0.6% of Carnot efficiency, while the corresponding value for most metallic coaxial Stirling-type PTCs is in the range of 4–11%.[15] The much poorer performance of the NNPTCs confirms the previous analysis, and the main cause is the use of the nonmetallic regenerator matrix.[12]

The remanent magnetic field and Johnson noise in the no.6 NNPTC can be negligible because all the components in the vicinity of the SQUID pickup loops are made of nonmagnetic and nonmetallic materials. According to the measurements[12], the interference induced by the translation and rotation of the cold head is about $50-60\,f_T/\sqrt{\text{Hz}}$, and the maximum temperature fluctuation of the cold head at 80 K with 130 mW applied heat load in 800 seconds was about 40 mK. The results indicate that the cooler can meet the basic noise requirements of most high Tc SQUIDs.

DISCUSSION

Successful application of high Tc SQUIDs is strongly tied to the development of satisfactory refrigeration technology. Pulse tube cryocoolers (PTCs) are promising candidates for providing low-noise cryogen-free cooling systems for high Tc SQUIDs because of their lower mechanical vibration and electromagnetic interference. Stirling-type pulse tube coolers are especially suitable for the task due to their compactness, portability, and lower vibration. Fabricating all of the cooler components in the vicinity of the SQUIDs' pickup loops using nonmagnetic and nonmetallic materials minimizes the cooler-generated EMI and opens the possibility of coupling the SQUIDs directly to the coolers.

The use of nonmetallic materials reduces the axial thermal conduction losses to some extent, but lower heat capacity per unit volume and the lower thermal penetration depth of the nonmetallic matrices than those of common metallic alternatives weaken the regenerator effectiveness significantly; higher operating frequencies and smaller dimensions make the situation worse.

Over 20 Stirling-type coaxial NNPTCs have been fabricated and tested systematically to obtain the optimum cooler geometry and working parameters. In the experiments, the optimal aspect ratio of the regenerator and the pulse tube is 5 - 6 and 13 - 16, respectively. Also, the optimal ratio of the volume of the pulse tube to the void volume of the regenerator is 0.5 - 0.6. The optimum operating frequency of the NNPTCs is a little lower than that of their metallic counterparts. The use of asymmetric double-inlet valves has a marked positive effect to restrain the intrinsic DC flow, which is similar to the situation for metallic PTCs.

A typical cooling power of 130 mW at 80 K for 70 W of input power has been achieved. The preliminary results indicate that the system can meet the basic cooling and noise requirements of high-Tc SQUIDs. In practical applications, larger cooling power and lower working temperatures are usually desired. So further performance optimization of the cooler is underway. In the future, practical applications of this new-style PTC are foreseeable.

ACKNOWLEDGMENT

This work is partly funded by the National Natural Science Foundation of China (Grant No. 50176052 and No. 50206025) and the Chinese Academy of Sciences. The authors would like to thank Dr. M. Thuerk in Jena University, Germany for his help on nonmetallic materials for the NNPTCs.

REFERENCES

1. Clarke, J., "High-Tc SQUIDs," *Current Opinion in Solid State & Materials Science,* vol. 2, no. 1 (1997), pp. 3-10.
2. Cantor, R., "DC SQUIDs: Design, optimization and practical applications," *SQUID Sensors: Fundamentals, Fabrication and Applications*, Weinstock, H., editor, Kluwer Academic Publishers, Dordrecht (1996), pp. 179-233.
3. Zimmerman, J.E., Radebaugh, R., and Siegwarth, J.D., "Possible cryocoolers for SQUID magnetometers," *Superconducting Quantum Interference Devices and their Applications,* Hahlbohm, H.D. et al. editors, Walter de Gruyter Publishers, Berlin (1977), pp. 287-296.
4. Kaiser, G., et al., "Cooling of HTSC Josephson Junctions and SQUIDs with Cryo-refrigerator," *Cryogenics,* vol. 34 (ICEC suppl.)(1994), pp. 891-894.
5. Van den Bosch, P.J., et al., "Cryogenic Design of a High-Tc SQUID-based Heart Scanner Cooled by Small Stirling Cryocoolers," *Cryogenics,* vol. 37, no. 3 (1997), pp.139-51.
6. Li, H., et al., "System Design of 60 K Stirling-type Coaxial Pulse Tube Coolers for HTS RF Filters," *Physica C,* vol. 282-287 (1997), pp. 2527-2528.
7. Heiden C., *Pulse tube refrigerators: a cooling option for high-Tc SQUIDs,* In: Weinstock H., editor. *SQUID Sensors: Fundamentals, Fabrication and Applications,* Kluwer Academic Publishers, Dordrecht (1996), pp. 289-305.
8. Gerster, J., et al., "Low Noise Cold Head of a Four-valve Pulse Tube Refrigerator," *Adv Cryo Eng.* vol. 43B(1998), pp. 2077-2084.
9. Lienerth, C., et al., "Low-Noise cooling of HTc-SQUIDs by means of a pulse-tube cooler with additional vibration compression," *ICEC18,* Narosa Publishing House, Mumbai (2000), pp. 555-558.
10. Dang, H.Z, Ju, Y.L, Liang, J.T. and Zhou, Y., "On the Development of a Non-metallic Non-Magnetic Miniature Pulse Tube Cooler," *Cryocoolers 12*, Kluwer Academic/Plenum Publishers, New York (2003), pp.799-804.
11. Dang, H.Z., Ju, Y.L., Liang, J.T., Cai, J.H., Zhao, M.G, and Zhou, Y., "Performance of Stirling-type non-magnetic and non-metallic co-axial pulse tube cryocoolers for high-Tc SQUIDs operation," (submitted to *Cryogenics*).

12. Dang, H.Z., *Investigation on high frequency Stirling-type nonmagnetic nonmetallic pulse tube cryocoolers*, Doctoral dissertation, Institute of Mechanics, Chinese Academy of Sciences, Beijing (2004), pp. 1-157.

13. Swift, G.W., *Thermoacoustics: a unifying perspective for some engines and refrigerators*, Acoustical Society of America Publications (2002), pp. 1-315.

14. Radebaugh, R., Marquardt, E. and Bradley, P., *Development of a Pulse Tube Refrigerator for Millimeter Array Sensor Cooling: Phase I,* ALMA Memo #281, NIST (1999), pp. 1-26.

15. Radebaugh, R., "Development of the Pulse Tube as an Efficient and Reliable Cryocooler," Proc. Institute of Refrigeration, London (2000), pp. 11-29.

Flow Circulations in Foil-Type Regenerators Produced by Non-Uniform Layer Spacing

D. Gedeon

Gedeon Associates
Athens, OH 45701

ABSTRACT

In a Stirling-cycle cryocooler model a foil-type regenerator is split into two parts. The foil spacing in one part is increased while decreased in the other. This gives rise to DC flow circulations between the two parts and degrades overall cryocooler performance.

Within the regenerator the internal temperature distribution tends to be skewed toward one end or the other, depending on the local direction of the DC flow. These temperature changes amplify the DC flow and significantly degrade performance unless prevented by means of transverse thermal coupling between the two parts of the regenerator.

The problem worsens with decreasing temperature and increasing foil spacing. In the temperature range of 30–100 K, it is easily possible for a foil regenerator to degrade overall cooling efficiency (heat lift / compressor PV power) by 15% or more for a foil spacing variation of only ±10% between different parts of the regenerator.

THE FOIL REGENERATOR RECORD

The common wisdom in the cryocooler industry is that foil regenerators (parallel-plates) do not work. Theoretically speaking they should work just fine. In fact they should work better than any other known regenerator type. This assertion is typically based on the evaluation of a figure of merit that measures the benefits of high heat transfer and low flow resistance. See for example the comparison by Ruhlich and Quack[1] which shows parallel-plate regenerators to be about 4 times better than stacked screens. Even computational models of complete cryocoolers, which consider more factors than just regenerator heat transfer and flow resistance, come to the conclusion that foil-type regenerators give the best coefficient of performance (COP) measured as heat lift per unit compressor PV power.

Apparently something goes wrong when one actually builds a foil regenerator. Typically foil regenerators are fabricated by winding a foil strip into a cylindrical or annular form, somehow spacing the layers to provide locally parallel flow paths. It is very difficult to achieve uniform spacing. One approach is to space the layers by dimpling the foil at intervals or inserting some sort of spacers between layers. If the dimples or spacers do not stack directly on top of each other then they can induce bending moments in the foil which tend to distort the spacing. Another approach is to etch the spacing features directly into the foil (Mitchell[2]), but maintaining uniform spacing between layers remains a challenge. Even if initial spacing is

Cryocoolers 13, edited by R. G. Ross, Jr.
Springer Science+Business Media, Inc., New York, 2004

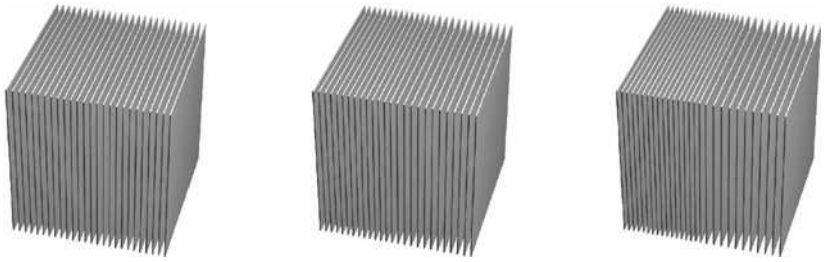

Figure 1. CAD renderings of parallel-plate regenerator matrices showing increasing spacing non-uniformities between the left and right halves of each matrix, ranging from uniform spacing (at left) to flow gap 25% smaller than the mean in one half and 25% larger in the other half (at right). The gap variation in the middle is ±10%.

perfect, non-uniform cooling or heating during operation can produce localized thermal expansions and contractions that may affect spacing.

Exactly how uniform foil spacing must be has been a relatively unexplored issue. Backhaus and Swift[3] discussed the matter in the context of a parallel-plate regenerator in a thermoacoustic stirling engine but did not come to a definitive conclusion. This paper takes a fresh look at the importance of foil spacing by using a mostly computational approach, backed by a bit of theory.

FORMULATING THE PROBLEM

There are infinitely many possible ways that foil spacing can vary within a regenerator. Consider the simplest case that captures the essential problem, namely a regenerator consisting of parallel plates divided into two parts of equal flow area as illustrated in Figure 1. Subject the two parts to equal but opposite perturbations in flow gap (gap between plates) and see what happens in the context of an operating Stirling cycle. The most interesting thing that happens is that equal but opposite DC flows develop in the two regenerator parts. Something like a slow convection cell superimposed on the baseline oscillating-flow traveling up one regenerator part and down the other.

In low Reynolds-number viscous flows, pressure drops are dependent on velocity shear rates whereas mass flows are dependent on the product of density and velocity. So variations in fluid density over the course of an oscillating-flow cycle may cause a net mass imbalance even though pressure drops are equal in the two directions. Or, if that is prevented by the lack of a return path for the surplus mass flow, there may arise a time-average pressure bias from one end of the flow path to the other. Or, anything between these two extremes. See Gedeon[4] for a discussion of DC flows in pulse-tube or Stirling-cycle cryocoolers employing closed-loop flow paths. In the present case, the relationship between time-mean pressure drop and DC flow differs between the two regenerator parts because of their different flow gaps. The result is that there is a little DC pressure drop and a little DC flow required in order to keep the laws of physics in balance.

ANALYTIC SOLUTION

There is an unpublished report[5] that derives the equation governing DC flow for such a two-part parallel-plate regenerator in detail. The procedure is briefly summarized here. Begin with the equation governing Darcy flow for a parallel-plate regenerator

$$u = -\frac{g^2}{12\mu}\frac{\partial P}{\partial x} \tag{1}$$

where u is section-mean velocity, g is flow gap, μ is viscosity and $\partial P/\partial x$ is the axial pressure gradient. Then assume that both velocity and density are the sum of a constant plus phasor part

(sinusoidally varying), $u = u_m + \vec{u}$, $\rho = \rho_m + \vec{\rho}$ and conclude after very little math that the DC flow per unit flow area may be written

$$(\rho u)_{dc} = \rho_m u_m + \tfrac{1}{2}\vec{\rho}\cdot\vec{u} \tag{2}$$

where $\vec{\rho}\cdot\vec{u}$ denotes the usual dot product for vectors. Use a linear superposition principle to apply the Darcy flow Equation (1) to both the mean and phasor velocity components, giving

$$(\rho u)_{dc} = -\frac{g^2}{12\mu}\left(\rho_m \frac{\partial P_m}{\partial x} + \tfrac{1}{2}\vec{\rho}\cdot\frac{\partial \vec{P}}{\partial x}\right) \tag{3}$$

Then make a few assumptions in order to conclude that there is a point, roughly the regenerator midpoint, where the local pressure gradients may be replaced by regenerator averages, i.e. $\partial P/\partial x \approx \Delta P/L$, where L is regenerator length. Denote that point by subscript c, and write Equation (3) as

$$(\rho u)_{dc} \approx -\frac{g^2}{12\mu_c L}\left(\rho_c \Delta P_m + \tfrac{1}{2}\vec{\rho}_c\cdot\Delta\vec{P}\right) \tag{4}$$

Apply Equation (4) to the two regenerator parts, denoting one part by subscript A and the other by subscript B. Add the equations. In order to conserve mass the left-hand sides must sum to zero (assuming there is no DC flow beyond the regenerators). Solve the resulting equation for DC pressure drop ΔP_m then substitute the result back into Equation (4). Replace phasor density variation $\vec{\rho}$ with an approximation based on the gas energy equation. Also assume the temperature distribution in the regenerator is approximately linear, that an ideal-gas equation of state applies and that gas viscosity and conductivity vary as $T^{0.7}$ (reasonably accurate for helium in the range of 10 to 1000 K). At this point the equation gets messy, but it can be simplified considerably if one is willing to assume a few things. First, that the regenerator *pressure-drop* phasor is 90 degrees out of phase with the *pressure* phasor (pressure and velocity in phase). Second, that the regenerator compliance (volume) is small. The first assumption is reasonable, since optimal regenerator performance requires that pressure and velocity fluctuations be roughly in phase. The second assumption is equivalent to saying that velocity phase does not vary much through the regenerator. Not a very good approximation, but it will have to do. The final oversimplified but instructive equation governing DC flow in regenerator A is

$$\frac{(\rho u)_{dc}}{(\rho u)_1} \approx \frac{\gamma P_m \Delta P_1 T_r^{1.4}}{48(\gamma-1)N_u k_r \mu_r L}\frac{\partial T}{\partial x}\left[\frac{g^4}{T_c^{3.4}}\right]_B^A \tag{5}$$

where the $[\cdot]_B^A$ notation means evaluate the difference $(\cdot)_A - (\cdot)_B$. The quantity on the left is the ratio of the DC mass flux to the amplitude of the oscillatory mass flux for the baseline unperturbed regenerator. Quantities on the right not yet defined are,

γ = ratio of specific heats (1.67 for helium)
P_m = mean pressure
ΔP_1 = amplitude of phasor pressure drop
T_r = Temperature at "rejection" end of regenerator (warmer end)
T_c = Temperature at a central point within regenerator (near midpoint)
$\partial T/\partial x$ = Temperature gradient within regenerator (representative average)
N_u = Nusselt number for laminar, developed parallel-plate flow (8.23)
k_r = gas conductivity at "rejection" end of regenerator
μ_r = gas viscosity at "rejection" end of regenerator

A similar equation governs the equal and opposite DC flow in regenerator B.

Note that the DC flow depends strongly on the gap difference between regenerator parts (g^4 dependence) and that the direction of DC flow reverses depending on the sign of the temperature gradient. For a cryocooler, where $\partial T/\partial x$ is negative, a positive gap perturbation in regenerator part A results in a negative DC flow. For an engine, where $\partial T/\partial x$ is positive, a positive gap perturbation results in a positive DC flow. In either case a positive gap perturbation produces DC flow from the colder end toward the warmer end of the regenerator. This DC flow combined

with the regenerator temperature gradient tends to remove heat from the interior of the regenerator, perturbing the temperature distribution *colder in the part with the larger gap.*

Another thing to note in Equation (5) is that DC flow depends roughly on the central regenerator temperature raised to the –3.4 power. This means that the drop in central regenerator temperature noted in the previous paragraph tends to amplify the DC flow. The exact gain factor for the amplification is difficult to evaluate analytically. The heat removal produced by DC flow is counteracted by other thermal-energy transport mechanisms in the regenerator including: gas conduction, solid conduction within the foil, the time-averaged enthalpy flux produced by the regenerator AC flow, and any transverse thermal conduction between the two regenerator parts. All of these effects tend to restore the temperature distribution to its baseline roughly-linear state. Backhaus and Swift[6] discuss a similar battle between DC flow temperature destabilization and stabilizing transport mechanisms in the context of closed-loop thermoacoustic Stirling engines.

SAGE MODEL

Because the available analytic solution is difficult to work with, highly approximate and does not adequately deal with the regenerator interior temperature perturbations produced by DC flow, the quantitative results presented in this paper are based on numerical analyses of two-part foil regenerators using the Sage computer program.[7] Sage employs a finite-difference solution of the regenerator gas-dynamic equations and resolves DC flows in reasonable agreement with the above analytic solution.

It is straight-forward to implement two regenerators in parallel within a Sage model. In the screen image on the left in Figure 2 the component labeled "parallel regenerators" contains two regenerator canisters as shown in the screen image on the right. A transverse thermal conduction link is established between the regenerator matrices inside each canister, as depicted by the connector arrows labeled Q_{Gx}. Transverse conduction is used as an optional means to restore thermal equilibrium to regenerator parts subject to DC flow. The transverse conduction distance between regenerators is an input to the model and can correspond to anything from heat flow across a single foil layer to heat flow between widely separated sections of the matrix.

The matrix stuffing in canisters A and B is "wrapped-foil," which is equivalent to ideal

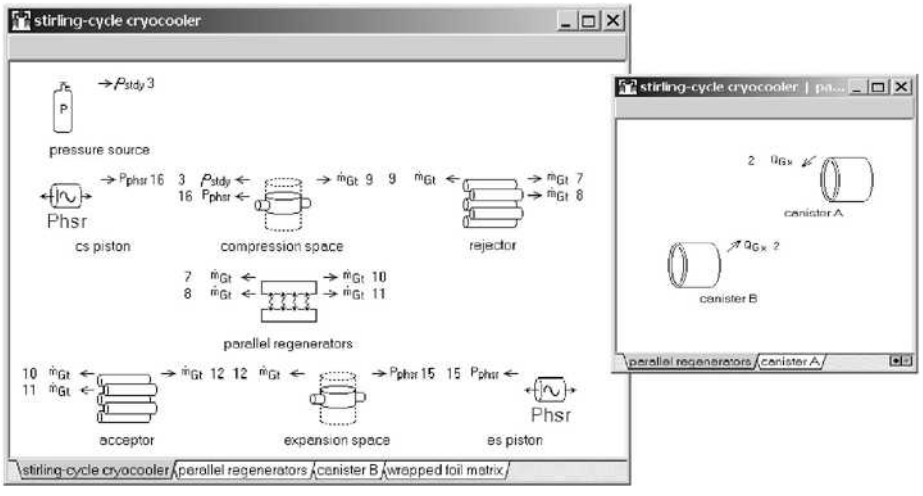

Figure 2. At left, Sage top-level model window for a simplified two-piston Stirling-cycle cryocooler. The model contains only the minimal number of components to implement the Stirling cycle using a two-part foil regenerator. Numbered arrows indicate connections between model components. At right, two canisters within the "parallel regenerators" component, each containing a foil-type regenerator matrix with the provision for transverse thermal conduction provided by the Q_{Gx} connectors.

parallel plates as far as the Sage model is concerned. It would also have been possible to fill the canisters with any other matrix type, such as stacked screens or random fibers. The reason for using wrapped-foil was that the phenomenon to be investigated is mainly thought to be a problem in foil-type regenerators. Another reason is that the above analytic solution is available for parallel-plate flow.

The remainder of the cryocooler model contains only those components necessary to implement a minimal Stirling-cycle cryocooler. The regenerator canisters have zero wall thickness and therefore zero thermal conduction loss. The rejector and acceptor heat exchangers at either end of the regenerators have isothermal wall boundary temperatures. The compression and expansion spaces are perfectly driven by sinusoidal volume-displacements provided by the CS and ES pistons, even though hardly any Stirling cryocooler employs two pistons in this way. There are no parasitic thermal conduction paths between the warm and cold ends of the cryocooler, except those provided by the regenerator foil and gas within the regenerators.

Model Optimization

To make the results most useful it is necessary to specify the various dimensional inputs to the Sage model in order that it represent a "good" cryocooler. Some variables are fixed at typical reasonable values, such as:

- Hot and cold temperature (see Table 2)
- Frequency = 30 Hz
- Charge Pressure = 25 bar (2.5 MPa)
- Piston amplitudes: CS = 5 mm, ES = 2 mm (both sinusoidal)
- Heat exchanger lengths: Rejector = 30 mm, Acceptor = 10 mm

Other variables strongly affect the overall performance and cannot be arbitrarily assigned. Sage's built-in optimizer selected these in order to achieve minimum PV power input with net heat lift normalized to 1.0 W. The variables optimized and constraints they are subject to are summarized in Table 1. During optimization the canister diameter, flow gap and foil thickness are constrained to be the same for both regenerator parts. So the optimization is equivalent to optimizing a single foil regenerator. After optimization, the flow gap (and only the flow gap) is manually varied between the two parts.

Table 1. Specifications used by Sage's optimizer in order to optimize the 1st, 2nd and 3rd stage regenerators and overall thermodynamic cycle.

Optimized Variable	Subject to
CS Piston	
Frontal area	
ES Piston	
Frontal area	
Phase angle (relative to CS piston)	
Compression and Expansion Spaces	
Mean volume	= 1.5 * swept volume amplitude
Wetted surface	= 1.5 * minimal right circular cylinder
Acceptor and Rejector	
Tube number	
Tube ID	
Regenerator	
Canister diameter	
Length	≤ 100 mm
Flow gap	
Foil thickness	≥ 15 microns

Table 2. Key values for optimized 1st, 2nd and 3rd stages used as the basis for computational experiments.

	1st stage	2nd stage	3rd stage
Boundary conditions			
Treject (K)	300	97	31
Taccept (K)	97	31	10
Foil Material	Stainless steel	Lead	Lead + Er_3Ni
Optimized regenerator dimensions and operating conditions			
Regenerator length (mm)	100*	100*	94
Flow gap (microns)	60	31	16
Foil thickness (microns)	15*	15*	63
Combined canister section area (mm^2)	18.3	23.1	111
Mean Reynolds number	56	168	522
Pressure variation (bar @ deg)	3.0 @ 46	3.8 @ 50	4.7 @ 46
Pressure drop (kPa @ deg)	6.1 @ -14.7	10.6 @ -140	11.4 @ -163
Mass flux Treject end (kg/s m^2 @ deg)	7.7 @ 64	21.6 @ 78	39.8 @ 79
Mass flux Taccept end (kg/s m^2 @ deg)	15.2 @ -13	48.9 @ -12	150 @ -29
Overall performance			
Heat lift @ Taccept (W)	1.0	1.0	1.0
PV power input (W)	2.96	3.38	3.80

* value limited by max or min constraint

Three Temperature Ranges

According to the above analytic solution, DC flow depends strongly on regenerator temperature. So the Sage model was optimized over three temperature ranges, roughly corresponding to those bounding the individual stages of a three-stage cryocooler operating between 300 K and 10 K. The resulting models are referred to as 1st, 2nd and 3rd stage models. In each case the ratio of warmer-end to cooler-end temperature is 3.1, as shown in Table 2. The various materials shown in Table 2 for the regenerator foil are intended to represent typical practice in order to maintain solid heat capacity at low temperatures. For greatest accuracy the models employ a so-called tabular-helium working gas, where the equation of state is based on tabulated values accurate down to 10 K, or lower.

In an actual three-stage cryocooler the heat lift rapidly diminishes in each successively higher stage, because the heat rejected by each stage adds to the heat lifted by the previous stage. This is unlike the three models of Table 2 where heat lift is normalized to 1.0 W for each. If the purpose were to put together an actual three-stage cryocooler from the specifications in the table, a scaling of the individual stages would be necessary.

COMPUTATIONAL EXPERIMENTS

For present purposes the main thing of interest is the relative change in regenerator performance and overall COP of each individual stage produced by perturbing the flow gap in the two regenerator parts by equal and opposite amounts — with the flow gap in one part larger than the mean value by Δg and in the other half smaller by Δg. This can be done with the two regenerator parts thermally isolated or in good thermal contact. The results of doing both are shown in Figure 3. As expected, COP goes down with increasing gap variation $\Delta g / g_0$. Roughly speaking, combined viscous dissipation losses go down, and combined net-cyclic enthalpy flows go up, as shown in Figure 4. The former reduces the required PV power input while the later subtracts directly from the heat lift. The reduced heat lift is more significant, so the net result is that overall COP goes down.

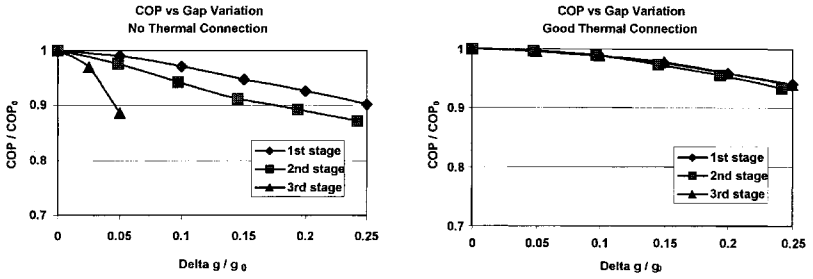

Figure 3. Degradation in cryocooler COP (heat lift / PV power) as a function of gap variations between two foil-type regenerator parts. $\Delta g/g_0$ may be thought of as the amplitude of the gap variation between the two regenerator parts

The COP degradation is much worse when the two regenerator parts are thermally disconnected (left plot of Figure 3). This is because the DC flow circulation skews the temperature profiles in the two regenerators. The temperature skewing effect can be seen in Figure 5, which shows the temperature distribution in the two 1st stage regenerator parts for the case $\Delta g/g_0 = 0.25$. Temperature skewing does two things: First, it tends to further increase the regenerator DC flow, as noted above. Second, it changes the viscosity, conductivity and density of the helium, which affects the net cyclic enthalpy flux carried by the AC flow. Consider the larger-gap regenerator part. Assuming pressure drop amplitude is roughly constant, which it is because of equal but opposite changes in the two regenerator parts, Darcy flow Equation (1) implies that mass flux amplitude is proportional to

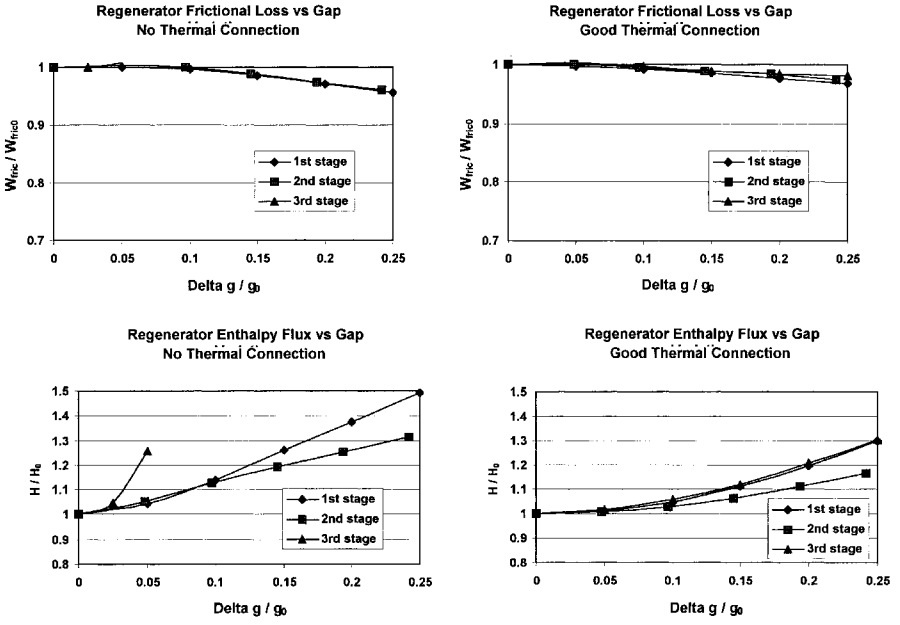

Figure 4. Changes in combined regenerator flow-frictional losses (pumping power) and net cyclic enthalpy flux as a function of gap variations between two foil-type regenerator parts. There is some beneficial effect of gap variation on combined frictional loss. But this is more than offset by increased enthalpy loss.

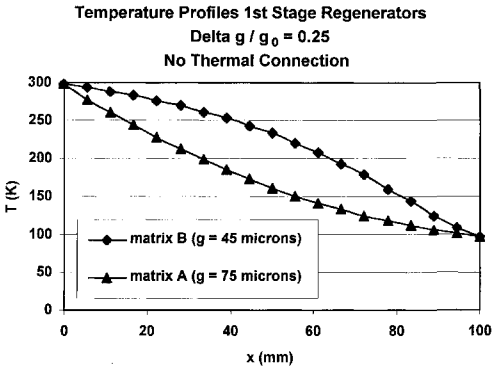

Figure 5. Typical internal temperature skewings in 1st stage regenerator parts *A* and *B* produced by DC flow. The effect illustrated is produced by a DC mass flux that is only about 0.13% of the AC part (0.011 kg/s·m^2 DC part compared to 8.5 kg/s·m^2 regenerator-average AC amplitude).

$$(\rho u)_1 \propto \frac{\rho g^2}{\mu} \tag{6}$$

So mass flux amplitude increases strongly with increasing gap. Moreover, because temperature decreases in the larger-channel regenerator, density ρ increases and viscosity μ decreases. Both tend to increase the mass flux amplitude beyond what it would increase as a result of the larger gap alone. Gas conductivity drops too, which means that the gas-to-foil temperature difference tends to increase more than it otherwise would. The result is increased net cyclic enthalpy flux ($\frac{1}{2} c_p (\rho \vec{u}) \cdot \vec{T}$) in the larger-gap regenerator part, with the increase being larger when its internal temperature is allowed to drop than if it does not. The effects are opposite in the smaller-gap regenerator part, but, because of the strong nonlinear dependence of enthalpy flux on gap and temperature, the increase in the larger-gap regenerator overwhelms the decrease in the smaller-gap regenerator.

Worse at Low Temperatures

In the thermally uncoupled case (left plot of Figure 3), for the same relative gap variation COP, degradation worsens with decreasing temperature — i.e. is worse for the 3rd stage than the 1st stage regenerator. The regenerator interior temperatures are free to drift and at-least two of the factors that tend to stabilize the regenerator temperature distribution — gas conduction and foil conduction — tend to be less effective at extremely cold temperatures. The net result is that the regenerator temperature skewing produced by DC flow gets progressively worse in low temperature regenerators, which increases the net cyclic enthalpy loss as noted above. At extremely low temperatures the temperature distribution may even go unstable. Some evidence for this is the failure of the Sage model to converge for gap perturbations beyond $\Delta g / g_0 = 0.05$ in the 3rd stage regenerator.

The thermally coupled case is substantially different (right plot of Figure 3). The COP drop-off is about the same for all three stages even though the relative DC flow increases in successive stages. Evidently, it is not so much the DC flow itself that affects COP in this case, as it is the effects of two non-optimal regenerators acting in parallel.

Worse for Large Flow Gaps

According to Equation (5) the relative DC flow depends on flow gap to the 4th power. However, pressure drop factor ΔP_1 in Equation (5) also depends on gap to the –2 power according to Darcy flow Equation (1). So, in the case of a fixed regenerator canister where the overall foil spacing changes, the tendency for DC flow increases approximately in proportion to

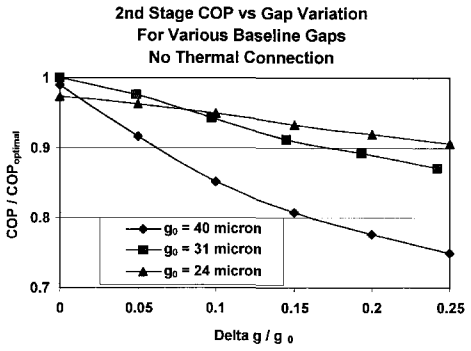

Figure 6. Sensitivity to gap variations increases dramatically with the size of the baseline regenerator gap.

the square of the flow gap. To investigate this, two additional models, corresponding to the 2nd stage regenerator with thermally disconnected parts, set the flow gap first about 30% higher, then 30% lower than the optimal gap. Systematically perturbing the gaps in the two regenerator parts as before produces the result shown in Figure 6. As expected the regenerator with the larger flow gap shows much greater sensitivity to gap variations compared to the regenerator with the smaller gap.

CONCLUSIONS

Computational experiments confirm that uniform foil spacing is critical to foil regenerator performance. Intra-regenerator DC flow circulation always results as a consequence of non-uniform foil spacing. If all parts of the regenerator are in good transverse thermal contact, the effects of such DC flow circulation are minimal. There is a drop in COP, but it results mainly from the effects of non-optimal regenerator parts acting in parallel. If the regenerator parts are thermally decoupled then the DC flow circulation alters the regenerator internal temperature distribution in such a way as to reduce COP much more dramatically. These internal temperature changes also tend to amplify DC flow. In other words there is a positive feedback mechanism between regenerator temperature change and DC flow. Especially at very low temperatures or if the flow gap is a bit larger than optimal. For a regenerator operating in the range of 30–100 K with a flow gap 30% higher than optimal, Figure 6 shows a degradation in COP by about 15% for a flow gap variation of only ± 10%.

To actually achieve something close to the theoretical performance of a foil regenerator a designer might do a few things. First, take care to space the layers very uniformly, e.g. with gap variations within ±10%. Second, design for a smaller flow gap than optimal. According to Figure 6 a gap reduction of 30% below optimal does not affect COP that much, and it results in greatly reduced sensitivity to gap variations. Third, provide for some sort of transverse thermal coupling within the regenerator. This may be easier said than done. Ideal would be a foil with high conductivity normal to the flow direction and low conductivity parallel to the flow direction. Providing some means to allow transverse mixing between adjacent gas passages, thereby promoting gas mixing, would accomplish the same thing, though at some risk for increased viscous dissipation due to flow separations and increased *axial* thermal conduction via the mechanism of thermal dispersion. Thermal dispersion is a phenomenon that looks like enhanced gas thermal conductivity on a macroscopic scale (see Hsu[8]). In addition to increasing effective transverse thermal conduction, inter-layer mixing would also tend to average out any local variations in flow gap, thereby reducing the tendency to produce DC flow circulations in the first place.

While the detailed study of this paper was based on foil-type regenerators the same sort of problems are likely to occur in non-foil regenerators, such as random fibers, screens and packed spheres, although to a lesser degree because transverse and axial thermal transports within such regenerators are typically much higher than for foils. Also, the flow in such regenerators lies somewhere between viscous-dominated Darcy flow and inertial flow, so the DC flow producing mechanism does not quite apply. Even so, there may come a point in low-temperature cryocoolers where an extreme sensitivity to local variations in matrix structure compounded by thermal amplification of DC flow begin to overwhelm the natural tendency of thermal dispersion to stabilize the axial temperature profile. An especially sensitive application would be high-power coolers where the regenerator transverse conduction distances are large.

ACKNOWLEDGMENT

This work would not have been possible without support over the past several years from NASA Glenn Research Center and DOE for regenerator development in Stirling-cycle engines and the collaboration with researchers at Cleveland State University and the University of Minnesota.

REFERENCES

1. Ruhlich, I. and Quack, H., "Investigations on Regenerative Heat Exchangers," *Cryocoolers 10,* Kluwer Academic/Plenum Publishers, New York (1999), pp. 265–274.
2. Mitchell, M. P. and Fabris, D., "Improved Flow Patterns in Etched Foil Regenerator," *Cryocoolers 12,* Kluwer Academic/Plenum Publishers, New York (2003), pp. 499–505.
3. Backhaus, S. and Swift, G. W., "Fabrication and use of Parallel Plate Regenerators in Thermo-acoustic Engines," *Proceedings of the 36th Intersociety Energy Conversion Engineering Conference,* ASME (2001), pp. 453–458.
4. Gedeon, D., "DC Gas Flows in Stirling and PulseTube Cryocoolers," *Cryocoolers 9,* Plenum Press, New York (1997), pp. 385–392.
5. Gedeon, D., *Intra-Regenerator Flow Streaming Theory,* unpublished memorandum (CSUIntraRegenStreamingTheory.pdf), Gedeon Associates, Athens OH, (2004).
6. Backhaus, S. and Swift, G. W., "An Acoustic Streaming Instability in Thermoacoustic Devices Utilizing Jet Pumps," *J. Acoust. Soc. Am.*, vol. 113, (2003), pp. 1317–1324.
7. Gedeon, D., *Sage Stirling-Cycle Model-Class Reference Guide, Third Edition*, Gedeon Associates, Athens OH, (1999).
8. Hsu, C.T. and Cheng, P., "Thermal Dispersion in a Porous Medium," *Int. J. Heat Mass Transfer*, vol. 33, no. 8 (1990), pp. 1587–1597.

A New Angle of View for Understanding and Evaluating Flow Characteristics of Cyclic Regenerators

Ercang Luo

Technical Institute of Physics and Chemistry
Chinese Academy of Sciences
Beijing 100080, China

ABSTRACT

Regenerators represent a crucial element of regenerative machines, where their flow characteristics have a strong impact on performance. Therefore, relatively extensive measurements on flow characteristics of regenerators have been made in recent years. These measurements have shown that the flow friction factors of regenerators under reciprocating flow are much larger than those under steady flow, sometimes larger by 2~6 times. Some of these measurement observations are true, but there are uncertainties about the evaluation methods behind others. Usually, these papers evaluated the flow friction factors of cyclic regenerators based on the view of steady flow, in which the pressure drop across the regenerator is caused only by the viscous effect of the fluid. As a result, the pressure drop was treated as a scalar quantity having the same phase as the velocity in the regenerator; in addition, the effects of inertia were usually neglected. In this paper, a new perspective for understanding and evaluating the flow characteristics in reciprocating-flow regenerators is proposed. Here, the inertia effect will be included, and the pressure drop is considered as a vector. In addition, the unusual increase of the pressure drop in the reciprocating-flow regenerator may result from early triggering or intensification of turbulence and entrance effects of the reciprocating flow in the complex geometry structure. The presented viewpoint may provide some new insights into the essence of the flow characteristics in reciprocating-flow regenerators.

INTRODUCTION

An oscillating flow can be classified as two types: a pulsating flow, and a reciprocating flow. In the former case the amplitude of the oscillating velocity is less than the time-averaged flow velocity, for which the flow direction never reverses. In the latter case, the amplitude of the oscillating velocity is greater than the time-averaged flow velocity, for which the flow direction can reverse periodically. Both types of oscillating flows have wide applications in the fields of acoustical, biological, chemical, and energy, as well as refrigeration and cryogenic engineering. Especially, in recent years, a great deal of effort has been devoted to the development of regenerative machines such as Stirling machines, pulse tube refrigerators and thermoacoustic machines. In regenerative machines, the regenerators used are the most important thermodynamic elements. For optimization of regenerative machines, it is important to accurately

Cryocoolers 13, edited by R. G. Ross, Jr.
Springer Science+Business Media, Inc., New York, 2004

predict the friction and heat transfer losses in the regenerators. However, at the present time, the flow-friction and heat-transfer-loss correlations used in the design of the regenerators are commonly based on steady flow conditions that are unrealistic, since the regenerative machines operate under reciprocating flow conditions. More recently, some experimental investigations on the flow characteristics of regenerators have been made that have shown that flow friction factors of regenerators under reciprocating flow are much larger than those under steady flow, sometimes increased by 2~6 times.[1,2,3] Some of these measurement observations are true, but there are questions over the validity of others. In this paper, the author presents a new perceptive on the flow characteristics of regenerators with the objective of attaining a deeper understanding of the flow behavior in regenerators and providing suggestions for future research directions.

PHYSICAL MODEL AND PRESSURE DROP OF CIRCULAR TUBE

Flow characteristics in a reciprocating-flow regenerator are very complex due to gas compressibility, entrance effects, turbulence effects, and the complex geometric structure. The complete analytical solution is too ambitious to be addressed directly. However, qualitatively, the flow characteristics in a regenerator are similar to those in a circular pipe. Therefore, we start with the following analysis by first considering reciprocating flow in a circular pipe. For simplicity, a simplified two-dimensional transient momentum equation for describing the circular pipe subjected to reciprocating flow is given as follows,

$$\frac{\partial u}{\partial t}+u\frac{\partial u}{\partial x}=-\frac{1}{\rho}\frac{dp}{dx}+\nu\frac{\partial^2 u}{\partial^2 y} \tag{1}$$

The following expression for the pressure drop over the length dx along the pipe can be obtained from Eq. (1),

$$\Delta p=\int\rho(\nu\frac{\partial^2 u}{\partial^2 y}-\frac{\partial u}{\partial t}-u\frac{\partial u}{\partial x})dx \tag{2}$$

This clearly shows that the pressure drop over the distance of dx along the pipe results from viscous friction, transient inertia, and local acceleration. We first consider a fully-developed laminar flow of an incompressible fluid. Therefore, the acceleration item, $u\frac{\partial u}{\partial x}$, will vanish. Adopting complex notation representing the thermodynamic variables appearing in Eq. (2), we have the following correlation between the pressure gradient, velocity and other operating parameters,

$$\frac{d\tilde{p}}{dx}=-\rho_0\omega[\frac{\mathrm{Im}(-f_\mu)}{|1-f_\mu|^2}+j\frac{1-\mathrm{Re}(f_\mu)}{|1-f_\mu|^2}]\tilde{u} \tag{3}$$

From Eq.(3), one can infer that the pressure drop over the distance dx consists of viscous and inertial contributions. The former is related to real friction losses, while the latter one is not. Even for the extreme case of a fluid with no viscosity, there is still a pressure drop over the distance dx due to the transient inertia of the fluid. It is important to note that the case of reciprocating flow is quite different from that of a steady flow. Keeping this in mind, it is useful to examine the important behaviors of reciprocating flow and to design appropriate experiments to obtain the correlations describing the dependence of pressure drop on the other thermodynamic parameters. Equation (3) gives a strict analytical solution for the pressure drop gradient dependence on the two similarity parameters and other thermodynamic variables that include zeroth-order and first-order Bessel functions. Because these are not straightforward for engineering design, Maa[4] has generated an approximate solution as follows,

$$\frac{d\tilde{p}}{dx}=-[\frac{8\mu}{r_0^2}\sqrt{1+\frac{1}{16}(r_0/\delta_\mu)^2}+j\omega\rho_0(1+\frac{1}{\sqrt{3^2+(r_0/\delta_\mu)^2}})]\tilde{u} \tag{4}$$

Figure 1 shows the flow characteristics of laminar and reciprocating flow in pipes. It is found that when the kinetic Reynolds number is smaller than eight (this corresponding to the dimensionless parameter r_0/δ_μ less than 1), the amplification of the pressure drop factor is no more than 1.1, and the phase of the pressure drop lags the velocity by about 20 degrees. In fact, a typical regenerator has the dimensionless parameter r_0/δ_μ less than 1. This means that the pressure drop of a reciprocating regenerator should not be much larger than that of its steady flow. However, recent experiments on reciprocating-flow regenerators have shown that reciprocating-flow regenerators have a 2 to 6 times increase in the pressure drop compared with steady-flow regenerators. We will expand our discussion on this issue in the following section. From the above analysis, we think that the appropriate similarity parameters are the peak Reynolds number and the kinetic Reynolds number. Figure 2 shows a comparison between the strict and approximate solutions. It is easily seen that the approximate solution agrees with the strict analytical solution very well, with errors being less than 10% for a wide range of r_0/δ_μ that cover most real cases of reciprocating flows. However, the viscous pressure drop is indeed increased due to the reciprocating flow. The larger the kinetic Reynolds number, the more obvious the phenomenon is. This interesting fact may be attributed to the more abrupt transverse velocity gradient with so-called "double boundary" layers or "annular effect".[6,7]

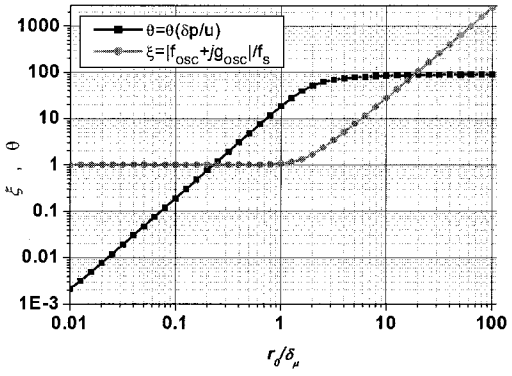

Figure 1. Flow characteristics of a reciprocating flow

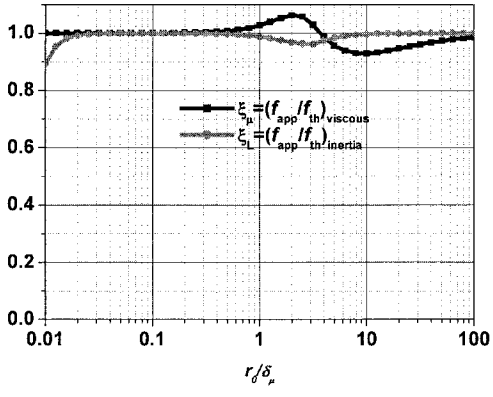

Figure 2. Comparison between the strict and approximate solutions

By introducing two similarity parameters, the peak Reynolds number, $R_{e,\max} = \rho_0 |\tilde{u}| D_h / \mu$, and the kinetic Reynolds number, $R_{e,\omega} = \rho_0 \omega D_h^2 / \mu$, we can rewrite Eq. (3) in the following form that is familiar to most engineers,

$$\frac{d\tilde{p}}{dx} = -\frac{1}{2}(f_{viscous} + jf_{inertia})\frac{1}{D_h}\rho_0 |\tilde{u}| \tilde{u} \tag{5}$$

where, $f_{viscous} = \frac{2R_{e,\omega}}{R_{e,\max}} \frac{\mathrm{Im}(-f_\mu)}{|1-f_\mu|^2}$, $f_{inertia} = \frac{2R_{e,\omega}}{R_{e,\max}} \frac{1-\mathrm{Re}(f_\mu)}{|1-f_\mu|^2}$, and f_μ is the viscous factor[5].

In a similar way, we can rewrite Eq.(4) in the following form,

$$\frac{d\tilde{p}}{dx} = -\frac{1}{2}(f_{viscous} + jf_{inertia})\frac{1}{D_h}\rho_0 |\tilde{u}| \tilde{u} \tag{6}$$

where, $f_{viscous} = \frac{64}{R_{e,\max}}\sqrt{1+\frac{1}{128}R_{e,\omega}}$ $f_{inertia} = \frac{2R_{e,\omega}}{R_{e,\max}}(1+\frac{1}{\sqrt{3^2+R_{e,\omega}/8}})$.

Furthermore, we can rewrite Eq.(6) in the following form,

$$\frac{d\tilde{p}}{dx} = -\frac{1}{2}\tilde{F}\frac{1}{D_h}\rho_0 |\tilde{u}| \tilde{u} = -\frac{1}{2}Fe^{j\theta}\frac{1}{D_h}\rho_0 |\tilde{u}| \tilde{u} \tag{7}$$

$$F = \frac{64}{R_{e,\max}}\sqrt{(1+\frac{R_{e,\omega}}{128})+\frac{R_{e,\omega}^2}{32^2}(1+\frac{1}{3^2+R_{e,\omega}/8}+\frac{2}{\sqrt{3^2+R_{e,\omega}/8}})}$$

where,

$$= \begin{cases} \frac{64}{R_{e,\max}} & (R_{e,\omega} << 32, \quad \textit{viscous controlling zone}) \\ \frac{2R_{e,\omega}}{R_{e,\max}} & (R_{e,\omega} >> 3200, \quad \textit{inertia controlling zone}) \end{cases}$$

and

$$\theta = arc\tan(\frac{R_{e,\omega}}{32}\frac{1+\frac{1}{\sqrt{3^2+R_{e,\omega}/8}}}{\sqrt{1+R_{e,\omega}/128}})$$

Based upon Eq.(7) and the expression for F and θ, it clearly shows these facts: (1) there is phase lag between the pressure drop and velocity, and the phase lag depends only upon the kinetic Reynolds number; (2) the "superficial" or "effective" pressure drop factor F is increased for a reciprocating flow compared with a steady flow by a factor of

$$\sqrt{(1+\frac{R_{e,\omega}}{128})+\frac{R_{e,\omega}^2}{32^2}(1+\frac{1}{3^2+R_{e,\omega}/8}+\frac{2}{\sqrt{3^2+R_{e,\omega}/8}})}.$$

The larger the kinetic Reynolds number $R_{e,\omega}$ is, the larger the amplification factor is. Actually, the kinetic Reynolds number is related to the dimensionless parameter r_0/δ_μ, where δ_μ is the viscous penetration length; that is, $R_{e,\omega} = 8(r_0/\delta_\mu)^2$. The reciprocating flow may be classified into three zones, viscosity controlling zone, transition zone and inertia controlling zone, corresponding to $R_{e,\omega} << 32$, $32 < R_{e,\omega} << 3200$ and $R_{e,\omega} >> 3200$. For the viscosity controlling zone, the pressure drop factor of the reciprocating flow is very close to that of steady, laminar flow, while for the inertia controlling zone, the "superficial" pressure drop factor can be much larger than that of a steady, laminar flow.

PHYSICAL MODEL AND PRESSURE DROP OF REGENERATORS

A regenerator has a much more complex geometric structure than a pipe. Thus, it is not easy to obtain the two-dimensional momentum equations for it. However, the above analysis based on a circular pipe should illuminate the issues associated with analyzing reciprocating-flow in a regenerator. At least we can imagine that the regenerator may function qualitatively as a pipe. Thus, we still can use the peak Reynolds number and the kinetic Reynolds number to depict its flowing performance. Due to the complex geometric structure of the regenerator, it is necessary to introduce an additional similarity parameter, the dimensionless shape factor. Moreover, the onset of turbulence, turbulence behavior, and entrance effects in the regenerator can be quite different from that of either steady flow in a regenerator or reciprocating flow in a circular pipe. First, we consider a correction for the regenerator due to its complex geometric structure,[7]

$$\frac{d\tilde{p}}{dx} = -\frac{1}{2}(C_{\mu,reg} f_{viscous} + jC_{L,reg} f_{inertia})\frac{1}{D_h}\rho_0 |\tilde{u}|\tilde{u} \tag{8}$$

where, $C_{\mu,reg} = C_{\mu,reg}(R_{e,\max}, R_{e,\omega}, \varphi)$ and $C_{L,reg} = C_{L,reg}(R_{e,\max}, R_{e,\omega}, \varphi)$. Both of these correction factors are functions of the peak Reynolds number, the kinetic Reynolds number, and the dimensionless geometry similarity parameter φ. As mentioned previously, if the reciprocating flow in the regenerator is still laminar, the superficial pressure drop factor for it should not be increased too much for typical operating conditions ($r_0/\delta_\mu < 1$ or $R_{e,\omega} < 8$). However, recent experiments on reciprocating regenerators have given a much larger pressure drop factor that ranges from 2 to 6 times larger than that expected. What is the reason is for this phenomenon? We think that there are two possibilities, turbulence effects and entrance effects.

Let us first look at the onset of turbulence with reciprocating flow in a pipe. According to previous extensive experimental investigations, the so-called acoustic Reynolds number is useful for characterizing the onset of turbulence with reciprocating flow. The acoustic Reynolds number is defined as follows,

$$R_{e,\delta_\mu} = \rho_0 |\tilde{u}| \delta_\mu / \mu \tag{9}$$

Actually, the acoustic Reynolds number is based on the mean peak cross-sectional velocity and the viscous penetration depth, δ_μ. These experiments showed that the critical value for turbulence onset, $(R_{e,\delta_\mu})_{cri}$, is about 500.[8,9,10] Figure 3 shows the pressure drop factors for laminar and turbulent flows in a pipe. It can be seen that, for the same kinetic Reynolds number, turbulent flow has a much larger pressure drop factor than laminar flow by 2 to 3 times. Due to its extremely complex geometric structure, a screen-woven or ball-packed regenerator may have a much lower $(R_{e,\delta_\mu})_{cri}$ for the onset of turbulence in the regenerator. There seems to have not been much investigation of the onset of turbulence in a reciprocating regenerator; this needs to be studied more in depth in the future.

We now examine the entrance effects for reciprocating flow in a pipe. It has been reported that the entrance length of reciprocating flow is time-dependent, and the time-averaged entrance length can be estimated using the following equation,[11,12]

$$\bar{x} \approx 0.05 R_{e,\delta_\mu} P_r D_h \tag{10}$$

Figure 4 shows that the pressure drop in the entrance zone is much larger than that in the fully developed zone (the figure is reproduced from Ref. 12). The definition for c_f, A_0 and $R_{e,\omega}$ can be found in the paper. Actually, A_0 is equal to $R_{e,\max}/R_{e,\omega}$. The author of the paper argued that it is better to select A_0 and $R_{e,\omega}$ as independent similarity parameters. However, our above analysis shows that it is actually better to select the peak Reynolds number and the kinetic Reynolds number as similarity parameters for reciprocating flow.

Also, due to its more complex geometric structure, a reciprocating-flow regenerator may have a much larger entrance effect than a steady-flow regenerator. We still use Eq. (8) to describe the pressure drop dependence on the peak Reynolds number, the kinetic Reynolds number, the dimensionless shape factor, and other relevant physical variables. However, we think that the two new correction factors should be expanded to include enhanced turbulence and entrance effects.

Now, let us take a look at changes to the acoustic Reynolds number and the time-averaged entrance length as a function of operating frequency, temperature, and pressure. In fact, the acoustic Reynolds number can be rewritten in the following form,

$$R_{e,\delta_\mu} = \frac{\rho_0 \mid \tilde{u} \mid \delta_\mu}{\mu} = \sqrt{\frac{\rho_0 \omega}{\mu}} X_{\max} \tag{11}$$

where, $X_{\max}$ is the displacement amplitude of gas particles.

In a typical experiment on a reciprocating-flow regenerator, one usually fixes the displacement amplitude of the piston, and this means that the displacement amplitude of the gas particles is fixed. Thus, if operating frequency is increased, the acoustic Reynolds number will be increased, and, consequently, the reciprocating flow trends toward earlier triggering or a stronger intensification of turbulence. In addition, for a gaseous fluid, if operating temperature is lowered, its density will increase and its dynamic viscosity will decrease. Both of these changes will increase the acoustic Reynolds number to trigger or intensify turbulence in the regenerator. Finally, a higher pressure will have a similar effect. These analyses may provide some reasons why the "superficial" pressure drop was 2 to 6 times larger for the cases having higher operating frequency and low-temperature.

Entrance effects in a reciprocating-flow regenerator are another challenging problem. It is believed that entrance effects may also play a significant role in creating increased pressure drop. This definitely needs to receive greater attention in future studies.

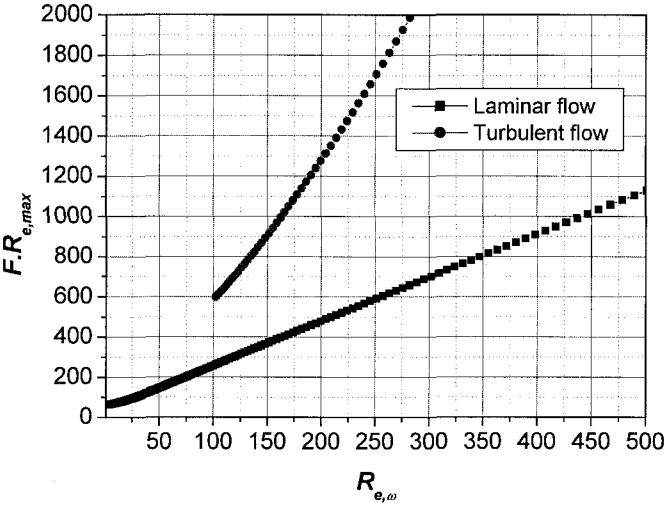

Figure 3. Turbulent effect in a pipe; the line for laminar flow is based on Eq. (7), while the line for turbulent flow is recalculated based on the experiment.[10]

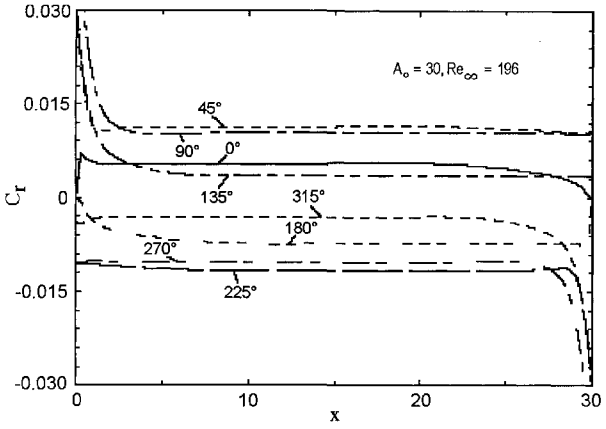

Figure 4. Entrance effect in limited long pipe.

CONCLUSIONS

Based on the presented study, the following conclusions are drawn:

(1) The pressure drop associated with reciprocating flow consists of three parts: viscous, inertia, and local acceleration. There are at least two similarity parameters for describing recipro-cating flow: peak Reynolds number and kinetic Reynolds Number. The superficial (or effective) pressure drop factor for oscillating flow in a pipe is amplified, resulting from the annular effect and the inertial effect. Certainly, the viscous part of the pressure drop will be amplified with reciprocating flow.

(2) For a regenerator having typical operating conditions, the unusual amplification of the superficial pressure drop factor may contribute to the triggering or intensification of turbulence and increased entrance effects associated with the oscillating flow in the regenerator. Both the onset of turbulence in a regenerator and entrance effects need to be studied more in-depth.

ACKNOWLEDGMENT

The financial support from the Chinese Academy of Sciences under Contract Number KJX2-SW-W12-1 is greatly appreciated. The authors would also like to thank Prof. Yuan Zhou and Prof. Jian-feng Wu for their helpful discussions.

REFERENCES

1. Helvensteijn B. Kashani A, Spivak A., Roach P., Lee J., Kittel P., "Pressure drop over regenerators in oscillating flow," *Adv. Cryo. Eng.*, vol. 43B, Plenum Press, New York (1998), pp.1619-1626.
2. Jiang Y., Ju Y., Zhou Y., "A study of oscillating flow characteristics of regenerators in a high frequency pulse tube refrigerators," *Adv. Cryo. Eng.*, vol. 43B, Plenum Press, New York (1998), pp. 1635-1641.
3. K. Yuan, L.Wang, Y.K. Hou, Y. Zhou, J.T. Liang, Y.L. Ju, "Oscillating flow characteristics of a regenerator under low temperature conditions," *Cryocooler 12*, Kluwer Academic/Plenum Publishers, New York (2003), pp. 539-546.
4. Maa Dah-you, *Theory and design of micro-perforated panel absorber*, Chinese Sciences Bulletin (1975), Vol. 1, pp. 38-50.
5. Rott N., "Thermoacoustics," *Adv. App. Mech.*, vol.20 (1980), p. 135.
6. Richardson E.G., Tyler E., "The transverse velocity gradient near the mouths of pipes in which an alternating or continuous flow of air is established," *Pro. Phys. Soc. London*, vol.42 (1929), pp.1-15.

7. Luo E.C., Liu H.D., He G. Q., Liang J.T., Zhou Y., "Flow characteristics of reciprocating flow in pipe and regenerator," *Cryogenics*, vol.4, no.110 (1999), pp. 68-173 (in Chinese).

8. M. Hino, M.Sawamoto, and S Takasu, "Experiments on the transition to turbulence in an oscillating pipe flow," *J. Fluid Mech.*, vol.75, Part 2 (1976), pp. 193-207.

9. P.Merkli and H. Thomann, "Transition to turbulence in oscillating pipe flow," *J. Fluid Mech.*, vol.68 (1975), pp. 567-575.

10. Zhao T.S., Cheng P., "Experimental investigation of the onset of turbulence and friction losses in an oscillatory pipe flow," *Int. J. Heat and Fluid Flow*, vol.17 (1996), pp. 356-362.

11. J.H.Gerrard and M.D.Hughes, "The flow due to an oscillating piston in a cylindrical tube: a comparison between experiment and simple entrance flow theory," *J. Fluid Mech.*, vol.50, no.1 (1971), pp. 97-106.

12. Zhao T.S., Cheng P., "Hydro-dynamically developing laminar flow in circular pipe," *J. Fluid. Eng.*, vol.17 (1996), pp. 167-172.

Experimental Flow Characteristics Study of a High Frequency Pulse Tube Regenerator

X.L. Wang, M.G. Zhao, J.H. Cai, J.T. Liang, W. Dai,

Cryogenic Laboratory
Technical Institute of Physics and Chemistry
Chinese Academy of Sciences
Beijing ,100080, P.R. China

ABSTRACT

In this paper, a one-dimensional regenerator hydrodynamic model has been developed. In the model, the definition of regenerator friction factor under oscillating flow is different from that for steady flow. A dynamic experimental apparatus has been designed and constructed to investigate the oscillating-flow characteristics of regenerators. In the prototype experimental system, a linear compressor was used to generate the oscillating pressure wave. Three different length regenerators were tested. Detailed experimental data have been obtained for the oscillating pressure and velocity wave that define the flow amplitude and the phase shift characteristics of a high frequency pulse tube cryocooler regenerator. The operational frequency of the system was run at 30 Hz, 40 Hz, 50 Hz and 60 Hz. The oscillating flow friction factor at these operational frequencies is shown in the experimental data. It was found that the relationship between the friction factor under oscillating flow and steady flow varied with the value of the instantaneous Reynolds numbers during one cycle. The ratio is not simply a scaler-multiple relationship as has been reported in other references. The results can be used to predict the performance of a pulse tube cryocooler and should be helpful in the design of a cryogenic regenerator using numerical simulation models.

INTRODUCTION

Interest in the pulse tube cryocooler has grown rapidly in recent years owing to its lack of moving components in the low temperature region. Therefore, it has merits in mechanical simplicity, high reliability, low vibration, and low cost. As a necessary component, the oscillating flow regenerator plays an important role in the refrigerator performance of the pulse tube cryocooler and other regenerative cryocoolers. An accurate prediction of the pressure drop across a regenerator is crucial to the design of these cryocoolers.

To date, the most popular pressure drop correlation used for the design of these devices is the one provided by Kays and London[1], who obtained experimental data for steady flows through a stack of wire screens. Similarly, there are also some correlations with pressure drop in regenerators[2-4], but most of them are based on unidirectional steady flow through a stack of screens. Since a pulse tube cryocooler operates under periodically reversing flow conditions, it is apparent that the correlation equations based on steady flow are not able to predict accurately the pressure drop in the oscillating flow regenerator.

Cryocoolers 13, edited by R. G. Ross, Jr.
Springer Science+Business Media, Inc., New York, 2004

Considerable prior research has been performed on the pressure drop in a packed column subjected to oscillating flow. Hsu et al.[5] performed oscillating-flow experiments with regenerators and revealed that the oscillating-flow friction factor is nearly the same as the steady friction factor at low operating frequencies. Yoshida et al.[6], Zhao and cheng[7], Helvensterjn et al.[8], and Ju et al.[9] found a higher friction factor with oscillating flow in the regenerator than with steady flow at the same Reynolds numbers based on the cross-sectional mean velocity. Recently, Nam and Jeong[10-11] measured the flow characteristics of a regenerator under actual operating conditions. Their experimental results show that when the operating frequency is less than 9 Hz, the oscillating-flow friction factor is nearly the same as the steady flow friction factor for Reynolds numbers up to 100. For 60-Hz operation, the ratio of the oscillating flow friction factor to that for steady flow increases as the hydraulic Reynolds number increases. Sungryel Chio[12] proposed a new oscillating flow model for the pressure drop with oscillating flow through a regenerator with pulsating pressure. Two correlations in the model were obtained from experiments with wire screen regenerators under various operating frequencies and inlet mass flow rates. The validity of these results for cryocooler regenerators is still questionable because the temperature effects on the flow characteristics were neglected in his model and experiments.

In this paper, the definition of the regenerator friction factor under an oscillating flow is obtained by analyzing a one-dimensional regenerator hydrodynamic model, which is different from the friction factor with steady flow. The pressure and velocity at the two ends of the regenerator were measured in a carefully designed apparatus to determine the oscillating flow friction factor. Finally, the friction factor is compared with the steady flow friction factor.

ANALYSIS

It is assumed that the flow in the regenerator is one-dimensional, the working gas is an ideal gas, the gas and matrix heat conduction along the matrix are neglected, and there is no temperature difference across the regenerator. The basic momentum equation is as follows:

$$\rho\frac{\partial u}{\partial t}+\rho u\frac{\partial u}{\partial x}+\rho u\frac{\partial u}{\partial r}=-\frac{\partial P}{\partial x}+\mu\frac{1}{r}\cdot\frac{\partial}{\partial r}(r\frac{\partial u}{\partial r})+\frac{\partial}{\partial x}(\mu\frac{\partial u}{\partial x}) \tag{1}$$

The second term on the right of Eq. (1) can be expressed in the following form[13]:

$$\mu\frac{1}{r}\cdot\frac{\partial}{\partial r}(r\frac{\partial u}{\partial r})+\frac{\partial}{\partial x}(\mu\frac{\partial u}{\partial x})\approx f\cdot\frac{1}{Dh}\cdot\frac{\rho u^2}{2} \tag{2}$$

The following definition of the oscillating flow friction factor can be obtained:

$$f_{inst}=\frac{-\frac{\partial P}{\partial x}-\rho\frac{\partial u}{\partial t}-\rho u\frac{\partial u}{\partial x}-\rho u\frac{\partial u}{\partial r}}{\frac{\rho u^2}{2D_h}} \tag{3}$$

where, D_h is the hydraulic diameter, f_{inst} is the instantaneous friction factor of the oscillating flow regenerator, which is a function of position x and time t.

In our experimental measurement, we can only obtain the pressure drop in a given length L, so the mean instantaneous friction factor in the length L:

$$f(t)=\frac{1}{L}\int_0^L f_{inst}(x,t)dx \tag{4}$$

The mean instantaneous velocity in the length is expressed as follows:

$$u(t)=\frac{1}{L}\int_0^L u(x,t)dx \tag{5}$$

Integrating Eq. (3) over the total length L of the regenerator, we have

$$f(t) = \frac{\Delta P}{\dfrac{\rho u(t)^2 \cdot L}{2D_h}} - \frac{2D_h}{u(t)^2} \cdot \frac{\partial u}{\partial t} - \frac{2D_h}{L} \cdot \frac{\Delta u}{u(t)} - \frac{2D_h}{u(t)} \cdot \frac{\partial u}{\partial r} \tag{6}$$

It is found that under our experimental conditions the pressure gradient term is far greater than the third and fourth terms in the right side of Eq. (5), so they can be neglected. The elimination of the two terms in Eq. (5) leads to the following simplified form of the mean instantaneous friction factor:

$$f(t) = \frac{\Delta P}{\dfrac{\rho u(t)^2 \cdot L}{2D_h}} - \frac{2D_h}{u(t)^2} \cdot \frac{\partial u}{\partial t} \tag{7}$$

where the oscillating flow friction factor includes two terms. The first term is similar to the steady flow friction factor in form, but the velocity is the mean instantaneous velocity. The second term is the inertial term, which cannot be neglected when the oscillating frequency of the flow is high.

EXPERIMENTAL SYSTEM

Figure 1 shows a schematic diagram of the experimental apparatus for testing the regenerator. The system is designed to measure the dynamic pressure and velocity of the oscillating flow gas at the two ends of the test regenerator. The test section consists of a packed column with both ends connected to the flow conditioning section made of stainless steel pipe of the same diameter. The two heat exchangers are provided at the two ends to maintain a constant temperature through the whole test section. This type of heat exchanger configuration is similar to other work.[4] The test section is connected to a reservoir with an adjustable needle orifice valve that is connected to the end of the second flow-conditioning section. A linear compressor (swept volume: 5 cc) is used to generate the oscillating pressure and flow at various frequencies (30–60 Hz).

A fine hot wire (DANTEC, Model 90N10) anemometer and two piezoelectric pressure transducers (KISTLER, Type 601A) are used to measure the dynamic pressure and the instantaneous cross-sectional mean velocity through the regenerator, respectively, as shown in Fig. 1. Detailed information about the experimental apparatus is similar to that in Ju, et al.[9]

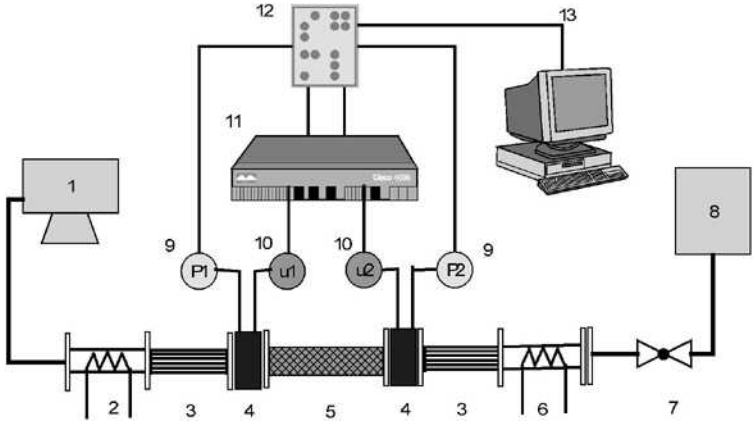

Figure 1. Schematic diagram of experimental apparatus: 1–compressor, 2–cooler, 3–flow straightener, 4–connector, 5–regenerator, 6–heater, 7–orifice, 8–reservoir, 9–pressure transducer, 10–hot-wire probe, 11–hot-wire anemometer, 12–A/D converter board, 13–computer.

Table 1 Properties of sample regenerators.

Regeneraor No.	Lengh (m)	Diameter (m)	Number of screens n	Mesh size	Wire diameter (mm)	Pitch (mm)	Hydraulic diameter (mm)
1	0.052	0.007	1261	500	0.021	0.0508	0.0392
2	0.050	0.008	1230	500	0.021	0.0508	0.0392
3	0.045	0.009	1124	500	0.021	0.0508	0.0392

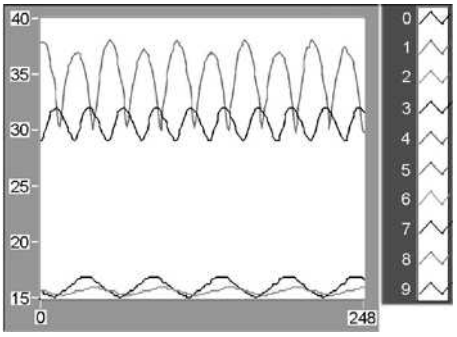

Figure 2. Typical prototype of the instantaneous gas velocity and pressure wave.

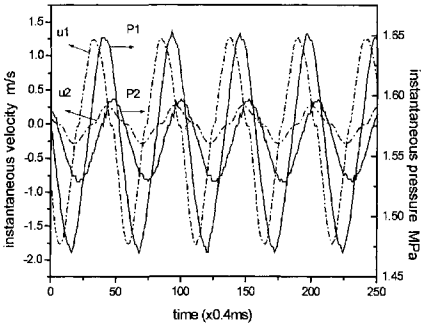

Figure 3. The processed experimental data.

EXPERIMENTAL RESULTS AND DISCUSSIONS

Three regenerators were made to confirm the reliability and repeatability of the experimental results in this study. The regenerators were made of stacks of stainless-steel plainly woven wire screens with 500 mesh size. The properties for the three regenerators are listed in Table 1 including the number of screens n, wire diameter d_w, pitch p, and hydraulic diameter d_h. The hydraulic diameter d_h of the regenerator was determined from the equation given in the work of Miyabe.[3]

Typical raw experimental data for the oscillating flow is shown in Fig. 2. The raw experimental data measured from the hot wire anemometer and the pressure transducers required data processing which included velocity transformation and correction. Figure 3 shows the real pressure and velocity wave at the inlet (V1, P1) and the outlet (V2, P2) of the test regenerator. Pressure and velocity for high frequency clearly show phase shift and amplitude attenuation. It is also observed from Fig. 3 that the positive and the negative amplitude of the velocity are different. These are typical phenomena for the valve (resistance) and the reservoir (capacitance) configuration, which were also found in the work of Kwanwoo[11] and theoretically verified in the work of Kuriyama et al.[14]

THE INSTANTANEOUS OSCILLATING FLOW FRICTION FACTOR

The pressure and velocity wave were measured for the oscillating flow at the two ends of the regenerator. The following correlation equation was used to calculate the instantaneous oscillating flow friction factor (Eq.7):

$$\Delta P(t) = P_1(t) - P_2(t) \tag{8}$$

$$u(t) = [u_1(t) + u_2(t)]/2 \tag{9}$$

Defining the instantaneous Reynolds number:

$$\mathrm{Re}(t) = \frac{\rho(t) \cdot u(t) \cdot D_h}{\mu} \tag{10}$$

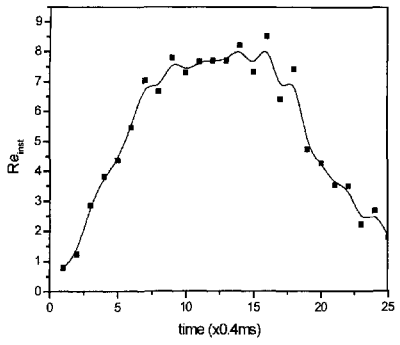

Figure 4. Variation of the instantaneous Reynolds number in terms of time in half cycle.

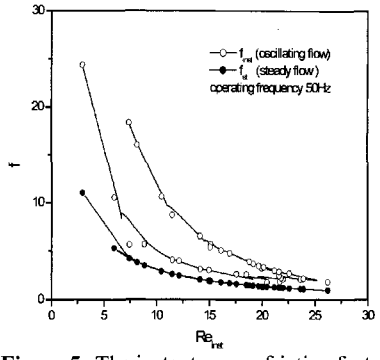

Figure 5. The instantaneous friction factor for 50 Hz.

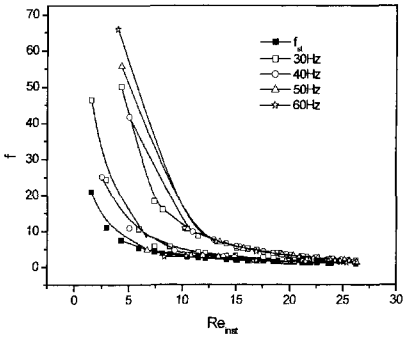

Figure 6. The instantaneous Reynolds number for different operating frequencies.

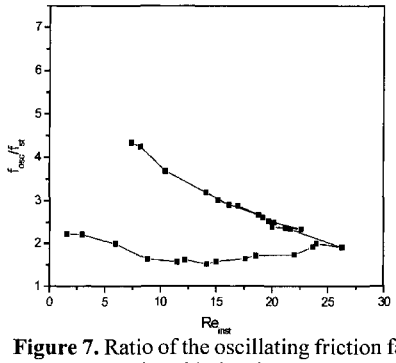

Figure 7. Ratio of the oscillating friction factor to the steady flow friction factor for 50 Hz.

To compare the pressure drops over the regenerator in oscillating flow with those in steady flow, we used the following correlation equation for predicting the friction factor of a steady flow through a stack of woven screens[3]:

$$f_M = \frac{33.6}{\mathrm{Re}_l} + 0.337 \quad , \quad f_M = \frac{\Delta P}{0.5\rho u^2 n} \quad , \quad u = u_0/\beta \tag{11}$$

where, u_0 is frontal flow velocity.

The instantaneous oscillating flow friction factor f_{inst} is computed and correlated according to Eqs. 7, 8, and 9 based on the experimental data. The instantaneous Reynolds number according to Eq. 10 for a half cycle is plotted in Fig. 4. Corresponding to the variation of the Reynolds number in Fig. 4, the relationships of the instantaneous Reynolds number and the oscillating flow friction factor are shown in Fig. 5. For comparison, the steady friction factor is also plotted. The measurement is performed at 50 Hz. It is clearly seen that the oscillating flow friction factor for increasing instantaneous Reynolds number exceeds the friction factor for decreasing Reynolds number, and there is an obvious asymmetry. This is a typical result for the data obtained in our experiments. Moreover, note that the asymmetry characteristics become more apparent when the operating frequency increases in Fig. 6. By investigating the processed experimental data, we found that the cause of this phenomenon lies in that—even though total integrated mass flow in the positive direction is equal to that in the negative direction—the instantaneous mass flow in the positive direction (from the compressor to the reservoir) is larger than that in the negative direction (towards the compressor), and the period of the positive direction is shorter than that of the negative direction.

It should also be noted that the oscillating-flow friction factor deviates from that for steady flow. The ratio of the oscillating-flow friction factor to the steady-flow friction factor at 50 Hz is presented in Fig. 7. The result indicates that the flow characteristics in the regenerator cannot be

treated in a quasi-steady manner for high frequencies. The ratio f_{inst}/f_{st} isn't simply a scaler-multiple relationship as has been reported in other work[6-8], as it is affected by the operating frequency and the instantaneous Reynolds number. For a 50 Hz operating frequency, from Fig. 7 we find that when the instantaneous Reynolds number is 0→25 in a half cycle, this ratio is about 2.2 ~1.9, and when the Reynolds number is 25→0 in the same half cycle, the ratio is 1.9~4.2.

CONCLUSIONS

In this paper, a definition of oscillating flow friction factor, which is different from the steady flow friction factor, has been presented by simplifying the momentum equation of the regenerator. A dynamic experimental apparatus has been designed and constructed to investigate the oscillating flow characteristics of regenerators. The oscillating flow friction factor was obtained by measuring the oscillating pressure and velocity wave at the two ends of the regenerator. The results show that the friction factor at high frequency operation deviates significantly from that for steady flow and cannot be treated in a quasi-steady manner. The ratio of the high frequency oscillating-flow friction factor to that for steady flow is not simply a scaler-multiple relationship, as the relationship changes under different operating frequencies and the instantaneous Reynolds number conditions. In addition, asymmetry characteristics associated with the oscillating friction factor in one cycle were found in our experiments, and the reason for the asymmetry was discussed.

ACKNOWLEDGMENT

The work is funded by the National Natural Science Foundation of China (Grant No. 50206025).

REFERENCES

1. Kays, W.M. and London, A.L., *Compact Heat Exchangers*, 2nd Ed. McGraw-Hill, New York, 1964.
2. Walker, G. and Vasishta, V., "Heat transfer and flow fiction characteristics of wire-screen Stirling engine regenerator," *Adv. Cry. Eng.*, vol. 16, Plenum Press, New York (1971), pp. 324-332.
3. Miyabe,H., Takahashi, S., and Hamaguchi, K., "An approach to the design of Stirling engine regenerator matrix using packs of wire gauzes," *Proc. 17th IECEC*, vol. 1 (1982), pp. 1839-1844.
4. Sodre. J. R., and Parise, J. A. R., "Friction factor determination for flow through finite wire-mesh matrices," *ASME Journal of fluid engineering*, Vol. 119 (1997), pp. 847-851.
5. Chin-Tsau Hsu, Huili Fu, Ping Cheng, "On pressure-velocity correlation of steady and oscillating flows in regenerators made of wire screens," *Transactions of the ASME*, vol. 121 (1999), pp.52-56.
6. Yoshida, S., Ravikumar, K. V. and Frederkng, T.H.K., "Friction factors of stacks of perforated regenerator plates," *Cryocoolers 8*, Plenum Press, New York (1995), pp. 259-268.
7. Zhao,T.S. and Cheng, P., "Oscillatory pressure drops through a woven-screen packed column subjected to a cycle flow," *Cryogenics*, vol. 36 (1996), pp. 333-341.
8. Helvensteijn, B.P.M., et al., Pressure Drop Over Regenerators in Oscillating Flow, *Adv. in Cryogenic Engin.*, vol. 43B, Plenum Publishing Corp., New York (1998), pp. 1619-1626.
9. Yonglin Ju, Yan jiang and Yuan Zhou, "Experimental study of the oscillating flow characteristics for a regenerator in a pulse tube cryocooler," *Cryogenics*, vol. 38 (1998), pp. 649-656.
10. Kwanwoo Nam and Sankwon Joeng, "Experimental study on the regenerator under actual operating conditions," *Adv. in Cryogenic Eng.*, Vol. 47, AIP, Melville, NY (2002), pp. 977-984.
11. Kwanwoo Nam and Sankwon Joeng, "Measurement of cryogenic regenerator characteristics under oscillating flow and pulsating pressure," *Cryogenics*, vol.43 (2003), pp. 575-581
12. Sungryel Choi, Kwanwoo Nam, Sangkwon Jeong, "Investigation on the pressure drop characteristics of cryocooler regenerators under oscillating flow and pulsating pressure conditions," *Cryogenics*, vol.44 (2004), pp. 203-210.
13. Smith W.R., "One-dimensional models for heat and mass transfer in pulse-tube refrigerators," *Cryogenics*, vol. 41 (2001), pp. 573-585.
14. Kuriyama F, Radebaugh R., "Analysis of mass and energy flow rates in an orifice pulse-tube refrigerator," *Cryogenics*; vol. 39 (1999), pp. 85-92.

Regenerator Flows Modeled Using the Method of Characteristics

Thomas P. Roberts[1] and Prateen V. Desai[2]

1. Air Force Research Laboratory
Kirtland AFB, NM 87117

2. Georgia Institute of Technology
Atlanta, GA 30332

ABSTRACT

A hyperbolic system of partial differential equations based on the volume averaged Navier Stokes system is discretized and used to portray the fluid and matrix interactions during oscillating regenerator flows. This system is solved using the Method of Characteristics for axial flow and time for the fluid phase while the matrix energy balance is solved using a discretized Fourier conduction equation axially and in time. Solution of the fluid phase is simplified by integration of the microscale diffusive flow friction and dissipative energy balance effects using volume averaging principles. The solution then uses a solution grid which is of the same order size as the volume averaging integration volumes. Correlations between previously obtained empirical regenerator performance data and these solution results indicate that this modeling approach appropriately describes the macroscopic performance character of a real regenerator.

INTRODUCTION

Cryocooler regenerator flows are characterized by unsteady gas dynamics, but the methods of describing these flows also take many attributes of the flows described in a variety of porous media sources which emphasize flows of incompressible fluids. The boundary between these approaches to the regenerator problem has been to this point unaddressed, and hence is the subject of this paper. Prior work has been dominated by one of two approaches to solution of the Navier Stokes Equations describing this system. Derivative from the Kays and London empirical treatise[1] are the various REGEN models such as that from Radebaugh et al.[2] This general approach describes the cryogenic regenerator as being a serial compilation of regenerators and flow and energy transfer impedances through the regenerator as a whole are essentially the sum of these serial parts. The other approach is that of thermoacoustics as exemplified by Swift.[3] A compromise between these two is the derivation of Shapiro's incompressible flow model[4] by Organ.[5] This paper will address a novel approach to Organ's derivation, and present preliminary results which illumine a set of empirical measurements of regenerator performance. This new derivation is based upon the modeling of compressible and combusting flows done by Fedkiw et al. [6,7,8]

Cryocoolers 13, edited by R. G. Ross, Jr.
Springer Science+Business Media, Inc., New York, 2004

A NUMERICAL MODEL FOR REGENERATOR FLOWS

The Navier Stokes System

Roberts and Desai[9] derived using volume averaging methods for porous media flows the following system of equations that describe the mass, momentum, and energy balances in the working fluid using the ideal-gas equation of state.

$$0 = \frac{\partial \langle \rho^\alpha \rangle^\alpha}{\partial t} + \frac{\partial \langle \rho^\alpha \rangle^\alpha \langle v^\alpha \rangle^\alpha}{\partial x}$$

$$-\frac{\Phi}{\varepsilon^\alpha} = \frac{\partial \langle v^\alpha \rangle^\alpha}{\partial t} + \langle v^\alpha \rangle^\alpha \frac{\partial \langle v^\alpha \rangle^\alpha}{\partial x} + \frac{1}{\langle \rho^\alpha \rangle^\alpha} \frac{\partial \langle P^\alpha \rangle^\alpha}{\partial x} \tag{1}$$

$$\langle \rho^\alpha \rangle^\alpha Q = \frac{\partial \langle \rho^\alpha \rangle^\alpha \langle u^\alpha \rangle^\alpha}{\partial t} + \frac{1}{2} \frac{\partial \langle \rho^\alpha \rangle^\alpha \left| \langle v^\alpha \rangle^\alpha \langle v^\alpha \rangle^\alpha \right|}{\partial t} +$$
$$\frac{\partial}{\partial x} \left(\langle \rho^\alpha \rangle^\alpha \langle v^\alpha \rangle^\alpha \langle u^\alpha \rangle^\alpha + \left(\langle P^\alpha \rangle^\alpha \langle v^\alpha \rangle^\alpha \right) + \frac{1}{2} \langle \rho^\alpha \rangle^\alpha \langle v^\alpha \rangle^\alpha \left| \langle v^\alpha \rangle^\alpha \langle v^\alpha \rangle^\alpha \right| \right)$$

$$\langle P^\alpha \rangle^\alpha = R \langle \rho^\alpha \rangle^\alpha \langle T^\alpha \rangle^\alpha \qquad \left[\langle c^\alpha \rangle^\alpha \right]^2 = \gamma R \langle T^\alpha \rangle^\alpha = \gamma \frac{\langle P^\alpha \rangle^\alpha}{\langle \rho^\alpha \rangle^\alpha} \tag{2}$$

The dissipative and diffusive terms in the momentum and energy balances are defined:

$$\Phi = F^1 \frac{\partial \left(\langle \rho^\alpha \rangle^\alpha \langle v^\alpha \rangle^\alpha \right)}{\partial t} + F^2 \langle v^\alpha \rangle^\alpha + F^3 \langle v^\alpha \rangle^\alpha \langle v^\alpha \rangle^\alpha$$
$$\langle \rho^\alpha \rangle^\alpha Q = \frac{h^{\alpha\beta}}{r_h} \left(T^\beta - \langle T^\alpha \rangle^\alpha \right) - \frac{G^1}{\varepsilon^\alpha} \frac{\partial \langle \rho^\alpha \rangle^\alpha \langle v^\alpha \rangle^\alpha}{\partial t} \tag{3}$$

The remainder of this paper will address these fluid properties as being volume averages, and henceforth drop the averaging notation (<*X*>).

The hyperbolic nature of this system is critical for characterizing the fluid flows within the regenerator, as hyperbolic systems are capable of propagating wave phenomena, and given the use of regenerators in oscillatory acoustic-mechanical systems, we would expect the model to describe this type of phenomena. Restating equation 1 in terms of density, mass flow rate, and energy:

$$\begin{bmatrix} \rho \\ \rho v \\ E \end{bmatrix}_t + \begin{bmatrix} \rho v \\ \rho v^2 + P \\ Ev + Pv \end{bmatrix}_x + \begin{bmatrix} 0 \\ \Phi / \varepsilon \\ -\rho Q \end{bmatrix} = 0 \tag{4}$$

with $E = c_v T + \rho v^2/2 + P/\rho$.

This system now has the general form of $U_t + F(U)_x + S = 0$ and can be numerically solved by determining the Jacobian of the flux vector, *S*, which is the transformation matrix between the *x-t* plane and the real space of the dependent variables: density, velocity, pressure, and specific energy. In this case the Jacobian can be used to restate equation 4,

$$\begin{bmatrix}\rho\\ \rho v\\ E\end{bmatrix}_t + \begin{bmatrix}v & v & 0\\ 1 & 3-\gamma & c_pT+v^2/2\\ 0 & \gamma-1 & \gamma v\end{bmatrix}\begin{bmatrix}\rho\\ \rho v\\ E\end{bmatrix}_x + \begin{bmatrix}0\\ \Phi/\varepsilon\\ -\rho Q\end{bmatrix} = 0 \tag{5}$$

by a simple implementation of the chain rule in R^3.

Eigensystems and Characteristic Fields

Solution for the eigensystem of the Jacobian is feasible numerically, and Fedkiw et al [1999] gave its eigenvalues as the set $\{ v+c, v-c, v\}$, which are consistent with the characteristic lines for this system given by Shapiro[4], among other texts. The eigenvectors describe how the fluid property solution propagate along these characteristics. Using the eigenvectors as the columns of matrix R.

$$J R = R\, Diag(\{ v+c, v-c, v\}) \tag{6}$$

Defining L to be the inverse of R, these two matrices can diagonalize the Jacobean.

$$L J R = Diag(\{ v+c, v-c, v\}) \tag{7}$$

Applying this system to a solution node, x_0, .and finding estimates for L_0 and R_0, equation can be used as an exact diagonalization of equation 4 at x_0, and used as a linear estimate in some neighborhood of x_0. The first step in accomplishing this is by multiplication of equation 4's general form by L_0.

$$L_0 U_t + L_0 F(U)_x + L_0 S = 0 \tag{8}$$

A discretized differential operator, Δ, is applied to $F(U)$, and then the resulting system is multiplied by R_0.

$$U_t + R_0 \Delta [L_0 F(U)] + S = 0 \tag{9}$$

Equation 9 clearly shows how the eigensystem has been used to transform the original non linear system to what is now a system three independent, linear ordinary differential equations. This is entirely consistent with how prior implementations of the Method of Characteristics solved along analytical characteristic lines, with one important caveat: the local region of valid linearization of the Jacobean is considerably smaller than what might be expected from Courant-Friedrichs-Lax criteria (in this case $(x_1 - x_0)/(v+c)$, the nodal separation divided by maximum propagation speed). Instead, due to the stiffness of this system and the way that pressure variations have been incorporated into the specific energy derivatives, the effective step size is usually on the order of the CFL condition divided by 100. Offsetting this is the highly linearized system now being solved which poses an extremely low computational overhead. In addition, the necessity for intermediate point interpolations of timestep starting data, which characterized prior Method of Characteristics implementations, has been eliminated.

Solution of the matrix Temperature field

The requirement that the energy transferred from gas to matrix in the source vector in the Navier Stokes system be used as the convective boundary condition for any matrix segment was the foundation of the implicit solution of the matrix temperatures at the end of each time step. In addition, both ends of the matrix were presumed to be attached to constant temperature sinks. Empirically measured conduction values for an actual regenerator were used, which were approximately an order of magnitude less than the usual values for 304 stainless steel.

IMPEDANCE VALUES FOR HEAT AND MOMENTUM TRANSFER

A major goal of this study was to determine whether the empirical trends noted in Roberts and Desai[10] and extended below can be numerically simulated. In that paper it was noted that a relation between flow impedance and both instantaneous flow values and flow history was evident.

$$f \approx C_1 Str + C_2/\mathrm{Re} \tag{10}$$

An investigation was conducted concerning whether a similar relationship could be confirmed for the heat transfer impedance exhibited by the regenerator. In this the energy balance can be depicted as a balance between the material derivatives of internal energy and the convection and dissipative thermal interactions between the fluid and matrix:

$$\begin{aligned}
&(\gamma-1)\langle\rho^\alpha\rangle^\alpha\left(Q+\langle v^\alpha\rangle^\alpha\Phi\right)\approx\frac{D\langle u^\alpha\rangle^\alpha}{Dt}\approx\frac{D\langle c_v^\alpha T^\alpha\rangle^\alpha}{Dt}\\
&\Phi\approx F^1\frac{d\left(\langle\rho^\alpha\rangle^\alpha\langle v^\alpha\rangle^\alpha\right)}{dt}+F^2\langle v^\alpha\rangle^\alpha+F^3\langle v^\alpha\rangle^\alpha\langle v^\alpha\rangle^\alpha\\
&\langle\rho^\alpha\rangle^\alpha Q=\frac{h^{\alpha\beta}}{r_h}\left(T^\beta-\langle T^\alpha\rangle^\alpha\right)-\frac{G^1}{\varepsilon^\alpha}\frac{\partial\langle\rho^\alpha\rangle^\alpha\langle v^\alpha\rangle^\alpha}{\partial t}
\end{aligned} \tag{11}$$

On a cyclic, integral basis this balance can be re-expressed as the balance between how the fluid loses internal energy in transiting the regenerator and its interactions with the matrix.

$$\begin{aligned}
&\gamma c_p\left(T_{hotend}-T_{coldend}\right)\omega\approx\frac{h}{r_h\rho}\left(T_{matrix}-T_{fluid}\right)+fv^2\omega\\
&\gamma\approx\frac{v}{r_h\omega}\frac{h}{vc_p\rho}c_1+f\frac{v^2}{c_p\left(T_{hotend}-T_{coldend}\right)}\\
&\left(\gamma-C_2 f\,Ec\right)Str\,C_1\approx St
\end{aligned} \tag{12}$$

Equation 12's manipulations allows for the f value to be either the actual data gathered on a regenerator, which would not be available on an a priori basis to any design, or an estimate of what f might be from Roberts and Desai.[10] The results of these two optional paths, compared to Kays and London's data[1] is shown below. The coefficients for the regressions, both of which had R-square values close to unity, were:

	f actual	f from Eqn. 13
C1	0.599	0.599
C2	-4.47E-05	-3.54E-05

In general the Strouhal numbers were in the area of 1e-4 and the Eckert numbers in the range of 5e-3 to 9e-4. As can be noted from figure 1, the results of this model correlated very closely with observed performance and differed greatly from the Kays and London trend.

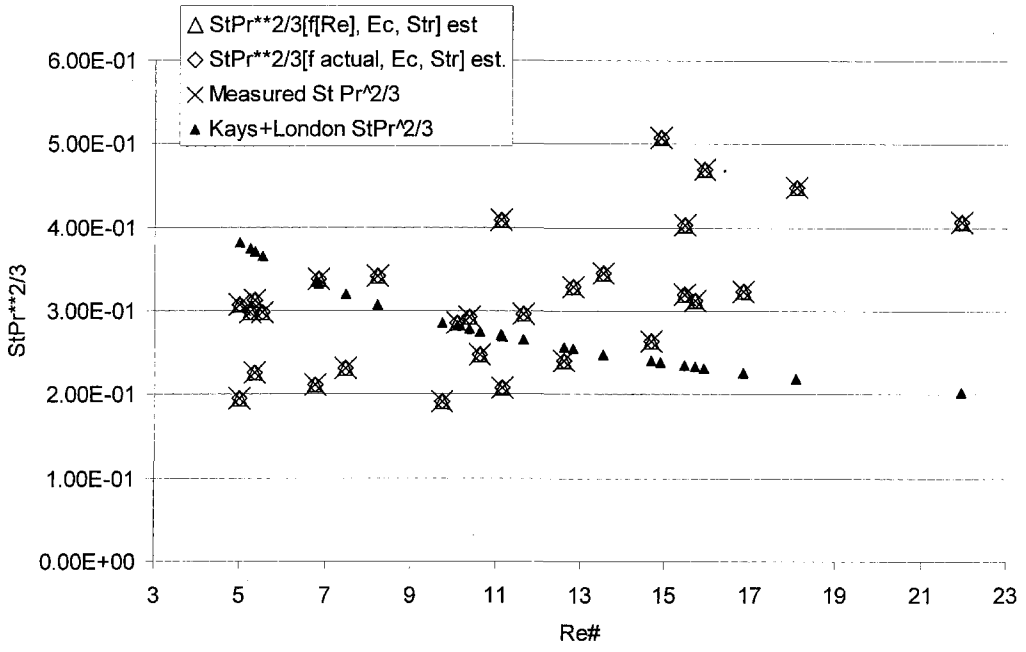

Figure 1. Results of correlation of Reynolds, Eckart, and Strouhal numbers with heat transfer impedance

NUMERICAL RESULTS

The numerical model was coded using *Mathematica* version 5. The subsidiary goals in this part of the study were:

1. Obtain a working code to model how wave phenomena propagate in this linearized model of the Navier Stokes equations.
2. Verify if the form of equations 10 and 12 indicates that on a local, instantaneous basis:

$$h \approx c1 \partial v/\partial t + c2\, v \qquad f \approx c3 \partial v/\partial t + c4\, v \tag{13}$$

In order to accomplish the second goal, the coefficients for the terms of these equations were modified in order to achieve two quantitative requirements:

1. Match the mass and enthalpy flow rates exiting from the model with experimental exit rates.
2. Obtain smooth propagation of the pressure waves through the regenerator (in short, no shock developments due to artificial numerical processes).

Preliminary results were obtained for simple sinusoidal entry conditions, as shown in Figures 2 through 5. The results for purely instanteous (*c1, c3 = 0,* no relationship of impedance with *dv/dt*) impedance dependancy are shown in Figure 2.

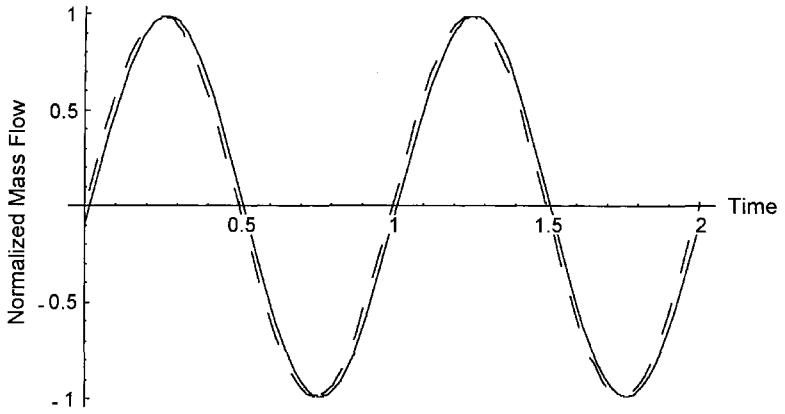

Figure 2. St and f only functions of v (dotted line is warm end trace, while solid is cold end trace).

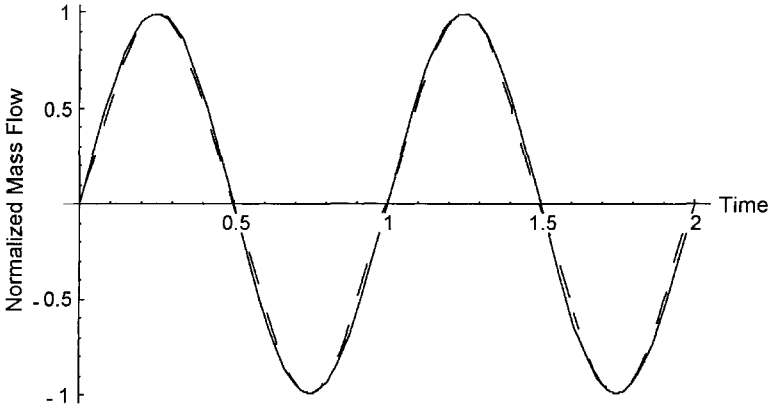

Figure 3. Comparison of warm end traces using St(u, u_t), f(u, u_t) [dashed line]vs. St(u), f(u) [solid].

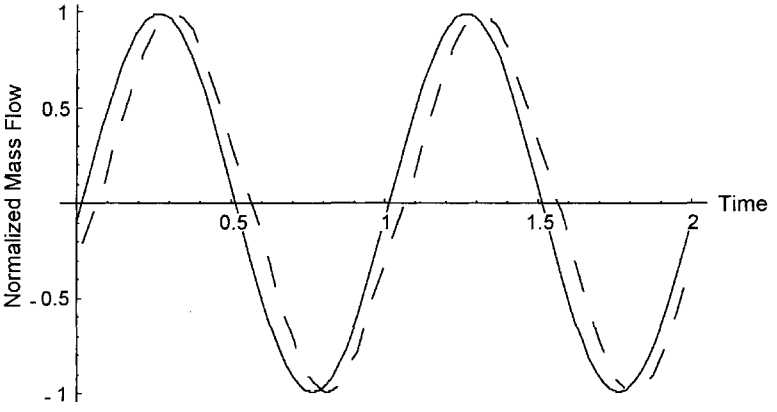

Figure 4. Comparison of cold end traces using St(u, u_t), f(u, u_t) [dashed line] vs. St(u), f(u) [solid].

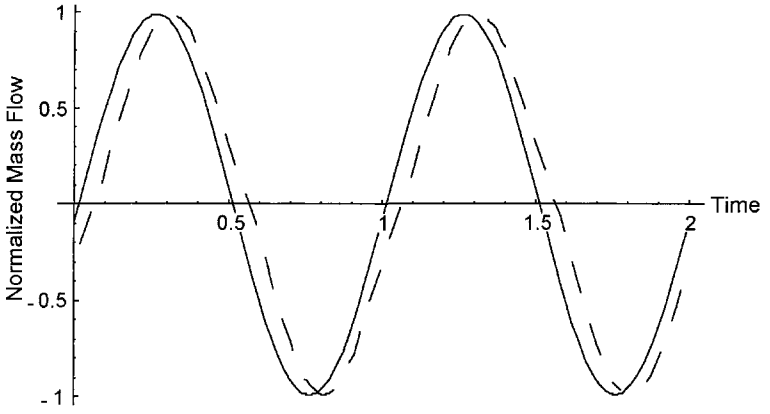

Figure 5. Warm [solid] and cold [dashed line] end traces using St(u, u_t), f(u, u_t).

As can be seen in Fig. 2, there is no significant phase shift between the two mass flow rates, but this changes as the coefficients for the equation 13's temporal derivatives are made non zero.

Matching Empirical Data

Experimentally measured mass flow, temperature, and pressure (Roberts and Desai [2003]) on a functional cooler regenerator was converted to enthalpy flow, and these flows were then approximately duplicated by the numerical mode; see Fig. 6 for mass flows and Fig. 7 for enthalpy flows.

In the modeled case presented above, the average temporal components of the heat transfer and flow friction factors were 14.5% and 15.1% of the cyclic average values for these factors, which implies that at maximum flow accelerations, this temporal factor is highly significant as a part of the overall momentum and energy transfer regime.

CONCLUSIONS

With some significant caveats (such as enthalpy flows being affected by warm end compression effects and cold end refrigeration effects), this model gives reasonable predictions of what

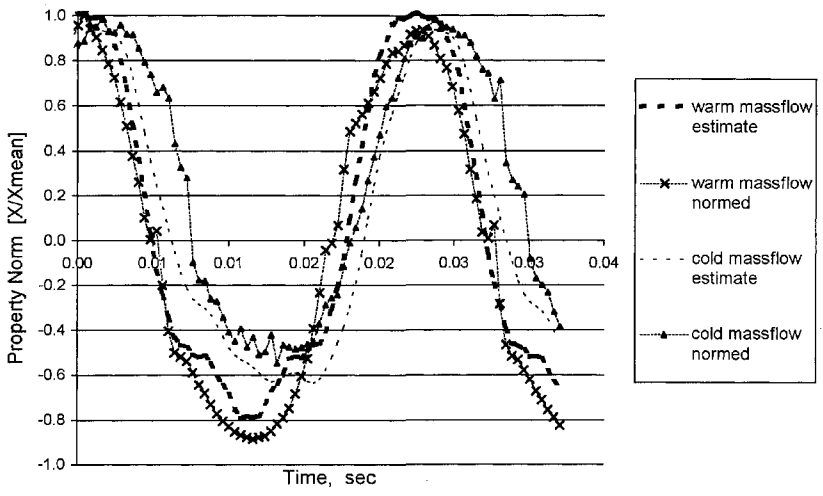

Figure 6. Matching mass flow rates from empirical data with model. (Normalizing factors were the cyclic averages using absolute values)

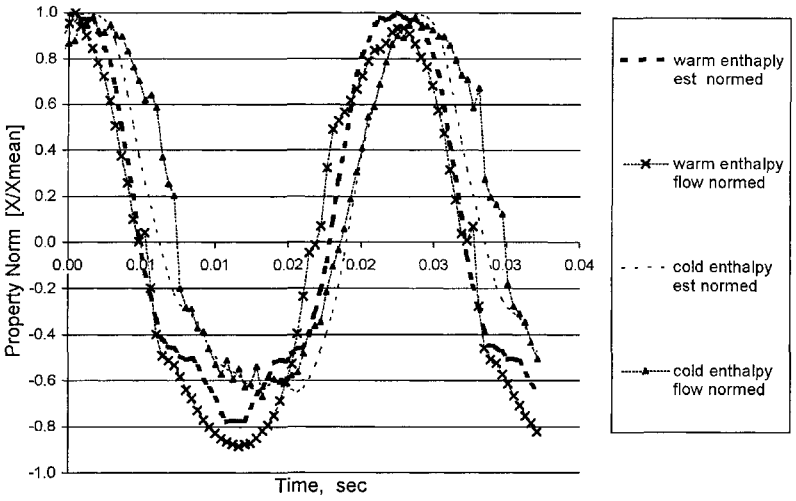

Figure 7. Matching enthalpy flow rates from empirical data with model.

phenomena are occurring in a Stirling or Pulse Tube regenerator. These reservations are largely due to the fact that any real regenerator's boundary conditions are simultaneously another components boundary conditions, and therefore a model which does not take into account the joint thermodynamic processes occurring in the cooler as a whole is bound to be simplified to a significant extent. Examples of this can be seen in comparison of the empirical versus model results, as the empirical results show many jagged variations in flows which are possibly due to reflection sites and entry and exit conditions. Other phenomena which also might significantly affect the estimate for enthalphy flow in particular is the probability that work extraction and cooling extend into the cold end of the regenerator, which is not incorporated in this model.

NOTATION

v_i = the velocity vector of the fluid, α
T = the temperature of the fluid, α
u = specific internal energy of the fluid, α
c = speed of sound
c_v, c_p = constant volume and pressure specific heats
γ = ratio of specific heats
ρ = density
P = pressure
f_i = friction factor
F, G = tensor coefficients in equation 3
Q = specific heat flux from porous media to fluid
α^a = subscript for fluid
β^a = subscript for solid matrix
ε^a = ratio of fluid volume to total volume
ω = frequency
r_h = hydraulic radius of matrix mesh
J = Jacobian
R, L = matrix of eigenvectors and its inverse
Re = Reynolds number based on r_h
Str = Strouhal number , $\omega r_h / v_{mean}$
Ec = Eckert number, $v^2/c_p(T_{warm} - T_{cold})$

REFERENCES

1. Kays, W. and London, A., *Compact Heat Exchangers*, 3rd ed., McGraw-Hill Book Co., NYC (1984).
2. Radebaugh, R., Gary, J., Marquardt, E., Louie, B. Daney, D., Arp, V., and Linenberger, D. *Measurement and calculation of regenerator ineffectiveness for temperatures of 5 to 40 K*, Wright Laboratory, WPAFB, OH, USA WL-TR-92-3074 (1992).
3. Swift, Greg, *Thermoacoustics*, Acoustical Soc. of Amer., Sewickley, PA (2002).
4. Shapiro, A. *The Dynamics and Thermodynamics of Compressible Fluid Flow*, Wiley, NYC (1953-4) (vol. 1 & 2).
5. Organ, A. *Thermodynamics and Gas Dynamics of the Stirling Cycle Machine*, Cambridge Univ. Press, Cambridge UK (1992).
6. Fedkiw, R., Merriman, B., Donat, R. and Osher, S., "The Penultimate Scheme for Systems of Conservation Laws: Finite Difference ENO with Marquina's Flux Splitting," UCLA CAM Report 96-18 (1996). http://www.math.ucla.edu/applied/cam/
7. Fedkiw, R., Merriman, B., and Osher, S., "Efficient Characteristic Projection in Upwind Difference Schemes for Hyperbolic Systems," *J. Comp. Physics*, v. 141 (1998), p. 22-36.
8. Fedkiw, R., Merriman, B., and Osher, S., "Simplified Discretization of Systems of Hyperbolic Conservation Laws Containing Advection Equations," UCLA CAM Report (1999). http://www.math.ucla.edu/applied/cam/
9. Roberts, T. and Desai, P., "Periodic Porous Media Flows in Regenerators," *Cryocoolers 12*, Kluwer Academic/Plenum Publishers, New York (2002), pp. 516-524.
10. Roberts, T. and Desai, P., "Working Fluid State Properties Measurements in Medium and High Frequency Cryocoolers," *Adv. in Cryogenic Engineering*, Vol. 49B, Amer. Institute of Physics, Melville, NY (2004), pp. 1146-1153.

A Fast and Accurate Regenerator Numerical Model

Jeremy P. Harvey[1], Carl S. Kirkconnell[1], and Prateen V. Desai[2]

[1]Raytheon Space and Airborne Systems
El Segundo, CA 90245-0902

[2]G.W. Woodruff School of Mechanical Engineering
Georgia Institute of Technology
Atlanta, GA 30332-0405

ABSTRACT

A complete, fast, and accurate numerical method for solving the regenerator one-dimensional conservation equations has been developed. This model utilizes an artificial convergence technique to advance the Method of Lines (MOL) solution to steady state within as little as 20 cycles of simulation time, which is much faster than traditional methods.

In addition to parameters which characterize the porous medium and regenerator dimensions, the model requires six boundary parameters; cold and hot mass flux amplitude and phase difference (3), cold and hot mean temperature (2), and mean pressure (1). Specified mean pressure and mean boundary temperatures are achieved using the artificial convergence technique. Constant regenerator net energy flow is demonstrated, and is the requirement for convergence.

This model has been used to quantify the effects of several limiting assumptions typically used in regenerator analysis such as ideal gas, constant properties, local thermal equilibrium, and constant temperature, i.e. $T = T(x)$. These assumptions all lead to under-prediction of regenerator net heat flux, or regenerator loss. Comparison of this model to experimental data and system level modeling using Sage is also included. Finally, the numerical method is validated using an exact solution test case, yielding normalized errors of order 10^{-6}.

INTRODUCTION

Regenerators in cryocoolers and power engines serve to thermally insulate the hot reservoir from the cold reservoir while allowing for pressure work transmission. Practical limitations on regenerator design prevent complete insulation and the resulting net enthalpy flow leads to a reduction in net refrigeration or power production. For modeling regenerative systems, the flow and heat transfer in the regenerator needs to be modeled by solving the system of conservation equations with appropriate boundary conditions.

Cryocoolers 13, edited by R. G. Ross, Jr.
Springer Science+Business Media, Inc., New York, 2004

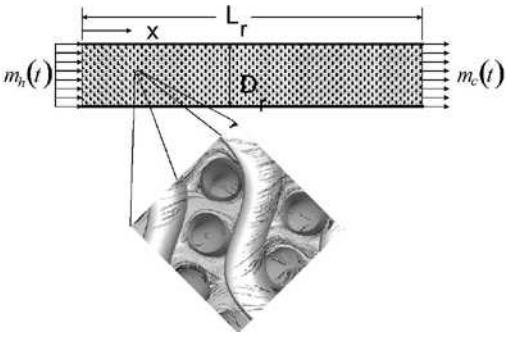

Figure 1. Diagram of the one-dimensional regenerator.

MATHEMATICAL MODEL FOR THE ONE-DIMENSIONAL REGENERATOR

The conservation equations for the one-dimensional regenerator (Fig. 1) have been derived using a volume averaging technique.[1] The result is a system of four coupled partial differential equations for gas density, ρ, gas mass flux, m, gas energy, E, and matrix temperature, T_β. Three decoupled auxiliary equations give the entropy generation in the gas, s'''_{gen}, matrix, $s'''_{\beta,gen}$, and the system, $s'''_{gen,sys}$. Lastly, two equations of state are necessary to define the gas temperature, T, and pressure, p, in terms of the density and energy. These equations are repeated here:

$$\frac{\partial \rho}{\partial t}+\frac{\partial m}{\partial x}=0 \tag{1}$$

$$\frac{\partial m}{\partial t}+\frac{\partial}{\partial x}\left(\frac{m^2}{\rho}+p\right)+\frac{\mu\varepsilon}{K}\frac{m}{\rho}+\frac{m^2}{\rho}\frac{\varepsilon^2 c_f}{K^{1/2}}sign[m]=0 \tag{2}$$

$$\frac{\partial E}{\partial t}+\frac{\partial}{\partial x}\left(mh-N_k k\frac{\partial T}{\partial x}\right)-a_v H\left(T_\beta-T\right)=0 \tag{3}$$

$$(\rho c)_\beta\frac{\partial T_\beta}{\partial t}-\frac{\partial}{\partial x}\left[k_\beta\tau_\beta\frac{\partial T_\beta}{\partial x}\right]+\frac{\varepsilon}{1-\varepsilon}a_v H\left(T_\beta-T\right)=0 \tag{4}$$

$$s'''_{gen}=\frac{N_k k}{T^2}\left(\frac{\partial T}{\partial x}\right)^2+\frac{a_v H}{TT_\beta}\left|T_\beta-T\right|^2-\frac{m}{\rho T}\frac{\partial p}{\partial x} \tag{5}$$

$$s'''_{\beta,gen}=\frac{k_\beta\tau_\beta}{T_\beta{}^2}\left(\frac{\partial T_\beta}{\partial x}\right)^2+\frac{\varepsilon}{1-\varepsilon}\frac{a_v H}{TT_\beta}\left|T_\beta-T\right|^2 \tag{6}$$

$$s'''_{gen,sys}=\varepsilon\frac{N_k k}{T^2}\left(\frac{\partial T}{\partial x}\right)^2+(1-\varepsilon)\frac{k_\beta\tau_\beta}{T_\beta{}^2}\left(\frac{\partial T_\beta}{\partial x}\right)^2+\frac{a_v H}{TT_\beta}\left|T_\beta-T\right|^2-\varepsilon\frac{m}{\rho T}\frac{\partial p}{\partial x}\geq 0 \tag{7}$$

$$T=f_1(\rho,E) \tag{8}$$

$$p=f_2(\rho,E) \tag{9}$$

$$\mathrm{Re}=\frac{m\sqrt{K}}{\mu} \tag{10}$$

The 1-D momentum equation contains two parameters, K and c_f, which characterize the flow friction due to viscous and inertial effects respectively. The gas viscosity, μ, is in general a fluid property and thusly dependent on temperature and pressure. The energy equations contain

a volumetric interfacial convection heat transfer coefficient, $a_v H$, which is dependent on the local instantaneous Reynolds number, Re. The length scale in the Reynolds number is chosen as the square root of the permeability which is the natural length scale derived from scale analysis of the momentum equation; thus the momentum and energy equations are united via a common scale. Dispersion in the gas phase has been shown to behave as a diffusive energy flux.[2] Gedeon acknowledges this as a loss mechanism in regenerators and labels it as enhanced axial conduction.[3] He utilizes a similar methodology for modeling the dispersion in the form of a dispersion coefficient, N_k. The porosity, ε, is the final parameter which characterizes the 1-D model. This general model represents a fully nonlinear, compressible model for the regenerator.

ARTIFICIAL CONVERGENCE TECHNIQUE

The total energy flux in the regenerator is composed of a diffusive/dispersive flux and an enthalpic flux. This total energy flux must be constant at steady state as will be shown. Cyclic averaging of the combined gas and matrix energy equations under the assumption of periodic steady state results in

$$\oint\left\{\frac{\partial}{\partial z}\left[h_{ss}+q_{g,ss}+q_{m,ss}\right]\right\}dt=0\,, \tag{11}$$

where the "ss" subscript indicates steady state. This conclusion is reached by noting that the cyclic average of the internal energy terms is identically zero at steady state. Let

$$h_{ss}=\rho u c_p T_{ss},\; q_{g,ss}=-N_k k\frac{\partial T_{ss}}{\partial x},\; q_{m,ss}=-\frac{1-\varepsilon}{\varepsilon}k_\beta\tau_\beta\frac{\partial T_{\beta,ss}}{\partial x}. \tag{12}$$

A simplification in terms of temperature gives

$$\oint\left\{\frac{\partial}{\partial x}\left[\rho u c_p T_{ss}-N_k k\frac{\partial T_{ss}}{\partial x}-\frac{1-\varepsilon}{\varepsilon}k_\beta\tau_\beta\frac{\partial T_{\beta,ss}}{\partial x}\right]\right\}dt=0. \tag{13}$$

The temperature field at the end of a cycle may not satisfy this relationship. In this case, this relation provides a means of calculating a correction for the initial condition of the following cycle. By defining the quasi steady-state temperature fields which satisfy Equation 12 exactly as

$$T_{ss}=T'(x)+T(x,t),\; T_{\beta,ss}=T'(x)+T_\beta(x,t)\,, \tag{14}$$

where the primed temperature is an axial correction. T(x,t) and T_β(x,t) are the temperatures of the gas and matrix, respectively, from the current cycle. These quantities can be substituted into Equation 13 and T'(z) can be solved to obtain

$$f_1(z)\frac{\partial^2 T'}{\partial z^2}+f_2(z)\frac{\partial T'}{\partial z}+f_3(z)=0\,, \tag{15}$$

where

$$\begin{aligned}
f_1(x)&=-\oint\left\{N_k k+\frac{1-\varepsilon}{\varepsilon}k_\beta\tau_\beta\right\}dt\\
f_2(x)&=\oint\{\rho u c_p\}dt\\
f_3(x)&=\oint\left\{\frac{\partial}{\partial x}\left[\rho u c_p T-N_k k\frac{\partial T}{\partial x}-\frac{1-\varepsilon}{\varepsilon}k_\beta\tau_\beta\frac{\partial T_\beta}{\partial x}\right]\right\}dt
\end{aligned} \tag{16}$$

For the case of constant specific heat,

$$f_2(x)=c_p\oint\{\rho u\}dt=0 \tag{17}$$

which follows from a cyclic-average of the continuity equation. Equation 14 is a second order ODE which can be solved for the temperature correction function. The boundary conditions are appropriately chosen as

$$T'(0) = 0$$
$$T'(L_r) = 0\,, \tag{18}$$

since the temperature field at the ends does not need a correction due to the boundary conditions which fix those values. T' can then be solved numerically with a finite difference technique. Then the initial conditions for the temperatures for the next period are

$$T(0,x) = T(\tau,x) + \lambda T'(x)$$
$$T_\beta(0,x) = T_\beta(\tau,x) + \lambda T'(x). \tag{19}$$

A relaxation factor, λ, is used to aid stability. Experimentation has indicated an optimum value of 0.30-0.35. This method has been used to advance the solution to steady state in as little as 20 cycles of simulation. In practice, the temperature correction is only applied once every three cycles.

SIMPLIFIED MODELS FOR THE REGENERATOR

A few special cases of the general model as presented in Equations 1-10 are worthy of notice since they can be used to 1) illustrate the non-conservative effect of simplifying assumptions and 2) decompose the total regenerator loss.

Constant Temperature Model (CTM)

In the limit of infinite convective heat transfer coefficient and infinite matrix heat capacity, the regenerator gas and matrix have constant temperatures which vary only with axial location. The gas and matrix temperatures must be identical. In this limit, the energy equations are eliminated altogether. A solution is achieved using the artificial convergence technique.

Local Thermal Equilibrium Model (LTEM)

A less restrictive model than the constant temperature model can be proposed by relaxing the infinite heat capacity assumption. In this case, the gas and matrix temperatures are still identical, except now there can be a time varying temperature field. A single energy equation can be written by relating the convective heat transfer terms. Under the assumption of ideal gas, this energy equation becomes

$$\frac{\partial T}{\partial t} + \frac{\rho u c_v}{C_{LTE}}\frac{\partial T}{\partial x} + \frac{1}{C_{LTE}}\frac{\partial}{\partial x}\left(Pu - N_k k \frac{\partial T}{\partial x} - \frac{1-\varepsilon}{\varepsilon} k_\beta \tau_\beta \frac{\partial T_\beta}{\partial x} \right) = 0. \tag{20}$$

where the combined volumetric heat capacity is defined as

$$C_{LTE} = \rho c_v + (\rho c)_\beta \frac{1-\varepsilon}{\varepsilon}. \tag{21}$$

Real Gas versus Ideal Gas/Constant Properties

The LTEM is limited in applicability to ideal gas and constant properties. The CTM and the full model both have variants based on the use of real gas or ideal gas equations of state. Properties such as the viscosity can vary with temperature and pressure in general. As a result, five models can be compared. An illustrative comparison is provided in the following section.

EFFECT OF LIMITING ASSUMPTIONS

The five models presented in the previous section were simulated under identical operating and boundary conditions. Figure 2 shows that the regenerator loss increases as the limiting assumptions are removed. Beginning with the CTM using ideal gas, the regenerator loss reported is totally due to conduction and dispersion, i.e. the net enthalpy flow is identically zero. Addition of the real gas shows that the net enthalpy flow becomes nonzero due to pressure dependence of the enthalpy. Pressure and mass flux are partially in-phase resulting in a net enthalpy flux. The LTEM model shows that the effect of finite matrix heat capacity, at least for this simulation, resulted in a net enthalpy flux increase comparable to the effect of real gas. The full model which utilized the dual energy equations and real gas represents the most accurate prediction of the regenerator loss. This model accounts for additional net enthalpy flow in the regenerator due to temperature differences between the matrix and gas. Figure 3 illustrates how the four loss mechanisms compare. The most significant loss that is commonly ignored is that due to real gas effects. It should be noted that temperature dependent properties such as viscosity were used only for the real gas simulations.

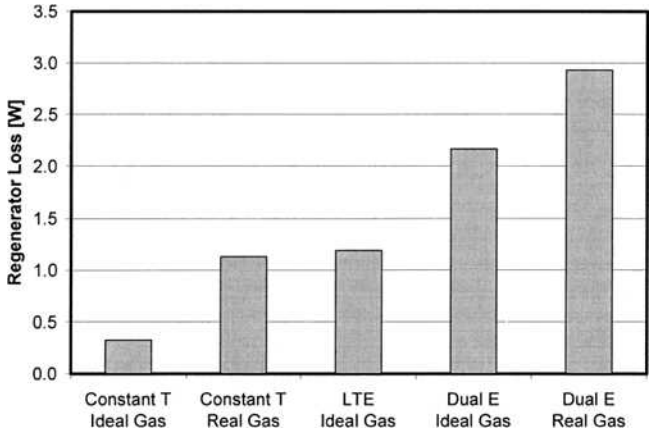

Figure 2. Comparison of regenerator loss calculated with limiting case models based on identical operating conditions (ideal gas assumes constant properties.)

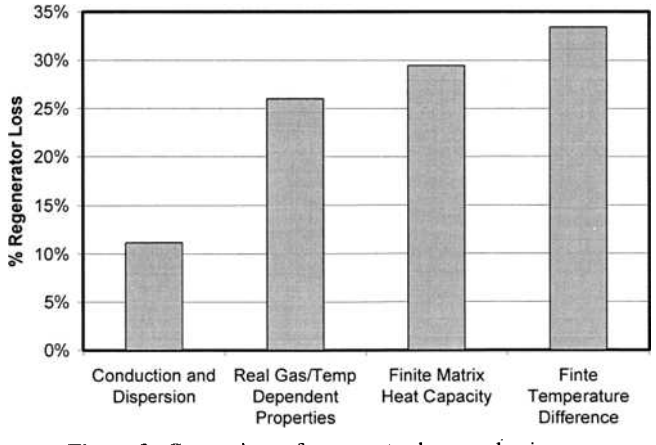

Figure 3. Comparison of regenerator loss mechanisms.

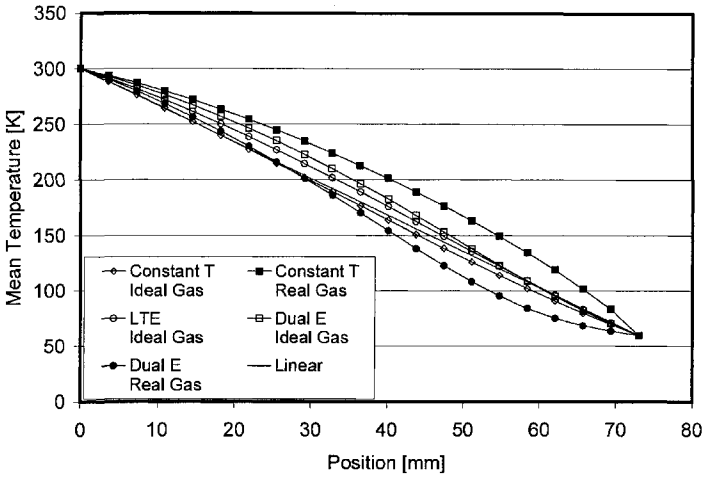

Figure 4. Comparison of mean temperature profiles calculated with the different models based on identical operating conditions.

These simulations were performed for a regenerator operating at no-load at 70 K. Figure 4 shows the mean temperature profiles for the five models and a linear profile. The profiles deviate by as much as 50 K (Constant T Real Gas versus Dual E Real Gas.) It is this temperature profile which produces a steady state solution. Beginning with a linear profile, a model must eventually converge on a temperature profile that produces a uniform energy flux along the regenerator.

MODEL COMPARISONS

This model was compared to two other regenerator models, Sage and REGEN3.2. The models compared reasonably well. It is expected that the Georgia Tech model is the most accurate based on the evidently more accurate energy balance and entropy generation discrepancy. Figure 5 shows the energy fluxes as predicted by the three models.

Each model has three curves: 1) for enthalpy flux, h, 2) conductive and dispersive flux, q, and 3) the total flux, h+q. As presented earlier, the total energy flux in the regenerator must be constant and uniform at steady state. The GT model demonstrates this uniformity while the Sage and REGEN models produce noticeably non-uniform total energy fluxes. Fortunately, Sage and REGEN over-predict the regenerator loss in comparison to the GT model.

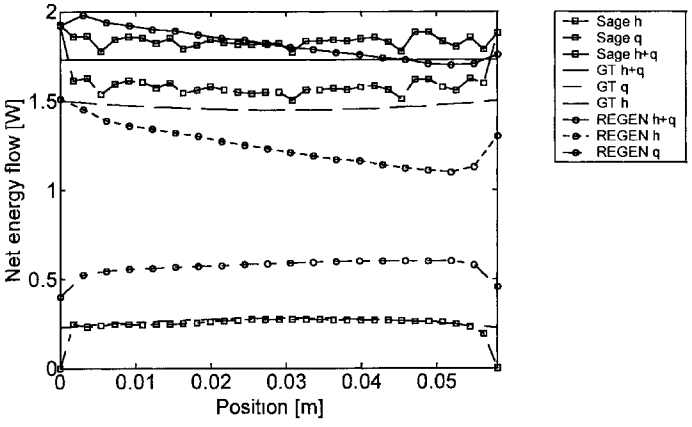

Figure 5. Comparison of Sage-predicted regenerator loss versus GT model.

Table 1. Sage Comparison Summary.

	GT			SAGE		
Net refrigeration	0.0	0.5	1.0	0.0	0.5	1.0
Regenerator Loss	1.73	1.60	1.54	1.84	1.744	1.671
Viscous and inertial lost power	15.3	14.2	14.1	15	14.18	14.02
Interfacial heat transfer lost power	3.17	2.36	1.87	3.15	2.34	1.85
Gas conduction and dispersion lost power	0.618	0.477	0.381	-	-	-
Matrix conduction lost power	0.129	0.105	0.087	-	-	-
Total gas and matrix conduction and disp.	0.747	0.582	0.469	0.713	0.553	0.441
Total lost power	19.2	17.2	16.4	18.9	17.1	16.3
Lost power based on external calculation	19.2	17.2	16.4	19.0	17.2	16.4
Lost power discrepancy	-0.029%	-0.012%	-0.060%	-0.734%	-0.481%	-0.270%
Warm end pressure ratio	1.30	1.31	1.33	1.30	1.31	1.33
Cold end pressure ratio	1.22	1.22	1.24	1.21	1.22	1.24
Warm end pressure phase angle	-42.6	-43.1	-44.9	-42.7	-43.27	-45.11
Cold end pressure phase angle	-62.8	-62.2	-63.4	-63.1	-62.5	-63.6

Sage provides listings which include the available energy losses and an available energy loss discrepancy. This discrepancy is a measure of the difference in available energy loss based on an internal and external control volume formulation. The discrepancy is a measure of numerical errors. Table 1 compares the results from the Sage and GT models for three runs. The GT model averaged 0.03% discrepancy, while Sage averaged 0.5% discrepancy.

SUMMARY

The model presented in the work represents a complete model which produces accurate results. Simulation time is reduced by a factor of 50 by utilizing an artificial convergence technique which drives the solution to the steady state solution without sacrificing accuracy. This technique works by predicting a correction to the mean temperature profile based on a partially converged solution.

This model was used to show the effect of simplifying assumptions on the regenerator loss prediction. The use of ideal gas and constant properties was shown to have a significant non-conservative result over real gas and temperature dependent properties.

A comparison of this model with Sage and REGEN3.2 shows that this model is at least if not more accurate based on the First and Second Laws of conservation.

ACKNOWLEDGMENT

The work described herein was performed with funds provided by Raytheon Space and Airborne Systems to the Georgia Tech Foundation.

REFERENCES

1. Harvey, J. P., *Compressible oscillatory flow and heat transfer in porous media: Application to cryocooler regenerators*, Doctoral Dissertation, Georgia Institute of Technology, Atlanta, Georgia, 2003.
2. Whitaker, S., *The Method of Volume Averaging*, Kluwer Academic Publishers, Netherlands, 1999.
3. Gedeon, D., *Sage Stirling Model—Class Reference Guide*, Gedeon Associates, 1999.

A Parametric Optimization of a Single Stage Regenerator Using REGEN 3.2

J.M. Pfotenhauer, J.L. Shi, and G.F. Nellis

University of Wisconsin - Madison
Madison, Wisconsin 53706

ABSTRACT

Regenerative heat exchangers define the crucial design component for high frequency cryocoolers such as Stirling and Pulse Tube refrigerators. To aid in their design, a parametric investigation has been carried out using the NIST code REGEN3.2 to optimize a single-stage regenerator operating with a warm end temperature of 300 K and a cold end temperature that varies between 60 and 80 K. The matrix choice in all the calculations is 400-mesh stainless steel. The optimization has been defined by maximizing the COP as a function of geometry, mass flow, and the phase between the cold-end mass flow and pressure. We have conducted the optimization investigation over a frequency range of 30 - 60 Hz using a constant average pressure of 20 bar and a pressure ratio of 1.2. Regenerator performance—defined by net cooling power, COP and losses—is presented along with the optimized parameters of geometry, mass flux, and phase angle as a function of cold end temperature and frequency in order to provide convenient design charts for single-stage regenerators.

Additionally, first order design approximations are explored such as the dependence of the optimized length on end temperature conditions alone, and the independence of an optimized mass flux over a wide range of cooling power.

INTRODUCTION

The regenerator-design code developed at NIST[1-3] in its most recent version, REGEN 3.2, provides a powerful tool for the user to investigate the influence of geometry, material selection, frequency, temperature, pressure ratio, and the phase between flow and pressure on regenerator performance. While the broad array of variable parameters enables a wide variety of questions to be investigated, the multiplicity of choices can be intimidating to the new user, and the optimal approach for utilizing REGEN 3.2 in regenerator design is not immediately obvious. In this report we present the sequential steps, and summary of trends observed, in a systematic use of REGEN 3.2 over range of what we consider to be 'typical' operating conditions for single stage cryocoolers. Here the cold end temperature varies between 60 K and 80 K and the frequency varies between 30 and 60 Hz. The pressure ratio ($P_r = P_{max} / P_{min}$) is fixed at 1.2, and stainless steel screens are chosen for the regenerator matrix.

The intent of this investigation is to identify 'rules of thumb' that can be used in a quantitative sense to optimize the design of regenerators without having to repeat the detailed investigation with REGEN. It should be noted that there are certainly many other uses one can

Cryocoolers 13, edited by R. G. Ross, Jr.
Springer Science+Business Media, Inc., New York, 2004

make of REGEN, and our investigation does not come near to exploring its full capabilities. For example, the real-gas properties of helium that are accommodated and influence regenerator design near 10 K are not explored in our investigation. Following a brief description of the key performance parameters within REGEN 3.2, we describe the approach used in our systematic investigation, and the resulting performance trends. The broad picture indeed provides a set of interesting and quantitative guidelines one can quickly apply for parametric analyses and regenerator designs.

KEY PARAMETERS

The thermal and fluid relations that form the foundation of REGEN are well detailed by Radebaugh and Louie[1] as is the numerical approach by Gary and Radebaugh[2,3]. From a user's perspective, the distinctive features afforded by REGEN include the temperature dependent properties of the matrix material, a large selection of materials (more than 30) and flow geometries (5), and the flexibility to add user-defined materials or geometries. REGEN accounts for the pressure drop across the regenerator and includes the non-ideal pressure dependence of enthalpy for the working gas. REGEN 3.2 permits these analyses to be carried out on standard PCs. Input parameters are required for the assumed sinusoidal mass flow at each end in terms of the frequency, amplitude, phase difference, and temperature. The average pressure is also required. Alternately, one can define the input in terms of the pressure ratio (P_r), the phase angle between pressure and mass flow at the cold end (θ), and the average pressure (P_o).

The output provided by REGEN 3.2 defines the performance of the regenerator in terms of its gross and net cooling power, thermal losses, associated PV work at the cold and warm ends, and various other parameters that describe the flow. In the present study, an optimized regenerator is defined by the design that minimizes the necessary work supplied at the warm end in order to achieve a desired cooling power at the cold end. In the variables supplied by REGEN 3.2 such an optimization is achieved by maximizing the net adjusted coefficient of performance (NTACOP). The coefficient of performance is calculated from the net adjusted cooling power (NTCADJ) and PV work at the warm end of the regenerator (PVWK0T) by:

$$\text{NTACOP} = \text{NTCADJ} / \text{PVWK0T} \tag{1}$$

The net adjusted cooling power is calculated beginning from the acoustic power at the cold end of the regenerator (PVWK1). The cold end acoustic power is determined from the integral of the product of the dynamic pressure and volumetric flow at the cold end of the regenerator around one cycle:

$$PVWK1 = \frac{1}{\tau}\int_{t-\tau}^{t} \frac{\varphi A v(L,t)\rho(L,t)P_d(t)}{\rho_L}dt. \tag{2}$$

Here φ and A are the porosity and cross sectional area of the regenerator respectively, while v(L,t) and ρ(L,t) are the instantaneous velocity and density of the gas at the cold end of the regenerator (see Fig. 1). $P_d(t)$ is the instantaneous dynamic pressure and ρ_L is the gas density at the constant cold end temperature. REGEN 3.2 modifies the cold end acoustic power by the loss terms ENTFLX, and HTFLUX, which respectively account for the regenerator ineffectiveness, and heat flux due to conduction through the cold end of the matrix, to calculate the net adjusted cooling power.

$$\text{GRCADJ} = (\text{PVWK1} - \text{PRLOSS})*\text{COOLING\_MULT} \tag{3}$$

$$\text{NTCADJ} = \text{GRCADJ} - \text{RGLOSS} - \text{HTFLUX} \tag{4}$$

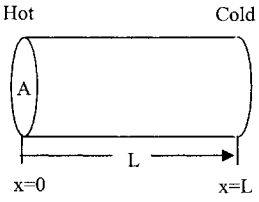

Figure 1. Regenerator configuration defined in REGEN 3.2

$$\text{RGLOSS} = \text{ENTFLX} - \text{PRLOSS} \tag{5}$$

ENTFLX is calculated from the cycle averaged enthalpy flow out the cold end of the regenerator:

$$\text{ENTFLX} = \frac{1}{\tau}\int_{t-\tau}^{t} \varphi A v(L,t)\rho(L,t)h(L,t,P)dt \tag{6}$$

The term COOLING_MULT allows one to estimate a reduced cooling power produced through a non-ideal expansion process in, for example, a pulse tube or Stirling cycle expander. However, throughout the present investigation, COOLING_MULT is set at unity. The term PRLOSS accounts for the non-ideal gas dependence of enthalpy on pressure. Separating this term out of ENTFLX allows RGLOSS to characterize the dependence of regenerator ineffectiveness on geometry parameters alone.

Combining equations (3), (4), and (5) in the case where COOLING_MULT =1 yields the expression for the net adjusted cooling power:

$$\text{NTCADJ} = \text{PVWK1} - \text{ENTFLX} - \text{HTFLUX} \tag{7}$$

The PV work at the warm end of the regenerator (PVWK0T) is determined in a similar fashion as that described by equation (2), except that the velocity and density terms are evaluated at the warm end (x=0), and the dynamic pressure amplitude is increased by an amount equal to the pressure loss through the regenerator. Notice that the net adjusted coefficient of performance defined by equation (1) accounts for both thermal and pressure losses in the regenerator, and thereby provides a realistic comparison of the net cooling power at the cold end and required acoustic power at the warm end.

OPTIMIZATION PROCEDURE

The results generated in the present investigation have been obtained by running REGEN 3.2 simultaneously and continuously on 4 different Pentium IV PC's over a period of approximately two months. In each run the program is halted after 50 cycles. As noted in the instruction manual that accompanies REGEN 3.2, the accuracy of the solution, and the approach to cyclic steady state, can be monitored through the ratio ETHDIF/ETHFLX that measures the energy balance through the regenerator. If ETHDIF is 5-10% of ETHFLX the solution is probably acceptable, a value of 50% is probably not acceptable. As shown in Fig. 2, most of our data produce ratios of approximately 25%. In view of our interest in trends and not necessarily precise quantitative information, and noting that accuracies of less than 10% would require 200 months for the same quantity of information, we have elected to accept the numerical inaccuracy. We note that the variance of NTACOP from 50 cycles to 5000 cycles is less than 10%.

A nested sequence of parameter loops, shown in Fig. 3, is used to generate performance data from REGEN 3.2. To begin, the values of the cold end temperature (T_c), frequency (f),

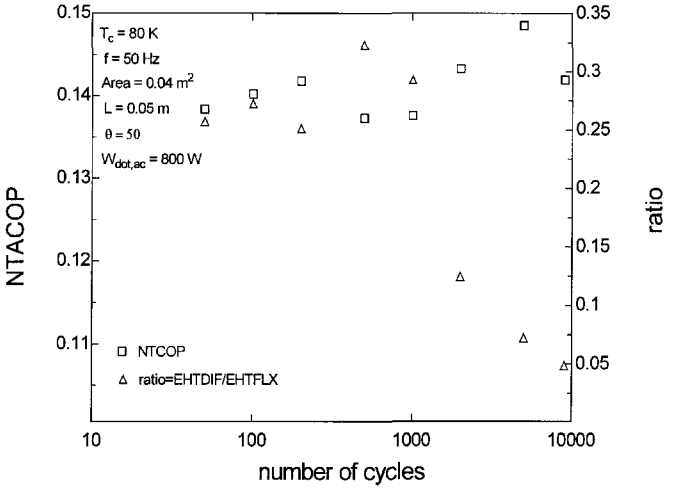

Figure 2. Variation of NTACOP (left) and solution accuracy (right) with number of cycles used in the solution

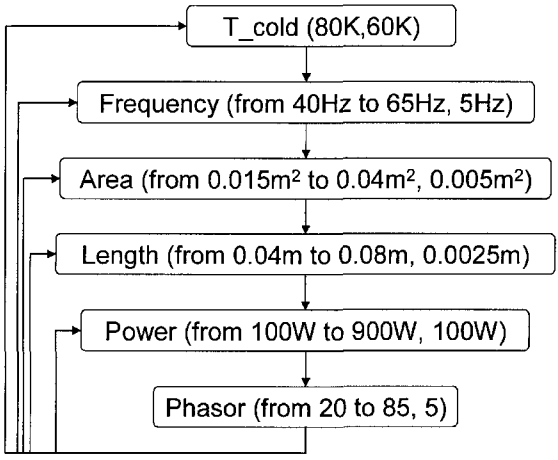

Figure 3. Systematic approach to determine the optimized regenerator geometry as a function of cold-end-temperature and frequency

regenerator area (A), regenerator length (L), and cold end mass flow rate ($\dot{m}_c$) are fixed. In a preliminary investigation, it was found that for the relatively small value of $P_r = 1.2$ used in this study, the term PVWK1 is essentially identical to the expression for acoustic power:

$$\dot{W}_{acoustic} = \tfrac{1}{2} R T_c \dot{m}_c \frac{P_d}{P_o} \cos\theta \qquad (8)$$

where R is the ideal gas constant. Thus, using Eq. (8), a set of runs can be performed for a constant value of acoustic power by varying $\dot{m}_c$ over a range of θ. The set of runs with various constant power curves are generated for each value of regenerator length indicated in Fig. 3. This group of runs is repeated for the each of areas indicated, with the systematic approach continuing through the full nested set of runs, finally generating more than 100,000 runs of REGEN 3.2.

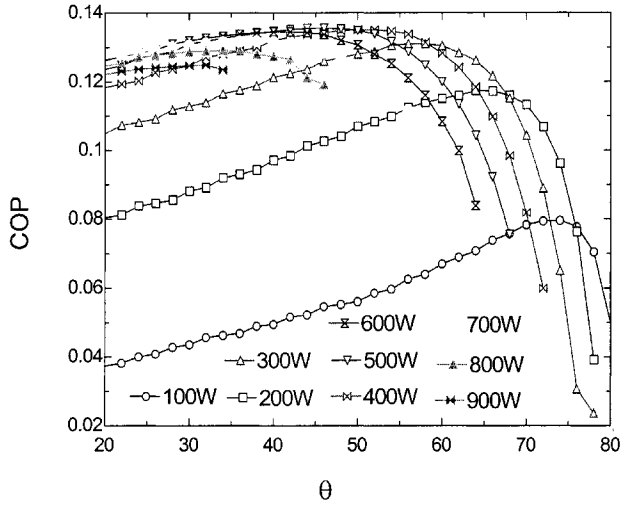

Figure 4. The dependence of COP on theta with variable power, but constant cold end temperature, area, length and frequency. In this case T_c = 80 K, f = 50 Hz, A = 0.02 m^2, and L = 0.05 m.

INVESTIGATION RESULTS

As noted above, the primary performance characteristic of interest for each run is the NTACOP. Results from a series of runs within the innermost loop of Fig. 3, carried out for different values of acoustic power, are shown in Fig. 4. From such data, the optimum acoustic power associated with the fixed values of T_c, f, A, and L is found by identifying the power and corresponding value of θ that produces a maximum NTACOP.

By repeating the above runs for a variety of regenerator lengths, a set of optimized values of power, phase angle, and COP are obtained for each length. An example of optimized COP - length data are shown in Fig. 5. In this case the associated values of acoustic power (PVWK1)

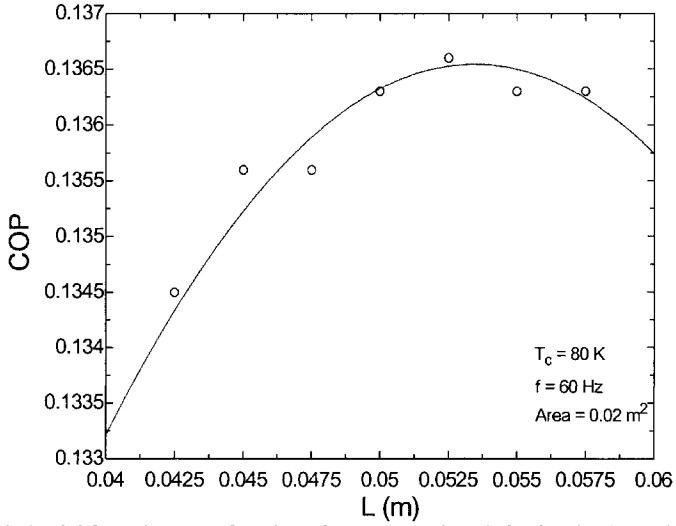

Figure 5. Optimized COP values as a function of regenerator length for fixed values of T_c, frequency, and area. The associated values of PVWK1 and θ are 500 W and 45 ° respectively.

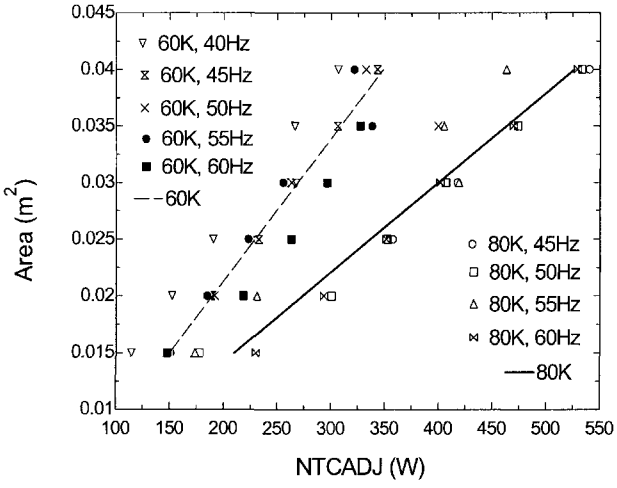

Figure 6. Correlation between the optimized cross sectional area of regenerator and the associated cooling power for two different cold end temperatures.

and phase angle are 500 W and 45 °. Repeating this investigation for other values of regenerator area, while holding frequency and cold end temperature fixed, reveals a strongly linear relationship between the optimum acoustic power and regenerator area. A corresponding linear relationship also exists between the net adjusted cooling power (NTCADJ) and the regenerator area, as illustrated in Fig. 6. Here the scatter of data is primarily a result of the course step size (100 W) used for the values of acoustic power. Fig. 6 also suggests a slight frequency dependence at 60 K in the relationship between the optimized area and cooling power. Fig. 7 explores this relationship explicitly for a fixed cooling power (300 W). Although the frequency dependence is evidenced in the 60 K data, more information is required at 80 K to make a similar conclusion at that temperature.

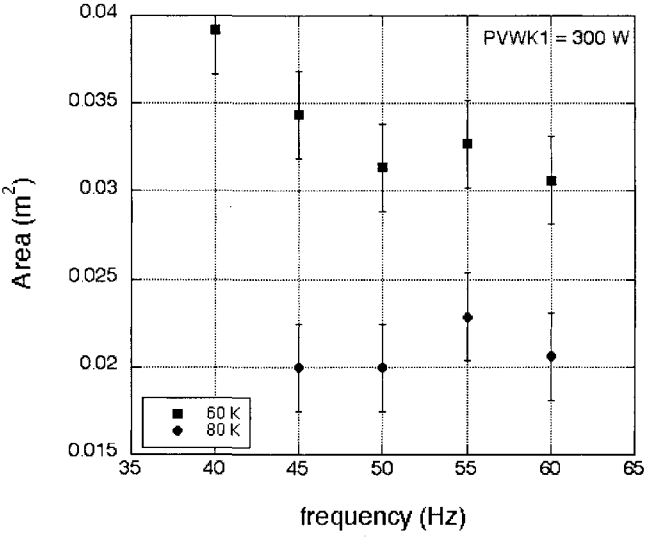

Figure 7. Frequency dependence of optimized area for constant cold end temperature (80 K) and cooling power (300 W).

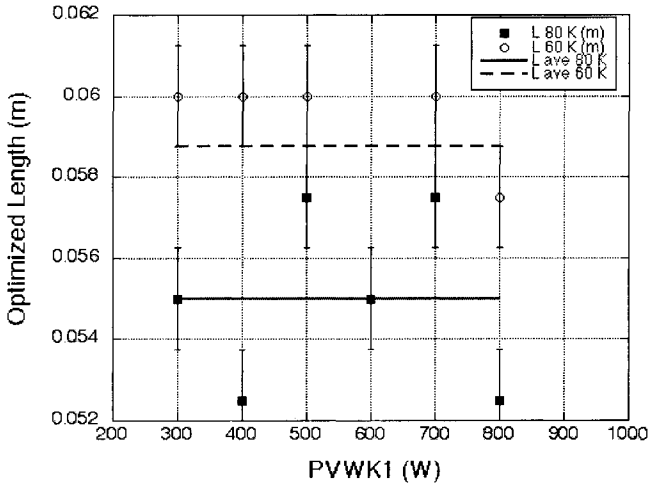

Figure 8. Optimized regenerator length at 80 K and 60 K.

In contrast to the clear correlation between cooling power and area, there is little, if any correlation between the cooling power and the optimized length. As shown in Fig. 8, the optimized regenerator length is insensitive to cooling power, but varies inversely with the cold end temperature. For a constant cold end temperature, one can also clearly identify a frequency dependence to the optimized length (see Fig. 9). Finally, the optimized values of NTACOP are found to be frequency independent, and vary inversely with the cold end temperature as expected. Fig. 10 displays that the optimized COP values, including the various real loss terms accounted by REGEN 3.2, are 0.14 at 80 K and 0.085 at 60 K. These values indicate that an optimized regenerator can be expected to perform with an efficiency of at best 38.5% and 34% of Carnot at 80 K and 60 K respectively.

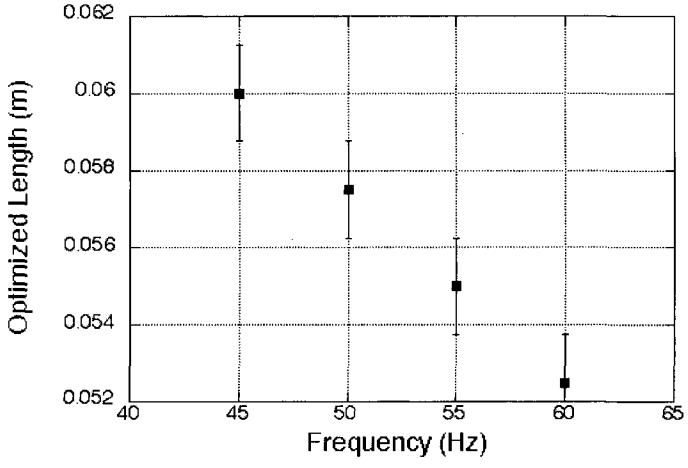

Figure 9. Frequency dependence of the optimized length. Here T_c = 80 K.

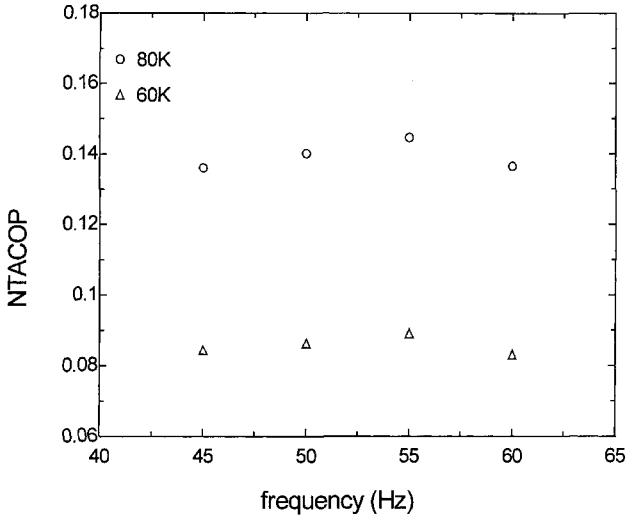

Figure 10. The coefficient of performance for an optimized regenerator, as determined by REGEN 3.2, operating at 80 K or 60 K.

CONCLUSIONS

A systematic use of REGEN 3.2 including over 100,000 runs reveals a number of useful 'rules of thumb' for designing single stage regenerators operating between a warm end temperature of 300 K and a range of cold end temperatures between 60 K and 80 K. The optimized length of the regenerator is independent of the cooling power but found to be inversely dependent on the cold end temperature and frequency. At 80 K and 60 Hz, the optimized length is 53±0.5 mm. Decreasing the frequency to 45 Hz increases the optimized length to 60 mm. A linear relationship exists between the optimized regenerator area and the desired cooling power. At 80 K the coefficient of proportionality is approximately 7.7 x 10^{-5} m^2/W. (This area represents the total cross section of the regenerator, including the screen matrix). The optimized area at 60 K is found to be somewhat frequency dependent, varying from 0.04±0.005 m^2 at 40 Hz to 0.03±0.005 m^2 at 60 Hz to provide 300 W of cooling power. In all of the runs at 80 K and 60 K, the optimized phase angle between the mass flow and pressure at the cold end of the regenerator is 45±5°. Finally, REGEN 3.2 calculates that the optimum COP of a regenerator operating at 80 K and 60 K will be 38.5% and 34% of Carnot respectively.

ACKNOWLEDGEMENTS

The authors extend their gratitude to Ray Radebaugh and Abbie O'Gallagher for many helpful discussions. This work was partially supported by a subcontract from Atlas Scientific.

REFERENCES

1. R. Radebaugh and B. Louie, "A Simple, First Step to the Optimization of Regenerator Geometry," *Proc. of the 3rd Cryocooler Conf.*, NBS Special Publication 698, Boulder, CO (1985), pp. 177-198.

2. J. Gary, D. Daney, and R. Radebaugh, "Computational Model for a Regenerator," *Proc. of the 3rd Cryocooler Conf.*, NBS Special Publication 698, Boulder, CO (1985), p. 199.

3. J. Gary and R. Radebaugh, "An Improved Numerical Model for Calculation of Regenerator Performance (REGEN 3.1)," *Proc. of the Fourth Interagency Meeting on Cryocoolers*, No. DTRC-91/003, David Taylor Research Center, Bethesda, MD (1991), pp. 165-176.

A Numerical Model of an Active Magnetic Regenerator Refrigeration System

K.L. Engelbrecht , G.F Nellis, and S.A Klein

University of Wisconsin
Madison, WI 53706

ABSTRACT

Active magnetic regenerative refrigeration (AMRR) systems represent an environmentally attractive space cooling and refrigeration alternative that do not use a fluorocarbon working fluid. Two recent developments have made AMRR's feasible in the near-term. A rotary regenerator bed utilizing practical and affordable permanent magnets has been demonstrated and shown to achieve a reasonable coefficient of performance (COP). Concurrently, families of magnetocaloric material alloys with adjustable Curie temperatures have been developed. Using these materials, it is possible to construct a layered regenerator bed that can achieve a high magnetocaloric effect across its entire operating range. This paper describes a numerical model capable of predicting the practical limits of the performance of this technology applied to space conditioning and refrigeration. The model treats the regenerator bed as a one dimensional matrix of magnetic material with a spatial variation in Curie temperature, and therefore magnetic properties. The matrix is subjected to a spatially and temporally varying magnetic field and fluid mass flow rate. The variation of these forcing functions is based on the implementation of a rotating, multiple bed configuration. The numerical model is solved using a fully implicit (in time and space) discretization of the governing energy equations. The nonlinear aspects of the governing equations (e.g., fluid and magnetic property variations) are handled using a relaxation technique. Some preliminary modeling results are presented which illustrate how an AMRR system can be optimized for a particular operating condition. The performance of the AMRR in a space cooling application with the layered vs non-layered bed is compared to current vapor compression technology.

INTRODUCTION

Magnetic cooling has the potential to become competitive with vapor compression systems. The metallic refrigerant has essentially zero vapor pressure and no ozone depletion potential or direct global warming potential. The theoretical limit on the efficiency (or COP) of an active magnetic regenerative refrigeration (AMRR) system is the Carnot limit. However, the temperature lift of an AMRR system is limited by the material properties of the magnetocaloric alloy. Practical limits on the performance of an AMRR have yet to be established as there is currently no directly applicable, non-proprietary model that considers the detailed, coupled thermal-fluid processes occurring within a layered magnetic bed.

Cryocoolers 13, edited by R. G. Ross, Jr.
Springer Science+Business Media, Inc., New York, 2004

The Magnetocaloric Effect

The thermal and magnetic properties of magnetocaloric materials are highly coupled over a certain, typically somewhat limited, temperature range, allowing them to be used within energy conversion systems. Temperature (T) and entropy (S) form what in thermodynamics is called a canonical conjugate property pair that, together, defines the transfer of heat. Pressure (P) and volume (V) form another such property pair defining the transfer of mechanical work. If hysteresis is ignored, then it is possible to define a similar pair of properties to describe the transfer of magnetic work: applied field ($\mu_o H$) and magnetic moment (VM) [1]. The fundamental property relation for a substance capable of experiencing magnetic work is shown in Eq. (1).

$$dU = T \cdot dS + \mu_o \cdot H \cdot d(V \cdot M) \tag{1}$$

Examination of Eq. (1) reveals that the applied field is analogous to pressure and magnetic moment is analogous to (the inverse of) volume. This analogy is physically revealing; increasing the applied field tends to align the magnetic dipoles, which can be thought of as small torsional springs, and the result is an increase in the magnetization and an increase in temperature. The process of aligning the magnetic dipoles requires work and reduces entropy. In a compressible substance increasing the pressure tends to reduce the space between molecules, which can be thought of as small linear springs. The process of reducing the volume requires work and reduces entropy and increases the temperature of the gas.

Using the analogy described above it becomes possible to apply all of the typical thermodynamic results and identities ordinarily used with a pure compressible substance to a magnetic material; including Maxwell's relations that describe relationships between partial derivatives of properties and the idea of an equation of state that describes the magnetization as a function of temperature and applied field.

Magnetic Refrigerator Configurations

The thermodynamic coupling between thermal and magnetic properties allows a magnetocaloric material to be used as the working fluid in a refrigeration cycle. In 1933, Giauque and MacDougall [2] reported using this effect to reach temperatures below 1 K, breaking the temperature barrier that was previously imposed by the properties of compressible fluids. These early, "one-shot" techniques utilized an isothermal magnetization followed by an adiabatic demagnetization. This cycle suffers from limited temperature lift due to the magnetic material properties.

This technical barrier has been overcome by the use of a regenerator in the active magnetic regenerative refrigeration (AMRR) cycle. A porous, packed bed of magnetic material is exposed to a time-varying magnetic field and a time-varying flow of heat transfer fluid. Each segment of the bed undergoes a unique refrigeration cycle and interacts with the adjacent material via the heat transfer fluid. The net result of these cascaded refrigeration cycles is a temperature lift that is much larger than can be achieved with a "one-shot" configuration. Different mechanical realizations of this cycle are possible. For example, the magnetic material may be stationary and the field varied by controlling the current in a solenoid. This configuration is feasible at very low temperatures where superconductors can be used to efficiently handle the large currents that are required to generate significant magnetic fields but is not practical near room temperature applications where the applied field variation is achieved by physically moving the magnetic regenerator into and out of a stationary magnetic field produced by a permanent magnet either linearly [3-6] or rotationally [7]. The practical limit on the efficiency that can be realized by an AMRR is then limited primarily by losses that are related to the regenerator and can only be assessed through the development of a detailed and realistic model of this component, as described in the subsequent sections.

Layered beds

Ideally, the regenerator in an active magnetic refrigerator (AMR) would utilize a magnetic material that undergoes a magnetic field induced change in entropy that is constant across the bed over its entire operating temperature range. However, pure magnetic materials exhibit a sharp peak in their magnetic-to-thermal coupling and therefore in the magnetically driven entropy change. This peak occurs at the Curie temperature (T_{Curie}). When used as a magnetic refrigerant in an AMR, this characteristic of the material results in there being only a very small temperature range (near the Curie temperature) where the AMR can maintain its otherwise potentially high performance.

Researchers have recently identified families of magnetic material alloys whose Curie temperatures can be engineered, within some range, through variation in the alloying formula [8-10]. Therefore, AMR beds may be constructed with engineered, spatial variations in their Curie temperature; the material with the lowest Curie temperature is placed at the cold end of the matrix and the Curie temperature of the material increases towards the hot end.

MODELING

The conventional equipment outside of the magnetic regenerator bed, including the pumps, heat exchangers, fans, drive motor, and permanent magnets are not explicitly modeled. Their effect on the bed is felt through an imposed time variation of the mass flow rate ($\dot{m}(t)$) and the variation of the magnetic field in time and space ($\mu_o H(x,t)$); these variations must somehow be related to the fluid-mechanical-magnetic configuration that is employed to operate the bed. When the fluid mass flow rate is positive, flow is in the positive x direction and therefore enters the hot end of the regenerator bed. A negative mass flow rate indicates flow entering from the cold end of the bed. The flow entering the bed is assumed to have the temperature of the adjacent thermal reservoir, T_H or T_C, depending on whether the flow rate is positive or negative, respectively. The fluid is assumed to be incompressible (ρ_f = constant). The remaining required fluid properties, specific heat capacity (c_f), viscosity (μ_f), and thermal conductivity (k_f), are assumed to be functions of temperature but not pressure.

The fluid flows within a regenerator matrix formed from a layered magnetic material. The layering causes the Curie temperature to vary spatially along the matrix ($T_{Curie(x)}$). The partial derivative of entropy with respect to applied field at constant temperature is assumed to be a function of the temperature of the material relative to the local Curie temperature and of the applied magnetic field ($\frac{\partial s_r}{\partial \mu_o H}_T (T - T_{Curie}, \mu_o H)$); this dependence implies that the magnetic effect of different alloys can be collapsed onto a common shape by shifting the temperature scale according to the Curie temperature. The specific heat capacity of the material at constant, zero applied field and the thermal conductivity of the material are assumed to be a function of the material's temperature, applied field, and its Curie temperature ($c_r(T, T_{Curie}, \mu_o H)$ and $k_r(T, T_{Curie}, \mu_o H)$).

The geometry of the matrix consists of many small passages that allow the fluid to flow in intimate thermal contact with the regenerator material. Regenerator geometries ranging from packed beds of spheres to screens to perforated plates may all be considered by this model. In order to maintain this flexibility, the regenerator geometry is characterized by a hydraulic diameter (d_h), porosity (ε), and specific surface area (a_s). The Nusselt number of the matrix is assumed to be a function of the local Reynolds number and Prandtl number of the fluid ($Nu(Re_f, Pr_f)$). The friction factor is assumed to be a function of the local Reynolds number ($f(Re_f)$). The matrix/fluid combination is characterized by an effective thermal conductivity (k_{eff}) that relates the actual axial conduction heat transfer through the composite solid/liquid structure to the heat transfer through a comparable solid piece of regenerator material. The overall size of the regenerator is specified according to its length (L) and total cross-sectional area (A_c).

Derivation of Governing Equations

The fluid and regenerator temperature variations over a periodic steady-state cycle are the eventual output of this model ($T_f(x,t)$ and $T_r(x,t)$). These variations, coupled with the prescribed mass flow rate and applied field, allow the calculation of cycle performance metrics such as refrigeration load and magnetic power. The temperature variations are obtained by solving a set of coupled, partial differential equations in time and space obtained from energy balances on the fluid and the matrix. After some simplification, the energy balance on the fluid is:

$$\dot{m}(t)c_f(T_f)\frac{\partial T_f}{\partial x}+\frac{Nu(Re_f,Pr_f)k_f(T_f)}{d_h}a_s\,A_c\,(T_f-T_r)+\rho_f\,A_c\,\varepsilon\,c_f(T_f)\frac{\partial T_f}{\partial t}=\left|\frac{\partial p}{\partial x}\frac{\dot{m}(t)}{\rho_f}\right| \quad (2)$$

The first term in Eq. (2) represents the enthalpy change of the flow, the second term represents heat transfer from the fluid to the magnetic material, the third term represents the energy stored by the fluid that is entrained in the matrix structure, and the fourth term represents viscous dissipation. Note that axial conduction is ignored in the fluid equation and instead is applied to the matrix and modeled using the concept of effective bed conductivity. The governing equations are simplified and the numerical solution is stabilized considerably if the entrained fluid heat capacity is "lumped" with the heat capacity of the matrix itself; therefore this term is removed from the fluid energy equation but will be included in the regenerator energy equation. Investigations are ongoing relative to the impact of this simplification, but it appears to be conservative; that is, this simplification tends to reduce the performance somewhat. After removing the entrained fluid heat capacity and expressing the pressure gradient in terms of a friction factor, Eq. (2) becomes:

$$\dot{m}(t)c_f(T_f)\frac{\partial T_f}{\partial x}+\frac{Nu(Re_f,Pr_f)k_f(T_f)}{d_h}a_s\,A_c\,(T_f-T_r)=\left|\frac{f(Re_f)\dot{m}(t)^3}{2\rho_f^2A_c^2d_h}\right| \quad (3)$$

The energy balance on the magnetic material in the regenerator is:

$$\frac{Nu(Re_f,Pr_f)k_f(T_f)}{d_h}a_s\,A_s(T_f-T_r)+A_c(1-\varepsilon)\mu_oH\frac{\partial M}{\partial t}+k_{eff}A_c\frac{\partial^2T_r}{\partial x^2}=\rho_r\,A_c(1-\varepsilon)\frac{\partial u_r}{\partial t} \quad (4)$$

where the first term represents heat transfer from the fluid to the regenerator, the second term represents the magnetic work transfer, the third term is axial conduction, and fourth term represents energy storage. The magnetic work term is grouped with the change in the internal energy in order obtain an expression involving the partial derivative of the entropy with respect to magnetic field. The fluid heat capacity, removed from Eq. (2) is added to the regenerator energy balance. The governing equation for the regenerator becomes:

$$\begin{aligned}&\frac{Nu(Re_f,Pr_f)k_f(T_f)}{d_h}a_s\,A_s(T_f-T_r)+k_{eff}A_c\frac{\partial^2T_r}{\partial x^2}=\\&A_c(1-\varepsilon)\rho_r\,T_r\frac{\partial s_r}{\partial\mu_oH}_T(T_r-T_{Curie},\mu_oH)\frac{\partial\mu_oH}{\partial t}\\&+A_c\left[\rho_f\,\varepsilon\,c_f(T_r)+(1-\varepsilon)\rho_r\,c_{\mu_oH}(T_r,T_{Curie},\mu_oH)\right]\frac{\partial T_r}{\partial t}\end{aligned} \quad (5)$$

The boundary conditions for Eq. (3) and (5) include that the fluid is assumed to enter the matrix at the temperature of the associated thermal reservoir, the ends of the regenerator are assumed to

be insulated from conductive heat transfer, and the regenerator must undergo a steady-state cycle. This last boundary condition leads to the constraint that the temperature at any location in the regenerator at time t must equal the temperature at the same point at time $t + \tau$ where τ is the duration of a cycle.

Numerical Model

The numerical solution for the fluid and regenerator temperatures is obtained on a numerical grid that extends from 0 to L in space and from 0 to τ in time. Initially, "guess" values for the temperatures at each node ($T^*_{r\,i,j}$ and $T^*_{f\,i,j}$) are assigned based on a spatially linear and time invariant assumption. The properties, local flow characteristics, and other temperature dependent aspects of the matrix behavior are computed for each control volume based on these "guess" temperature values. The fluid and regenerator governing equations are linearized, discretized and written for each control volume. These equations are solved using a sparse matrix decomposition algorithm. The absolute value of the maximum error between the "guess" values of the regenerator and fluid temperatures and the calculated values is determined. If the error is less than a relaxation tolerance (*tol*) then the relaxation process is complete. If not, then a new set of guess values is used in a subsequent iteration. These new "guess" values (T^{*+}) are computed as the weighted average of the calculated and "guess" values.

Material Properties

The fluid properties are obtained by implementing polynomial correlations for the specific heat capacity, thermal conductivity, and viscosity as a function of temperature over the temperature range of interest. Water and other heat transfer fluids such as propylene/glycol and ethylene/glycol solutions can be implemented using this technique. Experimental property data for a 94% gadolinium 4% erbium alloy measured at Ames Lab and provided by Astronautics Corporation were used to provide entropy over a range of temperatures and applied fields. These experimental data are interpolated using a two-dimensional spline technique and the interpolated entropy data are numerically differentiated to determine the required model inputs: constant field specific heat capacity and the partial derivative of entropy with respect to applied field.

Thermal/Hydraulic Performance of Matrix

Although the model is generally applicable to a number of matrix configurations, the initial analyses have focused on a packed sphere regenerator. The effective conductivity of the regenerator/fluid matrix is computed using the correlation presented by Kunii and Smith [11]. The friction factor is computed using the Ergun equation [12] and the Nusselt number is calculated using a correlation for a bed of uniform diameter spheres found in Rohsenow [13].

The Biot number associated with the magnetic material is not generally much less than unity throughout the entire cycle, particularly in the flow periods. Therefore, the temperature in the spheres that comprise the regenerator matrix cannot be considered spatially uniform. As a result, the heat transfer from the fluid to magnetic material is significantly affected by conduction from the center of the spheres to the outer surface as well as by the convection from the surface of the spheres to the fluid. This effect is accounted for by modifying the heat transfer coefficient as suggested by Jeffreson [14].

Validation of the Numerical Model

There are few analytical solutions to the regenerator equations. However, in the limit of constant properties and no axial conduction, the thermal effectiveness (ε) of a conventional regenerator (i.e., one with no magnetocaloric effect) subjected to a constant, alternating mass flow rate (i.e., constant in time and with the same value during both the cold-to-hot and hot-to-cold flow periods) is well-known.

The thermal effectiveness (ε_t) in this case is defined as:

$$\varepsilon_t \equiv \frac{\dot{q}_{f-r}}{\bar{\dot{m}}\, c_f \left(T_H - T_C\right)} \tag{6}$$

where $\bar{\dot{m}}$ is the magnitude of the mass flow rate and $\dot{q}_{f-r}$ is the average heat transfer rate between the fluid and the matrix during the cycle:

$$\dot{q}_{f-r} = \bar{\dot{m}}\, c_f \int_0^{\tau/2} \left(T_H - T_f\left(x = L, t\right)\right) dt \tag{7}$$

The typical variables used to characterize this problem are the number of transfer units (*NTU*, sometimes also referred to as the reduced length of the regenerator) and the utilization ratio (*U*, the inverse of the matrix capacity rate ratio [15]).

$$NTU \equiv \frac{Nu\, k_f\, a_s\, L\, A_c}{d_h\, \bar{\dot{m}}\, c_f} \tag{8}$$

$$U = \frac{\bar{\dot{m}}\, c_f\, \tau}{2\, A_c\, L\left(1-\varepsilon\right)\rho_r\, c_{\mu_0 H}} \tag{9}$$

Dragutinovic and Baclic [16] present tables for the ε_t as a function of *NTU* and *U* in this limiting condition and the passive behavior of the numerical model can be verified against these solutions. The numerical model was implemented in this limiting (passive) condition by specifying constant material properties, removing the axial conduction and viscous dissipation terms in the governing equations, setting the matrix porosity to zero, and eliminating the magnetocaloric effect. A grid with 80 spatial control volumes (n = 80) and 100 time steps (m = 100) was used and the results are illustrated in Fig. 1. Excellent agreement between the published and predicted results is observed, verifying the accuracy of the numerical model in this limit.

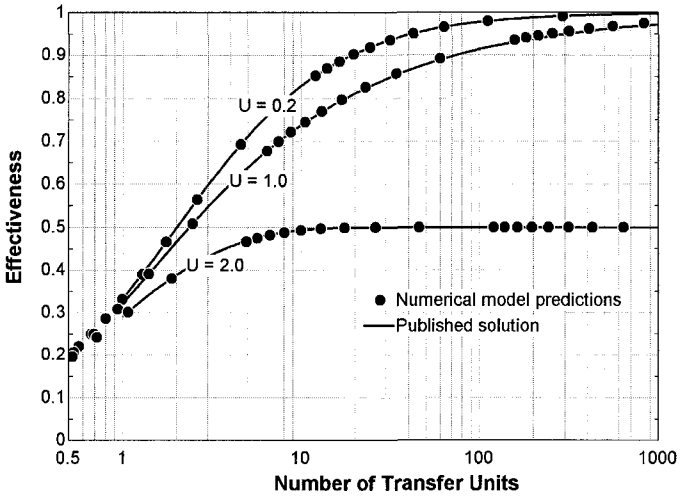

Figure 1. Comparison between model and published regenerator solution in passive limit.

Heat Exchangers

A practical AMRR device will interact with the conditioned space and the ambient environment via conventional heat exchangers. The hot and cold heat exchangers, the equivalent of the condenser and evaporator in a vapor compression cycle, are modeled as cross flow air-to-liquid heat exchangers. The overall conductance, UA, and mass flow rate of air through each heat exchanger are specified based on values that are reasonable for an equivalent vapor compression system. Unlike the evaporator and condenser in a vapor compression cycle, the heat exchangers in an AMRR will have a finite capacity ratio and therefore the performance, as indicated by an approach temperature difference, will not remain constant as the mass flow rate of the refrigerant (in this case the heat transfer fluid) is varied. An iterative calculation is required to ensure that the reservoir temperatures used as the fluid temperature boundary conditions for the numerical model of the AMR bed (T_H and T_C) are consistent with the mass flow rates of the air and heat transfer fluid and the operating temperatures.

The fluid entering the hot end of the AMR is assumed to be at a constant hot reservoir temperature, T_H. During the cold-to-hot flow process, fluid leaves from the hot end of the AMR bed with a time varying temperature $T_{AMR,out}(t)$ that is predicted by the model. The fluid exiting the AMR is assumed to fully mix prior to entering the hot heat exchanger (the equivalent of the condenser) at a constant temperature $T_{HX,in}$, the enthalpy average temperature of the fluid flow. Air from the surroundings is used as a heat transfer medium and enters the heat exchanger at $T_{ambient}$, a temperature that is typically specified according to an Air-Conditioning and Refrigeration Institute (ARI) standard test condition. Knowledge of the mass flow rates and temperatures on each side of the hot heat exchanger allows the heat exchanger effectiveness to be computed, using the ε-NTU for a cross-flow heat exchanger with both fluids unmixed [17]. The effectiveness is then used to compute the heat exchanger load and finally the exit enthalpy and temperature of the heat transfer fluid. The calculated exit temperature will not in general be equal to the value T_H used in the model, necessitating an iteration loop in which this temperature is adjusted. An analogous process is applied to the cold heat exchanger (the equivalent of the evaporator).

RESULTS

It is useful to directly compare the predicted performance of an AMR to a standard vapor compression system. To accomplish this, the DOE/ORNL Heat Pump Design Model developed by Rice [18] and available online was exercised using its default conditions with the one exception that dry indoor and outdoor air conditions were used rather than the default relative humidity values. Currently the heat exchanger models used for the AMR cycle do not accurately model the dehumidification process. The parameters used to carry out the comparison are summarized in Table 1. The AMR bed model coupled to the heat exchanger model described above was operated in order to determine how system performance varies with the regenerator volume, aspect ratio (L/d), and bed layering.

Table 1. Parameters used for comparative study.

Parameter	Value	Parameter	Value
heat rejection temp.	308.2 K	hot heat exchanger UA	957 W/K
load temperature	299.8 K	motor efficiency	0.9
cooling capacity	7.3 kW	pump efficiency	0.7
maximum applied field	1.5 Tesla	heat transfer fluid	Water
cold air mass flow rate	0.58 kg/s	number of beds	6
hot air mass flow rate	1.35 kg/s	period	0.2 sec (5 Hz)
cold heat exchanger UA	577 W/K	sphere size for packing	0.1 mm

Figure 2 illustrates the refrigeration capacity and COP for an AMR system using the parameters listed in Table 1 and a regenerator of a fixed volume (25 L) and aspect ratio (L/d = 0.34). The results are shown both for a regenerator consisting of a single magnetic material alloy (i.e. a non-layered bed) as well as for a layered regenerator bed. The layered regenerator has a Curie temperature that varies linearly along the bed from the AMR hot reservoir temperature to the cold reservoir temperature, and the non-layered regenerator contains a constant Curie temperature magnetic material that is set at the midpoint between the hot and the cold reservoir temperature. The COP curve of the non-layered bed lies almost directly on top of the COP curve of the layered bed plotted against water mass flow rate. This shows that a layered bed can produce a higher cooling capacity than a non-layered bed at approximately the same efficiency. Notice that for each type of bed configuration it is possible to produce a specified refrigeration capacity using one of two possible mass flow rates. In the figure, the lower mass flow rate always corresponds to a higher COP. In order to design a bed for a given refrigeration capacity (7.3 kW in this case) it is therefore necessary to vary the water mass flow rate in order to generate refrigeration capacity and COP vs. mass flow rate information. This information is interpolated using a piecewise cubic hermite interpolating polynomial in order to select the mass flow rate required to produce the desired cooling capacity; the lower mass flow rate is selected by constraining the solution to those values where the slope of capacity against mass flow rate is positive.

Figure 3 illustrates the COP as a function of aspect ratio for a 25 L layered bed producing 7.3 kW of refrigeration. Figure 3 shows that there exists an optimal aspect ratio where the COP is maximized; lower aspect ratios result in excessive conduction losses and higher aspect ratios result in excessive pumping losses.

Preliminary Comparison with Vapor Compression System

The DOE/ORNL Heat Pump Design Model predicts a COP of 2.51 for the vapor compression cycle including 0.59 kW of fan power. The AMR model was subsequently run at the same conditions and using the same heat exchanger sizes (as indicated by the UA values in Table 1) and air flow rates. The numerical model does not account for fan power, so the fan power from the Heat Pump Design Model was added to the total power predicted by the numerical model and used to correct the predicted COP for the AMR cycle.

Figure 4 illustrates the predicted COP as a function of regenerator volume for a layered and non-layered bed; these curves were generated using a refrigeration capacity of 7.3 kW and the optimal aspect ratio for each volume. Figure 4 shows that an AMR cycle may be capable of achieving higher values of COP than an equivalent vapor compression cycle, depending on the volume of the magnetic regenerator bed used. As the AMR regenerator volume increases, the operating efficiency also increases and the layered bed out-performs the non-layered bed. Of course, larger regenerator volumes are also associated with higher initial investments and therefore there must be an economically optimum regenerator volume.

CONCLUSIONS

The numerical model presented in this paper is capable of predicting the performance of an AMRR with a layered regenerator matrix. The model was verified in its passive limit and subsequently used to analyze the effects of regenerator volume and aspect ratio. An initial optimization of the AMRR cycle was presented to demonstrate how this space cooling efficiency of this technology compares to current vapor compression technology.

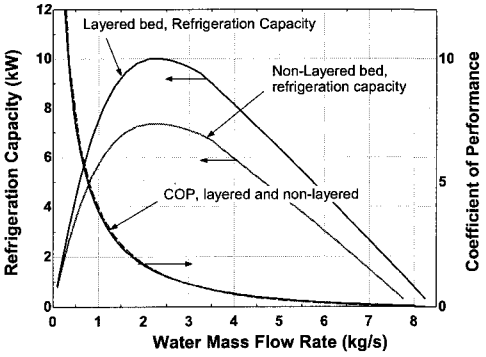

Figure 2. Refrigeration capacity and COP of a 25 L layered and non-layered bed as a function of the water mass flow rate.

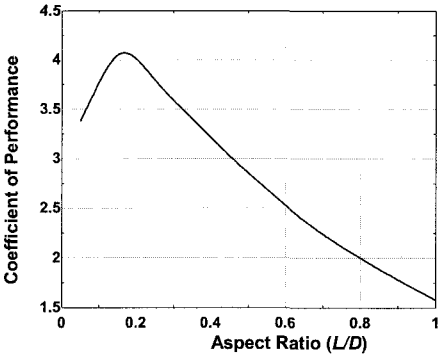

Figure 3. COP of a 25 L layered bed producing 7.3 kW of refrigeration as a function of the aspect ratio.

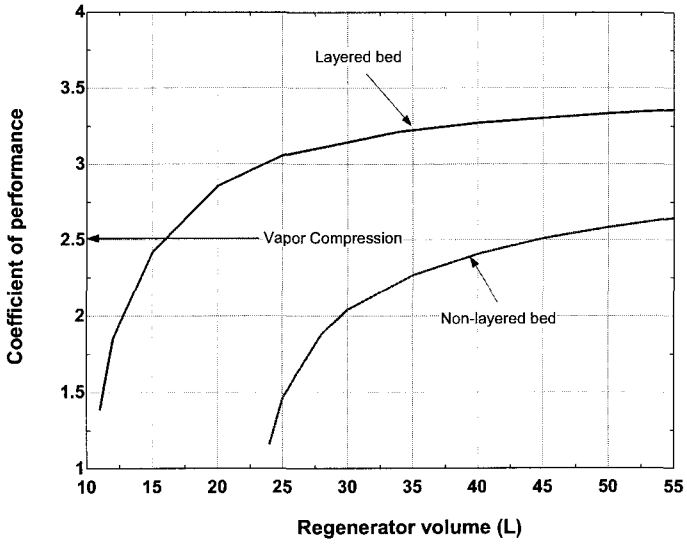

Figure 4. COP of a layered and non-layered bed producing 7.3 kW of refrigeration at its optimal aspect ratio. Also shown is the COP for a comparable vapor compression cycle.

ACKNOWLEDGMENT

Financial support for this project was provided by the Air-Conditioning and Refrigeration Technology Institute (ARTI). The technical assistance of personnel at Astronautics Corporation is gratefully acknowledged.

REFERENCES

1. Guggenheim, E.A., Thermodynamics, An Advanced Treatment for Chemists and Physicists, North Holland, Amsterdam (1967).
2. Giauque, W. F., and MacDougall, D. P., "Attainment of temperatures below 1° absolute by demagnetization of $Gd_2(SO_4)_3$ $8H_2O$", Phys. Rev., vol. 43 (1933), pp. 7768.
3. Rowe, A. M., and Barclay, J. A., "Design of an Active Magnetic Regenerator Test Apparatus", Advances in Cryogenic Engineering, vol. 47 (2002), pp. 995.

4. Hirano, N., Nagaya, S., Takahashi, M., Kuriyama, T., Ito, K., and Nomura, S., "Development of Magnetic Refrigerator for Room Temperature Application," *Advances in Cryogenic Engineering*, vol. 47 (2002), pp. 1027.

5. Wu, W., "Room Temperature Magnetic Refrigerator using a 1.4 T Permanent Magnet Field Source," Abstract K7.004, American Physical Society Conference, Austin, TX (2003).

6. Zimm, C., Jastrab, A., Sternberg, A., Pecharsky, V., Gschneidner, K. Jr., Osborne, M., and Anderson, I., "Decription and Performance of a Near-Room Temperature Refrigerator," *Advances in Cryogenic Engineering*, vol. 43B (1998), pp. 1759.

7. Zimm, C. B., Sternberg, A., Jastrab, A. G., Boeder, A. M., Lawton, L. M. Jr., and Chell, J. J., 2002, "Rotating Bed Magnetic Refrigeration Apparatus", U.S. Patent Application, US 2002/0053209 A1.

8. Pecharsky, V. K., and Gschneidner, K. A. Jr., "Giant Magnetocaloric Effect in $Gd_5(Si_2Ge_2)$," *Physical Review Letters*, vol. 78, no. 23, pp. 4494.

9. Chen, Y., Wang, F., Shen, B., Hu, F., Sun, J., Wang, G., and Cheng, Z., "Magnetic properties and magnetic entropy change of $LaFe_{11.5}Si_{1.5}H_y$," *J. Phys.: Condens. Matter*, vol. 15, no. L161 (2003), pp. 7.

10. Hu, F., Shen, B., Sun, J., and Cheng, Z., "Influence of negative lattice expansion and metamagnetic transition on magnetic entropy change in the compound $LaFe_{11.4}Si_{1.6}$," *Applied Physics Letters*, vol. 78, no. 23 (2001), pp. 3675.

11. Kunii, D. and Smith, J. M., "Heat Transfer Characteristics of Porous Rocks," *AIChE Journal*, vol. 71 (1960).

12. Ergun, S., "Fluid flow through packed columns," *Chem. Eng. Prog.*, Vol. 48 (1952), pp. 89-94.

13. Rohsenow, W.M., Hartnett, J. P. and Cho, Y.I., *Handbook of Heat Transfer*, McGraw-Hill, New York (1998).

14. Jeffreson, C.P., "Prediction of Breakthrough Curves in Packed Beds," *AIChE Journal*, vol. 18, vo.2 (1972), pp. 409.

15. Ackermann, R. A, *Cryogenic Regenerative Heat Exchangers*, Plenum Press, New York (1997).

16. Dragutinovic, G. D., and Baclic, B. S., *Operation of Counterflow Regenerators*, Computational Mechanics Inc., Billerica, MA (1998).

17. Incropera, F. P., and DeWitt, D. P., *Fundamentals of Heat and Mass Transfer*, John Wiley & Sons, New York (1996).

18. Keith Rice, DOE/ORNL Heat Pump Design Model, Mark V Version, http://www.ornl.gov/~wlj/hpdm/

Comparative Performance of Throttle Cycle Cryotiger Coolers Operating with Different Mixed Refrigerants

Mikhail Boiarski, Oleg Podtcherniaev, Kevin Flynn

IGC Polycold Systems, Inc.
Petaluma, CA 94954 USA

ABSTRACT

Small-scale Cryotiger coolers are based on commercially available hermetic oil-lubricated compressors and operate in a range of 70 to 200 K with different mixed refrigerants. Modern coolers efficiently operate with both flammable HC-based and nonflammable HFC-based refrigerants. This allows compliance with the requirements of many customers involved in the design of integrated systems.

New HFC mixed refrigerants are compatible with the selected oils, and a family of refrigerant candidates allows retrofitting of the coolers with an optimal composition for a given temperature range. However, the configuration of the counter flow heat exchanger significantly influences refrigeration performance. Test data obtained for tube-in-tube heat exchangers are in a good agreement with computer modeling. This allows optimization of the performance and dimensions of the heat exchanger for a particular cooler. This paper compares the performance of the new nonflammable refrigerant mixtures with prior flammable refrigerant mixtures. Test data on the performance and operating parameters are presented for both steady state and cool down regimes.

INTRODUCTION

Small-scale Cryotiger coolers have been developing since the mid 1990s.[1,2] They are based on commercially available hermetic oil-lubricated compressors and operate in a range of 70 to 200 K with different mixed refrigerants (MR). A schematic of the simplest single-stage throttle cycle cooler is presented in Fig. 1. It consists of a single flowloop comprising of a compressor unit (CM), recuperative heat exchanger (HE), throttle capillary (TH), and evaporator (EV) connected to an interface plate that removes heat from the object to be cooled. The compressor unit includes an oil separator and an air cooled after-cooler that removes heat (Q_A) to the environment. The cryostat of the cooler consists of the HE, TH, and EV. It is connected to the CM with flexible lines that can be configured in various lengths, typically ranging from 3 to 20 m and longer.

In general, the schematic of a closed cycle MR cooler operating with a single compressor varies depending on the application and objective functions in design. The Klimenko auto-cascade cycle can be efficiently used for larger scale coolers designed for industrial applications.[3] As distinct from the Cryotiger coolers, they operate with the multistage refrigeration process providing

Cryocoolers 13, edited by R. G. Ross, Jr.
Springer Science+Business Media, Inc., New York, 2004

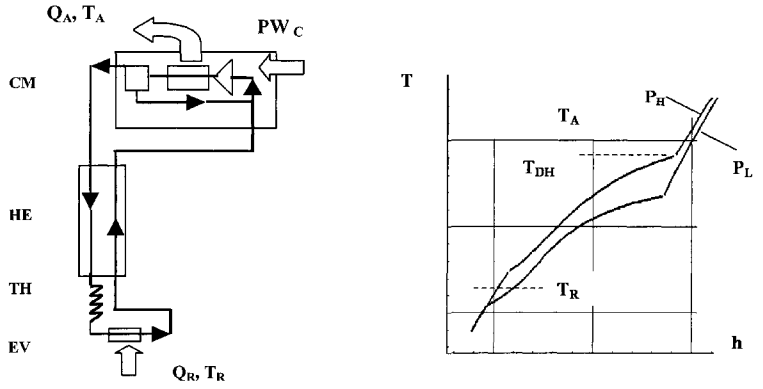

Figure 1. Cryotiger schematic and temperature- enthalpy diagram.

different operational modes: cool, rapid defrost, and standby. The standby mode allows the cryostat to be prepared for rapid cool down.

A single-stage MR cooler can operate with the MR supplied to the cryostat either partially liquefied (LRS technology) or gas mixed refrigerant (GRS technology). Although the LRS provides the higher refrigeration capacity (Q_R) and power efficiency[2], the GRS was selected for designing the Cryotiger coolers. Initially, they were designed to be integrated with various electronic devices that need a relatively low Q_R. The GRS technology also avoids two-phase flow transportation through the long, flexible lines. In addition, it makes possible a compact cryostat and oil separation system.

First-generation coolers perform efficiently with different flammable hydrocarbon (HC-based) MR in the range of 80 to 130 K.[4] New applications, like Charged-Coupled Device (CCD) cameras, need refrigeration at elevated temperature ranges up to 200 K. Both traditional and new applications need coolers operating with nonflammable MR. This would satisfy the requirements of many customers involved in the design of systems integrated with coolers.

This paper compares the new HFC-based nonflammable mixed refrigerants (NF MR) with traditional HC-based flammable mixed refrigerants (FL MR) operating in the range of 120 K to 200 K. Performance of standard-design coolers and possibilities for customizing them have also been analyzed with computer models developed in our previous research.

DESIGNING NONFLAMMABLE MIXED REFRIGERANTS

The modern MR design must consider the thermo-physical properties of the ingredients and the environmental characteristics, as well.[5,6] In cryogenic applications, HC components are widely used due to their good thermodynamic properties, good solubility with compressor oils, and zero ozone depletion potential. However, these components are flammable and are not suitable for all customer applications. In systems, such as the traditional Cryotiger with a standard design, application of HC-based MR is possible because the system volume is rather small. Typically, less than 150 g of MR is required. In developing nonflammable mixed refrigerants, either FC (fluorocarbons) or HFC (hydroflurocarbons) components have been considered. They have zero ODP and are commercially available. The freezing temperature (T_{FRZ}) is one of the essential issues in designing a NF MR. It must be lower than the lowest operating temperature of the cooler without heat load. Table 1 shows comparative data for potential MR ingredients.[6]

We can see that T_{FRZ} for high-boiling nonflammable (NF) candidates is essentially higher compared to the previously used flammable (FL) HC components of MR. Based on preliminary modeling and testing, nonflammable MR have been developed for the selected T_R in the range of 120 to 200 K. These are presented and covered by US Patent 6502410.[7] Test data on freezing temperatures of the selected MR are presented in Table 2.

Table 1. Thermodynamic properties [6] of the potential candidates for MR design.

No.	Formula	(Prefix) & ASHRAE No.	Boiling T, K	Freezing T_{FRZ}, K	Molecular Mass
1-FL	CH4	(HC) R50	111.6	90.9	16.04
1-NF	CF4	(FC) R14	145.2	89.3	88.01
2- FL	C2H6	(HC) R170	184.3	90.4	30.07
2- NF	CHF3	(HFC) R23	191.0	118.1	70.02
3- FL	C3H8	(HC) R290	231.0	85.5	44.10
3- NF	C2HF5	(HFC) R125	224.6	170.0	120.03
4- FL	i-C4H10	(HC) R600a	261.5	113.0	58.13
5- NF	CF3CH2CF3	(HFC) R236fa	271.8	180.0 *	152.04

*) Polycold test data.

Table 2. Test data on freezing temperatures: MR composition in %, mole.

No	T_{FRZ}, K	NE	AR	R-14	R-23	R-125	R-134a	R-236fa
1	< 113	-	24.2	46.8	12.5	14.5	-	-
2	< 116	-	41.0	32.0	18.0	9.0	-	-
3	115...116	8.5	14.0	29.0	48.5	-	-	-
4	116	5.0	33.0	23.0	39.0	-	-	-
5	120	-	17.3	20.0	33.0	21.5	3.7	5.3
6	130	-	19.0	22.0	27.5	19.5	3.0	9.0

Another aspect is compatibility of nonflammable MR with compressor oil. A compressor designed to operate with HFC refrigerants typically uses either polyolesters (POE) or polyalkylene glycols (PAG) type of oil to ensure long-term operation. POE oil Solest LT-32 has a pour point temperature of 223 K. Test data shows that blended with R23 (95% by weight) the pour point temperature reduces to 167 K; the same proportion with R125 gives T_{FRZ} = 170 K. Three component MR consisting of R14, R23 and R125 provides T_{FRZ} = 167 K if the oil content equals 3.5 %. Also, reduction of oil content to 1% decreases T_{FRZ} to 150 K. Thus, to provide long-term operation with the nonflammable MR, the cooler should be equipped with an appropriate oil separator providing oil content below these levels. The combinations of these oils with nonflammable mixed refrigerants are also presented and covered by US Patent 6502410.[7]

Table 1 also shows that the molecular mass of the HFC components is essentially higher compared to their HC equivalents. This affects the MR flow rate and performance of the cooler basic components: CM, HE, TH and EV, especially for replacing the flammable MR in the existing coolers.

Thus, modeling combined with test data is needed to identify minor hardware modifications required to achieve the needed refrigeration capacity Q_R and other objective functions.

PERFORMANCE OF THE COOLER COMPONENTS

Adiabatic Compressor

Cryotiger coolers operate with single-stage adiabatic compressors designed for a traditional vapor-compression refrigeration cycle. For GRS technology, it would be more efficient to use an isothermal compressor for reduced power consumption (PW_C). Using an adiabatic compressor would reduce the Carnot efficiency (CEF) by about 20%.[2] However, due to practical reasons, we are limited to commercially available components to provide a cooler at reasonable cost.

A simple equation shows the compressor influence on the cooler efficiency:

$$CEF = CEF_{SI} \times \eta_{CA} \quad (1)$$

where CEF_{SI} is for a system operating with an ideal adiabatic compressor.

Power efficiency of an adiabatic compressor $\eta_{CA} = \Delta H_S / PW_{CR}$ could be calculated if PW_{CR} is known either from testing or from catalog data. Volumetric efficiency (λ) is another important

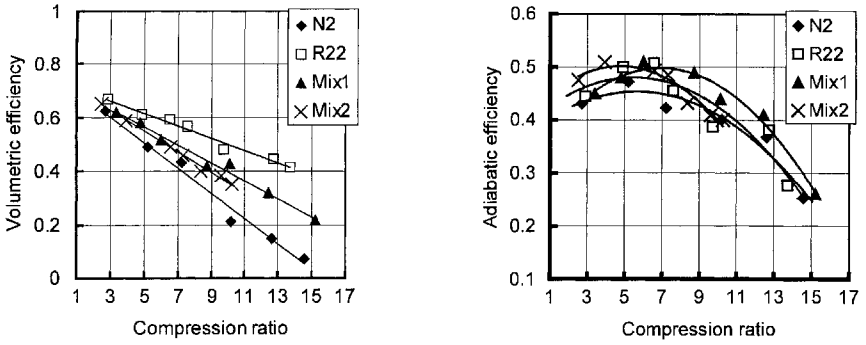

Figure 2. Test data on adiabatic compressor efficiency.

parameter as it influences the MR flow rate. It affects the ratio of the actual volumetric flow entering the compressor suction port to the compressor displacement V_H. Figure 2 shows test data obtained by A. Lunin for a rotary piston compressor of $V_H = 28$ L /min (1 cfm). The efficiency data are shown as a function of compression ratio ($\varepsilon = P_H / P_L$). In modeling the cooler performance, it is necessary to correlate compressor efficiency with the properties of pure and mixed refrigerants. The volumetric efficiency data can be correlated with the equation:

$$\lambda = A + B\,(\varepsilon^{1/k} - 1) \qquad (2)$$

where k is the ideal-gas adiabatic constant. For blends, k was calculated as $k = \sum z_i k_i$, where z_i and k_i are the mole fraction and individual coefficient of the blend component, respectively. For Mix (1): $k = 1.13$; for Mix (2): $k = 1.28$. For the presented data, the calculated values of λ are accurate within 5% when the following coefficients are used: $A = 0.71$ and $B = 0.35 - 0.34 \times k$.

It is more difficult to find a correlation for adiabatic efficiency η_{CA} due to significant deviations in the test data. However, we can see that, in the practical range of $\varepsilon = P_H / P_L = 3 \ldots 9$, all the tested refrigerants are quite identical, providing $\eta_{CA} = 0.46$ on average. A little increase in performance can be noticed for those having lower adiabatic constants.

Throttle Device

A throttle capillary is used for pressure reduction from the high discharge pressure (P_H) to the low pressure at the evaporator (P_{EV}). This component of the hardware, which is the simplest in design, essentially influences the cooler performance when combined with a given compressor and heat exchanger. Both the inner diameter (ID) and length of the capillary (L_{CAP}) determine the value of P_{EV} and the MR flow rate (G). Modeling data may be obtained with a simple assumption about the homogeneous structure of the two-phase MR flow.

Figure 3 shows the capillary characteristics of different four-component MRs: flammable (FL) consisting of AR and HC components and nonflammable (NF) in which HCs are substituted with HFCs. These modeling data were obtained for the case of T= 130 K and P=2.0 MPa at the capillary

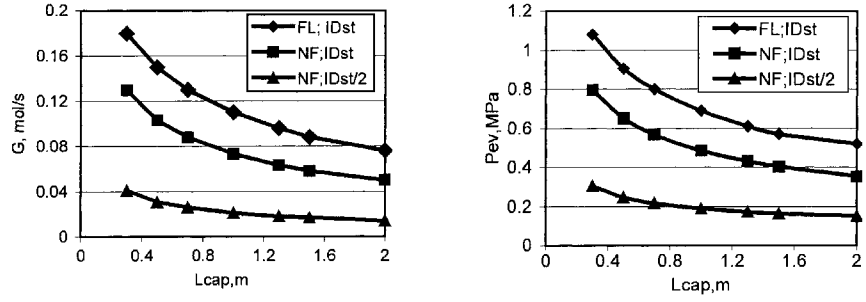

Figure 3. Calculated characteristics of the throttle capillary tube.

inlet. It can be noted that the same standard-size capillary would provide about 50 % lower flow rate for a NF MR as compared to a flammable one. As a result, direct retrofitting with a NF MR will reduce the refrigeration capacity Q_R.

Computer modeling shows that the effective capillary length is shortened when the inner diameter is reduced. For example, for a standard size capillary ID_{ST}, increasing L_{CAP} above 2 m does not cause a significant flow change. At the same time, this length is in the range of 0.5 to 0.7 m if the capillary size is reduced to $ID = ID_{ST} / 2$.

Thus, to provide identical refrigeration capacity Q_R at the MR replacement, adjusting the capillary size is required. Accuracy of modeling can be improved with adjustable coefficients obtained with limited experimental data.

Recuperative Heat Exchanger

A simple criterion has been proposed [9] to identify the effectiveness (HEE) of a heat exchanger operating within a cryocooler. This is a ratio of the design objective function in the real cycle to that in a highly idealized cycle. In the last case the cycle includes intrinsic losses only, which could not be eliminated for the selected refrigerant. These losses inherently belong to the analyzed process and are associated only with the thermodynamic properties of the refrigerant.

For Cryotiger coolers, the refrigeration capacity Q_R was selected as the design objective function; thus: $HEE_Q = Q_R^{RL} / Q_R^{ID}$. For a different case designed to minimize PW_C, the HEE should be modified to: $HEE_{PW} = PW^{ID} / PW^{RL}$.

In this analysis we consider maximizing Q_R as the design objective function and use HEE_Q as the heat exchanger efficiency. Values for HEE_Q can be in the range of 0 to 1. This function helps in finding the conditions for the most effective application of a heat exchanger. Both the refrigeration capacity of the real cycle with a given heat exchanger $Q_R^{RL} = f(\Delta T_{MIN}, \Delta P_L, Z_{MR},)$, and the refrigeration capacity of the idealized cycle $Q_R^{ID} = f(\Delta T_{MIN} = 0, \Delta P_L = 0, Z_{MR})$ have been calculated with computer software described elsewhere.[2,4]

Computer models and test setups developed allow evaluating and comparing tube-in-tube coil type HE performance of different patterns. Table 3a presents the geometry characteristics of the tested HE. Modeling and test data for HE_B operating at elevated T_R = 120–140 K is presented in Table 3b. Good agreement is seen among the calculated and experimental data that were obtained by adjusting the overall heat transfer coefficients and the measured pressure drop in the discharge ΔP_D and suction ΔP_S lines of the cooler. These coefficients have been also used in obtaining the modeling data presented in Fig. 4.

Modeling and test data for $T_R < 100$ K is presented elsewhere.[2,4] The best results were obtained for the HE_B with enlarged tubes that were matched to the standard cryostat dimensions. Meanwhile, investigating the standard-size HE_S is of practical interest as well, as this HE is more compact and could be used with a direct retrofit of the MR.

The data presented in Fig. 4 allow evaluation of the HE length influence on the cooler performance when operating with NF MR. We can see that at PR = 3 and T_R = 130 K, HE_B could provide a Q_R about 25 % higher compared to the standard HE_S. At a pressure ratio PR = 5, Q_R is essentially the same at $L = 0.75\ L_{ST}$. At the same time, at PR = 3, which can be achieved with elevated pressure in the suction line, Q_R increases with increasing L up to the cryostat-size limiting value of L< 4 m. In most of the analyzed cases, Q_R monotonically increases with increasing L. The result depends on both the ΔT and ΔP influence on Q_R. In some cases the length increase does not improve the performance at all: PR = 3 in a range of $L = 0.75\ L_{ST}$ to $0.9\ L_{ST}$.

Table 3a. Counter-flow Heat Exchangers (HE) tested in the Tiger Cooler.

HE Type	HE_S, 7 in 1	HE_B, 7 in 1	HE_B, 7 in 1	HE_B, 10 in 1
Length	L_{STD}	L_{STD}	$0.9*L_{STD}$	$0.75*L_{STD}$
ID_B	ID_{STD}	$1.2*ID_{STD}$	$1.2*ID_{STD}$	$1.8*ID_{STD}$
OD_S	OD_{STD}	$1.35*\ OD_{STD}$	$1.35*\ OD_{STD}$	$1.55*\ OD_{STD}$
Area-A_{HE}	A_{STD}	$1.4*\ A_{STD}$	$1.2*\ A_{STD}$	$1.7*\ A_{STD}$
Best HEE_Q	0.42	0.58	0.56	0.32

Table 3b. Comparing HE_B (7 in 1) performance data from testing and modeling.

Data from:	Q_R, W	PW_C, W	ΔP_S, MPa	ΔP_D, MPa	ΔT_{WE}, K	ΔT_{CE}, K
L_{STD}; FL MR: N_C=4, AR+HC, T_R = 123 K, P_D=2.24 MPa, P_E = 0.73 MPa						
Testing	40	460	1.5	1.7	6.7	2.2
Mod- real	38	556	1.6	1.0	5.6	4.2
Mod- ideal	72	640	0.02	0.02	1.9	2.7
L= 1.14 L_{STD}; FL MR: N_C=3, N2+HC, T_R = 140 K, P_D=2.02 MPa, P_E = 0.62 MPa						
Testing	20	482	0.9	-	2.0	8.1
Mod- real	23.7	625	1.5	2.4	2.9	12
Mod- ideal	44	650	0.02	0.02	0.1	10
L= 1.14 L_{STD}; FL MR: N_C=4, N2+HC, T_R = 142 K, P_D=1.64 MPa, P_E = 0.53 MPa						
Testing	20	465	0.9	-	4.2	0.6
Mod- real	18.1	451	1.0	1.6	4.1	0.6
Mod- ideal	25	480	0.02	0.02	3.6	0.1
L_{STD}; NF MR: Nc=4, AR+HFC, T_R = 138 K, P_D=2.12MPa, P_E = 0.62 MPa						
Testing	25.0	520	2.8	2.3	4.5	2.5
Mod- real	26.6	495	2.5	1.7	4.0	3.5
Mod- ideal	71.3	621	0.02	0.04	0.1	2.7

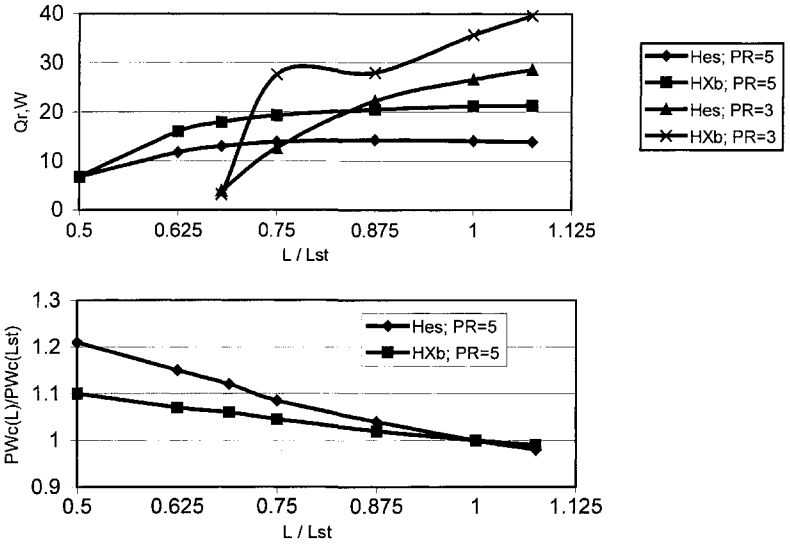

Figure 4. Heat exchanger performance operating with NF MR at T_R = 130 K.

Reduction of the HE length is beneficial in developing compact coolers. This may be attractive for coolers integrated with electronic devices. However, at a certain HE length the power consumption could exceed the nominal power of the given compressor motor. The potential PW_C increase relative to the standard cooler PW_C (L) / PW_C (L_{ST}) is shown at Fig. 4b as a function of the HE length.

Based on preliminary testing and modeling the refrigeration performance, the standard size heat exchanger was selected for the NF MR development at T_R = 130 K. However, both refrigeration capacity and dimensions of the cryostat can be customized, if necessary.

STANDARD COOLER OPERATING WITH NF MR

Preliminary test data and modeling show that a standard design cooler provides as much refrigeration capacity as is required for a number of electronic-instrumentation applications. Only a minor hardware modification is needed to adjust the throttle capillary size to operate with the NF MR in the range of T_R = 130 to 200 K.

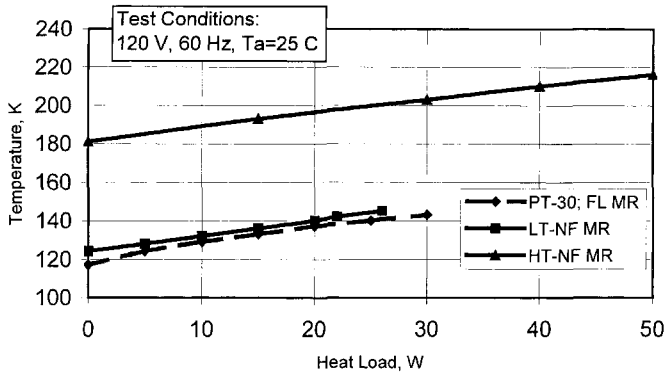

Figure 5. Refrigeration map of the standard Cryotiger operating with NF MR.

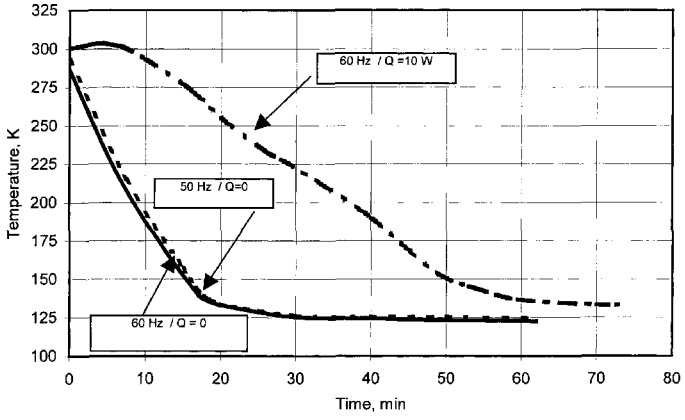

Figure 6. Cool down regimes of the LT cooler operating with NF MR.

Two cases have been considered for development: 1) a relatively low temperature cooler (LT) designed for T_R = 130...150 K, and 2) a higher temperature cooler (HT) designed for the higher temperature range of T_R = 180...220 K. An experimental refrigeration capacity map that plots $T_R = f(Q_R)$ is presented in Fig. 5 for both coolers.

Although the coolers are designed to operate with both electrical-voltage standards: 120 V 60 Hz and 230 V 50 Hz, for a frequency of 50 Hz, refrigeration capacity is about 15% lower as compared to at 60 Hz. The LT cooler provides a Q_R that is 3~5 W lower than for the flammable PT-30 MR, which consists of AR and HC components. Cooldown time of the LT cooler was less than 25 min without a heat load, as is shown in Fig. 6. With a heat load of 10 W applied at the start, cooldown time was less than 60 minutes.

CONCLUSIONS

The proposed nonflammable mixed refrigerants provide a refrigeration capacity with the standard-design Cryotiger coolers of 25 to 50 W in the temperature range of 120 to 210 K; this is consistent with the cooling required for many applications. Throttle capillary size must be adjusted to the selected mixed refrigerant to operate efficiently in a specified temperature range.

A counter flow heat exchanger with enlarged tubes that matches the standard cryostat size would allow a 30 % increase in refrigeration capacity.

The Cryotiger cooler could be customized to provide either more refrigeration capacity or a smaller size cryostat with a minor modification in design.

ACKNOWLEDGMENT

We are grateful to A. Lunin, B. Qiu, M. Losada and C. Rebecchi for supporting of this research with the obtained test data.

REFERENCES

1. Boiarski, M., et al., "Retrospective of mixed refrigerant technology and modern status of cryocoolers based on one-stage, oil-lubricated compressors," *Advances in Cryogenic Engineering*, Plenum Press, NY, 1997, vol.43, p. 1701-1708.
2. Boiarski, M., et al., "Modern trends in designing small-scale coolers operating with mixed Refrigerants," *Cryocoolers 11*, Kluwer Academic/Plenum Publishers, 2001, pp. 513-521.
3. Podtcherniaev, O., et al., "Performance of throttle-cycle coolers operating with mixed refrigerants designed for industrial applications in a temperature range 110 to 190 K," *Advance in Cryogenic Engineering*, Melville, NY, 2002, vol. 47A, p. 863-872.
4. Boiarski, M., et al., "Enhanced refrigeration performance of the throttle-cycle coolers operating with mixed refrigerants", *Advances in Cryogenic Engineering*, Kluwer Academic/Plenum Publishers, NY, 2000, vol.45, pp. 291-297.
5. Calm, J. "Property, safety and environmental data for alternative refrigerants," Proc. The Earth Technology forum, 1998, Washington DC, pp. 192-205.
6. *ASHRAE Handbook—Fundamentals,* 1997.
7. Podtcherniaev, O. et al. "Nonflammable mixed refrigerants", US Patent 06502410 B1, Jan.7, 2003.
8. Podtcherniaev, O., et al., "Comparative performance of two-stage cascade and mixed refrigerant systems in a temperature range from –100 C to –70 C°," *9th Int. Refrigeration and Air Conditioning Conference at Purdue*, 2002. Paper R18-3 on CD.
9. Boiarski, M., et al., "Design optimization of throttle–cycle cooler with mixed refrigerant," *10th Int. Cryocooler Conference*, Plenum Press, New York, 1999, pp. 457-465.

Progress in Micro Joule-Thomson Cooling at Twente University

P.P.P.M. Lerou, H. Jansen*, G.C.F. Venhorst, J.F. Burger, T.T. Veenstra, H.J. Holland, H.J.M. ter Brake, M. Elwenspoek* and H. Rogalla

University of Twente, Faculty of Science and Technology, *Faculty of Electrical Engineering, Mathematics and Computer Science
7500 AE Enschede, The Netherlands

ABSTRACT

At the University of Twente, research on the development of a sorption-based micro cooler is in progress. Because of the absence of moving parts, such a cooler is virtually vibration free and highly durable, which potentially results in a long lifetime. A miniature cryogenic cooler with these properties would be appealing in a wide variety of applications including the cooling of vibration-sensitive detectors in space missions, low-noise amplifiers and semi- and superconducting circuitry.

The objective of the present project is to scale down a Joule-Thomson (JT) cold stage to a total volume of a few hundredths of a cm^3. This size reduction introduces many problems. The proposed cold stage volume results in a restriction cross-sectional area of about a thousandth of a mm^2 which may cause clogging problems. Flow channels with a cross-sectional area of a few hundredths of a mm^2 will produce high pressure drops influencing the JT cycle. Furthermore, the micro channels must be capable of withstanding high pressures and maintaining a large temperature gradient over a relatively short length.

The project aim is to develop a reliable micro JT cold stage that is fabricated out of one material with a relatively simple and reproducible fabrication method. The length of the cold stage is calculated at about 20 mm with a width of 1.7 mm and height of about 0.3 mm. The mass flow is in the order of one mg per second to create a net cooling power of 10 mW at 96 K. The final objective of the project is to integrate the cold stage, vacuum chamber and device into one compact design. This paper discusses possible solutions to the problems mentioned and presents a concept design of such a miniature JT cold stage.

INTRODUCTION

Cooling of low-noise amplifiers, infrared detectors, and other electronic circuitry to cryogenic temperatures can be advantageous. It improves the signal-to-noise ratio and bandwidth of the system. For superconducting devices it is crucial that they are cooled below their critical temperature in order to operate properly. In many cases the system, which is to be cooled, is very small so an accompanying small cryocooler would be obvious. Several attempts have been made to construct such a miniature refrigerator.[1]

Cryocoolers 13, edited by R. G. Ross, Jr.
Springer Science+Business Media, Inc., New York, 2004

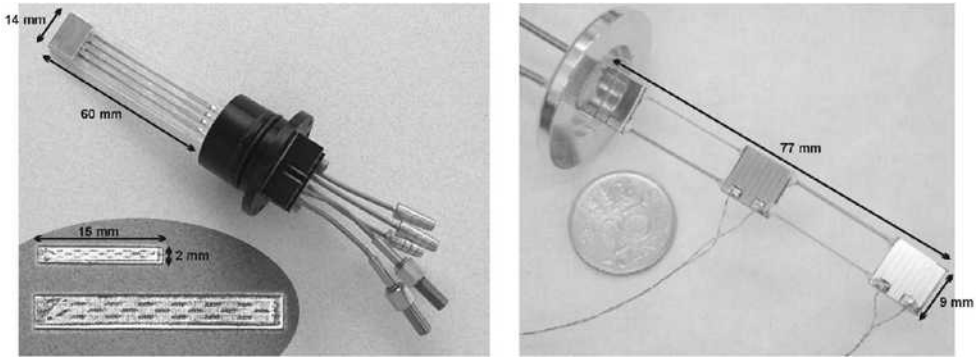

Figure 1. On the left: a two stage nitrogen/neon refrigerator made by MMR technologies, Inc.[4] and a prototype of a micro miniature N_2 refrigerator made by Little et al.[2] On the right: a micro machined ethylene cold stage fabricated by Burger et al.[5]

Much pioneering work on micro coolers was done by Little et al, who made different miniature cold stages [2,3]. The smallest had a size of 15x2x0.5 mm (0.015 cm^3). This cooler was used in an open-loop cycle with N_2 gas at a high pressure gas of 165 bar and a flow rate of 3 mg/s. It had a cooling power of 25 mW at a temperature of 101 K and with no heat load the cold stage temperature reached 95 K. It was constructed through an abrasive etching process. Unfortunately, this achievement was not reproduced or turned into an industrial product. However, larger coolers of this design are nowadays commercially available from MMR Technologies, Inc. [4]. The smallest has a size of about 60 x 14 x 2 mm (1.68 cm^3) (Fig. 1). It can cool down to 35 K with a cooling power of 50 mW using a two-stage nitrogen/neon Linde-Hampson configuration.

Burger et al. developed a Joule-Thomson (JT) cold stage with a total volume of 0.76 cm^3 (77 x 9 x 1.1 mm) combined with a sorption compressor, thus realizing a closed-cycle micro cooler.[5] This miniature cooler had a cooling power of 200 mW at 170 K (Fig. 1). Burger used Micro Electro Mechanical System (MEMS) technology to construct different components of the cold stage. Wet KOH etching and wafer bonding techniques were used for the fabrication of a condenser, restriction and evaporator in silicon. Counter flow heat exchangers were made out of tiny glass capillaries. After fabrication the different cold stage parts were glued together.

As a continuation of this previous research we present an approach for the development of a miniature cold stage with a total volume of about 0.010 cm^3. Compared to the previous work, the present project will only use MEMS technology to fabricate the cold stage. By using a sorption compressor the gas cycle will be closed in combination with a total exclusion of any mechanical moving parts. The cold stage temperature will be about 96 K with a net cooling power of about 10 mW. In addition, the cold stage will be highly reproducible by applying a relatively simple production process. As a final goal we are aiming at the integration of cold stage, vacuum chamber and device into one compact easy-to-use device.

CHOOSING WORKING GAS AND PRESSURES

In a Linde-Hampson cycle, gas is pressurized using a compressor (Fig. 2, 1→2). After compression the gas flows from the compressor through a counter flow heat exchanger (CFHX) to a flow restriction (2→3). Through this restriction, the gas undergoes isenthalpic expansion to the low-pressure side and usually changes its phase to a liquid (3→4). By absorbing heat from its surroundings the liquid evaporates (4→5) and the produced vapor flows back through the CFHX absorbing heat from the warm high-pressure side (5→1). Once the gas has reached the compressor it can be compressed again, closing the cycle.

In certain applications the device to be cooled has a very low dissipation or no dissipation at all. In these cases the required cooling power is determined by the total parasitic heat load from the

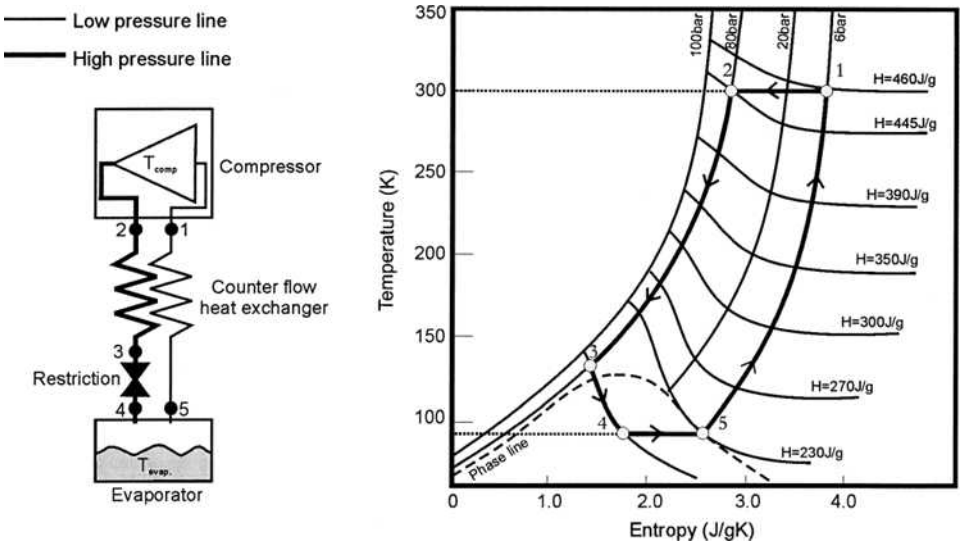

Figure 2. On the left side, a schematic scheme of the Linde-Hampson cycle. On the right side, the T-S diagram of nitrogen with isobars and isenthalps. The bold line with numbers represents the cycle.

environment. By a clever design of the cryogenic enclosure of such a small device, the required cooling power can be limited to a few mW only.

The gas used in a Linde-Hampson cycle in combination with the chosen low pressure will determine the temperature of the cold stage. In the search for a cheap, non toxic and nonflammable gas which can create a cryogenic temperature (roughly T<120 K), nitrogen is an obvious choice. The boiling temperature of nitrogen at 1 bar is about 77 K.

With the change in pressure during compression, the gas undergoes a change in enthalpy. Theoretically this change in enthalpy will determine the available gross cooling power of the cold stage. To create sufficient cooling power with nitrogen, a relatively high pressure (80 bar) is chosen at the high-pressure side of the cycle (Fig. 2). It is our intention in the future to combine the cold stage with a sorption compressor.[6] Based on first calculations of a two-stage nitrogen sorption compressor the low-pressure side is chosen at 6 bar. At this pressure the sorption material of the compressor has considerably more sorption capacity than at lower pressures. This way a cooler with acceptable efficiency can be designed.

A pressure change from 80 to 6 bar results for nitrogen in a cooling enthalpy of about 15 J/g. The cold stage temperature at 6 bar is about 96 K. Since the gross cooling power is given by $\dot{m}dh_{45}$, where $\dot{m}$ is the mass flow and dh_{45} the cooling enthalpy, the mass flow will have to be in the order of 1 mg/s to create a net cooling power of 10 mW.

FABRICATION OF MICROSTRUCTURES

The abrasive etching technique used by Little et al. is based on powder blasting.[2] This is a micromachining technique where a high pressure mixture of air and powder particles is accelerated towards a substrate[7]. The powder consists of Al_2O_3 particles and is accelerated through a nozzle (Fig. 3). Once the particles hit the target they erode surface particles. A mask protects parts of the target to create different structures. Wensink et al. found a removal rate for glass and silicon of approximately 25 μm/min.[7] The smallest feature size attainable is about 30 μm with an aspect ratio of 2.5.

The main disadvantage of powder blasting is the relatively high roughness of the blasted surface which goes hand in hand with the process. Small imperfections at the sides of the channels are likely to be the starting point of a rupture when a micro channel is pressurized to a high pressure.

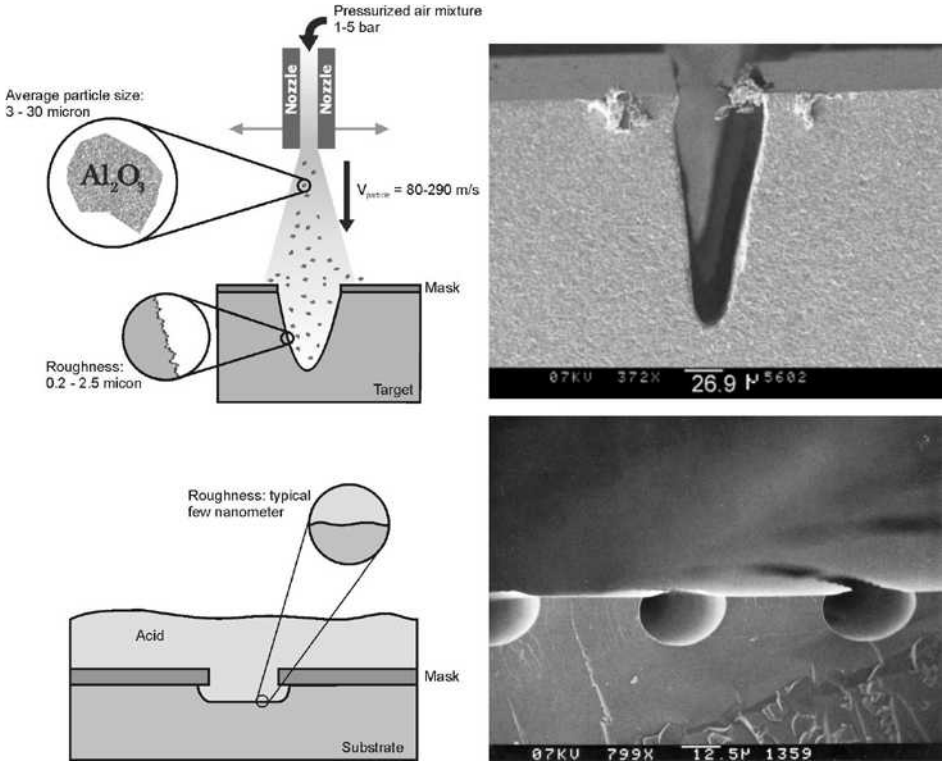

Figure 3. The top two figures show a schematic impression of the powder blast process and a 50 µm wide channel in Pyrex with an aspect ratio of 2.5 (blasted with 9 µm alumina particles at 290 m/s).[7] The lower two figures show a schematic impression of the isotropic wet etch process and three etched channels with a width of approximately 30 µm.[9]

Also the flow behaviour through the micro channels is influenced. Higher roughness results in a higher flow resistance and associated pressure drop. The rough surface can also be more sensitive to clogging. This is why we prefer to use a wet etching process for fabricating a miniature cold stage.

As an alternative, photolithography can be used, which is a widely used technique in MEMS technology.[5,8] A wafer is coated with a photo resist layer and exposed through a mask to ultraviolet light. Using positive resist the exposed areas are removed with a development solution. Now the wafer can be etched using an acid, usually hydrogen fluoride (HF) (Fig. 3). After etching the resist layers are stripped from the wafer and the wafer is cleaned. These processing steps can be repeated to create different structures and depths in the wafer. To create closed channels the processed wafer is closed with another wafer through an anodic or fusion bonding process. Miniaturizing cold stage parts using MEMS technology

One of the most crucial parts in a Linde-Hampson cycle is the counter flow heat exchanger (CFHX). The CFHX maintains the temperature gradient between the warm and cold ends of the cooler. The CFHX also improves the efficiency of the cooler by exchanging enthalpy between the high and low-pressure side. In an ideal cycle we presume that the counter flow heat exchanger works with an efficiency of 100%, theoretically corresponding to an infinite length. Inefficiency of a CFHX results in a loss of the cold stage's gross cooling power.

To maximize the efficiency of the CFHX we are looking for a geometry that results in an optimal enthalpy exchange between the high and low-pressure lines. In general, this means that the heat-exchange surface between these lines has to be maximized. Two rectangular channels on top of each other seem to be a convenient configuration. A very thin layer separates the channels (Figs. 4 and 5).

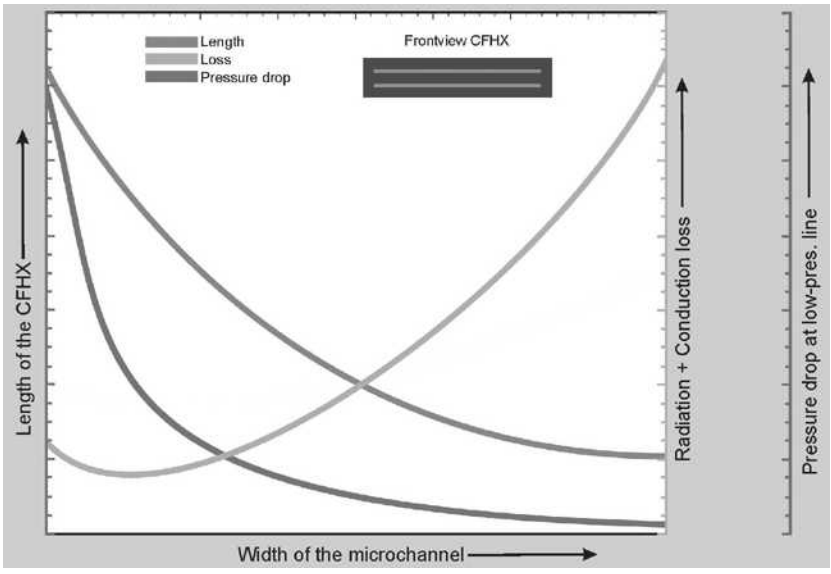

Figure 4. Width of a microchannel versus CFHX length, total loss and pressure drop at the low-pressure line. The graph is calculated for two symmetrical channels with constant high and low pressure, CFHX efficiency, wall thickness, channel height and mass flow.

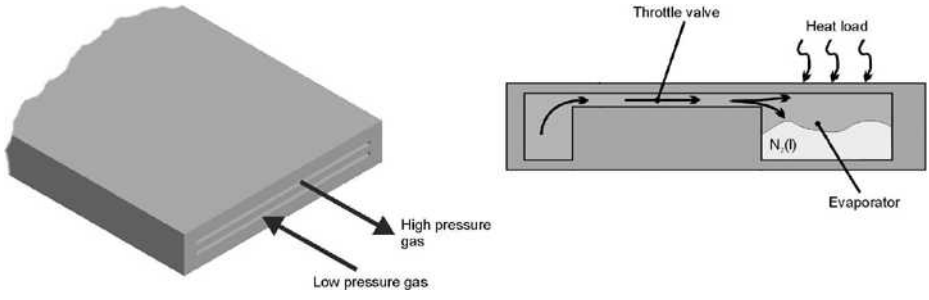

Figure 5. On the left: cross-section of a CFHX. On the right: crosscut of a restriction and evaporator. The throttle valve and evaporator will be etched into the glass.

To optimize the geometry we study the effect of different parameters on the operation of a CFHX. Next to a high efficiency in exchanging enthalpy per unit length of the CFHX, only a small pressure drop over the high and low-pressure lines can be accepted. A large pressure drop at the high-pressure side will increase power loss and a drop at the low-pressure side will result in an increase of the cold-stage temperature. For a constant shape of the channel, the cross-sectional area will mainly determine the pressure drop per unit length of the CFHX. The smaller the area the higher the pressure drop. However, a smaller cross-sectional area will improve heat-exchange properties. Another very important parameter influenced by the geometry of the CFHX is the loss in the gross cooling power due to conduction from the warm side of the CFHX to the cold side.

The objective is to make a very small, highly efficient heat exchanger. However small, or in other words short, goes hand in hand with a high conduction loss. The task is to optimize the heat exchanger's geometry for minimal pressure drop and heat losses (conduction and radiation) in combination with very small dimensions. Figure 4 shows the general behavior of all parameters for a constant height and changing width of the CFHX-channels.

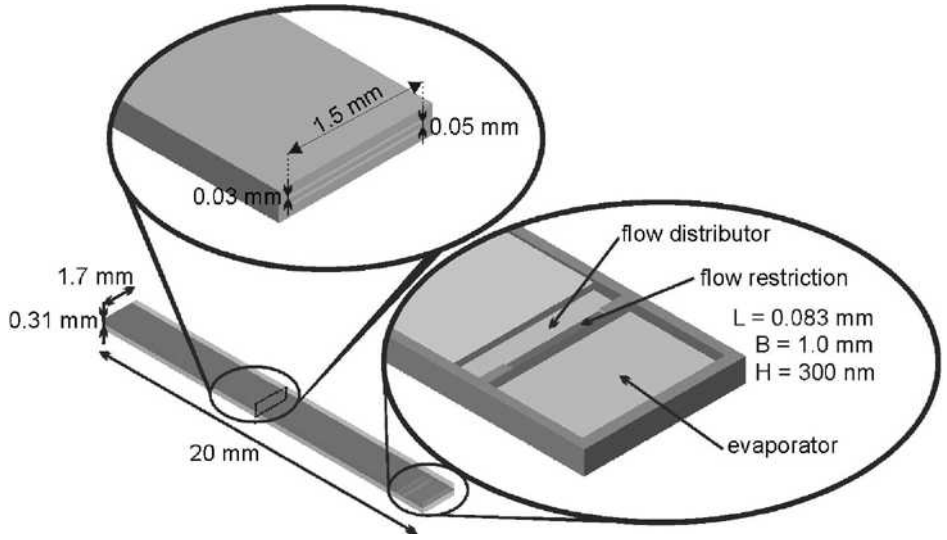

Figure 6. Concept design for a N_2 miniature cryocooler with a net cooling power of about 10 mW at 96 K.

Similar calculations can be made for different geometries. In this way an optimal configuration can be found. Aiming at a net cooling power of about 10 mW, an optimal channel geometry of (L x W x H) = (18.9 x 1.5 x 0.03) mm was found. The thickness of the wall between the two channels is calculated at 50 μm. The mass flow is 1 mg/s and the total parasitic heat loss is about 4.57 mW. The pressure drop over the low-pressure line is about 0.15 bar resulting in a cold-stage temperature of 97 K.

A wide and shallow channel will be etched in the glass wafer to serve as the restriction establishing a flow of 1 mg/s at a pressure drop of 80 to 6 bar. The dimensions of this channel are calculated at (L x W x H) = (0.083 x 1.0 x $0.3 \cdot 10^{-3}$) mm. An etched reservoir in the wafer will serve as the evaporator (figure 5). Combining all the different designed parts a concept design for a miniature N_2 cooler is made (Fig. 6).

Since the miniature coolers will be etched in glass wafers it is possible to fabricate a high number of coolers at the same time. Some test structures are etched in glass to test the technology and some properties of micro channels and restrictions (Fig. 7). Micro channels with varying widths and lengths and different flow restrictions are fabricated.

TOTAL INTEGRATED COMPACT DEVICE

One of the final objectives is to integrate the miniature cold stage with the device that is to be cooled and a vacuum chamber into one compact design. Since the construction material of the cold stage is glass (Pyrex) it is expected that it is possible to connect the cooler to devices made out of silicon (e.g. integrated circuits or MEMS devices).

It is our aim to combine the integrated cold stage package with a small sorption compressor. Optimization of sorption compressor configurations is ongoing at the University of Twente.[6]

CONCLUSIONS

An approach for the fabrication of a miniature N_2 cold stage using MEMS technology was presented. The total volume of the cold stage is about 0.010 cm^3. An optimal channel geometry for the counter flow heat exchanger was calculated at (L x W x H) = (18.9 x 1.5 x 0.03) mm with a wall thickness between the two channels of 50 μm. A wide and shallow channel with the dimensions (L x W x H) = (0.083 x 1.0 x $0.3 \cdot 10^{-3}$) mm will serve as flow restriction. A high pressure of 80 bar and a low pressure of 6 bar in combination with a mass flow of 1 mg/s results in a net cooling power

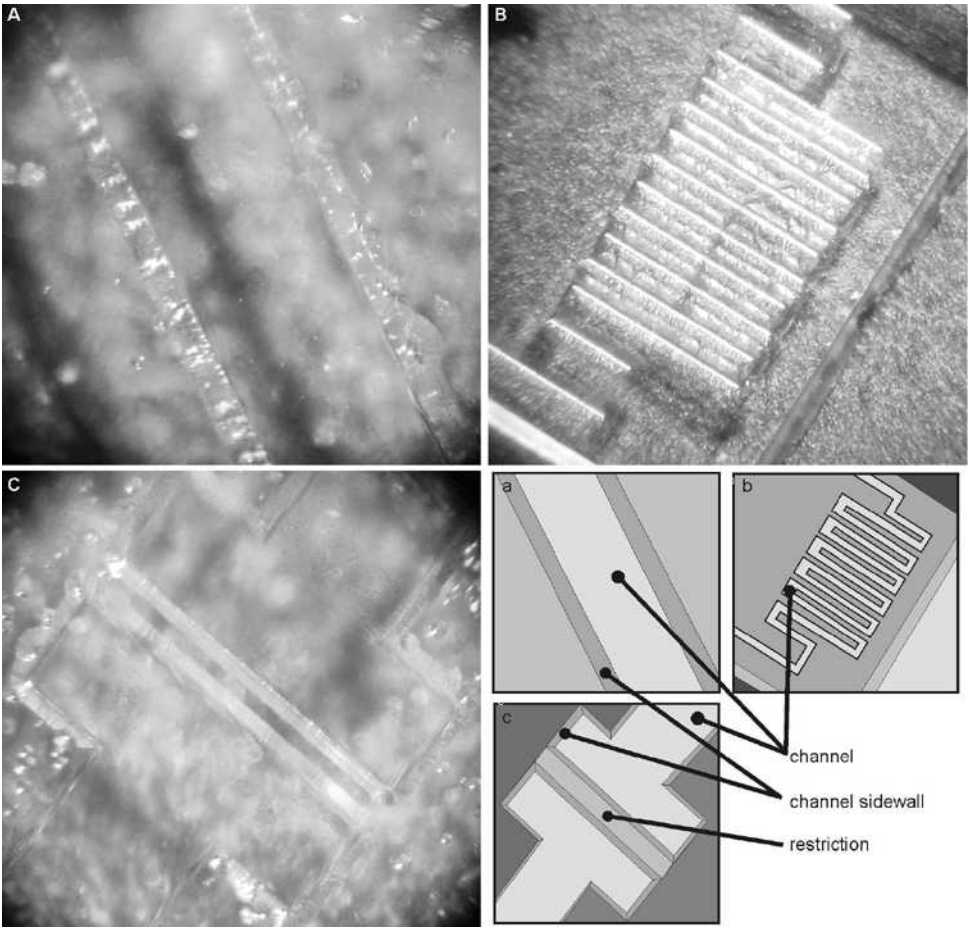

Figure 7. Micro test structures etched in glass with HF. A channel with a width of 110 μm (A), a meandering channel structure, channel width is 140 μm (B), a flow restriction with a width of 3 mm, a length of 0.253 mm and a height of 248 nm (C)

of 10 mW and a cold stage temperature of 97 K. The pressure drop over the low-pressure line is about 0.15 bar. Since a photolithography fabrication method is used it is possible to fabricate a high number of coolers at the same time. It is our aim to combine the cold stage with a small sorption compressor and to integrate the miniature cold stage and vacuum chamber with the device that is to be cooled into a totally integrated compact device.

ACKNOWLEDGMENT

This work is supported by the Dutch Technology Foundation (STW) and Thales Cryogenics.

REFERENCES

1. Sangkwon Jeong, "How difficult is it to make a micro refrigerator?" *Int Journal of Refrigeration*, vol. 27 (2004), pp. 309-313.

2. Garvey, S., Logan, S., Rowe, R., Little, W.A., "Performance characteristics of a low-flow rate 25 mW, LN_2 Joule-Thomson refrigerator fabricated by photolithographic means," *Appl. Phys. Lett*, vol. 42 (1983), p. 1048.

3. Little, W.A., "Microminiature refrigeration," *Rev Sci Instrum*, No. 55(5) (1984), pp. 661-680.

4. MMR Technologies, Inc., Internet URL: http://www.mmr.com

5. Burger, J.F., Holland, H.J., Seppenwoolde, J.H., Berenschot, E., ter Brake, H.J.M., Gardeniers, J.G.E., Elwenspoek, M., and Rogalla, H., "165 K microcooler operating with a sorption compressor and a micromachined cold stage," *Cryocoolers 11*, Kluwer Academic/Plenum Publishers, New York (2001), pp. 551-560.

6. Wiegerinck, G.F.M., Burger, J.F., Holland, H.J., Hondebrink, E., ter Brake, H.J.M. and Rogalla, H., "Improvements in sorption compressor design," *Cryocoolers 13*, Kluwer Academic/Plenum Publishers, New York (2005).

7. Wensink, H., Elwenspoek, M.C., "Reduction of sidewall inclination and blast lag of powder blasted channels," *Sensors and Actuators*, A 102 (2002), pp. 157-164.

8. Elwenspoek, M.C., Jansen, H., *Silicon Micromachining,* Cambridge University Press, Cambridge (1998).

9. Burger, J.F., "Cryogenic microcooling—a micromachined cold stage operating with a sorption compressor in a vapor compression cycle," *Ph.D. Thesis*, University of Twente, 2001.

The Performance of Joule Thomson Refrigerator

Yong-Ju Hong, Seong-Je Park and Hyo-Bong Kim

HVAC & Cryogenic Engineering Group
Korea Institute of Machinery & Materials
Taejeon, 305-600, Korea

Young-Don Choi

Department of Mechanical Engineering
Korea University
Seoul, 136-701, Korea

ABSTRACT

Miniature Joule Thomson refrigerators have been widely used for the cooling of infrared detectors, cryosurgery, thermal cameras, missile homing heads, and guidance systems because they have a simple, compact structure and rapid cooldown characteristics.

The purpose of the present study was to characterize the thermal performance of a commercial demand-flow miniature Joule Thomson refrigerator designed for cooling infrared detectors. It has an O.D. of 5 mm and has a bellows flow-control mechanism to provide temperature control. Experimental data have been gathered on cooldown characteristics, no-load temperature, and cooling capacity for different pressures of nitrogen (NBP 77.3 K) and argon (NBP 87.4 K) gas.

The test refrigerator was installed into a dewar that has a vacuum connection and radiation shields to diminish the heat load through conduction and radiation heat transfer. In the experiments, a pressure regulator was used to adjust the high-pressure supply gas to a constant pressure.

The presented results show that there exists a minimum supply pressure for getting the required coldend temperature, and higher supply pressure to the Joule Thomson refrigerator results in more rapid cooldown performance.

INTRODUCTION

Miniature Joule Thomson refrigerators have been widely used for the cooling of infrared detectors, cryosurgery, thermal cameras, missile homing heads, and guidance systems because they have a simple, compact structure and rapid cooldown characteristics. [1,2]

Different working fluids can be used to achieve a wide range of cooling temperatures. In the basic Joule Thomson cycle, the high pressure gas from a compressor or bottle passes through a counterflow heat exchanger and is precooled by the returning low pressure gas stream. The precooled gas is expanded isenthalpically through the Joule Thomson nozzle, which produces a two phase fluid. The liquid is used to adsorb the heat load at constant temperature. The low pressure gas is exhausted to the compressor or atmosphere to complete the cycle.

Cryocoolers 13, edited by R. G. Ross, Jr.
Springer Science+Business Media, Inc., New York, 2004

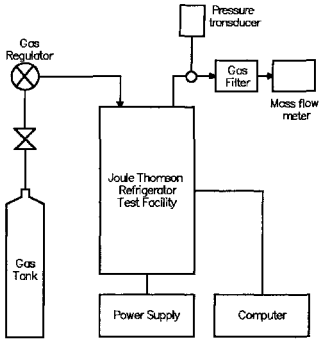

Figure 1. Configuration of experimental apparatus.

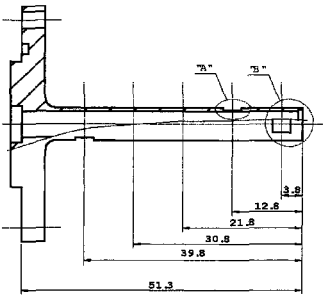

Figure 2. Dewar and installation position silicon-diode of thermometers.

Fixed orifice Joule Thomson refrigerators do not contain a control mechanism to vary the refrigerant flow during operation, so they produce refrigeration at a continuous high rate when the supply pressure is high. They are good for fast cooldown applications, but are not suitable for long-term steady-state operation.

Demand-flow Joule Thomson refrigerators contain a flow control mechanism to adjust the refrigerant flow rate according to the heat load in order to conserve refrigerant. Although a variety of configurations of flow control mechanisms have been proposed, the bellows control mechanism is the most widely adopted. [3,4]

The performance of the Joule Thomson refrigerator is strongly dependent on the effectiveness of the heat exchanger and the operating pressures. [5,6]

Nitrogen and argon are widely used as refrigerants for the Joule Thomson refrigerator. Compared with nitrogen, the performance of argon as a refrigerant appears to be very superior.[7]

The purpose of the present study has been to examine the thermal performance of a miniature Joule Thomson refrigerator. In particular, the cooldown characteristics, no load temperature and cooling capacity were investigated by experiment for different pressures of nitrogen (NBP 77.3 K) and argon (NBP 87.4 K) gas. In addition, the mass flow rate through the refrigerator and temperature profile on the surface of dewar were measured during the cooldown process.

EXPERIMENTAL SETUP

The Joule Thomson refrigerator test unit was a commercial demand-flow miniature refrigerator for cooling of infrared detectors. It has an O.D. of 5 mm and has a bellows flow control mechanism. The configuration of the experimental apparatus is shown schematically in Figs. 1 and 2.

Pure nitrogen or argon gas was supplied from a high pressure gas tank into the miniature Joule Thomson refrigerator. The supply pressure of the gas was adjusted by a pressure regulator. The Joule Thomson refrigerator with dewar was installed in a vacuum chamber where the pressure was maintained below 10^{-5} torr using a turbo molecular vacuum pump to reduce the thermal load during the measurements.

Two types of dewars were used for the measurements: a glass dewar and a stainless steel dewar:

Glass dewar. A glass dewar (thickness 1.2 mm) was used for the measurement of cooldown performance and cooling capacity. A manganin resistance wire was wound on the cold end to measure cooling capacity. The cooling load was introduced by an external DC power supply. A silicon-diode thermometer was attached to measure the temperature at the cold end.

Stainless steel dewar. This was used for measurement of the mass flow rate and the surface temperature profiles. A gas filter was installed between the Joule Thomson refrigerator and the mass flow meter. Pressure transducers were employed to record the supply and exhaust pressures.

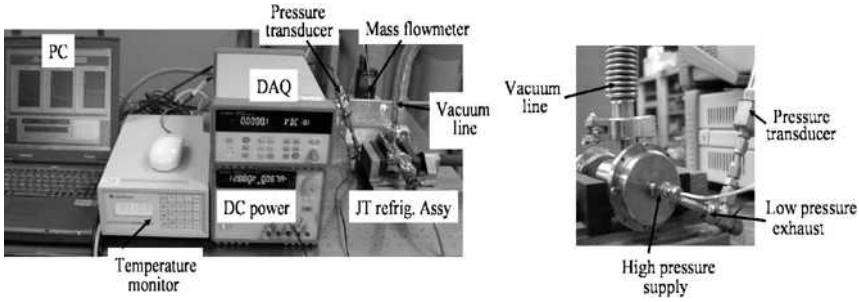

Figure 3. Photograph of experimental apparatus.

As shown in Fig. 2, the five silicon-diode thermometers were attached on the surface of the stainless steel dewar to measure the temperature distribution. Instantaneous mass flow rate through the refrigerator was measured by the mass flow meter.

All sensors were connected to an HP 34970A data logger. A photograph of the experimental system is shown in Fig. 3.

EXPERIMENTAL RESULTS

Cool down and cooling capacity

Figure 4 shows the cooldown performance of the Joule Thomson refrigerator with glass dewar for seven different supply pressures of nitrogen. The measurements were performed during 10 minutes. It is observed that the Joule Thomson refrigerator has a rapid cooldown rate at higher supply pressure, typically about 2 minutes, and there exists a minimum supply pressure for achieving the required cold-end temperature. The minimum temperature achieved at the cold end is around 84 K. Steady state conditions were achieved in less than 4 minutes when the supply pressure is above 8 MPa. The cooldown rate increases to around 110 K for all test cases.

Figure 5 shows the cooldown process with argon. The cooldown rate increases as the supply pressure increases. At a supply pressure of 10 MPa, the cool down time to reach 100 K at the cold end is around 1.4 minutes, which is about 1.43 times faster than with nitrogen. Steady state conditions were achieved in less than 4 minutes when the supply pressure was above 7 MPa. The minimum temperature achieved at the cold end was around 90 K. The temperature does not reach the NBP due to the pressure drop of the heat exchanger. At the end of cooldown process, temperature oscillation occurred.

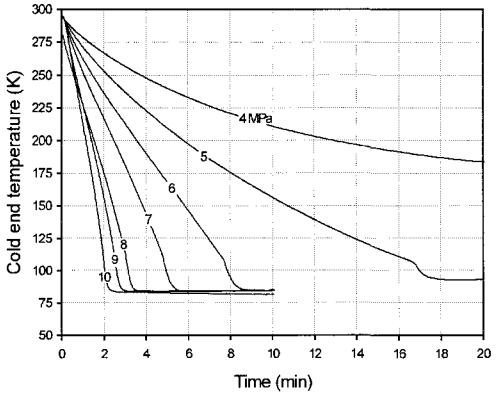

Figure 4. Cooldown process of the Joule Thomson refrigerator with nitrogen at various pressures.

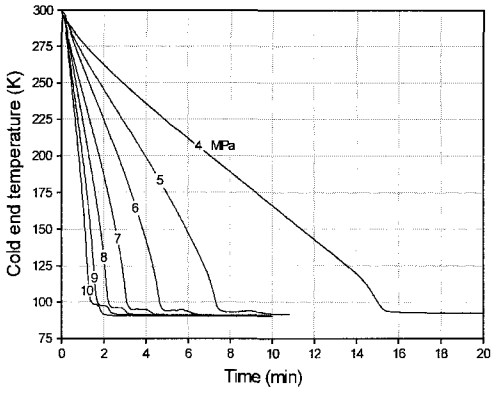

Figure 5. Cooldown process of the Joule Thomson refrigerator with argon at various pressures.

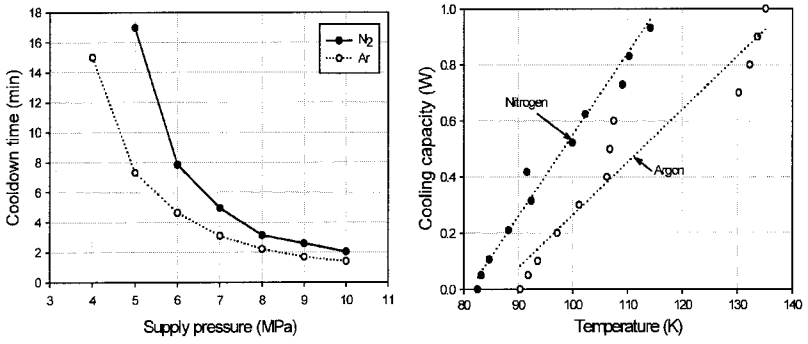

Figure 6. Cooldown time to reach 100 K at cold end and cooling capacity.

Figure 6 shows the cooldown time to reach 100 K at the cold end and the cooling capacity when the supply pressure is 10 MPa. The cooldown time decreases as the supply pressure increases. Argon has a faster cooldown performance than nitrogen for all test cases. When the supply pressure is low, the cooldown time of argon is about 2 times faster than that with nitrogen. As the supply pressure increases, the ratio of cooldown time with argon to that with nitrogen decreases.

The cooling capacity of the refrigerator increases as the temperature at the cold end increases. The refrigerator with nitrogen has 0.5 W cooling capacity at 100 K, but with argon it has about 0.3 W. For the same temperature at the cold end, the refrigerator with nitrogen has more cooling capacity than with argon.

Mass Flow Rate and Temperature Profiles

Figure 7 shows the transient temperature profiles and mass flow rates through the refrigerator with nitrogen at 10 MPa. The mass flow rate increases as the cold end temperature decreases.

After 1 minute, the cooldown rate increases due to the increased mass flow rate. The maximum mass flow rate is around 8 SLPM. The mass flow rate suddenly decreases when the temperature at cold end reaches steady state. These phenomena is the result of the operation of the flow control mechanism. It is observed that a small amount of nitrogen is supplied to keep the temperature at steady state. As time increases, the temperature near the cold end decreases. After 2.5 minutes, a large temperature gradient along the surface of the stainless steel dewar is established.

For comparison, Fig. 8 shows results with argon using a supply pressure of 10 MPa. In this case, large variations of the mass flow rate and oscillation of the temperature were observed. The maximum mass flow rate was around 9 SLPM.

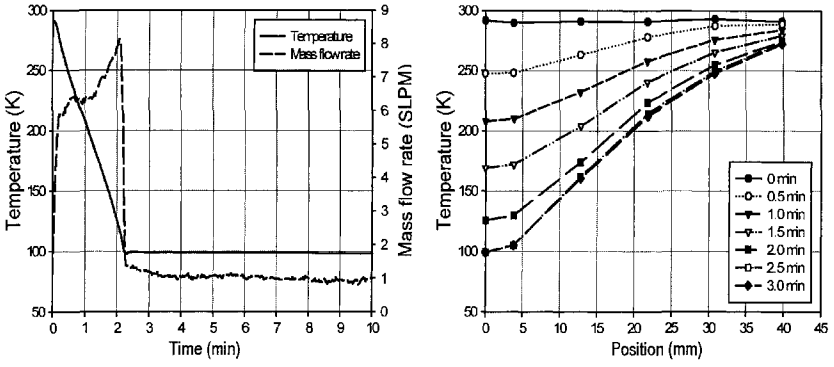

Figure 7. Mass flow rate and temperature profiles with nitrogen.

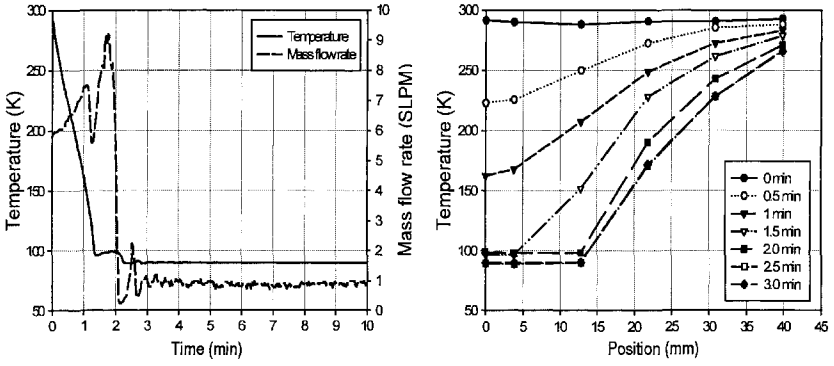

Figure 8. Mass flow rate and temperature profiles with argon.

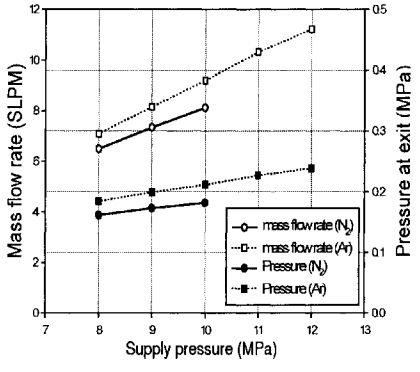

Figure 9. Mass flow rate and exhaust pressure

Early in the cooldown process, the temperature profile with argon in the stainless dewar is similar to that with nitrogen. After the temperature at the cold end reaches the minimum temperature, the cold region on the surface of the dewar spreads out. Therefore, the temperature profile has a steep slope at steady state.

Figure 9 shows the maximum mass flow rate through the refrigerator and the exhaust pressure. The maximum mass flow rate occurred at the end of cooldown process and increases as the supply pressure increases. At the same supply pressure, the mass flow rate of argon is larger than that of nitrogen.

The exhaust pressure of the refrigerator increases as the supply pressure increases. These increases of the exhaust pressure result from the pressure drop of the gas filter. The larger mass flow rate through the gas filter results in the higher pressure drop.

SUMMARY

In the present study, the cooldown characteristics, no load temperature and cooling capacity of a miniature Joule Thomson refrigerator were investigated by experiment using different pressures of nitrogen and argon gas. In addition, the mass flow rate and temperature profile on the surface of the dewar were measured during the cooldown process.

The results show that there exists a minimum supply pressure for getting the required cold end temperature, and higher supply pressure to the Joule Thomson refrigerator results in more rapid cooldown performance. The mass flow rate increases during the cooldown process, then a small amount of gas is supplied to keep the temperature at steady state. The maximum mass flow rate increases as the supply pressure increases.

ACKNOWLEDGMENT

The authors are grateful to the Ministry of Science and Technology (MOST) and the Agency for Defense Development (ADD) for support of this work through the Dual Use Technology project.

REFERENCES

1. R. Levenduski and R. Scarlotti, "Joule-Thomson cryocooler for space applications," *Cryogenics*, vol. 36, no. 10 (1996), pp. 859-866.
2. W. A. Little, "Microminiature Refrigerators for Joule-Thomson Cooling of Electronic Chips and Devices," *Advances in Cryogenic Engineering*, vol. 35, Plenum Press, New York (1990), pp. 1325-1333.
3. Graham Walker, *Miniature Refrigerators for Cryogenic Sensors and Cold Electronics*, Clarendon Press, Oxford (1989), pp. 23-35.
4. Martin Donabedian, *Spacecraft Thermal Control Handbook Volume II: Cryogenics*, The Aerospace Press, California, (2003), pp. 44.
5. H. Xue, K. C. Ng, J. B. Wang, "Performance evaluation of the recuperative heat exchanger in a miniature Joule-Thomson cooler," *Applied Thermal Engineering*, vol. 21 (2001), pp. 1829-1844.
6. B. Z. Maytal, "Performance of ideal flow regulated Joule-Thomson cryocooler," *Cryogenics*, vol. 34. no. 9 (1994), pp. 723-726.
7. J. S. Buller, "A miniature self-regulating rapid-cooling Joule Thomson cryostat," *Adv. Cryo. Eng.*, Vol. 16, Plenum Press, New York (1971), pp. 205-213.

Development of a 4K Sorption Cooler for ESA's Darwin Mission: System-Level Design Considerations

J.F. Burger[1], H.J.M. ter Brake[1], H.J. Holland[1], G. Venhorst[1], E. Hondebrink[1], R.J. Meijer[1], T.T. Veenstra[1], H. Rogalla[1], M. Coesel[2], D. Lozano-Castello[3], A. Sirbi[4]

[1] University of Twente, Faculty of Science and Technology
7500 AE Enschede, The Netherlands
[2] Dutch Space, The Netherlands; [3] University of Alicante, Spain
[4] ESA-ESTEC, The Netherlands

ABSTRACT

ESA's Darwin mission is a future space interferometer that consists of six free-flying telescopes. To guarantee a proper mechanical stability of this system, hardly any vibration of the optical system with integrated cryocoolers can be tolerated. This paper presents the system design of a 4.5 K, 10 mW vibration-free sorption cooler chain, of which the helium stage is currently in development under an ESA-TRP contract. A sorption cooler is a favorite option because it has no moving parts and it is, therefore, essentially vibration-free. A two-stage helium/hydrogen cooler is proposed which needs 5 Watts of input power and which applies two passive radiators at 50 K and 80 K. The paper includes the following aspects: system modelling, radiator configurations, activated carbons, different multi-stage cooler options, and integration aspects of the compressor cells with the radiators.

INTRODUCTION

ESA's Darwin mission is an Infrared Space Interferometer that will search for terrestrial planets in orbit around other stars[1]. Until now, there are a number of *indirect* methods to search for these. For example, the radial velocity of stars can be determined very accurately using the Doppler shift (wobble) of the star spectra[2]. Alternatively, photometric transit methods can be used to detect the brightness drop in the stellar light produced by the planet when it passes the star's line of sight[3]. With these indirect methods, only the existence of some massive planets dissimilar of our own was proved. Darwin hopes to look directly at smaller terrestrial planets by – for the first time – making use of space-based 'nulling' interferometry, which allows for a serious search for life on other planets with a very real chance of success. By using a combination of six free-flying 1.5 m telescopes and 1 central hub with a baseline of 50 - 500 m (see Fig. 1), a symmetric transmission map can be produced, allowing the search for a planet in a specific zone (e.g. where water is in the liquid phase) around the star. Once a planet is found, the same system can be used to observe it in more detail.

Cryocoolers 13, edited by R. G. Ross, Jr.
Springer Science+Business Media, Inc., New York, 2004

Figure 1. Artist impression of the Darwin free-flying interferometer concept (Courtesy of Alcatel Space). It consists of six free-flying telescopes in a hexagonal configuration that redirect the beams to the central spacecraft.

The optical paths between the central hub and the six telescopes are controlled and stabilized to less than 10 nm by making use of micro-Newton ion thrusters that operate in a control loop in combination with RF, optical and laser metrology. To guarantee the pointing and dimensional stability, no vibration of the optical system with integrated cryocoolers can be tolerated. As a consequence, zero-vibration is one of the central requirements for the cryocooler, and the main reason to investigate the use of sorption coolers.

Darwin will have to operate at the L2 Lagrange point in the sun-earth system – the point at which the gravitational forces of the sun and earth balance, leaving the spacecraft almost completely still in the sun-earth space.[1] The reason for this is that otherwise there will be too much background zodiacal dust, interfering with any readings taken. In addition, the L2 position makes it possible to apply passive radiative precooling for temperatures larger than ~ 30 K, a temperature impossible to reach for low earth or geostationary orbits.[4] In this way, all Darwin's optical elements are passively cooled to 40 K. Low-temperature radiative cooling can also be used to precool an active cryocooler that is applied to reach temperatures below 30 K.

Active sub-10 K cooling is required in the central hub of Darwin to cool the mid-IR camera (5 - 30 μm), which could consist of a Si:As array.[1] Wade and Lindensmith[5] argued that in such a system the cooling power can be reduced to a few mW's by careful thermal design of the integrated package of cooler and camera, and by providing proper precooling and shielding at somewhat higher temperatures. To be conservative, in this study a required cooling power of 10 mW at 4.5 K is assumed.

Darwin's essential cryocooler requirements that were discussed in this section are summarized in Table 1, together with some additional requirements regarding mass, lifetime, power input, etc.[1]

Table 1. Summary of cryocooler requirements for Darwin.

cooling power and cold-stage temp.	10 mW @ 4.5 K
radiative precooling power and temperature	1. < 5 W @ 50 K, resulting in max. 17 m^2 radiator area (or scaled to other temperatures using T^4 law) 2. < 200 W @ 300 K on spacecraft bus
exported mechanical vibrations	< 1 μN/√Hz for f > 0.1 Hz or < 1 μN RMS
input power	< 200 W
mass target	< 10 kg
temperature stability	< 1 mK for 1 hour, < 10 mK for 2 weeks, < 0.1 K for lifetime
lifetime	> 5 years
others: continuous operation; resistant to launch loads; resistant to radiative environment	

CRYOCOOLER OPTIONS

Active cooling of the mid-IR camera can be done either by stored cryogens (open cycle), or by closed-cycle cryocoolers. Important advantages of stored cryogens are: no vibrations and no power consumption. On the other hand, important disadvantages are: a limited lifetime and a large volume and mass. Two candidates have been considered for Darwin: superfluid helium around 2 K and solid hydrogen at 10 K.[1] Superfluid helium was used on a previous European spacecraft (ISO) and will be used for the Herschel mission. If the parasitic heat losses are reduced to 30 mW by technological improvements (50 mW for Herschel), then still a 5 m^3 cryostat is required for a 5 years lifetime. This makes superfluid helium an unsuitable option. Solid hydrogen, on the other hand, could provide a suitable cooling power at 10 K during 5 years of operation, assuming a cryostat mass of 300 kg and a hydrogen mass of around 75 kg, contained in a volume of 1 m^3. This technology appears compatible with the Darwin mission, provided that the detector does not need to be cooled below 10 K. However, there are disadvantages that make this option less favorable: a substantial mass and volume is required to reach a lifetime that is still limited, and hydrogen in such large amounts is dangerous to handle.

There are a very limited number of closed cycle coolers that could be considered as an option for Darwin. Space qualified Stirling and Pulse-Tube coolers that have been developed in recent years are based on the 'Oxford' technology: a clearance seal is used around the piston to guarantee leak tightness without mechanical contact.[6] The seal is rigidly maintained in lateral position by a set of diaphragm springs. Control electronics have been developed to minimize the exported vibration of a pair of back-to-back compressors to the order of a few 10 mN. Such vibrations, however, are still incompatible with Darwin – which makes use of μN ion thrusters. Another reason that makes this type of regenerative coolers less suitable is the relatively small distance between the cold stage and the 300 K heat sink of the compressors; for Darwin it is better to have 300 K components far away from the optical components because of stray light concerns. For that same reason, it is more attractive to apply a continuous flow cooler such as a Joule Thomson (JT) or Turbo-Brayton, where complete separation of the cold stage and warm compressor is possible – if required.

A Turbo-Brayton cryocooler was space qualified and demonstrated for use in the Near Infrared Camera/Multi-Object Spectrometer (NICMOS) of the Hubble Space Telescope.[7] A cooling power of 8 W is obtained at 70 K by the expansion of a gas by means of a mechanical turbine that operates with a very high rotational speed (4500 rev/s). The compressor also operates at such high speed, so that very limited low-frequency mechanical vibrations are expected. Developments are reported to adapt this system to lower temperatures (4 - 35 K) and lower cooling powers (20 - 100 mW), but this requires the development of a full-balanced expander of an extraordinarily small size that operates with a very high speed.[8] Such kind of expander is challenged by fundamental scaling laws.

In recent years, space-qualified closed-cycle JT coolers were developed that can supply enough cooling power for Darwin.[9] They operate with the same type of piston-compressors based on 'Oxford' technology that was discussed above. As a consequence, the zero-vibration requirement cannot be met. As an alternative, Ball Aerospace is developing a 6 - 8 K hydrogen-helium JT cooler for NGST that is driven by a mechanical rotary vane compressor.[10] Although the exported vibrations of such compressor are less than for linear compressors, it is uncertain whether the exported vibrations are compatible with Darwin's micro-Newton requirements.

An attractive alternative is the use of a sorption compressor that drives a JT cold stage, in combination with passive radiative precooling around 50 K. Such sorption cooler has no moving parts and is, therefore, essentially vibration-free. In addition, the absence of moving parts simplifies scaling of the cooler to small sizes, and it contributes to achieving a long lifetime. These two properties make sorption coolers even more attractive for future scientific space missions. A 20 K hydrogen cooler based on this technology is currently being built for ESA's Planck mission[11], and a 169 K ethylene sorption microcooler was developed at the University of Twente to illustrate the attractive scaling possibilities of this technology.[12] Details on the basic operating principles of sorption coolers can be found in a few recent publications.[13, 14]

PERFORMANCE OF A SINGLE HELIUM SORPTION STAGE

Modelling approach

Most sorption coolers can produce a limited temperature drop from the compressor heat sink temperature to the refrigeration low temperature – especially when physical adsorption is applied such as with helium gas in combination with activated carbon. To reach larger temperature differences, a number of cascaded sorption stages can be used – possibly in combination with other cooler types. Later on in this paper, different combinations of cascaded stages will be discussed. For a proper design of such a cascaded system, it is important that each individual sorption cooler stage is understood, modelled and optimized properly. This section describes our modelling approach, input parameters, and some performance trends of a single helium stage.

A thermodynamic model was developed that calculates the basic thermodynamic performance of a sorption cooler stage. In essence, the compressor and cold stage *COP*'s are calculated, with realistic gas and adsorption properties as input. The model includes 'intrinsic' loss factors, these are loss terms that are firmly associated with the sorption cooler architecture, and that cannot be reduced by clever design of the individual cooler components - once the gas, adsorption material, and compressor cylinder material are chosen. An example of an intrinsic loss term is the heat that is put in the heat capacity of the sorption material and compressor walls. The results of this model are basically independent of cooler size, i.e. the resulting cooler input power and radiator areas are scalable with the required cooling power. This is an important and characteristic feature for sorption coolers, which is usually not found for mechanical cryocoolers.

Input parameters and boundary conditions

Radiator thermal performance. The radiator temperature that must be chosen is not fixed at 50 K. In fact, the design of the radiator plus sorption cooler should be such that the radiator area is minimized. The design constraint of the precooling radiators can be expressed as:

$$P_{rad} = \varepsilon A \sigma \left(T_{rad}^4 - T_{sink}^4 \right) \qquad (1)$$

Here, T_{sink} gives the temperature of the radiator in case of no heat load. This temperature is determined by the parasitic load coming from the spacecraft; it depends on the detailed design of the radiators. In this project, it was decided to work with a radiator in the shape of a truncated pyramid, which resulted in $T_{sink} = 20.5$ K. Furthermore, a value of 0.8 was taken for the radiator emissivity.

Adsorption materials. The performance of a sorption cooler is very much influenced by the selected adsorption material. Activated carbons are generally believed to be the preferred adsorption material (compared to zeolites and silica gels) for helium sorption compressors. An important parameter of an activated carbon is the amount of gas (per mass/volume of sorber material) that can be liberated from a sorption cell during one thermal cycle of the compressor. This is essentially coupled to two properties of the activated carbon: the adsorption capacity at low pressure and temperature (e.g. 50K and 1 bar for the helium stage) and the void volume – since gas is stored and lost in this volume when the gas is compressed to a high pressure.

Table 2 lists properties of three different types of activated carbon. Saran is a microporous monolithic carbon that is produced from Polyvinylidene Chloride – a carbon historically considered favorite for sorption compressors because of it's high adsorption capacity at low pressure and its very low void volume. Unfortunately, it cannot easily be produced because its precursor material is on an international hazard list. ESA1 and ESA2 are carbons from Spanish anthracite, developed in this project. The table also compares the amount of delivered gas for the different carbons, for sorption compressors heat sunk at 20 K and 50 K. From the numbers, it can be concluded that at 50 K the void volume is affecting the amount of delivered gas much more than at 20 K, whereas at 20 K the adsorption capacity plays the major role. Since we prefer to apply radiative precooling of the helium sorption compressor, ESA1 in a monolithic shape is currently selected as the preferred material. Fig. 2 compares some of the isotherms of ESA1 and ESA2.

Table 2. Properties of three different types of activated carbon, together with an example of helium adsorption properties in a sorption cell that is heat sinked at 20 K and 50 K.

carbon	Saran		ESA1		ESA2	
shape	monolith		monolith		pressed powder	
density (mg/ml)	1.0		0.7		0.5	
void volume fraction	0.545		0.68		0.77	
Adsorption properties (all expressed in mg gas per gram of sorber material):						
Adsorption low temp., T_L	20 K	50 K	20 K	20 K	20 K	50 K
Adsorbed gas at T_L and 1.25 bar	58.5	8.7	77.4	7.5	105	7.5
Gas in voids at T_L and 1.25 bar	0.3	0.6	1.9	1.1	3.3	1.8
Total gas in cell at T_L and 1.25 bar (A)	58.8	9.3	79.3	8.6	108.3	9.3
Adsorbed gas at 120 K and 13 bar	2.5	2.5	2.25	2.25	2.25	4.2
Gas in voids at 120 K and 13 bar	2.8	2.8	5.01	5.01	7.9	7.9
Total gas in cell at 120 K and 13 bar (B)	5.3	5.3	7.26	7.26	10.15	12.1
Amount of delivered gas (= A – B)	**53.5**	**4**	**72.04**	**1.34**	**98.15**	**-2.8**

Gas and sorption container properties. Gas properties are obtained from Cryodata's Gaspak.[15] Three material properties of Stainless Steel 316L (compressor material) are used: the temperature-dependent specific heat, the density and the yield strength. The yield strength is used to calculate the required thickness of the compressor container wall, and this required thickness is translated into a ratio of the container-to-sorber mass. A yield strength is assumed of 295 MPa at 300 K; in the temperature range of 20 – 150 K the yield strength can be considered significantly higher. In the model, a maximum allowable stress is taken as 100 MPa, resulting in a suitable margin of safety to account for the repeated thermal and mechanical cycling.

Performance trends of a single helium sorption stage

The thermodynamic model was used to calculate performance trends as a function of relevant cooler operating parameters, such as: the compressor low and high temperatures, system pressures, precooling temperatures, void volumes, etc. As an example, Fig. 3a shows the radiator area as a function of the radiator temperature, for a radiator that directly heat sinks a single-stage helium sorption compressor. The total cooler performance is made up by the product of the radiator performance and the sorption stage performance. Clearly, for lower temperatures the radiator performance (expressed in radiator area per Watt of radiative power) deteriorates the system performance, and for higher temperatures the sorption compressor performance deteriorates the system performance, which explains the optimum operating temperature of about 45 K for this specific case. As a second example, Fig. 3b shows the cooler COP as a function of the void volume fraction of the activated carbon, for a compressor heat sunk from 20 K and 50 K. For a heat sink temperature of 20 K, the amount of gas produced in one compressor cycle

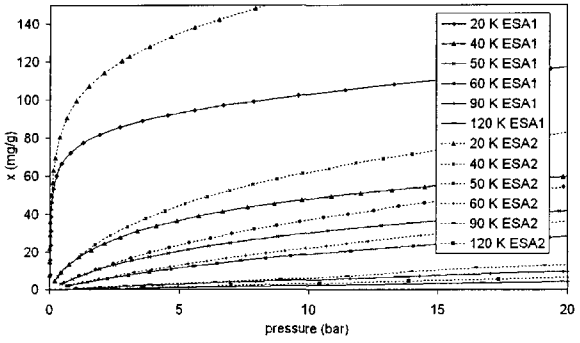

Figure 2. Measured isotherms of two different activated carbons: ESA 1 and ESA 2.

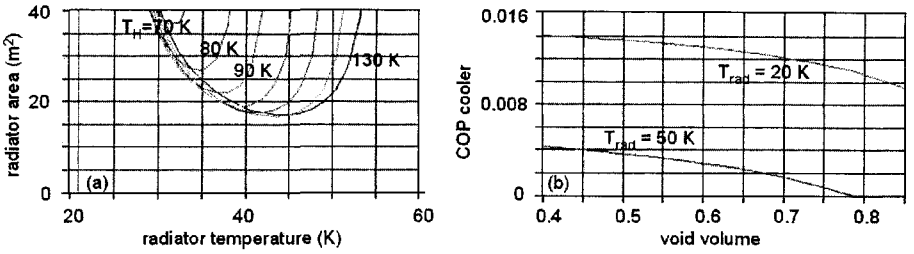

Figure 3. (a) Radiator area as a function of the compressor low and high temperature; (b) effect of the void volume on the efficiency of the cooler. Pressure settings: p_L = 1.3 bar; p_H = 13 bar.

is so big that the influence of the void volume is very limited – even for large void volumes of 85% of the compressor cell. This is clearly not the case for a helium compressor operating from 50 K: then the influence of the void volume is very significant.

COMPARISON OF DIFFERENT MULTI-STAGE SORPTION COOLER CHAINS

A number of different multi-stage sorption coolers were compared, some of them having non-sorption precooling stages. Some relevant characteristics are listed in Table 3. For all cooler configurations it was assumed that they should supply a cooling power of 10 mW at 4.5 K. Optimized operating parameters were determined with the models that were briefly described in the previous section of this paper; proper margins were taken into account. In cases where a trade-off was found between input power (*COP*) and radiator area, then the radiator area was minimized – with the penalty of a higher compressor input power. Optimization of the multi-stage sorption coolers was done by combining the results of individually optimized (sorption) stages, and subsequent variation of the interfacing temperature(s). Furthermore, three contributions were taken into account to estimate the cooler-chain masses: the estimated cooler masses itself, the radiator mass, and the mass needed to provide the required power to the cryocoolers. The main characteristics of the six cooler-chains are summarized below.

Configuration 1. Fig. 4a shows a schematic picture of configuration 1, including the most important operating parameters. This cooler makes use of two rather small sorption stages, which can both be located at the cold end of the spacecraft. The helium and hydrogen stages both apply activated carbon as the adsorption material, and also both operate as a *two-stage* sorption compressor (i.e. the gas is compressed in two steps from a low to a high pressure). Two-stage sorption compressors have a better performance, compared to single-stage compressors. Precooling of the sorption compressors is done by two radiators at 50 and 80 K. The hydrogen stage is supplying a tiny 25 mW at 14.5 K for precooling the helium cold stage and shielding purposes. The disadvantage of this cycle is the large total radiator area, which is mainly related to the helium stage. However, a number of advantages are present: the cooler itself is small, light and compact; it requires a very small input power; it can easily be made redundant without sacrificing total system mass; the small compressor cells can be integrated with the radiator, thus spreading the thermal load over the radiator area. This cooler configuration is chosen as the baseline design, and will be described in somewhat more detail later in this paper.

Table 3. Overview of the different cooler options with their most important characteristics. This comparison is a thorough update of a previously reported comparison.[16]

option:	1	2	3	4	5	6
stage 1:	2-st C/H2	solid Ne	1-st LaNi/H2	2-st C/H2	Turbo-Brayton	solid Ne
stage 2:	2-st C/He	2-st C/He	1-st C/He	2-st C/He	1-st C/He	1-st C/He
P input (W)	7.9	7.9	194 W @ 300 K	151	318 W @ 300 K	0.85 W
T rad (K)	49 / 52 / 80	50 / 55	50 / 300	105 / 135	50 / 300	-
A total (m^2)	18.6	23.25	4.4	23.1	5.1	-
total mass (kg)	83	295	153	171	190	2000

Configuration 2. This option applies a solid neon cryostat to precool the helium cold stage – replacing the small hydrogen stage. It does not reduce the radiator area, but it removes the possible development risks that come with the hydrogen stage – with the price of a bigger radiator area and a higher total mass (or shorter lifetime). On the other hand, the neon may be useful for other (cooling) purposes in a spacecraft. A cooling enthalpy of 105 J/g was assumed for the neon solid-vapor transition, leading to a required neon mass of 47 kg to provide a cooling power of 25 mW for 5 years. The total mass of the neon cryostat was estimated at 200 kg.

Configuration 3. Fig. 4b shows a schematic picture of configuration 3. It makes use of a metal hydride sorption compressor that operates from a heat sink around 280 K, so that this hydride compressor must be located at the warm side of the spacecraft. The hydrogen gas is precooled by a radiator operating at 50 K. Compared to option 1 and 2, the advantage of this system is the limited radiator area, which can be further reduced to less than 2 m^2 by using a multi-stage radiator. Also, the technology is available for space application.[11] A significant disadvantage is that metal hydride technology is based on chemical absorption, which is inevitably related to degradation effects that can significantly limit the useful lifetime.[13] This is not the case for carbon-based sorption technology, which is based on intrinsically reversible physical adsorption. Other disadvantages of configuration 3 are: a high cost, a high input power, and a more complicated system integration – because the compressor is located at the warm side of the spacecraft, and hydride technology requires delicate handling to prevent hydride contamination.

Configuration 4. In this option, a hydrogen-carbon sorption stage is applied to provide active heat sinking of the entire helium-carbon stage at 18 K. Unfortunately, the total radiator area is very large. A second hydrogen/carbon stage can be added to precool the helium cold stage to 14.5 K, adding more complexity; this would reduce the input power and radiator area of the upper hydrogen stage with a factor of 0.67. However, the total radiator area will still be bigger than 15 m^2 – for a very complex, inefficient and heavy cooler-chain. Notice that the high mass-flow of the hydrogen stage will require significantly bigger compressor cells, tubing etc. than required for the small hydrogen stage that is used in cooler option 1. In addition, the upper hydrogen stage applies radiators at 105 K and 135 K that radiate more than 150 W at the cold side of the spacecraft – which makes this option less attractive as compared to the other options.

Configuration 5. Creare is currently developing a Turbo-Brayton cooler that will be able to cool to 20 K with a cooling power of about 1 W.[17] This Turbo-Brayton cooler is used in option 5 to heat sink the helium sorption stage at 20 K. Preliminary performance data was obtained from Creare: 1.04 W of cooling at 20 K, for 1 W heat sinking at 50 K and a compressor electrical input power of 200 W at 300 K. The data was scaled to accommodate the required 1.3 W of

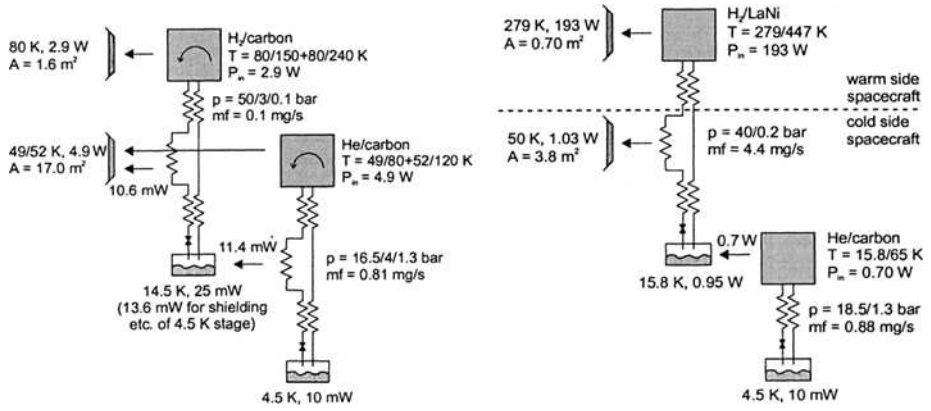

Figure 4. (a and b) Schematic picture of cooler configuration 1 and of cooler configuration 3.

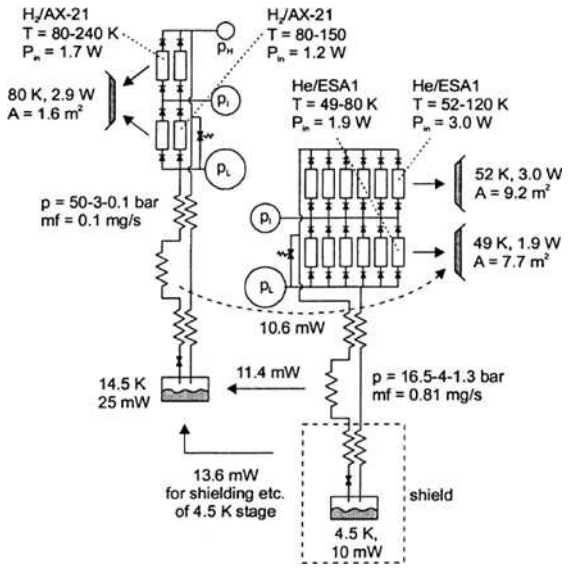

Figure 5. Schematic picture of the baseline design of the entire 4K sorption cooler chain.

cooling power. Like for the sorption stages, a 25% margin was added. According to information from Creare[17], it may be possible to increase the 50 K precooling temperature somewhat – which would significantly reduce the radiator area. Advantages of this system are: a limited radiator area, existing technology and a proper lifetime. Disadvantages are: a high input power and system-mass, and the use of moving parts and high gas flows that may cause vibrations.

Configuration 6. For completeness, an option is included in which a solid neon cryostat heat sinks the helium sorption compressor at 18 K. Clearly, this option is not attractive because of the extreme large mass, although no radiator is required at all.

BASELINE COOLER DESIGN

Fig. 5 shows a schematic picture of the proposed baseline design of the entire 4K sorption cooler chain, with some relevant parameter settings included in the picture. The mentioned parameters include a 25% loss-budget.

Gas buffers are used at the intermediate and low pressure for the helium sorption stage, and for the intermediate, low and high pressure in the case of the hydrogen sorption stage. These gas buffers have several functions. Firstly, the gas buffers facilitate the discontinuous and independent use of the individual compressor cells[18], which has several advantages at the low and intermediate pressure-side. Secondly, the low-pressure buffers are needed to limit the system pressure to acceptable values when the system is stored at 300 K. At 300 K, virtually no gas is adsorbed on the activated carbon – independent of the pressure. If no low-pressure buffer is used, then pressures higher than 100 bar will be present in the system or, alternatively, the system will burst. All parts of the system could be designed to stand such high pressures, but for the compressor cells this is not feasible: it would result in very thick walls that would deteriorate the cooler performance dramatically due to the added thermal mass. No high-pressure buffer is used for the helium stage: in the current design there are more than enough sorption cells to provide a continuous high-pressure gas flow, and a high pressure buffer rapidly increases the required size of the low pressure buffer.

In addition to the low-pressure buffer, an excess-pressure relief-valve is required between the high pressure and the low pressure side, which opens at a pressure somewhat above the highest system pressure – for instance at 18 - 20 bar in the case of a high pressure of 16.5 bar.

This relief-valve is needed for the situation that the cooler temporarily stops operating, and the compressor sink temperature is raised. In that situation, all compressor cells are raised in temperature and the adsorbed gas is released and flowing through the check valves to the high pressure side, while at the same time the flow through the cold stage is reducing because of the temperature increase of the JT-restriction and the lack of precooling at 14.5 K.

For the helium stage, currently 2 x 6 sorption cells of 1.5 cm in diameter and 15 cm in length are foreseen, each having a cycle period of more than 10 minutes. This architecture is based on the following ideas. The twelve cells (each combined with two check valves) can be distributed over the radiator area, resulting in a limited temperature gradient from the activated carbon to the radiator surface. In addition, it facilitates the design of very light and thin radiators. Furthermore, this number of cells makes it possible to loose one or two cells: the system becomes redundant. Obviously, gas leaks remain single-point failures, but a defect in one of the following cell-components can be handled by the remaining cells: heater, gas-gap heat switch, mechanical support, temperature sensor, (leaking) check valve, a clogged filter.

For the hydrogen stage the situation is slightly different. Here, the gas flow is so low that it is not required to distribute more cells over the radiator area. Therefore, 2 x 2 cells of 1.5 cm in diameter and 15 cm in length are proposed, in combination with three buffers. In this way, there is redundancy in the system and at least one of the cells may be lost.

Different alternatives for the radiator design were compared, including deployable radiator options. Fig. 6 shows a side view of one of the favorite design options, consisting of a fixed radiator integrated in the beam combiner design. The design is such that there is a gradual temperature decrease from the sun-side of the spacecraft to the cold optical bench that is located at the other side of the spacecraft – in order to provide optimal passive cooling for the heat conduction losses. The cryocooler cold stage is located inside the optical bench, to provide the required cooling power at 4.5 K to the IR detectors. A sun-shield in combination with a V-groove radiator is proposed to shield the passive radiators from the warm side of the spacecraft – similar to the original Alcatel-design. The 80 K and 50 K radiators have the shape of a six-sided truncated pyramid, to obtain an optimal view-factor to space. The helium compressor cells are distributed over the inside of the radiator surface. The individual compressor cells (plus two check valves) are connected to three ring-lines for the low, medium and high pressures.

From these drawings, it clearly appears that the radiator is very big – although the present design can be accommodated in the Ariane 5, which is currently the preferred launcher for Darwin. We are considering two options to reduce the radiator area: further improvement of the activated carbon adsorption properties, and a reduction of the required cooling power at 4.5 K.

CONCLUSIONS

A system-level design of a 4.5 K sorption cooler was made. Different options for vibration-free precooling and/or heat sinking of a 4.5 K helium sorption stage were compared: a small carbon-hydrogen sorption cooler, a hydride-hydrogen sorption cooler, a solid neon cryostat, and a Turbo-Brayton cooler. All of these cooler chains make use op passive radiative cooling to as low as 50 K, which is made possible by Darwin's far-away position L2. According to this study,

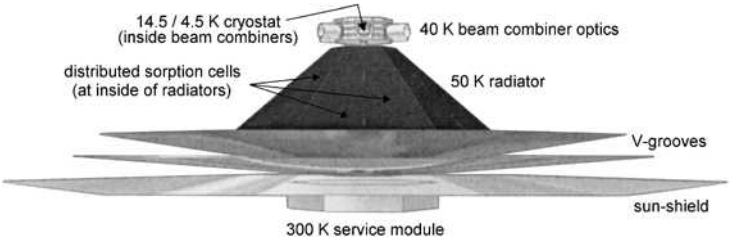

Figure 6. Design impression (side-view) of the radiators integrated in the beam combiner spacecraft.

the properties of a few different cooler chains satisfy the requirements. More specific, a helium/hydrogen sorption cooler precooled by two radiators at 50 and 70 K has several distinctive advantages: the cooler itself is small, light and compact; it requires a very small input power; it can easily be made redundant; the small compressor cells can be integrated with the radiator. The big radiator area is a disadvantage; further improvements of the activated carbon and/or a smaller cooling power at 4.5 K can reduce the required area.

REFERENCES

1. *Darwin – The InfraRed Space Interferometer, The search for Terrestrial Exoplanets and High Resolution Imaging of the Universe*, Concept and Feasibility Study Report, ESA-SCI (2000).
2. Queloz D. *Planets outside the solar system: Theory and observations*, eds. J.M. Mariotti and D. Alloin, Kluwer (1999), pp. 107.
3. Charbonneau D., Brown T.M., Latham D.W., Mayor M.,"Detection of planetary transits across a sun-like star," *The Astrophysics Journal*, vol. 529 (2000), pp. L45-L48.
4. Collaudin B., Rando N.,"Cryogenics in space: a review of the missions and of the technologies," *Cryogenics*, vol. 40 (2000), pp. 797-819.
5. Wade L.A., Lindensmith C.A.,"Low-power, zero-vibration 5 K sorption coolers for astrophysics instruments,"*Adv. in Cryogenic Engineering* (2002), pp. 47.
6. Davey, G.,"Review of the Oxford cryocooler,"*Adv. in Cryogenic Engineering*, vol. 35 (1990), pp. 1423-1430.
7. Nellis G.F., Dolan F.X., McCormick J.A., Swift W.L., Sixsmith H.,"Reverse Brayton Cryocooler for NICMOS," *Cryocoolers 10*, Kluwer Academic/Plenum Publishers, New York (1999), pp. 431-438.
8. McCormick J.A., Nellis G.F., Sixsmith H., Zagarola M.V., Gibbon J.A., Izenson M.G., Swift W.L., "Advanced developments for Low Temperature Turbo-Brayton Cryocoolers," *Cryocoolers 11*, Kluwer Academic/Plenum Publishers, New York (2001), pp. 481-488.
9. Fernandez R., Levenduski R., "Flight demonstration of the Ball Joule-Thomson cryocooler," *Cryocoolers 10*, Kluwer Academic/Plenum Publishers, New York (1999), pp. 449-456.
10. Oonk R.L., Glaister D.S., Gully W.L., Lieber M.D.,"Low-temperature, low-vibration cryocooler for Next Generation Space Telescope Instruments," *Cryocoolers 11*, Kluwer Academic/Plenum Publishers, New York (2001), pp. 775-782.
11. Prina, M., Loc, A., Schmelzel, M.E., Pearson, D., Borders, J., Bowman, R.C., Sirbi, A., Bhandari, P., Wade, L.A., Nash, A., Morgante, G.,"Initial test performance of a closed-cycle continuous hydrogen sorption cooler, the Planck sorption breadboard cooler," *Cryocoolers 12*, Kluwer Academic/Plenum Publishers, New York (2003), pp. 637-642.
12. Burger, J.F., Holland, H.J., ter Brake, H.J.M., Elwenspoek, M.C. and Rogalla, H.,"Construction and operation of a 165 K microcooler with a sorption compressor and a micromachined cold stage," *Cryocoolers 12*, Kluwer Academic/Plenum Publishers, New York (2003), pp. 643-650.
13. Bowman Jr., R.C., Kiehl, B. and Marquardt, E., "Closed-Cycle Joule-Thomson Cryocoolers," *Spacecraft Thermal Control Handbook, Volume II: Cryogenics*, edited by M. Donabedian, The Aerospace Press, El Segundo, CA (2003), pp. 187-216.
14. Burger, J.F., Holland, H.J., Wade, L.A., ter Brake, H.J.M., Rogalla, H., "Thermodynamic considerations on a microminiature sorption cooler," *Cryocoolers 10*, Plenum Press, New York (1999), pp. 553-564.
15. *Gaspak – fluid property program*, version 3.30, Cryodata Inc., Niwot, CO, USA.
16. Burger, J.F., ter Brake H.J.M., Rogalla H., Linder M.,"Vibration-free 5 K sorption cooler for ESA's Darwin mission," *Cryogenics*, vol. 42 (2002), pp. 97-108.
17. W.L. Swift, Creare Inc., personal communication (2003).
18. Wiegerinck, G.F.M., Burger, J.F., Holland, H.J., Hondebrink, E., ter Brake, H.J.M., Rogalla, H., "Improvements in sorption compressor design," Presented at this conference.

Improvements in Sorption Compressor Design

G.F.M. Wiegerinck, J.F. Burger, H.J. Holland, E. Hondebrink, H.J.M. ter Brake, and H. Rogalla

University of Twente, Faculty of Science and Technology
7500 AE Enschede, The Netherlands

ABSTRACT

A single sorption compressor cell that is thermally cycled provides an intermittent flow. For a Joule-Thomson expansion stage, a more or less continuous flow is required. The standard method to obtain a continuous flow out of a sorption compressor is to use three or more compressor cells that are operated out of phase. This paper presents an alternative compressor concept that uses only one compressor cell, two buffer volumes and two check valves. Such a compressor is easier to construct and to operate and has a higher reliability at the expense of a slight variation in the cooler's cold-end temperature. The principle was demonstrated using a sorption compressor cell that is equipped with a gas-gap heat-switch, is filled with Maxsorb activated carbon, and uses xenon as a working fluid. A flow of 0.5 mg/s was achieved with a low pressure of 2.0 bar and a high pressure of 12.6 bar. The compression ratio can be increased by reduction of the void volume and by optimization of the compressor control system.

INTRODUCTION

A sorption compressor cell basically consists of a container that is filled with an adsorbent. It can act as a compressor by thermally cycling the adsorbent and at the same time controlling the gas flow to and from the system. This gas flow can be controlled either actively or passively. One can distinguish four different parts in the cycle. These are schematically shown in Fig. 1. Starting from an initial low (heat-sink) temperature and pressure, during the first part of the cycle (A) the sorber container is heated while no gas can flow into or out of the compressor cell. Adsorbed gas comes off the surface and builds up pressure in the void volume of the container. If, at some point, the container is opened, high-pressure gas flows out (phase B). In this phase, further heating of the container is required to keep the pressure constant. When most of the gas has come off the surface, the container is cooled back to the heat-sink temperature and the container is closed (phase C). Gas from the void volume now adsorbs onto the surface of the sorber material, causing the pressure in the container to drop. At a sufficiently low pressure, gas should be supplied to the sorber container in order to return to the starting point (phase D). So, during only one phase of the cycle (phase B) high-pressure gas is supplied by the cell and during another phase (phase D) low-pressure gas is taken up by the cell. In the other two phases no gas flows into or out of the system.

While an individual sorption cell provides an intermittent flow, a Joule-Thomson expansion stage needs a more or less continuous mass flow in order to provide continuous cooling power. In general, a continuous flow is obtained by using three or more compressor cells. They are operated

Cryocoolers 13, edited by R. G. Ross, Jr.
Springer Science+Business Media, Inc., New York, 2004

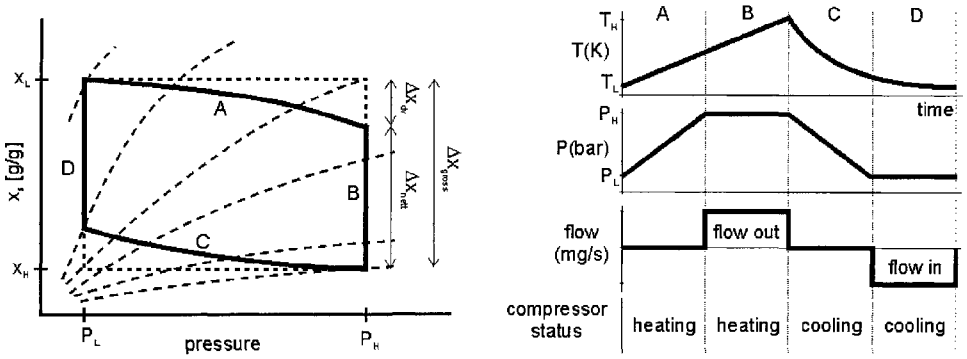

Figure 1 (a) Amount of adsorbed gas per gram of sorber material during the sorption cycle. (b) Temperature, pressure, flow and compressor status with time during the sorption cycle.

out of phase and their phases are synchronized. A check valve unit is used to convert the intermittent flows of the individual cells to a continuous flow through the cold stage. A schematic picture of such a cooler using four sorption cells is shown in Fig. 2. Bowman *et al.*[1] recently published an overview of closed-cycle Joule-Thomson cryocoolers.

Coolers that consist of a sorption compressor with a Linde-Hampson cold stage have several advantages. They are thermally driven and have no moving parts, apart from some check valves. As a consequence, they can be scaled to small sizes and can operate with an absolute minimum vibration level. Besides, wear-related issues hardly play a role giving the potential for a long cooler lifetime.

A disadvantage of this cooler type is the relatively complex compressor design including three or more compressor cells, each consisting of a container filled with sorber material and equipped

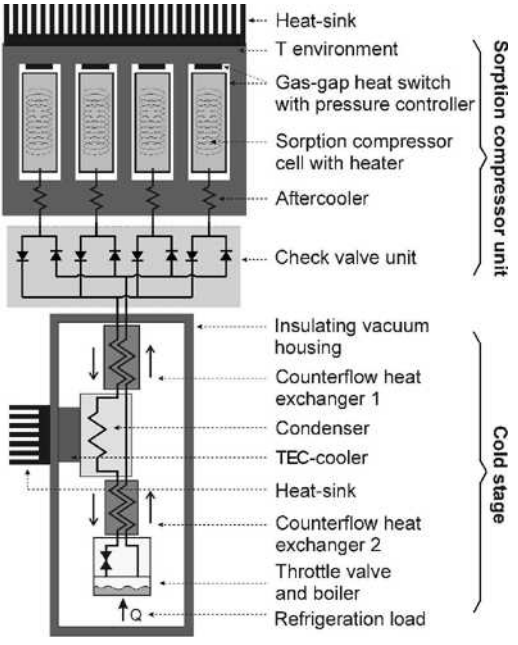

Figure 2. Sorption compressor with a Linde-Hampson cold stage using four sorption compressor cells operating 90 degrees out of phase.

with a heater, a heat-switch with an actuator, and some means to control the heater and the heat-switch actuator. As more complicated components in a system increase the risk of failures, a reduction of complexity would increase the reliability of the cooler. Another drawback is that, in many cases, the cooler is relatively inefficient compared to other types of coolers. Every time the gas in the container is pressurized, the complete container including sorber material, heater, and walls needs to be heated. The contribution of the heat capacity of the container to the total amount of heat input is significant. Furthermore, a considerable amount of gas is lost in the void volume of the sorber material.

In the next section, we present a new design to create a continuous flow out of a single compressor cell. Then, the setup to test the proposed compressor configuration is discussed and the first experimental results are presented. The paper concludes with a discussion on the principle and on the measurement results.

1-CELL SORPTION COMPRESSOR

A Joule-Thomson expansion stage requires a more or less continuous mass flow in order to obtain a continuous cooling power. Besides, the compressor should supply a constant low pressure as this pressure is directly related to the low-end temperature of the cold stage. As set out in the previous section, a single sorption cell supplies an inherently non-continuous flow. As far as we are aware, up to now all coolers of this type use a number of sorption compressor cells that are operated out of phase. As a simpler alternative, we present a design that uses only a single sorption compressor cell and two buffer volumes. This design is shown in Fig. 3.

During phase A of the sorption cycle, the sorber container is heated and pressure builds up in the sorber container as both check valves are closed because of the pressure differences over the valves. The high-pressure buffer supplies gas to the cold stage which is taken up by the low-pressure buffer, while no gas flows to or from the compressor cell. As a consequence, the pressure of the high-pressure buffer slowly decreases while that of the low-pressure buffer steadily increases. Once the pressure in the container has become higher than that of the high-pressure buffer, the high-

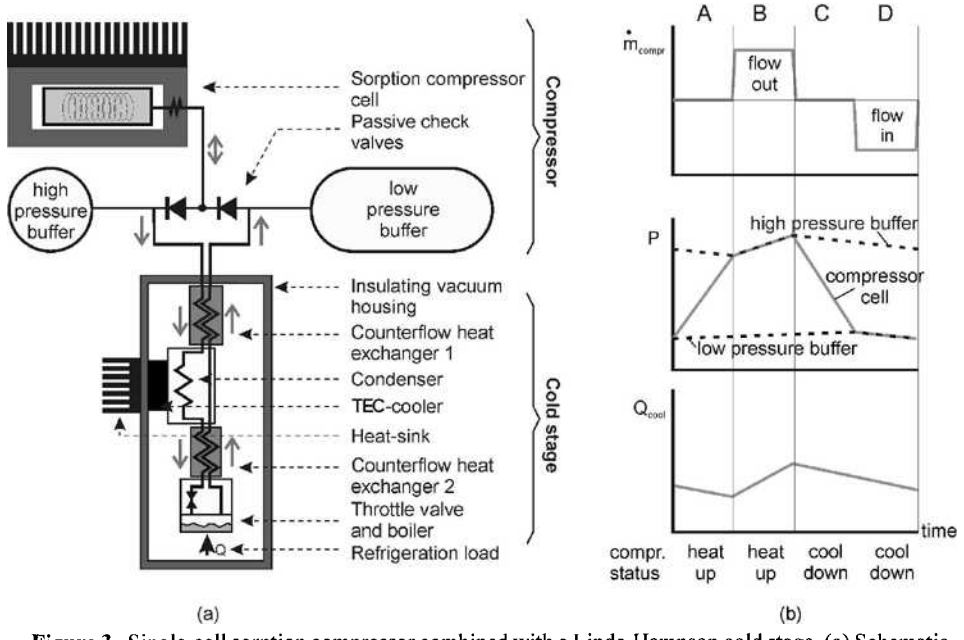

Figure 3. Single-cell sorption compressor combined with a Linde-Hampson cold stage. (a) Schematic drawing of the configuration. (b) Mass flow, pressure and cooling power (exaggerated) with time.

pressure check valve opens and a relatively large gas flow is supplied to the high-pressure buffer, causing the pressure of that buffer to rise (phase B). When the container has cooled down, the pressure in the container decreases and the high-pressure check valve closes (phase C). Again, the flow through the cold stage is maintained by the buffers. When the pressure in the container has dropped to below that of the low-pressure buffer, the low-pressure check valve opens and gas flows from the buffer to the cell (phase D).

The configuration has a number of advantages. First of all, the number of components is reduced. This increases the reliability of the compressor. Besides, controlling the cooler has become easier as only one sorption compressor cell needs to be driven. The reliability of the design can be further increased by mounting a second compressor cell between the low-pressure and high-pressure buffers. The two parallel cells can be operated completely independently. If one of the compressor cells fails, the compressor can still operate (redundancy). The advantage of reduction of complexity becomes even more pronounced when multistaged compression is applied as suggested by Bard.[2] Then, instead of two compressor units consisting of in total eight sorption compressor cells and 16 check valves, only two sorption compressor cells, three buffer volumes and four check valves are needed. With a two-stage compression approach, the COP of the cooler can be increased.[2,3] Besides, in the proposed layout no synchronization between the different compressor cells is needed. As a result, each cell can be cycled at its optimum cycle frequency, and does not have to be tuned to others as is the case in the traditional layout.

A disadvantage of the proposed design compared to the traditional layout is the slight fluctuation in pressure of the low-pressure buffer. This will result in some variation of the cold stage temperature. Proper design of the low-pressure buffer can minimize this temperature variation. Furthermore, this temperature fluctuation can be damped passively or actively. Another disadvantage of the pressure fluctuations in the buffers is that both the flow through the cold stage and the enthalpy of cooling will slightly vary with time as shown with some exaggeration in Fig. 3. However, the actual cooling power of the cold stage is buffered by the evaporating liquid in the boiler.

EXPERIMENTAL SETUP

Thermodynamical Set Points

To demonstrate the single cell sorption compressor, we selected xenon as the working fluid. This gas adsorbs reasonably well at room temperature while at the same time a relatively low temperature of 165 K can be reached for a compressor low pressure of 1 bar. We plan to apply a thermoelectric cooler (TEC) to precool the high-pressure gas. Such a TEC-cooler increases the efficiency of the sorption compressor combined with the Linde-Hampson cold stage without compromising its advantages over other types of coolers. Precooling of the high-pressure gas is useful as the enthalpy related to the gas-liquid phase change adds to the enthalpy of cooling.[4] To liquefy the fluid in the precooler, the high-pressure gas should be precooled below the boiling point of the fluid at that pressure. For a 2-stage TEC-cooler, a temperature of about 235 – 240 K seems achievable with sufficient cooling power.[5] This implies a compressor high pressure in the range of 16 – 19 bar. Of course, the selection of the working fluid and the thermodynamic setpoints is rather arbitrary. Also other gases can be taken depending on the requirements of the cooler.

Sorption Compressor Cell

The design of the compressor cell is shown schematically in Fig. 4. The sorber container is made of stainless steel, has an inner diameter of 9.4 mm and a length of 10 cm. It is filled with commercially available Maxsorb MSC-30 high surface area activated carbon. This sorber material has a surface area of 3290 m^2/g and an apparent density of 0.28 g/ml.[6,7] The charcoal was filtered and only particles with a diameter between 210 – 420 μm were selected. On top of the sorber container, a 2 μm stainless steel filter is placed. In this filter, a feedthrough for a thermocouple is welded. This thermocouple is used both for sensing the temperature and as a heating element. While thermally cycling the sorber container, the thermocouple is switched between heating mode and sensing mode. The sorber container is gold-plated to reduce radiative heat loss and it is cen-

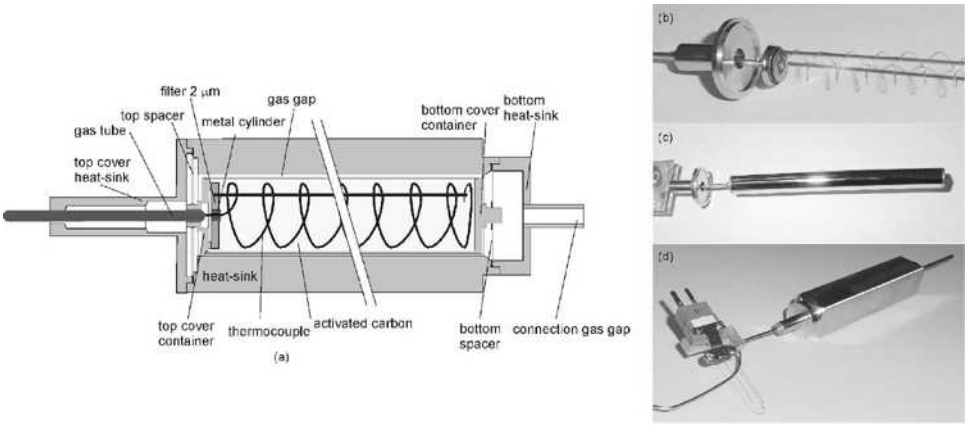

Figure 4. *Sorption compressor cell* (a) Schematic drawing. (b) Top cover and filter of the sorber container with the thermocouple attached. (c) Gold-plated sorber container before installation of the heat-sink. (d) Finished compressor cell.

tered in a stainless steel heat-sink by means of two spacers. For a more detailed description of the compressor cell, the reader is referred to Burger *et al.*[8]

The sorption compressor cell is embedded in an aluminum heat sink. Cooling fins are mounted on top. An axial flow fan (Papst 9956L) is applied to further improve the thermal contact with the environment. A powerful TEC-cooler is positioned between the compressor cell and the cooling fins to keep the heat-sink temperature constant to 20 °C. The pressure in the sorber container is measured outside the cell with a low-void volume Kulite pressure sensor (type XTL-190). The thermocouple in the sorption compressor is an Omega E-type with an outer diameter of 0.25 mm and a length of 51 cm of which 37 cm is inside the sorber material while the remaining 14 cm is located outside the sorber container. The total thermocouple resistance is 393 Ω. The temperature of the heat sink and of the 'cold junction' of the thermocouple was monitored with Heraeus PT1000-resistors. The total void volume between the filter of the sorption compressor cell and the check valves is estimated to be 1.2 cm^3.

Gas-Gap

When heating the sorber container the thermal contact between the container and the surrounding heat-sink should be bad. When cooling down the container, a good thermal contact is required. To achieve this, a gas-gap heat switch is integrated in the sorption compressor cell. This is the narrow slit between the sorber container and the heat-sink and has a width of 300 µm. We selected helium as the contact gas. If the gas in the slit is in the viscous state, a relatively good thermal contact between the sorber container and the heat-sink exists. If the gas in the gap is in the molecular regime, the heat transfer scales with the pressure and hence a lower pressure implies a worse thermal contact.[9,10] Figure 5a shows the theoretical heat transfer coefficient for the gas-gap assuming an accommodation coefficient $\alpha = 0.3$ for the helium gas.[10] For the gas-gap high pressure 50 mbar was selected. The gas-gap low pressure should be as low as possible. A pressure below $5 \cdot 10^{-3}$ mbar gives a maximum conduction heat loss of 0.1 W which seems low enough for our application.

We intend to vary the pressure in the gas-gap by a separated sorption compressor unit that is integrated in the gas-gap. This unit can e.g. be a metal-hydride acting as sorber material with H_2 as the working gas.[9,11] To test the compressor operation in a laboratory setup, we created the pressure swing in the gas-gap by switching the gas-gap volume between a low-pressure and a high-pressure 'reservoir' with the help of two active valves. This, and the other components of the experimental setup, is shown schematically in Fig. 6. A vacuum pump is used as the low-pressure 'reservoir'. For the high-pressure reservoir, helium gas of 1.5 bar is expanded over two flow restrictions to a

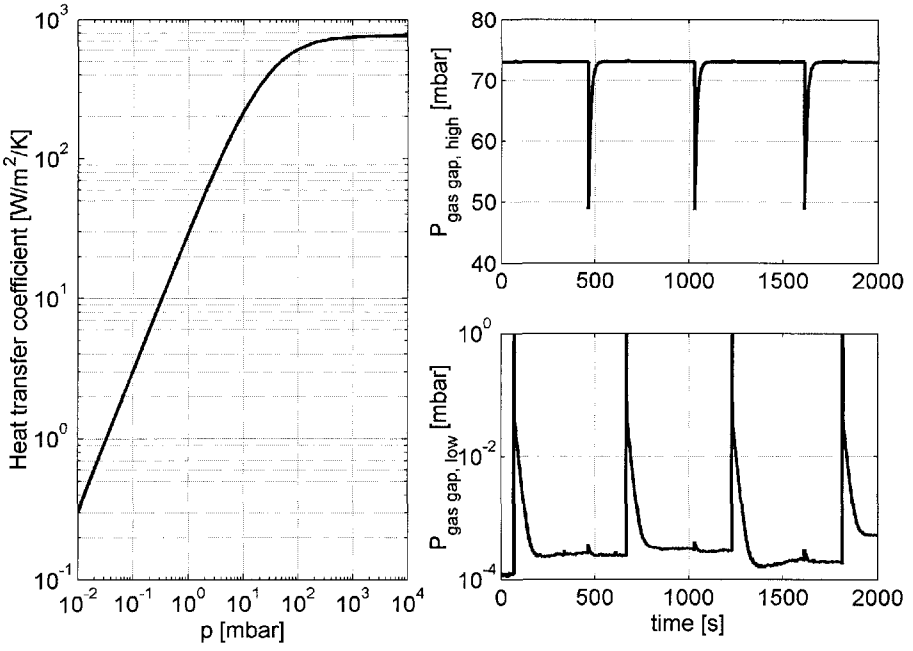

Figure 5. (a) Theoretic heat transfer coefficient in the gas gap for helium gas with an accommodation coefficient of 0.3. (b) Pressure in the high-pressure (top) and low-pressure 'reservoir' of the gas-gap control system.

vacuum pump. The volume between the two restrictions acts as the high-pressure 'reservoir'. Note that the pressure dependent heat transfer of hydrogen does not deviate much from that of helium gas. Figure 5b shows the time-dependent behavior of the pressure in the reservoirs as the active valves are switched. The pressures in both the high-pressure and the low-pressure reservoir are measured with MKS Baratron 627B pressure transducers that are located directly behind the active valves. The gas gap high pressure was set to 73 mbar. With this setting, the pressure in the reservoir is nearly always above 50 mbar. After opening the valve, the pressure in the high-pressure reservoir reaches its equilibrium value again within about 30 seconds. For the low-pressure reservoir, equilibrium takes about 100 seconds, but within the first 3 seconds, the pressure has dropped with more than a factor 1000. According to Fig. 5b, the heat transfer rate has dropped with a factor of about 500. These time periods are acceptable for our application.

Buffer Volumes

The size of the pressure variations in both the high-pressure and the low-pressure buffer depend on the mass flow through the cold stage, the cycle time and the volume as described by Eq. 1.

$$\Delta p = \frac{\dot{m}_{cool} RT}{VM}\left(t_{cycle} - t_{flow}\right) \tag{1}$$

Here, Δp [Pa] is the pressure variation in the buffer, $\dot{m}$ [kg/s] the average mass flow through the cold stage, R [Jmol^{-1}K^{-1}] the universal gas constant, T [K] the absolute temperature, V [m^3] the buffer volume, M [kg/mol] the mole mass of the working fluid, t_{cycle} [s] the cycle time and t_{flow} [s] the period during which there is a gas flow between the compressor cell and the buffer under consideration. For the low-pressure buffer a volume of 300 cm^3 was selected while for the high-pressure buffer a volume of 75 cm^3 was taken.

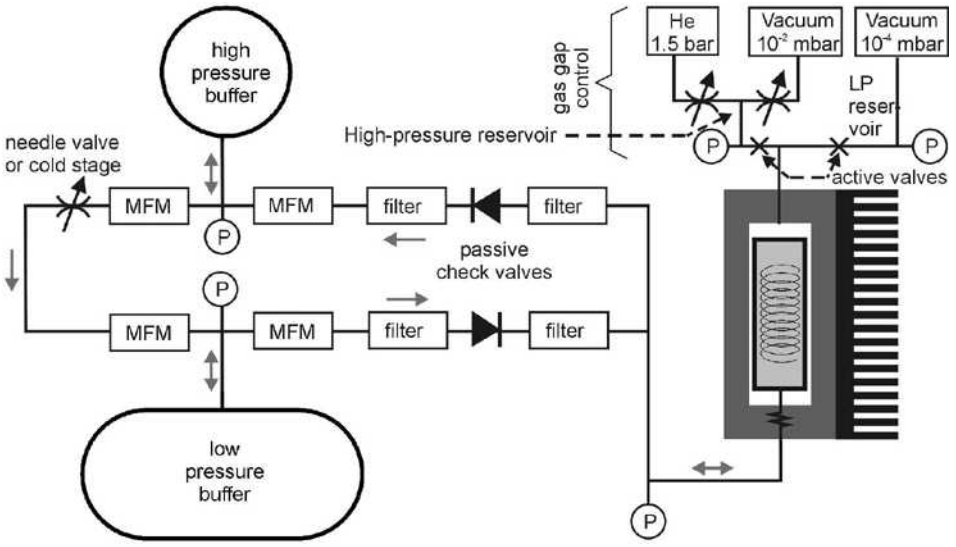

Figure 6. Schematic overview of the experimental setup. See text for details.

Other Components

For the check valve we used Swagelok 6L-CW4S4 valves. This is an all-welded check valve with a fluorocarbon coating on the poppet. They have a cracking pressure of 10 ± 2 mbar, an estimated xenon leak flow of 11 μg/s and an estimated pressure drop of $1 \cdot 10^{1}$ mbar for a xenon flow of 2 mg/s at 1 bar absolute pressure. To prevent pollution of the check valves, Valco filters with screens of 10 μm pore size are applied on both sides of the check valves.

To test the compressor performance, the first experiments were performed without a cold stage. Instead, a tunable needle valve is used over which the pressure can drop. The pressures of the high and low-pressure buffers are measured with Druck PTX1400 sensors. The mass flows between the buffers and the sorption compressor cell and between the buffers and the flow restriction are measured with Bronkhorst EL-FLOW mass flow controllers. The data are sampled with a National Instruments multiplexer board connected to an E-series DAQ-card. Each channel is sampled with 500 Hz and averaged over 200 samples before the data was further processed. A custom written LabVIEW program is used to control the system.

RESULTS AND DISCUSSION

Measurement Results

The behavior of pressure, mass flow and the temperature of the thermocouple as measured are shown in Fig. 7. During phase A, the sorber container is heated with a duty cycle of 80%. This resulted in a time-averaged input power of 3.7 W. During the other 20%, the temperature is measured. Directly after having heated the container, the observed temperature reduces rapidly. The heat distributes more uniformly over the sorber container resulting in a temperature decrease at the position of the thermocouple. During phase B, the sorber container is heated during only 50% of the time, resulting in an average input power of 2.3 W. In this way, the temperature profile in the sorber container is smaller compared to phase A, and more gas will be desorbed at the maximum temperature that is allowed. During this experiment the maximum temperature was set to 550 K.

The behavior of the pressures in the sorber container and the buffers is as expected (compare Fig. 7 with Fig. 3). The pressure in the container alternates between 2.0 and 12.6 bar. The high-pressure buffer fluctuates between 11.8 and 12.4 bar and that of the low-pressure buffer varies between 2.1 bar and 2.3 bar. The average mass flow through the flow restriction is 0.50 mg/s. The

maximum flow through the cold stage is 8% larger than the average flow; the minimum flow is 5% less than the average. The broad band in the mass flow from the cell to the high-pressure buffer is caused by the intermittent heating during phase B.

Once the compressor operation is stable, the time period each phase takes is nearly constant. The average time of each phase is 207 s for phase A, 174 s for phase B, 65 s for phase C and 135 s for phase D. When considering the individual cycles, the deviations fall within a band of 3% from the average. Of course, for a detailed analysis of the stability of the compressor many more cycles should be considered. When applying equation (1) to these times a pressure variation in the high-pressure buffer of 0.63 bar results and 0.14 bar for the low-pressure buffer. The number for the low-pressure buffer agrees exactly, for the high-pressure buffer the deviation is 0.09 bar. This may be caused by an error in the estimate of the total high-pressure volume.

Consequences for Cooler Behavior

As stated before, if the compressor is connected to a Linde-Hampson cold stage, the variation of the pressure in the low-pressure buffer affects the temperature of the liquid in the boiler of the cold stage. In Fig. 8, the measured pressures from the low-pressure buffer are converted to the temperature of the liquid within the boiler using GasPak.[12] It turns out that the temperature varies between 178.8 K and 180.3 K, a fluctuation of 1.5 K. Apart from common techniques to control a cooler's cold tip temperature, with this configuration one can reduce the variation by increasing the buffer volume size.

Also the cooling power will vary somewhat because of the time-dependent flow through the cold stage and the pressure-dependent enthalpy of cooling. This will result in a variable liquid production rate and is in general not a problem.

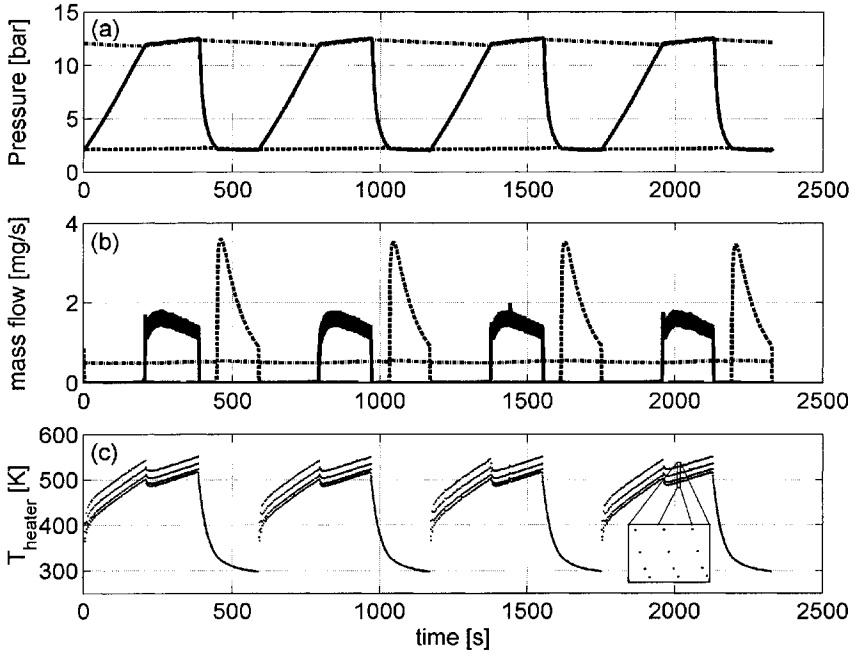

Figure 7. Performance of a single cell compressor (a) Pressure with time; P_{cell} (solid), $P_{LP,buffer}$ (dashed), $P_{HP,buffer}$ (dash-dotted). (b) Mass flow with time; cell to HP_{buffer} (solid), flow through restriction (dash-dotted), LP_{buffer} to cell (dashed). (c) T_{heater} with time. The measured temperatures are shown as dots (see inset). While heating, the temperature cannot be determined.

Possible Improvements

At the moment, a pressure difference from 2.0 to 12.6 bar is achieved. As discussed earlier, a minimum high-pressure of 16 bar is required in order to liquefy the gas in the precooler and, as a result, to largely increase the cooling power. A way to improve the current setup is to reduce the void volume in the sorber container part of the setup. Ways to do this include filling up void volume in the tubing, using smaller check valves[13], and using other activated carbons with inherently lower void volume fractions. Another improvement can be made by optimizing the compressor cell control software. A shorter cycle time will increase the pressure difference between the high-pressure and low-pressure buffers as long as this effect is not counteracted by a decrease in the amount of desorbed gas because of a larger temperature profile in the sorber container. Another way to improve the cooler performance is to increase the maximum temperature that is allowed in the sorber container.

CONCLUSIONS

A new sorption compressor design was proposed consisting of only one compressor cell, two check valves and two buffer volumes. Such a design is easier to operate compared to a compressor consisting of multiple cells and increases the reliability of the cooler. The principle was demonstrated using a setup with a sorption compressor with a volume of about 8 cm^3 that was filled with Maxsorb activated carbon and xenon as a working fluid. A continuous flow of 0.5 mg/s was established with a pressure difference from 2.0 to 12.6 bar. The low-pressure buffer had a pressure fluctuation of 0.2 bar resulting in a theoretical fluctuation in the temperature of the liquid in the boiler of 1.5 K. A high pressure of 16 bar is required to liquefy the high-pressure gas by a thermoelectric precooler and hence largely increase the cooling power. Ways to achieve this with the current setup include reduction of the void volume of the sorber container and optimization of the heater control. The proposed design is an alternative to the sorption compressor units consisting of multiple compressor cells that are operated out of phase.

ACKNOWLEDGMENT

This research was supported by the MESA+ research institute of the University of Twente.

REFERENCES

1. Bowman Jr., R.C., Kiehl, B. and Marquardt, E. "Closed-Cycle Joule-Thomson Cryocoolers," *Spacecraft Thermal Control Handbook, Volume II: Cryogenics*, edited by M. Donabedian, The Aerospace Press, El Segundo, CA (2003), pp. 187-216.

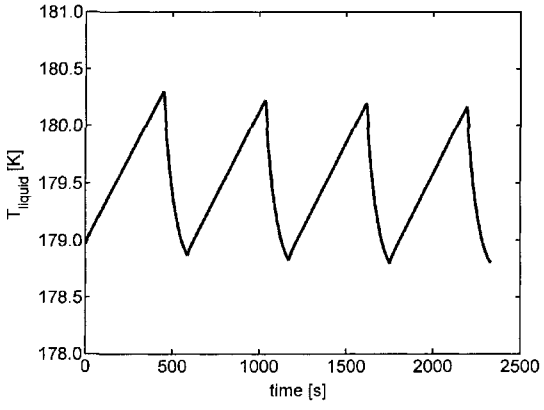

Figure 8. Calculated temperature of the liquid in the boiler of a cold stage as derived from the pressure in the low-pressure buffer.

2. Bard, S., "Improving adsorption cryocoolers by multi-stage compression and reducing void volume," *Cryogenics*, vol. 26 (1986), pp. 450 – 458.

3. Burger, J.F., Ter Brake, H.J.M., Holland, H.J., Venhorst, G., Hondebrink, E., Meijer, R.J., Veenstra, T.T., Rogalla, H., Coesel, M., Lozano-Castello, D. and Sirbi A., "Development of a 4 K Sorption Cooler for ESA's Darwin Mission: System-Level Design considerations," *Cryocoolers 13*, Kluwer Academic/Plenum Publishers, New York (2005).

4. Burger, J.F., Holland, H.J., Wade, L.A., Ter Brake, H.J.M., and Rogalla, H., "Thermodynamic considerations on a microminiature sorption cooler," *Cryocoolers 10*, Kluwer Academic/Plenum Publishers, New York (1999), pp. 553-563.

5. Marlow Industries, Inc., 10451 Vista Park Road, Dallas, Texas, USA. http://www.marlow.com

6. The Kansai Coke & Chemicals Co. Ltd., 1-1 Oh-Hama, Amagasaki, Japan 660.

7. Otowa, T., Tanibata, R., and Itoh, M., "Production and adsorption characteristics of MAXSORB: high-surface-area active carbon," *Gas separation & purification*, vol. 7, no. 4 (1993), pp. 241-245.

8. Burger, J.F., Holland, H.J., Seppenwoolde, J.H., Berenschot, E., Ter Brake, H.J.M., Gardeniers, J.G.E., Elwenspoek, M. and Rogalla, H., "165 K microcooler operating with a sorption compressor and a micromachined cold stage," *Cryocoolers 11*, Kluwer Academic/Plenum Publishers, New York (2001), pp. 551-560.

9. Burger, J.F., Holland, H.J., Van Egmond, H., Elwenspoek, M., Ter Brake, H.J.M., and Rogalla, H., "Fast gas-gap heat switch for a microcooler," *Cryocoolers 10,* Kluwer Academic/Plenum Publishers, New York (1999), pp. 565 – 574.

10. Corruccini, R.J., "Gaseous heat conduction at low pressures and temperatures," *Vacuum*, vol. VII & VIII, 1957-1958, pp. 19-29.

11. Gardeniers, J.G.E., Burger, J.F., van Egmond, H., Holland, H.J., Ter Brake, H.J.M., Elwenspoek, M., "ZrNi thin films for fast reversible hydrogen pressure actuation," *ACTUATOR 2000.* 7th International Conference on New Actuators and International Exhibition on Smart Actuators and Drive Systems. Conference Proceedings, 2000, pp. 208-211.

12. Cryodata. Inc, http://www.cryodata.com

13. Burger, J.F., Van der Wekken, M.C., Berenschot, E., Holland, H.J., Ter Brake, H.J.M., Rogalla, H., Gardeniers, J.G.E., and Elwenspoek. M.,"High pressure check valve for application in a miniature cryogenic sorption cooler," *Twelfth IEEE International Conference on Micro Electro Mechanical Systems* (1999), pp. 183-188.

Cryogenic Testing of Planck Sorption Cooler Test Facility

B. Zhang, D. Pearson, J. Borders, B. Franklin, M. Prina and J. Hardy

Jet Propulsion Laboratory
California Institute of Technology
Pasadena, CA 91109

D. Crumb

Swales Aerospace
Pasadena, CA 91107

ABSTRACT

A test facility has been upgraded in preparation for testing of two hydrogen sorption cryocoolers operating at 18/20 K. These sorption coolers are currently under development at the Jet Propulsion Laboratory (JPL) for the Planck mission sponsored by the European Space Agency (ESA). The two units share the same process and component design with different plumbing configurations required for spacecraft integration. Previous effort at JPL has led to the successful demonstration of a prototype of the sorption cooler. Each flight unit of the sorption cooler will be tested in a vacuum chamber with simulated background environment for the spacecraft. GM cryocoolers, bulk LN2, and a chiller unit are used to establish nominal temperature stages at 50, 100, and 280 K, respectively, allowing the cold end of the sorption cooler to operate at 18/20 K.

This work summarizes the scope of the test facility upgrade, including design for cryogenic cooling power delivery, system thermal management, insulation schemes, and data acquisition techniques. Ground support equipment for the sorption coolers, structural features of the test chamber, and the vacuum system involved for system testing are also described in detail.

INTRODUCTION

Two Planck Sorption Cooler units are to be tested at the Planck test facility. The facility has been upgraded from the Engineering Breadboard (EBB) configuration to the current configuration for the testing of flight sorption cooler units.

The two units share the same process and component design with different plumbing configurations required for spacecraft integration. Previous effort had led to successful demonstration of a prototype of the sorption cooler. Each flight unit of the sorption cooler will be tested in a vacuum chamber with simulated background environment for the spacecraft. Two Gifford-McMahon (GM) cryocoolers, bulk liquid nitrogen (LN2), and a chiller unit are used to establish nominal temperature stages at 50, 100, and 280 K, respectively, allowing the cold end of the sorption cooler to operate at 18/20 K.

Cryocoolers 13, edited by R. G. Ross, Jr.
Springer Science+Business Media, Inc., New York, 2004

The sorption cooler incorporates hydrogen hydride compressor technology[3] with a Joule-Thomson refrigerator cold end and hence eliminates moving parts in both the warm and cold ends. This type of configuration is especially suitable for certain space applications where low vibration levels are crucial.

TEST OBJECTIVES

Objectives for the cryogenic test are to verify chamber vacuum system integrity and cryogenic cooling capabilities for simulating operating environment of the flight hardware. Specifics are summarized as follows:

- Vacuum leak rate < 1.0×10^{-9} atm.- cc/s
- Ultimate chamber pressure < 1.0×10^{-6} torr
- Temperature of 50 K shroud reaches 90 K within 48 hours
- All other temperatures reach 90 K within 24 hours
- Temperature at PC3C reaches 45 K within 24 hours.
- 100 K plate temperature < 120 K
- 50 K plate temperature < 60 K within 7 days
- PC3C < 40 K with zero power input
- PC3C < 45 K with 3 W applied
- PC3A and B < 60 K
- 50 K shroud temperature < 45 K
- LN2 tank holding time > 72 hours.

CHAMBER DESCRIPTION

The test chamber has an outer diameter of 1.8 m with an internal height of 2.8 m, which provides sufficient room to accommodate the testing of the sorption coolers.

Structural Features and Analysis

As shown in Figure 1, the 50 K (V3) plate of the Piping and Cold End (PACE) assembly is supported by four struts which therefore bear almost the entire weight of PACE. These struts are secured to the 100 K plate. The 100 K shroud is supported by the 100 K plate. The bottom flange of the 100 K shroud is bolted to the 100 K plate. Together they form the enclosure for the 50 K stage. The LN2 tank is both mechanically and thermally attached to the top of the 100 K shroud. Six posts sit on top of a base plate and support the 100 K plate. The Sorption Cooler Compressor (SCC) and Chiller Panel Assembly (CPA) will be bolted down to the base plate. Finally, the base plate is supported by three pads at the bottom of the vacuum chamber. These pads are situated directly above the three legs of the chamber. Detailed description and design analysis for the chamber structure are given in Ref. 4.

Thermal Design

For the cryogenic test alone, two temperature stages are established inside the test chamber for thermal management. Nominal temperatures for these stages are set at 50 K and 100 K. Two additional stages at 18/20 K and 260 K will be further established for flight hardware testing.

The 50 K stage is cooled by two GM cryocoolers, while the 100 K stage is cooled by the LN2 tank. LN2 precoolers are installed in 50 K and 100 K plates to accelerate the initial cool down from ambient temperature to 90 K. Cooling power from these GM cryocoolers is delivered through flexible thermal straps and solid thermal bus bars. The thermal strap is made of braided multi-strand copper wires. Each strap consists of 1000 wires with a nominal diameter of 0.01 in. The straps are individually trimmed to length in order to reduce their thermal impedance.

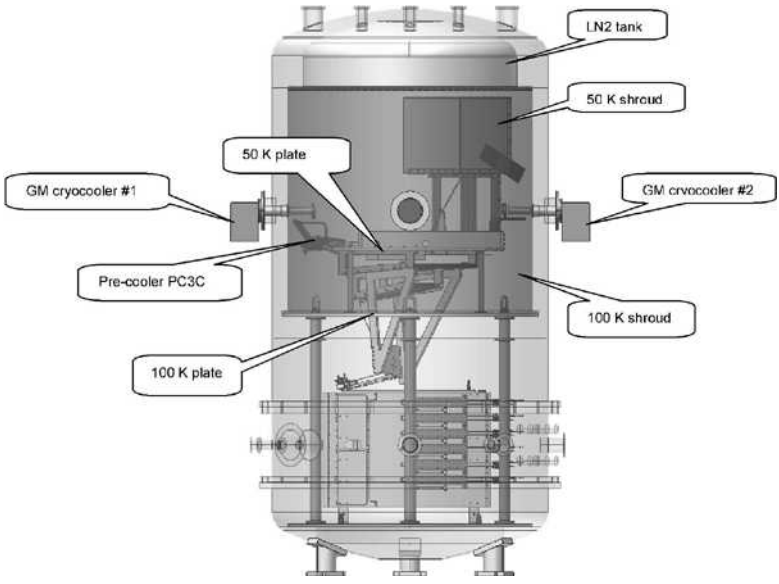

Figure 1. Test chamber schematic.

A substantial amount of multilayer insulation (MLI) has been installed in the vacuum chamber for thermal insulation of the 50 K and 100 K temperature stages. Each blanket consists of 20 alternating layers of 0.5 mil, perforated aluminized mylar and Dacron spacer material. Detailed thermal system management schemes and chamber thermal analysis are given in Ref 5.

Facility and Testing Equipment

Supporting equipment for the test chamber includes vacuum pumps and cooling equipment including cryogenic cooling equipment.

A vacuum pump (Stokes Model 212-11) equipped with a roots blower (Stokes Model 607-1) serves as the main roughing pump for the chamber. The throughput of the pump is rated at 150 cfm, while the roots blower is rated at 600 cfm with an ultimate below milli-torr vacuum level.

A turbo molecular pump or TMP (Seiko Seiki Model STP400) handles pumping in the high vacuum range. The TMP has a pumping speed of 420 liter/s for nitrogen at vacuum levels below 1.0×10^{-4} torr. The TMP is backed up by an explosion-proof rotary pump (Edwards Model E2M30FX). A solenoid valve between the TMP and the fore-line pump closes in the event of power failure to prevent system contamination due to oil backstreaming from the fore-line pump.

A chiller (BOC Edwards Model TCU 40/80) removes the heater input power of the sorption compressor elements. The TCU 40/80 is a single-channel temperature control unit with a cooling capacity of 350 W at –40 °C or 2000 W at –20 °C. The chiller unit was not used during the cryo test.

Two GM cryocoolers of the same model (CTI Model 1020 Cryodyne) maintain the operating temperature of the precoolers (PC1-3) and the 50 K stage environment. The 1020 is a two-stage regenerative type cryocooler. With a 10-W heat load applied to the first-stage cold station at 42 K, it is capable of lifting 4 W at 14.5 K or 15 W at 26 K at the second stage. The first-stage cooling capacity reaches a maximum of 50 W at 93 K while the second stage capacity remains the same.

A 300-liter liquid nitrogen tank sits on top of the 100 K shroud and cools the entire 100 K stage. During normal operation, this LN2 tank needs to be filled once a week. Gaseous nitrogen is exhausted through a vent stack to atmosphere outside the test facility. LN2 Pre-cooling loops are mounted on the 50 K and 100 K plates to speed up the initial cool-down. These cooling loops will be shut off and evacuated once the plates cool down to below 90 K.

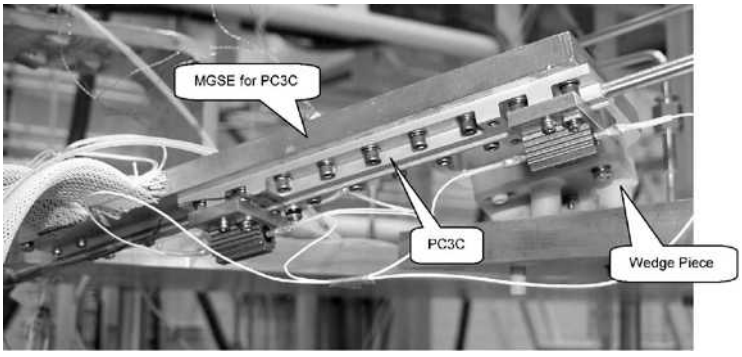

Figure 2. Instrumentation for PC3C.

Instrumentation and Data Acquisition

Temperature sensors are strategically located in the chamber to collect data at all temperature stages. Heaters are used to maintain preset temperature levels at PC3C, 50 K shroud, and 50 K plate. The high vacuum range is monitored by hot and cold cathode gauges, while the rough vacuum end is covered by a mechanical pressure gauge (Leybold Diavac DV1000). A data acquisition system based on Labview logs readings from temperature sensors and power input to instrument heaters.

As a critical element of the cryogenic testing, pre-cooler PC3C is equipped with temperature sensors and heaters to simulate the operating condition of the sorption cooler. A photo of PC3C mounted on its MGSE is shown in Figure 2. PC3C is bolted to its MGSE by eighteen M4 stainless steel bolts. These bolts are lubricated and torqued to 5 in-lbf to achieve a compression of 286 lbf per bolt to avoid reaching the yield point of copper. Heaters mounted on the PC3C side, together with temperature sensors mounted on both the PC3C and its MGSE sides, allow a rough assessment of the temperature drop across their interface. The surface of PC3C is gold coated to improve thermal contact at the interface with its MGSE.

The MGSE plate for PC3C is anchored to the 50 K plate via a wedge piece made of G10 material to reduce parasitic heat leak from the 50 K plate.

Test Setup

A photo of the chamber top view is presented in Figure 3 with major elements called out as shown. The dummy 50 K plate built solely for the cryogenic test will be replace by the PACE assembly for sorption cooler system test. The rest shown in the photo are actual MGSE parts to be used for flight hardware testing.

TEST RESULTS

The cryogenic test commenced in late January of 2004 and completed in less than ten days. Experimental data, including temperature readings and heater input power, were continuously recorded. Selective data reflecting typical operating environments are presented in this section.

Chamber Cool-down

During the initial vacuum pump-down, warm nitrogen gas (GN2) was used to back-fill the chamber. This process was repeated three times and each time the chamber pressure was cycled between 10^{-2} torr and 300 ~ 500 torr. The two GM cryocoolers were turned on once the chamber vacuum level was brought down to below 10^{-5} torr by the turbo molecular pump. Immediately following that, liquid nitrogen from an external storage tank was supplied to run the pro-coolers and to fill the LN2 tank.

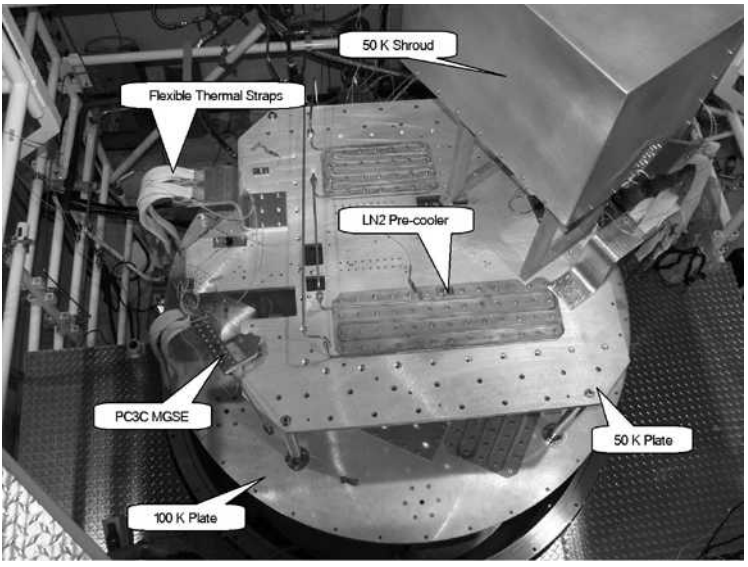

Figure 3. Top view of chamber setup.

The 50 K and 100 K stages (with the exception of the 50 K shroud) were cooled down to 90 K within a day. The 50 K shroud was cooled down by the second stage of GM #2 alone without any LN2 pre-cooling. It took less than 42 hours for the rear side of the shroud to reach 90 K, but slightly more than 4 days to reach 20 K.

Temperature readings from all sensors during the cool-down and cryogenic test are graphically presented in Figure 4.

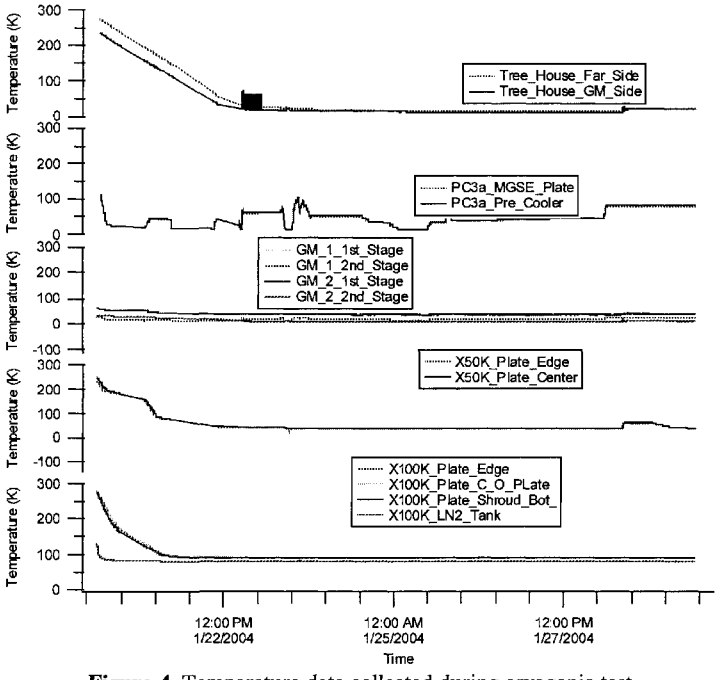

Figure 4. Temperature data collected during cryogenic test.

Temperature Control at PC3C

The temperature at pre-cooler PC3C is controlled by the Proportional Integral and Derivative (PID) algorithm of Labview. Heaters are used to simulate the actual cooling requirement of approximately 3 W. At zero heater input power, the temperature at PC3C bottomed out below 13 K. The heater input power was subsequently ramped up in several steps and reached a maximum of 10 W, exceeding the required level by more than a factor of three. The additional power elevated the temperature at PC3C and made it possible to test the sorption cooler with PC3C running at temperatures up to 70 K.

Two temperature sensors on each side of the interface between PC3C and its mechanical ground support equipment (MGSE) are located approximately 80 mm apart. As such, the difference between their readings (ΔT_{Total}) includes not only the temperature drop across the interface, designated by $\Delta T_{Interface}$, but also the temperature drop through the 80-mm spacing in the MGSE plate. The later was then analytically evaluated and subtracted from ΔT_{Total} to obtain $\Delta T_{Interface}$. The dependence of these temperature differences on input power can be best described in polynomial terms through regression as follows:

$$\Delta T_{Total} = 0.0049\dot{Q}^3 - 0.0329\dot{Q}^2 + 0.197\dot{Q} + 0.0106 \quad (1)$$

$$\Delta T_{Interface} = 0.0079\dot{Q}^2 + 0.0026\dot{Q} + 0.0507 \quad (2)$$

The conductance across the interface $C_{Interface}$ is also calculated and plotted in Figure 5 as a function of heater input power. The data points can be best fitted with the following fourth order polynomial:

$$C_{Interface} = -0.0055\dot{Q}^4 + 0.1746\dot{Q}^3 - 1.9867\dot{Q}^2 + 7.931\dot{Q} + 10.886 \quad (3)$$

Temperature Control at 50 K Shroud

Heaters mounted on the 50 K shroud allow the control of the shroud temperature. To simulate the operating environment of the spacecraft, the heater mounted on the front end of the shroud was turned on at 1.814 W. Temperature readings at this input power level and those at zero input power are given in Table 1.

Temperature Control at 50 K Plate

Temperature readings from sensors on the 50 K plate and GM#2 first stage are given in Table 2 at zero and 13.91 W heater input power, respectively.

Vacuum System Integrity

The vacuum system integrity was successfully verified through the cryogenic test. The chamber had no detectible leak that could be picked up by a helium leak detector with a sensitivity of 1.0×10^{-12} atm-cc/s. In the initial pump-down, the chamber vacuum reached levels at 10^{-3} torr and

Table 1. Temperature control at 50 K shroud.

Sensor Designation	Temperature (K)	
	Power = 0 W	Power = 1.814 W
GM #2, 2nd stage	7.7	10.2
50 K shroud, front	11.14	18.5
50 K shroud, rear	13.57	20.2

Table 2. Temperatures control at 50 K plate.

Sensor Designation	Temperature (K)	
	Power = 0 W	Power = 13.91 W
GM #2, 1st stage	35.01	39.65
50 K plate, center	36.45	59.47
50 K plate, edge	36.56	59.99

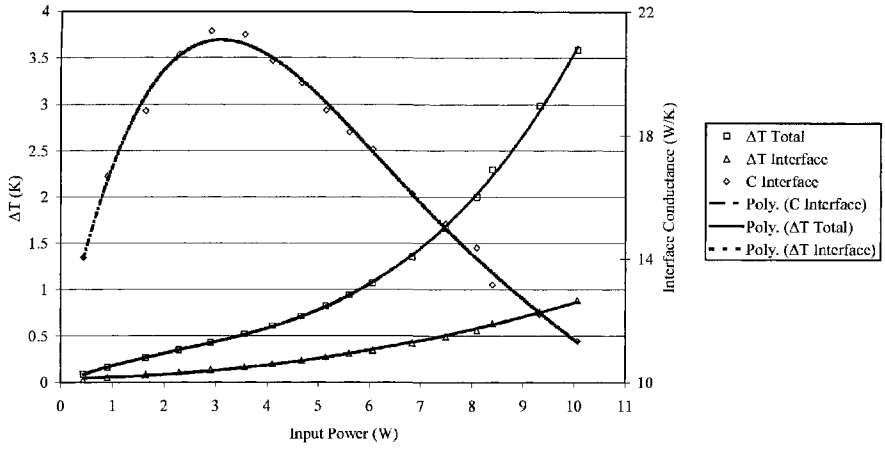

Figure 5. Temperature control at PC3C.

10^{-6} torr in two hours and twenty-four hours, respectively. The ultimate chamber vacuum reached was 6.7 x 10^{-7} torr.

LN2 Tank Holding Time

The LN2 tank has a capacity of approximately 300 liters. The holding time of the tank under normal operation directly reflects the parasitic heat leak into the 100 K stage. The recorded holding time was more than a week (177 hours) after it was filled the last time. This translates into a boil-off rate close to 0.381 g/s, or a heat leak of 74.7 W. It should be noted that part of this heat leak directly entered the LN2 tank from the top of the chamber and had no impact on the thermal performance of the 100 K stage.

DATA ANALYSIS

Conductance of Thermal Straps

As mentioned previously, cryogenic cooling power from the GM cryocoolers was delivered to the 50 K stage through flexible copper thermal straps. Thermal conductivity of copper is a strong function of temperature at cryogenic temperatures. This temperature dependence becomes most significant around 20 K. To correlate experimental data with theoretical predictions, temperature readings from three thermal straps are analyzed. These straps are used to cool PC3C, the 50 K shroud, and the 50 K plate. For each strap, temperature readings from sensors attached to both ends are used in conjunction with heater input power and strap geometry to obtain a value for the thermal conductivity integral over the temperature range experienced by the strap based on the equation

$$\int_{T_{GM}}^{T_{LOAD}} k dT = \frac{\dot{Q}}{A/L} \tag{4}$$

where k is thermal conductivity; T_{LOAD} and T_{GM} are temperatures at the load and GM cold head, respectively; $\dot{Q}$ is the heater power input, A is the cross-sectional area of the strap, and L is the length of the strap. Once the value of the thermal conductivity integral is calculated, it is then compared with that generated by a commercial database CRYOCOMP [6] through an iteration process to determine the ratio of residue resistance or RRR value for the strap. The RRR values calculated in this way for the three thermal straps are given in Figure 6. To estimate the parasitic heat leak at zero heater input power, a conductivity integral is generated by CRYOCOMP by using temperature readings and a RRR value either interpolated or extrapolated from all the RRR values calculated at various input power levels.

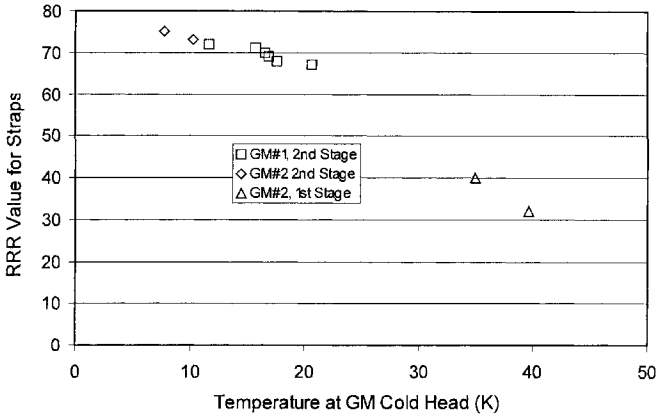

Figure 6. RRR values calculated for three thermal straps.

Table 3. Test facility heat leak summary.

Temperature Stage	Cooling Source	Heat Leak (W)
PC3C	GM #1, 2nd stage	0.28
50 K Shroud	GM #2, 2nd stage	0.77
50 K plate	GM # 1 and #2, 1st stage	1.5
100 K stage	LN2 tank	74.7

Heat Leak Summary

Parasitic heat leaks into the system are estimated mostly based experimental data. For system components cooled by flexible copper thermal straps, thermal properties for copper derived from CRYOCOMP are used. Heat leak into the 100 K stage is calculated from the boil-off rate of liquid nitrogen in the LN2 tank. Heat leaks are summarized in Table 3.

Due to the small size of PC3C, heat leak through the MLI blanket is negligible. The total heat leak of 0.28 W can be considered to come from the G10 wedge piece that supports PC3C over the 50 K plate. Neglecting the conduction through three G10 legs, heat leak into the 50 K shroud is through the MLI blanket. Considering a surface area of 1.6 m^2, the average heat leak per unit surface area is approximately 0.48 W/m^2. Among the 1.5 W heat leak into the 50 K plate, 0.69 W are attributed to the four stainless steel struts. This value is analytically evaluated based on the strut geometry and conductivity integral at the actual temperature boundary conditions of 36 K and 90 K. Over an approximate surface area of 2.66 m^2 (1.33 m^2 per side) for the 50 K plate, the average heat leak through the 50 K plate MLI blanket is about 0.3 W/m^2.

To estimate the heat leak into the 100 K stage excluding the LN2 tank, heat flux along the shroud is roughly assessed by considering conduction alone. Using the ratio of cross-sectional area over length for the shroud at 0.22 m and temperature boundary conditions at 77.8 and 88.86 K, a thermal conductivity integral is evaluated at 1300 W/m, which yields a heat transfer rate at 28.19 W.

Conduction through the six posts supporting the 100 K stage is estimated at 8.68 W. Subtracting this amount of heat leak, the heat leak through the MLI blankets becomes 19.51 W. The total surface area of the 100 K stage exposed to the 300 K environment is about 9.34 m^2. The average heat leak over unit area of MLI blanket is about 2.1 W/m^2. It should be noted that this approach underestimates the actual heat leak through the MLI blankets, since it neglected the interaction of radiation and conduction along the shroud. Heat leaks into different temperature stages are summarized in Table 3.

Comparison of Experimental Data with Test Objectives

Experimental data collected through the cryogenic test serve as references for future chamber operation. As shown in Table 4, they compare favorably against the test objective.

Table 4. Comparison of test results with objectives.

Performance Criterion	Test Objective	Results
Chamber vacuum leak rate	$< 1.0 \times 10^{-9}$ atm.-cc/s	$< 1.0 \times 10^{-9}$ atm.-cc/s
Ultimate chamber vacuum	$< 1.0 \times 10^{-6}$ torr	6.7×10^{-7} torr
50 K shroud reaches 90 K	48 hrs	41.5 hrs
50 K stage reaches 90 K	24 hrs	12 hrs
100 K stage reaches 90 K	24 hrs	13.7 hrs
50 K plate reaches 60 K	7 days	49.2 hrs
PC3C reaches 45 K	24 hrs	7.7 hrs
PC3C no-load temperature	< 40 K	13 K
PC3C operating temperature	< 45 K at 3 W	< 32 K at 4.67 W
PC3A and B operating temperature	< 60 K	< 37 K
50 K shroud operating temperature	< 45 K	< 25 K
100 K plate operating temperature	< 120 K	< 90 K
LN2 tank holding time	> 72 hrs	177 hrs

DISCUSSION AND CONCLUSIONS

The 50 K shroud had the longest cool-down time compared to the rest of the system mainly due to the absence of an LN2 pre-cooling circuit. Other factors include the fact that the low heat leak into the shroud led to a low operating temperature at the GM cold head, where cooling capacity is low, and the thin wall of the shroud is a compromise between less thermal mass and higher conductance. Nevertheless, the cool-down speed of the 50 K shroud can be considered acceptable and no improvement measures seem to be necessary.

In conclusion, the cryogenic test of the Planck test facility was carried out successfully. Experimental data compare favorably against those from previous testing of the sorption cooler prototype. With all test objectives achieved or succeeded, this experiment demonstrated that the test facility has adequate cryogenic cooling power and proper delivery means to create and maintain required testing environment for future testing of flight units of the Planck sorption coolers.

ACKNOWLEDGMENT

The research described in this paper was carried out by the Jet Propulsion Laboratory, California Institute of Technology, under a contract with the National Aeronautics and Space Administration.

REFERENCES

1. Collaudin, B. and Passvogel, T., "The FIRST and PLANCK 'Carrier' Missions. Description of the Cryogenic Systems," *Cryogenics,* Vol. 39 (1999) pp. 157-165
2. Prina, M., et al., "Initial Test Performance of a Closed-Cycle Continuous Hydrogen Sorption Cooler, the Planck Sorption Breadboard Cooler," *Cryocoolers 12*, Kluwer Academic/Plenum Press, New York (2003), pp. 637-642.
3. Bowman, Jr., R.C., et al., "Evaluation of Hydride Compressor Elements for the Planck Sorption Cooler," *Cryocoolers 12*, Kluwer Academic/Plenum Publishers, New York (2003), pp. 627-635.
4. Zhang, B. "Structural Analysis of Test Chamber for Planck Sorption Cooler Non-flight Configuration Testing," *Design Monograph*, JPL (2003).
5. Zhang, B. "Facility Thermal Analysis for Planck Sorption Cooler Non-flight Configuration System Testing," *Design Monograph*, JPL (2003).
6. Cryodata, "User's Guide to CRYOCOMP," version 3.0, Colorado, (1997).

Cryogenic Tests of a 0.1 K Dilution Cooler for Planck-HFI

L. Sentis and J. Delmas[1], Ph. Camus[2], G. Guyot[3], and Y. Blanc[4]

[1]Air Liquide Advanced Technology Division, AL/DTA
Sassenage, France
[2]National Center for Scientific Research
Centre de Recherche des Très Basses Températures, CNRS/CRTBT
Grenoble, France
[3]Institut d'Astrophysique Spatiale, CNRS/IAS
Orsay, France
[4]French National Space Agency, CNES
Toulouse, France

ABSTRACT

Planck is the third medium-size scientific mission (M3) of the ESA HORIZON 2000 program and is to be launched in 2007. The bolometer-based Planck/HFI (High Frequency Instrument) is cooled down to 100 mK in order to measure the Cosmic Microwave Background (CMB) radiation with sensitivity close to the fundamental photon noise limit. We report the critical design drivers for the open-cycle dilution system and the solutions adopted.

The system must be able to operate for 24 months in space with severe constraints on the temperature stability. The thermomechanical architecture is described with the strong integration of the dilution with the focal plane. Thin NbTi superconducting tubes are used to achieve both a mechanical stiffness and a low thermal conductivity for the supporting focal plane. A passive thermal filter based on the high heat capacity of the Holmium-Yttrium alloy is used to achieve the low 20 nK/$\sqrt{\text{Hz}}$ thermal fluctuation spectrum required. In order to survive the vibration level during launch, a locking mechanism, based on the shape memory alloy NiTi, has been designed to hold the focal plane while at ambient temperature. Control of the purity of the ^{3}He and ^{4}He isotopes is essential for long-term operation. In addition to the initial purity control, several filtering systems are implemented within the injection system.

The different critical items have been validated with an Elegant Breadboard whose results are reported in this article.

INTRODUCTION

The Planck satellite design is driven by the thermal requirements. The scientific payload is cooled by passive radiators (V-grooves) down to 50 K.[1] A Joule-Thomson (JT) expansion of hydrogen using a sorption compressor cools the instrument down to 20 K.[1] A JT expansion with helium using mechanical compressors provides 4 K cooling for HFI. The system provides both 100 mK, thanks to an open-cycle dilution, and 1.6 K with a JT expansion on the isotope mixture

Cryocoolers 13, edited by R. G. Ross, Jr.
Springer Science+Business Media, Inc., New York, 2004

Figure 1. The 51 L helium tank for the PLANCK-HFI dilution cooler.

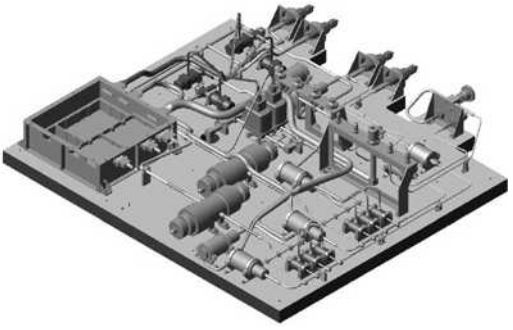

Figure 2. The Dilution Cooler Pneumatic Control Unit.

exhaust flow. A complex optical filtering arrangement defines the different photometric bands for 48 bolometers. Severe constraints are put on the optical filters and the focal plane thermal stability in the useful bandwidth of the scientific signal (0.016-100 Hz).[5] They required a temperature noise spectral density lower than 20 nK/$\sqrt{\text{Hz}}$ at 100mK +/-5mK and 28 μK/$\sqrt{\text{Hz}}$ at a temperature lower than 2.1 K.

The dilution Cooler is composed of:

- 4 tanks mounted on the Service Module (SVM), one for ^{3}He and three for ^{4}He, to store the helium isotopes required for the 24-month PLANCK mission
- A Pneumatic Control Unit mounted on the SVM, used to monitor and regulate the isotope flows and pressure throughout the mission
- Piping from the Pneumatic Control Unit at 300 K to the Focal Plane Unit (FPU), composed of counterflow heat exchangers and charcoal filters at the 50 K and 18 K level
- The Focal Plane Unit (18 K-100 mK) on which will be mounted the HFI bolometers (100 mK), filters (1.6 K) and horns (4 K). This unit is designed for cryogenic performance, to withstand launch vibrations, and to provide suitable alignment of the 100 mK, 1.6 K and 4 K plates at 100 mK.

MECHANICAL DESIGN

The 51 L tanks (Fig. 1) are made with a titanium liner over-wrapped with a multi-planar Kevlar® filament envelope. They are filled up to 295 bars before launch.

The Pneumatic Control Unit (Fig. 2) is composed of pneumatic components set onto an aluminium honeycomb panel. Latch valves isolate the high-pressure circuitry from the lower one during launch phase. High stability pressure regulators provide 18 bar to the cooler throughout the mission. Discrete flow control allows increasing the flow rate if additional cold power is required during the mission. Fill and drain valves are connectable with a pump or a tank-filling compressor during testing or ground operations. An electronic unit is designed to monitor and actuate the active components: valves, pressure sensors, and thermometers.

The piping from 300 K to 18 K is composed of isotope injection pipes routed inside the exhaust pipe to create a counter flow exchanger. It is designed to minimize heat loads on the payload module and to withstand the acoustic vibrations of the V-grooves on which the pipes are attached (Fig. 3).

The Focal Plane Unit mechanical design (Figs. 4, 5 and 6) is driven by mass and volume constraints, by the material thermal properties at low temperature, and by the mechanical loads during launch. The radiation shields at 4 K and 1.6 K are made of Al 6061. The counterflow dilution heat exchanger stiffness is achieved with NbTi tubes and 12 Stainless Steel annular plates for thermalization (Fig. 7). The thermal contractions of the various materials are carefully taken into account to achieve the required alignment of each optical plate. During launch, an equivalent

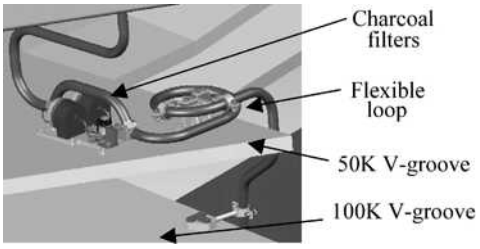

Figure 3. Complex piping assemblies.

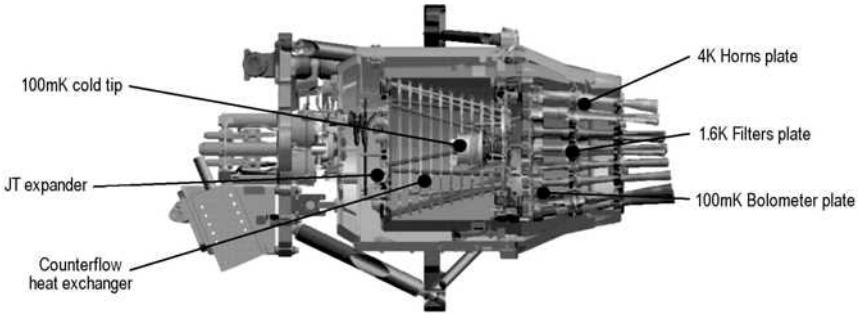

Figure 4. The Focal Plane Unit.

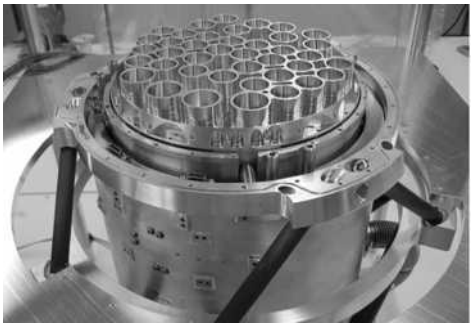

Figure 5. The Focal Plane Unit with the bolometer plate.

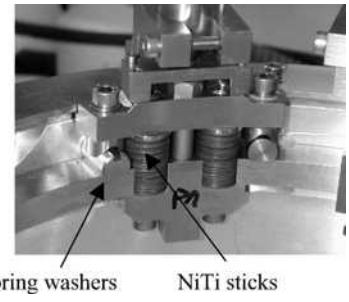

Figure 6. Launch blocking clamps. The opening is actuated by NiTi shape memory alloy + spring washers.

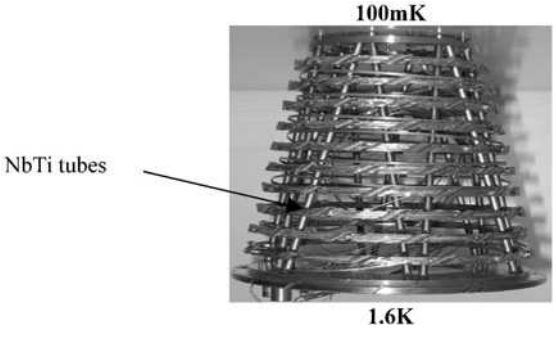

Figure 7. The Dilution Cooler heat exchanger between 100 mK and JT expansion.

static load of 30 g is applied onto the structure. A blocking mechanism including three clamps firmly tightening the Focal Plane with the 4 K shield. The clamp's opening is actuated using NiTi shape memory alloy sticks. The austenitic-martensitic transition of TiNi occurs at roughly 200 K. The NiTi stick applies a force of 1500 N at room temperature. After the transition, springs washers applying a compression of about 1500 N on the NiTi relax the system, allowing a displacement of 1.15 mm of the clamps. In the open position, the 100 mK structure is isolated from the 4 K shield.

OPEN-CYCLE DILUTION THERMAL PERFORMANCE

Process patented by CNES, n° 93.08201.

The operation of the open-cycle dilution cooler in space has been discussed in previous articles[2,3] and used in the balloon experiment Archeops.[4,6] The temperature response of the 100 mK cold tip can be explained by the thermodynamical properties of the ^{3}He-^{4}He mixture. As the open-cycle dilution operates with an excess of ^{3}He (>15%)[2] (as compared with the 6.4% solubility limit below 0.1 K), the theoretical cooling power is only a function of the ^{4}He mass flow and the temperature. The available cooling power is measured with an electrical heater. Under 0.4 K and with constant isotope mass-flow, the temperature response of the dilution cold tip is accurately described by the classical square-temperature law: $P = \dot{n}_4 \cdot q_{DIL} \cdot T^2 - P_0$ where $q_{DIL} = 0.73\ J/K^2/mol$ depends on the heat exchanger design and P_0 is a rough estimation of the cold losses (conduction in supports and wires, viscous dissipation, ...etc). Due to the excess of ^{3}He, the dilution provides a cooling power along a Counter-Flow Heat Exchanger (CFHE) located between the isotopes injection and the mixture exhaust capillaries. A Joule-Thomson expansion on the exhaust circuitry provides 1.45 K. Between the JT stage and the 100 mK cold tip, the structure on which the CFHE is routed is designed to reduce the conductive loads on the cold tip.[3] The efficiency of the CFHE thermalization can be explained by a simple analytical consideration. We suppose here that the heat exchanger is perfect (i.e. no temperature difference between the incoming isotopes and the return mixture). The thermal balance of a given volume including the cold tip and a section of the heat exchanger at temperature T gives the formula:

$$P_{CT} + kA \cdot \frac{dT}{dl} = \dot{n}_4 \cdot q_{DIL} \cdot T^2 - P_0 \qquad (1)$$

where P_{CT} is the external power on the cold tip, the second term is the conductive load, and l is the distance from the cold tip. Using the Wiedemann-Franz law valid for a normal metal, it is straightforward from (Eq. 1) to obtain an approximation of the conductive load on the cold tip:

$$P_{WIRES} = kA \cdot \left.\frac{dT}{dl}\right|_{l=0} = \frac{\dot{n}_4 \cdot q_{DIL} \cdot \left(T_{JT}^2 - T_0^2\right)}{\exp\left(\frac{2 \cdot \dot{n}_4 \cdot q_{DIL} \cdot R}{L_0}\right) - 1} \qquad (2)$$

where L_0 is the Lorenz constant ($2.45\ 10^{-8}\ W \cdot \Omega/K^2$), R is the electrical resistance, and T_0 and T_{JT} are the cold tip and JT stage temperatures.

The limit where the heat load equals the maximum cooling power $\left(\dot{n}_4 \cdot q_{DIL} \cdot T_0^2\right)$ is given by $\dot{n}_4 \cdot R \geq L_0 / q_{DIL} \cdot \ln\left(T_{JT}/T_0\right) \approx 20(\mu mol/s)(m\Omega)$. The thermalization reduces the conductive load by more than a factor 30. For quantitative results, a detailed conductive model must take into account the thermodynamic properties of ^{3}He-^{4}He up to T_{JT} (1.5 K).

The instrument requires 80 shielded cryogenic cables made with stainless steel braid and a pair of conductors (60 Ω/m). The linear thermal conductance has been measured to be $0.47 \cdot T\ \mu W \cdot cm\ K$ ($T < 2K$), dominated by the braid (equivalent to 5.2 Ω/m). The mechanical support is made of NbTi superconductive alloy (very low thermal conductivity).

As the available power at 100 mK is very low (about 100 nW), the performance of the open-dilution relies on the quality of the 100 mK-1.6 K structure design. In Planck/HFI, we only need about 50 nW to regulate the focal plane temperature with the required stability[5] and 20 nW for the

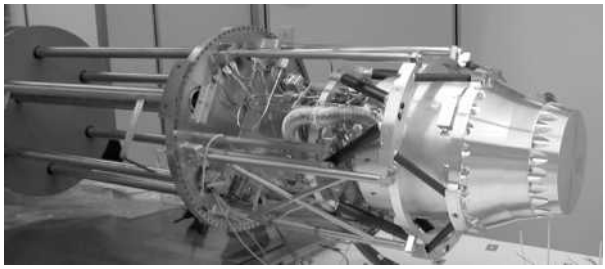

Figure 8. The FPU qualification model, ready for integration in the test cryostat.

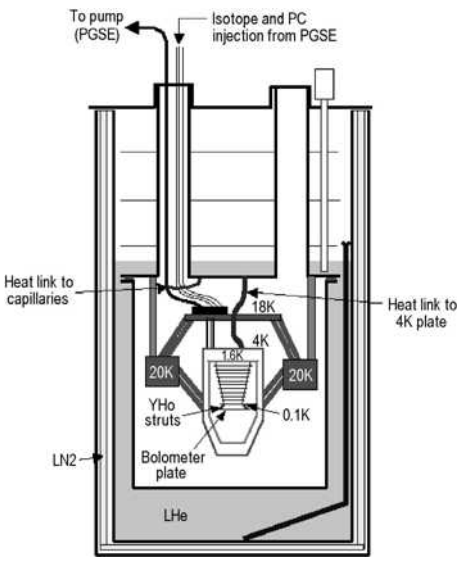

Figure 9. The FPS installed in the test cryostat.

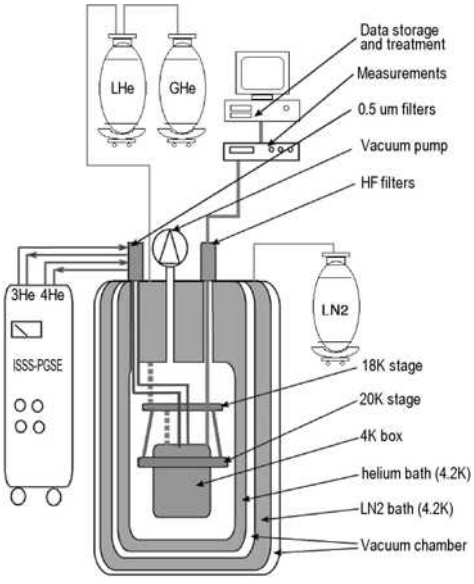

Figure 10. The whole test installation.

power dissipated by detectors and high-energy particles (energy deposited into the focal plane material).

CRYOGENIC TESTS

The main purpose of the test facilities is to recreate a "space-like" environment in which the FPU can be qualified under representative conditions. These test facilities (Figs. 8 to 10) are composed of a liquid helium cryostat in which a vacuum chamber containing the dilution unit is immersed. This helium bath provides the base temperature of the system via heat links between the vacuum chamber and the 4 K interface of the FPS. The 18 K and 20 K plates are then actively regulated. We monitor temperatures of the 1.6 K stage, middle of the heat exchanger, dilution plate, and bolometer plate. The cooling power of the system is determined at each stage by electrical heating. The DCPU is simulated by a test bench (ISSS-PGSE), which provides both isotopes supply, isotopes molar flow control, mixture pumping, and storage. This bench also provides supply and molar flow regulation of He for the precooling circuit. Figure 9 depicts the whole installation.

Joule Thompson (JT) Expansion Performance

The JT expansion performances are critical for a good operation of the dilution unit. It indeed provides most of the cooling power used in the heat exchanger to cool down the helium coming

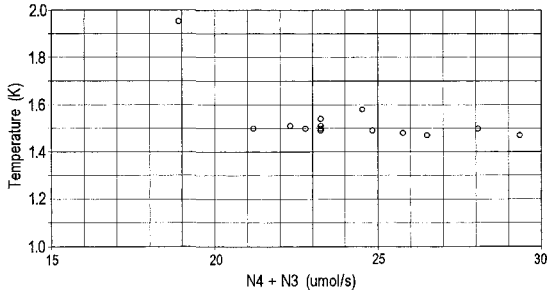

Figure 11. Temperature of the 1.6 K stage as a function of the total molar flow

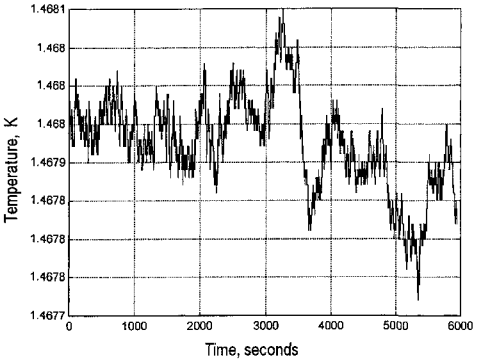

Figure 12. Temperature stability versus time.

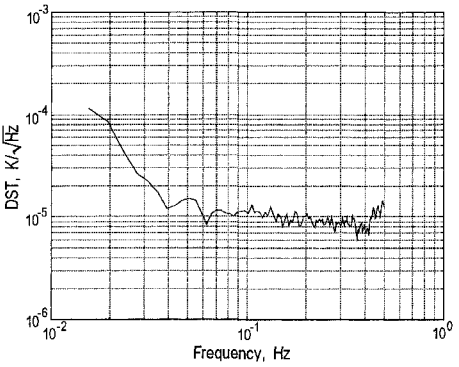

Figure 13. Noise spectrum.

from the 4 K stage. We could investigate both the JT behavior as a function of isotopes molar-flow and verify the thermal stability of the 1.6 K stage.

The temperature of the JT stage is governed by the total molar flow. By decreasing the total molar flow we have observed a discontinuity in the 1.6 K stage temperature. This discontinuity appears when molar flow is lower than 20 μmols/s. We had already observed this phenomenon during the first prototype test session. It can be explained by the gas phase inside the JT heat exchanger. This phase reduces the heat exchange coefficient, and thus the temperature of the plate increases. Thermodynamic analysis suggests that this limit essentially depends on the ^{4}He molar flow. In Fig. 11, the molar flow threshold around 20 μmols/s is clearly visible. If the total molar flow is greater than 20 μmols/s we can see that the temperature does not strongly depend on the molar flow ($\Delta T < 0.1$ K).

The temperature stability has also been investigated, and we have found that this stage is remarkably stable. Figures 12 and 13 show the temperature stability as a function of time and the noise spectrum. These graphs were made with ^{4}He and ^{3}He molar flow of respectively 19.5 μmol/s and 7.0 μmol/s. The suction pressure was 400 Pa. The temperature measured on the bolometer plate was 92.55 mK with 100 nW applied on the dilution stage. The sampling frequency is 1 Hz. We can see in Fig. 13 that the stability specification is entirely fulfilled. We have indeed 80 $\mu K/\sqrt{Hz}$ at 0.02 Hz.

The dilution cooler performance is critical for bolometer operation. It is necessary to have both cooling power and temperature stability at 100 mK. During the mission, the temperature stability is achieved by regulating the dilution plate through a PID system and by mounting the bolometer plate on HoY supports. In our experiments HoY is replaced by brass in order to decrease the time response of the system. PID is not used. We thus consider the stability of the dilution itself. We have investigated both the cooling power and the molar flow dependence for the minimum dilution temperature. These results have allowed verifying the theoretical model of the dilution cooler.

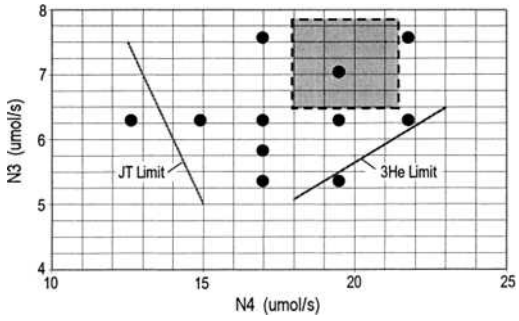

Figure 14. Measurement points in the molar flow plane.

Figure 14 depicts the experimental plan we have followed. All the points have been measured with 100 nW applied on the cold tip. In this graph we have represented the JT limit (explained above) and the ^{3}He limit we will discuss in this section. As the mission is 24 months long, the total isotope flow is limited. The gray square in Fig. 14 represents the molar flow domain usable for the Planck mission. Both temperature and cooling power specifications are fulfilled in this domain. This window has been determined using measurement results as well as a theoretical model.

The minimum dilution temperature and cooling power depends on the ^{3}He flow and ^{4}He flow. The temperature response of the ^{4}He molar flow does not depends on the ^{3}He flow if the latter is greater than 6.3 μmol/s. For all ^{4}He flows investigated it is also the condition to keep the ^{4}He molar flow optimum in the left hand side of the graph, i.e. far from the ^{3}He limit. The whole window can be modeled with accuracy, and we thus are able to foresee temperature and cooling power for given molar flows.

Figures 15 and 16 represent the cold tip temperature as a function of ^{3}He and ^{4}He flows.

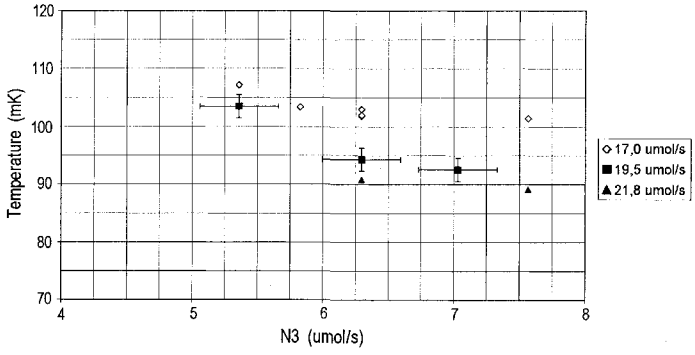

Figure 15. Temperature of the cold tip versus ^{3}He molar flow.

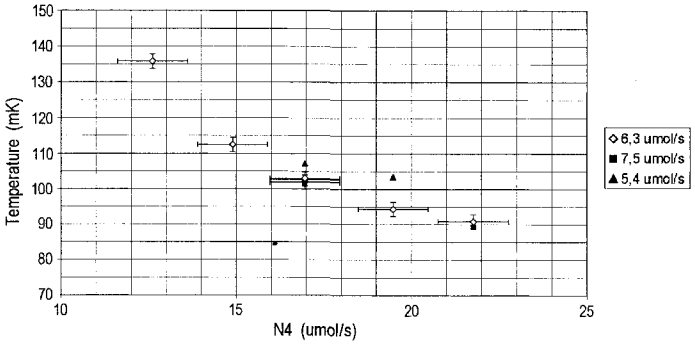

Figure 16. Temperature of the cold tip versus ^{4}He molar flow.

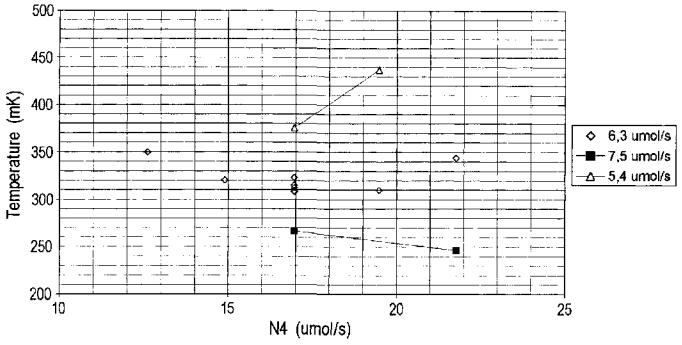

Figure 17. Temperature of plate 6 vs. ^{4}He molar flow.

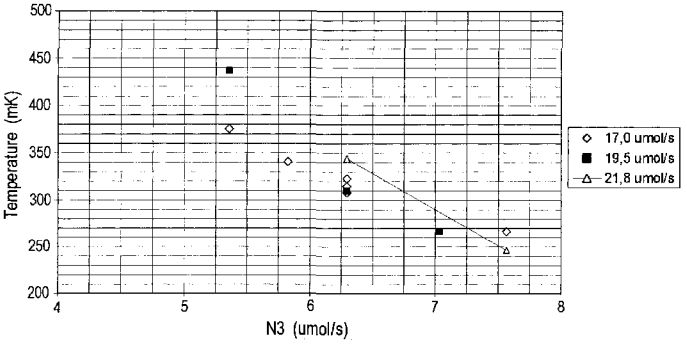

Figure 18. Temperature of plate 6 vs. ^{3}He molar flow.

As we can see in Figs. 15 and 16 the temperature of the cold tip decreases with an increase of ^{4}He molar flow and reaches a saturation value that depends on the ^{3}He molar flow. Meanwhile, if we increase the ^{3}He molar flow, we first obtain a decrease of the cold tip temperature, but then this temperature increases again because of viscous losses. We can see this behavior in Fig. 15 with 17 μmols/s of ^{4}He.

The ratio (X) of ^{3}He to ^{4}He is also a key parameter, because it determines the "quantity" of the dilution process along the heat exchanger. Increasing this ratio increases the cooling power, but as we have seen above, it also increases viscous losses along the heat exchanger. On the other hand, a smaller ratio will stop the dilution process earlier, and the heat exchanger performance will be worse. We can easily see that an increase of this ratio leads to a significant decrease of the heat exchanger temperature.

Figures 17 and 18 show the temperature of the middle of the heat exchanger when varying the isotope's molar flows. These figures point out an interesting behavior. With a fixed ^{3}He molar flow the temperature increases if the ^{4}He molar flow is greater than an optimum value. This optimum value increases with increasing ^{3}He flow. In the worst case (5.4/19.5 μmol/s) we have observed a strong increase of plate 6 temperature instability. This phenomenon is explained by a complete dilution of the ^{3}He before the extractor. As we have seen, above the limit is given by the ratio of ^{3}He to ^{4}He. From these data we can determine the value of this limit so that we can remain in favorable conditions. During these tests the limit was determined to be X > 22%.

The dilution cooling power has been measured for the molar flows defined by of the gray area in the top right corner of Fig. 14. The results are plotted in Fig. 19. As we can see, the temperature squared variation predicted by the theoretical model is demonstrated. From these data we have evaluated the residual power. It is equal to 308 nW, which is in agreement with our model.

Using the power and temperature response we determine the parameters required to fit the theoretical model, that is to say Q_{DIL}, P_0 and T_{JT}. The difference between the model and the

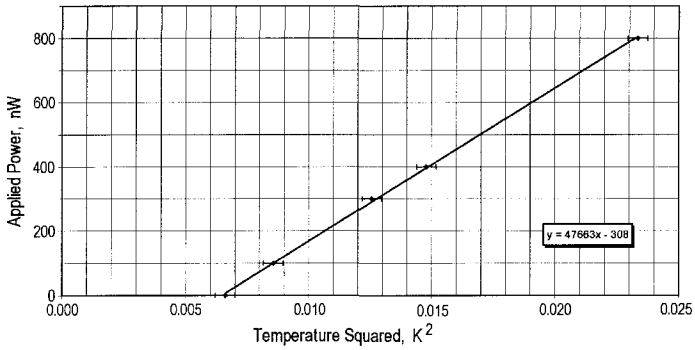

Figure 19. Power applied versus temperature squared.

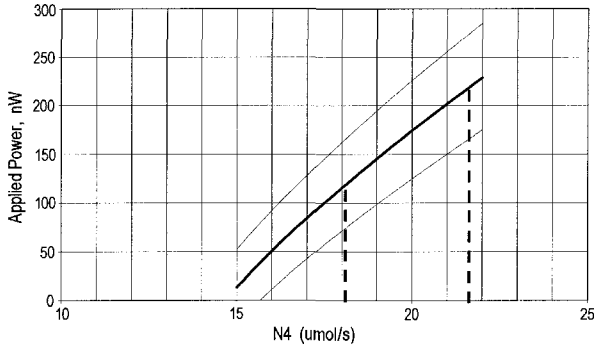

Figure 20. Cooling power versus ^{4}He molar flow.

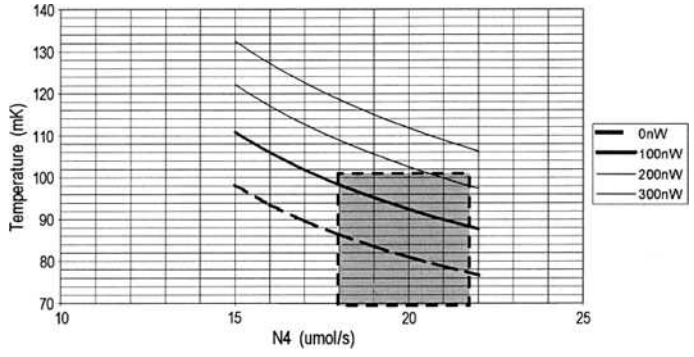

Figure 21. Minimum temperature versus ^{4}He molar flow.

measurements is then lower than 1%. Figures 20 and 21 show the model behavior. The molar flow domain has also been represented. We can see in these figures that the cooling power is larger than 100 nW in the whole molar flow domain. The temperature stability of the bolometer plate is also a key point, but as in our system the HoY supports are not used, the stability we obtained is worse than the one expected in real conditions. Nevertheless, we obtained 15 $\mu K/\sqrt{Hz}$ at 0.02 Hz, which allows us to expect that the specification will be fulfilled with HoY supports.

These graphs were made with ^{4}He and ^{3}He molar flow of 19.5 μmol/s and 7.0 μmol/s, respectively. The suction pressure was 400 Pa. The temperature measured on the bolometer plate was 92.55 mK with 100 nW applied on the dilution stage. The sampling frequency was 1 Hz.

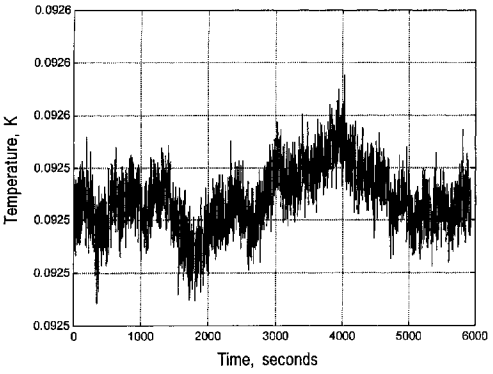

Figure 22. Temperature stability of cold tip stage.

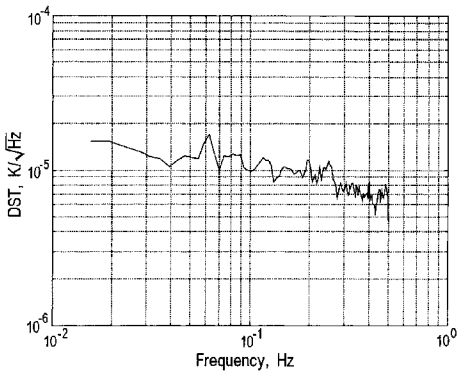

Figure 23. Noise spectrum.

CONCLUSIONS

The cryogenic tests of the Elegant Breadboard have successfully demonstrated the ability of the open-cycle dilution cooler to match the theoretical model and to achieve the required cryogenic performance. The 1.6 K-JT behavior is also satisfactory. These results have allowed the manufacture of the FPU qualification model to be started using the same configuration.

Air Liquide is now carrying out the cryogenic tests of this qualification model. During cool down, the launch blocking clamps opened successfully. The dilution is being tested with the HoY supports and with active regulation; this will allow verifying the thermal stability at 100 mK and 1.6 K. The unit will then undergo vibration tests and final cryogenic tests to complete the qualification sequence.

ACKNOWLEDGMENT

The authors thank A. Benoit from CRTBT for his strong support from the beginning of the project as technical expert of the open-cycle dilution, IAS HFI and the Air Liquide team for their active participation and availability during the design, integration, and tests phases.

REFERENCES

1. Collaudin B., Passvogel T., "The FIRST and Planck 'Carrier' Missions: Description of the Cryogenic Systems," *SPIE Conf Proc.*, January 1998.
2. A.Benoit, S.Pujol, "Dilution Refrigerator for Space Applications with a Cryocooler," *Cryogenics,* 34 (1994). pp. 421-423.
3. Benoît A., Bradshaw T., Jewell C., et al., "A Long Life Refrigerator for 0.1 K Cooling in Space," SAE Technical Paper Series No. 941276 (1994).
4. Benoit A. et al, "Archeops: a Balloon Experiment for Measuring the Cosmic Microwave Background Anisotropies," *Proc of the 15th ESA Symp. on European Rocket and Balloon Prog. and Rel. Research,* ESA SP-471, Aug. 2001.
5. Lamarre J-M et al, "Use of High Sensitivity Bolometers for Astronomy: Planck High Frequency Instrument," *Proceedings of the 9th International Workshop on Low Temperature Detectors*, 22-27 July 2001, AIP Conf. Proc., p. 605.
6. Madet K., Benoit A., Gautier B., "The Archeops Cryostat : a Dilution Refrigerator for Balloon Experiment, ICEC 19.

HERSCHEL Sorption Cooler Qualification Models

L. Duband, L. Clerc, L. Guillemet and R. Vallcorba

CEA/DRFMC/Service des Basses Températures
Grenoble France

ABSTRACT

The HERSCHEL/PLANCK mission of the ESA Horizon 2000 Science Program accommodates two spacecrafts for a joined launch on ARIANE 5 in 2007. HERSCHEL, a multi-user observatory type mission, is a giant space telescope. It will be able to collect light from very distant galaxies and to observe, for the first time, objects completely enshrouded by dust such as the primeval galaxies. The HERSCHEL payload consists in three instruments built by international scientific consortia, HIFI (Heterodyne Instrument for FIRST), PACS (Photo-conductor Array Camera & Spectrometer) and SPIRE (Spectral and Photometric Imaging REceiver). The spacecraft provides the environment for astronomical observations in the infrared and sub-millimeter wavelength range requiring cryogenic temperatures for the cold focal plane units. A key requirement for the bolometric detectors, used in PACS and SPIRE, is that they will have to be cooled down to 290 mK. This will be achieved by two ^{3}He adsorption coolers for which CEA-SBT is responsible. The sub-Kelvin sorption coolers provide a wide range of heat lift capability at temperature below 400 mK. Helium adsorption coolers rely on the capability of porous materials to adsorb or release a gas when cyclically cooled or heated. Using this physical process one can design a compressor/pump which, by managing the gas pressure in a closed system, can condense liquid at some appropriate location, and then perform an evaporative pumping on the liquid bath to reduce its temperature.

The structural and cryogenic qualification models have been developed and qualified. This paper deals with this program.

INTRODUCTION

Evaporative cooling is widely used in low-temperature laboratories where liquid helium pumped cryostats allow temperatures slightly below 1 K to be reached. Our cooler uses the same principle but with some distinctive features, some of which are dictated by the space environment.

The first feature is the use of an isotope of helium, namely helium 3 (^{3}He), whose physical characteristics allow temperatures as low as 250 mK to be reached. However, the cooler alone does not cover the temperature range from ambient down to sub-kelvin temperatures. It requires a pre-cooling stage with enough cooling power at a temperature lower than 3.2 K, the ^{3}He critical temperature. This can either be achieved using a helium bath (typical for laboratory units or on HERSCHEL), or a mechanical cryocooler.

Cryocoolers 13, edited by R. G. Ross, Jr.
Springer Science+Business Media, Inc., New York, 2004

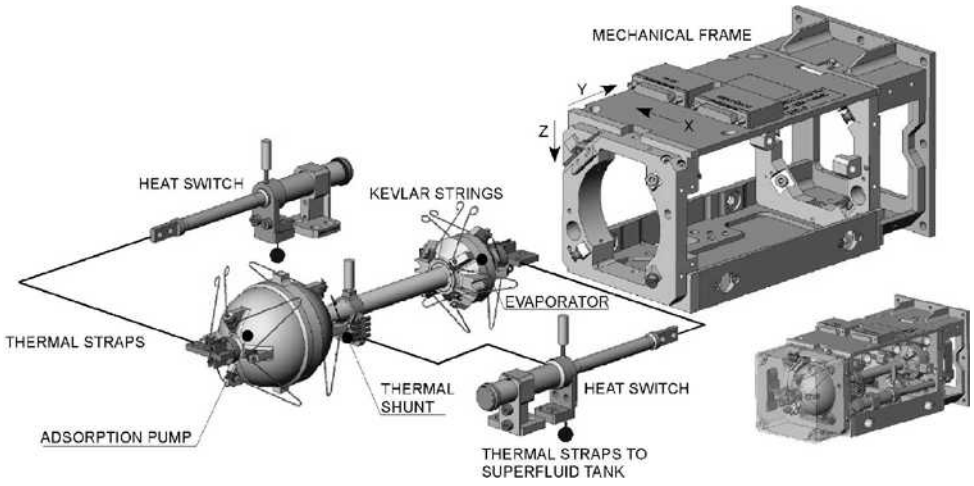

Figure 1. Actual 3D view of the HERSCHEL cooler.

The second feature lies in the technique used to achieve the pumping effect. To suppress all moving parts, and hence improve the reliability, we have recourse to the adsorption pump capabilities. Adsorption is the physical mechanism in which a gas can be trapped onto a surface. Material with a high specific area such as activated charcoal (typically 1200 m^2/g) is required. The amount of adsorbed gas strongly increases with pressure, and decreases with temperature. Thus, in a closed box filled with some gas and activated charcoal, it is possible to provide either an increase (gas release) or a decrease (gas trapping) of the pressure simply by varying the temperature of the adsorbant (the charcoal). Consequently, below its critical temperature, a gas can be compressed until it forms a liquid. Then, lowering the equilibrium pressure, the temperature of the condensed liquid can be reduced.

The third feature is related to the zero gravity environment. In a laboratory adsorption cooler, gravity confines the liquid in the evaporator. Unfortunately, in space, we cannot rely on gravitational forces. The alternative is to include a porous material (such as an alumina sponge) in the evaporator, which confines the liquid by capillary attraction. For the cooling, the gas has to be first condensed directly into the evaporator and then evaporated by pumping. Thus, during condensation the evaporator needs to be thermally connected to the cold heat sink, and during the low temperature step, it must be thermally isolated.

The fourth feature is related to the heat switches to make or break thermal contact. We have designed very efficient gas gap heat switches where the presence or absence of gas between two interlocked copper parts changes drastically the heat flow between them. The gas handling is achieved with a miniature cryogenic adsorption pump.

The final feature is related to the structural strength required to survive the launch. The cooler must be firmly fixed while the parasitic heat loads on the cold parts must be minimized. To fulfil these two contradictory requirements, we have developed a suspension system making use of Kevlar® strings. This material is chosen for its unique mechanical and thermal properties.

As described above, the space-borne adsorption cooler comprises an adsorption pump containing the activated charcoal, which will control the gas pressure, a pumping line, an evaporator holding the porous material, and two heat switches to control the temperature gradient during the various phases. Part of this assembly (pump, line and evaporator referred as the cooler heart) is suspended with Kevlar strings inside a mechanical frame as depicted in Fig. 1. The cooler is loaded with helium and sealed. The only links to ambient temperature are the heater wires used to drive the adsorption pump and the heat switches.

Once the cooler is thermally mounted on the cold heat sink and cooled down to below the critical temperature of ^3He (3.2 K), operation can begin.

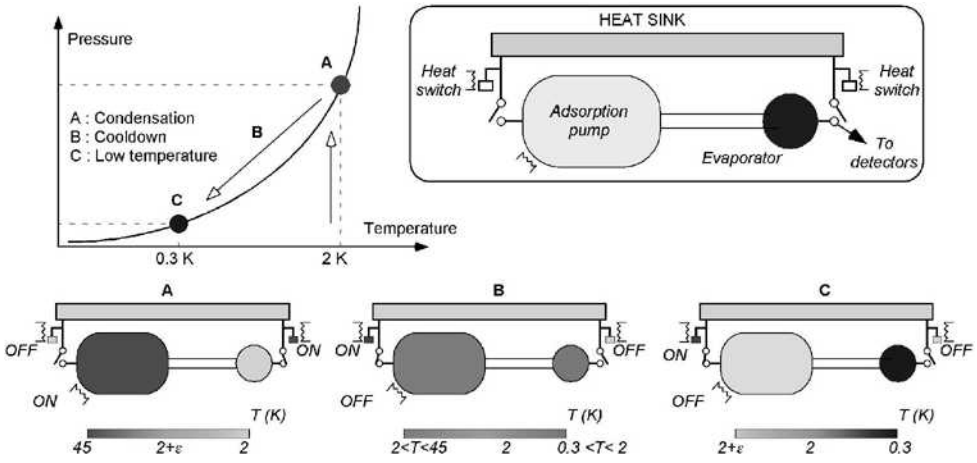

Figure 2. Steps of the cooling operation; Steps A and B account for less than 5% of the running time.

In brief, helium sorption refrigerators have no moving parts, are vibrationless, and can be designed to be self contained and compact with a high duty cycle efficiency. These features and the expected reliability that follows make them very attractive for space applications. Concerning the drawbacks, relatively poor thermodynamic efficiency with regards to Carnot due to the heat of adsorption, and non continuous operations can be noted. Details on their principle of operation have been described in numerous papers and the reader is referred to the relevant publications.[1,2] Nevertheless a typical cycle is summarized in Fig. 2.

CEA-SBT has acquired a long time experience in sorption cooler technology. Numerous laboratory systems ranging from single to three stages units have been developed, and several rocket or space borne systems have been flown.[3,4]

HERSCHEL COOLER DESCRIPTION

The SPIRE and PACS sorption coolers were both designed following the same overall specifications (see Table 1) and were sized using a software tool developed at CEA-SBT for the thermal aspects and ANSYS for the mechanical ones. They are designed to be interchangeable and thus feature both instrument mechanical interfaces. The thermal architecture in the satellite is such that the coolers are mechanically mounted off of a structure at 4 K or above (level 1) and thermal paths are then provided to the superfluid helium tank (level 0) for the cooler operation. This constraint calls for a specific thermal architecture (see Fig. 2) and design. In particular, during the recycling phase of cooler operation the heat flowing to the tank from the sorption pump and from the evaporator are significantly different.

Table 1. HERSCHEL Cooler specifications.

Safety	Structural failure mode shall be "leak before burst"
Mechanical (worse case axis)	• Sine sweep vibration: 22.5 G peak up to 100 Hz / Random : 20–150 Hz: 11.5 G RMS • First eigenfrequency above 120 Hz • Proof pressure: 2 x maximun operating pressure
Thermal	• Heat lift capability: 10 μW minimum at 290 mK • Hold time: no less than 46 hours • Recycling time: no more than 2 hours • Total energy dissipated per cycle: no more than 860 J
Electrical	Cold interface (cooler heart) electrically isolated from the mechanical interfaces
Geometry and Interface	• Volume and Mass: 100 x 100 x 230 mm maximum - < 1.8 Kg • Mechanical interface: with a 4 K structure • Thermal interface: with a 1.7 K He II bath

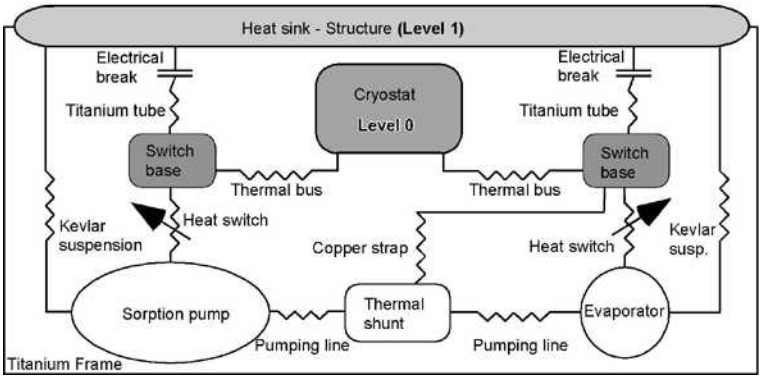

Figure 3. Cooler thermal architecture.

During this phase it is crucial to keep the evaporator temperature as cold as possible to increase the condensation efficiency and reduce the liquid fraction lost during cooldown. Consequently, two thermal interfaces and thus two thermal buses are required (see Fig.1 and 3). Finally, to fulfil the electrical isolation requirement, the two heat switches are mounted on the mechanical frame using Kapton spacers.

A picture of the cooler is shown on Fig. 4, and Table 2 summarizes its main characteristics. Most of the cooler, i.e. the evaporator and sorption pump envelope, the pumping line and heat switch tubing and support structure, is made of titanium 6Al-4V. All thermal interfaces are made of high purity gold-plated copper. The heat switches feature thermal interfaces to the main tank. The thermal switches are fixed at one end and behave like cantilever beams. Moreover, as a flexible copper strap is bolted on the free end, the first vibration natural frequency is lowered by this added mass. As a result, the first vibration frequency in the transverse axes is quite low. Consequently, both switches feature snubbers that are very efficient at limiting the thermal switch's motion, and are mandatory to protect them from damage. Snubbers are also implemented on the miniature pump side.

The cooler is charged with ^{3}He gas and permanently sealed. The pressure at room temperature is close to 8 MPa. To qualify as "leak before burst," both coolers are designed so that the pumping line with a calculated burst pressure of 35 MPa is the weakest point with regards to internal pressure. Both systems are proof pressure tested to 20 MPa.

The switches are also charged with ^{3}He gas at room temperature, as the use of ^{3}He gas substantially improves the performance in the ON position, since in the 2K range ^{3}He has a thermal conductivity three times higher than ^{4}He.

The Kevlar suspension system has been improved since the engineering models[5] and now features a ratchet mechanism to ease the tensioning of the strings. The behaviour of Kevlar strings under various conditions has been extensively studied and has led to some unexpected results. For instance, it was demonstrated that the Kevlar tension is substantially affected by the successive 80°C bake out (required during the qualification program). A procedure was then established to train and stabilize the Kevlar under tension.

The PACS unit uses 500 μm diameter braided Kevlar strings everywhere, and the SPIRE unit uses 500 μm diameter strings on the pump side and 290 μm diameter strings on the evaporator side.

Table 2. Cooler main characteristics.

He charge	6 STP dm^3
Pressure at room temperature	7.5 MPa
Overall dimensions	100 x 100 x 229 mm
Overall mass	1750 grams
Suspended mass (cooler "heart")	281 grams

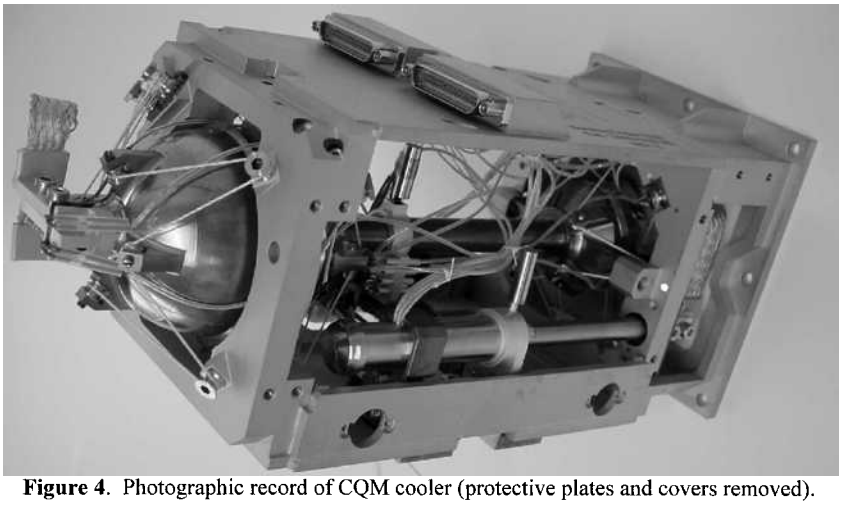

Figure 4. Photographic record of CQM cooler (protective plates and covers removed).

QUALIFICATION PROGRAM

A test cryostat, CRYOTEDI III, has been designed and manufactured. This cryostat contains a nitrogen and a helium tank, both supporting thermal shields. The useful volume on the cold plate is about 370 mm in diameter and 250 mm height. This cryostat provides autonomy of about a week at 1.7 K. A particular feature of the cryostat is the possibility to operate in any orientation between –90° and +90° as long as the liquid level is equals or below 50% (which is usually the case once the helium bath has been brought down from 4.2 K to 1.7 K). This feature allows the sorption cooler to be tested in any orientation. The cold plate features an additional aluminium plate which simulates the instrument interface (Level 1) and can be temperature regulated.

A test plan has been established and comprises a test sequence to be performed on the sorption coolers that, together with analysis and other verification methods, contributes to qualification. This test program covers the functional performance and environmental tests required to provide confidence in the ability of the coolers to meet the specified requirements. Performance measurements have been made before and after the environmental tests, designed to detect changes in performance parameters that may indicate a potential failure.

The main tests are listed in chronological order in Table 3 together with a summary of the results.

Thermal performance

A typical recycling curve is displayed on Fig. 5. For this run, the input power to the pump is 300 mW until the latter reaches 45 K, at which point this power is reduced to 50 mW. The heat switch on the evaporator is maintained in the ON position with 800 µW. Once the sorption pump is at 45 K, most of the helium is desorbed from the charcoal.

Table 3. Test Plan – Main results

Test	*Experimental result*
Leaktightness and proof pressure test	20.5 MPa for 3 minutes – leak rates < 10^{-10} mb.l^{-1}.s^{-1}
Thermal performance – bath @ 1.6 K	SPIRE unit: 248 mK ultimate T, orientation independent
Cooler bake out at 80°C for one week	Passed
Verification of thermal performance	Consistent with first set
Vibration tests	Passed (see Table 4)
Verification of thermal performance	Consistent with first set
Autonomy tests	Problem at first (see further) – within specif. at delivery

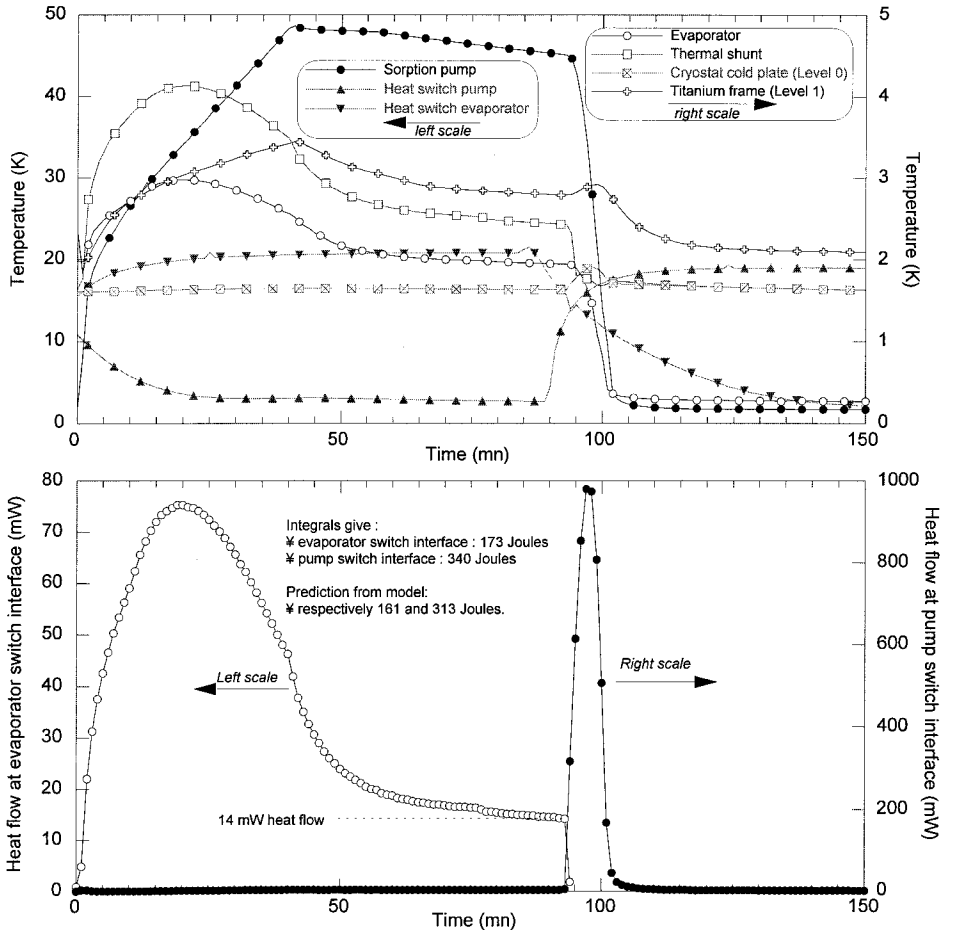

Figure 5 : Typical cooler recycling and associated heat flows to heat sink

The enthalpy of the hot gas as well as the latent heat of condensation is evacuated to the cryostat cold plate through the finite thermal conductance of the switch and straps. The end of this phase occurs once the evaporator temperature drops below 2 K, at which point the input powers to the pump and to the evaporator switch are turned OFF. Shortly after the switch on the pump is turned ON. The pump temperature decreases quickly and the evaporator reaches 300 mK within minutes. During the recycling phase and for ground test only, the cooler must be set so that the main sorption pump is above the evaporator to avoid any convective effect which would otherwise prevent any condensation. Once the cooler has reached its ultimate temperature, it is insensitive to orientation and can even be operated against gravity as shown further.

Both straps to the cryostat are instrumented with thermometers and heaters, and were fully characterized prior to the cooler tests. Then, using a simple shunt technique, one can easily extract from the thermal data the powers flowing through each of the straps (Fig. 5). These measured powers are consistent with predictions and contribute to the sizing of the thermal bus within HERSCHEL.

The cooling power curves of both coolers were measured before and after each environmental test. In addition the tests were carried out for three cooler orientations, right-side up, horizontal and upside down.

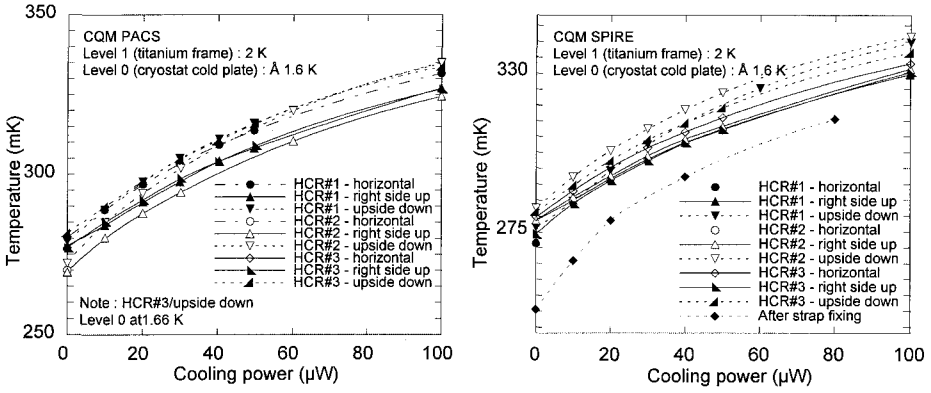

Figure 6. Cooling power curves for both units (SPIRE and PACS).

These tests allow verification of the "zero-G" operation and, for instance, check for any potential damage to the internal porous material after vibration tests. The results displayed in Fig. 6 do not show any significant differences between each set of tests.

Probably the most critical tests are the autonomy tests. For these tests the cooler is recycled and the autonomy at low temperature is then measured for a given applied load on the cold tip. These tests allow for both a verification of the correct filling of the coolers, and a very precise measurement of the parasitic heat loads internal to the cooler. It is important to emphasize that this aspect is critical for the SPIRE and PACS instruments as any loss in autonomy can substantially impact the mission and the amount of data expected.

The first set of autonomy tests revealed two anomalies as illustrated on Fig. 7. On this figure we have reported the autonomy (in fact the inverse of the autonomy) versus the load applied. For each data point the cooler was recycled in the exact same thermodynamic conditions and one can then assume the initial amount of liquid produced is the same. In addition, the operating temperatures were close enough so that the latent heat (L) can be considered constant. We can then simply write that the amount of "cold" joules produced is equal to the total load times the autonomy : $m_0 \cdot L = (P_{applied} + P_{parasitics}) \times$ time (where m_0 is the quantity of liquid at the beginning of the low temperature phase). Plotting 1/time versus $P_{applied}$ should then give a curve of slope $1/(m_0 \cdot L)$ and of ordinate $P_{parasitics}/(m_0 \cdot L)$. This analysis, performed for both coolers and reported on Fig. 7, clearly shows the underfilling and extra parasitic aspects.

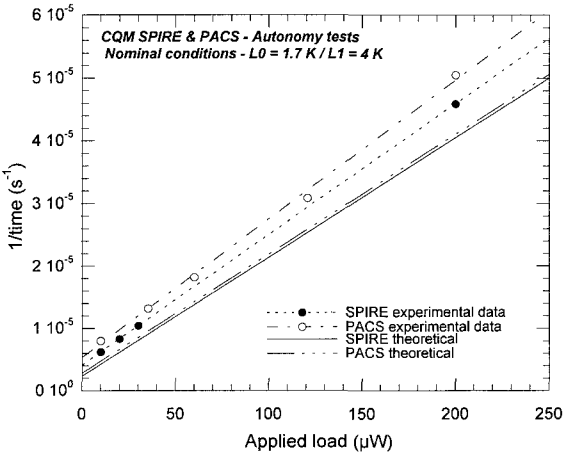

Figure 7. Thermal performance analysis – Autonomy tests.

Table 4. Vibration test – first natural frequencies.

	Cold tip	Structure	HS evap. I/F	HS pump I/F
X_{SPIRE}	386	826	138	138
Y_{SPIRE}	561	1360	705	705
Z_{SPIRE}	291	1130	127	136
X_{PACS}	558	1230	126	132
Y_{PACS}	653	1180	302	325
Z_{PACS}	460	923	128	134

As it would be too complicated to keep ^{3}He gas bottles under high pressure (> 8 MPa), the filling of the coolers is performed at low temperature and relies on a perfect knowledge of all void volumes in the circuitry as well as the cooler volume. Because the cooler internal volume is small and difficult to calculate accurately (activated charcoal, etc...) an error of a few percent is within the realms of possibility. Indeed, the analysis of the results indicates a few percent underfilling for both coolers. The coolers are sealed and the amount of gas cannot be changed anymore, however this anomaly is not regarded as major as a new fill procedure has been established for the flight models.

The second anomaly is related to an unexpected parasitic load (few μW). After investigation, it was found that the braided copper strap used between the evaporator heat switch and the cold tip induced stress on the switch and thus a slight internal contact between the two interlocked copper parts. Although the straps were initially very flexible, it turned out that the gold plating of the entire straps substantially changed their mechanical performance and led to these results. Operating the cooler without strap — i.e. without heat switch and thus making use of the gravity — gave results in accordance with predictions. The design of the strap was changed and the tests were successfully repeated leading to results consistent with predictions (see Fig. 6 – SPIRE unit). For instance, under the nominal conditions, i.e. L_0 = 1.7 K and L_1 = 4 K, the autonomy of the PACS CQM unit was measured to be 47 hours with a 10 μW applied load. The analysis of this result gives a 13 μW parasitic load compared with 14 μW predicted.

Mechanical performance

Both coolers were successfully vibration tested at the Centre Spatial de Lieges (CSL – Belgium) without apparent failure or helium leakage. Accelerometers were mounted on both thermal switch interfaces (HS I/F), on the titanium structure, and on the evaporator cold tip. Table 4 summarizes the first natural frequencies measured on the various interfaces. The axes are defined as follows (see Fig. 1): Y is along the pumping line, and X is along the upper plate (connector side).

These tests were carried out at room temperature. The HERSCHEL satellite embarks a large superfluid helium tank, and the instruments and coolers will be launched cold. Consequently, the ultimate qualification of the coolers will be performed during the cold vibration tests of the instrument qualification models.

The post-vibration-test thermal performance of both coolers was checked and found to be similar to previous measurements (see Fig. 6).

CONCLUSION

The two qualification models of the sorption coolers to be used onboard HERSCHEL for the SPIRE and PACS instruments successfully completed their qualification programs. Both units have been delivered to the instrument projects.

The SPIRE unit has been integrated into the instrument qualification model, and the first set of tests have demonstrated satisfactory performance for the cooler. The SPIRE instrument will be cold vibration tested in the near future and shall demonstrate the final qualification of the cooler.

Preliminary tests of the PACS cooler integrated in the instrument are also satisfactory. Manufacturing of the flight models have been initiated.

ACKNOWLEDGEMENT

We wish to thank J.L. Durand and E. Ercolani who developed the Kevlar string tensiometer and contributed to the mechanical analysis, and N. Luchier who performed various measurements on the Kevlar.

REFERENCES

1. Torre, J.P. & Chanin G., "Miniature liquid ^{3}He refrigerator," *Rev. Sci. Instrum.*, 56 (1985) pp. 318-320.
2. Duband, L., "Space-borne helium adsorption coolers," *ESA SP-401* (1997) pp. 357-360.
3. Duband, L. and Collaudin B., "Sorption coolers development at CEA-SBT," *Cryogenics,* 39 (1999) pp. 659-663.
4. Duband, L., Hui, L. & Lange, A.E., "A space-borne ^{3}He refrigerator", *Cryogenics,* 30 (1990) pp. 263-270.
5. Duband, L., Collaudin, B. and Jamotton, "Sub-Kelvin sorption coolers for space applications," *Cryocoolers 11,* Kluwer Academic/plenum Publishers, New York (2001), pp. 567-576.

ADR Configurations and Optimization for Cryocooler-Based Operation

P.J. Shirron, M.J. DiPirro, J.G. Tuttle, E.R. Canavan

NASA/Goddard Space Flight Center, Code 552
Greenbelt, MD 20771

ABSTRACT

Because of renewed interest in low temperature refrigeration for space missions, there has been considerable developmental work on adiabatic demagnetization refrigerators (ADR) over the last decade or so. As a result, they have expanded from single-stage systems requiring relatively low heat sink temperatures to multi-stage systems capable of rejecting heat to 5 K and higher. This capability enables the use of cryocoolers for heat sinking instead of superfluid helium — a critical step in meeting the space community's need for long-life, low temperature coolers. Since there is no intrinsic limit to an ADR's operating range, the interface temperature for a hybrid ADR/cryocooler system can be set to achieve various performance goals, such as maximizing total system efficiency or minimizing mass. In addition, a larger operating range affords greater flexibility in selecting a cryocooler. In this paper we compare the specific power of ADRs and cryocoolers to develop guidelines for optimizing total system performance, and discuss configurations and operating modes for higher temperature ADRs, along with future technology developments needed to implement them.

INTRODUCTION

Cooling requirements for space telescopes fall into two categories: cooling of the detector focal plane and cooling of the telescope structure. The temperatures required can be quite different. Microcalorimeters generally need to be cooled to less than 100 mK to achieve background-limited performance, while the telescope and other instrument components need only be cooled, in the case of infrared sensing, to ~4 K to limit the amount of stray radiation reaching the detectors. To date, this has been achieved using a low temperature cooler, such as an ADR or ^{3}He refrigerator, connected to a superfluid helium bath. The helium bath may provide cooling directly, as on the Cosmic Background Explorer (COBE)[1], or indirectly by vapor cooling, as is the case for the Spitzer Space Telescope.[2]

The limited lifetime of stored cryogens provides a strong incentive for using cryocoolers on future missions, particularly for very large telescopes. This provides a pressure to develop low temperature coolers capable of operating with significantly higher heat sink temperatures than superfluid helium. At NASA/Goddard Space Flight Center, we have recently developed a 4-stage ADR[3] that operates continuously at 100 mK and below while rejecting heat at 5 K. The efficiency, computed as the ratio of "useful" entropy absorbed at the cold stage to the total entropy expelled to the heat sink, is quite high — just under 50% at 100 mK. Since there is no

Cryocoolers 13, edited by R. G. Ross, Jr.
Springer Science+Business Media, Inc., New York, 2004

intrinsic limit to an ADR's operating temperature, the total efficiency for a hybrid ADR/cryocooler system may be improved by having the ADR operate over a wider and wider range. This paper addresses that possibility by assessing the relative performance of ADRs and cryocoolers in their temperature range either one could be used.

For this analysis, the relevant parameter is specific power. One difficulty is that comparisons of specific power can be misleading if the inlet and outlet temperatures are not the same. Cryocoolers are generally designed to reject heat at room temperature while ADRs operate much colder. We therefore present two analyses. The first is the performance of a single optimized ADR stage operating at temperatures between 1 and 30 K. The second is the performance of a hybrid system, shown schematically in Figure 1, consisting of a cryocooler operating between 30 K and room temperature, and an ADR cooling to lower temperature. A more complete analysis could be performed in which the interface temperature is varied, however this case seems to adequately illustrate the potential for using ADRs at higher temperature.

ADR PERFORMANCE PARAMETERS

The magnetic cooling cycle lends itself to an assessment of specific power, especially if we use the standard practice of considering only the input power to each refrigeration stage, not the total power dissipation of the drive electronics. In general, the input power has three terms: the energy of the magnetic fields used to drive the cycle, energy dissipated in the magnet leads, and power used to operate heat switches. In our case, the gas-gap heat switches are passive and have no dissipation. For the hybrid cooler depicted in Figure 1, a fourth term is the cryocooler's input power needed to reject the ADR's waste heat. Cooling power can be estimated from measurements of entropy versus temperature and magnetic field for a given refrigerant, or, where that is lacking, from the entropy of a system of non-interacting spins if an internal magnetic field is added to account for magnetic interactions.

The impact of parasitic effects such as heat conduction, for example in the suspension system supporting each "salt pill", and thermal gradients within the heat switch and salt pill, is captured in an efficiency factor, ε, as defined above. Historically, ADR efficiencies approach 90% at the temperatures of interest here, but in this analysis we use 80% to be conservative.

Cooling Power

For a stage of molar mass m operating between temperatures T_{high} and T_{low}, with a maximum magnetic field B, a cycle time τ, and an efficiency ε, the cooling power is given by

$$\dot{Q}_{in} = \varepsilon m T_{low} \Delta S / \tau \tag{1}$$

where ΔS is the difference in molar entropy of the refrigerant at low temperature and zero field and at high temperature and field B:

$$\Delta S = S(T_{low}, 0\ Tesla) - S(T_{high}, B) \tag{2}$$

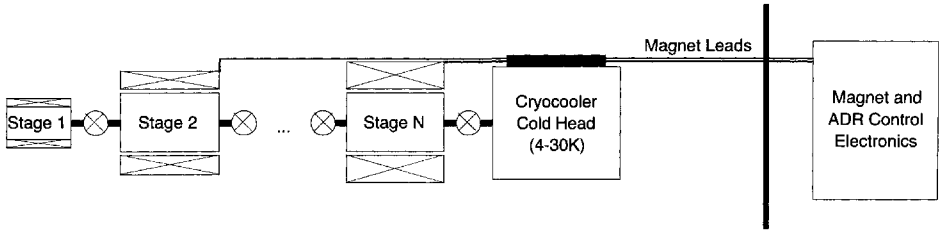

Figure 1. Schematic of a hybrid cooler consisting of an N-stage ADR and a cryocooler. The latter cools the ADR's magnets and electrical leads, and absorbs heat from the stage N refrigerant. The cryocooler is assumed to reject heat at room temperature.

Magnetic field considerations favor refrigerants with the highest possible entropy density over their cooling range. This has the effect of lowering the magnet's input power relative to the refrigerant's cooling power. At temperatures above a few Kelvin, gadolinium gallium garnet (GGG) has been used successfully in two-stage ADRs[4]. It is a readily available material and has significantly higher entropy capacity than the hydrated salts typically used at lower temperature. However, many other compounds, such as Gd fluoride, whose entropy properties are shown in Figure 2, have significantly higher density than GGG and low enough ordering temperatures to be useful in the 4-30 K range.

At higher temperatures than those shown, the entropy function

$$S(T,B)/R = x\coth(x) - (2J+1)x\coth((2J+1)x) + \ln\left(\frac{\sinh((2J+1)x)}{\sinh(x)}\right) \qquad (3)$$

$$x \equiv \mu_B gB/2k_BT = (0.336\ \mathrm{K/T})\, gB_{eff}/T$$

is an acceptable approximation, using, for GdF_3, J=7/2, g=2, and $B_{eff}^2=B^2+b^2$ with b~1 T. R=8.312 J/mol•K is the universal gas constant.

The variety of magnetic materials that could be used as refrigerants might inspire a more intensive optimization study, but it is unlikely to yield qualitatively different results from those we present using the properties of GdF_3.

Input Power

Magnet Energy. The energy required to create a magnetic field in a superconducting coil can be calculated exactly from the physical parameters of the coil (assuming a uniform distribution of windings): number of turns, inner and outer radii, and length. From these parameters, one can compute the coil's field to current ratio and inductance L, and subsequently the magnet's stored energy at current I. The average power input to the magnet is then given by

$$\dot{Q}_{magnet} = \frac{1}{2}LI^2/\tau \qquad (4)$$

This expression is cast in terms of current rather than field because the input power for the magnet leads depends only on the current.

A substantial enhancement of the inductance can result from the addition of ferromagnetic shielding, and a substantial reduction can result from the inclusion of bucking or shield coils.

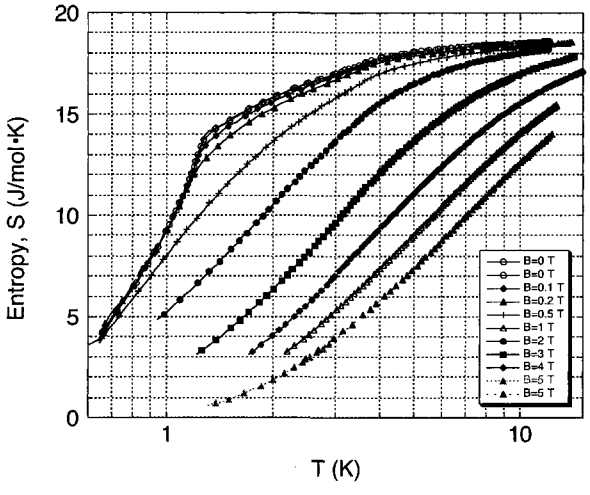

Figure 2. Measured entropy of GdF_3.

While field energy can still be calculated exactly, it is more enlightening to develop scaling laws for its dependence on parameters such as refrigerant volume and magnetic field capability.

We consider two regimes. For small magnets with modest field to current ratios ($\lesssim$0.5 T/A), the windings are generally thin compared to their diameter and higher fields can be obtained either by applying higher current or adding proportionally more turns. In the latter case, the inductance increases as the square of the number of turns, but in both cases the magnet's stored energy is quadratic in the peak field and proportional to the refrigerant volume V. For higher field magnets ($\gtrsim$1 T/A), the dependences are complicated by the inverse relationship between critical current of superconducting wire and magnetic field. Higher fields are produced by increasing the number of turns *and* reducing the current. Using our high field magnets as a basis for scaling, the number of turns required for a given field grows approximately as the square of the field, but the energy only grows as $B^{2.25}$ and as $V^{0.75}$. Since these dependences are only slightly different than for small fields, we use these scaling rules for all field values and volumes.

With B in Tesla and V in cm^3, magnet input power can be summarized

$$\dot{Q}_{magnet} = (2.74J)B^{2.25}V^{0.75}/\tau \qquad (5)$$

Hysteresis. While the vast majority of magnet's energy is dissipated at room temperature, a small amount is converted to heat through hysteresis in both the magnet and shielding. It is potentially significant because this heat is amplified by the cryocooler's specific power. Fortunately the magnitudes turn out to be negligible compared to the magnet's energy. Hysteresis heating in the magnet is proportional to the volume of superconductor and the total field excursion (up and down), while in the shield it is proportional only to the volume of ferromagnetic material. Some differences may be expected for other materials, but for the NbTi and silicon iron "C"[5] used in our ADRs, the magnitudes are 1.44 mJ/T•cm^3 and 58 μJ/cm^3.

Magnet Leads. In general, each ADR stage has independent magnet leads for temperature control. The leads must carry currents up to several amps, depending on the stage's temperature, with a duty cycle of between 25 and 50%. They can be normal metal or a combination of high temperature superconductors (HTS) and normal metal. In either case, the heat load to low temperature depends strongly on the presence (or absence) of upper cooling stages to which they can be thermally anchored. For this analysis, we assume there is either an intermediate cryocooler stage or a spacecraft radiator at 60 K. It is also assumed that the magnets are cooled by the cryocooler, which intercepts all heat conducted to low temperature. Heat absorbed at the 60 K stage is scaled in temperature to give an equivalent heat load on the cold stage.

Brass/HTS hybrid leads have a distinct advantage over all-brass leads, in both lower steady state heat conduction and the absence of ohmic heating in the superconducting portion. Using data for the HTS leads developed for the X-Ray Spectrometer instrument on Astro-E[6], a pair of leads sized to carry 1 A will conduct 19 mW from room temperature to 60 K, and about 0.79 mW from 60 K to low temperature (30 K or lower). In the brass, the round trip resistance of 35 mΩ approximately doubles the heat conducted to 60 K at full (1 A) current. The average heat load consequently depends on the magnet's duty cycle, which is typically about 30%.

Cryocooler Efficiency. The cryocooler absorbs heat from the warmest ADR stage and magnet leads, and rejects it to room temperature. Its input power is computed from total effective heat load at the cold tip times the coefficient of performance for representative coolers. At 30 K, a reasonable range is 50-200 W/W, with the higher figure being more appropriate for low cooling power systems[7].

OPTIMIZED ADR PERFORMANCE

The preceding analysis was used to optimize a multi-stage ADR operating between 1 and 30 K. The system uses 8 stages, mainly because of the energy penalty associated with using magnetic fields much above 4 T. Using such modest fields, the highest temperature stages have appreciable cooling capacity only if their range is limited to about 4 K. The optimization parameter was the total input power divided by the cooling power at 1 K. Figure 3 shows the

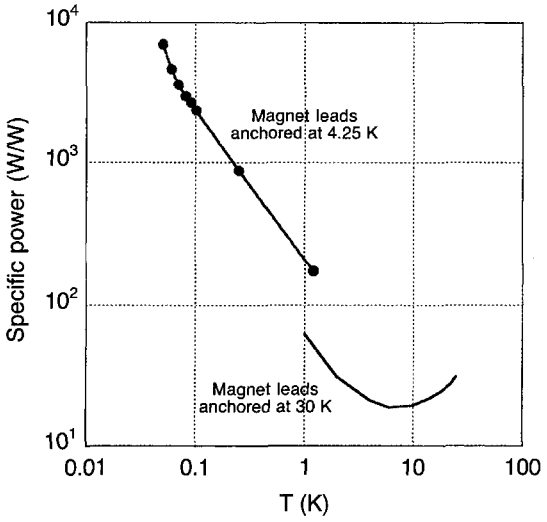

Figure 3. Specific power of individual stages of an optimized ADR operating between 1 and 30 K, compared to the performance of the existing 4-stage ADR operating over the range from 50 mK to 4.2 K.

relative performance of each ADR stage in the system. For this comparison, specific power is computed using only the input power and cooling power associated with each stage. Figure 3 also includes the performance of each stage in our 4-stage ADR.

The most notable feature is the minimum in specific power just below 10 K. This occurs because, as can be seen in Figure 2, the entropy capacity of GdF_3 (per applied field) diminishes markedly above 10 K, and the magnetic field energy begins to rise rapidly relative to cooling capacity. The calculation suggests ADRs have better or at least competitive performance compared to mechanical cryocoolers up to about 30 K.

The discontinuity near 1 K for the two ADR systems illustrates the earlier point about the importance of high-density refrigerants. Chrome potassium alum salt, used below 1 K, has relatively low entropy density (and consequently a low ordering temperature) and requires extra volume for a thermal bus, making the magnet volume and energy significantly larger than is possible with GdF_3 at higher temperature.

The performance of a hybrid ADR/cryocooler system is shown in Figure 4. The cryocooler is taken to have specific powers of 50 and 200 W/W. The points for each stage reflect its cooling power and input power, plus the input power of all warmer stages and the cryocooler. The more or less constant offset between curves indicates the system's efficiency is dominated by the cryocooler's input power. At 4 K, the specific power is in the 1000-4000 range. From a compilation of data for space coolers[7], the efficiency of hybrid JT coolers ranges from 4000-15000 W/W at 4 K, with some laboratory units as low as 1500 W/W. So we conclude that there is a potentially significant performance advantage to ADRs over the 4-30 K range which, coupled to their inherently higher reliability, makes them very attractive for space applications.

CONFIGURATIONS FOR HIGH TEMPERATURE OPERATION

The need for multiple cooling stages to span higher temperatures may give rise to concerns about the system's complexity. Indeed, if as many as 8 stages needed to be operated independently, the concerns would be well-founded. However, it is possible to configure the system in such a way that only two independent magnet controllers are required. This introduces some inefficiency, but it is more than offset by the reduced magnet lead heat load.

The 8-stage ADR is shown in Figure 5. The extra stage for stabilizing the base temperature is optional. The 8 stages are divided into two groups in an alternating fashion. Each group of

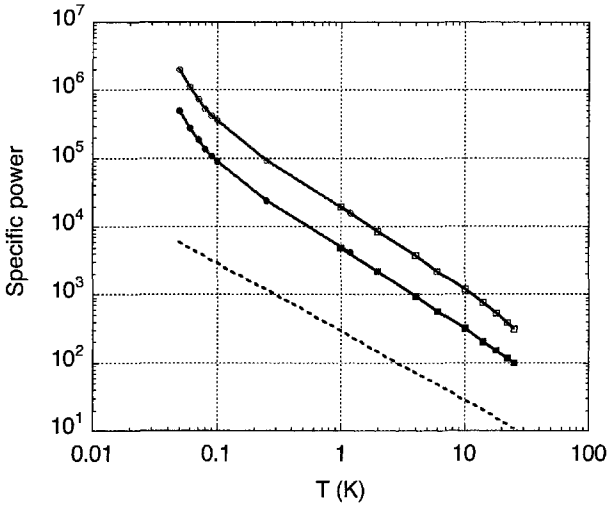

Figure 4. Specific power for a hybrid ADR/cryocooler system over the ADR's operating range. Solid symbols correspond to 50 W/W at 30 K for the cryocooler, and open symbols correspond to 200 W/W. The dashed line represents ideal performance.

four is controlled by the same power supply, so all four stages warm and cool in concert. The interconnecting heat switches are passive gas-gap[8] with carefully sequenced on/off transition temperatures such that when one group is demagnetized, each stage cools into the range where its heat switch turns off, and as the other group is magnetized, each stage warms into the range where its heat switch turns on. For proper selection of refrigerant masses and magnetic field strengths, such a system is actually self-stabilizing. In other words, inefficiencies resulting from off-nominal temperature distributions will bias each stage toward its nominal operating point.

Figure 6 shows a plot of an initial cooldown from 30 K, and subsequent stable operation with an applied heat load of 5 mW at ~4 K. Heat is rejected to 30 K at an average rate of 130 mW, giving an overall heat transfer efficiency of 29%, or roughly 85% for each stage.

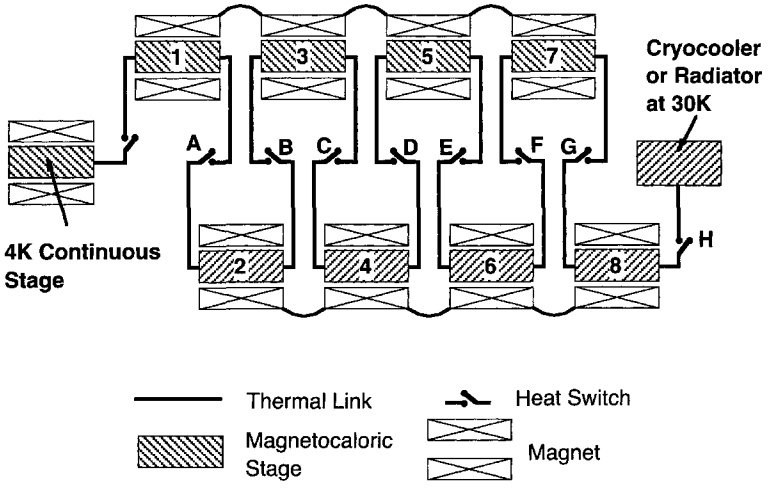

Figure 5. Configuration of an 8-stage ADR operating between 4 and 30 K.

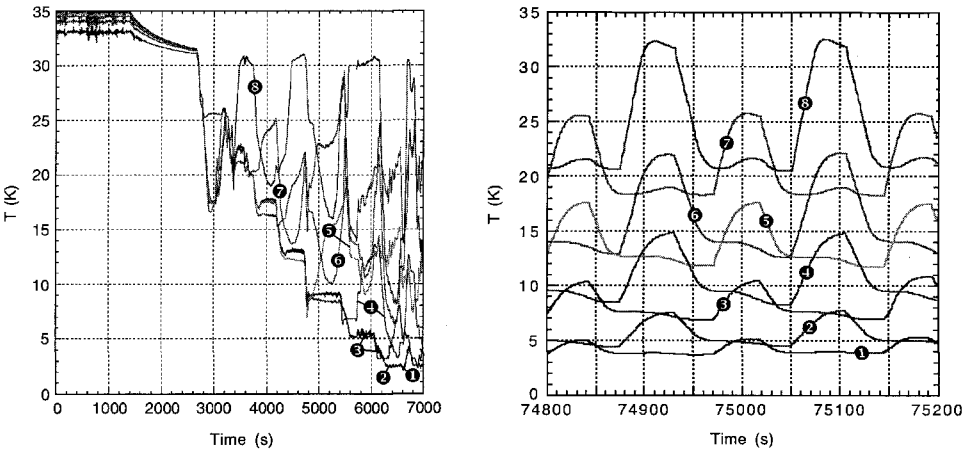

Figure 6. Cooldown and continuous cycling of an 8-stage ADR; numbers on curves are stage number.

FUTURE DEVELOPMENT

The implementation of higher temperature ADRs relies critically on superconducting magnet technology. NbTi can generate suitable fields (up to 4 T) at no higher than about 6 K. While other materials can in principle extend the usable range, none presently has the capability we require. The main obstacle is the production of sufficiently fine wire to build low-current ($\lesssim$10 A), high-field magnets. Progress is being made, though. Superconducting Solutions, Inc. is working on a "react and wind" process for Nb_3Sn that has successfully yielded 0.2 mm wire with a critical current of 14.5 A at 10 K in a 3 T field.[9] The wire is designed to withstand handling and magnet winding after reaction to form the superconductor. The goal is to produce an 8 A, 3 T magnet for 10 K operation.

Other materials, such as MgB_2 (T_c~39 K) and HTS, have significantly higher operating range, but the prospects for their application in ADRs is uncertain. MgB_2 has not yet demonstrated high enough critical current densities for practical magnets, and HTS materials are difficult to manufacture in sufficiently long lengths and with small cross-sectional areas. Should this change in the future, their availability would be enabling for higher temperature ADRs.

At present, we are working to incorporate Nb_3Sn magnets into a system[10] that will operate between 4 and 10 K. The overall goal, beyond development of the basic components, is to demonstrate cooling capacities suitable for future IR telescopes. Estimates are highly dependent on details of individual designs, but they tend to fall in the 10-100 mW range at 4 K. The plan would then be to integrate this system with our 4-stage ADR and a 10 K cryocooler to demonstrate cooling for both detectors and instrument components with good efficiency.

ACKNOWLEDGMENT

This work has been funded by NASA's Office of Aerospace Technology through its Cross-Enterprise Technology Development Program.

REFERENCES

1. Volz, S.M., DiPirro, M.J., "Anomalous On-orbit behavior of the NASA Cosmic Background Explorer (COBE) Dewar," *Cryogenics*, vol. 32 (1992), p. 77.

2. Hopkins, R.A., Nieczkoski, S.J., Russell, K.L., Lysek, M.J., Klavins, A., "Cryogenic/Thermal System for the SIRTF Observatory," *Adv. in Cryogenic Engineering*, Vol. 43A, Plenum Publishing Corp., New York (1998), pp. 973-979.

3. Shirron, P.J., Canavan, E.R., DiPirro, M.J., Francis, J., Jackson, M., Tuttle, J.G., King, T.T., Grabowski, M., "Development of a Cryogen-Free Continuous ADR for the Constellation-X Mission," *Cryogenics*, Vol. 44, Issue: 6-8, June-August, 2004, pp. 581-588.

4. Hagmann, C., Richards, P.L., "Two-stage magnetic refrigerator for astronomical applications with reservoir temperatures above 4K," *Cryogenics,* vol. 34, no. 221 (1994).

5. Tuttle, J.G., Hait, T.P., Boyle, R.F., Muller, H.J., Hodge, J.D., Breon, S.R., "A High T_C Superconducting Current Lead Assembly for the XDS Helium Cryostat," *Adv. in Cryogenic Engineering*, Vol. 43A, Plenum Publishing Corp., New York (1998), pp. 965-972.

6. Silicon Iron "C" (4% silicon, 96% Fe), source of supply: Scientific Materials Inc., 70 Old Hopkinton Rd, Westerly, RI 02891.

7. Dean Johnson, NASA/Jet Propulsion Laboratory, private communication.

8. DiPirro, M.J., Shirron, P.J., Tuttle, J.G., Canavan, E.R., "Design and Test of Passively Operated Heat Switches for 0.2 to 15 K," *Adv. in Cryogenic Engineering*, Vol. 49A, Amer. Institute of Physics, Melville, NY (2004), pp. 436-442.

9. Tuttle, J.G., Shirron, P.J., Canavan, E.R., DiPirro, M.J., Riall, S., Pourrahimi, S., "A 10 K magnet for space-flight ADRs," *Cryogenics*, Vol. 44, Issue: 6-8, June-August, 2004, pp. 383-388.

10. DiPirro, M.J., Canavan, E.R., Shirron, P.J., Tuttle, J.G., "Continuous Cooling from 10 to 4 K Using a Toroidal ADR," *Cryogenics*, Vol. 44, Issue: 6-8, June-August, 2004, pp. 559-564.

Small Adiabatic Demagnetization Refrigerator for Space Missions

N. Luchier, L. Duband

CEA/DRFMC/Services des basses Températures
Grenoble, France

ABSTRACT

In future space missions, it is likely there will be an increasing need for ultra low temperatures. For instance, XEUS is expected to employ a series of superconducting tunnel junctions and transition edge sensors that will require cooling down to 100 mK and below. Only a few technologies are capable of producing such low temperatures: dilution refrigerators, adiabatic demagnetization refrigerators (ADRs), and pomeranchuk cells, to name the most known.

Space missions call for demanding specifications as far as the refrigerator design is concerned. In particular, they need to be extremely reliable, which implies that there should be no moving parts, and they should be as light and electrically efficient as possible. These requirements rule out most of the technologies except for the ADR and a promising new cooling technology: the SINIS junction. The main drawbacks of the ADR are its weight and electrical needs, which can both be quite high.

To address these issues, CEA-SBT has chosen to take advantage of its sorption-cooler know-how to design a small ADR that is composed of a 1 Tesla superconducting coil (0.2T/A) coupled with a chromium-based salt refrigerant material; the ADR is then precooled by a 300 mK sorption cooler.

This paper presents the design of the 100 mK refrigerator system and the first experimental results obtained.

INTRODUCTION

For several decades since the first successful experiments at achieving sub-Kelvin temperatures[1,2], adiabatic demagnetization has been the only means of reaching ultra low temperatures—as low as 1 mK for electronic paramagnetism, even lower for nuclear demagnetization. It was only in the 1960s that a more practical way of producing ultra low temperatures was found: the dilution refrigerator. This refrigerator also has the advantage of producing continuous cooling with fairly high cooling power, even at the lowest temperatures. However, as far as space applications are concerned, dilution refrigerators are very complicated to use. The classical systems rely on gravity to work, although a dilution refrigerator has been designed for the Planck space mission.[3] An efficient solution has yet to be found to confine the needed interface between dilute/concentrate mixtures. In addition, a continuous system either requires large cryogen vessels or a way to recover the gas mixture. Until such a solution is found, the ADR retains considerable interest for space applications due to its non sensitivity to gravity and its absence of any moving parts.

Cryocoolers 13, edited by R. G. Ross, Jr.
Springer Science+Business Media, Inc., New York, 2004

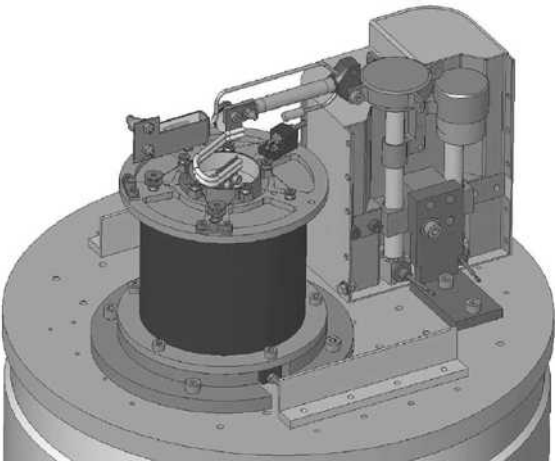

Figure 1. 3D view of the prototype.

CEA/SBT chose to combine an ADR with a sorption cooler to address the drawbacks of both solutions. The combination, equivalent to a multistage ADR, should be able to reach lower temperatures than those achievable with a ^{3}He sorption cooler alone (typically 260 mK). In addition, because the ADR is pre cooled, lower magnetic fields are needed compared to a multistage ADR, leading to lower electrical consumption and a lighter system. Finally, an ADR stage coupled with a sorption cooler can allow continuous cooling at 300 mK to be provided.

THE SYSTEM

Figure 1 shows an illustration of the integrated system. It is thermally connected to a 4.2 K heat sink and is composed of two main parts:

1) *The double-staged sorption cooler:* A ^{4}He sorption stage pre cools and liquefies the ^{3}He stage allowing temperatures as low as 250-300 mK to be reached. The complete description of the sorption cooler is beyond the scope of this article (see Ref. 4 for an in-depth description of the system).
2) *The ADR:* This consists of a salt pill and a coil thermally isolated from each other through Kevlar cords.

In the expected starting temperature range of our ADR (roughly 500-300 mK), the choice of the refrigerant is limited to Chromic Potassium Alum (CPA), Ferric Ammonium Alum (FAA), and Chromic Cesium Alum (CCA). Between 0.5 and 0.05 K, each of these salts has around the same capability as a refrigerant, with maybe a little superiority for the FAA. However, the melting point of FAA is quite low (around 39°C[5]), which can be a problem in space missions where the systems are usually baked around 80°C. In addition, there are the difficulties of handling during the building of the pill (which may imply some TIG welding). As far as melting point is concerned, the best paramagnetic salt is CCA (116°C).[5] However, CCA is quite difficult to grow.[6] So, for our first prototype, we made a trade-off and chose the CPA salt (melting point of 89°C[5]). Table 1 summarizes the key data for this salt.

Table 1. CPA salts data[5]

Molar weight (g/mole)	499
Density (g/cm^3)	1.83
Néel temperature (K)	≈0.01
Landé factor g	1.97
total electronic angular momentum J	½
Local magnetic field (interactions) (T)	0.01

The salt pill is connected to the double-staged sorption cooler ^{3}He evaporator through a ^{3}He gas gap heat switch. This heat switch has a similar design to our ^{4}He gas gap heat switch[7] but is able to work at a lower temperature. According to our model, with the ^{3}He evaporator at 0.3 K, the switch will create a load of about 0.17 μW on the salts at 0.1 K, which is quite low. The pill is suspended in the center of the coil using Kevlar strings that bring a total load of around 1.3 μW.

PERFORMANCE PREDICTIONS

In order to be able to determine the quantity of salts as well as the field intensity needed, a modeling of the adiabatic demagnetization transformation was performed. We choose the simple free ion approximation. However, this model alone does not take any interaction into account. Thus, a simple model correction was made for these interactions (mainly the dipolar interactions) via a small local field added to the applied field: i.e. $H_{tot} = \sqrt{H_{app}^2 + h^2}$. The crystal field splitting effects were completely neglected in this model, but the variation between an 'exact' calculation and the free ion approximation is small enough (around 1% at most) to provide confidence that the results of our calculations are accurate.

From the free ion approximation, we can derive the following expression for the entropy[8,9]:

$$\frac{S(H,T)}{R} = \ln\left(\frac{\sinh((2J+1)x/2)}{\sinh(x/2)}\right) + \frac{x}{2}\coth\frac{x}{2} - \frac{(2J+1)x}{2}\coth\frac{(2J+1)x}{2} \qquad (1)$$

with $x = \frac{g\mu_B\sqrt{H_{app}^2 + h^2}}{kT}$. J is the total electronic angular momentum, g is the Landé factor, μ_B is the Bohr magneton.

Fig. 2a shows the entropy versus the applied magnetic field for a temperature of 0.3 K according to equation 1. At this temperature, it is useless to apply a magnetic field above 1T. With this field, 95% of the entropy is already removed and removing the few percent left would be too high a cost in field intensity.

At 1T, the heat rejected at the ADR heat sink (the cold tip of the double-staged sorption cooler) is $q_r = 0.3 \times [S(0.3K, 0T) - S(0.3K, 1T)] = 3.3$ J/mole.

One of the consequences of the free ion approximation is that entropy is a function of H/T. Since the demagnetization is adiabatic, the final magnetic field available to regulate the system at the final temperature is defined by the following expression:

$$\left.\frac{\sqrt{H_{app}^2 + h^2}}{T}\right|_{0.1K} = \left.\frac{\sqrt{H_{app}^2 + h^2}}{T}\right|_{0.3K} \qquad (2)$$

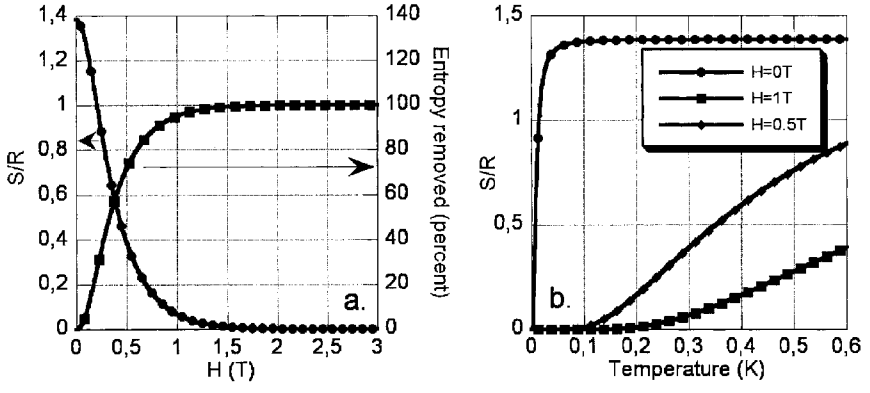

Figure 2. Entropy variation: as a function of the magnetic field for a temperature of 0.3 K and as a function of the temperature for different applied magnetic fields.

With a starting applied field of 1 T, there is about 0.33 T left to allow for temperature regulation at 0.1 K.

Fig. 2b shows the entropy of the salts at various magnetic fields. Assuming the demagnetization is perfectly adiabatic, the energy at our disposal at 0.1K is $q_d = 0.1 \times [\, S(0.1K,0T) - S(0.3K,1T) \,] = 1.1$ J/mole.

ADR SETUP

Salt Growth

When growing the paramagnetic salts, one has to be careful to fully thermalize them. In particular, the condition of having inter grain boundaries must be avoided. In order to fulfill this requirement, a thermal bus composed of 365 copper wires 250 μm in diameter brazed on the cold tip has been designed (see Fig. 3). The wires are organized in a triangular array and spaced 2 mm from each other. The aim of such a thermal bus is to ensure that the crystal's sizes are at least of the same size as the wire spacing. Hagmann *et al.*[6] built such a thermal bus to grow CCA crystals. We have built an equivalent bus for CPA, which grows in larger crystals.

The growing apparatus is quite similar to the one of Hagmann: the copper bus is cooled by a Peltier cell in order to ensure that the growth occurs preferentially on the copper wires. The growth results in crystals of around 1 cm in size for the largest. In the whole, every crystal seems to have grown on a copper wire, and it does not appear that there were any crystals without connections to the thermal bus. Because these salts need to be hermetically sealed to avoid any loss of water (which would impact their paramagnetic properties), the salts were sealed in a stainless steel pill.

In total, 0.2 moles of salt have been grown. This will yield a refrigerator "autonomy," or dwell time, of about 12 hours with a 5 μW load for a magnetization field of 1 T.

The Coil

We used a homemade coil built with 0.3 mm NbTi wire. The coil is 100 mm long with a field hole 50 mm in diameter. It is composed of 66 layers of around 250 turns each.

Each layer was potted with Araldite in order to ensure that the wire won't move in the magnetic field (which would lower the coil heat dissipation). Since the coil is cooled only by conduction, we built the mandrel of pure copper to ensure good thermal conduction between the 4.2 K heatsink and the wires. Despite this mandrel, our first tests showed that this is not enough to keep the whole wiring cooled during the manipulations. When the current is varying, the outer part of the wiring is heated, even at low current, which lowered the maximum field that could be applied. Solutions are currently being evaluated to prevent this heating.

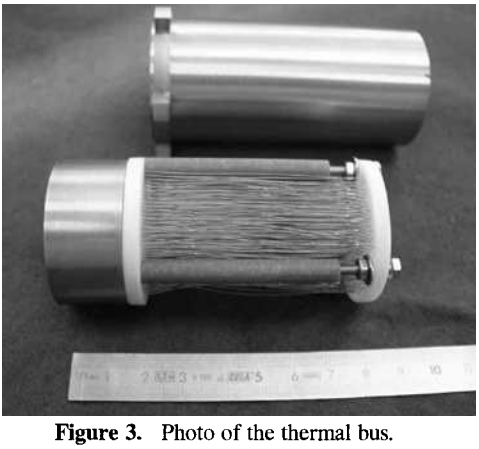

Figure 3. Photo of the thermal bus.

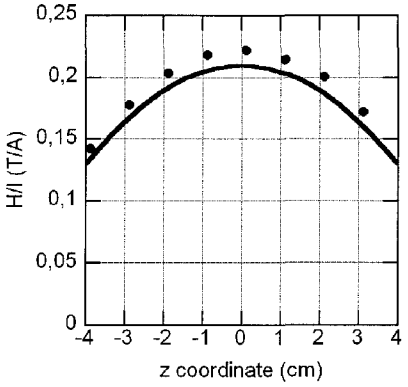

Figure 4. The coil measured field (dots) along with the expected calculated field (line).

Plunged in liquid Helium, the coil critical current is 34 A for a field of 7.5 T and a field over current ratio of 0.22 T/A at the coil center. The coil weights 2.5 kg for a total system weight around 5 kg (without any magnetic screening solutions that often represent a good part of the total weight of ADRs). Figure 4 displays the measured field profile as well as the predicted field. This field was calculated using roughly the same coil geometry and current intensity. It is important to emphasize that this coil is a homemade prototype. When designed by a specialist manufacturer, the weight is expected to be significantly less.

EXPERIMENTAL RESULTS

As mentioned previously, to validate this concept, we have used a double-stage helium sorption cooler as the pre cooling unit. The first ^{4}He stage is used to cool down and condense the ^{3}He stage at a temperature of about 2.4 K (for this particular setup). The ^{3}He then provides about 3 Joules of "cold Joules." This value is compatible with the operation of the ADR considering that:

1. The specific heat of CPA is given by[8] $C/R = aT^3 + b/T^2$, with $a \approx 4.10^{-4}$ K^{-3} and $b \approx 0.016$ K^2. (According to these values, cooling 0.2 moles of CPA from 2.4 to 0.3 K requires 83 mJ).
2. The heat rejected at 0.3 K during the 1 T magnetization is $Q_r = 660$ mJ.

Due to schedule constraints the gas gap heat switch to be used in the framework of this project was not available at the time of writing. Consequently, for the first set of tests, the switch was replaced by a copper strap. In this case the performance of the ADR is significantly degraded because, as the salt pill is thermally grounded to the ^{3}He evaporator, a large fraction of the demagnetization energy is used to cool down the ^{3}He liquid. In addition, the parasitic load to the pill is substantially higher. Nevertheless, using this setup, preliminary experiments were carried out. Since the enthalpy of the ^{3}He liquid is fairly large, the ADR cooling effect depends on the amount left in the evaporator. On the other hand, the amount of liquid must be large enough so that the sorption cooler does not run out during the magnetization process. For one of the best cycles, the salt pill was magnetized at a temperature around 500 mK with a limited field of 0.4 Tesla. The subsequent demagnetization provided a 300 mK cooling effect (ultimate temperature of about 200 mK). These first results are very encouraging and demonstrate that the ADR is operating correctly. Yet they revealed two main areas for future improvements: a better overall thermalization of the coil, and probably a review of the thermal bus design.

CONTINUOUS HELIUM SORPTION COOLER

One of the drawbacks of helium sorption coolers is the single shot operation. Although typical duty-cycle efficiencies are in excess of 95%, the demand for continuous operation has been identified. As mentioned previously, the addition of the ADR stage to the helium sorption cooler can

satisfy this objective. In this operating mode, the sorption cooler is recycled and the experiment is cooled down to a temperature slightly above its ultimate temperature. This mode, achieved by controlling the temperature of the sorption pump, allows retaining some margin in cooling power or rather in available "cold" Joules. In the first phase, only the sorption cooler is used. Then the ADR stage is slowly magnetized while the temperature of the experiment is temperature regulated using the additional cooling power available. Once the helium sorption cooler is close to being out of liquid helium, the ADR is thermally disconnected from the latter using the heat switch. In the meantime the ADR is demagnetized to maintain the experiment at constant temperature. The sorption cooler is then recycled, and, once the evaporator is back at the operating temperature, the ADR stage is thermally reconnected. The cycle can then be repeated. The required ADR field is limited, as the autonomy of the ADR stage is set to compensate for the load from the experiment and from the heat switch OFF thermal leak during the sorption cooler recycling phase (less than ~5% of the overall cycle).

CONCLUSIONS AND PERSPECTIVES

The design and first test results have been presented for a small adiabatic demagnetization refrigerator coupled with a double-stage sorption cooler to reach temperature as low as 50 mK. The objective has been to come up with a sub-Kelvin cooling solution for space use, with limited mass and magnetic fields. In addition, this thermal architecture could be used to develop a continuous ^{3}He refrigerator.

Due to the unavailability of the heat switch at the time of writing, this first set of tests was carried out with a degraded setup. Nevertheless, these preliminary results have demonstrated a cooling effect of 300 mK from a starting temperature of 500 mK. The next set of tests will be performed with the nominal setup, i.e. with a ^{3}He gas gap heat switch.

ACKNOWLEDGMENTS

We wish to thank Laurent Clerc for the use of the sorption coolers, Laurent Guillemet for his help in the use of the design tools, Alain Boulbès (CNRS/CRTBT, Grenoble, France) for all the advice he provided on how to build the coil, and Laurent Miquet for the invaluable help in the design and building of the ADR.

REFERENCES

1. Giauque W.F. and D.P. Macdougall, *Phys.Rev.* 43, 7689 (1933).
2. W.J. De Hass, E.C. Wiersma and H.A. Krmaers, *Physica* 1, 1 (1933).
3. A. Benoit, et al., SAE *Technical Paper Series* No. 941276 (1994).
4. L. Duband, "Double Stage Helium Sorption Coolers," *Cryocoolers 11,* Kluwer Academic/Plenum Publishers, New York (2001), pp. 561-566.
5. I.D. Hepburn, "Adiabatic Demagnetization Refrigeration in Space, A Design Study," *ESA contract Final Report 153018.*
6. C. Hagmann, et al., "Paramagnetic salt pill design for magnetic refrigerators used in space applications," *Cryogenics,* vol. 34, Number 3 (1994), pp. 213-219.
7. L. Duband, "A thermal switch for use at liquid helium temperature in space borne cryogenic systems," *Cryocoolers 8,* Plenum Press, NY (1995), pp. 731-741.
8. R.P. Hudson, *Principles and application of magnetic cooling*, North-Holland Publishing Company-Amsterdam, London (1972).
9. N.W. Ashcroft and N.D. Mermin, *Solid State Physics*, Saunder College Publishing (1976).

Magnetoresistive Heat Switches and Compact Superconducting Magnets for a Miniature Adiabatic Demagnetization Refrigerator

J-M. Duval, B.M. Cain and P.T. Timbie

Department of Physics
University of Wisconsin
Madison, Wisconsin, 53706, USA

ABSTRACT

In order to provide continuous cooling at 50 mK for space or laboratory applications, we are designing a miniature adiabatic demagnetization refrigerator (MADR) anchored at a reservoir at 5 K. Continuous cooling is obtained by the use of several paramagnetic pills placed in series with heat switches. We are aiming for a fast cycling process ($\approx$ 500 s) in order to reduce the size of the pills. For that purpose, we developed and tested magnetoresistive heat switches based on single crystals of tungsten. They provide good thermal performance for a very short switching time, depending only on the ramping speed of the magnet used. Measurements of heat conductivity between 150 mK and 10 K with fields ranging from 0 T to 3 T are presented for different tungsten crystals. Small superconducting magnets have been designed and manufactured from high current density NbTi wires. The shielding is achieved using ferromagnetic material, and a holmium core is used as a flux concentrator. Superconducting shielding is envisioned. Results of numerical simulations and measurements of magnetic field are compared. A prototype continuous MADR, using magnetoresistive heat switches, small paramagnetic pills, and compact magnets has been tested. A design of a MADR that would provide continuous cooling below 100 mK is described.

INTRODUCTION

The development of smaller and more reliable coolers for temperature under 200 mK is necessary to permit the utilization of new sensitive detectors[1] for space-based or ground-based applications. The design of reliable heat switches is essential for low temperature coolers. The characterization of tungsten crystal magnetoresistive heat switches is presented in this paper. We measured the conductivity of different crystals and discuss its uses and limitations. ADRs can provide cooling in this range of temperatures and they offer the advantage of being totally electronic and of not using any gas. ADRs are therefore independent of gravity and do not require any plumbing or moving parts. A design of a multistage ADR based on magnetoresistive heat switches is described. As part of an effort to reduce the mass of the full device and to limit stray field on the detectors, we present progress in the design of a multilayer shield. Finally, the latest developments and tests of a prototype of a continuous miniature ADR are described.

Cryocoolers 13, edited by R. G. Ross, Jr.
Springer Science+Business Media, Inc., New York, 2004

CONFIGURATION AND OBJECTIVES

Our goal is to realize a MADR that can provide continuous cooling at 50 mK from a 5 K reservoir. Our design[2] is comparable in principle to the continuous ADR described by Shirron.[3,4] The main feature is that the temperature of the last pill (starting from the bath) of the series is kept constant by control of its magnetization and demagnetization rate.

The adjacent pills provide cooling during the magnetization process and allow a continuous process. This cascade type of cooling can be implemented with any number of pills greater than two. Depending on the number of stages, these devices could be used with a different bath temperature or pre-cooler temperature. Our design aims at using the smallest pills possible.

For that purpose, the cycling time has been minimized. As has been discussed[2], the limiting factor for increasing the frequency of cycling is the eddy currents in the magnets and the copper thermal bus that connect the salt pills and switches. CPA (chromic potassium alum) salt is used. It provides good thermal properties and the crystal is relatively easy to grow. Use of GGG (gadolinium gallium garnet) is envisioned for the higher temperature stages. The cycling time of our prototype is of the order of 500 s, with the switching time of each magnet being between 10 and 30 s. Ultimately, a 5K / 50 mK MADR would require a succession of four pills. We describe, in the last section, experimental results obtained with two pills.

MAGNETORESISTIVE HEAT SWITCHES

Magnetoresistive heat switches are used because of their simplicity, reliability and short switching time.[5] These switches require superconducting magnets providing a field of several Tesla, as is described in the next section. We acquired different commercial tungsten crystals, vacuum brazed them to a copper bus, and measured their thermal conductivity as a function of temperature (from 150 mK to 10 K) and magnetic field (from 0 to 3 T). The values of the measured thermal conductivity for two of these crystals (a square crystal of size 0.5 × 0.5 × 20 mm^3 and a cylindrical crystal of diameter 0.5 mm and length 25 mm) are presented in Figures 1 and 2. The magnetic field has been obtained with the magnet described in the next section, therefore, as can be seen in Figure 3, the field is not homogeneous in the length of the crystal. Typically, the field on the edge of the crystal is half of the maximum field. For simplicity, we decided to represent the heat conductivity in the crystal as a function of the field in the center of the magnet. This approach leads to underestimation of the effect of the field and to overestimation of the crystal conductivity by around 40% for the

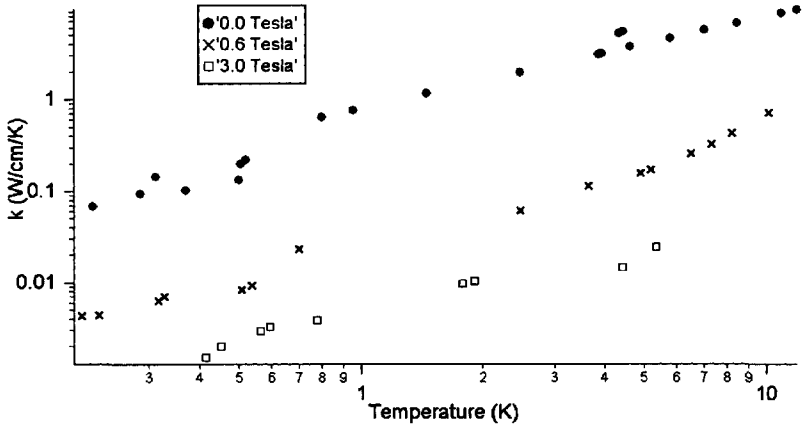

Figure 1. Thermal conductivity of a single crystal of tungsten as a function of temperature and applied magnetic field. The temperature represents the average temperature between the two sides of the crystal. The value of the field indicated is the field in the center of the magnet during the measurements. Measurements at high field are similar for all crystals. Differences with no field are discussed.

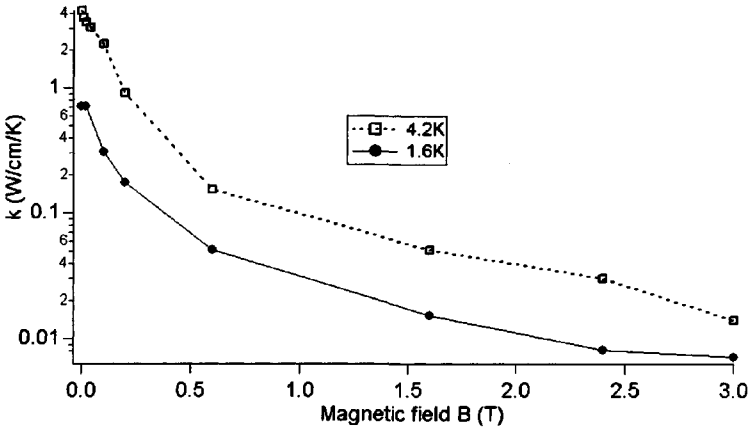

Figure 2. Thermal conductivity of a single crystal of tungsten as a function of applied magnetic field for two temperature.

maximum field. The value of the conductivity should therefore be lower than what is represented. We found that the measurements at a field greater than 0.5 Tesla agree well and are consistent with the data[6] of Batdalov to within less than 40 %. We explain this difference by the inhomogeneous field in our crystal.

The discrepancy for measurements of conductivity with a field of zero is more important. Specifically, the conductivity is several orders of magnitude lower than the one reported by Batdalov.[6] We measured the RRR (residual resistivity ratio) of the crystals, and found values of the order of 100 to 200, as to be compared to Batdalov's value[6] of 1.5×10^6. We expected that the small size of the crystal compared to the mean free path of electrons in the crystal[7] could be a limitation to the RRR and heat conductivity in the absence of magnetic field. We therefore got a crystal of larger size ($1.0 \times 1.0 \times 20$ mm^3) and measured its heat conductivity and RRR. The RRR measured was lower than 50 and the heat conductivity in the absence of field is also low, showing a much lower purity. We haven't found an explanation for the poor quality of this crystal and are investigating this.

As a conclusion, we can be confident of the reproducibility of the thermal conductivity of these heat switches in the presence of a magnetic field on the order of a few Tesla. The conductivity without magnetic field can be determined by electrical measurements and is largely dependent on the purity of the crystal. In order to achieve a conductivity ratio of 500, which would be suitable for our design, crystals with an RRR higher than 200 have to be found.

Magnetoresistive heat switches with tungsten crystal of RRR of the order of 100 can be used at the expense of a lower efficiency and limitations on the lowest achievable temperature.

MAGNETIC SHIELDING

Superconducting magnets are required both for the paramagnetic pills and for the magnetoresistive heat switches. Each magnet has to be shielded in order to limit the stray field on the detectors and on the neighboring heat switches or pills. The magnets, and especially their shields, are responsible for most of the mass and volume of the MADR. We first designed and built shields out of vanadium permendur (VP) and silicon iron. The magnetic field in the center of the magnet, as well as outside of the magnets has been measured and compared to the simulation (Figure 3). The field fits our prediction to better than 20%. The difference is explained by uncertainties in the purity and heat treatment of the materials.

In order to limit the size and mass of the magnet even more, as well as the stray magnetic field on the detectors, we are exploring the possibility of using a layer of superconductor as a shield. Superconductors can be used as shields by taking advantage of their perfect diamagnetism. The

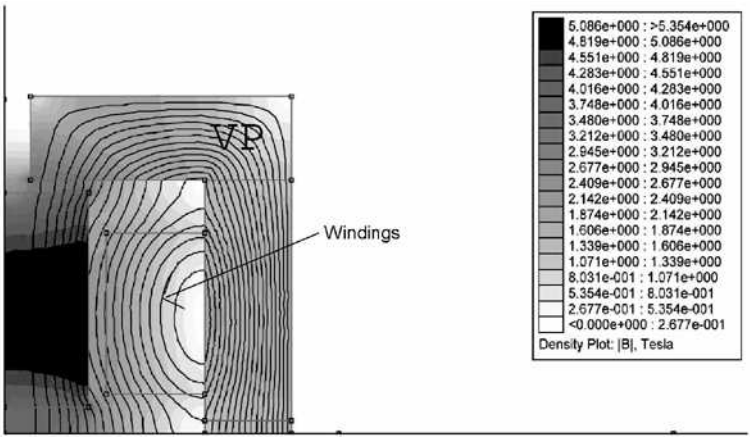

Figure 3. Simulation of magnetic field in the magnet and shields. Cross section of one quadrant of cylindrical symmetric design. Simulation done with software FEMM.[8])

limitation of using superconductors is that the magnetic field must always be kept below the material's critical field. As a preliminary experiment, we wrapped Pb foil around a 3 T magnet and its VP shield and measured the field on the mid plane 5 cm from the center. The comparison is presented in Figure 4. When the critical flux is not exceeded the magnetic field outside is kept very low. If, on the contrary, the critical flux is exceeded, part of the Pb becomes normal and is penetrated by the field. Furthermore, when the field decreases, the magnetic field is trapped in the superconductor. At maximum current, we believe that the field with superconductor is lower than the field without because part of Pb is still superconductor. In order to realize an efficient shielding, all of the material has to stay superconducting. This could be achieved by using a material with a higher critical field, like Nb, by using a thicker shield, or by placing the superconductor layer away from the inner shield. With appropriate superconducting shielding, we are aiming at a stray field at the position of the detectors of less than 0.1 mT.

TWO STAGE PROTOTYPE AND TEST

We built and tested a two-stage MADR to validate the concept of using small pills, magnetoresistive heat switches, and fast switching times (see Figure 5). The control of temperature and of the different phases of the cycle is fully automated using a computer controlled PID loop.[9]

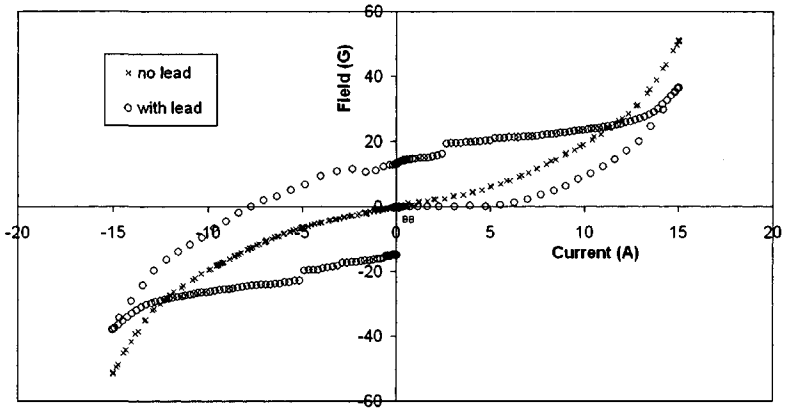

Figure 4. Field 5 cm away from the center of the magnet with and without a layer of Pb tape around the VP shield. The field in the center of the magnet is 3 T when the current (shown on horizontal axis) is 15 A.

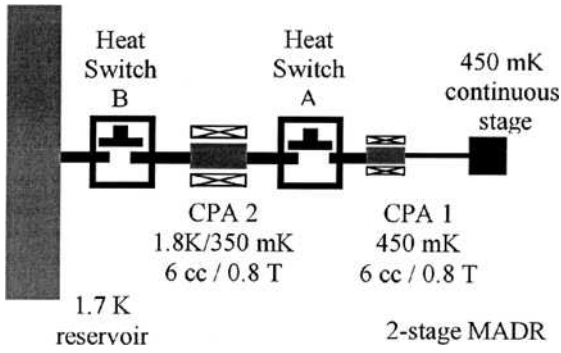

Figure 5. Experiment with two pills for a continuous temperature of 450 mK. The magnet and size for CPA1 (0.8 T/6 cc is oversized for this experiment allowing more freedom to tune the parameters.

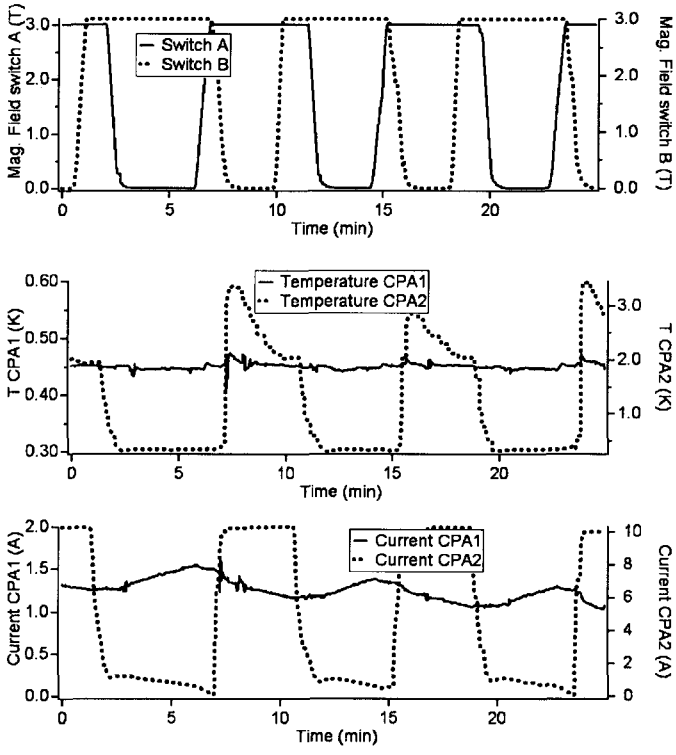

Figure 6. Validation of the principle by the test of a two-stage ADR. Top panel : magnetic field at center of heat switches vs time. Middle panel : Temperature of continuous stage (CPA1) and second stage (CPA2). Bottom panel : Current in the magnet for both stages. Values of the magnetic field are proportional to the values of the current with a ratio of around 15 A/T.

The temperature variations are shown in Figure 6. The fluctuations are on the order of 1 mK. Stability will be improved in future experiments by optimizing the PID parameters, using a more accurate power supply, and increasing the frequency of temperature acquisition. The continuous temperature achieved in this example is 450 mK, with a bath temperature of 1.6 K. In the example shown in Figure 6, a drift appears in the current on CPA1, showing that the temperature chosen is slightly too

Table 1. Parameters for a four-stage MADR. Power is the heat load through the heat switches connecting the next stages. Q is heat extracted per cycle. Size is the size of the paramagnetic pills and field, the magnetic field of the corresponding magnet. Tmin and Tmax are the maximum and minimum temperature of the pill during a full cycle.

Pills	Tmax (K)	Tmin (K)	Power (uW)	Q (mJ)	size (cm^3)	Field (T)
CPA1	0.050	0.050	15.8	4	3	0.15
CPA2	0.8	0.047	35	8.6	10	1.2
CPA3	1.5	0.78	1100	250	15	1.5
GGG	5	1.46	2200	550	15	2.0

low. For a temperature of 500 mK, the drift was negligible, and for a temperature of 550 mK, the drift was positive.

Also, for a full prototype, the whole control process could be implemented using electronic components which would provide faster and more accurate temperature control. Each phase of the cycle is determined by measurements of temperature or of voltage (equivalent to field) of magnet, providing a fully self-controlled setup. This experiment shows the possibility of using miniature pills and magnets with fast cycling time. We are now working on the implementation of a third stage in order to reach a lower continuous temperature.

DESIGN OF A FULL STAGE MADR

Mainly because of the limitation in the heat conductivity of the tungsten crystal in the absence of magnetic field, and hence the limitation in the ratio on/off of conductivity, a four-stage MADR reaching a temperature of 50 mK cannot be made with the quality of crystal we have obtained so far. Several possibilities, however, should be explored in order to realize this promising cooler. Crystals exhibiting RRR of around 500 would be adequate to realize such a prototype.

Measurements on such a crystal have been published[10], the main difficulty being to find a crystal with such a purity with the size we are looking for and at a reasonable price. The utilization of other types of heat switches such as passive gas-gap heat switches[11], or at the lower temperature, superconducting switches would allow the possibility of such a prototype.

Following our measurements of heat conductivity of magnetoresistive heat switches, and assuming that crystals with RRR of 500 can be found, we calculated the requirements for a MADR capable of reaching a temperature of 50 mK with a reservoir at 5K. CPA pills would be used for the three colder stages whereas GGG would be used for the stage ranging from 5 K to 1.6 K. The results of this estimation of size and magnetic field are shown in Table 1. The mass of such a cooler would be less than 5 kg.

RESULTS AND CONCLUSION

We designed a light and compact four-stage MADR for continuous operation under 100 mK. A magnetoresistive heat switch based on a tungsten crystal has been designed, and its conductivity has been measured. We determined that this type of heat switch can be used if the crystal has the necessary purity—typically an RRR greater than 500. Other heat switches, like Al superconducting switches or gas gap switches, could be used for lower-temperature switches. We built a continuous MADR with a succession of 2 pills showing the feasibility of the design and of the temperature control technique. We are working on the implementation of one more stage in order to reach continuous cooling at 150 mK. Future development of lower temperature coolers will require a focus on efficient heat switches.

ACKNOWLEDGMENTS

This work is supported by NASA grant NAG5-10204.

REFERENCES

1. *Proceedings of the Tenth International Workshop on Low Temperature Detectors*, AIP Conference Proceedings, NIM-A(2004), p. 520.
2. Duval, J.-M., Cain, B. and Timbie, P., "A Miniature Adiabatic Demagnetization Refrigerator," *Adv. in Cryogenic Engineering*, Vol. 49B, Amer. Institute of Physics, Melville, NY (2004), pp. 1729-1736.
3. Shirron, P., Canavan, E., DiPirro, M., Tuttle, J. and Yeager, C., "A multistage continuous-duty adiabatic demagnetization refrigerator," *Adv. Cryo. Eng.*, 45B, Kluwer Academic/Plenum publishers, NewYork (2000), pp. 1629-1638.
4. Shirron, P., Canavan, E., DiPirro, M., Jackson, M., King, T., Panek, J. and Tuttle, J., "A compact, high performance continuous magnetic refrigerator for space missions," *Cryogenics,* 41 (2001), pp. 789-795.
5. Supanich, M. and Timbie, P., "A miniature adiabatic demagnetization refrigerator and magnetoresistive heat switch," AIP Conference Proceedings 605, edited by Porter, McCammon, Galeazzi and Stahle (2002), pp. 387-90.
6. Batdalov, A. and Red'Ko, N., "Lattice and electronic thermal conductivities of pure tungsten at low temperature," *Sov. Phys. Solid State,* 22 (1980), pp. 664-6.
7. Canavan, E., DiPirro, M., Jackson, M., Panek, J., Shirron, P. and Tuttle, J., "A magnetoresistive heat switch for the continuous ADR," *AIP Conference Proceedings,* 613B (2002), pp. 1183-90.
8. Finite Element Method Magnetics, http://femm.foster-miller.net/.
9. National Instrument LabVIEW, PID control software.
10. Touloukian, Y.S., *Thermophysical Properties of Matter*, Ed. by IFI/Plenum, New York (1970).
11. Shirron, P., Canavan, E., DiPirro, M., Tuttle, J. and Yeager, C., "Passive gas gap heat switches for use in adiabatic demagnetization refrigerators," *AIP Conference Proceedings,* 613 (1) (2002), pp. 1175-1182.

The Performance of a Laboratory Optical Refrigerator

G.L. Mills, D.S. Glaister, W.S. Good, A. J. Mord

Ball Aerospace & Technologies Corp.
Boulder, CO, USA 80301

ABSTRACT

Optical refrigeration using anti-Stokes fluorescence in solids has several advantages over more conventional techniques, including low mass, low volume, low cost and no vibration. It has been the topic of analysis and experimental work by several organizations. We recently demonstrated the first optical refrigerator which cooled an attached load 11.8°C below the surroundings. Our laboratory refrigerator is pumped by a 30 watt, tunable, ytterbium doped yttrium aluminum garnet (Yb:YAG), continuous wave, disk laser and uses a ytterbium doped fluorescent cooling element external to the laser cavity.

In this paper, we report on the operation of our laboratory optical refrigerator at different pump wavelengths, power inputs and loads. We have modeled the refrigeration cycle based on the fluorescent material emission and absorption data at ambient and reduced temperature. We have also calculated the expected heat transfer into the refrigerator cold assembly. The measured performance of the refrigerator is presented and compared to the expected performance.

INTRODUCTION

The basic principle of cooling by anti-Stokes fluorescence was suggested as early as 1929,[1] but it was not until 1995 that the actual cooling of a solid was first demonstrated by Epstein et al. at Los Alamos National Laboratory (LANL) using Ytterbium doped Zirconium Fluoride (Yb:ZBLAN) glass.[2,3] In 1996, Clark and Rumbles reported cooling in a dye solution of rhodamine 101 and ethanol.[4] A collaborative effort by LANL and Ball Aerospace resulted in an isolated cylinder of Yb:ZBLAN cooling 48°C below the ambient temperature.[5] Gosnell has reported cooling of 65°C in a Yb:ZBLAN fiber.[6] In 2003, we demonstrated the first optical refrigerator. It cooled an attached load 11.8°C below the surroundings.[7]

The fundamental refrigeration cycle of fluorescent cooling is simple. In the case of the Yb: ZBLAN material, the presence of the internal electric fields of the host ZBLAN cause the ground and first excited states of the Yb^{3+} ion to be split into multilevel manifolds as shown in Fig. 1. A photon from a laser tuned appropriately will be absorbed only by an ion that has been thermally excited to the highest level of the ground-state manifold and will promote that ion to the lowest level of the excited-state manifold. When that ion decays radiatively, it can fall to any of the four ground-state levels. On average, the outgoing fluorescent photon will carry slightly more energy

Cryocoolers 13, edited by R. G. Ross, Jr.
Springer Science+Business Media, Inc., New York, 2004

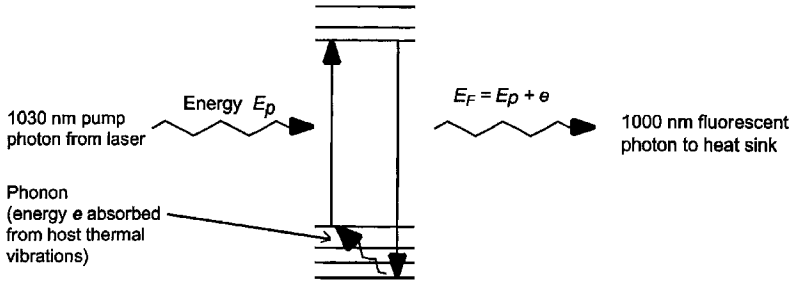

Figure 1. The photon-phonon refrigeration cycle results from the energy levels of the Yb^{3+} ion in the ZBLAN glass host material.

than the pump photon. By selectively "picking off" the "hottest" ions, this process depletes the population of the highest ground-state level. Thermal equilibrium is re-established when another ion is promoted to that level by absorbing a phonon from the host material. The absorption of this phonon constitutes the refrigeration. In summary, a Yb^{3+} dopant ion absorbs a pump photon and the photon is re-emitted slightly bluer (higher energy). This energy difference comes from thermal vibrations (phonons) of the host material.

The simplest implementation of a cryocooler based on this principle is a simple Yb:ZBLAN cylinder (cooling element) with high-reflectivity dielectric mirrors deposited on the ends as shown in Fig. 2. The pump beam is introduced through a small feed hole in one mirror, and then bounces back and forth until it is absorbed. A key feature of this arrangement is that the pump light is confined to a nearly parallel beam, while the fluorescence is emitted randomly into 4p steradians. This makes it possible for fluorescence to escape while trapping the pump light inside. The fluorescent photons that are nearly parallel to the pump beam are also trapped. They are reabsorbed and then simply try again to escape with a small and calculable degradation to the overall efficiency

The potential advantages of optical cooling have been identified in previous work.[8] The overall system mass for mechanical coolers, thermoelectric coolers and optical cryocoolers for an optimized spacecraft application were calculated. An optical cryocooling will likely have the lowest system mass when the load is less than 1.0 W and the temperature is between 80 and 200 K. Optical refrigeration has the potential to extend benefits of solid-state cooling to a new, lower temperature region. Optical cryocooling can potentially be miniaturized to a much smaller level than conventional methods. We have a preliminary design for a cryocooler with a total volume of 0.3 cubic centimeters that could provide 3 milliwatts net refrigeration at 80 K.[9]

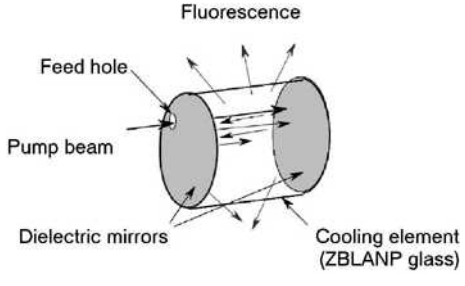

Figure 2. Dielectric mirrors provide long pump path.

LABORATORY REFRIGERATOR DESCRIPTION

A sketch of the laboratory optical refrigerator is shown in Fig. 3. The refrigerator is contained in a small vacuum chamber (not shown), which contains a window for the pump beam. The vacuum chamber is pumped to a pressure less than 10^{-4} torr using a turbo molecular pumping station. The chamber is maintained at a constant temperature about 10°C above the ambient to eliminate the effect of swings in the laboratory temperature. This allows for more precise measurements of heat conductance and cooling.

A copper heat sink completely surrounds the cooling assembly and is mounted to the vacuum chamber wall. A significant issue with the heat sink is the surface facing the cooling assembly. This surface needs to selectively absorb the near 1 micron fluorescence while having low emittance to the ambient radiation. The cooling assembly, which includes the fluorescent element, thermal link and the load mass, is mechanically supported within the heat sink using a fiberglass epoxy support.

The fluorescent cooling element is made from Yb:doped Zirconium Fluoride glass (ZBLAN). It is cylindrical and coated on both ends with high performance dielectric mirrors. The fluorescent element is 12 mm in diameter and 13 mm long and weighs 8.5 grams. It is doped with 2% by mass Ytterbium Fluoride.

A critical issue in the design of an optical refrigerator is that the load to be cooled will invariably be light absorbing and must be shielded from the light from the cooling element fluorescence while being in thermal contact with it. This occurs even when the load appears to be shielded by one the dielectric mirrors since it has been found that the dielectric mirrors leak a significant amount of fluorescence.[10] The fluorescent element is attached to the load with a proprietary thermal link that provides high thermal conductance but prevents the leaked fluorescence from being absorbed by the load.

The load mass is intended to simulate a small infrared focal plane or other small sensor. It consists of an aluminum cylinder 10 mm in diameter and 6 mm thick and weighs 1.1 grams, Fig 4. A silicon diode thermometer and an 1/8 watt, 240 ohm, carbon resistor are mounted with adhesive in a slot in the load mass cylinder. The carbon resistor is used as a heater to impose a heat load and can also serve as a backup thermometer. Four, 36-gauge phosphor bronze wires are connected to the silicon diode thermometer and carbon resistor. The load mass is thermally connected to the fluorescent cooling element through a device which isolates it from the light leaking through the dielectric mirror.

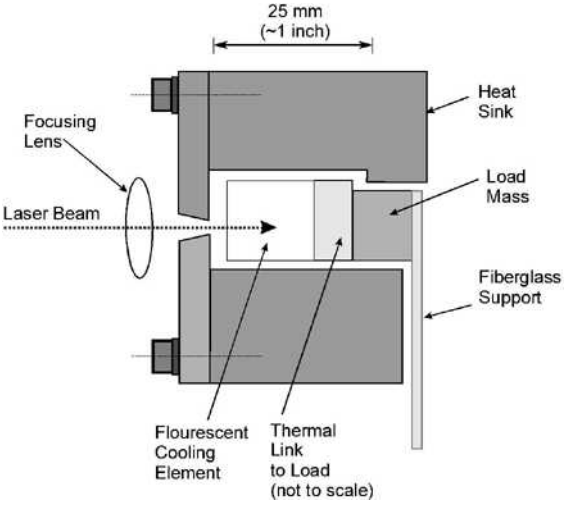

Figure 3. The laboratory optical refrigerator

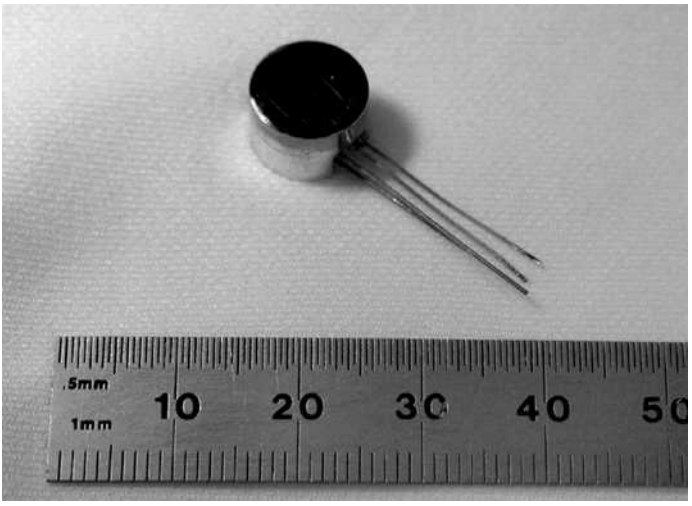

Figure 4. A photo of the load mass. The top and sides have been polished and coated with gold and the heater resistor and silicon diode thermometer are bonded in a groove in the aluminum.

The fluorescent element was pumped using a commercial Yb:YAG disk laser, which could be tuned from 1015 to 1050 nm. Tests were done at wavelengths of 1020 to 1040 nm. The laser could produce output powers of up to 25 watts but only near the 1030 nm optimum power wavelength. The laser powers reported here are our estimate of the laser power at the fluorescent element, based on the power measured at the laser and measurement of the feed optics attenuation.

TEST REFRIGERATOR PERFORMANCE

The test refrigerator was operated after carefully aligning and focusing the laser beam into the fluorescent element to achieve the maximum fluorescence as measured by a photodiode. The laser beam was then turned off, the vacuum chamber was pumped down and the cooling assembly was allowed to come into thermal equilibrium with the heat sink. The laser beam was then turned on and the temperatures of the load mass and heat sink were monitored. The beam remained focused on the fluorescent element until a near steady state condition was achieved. The beam was then turned off and the temperatures continued to be monitored.

A typical result is shown in Fig. 5 for 7.4 watts of laser power. When the beam is introduced into the fluorescent element the load mass thermometer initially heats and then the cooling effect appears to take over and the assembly cools. When the beam is turned off, the assembly continues to cool for a brief period. We conclude from this, that there is a heat source that gets to the load mass very quickly once the beam is turned on and is eventually overwhelmed by the cooling effect of the fluorescent element. The most likely explanation is that some fluorescence is still being absorbed by the load mass. The fluorescence being absorbed by the heat sink caused its temperature to rise until it came into thermal equilibrium with the chamber wall. At equilibrium, the load mass was cooled 7.9°C below the starting temperature and 11.8°C below the heat sink. The maximum steady state temperature measured was 15.6°C for 14 watts of laser power.

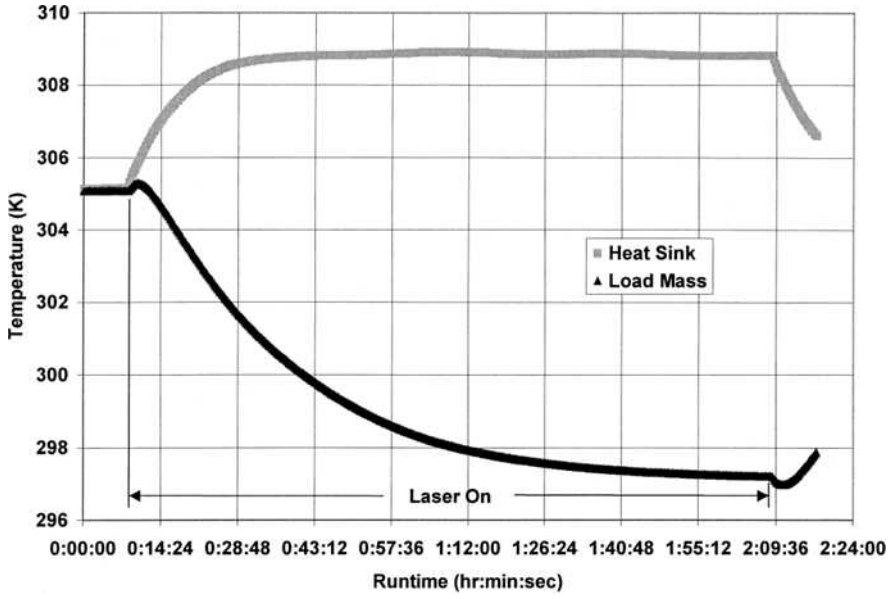

Figure 5. Effect of pumping the fluorescent element with 7.4 watts of 1030 nm laser light for the indicated time period.

We also explored the heat loads that could be lifted by a cooling assembly, for a given laser power, by putting various electric powers through the resistor.

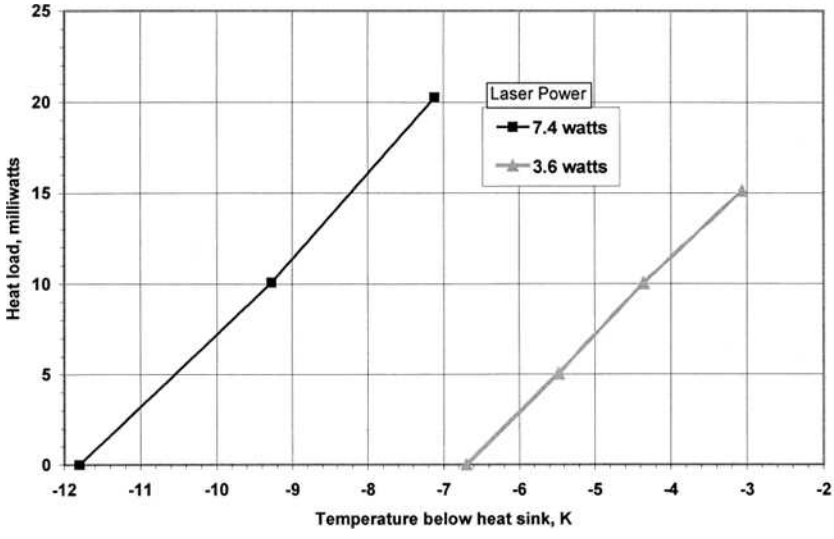

Figure 6. Test refrigerator load curve for the laser powers shown and a wavelength of 1030 nm.

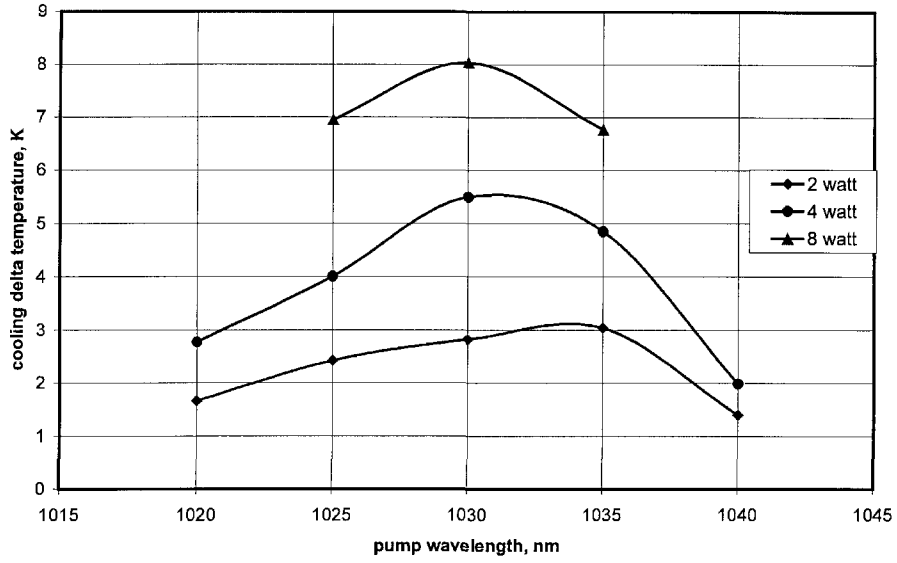

Figure 7. Cooling delta temperature at various powers and wavelengths.

The result is a load curve for the test refrigerator as shown in Fig. 6. The power was also applied to the resistor without having the laser on to measure the thermal conductance between the cooling assembly and the heat sink. This was determined to be 4.32 watts/K. When the cooling assembly was 11.8°C below the heat sink, the refrigeration was 67.4 milliwatts.

Modifications were made to reduce the radiation heat transfer between the cooling assembly and the heat sink. The conductance between the cooling assembly and the heat sink was modeled using standard thermal modeling techniques. The value estimated by the model was 2.5 milliwatt/K which is 17% less than the 3.0 milliwatts/Kelvin that was measured.

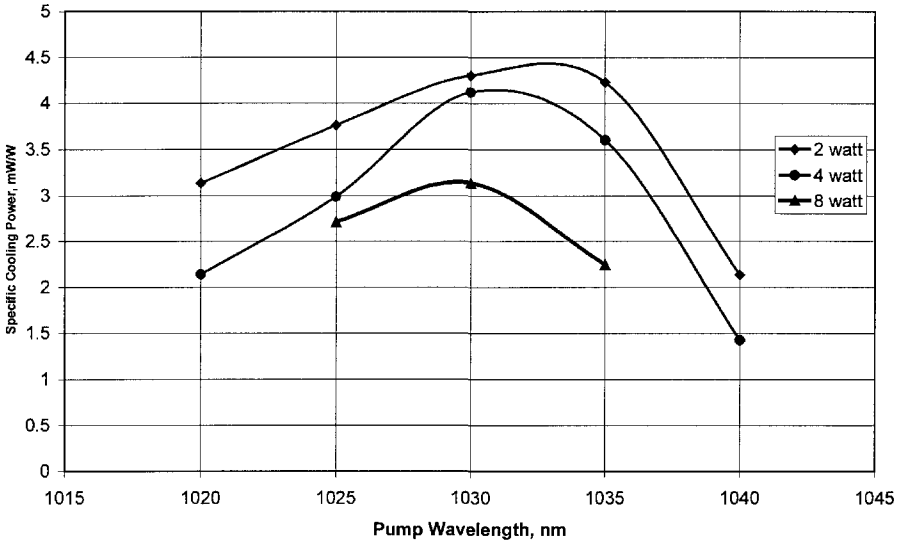

Figure 8. Specific Cooling Power at various input powers and wavelengths

The refrigerator was operated at a variety of powers and wavelengths. The resulting temperatures are shown in Fig. 7. As expected higher power levels produced increased cooling and lower temperatures. At all power levels, the maximum cooling occurred at 1030 nm. Based on the measured conductance of the cooling assembly to the sink, the refrigeration power was determined and a specific refrigeration was calculated by dividing by the input power. The results are shown in Fig. 8. As the input power was increased, the specific refrigeration was reduced. This was expected because as pump power, is increased, the electrons in the lower manifold are depleted.

CONCLUSIONS

We have developed a method for thermally attaching the fluorescent element to a load mass, while isolating it from the mirror leakage. This has allowed us to demonstrate optical refrigeration of a load mass that simulates an infrared focal plane or other small sensor. We have also created a refrigerator test bed that will allow accurate tests of the refrigeration capacity of fluorescent elements.

Our laboratory optical refrigerator was operated at various wavelengths and powers. The optimum wavelength was found to be 1030 nm at all powers. Operation of our laboratory refrigerator resulted in a maximum cooling of 15.6°C and a heat lift of 67.4 milliwatts. The highest specific cooling was 6.9 milliwatt/watt. As the input power was increased, the specific refrigeration was reduced.

Further work on cooling assembly packaging and fluorescence control may further reduce the effect of fluorescence heating. We anticipate substantially increased refrigeration and lower temperatures as these and other refinements are made and higher laser powers are used.

ACKNOWLEDGMENT

This work was performed as part of NASA contract NAS1-00115.

REFERENCES

1. Pringsheim, P., *Z. Phys* 57, (1929), p. 739.
2. Epstein, R.I., M.I. Buchwald, B.C. Edwards, T.R. Gosnell and C.E. Mugan, "Observations of Laser-Induced Fluorescent Cooling of a Solid," *Nature* 377, 500 (1995)
3. Epstein, R.I., et al., "Fluorescent Refrigeration," U.S. Patent. No. 5,447,032 (University of California).
4. Clark, J.L., G. Rumbles, *Phys. Rev. Letters*, 76, 2037 (1996).
5. Edwards, B.C., J.E. Anderson, R.I. Epstein, G.L. Mills, and A.J. Mord, "Demonstration of a Solid-State Optical Cooler: An Approach to Cryogenic Refrigeration," *Journal of Applied Physics*, 86 (1999).
6. Gosnell, T.R. "Laser Cooling of a Solid by 65 K Starting from Room Temperature," *Optics Letters*, vol. 24, no. 15 (1999).
7. G.L. Mills, J. A. Turner-Valle, M. I. Buchwald, "The First Demonstration of an Optical Refrigerator," *Adv. in Cryogenic Engineering*, Vol. 49, Amer. Institute of Physics, Melville, NY (2004), pp. 1845-1852.
8. Mills, G.L., Mord, A.J., Slaymaker. P. A., "Design and Predicted Performance of an Optical Cryocooler for a Focal Plane Application," *Cryocoolers 11*, Kluwer Academic/Plenum Publishers, New York (2001), pp. 613-620.
9. Mills, G.L., "Progress in Optical Refrigeration," *Proceedings of the Fourth Workshop on Military and Commercial Applications of Low-Cost Crycoolers*, November 20-21, 2003, San Diego, CA.
10. Mills, G.L., Fleming J. , Wei Z., Turner-Valle, J., "Dielectric Mirror Leakage and its Effects on Optical Cryocooling," *Cryocoolers 12*, Kluwer Academic/Plenum Publishers, New York (2003), pp. 687-692.

A Thermal Storage Unit For Low Temperature Cryocoolers

R.C. Levenduski and J.M. Lester

Redstone Aerospace Corp.
Longmont, CO 80501

ABSTRACT

The Air Force has developed a 10K Cryocooler based on a hybrid approach of combining different cooling technologies into a single cryocooler. The Air Force Hybrid 10K Cryocooler combines a Stirling cryocooler as a precooler and a Joule-Thomson cooling stage to create a cryocooler that produces cooling at 10K.

Redstone Aerospace has completed a Small Business Innovation Research contract to develop a unique thermal storage unit (TSU) for the AFRL 10K cryocooler. The purpose of the development was to demonstrate an effective method of substantially increasing the cryocooler's peak cooling capacity for short periods of time. This would enable a cryocooler sized for the average load to meet the needs of future missions, thereby reducing the overall size, weight and input power of the cryocooler. This new TSU technology allows the AFRL 10K Cryocooler, which is based on the Redstone Interface concept, to maintain the sensor temperature at precisely 10K in the presence of a widely varying load. In addition, analysis has shown that this TSU technology can be effectively applied to systems down to 4K.

Testing has demonstrated that the TSU is highly effective in increasing both the magnitude and duration of the AFRL 10K Cryocooler's peak cooling capacity. The peak cooling capacity at 10K increased in both magnitude and duration. This paper describes the cryocooler and presents the test results.

INTRODUCTION

Cryocoolers for space applications have traditionally supported low and steady cooling loads. Consequently, their input power requirements, size, and weight have been low and manageable for the spacecraft. We are now entering a period where cooling loads are becoming much larger and varying greatly in time. This new level of operation can seriously impact the design of the whole spacecraft as the peak power drain and other aspects of the cryocooler become less tolerable. This has driven the development of Thermal Storage Units (TSUs) as a way to satisfy the cooling requirements while minimizing impacts to the spacecraft. Incorporating a TSU minimizes the cryocooler's size, weight and peak input power and enables the sensor temperature to be held constant over widely varying load conditions.

To date, development work has concentrated on fixed temperature TSUs. Fixed temperature TSUs absorb high heat loads at constant temperature by the mechanism of phase change in a

Cryocoolers 13, edited by R. G. Ross, Jr.
Springer Science+Business Media, Inc., New York, 2004

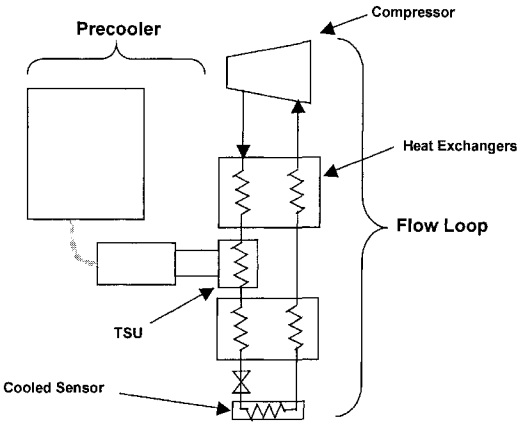

Figure 1. Schematic of the Redstone Interface

cryogen located at the cooled device. A new approach using variable temperature TSUs has been investigated to solve the variable heat load problem without the need for phase-change cryogens. This approach is particularly useful for very low temperature applications (below 15K) where there are no phase-change cryogens useful for TSUs. Variable temperature TSUs also have applications at higher temperatures. This approach has advantages in temperature control, weight reduction and system integration. The concept, called the Redstone Interface, is shown in Figure 1.

The Redstone Interface comprises a precooler, a TSU and a flow loop. The precooler can be a Stirling, Pulse Tube, J-T or Reverse Brayton. The precooler runs at the constant average cooling load, thereby minimizing its power input and size. The TSU is integrated with the precooler and the flow loop remotely from the sensor. The TSU cools down when the cooling load is low because the precooler has excess capacity. In this way the TSU stores a reserve of cooling to support the following high load. The TSU warms up slowly when the cooling load is high thereby providing extra cooling capacity for a short time. The sensor temperature control function is implemented by active control of the flow loop. Sensor temperature is measured and a small circulator or compressor changes speed to adjust the loop flow in order to control temperature.

DESIGN APPROACH FOR THE 10K CRYOCOOLER

The 10K Cryocooler used for demonstrating the variable temperature TSU concept included a commercial G-M cryocooler, commercial compressors for the J-T loop with a bypass loop to control output, and a custom-designed, modular cold head. A schematic is shown in Figure 2. The cold head was designed with three stages of precooling to simulate a flight precooler. The cold head was also designed to operate with and without a TSU so that the relative performance could be determined.

The variable temperature TSU concept does not require materials that change phase at constant temperature but does require materials that have high thermal capacity to keep the size and weight of the TSU manageable. The choice of thermal storage materials is very limited at low temperatures. The Phase I study revealed that even high specific heat materials such as lead or rare earths are not useful for 10K applications because of the large amount of material required. The study's conclusion was that helium and hydrogen are the only materials with acceptably high heat capacities in that temperature range.

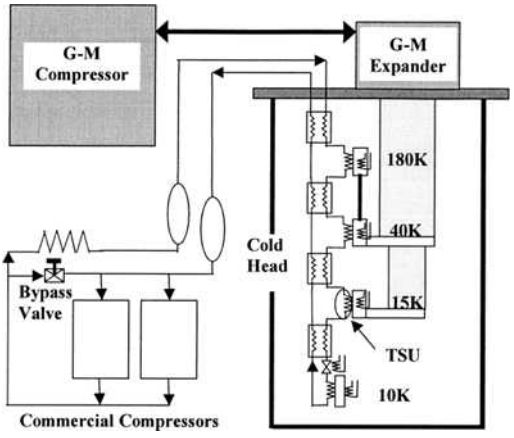

Figure 2. Schematic of 10K Cryocooler

Several designs were devised that incorporated a helium-filled TSU onto the precooler. However, the variation in internal pressure from room temperature to operating temperature (15K) required that an additional bottle be used to store the gas at a reasonable pressure. This was unattractive from a packaging and heat leak perspective. Consequently, an approach that incorporated the TSU directly into the J-T loop was selected. In this approach, helium gas flows through the TSU and is cooled by the precooler to near liquid density. This stored mass of helium has significant heat capacity that is used to delay warming of the precooler during the high load period. Additionally, as the gas in the TSU warms, the pressure in the J-T loop increases, which increases the mass flow rate and cooling capacity to counteract the warming.

An analysis showed that using charcoal adsorbent to concentrate helium in the TSU offered an improvement over using an empty volume, so this became the baseline approach. The TSU was designed as a toroid to enable it to be inserted in the high-pressure stream of the J-T loop and also be efficiently integrated with the G-M cold finger. The inside was filled with several layers of copper screens and charcoal.

PREDICTED PERFORMANCE

A mathematical model was created to analyze the performance of the cryocooler. The model links to a fluid properties program that calculates real gas properties over the entire operating range of pressure and temperature. The model is a dynamic simulation of the cryocooler that has inputs to define the hardware and outputs that describe its performance. Inputs include charge pressure, ambient temperature, heat exchanger volumes and supplemental gas volumes, heat exchanger efficiencies and parasitic heat leaks at design operating conditions, masses at each interface, compressor swept volume, internal leakage and operating speed range, an interface temperature control algorithm to control the compressor speed, isotherms for and the amount of charcoal in the TSU, and cooling capacity functions for each stage of the three-stage flight precooler. Outputs include pressure and temperature of the gas at each node, heat load on each interface, mass flow rate, and compressor input power. The output parameters are calculated and presented as a function of time.

Two versions of the model were created to analyze the cryocooler. The Flight Cryocooler version includes performance projections for a 3-stage precooler that provides the necessary cooling capacity at each stage. A cryocooler having the specified performance has not yet been

built, so the performance projections were based on a combination of test data from an existing 2-stage 30K cryocooler and other test results.

The TSU Demo version was created to reflect the hardware that was built as opposed to a flight version that could be built. It includes performance data for the 2-stage commercial G-M refrigerator that was used as the precooler. This model contains several features that differ from the flight cryocooler model. One difference is the modeling of the 180K cooling stage. The flight model assumes the precooler has a separate cooling stage at 180K whereas the TSU Demo model creates an 180K stage by incorporating thermal isolators from the G-M refrigerator's 40K stage. This approach was used to create a 3-stage precooler from the 2-stage G-M so that the TSU Demo unit's performance could be extrapolated to a flight unit. Another major difference is that the G-M precooler had excess cooling capacity at 15K, which had to be offset with heaters in order to replicate the performance of the flight cooler. Both the Flight Cryocooler and TSU Demo versions include performance projections for a two-stage, variable speed, J-T loop compressor.

The model assumed a cryocooler that was designed to provide 250mW of continuous cooling at 10K. The cold stage of the precooler was assumed to operate at 15K under the design conditions and the J-T compressor was assumed to produce a flow rate of 45mg/sec of helium at supply and return pressures of 140 psia and 70 psia, respectively.

Baseline Load Profile Case (No TSU)

The first task was to determine the cryocooler's predicted peak cooling capacity without a TSU for a given load profile scenario. The load profile specified in the requirements were:

- Low load = 0.100 W
- Load profile cycle time: 90 minutes
- High load duty cycle = 15% (13.5 minutes at high load followed by 76.5 minutes at low load)

The peak cooling capacity of the cooler was determined by trial and error. A peak load value was selected before each run and the temperature of the 10K interface was reviewed. The peak load was reduced in the subsequent run if the 10K interface exceeded 10K during any portion of the load profile. The peak load was reduced in 1 mW steps until the 10K interface remained at 10K throughout the load profile.

The baseline load profile run established that the peak cooling capacity of the flight 10K cryocooler was 307 mW. This is shown in Figure 3. This was 57 mW greater its designed steady state cooling capacity of 250 mW. The increase in the short term cooling capacity arises from two factors: a greater pressure ratio and mass flow rate during the high load period and an initially lower precooler temperature than the design point of 15K.

The heat load during the low load period is only 100 mW, so the compressor, which is designed to produce 250 mW of cooling at its design speed of 24 Hz, operates at a slower speed to match the lower heat load. The slower operating speed decreases the compressor's pressure ratio and mass flow rate, which in turn decreases the load on the precooler. Figure 3 shows that the 15K Interface drops to 11.2K under low load conditions. Figure 4 shows the cryocooler's pressures and flow before and during the load profile. The pressures clearly exceeded the nominal design values during the high load period, giving rise to additional cooling capacity.

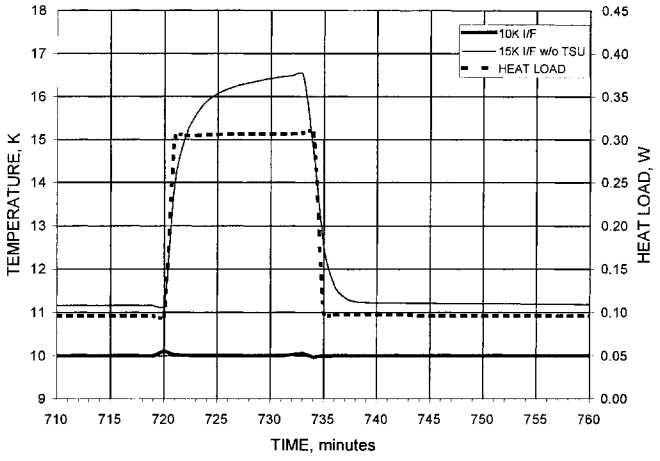

Figure 3. Model results: Interface temperatures and max heat load during load profile without TSU

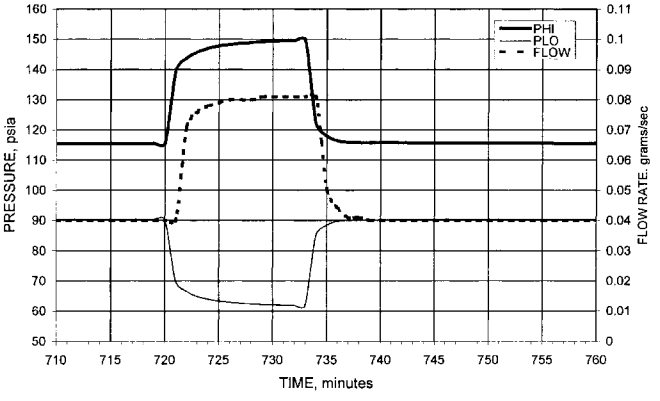

Figure 4. Model results: Cryocooler pressures and flow during load profile without TSU.

Load Profile Case with Charcoal TSU

A charcoal Thermal Storage Unit (TSU) was added to the cold head model to investigate its impact on the peak cooling capacity of the 10K cryocooler. The charcoal TSU was modeled as a container filled with charcoal that was intimately attached to the 15K Interface and through which the working gas flowed. The helium adsorption isotherms for the Barnabey-Cheney 580-26 (carbon A) were used to calculate the amount of helium adsorbed by the charcoal and the associated heat of adsorption.

The model was used to investigate the effects of various amounts of charcoal and the effects of placing the TSU in the high-pressure and low-pressure sides of the cold head. Charcoal amounts of 10, 20, 40, 60 and 80 grams were analyzed. The modeling results for a TSU

containing 40 grams of charcoal will be discussed here because that is what the cold head was tested with. However, Table 1 summarizes the key performance parameters for all runs.

Figure 5 shows that the cryocooler's predicted peak cooling capacity increased from 307mW to 458mW for the same duration of high load when the TSU was placed in the high-pressure side of the cold head. This increase is attributed to the helium gas that was desorbed from the charcoal as the TSU warmed. The extra gas in the system increased the pressures and flow rate beyond the values attained in the baseline case, as shown in Figure 6, thereby increasing the cooling capacity. The 15K Interface warmed more slowly during the high load period because much of the additional heat load went into liberating the helium from the charcoal in the TSU. This kept the gas temperature at the J-T valve colder longer than in the baseline case, further increasing the cooling capacity. Note too however, that the TSU

Table 1. Summary Of Load Profile Modeling Results

TSU Size & Location	Peak Load (mW)	High Pressure (psia)	Low Pressure (psia)	Mass Flow (mg/s)	Max 15K I/F Temp (K)
No TSU	307	149.7	61.8	81	16.5
10g HP Side	343	159.0	65.4	86	16.6
20g HP Side	387	164.9	68.1	90	16.2
40g HP Side	458	169.9	67.2	92	15.4
60g HP Side	503	171.4	63.2	93	14.8
80g HP Side	528	171.5	61.1	94	14.4
10g LP Side	356	171.3	70.5	93	17.2
20g LP Side	420	188.8	76.0	102	17.3
40g LP Side	540	218.4	73.2	117	17.3
60g LP Side	616	233.0	72.3	125	17.0
80g LP Side	661	240.5	72.5	129	16.8

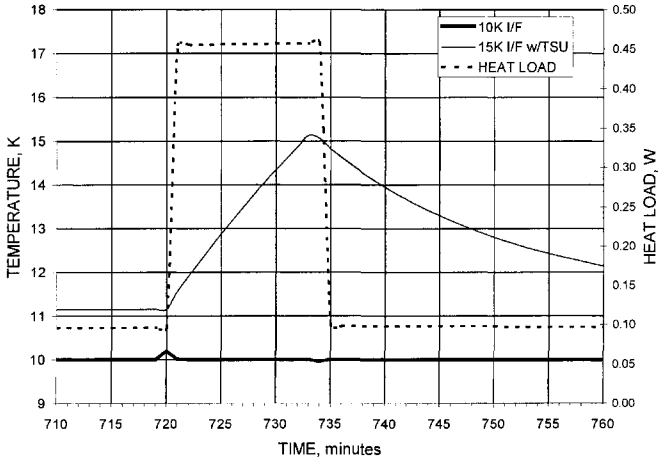

Figure 5. Model results: Interface temperatures and max heat load during load profile with TSU

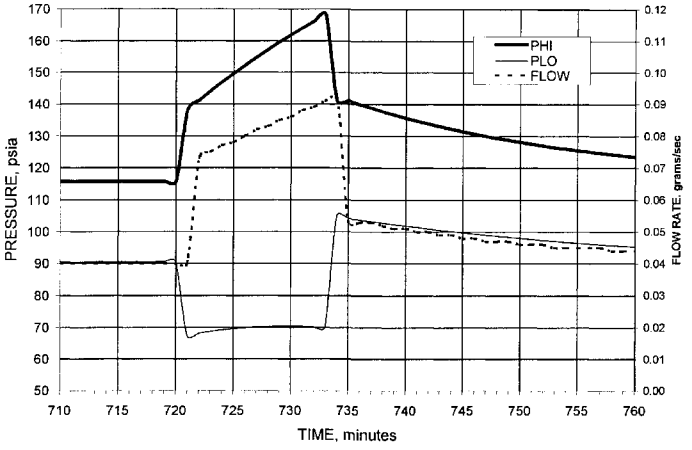

Figure 6. Model results: Cryocooler pressures and flow during load profile with TSU.

temperature decreased more slowly during the subsequent low load period because of the heat of adsorption of the helium onto the charcoal.

TEST RESULTS

As noted previously, the G-M precooler had more cooling capacity at 15K than the flight precooler would have, so the excess capacity had to be offset with heaters to simulate the performance of the flight precooler. Another factor to consider was that the cooling capacity curve of the G-M precooler was steeper than the flight unit. This meant that the TSU would not warm as much or as quickly as it would with the flight precooler, so this effect also had to be negated with the heaters. A series of tests determined that an additional heat load of 0.77W had to be added to the TSU during the load profile to simulate the performance of the flight precooler. This additional heat load is evident in the data.

Component testing of the cold head revealed a partial blockage in the high pressure tubing that caused a significant pressure drop. Since the pressure transducers were located outside the cold head, this significantly reduced the cooling capacity under the indicated supply and return pressures. Although the restriction reduced the net cooling capacity, the relative effect of the TSU could still be determined so the decision was made to proceed with the testing without reworking the hardware at that time.

The test approach was to establish low load operating conditions as close to the model predictions as possible, i.e. at nearly the same pressures and flow with a 100mW heat load, and then conduct load profile testing to determine the effect of the TSU. The low load conditions were best achieved with no applied heater load, so this became the baseline low load condition.

Test Results Without TSU

Testing was conducted without the TSU and with a small heat exchanger attached to the 15K Interface to cool the gas. The peak cooling capacity was determined by trial and error, just like it was done for the model. The heat load was changed incrementally until the cryocooler maintained the load interface at 10K for seven minutes. The peak cooling capacity, shown in Figure 7, was 118mW. As expected, the 15K Interface temperature rose sharply during the load profile. Without the TSU, the operating pressures in the cold head change solely as a result of an increase in compressor pumping capacity (speed) and reaches its maximum value quickly. The

high pressure during this test, as shown in Figure 8, increased by 15 psia to 130 psia. This increased the mass flow rate to 58 mg/s, which provided the higher capacity.

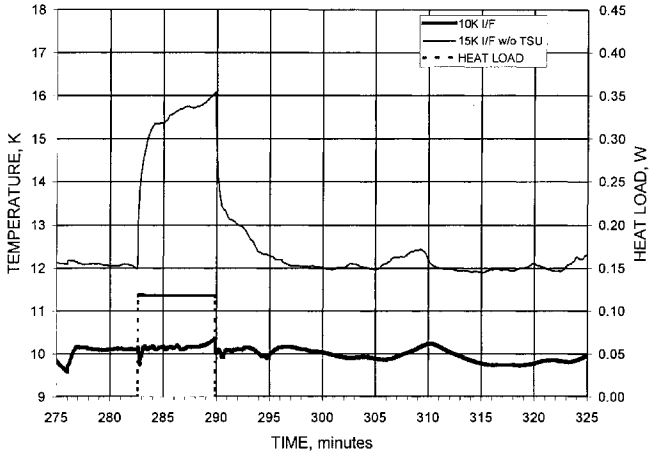

Figure 7. Test results: Heat load and temperatures during load profile without TSU.

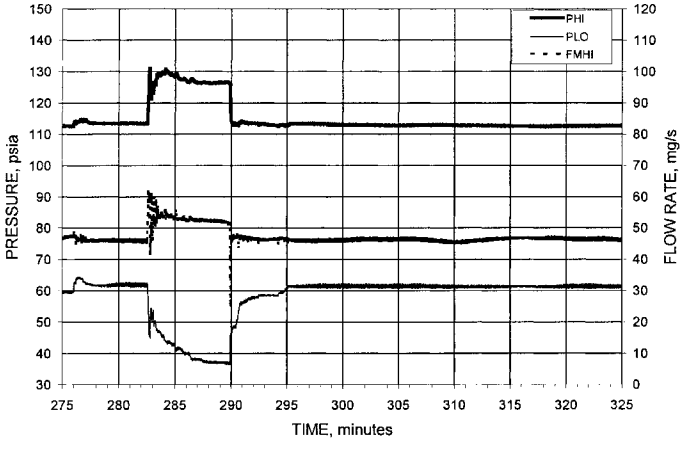

Figure 8. Test results: Cryocooler pressures and flow during load profile without TSU.

Test Results with Charcoal TSU

Testing with the charcoal TSU was conducted under the same low load conditions as without the TSU. The peak cooling capacity was again determined by incrementally changing the heat load until the cryocooler maintained the load interface at 10K for seven minutes.

The applied heat loads during the load profile are shown in Figure 9. The graph shows that the peak cooling capacity increased from 118mW to 275 mW for seven minutes. The graph also shows that the TSU temperature warmed much more slowly than without a TSU. Figure 10 shows that as expected, the gas that desorbed from the warming TSU increased the operating pressures and mass flow rate, thereby increasing the cooling capacity. This test demonstrated the effectiveness of a charcoal TSU in increasing the short term, peak cooling capacity of a 10K cryocooler.

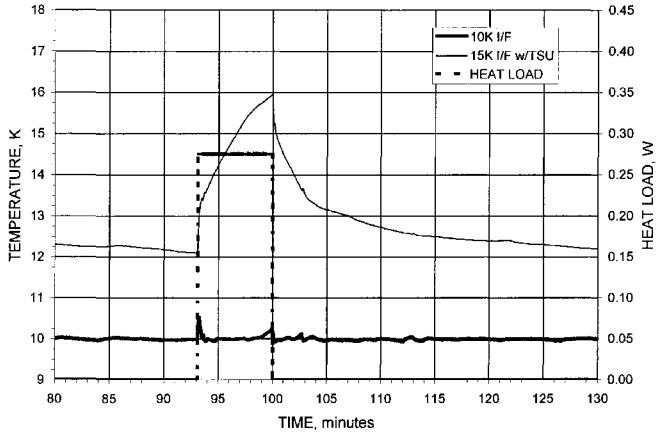

Figure 9. Test results: Heat load and temperatures during load profile with TSU.

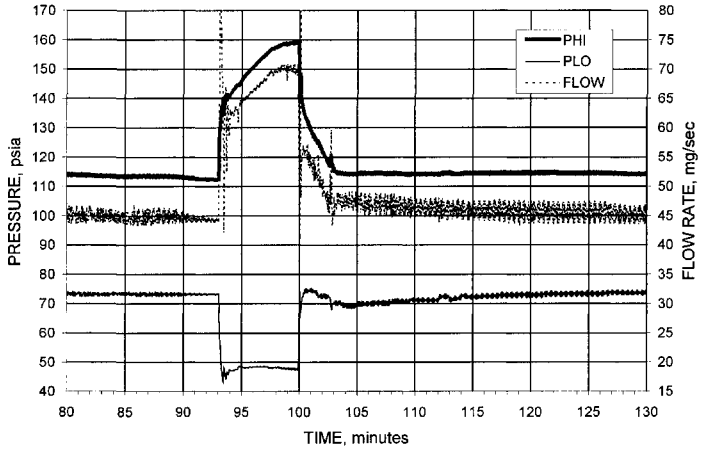

Figure 10. Test results: Cryocooler pressures and flow during load profile with TSU.

CONCLUSIONS

A concept that incorporates a unique thermal storage unit into a low temperature cryocooler comprising a precooler and J-T flow loop has been identified. An analytical model has been developed to parametrically analyze the cryocooler's performance and enables the design of a 10K cryocooler for variable load applications. Testing has demonstrated that a TSU filled with charcoal can be placed in the flow stream of a J-T stage to store helium and provide thermal capacity for intermittent high loads.

ACKNOWLEDGMENT

Financial support for this effort was provided by the Air Force Research Laboratory, Kirtland AFB. The authors would also like to thank Ball Aerospace and Technologies Corporation for their support of this effort.

REFERENCES

1. I. Vazquez, M.P. Russell, D.R. Smith, R. Radebaugh, "Helium Adsorption on Activated Carbons at Temperatures Between 4 K and 76 K," *Advances in Cryogenic Engineering*, Vol. 33, Plenum Publishing Corp., New York (1988), pp. 1013-1021.
2. Lester, J.M., "Redstone Interface Cooling System," *Adv. in Cryogenic Engineering*, Vol. 43A, Plenum Publishing Corp., New York (1998), pp. 1025-1030.
3. Levenduski, R.C., Lester, J.M., Marquardt, E., "A Hybrid, Multistage 10K Cryocooler for Space Applications," *Cryocoolers 12,* Kluwer Academic/Plenum Publishers, New York (2003), pp. 579-585.

Development of a Nitrogen Thermosiphon for Remote Cryogenic Devices

J. Yuan and J. Maguire

American Superconductor Co.
Westborough, MA 01581 U.S.A.

ABSTRACT

A group of optical sensors is required to operate at a temperature of less than 77 K with minimum vibration. To that end, a thermosiphon integrated with a GM Cryocooler has been designed and fabricated. The thermosiphon system has the capability to operate at 77 K with a total heat lift rate of 120 watts. The system was required to cool two sets of sensors, therefore two thermosiphon loops sharing one cryocooler have been designed, and each loop has the capability to operate independently. Based on the working conditions, nitrogen has been selected as the working fluid. A CryoMech AL200, which can supply 160 watts at 70 K, is utilized as the cooling source. A coil type condenser, which is easier to fabricate and less costly, was also selected. The condenser and evaporator are connected through flexible transfer lines. This paper provides the details of the system and component design. Descriptions of the test apparatus and temperature control system are also provided. Additionally, the cooldown process, the load map, and the effect of working fluid inventory on system performance are discussed in the paper.

INTRODUCTION

Thermosiphons provide a cooling method with reduced levels of vibration and tighter temperature control for a variety of cryogenic applications. Since the latent heat of the working fluid is used to absorb and reject heat, a thermosiphon enables the possibility of having a high thermal conductance interface between the cooling device and the cooling source over a long distance. In addition, the cooling of multiple cryogenic devices can easily be achieved by using a thermosiphon with multiple circulating loops but sharing one cooling source. The merits of a thermosiphon over other types of circulation cooling methods are greater simplicity and higher potential reliability due to the fact that there is no recuperative heat exchanger or driving device such as a pump. The major disadvantage of a thermosiphon system is the working temperature is limited by the properties of the available fluids.

In this paper, the design of a thermosiphon with two circulating loops that share one cryocooler is presented. The paper also includes descriptions of the test apparatus and temperature control system, the cooldown process, the load map, and the effect of working fluid inventory on system performance. Tests indicate the system is capable of lifting a total of 120 watts at 77 K over a distance of 12 feet with less than 7 K temperature gradient.

Cryocoolers 13, edited by R. G. Ross, Jr.
Springer Science+Business Media, Inc., New York, 2004

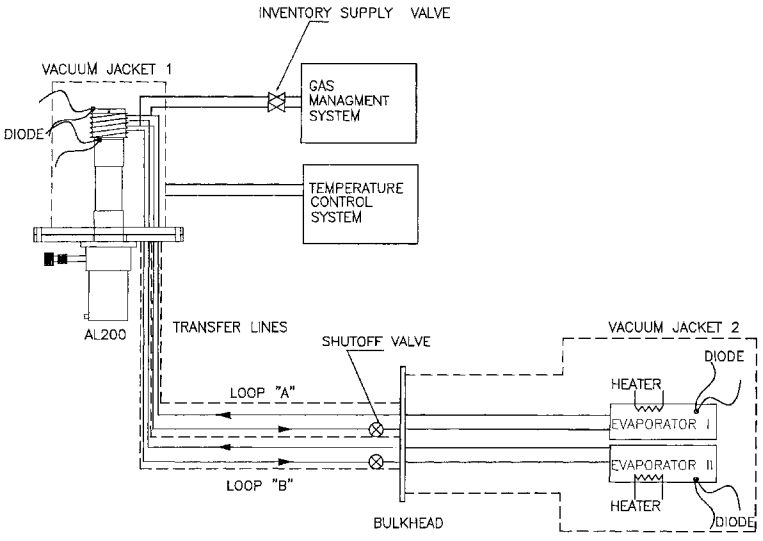

Figure 1. Thermosiphon system

THERMOSIPHON DESIGN

System Design

The schematic configuration of the thermosiphon is illustrated in Fig. 1. Fundamental features of this system include one single stage GM cryocooler, one coil type condenser, two pairs of flexible transfer lines to link the condenser and evaporators, two cryogenic shutoff valves, two evaporators, two vacuum jackets, one gas management system and one temperature control system. The design objective was to have two thermosiphon loops with one cryocooler and have the two systems work independently. The required heat lift rate was 50 watts at 77 K for each loop. In order to independently control each loop, two cryogenic shutoff valves are connected in series with liquid flow passages. Vacuum Jacket "1" and Vacuum Jacket "2" are connected through insulated flexible transfer lines with bayonets. A coil type condenser which is easier to fabricate and less costly was used. The evaporators are tube type heat exchangers. Gas inventory is controlled by the gas management system. Condenser temperature is maintained by a temperature control system.

In order for a thermosiphon to work properly, a few criteria must be met. The criteria include a pressure head limit, a sonic limit, a boiling limit and an entrainment limit. For a gravity driven thermosiphon, the pressure head limit is probably the most important one. During steady state operation of the thermosiphon, the working fluid in the vapor phase flows continuously from the evaporator to the condenser, and returns to the evaporator in the liquid phase. The maximum pressure head P_{max} must be greater than the total pressure drop in the flow passages [1].

$$P_{max} \geq \Delta P_l + \Delta P_v \tag{1}$$

where ΔP_l is the pressure drop over liquid flow passage and ΔP_v is the pressure drop over vapor flow passage. The pressure head of a thermosiphon is mainly due to the gravity force. The total pressure head is the summation of capillary head and gravitational head.

$$P_{max} = P_c + P_g = \frac{2\sigma}{r_c} + (\rho_l - \rho_v)gh \tag{2}$$

where σ is the surface tension coefficient, r_e is effective capillary radius and h is the elevation difference between condenser and evaporator. Compared to the gravitational head, the capillary head is negligible in this case. The pressure drop of this system depends on circulating rate of working fluid, pipe diameter, pipe roughness and pipe length. The circulating rate of the working fluid can be readily obtained by the following relationship

$$Q = \dot{m}L \tag{3}$$

where Q is the required heat lift rate, $\dot{m}$ is the mass flow rate at steady state, and L is the latent heat of the working fluid. Key parameters of the system including the elevation of the condenser and the diameter of each flow passage can be obtained by applying Eq. (1), (2) and (3).

Based on the system requirement, nitrogen has been selected as working fluid, which has a triple point temperature of 63.15 K and wide working temperature range up to 126 K.

Component Design

Cryocooler. Selection of the cryocooler was based on the required heat lift rate and the following temperature relationship

$$T_{evaporator} = T_{coldhead} + \delta T_{condenser} + \delta T_{evaporator} \tag{4}$$

where $T_{coldhead}$ is cold head temperature, $\delta T_{condenser}$ is the temperature drop of condenser, and $\delta T_{evaporator}$ is the temperature drop of the evaporator. Assuming the parasitic losses of the entire system are about 40 watts and a total temperature drop of about 7 K, to lift 100 watts at 77 K, a cryocooler has to have a minimum of 140 watts at 70 K. To that end, a CryoMech AL200, which can supply 160 watts at 70 K, is utilized as the cooling source.

Condenser. A coil type condenser was used in the present design, which is easier to make and less costly. Two tubes coiled side by side are soldered onto a copper mandrel. Heating elements embedded inside copper mandrel are used to control the condensation temperature. During normal operation, vapor flows into the top section of the condenser and condenses inside the coiled tubing and flows down. Vapor condensation inside tubes depends strongly on the velocity of the vapor flowing through the tubes. When the vapor velocities are low (Re < 35000), a correlation of the form

$$\bar{h}_D = 0.555\left[\frac{g\rho_l(\rho_l - \rho_v)k_l^3 h_{fg}'}{\mu_l(T_{sat} - T_s)D}\right]^{1/4} \tag{5}$$

has been recommended[2] to obtain the convection coefficient, where h_{fg}' is the modified latent heat, k_l is liquid conductivity, T_s is tube wall temperature and D is tube diameter. To transfer 100 watts with a temperature drop of 2 K, a ½" copper tube with 75 cm length was selected.

Flexible Transfer line. Four flexible transfer lines have been built based on a coaxial configuration. Two are for liquid flow while the other two are for vapor flow. Each transfer line consists of two corrugated stainless steel tubes, the inner small tube forms the flow passage for working fluid while the outer large tube forms the vacuum envelope. Multi layers of Mylar have been wrapped around inner tube to minimize thermal radiation. To avoid the inner tube having direct contact with outer tube, G10 spacers have been placed every 2 ft along transfer tube.

Evaporator. A tube type evaporator has also been designed and fabricated. A "U" shape ½" copper tube is soldered onto a rectangular copper plate. The total length of copper tube is about 75 cm. The total heat transfer area of the evaporator is about 2.67×10^{-2} m^2. To transfer 50 watts, a 3 K temperature drop was expected.

Fill Tube. The fill tube provides the only access to the thermosiphon for evacuation and fluid charging. Since the fill tube is connected between the condenser and the charging bottle is at room temperature, a stainless steel tube of 1/4" diameter was used to reduce the heat leak from the ambient environment.

Temperature Control System. The temperature control system consists of one trim heater, one type "E" thermocouple, one solid state relay, one Omega iSeries Temperature & Process Controller Cni8A23.

Gas Management System. The gas management system consists of supply bottle, flow meter, evacuation port, relief valve and pressure gauge. The flow meter is used to control the working fluid inventory.

THERMOSIPHON PERPORMANCE

Test Setup

The test apparatus is detailed schematically in Fig. 1. Both the condenser and the evaporators are contained within vacuum chambers which are evacuated to a pressure of 1×10^{-5} torr. In order to reduce the thermal radiation loss at low temperature, more than 20 layers of aluminized Mylar were wrapped around the inside of vacuum chambers. A 150-watt heater is placed inside of the condenser mandrel as a trim heater to control the condensation temperature. For test purposes, each evaporator has one heater block which can supply 150 watts to simulate the future application heat load. Two diode thermometers are placed on the condenser to monitor temperature, while one type "E" thermocouple is installed on the condenser to control the condensation temperature. Each evaporator has one diode to monitor evaporator temperature.

Cool Down

Tests have been carried out to study the system cooldown. The two thermosiphon loops were tested separately. After evacuating and purging both systems, the shutoff and supply valves of Loop "B" were closed while the shutoff and supply valves of Loop "A" were opened. At this time, both systems were charged with pure nitrogen gas at 20 psig. No extra heat load was added to both evaporators at initial setup. The temperature of cold head controller was set at 76 K and the nitrogen bottle supply regulator was set at 200 psig. A flow meter installed between the supply bottle and the thermosiphon was utilized to measure the system gas inventory.

Fig. 2 shows the experimental results of the cooldown process. After turning on the cold head, the condenser rapidly cooled to 76 K and started to condense nitrogen. Nitrogen was continuously drawn in from the supply bottle and began to cool the liquid flow passage of Loop "A". After about 20 minutes, evaporator I started to cool down quickly and reached 77 K in about 90 minutes. After evaporator I reached steady state, the supply valve of Loop "A" was closed and total inventory for Loop "A" was found to be about 200 g. During this time period, evaporator II of Loop "B" was still at room temperature as the shutoff valve was still closed. After evaporator I reached the minimum temperature, the shutoff and inventory valves of Loop "B" were opened and evaporator II started to cool down in about 20 minutes. When evaporator II reached 225K, a 20W heat load was added to the evaporator to study the thermosiphon behavior with an additional heat load. As seen, the cooldown slope decreased slightly due to this extra heat load. After about 100 min, evaporator II reached 77 K. After evaporator II reached steady state, the supply valve of Loop "B" was closed. The total inventory for Loop "B" was the same as Loop "A". During the cool down process of both loops, system pressures were about 2 psig.

Parasitic Losses

System parasitic losses have also been estimated based on zero heat load performance of the

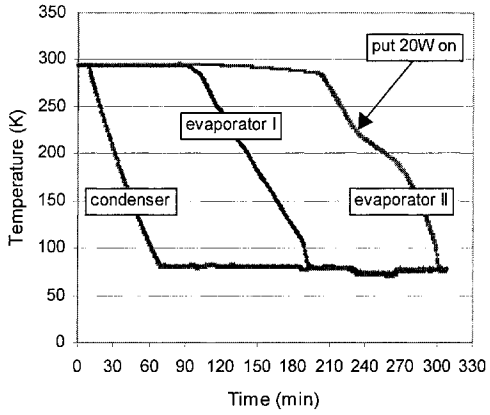

Figure 2. Cooldown process

thermosiphon. At zero heat load on the evaporators, the cold head temperature was set at 76 K and the trim heater was found to be supplying 145 watts. According to the performance data of coldhead, the total heat load was 185 watts at this temperature. Based on this information, we estimated that system parasitic losses were about 40 watts which is in very good agreement with our initial estimation.

Load Map

After both evaporators reached steady state a heat load was added on evaporators to map the system performance. In order to have performance data at 77 K, the temperature controller was set at 67K during the entire experiment. At this temperature, the cooling capacity of cryocooler is around 150 watts. When total heat load on the evaporators was less than 110 watts (150 watts subtracting 40 watts for parasitic losses), the condenser maintained a constant temperature of 67 K by energizing the trim heater. The temperature of condenser increased slightly when the total heat load on evaporator was larger than 110 watts. With total heat load of 120 watts on the evaporators, the condenser temperature was found to be about 70.5 K. Fig. 3 presents the test results. As expected, the coupling effect between the two evaporator was relatively weak. As

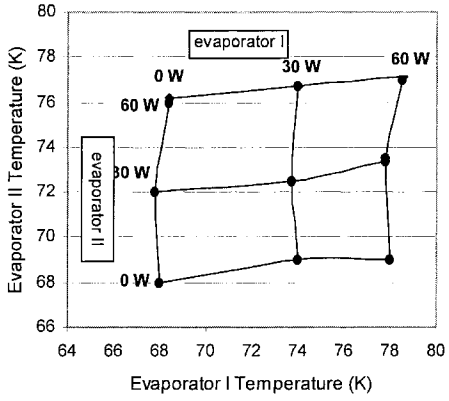

Figure 3. System load map

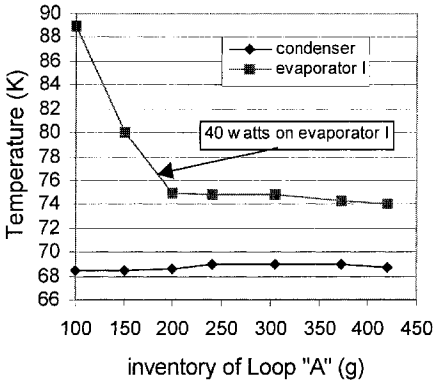

Figure 4. Effects of inventory on system performance

Seen in the load map, when heat load on evaporator II was zero while heat load on evaporator I ramping from zero watts to 60 watts, the temperature of evaporator II only increased slightly. The performance of the two thermosiphons was slightly different. Loop "B" was 1 K better than Loop "A" when the heat loads were 60 watts on both evaporators.

Effect of Inventory

The effect of the working fluid inventory on the system performance has been investigated. Different inventories of Loop "A" were tested while the inventory of Loop "B" was kept the same during the entire test. For each inventory, a fixed heat load was applied to evaporator I and the temperature was recorded after it reached steady state. Figure 4 presents the test results. As observed, the inventory plays an important role in the system performance. In general, system performance increased with adding more inventory. However, this effect became insignificant when a certain inventory level has been reached. For the present test setup, 200 g was the minimum inventory.

CONCLUSION

A thermosiphon system with two circulating loops but sharing one cryocooler has been successfully designed, constructed and tested. Tests indicate that the thermosiphon can be utilized as a very efficient way to transfer heat loads over long distance. A low thermal resistance between the cooling device and the cooling source has been achieved in the present design. A coil type condenser has also been successfully tested. Test results show that present system has heat lift rate of 120 W at 77 K over distance of 12 ft with less than 7 K temperature gradient.

ACKNOWLEDGMENT

The authors would like to thank our coworkers at American Superconductor for their assistance and support.

REFERENCES

1. Chi, S.W., *Heat pipe theory and practice : a sourcebook*, McGraw-Hill, New York, 1976.
2. Rohsenow, W.M., "Film Condensation," *Handbook of Heat Transfer*, Chapter 12A, W.M. Rohsenow and J.P. Hartnett Eds., McGraw-Hill, New York, 1973.

Long Life Cryocoolers for Space Applications A Database Update

Thom Davis[1], Nandu Abhyankar[2]

[1]Space Vehicles Directorate
Air Force Research Laboratory
Albuquerque, NM, USA

[2]Dynacs Military and Defense, Inc
Albuquerque, NM, USA

ABSTRACT

The Air Force Research Laboratory (AFRL) sponsored creation of a database on the performance and maturity of space cryocoolers in the prototype, flight qualified, and flight categories. The database was originally developed by The Aerospace Corporation a few years ago and was presented to the community in printed as well as in electronics format. With the help of industry partners such as Ball Aerospace, Raytheon, Northrop Grumman, Lockheed, Jet Propulsion Laboratory, and others, the database has been updated with more current information. The additional information on the coolers, along with the interactive form and search feature, are presented in the paper. The data are supported with graphics indicating the changes in the performance trends. AFRL is actively soliciting input from space cryocooler industries and agencies to provide information for coolers not included in the survey.

INTRODUCTION

Mechanical cryocoolers, such as pulse tube, split Stirling and turbo-Brayton variants, have been reliably used on space missions involving infrared sensors for surveillance purpose. The Air Force Research Laboratory (AFRL), in cooperation with the Missile Defense Agency (MDA, previously BMDO), the Space Tracking and Surveillance System (STSS, previously SBIRS Low) and other Space Agencies, has played an instrumental role in their development over the last decade. In continuation with the role of supporting development of cryogenics technology and its space application, AFRL had sponsored building a database of long life cryocoolers.[1-2] The report was prepared by The Aerospace Corporation with assistance from AFRL. The information was communicated to the cryogenics community through a printed report, a CD, and a conference paper presentation. The objective was to consolidate available information from manufacturers and the user community, and provide a comparative assessment of technology, performance, and suitability for space application, for both military and civilian use. It also allowed independent data gathering and assessment without a bias for marketing. Since the initial

Cryocoolers 13, edited by R. G. Ross, Jr.
Springer Science+Business Media, Inc., New York, 2004

data collection was undertaken and was conveyed in the survey, many new developments have taken place that are reported as an update in this presentation. It is hoped that the presentation will prompt other space cooler developers that are missing from this presentation list to provide additional information that can be included in the survey report to be dated 2004.

The coolers included in the survey have expected operational life expectancy of 5 to 10 years. The category of "long-life" mentioned in the title is indicative of the requirement that cryocoolers developed for space use are reliable and continue to perform as designed for long missions. Their use depends on the duration of the mission. There have been a few coolers, not meant for long operation, that have flown on short space missions. These coolers will be included in the future version of the database consolidating all space applicable coolers.

There have been a number of surveys done for cryocoolers over time[1-11] with recent overviews for NASA programs.[12-15] Strobridge's survey[5-6] in 1969 and 1974 appears to be the first baseline for Carnot efficiency comparison followed by others.[4,8] The US Navy survey, conducted by then Nichols Research Corporation (NRC), was comprehensive.[9-10] The most recent survey, an expanded version of NRC, was undertaken for cryocoolers by ter Brake and Wiegerinck at the Center for Interfacing Low Temperature Electronics and Coolers (CILTEC) involving 235 coolers in the 4-120 K range with emphasis on the use of 80 K improvements and also for non-military applications. The trends in performance, mass, as well as cost are included for different temperature and cooling power ranges. The cost is not a driving factor for space missions where reliability and performance are major issues.

DATABASE SUMMARY

There are approximately 50 cryocoolers in the current AFRL database. They are divided among the following categories: integral pulse tube, split Stirling, turbo and reverse Brayton, sorption, Joule-Thomson, and hybrids. Coolers added since the initial database preparation are listed in Table 1a and 1b along with their performance summary, mass, and maturity. Sunpower and Thales are recently added vendors. Lockheed Martin ATC, Northrop-Grumman (formerly TRW), and Raytheon have introduced multi-stage pulse tube coolers in their inventory. Among hybrid coolers, to achieve a lower temperature than their individual units, Raytheon has a Stirling and pulse tube hybrid, Northrop-Grumman has a Joule-Thomson and pulse tube hybrid, and Ball Aerospace has a Joule-Thomson/split Stirling hybrid. Ball Aerospace continues with the multistage Stirling designs with advanced "next-generation" designation. The thrust to achieve 6 K to 10 K temperatures is evident in the research pursued by Ball Aerospace, Creare, Raytheon, Northrop Grumman, and Lockheed Martin with support from MDA, NASA, AFRL, and their internal research and development (IRAD.)

Figures 1 through 4 portray comparisons of coolers for the parameters Carnot efficiency, load-lift capacity (QL), specific power, and mass. Percent Carnot efficiency is given by the ratio of coefficient of performance (COP=QL/Pin, an inverse of specific power) to the Carnot Efficiency (Tc/(Th-Tc)) where Th (or TR) is the heat sink/rejection temperature, Pin the input power, and Tc the cold end temperature. For multistage coolers, percent Carnot efficiency is calculated as second law efficiency combining the ratio QL*(Th-Tc)/Tc for individual stages. Thus for individual stages denoted by index "i,"

$$\%\text{Carnot} = 100 * \left[\sum_i \text{QL}_i * \left(\frac{Th - Tc_i}{Tc_i} \right) \right] / Pin \qquad (1)$$

For COP calculation, the numerator is the combined load lifted by the cold end of the cooler. The percent Carnot efficiency gauges the thermodynamic performance of the cooler. For space application, the combination of temperature, heat load capacity, required input power, reliability and maturity of the cooler and electronics provide a basis in the mission selection.

Table 1a. Coolers added in the update[1].

Vendor	Ball	Ball	Ball	Ball	Creare	Raytheon	Raytheon	Sunpower	Thales	Thales
Model	4-10K (ACTDP)	SB235 (NGe 35 K)	SB235E (ENGe 35 K)	OC190	6K-10K RB	RS1	RSP2	CryoTelCT	LSF9330-1	MPT
Type/Stages	HybJT SpSt/2	SpSt/2	SpSt/2	Optical/1	ReverseBrayt/1	SpSt/1	Hybrid/2	IntegralSt/1	SpSt/1	SplitPT/1
DesignLoad (W)	0.02	0.5	1.2	0.4	0.01	4.5	1.75	10	6	1
DesignTemp (K)	6	40	40	90	6	60	58	77	80	80
DesignPower (W)	150	90	170	100	100	142	131	160	100	35
RejectionTemp (K)	300	300	300	300	260	300	300	300	300	290
Stage1Load (W)	0.15	3.5	12				5			
Stage1Temp (K)	18	110	110				110			
CombinedLoad (W)	0.17	4	13.2	0.4	0.01	4.5	6.75	10	6	1
TMUMass (Kg)	30	10.5	12.9	0.5	35	13.8	7	2.7	8.6	2.8
Maturity	BB/QM	QM/FM	QM/FM	BB/CD	BB	FM/EDM	BB/EDM	FM	EM	BB

[1]BB: bread/brassboard, QM: Qualification Model, EDM: Engineering developmental model, FM: Flight Model, CD:Conceptual Design PT:Pulse Tube, SpSt:Split Stirling, TMU: Thermo-mechanical Unit. IRAD: Internal research and development.

Table 1b. Coolers added in the update (continued)[1].

Vendor	NG	NG	NG	NG	NG	LM	LM	LM	LM	LM
Model	HEC-2St	HCC	10K	6K (ACTDP)	MPT-HEC	ESAIntPT	IRAD2PT	IRAD3PT	HCC2PT	JPLGam-Ray
Type/Stages	PT/2	PT/2	PT/3	Hyb PT-JT/4	PT/1	PT/1	PT/2	PT/3	PT/2	PT/1
DesignLoad (W)	8.1	2	0.1	0.03	1.5	2.5	0.5	0.13	1.7	1.32
DesignTemp (K)	95	35	10	6	65	77	35	10	35	80
DesignPower (W)	147	500	500	200	65	89	56	240	600	30
RejectionTemp (K)	300	300	300	300	300	303	295	290	303	295
Stage1Load (W)	5.3	18.5	0.3	0.15					17	
Stage1Temp (K)	170	85	75	18					85	
CombinedLoad (W)	13.4	20.5	0.4	0.18	1.5	2.5	0.5	0.13	18.7	1.32
TMUMass (Kg)	5.3	14.3	14.3	14.3	1.5	2.4	7	14	23	2.5
Maturity	FM/FM	EDM/EDM	BB	BB	EDM/FM	EDM/EDM	BB	BB	EDM	BB

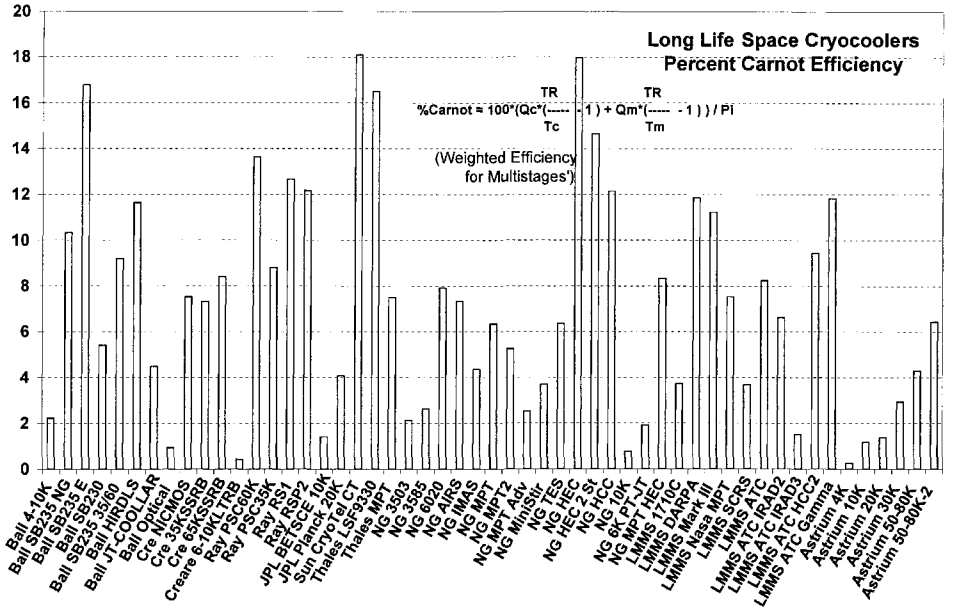

Figure 1. Percent Carnot efficiency comparison for AFRL database coolers.

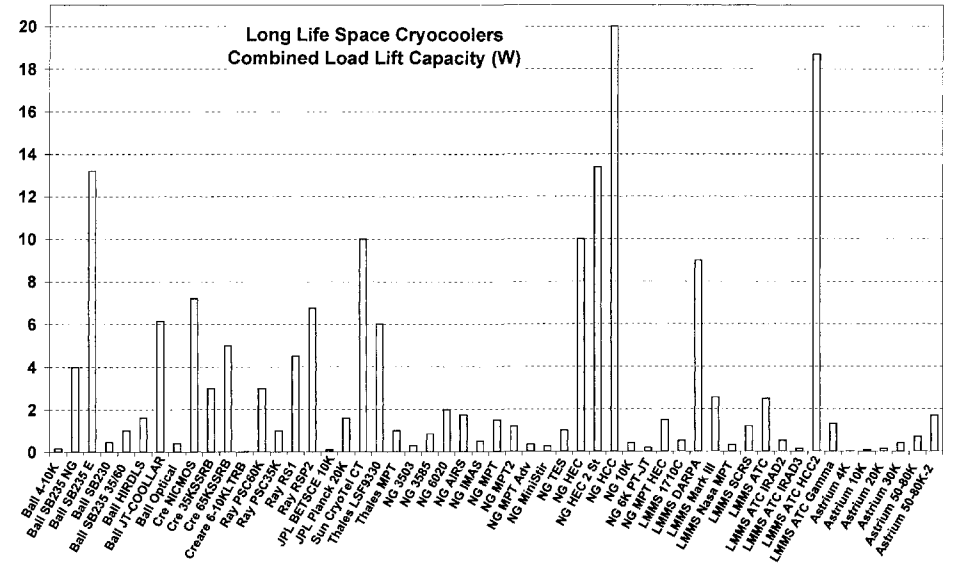

Figure 2. Heat load capacity comparison for AFRL database coolers.

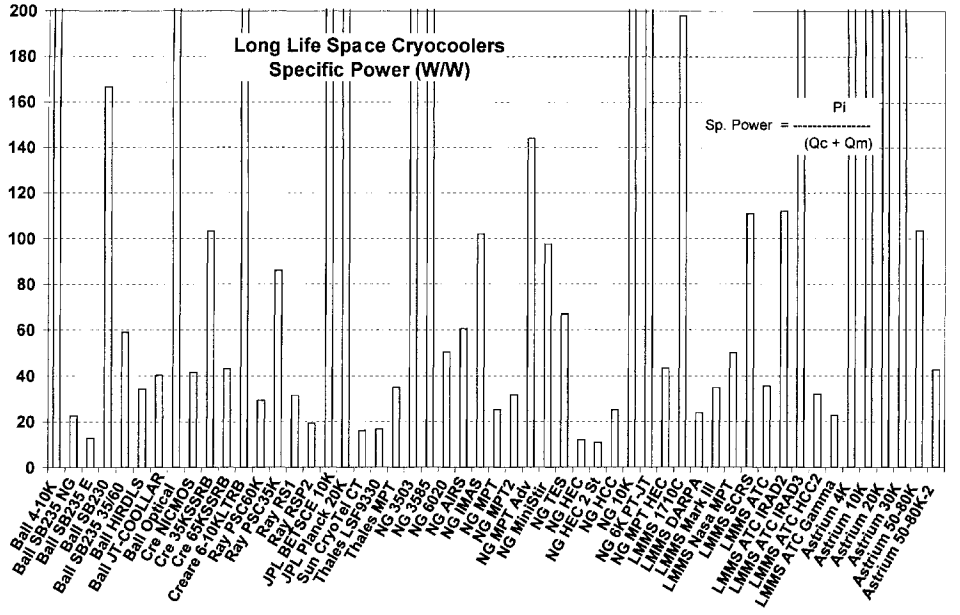

Figure 3. Specific power comparison for AFRL database coolers.

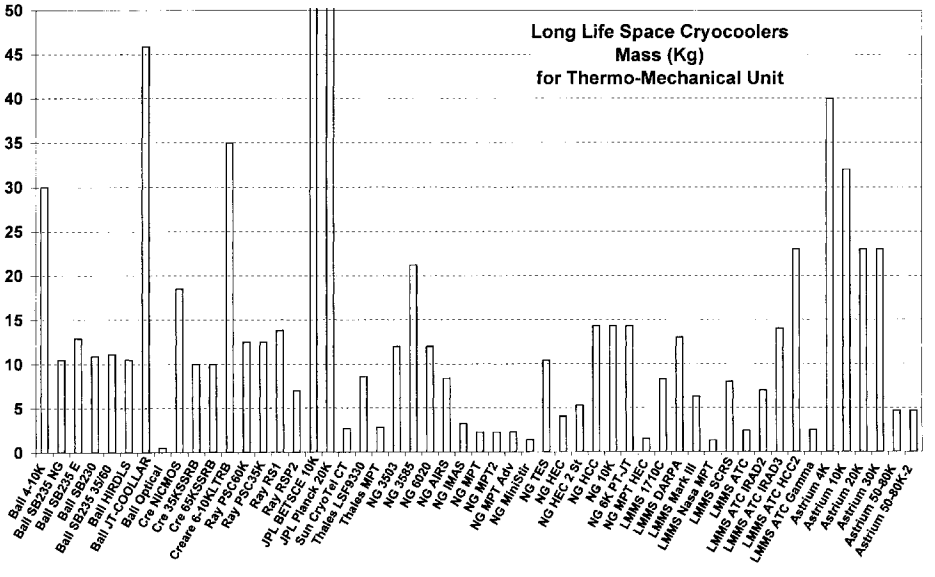

Figure 4. Mass of the thermo-mechanical unit for AFRL database coolers.

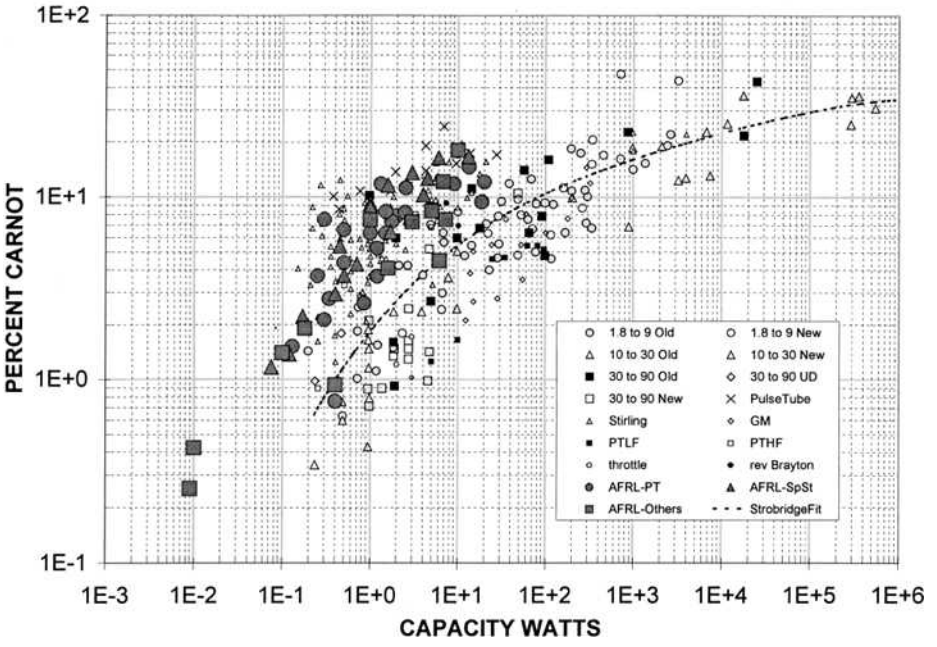

Figure 5. Percent Carnot Efficiency versus heat load of AFRL database coolers along with coolers covered by Strobridge (Ref 6) and ter Brake/ Wiegerinck (Ref 3.)

It is instructional to compare the current database parameters with the surveys done in the past, notably the data available from previous surveys by Strobridge in 1974 and ter Brake and Wiegerinck in 2002. Both considered general types of non-military based cryocoolers and provided trends in efficiency, mass, and cost in historical perspective. In order to provide a comparative basis, the percent Carnot effieiency for AFRL database coolers is plotted along with their cooler data in Figure 5 and isolated in Figure 6. The categories presented by both the surveyors are retained. Curve fits are given as follows:

AFRL Space coolers database:

$$\log C = 0.73719 + 0.45936 * \log Q - 0.08743 * \log Q^{2}$$

Strobridge (Ref 6):

$$\log C = 0.264392 + 0.60539 * \log Q + 0.15656 * \log Q^{2} + 0.02452 * \log Q^{3} + 0.0015595 * \log Q^{4}$$

where C stands for percent Carnot efficiency and Q for the heat capacity of the cooler. Considering the scatter, a quadratic fit is sufficient for the AFRL coolers database. An accurate fourth order polynomial fit for Strobridge plot line is given for reference and was obtained from the original chart. Strobridge does mention that such lines "represent the author's judgment of an average and are thus subject to arbitration." It is seen that the coolers with very low cold end temperature are not efficient thermodynamically although their advantage has to be weighed with their application for specific sensor design requirements.

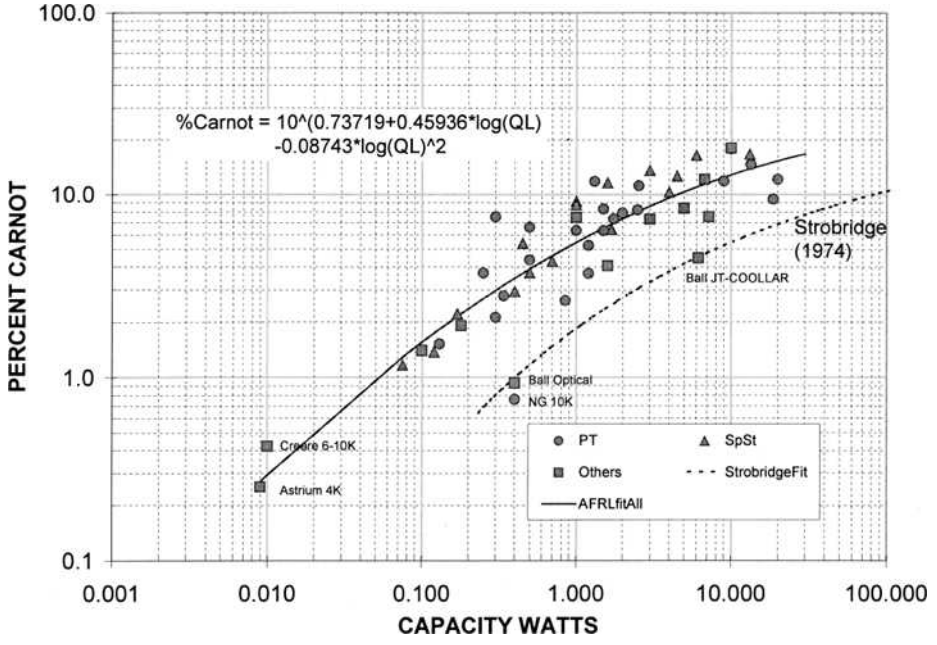

Figure 6. Percent Carnot Efficiency of AFRL database coolers.

The cooler mass is plotted against the input power in Figure 7 for combined cooler database and in Figure 8 for AFRL cooler database. The trends are comparable with previous data fit. CILTEC survey gives $m = 0.0711\ Pin^{0.905}$. The AFRL survey shows $m = 0.082\ Pin^{0.998}$. If the heavy sorption coolers and the optical low mass cooler are avoided, the curve gets shifted to $0.1762\ Pin^{0.8266}$. There is much scatter in the data for it to be considered reliable estimate.

DATABASE DISPLAY FEATURES

A sample of the front panel capture of the MS Access AFRL cryocooler database is shown in Figure 9. It is a valuable tool for space cryogenics development. It includes geometrical and thermodynamical performance parameters, maturity status, company information, thumbnails of the coolers linked to images, and hyperlinks to references of individual coolers. The database also provides links and summaries of web pages (Figure 10) for agencies and manufacturers related to space cryogenics.

FUTURE CONSIDERATIONS

It is projected that future updates of the database will include all space-applicable coolers. Space cryocooler developments in Europe and Japan are not sufficiently represented in the present survey, and it will be useful to include them.

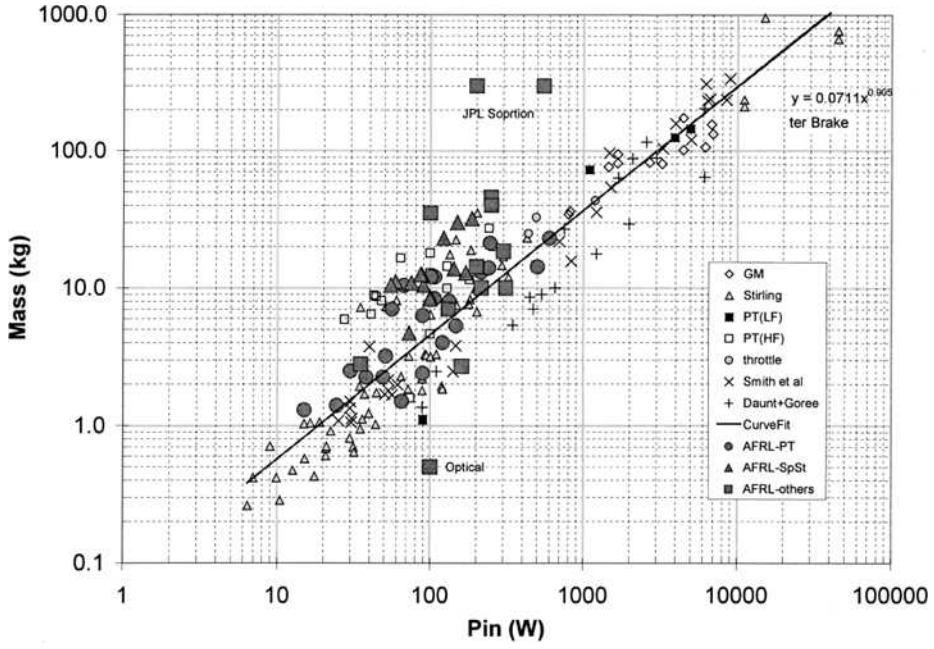

Figure 7. TMU mass versus input power of AFRL database coolers along with coolers covered by ter Brake/ Wiegerinck (Ref 3.)

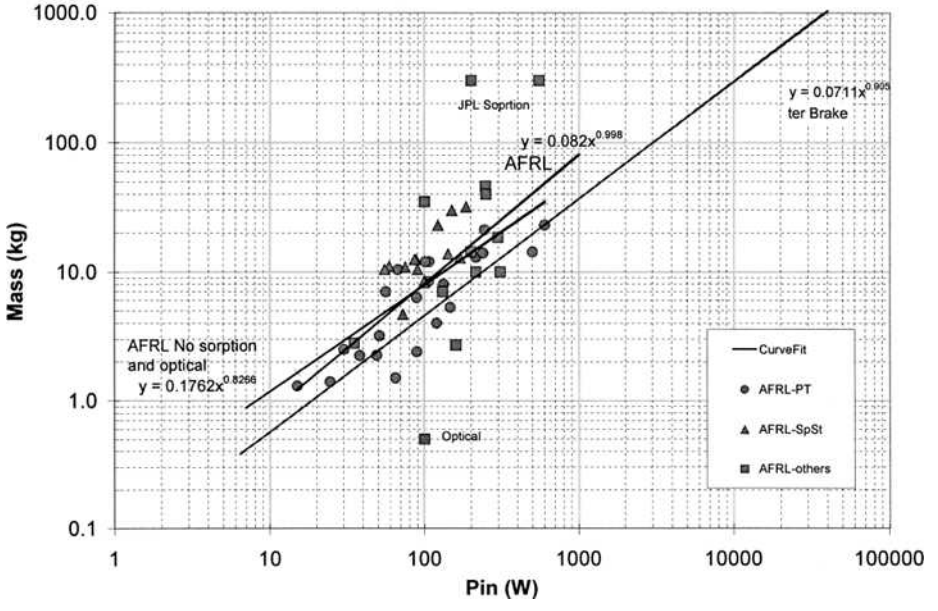

Figure 8. TMU mass versus input power of AFRL database coolers.

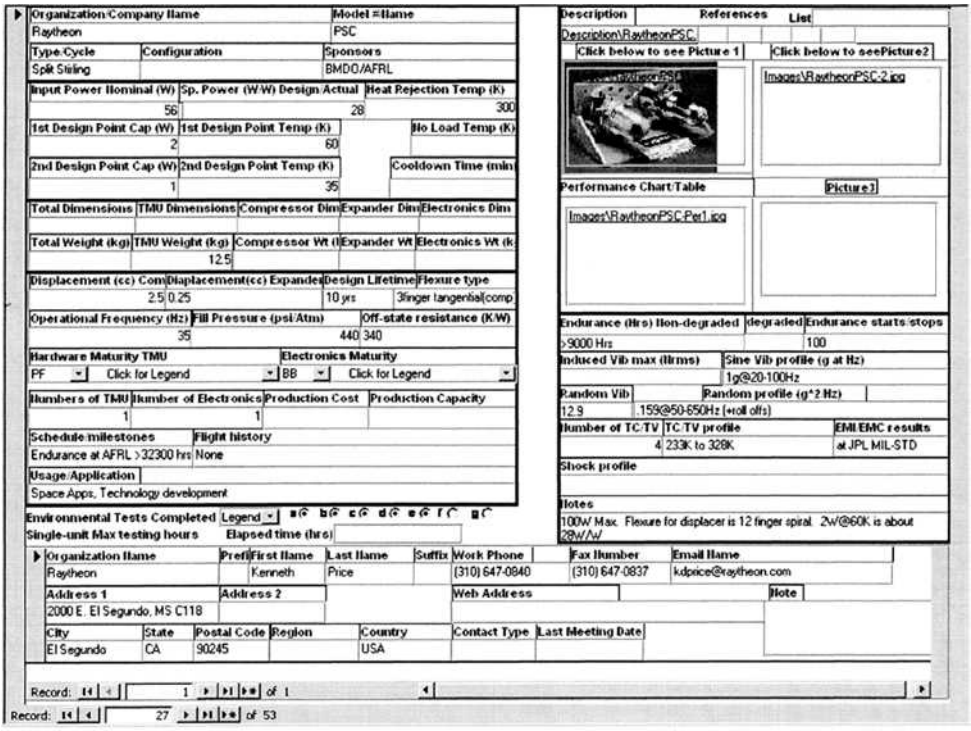

Figure 9. Front panel sample of the AFRL coolers MS Access database.

Figure 10. Example of links in the AFRL coolers MS Access database.

ACKNOWLEDGEMENT

We gratefully acknowledge the support of the following individuals to update the cooler information. Dave Glaister of Ball Aerospace; Walt Swift of Creare; Bob Bowman of JPL; Jeffrey R. Olson and Ted Nast of Lockheed Martin; Tanh Nguyen and Manny Tward of Northrop Grumman NGST/TRW; Ken Price and Carl Kirkconnell of Raytheon; Doug Keiter of Sunpower; Peter Bruins, Wim van den Hil, and Jeroen Mullie of Thales Cryogenics; and Peter Kittel of NASA.

REFERENCES

1. Donabedian, M., Curran, D.G.T., Glaister, D.S., Davis, T., Tomlinson, B.J., "An Overview of the Performance and Maturity of Long Life Cryocoolers for Space Applications," Aerospace Report No. TOR-98(1057)-3, Revision A.
2. Glaister D.S., Donabedian M., Curran D.G.T., Davis T., "An overview of the performance and maturity of long life cryocoolers for space applications," Ross R.G., (Ed.), *Cryocoolers 10*, Plenum Press, New York (1999), pp. 1-20.
3. ter Brake, H.J.M., Wiegerinck, "Low-power Cryocooler Survey," Cryogenics 42 (2002), pp. 705-718.
4. Daunt, J.G., Goree, W.S., "Miniature cryogenic refrigerators. Report Office of Naval Research, July 1969, contracts Nonr-263(70) and N00014-67-C-0393.
5. Strobridge T.R., "Refrigeration for superconducting and cryogenic systems," IEEE Trans. Nucl. Sci., Volume: NS-16, Issue: 3, part 1 (1969), pp. 1104-1108.
6. Strobridge T.R., Cryogenic refrigerators--An updated survey. National Bureau of Standards Technical Note 655 (Supt. Documents, U.S. Govt. Printing Off.), 1974.
7. Crawford, A.H., "Specifications of cryogenic refrigerators," Cryogenics, Volume: 10, (1970), pp. 28-37.
8. Smith, Jr J.L., Robinson, Jr G.Y., Iwasa, Y., "Survey of the state-of-the-art of miniature cryocoolers for superconducting devices," NRL Memorandum Report 5490, Naval Research Laboratory, Washington DC, 1984.
9. Naval Research Laboratory "Cryo Cooler Database," Version 1.0, April 1999," Prepared by Nichols Research, Albuquerque, NM, USA.
10. Bruning J.L., Torrison R., Radebaugh R., Nisenoff M., "Survey of cryocoolers for electronic applications (C-SEA)," Ross R.G., (Ed.) *Cryocoolers 10*, Plenum Press, New York (1999), pp. 829-835
11. Collaudin, B., Rando, N., "Cryogenics in Space: a Review of the Missions and of the Technologies," *Cryogenics*, Vol. 40, (2000), pp. 797-819.
12. Ross, R.G., Jr., "JPL Cryocooler Development and Test Program: A 10-year Overview," *Proceedings of the 1999 IEEE Aerospace Conference*, Snowmass, Colorado, Cat. No. 99TH8403C, ISBN 0-7803-5427-3, 1999, p. 115-124.
13. Boyle, R. and Ross, R.G., Jr., "Overview of NASA Space Cryocooler Programs," *Adv. in Cryogenic Engin.*, Vol 47B, Amer. Inst. of Physics, New York (2002), pp. 1037-1044.
14. Ross, R.G., Jr. and Boyle, R. "NASA Space Cryocooler Programs—An Overview," *Cryocoolers 12*, Kluwer Academic/Plenum Publishers, New York (2003), pp. 1-8.
15. Ross, R.G., Jr., Boyle, R.F., and. Kittel, P., "Overview of NASA Space Cryocooler Programs — A 2003 Summary," *Adv. in Cryogenic Engin.*, Vol 49B, Amer. Inst. of Physics, New York (2004), pp. 1197-1204.

Active Versus Standby Redundancy for Improved Cryocooler Reliability in Space

R.G. Ross, Jr.

Jet Propulsion Laboratory
California Institute of Technology
Pasadena, CA 91109

ABSTRACT

Long-life space cryocooler applications, such as NASA's Atmospheric Infrared Sounder (AIRS) instrument, require that the cryocooler system possess a very high level of reliability. This need for high reliability not only demands that high reliability coolers be used, but often requires that some form of redundancy be incorporated. One common implementation is standby redundancy; however, active redundancy is another equally viable choice. Recently, experience with both types of redundancy has been gained with the AIRS instrument. The AIRS cryocoolers were initially designed and launched as standby redundant units; they were then switched over to active redundancy after six months of in-space operation.

This paper examines the performance trade for the two redundancy approaches with explicit treatment of the effect of operational level (off, versus low power, versus high power) on the reliability of the redundant and primary unit. This is accomplished through the derivation and use of a new reliability model that explicitly includes the probability of failure both prior to and after the time of a cooler failure. Also presented, is a discussion of the effect of the two redundancy approaches on the overall space-instrument system including input power level, robustness to transient single-event shutdowns, and robustness to in-space load increases—such as from in-space contamination of cryogenic surfaces. The active redundancy approach is shown to have advantages in terms of improved reliability as well as improved overall system performance.

INTRODUCTION

One key means of improving the reliability of systems required to provide continuous cooling during multi-year space missions is to incorporate redundant components to protect against individual failures. There are many options for incorporating redundancy; four common ones, highlighted in Fig. 1, have been analyzed previously by this author with respect to their total systems advantages and disadvantages.[1] Although most space cryocooler missions to date have not incorporated redundancy, the 'dual coolers with dual electronics and no switches' approach in the lower left corner of Fig. 1 was adopted by the NASA AIRS mission, which was launched in May 2002.[2-5] The original analysis of the reliability of that configuration utilized the classic equations for the reliability of a two-parallel redundant system as noted in Eq. 1. This classical equation describes the reliability (R_{clrsys}) of the two-cooler system over (T) years of operation as:

Cryocoolers 13, edited by R. G. Ross, Jr.
Springer Science+Business Media, Inc., New York, 2004

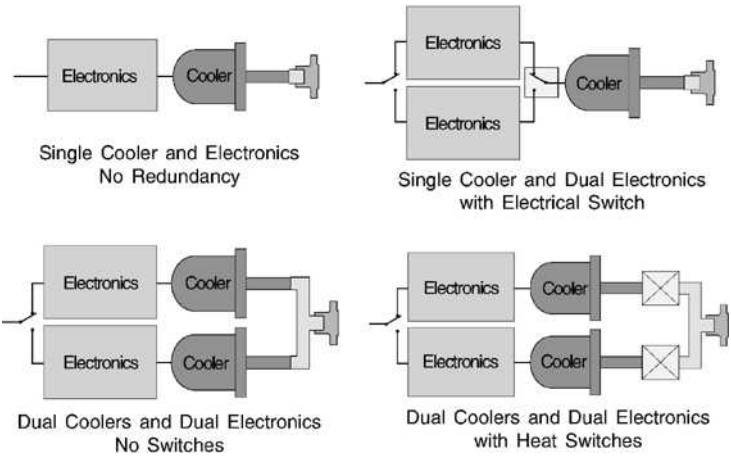

Figure 1. Example cryocooler redundancy options.

$$R_{clrsys} = 1 - (\dot{P}_u \cdot T)^2 \tag{1}$$

where P_u is the probability of failure per year of each integrated cooler unit (mechanical cooler plus electronics). Given that the electronics and mechanical cooler are in series (i.e. both must work for the integrated cooler unit to work) we get that

$$\dot{P}_u \approx \dot{P}_e + \dot{P}_m \tag{2}$$

where $\dot{P}_e$ is the probability of failure per year of the electronics and $\dot{P}_m$ is the probability of failure per year (failure rate) of the mechanical cooler. This simplified equation assumes that the probabilities of failure are small ($\dot{P} \ll 1$). More accurately

$$\dot{P}_u = \dot{P}_e + \dot{P}_m - \dot{P}_e\dot{P}_m \tag{3}$$

Also imbedded in these classical equations for series/parallel redundancy are assumptions as to how the coolers are operated. For example, is the redundant unit 'on' or 'off' while the second unit is operating, and what is the effect of whether it is on or off on its probability of failure?

For the AIRS instrument, an operational strategy referred to as *standby redundancy* was initially selected. With this approach, the second, or redundant cooler, was assumed to be not operating while the primary unit was operating; this minimizes the chance of failure of the backup unit during operation of the primary unit. A second operational strategy available with the AIRS cooler configuration was to operate both coolers at reduced power until one fails, then to depend on the remaining good cooler to operate alone for the rest of the mission life, or until it fails. This is referred to as *active redundancy.*

For either operational strategy, each cooler must be sized to carry both the active cooling load of the instrument as well as the parasitic cooling load caused by heat conduction through the turned-off cooler. For the AIRS cryogenic system, the parasitic load through the off-cooler represents nearly half of the total load on the operating cooler.[3] Thus, when two coolers are sharing the load, they have only about one quarter of the load carried when a single cooler is operating.

To properly quantify and understand the reliability of these two operational strategies, one must explicitly address the effect of operational level (off, versus low power, versus high power) on the reliability of the redundant and primary unit during all periods of the mission. This requires an analytical formulation for reliability that is considerably more complete than the classical representation presented above in Eqs. 1 to 3. Also, when considering the merits of the two operational strategies, it is important to consider the effect of the two redundancy approaches on the overall space-instrument system including input power level, robustness to transient single-

event shutdowns, and robustness to in-space load increases—such as from in-space contamination of cryogenic surfaces.

This paper first addresses this comparison through the derivation and use of a new reliability model that explicitly includes the probability of failure, both prior to, and after the time of a cooler failure. This is then followed by an examination of the effect of the two redundancy approaches on the overall space-instrument system.

RELIABILITY MODEL DERIVATION

To understand the reliability of the complex operational scenario associated with active redundancy it is necessary to examine the details of what it takes to survive the mission. Let us assume that there are two parallel cooler units (A and B), and that cooler A fails first, and then cooler B continues on until cooler B fails. Successful outcomes include both:

a) Those cases when cooler A never fails and operates for the complete mission, and

b) Those cases where cooler A fails, cooler B is still functional when cooler A fails, AND cooler B does not fail for the remainder of the mission.

Examination of the above indicates that there are three failure-rate terms that govern the system-level reliability: 1) the probability of failure per year ($\dot{P}_A$) of cooler A prior to its failure, 2) the probability of failure per year ($\dot{P}_{B1}$) of cooler B prior to the failure of cooler A, and 3) the probability of failure per year ($\dot{P}_{B2}$) of cooler B after the failure of cooler A. Introducing these three distinct failure-rate probabilities ($\dot{P}_A$, $\dot{P}_{B1}$, and $\dot{P}_{B2}$) allows us to assign different failure rates to the two coolers before and after the switch-over to the redundant unit.

Stepping back to basic principals, we can now calculate the reliability of the complete system over mission length (T) as the fraction of successful outcomes out of all possible operational outcomes. Successful outcomes include: 1) cases where cooler A never fails, and 2) all cases where cooler A fails at time (t), cooler B is still functional (has not failed) at time (t), AND cooler B continues to run for the remainder of the mission (T- t).

Mathematically, the fraction of possible outcomes where cooler A never fails is given by the reliability of cooler A, i.e.

$$R_A = 1 - \dot{P}_A T \tag{4}$$

For all other possible outcomes, consider the calculational process schematically illustrated in Fig. 2. Here, we divide up the mission duration (T) into numerous time intervals Δt, each defined by the time (t) since the start of the mission. For each of these time intervals we ask what is the probability of a cooler A failure during this interval, and what is the fraction of these failure cases where cooler B successfully completes the mission. This fraction of cases where cooler B works successfully can be most easily computed as one minus the probability of cooler B failing either before or after the switch-over. Thus, the fraction of successful outcomes for each Δt interval at each time (t) is given by

$$R_t = \dot{P}_A \Delta t \left(1 - \dot{P}_{B1} t - \dot{P}_{B2}(T - t)\right) \tag{5}$$

where $\dot{P}_A \Delta t$ is the probability of a cooler A failure during time interval Δt, $\dot{P}_{B1} t$ is the probability of cooler B failing prior to time (t), and $\dot{P}_{B2}(T - t)$ is the probability of cooler B failing after time (t).

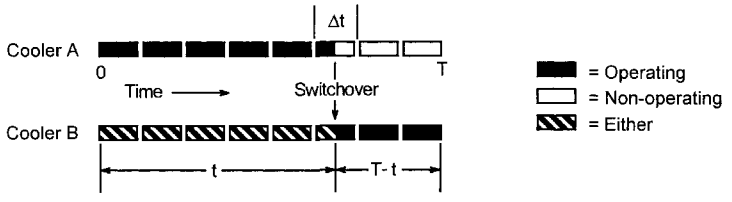

Figure 2. Schematic illustration of reliability calculation interval (Δt) of mission life (T).

Now, the complete mission reliability (the fraction of successful outcomes out of all possible operational outcomes) is just Eq. 4 plus the sum of Eq. 5 over all possible Δt's from 0 to T, i.e.

$$R_{clrsys} = 1 - \dot{P}_A T + \sum R_t \tag{6}$$

Converting this to an integral for a vanishingly small Δt we get

$$R_{clrsys} = 1 - \dot{P}_A T + \int \dot{P}_A (1 - \dot{P}_{B1} t - \dot{P}_{B2}(T - t))dt \tag{7}$$

which gives

$$\boxed{R_{clrsys} = 1 - \tfrac{1}{2} T^2 \dot{P}_A (\dot{P}_{B1} + \dot{P}_{B2})} \tag{8}$$

or

$$\boxed{P_{clrsys} = \tfrac{1}{2} T^2 \dot{P}_A (\dot{P}_{B1} + \dot{P}_{B2})} \tag{9}$$

where

R_{clrsys} = reliability of cooler system over T years operation
P_{clrsys} = probability of failure of cooler system in T years
$\dot{P}_A$ = probability of failure/year of cooler A + electronics A, where unit A is the 1st to fail
$\dot{P}_{B1}$ = probability of failure/year of cooler B + electronics B in period before unit A fails
$\dot{P}_{B2}$ = probability of failure/year of cooler B + electronics B in period after unit A fails

In the above, recall that the probability of failure of the mechanical cooler plus electronics is given by Eqs. 2 and 3. For example, for cooler A

$$\dot{P}_A \approx \dot{P}_{mA} + \dot{P}_{eA} \tag{10}$$

Comparing Eq. 9 with Eq. 1, we see that Eq. 1 assumes that $\dot{P}_{B1} = \dot{P}_{B2} = \dot{P}_A$, i.e. that cooler B's probability of failure is independent of whether it is operating or not, or whether cooler A has failed or not. Equations 8 and 9 now provide access to these important functional dependencies.

SYSTEM IMPLICATIONS OF ACTIVE VERSUS PASSIVE REDUNDANCY

Equations 8 and 9, provide one means for providing visibility into the reliability strengths and weaknesses behind active versus passive redundancy. However, before conducting numerical comparisons it is useful to first explore the system level implications of the two redundancy options; this can provide insight into additional reliability factors that may need to be addressed.

Important distinctions between active versus passive redundancy include:

- The drive level (power, piston stroke, speed) associated with each cooler, both before and after a first cooler failure, and how the drive level reflects into the projected failure rate of the coolers and their electronics
- The impact of two-cooler operation on the total input power required from the spacecraft and the amount of heat that must be rejected from the spacecraft heat rejection system
- Possible implications of two-cooler operation on closed-loop temperature control of the cryogenic load
- Possible implications of two-cooler operation on such things as closed-loop cryocooler vibration suppression systems and limits on allowable input ripple current to the spacecraft power system
- The extent to which two-cooler operation minimizes thermal cycling of the overall cryogenic load to elevated temperatures during the mission due to things such as spurious safety trip-outs and warm-ups required to boil-off contamination condensed on cryogenic surfaces

Each of these is discussed below.

Implications on Required Range of Cooler Drive Levels

With active redundancy, both coolers (the primary and the backup) run simultaneously until one of the two coolers fails. From an input-power perspective, the impact of simultaneous two-

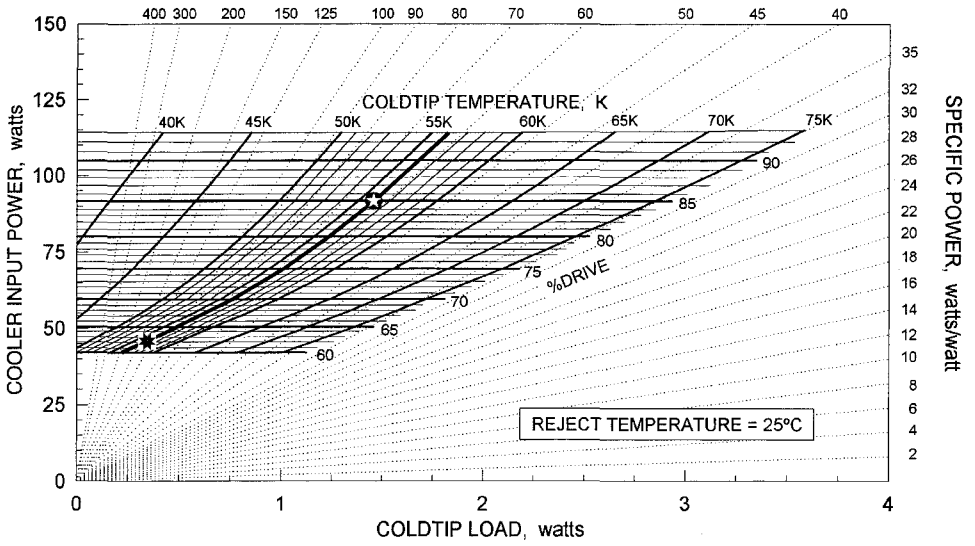

Figure 3. Cryocooler operating point in the AIRS instrument with single cooler operating ✪ and with load shared by two coolers in active redundancy mode ✷.

Table 1. Cooler drive status for the three operating regimes.

Redundancy Implementation	Cooler Drive Level		
	Cooler A Before Failure	Cooler B Before Cooler A Fails	Cooler B After Cooler A Fails
Standby Redundancy	85% drive	unpowered	85% drive
Active Redundancy	62% drive	62% drive	85% drive

cooler operation may be greatly alleviated by the fact that, with some cooler designs, as much as 50% of the total cryogenic load may be the parasitic load of the non-operating redundant cooler.[3] Specifically, with both coolers operating, the parasitic load of the standby cooler disappears, and the total cooling load shared by the two operating coolers may be only half of the load carried by a single operating cooler. This can result in each of the operating coolers in an active redundant system carrying only one quarter of the cryogenic load of the single operating cooler in a standby redundant system, and cause the required spacecraft power for the active redundant system to be comparable to that for the passive redundant system.

As an example, Fig. 3 illustrates the operating points of the pulse tube cryocoolers in the AIRS instrument in both standby redundancy mode (single cooler operating) and active redundancy mode (both coolers sharing the load until one cooler fails). Table 1 summarizes the resulting drive levels for this application in both the standby and active-redundancy implementations. For the AIRS cooler, '%-drive' is the relative input drive level that is commanded to the power amplifier; for the mechanical unit, it roughly equates to the percent of maximum available piston stroke.

Implications of Cooler Drive Level on Failure Probabilities

As shown in Table 1, active versus standby redundancy leads to significantly different drive levels (stroke levels) on the coolers prior to a first cooler failure. Specifically, the trade is between a single, heavily-loaded cooler plus a non-operating standby unit and two lightly-loaded coolers. Estimating the failure rates associated with these drive levels depends heavily on the specific cooler design and must draw upon test experience and understanding of the governing physics underlying the individual failure mechanisms.

Table 2. Failure rate (%/year) vs. input power level for example cryocooler mechanical unit.

FAILURE MECHANISM	0% Power 0% Stroke	40% Power 65% Stroke	60% Power 75% Stroke	75% Power 85% Stroke	100% Power 95% Stroke
Coldend blockage by Internal Contamination	0.05	0.05	0.08	0.15	0.22
Leakage from Seal or Feedthrough Failure	0.15	0.15	0.15	0.15	0.15
Comp. Flexure Spring Breakage from Fatigue	0	0.02	0.03	0.05	0.07
Comp. Motor Wiring Isolation Breakdown	0.05	0.12	0.15	0.25	0.35
Compressor Piston Wear or Seizure	0	0.06	0.09	0.15	0.22
Compressor Piston Position Sensor Failure	0	0.04	0.06	0.10	0.14
Wear and Leakage of Internal O-ring Seals	0	0.06	0.09	0.15	0.20
Total Failure Probability (%)	**0.25**	**0.50**	**0.65**	**1.00**	**1.35**

Table 3. Failure rate (%/year) vs. input power level for example cryocooler drive electronics.

FAILURE MECHANISM	0% Power 20°C	40% Power 25°C	60% Power 28°C	75% Power 30°C	100% Power 33°C
Transient/Peak Voltage-Current Stress	0	0.20	0.25	0.30	0.40
Arrhenius Time-Temp-Voltage Mechanisms	0.15	0.25	0.30	0.35	0.45
Thermal-cycle Fatigue Stress	0.05	0.10	0.15	0.20	0.25
Long-term Radiation Damage	0.15	0.15	0.15	0.15	0.15
Total Failure Probability (%)	**0.35**	**0.70**	**0.85**	**1.00**	**1.25**

Tables 2 and 3 provide examples of mechanism-level failure-rate estimates for both the mechanical cooler and its drive electronics. Such estimates, based on the methodology published previously by this author,[1] allow the effect of drive level to be explicitly observed. These particular estimates were generated by first scaling the mechanism failure rates at the 75% power level (which equates to an 85% stroke level) to give a total probability of failure of 1%/year; this corresponds to a 95% reliability after five years—which is felt to be a representative value. To scale the probabilities for different drive levels, the mechanisms were categorized by their underlying physics into those that had minimal dependency on drive level (such as leakage and parts radiation damage), those with a strong dependency on stroke level (such as flexure fatigue, contamination, and O-ring wear), and those with an Arrhenius-like temperature dependence on case temperature (such as many electronic-parts failure mechanisms). Included in the column headings is an estimate of the variation in total cooler input power, the percent of maximum piston stroke, and the electronic part case temperature associated with the various drive levels; these data were drawn from the AIRS cooler application.[3,4]

For the stroke-sensitive failure mechanisms, the failure probability was assumed to increase 10x for each factor of two increase in stroke level (S), i.e. $\dot{P}_S = \dot{P}_{75\%} \times 10^{\alpha}$, where $\alpha = \log(S/S_{75\%})/\log 2$, and $\dot{P}_{75\%}$ and $S_{75\%}$ are the failure rate and stroke for 75% power. This is representative of the power-law dependence of fatigue life on strain level and is felt to perhaps be a useful model for piston-generated contamination and piston-head O-ring wear, since piston forces and compression-space temperature both increase rapidly with increasing compressor stroke and input power. For Arrhenius mechanisms, where log failure rate is linearly proportional to inverse absolute temperature, P was assumed to increase 2x for each 10°C increase in case temperature (T), i.e. $\dot{P} = \dot{P}_{75\%} \times 2^{\beta}$, where $\beta = (T - T_{75\%})/10$. Note that these assumptions result in a significant reduction in failure probability at low drive-levels for both the cooler mechanical unit and its electronics.

Implications on Closed-loop Temperature Control, Vibration Control, and EMI

Another class of considerations that must be addressed in trading-off passive versus active redundancy is the effects on various control functions of running two coolers simultaneously. Specifically, closed-loop temperature control of the cryogenic load and closed-loop vibration suppression of cooler-generated vibration. The effect of ripple current fed back to the spacecraft

power subsystem and AC magnetic fields of two coolers running simultaneously are additional considerations.

Closed-loop Temperature Control. For most space cryocooler applications, closed-loop control of the temperature of the cryogenic load is an extremely important function of the cooler system. Therefore, accommodating closed-loop temperature control with either one or both coolers operating is an important consideration in selecting cooler redundancy. As an example, with the AIRS cooler system, each of the two coolers is connected to the focal plane load with its own flexible braid that has a finite thermal impedance. This thermal impedance between the temperature-controlled cold tip and the focal plane allows the two coolers to run simultaneously, each with its own independent closed-loop temperature control. Thus, either active or standby redundancy is possible with this system.

Closed-loop Vibration Suppression. The closed-loop control of cooler-generated vibration is another common requirement of space cryocooler applications. Distinguishing between the vibration output of two simultaneously-operating coolers and applying the appropriate suppression feedback often requires special design features and control algorithms that must be specifically addressed in light of the cooler redundancy approach.

Generated EMI. A third area affected by the redundancy approach is control of ripple currents fed back into the spacecraft power bus from the drive electronics as well as the magnetic fields radiated from the compressor drive motors. Since two coolers running at partial load are likely to have offending current and magnetic field levels similar to a single heavily-loaded cooler, EMI is probably not a decision driver, but it is a difference that should be considered at the systems level.

Implications on Payload Thermal Cycling

Cycling the cryocooler off for any reason will generally result in warm-up of the cryogenic payload elements such as focal planes, and require a cooldown and re-stabilization period that adversely impacts payload operational time. The resulting thermal cycling can also lead to mechanical fatigue of payload elements, with serious reliability consequences. Thus, the manner in which standby versus active redundancy influences the likelihood and number of payload warm-ups can be an important consideration.

With the AIRS instrument,[5] two types of cooler outages were found to be significant during the first few months of space operation: 1) planned warm-ups to decontaminate the cryogenic load elements and cooler coldend of high-emittance surface films (water ice), and 2) unplanned warm-ups associated with spurious safety trips caused by single event effects (SEEs) associated with passage through the South Atlantic Anomaly (SAA) during times of exceptionally severe radiation levels.

Implications of Redundancy on Deicing Warm-ups. Gettering of frozen contaminants on the cryogenic surfaces of the payload is a common space-instrument problem often addressed by planned periodic warm-ups to defrost the critical surfaces.[6] When the problem of contaminant buildup is solely an issue of cooler load increase, as opposed to degradation of optical or science performance, then a second active-standby cooler may be able to share the increased load and greatly extend the time between required decontamination events. In contrast, a single cooler in standby-redundant mode may be quickly overwhelmed by the contaminant-induced load increase and require frequent decontamination shutdowns. Over the mission life the rate of recontamination gradually diminishes, so the initial higher-power operation is likely to be well matched to the availability of the redundant unit and coincide with the availability of excess spacecraft power early in the mission.

As an example, Fig. 4 highlights the large reduction in payload warm-ups of the AIRS instrument following the switch-over from standby-redundant operation to active-redundant operation in November 2002. Since the switch-over, there has been only a single warm-up—that a precautionary shutdown of the entire instrument prior to the arrival of the radiation from a 100-year worst case solar storm spotted on the surface of the sun around the first of November 2003.

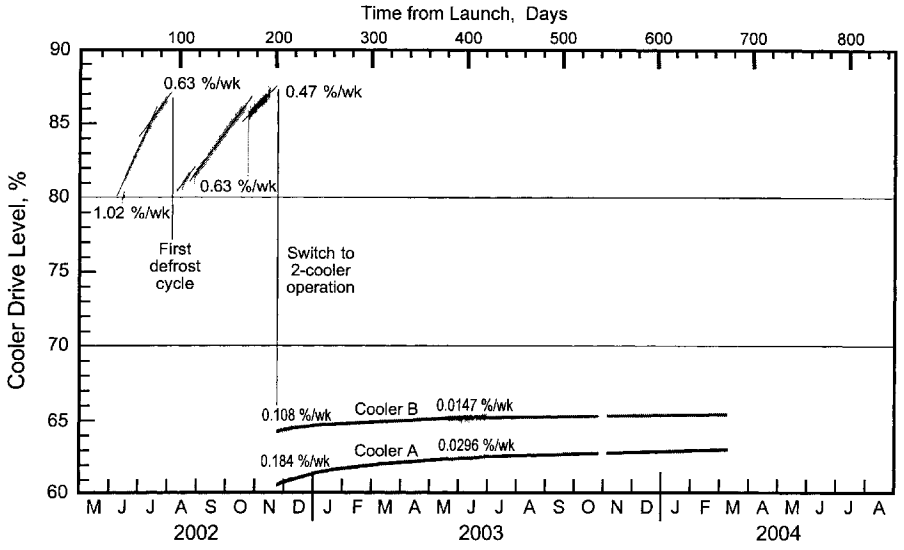

Figure 4. Overall summary of AIRS cooler drive level over the first two years of operation.

Implications of Redundancy on Safety Shutdowns. Random safety shutdowns are a possibility with any cooler due to such things as radiation hits received by the cooler electronics when passing through particularly severe radiation environments. With a single cooler operating in standby redundant mode, the safety shutdown is likely to cause a complete payload warm-up as the failure data is reviewed and a decision is made to resume cooler operation. By the time thermal equilibrium is returned, several days of operation may have been lost.

With active redundancy, the coolers may be programmed so that the second, unaffected cooler simply picks up the total load while the tripped-out cooler is being analyzed and restarted. For some applications, the reduced stroke and power associated with load sharing may also make the operating coolers less susceptible to shutdown events.

TWO-COOLER SYSTEM-LEVEL RELIABILITY ANALYSIS

With the reliability equations derived earlier and the system-level implications noted above, we are now prepared to work a numerical example assessing the reliability of the two redundancy approaches. To the earlier equation (Eq. 9) we now add the dependency of a focal-plane failure rate on thermal cycling, and the additional probability of a cooler unit failing during launch. This launch failure risk is not a function of operating time, so it is added as a discrete new term. Thus:

$$P_{sys} = P_{clrsys} + P_{FP} = (\dot{P}_A T + P_L)(\dot{P}_{B1} T/2 + \dot{P}_{B2} T/2 + P_L) + \dot{P}_{FP} T \qquad (10)$$

where

P_{sys} = probability of failure of total cryogenic payload system in T years
P_{clrsys} = probability of failure of the redundant cryocooler system in T years
$\dot{P}_A$ = failure rate for cooler A + electronics A, where unit A is the first to fail
$\dot{P}_{B1}$ = failure rate for cooler B + electronics B in period before unit A fails
$\dot{P}_{B2}$ = failure rate for cooler B + electronics B in period after unit A fails
P_L = probability of failure of a cooler/electronics unit during launch
$\dot{P}_{FP}$ = failure rate per year for focal plane (assumed not redundant)

Table 4 summarizes example values for the above failure probabilities. The cooler failure rates were derived from those in Tables 2 and 3 for the appropriate drive levels, while the focal plane failure rates are representative values selected for illustrative purposes.

Table 4. Example failure probabilities for cooler system components.

Cooler Drive Level	Focal Plane Thermal Cycling	Mechanical Cooler	Cooler Electronics	Focal Plane
Cooler at 85% stroke	extensive	0.010/yr	0.010/yr	0.010/yr
Cooler at 65% stroke	minimal	0.005/yr	0.007/yr	0.002/yr
Cooler unpowered	n/a	0.0025/yr	0.0035/yr	n/a
Launch Environment	n/a	0.01	0.01	n/a

Active Redundancy. Using the values from Table 4 for the case of active redundancy, and defining a cooler unit as a mechanical cooler plus its drive electronics gives:

$\dot{P}_A$ = failure rate for unit A in operation = 0.005 + 0.007 = 0.012/year
$\dot{P}_{B1}$ = failure rate for unit B *before* unit A fails = 0.005 + 0.007 = 0.012/year
$\dot{P}_{B2}$ = failure rate for unit B *after* unit A fails = 0.010 + 0.010 = 0.020/year
$\dot{P}_{FP}$ = failure rate for focal plane = 0.002/year
P_L = probability of a cooler unit failing during launch = 0.01 + 0.01 = 0.02

Entering these numbers into Eq. 10 for a mission duration of T=5 years gives:

$$P_{Active} = (0.012\times5 + 0.02)(0.012\times2.5 + 0.02\times2.5 + 0.02) + 0.002\times5$$
$$= 0.0080 \text{ (for coolers)} + 0.010 \text{ (for focal plane)} = \boxed{0.018} \quad (11)$$

Noting that the system reliability is just one minus the probability of failure, we get

$$R_{Active} = 1 - 0.018 = \boxed{98.2\%}$$

Standby Redundancy. Using the values from Table 4 for the case of standby redundancy, and again defining a cooler unit as a mechanical cooler plus its drive electronics gives:

$\dot{P}_A$ = failure rate/year for unit A in operation = 0.01 + 0.01 = 0.020/year
$\dot{P}_{B1}$ = failure rate/year for unit B *before* unit A fails = 0.0025 + 0.0035 = 0.006/year
$\dot{P}_{B2}$ = failure rate/year for unit B *after* unit A fails = 0.010 + 0.010 = 0.020/year
$\dot{P}_{FP}$ = failure rate/year for focal plane = 0.010/year
P_L = probability of a cooler unit failing during launch = 0.01 + 0.01 = 0.02

Entering these numbers into Eq. 10 for a mission duration of T=5 years gives:

$$P_{Standby} = (0.02\times5 + 0.02)(0.006\times2.5 + 0.02\times2.5 + 0.02) + 0.01\times5$$
$$= 0.0102 \text{ (for coolers)} + 0.050 \text{ (for focal plane)} = \boxed{0.0602} \quad (12)$$

and

$$R_{Standby} = 1 - 0.0602 = \boxed{94.0\%}$$

Interpretation of the Results

First, ignoring the contribution of the focal plane reliability, the numbers in Eqs. 11 and 12 indicate that the analyzed coolers configured with active redundancy are around 20% more reliable than the same coolers configured in a standby redundancy configuration. However, when the effect of reduced thermal cycling on the focal plane is also included, the reliability of the active redundancy system is seen to be vastly superior. Thus, adding the systems considerations into the cooler reliability analysis can be an important factor in selecting the optimum cooler redundancy approach.

SUMMARY

This paper has examined the performance trade between active and standby redundancy through the derivation and use of a new reliability model that explicitly includes the probability of failure of the redundant unit both prior to and after the time of a cooler failure. This allows the explicit treatment of the effect of operational level (off, versus low power, versus high power) on the reliability of the redundant and primary unit. Also presented, is a discussion of the effect of the two redundancy approaches on the overall space-instrument system including input power level, robustness to transient single-event shutdowns, and robustness to in-space load increases—such as from in-space contamination of cryogenic surfaces. The active redundancy approach is shown to have advantages in terms of improved reliability as well as improved overall system performance.

ACKNOWLEDGMENT

The work described in this paper was carried out at the Jet Propulsion Laboratory, California Institute of Technology, and was sponsored by the NASA EOS AIRS Project through an agreement with the National Aeronautics and Space Administration.

REFERENCES

1. Ross, R.G., Jr., "Cryocooler Reliability and Redundancy Considerations for Long-Life Space Missions," *Cryocoolers 11*, Kluwer Academic/Plenum Publishers, New York, 2001, pp. 637-648.
2. Ross, R.G., Jr. and Green K., "AIRS Cryocooler System Design and Development," *Cryocoolers 9*, Plenum Publishing Corp., New York, 1997, pp. 885-894.
3. Ross, R.G., Jr., Johnson, D.L., Collins, S.A., Green K. and Wickman, H. "AIRS PFM Pulse Tube Cooler System-level Performance," *Cryocoolers 10*, Plenum, New York, 1999, pp. 119-128.
4. Ross, R.G., Jr., "AIRS Pulse Tube Cooler System Level Performance and In-Space Performance Comparison," *Cryocoolers 12*, Kluwer Academic/Plenum Publishers, New York, 2003, pp. 747-754.
5. Ross, R.G., Jr. and Rodriguez, J.I., "Performance of the AIRS Pulse Tube Coolers and Instrument—A first Year in Space," *Adv. in Cryogenic Engin.*, Vol 49B, Amer. Inst. of Physics, New York, 2004, pp. 1293-1300.
6. Ross, R.G., Jr., "Cryocooler Load Increase due to External Contamination of Low-ϵ Cryogenic Surfaces," *Cryocoolers 12*, Kluwer Academic/Plenum Publishers, New York, 2003, pp. 727-736.

INTEGRAL Spectrometer Cryostat Design and Performance after 1.5 Years in Orbit

R. Briet and F. Serene

CNES - Centre National d'Etudes Spatiales
Toulouse, 31401, France

ABSTRACT

The INTERnational Gamma-Ray Astrophysics Laboratory (INTEGRAL) is an ESA satellite that was launched on October 17, 2002. One of the payloads is a Spectrometer (20 keV-8 MeV energy range, 2.5 m high, 1.1 m dia., around 1300 kg). It was supplied by CNES who managed, developed, assembled, and tested the instrument before delivery to ESA for satellite-level activities.

This instrument uses a detection plane containing 19 Germanium detectors that need to be cooled to 85 K during observation and periodically annealed up to 379 K (106°C) to recover energy resolution. The 25 kg cold stage operational temperature is achieved by four 50-80 K EADS-Astrium Stirling coolers, while a passive radiator provides (through a heat pipe connection) a 210 K housing around the detectors. This intermediate stage results in a reduction of cryocooler heat loads, and provides a cold and stable temperature for the preamplifiers. The housing can be configured to be vacuum-tight for ground testing, while it is open in the launch/space configuration.

This paper briefly reviews the flight model design of this double-stage cryostat and the main results from thermal vacuum testing at the satellite level. The excellent in-flight performance is then described together with data on the contamination-decontamination process that has been observed with the cold parts. Cryostat operability and lessons learned from the development and 1.5 years of in-flight data are also discussed.

INTRODUCTION

Gamma-ray emissions coming from celestial objects represent a trace of violent phenomena that have occurred in the vicinity of particular objects such as supernovae, neutron stars, and black holes. Detailed observation of the emissions allows understanding of these phenomena and nucleosynthesis in the universe.

The European Space Agency 2nd midterm scientific mission plan (ESA M2) includes the INTEGRAL observatory which carries four complementary instruments. The Spectrometer SPI, shown in Figs. 1 and 2, has a very high energy resolution of 2.5 keV in the range of 20 keV to 8 MeV. An Imager allows accurate location of the emitting sources, while the JEMX and OMC instruments complete the observation in the X-ray and visible wavelengths, respectively. The INTEGRAL satellite was launched on October 17, 2002 on a Proton launch vehicle; it reached an orbit with an altitude of 9000 km to 154000 km, a 300° perigee, 51.6° inclination, and a 72 hour period.

Organizationally, management of the spectrometer, including its development plan, technical specifications, and its integration and validation tests were under CNES responsibility. Many sub-

Cryocoolers 13, edited by R. G. Ross, Jr.
Springer Science+Business Media, Inc., New York, 2004

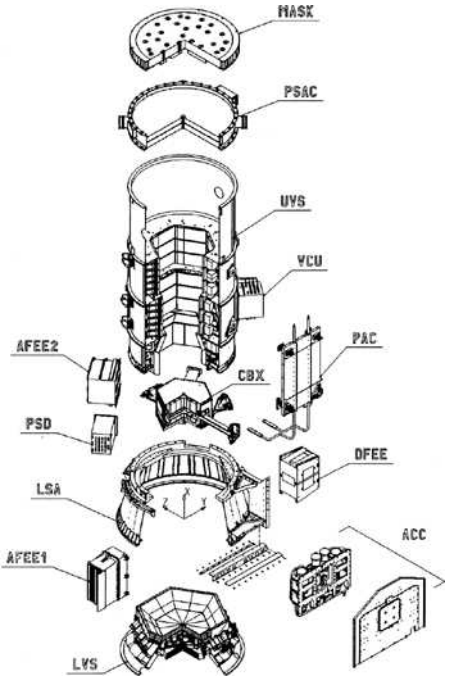

Figure 1. General spectrometer design.

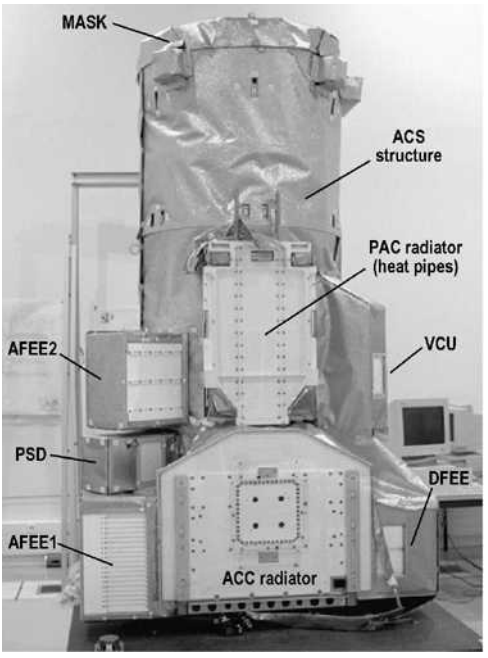

Figures 2. Flight Model Spectrometer in CNES Integration facilities.

systems were funded and provided by French and foreign laboratories involved in gamma-ray astrophysics. CNES also took part in this instrument by providing "in-house," from conception to manufacturing and tests, some key subassemblies such as the main structure, the on-board software, and the cryostat (see Fig. 3).

The core of the Spectrometer consists of 19 high purity Germanium Detectors (GeDs) requiring an operating temperature of 85–100 K to achieve a 2.5 keV resolution at 1.1 MeV. Resolution degradation occurs in time due to irradiation in space with a degradation rate proportional to temperature. A periodic annealing process at 106°C allows the recovery of initial performance.

The 25 kg cold stage operational temperature is achieved by four fully redundant 50-80 K EADS-Astrium Stirling coolers (Fig. 4), while a passive radiator (PAC in Figs. 2 and 3) provides (through a heat pipe connection) a 210 K housing environment around the detectors. This intermediate stage results in a reduction of cryocooler heat loads, provides a cold and stable preamplifier temperature, and eases ground testing.

After a brief instrument and cryogenic system description, this paper reviews the main results from thermal testing at the satellite level, the in-flight performance after 17 months operations, the annealing process effect that benefits the contamination process identified, and lessons learned from this cryogenic system development up to and including operation in space.

INSTRUMENT DESCRIPTION AND OPERATION

During the operation of the scientific instrument, the incident radiation coming from sources located in the field of view is intercepted by a passive MASK composed of pixels that either stop rays (tungsten blocks) or allow them to pass through. Once the photon beam has been coded by the mask, it reaches a pixelized 500 cm^2 detection plane and projects onto it a coded mask shadowgram characteristic of the source location in the sky. The energy range and the energy resolution impose the choice of Germanium crystal detectors.

Photons react with the detectors that are polarized at 5000 volts by creating a current proportional to the energy deposited by the incoming photons. To achieve the needed sensitivity requires that the detectors be operated below 110 K.

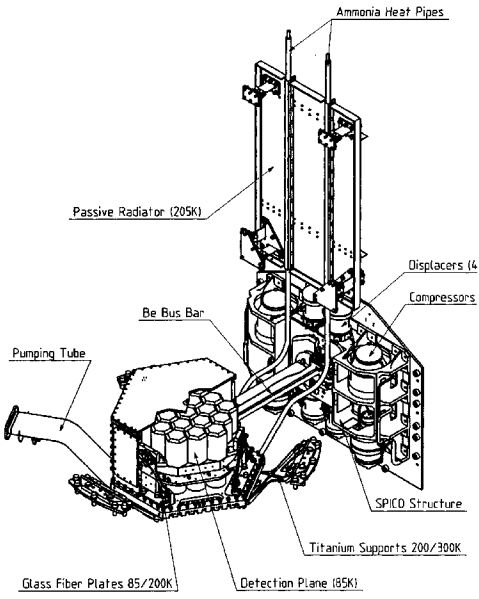

Figure 3. Cryostat overview.

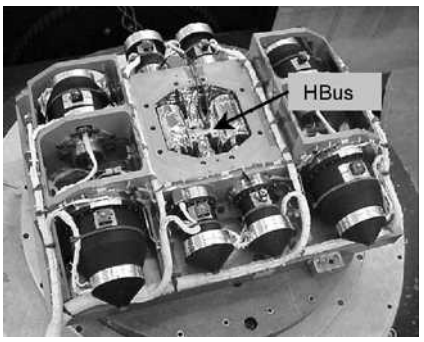

Figure 4. SPI Cooler assembly on EADS-Astrium shaker (HBus i.e. cold I/F to Be Bus Bar).

The optimized 85 K working temperature is achieved using two pairs of cryocoolers (ACC). The detection plane is enclosed in a Beryllium structure (CBX) controlled to around 208 K through a passive cooling device (PAC) to reduce the heat loads.

In order to shield the Germanium detector from the background, the cryostat with its Ge detector array is surrounded by an anticoincidence subassembly (UVS, LVS and VCU) composed of crystal scintillators and photomultipliers, keeping a free field of view. A plastic scintillator (PSAC), located under the mask, also reduces the background. All the signal output data produced from both detection plane and active shielding are then processed by several electronic modules (PSD, AFEE1 and two DFEE). Mechanical loads are supported by the main structure (LSA), which also acts as a single mechanical interface with the platform.

CRYOSTAT DESIGN

The detection plane is composed of 19 Germanium Detectors (GeD) mounted on a Beryllium plate. The overall volume of this hardware is a 100 mm high by 305 mm diameter cylinder which weights 25 kg. The main requirements associated with the GeD are a 85–90 K temperature during observation in order to get high sensitivity and low degradation rate; they also have to be heated up once a year to 380 K for the annealing process.

CNES thus conceived a cryostat composed of the three following subassemblies:

Cold Box (CBX)

The detection array and associated 19 preamplifiers are located inside a housing (CBX) controlled at about 208 K. Heat load reduction is mainly achieved by using MLI, GFRP plates, as well as low conductance wires. The heat lift of the cold stage is transferred to the cooler's cold tips through a Be Bus Bar and a complex 2-stage flexible link assembly.[1,2] This design mainly results from meeting background noise constraints and insuring that the lateral forces imposed on the displacers are low.

To limit the background noise, the detector plate, the chamber structure, and the cold bus bar are made of beryllium. The enclosure, composed of this chamber and a tube surrounding the Be Bus Bar, is vacuum tight to allow simple and low-cost ground testing. A "pumping tube" is thus fitted to the bottom plate of the housing for connection to an external pump or space. This equipment, as

well as the GFRP detectors-to-chamber supports, the titanium chamber-to-main-structure supports, and the electrical harness, constitute the CBX.

Passive Cooling (PAC)

The location of the Spectrometer on the anti-solar face of this sun-pointed satellite was requested early since it eases the use of an intermediate stage. Indeed, the structural envelope of the cold box is cooled at about 208 K by a subassembly called Passive Cooling (PAC). It consists of two ammonia heat pipes linked to an external radiator that is supported from the instrument by means of GFRP struts. The thermal loads rejected by the radiator at 205 K include heat that leaks into the intermediate stage as well as dissipation of the preamplifiers and the antifreeze safety system heating power (see Table 1). Indeed, to optimize the intermediate stage efficiency, heat pipes are used near the freezing point (196 K). A thaw system is implemented to re-prime the heat pipes after any survival mode.

Active Cooling (ACC)

Detector cooling is provided by the four 50-80 K EADS-Astrium Stirling coolers shown earlier in Fig. 4. These coolers are mounted to an outside radiator to reduce background noise transmitted to the detectors, and they are controlled by "independent" command electronics (CDEs) located on the platform. The cryocooler system design and flight operability (TM/TC) is described later in this paper and by Gibson.[2]

Easier integration and system ground testing, with regards to the cold GeD in a lab environment, was made possible by a specific design of the ACC radiator as well as by a special interface between the CBX airtight tube and the ACC structure. A bellows system allows for either a vacuum-tight connection for ground testing or for a full disconnection in the launch and flight configuration. This operation can be achieved through a trap door located on the cooler's radiator, which also permits connection of cryogenic ground support equipment (for faster cool down) and gives access for integration of the flight cooling system to the Hbus, at the end of the bus bar and its first stage flexible link.

Tables 1 and 2 summarize the cold-stage and intermediate-stage thermal loads, while Fig. 5 presents a schematic view of the above described 3-stage thermal system: the 90 K stage for the detectors and the 1st stage of preamplifiers, the 205 K stage for the 2nd stage of preamplifiers and a cold-stage thermal shield, and the 300 K stage for coolers and electronics.

CRYOGENIC SYSTEM OPERATIONS

Global Thermal control

Apart from the cryocooler drive electronics, operation and thermal management of the cryostat requires the following heater power lines (all fully redundant):

- Antifreeze safety system (electronic regulation: 12 W installed under 28 volts),
- Annealing / Outgassing heating system (electronic regulation: 15 W under 28 volts),
- Heat Pipe thaw system (simple On/Off: 38 W)
- Cryocooler switch-on system (mechanical thermostat: 87 W)
- Cryocooler compensation heating system (mechanical thermostat: 37 W)

The annealing/outgassing heater lines can be used in both outgassing and annealing modes by using a telecommandable threshold (37°C or 106°C). Heat pipe thaw nominal and redundant lines are both used to outgas the intermediate stage, which is the CBX and PAC, at 28°C. The cryocooler switch-on system guarantees start-up temperatures (-20°C), while compensation heaters ensure an acceptable minimum cooler operating temperature in nominal mode (4 coolers available).

Cooler Configuration

The cryostat uses two pairs of EADS-Astrium Stirling coolers as shown in Fig. 4 driven by two Cooler Drive Electronics (CDEs) for "standard" back-to-back operation. Even if a three-running-coolers configuration is available, and acceptable with regards to micro-vibrations, the de-

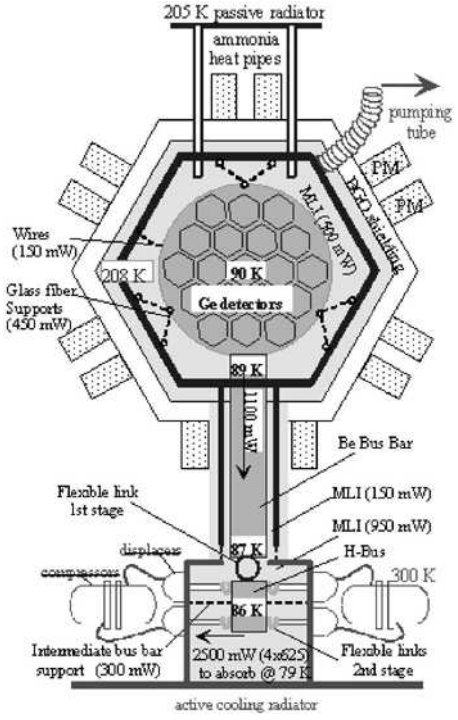

Figure 5. Cryostat concept and heat leaks towards cold stage.

Table 1. "90 K stage" thermal balance.

	Heat leaks => 90 K stage
MLI Detectors	500 mW
Mechanical Supports	450 mW
LV and HV wires	120 mW
Annealing and HK wires	30 mW
MLI Cold rod -Tube	150 mW
Heat lift at HBus (86 K)	**1250 mW**
Intermediate bus bar support	300 mW
MLI around coolers ends	950 mW
Coolers heat lift (79 K)	**≈ 2500 mW**

Table 2. "200 K stage" thermal balance.

	Worst cold case	**Worst hot case**
PA Dissipations	4.4 W	4.4 W
MLI CBX and Tube	1.5 W	2.8 W
Pumping tube	0.7 W	1.4 W
CBX supports	2.9 W	5.9 W
CBX wires	1.9 W	3.4 W
Leaks => 90 K stage	-1.2 W	-1.4 W
Heat pipes heat lift	**10.2 W**	**16.5 W**
MLI radiator	0.4 W	0.7 W
PAC Radiator supports	0.5 W	1.0 W
PAC heaters and sensors	0.9 W	1.6 W
Antifreeze power	6.5 W	0
Radiator rejection	**18.5 W**	**19.8 W**

graded case studied just assumes the availability of a single pair of coolers (CDE failure case).

Full redundancy is not really available on this instrument for GeD degradation rate and peak power reasons. Indeed, a single pair of coolers is sufficient to cool the GeDs to 95-100 K, which satisfies resolution requirements, but with an important degradation rate in time. This implies a long annealing sequence is required every 1.5 months, which is not desirable due to reduced instrument availability for science (taking into account a 15-day cooling sequence from 106°C to 100 K). Moreover, this configuration results in peak currents of 11.5 A on the power bus.

The ACC radiator was thus sized quite large (0.33 m^2) to get an instrument operability and reject high dissipations when using a single pair of coolers running nearly to full stroke in order to operate them at "low temperature", improving efficiency in a so-called "degraded mode." In nominal mode, all four coolers are activated, resulting in a lower load, lower stroke setting, and less dissipation. This latter case is so low that the running coolers must be heated to maintain their temperature in the flight operating range and to pass eclipse with even less power. The solution of using a higher stroke to achieve a higher dissipation was not feasible, since this would result in the GeDs operating below their qualification temperature range.

Cooler / Electronics Operation

CDE modes available are Off, Standby, Launch Lock, and Operating. In launch-lock mode, the piston's and displacer's position pick-off control loops (PPOs) are enabled and set to zero. In operating mode, displacer amplitudes are fixed at 3.4 mm peak to peak, while the compressor piston strokes are adjusted through a 6-bit telemetry command word from 0 to 9.0 mm peak to peak.

No temperature control loop is available. In order to reduce peak currents seen from the bus, the CDEs are linked and operated in a Master/Slave condition with the two pairs of coolers having a 90° phase shift between them. This globally results in a reduced peak current, representing 60% of the total combined CDE1 and 2 individual peak currents.[2]

In terms of telemetry, the CDE peak currents and the compressor drive and demand parameters are available. The demand telemetry reflects the telemetry command sent, this is the setting required at the PPO loop entry, while drive telemetry reflects the exit of the PPO control loop; this is the current sent to the coils.

In nominal configuration, all four coolers are operated with a typical 5.1 mm peak to peak compressor piston stroke (57%) resulting in a 60 W mean input power to the coolers (100 W to CDE). Master/Slave operation limits to 150 W the peak power drawn from the PLM PDU. In degraded mode, the two operating coolers are set at 8.7 mm compressor strokes, requiring 88 W of electrical input power to the coolers, 135 W to the CDEs, and peak currents up to 11.5 amps.

MAIN THERMAL GROUND TEST RESULTS

Thermal vacuum tests with the Flight Model (FM) instrument and at the FM satellite level validated the cryostat performance and power consumption. Electrical and mechanical thermostat controlled heater lines worked in accordance with manufacturing settings and predicted consumption. Stability of active regulation for antifreeze, outgassing, and annealing purposes was better than ±0.5°C.

The cryogenic chain performance was quite excellent, since 90 K was achieved for the GeDs in the 2-, 4- and even for the 3-cooler mode while respecting the 140 W electrical mean power budget. Nevertheless, some discrepancies occurred with respect to predictions. Indeed, cold stage thermal-leak measurements were always lower than theoretical capabilities of the cooling system as measured before delivery. At this time this was explained by deltas in the test configuration between the unit and system level, and was attributed to an increased heat load in the global thermal balance. As described below, long-term in-orbit operation subsequently demonstrated that during ground testing we were facing a contamination issue increasing the coolers' heat load.

IN-ORBIT ACTIVITIES AND RESULTS

Outgassing and First Cooling Phase

The INTEGRAL satellite was launched on October 17, 2002 05:41 UT from Baikonour. Initial telemetry proved that the CDEs and coolers survived launch in active launch-lock mode. A few hours later, instruments and units were switched on to warm the satellite and start the outgassing process. The cryostat outgassing phase lasted 11 days with "cold parts" at 38°C plus 1 day at 82°C. The intermediate stage, heated through the heat-pipe thaw lines, quickly reached 28°C, while the cryocooler's switch-on heaters maintained them cycling between -17°C and -11°C.

Annealing and thaw heaters were then switched off, leading to natural cooling down of both the cold and intermediate stages. About two days later, the antifreeze system automatically stabilized the latter at 208 K with a typical 6 W consumption, while all cold parts were lower than 35°C, which was suitable for start-up of the coolers. Natural GeD cooling at roughly -1°C/hour was thus followed by active cooling with piston strokes set at 72% maximum. As expected from ground testing, 5 days were necessary before the 25 kg cold stage reached the 90 ±1 K operational range; this finally required 4 x 5.14 mm peak to peak piston stroke (56% max).

Observation Phases

The first observation phase and commissioning activities occurred from November 5, 2002 to February 6, 2003. During this period it was noticed that the performance of GeD#15 was atypical in terms of leakage current and resolution, which might indicate contamination. Moreover the actual radiation background was excessive with regards to predictions, which resulted in degrading detector resolution far quicker than expected. After 3 months in orbit, resolution was about 20% worse compared to the initial value, so the scientists decided to anneal the detectors before calibration and to make future observations with the GeDs at 85 K to lower their degradation rate.

As can be seen in Fig. 6, annealing was then requested two more times by the Principal Investigator (PI) in July and November 2003, with the GeDs maintained at 106°C for 36 and 126 hours, respectively.

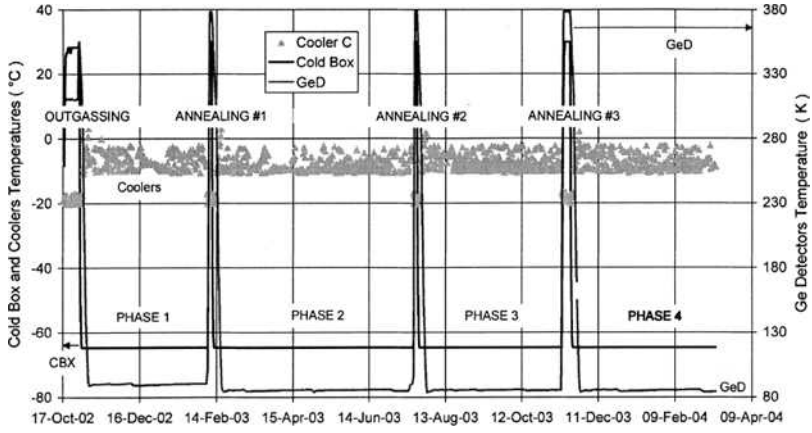

Figure 6. Cryostat main temperatures and phases.

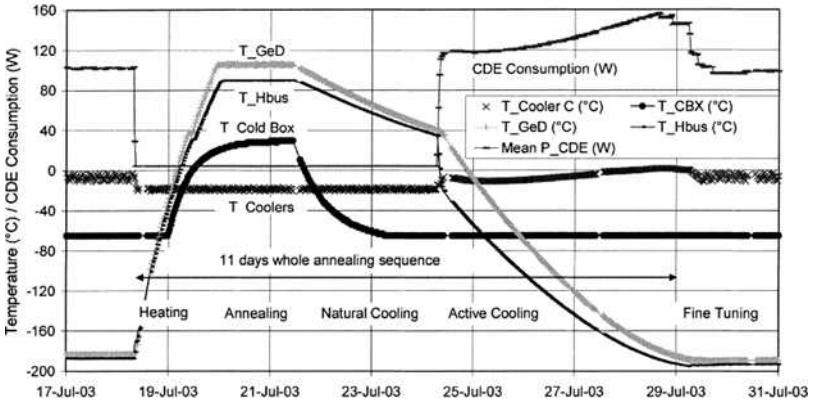

Figure 7. Temperatures and Cooler system power during a typical annealing sequence.

Annealing Sequence

Figure 7 shows temperature profiles for the coolers, cold box, HBus (cold interface with the coolers; this is a single interface connected to the four cold tips) and detectors during annealing #2 and the subsequent cooling sequence.

The compressor temperature profile (C) easily shows -7°C/-2°C oscillations due to the compensation heaters and thermostat cycling when the coolers are active. The switch-on thermostat cycling is then visible on 18-July when the CDEs remain in standby mode before compensation heaters and self-dissipations quickly reheat the coolers (24-July). This rate then decreases after the compensation thermostat is opened. Once the GeD temperature target is reached, the cooler stroke was reduced for fine tuning activities. As a consequence of the smaller input power, the compensation heaters quickly cycle again. During this mode, the intermediate stage is heated, as it was during the initial outgassing phase.

From the GeD temperature profile, we can easily extract a first phase up to "outgassing level" regulation at 310 K (37°C) to calibrate on-board annealing safety alarm, a second phase heating to annealing threshold followed by 106°C electronic regulation. Once the duration criteria defined by the PI is reached, the heaters are switched off, leading to natural cooling, which occurs during 3 days before the coolers can be restarted for 5 more days of cooldown mode. The complete annealing process thus lasts 11 days, remaining at 106°C for only 36 hours before a new observation is started.

Piston stroke requested in phase 1 was 55 to 59% of maximum to maintain the GeDs at 90±1K. The stroke settings were in the range 54 to 63% of maximum to get 85±1K during other observation

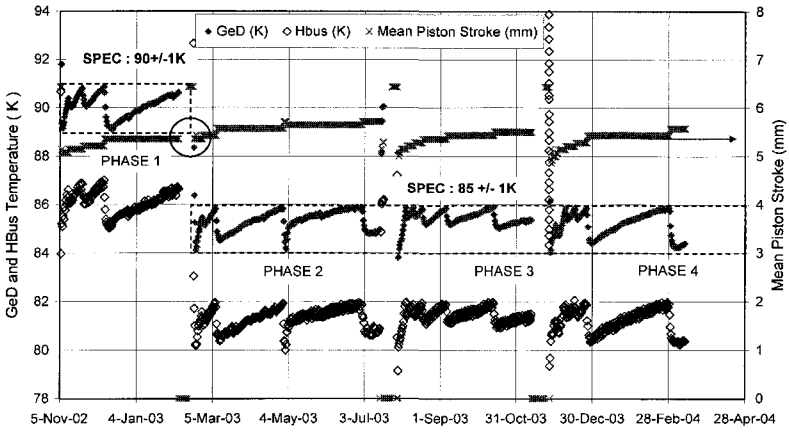

Figure 8. *Piston stroke adjustments and resulting GeD / HBus temperatures*

phases. Indeed, the cooler settings had to be adjusted to compensate for the GeD temperature drift.

Note that the maximum temperature reached by the HBus during annealing is 90.1°C, so the displacers tips were exposed (without degradation) to about 80°C—not far from their vacuum bakeout temperature level.

Contamination Occurrence

As can be seen in Fig. 8, the initial GeD temperature profile exhibited a positive drift that was easily compensated for by periodic increases of piston stroke to maintain the GeDs within the required range; this is 90±1 K up to February 2003, then 85±1 K. Analysis of cryocooler parameters did not show any drift nor discrepancy with regards to ground testing and typical telemetry. Nominal functioning of the cryocooler system was conclusively demonstrated after the first annealing occurred. Indeed, telemetry and efficiency during the subsequent cooling mode was similar to the first one (Nov 2002). Moreover, the piston stroke and power consumption required to achieve 85 K on the detectors after the first annealing was identical to that required to reach 90 K two weeks before, prior to annealing (see circled area on Fig. 8). This also showed that venting occurred during this process. Thus, annealing not only benefits the GeD resolution, but also improves the thermal insulation efficiency and lowers the emissivity of the cold parts.

Figure 9 presents the GeD temperature compared to the target temperature (either 90 or 85 K) during all mission phases, with time reset after each annealing. As expected from typical contamination, each phase temperature profile shows a drift that decreases in time.[3] Whether this results from a gradual decrease in the contamination source or only a saturation in its effect is not clear. This figure also shows that the GeD temperature profile and drift is fully repeatable from one phase to another (typically +1 K/month after 1.5 months and + 0.5 K/month after 4 months).

This drift occurrence can be explained by two candidate mechanisms, the last one looking more probable: 1) we are facing a constant contamination flow through cryostat apertures from the instrument (internal) and platform (external), and 2) heating the cold parts makes the contaminants trapped inside MLI blankets go towards the external layers. Thus, each annealing makes the MLI a bit cleaner, but contaminants still trapped in the MLI come back in time on the coldest parts due to cryopumping.

The location of the contaminated area can be assessed through analysis of thermal gradients (heat fluxes) along the cold chain. The total heat leak from the cold box towards the detection plane flows through the Be bus Bar and Flexible link reaching the HBus (see Figs. 3 and 5) before it is absorbed by the coolers. Since launch, the thermal gradient between the GeDs and the HBus has remained fully consistent, implying a stable heat flow in the observation phase: 3.90 K for GeDs at 90 K and Cold Box at 208 K; this is 1050 mW. This implies that no contamination and no loss of thermal insulation efficiency has occurred in the cold box / detector enclosure.

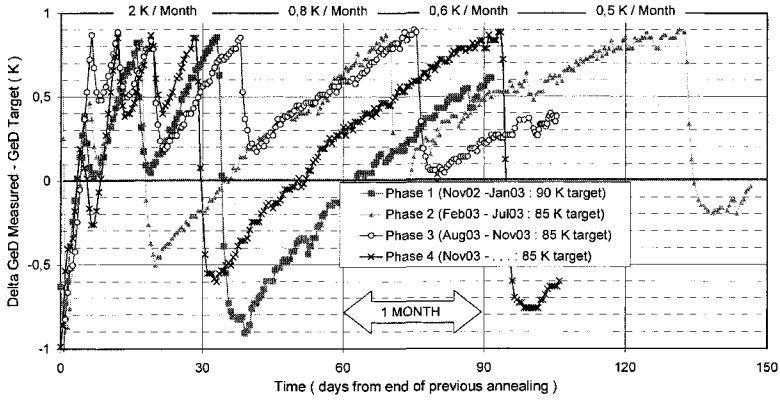

Figure 9. Ge detector temperature during each observation phase (comparison to target).

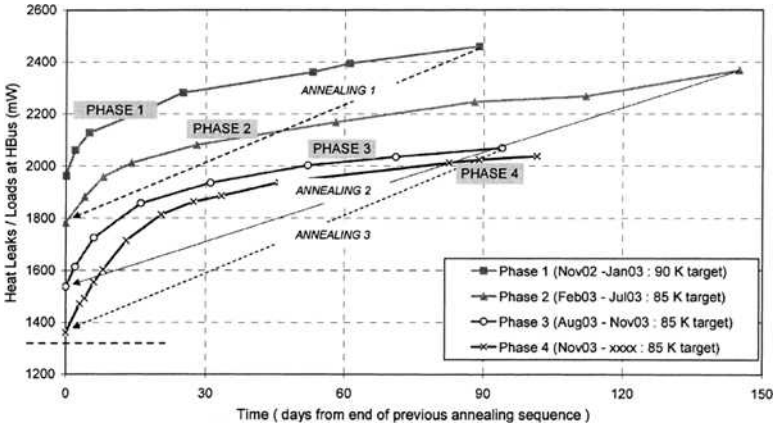

Figure 10. Evolution of thermal heat loads at HBus.

Any increase of emissivity and contamination is thus located in the HBus-displacer enclosure. Indeed, looking back on the HBus MLI as well as the overall displacer enclosure, the venting appears to be marginal. Moreover, the "hot" structure surrounding this volume—this is the coolers' support structure—has never been well outgassed in orbit. No specific heaters were foreseen to outgas this area, so during the so-called outgassing or annealing phases, the cooler switch-on heaters just maintained a temperature of about -15°C; a maximum +10°C was reached in cooldown mode.

Huge Benefits of Decontamination Sequences

Starting after launch with the same performance as during FM satellite thermal vacuum tests, successive annealing sequences highly benefited the thermal performance as shown in Fig. 10. Assuming the coolers' efficiency to be fully nominal after more than 14000 running hours allowed the cooler operating points to be used to compute the heat loads absorbed at HBus level.

This plot clearly highlights that each annealing saves several hundred milliwatts! Contamination is evident at the beginning, whereas its effect on heat load greatly decreases after 15 days post annealing sequence. The very first performance achieved after the annealing process tends to an asymptotic value that is in line with the predicted heat load as quantified in Table 1.

Cryostat System Margins with Regards to Contamination Issues

The heating sequence requested by the scientists to anneal the detectors, also highly benefited the cryostat thermal efficiency. As a result, contamination issues never had a real effect on instru-

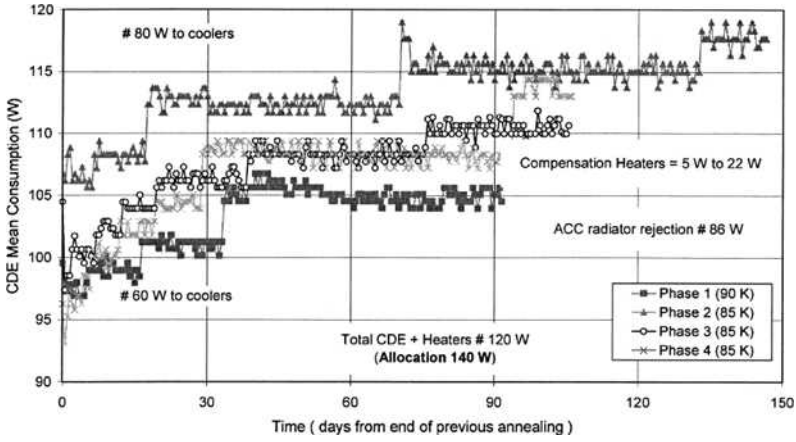

Figure 11. Mean CDEs (total CDE1 + CDE2) power consumption.

ment availability for science. Nevertheless, it is useful to examine the operational margin of the thermal design of the cryostat. Even without the annealing events performed, the GeDs can be maintained in the requested temperature range for 1.5 years without exceeding the allocated power budget. This can be extrapolated from Fig. 11, which shows the CDE mean power consumption. As previously explained, successive stroke (compressors dissipation) increases are associated with a corresponding decrease in the thermostated compensation heaters, leading to a total of 120 W constant power for both CDEs and heaters. The CDE power reached a maximum of 118 W after 5 months post-annealing. At this level, the CDE power increase due to contamination is assessed to be lower than 2 W per month. We can thus state a total capability of a minimum of 18 months before annealing would be requested only for thermal and power reasons.

CONCLUSIONS

The design, operation, and performance of the SPI cryostat has fully satisfied the technical objectives and the scientists. The cryocooler system, including electronics, exhibits nominal and stable performance and telemetry after 14000+ running hours.

The piston stroke used to maintain the GeDs at 85±1 K has never exceeded 62% of maximum. As per the MOPITT instrument[3], strokes have to be regularly increased to compensate for the contamination process (external to coolers). The annealing required to recover the resolution of the GeDs due to radiation damage greatly helps to outgas the cryostat. This allows the cryogenic performance to increase after each annealing and to be improved compared to system ground tests.

Apart from typical development difficulties linked to cryogenic space projects, the main issue we can emphasize is validation by tests. Indeed, cost and planning are generally not compatible with the duration needed for outgassing, actual stabilization (criteria adapted to mass / thermal balance), and for tracking any drift. With in-flight experience, we can state that what was identified as a performance deviation on the ground was clearly due to contamination effects.

Notably, the mission of this fully functional γ-ray observatory has been extended to 6 years.

REFERENCES

1. Briet, R, "INTEGRAL Spectrometer cryostat design and STM performances," *Advances in Cryogenic Engineering*, vol 45, Kluwer Academic / Plenum Publishers, New York (2000), pp. 489-498.
2. Gibson, A., "The FM Stirling Cryocooler System for the INTEGRAL Spectrometer," ICES01-2380.
3. Ross, R.G., Jr., "Cryocooler Load Increase due to External Contamination of Low-ε Cryogenic Surfaces," *Cryocoolers 12,* Kluwer Academic / Plenum Publishers, New York (2003), pp. 727-736.

Two Year Performance of the RHESSI Cryocooler

Robert Boyle

NASA/Goddard Space Flight Center
Greenbelt, MD 20771

ABSTRACT

The Ramaty High Energy Solar Spectroscopic Imager (RHESSI) spacecraft was launched on February 5, 2002. With two years of operation on-orbit, its Sunpower M77 cryocooler is maintaining the array of nine germanium detectors at 86K, at higher temperature and input power than intitial conditions. As commercial coolers similar to this are of some interest for other flight instruments, we offer an update on its status and health, and discuss the prospects for continued operation.

CRYOCOOLER BEHAVIOR

The Ramaty High Energy Solar Spectroscopic Imager (RHESSI) was launched in February 2002 to observe solar flare activity near and slightly after the peak of the eleven-year solar cycle. The spectrometer uses an array of nine large germanium detectors, mounted in a cryostat on a common coldplate.[1,2] An off-the-shelf Sunpower M77B Stirling-cycle cryocooler was chosen to maintain the coldplate at 75K and a thermal shield at 150K. The RHESSI cryocooler had seen approximately 11,000 hours of operation by the time it was launched, and has accumulated an additional 19,000 hours on orbit as of April 2004. Though the cooler is nominally non-contacting, wear products have been found in similar machines, so wear of this cooler has always been a possible concern.

After approximately six months on orbit the instrument team noticed a trend in the cryocooler power as shown in Fig. 1, increasing at a rate of 13-15mW each day.[3] The cooler is driven with a constant drive voltage, and no temperature feedback, so the power trend was unexpected and unexplained. The power increase seems to be consistent with the increase in temperature drop from the cryocooler to its radiator, and an increase in dissipation in the cryocooler drive electronics. During this time, heaters on the cryocooler radiator were gradually trimmed back, maintaining a roughly constant spectrometer shell temperature. Cryocooler vibration increased roughly in proportion to cryocooler power, suggesting that something was indeed changing within the cryocooler system. For the early part of the mission, the cryocooler cold tip temperature remained a constant, well-behaved function of orbital conditions. There was no apparent effect from changes in the cryocooler. But around the twelve month mark, temperatures in the spectrometer began to change as well, increasing as a cubic function of time as shown in Fig. 2. The temperature drop across the sapphire cold link to the cold tip increased, but only in proportion to the decrease in the conductivity of the sapphire. The overall heat load on the cold tip seemed to remain constant,

Cryocoolers 13, edited by R. G. Ross, Jr.
Springer Science+Business Media, Inc., New York, 2004

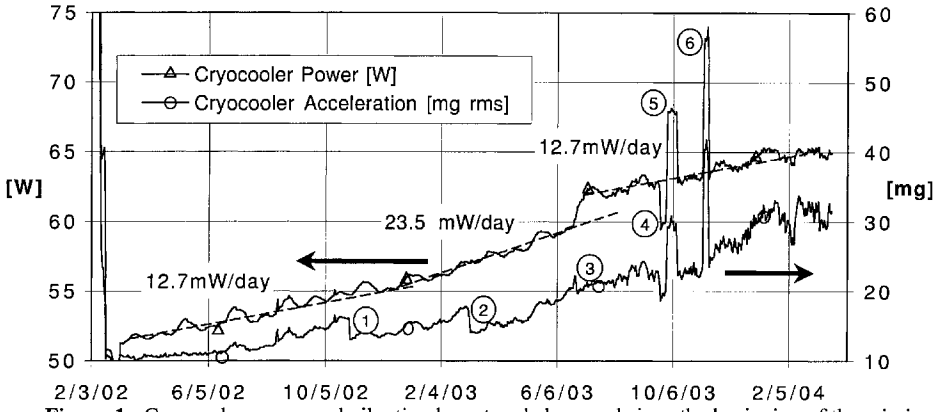

Figure 1. Cryocooler power and vibration have trended upward since the beginning of the mission. Cyclic variations in power are the result of orbital variations in temperature. The long-term drift in power is apparently the result of decreasing impedance of the cooler. Vibration changes at 1, 2, and 3 correspond to adjustments of the cryocooler counterbalance. Power changes at 4, 5 and 6 correspond to commanded changes in cryocooler power.

suggesting that the spectrometer vacuum space was not suffering from contamination. The vacuum space was sealed, with a one-time vacuum valve mechanism available for contingency purposes, and the mechanism was not actuated until February 5, 2004. From the time the vacuum valve was opened, the temperature increase seems to have halted, suggesting that some sort of contamination was occurring in the spectrometer.

POSSIBLE CAUSES

Failure of instrumentation and electronics are certainly not unlikely causes of flight anomalies, and have been suggested to explain some of the data from the RHESSI cooler. But the rising power and vibration of the cryocooler together suggest a real mechanical cause, such as wear of the clearance seals, accumulation of wear products in the regenerator, leakage of helium from the cooler, or degradation of the cryocooler counterbalance. From the available instrumentation, there doesn't seem to be a way to discriminate among the possible failure modes, and experience with similar coolers has not been illuminating.

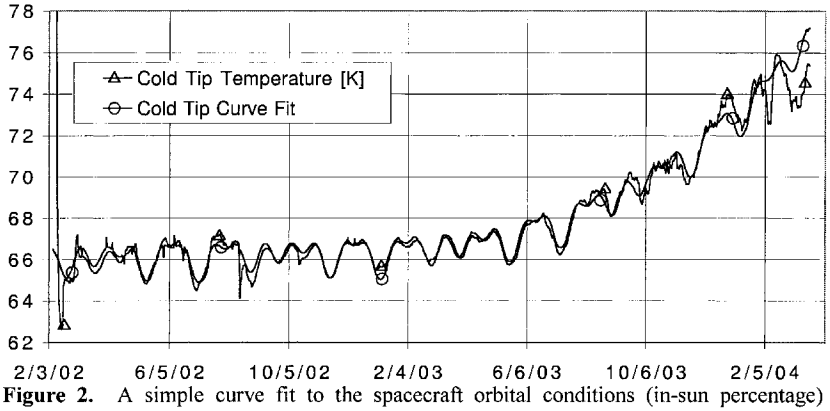

Figure 2. A simple curve fit to the spacecraft orbital conditions (in-sun percentage) closely describes the cold tip temperature for the first year of operation. A cubic function is added at that point to describe the deviation upwards in temperature. The departure between curve fit and actual data in February 2004 coincides with the opening of the spectrometer vacuum valve.

The temperature history of the system is also consistent with a degrading cryocooler, but the change in performance after opening the vacuum valve suggests a secondary contribution from contamination. The fact that the cold tip temperature did not actually decrease when the vacuum space was vented indicates that the contaminant was not helium. However, the thermal blankets in the spectrometer, composed of about 20 m^2 each of Dacron mesh and 6 μm Mylar, provide a large reservoir of water with a long time constant. While the temperature history of the spectrometer is quite different from what might be expected in a contaminated cryostat[4], it's possible that design details could have played a role. In the volume between the 180K thermal shield and the 85K coldplate assembly is a zeolite getter, thermally anchored to the cryocooler cold tip at approximately 75K. If the getter finally became saturated with water at around twelve months, deposition on the warmer surfaces within the spectrometer might have begun to affect the thermal performance. The sizing of the getter relative to the volume of MLI is currently under investigation.

CONCLUSIONS

The RHESSI cryocooler has successfully operated for over two years on orbit. Thermal operation of the spectrometer has degraded since launch, but the cryocooler performance is still sufficient to allow normal operation of the instrument. Observation and occasional experimentation continue, with the hope that the cryocooler will last until ICC'14.

REFERENCES

1. Boyle, R., Banks, S., Cleveland, P., Turin, P., "Design and Performance of the HESSI Cryostat," *Cryogenics*, vol. 39, no. 12 (1999), pp. 969-973.
2. Boyle, R., Banks, S., Shirey, K., "Final Qualification and Early On-Orbit Performance of the RHESSI Cryocooler," *Cryocoolers 12*, Kluwer Academic/Plenum Publishers, New York (2003), pp. 755-760.
3. Boyle, R., "On-Orbit Performance of the RHESSI Cryocooler," *Cryogenics*, Vol. 44, Issue: 6-8, June-August, 2004, pp. 389-393.
4. Ross, R.G., Jr., "Cryocooler Load Increase due to External Contamination of Low-e Cryogenic Surfaces," *Cryocoolers 12*, Kluwer Academic/Plenum Publishers, New York (2003), pp.727-736.

The NICMOS Turbo-Brayton Cryocooler – Two Years in Orbit

Walter L. Swift, John A. McCormack, Mark V. Zagarola, Francis X. Dolan, and Herby Sixsmith

Creare Inc.
Hanover, NH 03755

ABSTRACT

A turbo-Brayton cryocooler was installed on the Hubble Space Telescope in March 2002 to restore cooling to the Near Infrared Camera and Multi-Object Spectrograph (NICMOS). The cryocooler delivers its refrigeration to the NICMOS cryostat by means of a separate cryogenic circulating loop that was packaged with the cryocooler. During two years of on-orbit operation, the cooler has maintained the NICMOS detectors within specified bounds of temperature at approximately 77 K. The cryocooler relies on temperature feedback from the gas stream into and out of the cryostat for temperature control. Compressor frequency is adjusted to increase or reduce net refrigeration available from the cryocooler to accommodate changes in the thermal environment and parasitic heat loads. This paper reviews the cryocooler design, describes the means for temperature control, and reviews operational history during the first two years in space.

INTRODUCTION

The NICMOS Cooling System (NCS) was installed on the Hubble Space Telescope (HST) in March 2002. The cooling system replaces the solid nitrogen that had depleted from the NICMOS instrument in late 1998. The installation and activation of the cooling system represented the completion of a five-year effort to restore cooling to the NICMOS instrument on the observatory. The program involved upgrading the technology from an earlier 5 W, 65 K engineering model turbo-Brayton cryocooler[1] to meet the unique requirements of the HST—a slightly different operating temperature and load, continuous and extended operation in a space environment, delivery of refrigeration to remote detectors, and low vibration.

The NCS uses high-speed turbomachines with gas bearings and high-effectiveness heat exchangers to achieve its performance, life, and operational characteristics with no vibration. Differences between the NCS and the earlier engineering model are discussed in reference 2. These differences, coupled with the qualification requirements for use on the telescope, resulted in an extensive series of ground qualification tests and a flight qualification test during 1998.[3,4] Following the flight qualification test, the NCS was modified to improve the overall system performance. Electronics were changed to reduce EMI and the nominal operating conditions for the circulator loop were modified. Both changes had the effect of reducing the input power to the system. The NCS was re-qualified through ground tests, and software for on-orbit control of the system was

Cryocoolers 13, edited by R. G. Ross, Jr.
Springer Science+Business Media, Inc., New York, 2004

finalized and verified through operational and performance testing in thermal vacuum chambers at Goddard Space Flight Center. Extensive contamination control procedures to protect the circulator loop during pre-launch activities were developed and verified through test.[5]

The NCS was integrated with NICMOS during Servicing Mission 3B to the HST. The integration included installation of the cryocooler and circulator loop, attaching bayonet-ended flexible tubes to the NICMOS cryostat panel, installing the electronics module to control the NCS, and the addition of a radiator and tubing connecting it to the cryocooler heat rejection interface. Following this installation, the NCS was activated, and a series of tests was performed to assess health and operational characteristics of the system.[5] These tests verified the operational control algorithms, demonstrated that cooler induced vibration was well below requirements, and provided data regarding the resolution of the detectors that was used to establish an operating temperature for the NCS. After more than three years of dormancy, the NICMOS instrument was returned to operational service in May 2002. Except for a brief interruption in August 2003, it has remained operational since that date. The following sections describe the cryocooler, its control features and its operational history during the past two years.

THE NICMOS COOLING SYSTEM (NCS)

The flow loops comprising the NCS are shown in Figure 1. They include a cryogenic circulator loop, a hermetic single stage turbo-Brayton cryocooler, and a capillary pumped loop to reject heat from the cryocooler. Details of the design are given in references 2 and 5. This section briefly reviews the functional elements of the system.

Heat from the NICMOS detectors is transported by conduction from the detector support structure through an aluminum matrix within the cryostat to a cooling coil attached to the cryostat shell. The cooling coil is part of a flow loop that terminates at valved flanges and bayonet fittings on a panel at the end of the cryostat. This portion of the loop was used to maintain the nitrogen at cryogenic temperature prior to its initial launch. The NCS was designed so that flexible lines with matching bayonet fittings could be attached to the NICMOS tube connections during the servicing mission to the telescope. After the connections are made, the circulator loop is charged with neon from a pressurized gas fill bottle contained in the NCS assembly. A centrifugal circulator produces a flow of neon through the loop, exchanging heat with the cryocooler loop at the cold load interface (CLI).

The closed loop cryocooler consists of a centrifugal compressor driven by a three-phase induction motor, a high-effectiveness recuperator, and a turbine that produces refrigeration by expansion of the neon. The work of expansion produced in the turbine is converted to electric power in the turboalternator and dissipated in resistors at the warm end of the system. The heat from the NICMOS cryostat (and from circulator loop parasitic loads) is absorbed at the cold load interface (CLI) and is rejected to the capillary pumped loop (CPL) at the heat rejection interface (HRI). Nominal operating parameters for the NCS are listed in Table 1.

Table 1. Nominal operating conditions for the NICMOS cooling system.

Compressor input power	315 W
Temperature at Heat Rejection Interface	278 K
Compressor nominal speed	7,200 rev/s
Turboalternator nominal speed	3,100 rev/s
Cryocooler pressure ratio	1.6 : 1
Cryocooler flow rate	1.8 g/s Ne
Heat load at Cold Load Interface	7 W
Circulator nominal speed	1,200 rev/s
Circulator flow rate	0.4 g/s Ne
Control Temperature	72.4 K

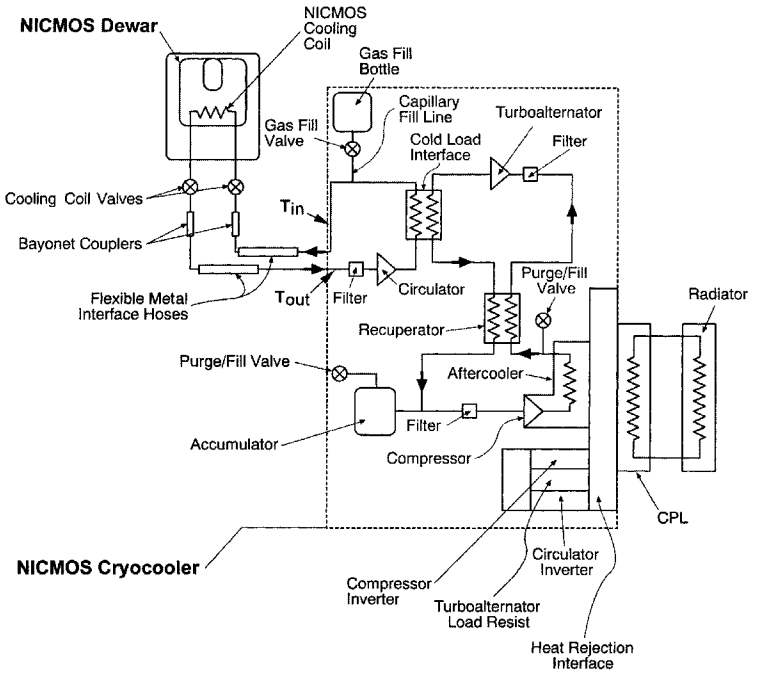

Figure 1. The NICMOS Cooling System (NCS).

The CPL provides temperature modulation between the radiator surface and the heat rejection interface. The telescope has an orbital period of about 90 minutes. Orbital, seasonal and observatory pointing variations produce a range of radiation heat loads on the cryostat and variations in the heat rejection temperatures. In general, the temperature difference between the radiator surface and the HRI is about 20°C. The variation in HRI temperature during the year is about ± 8°C around its nominal value of 278 K.

During cooldown, the compressor is driven at maximum speed. A control temperature derived from circulator loop measurements is continually calculated and compared with a commanded set-point value. After the control temperature reaches the desired set point, NCS operation is controlled using PID algorithms to maintain the control temperature within +/- 0.1°C of the set-point. This is done by increasing or decreasing compressor speed to increase or decrease the amount of refrigeration produced by the cooler.

TEMPERATURE CONTROL

A temperature sensor on the optical bench near the detectors is used as the primary measurement for continuous monitoring of detector temperature. This sensor reads about 4.7 K above the temperature at the cooling coil, which is located at the opposite end of the aluminum matrix in the cryostat. The temperature difference is mildly sensitive to the radiation heat load on the cryostat which varies with orbit, season and pointing attitude of the telescope. Two temperature sensors, labeled Tin and Tout in Figure 1, are attached to the outer surfaces of the solid tubes in close proximity to the cold load interface. These sensors give a relatively accurate indication of the temperature of the neon as it leaves the CLI flowing to the cryostat, and as the fluid leaves the cryostat before entering the circulator. These temperature measurements,

together with the circulator flow rate and the neon properties, provide a reasonable estimate of the heat load in the circulator loop.

An instrumented simulator of the tubing loop in the cryostat was used during ground tests to quantify the temperature distribution in the loop as a function of circulator operating conditions and environmental temperature. The simulator and the tests provided an empirical relationship between Tin, Tout and the control temperature – the temperature at a connection point between the aluminum matrix and the coil. This temperature ($T_{control}$) is used as the control parameter for the operation of the cryocooler. Because the radiation heat load from the aft shroud to the detectors and to the circulator loop tubes was not known exactly, the final operating set-point for the cryocooler was determined during a series of tests following the installation and activation of the cooler on-orbit. During these tests, the temperature sensors at the optical bench in the cryostat were monitored while the set-point temperature of the cooler was systematically varied over temperatures between 71.5 K and 72.5 K. These orbital tests verified that the empirical relations determined during ground tests were sufficient for control without modification.

COOLING SYSTEM PERFORMANCE

The performance of the cryogenic portion of the cooling system over time can be assessed by treating the circulator loop and the cryocooler loop independently. There are several potential sources of degradation that can affect the performance of the combined system.

1. Leakage. Some degree of degradation of performance in the circulator loop was expected because of the diffusion of neon through o-rings at the bayonet fittings. The cryocooler loop is hermetic, and no leakage is anticipated in this loop.
2. External contaminants. Because the cryocooler and circulator loop tubing are the coldest surfaces in the aft shroud, it is possible that contaminants would migrate to the multi-layer insulation wrap surrounding these surfaces. This would reduce the effective insulation of the blankets and increase the parasitic heat load to the cooler.
3. Internal contaminants. Outgassing and freeze out of contaminants within the cryocooler or the circulator loop would also decrease the effective performance of the two loops by either blocking flow passages or by reducing heat transfer in the recuperator or the thermal interfaces.

To date the minor changes in performance are within the bounds of expectations and predictions, and appear to be solely the result of the diffusion of neon from the circulator loop. Figure 2 shows some of the key parameters that are used to monitor and assess behavior during operation. The figure shows temperatures at the cryostat inlet and outlet (T_{in} and T_{out}), the calculated control temperature ($T_{control}$), and the temperature near the detectors on the optical bench ($T_{detector}$). The figure also shows the temperature rise through the circulator loop (ΔT_{NICMOS} = Tout – Tin). The periodic fluctuations in ΔT_{NICMOS} reflect the variations in radiation heat load on the cryostat caused by orientation of the telescope and orbital effects. Even the periodic change in solar flux intensity is visible within the data. The gap in the data was caused by a shutdown in August 2003.

Circulator Loop

The circulator loop is not hermetic. The bayonets are sealed within their fittings by means of elastomeric o-rings. Although the leakage is minimized by maintaining the temperature of the seals close to ambient, some diffusion of neon through the elastomers is to be expected. The predicted diffusion rate had been confirmed early in the development of the seals through tests. The tests and calculations resulted in an estimated leakage between 1 % and 5 % of the total neon mass in the circulator loop per year.

On-orbit telemetry provides measurements of pressure in the circulator loop. The nominal pressure in this loop during cryogenic operation is approximately 3.67 atm (54 psia). The telemetry gives a resolution of 2.2 % of the nominal pressure. A detailed accounting of the mass distribution in the circulator loop is required to accurately assess mass depletion. Approximately

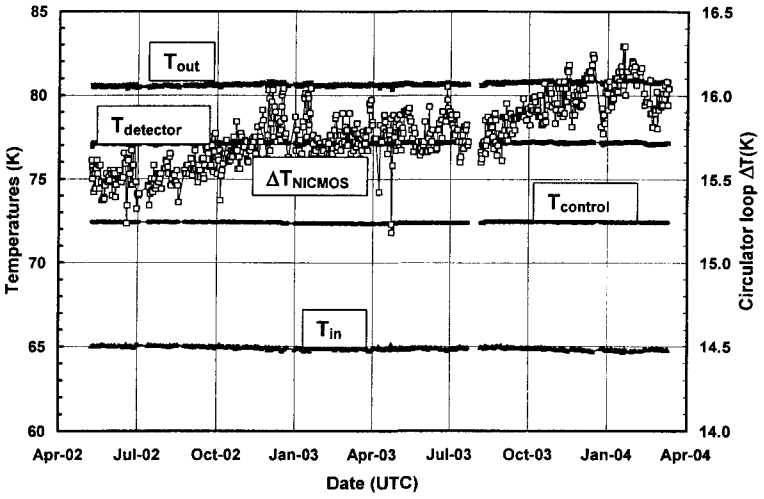

Figure 2. NCS on-orbit temperatures during the first two years of operation.

90 % of the circulator loop volume is subject to the temperature changes in the fill tank (which is nominally at ambient temperature). At normal steady operating conditions, approximately 30 % of the neon mass is in the cryogenic portion of the circulator loop. Because of the limited number of temperature measurements through this loop, the distribution of temperature is only approximately known and is subject to some uncertainty beyond that introduced by the pressure transducer resolution. This distribution and that of the volumes affect the precision with which the inventory can be determined.

Measurements and supporting calculations show that the mass of neon that has diffused through the bayonets is within the bounds of the initial estimates. At present the decrease in mass is about 2.3 % of the initial charge and is decreasing at a nearly constant rate. This decrease in mass inventory produces a small shift away from the optimum circulator operating point because the density of the circulated fluid is decreased. This results in a reduction in the mass flow rate and a corresponding increase in ($T_{out} - T_{in}$). The increase can be seen in Figure 2. The result is a minor decrease in the effective load temperature for the cryocooler and a slight decrease in the cryocooler cycle efficiency. Based on the other operating parameters in the loop and the margin of operation in the cryocooler, it is unlikely that the circulator loop will require recharging for at least two more years. If the recharge is required, only a negligible amount of the total capacity of the refill tank will be needed.

Cryocooler

The performance of the cryocooler can be assessed by calculating the cycle efficiency relative to Carnot, and monitoring this figure of merit over time. Small variations in the value are expected because of the resolution of some of the instruments used in the calculation, and because the efficiency is mildly dependent on the cooling load and load temperature. However, over a long period of time, the average value should remain constant if there is no degradation.

The efficiency of an ideal Carnot cycle operating between a rejection temperature T_{rej} and a load temperature T_l reflects the amount of refrigeration Q_l that could be expected for an input power P and is given by the relation:

$$\eta_C = T_l / (T_{rej} - T_l) \quad (1)$$

The refrigeration delivered by the cooler (Q_l) is the sum of the input power to the circulator and the heat removed from the circulator loop. The power to the circulator is given by the product of voltage and current measurements, reduced by the inefficiency in the motor controller. The heat removed from the circulator loop is given by measurements T_{in}, T_{out}, the specific heat of the neon and the mass flow rate. Because there is no flow meter in the circulator loop, the flow rate is derived from performance data measured during ground tests. There is also a small additional heat load to the cryocooler due to radiation parasitics at the cold load interface and along the recuperator length. However, these contributions are low relative to the circulator loop heat load and are accounted for in the performance of the cryocooler.

The rejection temperature used in the calculation is measured at the heat rejection surface on which the compressor is mounted. The load temperature is taken as the calculated value using the approximating relation derived for the control temperature. The input power to the compressor (Pc) is the product of current and voltage derived from telemetry for the compressor leads. The efficiency of the cryocooler relative to a Carnot cycle is then given by:

$$\eta = (Q_l / T_l) \times (T_{rej} - T_l) / (P_c) \quad (2)$$

Figure 3 shows the cycle efficiency relative to Carnot for the two-year period of operation to date. The average value has remained constant at about 6.25 %. Imposed on the changes that result from orbital, seasonal and pointing changes is a slight decrease in the value over time. This decrease is caused by the slight reduction in the effective load temperature caused by the diffusion of neon from the circulator loop.

SHUTDOWN AND RESTART

In August 2003, the NCS shut down for a period of about 6 days. The shutdown occurred during passage through the South American Anomaly (SAA) an area of elevated radiation. During this transit, an anomalous command was registered in the commanded circulator voltage, a parameter that is kept constant except by intervention from ground commanding. The event was diagnosed as a Single Event Upset (SEU) resulting in a commanded voltage that exceeded maximum limits set in the software. The control software shut down the cryocooler and the NCS cooling system. Following several days of telemetry review and diagnosis, the system was restarted without incident. Figure 4 shows temperatures at the cold end of the system and the temperature rise through the cryostat for the time period surrounding the shut down and restart. Temperatures in the circulator lines increased to about 200 K during the shutdown interval. However, because of the well insulated, large thermal mass in the cryostat, the cooldown was rapid. Detector temperatures stabilized within a few days, and NICMOS was returned to normal operation 13 days after the event.

CONCLUSIONS

The NICMOS cooling system has successfully met performance and operational expectations during its first two years on the HST. Temperature controls have maintained the detectors within desired stability bands, ad the system has recovered successfully from an SEU in an elevated radiation environment. Diffusion of neon through the bayonet o-rings is within predicted bounds, and a recharge of the circulating loop to restore the original design point pressure is not likely to be required for another two years. The system has confirmed the viability of turbo-Brayton cryooolers for use in space environments demanding low vibration and long life.

ACKNOWLEDGMENT

The development of the NICMOS cryocooler was sponsored by NASA, the Air Force and MDA. We are grateful for their support and for the additional contributions by the Hubble Space Telescope Project and their subcontractors.

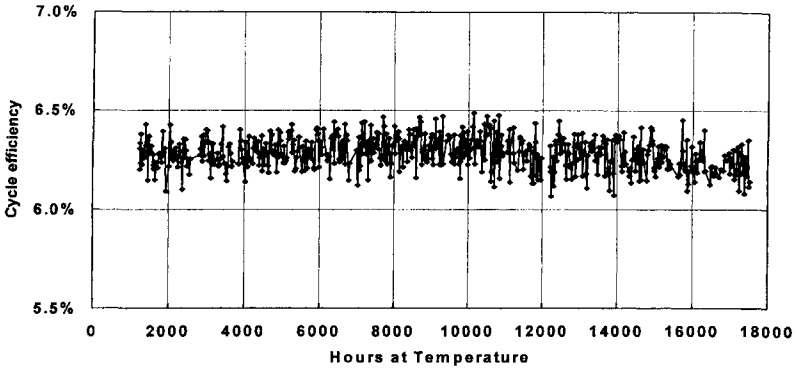

Figure 3. Cryocooler cycle efficiency during the first two years of operation at temperature.

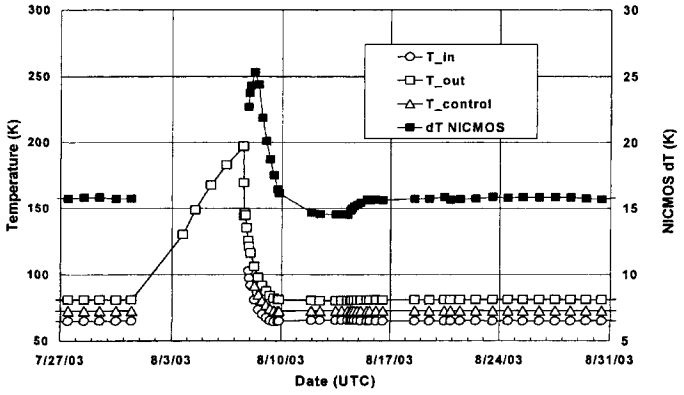

Figure 4. Cold end temperatures during the SEU shutdown and restart.

REFERENCES

1. Swift, W. L., "Single Stage Reverse Brayton Cryocooler: Performance of the Engineering Model," Cryocoolers 8, Plenum Press, New York, 1995, pp. 499-506.
2. Nellis, G., et al, "Reverse Brayton Cryocooler for NICMOS," Cryocoolers 10, Plenum Press, New York, 1999, pp.431-438.
3. Dolan, F.X., McCormick, J.A., Nellis, G.F., Sixsmith, H., Swift, W.L., Gibbon, J. A., "Flight Test Results for the NICMOS Cryocooler," *Advances in Cryogenic Engineering*, Vol. 45A. Kluwer Academic/Plenum Publishers, New York (2000), pp. 481-488.
4. Breedlove, J.J., Zagarola, M.V., Nellis, G.F., Gibbon, J.A., Dolan, F.X. and Swift, W.L., "Life and Reliability Characteristics of Turbo-Brayton Coolers," *Cryocoolers 11*, Kluwer Academic/Plenum Publishers, New York (2001), pp. 489-498.
5. Swift, W.L., McCormick, J.A., Breedlove, J.J., Dolan, F.X. and Sixsmith H., "Initial Operation of the NICMOS Cryocooler on the Hubble Space Telescope," *Cryocoolers 12*, Kluwer Academic/Plenum Publishers, New York (2002), pp. 563-570

Model for Orbit-Induced Temperature Oscillations in a Miniature Pulse Tube Cryocooler, Part 1: Warm End Components

Daniel R. Ladner

Lockheed Martin
Space Systems Company
Denver, Colorado, 80201, USA

ABSTRACT

An analysis of the thermal oscillations observed during the two-stage Miniature Pulse Tube Flight Cryocooler (MPTFC) experiment on STS-108 (Dec. 2001) is presented. Orbit-induced thermal oscillations at the heat rejection surface produce sympathetic oscillations in the cryocooler warm components, which in turn propagate to the cold stages during cooler operation. The warm component analytical model discussed here was derived by solving a system of coupled differential equations that include heat flows from the experiment, the periodic solar incident radiation, and the IR heat rejection. In order to model the cold stage thermal behavior it is first necessary to ascertain the thermal behavior at both the heat rejection surface (EMP) and the aftercooler, which directly drives those oscillations. Unfortunately, there was relatively poor temperature resolution by sensors on those two components, but very high resolution on other warm end components. The model therefore seeks to determine unambiguously the EMP and aftercooler periodic thermal behavior. Results are compared graphically to the on-orbit temperature measurements.

INTRODUCTION

Background

The NIST/Lockheed Martin Miniature Pulse Tube Flight Cryocooler (MPTFC) experiment was flown and operated successfully as a self-contained payload (G-785) aboard the Space Shuttle Endeavour in December 2001. The design and cooling performance of the MPTFC were previously reported.[1,2] The occurrence of orbit-induced thermal oscillations on the cryocooler warm components and cold stages was described briefly in Ref. 2 and depicted there in Figs. 8 and 9. Orbit-induced temperature oscillations are typically observed on space hardware as a result of solar/earth albedo radiation absorption and nocturnal IR radiation cooling. However, it was noted that a pronounced increase (factor of ~3) in the oscillation amplitudes at the Experiment Mounting Plate (EMP) and other warm end components occurred almost simultaneously with the activation of the cryocooler from the standby mode. The uninsulated EMP is the lid of the flight canister and serves as the single heat sink and heat rejection surface for the experiment. The rest of the payload external surface, including the bottom end plate, is well insulated against the external thermal environment. The

Cryocoolers 13, edited by R. G. Ross, Jr.
Springer Science+Business Media, Inc., New York, 2004

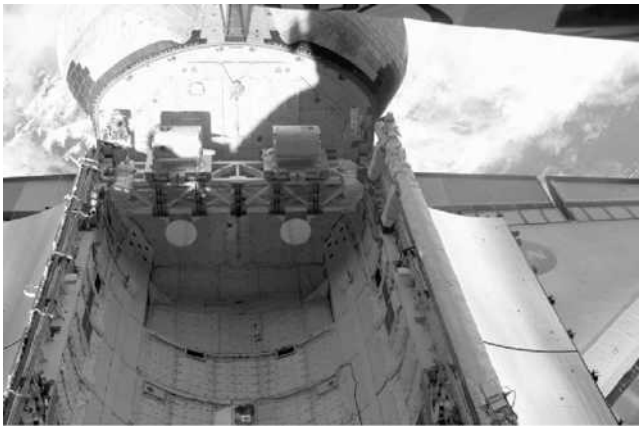

Figure 1. G-785 Payload as viewed from the ISS. It is the canister located in the shadow on the top right side of the truss (Shuttle port side).

preliminary explanation for the increase in the oscillation amplitudes given in Ref. 2 was that it was primarily attributable to the significant increase in experiment power from ~3 W in standby mode to ~38 W with the compressor operating. However, the model results presented in this paper do not substantiate that explanation, indicating only a slight effect from that source. The validity of this negative result is discussed below.

Thermal Environment

The G-785 payload was operated during flight days 1 to 5 during the STS-108 mission. The exact period of operation corresponds to the mission elapsed time (MET) from 00/19:19 to 04/11:53 (last data). Flight day 1 begins at MET 00/00:00 (day, hr, min). The cooler performance was demonstrated from MET 01/03:05 to MET 01/22:43 as the Shuttle was approaching the International Space Station (ISS). The position of the G-785 canister in the Shuttle bay is shown in Fig. 1. This NASA photo was taken from the ISS after the primary payload had been transferred from the bay to the ISS. Note that the EMP faces outward on the port side of the bay and is partially above it. This orientation obviously presents a quite complicated radiation view-factor, since the EMP looks at both the bay and space and/or earth depending on the Shuttle attitude.

During the approach to the ISS the Shuttle maintains various attitudes that are described with respect to the Orbiter Dynamic Coordinate System, which has the positive X axis pointing in the Shuttle nose direction and the positive Z axis pointing perpendicular to and outward from the Shuttle belly. A fixed Shuttle attitude with respect to the earth is described as local vertical/velocity vector, or _LV_VV, where the dynamic coordinate axes are inserted to specify the attitude. LV points toward earth center and VV points in the direction of the velocity.[3] Therefore, –ZLV–XVV has the Shuttle flying with its cargo bay facing earth and tail forward, while –XLV+ZVV has the Shuttle flying with tail toward earth and belly forward. Different attitudes present quite different thermal radiation heating and cooling factors for experiments situated in the cargo bay.

MODEL AND DERIVATION

Model

Figure 2 shows the G-785 payload during deintegration at NASA/KSC (as flown, but after the flight canister was detached). The EMP is the upper plate to which all parts of the experiment are fastened. The larger can, which is supported by four 6061 Al tubes comprising a cantilevered frame, contains the battery modules and the flight electronics. The electronics are located in a partitioned GN2-filled upper compartment within the larger can. This compartment contains the

Figure 2. G-785 Experiment at NASA/KSC.

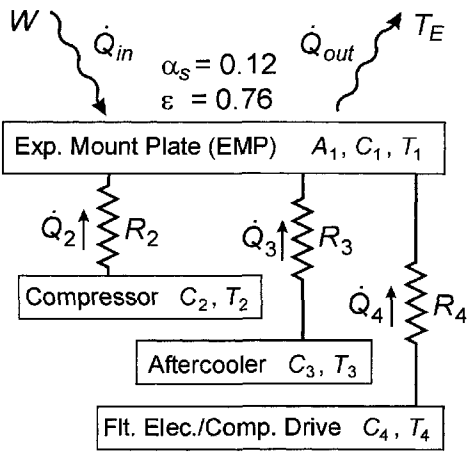

Figure3. Thermal model schematic.

cryocooler compressor drive electronics as well as signal conditioners and power converters. It is thermally well coupled to the EMP via the four thick wall support tubes. The smaller can (experiment housing) attached to the underside of the EMP contains the cryocooler, including the compressor and cold head components. The compressor and cold head warm end (aftercooler) are separately fastened to the EMP by thick-wall 6061 Al support tubes/flanges such that their effective thermal resistances, including contact resistances, are about 1K/W, as determined in pre-flight tests.

The model schematic is shown in Fig. 3 and is configured as a four lump thermal system. A lumped system is a valid approximation when the temperature gradients within each lump component are small compared to the gradients across the resistive legs.[4] The heat sink / heat rejection surface, depicted as capacity C_1 with surface area A_1, is the EMP. Radiation into and out of the 0.576 m diameter EMP is characterized by the solar absorptivity constant $\alpha_s = 0.12$ and the IR emissivity $\varepsilon = 0.76$. These are the nominal values for the silverized teflon tape which covers the external surface of the uninsulated EMP.[5] The solar heat flux (~1400 W / m^2) is denoted by W, and T_E is the effective (weighted average) environment temperature for IR radiation exchange. The components with capacities C_2, C_3 and C_4, temperatures T_2, T_3, and T_4, and dissipation powers $\dot{Q}_2$, $\dot{Q}_3$ and $\dot{Q}_4$, and legs with resistances R_2, R_3 and R_4, correspond to the compressor, the cold head aftercooler, and the flight electronics, respectively. Since the temperature difference between the EMP and the flight electronics is small and oscillations there are suppressed by the capacity C_4, the resistance R4 is taken to be a thermal short, i.e., $\dot{Q}_4$ is assumed to be an embedded non-negligible heat source within C_1. This assumption reduces the thermal model to a system of three equations and simplifies the analytical solution without compromising its ability to describe the thermal behavior of the components of interest.

Values for the thermal capacities can be estimated from the known dimensions and materials of these components. Calculated resistances of the supports associated with the compressor and aftercooler are ~0.27 K/W and 0.35 K/W. However, the effective thermal resistances R_2 and R_3 are dominated by contact resistance between the support flanges and the EMP, as observed in pre-flight measurements. The dissipation powers $\dot{Q}_2$, $\dot{Q}_3$ and $\dot{Q}_4$ can be determined from the laboratory measurements of standby power (~3 W), total DC power input at the compressor drive electronics, and the AC current, voltage, and phase angle at the driver output. The measured driver efficiency is 0.65. The driver pre-flight input power was set to ~34 W, so ~22 W is dissipated at the compressor/cold head. Approximate values of these parameters at the on-orbit initial experiment temperature of about 271 K are as follows:

$C_1 = 9970$ J/K, $C_2 = 910$ J/K, $C_3 = 380$ J/K
$R_2 = \sim 1$ K/W, $R_3 = \sim 1$ K/W
$\dot{Q}_2 = 14$ W, $\dot{Q}_3 = 8$ W, $\dot{Q}_4 = 12$ W + 3 W ($\dot{Q}_{standby}$) = 15 W, and $\dot{Q}_{total} = 37$ W.

Derivation

The three first-order linear differential equations describing the time dependence of the component temperatures are given by

$$dT_1/dt = k_{21}(T_2 - T_1) + k_{31}(T_3 - T_1) + K_A(1 + \sin(\omega t + \delta)) + K_B(T_E - T_1) + Q_{41} \quad (1)$$

$$dT_2/dt = k_{22}(T_1 - T_2) + Q_{22} \quad (2)$$

$$dT_3/dt = k_{33}(T_1 - T_3) + Q_{33} \quad (3)$$

where

$k_{21} = 1/R_2 C_1$
$k_{31} = 1/R_3 C_1$
$k_{22} = 1/R_2 C_2$
$k_{33} = 1/R_3 C_3$
$K_A = \alpha_S f_S A_1 W / C_1$
$K_B = \sigma \varepsilon A_1 (T_1 + T_E)(T_1^2 + T_E^2) / C_1$
$Q_{22} = \dot{Q}_2 / C_2$
$Q_{33} = \dot{Q}_3 / C_3$
$Q_{41} = \dot{Q}_4 / C_1$

and

α_S = solar absorptivity of EMP surface
σ = Stephan Boltzmann constant
ε = IR emissivity of EMP surface
ω = orbital angular frequency
δ = orbital initial phase angle
T_E = effective environment temperature
A_1 = EMP surface area
W = solar heat flux
f_S = effective solar heating factor

The EMP emitted IR radiation term has been factored to separate the temperature difference ($T_1 - T_E$) and treat the coefficient $K_B(T_1)$ as a constant to linearize Eq. (1) in T_1. For small fractional changes in T_1, this approximation introduces a small error in the solution. In the implementation of the model as an EXCEL© spreadsheet, K_B is updated at each time increment using the previous value of T_1, further reducing the error. The parameter f_S, the effective EMP solar heating factor, is associated with the duty cycle of incident solar radiation (~1400 W/ m^2) and/or earth albedo. For a Shuttle attitude of –XLV +ZVV (see below), the albedo radiation is not applicable. The factor $(1 + \sin(\omega t + \delta))$ is a simplification that nonetheless embodies the fundamental periodicity of the incident radiation and makes the model's analytical solution more tractable. The phase angle δ can in principle be determined from the cyclic temperature pattern prior to compressor activation. Although a Fourier approximation for half wave rectification[6] could be used with a numerical solution technique, the actual solar radiation waveform is typically neither purely sinusoidal nor half wave sinusoidal, but rather it is strongly dependent on the Shuttle's orbital parameters (beta angle and right ascension) and especially on the Shuttle attitude and the location / exposure orientation of the payload within the cargo bay.[7]

The system of equations (1) to (3) is solved analytically using the differential operator method directly to eliminate T2 and T3. Equivalently, a determinant method can be used. [8] In operator form, with D = d ( ) / dt , these equations become:

$$(D + K_{B23})\, T_1 = k_{21}\, T_2 + k_{31}\, T_3 + (K_{A4} + K_B\, T_E) + K_A \sin(\omega t + \delta) \tag{4}$$

$$(D + k_{22})\, T_2 = k_{22}\, T_1 + Q_{22} \tag{5}$$

$$(D + k_{33})\, T_3 = k_{33}\, T_1 + Q_{33} \tag{6}$$

where

$$K_{B23} = K_B + k_{21} + k_{31}$$
$$K_{A4} = K_A + Q_{41}$$

Operating on Eq. (4) with $(D + k_{22})\,(D + k_{33})$, Eq. (5) with $(D + k_{33})\, k_{21}$, and Eq. (6) with $(D + k_{22})\, k_{31}$, and eliminating the T_2 and T_3 terms on the right side of Eq. (4) gives

$$\{D^3 + (k_{22} + k_{33} + K_{B23})\, D^2 + [k_{22} k_{33} + k_{21} k_{33} + k_{31} k_{22} + K_B (k_{22} + k_{33})]\, D + k_{22} k_{33} K_B\}\, T_1 = k_{33} k_{21} Q_{22} + k_{22} k_{31} Q_{33} + k_{22} k_{33} (K_{A4} + K_B T_E) + [D^2 + (k_{22} + k_{33})\, D + k_{22} k_{33}]\, K_A \sin(\omega t + \delta) \tag{7}$$

The complementary function for Eq. (7) is found from the cubic auxiliary equation

$$m^3 + pm^2 + qm + r = 0 \tag{8}$$

where

$$p = k_{22} + k_{33} + K_{B23}$$
$$q = k_{22} k_{33} + k_{21} k_{33} + k_{31} k_{22} + K_B (k_{22} + k_{33})$$
$$r = k_{22} k_{33} K_B$$

Only real roots of Eq. (8) are admitted, and its analytical solution is expedited using the substitution $x = m - p/3$. [9] In the analysis here there are no repeated roots, so the complementary function for T_1 is of the form

$$T_{1C} = c_1 \exp(m_1 t) + c_2 \exp(m_2 t) + c_3 \exp(m_3 t) \tag{9}$$

where the coefficients c_1, c_2, and c_3 are to be determined from the initial conditions of T_1 and its derivatives. The particular solution for T_1 is determined by considering constant and time-dependent terms on the right side of Eq. (7) separately. By inspection,

$$T_{1P1} = [k_{33} k_{21} Q_{22} + k_{22} k_{31} Q_{33} + k_{22} k_{33} (K_{A4} + K_B T_E)] / k_{22} k_{33} K_B \tag{10}$$

The time-dependent particular solution of Eq. (7) is found by assuming the form

$$T_{1P2} = A \sin(\omega t + \delta) + B \cos(\omega t + \delta) \tag{11}$$

and using the method of undetermined coefficients to solve for A and B. (Alternatively, a complex solution of the form C exp (i(ωt + δ)) may be used.) Substituting Eq. (11) into Eq. (7), carrying out the indicated operations, and equating coefficients of the sin (ωt + δ) and cos (ωt + δ) terms, leads to

$$MA + NB = K_A (k_{22} k_{33} - \omega^2) \tag{12}$$

$$-NA + MB = K_A (k_{22} + k_{33}) \omega \tag{13}$$

where

$$M = k_{22} k_{33} K_B - (k_{22} + k_{33} + K_{B23}) \omega^2 \tag{14}$$

$$N = \omega^3 - [(k_{22} k_{33} + k_{21} k_{33} + k_{31} k_{22} + K_B (k_{22} + k_{33})] \omega. \tag{15}$$

The solutions are

$$B = K_A [N (k_{22} k_{33} - \omega^2) + M (k_{22} + k_{33}) \omega] / (M^2 + N^2) \tag{16}$$

and by Eq. (12)

$$A = [K_A (k_{22} k_{33} - \omega^2) - NB] / M \tag{17}$$

Then the general solution for T_1 is the sum of the complementary and particular solutions,

$$T_1(t) = \sum_1^3 c_i \exp (m_i t) + T_{1\,P1} + A \sin (\omega t + \delta) + B \cos (\omega t + \delta) \tag{18}$$

and the constants c_1, c_2 ,and c_3 can be determined by solving the three simultaneous equations (18), $T_1(t)$, $DT_1(t)$, and $D^2T_1(t)$, evaluated at $t = 0$ using known initial values.

Solutions for T_2 and T_3 follow immediately from the direct integration of the linear nonhomogeneous equations (2) and (3) using Eq. (18) for T_1. Equations (2) and (3) become

$$dT_2 + k_{22} T_2 dt = (k_{22} T_1 + Q_{22}) dt \tag{19}$$

$$dT_3 + k_{33} T_3 dt = (k_{33} T_1 + Q_{33}) dt \tag{20}$$

with integrating factors $\exp (\int k_{22} dt)$ and $\exp (\int k_{33} dt)$, respectively.

The solutions for T_2 and T_3 are

$$T_2(t) = k_{22} \sum_1^3 \{ c_i / (k_{22} + m_i) [\exp (m_i t) - \exp (-k_{22} t)] \} + \{ (T_{1\,P1} + Q_{22} / k_{22}) \times [1 - \exp (-k_{22} t)] \} + k_{22} / (k_{22}^2 + \omega^2) \{ C [k_{22} \sin (\omega t) - \omega \cos (\omega t)] + E [\omega \sin (\omega t) + k_{22} \cos (\omega t)] + (C\omega - E k_{22}) \exp (-k_{22} t) \} + T_2(0) \exp (-k_{22} t) \tag{21}$$

and

$$T_3(t) = k_{33} \sum_1^3 \{ c_i / (k_{33} + m_i) [\exp (m_i t) - \exp (-k_{33} t)] \} + \{ (T_{1P1} + Q_{33} / k_{33}) \times [1 - \exp (-k_{33} t)] \} + k_{33} / (k_{33}^2 + \omega^2) \{ C [k_{33} \sin (\omega t) - \omega \cos (\omega t)] + E [\omega \sin (\omega t) + k_{33} \cos (\omega t)] + (C\omega - E k_{33}) \exp (-k_{33} t) \} + T_3(0) \exp (-k_{33} t) \tag{22}$$

where

$$C = A \cos \delta - B \sin \delta \quad \text{and} \quad E = A \sin \delta + B \cos \delta \tag{23}$$

and $T_2(0)$ and $T_3(0)$ are the initial values of T_2 and T_3.

RESULTS

Implementation of the Model

The foregoing sequence for analytically solving the system of equations (1) to (3) was implemented as an EXCEL© spreadsheet. The estimated input parameters as given above (cf. Model) were used initially, and it was assumed that the EMP nominal values $\alpha_S = 0.12$ and $\varepsilon = 0.76$ were

correct. Using initial values of C_2 and C_3 given above, more exact values of C_2 and C_3, and therefore R_2 and R_3, were determined by iteration for consistency with the on-orbit measurements, particularly with the compressor data. The solar heating factor f_S was then determined in conjunction with C_1 so that the oscillation amplitude at the EMP was also consistent with the data. Finally, the effective environment temperature T_E was determined to provide the required energy balance between the sum of the solar and experiment input powers into the EMP and the radiated IR output power. Single entry parameter inputs to the spreadsheet and charting of the solutions over the time interval of interest resulted in rapid convergence of the model.

Parameter Values

The final input parameter values and resulting Eq. (9) constants were:

$C_1 = 9750$ J/K, $C_2 = 960$ J/K, $C_3 = 420$ J/K, $R_2 = 0.80$ K/W, $R_3 = 1.05$ K/W
$\dot{Q}_2 = 14.3$ W, $\dot{Q}_3 = 7.8$ W, $\dot{Q}_4 = 14.9$ W (incl. $\dot{Q}_{standby}$) and $\dot{Q}_{total} = 37.0$ W
$f_S = 0.40$, $T_E = 189.5$ K, $\omega = 1.1482\text{E-}3$ /s, $\delta = 1.70$ rad, $\alpha_S = 0.12$, $\varepsilon = 0.76$
$m_1 = -5.8730\text{E-}5$ /s, $m_2 = -2.5082\text{E-}3$ /s, $m_3 = -1.3020\text{E-}3$ /s
$c_1 = -3.88955$ K, $c_2 = -0.36107$ K, $c_3 = +0.24377$ K

Model Results

Figure 4 compares the model results (dashed curves) to the experimental data (open symbols) as a function of the experiment elapsed time during compressor operation. Data were obtained using 4-wire 100 Ω and 1 kΩ RTDs at 100 mA excitation with 8 bit voltage digitization. It can be seen that the EMP and aftercooler data from the 100 Ω RTDs are low resolution (± 0.4 K), although with regard to the EMP data, a periodic waveform is quite apparent. (Note that in Fig. 8 of Ref. 2 the data for those components are smoothed moving averages). The compressor data (1 kΩ RTD) are high resolution (± 0.04 K), and the T_2 model solution tracks very closely with that waveform. Data from the experiment vacuum housing (1 kΩ RTD) are also included for enhanced clarity of the thermal oscillation waveforms in the warm end components. The housing provides a parallel conduction path for the compressor, and its resistance is used in the estimated value of R_2. The measured orbit-induced oscillations are seen to be distorted sine waves, partly because of the upward temperature drift during equilibration, but also because the incident radiation intensity obeys a cosine squared law and because it is present for only ~ 40 % of each orbit. The solutions obtained here are nonetheless in reasonably good agreement with the overall system dynamic, including oscillation amplitudes, phase shifting of the compressor and aftercooler waveforms with respect to the EMP, and long relaxation times associated with system equilibrium. However, the solution initial transients slightly overshoot the data such that the model's first oscillation is remarkably absent in the data (note plateau at ~ 480 to 530 min.). A transient downward EMP temperature drift due to a Shuttle maneuver (see below) has been approximated in Figure 4 to ~ 600 min., but only partially corrects the solutions. Finally, it is noted that a true steady state equilibrium condition was never observed during the ~ 20 hour cooling performance, but for t > 980 min. the average radiation output was about –54 W, nearly balancing the 37 W of experiment power and the average solar input power of 18 W.

Shuttle Attitude Maneuver

The Shuttle orbital parameters of interest during the time interval of Fig. 4 were $\beta = 16$ degrees (orbit plane inclination with respect to the ecliptic) and right ascension of the ascending node (RAAN) = 304 degrees.[10] The RAAN gives the orbit plane rotational direction with respect to the direction of the sun. On Dec. 8 the RAAN was ~ 258 degrees, for which the rotation of the plane was ~ 46 degrees. Prior to the time interval shown in Fig. 4, the Shuttle had been flying with attitude –ZLV–XVV for several hours. The standby data for the cryocooler warm components

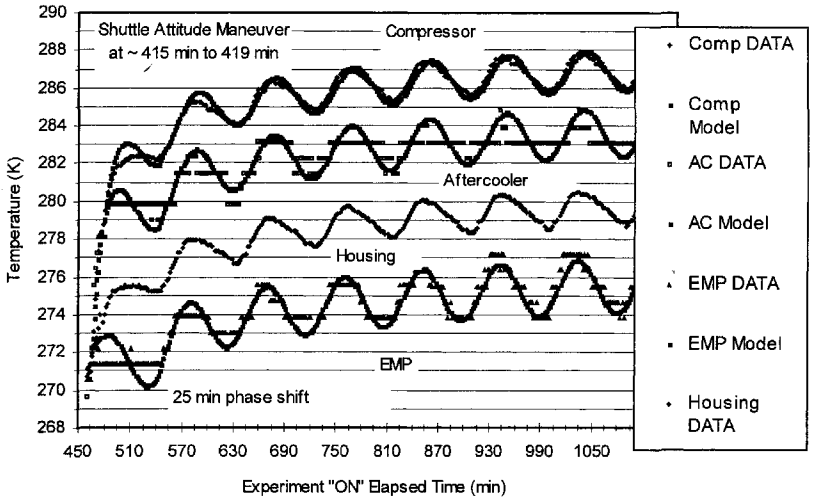

Figure 4. Model Results. T_1 (EMP), T_2 (compressor), and T_3 (aftercooler) solutions (dashed lines) plotted with on-orbit data (open symbols). The housing profile is shown to illustrate the typical waveform.

clearly show low amplitude (< 1 K) orbit-induced thermal oscillations over a seven hour period preceding Figure 4. However, a Shuttle maneuver to BIAS –XLV+ZVV was executed during MET 001/02:14 to 001/02:19, or 415 to 419 min. experiment elapsed time, only 47 min. before compressor activation at 466 min. The bias (pitch) angle was established at 70 degrees, meaning that the Shuttle's nose was tipped 20 degrees off the vertical to earth center.

One effect of this attitude change on the experiment temperatures was to upset the EMP thermal equilibrium, decreasing the average EMP temperature from ~271.5 K to ~270.5 K in the 47 min. preceding compressor activation. The downward temperature drift of the EMP may provide an explanation for the data plateau (noted above), because initial short-term drift was not included in Eq. (1). Secondly, the oscillations noted during standby were distorted by the downward drift after the maneuver, so it is impossible to determine the initial phase parameter δ from the standby data. That parameter can only be determined directly from the best fit to the data in Fig. 4, which gives $\delta = 1.7$ radians. The attitude maneuver also affected parameters f_S and T_E such that f_S increased while T_E decreased. In fact, this is the primary explanation, rather than the increase in experiment power, for larger oscillation amplitudes that occurred coincidently with experiment compressor activation. A secondary effect of the attitude change was to create a delay of ~ 20 min. in the occurrence of incident solar radiation at the EMP. This shift is clearly measurable when the standby oscillations (t < 415 min) are extrapolated to t > ~550 min. in Fig. 4, while the orbital period remains at ~91.2 min.

CONCLUSIONS

The analytical model results are in very close agreement with the flight data using the simple approximation given by Eq. (11) and three adjustable parameters, the solar heating factor, the effective environment temperature, and the experimentally determined orbit phase angle at compressor activation. The model successfully describes the equilibrium relaxation time, phase shifts between warm end component waveforms, and oscillation amplitudes. An improved approximation for the time dependent term in Eq. (1), based on better information regarding shadowing effects in the Shuttle cargo bay, might render improved fidelity to the observed waveforms, but a numerical solution would likely be required. One advantage to the analytical model as implemented here is to observe how small changes in critical parameters, such as f_S and T_E (or equivalently α_S and ε, which were not varied for the actual solution), can strongly affect the system thermal equilibrium.

A preliminary conclusion of Ref. 2, viz., that oscillation amplitudes were strongly coupled to total input power at the EMP, turned out to be wrong. The actual cause was associated with an increase in the solar heating factor f_S and a decrease in the temperature T_E due to a Shuttle attitude maneuver nearly coincident with compressor activation. The model result for the value of f_S is 0.40, which corresponds closely to the observed solar input duty cycle of 0.41.

It is also noteworthy that the model is quite sensitive to values of the component heat capacities, thermal resistances, and power inputs. The solution values for these parameters were found to be in excellent agreement with the experimental or calculated values, giving credibility to the lumped capacity model approach. Finally, a primary objective of the model, to ascertain the temperature waveform at the aftercooler as required for modeling the thermal behavior at the cold stages, was satisfactorily accomplished.

ACKNOWLEDGMENTS

I would like to thank Dr. Ray Radebaugh of NIST Boulder Laboratory for contributing Fig. 3, Dr. Joe Martin for proofing the model derivation, and Dr. Peter Kittel of NASA / ARC for sponsorship of the G-785 payload on STS-108.

REFERENCES

1. Bradley, P., Radebaugh, R., Xiao, J. H., and Ladner, D. R., "Design and Test of the NIST/Lockheed Martin Miniature Pulse Tube Cryocooler," *Cryocoolers 11*, edited by R. G. Ross, Jr., Kluwer Academic/Plenum Publishers, New York, 2001, p. 189.
2. Ladner, D. R., Radebaugh, R., Bradley, P., Lewis, M., Kittel, P., and Xiao, J. H., "On-Orbit Performance of a Miniature Pulse Tube Flight Cryocooler," *Cryocoolers 12*, edited by R. G. Ross, Jr., Kluwer Academic/Plenum Publishers, New York, 2003, p. 777.
3. "Orbiter Reference Information," *The Hitchhiker Customer Accommodations and Requirements Specifications*, Appendix X, NASA Publication 740-SPEC-008, NASA/GSFC, 2002.
4. Holman, J. P., *Heat Transfer*, 4th Edition, McGraw-Hill, Inc., New York, 1976, Chapter 4, pp. 99-102.
5. *GAS Experimenter Handbook*, NASA/GSFC, "Thermal Considerations," 1997.
6. Krezig, E., *Advanced Engineering Mathematics*, 2nd Edition, John Wiley and Sons, Inc., New York, 1967, pp. 446-447.
7. Serna, R. and Ortiz, C. R., "Orbital Incident Heating Fluxes for Six-Sided Box Cube," *NASA/JSC Technical Memorandum ES34-86-44M*, May, 1986.
8. Rainville, E. D., *Elementary Differential Equations*, 3rd Edition, Macmillan Co., N. Y. 1964, Chap. 14.
9. *Handbook of Chemistry and Physics*, 48th Ed., Chemical Rubber Company, Cleveland, OH, 1967, p. A-245.
10. "Attitude Timeline for the As-Flown STS-108 Mission," NASA STS-108 document, Tony Foster, Omitron Corp., 2003 (personal communication).

Model for Orbit-Induced Temperature Oscillations in a Miniature Pulse Tube Cryocooler, Part 2: Cold Head Components

Daniel R. Ladner

Lockheed Martin
Space Systems Company
Denver, Colorado 80201, USA

ABSTRACT

An analysis of the thermal oscillations observed during the two-stage Miniature Pulse Tube Flight Cryocooler (MPTFC) experiment on STS-108 (Dec. 2001) is presented. The previous analysis (Part 1) was required to determine the magnitudes and phases of the aftercooler and heat rejection surface temperature waveforms that drive the cold head responses. The aftercooler temperature in particular was poorly resolved due to low resolution (± 0.40 K) on its flight sensors. In Part 1 a system of differential equations describing the transient heat flow from parallel sources into the heat rejection surface was solved to recover the aftercooler waveform unambiguously. This companion paper analyzes the propagation of the warm aftercooler temperature waveform into the first and second stages of the MPTFC during cooler operation. This analysis comprises a similar system of equations that describe the series heat flow between the two stages and the aftercooler, including the stage cooldown from the on-orbit ambient temperature of ~ 271 K. The oscillating cold stage temperature waveforms were determined at high resolution (± 0.04 K) and their amplitudes were found to be significantly smaller than would be expected from the steady state pre-flight measurements at various rejection temperatures. Dynamic results of the model are compared graphically to the on-orbit data.

INTRODUCTION

Background

The NIST/Lockheed Martin Miniature Pulse Tube Flight Cryocooler (MPTFC) experiment was flown and operated successfully as a self-contained payload (G-785) aboard the Space Shuttle Endeavour in December 2001. The design and cooling performance of the MPTFC were previously reported.[1,2] The occurrence of orbit-induced thermal oscillations on the cryocooler warm components and cold stages was described briefly in Reference 2 and depicted there in Figs. 8 and 9. Orbit-induced temperature oscillations are typically observed on space hardware as a result of solar/earth albedo radiation absorption and nocturnal IR radiation cooling. In Part 1[3], it was noted that a simplified analysis of the thermal oscillations at the cold stages requires an unambiguous determination of the temperature waveform at the aftercooler where the cold head heat is re-

Cryocoolers 13, edited by R. G. Ross, Jr.
Springer Science+Business Media, Inc., New York, 2004

jected. This was satisfactorily accomplished and is consistent with the low resolution data from two sensors mounted to that component. The model results for the important warm components are given in Fig. 4 of Reference 3.

MODEL AND DERIVATION

Model

A thermal model for ascertaining the parasitic heat loads into the MPTFC cold head and the thermal degradation factors of the regenerators was developed and presented in a previous paper.[4] A schematic of the two-stage MPTFC cold head and thermal model schematic are given in Fig. 2 of Reference 4. The estimated net parasitic heat loads from conduction and radiation were found to be ~0.32 W into stage 1 at 198 K and ~0.21 W into stage 2 at 112 K for a stable ambient laboratory temperature of 294 K. These temperatures were somewhat warmer than the space environment on STS-108, but the temperature differences between cold head components are comparable. Two primary differences, however, are that on-orbit the warm components do not have a convective environment for a heat sink and so warm up rapidly to higher temperatures, and secondly they exhibit orbit-induced diurnal thermal oscillations which are absent in the lab.

Figure 1 shows the aftercooler data and the thermal waveform as deduced from the model in Part 1 and described there in Eq. (22) as component T_3. Also shown in the figure is a second waveform that is virtually identical but which is represented by a somewhat simpler equation (Eq. (3) below) for the purpose of expediting the cold head analysis.

Figure 2 shows the thermal model schematic used in the derivation below. The thermal model is configured as a two lump thermal system with heat rejection to the aftercooler (T_3) having the dynamic temperature previously modeled. The stage 1 temperature is designated as T_1 and the stage 2 temperature as T_2, but these should not be confused with the same component nomenclature in Part 1 used for the EMP and compressor, respectively. A lumped system is a valid approximation when the temperature gradients within each lump component are small compared to the gradients across the resistive legs.[5] Several heat flows representing refrigerative cooling and parasitic heat loads are shown. These heat flows are all taken as positive values, with flow directions accounted for by signs in the equations. The thermal resistances R_1 and R_2 are effective values, combining both conduction and linearized radiation[3] into single parameters. The parasitic heat flows associated with these resistances and temperature gradients are included as known refrigeration

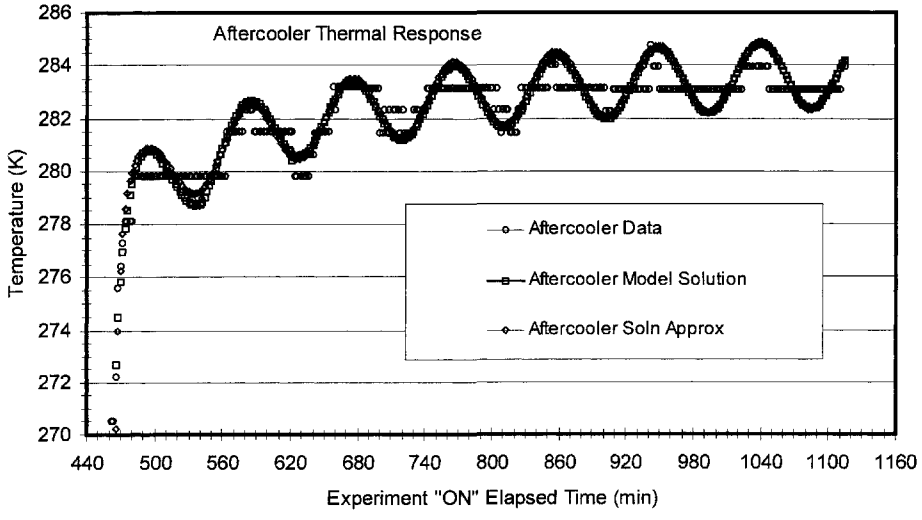

Figure 1. Aftercooler temperature versus time.

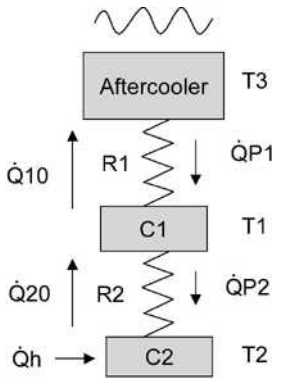

Figure 2. Thermal model schematic.

losses in the model. The capacity C_1 represents the stage 1 headers and an attached radiation shield. The capacity C_2 represents the stage 2 cold header and cold finger. Values for the thermal capacities can be estimated from the known dimensions and materials of these components. The approximate refrigerative powers $\dot{Q}_{10}$ and $\dot{Q}_{20}$ and loss $\dot{Q}_{1L}$ (for stage 1, Fig. 3) can be determined directly from the experimental cooldown data, taking into account the known temperature-dependent parasitics that can be determined from laboratory warm-up rate data.[4] The heater power $\dot{Q}_h$ is constant and represents a heat load at stage 2. It is equal to zero in the timeframe analyzed in this paper, but it is included in the model for analysis of other on-orbit data with heater power applied.[2]

It should be noted that any simplified modeling of the two-stage pulse tube (PT) cold head thermal performance is much less trivial than modeling the warm end components as described in Part 1.[3] Because of the large temperature differences between initial and final steady state values, the equation coefficients are not constant, although the parameters of interest (e.g., k_{11}) typically vary by less than 5% because of offsetting temperature factors. However, final stage temperature differences are proportional to the effective cold thermal resistances, and oscillation amplitudes are inversely related to the stage cold heat capacities. But the more difficult problem is retaining equation linearity when modeling the nonlinear refrigeration. Pulse tube cooling efficiency is known to be proportional to the dynamic cold-to-hot end temperature ratio for each stage. This is clearly shown in Fig. 3 during the cooldown of the MPTFC. Since the stage 1 refrigeration is proportional to T_1/T_3, with the aftercooler temperature change being small compared to the stage 1 change, such

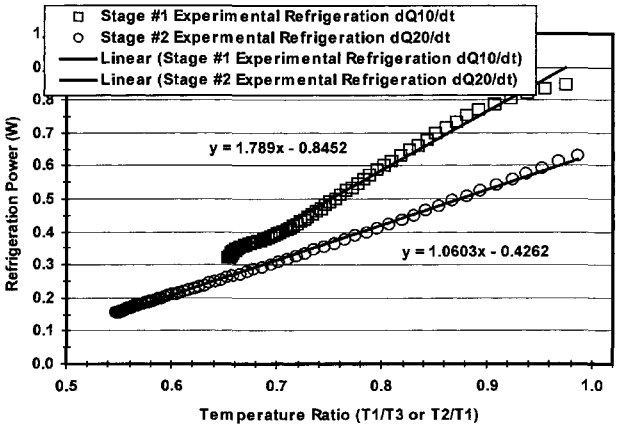

Figure 3. Experimental refrigeration versus temperature ratio.

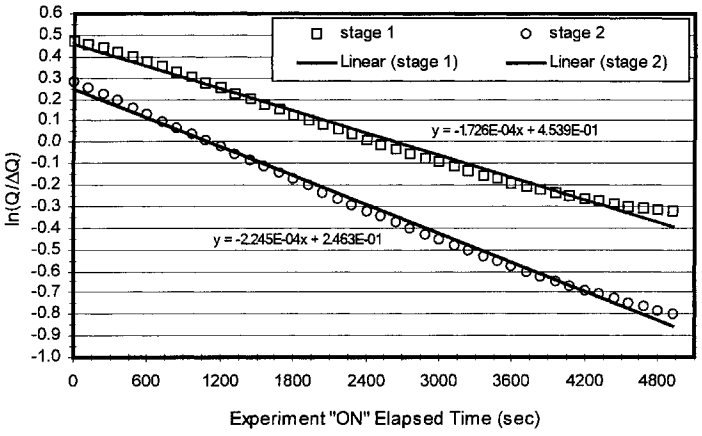

Figure 4. Experimental refrigeration versus time.

a relation can be used to advantage for the differential equation involving T_1. Note that this plot provides a measure of non-parasitic losses, since such losses are not directly included in the model (cf. Fig. 2). For the stage 2 equation, however, the similar relation T_2 / T_1 would be problematical because T_1 is not constant.

Fortunately, both stages exhibit nearly exponential cooling rates over much of their temperature change during cooldown, and this time dependence can be used to advantage for the stage 2 equation. In the cooldown plots shown in Fig. 4 the non-parasitic losses are not so obvious and are absorbed into the exponential curvefit coefficients.

Estimated values of the important model parameters are as follows:

$C_1 = 26.6$ J/K (271 K) → $C_1 = 22.6$ J/K (184 K)
$C_2 = 9.5$ J/K (271 K) → $C_2 = 6.0$ J/K (97 K)
$R_1 = 168$ K/W (271 K) → $R_1 = 215$ K/W (184 K)
$R_2 = 363$ K/W (271 K) → $R_2 = 564$ K/W (97 K)
$\dot{Q}_{10} = 1.789$ W, $\dot{Q}_{1L} = -0.845$ W (all temperatures, per Figure 3 curvefit)
$\dot{Q}_{20} = 0.608$ W, $m_5 = 2.245\text{E-}4$ / s (all temperatures, per Figure 4 curvefit)
$\dot{Q}_{P1} = 0.32$ W (184 K)
$\dot{Q}_{P2} = 0.21$ W (97 K)

The initial R and C inputs are the 271 K estimated values and the model then calculates their variation with temperature as the cooldown proceeds.

Derivation

The two first-order linear differential equations describing the time dependence of the cold stage temperatures are given by

$$dT_1/dt = k_{11}(T_3 - T_1) - k_{21}(T_1 - T_2) - Q_{11} \quad (1)$$

and

$$dT_2/dt = k_{22}(T_1 - T_2) + Q_{h2} - Q_{22} \quad (2)$$

where

$k_{11} = 1/R_1 C_1$ $k_{21} = 1/R_2 C_1$ $k_{22} = 1/R_2 C_2$
$Q_{11} = Q_{101} T_1 - Q_{1L1}$ where $Q_{101} = \dot{Q}_{10} / T_3 C_1$ and $Q_{1L1} = \dot{Q}_{1L} / C_1$

$Q_{22} = Q_{202} \exp(m_5 t) + Q_{P2} [1 - \exp(m_5 t)]$ where $Q_{202} = \dot{Q}_{20} / C_2$

$Q_{h2} = \dot{Q}_h / C_2$, $\dot{Q}_h$ = 0 W "off", 0.050 W "on" = stage 2 heater power

$Q_{P11} = \dot{Q}_{P1} / C_1$, $\dot{Q}_{P1}$ = the parasitic heat load into stage 1

$Q_{P22} = \dot{Q}_{P2} / C_2$, $\dot{Q}_{P2}$ = the parasitic heat load into stage 2 , and

$$T_3 = c_1 \sin(\omega t + \delta) + c_2 \cos(\omega t + \delta) + c_3 \exp(m_3 t) + c_4 \exp(m_4 t) + c_5 \qquad (3)$$

is an approximation for Eq. (22) in Part 1.[3] The dummy parameters used in Eq. (3) that result in the curve shown in Fig. 1 above are found to be

$c_1 = -0.92$ K $c_2 = +0.90$ K $c_3 = -4.90$ K $c_4 = -8.40$ K $c_5 = +283.8$ K

$m_3 = -9.00$ E-5 /s $m_4 = -4.50$ E-3 /s $\delta = +2.14$ rad. $\omega = 1.1482$ E-3/s

The system of equations (1) to (3) is solved analytically using the differential operator method directly to eliminate T_2. In operator form, with D = d ( ) / dt , these equations become:

$$(D + k_{11} + k_{21}) T_1 = k_{11} T_3 + k_{21} T_2 - Q_{11} \qquad (4)$$

$$(D + k_{22}) T_2 = k_{22} T_1 + Q_{h2} - Q_{22} \qquad (5)$$

Operating on Eq. (4) with $(D + k_{22})$ and Eq. (5) with k_{21}, and eliminating T_2 from the right side of Eq. (4) gives an equation for T_1 in terms of T_3 :

$$[D^2 + (k_{11} + k_{21} + k_{22}) D + k_{11} k_{22}] T_1 = k_{11} (D + k_{22}) T_3 + k_{21} (Q_{h2} - Q_{P22}) + k_{21} (Q_{P22} - Q_{202}) \exp(m_5 t) - (D + k_{22}) (Q_{101} T_1 - Q_{1L1}) \qquad (6)$$

Substituting for T_3 from Eq. (3) and collecting the T_1 terms gives

$$[D^2 + (k_{11} + k_{21} + k_{22} + Q_{101}) D + k_{22} (k_{11} + Q_{101})] T_1 = [k_{21} (Q_{h2} - Q_{P22}) + k_{22} (Q_{1L1} + k_{11} c_5)] + k_{11} c_3 (k_{22} + m_3) \exp(m_3 t) + k_{11} c_4 (k_{22} + m_4) \exp(m_4 t) + k_{21} (Q_{P22} - Q_{202}) \exp(m_5 t) + k_{11} (c_1 \omega + c_2 k_{22}) \cos(\omega t + \delta) + k_{11} (c_1 k_{22} - c_2 \omega) \sin(\omega t + \delta) \qquad (7)$$

The complementary function for Eq. (7) is found from the auxiliary equation

$$m^2 + pm + q = 0 \qquad (8)$$

where $p = k_{11} + k_{21} + k_{22} + Q_{101}$ and $q = k_{22} (k_{11} + Q_{101})$

Only real roots of Eq. (8) are admitted. In this analysis it is assumed that there are no repeated roots, so the complementary function for T_1 is of the form

$$T_{1C} = k_1 \exp(m_1 t) + k_2 \exp(m_2 t) \qquad (9)$$

where m_1 and m_2 are given by the quadratic solutions to Eq. (8), and the coefficients k_1 and k_2 are to be determined from the initial values of T_1 and its first derivative. The particular solutions for T_1 are determined by considering constant and time-dependent terms on the right side of Eq. (7) separately.

By inspection,

$$T_{1\,P1} = [\,k_{21}\,(Q_{h2} - Q_{P22}) + k_{22}\,(Q_{1L1} + k_{11}\,c_5\,)] / [\,k_{22}\,(\,k_{11} + Q_{101}\,)] \tag{10}$$

The time-dependent exponential particular solutions of Eq. (7) are found by assuming

$$T_{1\,P2} = k_3 \exp(m_3 t) \qquad T_{1\,P3} = k_4 \exp(m_4 t) \qquad T_{1\,P5} = k_5 \exp(m_5 t) \tag{11}$$

By substitution into Eq. (7) the coefficients are found to be

$$k_3 = k_{11} c_3\,(k_{22} + m_3) / [m_3^2 + p\,m_3 + q\,] \tag{12}$$

$$k_4 = k_{11} c_4\,(k_{22} + m_4) / [m_4^2 + p\,m_4 + q\,] \tag{13}$$

$$k_5 = k_{21}\,(Q_{P22} - Q_{202}\,) / [m_5^2 + p\,m_5 + q] \tag{14}$$

The time-dependent sinusoidal particular solution of Eq. (7) is found from

$$T_{1\,P4} = A \sin(\omega t + d) + B \cos(\omega t + d) \tag{15}$$

by using the method of undetermined coefficients to solve for A and B. Substituting Eq. (15) into Eq. (7), carrying out the indicated operations, and equating coefficients of the $\sin(\omega t + \delta)$ and $\cos(\omega t + \delta)$ terms, leads to

$$MA + NB = k_{11}\,(c_1\,\omega + c_2\,k_{22}\,) = k_7 \tag{16}$$

$$-NA + MB = k_{11}\,(c_1\,k_{22} - c_2\,\omega\,) = k_6 \tag{17}$$

where

$$M = q - \omega^2 \tag{18}$$

$$N = p\,\omega. \tag{19}$$

The solutions are

$$A = [\,M\,k_6 + N\,k_7\,] / (M^2 + N^2) \tag{20}$$

and

$$B = [\,M\,k_7 - N\,k_6\,] / (M^2 + N^2) \tag{21}$$

Then the general solution for T_1 is the sum of the complementary and particular solutions,

$$T_1(t) = \sum_{1}^{5} k_i\,\exp(m_i\,t\,) + T_{1\,P1} + A \sin(\omega t + \delta) + B \cos(\omega t + \delta) \tag{22}$$

and the constants k_1 and k_2 can be determined by solving the two simultaneous Eqs. (22), with T_1 (t) and DT_1 (t) evaluated at t = 0 using known initial values.

The solution for T_2 follows immediately from the direct integration of the linear nonhomogeneous Eq. (2) using Eq. (22) for T_1. Equation (2) becomes

$$dT_2 + k_{22}\,T_2\,dt = k_{22}\,T_1\,dt + (Q_{h2} - Q_{P22})\,dt + (Q_{P22} - Q_{202}\,)\exp(m_5\,t)\,dt \tag{23}$$

for which the integrating factor is $\exp(\int k_{22}\,dt\,) = \exp(\,k_{22}\,t)$. The solution for T_2 is

$$\begin{aligned} T_2(t) = {} & k_{22} \sum_{1}^{4} \{k_i / (k_{22} + m_i\,)\,[\exp(m_i\,t) - \exp(-k_{22}\,t)]\} + [(Q_{P22} - Q_{202}) / (k_{22} + m_5)] \times \\ & [\exp(m_5\,t\,) - \exp(-k_{22}\,t)] + [\,T_{1\,P1} + (Q_{h2} - Q_{P22}) / k_{22}]\,[1 - \exp(-\,k_{22}\,t)] + \\ & k_{22} / (k_{22}^2 + \omega^2)\,\{\,C\,[k_{22} \sin(\omega t) - \omega \cos(\omega t)] + E\,[\omega \sin(\omega t) + k_{22} \cos(\omega t)] + \\ & (C\omega - E k_{22}\,) \exp(-k_{22}\,t\,)\,\} + T_2(0) \exp(-k_{22}\,t) \end{aligned} \tag{24}$$

where T_2 (0) is the initial value of T_2 , and

$$C = A \cos(\delta) - B \sin(\delta) \quad \text{and} \quad E = A \sin(\delta) + B \cos(\delta) \tag{25}$$

RESULTS

Implementation of the Model

The foregoing sequence for analytically solving the system of equations (1) to (3) was implemented as an EXCEL© spreadsheet. The estimated values for the C, R and $\dot{Q}$ input parameters as given above (cf. Model) were used initially; the T_3 parameters were always fixed. More exact parameter values were then determined by iteration for consistency with the on-orbit temperature measurements. Single entry parameter inputs to the spreadsheet and charting of the solutions over the time interval of interest resulted in rapid convergence of the model.

Parameter Values

The final input parameter values were:

C_1 = 18.6 J/K (271 K) → C_1 = 15.8 J/K (184 K)
C_2 = 5.9 J/K (271 K) → C_2 = 3.6 J/K (97 K)
R_1 = 162 K/W (271 K) → R_1 = 209 K/W (184 K)
R_2 = 344 K/W (271 K) → R_2 = 540 K/W (97 K)
$\dot{Q}_{10}$ = 1.762 W, $\dot{Q}_{1L}$ = -0.827 W (all temperatures)
$\dot{Q}_{20}$ = 0.410 W , m_5 = 4.000E-4 / s (all temperatures)
$\dot{Q}_{P1}$ = 0.32 W (184 K)
$\dot{Q}_{P2}$ = 0.16 W (97 K)

It is seen that the only parameters that required any significant variation from the nominal estimates for a best fit to the data were C_2 (6.0 vs. 9.5 J/K) and the $\dot{Q}_{20}$ parameters (the stage 2 refrigeration). The ~30% decrease from the calculated capacity C_2 would seem to be larger than expected from experimental error. The stage 2 refrigeration parameters that were estimated using the Fig. 4 exponential curvefit were also incorrect; the model wanted a lower initial refrigeration and a longer time constant. These parameters are interrelated, since the magnitude of the net refrigeration power for stage 2 is $C_2\dot{T}_2 - \dot{Q}_{P2}$. However, the final input parameters are in reasonably good agreement with the initial estimates. An automatic optimization of all values (e.g., using "Solver") might reduce the differences between estimated and final parameter values.

Model Results

Figures 5 to 7 compare the model results to the experimental data (open symbols) as a function of the experiment elapsed time during compressor operation. In Fig. 5 the model predictions are seen to overlie the data almost perfectly to within the resolution of the figure scale. Figure 6 is the comparison of the model to the high resolution (± 0.04 K) stage 1 data. Likewise Fig. 7 compares the model to the stage 2 data. For both stages it is seen that the qualitative features and amplitudes of the steady state oscillations in the data are closely duplicated by the model, although a slight phase difference is also evident.

CONCLUSIONS

The analytical model developed here provides reasonably good results in comparison to the MPTFC cold stage on-orbit temperature measurements. The cooldown curves are in very close agreement with the flight data with most of the adjustable parameters held very close to the original

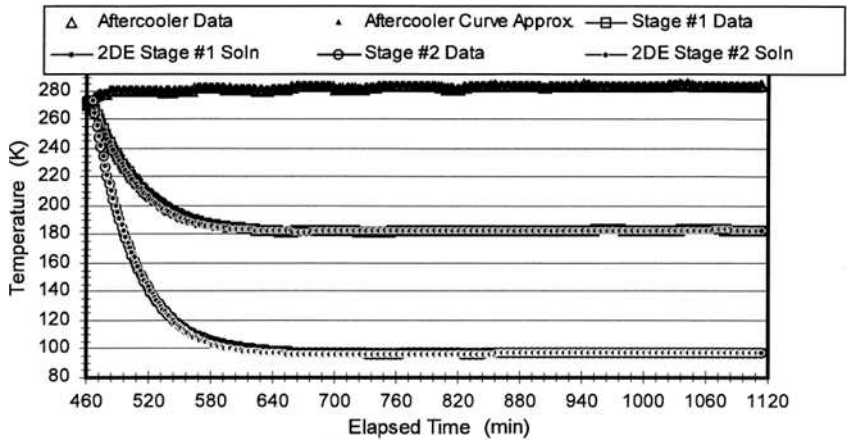

Figure 5. Model compared to flight data for both stages.

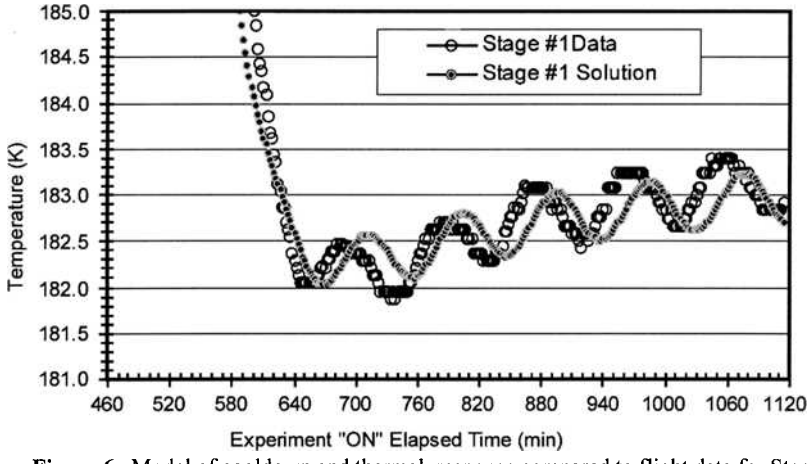

Figure 6. Model of cooldown and thermal response compared to flight data for Stage 1.

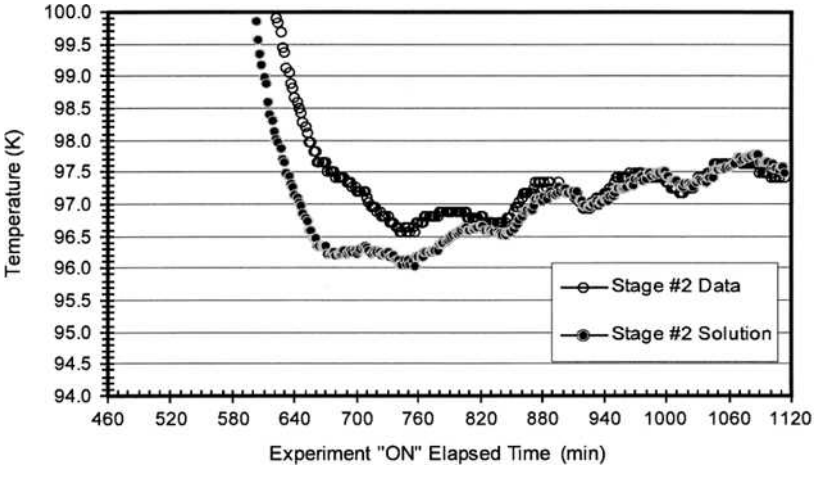

Figure 7. Model of cooldown and thermal response compared to flight data for Stage 2.

best estimates. The model successfully describes the cold stage relaxation times and the subsequent upward temperature drift that follows the aftercooler and EMP heat-sink temperatures. It also predicts oscillation amplitudes for each stage that are close to the measured values, and which are approximately 50% lower than would be predicted by steady state laboratory measurements for the same dc variation of the heat rejection temperature (aftercooler).[1,2] The predicted phase angles between the warm end aftercooler and the cold stage data waveforms are slightly greater than observed. This may reflect the temperature variation of the lump components, which causes the equation coefficients not to be constant, an assumption of the model. With some minor improvements the model could be used to accurately predict cryocooler coldhead behavior in any cyclical thermal environment, e.g., diurnal loading oscillations in space-based or lunar / planetary-based cryocoolers.

ACKNOWLEDGMENT

I would like to thank Dr. Ray Radebaugh of the NIST Boulder Laboratory for reviewing the model derivation, and Dr. Peter Kittel of NASA / ARC for sponsorship of the G-785 payload on STS-108.

REFERENCES

1. Bradley, P., Radebaugh, R., Xiao, J. H., and Ladner, D. R., "Design and Test of the NIST/Lockheed Martin Miniature Pulse Tube Cryocooler," *Cryocoolers 11*, edited by R. G. Ross, Jr., Kluwer Academic/Plenum Publishers, New York, 2001, p. 189.
2. Ladner, D.R., Radebaugh, R., Bradley, P., Lewis, M., Kittel, P., and Xiao, J. H., "On-Orbit Performance of a Miniature Pulse Tube Flight Cryocooler," *Cryocoolers 12*, edited by R. G. Ross, Jr., Kluwer Academic/Plenum Publishers, New York, 2003, p. 777.
3. Ladner, D.R. "Model for Orbit-Induced Temperature Oscillations in a Miniature PT Cryocooler, Part 1: Warm End Components," *Cryocoolers 13*, Kluwer Academic/Plenum Publishers, New York (2005).
4. Ladner, D.R., "Model for Two-Stage Pulse Tube Coldhead Parasitic Heat Load," *Advances in Cryogenic Engineering 47B*, American Inst. of Physics, Melville, NY, p. 1149.
5. Holman, J.P., *Heat Transfer*, 4th Edition, McGraw-Hill, Inc., New York, 1976, Chapter 4, pp. 99-102.

Cryogenic Tests of a Development Model for the 90 K Freezer for the International Space Station

T. Trollier[1], C. Aubry[1], J. Butterworth[1], S. Martha[1]
A. Seidel[2], and L. De Parolis[3]

(1) Air Liquide Advanced Technology Division, AL/DTA
Sassenage, France
(2) EADS Space and Transportation
Friedrischafen, Germany
(3) European Space Agency, ESA/ESTEC
Noordwijk, The Netherlands

ABSTRACT

A 90 K freezer, currently named CRYOSYSTEM, will support biological and medical experiments on board the International Space Station. The samples produced are intermediately stored under cryogenic conditions and downloaded to ground for further examination. Typical samples are animal tissue, organs, and plants, as well as organic fluids and protein crystals.

A Development Model (DM) of the freezer has been manufactured and tested by AIR LIQUIDE. The system is composed of a vacuum insulated shell equipped with a revolving magazine capable of freezing and storing up to 880 2-ml vials. The cryogenic cooling is produced by an engineering model Stirling cryocooler specially adapted for the needs of CRYOSYSTEM from a THALES Cryogenics BV tactical cryocooler.

This paper presents test results regarding the quick freezing of liquid samples, the snap freezing of solid samples, and the capability of the freezer to withstand power-off periods and to recover within the allocated time. Some preliminary correlations with ESATAN predictions are discussed.

INTRODUCTION

AL/DTA was selected by EADS in February 2002 for the delivery of the Cryogenic Sub-System of the CRYOSYSTEM. CRYOSYSTEM will support biological experiments on board the ISS. The samples produced are intermediately stored under cryogenic conditions and downloaded to ground for further examination. Typical samples are tissues of animals, organs, and plants, as well as organic fluids and protein crystals. The freezing and storage functions are performed by the so-called Cryogenic Vial Freezer (CVF), a 14 Panel Unit (PU) transportable drawer. On-orbit, up to three CVF may be accommodated inside the dedicated rack, called CRYORACK. The Cryogenic Sub-System consists of the vial freezer, specimen storage containers (2 ml or 5 ml vials) for quick and snap freezing of biological samples, and Orbital Support Equipment (OSE) including all cryogenic tools and supplies needed for the on-orbit operations of the CRYOSYSTEM. An illustration of the PDR design of the Vial Freezer is shown in the Fig. 1.

Cryocoolers 13, edited by R. G. Ross, Jr.
Springer Science+Business Media, Inc., New York, 2004

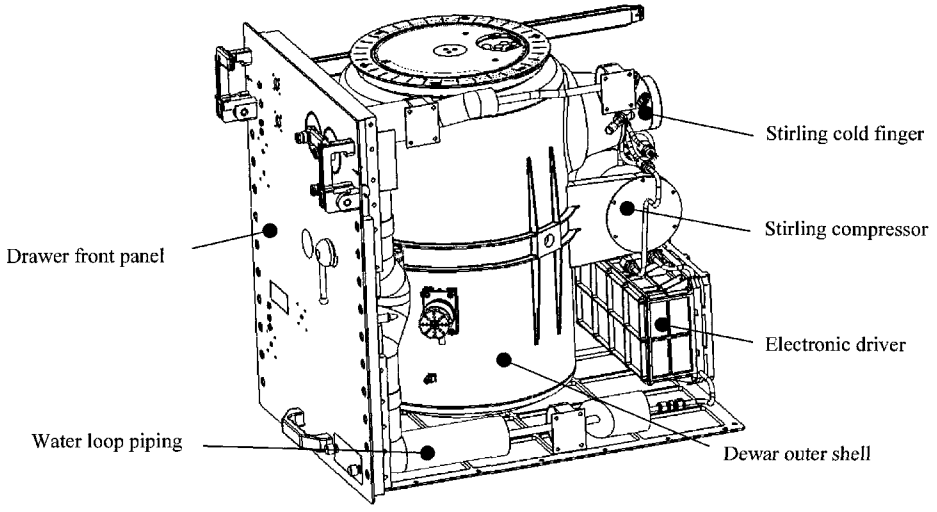

Figure 1. PDR design of the Cryogenic Vial Freezer (AL/DTA).

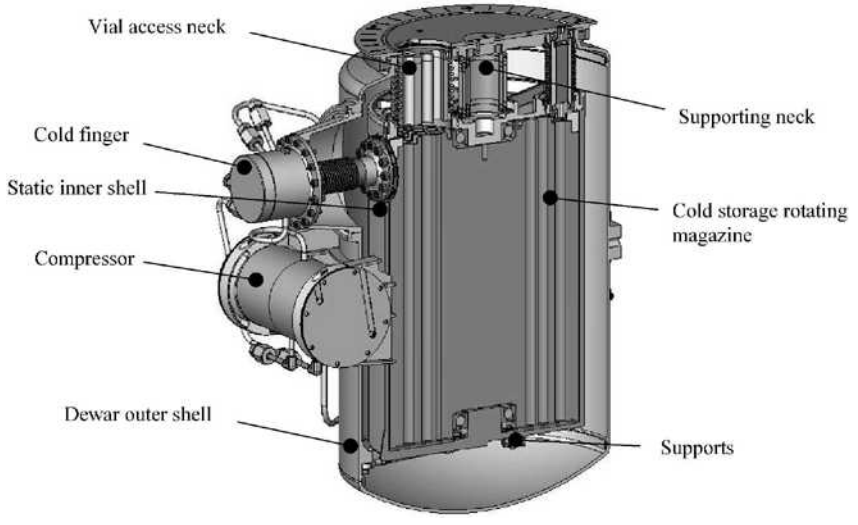

Figure 2. Cutaway view of the CRYOSYSTEM Dewar under design.

As shown in Fig. 2, the cold parts of the CVF consist of an inner shell and a storage magazine; these are suspended inside the outer shell with appropriate supports. This cold assembly weighs about 42 kg. The relative displacement between the inner shell and the cold finger cold tip is predicted to be 0.42 mm for combined launch and thermo-elastic loads (CRYOSYSTEM being launched cold). This will be accommodated by a dedicated Liquid Thermal Link Assembly with a mechanical stiffness of about 18 N/mm and a thermal resistance in the range of 0.5 K/W.[1]

VIAL FREEZER DM DESIGN

The CRYOSYSTEM project constitutes a brand new development with very challenging functional and performance requirements. It is therefore mandatory to verify in the project Phase B that the design meets the most critical requirements. The objectives of the DM CVF is to validate the functional performance of the system from the thermal and operational point-of-view. It therefore

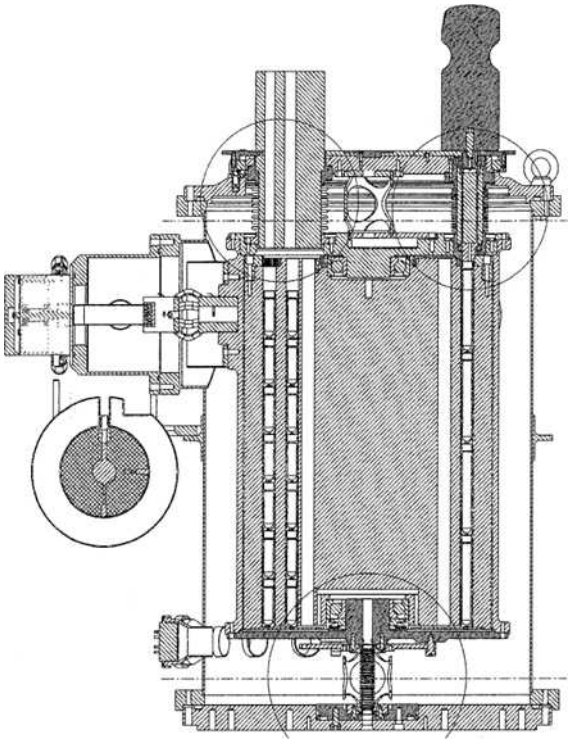

Figure 3. CRYOSYSTEM Dewar DM design.

consists of a representative magazine (capacity of 880 of 2 ml vial samples) with a representative door aperture that is put into a system providing thermal boundary conditions identical to that of the flight system. In this respect, heat entries through the Multi Layer Insulation (MLI) and the supports shall be equivalent to that of the flight design even if the DM supports are not structurally representative. This configuration corresponds to the ESATAN thermal simulations. The magazine is supported by two thermally representative epoxy supports. The DM CVF is cooled by a representative Stirling cooler[2] equipped with a copper-braid thermal link to the inner shell with characterized conductance. The outer shell is not flight representative and is demountable. The vacuum insulation will be dynamically pumped. All the upper interfaces are representative: upper faying surface and interface with the Cryogenic Orbital support equipment and Sample Containers (COSC provided by DAMEC Research). All the cold parts, with the exception of the inner shell vacuum seals, are representative of the flight design: revolving magazine, rotation system, and bearings. The DM design is shown in the Fig. 3.

Two photographs of the DM dewar, with and without insulation foam, are shown in the Fig. 4. The thermal insulation foam is used to prevent condensation during power OFF (the CVF being connected to the water loop of the ISS in order to remove heat from the cooler and the drive electronics).

For instrumentation, a series of PT100 thermal sensors are bonded onto the inner shell, the cold finger interface, and the outer shell. In particular, the rotating cold magazine contains twelve thermal sensors located in three different sections of the magazine (upper, mid, and lower) as shown in the Fig. 5. Four thermal sensors are located 90° apart at each section.

The vials used for Quick Freezing experiments are equipped with a PT100 thermal sensor plunged into saline solution, while the vials used for the Snap Freezing experiments contain a copper cylinder on which a PT100 thermal sensor is bonded. Thus, direct measurement of the sample temperature is made during the test campaign.

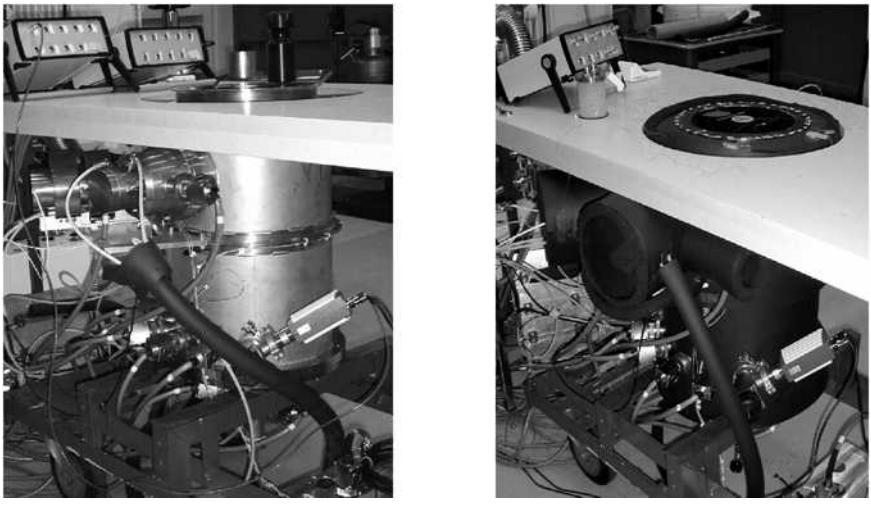

Figure 4. CRYOSYSTEM Dewar DM hardware (with and without thermal insulation foam).

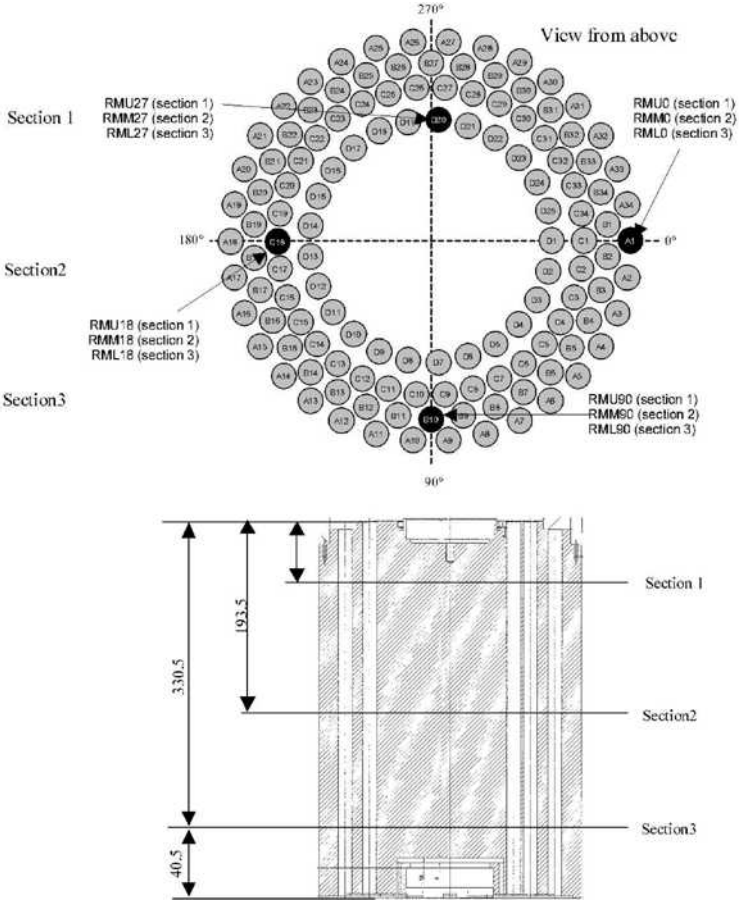

Figure 5. Rotative cold magazine thermal sensors location.

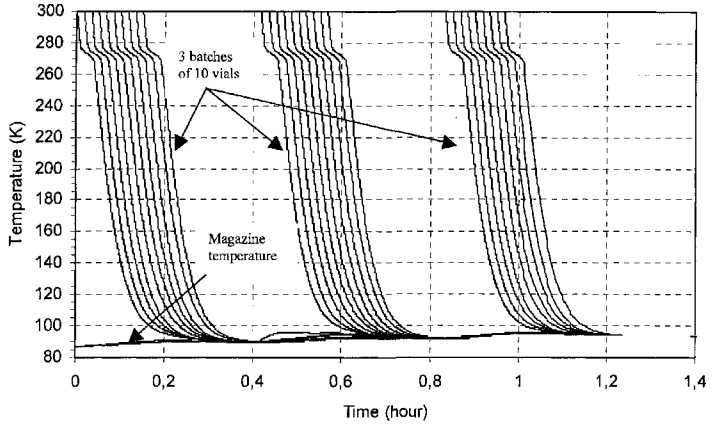

Figure 6. Quick Freezing simulation (ESATAN thermal model).

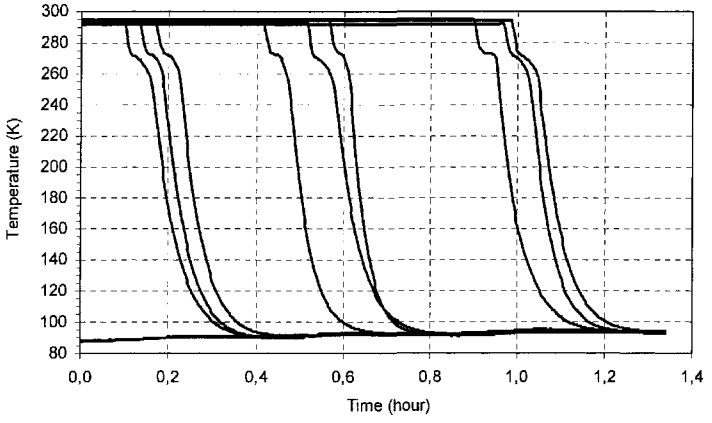

Figure 7. Temperature measurements during Quick Freezing (DM tests).

DM TESTS RESULTS AND ANALYSIS

Regulated Mode

Thermal mapping of the magazine was performed in the Regulated Mode using a set-point temperature of 84.9 K ±0.2K applied at the cold finger connection to the inner shell. A maximal thermal gradient of 0.3 K was observed in the magazine, and a mean temperature difference was noticed between the inner shell and the magazine.

Quick Freezing Tests

Quick freezing consists of a rapid cooldown of the vials from ambient to 113 K in less than ten minutes. Once frozen, the vials must always remain colder than 93 K inside the cold storage magazine. The worst case operational scenario consists of inserting three batches of ten warm vials (ambient temperature) with a cadence of one vial per minute. A 15-minute pause is made between batches. The specification states that the vial freezer shall sustain this scenario and recover (in order to allow for performance of another identical scenario) in a 24-hour period. The ESATAN model prediction of this scenario is shown in the Fig. 6, where the temperature of the three vial batches and the temperature of the magazine are presented. In Fig. 7 we report the temperature measurements during the performance of the test. Notice that only three vials are instrumented per batch of ten vials due to operational constraints linked to the cold rotary magazine.

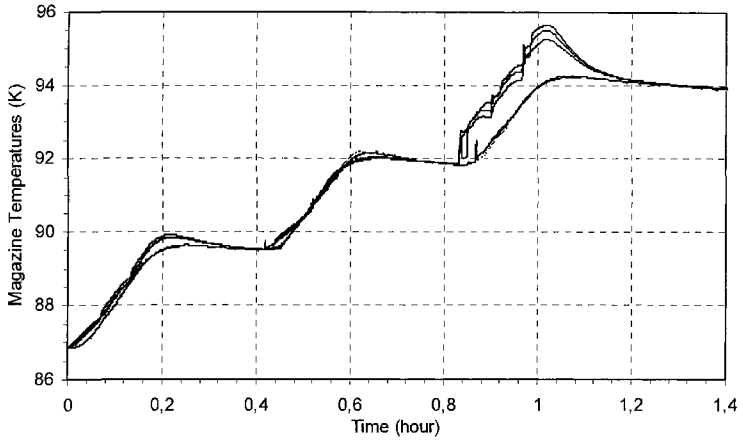

Figure 8. Magazine warm up during insertion of vials (ESATAN thermal model).

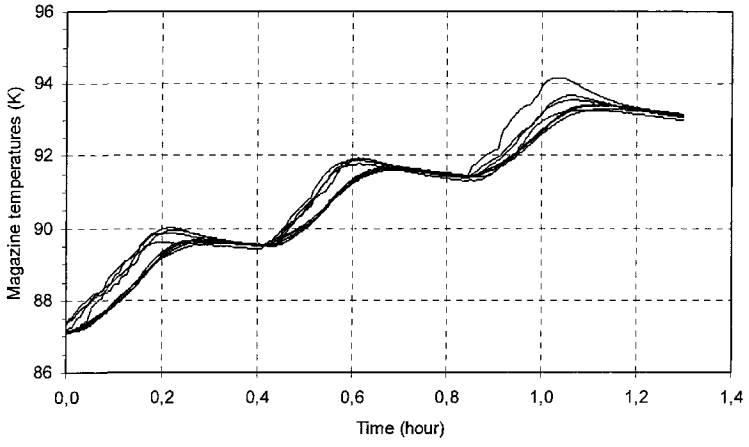

Figure 9. Magazine warm up records during insertion of vials (DM tests).

In Figs. 8 and 9 we report the warm up of the magazine during the insertion of the vials (ESATAN predictions and DM test performance, respectively). The magazine temperature rise predicted during insertion of the vials was greater than the measurements mainly due to the higher cooling capacity provided by the Stirling Engineering Model (the cooler used during the DM tests) in comparison to the cooling capacity implemented in the ESATAN thermal modelling. Also, the large temperature increase shown in the ESATAN thermal model for the last batch is related to a very stringent scenario where the vials insertion is concentrated in the same area.

After performance of the Quick Freezing scenario, the recovery capability of the freezer was investigated. The performance test results shown in Fig. 10 are compared to the simulations presented in Fig. 11. Again, due to the cooling capacity of the Stirling cooler used, the recovery is achieved a bit more quickly than in the predictions. The recovery is achieved in about twenty hours, which is fully compliant with the specification.

Snap Freezing Tests

Snap freezing is an ultra-rapid freezing so that the cells are instantaneously frozen so that water does not destroy the subcellular structure. It is performed by thrusting a biological sample against a precooled piece of copper with the help of a piston rod as shown in Fig. 12. The main

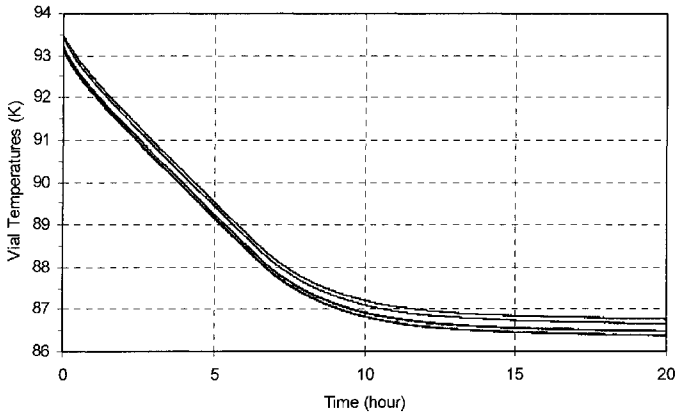

Figure 10. Temperature recovery after Quick Freezing operations (DM tests).

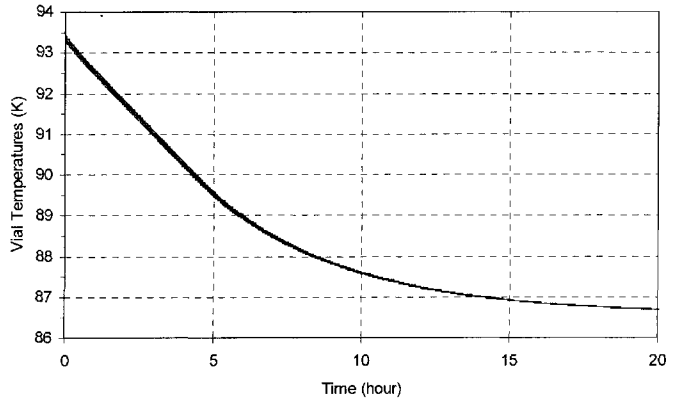

Figure 11. Temperature recovery after Quick Freezing operations (ESATAN thermal model).

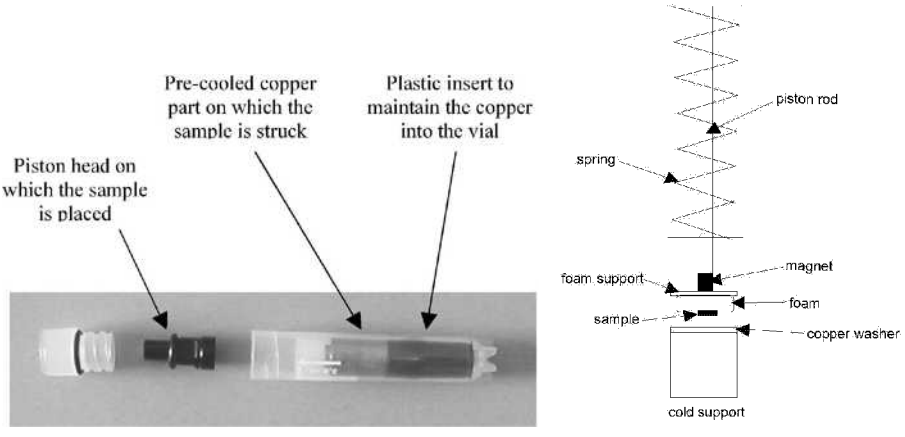

Figure 12. Snap freezing vial type and snap freezing process used for DM tests.

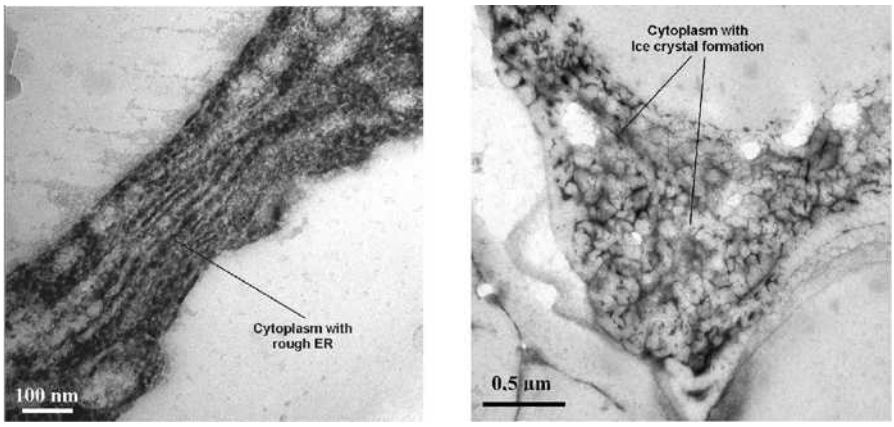

Figure 13. Electronic transmission microscope observations of snap frozen samples; left picture: cut depth 45 µm, right picture: cut depth 80 µm.

requirement on the snap freezing process is that the ice crystals shall be smaller than 10 nm to a depth of 15 µm. During the test campaign, ten samples of lettuce roots were snap frozen with the DM freezer apparatus. Compliance of the snap freezing with the requirements was confirmed by analysis using an electronic transmission microscope to view ultra fine cuts of the snap samples (cryo-substitution process). In Fig. 13, we show two examples of the observations made during the snap freezing analysis. The picture on the left is representative of a cut performed at a depth of 45 µm (three times more than specified). The observation shows that there is no ice crystal formation at this depth. As shown in the right hand picture, one must perform observations at a depth of 80 µm in order to see the formation of ice crystals. With respect to the specification, the snap freezing process used with our DM freezer was declared successful.

Power OFF Tests

The definition of "power OFF" is an operational phase without any resources (power, water) from the International Space Station or the transportation module (MPLM). The maximal duration of the power-OFF state is 8 hours, during which the vials stored in the freezer shall remain colder than 93 K. Furthermore, the freezer shall be capable of recovering from a power OFF in less than $2n$ hours (if the power OFF lasts n hours). The power-OFF scenario and the recovery phases were simulated with the ESATAN thermal model and experimentally investigated on the freezer DM. The worst-case condition used for sizing of the freezer (and for demonstration of compliance to the specification) involved performing the power OFF with an empty magazine (reduced thermal mass for faster warm up) and performing the recovery with a full magazine (highest thermal mass for slow cool down).

Figures 14 and 15 show, respectively, the magazine temperatures predicted during the power OFF and the experimental results. The warm-up of the magazine is slightly quicker than predicted due to higher heat loads than expected.

The temperature recovery after 8 hours power OFF and with a magazine filled with 500 of the 5 ml vials (full capability) is shown in Fig. 16. After 16 hours of cooling down, the magazine is fully recovered so that it is capable of sustaining another power OFF or performing any other operational scenario (e.g. quick or nap freezing).

CONCLUSIONS

The Development Model of the CRYOSYSTEM freezer allowed for successful demonstration of the operational constraints. The test results are in good agreement with the ESATAN model

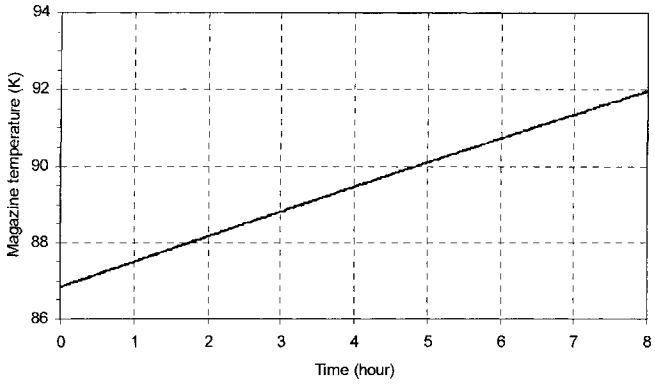

Figure 14. Magazine temperature during 8 hours power OFF (ESATAN thermal model).

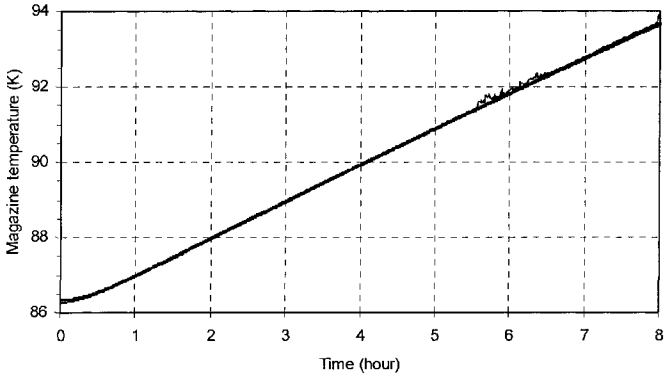

Figure 15. Magazine temperature during 8 hours power OFF (DM tests).

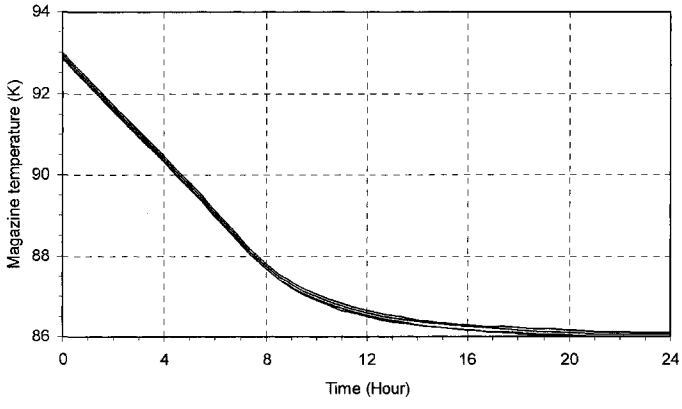

Figure 16. Temperature recovery after 8 hours power OFF (DM tests).

predictions. The DM test results are currently being used to refine the thermal model, particularly the heat losses thermal budget. For better optimization, other vial arrangements have also been tested.

Start of phase C/D for the CRYSOSYTEM is expected in October 2004. A Qualification Model (QM) of the freezer will be tested (thermal and mechanical) around end of 2005.

ACKNOWLEDGMENT

The authors wish to thank the European Space Agency and the complete CRYOSYSTEM industrial team for their contributions to the ongoing development.

REFERENCES

1 T. Trollier, A. Ravex, C. Aubry, A. Seidel, H. Stephan, L. De Parolis, A. Sirbi and R. Kujala, "Solutions for the Cryosystem Cryocooler On-Board the International Space Station," *Adv. in Cryogenic Engineering*, Vol. 49B, Amer. Institute of Physics, Melville, NY (2004), pp. 1187-1196.

2 T. Trollier, A. Ravex, P. Crespi, J. Mullié, P. Bruins, T. Benschop "High capacity flexure bearing Stirling cryocooler on-board the ISS," Proceedings of the nineteenth International Cryogenic Engineering Conference, ICEC19, pp. 381-384.

Comparison of Measurements and Models for a Pulse Tube Refrigerator to Cool Cryo-Surgical Probes

P.E. Bradley[1], R. Radebaugh[1], M. Lewis[1], R. Bailey[2], and M. Haas M.D.[2]

[1]National Institute of Standards and Technology
Boulder, Colorado, 80305, USA

[2]CIMEX BioTech L.L.C.
Covington, LA 70435 USA

ABSTRACT

This paper describes the performance measurements of a pulse tube refrigerator (PTR), originally developed for cooling cryo-surgical probes (CryoPens) to about 180 K for dermatological applications. The linear compressor, which has a maximum swept volume of 3.9 cc, was instrumented to measure the piston position with a laser position sensor shining through a sapphire window on one end of the compressor. These results along with pressures measured at the reservoir, pulse tube, and compressor allowed us to determine the flow and PV power at various locations, which were then compared with the predictions from our models. Comparisons were also made between the calculated and measured thermal load curve. The cooling rate for insertion of warm CryoPens was measured and the resulting thermal load on the PTR was determined, which agreed well with calculations.

INTRODUCTION

Background and Application

One of the more interesting recent applications for cryogenics is the use of low temperatures to surgically remove or destroy human skin surface lesions, warts, and in some instances tumors. The only requirement for such cryo-ablation is the development of low temperatures, at or below -50 C, in the surrounding tissue of interest for a rather short time, 3 minutes or less. For some time now it has been common practice to dab liquid nitrogen on these skin irregularities. However, for deep tissue procedures liquid nitrogen spray, sublimated carbon dioxide, or even Joule Thompson type cooler probes (which often operate at fairly high pressures) have been employed. A simple easy to use approach using low cost reusable foam-insulated probes called CryoPens™ which are cooled to below -50 C (223 K) has been developed by CIMEX BioTech to perform this procedure.

Surface lesions are removed by single or multiple short term contact with a cryogenic probe. The number of procedures and time of duration for cryo-ablation is determined from the amount,

Cryocoolers 13, edited by R. G. Ross, Jr.
Springer Science+Business Media, Inc., New York, 2004

size and depth of tissue needing to be removed. Usually there is little scarring and recovery times are reduced compared with conventional scalpel excision techniques. Furthermore, pain and discomfort are minimal and there is no blood loss associated with this procedure.

The CryoPen system consists of the CryoPens and the pen manifold support and cooling assembly. The entire assembly is cooled by an appropriate cryocooler (pulse tube in this case) to about -90C (183 K). The tips of the pens are cooled through contact with a fluid heat transfer medium in a reservoir/manifold, which in turn is cooled by the pulse tube cooler. The pens make minimal direct contact with the cooler to allow for easy removal and replacement. Once cold, a pen of specific tip size is chosen (based upon the size of the lesion to be frozen) and removed from the cold reservoir. Then an appropriate sterile shield is placed over the tip of the pen, thus readying the pen for a procedure. The sterile shield consists of a foam plastic cylinder which holds a pre-formed 51μm thick aluminum foil shield, which slips over the pen tip and makes direct contact with the patient's lesion.

Each cryo-surgical probe consists of a central core of nickel plated copper that is surrounded by foam, which is injected in the annular space between the core and an injected/extruded plastic holder. The outer surface of the plastic holder remains at room temperature, thus the probe may be handled without any special handling equipment. The entire probe assembly is about 18 cm in length and 4 cm in diameter. Each pen (without insulation) has a mass of about 272 grams, slightly higher or lower depending upon tip size. Figures 1 and 2 show cool down times for the cooler with and without pen assembly and a representative operating duty cycle for the pens respectively. The cool down time for the cooler is quite rapid at less than 15 minutes from 295 K to 193 K. With the added mass and surface area the cool down for the pens is considerably longer at about 135 minutes from 295 K to 193 K (typical starting temperature to begin initiating an operating procedure). Figure 3 shows a CryoPen, assembly, and cooler during test evaluation.

Pulse Tube Cooler

To provide cooling for the CryoPen assembly a suitable cooler is needed. For this program a pulse tube cooler was chosen. It is a u-tube configuration with an inertance tube phase shifter. The cold end is upright to allow easy access for removal and replacement of the CryoPens. This design is simple and low cost to fabricate as standard off the shelf materials are incorporated where possible. For instance polystyrene insulation is employed around the cold head rather than vacuum dewar insulation. This insulation is machined to fit closely around the cold head and is also used for the CryoPen and reservoir assembly. Additionally, standard off the shelf computer CPU heat sinks with fan assemblies are employed to remove heat from the aftercooler and pulse tube warm end heat exchangers. Figure 4 shows a cross-section view of the pulse tube cooler highlighting some of these elements.

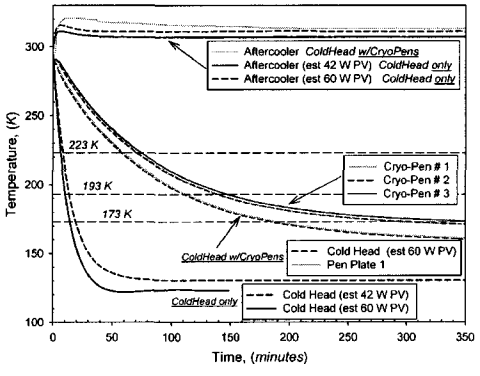

Figure 1. Cool down times using DRS compressor.

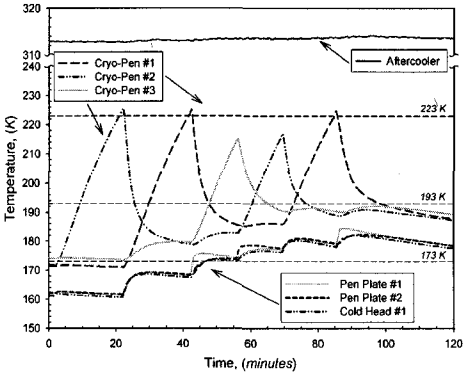

Figure 2. Representative duty cycle for Pens w/DRS comp.

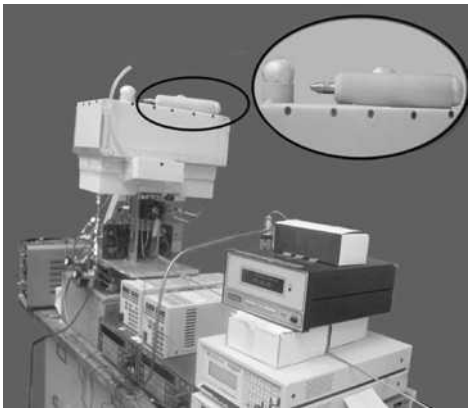

Figure 3. Pulse tube cooler and CryoPen during evaluation.

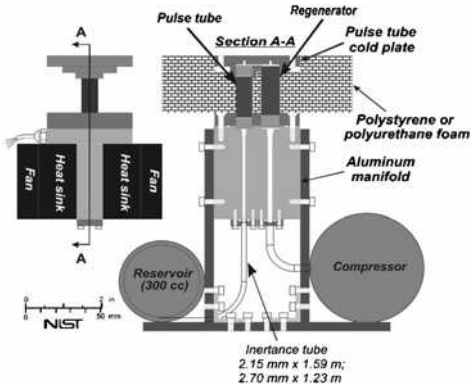

Figure 4. Cross-section of pulse tube cooler.

The pulse tube refrigerator is designed using the analytical model for an orifice pulse tube refrigerator as outlined by Storch, et al.[1] and the NIST numerical model for regenerators, REGEN3.2 (updated from REGEN3.1).[2] The inertance tube portion is designed using the electrical transmission line model developed by Radebaugh, et al.[3] Making reasonable assumptions for insulation and conduction losses for the CryoPen assembly (with pens) a goal of 10 W of net refrigeration at 170 K was set. To meet this goal the cooler was designed to operate at 60 Hz with a 2.5 MPa average system pressure, a pressure ratio (P_{max}/P_{min}) of 1.30 at the cold end, and heat rejected from the warm end at 300 K.

Cooler Performance

The pulse tube cooler has been operated with two similar linear opposed piston type compressors. They are off-the-shelf tactical compressors that are normally used with Stirling cold heads operating at about 50 Hz. Early performance was evaluated with a DRS compressor that has a nominal swept volume of about 3.9 cc but is not instrumented. Later performance was evaluated with an AIM compressor that has a maximum swept volume of about 3.8 cc and is instrumented to measure the piston position with a laser position sensor shining through a sapphire window on one end of the compressor. The performance with both compressors is shown in Figs. 5 and 6. The cooler driven with the DRS compressor was operated at higher powers from the outset (delivering pressure ratios above ~1.23 at the pulse tube) in order to rapidly optimize the inertance tube lengths for best performance. However, the cooler driven with the AIM compressor was operated at lower

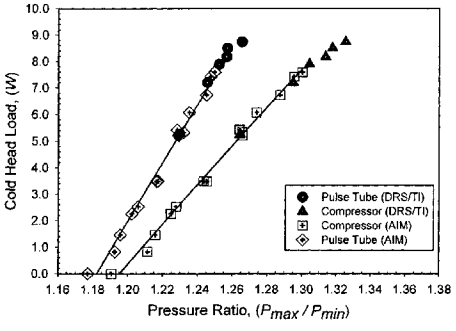

Figure 5. Cooling performance at 170 K for AIM and DRS compressors.

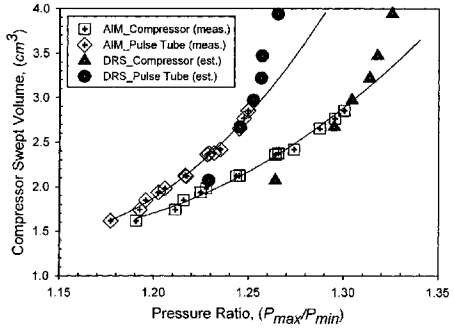

Figure 6. Swept volumes for AIM and DRS compressors with cold end at 170 K.

powers, delivering pressure ratios of 1.18 to 1.25 at the pulse tube, to more thoroughly characterize the system performance. The cooler performance for a given pressure ratio, as shown in Fig. 5, compares quite well between the two compressors, as expected.

Figure 6 shows the swept volume corresponding to pressure ratios for both compressors. At a given pressure ratio the swept volume for the first compressor differs somewhat from the second and requires an adjustment/correction. This difference is understandable since estimates of the swept volume for the first compressor are made based upon the piston position (or stroke) being proportional to the supplied voltage, making appropriate assumptions of adiabatic, sinusoidal compression and symmetry in piston oscillation (no inherent DC drift). Thus, at maximum stroke, the swept volume is calculated for the corresponding input voltage. This proportionality remains relatively constant for a given input voltage, so volume estimates at varying voltages can be made. This is only a relatively good estimate without position sensors to determine the actual stroke however as readily observed from Fig. 4. Without the piston position measurement, PV power can only be estimated based upon a sinusoidal, adiabatic compression. So the values from the measurements of the second compressor are used to anchor previous estimates for the PV power and swept volume with the first compressor. This is a valid approach, because a given swept volume results in a given pressure ratio delivered from the compressor to the pulse tube resulting in a given refrigeration power (see Fig. 5).

Swept volumes for the second compressor at any instant in time are calculated from the laser sensor that operates at 50 kHz. Both pistons are assumed to be in the same relative position at any instant in time with respect to the compression space. The second compressor has a maximum possible swept volume of about 3.8 cc. But due to a bias of the piston centering, which leads to hitting the inner stops, a maximum swept volume of only about 2.8 cc was attainable. This proved to be sufficient to obtain the desired measurements of phase shifts and for calculating the PV power at the compressor and power flows within the system to compare with the design models.

MODEL AND MEASUREMENTS

Phasor Model

A very instructive and valuable technique to estimate and evaluate a cryocooler is to construct a mass flow phasor diagram. This can be done for each individual segment or component within the cooler such as for the regenerator, the pulse tube, the inertance tube, etc. An even more valuable technique is to combine all of these elements into a single diagram that uses the cold end of the pulse tube as reference. From this diagram the magnitudes and phase angles, leading or lagging, can be visualized along with their importance and influence on the overall performance. Figure 7 shows the design phasor diagram for the pulse tube cooler. From this we see that mass flows in the regenerator, aftercooler, and compressor lead the pulse tube pressure at the cold end, while mass flows at the inertance tube entrance and reservoir lag the pulse tube pressure at the cold end. The shape or relative skewing between different elements can show what type of process occurs such as whether compression at the compressor is isothermal, or pseudo-adiabatic.

Cryocoolers often perform somewhat differently than expected so it is quite useful to evaluate some key performance parameters. Some that are very helpful are phase shifts and mass flows in the reservoir, inertance tube, regenerator, and aftercooler. However, making flow measurements in the regenerator and inertance tube are more difficult to make directly and introduce additional volume to the system that can affect system performance, sometimes reducing or even detracting their value for a given system. In practice a good design with well understood system geometries can still lead to uncertainties about some elements within the system and their effects on performance. But at a development or prototype stage a little thought and consideration given to including a few simple and easy to install pressure and temperature sensors can provide for an easy method whereby flows and phase shifts can be evaluated. These flows and phase shifts can be plotted and compared with the design phasor diagram, thus providing particular insight to the performance of the compressor, transfer line, and inertance tube while providing additional information about unforeseen and often detrimental volumes within the system.

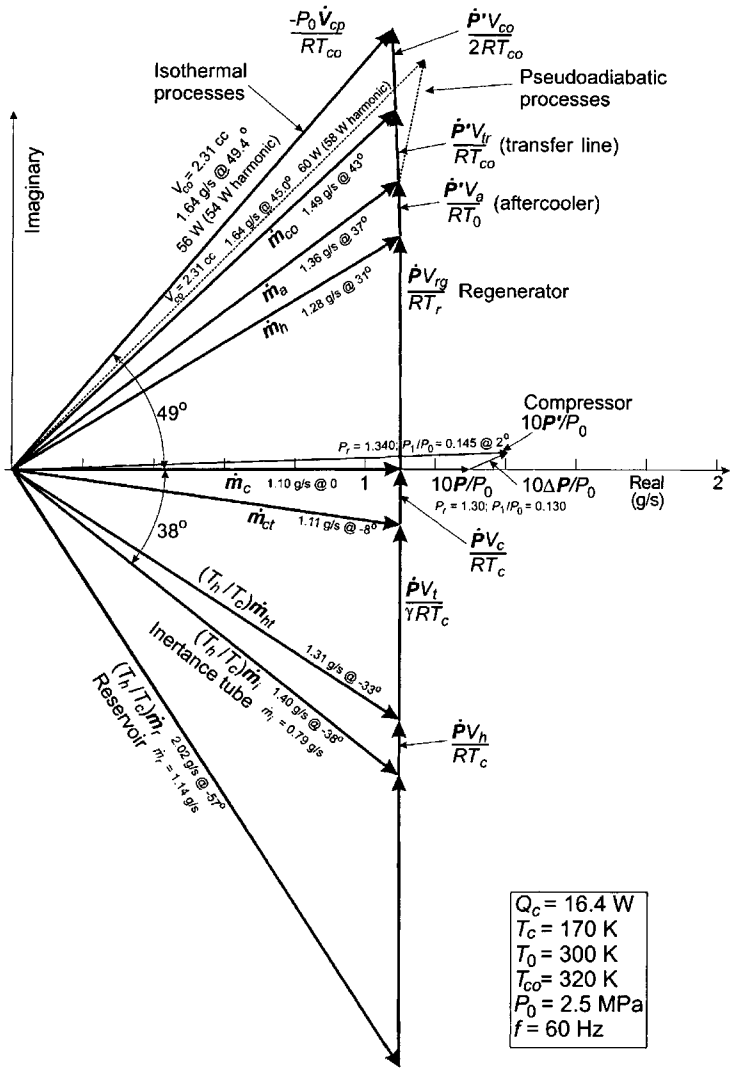

Figure 7. Design Phasor diagram for PT cooler.

Flow and Phase Shift Measurements

To evaluate the system we desire flow and phase shifts for the compressor, aftercooler, warm end of the pulse tube, and the reservoir. These can easily be found by installing sensors as follows. Pressure sensors (usually piezoresistive type) should be located at or near the transfer line leading from the compressor to the coldhead/aftercooler, the warm end of the pulse tube, and the reservoir. Temperature sensors should be placed on the compressor, transfer line, aftercooler, cold end of the pulse tube, and the reservoir (these can range from thermocouples for room temperatures to platinum resistance temperature detectors or diode thermometers at the cold temperatures depending upon the accuracy desired). For the ambient temperatures type E thermocouples were employed at the compressor, reservoir, aftercooler, and transfer line. Diode thermometers were employed at the coldhead and type T thermocouples were employed within the CryoPens.

The measurements we need are as follows. First we measure the phase between the pressure at the compressor and the warm end of the pulse tube. The value is rather low (at 2° to 4° for this

system) which can be measured using a lock-in amplifier or an oscilloscope. Second the phase between pressure and the mass flow at the piston of the compressor must be measured. Because mass flow $\dot{m}$ is in phase with the volume flow $\dot{V}$, the phase between flow and pressure can simply be measured as the phase between the volume flow and the pressure at the compressor. The pressure is measured from the piezoresistive pressure transducer, while $\dot{V}$ is measured from the laser position sensor. With a measured $\dot{V}$, combined with the temperature of the compressor along with the average pressure at the compressor a value for the mass flow at the piston face of the compressor (with or without coldhead) is calculated from;

$$\left|\dot{m}_{comp}\right| = 2\pi f \left|V_{comp}\right| \rho = \frac{2\pi f \left|V_{comp}\right| P_{mean}}{ZRT_{comp}}, \tag{1}$$

where f is the frequency of operation, $|V_{comp}|$ is the amplitude of the volume variation, P_{mean} is the average pressure at the compressor, Z is the compressibility factor for helium (=1), R is the gas constant, and T_{comp} is the temperature of the compressor.

We now need to determine the mass flow and phase angle for the reservoir with respect to pressure at the warm end of the pulse tube. Using either a lock-in amplifier (or suitable oscilloscope) to measure the pressure amplitude along with a known reservoir volume, operating frequency, and temperature of the reservoir the mass flow at the reservoir is found from;

$$\left|\dot{m}_{res}\right| = \frac{2\pi f \left|P\right| V_{res}}{\gamma R T_{res}}, \tag{2}$$

where f is the frequency of operation, $|P|$ is the amplitude of the pressure in the reservoir, V_{res} is the reservoir volume, γ is the ratio of specific heats, R is the gas constant, and T_{res} is the temperature of the reservoir. To plot on the system phasor diagram $|\dot{m}_{res}|$ must be multiplied by the temperature ratio T_h/T_c (see Ref. 2). The phase shift between the pressure at the pulse tube warm end and the reservoir is again found by employing a lock-in amplifier or suitable oscilloscope to measure the phase angle. Next, we measure the dead volume for the compressor: 1) with a cold head attached, V_{deadCH} and 2) without the cold head attached (referred to as blanked), $V_{deadBlank}$. These values are determined from the zero or null position about which the piston oscillates. Figures 8, 9, and 10 show the mass flow, dead volume, and derived phase angles.

Lastly, we calculate the average PV power delivered by the compressor to the coldhead. This is easy to accomplish since we measure the pressure at the compressor and the volume flow, $\dot{V}$ from the laser position sensor. From this we find the time averaged PV power to be;

$$\left\langle P\dot{V}\right\rangle = \frac{1}{\tau}\int_0^{\tau} P\dot{V}dt = \tfrac{1}{2}\left|P\right|\left|\dot{V}\right|\cos\theta \tag{3}$$

where τ is the period of one cycle, P is the dynamic pressure, $\dot{V}$ is the volume flow, and θ is the

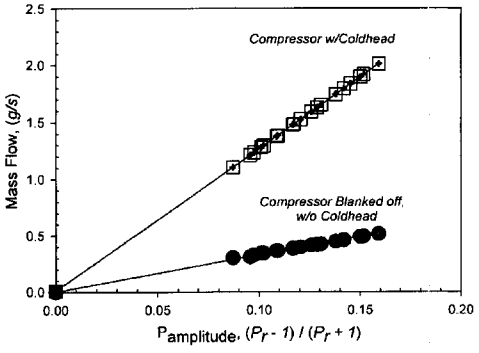

Figure 8. Mass flow at piston face of compressor.

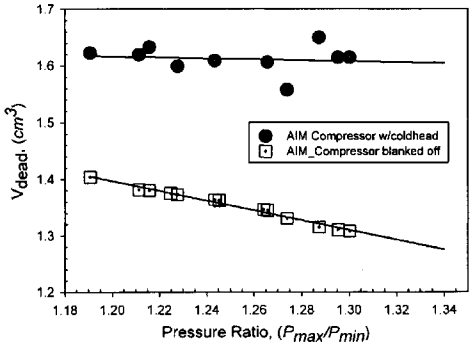

Figure 9. Dead volumes for compressor.

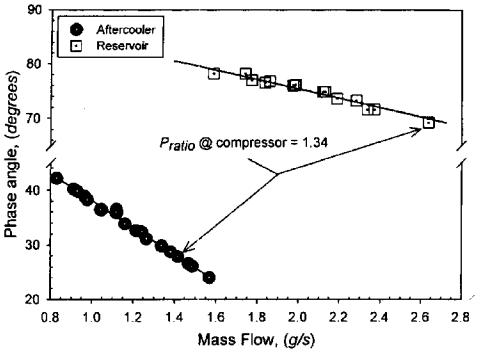

Figure 10. Phase angles measured.

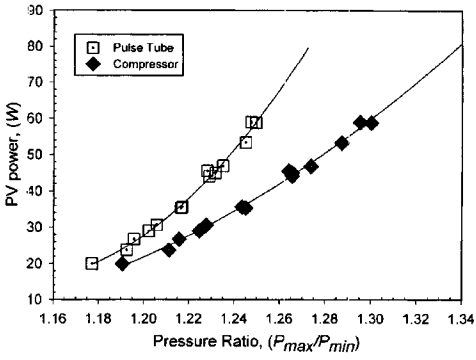

Figure 11. PV power from compressor.

phase angle between $\dot{V}$ and the pressure. From this we find the PV power required for a given pressure ratio as shown in Fig. 11.

Construct Phasor Model

Now we construct the phasor diagram using the convention that all phase angles are relative to pressure at the warm end of the pulse tube which aligns with the real axis. Because we want to measure only the major elements (ones that are easy to measure) we must lump some of the elements together for a more macroscopic comparison with the design phasor model. Thus, the phasors representing the rate of mass change in the regenerator, pulse tube, and inertance tube are lumped together while the phasors representing the rate of mass change in the volume due to the transfer line and compressor dead volume are lumped together as well. This simplifies the model which for comparative purposes proves quite valuable.

We construct the diagram for a design pressure ratio of 1.34 at the compressor. First a phasor representing the pressure for the compressor leading the pulse tube warm end pressure is drawn (see Fig. 12). Next we construct the phasor representing mass changes in volumes for the transfer line and dead volume of the compressor, (average volume on front side of the piston) the magnitude of which is found from correcting the $\dot{m}_{Blank}$ by multiplying by the ratio of the compressor dead

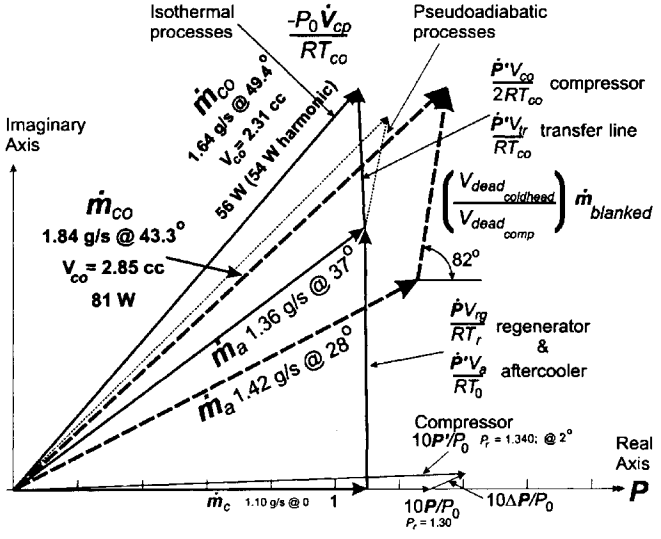

Figure 12. Phasor diagram for mass flow at aftercooler (dashed line).

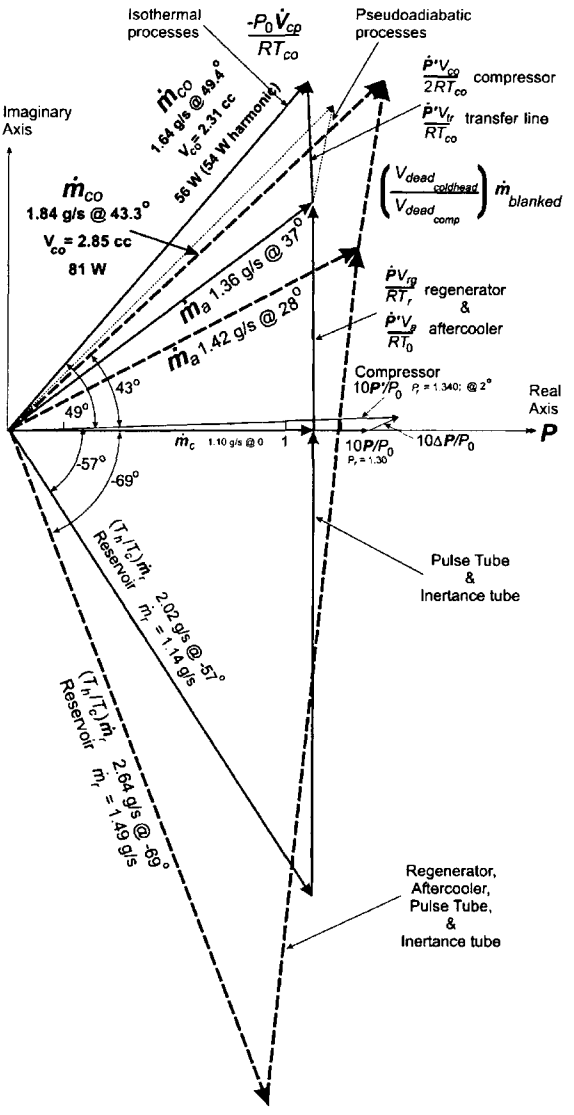

Figure 13. Complete phasor diagram for measured (dashed lines)and design (solid lines) flows and phase shifts.

volume, with coldhead attached, V_{deadCH} divided by the compressor dead volume for blanked off condition, $V_{deadBlank}$ as follows

$$\dot{m}_{corr} = \dot{m}_{blank} \frac{V_{deadCH}}{V_{deadBlank}}. \tag{4}$$

This phasor connects to phasor $\dot{m}_{co}$, which represents the mass flow at the piston face of the compressor (with coldhead attached) at the same phase angle with respect to the pressure at the compressor. Once this portion is constructed the $\dot{m}_{aftercooler}$ phasor is constructed from zero and connects to the start of the $\dot{m}_{corr}$ phasor. Now with trigonometry we calculate the magnitude and phase angle for $\dot{m}_{aftercooler}$ labeled as $\dot{m}_a$ in Figs. 7, 12, and 13.

The reservoir mass flow phasor, $\dot{m}_{res}$ is constructed similarly but its magnitude must be corrected by multiplying by a ratio of the warm and cold temperatures, (T_h/T_c). Now we construct the phasor that represents the lumped aftercooler, regenerator, pulse tube, and inertance tube by starting at the end of the reservoir mass flow phasor and connecting to the end of $\dot{m}_{aftercooler}$, the magnitude of which may be calculated with a little trigonometry. Figure 13 shows the completed diagram for design and measured flows and phase angles.

From the diagram we observe quite a phase shift for the mass flow into the reservoir indicating that we have a greater than expected phase shift from the inertance tube. We also see that greater power and mass flow is required from the compressor than expected, thus leading toward a pseudo-adiabatic process which is less efficient than the desired isothermal process. We also find that the volume estimates for the transfer line and the dead volume in the compressor are somewhat larger than that used in the model as well, though not significantly as evidenced from the cooler performance. The non-vertical nature of the phasor representing mass change in the aftercooler, regenerator, pulse tube, and inertance tube indicates loses due to irreversible heat transfer not accounted for in the simple phasor analysis.

CONCLUSIONS

We discussed a very simple method to evaluate a cryocooler by making a few easy measurements of key operating parameters which can then be used to model the behavior for the cooler. This model is very easy to construct and provides very valuable information to compare and evaluate the system, for the overall design as well as for individual key elements such as the compressor and inertance tube. It also provides valuable insight into undesirable volumes that are often introduced unintentionally. From this information valuable knowledge and improvement of the system can be made.

ACKNOWLEDGMENT

We gratefully acknowledge; Dr. Richard Rawlings and DRS Infrared Technologies for the compressor used in the first phase to optimize the pulse tube cryocooler, Dr. Ingo Ruhlich and AIM GmbH for the instrumented compressor used in the second phase to characterize the pulse tube cooler, and lastly CIMEX BioTech for their financial support.

REFERENCES

1. Storch, P.J., Radebaugh, R., and Zimmerman J.E., "Analytical Model for the Refrigeration Power of the Orifice Pulse Tube Refrigerator," NIST Technical Note 1343 (1990).
2. Gary J., Radebaugh R., "An improved numerical model for calculation of regenerator performance (REGEN3.1)," *Proceedings of Fourth Interagency Meeting on Cryocoolers,* David Taylor Research Center, Report DTRC-91/003, (1991), P. 165.
3. Schunk, L.O., Pfotenhauer, J.M., Nellis, G.F., Radebaugh, R., and Luo, E., "Inertance Tubes Optimization for kW-Class Pulse Tubes," *Adv. in Cryogenic Engineering*, Vol. 49B, Amer. Institute of Physics, Melville, NY (2004), pp. 1269-1276.

Development of a GM-Type Pulse Tube Refrigerator Cooling System for Superconducting Maglev Vehicles

Y. Kondo[1], M. Terai[1], Y. Nishikawa[1], O. Sugiyama[1], T. Inoue[2], A. Hirano[2], T. Goto[2], S. Fujii[2], Y. Jizo[3] and T. Amano[3]

[1]Central Japan Railway Company, Tokyo, 103-8288, JAPAN
[2]Aisin Seiki Co., Ltd, Kariya, Aichi, 448-8650, JAPAN
[3]Mitsubishi Electric Corp., Amagasaki, Hyogo, 661-8661, JAPAN

ABSTRACT

A superconducting maglev train is an innovative transportation system in which trains are levitated and driven at speeds of up to 311 mph. The Central Japan Railway Company and Japan Railway Technical Research Institute have developed and have been operating maglev trains on the Yamanashi Maglev Test Line for several years.

The superconducting coils of the maglev vehicles are cooled by liquid helium, and the radiation shields of the magnets are cooled using liquid nitrogen. Currently, Gifford-McMahon and Stirling refrigerators are used in the cooling system of the maglev vehicles. However, in recent years pulse tube refrigerators have been developed. It is expected that this type of refrigerator will be able to reduce the cost of both maintenance and production.

The Central Japan Railway Company, Aisin Seiki Co., Ltd., and Mitsubishi Electric Corporation have developed an 80 K GM-type pulse tube refrigerator as a recondenser for the liquid nitrogen used to cool the radiation shield plates of the magnets. The pulse tube refrigerator has achieved a cooling power of 170 W at 80 K and has operated safe and stably under the on-board conditions of the maglev running tests.

We have been operating this cooling system on the maglev vehicle for the last ten months. As a result, it has been proven that the pulse tube refrigerator is applicable to the maglev cooling system for practical use. The results also show that the pulse tube refrigerator can possibly be applied to the 4K-level cooling system for the maglev vehicle.

INTRODUCTION

The superconducting maglev train is an innovative transportation system in which trains are levitated and driven at speeds of up to 311 mph. The Central Japan Railway Company and the Japan Railway Technical Research Institute have developed and have been operating maglev trains on the Yamanashi Maglev Test Line since April 1997. The Yamanashi Maglev Test Line, which is 11.4 miles long, has several features presumed to be included in a commercial line; these include tunnels, curves and slopes. Tunnels, in particular, occupy 90% of the entire test line. The minimum

Cryocoolers 13, edited by R. G. Ross, Jr.
Springer Science+Business Media, Inc., New York, 2004

radius of the curve is five miles with 10 degrees superelevation. The steepest slope is 4% (about 2.3-degrees). In this test line, the maglev train attained a world record with its maximum railway speed of 361 mph. The cumulative distance covered by the train has reached 213,000 miles, and the number of people who have experienced a test ride has exceeded 65,000.

From the operational test results obtained to date, the prospective technical and economic performance has been estimated, and it has become clear that we must address three main issues. These are the verification of the reliability and durability over long-term operation, the reduction of initial/operational cost, and improvement of the aerodynamic characteristics of vehicles.

The superconducting magnets of the maglev vehicles have been cooled by 4 K and 80 K refrigerators. Currently, Gifford-McMahon and Stirling refrigerators are applied in the cooling system. These refrigerators have been safely and stably operating under the on-board conditions for seven years. However, these refrigerators need maintenance once a year, with high maintenance costs. It generally takes about two weeks or more for the maintenance.

On the other hand, pulse tube refrigerators have made remarkable progress in recent years. It is expected that this type of refrigerator will be able to reduce the costs of both maintenance and production.

THE SUPERCONDUCTING MAGNET AND ITS COOLING SYSTEM ON THE MAGLEV VEHICLES

Liquid helium and liquid nitrogen are used for cooling the superconducting coils and the radiation shields of the magnets of the maglev vehicles. Operation of the superconducting magnets without the need for a continual resupply of liquid helium and liquid nitrogen was achieved through the use of on-board refrigerators that have a large cooling capacity.

To meet the future needs of maglev vehicles, the on-board refrigeration system for the magnets should have the following attributes:

1. Achieve highly reliable operation in severe environments such as magnetic fields, vibration, humidity, and variable ambient temperature.
2. Be consistent with the limited space and weight to be allowed in the vehicle.
3. Meet restrictions on allowable on-board power supply and consumption.
4. Have excellent cost performance and long-term operation without maintenance for about 10,000 hours or longer.

Figure 1 shows a schematic drawing of the superconducting magnet and refrigeration system of the maglev vehicles. The magnets have four superconducting racetrack-shape coils cooled with liquid helium and radiation shield plates cooled with liquid nitrogen. The liquid helium is kept liquid by a two-stage 4 K GM/JT refrigerator, and the liquid nitrogen is kept liquid by a single-stage

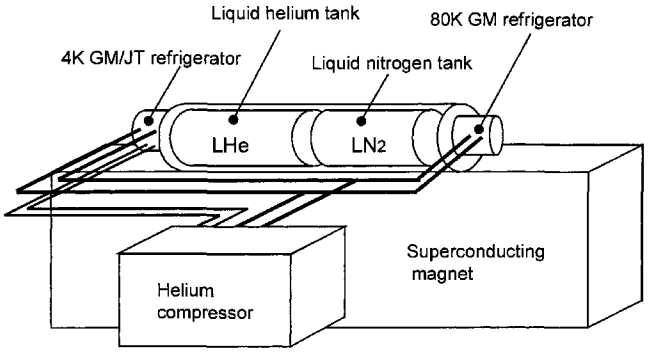

Figure 1. Schematic drawing of superconducting magnet and refrigeration system.

Table 1. Provisional specification of pulse tube refrigerator for the maglev.

80 K cooling power	> 150 W
Circulating mass flow rate	4 g/sec
Tolerable acceleration	±10 G
Tolerable magnetic field	0.06 T
Ambient temperature	-20 °C ~ 40° C
Mean time between maintenance	> 10,000 hours

80 K GM refrigerator. High-pressure helium is supplied to both refrigerators by a common compressor unit mounted on the body of the vehicle. The flow rate balance must be adjusted because of the common use of the compressor for the 4 K and 80 K refrigerators.

DEVELOPMENT OF A GM-TYPE PULSE TUBE REFRIGERATOR FOR MAGLEV VEHICLES

In recent years, pulse tube refrigerators have been developed and improved. It is believed that pulse tube refrigerator will be the next generation refrigeration system for most of cryogenic applications. This type of refrigerator is expected to reduce the costs of maintenance and production because of the lack of a displacer and having a simpler structure.

The Central Japan Railway Company, Aisin Seiki Co., Ltd., and Mitsubishi Electric Corporation originally planned to apply pulse tube refrigerators to the maglev vehicles. However, there was no pulse tube refrigerator that satisfied the required specifications for maglev use at that time. As a first task, we constructed an 80 K GM-type pulse tube refrigeration system and performed experiments and examinations evaluating the components of the pulse tube refrigerator. Table 1 shows the provisional specifications that were set up from requirements for maglev use.

Increasing Cooling Power of the Refrigerator

We studied ways to increase the cooling power of the refrigerator to more than 150 W at 80 K as a target value. The effort was focused on optimization of the shape and volume of the pulse tube, regenerator, and buffer tank, adjustment of the opening-and-closing time of the pressure switching valve, and improved heat removal in the vicinity of the hot end of the pulse tube.

Firstly, several trial products that had different shapes and sizes were manufactured; then the optimal shape and size were determined by operational tests. The optimal opening-and-closing time adjustment of the pressure switching valve was determined by repeated trial and error. For improved heat removal at the hot end of the pulse tube wall, high-pressure helium gas was used; this was provided from the compressor through a pressure switching valve unit. These design changes gained an additional cooling power of 45 W and enabled the refrigerator to satisfy the target value.

Improvement of the On-Board Refrigerator Performance in Severe Conditions

The on-board refrigerator is required to safely operate in severe conditions, such as vibration, magnetic fields, humidity and variable ambient temperature. Some improvements of this refrigerator have been performed in order to operate under these severe conditions.

The thermally insulated support of a pulse tube cold end was improved to tolerable vibration based on vibratory examinations. This improvement enabled the refrigerator to operate safely at 10 G acceleration up to a frequency of 350 Hz.

The magnetic shield was then developed considering the magnetic field distribution near the motor of the pressure switching valve unit. This shield enabled the refrigerator to operate safely just above the superconducting magnet.

The effect of atmospheric temperature on the cooling performance of the refrigerator was made clear by temperature environmental examinations. The results of these examinations proved that the pulse tube refrigerator satisfied the specifications of the maximum expected temperature.

Furthermore, because the maglev system has characteristic track conditions, the on-board pulse tube refrigerator is inclined in the running tests. Therefore the inclined pulse tube was examined and sufficient cooling capability was confirmed in the refrigerator.

Availability of the Refrigerator

Availability of refrigerator means reducing the ratio of the non-operating time for maintenance work to the operating time. Improvement of the availability includes lengthening the maintenance interval, and shortening the time of the maintenance work. Generally, since there is no displacer in the pulse tube refrigerator, there is minimal wear of its seal ring in the low-temperature level, and therefore minimal contamination into the regenerator by powder fragments of seal ring wear. Therefore the maintenance interval of the pulse tube refrigerator can be made longer than that of a GM refrigerator.

This pulse tube refrigerator was able to achieve mean time between maintenance 10,000 hours or longer by improving the durability of the frictional parts of the pressure switching valve that were the only wearing parts. The poppet-type valves have been applied to the pressure switching valve since it has a longer life-span than a conventional rotary-type valve.

Moreover, in order to shorten the time of maintenance and to reduce liquid helium loss caused by the refrigerator stopping due to maintenance, the refrigerator was designed to enable maintenance without raising the temperature of the superconducting magnets. To achieve short and easy maintenance, the refrigerator was outfitted with self-sealing, quick-disconnect couplings to the pressure switching valve unit and to the pulse tube and buffer tanks; this allows easy change-out of the entire pressure switching valve. As all of the connection ports are made with self-seal type couplings, atmospheric gases do not contaminate the refrigerator inside during maintenance.

As a result of these design features, the maintenance time for the pulse tube refrigerator has been significantly shortened from that required by the GM refrigerator.

The Refrigerator Manufactured as a Result of Development

As a result of the various kinds of experimental investigations and trial production, the development of the on-board 80 K GM-type pulse tube refrigerator was successful. Figure 2 shows a schematic drawing of the developed refrigerator system.

This refrigerator has a recondenser of nitrogen in the cold end of regenerator, and a heat exchanger cooled by helium gas in the hot end of pulse tube wall. The interface to the liquid nitrogen tank is completely identical to that of the 80 K GM refrigerator. Although the GM refrigerator was inserted horizontally, the pulse tube refrigerator is set vertically to avoid a loss caused by

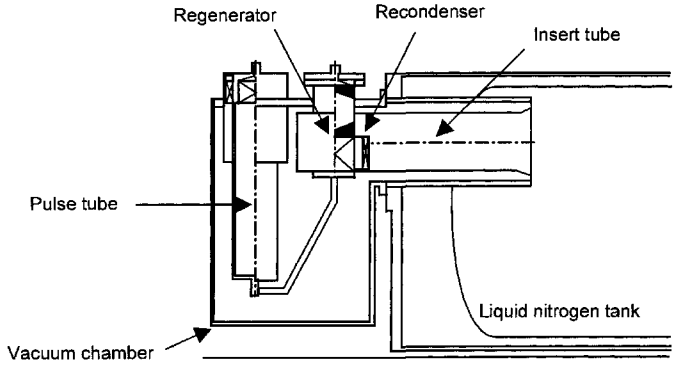

Figure 2. Schematic drawing of 80 K GM-type pulse tube refrigerator.

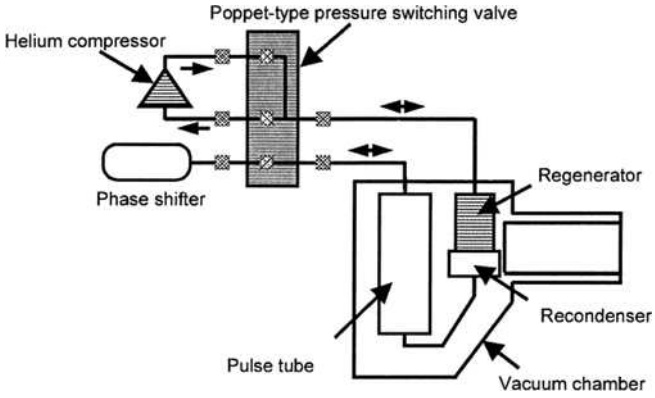

Figure 3. Flow diagram of pulse tube refrigerator.

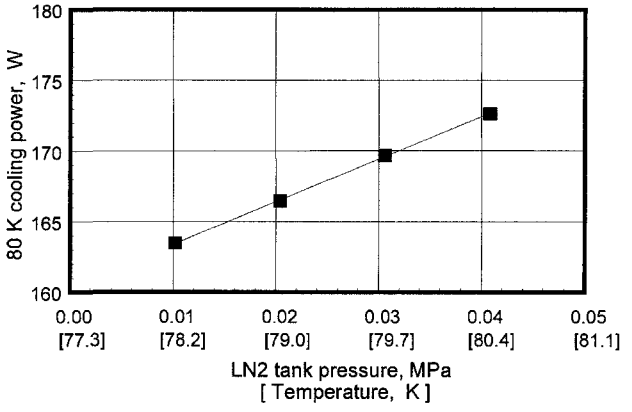

Figure 4. Cooling performance of pulse tube refrigerator.

natural convection in the pulse tube. The pressure switching valve unit, which has a phase shifting mechanism, is set next to the refrigerator, and connected with pipes.

Figure 3 shows the flow diagram of this refrigerator, while Fig. 4 shows the cooling performance of the refrigerator. As seen, the refrigerator has 170 W at 80 K of recondensation capability when using a GM refrigerator compressor, which is more than the target value. When the condition of gas flow and pressure was optimized in a heater load examination, the highest performance was more than 200 W.

RESULTS OF ACTUAL OPERATION ON THE YAMANASHI MAGLEV TEST LINE

Since the development of the 80 K pulse tube refrigerator was successful, we attached the refrigerator on a maglev vehicle to operate for practical use on the Yamanashi Maglev Test Line. This refrigerator was transported to the Yamanashi Maglev Test Line in May 2003, where initial checkout and operational adjustments were performed. The refrigerator has been operating smoothly, without any unfavorable influence on the combined operation of the 4 K GM/JT refrigerator. It was certified that this refrigerator had 170 W of cooling power at 80 K. In the operation of the refrigerator in magnetic fields, the waveform of the buffer tank pressure and the pressure of the nitrogen tank were measured, and they were compared for the conditions of energized and non-energized superconducting magnets. Since the results did not differ for these two conditions, the refrigerator was confirmed to operate smoothly in the magnetic fields of the maglev vehicle.

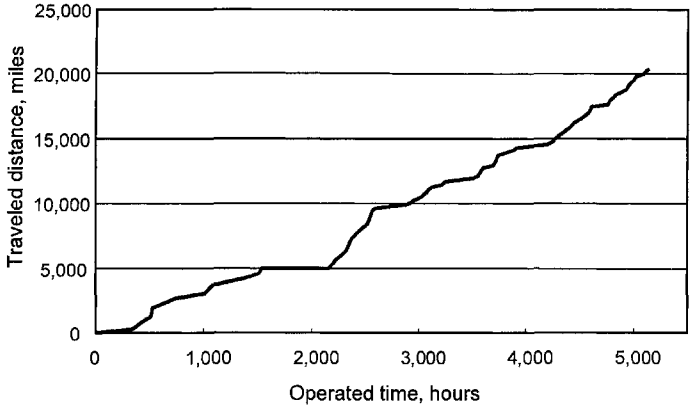

Figure 5. Traveled distance of pulse tube refrigerator.

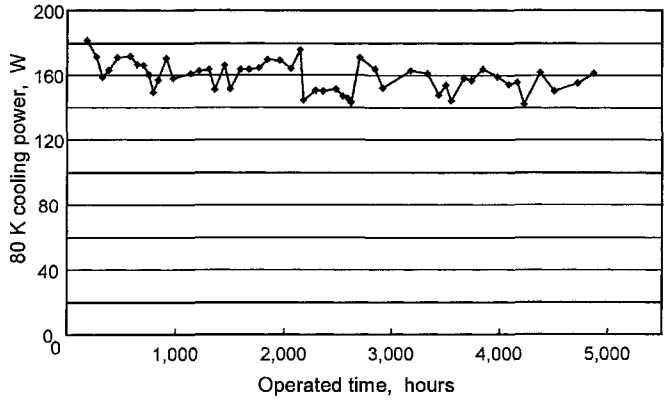

Figure 6. Long-term cooling power of the pulse tube refrigerator.

The vehicle running tests using this refrigerator on-board started in June 2003. The basic performance of the refrigerator, such as the cooling power, pressure waveforms of the buffer tank, and nitrogen tank pressure under vehicle running conditions were checked for speeds up to the maximum speed of 311.5 mph. Consequently, the operation stability of this refrigerator has been certified in actual vehicle running conditions in terms of the magnetic fields, vibration, track conditions of curves and slopes, acceleration, and deceleration. Furthermore, the maximum speed was increased up to 342.3 mph on October 29.

The long-term operation of the refrigerator has been monitored continuously from the start of operation, and, as of March 1, 2004, operation time has exceeded 5,200 hours without any problems. Figure 5 shows the distance traveled by the maglev vehicle carrying the pulse tube refrigerator, up to March 1. The total traveled distance amounts to more than 21,000 miles.

The variation of cooling power during the long-term operation is shown in Fig. 6. This refrigerator has had stable cooling power of 150 W or more, and its cooling power did not decrease as operation time passed and traveled distance was extended.

CONCLUSION

An 80 K GM-type pulse tube refrigerator for the maglev vehicle was developed successfully, satisfying specifications. Based on actual vehicle running tests carried out on the Yamanashi Maglev Test Line, it was confirmed that this refrigerator could be used for the cooling system of the super-

conducting magnets on-board the maglev vehicle at speeds of over 311 mph. The continuous operation of this refrigeration system was satisfactory even after over 5,000 hours of operation.

REFERENCES

1. N. Shirakuni et al., "Overview of new vehicles for the Yamanashi Maglev Test Line," *Proceedings of the 17th International Conference on Magnetically Levitated Systems (Maglev 2002),* 2002.
2. S. Fujimoto et al., "Development of 4K GM/JT Refrigerator for Maglev Vehicle," *Proceedings of the 16th International Cryogenic Engineering Conference / International Cryogenic Materials Conference,* Part1 (1996), pp. 331-334.
3. H. Nakao et al., "Development of the New Type On-board GM Refrigeration System for the Superconducting Magnet in Maglev Use," *Proceedings of the 15th International Conference on Magnetically Levitated Systems (Maglev'98),* 1998, pp. 250-255.
4. H. Nakao et al., "Developments of a Superconducting Magnet and an On-Board GM Refrigeration System for Maglev Vehicle," *Proceedings of the 15th International Conference on Magnet Technology,* 1997.

High-Power Pulse Tube Cryocooler for Liquid Xenon Particle Detectors

T. Haruyama[1], K. Kasami[1], Y. Matsubara[2], T. Nishitani[3], Y. Maruno[3], K. Giboni [4] and E. Aprile[4]

[1]KEK, High Energy Accelerator Research Organization
Oho, Tsukuba, Ibaraki 305-0801, Japan

[2]Nihon University
Funabashi, Chiba 274-0063, Japan

[3]Iwatani Industrial Gases Corp.
Moriyama, Shiga 524-0041, Japan

[4]Columbia University
New York, USA

ABSTRACT

A high-power and high-temperature pulse tube cryocooler has been developed for xenon liquefaction and re-condensation for high-energy particle detectors. To meet a cooling power requirement of around 70 W at 165 K, KEK and Nihon University have developed a co-axial pulse tube cryocooler with a configuration of inside regenerator.

This proto-type cryocooler has been used for a liquid xenon calorimeter, which detects the scintillation light energized by incoming γ-rays. The obtained cooling power is 70 W at 165 K by using a 2.2 kW GM-type compressor, and 120 W by using a 4.8 kW compressor.

The basic technology of this coaxial pulse tube cryocooler with an inside-regenerator has been transferred to Iwatani Industrial Gases Corp (IIGC). IIGC fabricated a manufacture-level high quality cryocooler for a dedicated liquid xenon time projection chamber (TPC) at Columbia University in New York. This Iwatani-cryocooler has about 90 W of cooling power at 165 K by using a 3 kW compressor.

Since a very clean liquid xenon atmosphere must be kept in this particle detector, the cold fin of the cryocooler is not directly reaching into the chamber, but installed on its outside. The cold stage of the cryocooler is attached to a copper plate, which works as an isolation flange and also as a re-condenser for evaporated xenon gas. Without liquid nitrogen, all the cooling procedures starting with initial cool-down, followed by xenon liquefaction and re-condensing operations were successfully completed without any troubles and difficulties.

INTRODUCTION

Recently, large-scale liquid xenon calorimeters have been proposed and fabricated for specific physics experiments, because of the fast response, large atomic number and high sensitivity of liquid xenon.[1] So called, MU-E-GAMMA (MEG), which detects rare muon decay has been

Cryocoolers 13, edited by R. G. Ross, Jr.
Springer Science+Business Media, Inc., New York, 2004

approved[2] and a lot of R&D experiments have been carried out.[3] A liquid xenon dark matter search experiment has also proposed.[4] The key technology of these experiments lies in cryogenic engineering including xenon liquefaction and re-condensation to keep the liquid state for long-term physics experiments, typically a few years. There are several ways to liquefy and re-condense xenon gas for long-term physics experiments. Conventionally, liquid nitrogen (LN_2) has been used for this purpose because of its simplicity. However, this method has disadvantages regarding temperature and pressure stability of the liquid xenon. It also wastes much LN_2 because of its inefficiency, and the handling of a cryogenic fluid might be troublesome in some cases.

The idea to apply a pulse tube cryocooler in place of liquid nitrogen has been proposed and experimentally realized.[5] The cryocooler has no moving parts in the low-temperature stage, resulting in no vibration and ensuring highly reliable long-term operation. An in-house pulse tube cryocooler has been operating to meet the requirement for canceling the heat load in a large prototype LXe calorimeter for the MEG experiments. The basic technology of this cryocooler has been transferred to Iwatani Industrial Gases Corp (IIGC). They fabricated a manufacture-level high quality cryocooler for the liquid xenon dark matter time projection chamber (TPC) development at Columbia University in New York.

Since this TPC requires a very clean xenon atmosphere, the cryocooler was installed outside of the inner xenon chamber as a "built-in" cryocooler. The cold stage of the cryocooler is attached to a copper plate, which works not only as the isolation flange, but also as a re-condenser for evaporated xenon gas. The initial cool-down, xenon liquefaction, and gas re-condensing were repeatedly completed without any troubles or difficulties.

LIQUID XENON PARTICLE DETECTORS

Property of liquid xenon

The detailed properties of xenon are given in Table 1.[6] It must be noted that xenon has a three times higher density than that of water, and a very narrow temperature margin between the triple point and saturated liquid temperature under atmospheric pressure. These properties imply the importance of temperature control during liquefaction and re-condensation. In these calorimeters a large number of photomultiplier tubes (PMT) are directly immersed into liquid xenon, and therefore solidification of xenon by accidental overcooling could cause permanent damage to the delicate PMTs. As shown in Table 1, the temperature margin between the liquid and solid phases is 3.4 K, and the latent heat for solidification is ~1/100 of that of liquefaction. These characteristics are important when a liquid xenon cryostat and refrigeration schemes are designed.

In addition to the physical properties of liquid xenon, we also investigated the heat transfer characteristics, such as convection and boiling heat transfer for the design of the calorimeter.[7]

Cooling requirements for particle detectors

The main purpose of developing a pulse tube cryocooler is to eliminate the consumption of liquid nitrogen during long-term normal operation, such as data taking. Since physics experiments will be kept running for a few years and more, cryocooler operation will make the maintenance of experiments much easier.

Table 1. Physical properties of liquid, gas xenon and liquid nitrogen

Property	LXe (saturated)	GXe (saturated)	LN_2 (saturated)
T(K): temperature	164.78	164.78	77.35
P(MPa): pressure	0.100	0.100	0.1013
Lv (kJ/kg): latent heat (liquid)	95.8	--	199.1
Ls (kJ/kg): latent heat (solid	1.2	--	28.4
Cp(kJ/kgK): specific heat	0.3484	173.4	2.03
ρ(kg/m^3): density	2947	9.883	804
T(K): / P(MPa): Triple point	161.36 / 0.0815	--	63.148 / 0.0125

In case of the MEG experiments, the heat load of the final liquid xenon calorimeter is estimated to about 130 W at 165 K including heat dissipated by 1000 PMTs, conduction heat leak through a thousand of signal cables and static heat load to the cryostat. A large prototype calorimeter has been constructed to study the sensitivity and stability of operation of a liquid xenon cryostat equipped with immersed PMTs. The system uses 120 L of liquid xenon and has 250 PMTs. The total heat load of this calorimeter is estimated to be about 52 W at 165 K.

The pulse tube cryocooler was designed with a cooling capacity of about 65 W at 165 K to meet the heat load of the xenon calorimeter. A re-condenser attached to the cold stage of the pulse tube cryocooler was directly located in the xenon atmosphere to enhance heat transfer performance. In this case, the most serious contaminant is water because of its strong absorption of the vacuum ultra violet light in liquid xenon.

For the dark matter proto-TPC at Columbia University, a heat load of the final detector is almost the same as that of the MEG calorimeter. Because the dark matter detector is very sensitive to many contaminants, such as water and oxygen, it requires ultra clean atmosphere. And so, we chose a way to install the cryocooler outside of the inner chamber. The cold stage of the cryocooler is attached to the copper plate, which works not only as isolation flange but also as re-condenser for evaporated xenon gas. More details are described later.

PULSE TUBE CRYOCOOLER

Coaxial configuration

The design criteria for the pulse tube cryocooler are the following: (1) a large cooling power at relatively high temperature around 165 K, (2) a simple procedure for assembly and maintenance and (3) compactness for space saving. To evaluate the cooling performance of this pulse tube cryocooler, we used a simulation code, so-called 'equivalent PV work' program code developed by one of the co-authors.[8] We calculated the cooling power to 65 W at 165 K under an assumption of using a 1.5-2 kW GM-type compressor.

A prototype pulse tube cryocooler was then fabricated and tested at KEK. It delivered a design cooling power of 70 W with a 2.2 kW GM-type compressor. Then, this technology has been transferred to Iwatani Industrial Gases (IIGC) to achieve much higher reliability and cooling performance. Figure 1 shows a conceptual drawing of the refrigerator designed and manufactured by IIGC.

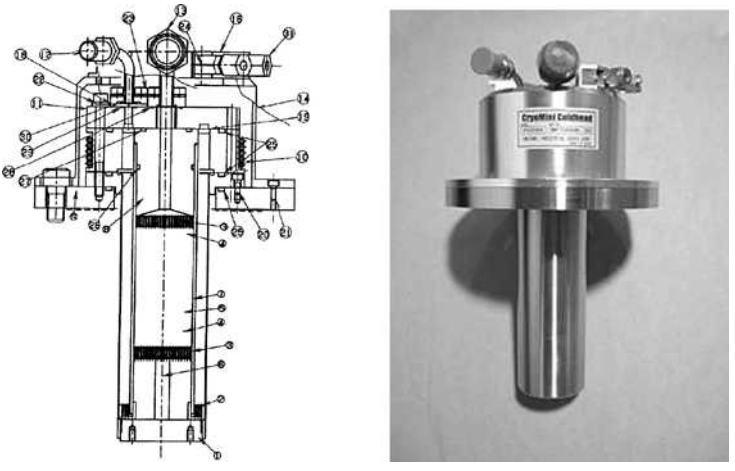

Figure 1. A conceptual drawing (left) and a picture (right) of the pulse tube cryocooler designed and fabricated by Iwatani Industrial Gases Corp.

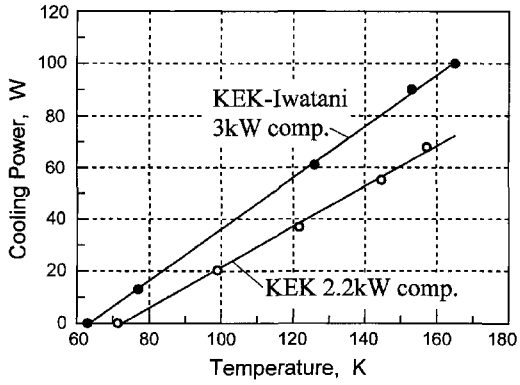

Figure 2. Cooling power of KEK-Iwatani pulse tube cryocooler operated by a 3 kW compressor. Original KEK cryocooler performance is also shown.

The diameter of the regenerator is 40 mm and the length is 80 mm. The regenerator is placed inside of a thin stainless pipe with 60 mm outer diameter, 0.5 mm wall thickness and 160 mm length. The gap between the outer pipe and a glass fiber reinforced plastic (GFRP) regenerator pipe works as a pulse tube. The cold-end heat exchanger was designed to absorb a relatively high heat load of about a few hundred watts.

To ensure a high cooling power, the cold-end heat exchanger was made of copper with 40 mm diameter. Forty radial slits with 0.3 mm width were machined in order to get enough heat exchanging surface area. A regenerator pipe was made from a GFRP cylinder of 40 mm diameter and 2 mm thickness. About 1000 sheets of #200 stainless steel mesh were stacked in the cylinder. A heater-mount with MINCO thermo-foil heaters[9] was attached and fixed by screws at the end of the cold stage for cooling power test and temperature control.

Cooling Power in Vacuum

An Iwatani GM-type CW404 water-cooled helium compressor was used for the cooling performance test. It was operated with an input power of 3.0 kW at 60 Hz. A 1000 cm^3 buffer tank and a rotary valve unit were connected to the cold head by 10 m long flexible hoses for the performance test. The hot end of the cold head was cooled by chilled water during the test. The timing of high-pressure charge and low-pressure expansion was controlled by the rotary valve operating system. The operating frequency was optimized by measuring the resulting lowest temperature at various frequencies. The frequency was changed between 2.4 and 3.6 Hz under a simple orifice mode keeping the orifice valve setting constant. The lowest temperature was obtained at an operating frequency of 2.4 Hz.

Cooling power measurement was carried out in a vacuum chamber. Figure 2 shows the obtained cooling power characteristics at several temperatures. The lowest temperature was about 63 K, and a cooling power of about 100 W was achieved at 165 K by using a 3 kW compressor. A calculated coefficient of performance (COP) is nearly 3%, which is similar to that of the original KEK cryocooler operated with a 2.2 kW compressor. The relationship between cooling power and temperature is well described by a straight line. This means that the cold end heat exchanger is capable to absorb more than 100 W.

PERFORMANCE TEST OF DARK MATTER PROTO-TPC

Preliminary Cooling Operation

Figure 3 shows the conceptual drawing of the prototype liquid xenon TPC at Columbia University with the pulse tube cryocooler. To ensure an ultra pure liquid xenon environment, the cold stage of the cryocooler is attached to the copper plate, which works as an isolation flange. Inside the

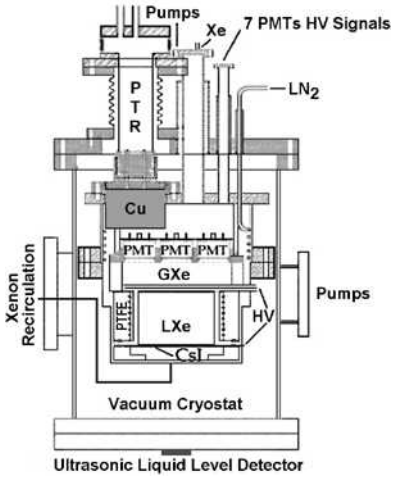

Figure 3. Schematic drawing of LXe proto-TPC at Columbia University with a "built-in cryocooler."

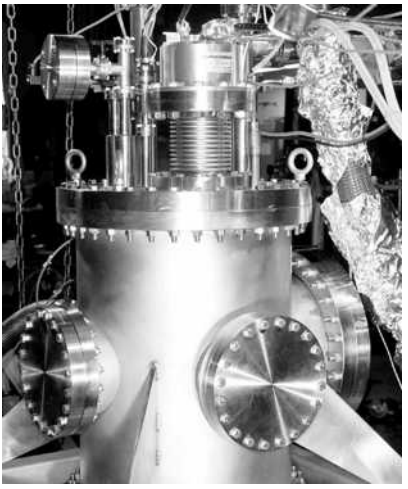

Figure 4. Picture of LXe dark matter proto-TPC.

chamber, a copper cylinder attached to the flange works as a re-condenser of evaporated xenon gas. The bellows shown in the figure is used to absorb thermal expansion of the pulse tube during operation. Figure 4 shows a picture of the chamber with the cryocooler. The bellows between the chamber and cryocooler can be seen.

A preliminary cooling test was carried out to verify the performance of the detector during operation with the cryocooler. After evacuation down to ~10^{-5} Pa, xenon gas was filled up to 0.2 MPa, and the cryocooler was operated for pre-cooling for about 12 hours. Then, only by using the cryocooler, 3 liters of liquid xenon were liquefied in the chamber. Once liquefied, a part of the gas was extracted, circulated through a purifier before re-condensing.

A rough estimate of the heat budget during the preliminary test is as follows: cooling power for cooling and re-condensing of circulating gas with 0.46 g/sec is 52 W; heater input to keep the cold stage temperature constant (about 170 K) is 24 W; heat leak into the chamber is 18 W.

The xenon temperature was kept constant within +/- 0.025 K by controlling the cold head with a Lakeshore Cryogenics temperature controller, model 340.[10] These tests were successfully repeated several times without experiencing any problems. During one of the tests the detector was operated continuously for about three weeks.

SUMMARY

A high-power and high-temperature pulse tube cryocooler was originally developed by KEK and Nihon University for xenon liquefaction and re-condensation in high-energy particle detectors.

The basic technology of this coaxial pulse tube cryocooler has been transferred to Iwatani Industrial Gases Corp., and a manufacture-level high quality cryocooler was fabricated and tested in a dedicated liquid xenon experiments at Columbia University in New York. It is confirmed that the Iwatani-cryocooler has about 100 W of cooling power at 165 K by using a 3 kW compressor. The cryocooler was isolated by a copper flange from the high purity liquid xenon in order to avoid contamination of the liquid with impurities. The copper flange also works as the thermal path for re-condensing evaporated xenon gas. A preliminary performance test as the cryocooler-equipped chamber was carried out successfully for over 3 weeks. The temperature stability of the liquid was measured to +/-0.025 K.

ACKNOWLEDGMENT

The authors would like to thank Prof. T. Doke and Dr. K. Terasawa of Waseda University for their useful comments and helpful arrangement. They also thank all the staff at Columbia's Nevis Laboratories for experimental setup and data taking during the first cooling test. They thank Mr. H. Inoue of the Mechanical Engineering Center at KEK for machining the prototype pulse tube cryocooler.

REFERENCES

1. Doke, T., et al., "Present status of liquid rare gas scintillation detectors and their new application to gamma-ray calorimeters," *Nucl. Instru. and Meth.* A420 (1999) pp. 62-80.
2. Mori, T., et al., Research Proposal to PSI. R-99.05.1, May 1999.
3. Mihara, S., et al., "Development of a liquid xenon photon detector – Toward the search for a muon rare decay mode at Paul Scherrer Institute" (in Japanese), *Cryogenic Engineering,* 38 (2003), pp. 94-99.
4. Aprile, E., et al., "Xenon: A 1 tonne liquid xenon experiment for a sensitive dark matter search," *Proceedings of Xenon 01*, World Scientific, New Jersey (2002), pp. 165-178.
5. Haruyama, T., et al., "Cryogenic performance of a 120 L liquid xenon photon calorimeter," *Proceedings of 19th ICEC*, Narosa Publishing House, India (2003), pp. 613-616.
6. Jacobsen, R.T., et al., *Thermodynamic Properties of Cryogenics Fluids*, Plenum Press, New York, 1997.
7. Haruyama, T., "Boiling heat transfer characteristics of liquid xenon," *Advances in Cryogenic Engineering,* 47B, AIP, New York (2002), pp. 1499-1506.
8. Matsubara, Y., et al., *7th International Cryocooler Conference Proceedings*, Air Force Phillips Laboratory Report PL-CP--93-1001, Kirtland Air Force Base, NM, April 1993, pp. 166-186.
9. MINCO products, Inc., Minneapolis, MN, USA.
10. Lakeshore Cryogenics, Inc., Westerville, OH, USA.

Vibration-Free Pulse Tube Cryocooler System for Gravitational Wave Detectors, Part I: Vibration-Reduction Method and Measurement

T. Tomaru[1], T. Suzuki[1], T. Haruyama[1], T. Shintomi[1], N. Sato[1], A. Yamamoto[1], Y. Ikushima[2], R. Li[2], T. Akutsu[3], T. Uchiyama[3] and S. Miyoki[3]

[1]High Energy Accelerator Research Organization (KEK)
Tsukuba, Ibaraki, 305-0801, Japan
[2]Sumitomo Heavy Industries Ltd.
Nishitokyo, Tokyo, 188-8585, Japan
[3]Institute for Cosmic Ray Research (ICRR), The University of Tokyo
Kashiwa, Chiba, 277-8582, Japan

ABSTRACT

We developed a vibration-free cryocooler system based on a 4 K pulse tube (PT) cryocooler for a cryogenic interferometric gravitational wave detector. In this system, we incorporated a vibration-reduction system that consists of a firm support for the cold head and a rigid cold table thermally linked to the cold stage to reduce both the vibrations of the overall cold head and those of the cold stage. Our cryocooler system reduced the cold-head vibration of the baseline PT cryocooler by over three orders of magnitude, where the vibration level was on the order of $10^{-9}/f^2$ m/$\sqrt{\text{Hz}}$.

INTRODUCTION

A vibration-free cryocooler can be useful. In particular, it is essential in cryogenic interferometric gravitational wave detectors[1] where vibration of the optical mirrors is one of the sensitivity limitations of the detectors. Figure 1 shows a schematic diagram of the cooling system of the Cryogenic Laser Interferometer Observatory (CLIO)[2], which is a prototype cryogenic gravitational wave interferometer being constructed in Japan. An optical mirror is cooled by conduction cooling using a 'vibration-free' cryocooler. 'Vibration-free' can be defined as the seismic vibration level, since mechanisms of any type are always moved by seismic vibration. Such vibration can not be eliminated without the use of special vibration isolators. The requirement concerning the vibration of the cryocooler in the CLIO is the seismic vibration level in the Kamioka mine (the site of the CLIO) where the seismic vibration level is $10^{-9}/f^2$ m/$\sqrt{\text{Hz}}$. The required cooling power of the cryocooler is 15 W at 40 K for the first stage and 0.5 W at 4.2 K for the second stage.

Cryocoolers 13, edited by R. G. Ross, Jr.
Springer Science+Business Media, Inc., New York, 2004

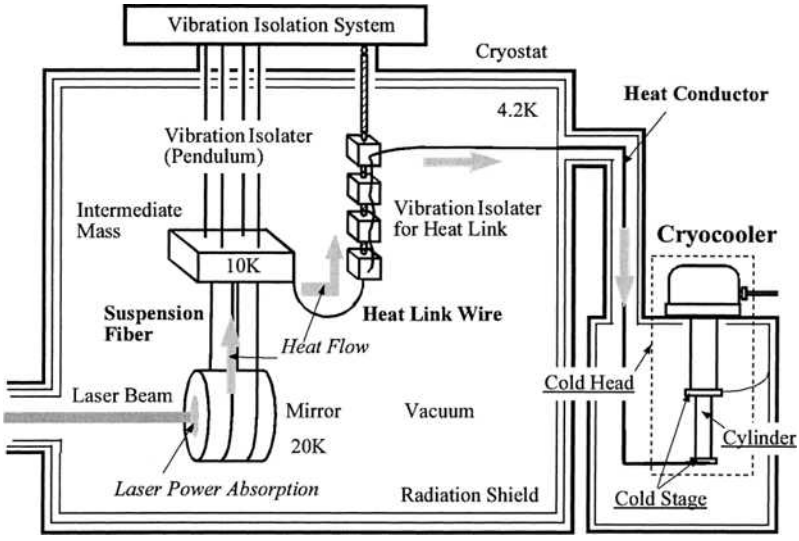

Figure 1. Schematic diagram of the mirror cooling system used in cryogenic interferometric gravitational wave detectors. Since the mirror has small laser power absorption (heat generation), it must be cooled continuously through heat links.

In our previous study[3], we confirmed that the vibration of a 4 K pulse tube (PT) cryocooler was much smaller than that of a 4 K Gifford-McMahon (GM) cryocooler.† However, even for the PT cryocooler, the observed vibration levels were too large for the requirement of the CLIO.

Therefore, we developed a vibration-reduction system for the PT cryocooler for the CLIO. In this system, vibrations of the overall cold head and the cold stage, which are different vibration components observed in our previous study, were reduced. The names of parts of the cryocoolers used in this paper are defined in Fig. 1.

In this paper, we report on the vibration-reduction method and the measurement for a vibration reduction of the overall cold head. Measurements of the cooling performance and the vibration reduction of the cold stage are reported elsewhere in this proceedings by Li.[4]

VIBRATION-REDUCTION SYSTEM

Investigation of Vibrations for a 4 K PT Cryocooler

Figure 2 shows vertical vibration spectra for a 4K PT cryocooler (SRP-052A, Sumitomo Heavy Industries Ltd.[5]) measured in our previous study.[3] The spectra can be described based on the displacement density[6], which is defined as

$$\tilde{x}(\omega)=\left[\lim_{T\to\infty}\frac{1}{T}\left|\int_{-T/2}^{T/2}x(t)\,e^{-i\omega t}\,dt\right|^2\right]^{1/2} \qquad \left[\mathrm{m}/\sqrt{\mathrm{Hz}}\right], \tag{1}$$

where ω is the angular frequency, T is the time length, and $x(t)$ is the displacement as a function of time.

† The vibration of the cold head for the 4K PT cryocooler was two orders of magnitude less than that of the 4K GM cryocooler. On the other hand, the cold-stage vibrations for both cryocoolers were at the same level. In this measurement, we used a setup of the PT cryocooler such that the rotary valve unit was separated from the cold head and they were connected by a rigid copper tube, which was anchored onto the ground.

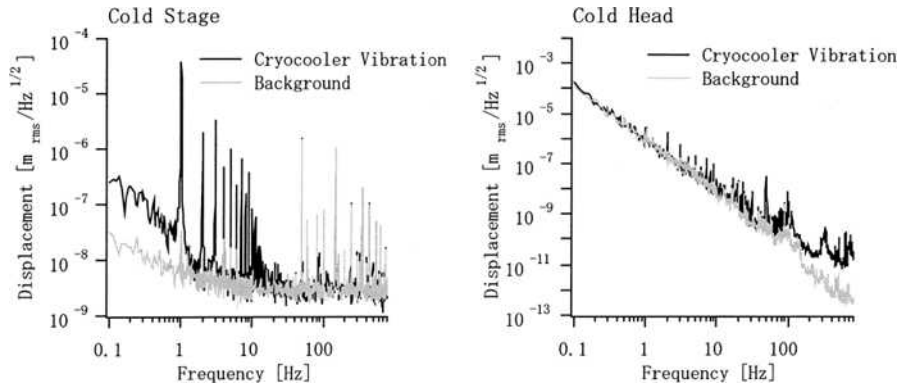

Figure 2. Vertical vibration spectra for a Sumitomo 4K PT cryocooler. The black lines show the vibration of the cryocooler and the gray lines show the sensor noise (background noise).

The features of the vibration include two points: one is the cold-stage vibration with the driving frequency (1 Hz) and its higher harmonics. The other is the cold-head vibration with the frequency components above about 50 Hz. From a spectrum analysis of the pressure oscillation of the working gas and an ANSYS simulation, we identified that this cold-stage vibration came from an elastic deformation of the cylinder due to the pressure oscillation of the working gas. Therefore, this is an inevitable problem for cryocoolers using oscillating gas. The cold-head vibration mainly came from reactions of a connecting tube between the cold head and the rotary valve unit, and so on.

Vibration-Reduction System

Based on the above study, we designed a vibration-reduction system for the 4K PT cryocooler. The design principle of this system is to separate all vibration sources from the cryostat and to anchor them to the ground. Figure 3 shows a schematic diagram of the system and Fig. 4 shows photographs of the system.

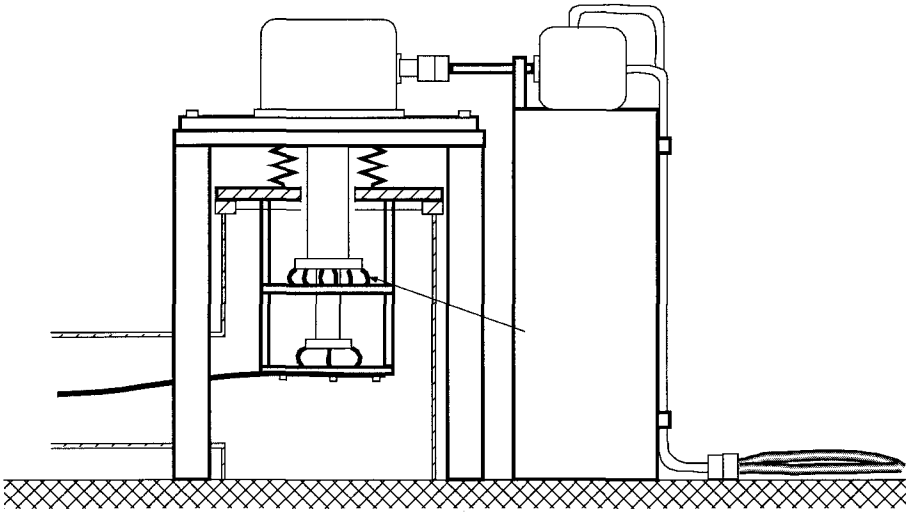

Figure 3. Schematic diagram of the vibration-reduction system for a 4K PT cryocooler.

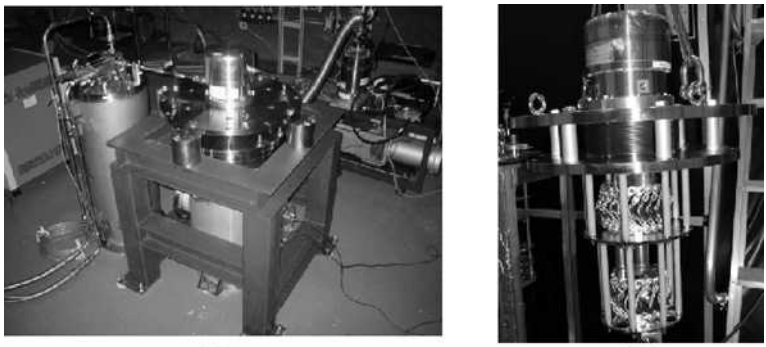

Figure 4. Photographs of the developed vibration-reduction system. (a) Support frame of the cold head and the rotary valve table; (b) Vibration-reduction stage for the cold stage.

To reduce the cold-head vibration of the PT cryocooler, we introduced a rigid frame to support the cold head, named 'support frame.' The cold head was mounted on the support frame and a welded bellows was connected between the cold head and the cryostat. A rotary valve unit, which could generate large vibrations, was not attached to the cold head directly, but was fixed onto an independent heavy table (rotary valve table). A connecting tube between the cold head and the rotary valve unit was also fixed on the rotary valve table. Flexible tubes from the compressor were converted to rigid pipes, and connected to the rotary valve unit. The pipes were also clamped onto the rotary valve table.

To reduce the cold-stage vibration, we used a rigid table, named 'vibration-reduction stage'. The vibration reduction of the cold stage through the use of a vibration-reduction stage has been reported by Lienerth et al.[7] An improved point concerning our vibration-reduction stage is that we set it under a lower flange of the bellows (named 'lower flange'), which was installed on the cryostat. Since the lower flange has minimal vibration, owing to being separated from the cold head, we can expect an absolute reduction of the cold-stage vibration by the vibration-reduction stage. The vibration-reduction stage consisted of eight alumina-FRP pipes, a copper plate and about forty heat-link cables for each stage. The reason why we used alumina-FRP is that it has a smaller thermal conductivity at 4 K, and a two times larger Young's modulus than that of glass-FRP. As the heat link, we used copper stranded cables for the first stage and pure aluminum stranded cables for the second stage (purity, 99.99%; size of each wire, ϕ0.1mm; total number of wires in a cable, 1666). The thermal conductivities of the second-stage metals strongly depend on their purities around 4 K; in contrast, they had a weak dependence of their purities around 40 K at the first stage. The reason why stranded cables with many thin wires were used is because the spring constant of the heat link is inversely proportional to the number of wires under the condition of a constant heat flow; therefore, the vibration conduction of the heat link could be reduced.

VIBRATION MEASUREMENT OF OVERALL SYSTEM

Since the vibration level of our system has been below the seismic vibration level in typical urban areas in our preliminary measurements, we checked the vibrations of the overall cryocooler system in Kamioka mine in Japan to reduce the background vibration noise. It is known that the seismic vibration in Kamioka mine is extremely small, the spectrum of which is about $10^{-9}/f^2$ m/$\sqrt{\text{Hz}}$ above a few hertz and two orders of magnitude smaller than that in the typical urban area.

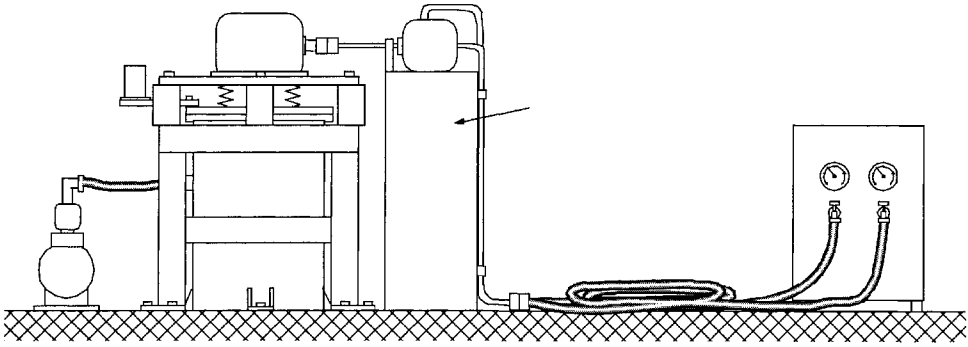

Figure 5. Schematic diagram of the experimental setup for vibration measurements of the overall cryocooler system (See Fig. 4). The vibration of our cryocooler system was measured by a laser accelerometer through a jig.

Figure 5 shows a schematic diagram of the experimental setup. The cold head was set onto a support frame through four posts of ϕ100mm in diameter and 90mm in height. The support frame was 690 mm in height and 670 mm in width, and consisted of H-beams of 100 mm in width. The lower flange of the bellows was mounted onto a cryostat. The length of the connecting tube between the rotary valve unit and the cold head was about 400 mm, and the weight of the rotary valve table was about 100 kg. The cryostat, the support frame and the rotary valve table were anchored onto the ground by thick bolts. The flexible tubes were 20 m in length and put on the ground in a coil. The distance between the cold head and the compressor was about 5 m. During the measurements, vacuum pumps were stopped so as to eliminate any influence of their vibration. We used a laser accelerometer (LA-50, Rion Co.) to measure the vibrations. The measured positions were on the ground and on the lower flange. Since the laser accelerometer had a large size, and it was difficult to set it onto the lower flange directly, we set it there by using a jig, which was a stainless-steel plate of 50 mm wide, 20 mm thick and 190 mm long.

Vibration spectra were acquired by a spectrum analyzer (Agilent 35670A). To achieve sufficient frequency resolution, we acquired the data by dividing them into three frequency ranges: 0.031 Hz resolution below 12.5 Hz, 0.25 Hz resolution between 12.5 Hz and 100 Hz, and 2Hz resolution between 100 Hz and 800 Hz. In this paper, we described the spectra in the displacement density defined by Eq. (1).

Figure 6 shows the measured results. The vibration level at the lower flange was two orders of magnitude smaller than the seismic vibration level in a typical urban area (our laboratory in KEK), and almost the same as the seismic vibration level in Kamioka mine. Since we observed that the seismic vibration in the Kamioka mine sometimes changed due to a change of the surrounding situations, and the maximum difference in the change was about one order of magnitude, the floor level in the seismic vibration spectrum could change by about one order of magnitude. Several jumps at the floor in the spectra also came from such a change of the surrounding situations, because the data were not acquired at the same time for all frequency ranges. A large peak at around 100 Hz came from a resonance of the jig for the laser accelerometer; we confirmed that this vibration did not come from the cryocooler system.

We observed sharp peaks at the driving frequency (1.2 Hz) and its higher harmonics in the vibration spectrum of the lower flange. After moving the compressor to outside of the experimental room, which was partitioned by a concrete-block wall, these sharp peaks disappeared. Figure 7 shows a comparison of the vibration levels at the lower flange when the compressor was set inside and outside of the experimental room. Based on this result, these sharp peaks could come from the motion of the compressor and the flexible tubes.

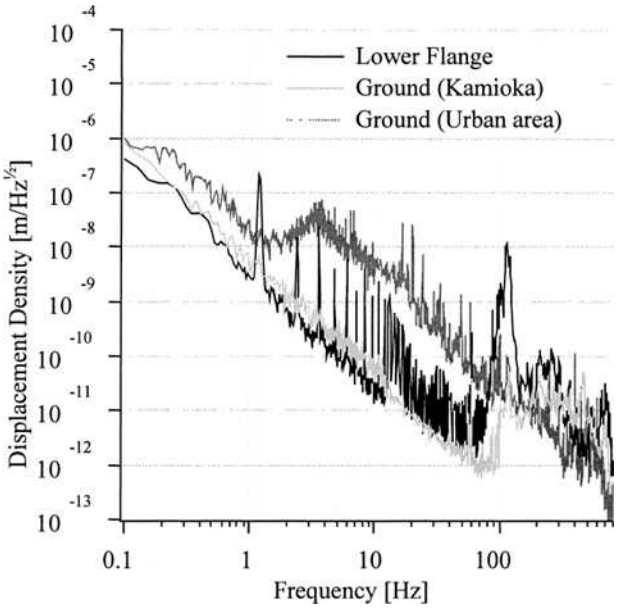

Figure 6. Vertical vibration spectra of the overall vibration-reduction cryocooler system. The black line shows the vibration at the lower flange, the gray line shows the seismic vibration (background noise) in Kamioka mine and the dotted line shows the seismic vibration in a typical urban area (KEK).

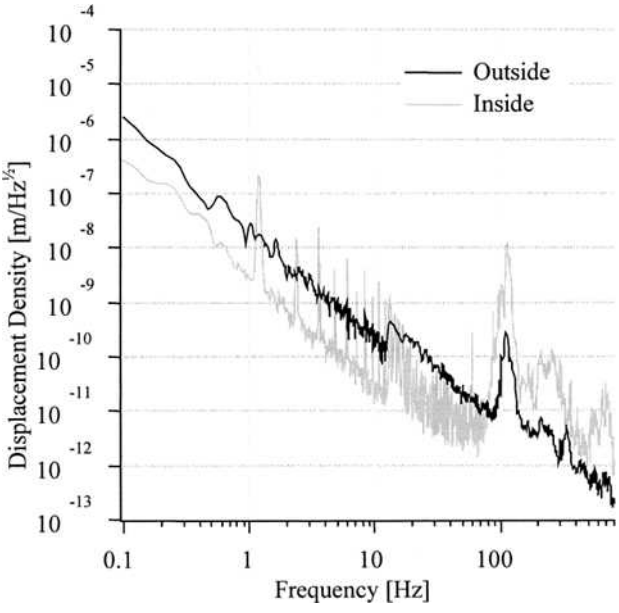

Figure 7. Comparison of the vertical vibration spectra when the compressor located outside of the experimental room (black line) and inside (gray line), which were partitioned by a concrete-block wall.

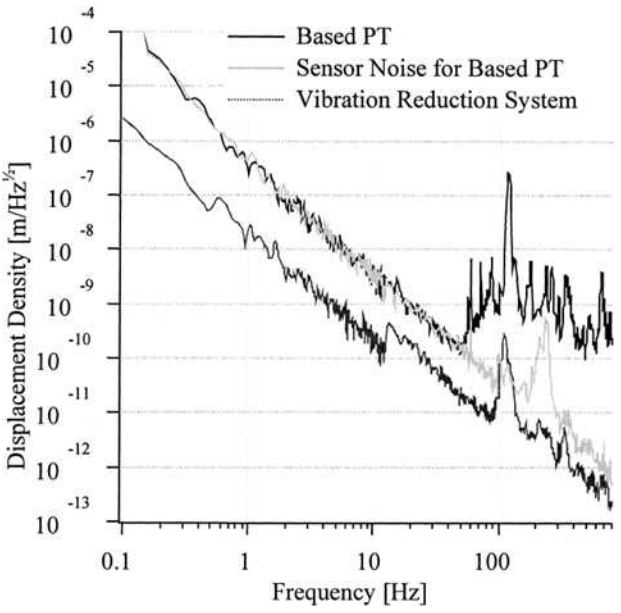

Figure 8. Vertical vibration spectrum of the based PT cryocooler (black line). The dotted line shows the vibration spectrum at the lower flange of the vibration-reduction cryocooler system when the compressor was located outside of the experimental room, and the gray line shows the sensor noise of the piezo-electric accelerometer used in the vibration measurement of the baseline PT cryocooler.

We also measured the cold-head vibration of the baseline 4K PT cryocooler in order to compare its vibration with that of our cryocooler system. We used the standard setup of the PT cryocooler, in which the rotary valve unit was attached to the cold head directly, the flexible tubes were connected to the rotary valve unit directly and the cold head was mounted on the cryostat directly. Figure 8 shows the measured result. Since we could not measure the vibration of the baseline PT cryocooler by the laser accelerometer, due to its large vibration, we used a piezo-electric accelerometer (Model 710, TEAC Co.) for the vibration measurement of the baseline PT cryocooler. Therefore, the sensor noise level of the piezo-electric accelerometer was larger than that of the laser accelerometer used in the measurement for the vibration-reduction cryocooler system. Above the 100 Hz frequency range, the vibration of the baseline PT cryocooler was over three orders of magnitude larger than that of the vibration-reduction cryocooler system. The motion of the rotary valve unit and the flexible tubes could generate this large vibration.

From the above results, we concluded that our vibration-reduction system reduced the cold-head vibration of the baseline PT cryocooler, and that the vibration level was almost the same as the seismic vibration level in Kamioka mine.

CONCLUSION

We developed a vibration-reduction system of a 4K PT cryocooler for the CLIO. The system consisted of a support frame and a vibration-reduction stage. The vibration sources in the cryocooler were separated from the cryostat and anchored onto the ground. From the vibration measurement for the overall system, we confirmed that the vibration of the system was more

than three orders of magnitude smaller than that of the baseline PT cryocooler. This vibration was much smaller than the seismic vibration level in a typical urban area ($10^{-7}/f^2$ m/$\sqrt{\text{Hz}}$), and was almost the same as the seismic vibration level in Kamioka mine ($10^{-9}/f^2$ m/$\sqrt{\text{Hz}}$). Therefore, we concluded that our cryocooler system could be designated as being 'vibration-free.'

ACKNOWLEDGMENT

This study was supported by a grant-in-aid for Scientific Research on Priority Area (14047217) prepared by Ministry of Education, Culture, Sports, Science and Technology in Japan.

REFERENCES

1. Kuroda K. et al., "Large-Scale Cryogenic Gravitational Wave Telescope", *Int. J. Mod. Phys.,* D Vol. 8 (1999), p. 557.
2. Ohashi, M. et al., "Design and Construction Status of CLIO," *Class. Quantum Grav.* Vol. 20 No. 17 (2003), pp. S599-S607.
3. Tomaru, T. et al., "Vibration Analysis of Cryocoolers," Accepted to *Cryogenics* (2004).
4. Li, R. et al., "Vibration-Free Pulse Tube Cryocooler System for Gravitational Wave Detectors, Part II: Cooling Performance and Vibration," *Cryocoolers 13*, Kluwer Academic/Plenum Publishers, New York (2005).
5. Xu M. Y. et al., "Development of a 4K Two-Stage Pulse Tube Cryocooler," *Cryocoolers 12*, Kluwer Academic/Plenum Publishers, New York (2003), pp. 301-308.
6. Bendat J. S. and Piersol A. G., *Random Data: Analysis and Measurement Procedures*, John Wiley & Sons, Inc., 1971.
7. C. Lienerth et al., *Proc. of ICEC*, Vol. 18 (2000), p. 555.

Vibration-Free Pulse Tube Cryocooler System for Gravitational Wave Detectors, Part II: Cooling Performance and Vibration

R. Li[1], Y. Ikushima[1], T. Koyama[1], T. Tomaru[2], T. Suzuki[2], T. Haruyama[2], T. Shintomi[2] and A. Yamamoto[2]

[1]Cryogenics Division, Sumitomo Heavy Industries, Ltd.
Nishitokyo, Tokyo, 188-8585, Japan
[2]High Energy Accelerator Research Organization (KEK)
Tsukuba, Ibaraki, 305-0801, Japan

ABSTRACT

A vibration-free pulse tube cryocooler system has been developed for gravitational wave detectors. A commercially available 4 K pulse tube cryocooler (SRP-052A, Sumitomo Heavy Industries, Ltd.) with a cooling capacity of 0.5 W at 4.2 K was applied in the system. In order to reduce the vibration of the 4 K pulse tube cryocooler to an ultra low level: (1) two vibration reduction stages (VR stages), (2) a cold head supporting frame, and (3) a valve unit mounting table were introduced as major components of the system. The cooling capacities of 15 W at 45 K and 0.4 W at 4.2 K were available at the first and the second VR stages simultaneously. Concerning the vibration, on the other hand, the displacement due to the elastic deformation of the pulse tubes was effectively reduced to be less than ± 1 μm. In the direction parallel to the pulse tubes, the displacement was lowered to ± 0.05 μm, which is two to three orders of magnitude less than that of the original 4 K pulse tube cryocooler, SRP-052A.

INTRODUCTION

A pulse tube cryocooler has no moving parts in its low temperature region, and in general has less vibration than a Gifford-McMahon (G-M) cycle cryocooler or Stirling cycle cryocooler. In the last ten years many kinds of pulse tube cryocoolers have for liquid nitrogen or liquid helium in various sensitive applications.[1-4]

As compared to a G-M or Stirling cycle cryocooler, the cold head of a pulse tube cryocooler has a significantly lower acceleration. A previous investigation indicated that the overall acceleration of the cold head of a 4 K pulse tube cryocooler is less than that of a 4 K G-M cryocooler by about two orders of magnitude.[5] However, the displacement of the cold stage is comparable between the 4 K pulse tube cryocooler and the 4 K G-M cryocooler. Therefore, the vibration of a pulse tube cryocooler is still not low enough for many sensitive applications. In the Cryogenic Laser Interferometer Observatory (CLIO)[6], which is a prototype of the Large-scale Cryogenic Gravitational wave Telescope (LCGT)[7], a number of mirrors and radiation shields were designed to be cooled by pulse tube cryocoolers. Although there are several vibration isolation components in the CLIO as part of its basic design, a pulse tube cryocooler system with a vibration level as low as possible is still essential for reaching the desired sensitivity with the state-of-the-art detectors.

Cryocoolers 13, edited by R. G. Ross, Jr.
Springer Science+Business Media, Inc., New York, 2004

By using a commercially available 4 K pulse tube cryocooler—SRP-052A, manufactured by Sumitomo Heavy Industries, Ltd.—a vibration-free pulse tube cryocooler system has been developed in this work. The key components introduced for reducing the vibration from the 4 K pulse tube cryocooler include: (1) two vibration reduction stages (VR stages), (2) a cold head supporting frame, and (3) a valve unit mounting table. In the present paper, the design concept of the system and the major components are described. The cooling performance and the vibration characteristics of the vibration-free system are also reported and discussed elsewhere in this proceedings.[8]

DESIGN OF CRYOCOOLER SYSTEM

Design Concept

As described by Tomaru, et al., the CLIO includes a number of mirrors that were designed to be cooled down to 20 K by about 10 pulse tube cryocooler units.[8] Liquid helium was a competitive option for cooling these mirrors without mechanical vibration. However, the Kamioka mine site of the CLIO is located in a remote area. For observation over long intervals, a regular refilling of liquid helium would be very inconvenient and uneconomic, and a cooling system based on 4 K pulse tube cryocoolers was chosen.

There were two major design concepts for developing a pulse tube cryocooler system with ultra low level vibration for this application. One approach would be to develop a special pulse tube cryocooler that has very low vibration and a reasonable cooling capacity; this would be a considerable effort. The second concept was to make use of a commercially available 4 K pulse tube cryocooler. After a feasibility study from the viewpoint of development difficulty, time, and expense, it was decided to use a commercially available 4 K pulse tube cryocooler.

A previous investigation had determined the vibration level and cold stage displacement of a commercially available 4 K pulse tube cryocooler.[5] The investigation has also made it clear that there are two kinds of vibration in a pulse tube cryocooler. One is the overall cold head vibration that is caused by the movement of compressor, rotary valve unit, and working gas flow. The other is cold stage vibration that is generated by elastic deformation of the pulse tubes and the regenerators due to the periodic pressure oscillation inside of the cryocooler.

Based on the investigation, the chosen design concept was to introduce several vibration reduction components for separating these two kinds of vibration and for reducing them effectively. Figure 1 is a schematic drawing of the pulse tube cryocooler system developed for the CLIO that incorporates the design concepts mentioned above.

Major Component

Besides a 4 K pulse tube cryocooler, the major components of the vibration-free pulse tube cryocooler system were two vibration reduction stages, a cold head supporting frame, and a valve unit mounting table. The following are detailed descriptions of these components.

4 K Pulse Tube Cryocooler. The 4 K pulse tube cryocooler employed in this development is manufactured by Sumitomo Heavy Industries Limited. The cryocooler is the SRP-052A, and its specified cooling capacity is 0.5 W at 4.2 K and 20 W at 45 K, simultaneously, with 7 kW power consumption. The cryocooler consists of a two-stage cold head, a rotary valve unit driven by a synchronous motor, two flexible hoses 20 meter long, and a helium compressor (the same as that used by a 4 K G-M cryocooler). The vibration of the pulse tube cryocooler has been previously investigated and compared with that of a 4 K G-M cryocooler.[5] In brief, the overall acceleration of the cold head is less than that of the G-M cryocooler by about two orders of magnitude, and the displacement of the cold stage is almost the same as that of the G-M cryocooler.

An attractive advantage of the SRP-052A is that the rotary valve unit is separated from the cold head with a self-sealing coupling. The standard setup recommended by the manufacture to achieve maximum cooling performance is to connect the rotary valve unit directly to the cold head without any extension connecting tube. From the viewpoint of vibration reduction, this configuration is

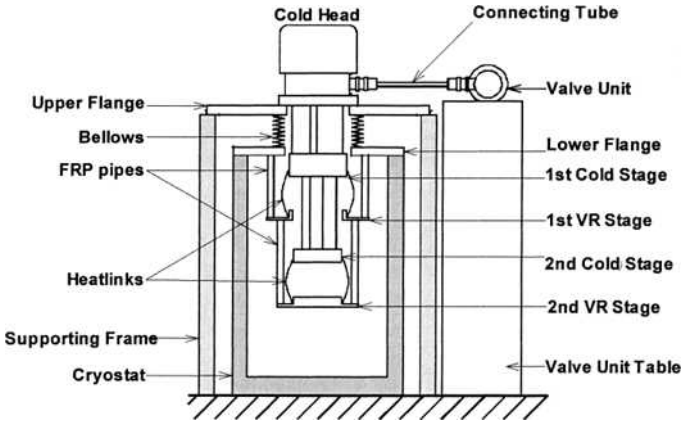

Figure 1. Schematic diagram of the vibration-free pulse tube cryocooler system. The compressor and the flexible hoses are not shown.

inconsistent with separating the rotary valve unit away from the cold head so as to reduce the vibration from the compressor and the valve unit as much as possible.

Vibration Reduction Stage. In order to reduce the cold stage vibration effectively, two vibration reduction stages were introduced for the first and the second stages of the cold head, respectively (see Fig. 1). The VR stages are the interfaces for delivering cooling to the mirrors and radiation shields of the CLIO. They are made of copper, thermally linked to the original cold stages of the cryocooler with braided wires, and tightly supported by eight FRP pipes fixed to the top flange (the lower flange in Fig. 1) of the cryostat.

For the first VR stage, the braided wires are made of oxygen free high conductivity copper, and for the second VR stage, they are braided wires of high purity aluminum. The copper wire has a higher thermal conductivity at temperatures above ~45 K. The high purity aluminum wire has the advantages of light weight, excellent thermal conductivity below 20 K, and very low Young's modulus.[9] The Young's modulus of the aluminum wire is only about 1/3 of that of copper wire.

The pipes for supporting the VR stages, on the other hand, are required to have poor thermal conductivity and a high Young's modulus. In this work, the FRP pipes applied to both VR stages are made of alumina fiber reinforced plastic (A-FRP). The A-FRP is well known for its low thermal conductivity below 40 K and its high Young's modulus compared with glass fiber reinforced plastic (G-FRP).

Cold Head Supporting Frame. The cold head supporting frame is an important component for separating the overall cold head vibration and the cold stage vibration. The cold head is fixed on the upper flange and supported by the supporting frame (Fig. 1). The frame is made of I-beams and has four strong supporting poles. There is a welded bellows between the upper flange and the lower flange for creating a vacuum space for the cryocooler and for isolating the vibration from the upper flange. With this configuration, the weight of the cold head is fully supported by the upper flange and the supporting frame, and the whole weight of the VR stages is supported by the lower flange and the cryostat. It is expected that the vibration-reduction function of the VR stages will be maximized by this configuration.

Valve Unit Mounting Table. Because the compressor and the drive motor of the rotary valve unit generate considerable mechanical vibration, effective vibration isolation between the rotary valve unit and the cold head is important for the present development. A steel table weighting more than 140 kg was used for mounting the rotary valve unit (Fig. 1). In addition, the table was also applied as an anchor for the helium gas lines from the compressor. Between the rotary valve unit and the cold head, a connecting tube of 40 cm long was employed. This configuration is not

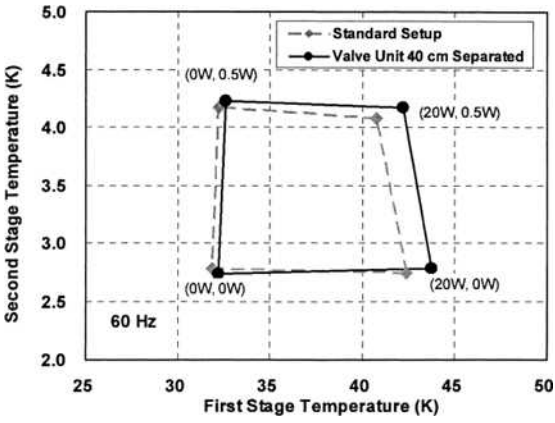

Figure 2. Comparison of load maps with and without a connecting tube of 40 cm.

recommended for getting the maximum cooling performance, but is important and convenient for reducing the vibration from the compressor and the valve drive motor.

COOLING PERFORMANCE

As described above, the VR stages and the valve unit mounting table were introduced into the pulse tube cryocooler system to reduce the vibration. From the point-of-view of cooling performance, these two improvements will negatively impact the cooling capacities available from the system. In particular, the extended connecting tube between the valve unit and the cold head is expected to reduce the cooling capacity compared with the original configuration. Also, the braided wires will produce a finite temperature difference between the VR stage and the original cold stage.

Influence of Valve Unit Separation

The influence of the valve unit separation was evaluated by comparing load maps of the cryocooler with and without the connecting tube of 40 cm. In Figure 2, two load maps show the comparison, but all data were measured without the VR stages. For the original configuration of the SRP-052A (i.e. without the connecting tube and with the rotary valve unit directly joined to the cold head), the cooling performance was 20 W at 40.8 K for the first stage and 0.5 W at 4.08 K for the second stage, simultaneously. After the introduction of the 40 cm long connecting tube, the cooling capacities became 20 W at 42.2 K on the first stage and 0.5 W at 4.17 K on the second stage. The decreased cooling capacity is observable, but limited, and the cooling performance still meets the specification of SRP-052A, even though the connecting tube is employed.

Load Map of VR Stage

In the CLIO, there are several vibration isolations between the 4 K cryocooler system and the 20 K mirrors. Because some of the isolation results in poor heat conduction, the cooling capacity available from the VR stages was required to be as large as possible. Figure 3 shows a load map of the VR stages with solid lines. As a reference, the load map of the cold stages measured at the same time is represented by broken lines in the figure. For a typical point with a head load of 15 W on the first stage and 0.5 W on the second stage, the temperature of the first VR stage was 43.7 K and that of the second VR stage was 4.43 K. At the same time, the cold stage temperatures were 41.2 K and 4.15 K, respectively.

Because the heat leak from room temperature via the A-FRP pipes was estimated to be only about 0.3 W to the first VR stage and about 10 mW to the second VR stage, the loss of cooling capacity was almost entirely caused by the thermal resistances of the braided-wire flex straps. The wires of the flex straps were made of high purity metals and were well heat treated. A high thermal

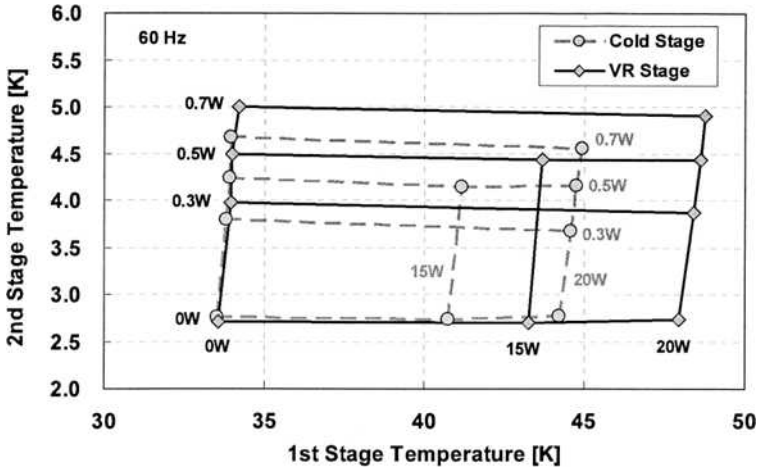

Figure 3. Load map of VR stages compared with that of cold stages.

conductivity of the braided wires is expected. The dominant thermal resistance is considered to come from the contact interface surfaces between the straps and the cold stages or the VR stages.

Although the VR stages have some negative effect on the cooling performance, the cryocooler system is able to deliver a net cooling capacity of at least 15 W at 45 K together with 0.4 W at 4.2 K.

VIBRATION OF VR STAGE

The overall vibration of the 4 K pulse tube cryocooler system has been reported by Tomaru et al. in the proceeding article of this proceedings.[8] The focus of the present paper is on the displacement of the cold stages and the VR stages.

Setup for Vibration Measurement

Figure 4 illustrates the vibration measurement setup for the pulse tube cryocooler system. The rotary valve unit was mounted on the valve unit table. The weights of the cold head and the VR stages were separately supported by an upper flange supporting frame and a lower flange supporting frame. The displacement was measured by a laser displacement sensor (LC-2420, Keyence, Co.), which was rigidly held on the lower flange supporting frame. An air damper was employed

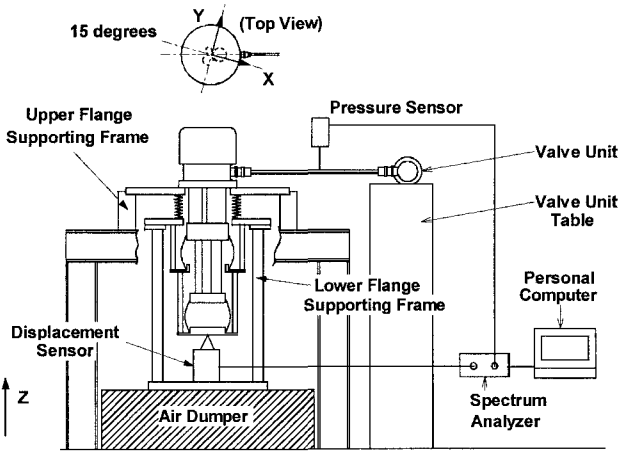

Figure 4. Setup of vibration measurement for the pulse tube cryocooler system.

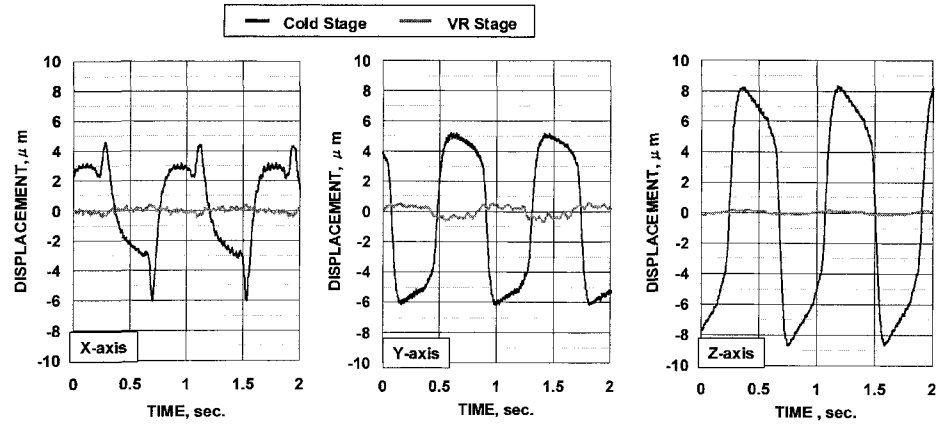

Figure 5. Displacement of the second VR stage and the second clod stag.

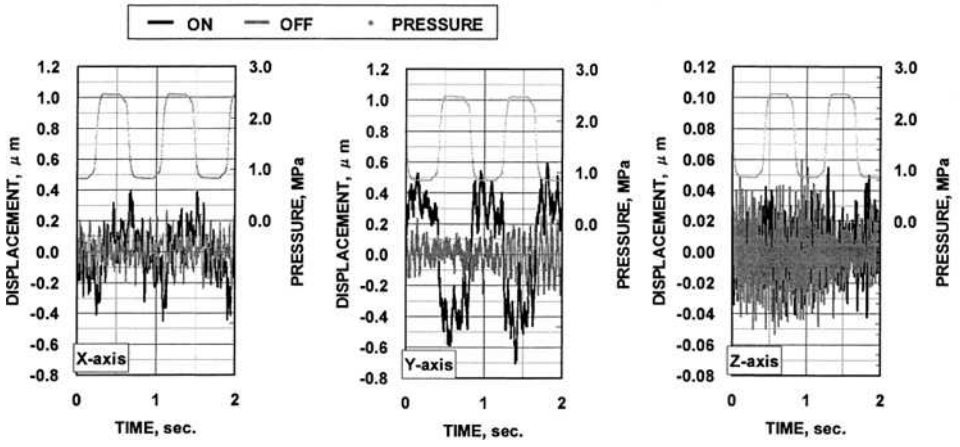

Figure 6. Displacement of the second VR stage for both cases of cryocooler turned on and turned off.

for isolating the vibration from the floor. The vibration was measured at room temperature, and the pressure oscillation in the cold head was monitored during the measurement. The data of the displacement and the pressure were acquired by a spectrum analyzer (OR24, Oros, SA) and a personal computer.

As shown in the Fig. 4, the vertical direction parallel to the pulse tubes was defined as the Z-axis, and the direction of 15 degrees rotated from the central axis of the connecting tube was defined as the X-axis.

Displacement of VR Stage

The measurement results for the second VR stage displacement are shown in Figs. 5, 6 and Table 1. For comparison, the displacements for the second cold stage (measured with the same setup) are also illustrated and listed. The displacements of the cold stage were $\pm 5.3\mu m$, $\pm 5.7\ \mu m$ and $\pm 8.5\ \mu m$ for the X, Y and Z directions, respectively. However, for the VR stage, the displacements for each axis were reduced down to less than $\pm 1\mu m$. The details of the VR stage displacement are shown in Fig. 6 by enlarging the vertical axis of Fig. 5. Figure 6 illustrates the second VR stage displacements for the cases of the pulse tube cryocooler turned off and turned on; it also shows the pressure wave inside of the cold head. From Fig. 6, it is seen that there is a higher level noise mixed in the displacement data for both cases of the cryocooler turned on and turned off. Including this noise, the displacements of the second VR stage were $\pm 0.42\ \mu m$, $\pm 0.65\ \mu m$ and

Table 1. Comparison of displacements between VR stage and cold stage (units: μg).

	X-axis	Y-axis	Z-axis
2nd Cold Stage	±5.3	±5.7	±8.5
2nd VR Stage	±0.42	±0.65	±0.05

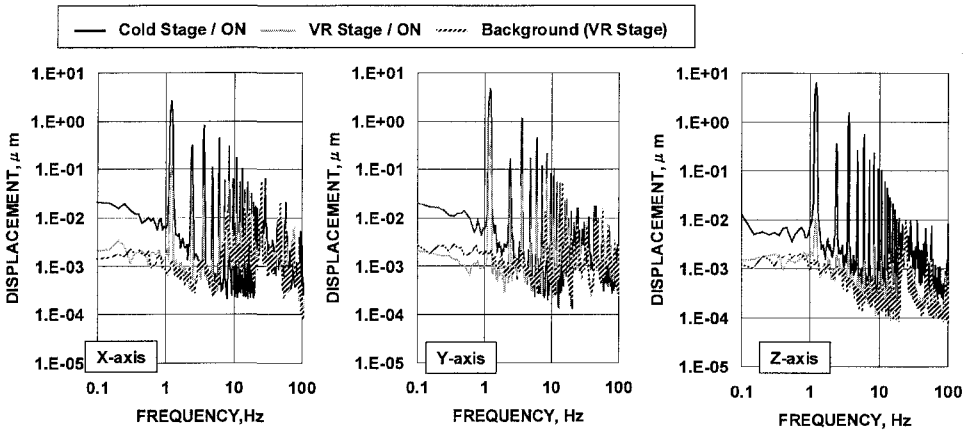

Figure 7. Spectrums of the second VR stage displacement.

±0.05 μm for the X, Y and Z directions, respectively. Especially for the Z-axis, there was almost no difference between the cases of the cryocooler turned on and turned off for the displacement. This means that the vibration of the VR stage in this direction has been successfully reduced to the background vibration level. In this sense, it can be said that the cryocooler system has achieved a vibration-free level—at least in the Z direction.

Figure 7 shows the spectrum of the displacements of the cold stage and the VR stage. For the cold stage, the peaks corresponding to the operating frequency (1.2 Hz) and its higher harmonics are sharp and high. For the VR stage, the peak at the operating frequency is still confirmed, but it is remarkably lower than that of the cold stage. The peak value for the Z-axis is 6.4 μm for the cold stage at 1.2 Hz, but is only 10 nm for the VR stage. For the X and Y directions, the peak value at 1.2 Hz is reduced from 2.6 μm to 0.12 μm and from 4.6 μm to 0.31 μm, respectively,

Both the time series data and the spectrum data indicate that the vibration has been reduced by one to two orders of magnitude in the X and Y directions and by two to three orders of magnitude in the Z direction. The effect of the VR stage was somewhat less for the X and Y directions. It is hypothesized that this was caused by the coupling of the pulse tubes and regenerators, but clarification with require more detailed investigation in the future.

Concerning the vibration of the first cold stage and the first VR stage, it was also evaluated in this work. Since the results for the first stages were similar to those for the second stages, they were not reported on in this paper. The displacements of the first stages, however, were much smaller because the length of the first-stage pulse tube and the first-stage regenerator are shorter.

CONCLUSION

A vibration-free pulse tube cryocooler system has been developed for gravitational wave detectors. In the cryocooler system, a commercially available 4 K pulse tube cryocooler has been employed. To achieve the necessary vibration reduction, three new components were introduced into the system. These included: (1) two vibration reduction stages, (2) a cold head supporting frame, and (3) a valve unit mounting table.

Although the VR stages and the valve unit mounting table affect the cooling performance negatively, the cryocooler system was able to deliver a net cooling capacity of 15 W at 45 K and

0.4 W at 4.2 K, simultaneously. This provides a large cooling margin for the mirrors and vibration isolation components of the CLIO.

The major components introduced by this work substantially reduced the vibration from the original 4 K pulse tube cryocooler. For X-axis and Y-axis, the displacement was reduced by one to two orders of magnitude, and was down to less than $\pm 1\mu m$. In particular, for the Z-axis, the displacement was lowered to be less than ± 0.05 μm and was two to three orders of magnitude less than that of the original cryocooler. The vibration level of the system was as low as expected for the gravitational wave detectors in the CLIO.

REFERENCES

1. Li, R., Ishikawa, A., Koyama, T., Ogura, T., Aoki, A. and Koizumi, T., "A Compact Liquid Nitrogen Recondenser with a Pulse Tube Cryocooler," *Advances in Cryogenic Engineering*, vol. 45, Kluwer Academic/Plenum Publishers, New York (2000), pp. 41-48.
2. Xu, M.Y., Yan, P.D., Koyama, T., Ogura, T. and Li, R., "Development of a 4 K Two-stage Pulse Tube Cryocooler," *Cryocooler 12*, Kluwer Academic/Plenum Publishers, New York (2003), pp. 301-307.
3. Wang, C. and P.E. Gifford, "Performance Characteristics of a 4 K Pulse Tube in Current Applications," *Cryocooler 11*, Kluwer Academic/Plenum Publishers, New York (2001), pp. 205-212.
4. C. Lienerth, G. Thummers and C. Heiden, "Low-Noise Cooling of HT-SQUIDs by Means of a Pulse Tube Cooler with Additional Vibration Compensation," *Proceedings of the 18th International Cryogenic Engineering Conference*, Narosa Publishing House, New Delhi (2000), pp. 555-558.
5. Tomaru, T., Suzuki, T., Haruyama, T., Shintomi, T., Yamamoto, A., Koyama, T., Li, R. and Matsubara, Y., "Vibration Analysis of Cryocoolers," *Journal of the Cryogenic Society of Japan*, Vol. 38, No. 12 (2003), pp. 693-702.
6. Ohashi, M. et al., "Design and Construction Status of CLIO," *Class. Quantum Grav.*, Vol. 20, No. 17 (2003), pp. S599-S607.
7. Kuroda, K. et al., "Large-Scale Cryogenic Gravitational Wave Telescope," *Int. J. Mod. Phys. D*, Vol. 8 (1999), p. 557.
8. Tomaru, T., Suzuki, T., Haruyama, T., Shintomi, T., Sato, N., Yamamoto, A., Ikushima, Y., Li, R., Akutsu, T., Uchiyama, T. and Miyoki, S., "Vibration-Free Pulse Tube Cryocooler System for Gravitational Wave Detectors, Part I: Reduction of Vibrations," *Cryocooler 13*, Kluwer Academic/Plenum Publishers, New York (2005).
9. Kasahara, K., Tomaru, T., Uchiyama, T., Suzuki, T., Yamamoto, K., Miyoki, S., Ohashi, M., Kuroda, K. and Shintomi, T., "Study of the Heat Links for a Cryogenic Laser Interferometric Gravitational Wave Detector," *Journal of the Cryogenic Society of Japan*, Vol. 39, No. 1 (2004), pp. 25-32.

Two-Stage Refrigeration for Subcooling Liquid Hydrogen and Oxygen as Densified Propellants

J.H. Baik[1], H.-M. Chang[2] and W. Notardonato[3]

[1]Florida Solar Energy Center, Cocoa, FL, USA 32922
[2]NHMFL, Tallahassee, FL, USA 32310 and Hong Ik University, Seoul, KOREA
[3]NASA-KSC, Kennedy Space Center, FL, USA 32899

ABSTRACT

The thermodynamic design on two-stage refrigeration cycles is performed as one of several feasibility studies for the densified propellant technologies funded by the NASA Glenn Research Center. The refrigeration is required to increase the density of liquid oxygen and liquid hydrogen by subcooling to 65 K and 15 K, respectively, and to reduce the gross lift-off weight of a launch vehicle by up to 20%. The objective of this study is to seek the most efficient and economic two-stage refrigeration cycle, which satisfies the specific cooling requirements at the two temperature levels so that both densified propellants can be supplied simultaneously on a scheduled launch countdown. Recuperative cycles such as Claude and reverse Brayton refrigeration can be modified for subcooling liquid oxygen and liquid hydrogen in a manner commonly used for large capacity flows at lower temperatures. It is proposed to use a hybrid or cascade cycle, combining recuperative heat exchangers, expander and Joule-Thomson (J-T) valve at 65 K and 15 K. A variety of two-stage cycles derived from J-T, reverse Brayton and Claude cycles are examined in this paper. The essential features and characteristics of selected hybrid two-stage cycles are reported through a rigorous thermodynamic analysis. Among the examined cycles, the two-stage reverse Brayton helium refrigeration system shows a very suitable possibility for cryogenic propellant densification technology.

INTRODUCTION

Since 2002, the Florida Solar Energy Center has conducted intensive research and development on cryogenic propellant densification technologies funded by NASA Glenn Research Center through the NASA Hydrogen Research at Florida Universities Program. By use of cryogenic propellants densification technologies, the single-stage-to-orbit (SSTO) and the reusable launch vehicles (RLV) become more attractive because of the reduced vehicle mass. The 8 ~ 10% denser cryogenic propellants at temperatures lower than those of the normal boiling point (NBP) can reduce the gross lift-off weight (GLOW) of a launch vehicle by up to 20% or increased payload capability.[1]

As an initial investigation, several promising densification systems were investigated based on various launch scenarios, and a rigorous thermodynamic analysis using real propellant properties was performed to suggest the most feasible and reliable system for the launch vehicle application.[2] It turned out from the investigation that a combination of a thermodynamic venting

Cryocoolers 13, edited by R. G. Ross, Jr.
Springer Science+Business Media, Inc., New York, 2004

system (TVS) and a Claude refrigerator for each propellant showed promise of being a highly efficient system from a thermodynamic point of view, but the system becomes rather complicated. The TVS system or subatmospheric boiling bath heat exchanger technology requires an additional gas compressor to densify NBP cryogenic propellants by lowering the vapor pressure. Furthermore, this technology requires two independent densification systems for liquid oxygen and liquid hydrogen, even though they may be suitable for large cooling power requirements.

In this paper, it is suggested for thermodynamic efficiency and economic practice that a two-stage refrigeration cycle be used to satisfy the specific cooling requirements at the two densification temperatures. The two-stage refrigeration cycle provides specific cooling powers at the two temperatures so that both densified propellants can be supplied simultaneously on a scheduled launch countdown. This technology is achievable by employing recuperative cycles such as the reverse Brayton and the Claude refrigeration cycle, which are commonly used for large capacity applications at lower temperatures. By designing a hybrid or cascade cycle with recuperative heat exchangers, expander, and Joule-Thomson valve, it is possible for us to provide the specific cooling requirements at specific densification temperatures at the same time. To verify the feasibility and characteristics of this new concept, rigorous thermodynamic analyses have been performed for a variety of two-stage cycles using combinations of J-T, reverse Brayton and Claude cycles.

IDEAL (REVERSIBLE) CYCLES

For the case where two cooling temperatures and their cooling capacities are given, we can classify possible refrigeration systems into three main categories as shown in Fig. 1. Figure 1(a) shows a 'Two single-stage coolers' system. Two separate cooling systems with two input powers provide the required cooling capacities at each cooling temperature. As the densification temperatures, 65K and 15K are selected for oxygen and hydrogen, respectively. Fig. 1(b) shows a 'One two-stage cooler' system that provides two independent cooling powers at two cooling temperatures and requires one input power. Also, the 'cascade cooler system' in Fig. 1(c) can be considered as one of the candidates for the two cooling temperatures and two cooling powers application. For ideal reversible refrigeration cycles, however, the minimum required input power should be the same for the three cases. By combining the energy and entropy balances, the minimum required work input for the three cases in Fig. 1 can be expressed as Eq. (1).

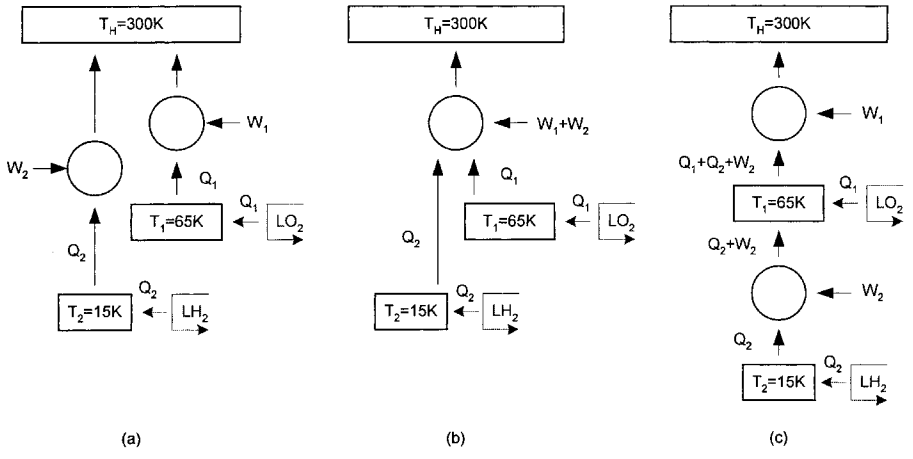

Figure 1. Ideal reversible cycles operating at two cooling temperatures; (a) two single-stage cooler system, (b) one two-stage cooler system, (c) cascade cooler system.

$$
\begin{aligned}
W_{A\ or\ B} &= W_1 + W_2 = Q_1\left(\frac{T_H}{T_1}-1\right)+Q_2\left(\frac{T_H}{T_2}-1\right) \\
W_C &= W_1 + W_2 = (Q_1+Q_2+W_2)\left(\frac{T_H}{T_1}-1\right)+Q_2\left(\frac{T_1}{T_2}-1\right) \\
&= Q_1\left(\frac{T_H}{T_1}-1\right)+Q_2\left(\frac{T_H}{T_1}-1\right)+Q_2\left(\frac{T_1}{T_2}-1\right)\left[\left(\frac{T_H}{T_1}-1\right)+1\right] \\
&= Q_1\left(\frac{T_H}{T_1}-1\right)+Q_2\left(\frac{T_H}{T_2}-1\right)
\end{aligned}
\tag{1}
$$

This implies that when we construct ideal cycles, any variation of system configuration does not affect the thermodynamic performances unless operating temperatures and cooling requirements are changed. In reality, however, there must be differences among them since their performances depend on thermodynamic and mechanical efficiencies of system components. For instance, system (a) and (c) in Fig. 1 have at least two work input components which is, in general, compressors. The requirement of two compressors to run the system may result in a more complicated, more expensive, less reliable, and less efficient system. On the other hand, system (b) in Fig. 1 can be operated by only one compressor, so that it has an inherent simplicity in system constitution. Furthermore, it can be a versatile system to provide various cooling powers at each cooling stage by controlling system design parameters such as work input, and cooling-power distribution ratios. Therefore, the choice of the appropriate refrigeration system and optimal operating condition based on both thermodynamic and practical considerations should be made at the design stage.

TWO-STAGE COOLERS

Figure 2 schematically shows a few simplified variations of the two-stage refrigeration cycle. Figure 2(a) depicts a two-stage reverse Brayton helium cycle. Two expanders are located at each densification stage to densify cryogenic propellants. The gas temperatures at the exits of the 1st and the 2nd expander are required to be low enough to densify saturated cryogenic propellants. Since helium is maintained in a gaseous state at the exit of the 2nd (lower temperature) expander, a dry expander can be used. The helium gas temperatures at the expander exits and the required cooling powers at each stage can be controlled by varying the mass flow fraction at the inlet of the first expander, the total mass flow rate in the compressor, and the compressor discharge pressure. Figure 2(b) shows another two-stage cooling cycle, a combination of reverse Brayton and Claude cycles with a J-T expansion valve. Even if a Claude cycle is self explanatory that it uses an expander in the 1st stage and a J-T expansion valve in the 2nd stage, this configuration is referred to as a two-stage reverse Brayton-Claude cycle in this paper because of the additional densification heat exchanger at the exit of the 1st stage expander. Since the isenthalpic process in the J-T expansion valve is a major source of irreversibility, a lower system efficiency is expected and a higher operating pressure is required. For hydrogen as a working fluid, we expect a benefit of obtaining subcooled liquid hydrogen at the exit of the J-T valve to enhance heat transfer in densifying saturated liquid hydrogen. Figures 2(c) and 2(d) depict more complicated combinations of reverse Brayton, J-T and Claude systems as references. These hybrid systems consist of both an expander at the liquid oxygen stage and a J-T expansion valve at the liquid hydrogen stage; this gives two independent helium or hydrogen cycles to take advantage of each system component. However, the system configurations tend to be complicated and maintenance issues can be evolved. Therefore, the two configurations in

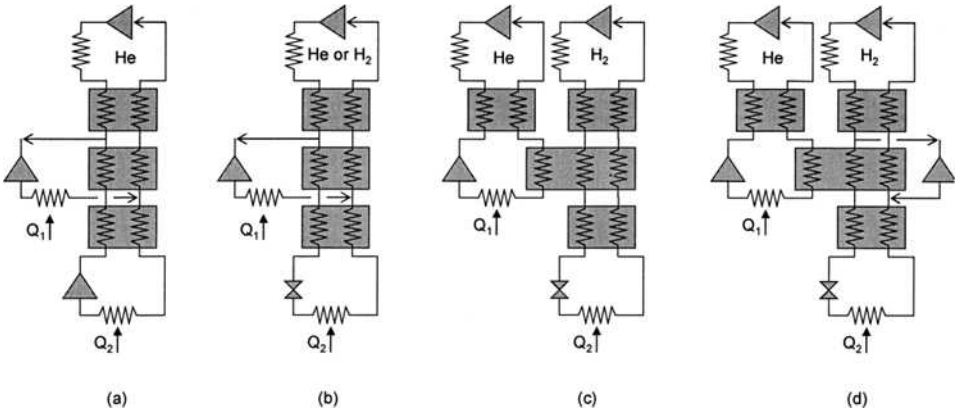

Figure 2. Two-stage cooler variations; (a) two-stage reverse Brayton helium cycle, (b) reverse Brayton-Claude helium/hydrogen cycle, (c) combination of reverse Brayton helium and J-T hydrogen cycle, (d) combination of reverse Brayton helium and Claude hydrogen cycle.

Figs. 2(a) and 2(b) are chosen in this paper to explore the possibility of using two-stage coolers to provide the required cooling powers at the required densification temperatures.

Two-Stage Reverse Brayton Helium Cycle

Based on the preliminary investigation on the required cooling power for various launch scenarios[2], the cooling powers that are required to densify 1 kg/s of liquid hydrogen and 6 kg/s of liquid oxygen are fixed in the rest of thermodynamic analysis. These flow rates depend on cooling the propellants before the start of the loading process. If the densification occurs during vehicle load, the rates become much higher. The corresponding cooling powers are 48 kW at 15 K and 268 kW at 65 K, respectively. In this analysis, discharge and suction pressures of the compressors are set to 2020 kPa and 101 kPa, respectively. The mass flow fraction at the inlet of the 1st expander, y, is defined as follows:

$$y \equiv \frac{\dot{m}_{\text{1st expander}}}{\dot{m}_{compressor}} \tag{2}$$

Figure 3 shows results of the thermodynamic cycle analysis for the two-stage reverse Brayton helium cycle. In this analysis, computerized real properties of helium are used.[3] Figures 3(a) and 3(b) show the required total mass flow rates of system and mass flow fractions at the inlet of the 1st expander as functions of densification stage temperatures. To obtain 65K and 15K of cold helium gas after the expanders at the densification stages, the system requires about 1.2 kg/s of total mass flowrate in the compressor and the mass flow fraction should be slightly over 50% of the total mass flow rate from Fig. 3(a) and (b). Figures 3(c) and 3(d) show the same results from a different angle of view. By changing the total mass flow rate of the system and the mass flow fraction, it is possible to get various densification temperatures at each stage for a fixed compressor discharge pressure. For a given total mass flow rate, the liquid oxygen densification temperature decreases as the mass flow fraction increases, since the mass flow rate expanded in the 1st expander increases for a fixed cooling power. However, the liquid hydrogen densification temperature has a minimum value, because the liquid hydrogen densification temperature is affected by the liquid oxygen densification temperature and mass flow rate at the 2nd stage at a fixed cooling power. In this analysis, the Figure of Merit (FOM: %Carnot) is calculated to be 0.54.

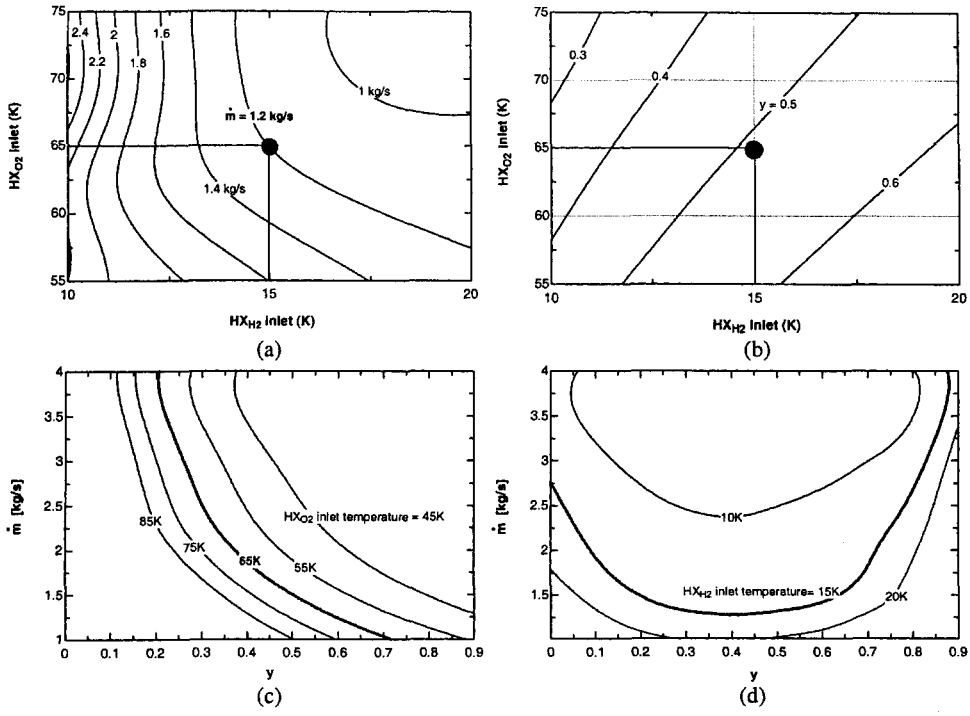

Figure 3. Selected analysis results of two-stage reverse Brayton helium cycle ($P_{discharge}$=2020 kPa, $P_{suction}$=101 kPa, heat exchanger effectiveness = 0.95, expander efficiency = 0.8)

Two-Stage Reverse Brayton-Claude Helium Cycle

The same analysis was performed for the two-stage reverse Brayton-Claude helium cycle, and the results are shown in Fig. 4. Since this cycle includes a J-T expansion valve, the calculated total mass flow rates of the system to satisfy the required cooling power at a given densification temperature are much higher than those of the two-stage reverse Brayton helium cycle for the same discharge pressure. In addition, available densification temperature ranges, in particular, for liquid oxygen are too low; thus, oxygen may be frozen or frosted in the heat exchanger. The same analyses were performed for higher and lower compressor discharge pressures, total mass flow rates, and mass flow fractions. In spite of intensive efforts to obtain better densification temperature ranges and operating conditions, this configuration seems to be inappropriate for this specific propellant densifier application.

Two-Stage Reverse Brayton-Claude Hydrogen Cycle

As in the previous analysis, real properties of hydrogen[4] are incorporated into the reverse Brayton-Claude hydrogen cycle analysis. First, various ranges of compressor discharge pressures were explored to obtain appropriate operating conditions that satisfy specific cooling requirements. Figure 5 shows that it is difficult for this hydrogen cycle to find the densification temperatures within a reasonable range. Again, the main reason for these imbalances is associated with the assumption that the ratio of cooling requirements associated with the ratio of mass flow rates of densified propellants (hydrogen:oxygen = 1:6) at each densification temperature are fixed. Also, the system efficiency becomes much lower than that of a two-stage reverse Brayton helium cycle because of the higher pressure ratio for J-T expansion. In addition, using hydrogen to cool oxygen in a heat exchanger has safety issues and may not be allowed at a launch site.

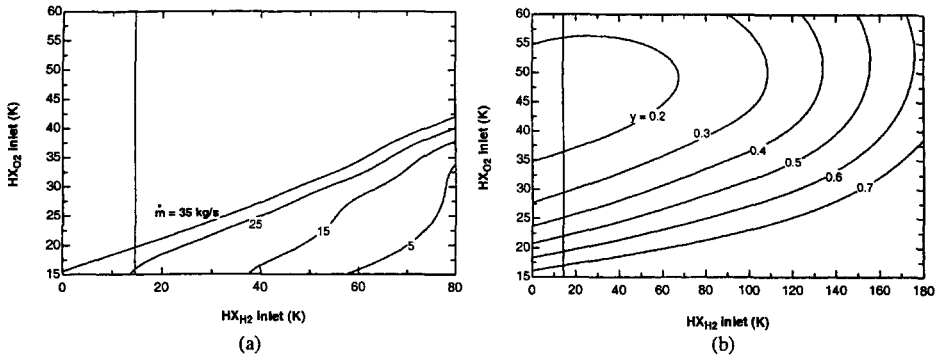

Figure 4. Selected analysis results of the two-stage reverse Brayton-Claude helium cycle. ($P_{discharge}$ = 2020 kPa, $P_{suction}$ = 101 kPa, heat exchanger effectiveness = 0.95, expander efficiency = 0.8)

From the thermodynamic analysis for the three two-stage refrigeration configurations, one of the best candidates for the cryogenic propellants densifier application seems to be the two-stage reverse Brayton helium cycle. This configuration has many attractive advantages. For instance, it uses helium as the working fluid, which is one of the most common fluids in the cryogenic engineering industry. It consists of heat exchangers, a helium compressor, and expanders; thus, all these system components are commercially available. This configuration can be dedicated to both propellants or to one of them independently. The cooling temperature and cooling power can be controlled by the operating pressure, the total mass flow rate and the mass flow fraction through the 1st expander. In addition, this cycle has proven to be scalable from the range of a few watts—for example, for the Hubble's Near Infrared Camera and Multi-Object Spectrometer (NICMOS) cooler—to a few kilowatts for particle accelerators, to many megawatts for large hydrogen liquefiers. In general, efficiency increases with increased capacity of the refrigerator due to increases in cycle complexity and greater efficiency in physically larger compressors and turbines. A useful rule of thumb to estimate the power required for hydrogen liquefiers is a simplified assumption of 2 kWh/100 scf for midsized units[5], so 834 kW of cooling power would be required for liquefaction of 1 million scf/day of hydrogen. This rate of hydrogen production is available via methane reformers in skid mounted systems, and an efficient liquefier to handle this capacity may have a market demand as hydrogen power becomes widely accepted. For this reason, this configuration might be a very promising design concept for other liquid hydrogen applications such as liquid hydrogen stationary storage facility for hydrogen fuel infrastructure development.

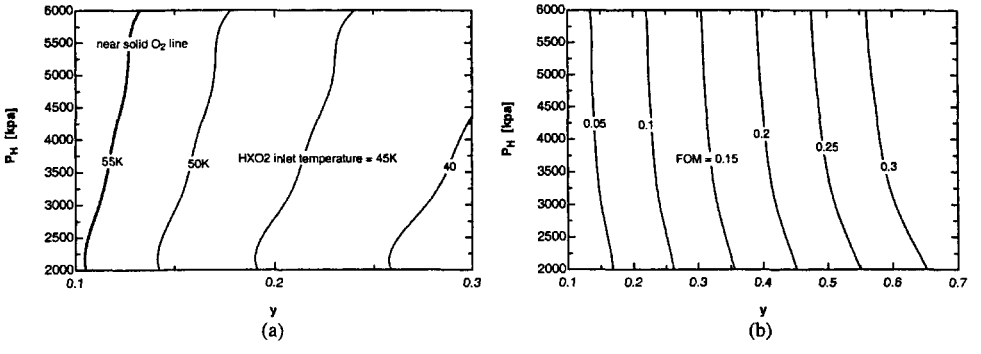

Figure 5. Selected analysis results of two-stage reverse Brayton-Claude hydrogen cycle. (P_H : compressor discharge pressure, heat exchanger effectiveness=0.95, expander efficiency=0.8)

Table 1. Comparison of thermodynamic performances between selected two single-stage cycles and one two-stage cycle.

Propellant	System	Power required	FOM
Hydrogen (1kg/s, 48kW@ 15K)	TVS+Claude cycle	1408 kW	0.648 (COP_{ideal}= 0.053)
Oxygen (6kg/s, 268kW@ 65K)	TVS+Claude cycle	1698 kW	0.571 (COP_{ideal}= 0.277)
Total	Two single-stage cycles	3106 kW	
Hydrogen(1kg/s)+Oxygen(6kg/s)	One two-stage reverse Brayton helium cycle	3990 kW	~0.54

This cycle is also a candidate for a combined hydrogen and oxygen liquefier for use on the surface of the moon or Mars, if a water source is found. One of the main concerns in realizing this concept would be obtaining appropriate expanders that provide specific cooling requirements.

COMPARISON WITH SINGLE-STAGE COOLERS

In the previous section, three two-stage systems were examined to suggest an appropriate cooling system for cryogenic densified propellants. In the recent report by authors[2], similar thermodynamic analyses were performed for various single-stage coolers for the same application. Now, it becomes interesting to compare their performance with that of two single-stage coolers for the same cooling requirements and densification temperatures. The detailed system configurations for various single-stage coolers can be found in the reference[2], and the final analysis results are discussed in this paper. Table 1 shows a comparison of the thermodynamic performance of the two single-stage cycles with that of one two-stage reverse Brayton helium cycle. In the analysis of the single-stage cycle, the same required cooling power and densification temperature are used. For both hydrogen and oxygen densification, a combination of thermodynamic venting system (TVS) and Claude cycle produces the best performance among selected single-stage systems. The total power required to operate independent hydrogen and oxygen systems becomes about 3 MW to densify 1 kg/s of liquid hydrogen and 6 kg/s of liquid oxygen. This value is comparable with the power required to operate the two-stage reverse Brayton cycle. For the same cooling requirements, the two-stage reverse Brayton helium cycle needs about 4 MW of work input and the overall system efficiency is about 54% of Carnot COP. Even if the two-stage cycle shows a slightly lower thermodynamic performance, it has considerable advantages over the combination of TVS and Claude cycle in reality regarding system reliability and potential safety concerns as listed in Table 2.

Table 2. System characteristics comparison.

Two single-stage TVS + Claude systems	One two-stage reverse Brayton helium system
• Two H_2 and N_2 compressors for main cycles	• One He compressor for main cycle
• Additional gas compressors for TVS are required	• No gas compressor for TVS is needed
• J-T expansion valve : potential clogging	• Gas expanders
• H_2 is used in main cycle	• H_2 is used in densification heat exchanger
• Liquid-to-liquid heat transfer in densification	• Gas-to-liquid heat transfer in densification

CONCLUSIONS

A two-stage hybrid refrigeration system is suggested to provide the most efficient, reliable and economic densification system for launch vehicle applications. A variety of hybrid systems, combining recuperative heat exchangers, expander and J-T expansion valve were examined by a rigorous thermodynamic analysis. In the analysis, three hybrid systems were selected based on their essential features and practical considerations to demonstrate system feasibilities. Thermodynamic cycle simulations using real fluid properties were performed for two-stage reverse Brayton helium system, two-stage reverse Brayton-Claude helium system and two-stage reverse Brayton-Claude hydrogen system. As a result, it is concluded that the two-stage reverse Brayton helium refrigeration system shows a very suitable possibility for the cryogenic propellant densification technology, and its feasibility in practical should be proved by a physical demonstration.

ACKNOWLEDGMENT

This work was funded by the NASA Glenn Research Center through NASA Hydrogen Research at Florida Universities Program administered by the Florida Solar Energy Center.

REFERENCES

1. Tomsik, T.M., "Recent Advances and Applications in Cryogenic Propellant Densification Technology," NASA TM 209941 (2000).
2. Baik, J.H. and Raissi, A-T., "R&D process for increasing density of cryogenic propellants at FSEC," *Cryogenics*, Vol. 44, Issue: 6-8, June-August, 2004, pp. 451-458.
3. McCarty, R.D. and Arp, V.D., "A New Wide Range Equation of State for Helium", *Advances in Cryogenic Engineering*, Vol. 35, Plenum Press, New York (1990), pp. 1465-1475.
4. McCarty, R.D., *Hydrogen, Technological Survey-Thermophysical Properties*, NASA SP-3089 (1975).
5. Evans, J., "The Economics of Small to Medium Liquid Hydrogen Facilities," *Cryogas International*, May 2003 (2003).

Proceedings Index

This book draws upon papers presented at the 13th International Cryocooler Conference, held in New Orleans, Louisiana on March 29 - April 1, 2004.. Although this is the thirteenth meeting of the conference, which has met every two years since 1980, the authors' works have only been available in hardcover book form since 1994; this book is thus the sixth hardcover volume. Prior to 1994, proceedings of the ICC were published as informal reports by the particular government organization sponsoring the conference—typically a different organization for each conference. Most of the previous proceedings were printed in limited quantity and are out of print at this time.

For those attempting to locate references to earlier conference proceedings, the following is a listing of the twelve previous proceedings of the International Cryocooler Conference.

1) *Refrigeration for Cryogenic Sensors and Electronic Systems*, Proceedings of a Conference held at the Nat'l Bureau of Standards, Boulder, CO, October 6-7, 1980, NBS Special Publication 607, Ed. by J.E. Zimmerman, D.B. Sullivan, and S.E. McCarthy, National Bureau of Standards, Boulder, CO, 1981.

2) *Refrigeration for Cryogenic Sensors*, Proceedings of the Second Biennial Conference on Refrigeration for Cryogenic Sensors and Electronics Systems held at NASA Goddard Space Flight Center, Greenbelt, MD, December 7-8, 1982, NASA Conference Publication 2287, Ed. by M. Gasser, NASA Goddard Space Flight Center, Greenbelt, MD, 1983.

3) *Proceedings of the Third Cryocooler Conference*, National Bureau of Standards, Boulder, CO, September 17-18, 1984, NBS Special Publication 698, Ed. by R. Radebaugh, B. Louie, and S. McCarthy, National Bureau of Standards, Boulder, CO, 1985.

4) *Proceedings of the Fourth International Cryocoolers Conference*, Easton, MD, September 25-26, 1986, Ed. by G. Green, G. Patton, and M. Knox, David Taylor Naval Ship Research and Development Center, Annapolis, MD, 1987.

5) *Proceedings of the International Cryocooler Conference*, Monterey, CA, August 18-19, 1988, Conference Chaired by P. Lindquist, AFWAL/FDSG, Wright-Patterson AFB, OH.

6) *Proceedings of the 6th International Cryocooler Conference*, Vols. 1-2, Plymouth, MA, October 25-26, 1990, David Taylor Research Center Report DTRC-91/001-002, Ed. by G. Green and M. Knox, Bethesda, MD, 1991.

7) *7th International Cryocooler Conference Proceedings*, Vols. 1-4, Santa Fe, NM, November 17-19, 1992, Air Force Phillips Laboratory Report PL-CP-93-1001, Kirtland Air Force Base, NM, 1993.

8) *Cryocoolers 8*, proceedings of the 8th ICC held in Vail, Colorado, June 28-30, 1994, Ed. by R.G. Ross, Jr., Plenum Press, New York, 1995.

9) *Cryocoolers 9*, proceedings of the 9th ICC held in Waterville Valley, New Hampshire, June 25-27, 1996, Ed. by R.G. Ross, Jr., Plenum Press, New York, 1997.

10) *Cryocoolers 10*, proceedings of the 10th ICC held in Monterey, California, May 26-28, 1998, Ed. by R.G. Ross, Jr., Kluwer Academic/Plenum Publishers, New York, 1999.

11) *Cryocoolers 11*, proceedings of the 11th ICC held in Keystone, Colorado, June 20-22, 2000, Ed. by R.G. Ross, Jr., Kluwer Academic/Plenum Publishers, New York, 2001.

12) *Cryocoolers 12*, proceedings of the 12th ICC held in Cambridge, Massachusetts, on June 18-20, 2002, Ed. by R.G. Ross, Jr., Kluwer Academic/Plenum Publishers, New York, 2003.

Author Index

Subject Index